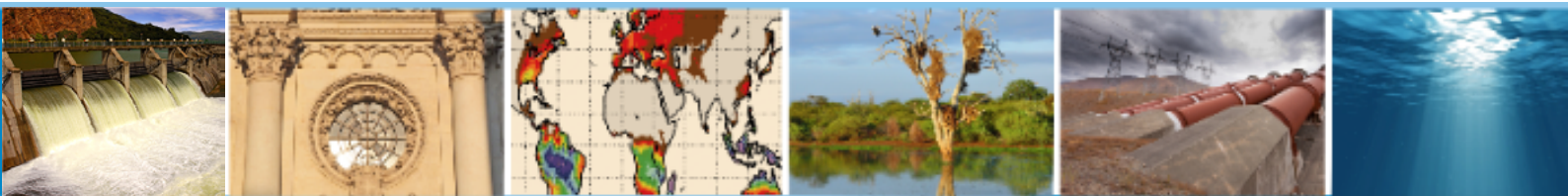


PROCEEDINGS



Climate change and its implications on ecosystem and society

Società Italiana per
le Scienze del Clima
SISC
First Annual Conference
Lecce, 23-24/09/2013

Partners:



In collaborazione con:



Con il patrocinio di:



PROCEEDINGS

Climate change
and its implications on
ecosystem and society

First Annual Conference

Lecce, 23-24/09/2013



More information on the Italian Society for the Climate Sciences - SISC
is available on the Internet: <http://www.sisclima.it>

ISBN 978 – 88 – 97666 – 08 – 0

© Società Italiana per le Scienze del Clima

Lecce, Italy - September 2013

CONTENTS

Introduction by Antonio Navarra	xi
Foreword by Donatella Spano	xii
SISC - A short description	xiii
Scientific Committee	xiv
Organizing Committee	xv
SISC First Annual Conference	xvi
ADVANCES IN CLIMATE SCIENCE	1
Modes of variability in the Pacific Ocean	2
ENSO Formation over the Equatorial Ocean	3
Intrinsic climate variability paced by external forcing: the Kuroshio Extension bimodality - North Pacific Oscillation case	11
Climatic trends of the equatorial undercurrent: A backup mechanism for sustaining the equatorial Pacific production	19
ENSO and Pacific Decadal Oscillation: decadal variability driven by tropical-extratropical interactions	30
Regional climate modelling and downscaling	40
A statistical downscaling system for seasonal projections using ensemble neural networks with Bayesian regularization	41
Multimodel SuperEnsemble Downscaling of Regional Climate Models in South-Western Alps	57
Implementation and validation of a precipitation downscaling chain for regional climate modelling	71
Performance evaluation of COSMO-CLM over Italy and climate projections for the XXI century	78
Variability and uncertainties using CMIP5 models	90
A data-driven causality analysis for the attribution of recent global warming	91
Reliability and skill of CMIP5 multi-model decadal hindcasts	102
Snow depth in the “Third Pole”: how do CMIP5 models represent it?	110

Heavy precipitation events over the Euro-Mediterranean region in a warmer climate: results from CMIP5 models	119
Modes of variability in the atmosphere and ocean	130
Effects of the North Atlantic Oscillation on winter precipitation in the Hindu-Kush Karakoram	131
Atmospheric blocking and Euro-Atlantic winter Mid-latitude climate variability	138
The temporal variability and associated spectral features of transient-eddy meridional heat transport	152
The Antarctic Circumpolar Wave scenario described as a combination of interannual signals	167
Climate processes in the Mediterranean region - I	183
Future storm surge distribution along the Mediterranean coast	184
Tropical-like cyclones in the Mediterranean sea: from the case study over Salento to a combined satellite-modelling approach	193
Sicily monthly high-resolution solar radiation climatologies	198
Reconstruction of long time series of monthly temperature values by statistical methods: an application to Europe and the Mediterranean region	210
Climate processes in the Mediterranean region - II	221
Daily precipitation statistics over the Po Basin: observation and post-processed RCM results	222
Climatological characterisation of the Ora del Garda wind in the Alps	235
Continuous measurements of climate altering halogenated gases at the Italian Climate Observatory O. Vittori	250
The myth of Scylla and Charybdis: a torrent in the Messina Strait	256
Poster Session	262
Intrinsic variability of the Antarctic Circumpolar Current: low-frequency fluctuations in the Argentine Basin flow	263
GNSS Analysis for Meteorological Applications and Climate Monitoring in the Mediterranean Area	271
Study of aerosol - water vapor - clouds interaction at CNR-IMAA Atmospheric Observatory	279
ACTRIS for coordinated long-term observation of aerosols, cloud-aerosol interactions, and trace gases in Europe	284
Space-borne measurements of carbon dioxide distribution: inverse modelling and data fusion techniques	291
Time Series Analyses of Climatological Records from a High Altitude Observatory in Southern Italy	303

Recent trends in daily temperature extremes over the Basilicata Region, Southern Italy (1951 – 2010)	328
Observed long term trend and low-frequency variability of spring discharge timing in the main Alpine rivers	339
Long term atmosphere-surface transfer studies in Salento Peninsula: a database	340
Statistical modelling of sequences of no rainy days	349
Mesoscale biological-physical interactions in the Sardinian Sea	361
Is global warming causing mass mortalities in the Mediterranean Sea upper layer?	382
High resolution coastal monitoring during the sea breeze event	388
Relationship between sahel rainfall and Mediterranean summer climate	410
Multivariate analysis for the influence of climate change on maritime structures design	419
IMPLICATIONS ON ECOSYSTEM SERVICES	426
Dynamic landscapes: hazard & risk assessment - I	427
An European HPC Infrastructure and the Climate Challenges	428
Exploring synergies for disaster risk reduction in Guatemala: the use of cognitive maps	440
Syndromes of Land Degradation and Implications for Ecosystem Services in Emilia-Romagna, Italy. An evaluation framework for the past and in face of a changing climate	461
Assessing environmental impacts of climate change at the regional scale to provide adaptation services: the Decision support System for Coastal climate change impact assessment	468
Dynamic landscapes: hazard & risk assessment - II	476
Towards flood risk assessment in a climate change perspective	477
A risk-based assessment of impacts affecting groundwater resources and related ecosystems in view of climate change	485
Climate change scenarios of minimum, maximum temperature and precipitation over Italian areas, period 2021-2050	496
Preliminary assessment of the effects of climate change on landslide activity of Orvieto clayey slope	507
Impacts on natural ecosystems - I	523
Distribution of bioclimate zones and their shifting due to climate change	524
Influence on population density and climate on the dynamics of the black grouse (<i>Tetrao tetrix</i>) populations in the Piedmont region (Italy)	542

Response to climate change of alpine glaciers in north-western Italian Alps	555
Has the ocean contributed to the decline of European eel recruitment? Results of a 40-year simulation experiment	566
Impacts on natural ecosystems - II	577
Climate Change Impacts on Distribution and Composition of the Alpine Natural Pasturelands	578
Larval Connectivity in the Central Pacific Ocean: Lagrangian simulations in the Northern Line Islands	587
The effects of climate change on cuatro cienegas aquatic ecosystem in the desert environment of northern Mexico	599
Impacts on forest and agricultural ecosystems - I	610
The impact of selective logging on Forest structure, Plant Diversity and above-ground biomass of African tropical forests	611
Assessing the resilience of Mediterranean trees diversity to climate change projections	624
Projected climate change impacts on staple crops in Nigeria	637
Evaluation of the potential of genomic tools and plant genes to mitigate the climate change impact and extremes on natural ecosystems and agriculture	650
Impacts on forest and agricultural ecosystems - II	669
Local impact assessment of climate change on fire season length	670
Analyzing changes in wildfire likelihood and intensity in Mediterranean areas: a case study from central Sardinia, Italy	685
Skill assessment of the global model EC-Earth in fire danger indices evaluation over the Greater Alpine Region: a comparison with the corresponding ERA-Interim Reanalysis parameters	707
Historical Trends and Future Predictions of Fire Emission Estimation in Italy	720
Poster Session	737
Assessing environmental impacts of climate change at the regional scale to provide adaptation services: the Decision support System for Coastal climate change impact assessment	468
Fluctuation in spatial patterns in semi-arid ecosystems under pressure	738
Application of the 3D-CMCC FEM (Three Dimension Forest Ecosystem Model) on multi-temporal NDVI satellite imagery and future scenarios	741
Are Cereals in Globally Trouble?	756
Assessing future land suitability of winter wheat crop	773
Water scarcity, climate change, and food security: challenges for the future	793
An analysis of the fire danger regime in Italy	808
A modelling framework to estimate CO ₂ fluxes under urban development scenarios	819

CLIMATE POLICY AND ECONOMIC ASSESSMENT	833
Economic analysis of climate change impacts: methods and approaches	834
Probabilistic economic impacts of climate change in an integrated assessment model framework	835
A Ricardian Analysis of the Impact of Climate Change on European Agriculture	845
Chaos in, chaos out: the effect of deterministic chaos in GCM scenarios on estimates of climate change impacts	848
Strategies for adaptation and mitigation policies - I	851
Putting climate change adaptation into action: an operational approach to implement the European Guidelines on developing adaptation strategies	852
The dynamic feedback of climate change impacts and catastrophic risk on mitigation and adaptation investments	863
Is Geoengineering a viable option for dealing with climate change?	891
Insurance and climate change adaptation: field experiments in Chilika Lagoon, India	898
Strategies for adaptation and mitigation policies - II	914
Guidelines for the implementation of the Regional Adaptation Strategy in Lombardy (RAS)	915
Beyond stationarity in planning renewables: The CLIM-RUN experience for the Euro-Mediterranean region	930
Eni's approach to mitigation and adaptation	935
Climatic change impacts on energy sectors over Italian region	944
Air quality and climate change mitigation policies	949
Including air pollutants' emissions in integrated assessment climate change modelling	950
Synergies and trade-offs between climate change mitigation strategies and air quality policies: the case of wood burning in domestic appliances	961
Ancillary benefits of climate change policy in China: air pollution impacts on household health, adaptation and government-controlled information in Beijing	974
Climate change and urbanization: implications, feedback and evaluation of strategies	997
Integrating the human dimension in ecosystem based adaptation to global changes	998
Vulnerability of Paris metropolitan area to future heat waves	1008
The role of climatic variability on cholera spreading in Bangladesh	1016
Albedo Modifications as Global Mitigation and Local Adaptation Strategy in European Cities: a geographically explicit investigation	1028

Economic assessment of climate change impacts	1041
An indicator-based assessment of vulnerability to climate change in Italian coastal cities	1042
Climate change, smoothing with water stock and impact on the agricultural sector in the Po valley (Italy)	1057
The economics of tropical cyclones under climate change: incorporating the impact of global hurricane characteristics and level of development	1076
Poster Session	1095
The Cost of Climate Change Inaction in the EU. A CGE Approach	1096
The informative role of farmers' perceptions of change for the development of robust climate change adaptation policies - a case study from Italy	1125
Evaluation of flood disaster risk in the Polesine sub-region	1126
 AUTHOR INDEX	 1147

INTRODUCTION



This book is a collection of the contributions presented at the First Annual Conference of the Italian Society for Climate Sciences. It has been created with the ambitious hope to testify the vast interdisciplinary character of climate change, which contributes in making climate research one of the most intriguing and important challenges of our time and of the near future for both the Italian and international scientific communities.

A single volume, in fact, includes contributions that address the issue of climate change and their implications on ecosystem services and society, proposing perspectives from various disciplines and converging them into a single integrated and interdisciplinary viewpoint on climate research.

In the following pages, authors from different backgrounds, agencies and institutions, offer useful information regarding state-of-the-art climate change research, our current ability to know and understand climate variability, and our ability to carry out projections and forecasts on climate change and their impacts.

At the same time, the research contained in this volume is evidence of an interdisciplinary research that is capable of sharing research methods, strategies, and knowledge. This book, therefore presents a possible way to achieve a common commitment to the analysis and the study of issues related to the climate and its changes.

While society, policy makers, and the public look to the scientific community in search of accurate, rigorous and current scientific information, the works collected in this book testify that climate research requires a greater joint effort in creating a common language that is capable of networking disciplines. Until now, these disciplines have been accustomed to working separately, divided by barriers created in the nineteenth century, which today, is not the only way to organize our knowledge.

This book represents a first step in the search of this new language and of a new spirit of interdisciplinary interaction, which is one of the main aims that motivate the Italian Society for Climate Sciences.

Antonio Navarra, SISC President

Co-chair Scientific Committee SISC First Annual Conference

A handwritten signature in black ink, which appears to read 'Antonio Navarra'.

FOREWORD



It is a great privilege to present the proceedings of the First Annual Conference of the Italian Society for Climate Sciences (SISC). The proceedings collect the papers presented during the Conference held in Lecce (Italy) from the 23rd to the 24th of September 2013.

The mission of SISC includes the concept of promoting the convergence of disciplines and multidisciplinary research. This concept stems from the awareness that combining the knowledge of different disciplines is essential for understanding all aspects of climate change and for a comprehensive analysis of its implications on society. We are aware that there is still much uncertainty about future climate, and we are also aware that progress in climate science requires innovative research based on the continuous exchange of information between various sectors of human knowledge.

Therefore, the aim of the first Annual SISC Conference has been to bring together scientists from different branches of knowledge in climate related science, as well as to foster scientific dialogue on policy making and strategies regarding adaptation, mitigation and sustainable growth.

The high quality of papers presented at the Conference represents the knowledge and experience of women and men who are actively working in the advancement of our understanding of climate sciences.

These papers range from atmospheric studies to forestry and agricultural sciences, from water resources management to public health, urbanization, and socio-economic studies. Given the importance of rapid environmental and climate changes, part of the Conference was dedicated to the discussion on the advancements of theories, observations, and models of atmospheric and oceanic fluid dynamics. Another session explored and discussed the implications of such dynamics on ecosystem services, by analyzing, projecting, and evaluating the climate change impact and extremes on hydrogeological systems, natural ecosystems, and agriculture. In addition, the Conference included presentations and debates on the translation of the interactions between climate and the processes concerning ecosystems into economic values.

The first Annual SISC Conference has been successful in attracting Italian and foreign experts of different disciplines under a unique umbrella that strives to effectively address the advancement of climate sciences and their implications on environmental and socio-economic systems.

We believe that SISC 2013 has been a benchmark in the exchange of ideas, creativity and the advancement of innovative interdisciplinary research, by bringing together such outstanding contributions to the issues of our future climate and the planetary changes driven by human causes. We are confident that these proceedings will provide an interesting contribution for further studies and research in climate science.

Donatella Spano

Co-chair Scientific Committee SISC First Annual Conference

University of Sassari

Euro-Mediterranean Center on Climate Change

Donatella Spano

SISC - A SHORT DESCRIPTION

The **Italian Society for the Climate Sciences (SISC)** was created in 2013 to serve as a meeting point for scientists from different disciplines, who use climate information for their research: from climatologists to physicists and chemists, geographers to agronomists, economists to political scientists, and all scholars that deal with climate-related sciences and their applications.

SISC aims at contributing to scientific progress and innovation of climatic sciences in Italy by promoting the convergence of disciplines and multidisciplinary research.

The institutional purposes of SISC are mainly to

The world of research:

- to foster the exchange of ideas, the creativity and the development of new interdisciplinary research;
- to promote communication and cooperation between universities and research institutions in Italy, strengthening the presence of climatic sciences in both Italian universities as well as higher education systems;
- to attract young talents to build a new interdisciplinary scientific community and increase overall productivity;
- to stimulate and coordinate the Italian contributions to the International programs in the field of climate sciences;
- to become the reference point and the meeting place for Italian scientists living abroad.

The society:

- to increase the impact of the studies and of the debate on climate issues, giving scientific rigour to the analysis of climate policies for mitigation and adaptation;
- to promote the dialogue among scientists, policy makers, businesses and citizens to support actions in the interest of the society and the environment;
- to provide research results to institutions, businesses and citizens.

SISC's aims are pursued in particular through:

- the organization of conferences and debates addressed to the scientific and policy communities;
- the implementation of web-communications;
- the promotion of training courses for young graduates;
- collaboration with multidisciplinary doctoral courses on climate sciences.

The SISC association is non-profit and non-advocacy, acts according to ethical principles and promotes policies for equal opportunities.

GOVERNANCE

Antonio Navarra – *President*

Carlo Carraro - *Vice-President*

Simona Masina – *Ordinary Member of the Executive Board*

Donatella Spano – *Ordinary Member of the Executive Board*

Riccardo Valentini – *Ordinary Member of the Executive Board*

Martina Marian – *Secretary General / Ordinary Member of the Executive Board*

SCIENTIFIC COMMITTEE

The Scientific Committee of the SISC First Annual Conference is composed by 20 experts and scientists from climate research areas. They reviewed all the papers received and selected those works accepted at the Conference, and then published in this volume.

Members of the SISC First Annual Conference Scientific Committee are:

Antonio Navarra (co-chair), Euro-Mediterranean Center on Climate Change

Donatella Spano (co-chair), Università di Sassari / Euro-Mediterranean Center on Climate Change

Anna Alberini, University of Maryland

Vincenzo Artale, ENEA

Sveva Avveduto, Istituto di Ricerche sulla Popolazione e le Politiche Sociali – CNR

Alberto Basset, Università del Salento

Anthony Bigio, George Washington University

Antonietta Capotondi, NOAA/ESRL/PSD and CIRES Climate Diagnostic Center

Carlo Carraro, Università Ca' Foscari di Venezia / Euro-Mediterranean Center on Climate Change

Raffaello Cervigni, World Bank

Marzio Galeotti, Università degli Studi di Milano

Paolo Gasparini, AMRA S.c. a r.l.

Piero Lionello, Università del Salento / Euro-Mediterranean Center on Climate Change

Simona Masina, Euro-Mediterranean Center on Climate Change

Claudia Pasquero, Università di Milano–Bicocca

Antonello Provenzale, Istituto di Scienze dell'Atmosfera e del Clima – CNR

Paolo Ruti, ENEA Centro Ricerche Casaccia

Cristina Sabbioni, Istituto di Scienze dell'Atmosfera e del Clima – CNR

Francesco Tubiello, FAO

Riccardo Valentini, Università degli Studi della Tuscia/ Euro-Mediterranean Center on Climate Change

ORGANIZING COMMITTEE

Donatella Spano (co-chair)

Università di Sassari / Euro-Mediterranean Center on Climate Change (CMCC), IAFENT Division

Simona Masina (co-chair)

Euro-Mediterranean Center on Climate Change (CMCC), ANS Division

Valentina Bosetti

Fondazione Eni Enrico Mattei (FEEM)/ Euro-Mediterranean Center on Climate Change (CMCC), CIP Division/ Bocconi University

Martina Marian

Fondazione Eni Enrico Mattei (FEEM)/ Euro-Mediterranean Center on Climate Change (CMCC), CIP Division

Valentina Bacciu

Università di Sassari / Euro-Mediterranean Center on Climate Change (CMCC), IAFENT Division

Mauro Buonocore

Euro-Mediterranean Center on Climate Change (CMCC), Communication Office

Alessandra Mazzai

Fondazione Eni Enrico Mattei (FEEM)/ Euro-Mediterranean Center on Climate Change (CMCC), CIP Division

Organizing Secretary - sisc.conference@sisclima.it

Mauro Buonocore

Euro-Mediterranean Center on Climate Change (CMCC), Communication Office

Gavriil Kyriakakis

Euro-Mediterranean Center on Climate Change (CMCC), IAFENT Division

Lucia Luperto

Euro-Mediterranean Center on Climate Change (CMCC), Communication Office

Manuela Santagata,

Euro-Mediterranean Center on Climate Change (CMCC), Communication Office

SISC First Annual Conference

The **First Annual Conference of the Italian Society for Climate Sciences** is entitled *Climate change and its implications on ecosystem services and society* and aims to involve scientists, researchers, policy makers, Italians and foreigners working in close contact with our country, whose activities closely affect aspects of climate change and their relationships on environmental and socio-economic systems.

The Conference aims to create and promote an interdisciplinary platform for discussion on climate systems and their interactions with the environment and the society. It also aims to promote a constructive and interdisciplinary dialogue between scientists, policy makers, service providers and the general public. At the Conference, scientists explore and model physical-chemical-biological-societal-economic responses to climate change through the most advanced techniques available and participants foster scientific dialogue on policy making and strategies regarding adaptation, mitigation, and sustainable growth.

The scientific presentations at the First Annual SISC Conference are divided into three parallel sessions.

The **“Advances in climate science”** session holds presentations of papers about theories, observations, and models of the dynamics of atmospheric and oceanic fluids. In particular, themes related to climate and environmental changes, forecasts and projections, mesoscale processes, and extreme events are explored and discussed.

Papers presented under the **“Implications on ecosystem services”** session address analysis, projections, models and the evaluation of climate change impact and extreme events on natural ecosystems and agriculture. This session also addresses changes in land-use and land-cover, also due to extreme hydrological events, as well as adaptation and mitigation strategies for hydrological and hydrogeological risks and water resource management.

The **“Climate policy and economic assessments”** session covers studies that translate the interactions between climate and the processes concerning ecosystems into economic values. Strategies for adaptation and mitigation policies are assessed, as well as the impacts of climate extremes and climate change on public health. Additionally, the theme of climate change and urbanization, including implications, feedback, and the evaluation of strategies and of public choices is addressed.

ADVANCES IN CLIMATE SCIENCE

ADVANCES IN CLIMATE SCIENCE

Modes of variability in the Pacific Ocean

ENSO Formation over the Equatorial Ocean

Miyakoda K.¹, Navarra A.², Masina S.², Cherchi A.², Ploshay J.³

¹Princeton University - USA,

²CMCC Bologna - Italy,

³GFDL, NOAA, Princeton NJ - USA

*Corresponding author: kikuro.miyakoda@noaa.gov

Abstract

The ENSO (El Niño-Southern Oscillation) extends horizontally over the equatorial Pacific and the equatorial Indian Oceans. Based on more than 10 cases of El Niño, it is noted that a substantial change took place around 1975, it is associated with the large change in the amount of condensation. In the cases of El Niño, a strong eastward current starts at 200~300 m depth in the eastern Indian Ocean, by a trigger of the Madden-Julian Oscillation in the atmosphere. This ocean current of ENSO spreads eastward as well as upward to a wide range of depth in the Pacific sector. The strong intensities of the surface currents over the Pacific are particularly concentrated near the equator. On the other hand, in the negative ENSO (*i.e.* La Niña), the opposite direction of currents prevail, which are initiated by the counter El Niño activities over the Pacific; the strong westward current is induced over the Indian Ocean.

Keywords: ENSO, Madden-Julian Oscillation, Equatorial Ocean, Indo-Pacific Ocean, El Niño



1. INTRODUCTION

In Miyakoda et al. (2012) (hereafter referred to as MNB12), the El Niño - Southern Oscillation (ENSO) process was discussed from the standpoint of the atmosphere. One of the main conclusions is that the ENSO in the atmosphere is formed over the Indian-Pacific sectors (instead of only the Pacific sector) with the width of $20^{\circ}\text{N}\sim 20^{\circ}\text{S}$ in meridian, and that the process is characterized as the biennial oscillation in the tropics. Besides, ENSO is basically an air-sea coupled phenomenon, and, therefore, in order to simulate or forecast it, the incorporation of the upper ocean in circulation models (GCM-General Circulation Models) is definitely required.

The domain of ENSO extends from the Indian Ocean to the Pacific Ocean with the Maritime Continent in the middle. Both lateral ends are bounded by sufficiently high mountains at Africa and Central America. On the other hand, the mountains in the middle, i.e., the Maritime Continent, are not so high, and therefore, the special westerly, i.e., the Madden-Julian Oscillation (MJO) in the atmosphere, can go through two areas (see Madden and Julian, 1994). This statement is rephrased as follows. What is the condition necessary for the ENSO activities to start over the Indian Ocean, to go through the Maritime Continent, and to develop into a substantial strength of El Niño over the Pacific Ocean?

The major issue of this paper is to analyze the results of ocean and atmosphere data assimilation, which has been obtained by the assimilation scheme of Masina et al. (2004). The main question is how the ENSO activities are initiated and organized within the frame-work of air-sea interaction. A specific question is how the atmospheric ENSO effects go through the half blocked area, i.e., the Indonesian archipelago. The existing observation suggests that the major ENSO effect first goes down to the depth of about 100 ~400 meter in the equatorial Indian Ocean, the effect then emerges at the surface of the Pacific Ocean, and the most substantial effect appears between the surface and 500 m depth in the Atlantic Ocean (Levitus et al., 2000, 2001 and 2009).

Another outstanding event is the 1976 transition of the atmospheric and oceanic state (for example, Zhang et al., 1997). The rainfall is increased rather suddenly after that year, particularly in the equatorial belt. The anomalous warmth of the atmosphere has started to cover many parts of the world. Although this change has been noticed to be more gradual for the atmospheric temperature, it is fairly sudden for the oceanic temperature. According to Kaplan et al. (2000), the 1976 type evolution of the oceanic

temperature occurred only once in the past 100 year history (see Levitus et al., 2000; 2001; Deser et al., 2004; Ishii et al., 2005).

2. PRECIPITATION ASSOCIATED WITH ENSO EVENTS

We use precipitation data from the reanalysis dataset obtained from the data-assimilation of ECMWF (European Centre for a Medium-Range Weather Forecasts). This dataset is most appropriate to describe here (see MNB12).

Fig. 1 shows NDJ mean precipitation anomalies averaged in the tropical Indian-Pacific sector of 20°S-20°N and 80°E-280°E. The number of data assimilated in ERA-40 re-analyses strongly increased from the end of the 1970's, and this may have artificially affected the mean precipitation.. The point of stress here is that the amount of condensation has increased substantially after about 1975.

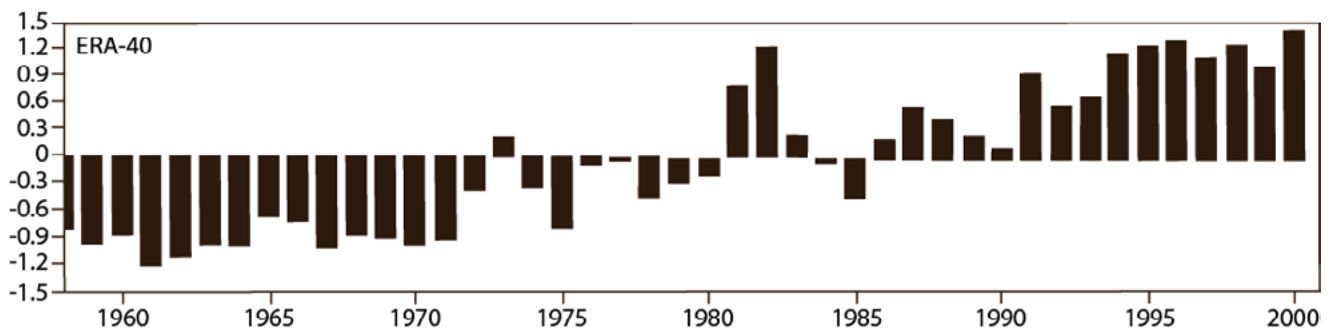


Fig. 1: shows NDJ mean precipitation anomalies (mm day⁻¹) averaged in the tropical Indo-Pacific sector of 20°S-20°N and 80°E-280°E, based on ERA-40 (Kallberg,P. et al, 2005).

Fig. 2 shows the zonal mean NDJ precipitation (mm,day⁻¹) in ERA-40. The difference between before and after 1975 emerges most intensely at the equatorial tropics (9°N~15°S) with more precipitation in the second half.

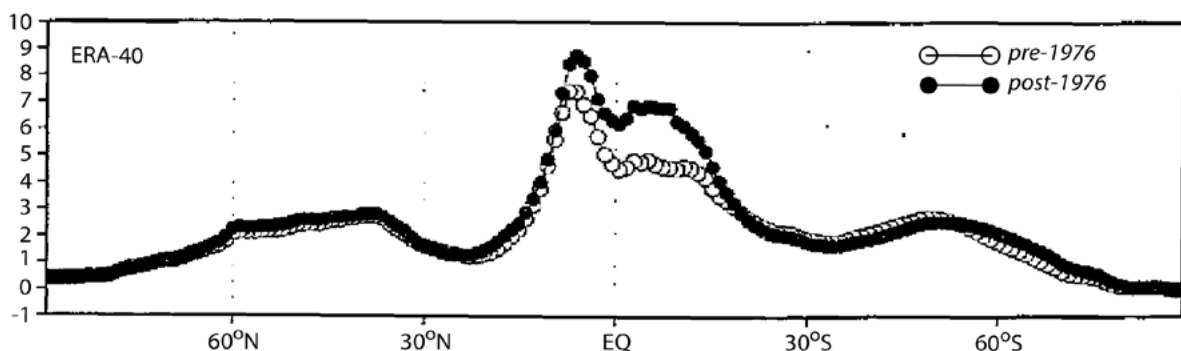


Fig. 2: Zonal mean precipitation (mm day⁻¹) in NDJ by ERA40 dataset, before and after 1976

3. ENSO BIENNIAL OSCILLATION

Summarizing the discussion above together with the description of MNB12, we re-define the basic concepts of ENSO oscillation, which consists of a biennial oscillation. The El Niño/La Niña activities are mainly the equatorial Pacific phenomena, while the oscillation of ENSO takes place over both the Indian Ocean and the Pacific Ocean.

It is amazing to see the center of a strong eastward anomaly-current at the depth of 200~300 m in the Indian Ocean. This anomaly current appears in all cases of El Niño history which are examined in this paper. Fig.3 is a particular example, which is a cartoon based on the El Niño case of Dec. 2006.

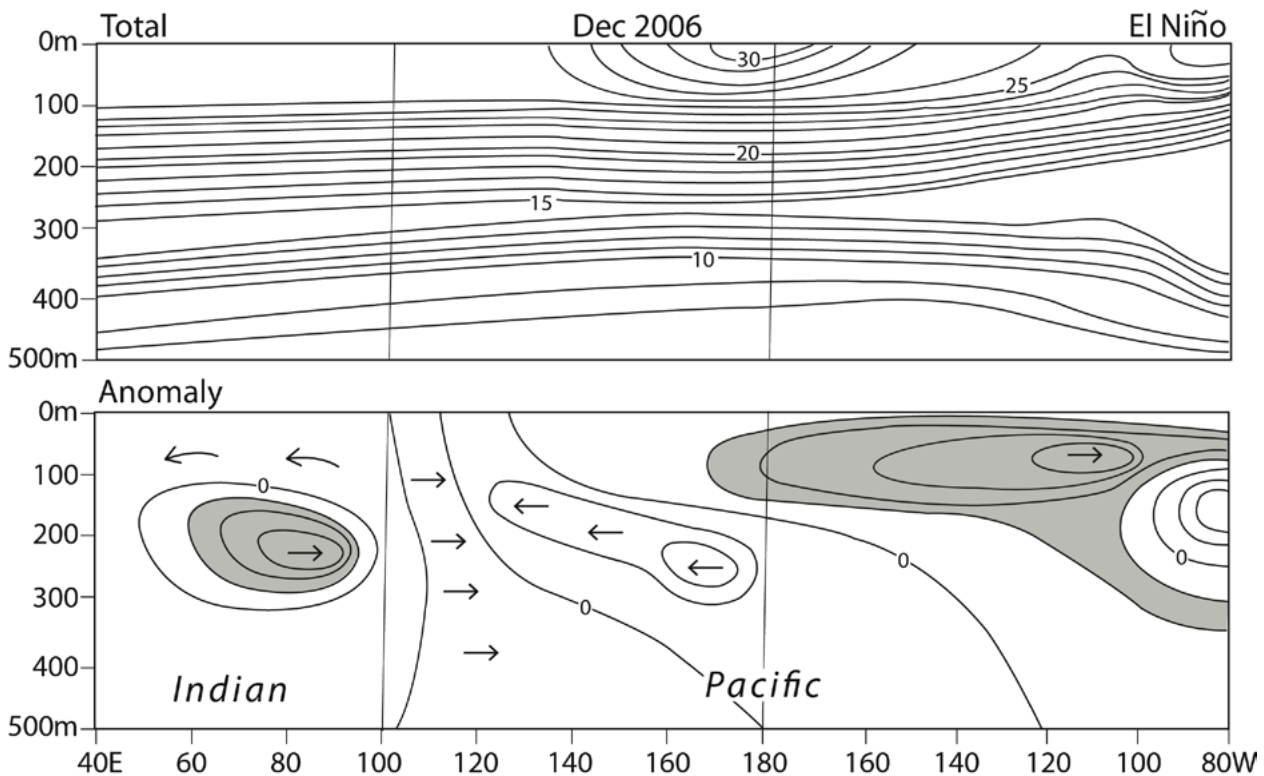


Fig. 3: A schematic picture of the Indo-Pacific ocean temperature at the initiation of the ENSO. The ocean temperature (upper) and the monthly anomaly (lower) in units of $^{\circ}\text{C}$. The arrows indicate the direction of anomaly components. The figure is based on the real data on December, 2006.

The equatorial flow has been studied theoretically for the atmosphere; see Salby et al. (1991) and Salby and Hendon (1994). However, the issue of MJO in the present paper is about the response under the water. The existing theory of MJO has not discussed this situation yet (see, for example, Zavala-Garay et. al, 2005).

The MJO is characterized by coherent eastward propagating atmospheric waves with a period range of 40-50 days, which appears between 10°N and 10°S around the globe (Madden and Julian, 1972; 1994, Waliser et al., 1999; and Zhang 2005).

The MJO is particularly strong over the Indian and western Pacific Oceans with increased rainfall. This atmospheric oscillation transmits itself horizontally along the equator, and at the same time the effect goes down vertically to the depth of 200~300 m in the Indian Ocean. Is there any constraint for the MJO to reach this depth and develop into El Niño? This question has not been investigated. Another question is whether it is possible to predict which year El Niño starts.

As was described so far, the problem consists of two issues, *i.e.*, the MJO and the ENSO. For example, Shinoda et al. (1998), Hendon (2000), and Wheeler and Hendon (2004) have demonstrated the experimental prediction of MJO, based on the “comprehensive mixed layer ocean model”. Huang and Kinter (2002), Guilyardi et al. (2003), and the present paper, try to handle realistic ENSO processes of the atmosphere and the ocean. In particular, Huang and Kinter (2001) describe the ENSO scenario for the first time in history as follows. “A significant zonal shift of the major convection during a large ENSO event can simultaneously cause anomalous equatorial winds over both the Indian and Pacific Ocean, which in turn initiate air-sea feedback processes in these two oceans.”

4. ENSO AND THE GLOBAL WARMING

In MNB12, it was concluded that the amount of rainfall is much larger after 1976 than before 1976, particularly in the equatorial tropics. Is this view applied to the oceanic case? Schopf and Burgman (2006) mentioned that “a simple mechanism that accounts for a change in the decadal scale mean of ocean temperature is the ENSO process”, and presented the SST anomaly record between 150°E and 80°W for 1860 ~ 2000 (see their Fig. 15). The 1976 transition is even clearer in the case of ocean, compared with that of atmosphere. The CMIP3 report (Meehl et al. 2009) also mentions that the transition occurs around 1975 (SST anomalies).

On the other hand, Levitus et al. (2000, 2001 and 2009) investigate the yearly time series of the observed ocean temperature between the surface and 500 m depth of the world ocean, and describe that the turning point between negative and positive value is around 1975.

In particular, according to Levitus et al. (2009), concerning the ocean heat content for the 0~700 m layer, the largest increase after 1976 is seen in the Atlantic, next in the Pacific, and the least is in the Indian Ocean. Ishii et al. (2003) also show (in their Fig. 8) that the temperature anomalies at 162°E-168°E in the depth of 150 m change their amplitude rather suddenly at about 1976 (the latitudes of 1°S-1°N).

5. CONCLUSIONS

The critical break-out of ENSO can be seen first in the ocean temperature anomaly of the Indian ocean centered at 200~300 m depth. The oscillations take place over the Indian and Pacific Oceans dominantly in the months of NDJ (possibly February too). This is true for all 10 cases of ENSO (therefore, of El Niño). The key area is the equatorial belt of 5°N-5°S under the ocean surface of the Indian Ocean. La Niña occurs over the Pacific Ocean some time after El Niño as the counter oscillation.

The El Niño forecasts consists of two steps, *i.e.*, first, the forecast of the impact of MJO over the Indian Ocean, and second, the forecast of the outbreak of El Niño also in the Indian Ocean. On the other hand, the La Niña forecasts consist of only one step, *i.e.*, the forecast of La Niña over the Pacific Ocean.

One of the outstanding characters in the equatorial belt of 5°N-5°S is that most of phenomena are reproducible or predictable, compared with those at the higher latitudes, and also compared with those in the atmosphere.

The second issue is the ENSO and the global warming. A most dramatic thing happened in the ocean and atmosphere around 1976. For the atmosphere, the increase of precipitation started around 1976. For the ocean, the increase in the ocean temperature occurred near the equator, at least, between the surface and 500 m depth, first in the Indian Ocean, secondly in the Pacific Ocean, and thirdly in the Atlantic Ocean, though for the magnitude, the largest is in the Atlantic Ocean, the second is in the Pacific, and the smallest is in the Indian Ocean (see Levitus et al. 2009).

6. REFERENCES

- Hendon H.H., (2000), *Impact of air-sea coupling on the Madden-Julian Oscillation in a general circulation model*. J. Atmos. Sci., 57, 3939-3952.
- Huang B. and Kinter J.L., (2002), *Interannual variability in the tropical Indian Ocean*. J. Geophys. Res., 107, 20-(1-23).
- Ishii M., Kimoto M., and Kachi M., (2003), *Historical ocean subsurface temperature analysis with error estimates*. Mon. Wea. Rev., 131, 51-78.
- Ishii M., Shouji A., Sugimoto S., and Matsumoto T., (2005), *Objective analyses of sea-surface temperature and marine meteorological variables for the 20th century using ICOADS and The Kobe collection*. Int. J. Climatol, 25, 865-879.
- Kallberg P. and Coauthors (2005), *Assimilation and modeling of the atmospheric hydrological cycle in the ECMWF forecasting system*. Bull. Amer. Meteor. Soc, S6, 387-402.
- Kaplan A., Kushnir Y., Cane M.A., (2000), *Reduced space optimal interpolation of historical marine sea level pressure:1854-1992*. J Climate, 13, 2987-3002.
- Larkin N.K. and D.E. Harrison (2001), *Tropical Pacific ENSO cold events, 1946-95: SST, SLP, and surface wind composite anomalies*. J. Climate, 14, 3904-3931.
- Levitus S., Antonov J.I., Boyer T.P., and C. Stephens, (2000), *Warming of the world ocean*. Science, 287, 2225-2229.
- Levitus S. and Coauthors (2001), *Anthropogenic warming of earth's climate system*. Science, 292, 267-270.
- Levitus S. and co-authors (2009), *Global ocean heat content 1955-2008 in light of recently revealed instrumentation problems*. Geophys. Res. Letters, 36, L07608, doi: 10.1029/20089L037155.
- Luther D.S., Harrison D.E., and Knox R.A. (1983), *Zonal winds in the central equatorial Pacific and El Niño*. Science, 222, 327-330.
- Madden R. and Julian P.R. (1972), *Description of global-scale circulation cells in tropics with a 40-50 day period*. J. Atm. Sci., 29, 1109-1123.
- Madden R. and Julian P. R. (1994), *Observations of the 40-50 day tropical oscillation – A review*. Mon. Wea. Rev., 122, 814-837.

- Masina, S., Di Pietro P., and Navarra A., (2004), *Interannual-to-decadal variability of the North Atlantic from an ocean data assimilation system*. *Clim. Dyn.*, 23, 531-540.
- Meehl G.A. and Co-authors (2009), *The WCRP CMIP3 multimodel dataset – A new era in climate change research*. *Bull. Amer. Meteor. Soc.*, 58, 1383-1394.
- Miyakoda, K., Navarra A., Masina S., Cherchi A. and Ploshay J. (2012), *ENSO and condensational heating*. *J. Meteor. Soc. Japan*, 90, 35-57.
- Saaji N.H., Goswami B.N., Vinajachandran P.N., and Yamagata T., (1999), *A dipole mode in the tropical Indian Ocean*. *Nature*, 401, 360-363.
- Salby M.L., Hendon H.H., Woodberry K., and Tanaka K., (1991), *Analysis of global cloud imagery from multiple satellites*. *Bull. Amer. Meteor. Soc.*, 72, 467-480.
- Salby M.L. and Hendon H.H. (1994), *Intraseasonal behavior of clouds, temperature, and motion in the Tropics*. *J. Atmos. Sci.*, 51, 2207-2224.
- Schoff P.S. and Burgman R.J. (2006), *A simple mechanism for ENSO residuals and asymmetry*. *J. Clim.*, 19, 3167-3179.
- Shinoda T., Hendon H.H., and Glick J. (1998), *Intraseasonal variability of surface fluxes and seasurface temperature in the tropical Indian and Pacific ocean*. *J. Clim.*, 11, 1685-1702.
- Waliser D.E., K.M. Lau, and J.-H. Kim, (1999), *The influence of coupled sea surface temperatures on the Madden-Julian Oscillation: a model perturbation experiment*. *J. Atmos. Sci.*, 56, 333-358.
- Wheeler M. and Hendon H., (2004), *An all-season real-time multivariate MJO index: Development of an index for monitoring and prediction*. *Mon. Wea. Rev.*, 132, 1917-1932.
- Zavala-Garay, Zhang C., Moore A.M., and Kleeman R., (2005), *The linear-response of ENSO to the Madden-Julian Oscillation*. *J. Clim.*, 18, 2441-2459.
- Zhang C., (2005), *Madden-Julian Oscillation*. *Amer. Geophys. Union, Reviews of Geophys.*, 43, 1- 36.
- Zhang Y., Wallace J.M., and Battisti D. (1997), *ENSO-like interdecadal variability: 1990-93*. *J. Climate*, 10, 1004-1020.

**Intrinsic climate variability paced by external forcing:
the Kuroshio Extension bimodality –
North Pacific Oscillation case**

Pierini S.*

*Dipartimento di Scienze e Tecnologie, Università di Napoli Parthenope
Centro Direzionale, Napoli - Italy*

**Corresponding author: stefano.pierini@uniparthenope.it*

Abstract

The North Pacific Oscillation is known to drive the North Pacific Gyre Oscillation (NPGO), and to excite Rossby waves that propagate the NPGO signature from the central North Pacific into the Kuroshio Extension (KE) region. This, in turn, is suggested to be the cause of the synchronization between the NPGO and the KE decadal bimodality as observed from satellite altimetry. In this communication modelling studies are presented supporting the hypothesis that such synchronization results from the excitation -via the Rossby wave field- of a KE relaxation oscillation, whose spatial structure and evolution is basically due to a highly nonlinear intrinsic oceanic mechanism. This is therefore a case of intrinsic variability paced by an external forcing, which is likely to be a common behaviour in climate dynamics.

Keywords: *Kuroshio Extension; North Pacific Oscillation; intrinsic variability; coherence resonance; synchronization*



The Kuroshio Extension (KE) is a highly stratified, eastward-flowing free inertial meandering jet formed by the confluence of the Kuroshio and Oyashio western boundary currents (Fig. 1); it constitutes, therefore, a front separating the warm subtropical and cold subpolar waters of the North Pacific Ocean [1].

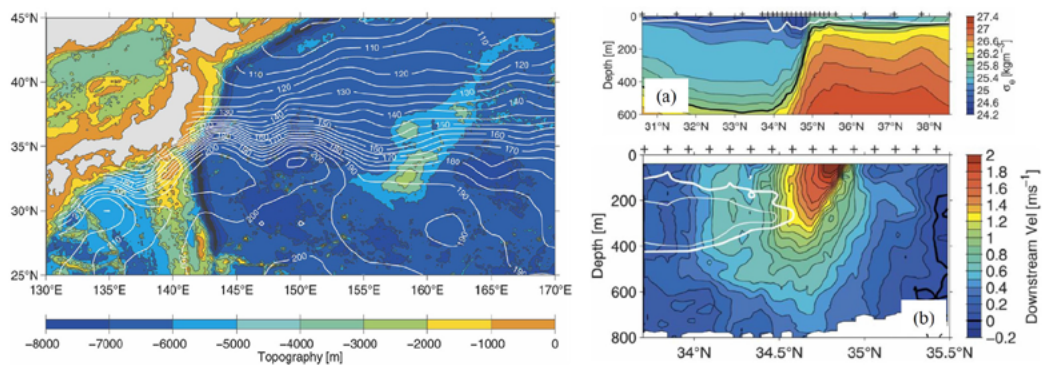


Fig. 1: Left panel: surface dynamic height field (cm) relative to 1000 dbar; colored map shows the bathymetry (from [2]). Right panels: (a): potential density along a KESS leg-1 transect across the KE system. (b): downstream velocity measured by shipboard ADCP along a KE section (adapted from [1]).

The KE displays a decadal variability of bimodal character connecting a zonally elongated, fairly stable, energetic meandering jet (the so-called elongated mode, Fig. 2c) and a much weaker, highly variable and convoluted jet with a reduced zonal penetration (the so-called contracted mode, Fig. 2a) [2,3]. Understanding the mechanisms that produce such low-frequency variability is relevant not only from a purely oceanographic viewpoint but also from a more general climatic perspective, as KE fluctuations are associated with vigorous air-sea heat exchanges known to affect considerably the variability of the midlatitude coupled ocean-atmosphere system in the North Pacific region and beyond.

Qiu and Chen [2] noticed that the first KE bimodal cycle (BC) observed through altimeter data was in synchrony with the arrival of baroclinic Rossby waves that propagated the Pacific Decadal Oscillation (PDO) signature from the central and eastern North Pacific into the KE region. This was confirmed also for the second documented cycle in a subsequent paper [3]: during the positive PDO phase (or negative North Pacific Gyre Oscillation -NPGO- phase, [4]), the intensified Aleutian Low generates negative SSH anomalies in the eastern North Pacific that propagate to the west as baroclinic Rossby waves: their arrival in the KE region is found to be in phase with the weakening and southward shift of

the KE jet, which marks the beginning of the so-called contracted mode. Naturally, it is of fundamental importance to identify the physical mechanisms that lead to this atmosphere-ocean mode of variability. A first fundamental question arises to this respect: is the KE low-frequency variability directly shaped by the incoming Rossby wave field, or is it due to a nonlinear intrinsic mode of the ocean system? The KE jet is a sharp ocean front, so the dramatic changes observed in its BC cannot be due to a linear superposition of a spatially broad field of Rossby waves, as clearly shown in [2]. On the other hand, an idealized KE reduced-gravity jet obtained in the eddy-permitting primitive equation process study by Pierini [5,6] yielded a decadal chaotic relaxation oscillation (RO) under steady climatological wind forcing in substantial agreement with altimeter observations (Fig. 2; see [7] for a detailed model-data comparison).

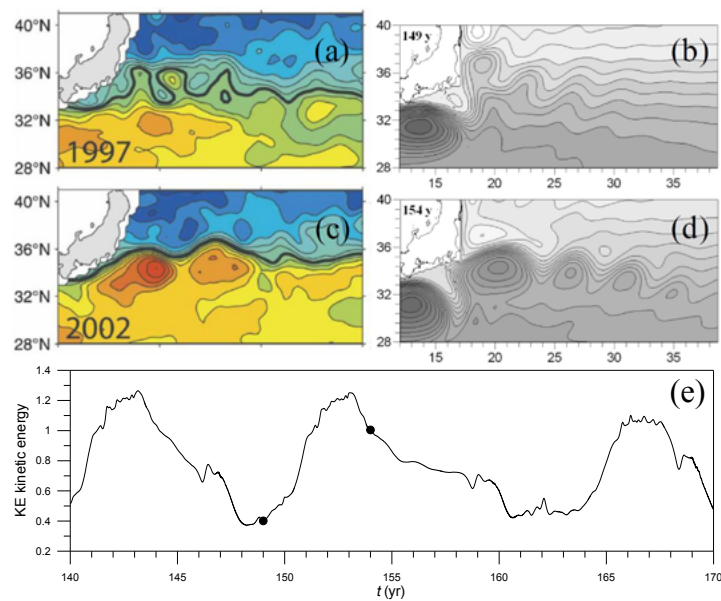


Fig. 2: (a,c): annually averaged sea surface height maps derived from altimeter data by Qiu and Chen [2] for the years 1997, 2002. (b,d): corresponding model analogues obtained by Pierini [5]. (e): time series of three modeled cycles of the KE kinetic energy (adapted from [2] and [5]).

This supports the hypothesis that the KE bimodality is essentially due to a highly nonlinear intrinsic RO (that may be self-sustained), in which the basic state (essentially the contracted mode) can spontaneously evolve through the various stages of the BC until the original state is recovered, the gross features of such evolution being basically unaffected by the wind forcing (substantially the same hypothesis was also supported by OGCM hindcasts [8-9]). In [5,7] it was shown that the KE RO is self-sustained in a parameter range past a homoclinic bifurcation in state space (a "tipping point"). Fig.

3 shows the bifurcation map with A_H (the lateral eddy viscosity) chosen as the control parameter (left panel), and the dramatic change of the system's behavior when the tipping point is passed (right panel).

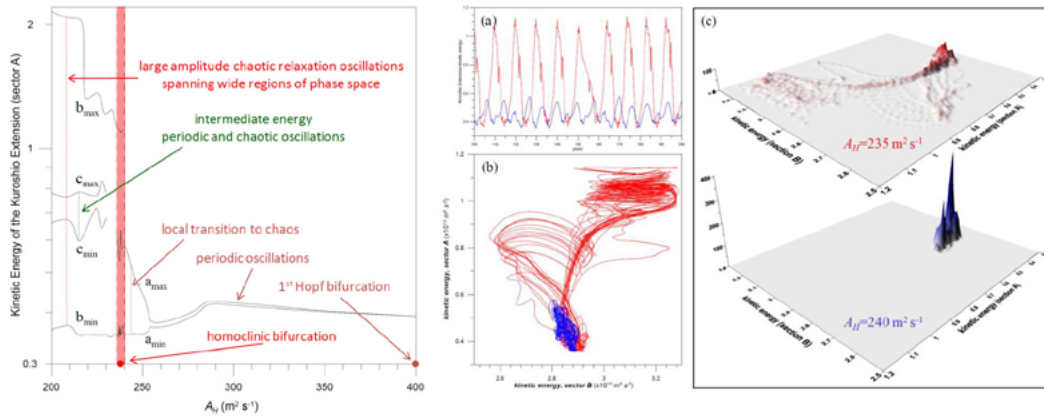


Fig. 3: Left panel: bifurcation diagram with A_H as the control parameter. Right panel: time series of the KE kinetic energy E_A (a) and projection of flow trajectory onto the $E_B - E_A$ plane (E_B is the energy of the Kuroshio south of Japan) (b), for $A_H=240 \text{ m}^2 \text{ s}^{-1}$ (blue line) and $A_H=235 \text{ m}^2 \text{ s}^{-1}$ (red line). (c): probability density function on the $E_B - E_A$ plane for $A_H=240 \text{ m}^2 \text{ s}^{-1}$ (lower panel) and $A_H=235 \text{ m}^2 \text{ s}^{-1}$ (upper panel; adapted from [7]).

In this scenario the KE bimodality must therefore be the manifestation of a nonlinear intrinsic ocean mode excited by a Rossby wave train. Based on their multidecadal hindcast by the OGCM for the Earth Simulator (OFES), Taguchi et al. [8] suggested that the broadscale Rossby waves generated by the basin-scale wind variability excite intrinsic modes of the KE jet, thus reorganizing the SSH variability in space. [3,9] share the same view, and point to the role played by mesoscale eddies and related feedbacks in the KE dynamics. An approach to the problem based also on the powerful concepts of dynamical systems theory was adopted by Pierini [10]: in that study the KE RO [5], that emerges spontaneously beyond the tipping point, can arise even below that threshold under an appropriate red noise wind forcing according to the coherence resonance mechanism (e.g., [11]). That case constitutes a paradigm of the observed synchronization described above, which is likely to be quite common in climate dynamics [12]. To study the same problem on a more conceptual level, a low-order ocean model was developed by Pierini [13]: the combined effect of coherence resonance and of a periodic forcing could then be analyzed, and general aspects of noise effects on abrupt climate transitions were investigated [14].

Although a consensus on the validity of this dynamical mechanism seems to have been reached, it is rather surprising that model studies showing a correct combination of KE bimodality and timing are

not yet available (e.g., [9, 15, 16]). In connection to this, Pierini [17] has developed a process study based on the North Pacific Ocean circulation model [5] in which both the KE bimodality and its synchronization with the NPGO in significant agreement with observations are obtained. The model includes a time-dependent North Pacific Oscillation (NPO, the second dominant mode of sea level pressure variability in the North Pacific) forcing component, which was derived from the NPGO under the assumption that the latter reflects the NPO with no lag.

In the reference simulation the model captures the main features of both the KE bimodality and its teleconnection with the NPO variability via the Rossby wave field. This is shown in Fig. 4 by means of the KE path length: the recharging phase shown by the large amplitude oscillations starts almost a year before (after) the actual beginning in the first (second) BC, and its duration in the first cycle is shorter than the real one (as already noted by [7]), but overall the underlying dynamics, teleconnection and synchronization are in significant agreement with data [17].

A series of sensitivity numerical experiments are also carried out in [17]. The model response to variations of the zonal location of the NPO forcing shows that the synchronization and teleconnection evidenced in the reference simulation are robust model features. Another sensitivity experiment shows that the emergence of the KE bimodality with a correct timing is extremely sensitive to changes in the

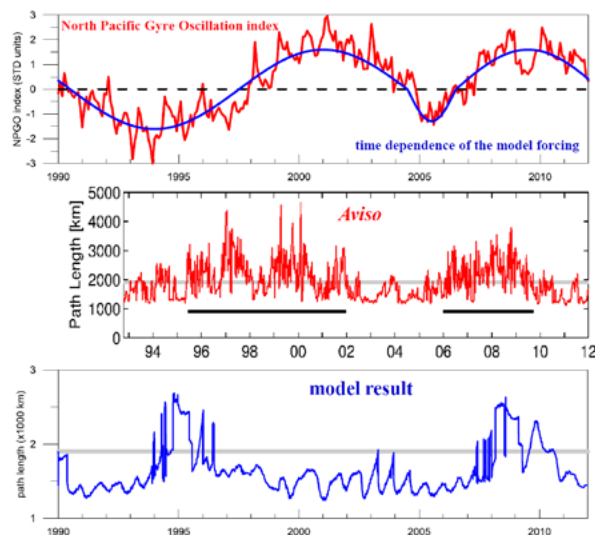


Fig. 4: Upper panel: NPGO index (red line, courtesy of E. Di Lorenzo [4]) and time dependence of the wind forcing used in [17] (blue line). Central panel: upstream KE path length derived from altimeter data (updated time series to Qiu and Chen [2-3], private communication). Bottom panel: modeled upstream KE path length obtained by Pierini [17].

dissipative parameterization. If dissipation is too high, ROs cannot emerge at all; if, on the other hand, dissipation is too low, the self-sustained nature of the ROs leads to a distorted synchronization, with a consequent lack of agreement with observations. It is important to stress that these two opposite scenarios correspond to a variation in the weight of dissipation of just ~15%. Such extreme sensitivity is suggested to be the main cause of the absence of a correct KE low-frequency variability in state-of-the-art OGCM simulations of the North Pacific Ocean. That sensitivity is also conjectured to be a model artifact, whose appearance may not, in fact, be limited to relatively idealized models such as the present one.

In conclusion, the complex mechanism emerged in this study is interpreted in terms of dynamical systems theory as a case of intrinsic variability in an excitable dynamical system triggered (and therefore paced) by an external forcing in a parameter range preceding the tipping point beyond which the intrinsic variability is self-sustained. This same mechanism is considered for the explanation of fundamental climate phenomena, such as the occurrence and timing of the glacial-interglacial cycles, the Heinrich and Dansgaard-Oeschger events, and the Atlantic multidecadal variability (e.g., [12, 18]).

ACKNOWLEDGMENTS

Valuable discussions with Henk A. Dijkstra, Bo Qiu and Emanuele di Lorenzo are kindly acknowledged. The research activities presented in this paper have been supported by the VI F.P. "High Performance Computing - Europa" Project of the European Commission (contr. n. RII3-CT-2003-506079), by the "Regione Campania" of Italy (L.R. n. 5/2002, Ann. 2005, contr. 1279), and by the Italian "Programma Nazionale di Ricerche in Antartide" (contr. n. 2010/A2.11-2753).

REFERENCES

- Qiu B., Hacker P., Chen S., Donohue K.A., Watts D.R., Mitsudera H., Hogg N.G. & Jayne S.R. (2006), *Observations of the Subtropical Mode Water evolution from the Kuroshio Extension System Study*, J. Phys. Oceanogr., No. 36, pp. 457-473. (1)
- Qiu, B. & Chen S. (2005), *Variability of the Kuroshio Extension jet, recirculation gyre and mesoscale eddies on decadal timescales*, J. Phys. Oceanogr., No. 35, pp. 2090-2103. (2)

- Qiu B. & Chen S. (2010), *Eddy-mean flow interaction in the decadal-modulating Kuroshio Extension system*, Deep-Sea Res. II, No. 57, pp. 1097-1110. (3)
- Di Lorenzo E., and co-authors (2008), *North Pacific Gyre Oscillation links ocean climate and ecosystem change*, Geophys. Res. Lett., No. 35, pp. L08607-1-6. (4)
- Pierini S. (2006), *A Kuroshio Extension System model study: decadal chaotic self-sustained oscillations*, J. Phys. Oceanogr., No. 36, pp. 1605-1625. (5)
- Pierini S. (2008), *On the crucial role of basin geometry in double-gyre models of the Kuroshio Extension*, J. Phys. Oceanogr., No. 38, pp. 1327-1333. (6)
- Pierini S., Dijkstra H. A. & Riccio A. (2009), *A nonlinear theory of the Kuroshio Extension bimodality*, J. Phys. Oceanogr., No. 39, pp. 2212-2229. (7)
- Taguchi B., Xie S.-P., Schneider N., Nonaka M., Sasaki H. & Sasai Y. (2007), *Decadal variability of the Kuroshio Extension: Observations and an eddy-resolving model hindcast*, J. Climate, No. 20, pp. 2357–2377. (8)
- Taguchi B., Qiu B., Nonaka M., Sasaki H., Xie S.-P. & Schneider N. (2010), *Decadal variability of the Kuroshio Extension: mesoscale eddies and recirculations*, Ocean Dyn., No. 60, pp. 673–691. (9)
- Pierini S. (2010), *Coherence resonance in a double-gyre model of the Kuroshio Extension*, J. Phys. Oceanogr., No. 40, pp. 238-248. (10)
- Pikovsky A.S. & Kurths J. (1997), *Coherence resonance in noise-driven excitable systems*, Phys. Rev. Lett., No. 78, pp. 775-778. (11)
- Crucifix M. (2012), *Oscillators and relaxation phenomena in Pleistocene climate theory*, Phil. Trans. R. Soc., No. A 370, pp. 1140-1165. (12)
- Pierini S. (2011), *Low-frequency variability, coherence resonance and phase selection in a low-order model of the wind-driven ocean circulation*, J. Phys. Oceanogr. No. 41, pp. 1585-1604. (13)
- Pierini S. (2012), *Stochastic tipping points in climate dynamics*, Phys. Rev. E, No. 85, pp. 027101-1-5. (14)
- Douglass E.M., Jayne S.R., Bryan F.O., Peacock S. & Maltrud M. (2012), *Kuroshio pathways in a climatologically forced model*, J. Oceanogr., No. 68, pp. 625-639. (15)
- Kurogi M., Hasumi H. & Tanaka Y (2013), *Effects of stretching on maintaining the Kuroshio meander*, J. Geophys. Res. Oceans, No. 118, pp. 1182-1194. (16)

- Pierini S. (2013), *Kuroshio Extension bimodality and the North Pacific Oscillation: a case of intrinsic variability paced by external forcing*, submitted to J. Climate. (17)
- Otterå O.H., Bentsen M., Drange H. & Suo L. (2010), *External forcing as a metronome for Atlantic multidecadal variability*, Nature Geoscience, No. 3, pp. 688-694. (18)

Climatic trends of the equatorial undercurrent: A backup mechanism for sustaining the equatorial Pacific production

Ruggio R.^{1,2*}, Vichi M.^{2,3}, Paparella F.⁴, and Masina S.^{2,3}

¹*Dipartimento di Scienze e Tecnologie Biologiche ed Ambientali, Università del Salento, Lecce - Italy,*

²*Centro Euro-Mediterraneo sui Cambiamenti Climatici, Bologna, Italy,*

³*Istituto Nazionale di Geofisica e Vulcanologia, Bologna, Italy*

⁴*Dipartimento di Matematica e Fisica E. De Giorgi, Università del Salento, Lecce, Italy*

*Corresponding author: raffaele.ruggio@unisalento.it

Abstract

The Equatorial Undercurrent (EUC) is the major source of iron to the equatorial Pacific and it is sensitive to climatic changes as other components of the tropical Pacific. This work proposes a methodology based on a Lagrangian approach aimed at understanding the changes in the transport of iron rich waters to the EUC in a future climate change scenario, using climate model data from an Earth system model. A selected set of regions from the northern and southern extra-equatorial Pacific has been chosen. These regions are characterized by the presence of iron sources from continental shelf processes like the Papua New Guinea region and atmospheric deposition like the northern subtropical gyre. The trajectories that reach the EUC during the 20th and the 21st century departing from these areas have been analysed using a set of statistics designed to determine variations in the amount of transport and in the travel times of the water masses. The transport of waters to the EUC from the north Pacific subtropical gyre and from the Bismarck Sea is projected to increase during the 21st century. The increase is particularly significant for water masses from the northern subtropical gyre, with travel times lower than 10 years in the second half of the 21st century. This increased interaction between the extra-tropics and the EUC may bring additional iron-rich waters in the high-nutrient low-chlorophyll region of the equatorial Pacific compatibly with the significant increase of the simulated net primary production found in the biogeochemical model, thus partly offsetting the anticipated decrease of production implied by the surface warming.

Keywords: *Equatorial circulation; Equatorial Undercurrents; Iron; Primary production; Lagrangian method*



1. INTRODUCTION

The Equatorial Undercurrent (EUC) is one of the major circulation patterns in the equatorial Pacific, flowing within the thermocline at around a 180 m depth and outcropping in proximity of the Galapagos Islands.

The origin of the EUC waters has been identified by means of modelling studies ([4]; [5]; [6]), which have revealed the contributions both from northern and southern sources off the equator [4].

The EUC plays a major role in controlling the biogeochemistry of the equatorial Pacific [7], via changes in the supply of dissolved iron (e.g. [2]). The area of upwelling in the eastern equatorial Pacific is a high nutrient low chlorophyll region where productivity is limited by iron. The iron found in the current has been shown to mostly originate in the western basin and its lithological characteristics have suggested its association with sedimentary sources from the Papua New Guinea shelves.

The equatorial Pacific is an important region to be considered for climate change studies, as it is expected to be quite sensitive to future climate change. These changes in the oceanic physical features are anticipated to impact the biological production of the equatorial ecosystem. It is likely that contrasting biological patterns may occur: for instance, [10] found a particularly evident increase in the simulated equatorial net primary production at the end of the 21st century using two different emission scenarios, the A1B and a 450 ppm stabilization scenario and they suggested a link with changes in the iron transport through the EUC. It is therefore of interest to investigate whether the intensity of the EUC water mass transport is affected by climate change and how this may impact the supply of iron from the known extra-equatorial sources. This work constructs a diagnostic analysis based on a combination of Lagrangian particle tracking and statistical tools that have been applied to the results of an Earth system model (ESM) forced with a climate change scenario. Of all the regions of the Pacific Ocean that have been identified as sources or important pathways of the EUC waters [4], we have considered a subset of those that may also provide a sustained iron input to the ocean, classifying them into regions of shelf (riverine or sedimentary) and atmospheric sources. The diagnostic tool is composed of a two-stage process. Initially, from the selected Pacific regions, a set of water mass trajectories have been evolved over the simulation period using a Lagrangian algorithm, which allows to compare their pathways to previous works on the sources of the EUC. Subsequently, a set of statistics has been designed and applied to the trajectory data to quantify the changes in the mass transport over the 20th and 21st centuries.

2. METHODS

The model used in this work is the INGV–CMCC carbon cycle Earth system model ([3]; [10]), a coupled climate model which represents explicitly the carbon cycle on land and in the ocean with detailed marine biogeochemical processes. The oceanic component of the model is PELAGOS ([11], [12]; [13]), a coupling between the ocean general circulation model OPA8.2 (Madec et al., 1999) and the biogeochemical flux model [11]. It is solved on the curvilinear grid ORCA2, with a resolution of 2° of longitude and a variable mesh of $0.5\text{--}2^\circ$ of latitudes. The vertical grid has 31 levels with variable depth and a constant 10 m step in the top 100 m.

In this study we have used model outputs consisting of monthly averages of the zonal, meridional and vertical velocities as well as temperature and salinity fields for the period from January 1900 to December 2099. The future scenario simulation (2000–2099) has been forced by the SRES A1B emission scenario. Biogeochemical model data at monthly resolution have been used to analyse the iron distribution and the response of phytoplankton production to climate change.

Lagrangian trajectories of water masses have been computed from these physical ocean model data using the ARIANE Lagrangian integrator ([1] <http://stockage.univ-brest.fr/grima/Ariane/>).

Three different areas have been chosen among the various regions of EUC water sources (Fig. 1): a broad region of the subtropical north Pacific gyre as representative of iron enrichment from atmospheric deposition, and two continental shelf regions from the southern Pacific. The Bismarck Sea is a closed sea directly in contact with the Papua New Guinea shelves and it is a region where iron sources are mostly due to bottom enrichment processes. The Solomon Sea is also a continental shelf sea, but in the model it is in direct contact with the southern subtropical gyre. It is important to remember here that there is no explicit parameterization of iron sources from bottom sediments in the current model, and therefore the concentration in the continental shelf areas is lower than observed (e.g. [8]).

More than 1000 seeding locations were implemented in the northern subtropical gyre area between $150^\circ\text{E}\text{--}130^\circ\text{W}$ and $20^\circ\text{N}\text{--}40^\circ\text{N}$ (pink area in Fig. 1). The points are equally spaced on a regular grid with 101 zonal points and 11 meridional points. All particles were placed at the same depth of 100 m. That is close to the base of the mixed layer, in order to catch the dynamics of water masses that have recently ventilated. About 200 seeding locations were implemented in the Bismarck Sea between $137^\circ\text{E}\text{--}155^\circ\text{E}$ and $2^\circ\text{S}\text{--}5^\circ\text{S}$ (yellow area in Fig. 1). Given the focus on shelf processes, the seeding

locations have been placed at different depths (every 50 m from 150 to 350 m) on a regular grid with 11 zonal points and 6 meridional points.

The Solomon Sea area is located between 152°E – 162°E and 6°S – 12°S (shown in cyan in Fig. 1). The seeding locations are on a regular grid of 6 zonal points and 6 meridional points placed at the same depth levels of the previous case.

The seeding frequency was every six months from January 1900 until June 2099 resulting in a sample of 597,600 seeded particles. Particles were considered as belonging the EUC when their trajectory crossed from west to east a closed volume with longitude between 155°W and 165°W , latitude between 3°S and 3°N and depth between 0 and 350 m (the blue area in Fig. 1 hereafter called EUC-box).

3. LAGRANGIAN RESULTS

We analyze trends in the water mass transport from the tropical and extratropical areas to the equatorial region by plotting the mean monthly arrivals in the EUC-box (Fig. 2). The arrivals from the north Pacific subtropical gyre area (Fig. 2a) show an evident trend for particles whose travel time does not exceed 10 years. The overall trend for particles that travel up to 5 years is a 27% increase of arrivals per century, and 150% increase per century if the regression is restricted to 2050–2099. For particles traveling 5 to 10 years, the 2050–2099 trend drops to a 74% increase per century.

For the particles seeded in the Bismarck Sea (Fig. 2b) the results are analogous: the particles that travel up to two years show an overall 10% increase per century of arrivals in the EUC-box, and a 30% increase per century restricting the regression to 2050–2099. Particles that arrive having traveled for more than two years do not show evident trends.

The particles seeded in the Solomon Sea (Fig. 2c) do not show evident trends on any time scale. However, if the Solomon Sea launch area is divided into two sub-domains, W and E of 155° , and the statistic is made separately for the particles seeded in each subdomain, then the particles launched in the western subdomain show an overall 9% increase of arrivals per century into the EUC-box, and the particles launched in the eastern subdomain show an overall 11% decrease when counting arrivals within two years from seeding.

The total number of arrivals in the EUC-box in the 20th century is always lower than in the 21st century, but the difference is small, particularly for the southern sources. To estimate whether the

differences between the centuries are statistically significant, we used a jack-knife procedure, which consists randomly subsampling 10% of the particle pathways from each seeding region for each century. The distribution of the fraction of arrived particles for each century is shown in Fig. 3 for both the 20th and the 21st century. There is no overlap in the histograms from the north Pacific subsamplings (Fig. 3a), indicating that arrivals in the 20th century are always less than in the 21st century subsamples. For the particles starting in the Bismarck Sea (Fig. 3b), the empirical distributions from the two centuries are also separated, but there is a small overlap. Finally in the case of Solomon Sea (Fig. 3c) the overlap is much more significant and the Mann-Whitney U test gives about 30% of probability that the two datasets are statistically indistinguishable.

The above statistics are a strong clue that the model exhibits a genuine centennial trend in two out of three cases.

It is also interesting to quantify the typical travel time of the particles that arrive in the EUC-box from the seeding regions. In Fig. 4 the number of particles arrived in the EUC-box is plotted as a function of their travel time and period of seeding (grouped in bins of 10 years). For the north Pacific area it is clear that the bulk of arrivals corresponds to particles that have traveled between 5 and 10 years.

The distribution of arrival times from the northern subtropical gyre changes after year 2050, with the shorter travel times becoming more frequent, as already suggested by the results of Fig. 2a. For the Bismarck and Solomon Sea areas (Fig. 2b and c) the highest frequency corresponds to particles that have traveled less than 2 years. In these cases, travel times show a much smaller change during the 21st century.

4. DISCUSSION

The Lagrangian analysis of coupled model simulations revealed that during the 21st century there is a statistically significant increase of water mass transport to the EUC both from the northern subtropical gyre and from the southern boundary sources.

In fact, even if it is weaker than the one detected in the north there is an increase in the number of arrivals from the seeding region located in the Bismarck Sea surrounding the Papua New Guinea shelves. By dividing the seeding area in two sub-sections we notice that in the west part (boundary section) there is actually an increase in the number of arrivals similar to the one detected from the northern sources while in the east part (interior pathways) there is a weak negative trend.

This is also valid for the Solomon Sea shelf, which represents the region more in contact with the open southern subtropical gyre. Here the statistical analysis presented did not detect any significant increase in the transport of water masses to the EUC although by dividing the seeding area as in the previous case we found two opposite weak trends that balance each other.

Under a future climate change scenario, in addition to the increased transport, we found that there is a substantial rise in the number of particles reaching the EUC within 10 years from their seeding.

[10] linked the increase of net primary production (NPP) and inorganic carbon uptake found in the model results in the eastern equatorial Pacific to changes in the EUC transport features. Our Lagrangian analysis is consistent with the hypothesis that the primary production increase observed in the model is due to an increment of iron-rich water transport through the EUC.

5. ACKNOWLEDGMENTS

This work has been funded by the Centro Euro Mediterraneo per i Cambiamenti Climatici through the GEMINA project.

6. REFERENCES

Blanke B., Raynaud S. (1997), *Kinematics of the Pacific Equatorial Undercurrent: An Eulerian and Lagrangian approach from GCM results*, J. Phys. Oceanogr. 27 (6), 1038–1053. (1)

- Coale K.H., Fitzwater S.E., Gordon R.M., Johnson K.S., Barber R.T. (1996), *Control of community growth and export production by upwelled iron in the equatorial Pacific ocean*, *Nature* 379, 621–624. (2)
- Fogli P.G., Manzini E., Vichi M., Alessandri A., L.P., Gualdi S. Scoccimarro E., Masina S., Navarra A. (2009), *INGV-CMCC carbon: A carbon cycle Earth system model*, Tech. Rep. RP0061. CMCC. (3)
- Goodman P.J., Hazeleger W., de Vries P., Cane M. (2005), *Pathways into the Pacific Equatorial Undercurrent: A trajectory analysis*, *J. Phys. Oceanogr.* 35 (11), 2134–2151 (2011/01/29). (4)
- Grenier M., Cravatte S., Blanke B., Menkes C., Koch-Larrouy A., Durand, F. Melet, A., Jeandel C., (2011), *From the western boundary currents to the Pacific Equatorial Undercurrent: modeled pathways and water mass evolutions*, *J. Geophys. Res.* 116 (C12044). (5)
- Gu D., Philander S. (1997), *Interdecadal climate fluctuations that depend on exchanges between the tropics and extratropics*, *Science* 275 (5301), 805. (6)
- Mackey D.J., O'sullivan J.E., Watson R.J. (2002), *Iron in the western Pacific: A riverine or hydrothermal source for iron in the equatorial undercurrent?*, *Deep-Sea Res. Part II* 49, 877 – 893. (7)
- Pennington J., Mahoney K., Kuwahara V., Kolber D., Calienes R., Chavez F. (2006), *Primary production in the eastern tropical pacific: A review*, *Prog. Oceanogr.* 69, 285–317. (8)
- Slemons L.O., Murray J.W., Resing J., Paul B., Dutrieux P. (2010), *Western pacific coastal sources of iron, manganese, and aluminum to the equatorial under current*, *Glob. Biogeochem.Cycles* 24 (3). (9)
- Vichi M., Manzini E., Fogli P., Alessandri A., Patara L., Scoccimarro E., Masina S., Navarra A. (2011), *Global and regional ocean carbon uptake and climate change: sensitivity to a substantial mitigation scenario*, *Clim. Dyn.* 37 (9), 1929–1947. (10)
- Vichi M., Masina S. (2009), *Skill assessment of the PELAGOS global ocean biogeochemistry model over the period 1980–2000*, *Biogeosciences* 6 (11), 2333–2353. (11)
- Vichi M., Masina S., Navarra A. (2007a), *A generalized model of pelagic bio geochemistry for the global ocean ecosystem. Part II: numerical simulations*, *J. Mar. Syst.* 64, 110–134. (12)
- Vichi M., Pinardi N., Masina S., (2007b), *A generalized model of pelagic bio geochemistry for the global ocean ecosystem. Part I: theory*, *J. Mar. Syst.* 64, 89–109. (13)

7. FIGURES

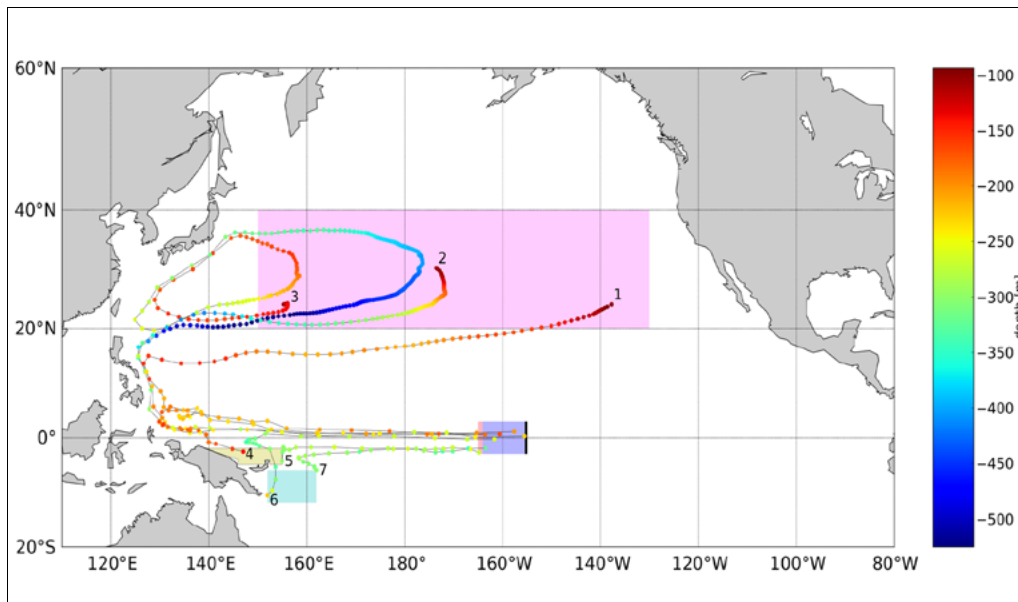


Fig. 1: Regions of particle seedings and examples of particle trajectories to the equatorial region. The large pink rectangle is the seeding area identified as the northern subtropical gyre area. The yellow irregular polygon represents the seeding area in the Bismarck Sea. The cyan rectangle represents the seeding area in the Solomon Sea and the small violet rectangle is the EUC-box where arrivals are counted.

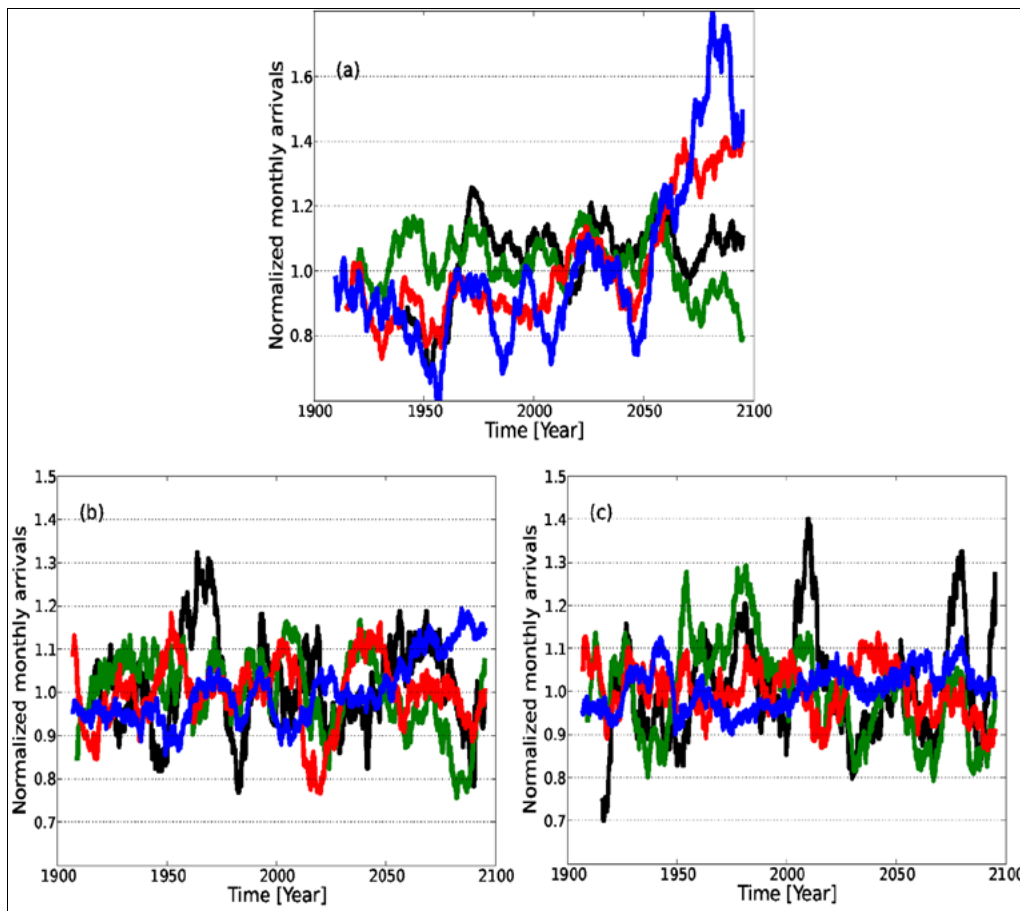


Fig. 2: Monthly arrivals of particles in the EUC-box, averaged with a 10 year running mean and normalized with the time series mean for (a) the northern subtropical gyre, (b) the Bismarck Sea and (c) the Solomon Sea. The curves show particle arrivals with travel times in the intervals 0–5 years (blue), 5–10 years (red), 10–20 years (green) and 20–40 years (black) for panel a and 0–2 years (blue), 2–4 years (red), 4–8 years (green) and 8–16 years (black) for panels b and c.

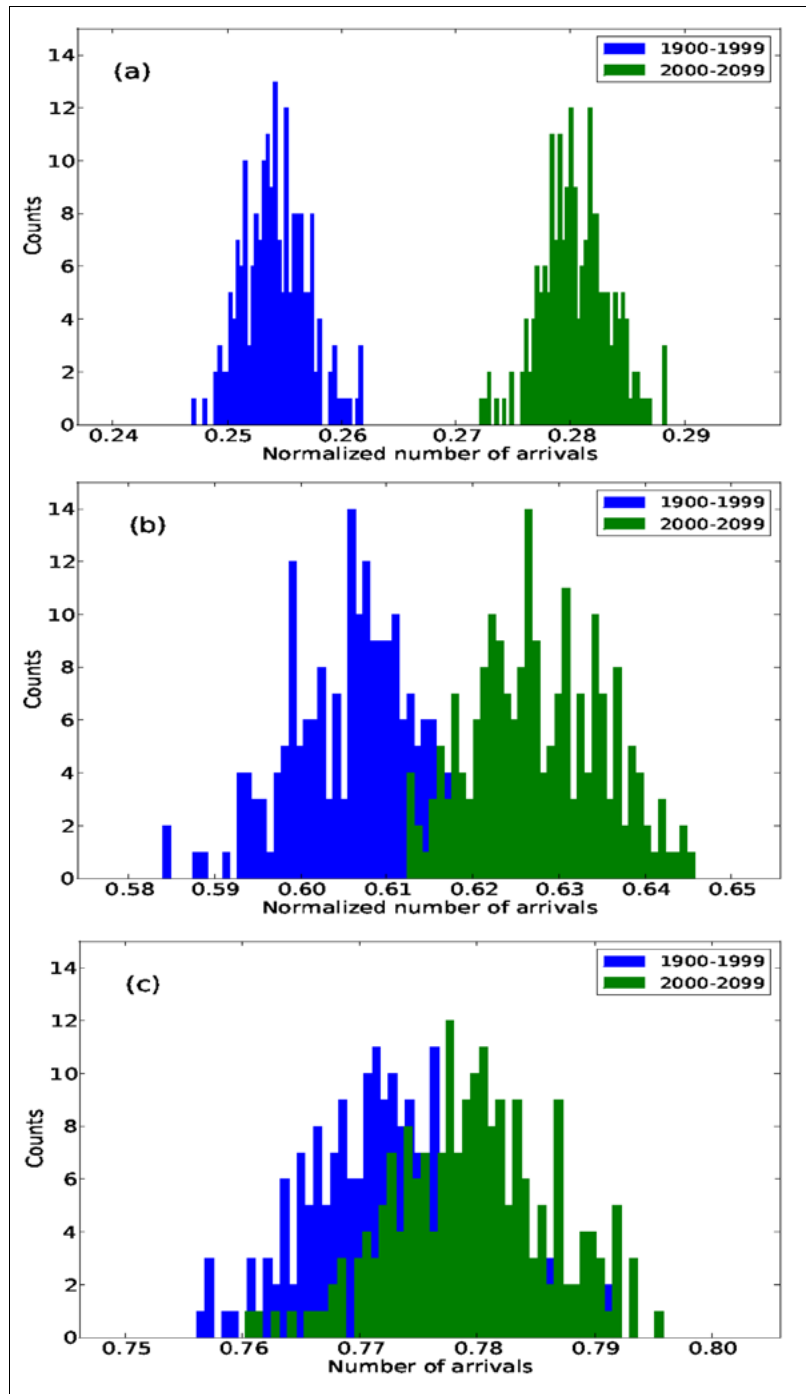


Fig. 3: Results of a jack-knife resampling on the particle arrivals in the EUC-box in the 20th (blue histogram) and in the 21st (green histogram) for (a) the northern subtropical gyre (b) the Bismarck Sea and (c) the Solomon Sea.

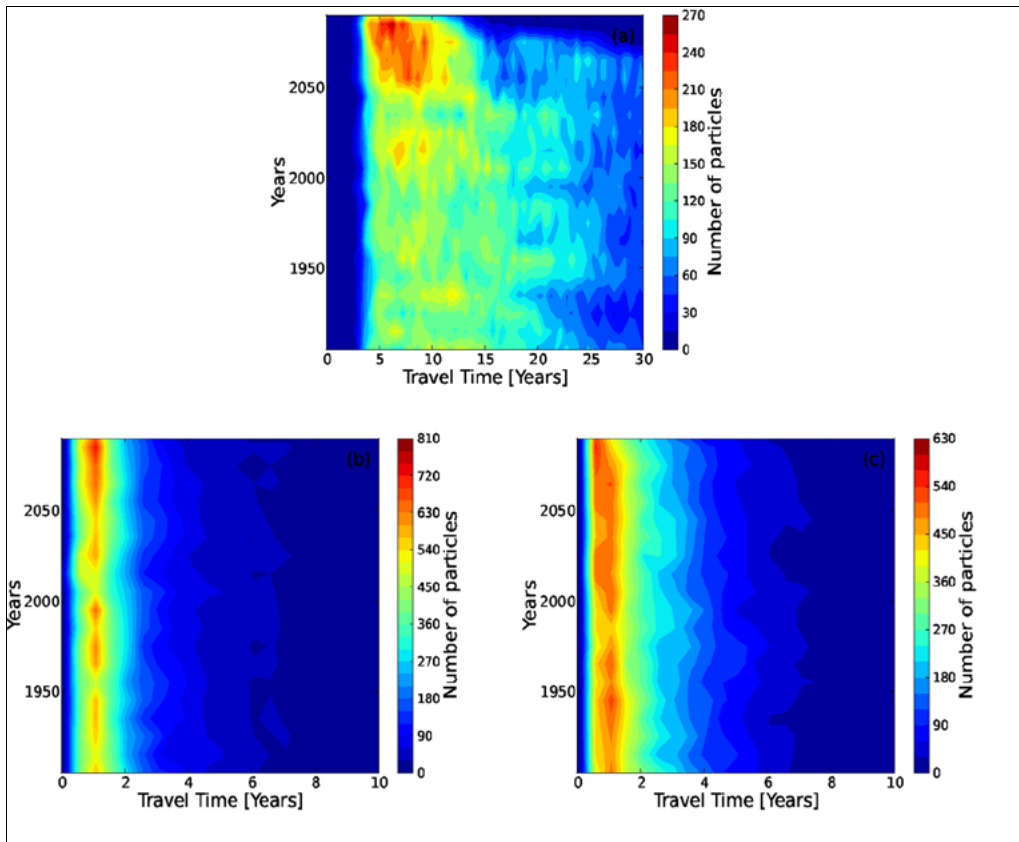


Fig. 4. Number of particles arrived in the EUC-box as a function of their travel time and of the time of seeding for (a) the northern subtropical gyre (b) the Bismarck Sea and (c) the Solomon Sea. Note that the range of particles is different between the panels to reflect the different amount of particles arriving from each region. The width of the bins is 6 months on the horizontal axes and 10 years on the vertical axes.

ENSO and Pacific Decadal Oscillation: decadal variability driven by tropical-extratropical interactions

Farneti R.^{1*}

¹*Earth System Physics, International Centre for Theoretical Physics, Trieste, Italy*

*Corresponding author: rfarneti@ictp.it

Abstract

In this paper, we investigate the observed Pacific decadal variability straddling the year 2000 and the mechanisms for the generation of ENSO decadal variability (EDV). We argue that some of the Pacific tropical Sea Surface Temperature (SST) decadal variability stems from the forcing of the Pacific subtropical gyre through the atmospheric response to ENSO. The resulting Ekman pumping anomaly alters the SubTropical Cell (STC) and oceanic heat transport, providing a negative feedback on the SST. Our results highlight the oceanic role in transmitting the subtropical anomalies back to the tropical ocean. We suggest that extratropical atmospheric responses to tropical forcing have feedbacks onto the ocean dynamics, leading to a time-delayed response of the tropical oceans, giving rise to a possible mechanism for multidecadal ocean-atmosphere coupled variability. The mechanism at play could also provide some degree of predictability to both decadal ENSO and the Pacific Decadal Oscillation (PDO).

Keywords: *Decadal Variability and Predictability, ENSO, PDO*



Understanding the mechanisms behind the generation of low-frequency El Niño-Southern Oscillation (ENSO), and its associated teleconnections to the Pacific Decadal Oscillation (PDO) and extratropical variability at large, is of fundamental and practical importance. Knowledge and prediction of this mode of variability could, for instance, lead to a better distinction between natural and anthropogenic contributions to tropical and extratropical climate variability. The origin of ENSO decadal variability (EDV) is still a matter of debate, and many different mechanisms have been proposed to date. Some studies point towards the role of an atmospheric bridge from the extratropics [1], while others have stressed the importance of internal stochastic atmospheric variability [2] or nonlinearities in ocean-atmosphere coupling within the Tropics [3] to drive the low-frequency variability.

Another possible mechanism for the modulation of ENSO on decadal time scales is through an oceanic teleconnection (or 'tunnel') involving the Pacific Subtropical Cells (STC), particularly the northern one [4]. The STCs are shallow meridional overturning cells straddling the tropical-subtropical regions in both hemispheres. They are characterized by poleward-flowing surface (primarily Ekman) flow and an equatorward geostrophic flow in the pycnocline, the two branches connected by subtropical subduction and equatorial upwelling [5]. Being particularly strong in the Pacific Ocean, they are also responsible for a large poleward heat transport. Changes in the strength of the STC have been shown to lead to variations in equatorial upwelling and decadal SST variability in the tropical Pacific [6]. Theories for the STC relate their strength to the subtropical wind stress [5], so that it is plausible to imagine decadal subtropical anomalies substantially affecting the tropical variability and to consider the STC as an effective oceanic mechanism for extratropical-tropical teleconnection. The strength of the Pacific STCs has been observed to weaken from the 1960s to 1990s [7], but they began to strengthen in the following decade starting in 2000 [8], suggesting the possibility of natural interdecadal variations. The focus of this study is on the ocean's role in generating decadal variability of tropical Pacific SST and on the atmospheric teleconnection that links tropical anomalies to the midlatitudes. We thus try to connect the two components of what might be a mechanism for coupled ocean-atmosphere multidecadal variability in the Pacific sector; namely, atmospheric and oceanic teleconnections giving rise to EDV.

We first use an atmospheric model to produce a 10-member ensemble response to the observed tropical Pacific SST. The atmospheric model is the International Centre for Theoretical Physics Atmospheric General Circulation Model (ICTP-AGCM) called SPEEDY. The model has a spectral dynamical core and is a hydrostatic sigma-coordinate model. The SST decadal anomalies, computed as

the difference between the 2000-2009 and the 1990-1999 period, are reminiscent of the PDO (Fig. 1). Cold anomalous SSTs at the equator are responsible for driving a weakening of the Hadley cell and hence atmospheric heat transport to the subtropics. This result is in agreement with previous studies, in which the atmospheric energy transport changes to the 1980s-1970s decadal anomaly were studied. In that case, the equatorial SST was anomalously warm, corresponding to the warm phase of EDV, and the atmosphere was found to respond with anomalies of opposite sign to the ones described here.

Then, we force a global ocean model with anomalous forcing fields derived from the atmospheric ensemble-mean run. The ocean-sea ice model is the Modular Ocean Model version 4p1 (MOM4p1). MOM4p1 is a free-surface primitive equation model, it uses a z^* -vertical coordinate and its resolution is 2 degrees in latitude and longitude, with refined meridional resolution equatorward of 30 degree, so that it reaches 1 degree of resolution at the equator. The applied decadal pattern of wind stress is very similar to the observed and modelled mode associated with subtropical decadal variability [4]. Initially, a PDO-like SST pattern is generated in its negative phase. Our results thus confirm the tropical role in driving and shaping part of the PDO signal at decadal time scales [2]. Subsequently, the northern STC weakened significantly (Fig. 2a), with a reduced transport of 4-6 Sv, consistent with recent observed estimates [7,8]. A weakened STC is consistent with a reduction in transport of colder subtropical water into, and surface warmer tropical water out of, the tropical Pacific. The oceanic heat transport (OHT), ascribed to both the wind-driven SubTropical Gyre (STG) and the STC, was found to be reduced (Fig. 2b). Significant equatorial SST warm anomalies are eventually generated, reversing the sign of the initial equatorial SSTs responsible for generating the extratropical wind anomalies in the first place (Fig. 2c). The STC thus seems to provide the connection between subtropical wind stress anomalies and equatorial SSTs.

To illustrate the proposed interactions between the STG, STC, and equatorial SST, we represent the system as an idealized set of ordinary differential equations. If G and C are suitably scaled indices of the anomalies in the intensity of the Pacific STG and STC respectively, and T represents the SST anomaly in central equatorial Pacific, we formulate our idealized model as follows:

$$\begin{aligned}
 (1a) \quad & dT/dt = T - \alpha T(t - \delta) - r_1 (T - T_0)^3 - E G \\
 (1b) \quad & dG/dt = E T - k G + \gamma r_2 \\
 (1c) \quad & dC/dt = -k (C - G)
 \end{aligned}$$

According to Eq. 1b, G spins up in response to a warming of tropical SST, T .

Similarly, C spins up in response to G . The atmospheric response tends to be in phase with the climatological wind stress during warm ENSO events (positive T) and of opposite phase during cold events (negative T ; as in this paper).

An acceleration of the STG will lead to an intensification of the Ekman pumping and associated equatorward thermocline flow, resulting in a strengthening of the subtropical cells and consequent equatorial upwelling (and viceversa). Since increased upwelling at the equator leads to a decrease in equatorial SST, this leads to a negative feedback on T .

In Eq. 1a, T_0 represents an equilibrium temperature for the equatorial SST which is related to the anomalous upwelling associated with the STC ($T_0 = -b C$). In Eq. 1a and Eq. 1b, the terms $(-E G)$ and $(E T)$ represent the exchange of energy between the equatorial upper ocean and the subtropical gyre, which are modulated by the atmospheric response to ENSO. The exchange coefficient E is written as a non-linear function of T , in order to represent the non-linear dependence of latent heat flux on SST. The interaction between the gyre and the subtropical cell is simulated by the relaxation term $(-k (C-G))$ in Eq. 1c. This term drives the anomaly in the subtropical cell towards a value in phase with the gyre anomaly; therefore, a spin-up of the gyre will lead to a spin-up of the subtropical cell, and vice-versa. Finally, in Eq. 1b the term r_2 represents the forcing of the subtropical gyre by atmospheric modes that are not connected with ENSO, and a linear dissipation term $(-k G)$ acts as a sink of energy.

Time series of the T , G and C variables (after subtraction of their long term mean, which is not strictly zero due to the non-linearities in the equations) are shown in the three panels of Fig. 3, with the black and blue lines showing values equivalent to monthly and 10-year means respectively.

The scale on the x-axis is in equivalent years, starting from an arbitrary value. Looking at the graph for the equatorial SST anomaly, T , we see variability between -3 and $+4$ units, with decadal modulations of the order of 0.5 units. The distance between consecutive (positive) maxima corresponds to an average period of about 4 to 5 years, with irregular episode of longer separation between consecutive warm peaks. This looks like an acceptable simulation of the actual ENSO variability. Decadal variability is clearly evident in the subtropical cell index C , while the spectrum of the subtropical gyre index G shows a similar ratio of decadal to interannual variability to the one found in T .

The proposed mechanism for the ocean-atmosphere multidecadal Pacific variability can be summarized by the schematic diagram in Fig.4. Suppose a negative SST pattern is present in the equatorial Pacific, as in the case of the decadal anomaly between the 2000-09 and 1990-99 period. The cooling at the equator forces an extratropical response through an atmospheric teleconnection (depicted by a large

curly arrow in Fig. 4). The extratropical atmospheric response is imprinted mainly in the subtropical winds, which subsequently generate a wind-stress-curl anomaly of opposite sign with respect to the climatological conditions, thereby weakening Ekman pumping there (horizontal arrows in the Ekman layer). The resulting anomalously weak downwelling (vertical arrow below the STG) results in a weaker equatorward geostrophic flow (horizontal arrows below the Ekman layer), which in turn spins-down the lower branch of the STC. The reduced mass flux in both the STG and STC also implies a weakening of the meridional heat transport, a slow-down of the eastward-flowing equatorial undercurrent (EUC) -- partially fed from water subducted in the subtropics -- and a reduction in equatorial upwelling (vertical arrow near the equator). A positive SST anomaly is thus generated at the equator, damping the initial one and giving rise to a negative feedback on decadal time scales through tropical-subtropical interactions, with an oceanic 'tunnel' transmitting the anomaly back to the equator via transport anomalies. The simulated decadal change is towards a positive PDO, i.e. an anomaly of opposite sign to the initial one, consistent with the overall hypothesis of a negative feedback associated with a reversal of the initial SST anomalies.

In summary, we have proposed a mechanism by which tropical-subtropical interactions can give rise to EDV. Further, the mechanism is based on observed variability of both the atmosphere and ocean. However, a few caveats should be placed on our results. The coarse grid of the ocean model might be responsible for non-trivial modifications to tropical dynamics and subtropical-tropical pathways of communication. Most importantly, the mechanism for multidecadal variability proposed here, involving atmospheric and oceanic teleconnections, is based on uncoupled integrations, neglecting potentially important processes and interactions present in a coupled framework. It remains to be tested whether the coupled tropical-extratropical mechanism leading to EDV, and involving oceanic and atmospheric teleconnections, still holds in a dynamically coupled ocean-atmosphere model.

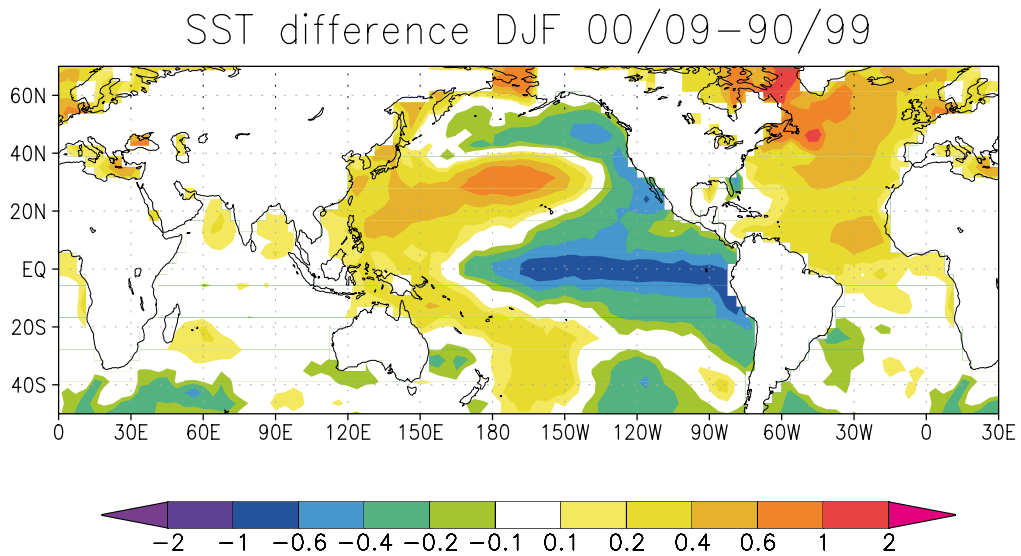


Fig. 1: December-to-February sea surface temperature anomaly, computed as the difference between the decades 2000-2009 and 1990-1999, used in the SST-forced AGCM integration. Units are K.

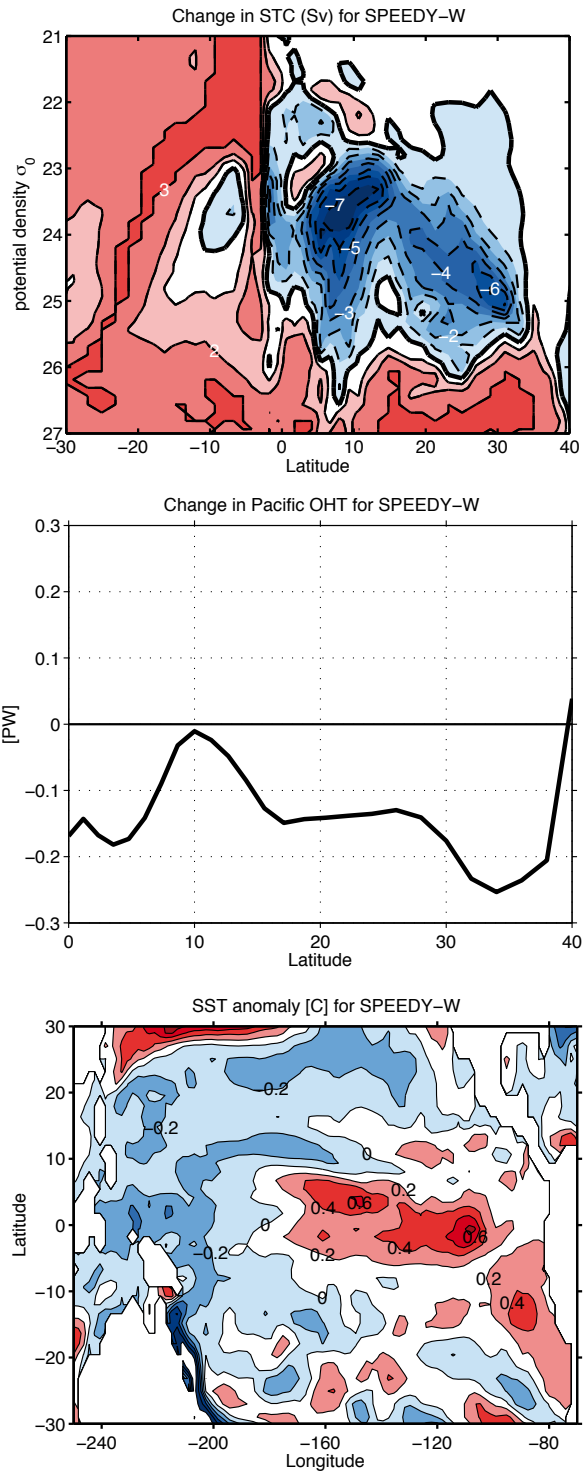


Fig. 2: Oceanic anomalies at the end of the perturbation experiment. (top) subtropical cells (STC) in density space, (middle) ocean heat transport (OHT), and (bottom) sea surface temperature (SST). Units are Sv (contour interval of 1), PW and C (contour interval of 0.2), respectively.

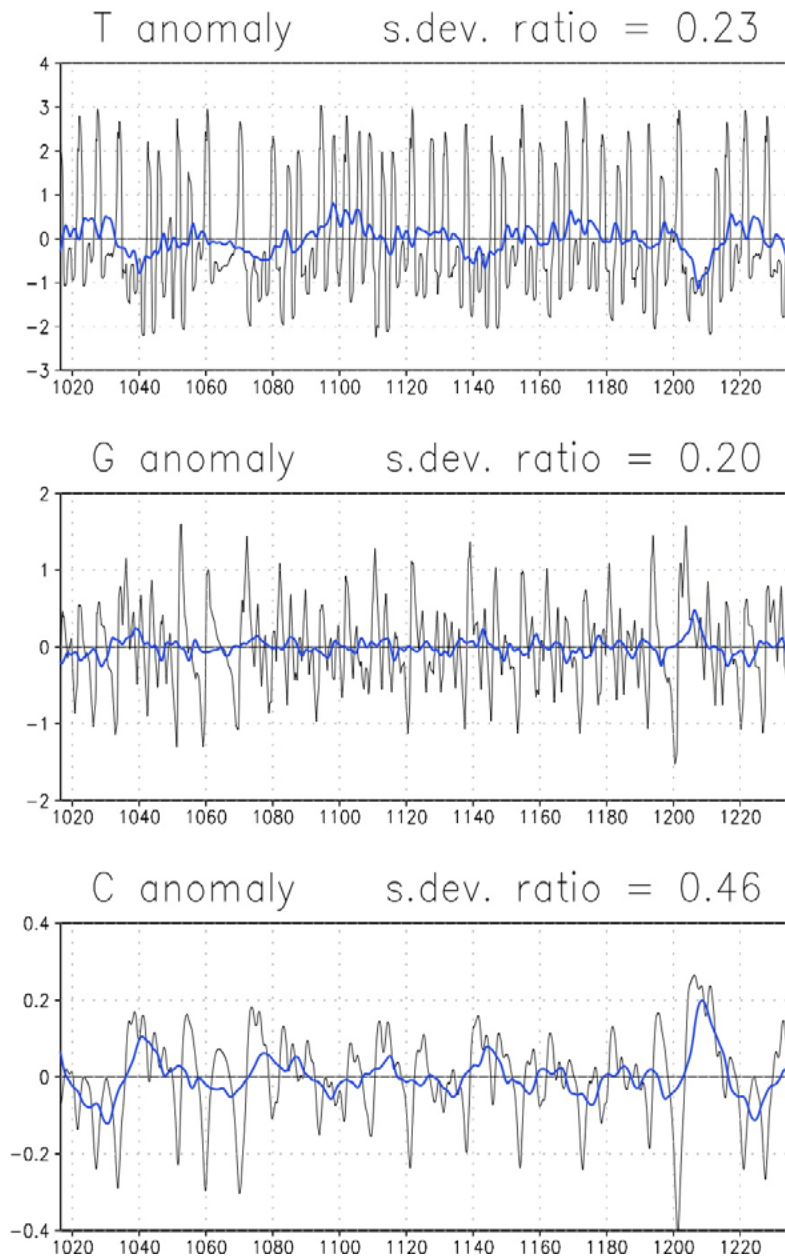


Fig. 3: Time series for the three variables T (ENSO SST) , G (subtropical gyre) and C (subtropical cell) in the model described by Eqs. 1a-b-c.

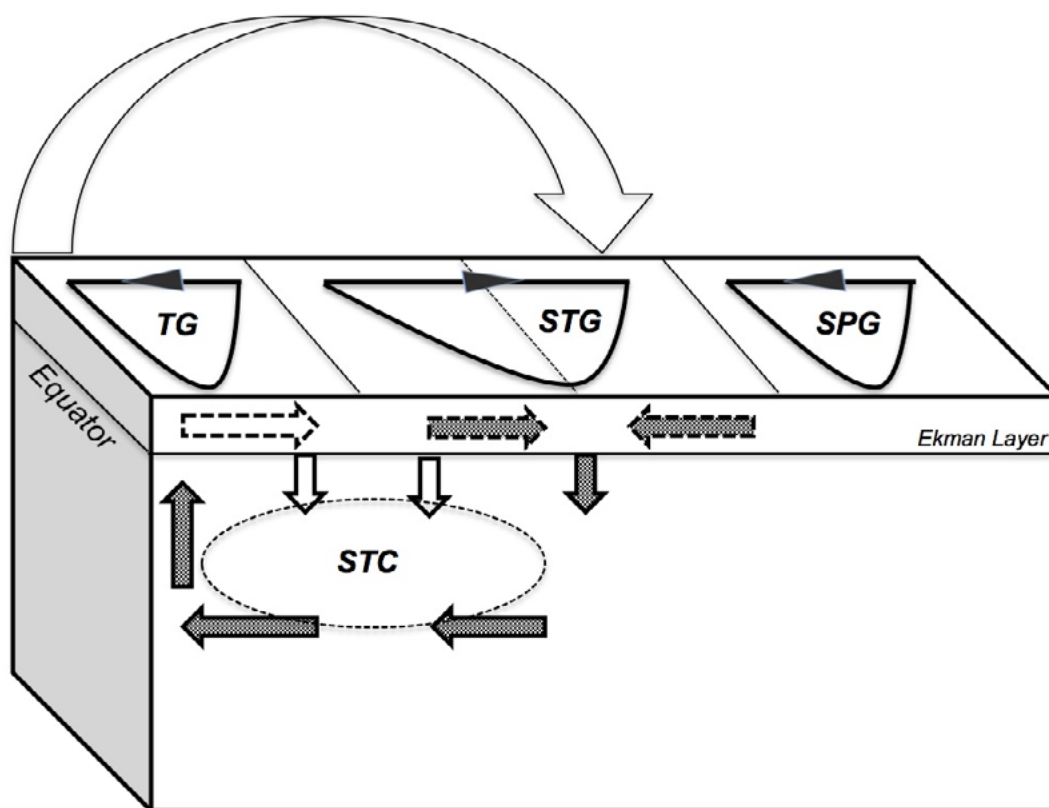


Fig. 4: Schematic of the putative tropical-extratropical Pacific interactions at decadal time scales. Shown are the horizontal gyres (TG: tropical gyre, STG: subtropical gyre, SPG: subpolar gyre) and subtropical vertical cell (STC: subtropical cell). See text for details.

ACKNOWLEDGMENTS

The author would like to acknowledge the contribution and help from his co-authors, Franco Molteni and Fred Kucharski, as well as fruitful conversations with Jay McCreary.

REFERENCES

- Barnett T.P., Pierce D.W., Latif M., Dommenges D. & Saravanan R. (1999), *Interdecadal interactions between the tropics and midlatitudes in the Pacific basin*. Geophys. Res. Lett., No. 26, pp. 615-618. (1)
- Newman M., Compo G.P. & Alexander M.A.. (2003), *ENSO-forced variability of the Pacific Decadal Oscillation*. J. Climate, No. 16, pp. 3853-3857. (2)
- Timmermann A. & Jin F.-F. (2002), *A nonlinear mechanism for decadal El Niño amplitude changes*. Geophys. Res. Lett., No. 29, doi:10.1029/2001GL013369. (3)
- Kleeman R., McCreary J.P. & Klinger B.A. (1999), *A mechanism for generating ENSO decadal variability*. Geophys. Res. Lett., No. 26, pp. 1743-1746. (4)
- McCreary J.P. & Lu P. (1994), *Interaction between the subtropical and equatorial ocean circulations: the subtropical cell*. J. Phys. Oceanogr., No. 24, pp. 466-497. (5)
- Nonaka M., Xie S.P. & McCreary J.P. (2002), *Decadal variations on the subtropical cells and equatorial Pacific SST*. Geophys. Res. Lett., No. 29, doi:10.1029/2001GL013717. (6)
- McPhaden M.J. & Zhang D. (2002), *Slowdown of the meridional overturning circulation in the upper Pacific Ocean*. Nature, No. 415, pp. 603-608. (7)
- McPhaden M.J. & Zhang D. (2002), *Pacific Ocean circulation rebounds*. Geophys. Res. Lett., No. 31, doi:10.1029/2004GL020727. (8)

ADVANCES IN CLIMATE SCIENCE

Regional climate modelling and downscaling

A statistical downscaling system for seasonal projections using ensemble neural networks with Bayesian regularization

Amendola S.^{1,2}, Maimone F.^{2*}, Ciciulla F.², and Pelino V.²

¹CMCC Bologna, Italy,

²Italian Air Force, CNMCA, Rome, Italy

*Corresponding author: maimone@meteoam.it

Abstract

A novel statistical downscaling system for seasonal projections is presented, based on the outputs of an ensemble of neural networks incorporating Bayesian regularization. The system is able to take as input multiple predictor fields, and/or time series, which may be either model outputs, past observations, and even a combination of them. Focusing on the southern European area, examples of the latter include observational SST in the North Atlantic (with a time-lag of several months with respect to winter season), and model-estimated Madden Julian Oscillation indices (with time-lags of few weeks relative to the October-March period). Here additional predictors are intended to help re-connecting, in a statistical sense, those climate ‘nodes’ (e.g. between tropics and middle latitudes) that are represented as quite disconnected by the present generation of coupled ocean-atmospheric models. Referring to the technical aspects of our statistical system, gridded fields are compressed using EOFs, after which a canonical correlation analysis is performed between predictors and predictands. Then the first canonical variates of the formers are used as effective predictors. Final outputs for each parameter is expressed as a probability distribution for each station/grid point in the space of observations, as a result of the convolution of Gaussian mixtures, one for each principal component considered. Some preliminary results of the first version of the system, focused on three-month projections over Italy, are shown, while possible extensions of the scheme, e.g. concerning the use of the model ensemble spread as an additional information supply, are discussed at the end of the paper.

Keywords: *Empirical statistical downscaling, seasonal climate projections, neural networks, Bayesian regularization*



The need for an extension of weather forecast range beyond the limit of ten days is becoming more and more compelling in our society. Recent guidelines from the World Meteorological Organization (WMO) have strongly posed the invitation to each National Meteorological Service (NMS) to build up the necessary infrastructures to provide a Climate Service at the national level. Time scales of interest would range from 5 days to several months, and the products would include, for example, projections by climate global/regional models, climate monitoring of the major climate indices and climatic alerts to warn of a particular condition within the climatic system (which could be lead, for example, to intense events). Reference points to provide regional-scale products are Regional Climate Centers, like for example DWD for WMO's region VI, while the specific *responsibility* for the dissemination of the ultimate products within each Nation should be left to the single NMS. For this reason, operatively tailoring and calibrating regional scale monthly and seasonal projections should be among the main tasks of the climatological departments of each NMS.

In the middle latitudes a major source of variability is associated with the North Atlantic Oscillation, which, as it is well known, is characterized by a quite stochastic signal, at variance with the quasi-periodic phenomena occurring in the tropics, particularly in the Pacific. Coupled ocean-atmospheric models for seasonal predictions do not capture satisfactorily this variability, and then should be supplemented by other techniques providing a proper calibration and downscaling. Several empirical statistical downscaling methods have been designed up to now, that have been proved to compete with the most sophisticated dynamical downscaling modelling (see e.g. Ref.[1] for a review). Here one new method is illustrated, based on the use of ensemble neural networks analysis, which allows us to build up a quite general probability distribution for the predictand (often constrained to be just a Gaussian in other approaches).

The system has been realized in the MATLAB programming language, its architecture is set up in an XML configuration file (*Image 1*), through which all system's parameters are established, so it can be used as an user interface to set up the various model options. For example, by the configuration file it is possible set up training, verification and forecast years for the neural network; is obviously possible to set up forecast parameters or select the predictors, or the type of plot the operator wants to visualize as output, and so on.

```

<Seasonal_Forecast>
  <conf>
    <directory_predictors>G:\Dati\DATA_Seasonal\SF_System4\System4_training_1981-2010\</directory_predictors>
    <directory_predictors_verification>G:\Dati\DATA_Seasonal\SF_System4\System4_2011\</directory_predictors_verification>
    <directory_predictors_forecast>G:\Dati\DATA_Seasonal\SF_System4\System4_2012\</directory_predictors_forecast>
    <directory_observations>G:\Dati\E-OBS\E-OBS_CPT\</directory_observations>
    <directory_output>\Output\</directory_output>
    <forecast_parameter>In</forecast_parameter>
    <predictors>In,Tx,Tp</predictors>
    <data_type>S</data_type>
    <predictor_number>3</predictor_number>
    <Month_Run>05</Month_Run>
    <lead_months>2</lead_months>
    <Projections_Months>3</Projections_Months>
    <climatological_period>all</climatological_period>
    <num_EOF_predictors>5</num_EOF_predictors>
    <num_EOF_observations>5</num_EOF_observations>
    <num_canonical_variates>2</num_canonical_variates>
    <training_years>1981-2009</training_years>
    <verification_years>2010</verification_years>
    <forecast_years>1</forecast_years>
  
```

Image 1: A screenshot of the xml type configuration file

Basic version of the system uses as predictors the outcomes (T max, T min, T mean or cumulated rainfall) of the seasonal forecast model System4 (S4) of ECMWF represented on a regular lat-long grid of 0.75 x 0.75 deg. Besides, S4 reforecast ensemble means (available from 1981 to 2010 with 15 ensemble members) have been used to train the neural network. It has to be noticed that as S4 model climatology, all the 450 available ensemble members (15 members x 30 years) have been considered, according to ECMWF seasonal products. These forcings (predictors) are then mapped onto the observations of the same parameter (predictand), consisting in the EOBS observational gridded dataset [2], interpolated on a finer lat-long grid than S4, such as 0.25 x 0.25 deg; direct observational station data could also be used. We illustrate here the preliminary results of three-month projections, the typical time period of a seasonal forecast, so that we will consider averages of daily data on this time period. Predictors and predictands are pre-processed before being used to train the neural network. First of all, original data or their anomalies (standardized or not) can be used as the relevant variables. All these possibilities can also be set in the configuration file. In case of precipitation as predictand/predictor, a log-transformation can be performed, which allows generally to deal with more regular (Gaussian like) distributions.

As a weighting function for the grid boxes, the product by the cosine of their latitudes has been adopted. At this point Empirical Orthogonal Functions analysis (EOFs) is performed to compress the

spatial area information into a few principal component coefficients (PCs) [1],[3],[4]. We are then left with a few simple time series, and the field for each observational time can be thought as consisting of a weighted sum of a small number of different basis EOFs (“loading patterns”) describing the most important variability modes. Now Canonical Correlation Analysis (CCA) is performed ([1],[3],[4]) on the leading PCs of predictand/predictor, which allows in general to extract the maximum correlation modes between them. Again, only a few *canonical variates* time series (the analogous for CCA modes of the principal components for EOF modes) retain the relevant information.

Image 2 shows a simple scheme illustrating also the pre-processing just described. At this point the neural network analysis (NN) comes into play [5,6].

Statistical downscaling system for seasonal projections on Italy: general scheme

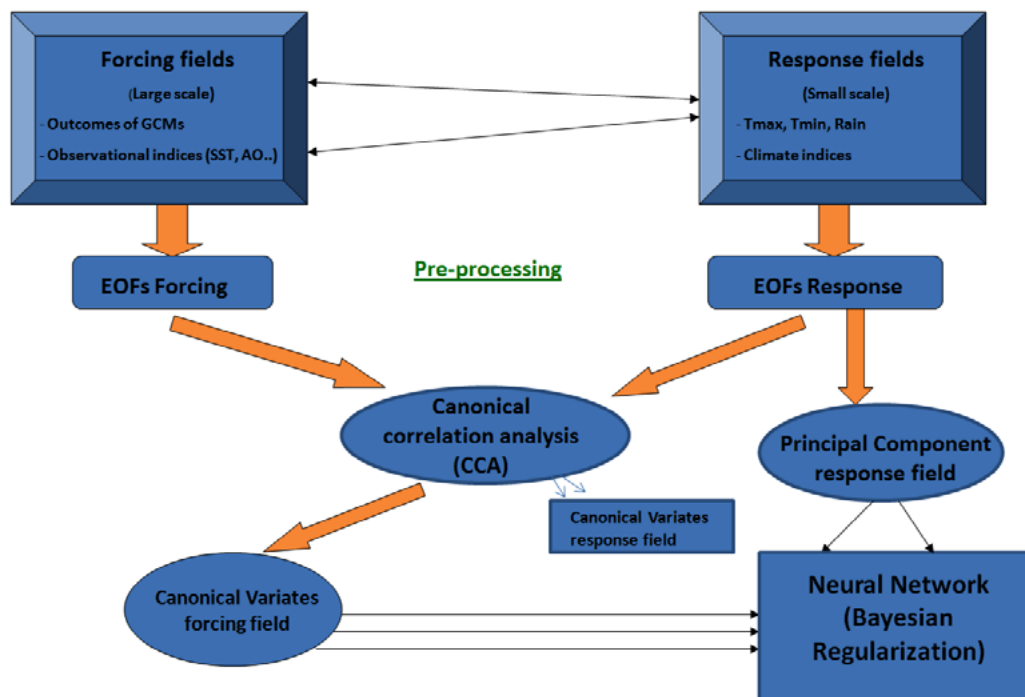


Image 2: A general scheme of the pre-processing of the downscaling system

The NN employed in the system is a feed forward multilayer perceptron. It is endowed with two hidden layers, the former having a number of neurons equal to the number of inputs, and the latter has a single neuron and finally the output layer with one outcome (Image 3). The NN take as input first n selected canonical variates of predictand (or forcing) and is trained to give as output first m selected

predictand PCs, one at a time, that is NN work separately for each *m-th* predictand PCs. Then in basic version of model the correspondent System4 parameter PCs on the smaller Italian area are given.

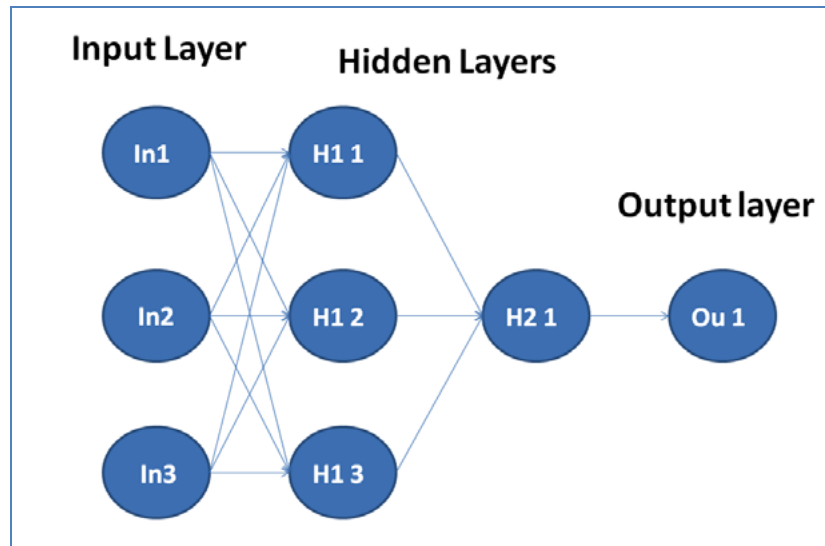


Image 3: Simple scheme of a neural network with two hidden layers

The input signal is mapped on first hidden layer by a hyperbolic tangent sigmoid transfer function, while a linear function is used in second hidden layer.

Generally a NN with a large number of neurons is able to reconstruct in detail the values of whatever target, but in that case NN risk to overfit data and no realistic regression law is obtained. So some input-output data pairs must be excluded from the training process (by means of which regression law is built) and a small number of hidden neurons should be used. Only if the NN is able to reproduce target data excluded from the training (*validation data*) a good system has been obtained. At this end data record has to be divided into *training data*, on which to train the NN, and *validation data* used to test the NN skill. Depending on the results, if necessary NN model can be modified.

When data records are not plentiful, *cross-validation* technique is applied in order to take advantage of the entire data set for validation. With this procedure data record is divided in K segments, then one segment is used as validation data and the other K-1 are used to train the NN, this process is repeated for all K segments. In this case some data must be left out of the cross-validation in order to measure the model forecast error. But this approach turns out to be rather bulky and does not allow us to use the entire data record to train our NN model, so a Bayesian approach has been implemented. The

method, based on Bayes theorem, allows to determine the NN weights without the need for validation data. Regularization methods add penalty coefficients to the weights in order to control non-linearity of the transfer function and reduce overfitting problems. To obtain an estimate of the associated error, an approach similar to the cross-validation has been adopted: the data record has been divided into K segments, one of which has been used to calculate the error and the others K-1 to train the network; this process is repeated for all the segments. Besides, this procedure has been repeated a certain number of times by re-initializing the NN weights using Nguyen-Widrow approach in order to decrease the training time [7]. In this way, we obtain an ensemble of NNs (*Figure 1*) each of which with its own associated mean error.

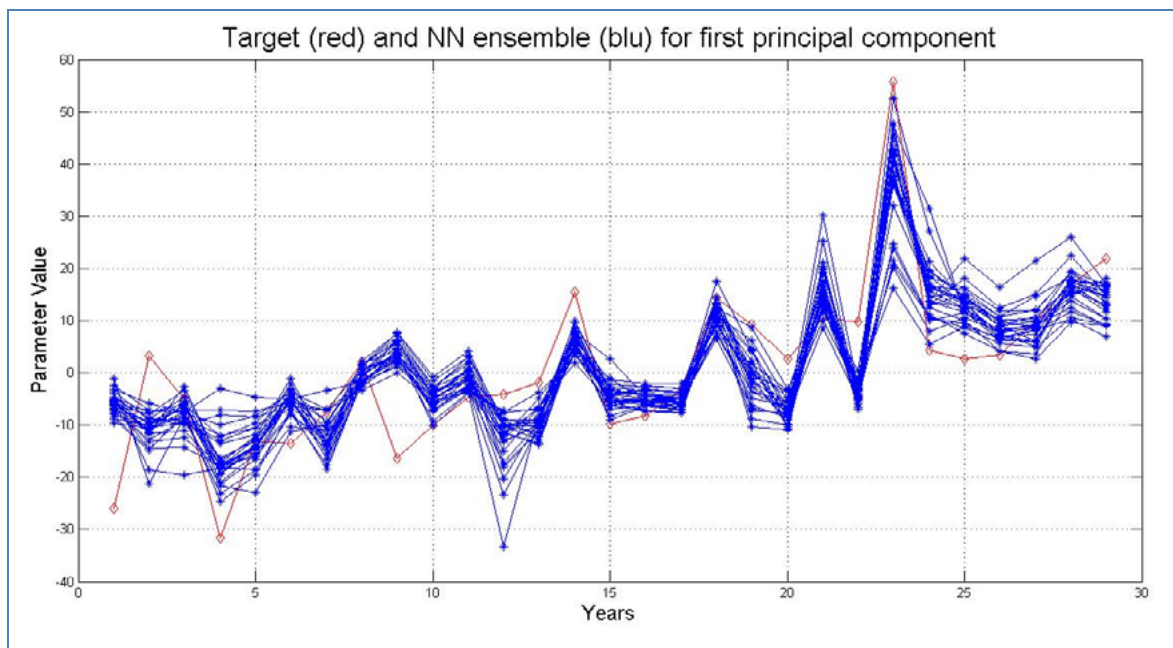


Fig. 1: An example of the outcomes of our neural network system. In red the target of the network, in blue the ensemble’s members. This ensemble reconstructs the first PCs of the response field; similar outputs are obtained for successive PCs.

As previously described, our NN is trained with Bayesian method using predictor and predictand datasets referred to their longest overlapping time period. At this point our system is ready to give a forecast by applying the appropriate input (the canonical variates obtained from the current operational ECMWF seasonal forecast model output) to the so constructed neural network model. In so doing, we obtain an ensemble for each of the first predictand PCs. We take advantage of these ensembles to reconstruct the probability density function (PDF) of each predictand PCs as a Gaussian mixture

distribution (GM distribution) of the different ensemble members, that is a weighted average of the Gaussian distributions, each of which related to a given ensemble member. In this way it is possible to take into account the effects of a number of physical mechanisms affecting the observed variables and hence to reproduce a more appropriate multimodal behaviour. Once obtained, these PDFs must be finally recombined to give the distribution of the response field (one distribution for each grid point/station data); this is the final output of the statistical downscaling model. In order to recombine these PDFs, Fourier transform (FT) convolution theorem is used. This theorem states that FT of the convolution between two functions is equal to the product of the FTs of the single functions :

$$F\{f * g\} = F\{f\} \cdot F\{g\}.$$

Dealing with a numerical approach, we have a set of discrete points, so discrete Fourier transform has to be used and indeed Fast Fourier Transform (FFT) is used. According to this approach, PDFs for each grid point are reconstructed sequentially applying convolution theorem to suitably rescaled principal component PDFs (*Figure 2*). Initially the convolution between the first two principal component PDFs is carried out; then convolution between the third one and the result of the first convolution is performed and so on, until the last PDF is taken into account. The final result on the grid-point space is then obtained by combining the various EOF response field. In *Figure 3* the case for a given grid point is shown, together with the climatological 33th and 66th percentiles.

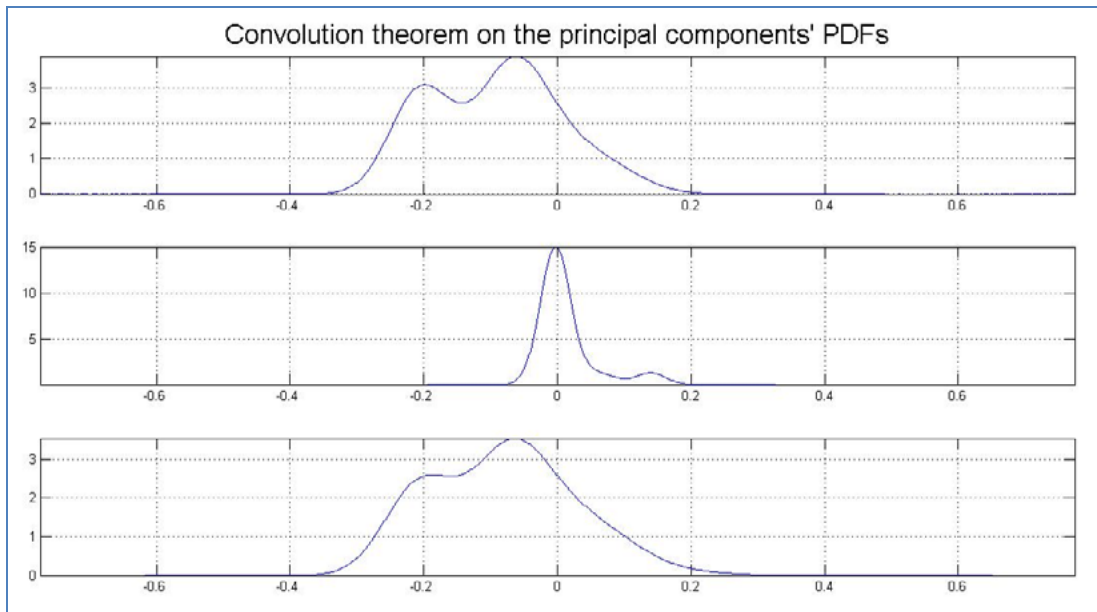


Fig. 2: An example of the application of the convolution theorem: in the upper figure there is the result of the convolution between first and second PCs' probability density functions; in the middle figure the third PC's PDF; in the below figure there is the convolution between first two. The procedure is applied for all involved PCs.

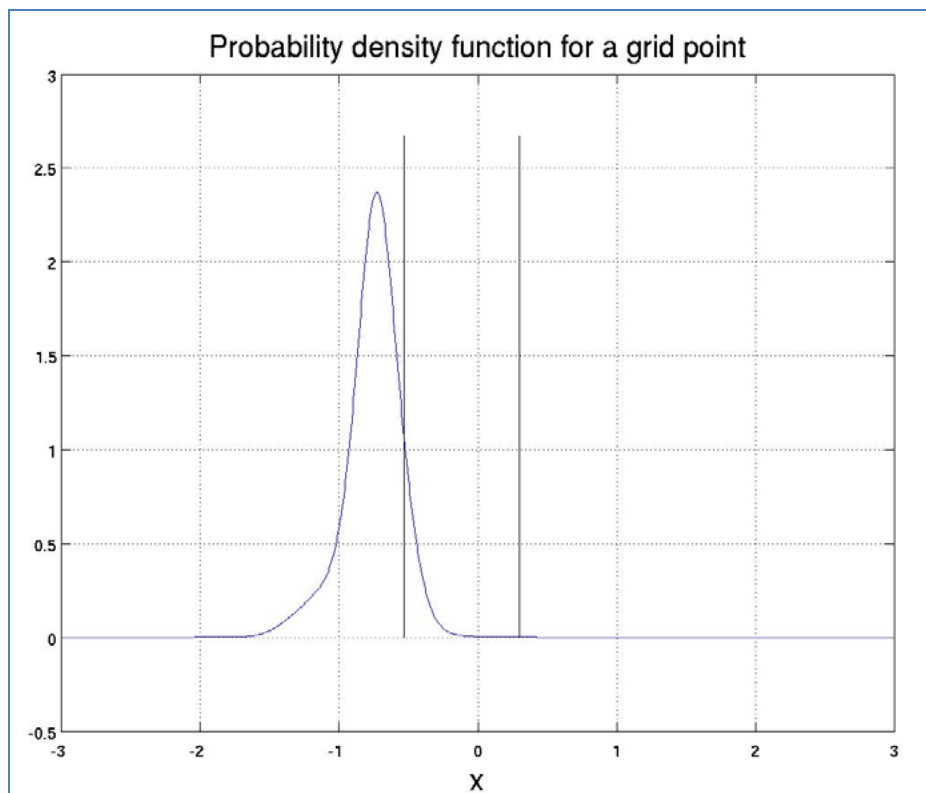


Fig. 3: An example of the output of the statistical model; a PDF for a grid point is shown together with climatological percentiles. A similar PDF is constructed for each grid point of the response field.

Starting from grid-point PDFs it is possible to obtain the various probabilistic seasonal forecast maps, similar to those provided by ECMWF for System4 direct output, by integrating them between the chosen threshold percentiles.

Moving now to the validation aspects, it should be stressed that our system output is constructed from input data not used in the training phase; a first qualitative skill estimate can then be given, since the corresponding observations are available. Then some three-month periods are left out of training in order to compare model output with EOBS dataset, and also with the direct System4 forecasts. As an example in *Figure 4* an outcome of the system for 1995 JJA mean maximum temperature is presented. This figure shows a tercile summary with the probability of the prevailing conditions relative to the considered percentile intervals (lower, central and upper tercile). For a qualitative comparison, the maps of system output (*Figure 4*), EOBS data (*Figure 5*) and System4 outcome (*Figure 6*) for the same period are shown. Concerning the System4 output, it should be noticed that the probability maps we use for comparison are obtained from the first 15 ensemble members (corresponding to the same set considered for model climatology) in spite of the fact that operational seasonal forecasts, available since 2011, are based on a total of 51 ensemble members.

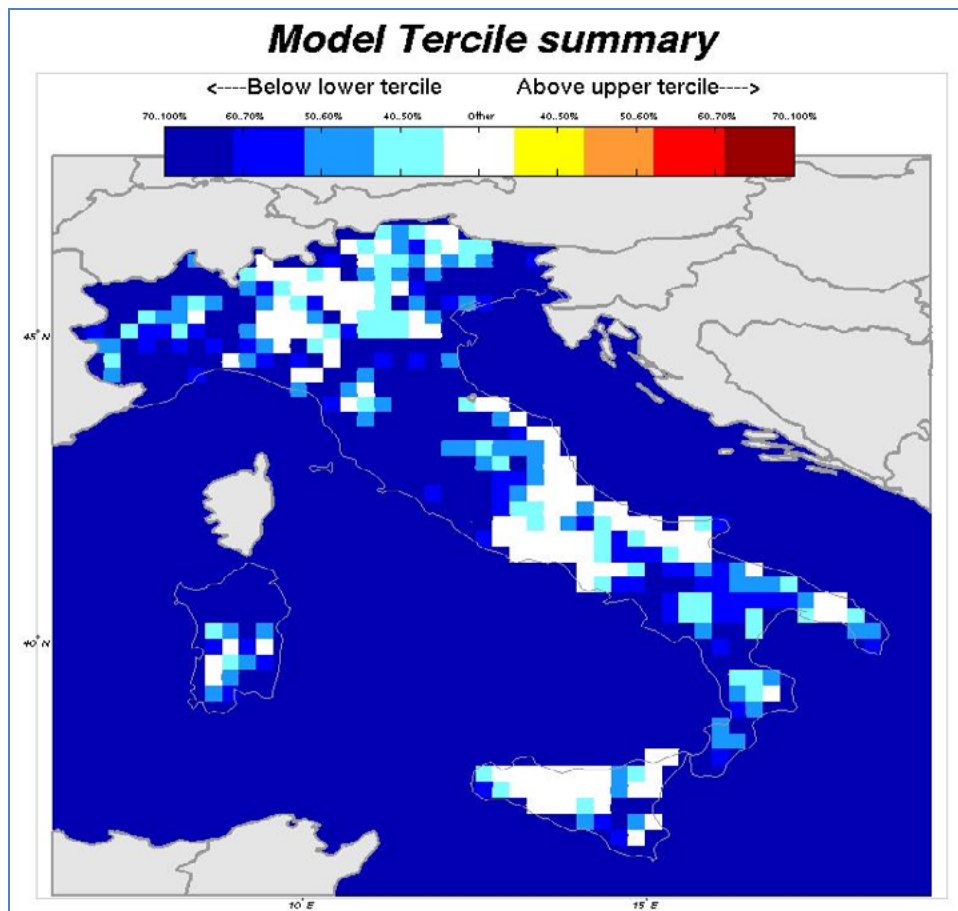


Fig. 4: An outcome of the downscaling system for Tmax mean relative to 1995 JJA quarter, period excluded from the training.

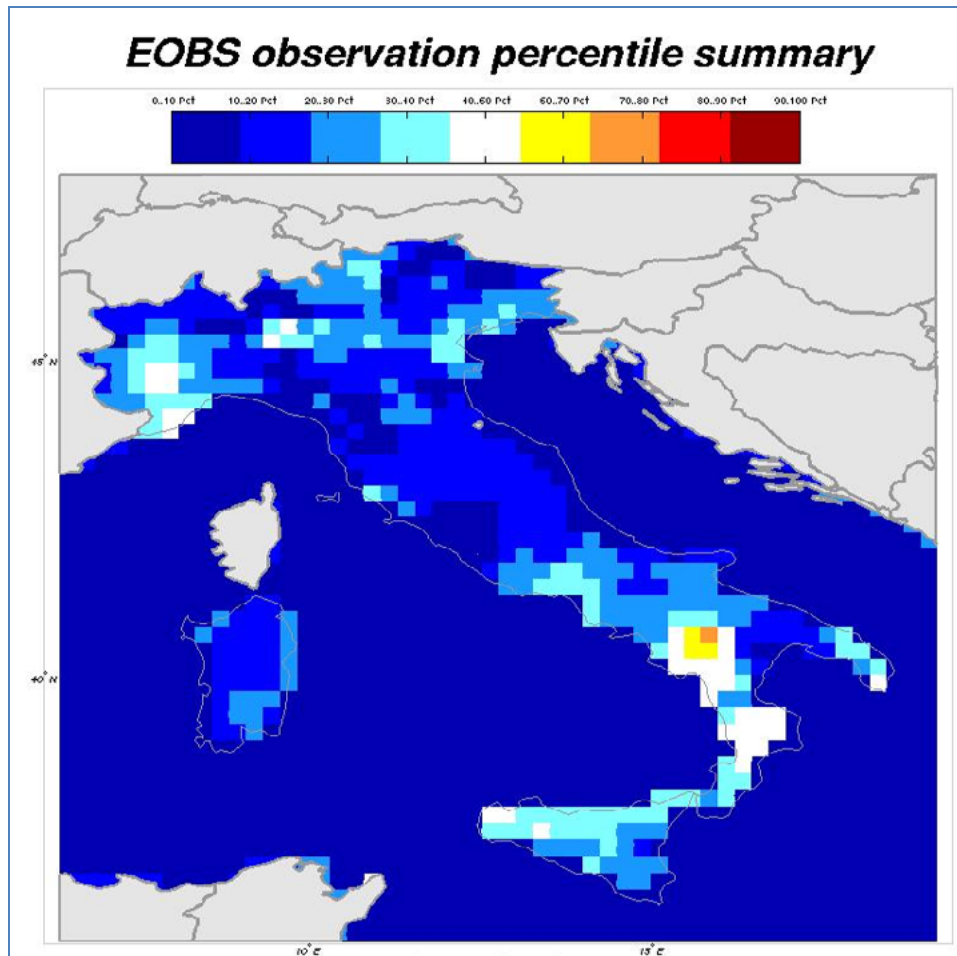


Fig. 5: EOBS observation for the same quarter as in Figures 4,6. The observed temperature is classified in various percentiles categories in confront with 1981-2010 climatology.

Comparing the *Figures 4, 5 and 6*, it is quite evident an overall improvement due to our downscaling system with respect to System4 outcome. Notice as our downscaling system is more able to detect regional details and reproduce the correct anomalies in a quite realistic way than a coarse resolution GCM. However, a deeper analysis of the performance of the system (evaluation of anomaly correlation, ROC area, reliability, etc.) is necessary to quantitatively asses its real skill.

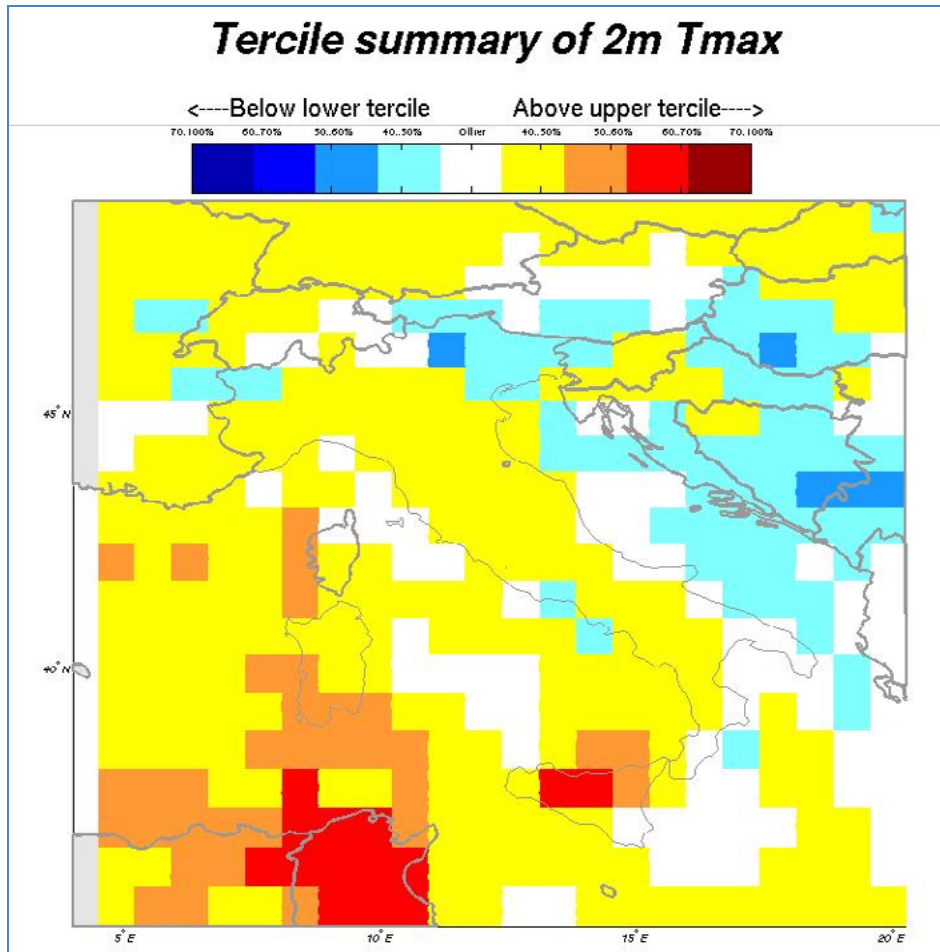


Fig. 6: The outcome of System4 model for the same quarter as in Figures 4-5. It is shown the same tercile summary as in Figure 4. Apart from the above qualitative comparison, a spatial Spearman correlation map calculated for the training period between model outputs and observations is shown in Figure 7. It is possible to see over which areas we may expect a better system performance.

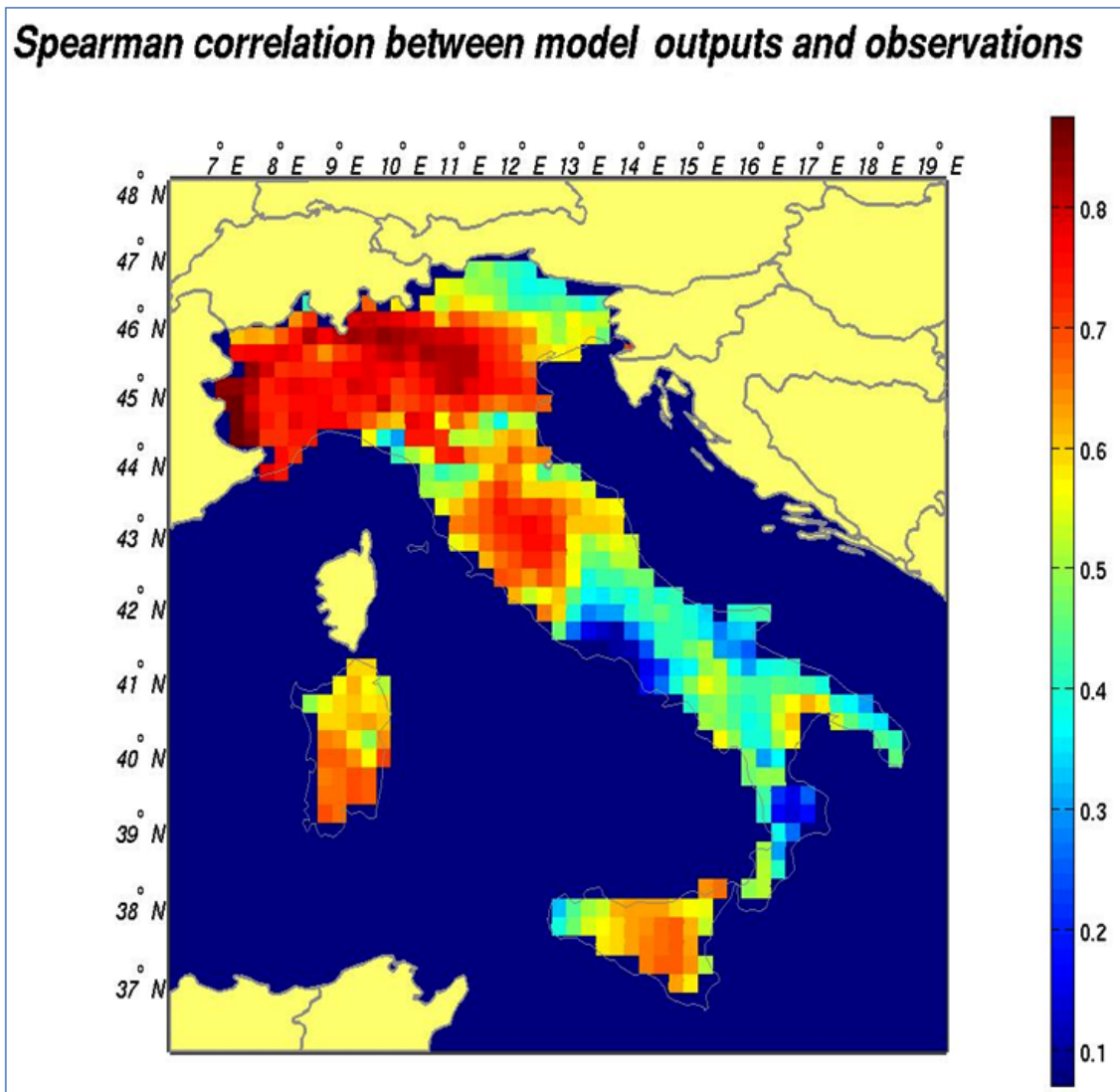


Fig. 7: A map of the Spearman correlation over the downscaling scenario between model output and observations relative to the training period.

Up to now we have used a single predictor field scheme. Nevertheless, our system is able also to ingest additional predictor fields. In general, when including more than one predictor into a statistical forecasting model, a typical problem one is faced with is whether to include all of them, or a particular subset, and in the latter case how to choose among the predictors. General criteria are: 1) maximize the information content; 2) avoid redundancy in the information [3]. Concerning this last point, it has been shown that redundancy is not just superfluous, but also undesirable. The method of ‘screening of predictors’ we have chosen is that of *forward selection* with linear regression. In practice, to begin with, one tries all the single predictors and finds the best one, based on the best correlation R between

predictors and predictand. Then one adds to the chosen predictor, another predictor at a time, and selects the best for the two-dimensional regression, and so on, finally obtaining a ranking of all the available predictors. As a stopping rule, we consider the RMSE minimum value on an independent sample. To be specific, a module of the system calculates the performance using successively one predictor, two predictors etc., taking each time a verification sample apart, and projecting the corresponding predictand onto it. Plotting the RMSE of the projections versus the number of predictors employed, one obtains a curve generally exhibiting a minimum. The number of predictors in coincidence with this minimum will be the chosen one. Parenthetically, linear regression is justified here by the regularization procedure adopted, by which neural network can be considered as a relatively small non-linear correction to a basic linear analysis.

As an example of the use of multiple predictor fields, we have included monthly SST field over North Atlantic ocean to project T_{max} mean onto the winter quarter DJF, with a time lag of 6 months. Retaining the first 4 canonical variates for both System4 T_{max} and SST fields, we have obtained an improvement on the Spearman correlation from 0.35 to 0.51, on the average over Italy.

On the predictands side, apart from the basic parameters like mean maximum temperature, cumulated precipitations, etc, it would be interesting to use some derived climatic indices (like, for example, CLIMDEX indices) which may be able to take into account also extreme conditions (say, heat waves during summertime, prolonged droughts, cold waves, etc.). In that case one could compute the same direct parameter for the seasonal forecast model, eventually using some additional predictors.

Another kind of extension that is being developed concerns the use of a different kind of preprocessing for the data in the space of observations, i.e. using cluster analysis. A cluster analysis based on monthly or seasonal data applied to a given parameter, or a set of parameters, is useful to find out the relative 'climatic zones'. Given that each climatic zone may be associated with a particular large-scale pattern of the forcing, it could be useful to apply the procedure to each cluster separately, and extract from the EOF and CCA analysis the most relevant signal appropriate to that particular zone.

Another forthcoming extension of the system refers to the use of model-ensemble spreading information. It is customary, and even safe, in the statistical downscaling practice to use just ensemble-mean fields as predictors, as we have done so far. Such a practice has at least three a-priori justifications. First, these fields typically present the best skill scores among all the ensemble members taken separately; second, statistical machinery (cross-validation) furnishes by itself probabilistic

forecasts, while taking into account other ensemble members would add a seemingly spurious extra level of probability; third, variability is often underestimated in many regions of the world. Nevertheless, variability remains an important part of the information content of GCM outputs, and considering the uncertainty associated with the model predictors could reveal itself an useful exercise. One possibility, that is being explored in the context of our system, is the use of ‘fuzzy PCs’ of the predictor fields. The associated uncertainty can be easily propagated on the linearly related canonical variates. Then, neural network can be used to calculate a ‘derivative’ associated to the predictor perturbations, and the resulting extra level of uncertainty added to the final PDFs.

In conclusion, we have presented the first version of a new integrated system for statistical downscaling of seasonal forecasts. The main strength points are 1) the account for non-linear relations between predictors and predictands by means of Bayesian regularization neural network ensembles; 2) the consideration of generally non-Gaussian PDFs for predictand outputs; 3) the possibility to take into account multiple predictor fields or time series.

A full assessment of the skill of the system, and an extension of it to include the spreading information associated with GCM ensemble outputs, is currently under development.

ACKNOWLEDGMENTS

Financial support of the project for one of us (S.A.) by CMCC, Euro-Mediterranean Center for Climate Change, is acknowledged.

We acknowledge also the E-OBS dataset from Eu-FP6 project ENSEMBLES (<http://ensembles-eu.metoffice.com>) and the data providers in the ECA&D project (<http://www.ecad.eu>).

REFERENCES

- Benestad R. E., Hanssen-Bauer I., Chen D. (2008), Empirical-Statistical Downscaling, *World Scientific Pub Co Inc.* (1)
- Haylock M.R., Hofstra N., Klein Tank A.M.G., Klok E.J., Jones P.D., New. M. (2008), *A European daily high-resolution gridded dataset of surface temperature and precipitation*. *J. Geophys. Res (Atmospheres)*, **113**, D20119, doi:10.1029/2008JD10201. (2)

- Wilks D.S. (2006), *Statistical Methods in the Atmospheric Sciences, Second Edition, International Geophysics Series*, Academic Press. (3)
- Peixoto J.P., Oort A.H. (1992), *Physics of Climate*, American Institute of Physics. (4)
- Hsieh W.W. (2009), *Machine Learning Methods in the Environmental Sciences Neural Networks and Kernel*, Cambridge University Press. (5)
- Pasini A., Langone R. (2012), *Influence of Circulation Patterns on Temperature Behavior at the Regional Scale: A Case Study Investigated via Neural Network Modeling*, *Journal of Climate*, **25**, 2123. (6)
- Nguyen D., Widrow B. (1990), *Improving the Learning Speed of 2-Layer Neural Networks by Choosing Initial Values of the Adaptive Weights*, in the Proceedings of the International Joint Conference on Neural Networks, 3:21–26. (7)

Multimodel SuperEnsemble Downscaling of Regional Climate Models in South-Western Alps

Cane D.^{1*}, Barbarino S.^{1,2}, Renier L. A.¹, Ronchi C.¹

¹Regional Agency for Environmental Protection - Arpa Piemonte, Torino, Italy,

²Istituto Scienze dell'Atmosfera e del Clima - ISAC-CNR, Torino, Italy

*Corresponding author: daniele.cane@arpa.piemonte.it

Abstract

The climatic scenarios show a strong signal of warming in the Alpine area already for the mid XXI century. The climate simulations, however, even when obtained with Regional Climate Models (RCMs), are affected by strong errors when compared with observations, due both to their difficulties in representing the complex orography of the Alps and to limitations in their physical parametrization.

The aim of this work is to reduce these model biases by using a specific post processing statistic technique, in order to obtain a more suitable projection of climate change scenarios in the Alpine area.

For our purposes we used a selection of Regional Climate Models (RCMs) runs which were developed in the framework of the ENSEMBLES project. They were carefully chosen with the aim to maximise the variety of leading Global Climate Models and of the RCMs themselves, calculated on the SRES scenario A1B. For the study area of Piedmont daily temperature and precipitation observations (covering the period from 1957 to the present) were carefully gridded on a 14-km grid over Piedmont Region through the use of an Optimal Interpolation technique.

Hence, we applied the Multimodel SuperEnsemble technique to temperature fields, reducing the high biases of RCMs temperature field compared to observations in the control period.

We also proposed the application of a brand new probabilistic Multimodel SuperEnsemble Dressing technique, already applied to weather forecast models successfully, to RCMs: the aim was to estimate precipitation fields, with careful description of precipitation Probability Density Functions conditioned to the model outputs. This technique allowed to reduce the strong precipitation overestimation, arising from the use of RCMs, over the alpine chain and to reproduce well the monthly behaviour of precipitation in the control period.

Keywords: *Regional Climatic Models, Multimodel SuperEnsemble, Alps*



1. INTRODUCTION

The Alps are a region very sensitive to the impacts of the climate change: the temperatures increased here more than the world average [1] and the projections for the XXI century show again an increase higher than the average.

Piedmont Region is located in North-Western Italy, at the South-Western edge of the Alpine chain. The temporal target of our work is the mid XXI century, to drive conclusions that can be used to concrete adaptation measures to the climate change in a reasonable time.

Then we chose to focus on a single scenario (SRES A1B) instead of a range of different scenarios as, for our time interval of interest, the largest variations occur among the different models, while the different scenarios do not differ so much [2].

In this work we applied Multimodel techniques on several Regional Climate Models (RCMs) outputs, which are combined together to obtain collective evaluations.

Multimodel combination is a pragmatic approach to estimate model uncertainties and to make climate projections more reliable. Their use in the climatic simulations is recommended by the Intergovernmental Panel on Climate Change [3]. The simplest Multimodel technique is the “Poor Man Ensemble”, which is an average of different models, without any bias correction or weighting (“equal weighting”), while more sophisticated approaches suggest applying model weights according to some measure of performance (“optimum weighting”). The results confirm that equally weighted multimodels on average outperform the single models [4, 5], and that projection errors can in principle be further reduced by optimum weighting. However, this not only requires accurate knowledge of the single model skill, but the relative contributions of the joint model error and unpredictable noise also need to be known to avoid biased weights [6]. Many weighting procedures were proposed on seasonal, decadal and climatic models [7, 8, 9]. Christensen et al. [10] showed that the use of model weights is sensitive to the aggregation procedure and showed different sensitivities to the selected metrics. They suggested that model weighting adds another level of uncertainty to the generation of ensemble-based climate projections, which should be suitably explored, although their results indicate that this uncertainty remains relatively small for the weighting procedures examined. In this study the uncertainty of the Multimodel techniques applied is carefully evaluated.

2. INPUT MODELS AND OBSERVATION

For the study area of Piedmont, daily temperature and precipitation observations (covering the period from 1957 to the present), collected by the Environmental Protection Agency of Piedmont Region, were gridded on a 14-km grid (0.125° resolution, with careful description of the complex orography of the region) over Piedmont Region (coordinates: 6.5625-9.4375 E/44.0625-46.4375N): an Optimal Interpolation (OI) technique was used to assimilate the low and high density ground station data, arbitrarily displaced in the region, on a regular three-dimensional grid map based on a background field [11].

Only for temperature, the background field is obtained by a linear tri-dimensional downscaling of ERA-40 archive spanning from 1957 to 2001 and of the ECMWF objective analysis from 2002 to 2009 on the selected grid.

The Regional Climate Models (RCMs) used in this study come from the EU project ENSEMBLES on the SRES scenario A1B basis: all the model runs refer to the same grid including Europe. The RCMs simulations used in this paper are a selection of 7 RCMs runs resulting from the ENSEMBLES project (Tab. 1), carefully chosen in order to maximise the variety of leading Global Climate Models and of the RCMs themselves, and with a data amount compatible with our elaboration and storage facilities. Models descriptions can be found at <http://ensemblesrt3.dmi.dk/>.

Acronym	Reg. Clim. Model	Global Clim. Model	Run by
DMI	HIRHAM5	Arpege	Danish Meteorological Institute
ICTP	REGCM3	ECHAM5	The Abdus Salam Intl. Centre for Theoretical Physics
HC	HadRM3Q0	HadCM3Q0	Hadley Centre for Climate Prediction and Research
CNRM	RM4.5	Arpege	Météo-France CNRM/GMGEC/EAC
ETHZ	CLM	HadCM3Q0	Swiss Institute of Technology (ETHZ)
KNMI	RACMO2	ECHAM5	The Royal Netherlands Meteorological Institute
MPI	REMO	ECHAM5	Max Plank Institute - Hamburg

Tab. 1: the models used in the Multimodel SuperEnsemble evaluation

For each model, the reanalysis runs from the ECMWF ERA-40 reanalysis (1961-2000) and the scenario runs (1961-2100) on SRES scenario A1B are available on a common grid at a resolution of 25 km.

We interpolated the daily data from the models on the OI grid with a simple bi-linear interpolation. The use of such an interpolating technique can introduce biases, but the Multimodel techniques include a bias removal before applying the model average.

3. DOWNSCALING OF TEMPERATURES

In the Multimodel SuperEnsemble technique [4] the models are unbiased and weighted with an adequate set of weights calculated during the so-called training period, with comparison with the observations. This technique is widely applied to weather forecast models (an example in Piedmont can be found in [12]) and to seasonal climate forecasts [13]. The standard Multimodel SuperEnsemble technique was here applied to the temperature fields regarding the period 1961-1980 as training dataset to calculate weights and to obtain daily fields of reanalyses (1981-2000) and scenarios (1981-2050).

We evaluated the Multimodel SuperEnsemble uncertainty with a explicit calculation of the model variances and covariances in the training period, and combining them with the multimodel weights to obtain the final multimodel variance (here calculated in the hypothesis of non-independent models).

We tested the technique on the past data, splitting the control period of the models into two halves: the first one (1961-1980) was used as training period, the second one (1981-2000) as forecast period.

We decomposed the models and Multimodel time series in the trends and seasonal components with the Seasonal Decomposition of Time Series by LOESS [14] and compared them with the observation series.

The Multimodel SuperEnsemble temperature fields show a very good reduction of model biases (Fig. 1) and a very close reproduction of the temperature monthly statistics (Fig. 2). In this paper we show only the validation results of the maximum temperature, but those of minimum temperature have identical skill. Please notice that, in the control period, the reanalyses and scenario runs from the models show not only strong biases towards the observed temperature but, more worrying, the trends sometime differ in a very significant way, and the reanalysis and scenario runs from the same model very often show a different behaviour.

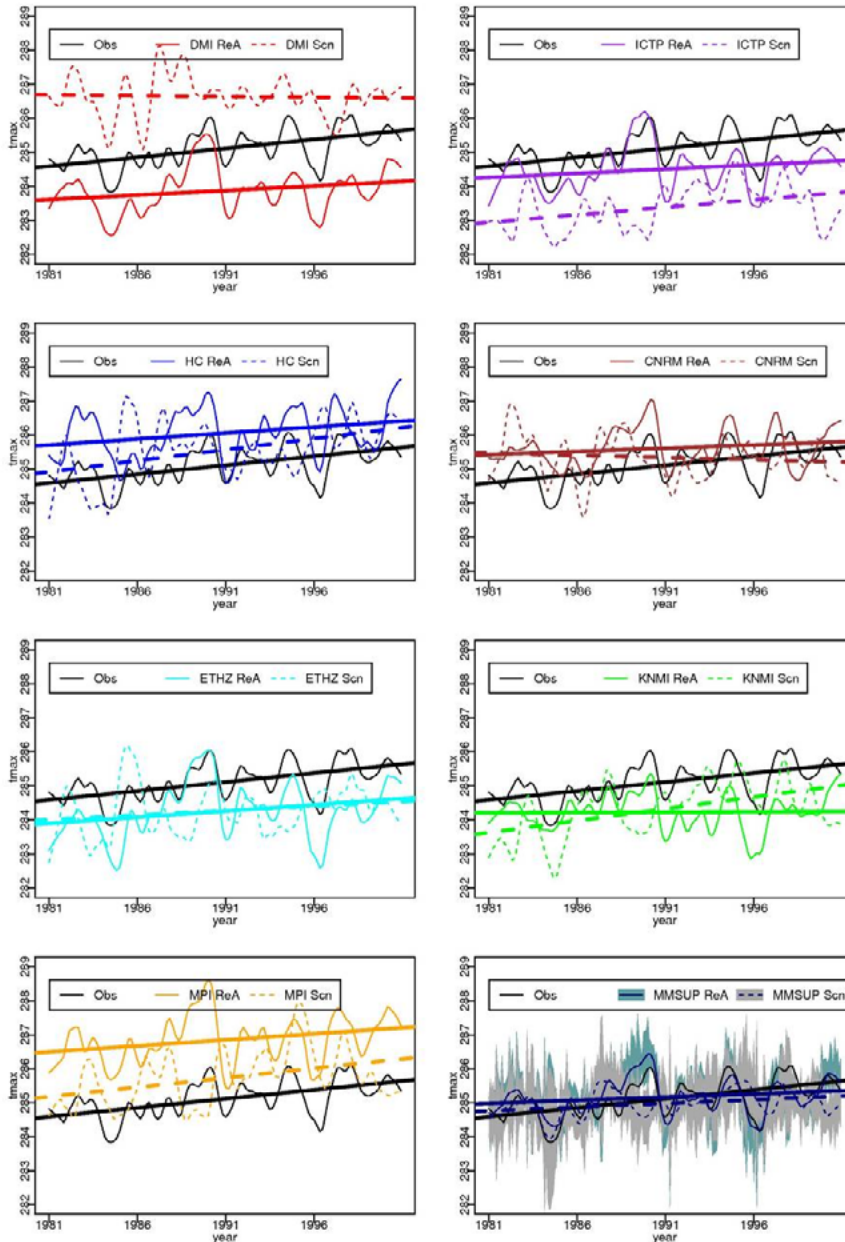


Fig. 1: Comparison between trends from observations obtained with Optimal Interpolation of Piemonte data (black lines), reanalysis runs (solid lines) and scenario runs (dashed lines) for different models (acronyms in Table 1) and Multimodel SuperEnsemble (MMSUP) in the period 1981-2000. Multimodel training period: 1961-1980. Multimodel uncertainty (square root of the total multi-Normal variance) is represented as confidence bands.

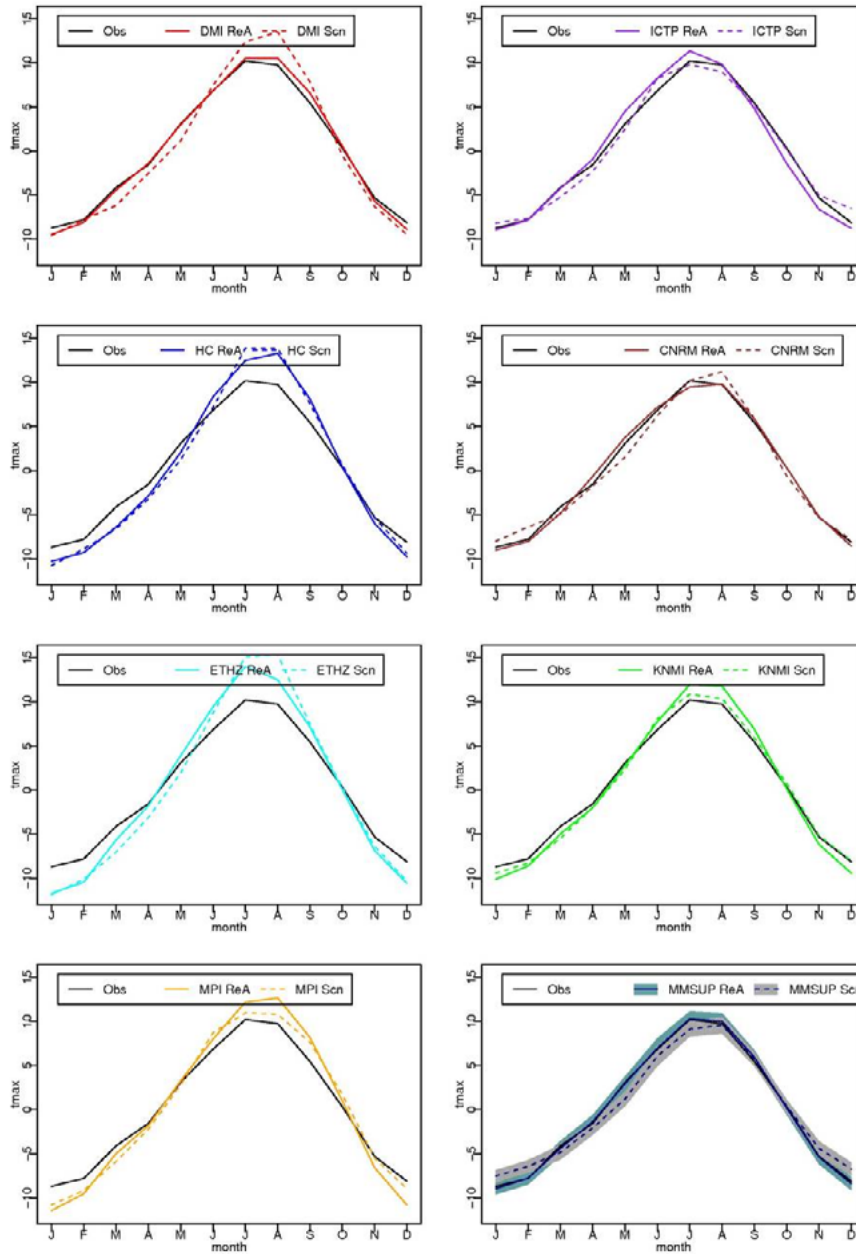


Fig. 2: Comparison between seasonal component from observations obtained with Optimal Interpolation of Piemonte data (black lines), reanalysis runs (solid lines) and scenario runs (dashed lines) for different models (acronyms in Table 1) and Multimodel SuperEnsemble (MMSUP) in the period 1981-2000. Multimodel training period: 1961-1980. Multimodel uncertainty (square root of the total multi-Normal variance) is represented as confidence bands.

We evaluated the difference between the Multimodel SuperEnsemble scenario data averaged over the period 2031-2050 with respect to the period 1981-2000, as a function of the season (comparison was made on the scenario for better consistency, but the scenario is very close to observations). The scenario projection shows a significant increase of the temperatures over the region. This increase is shown also by the original RCMs, but the post-processed data allow a better characterization of the alpine region, with an increasing and more realistic variance of temperature variations as a function of the altitude, thanks to the calibration with observations (Fig. 3).

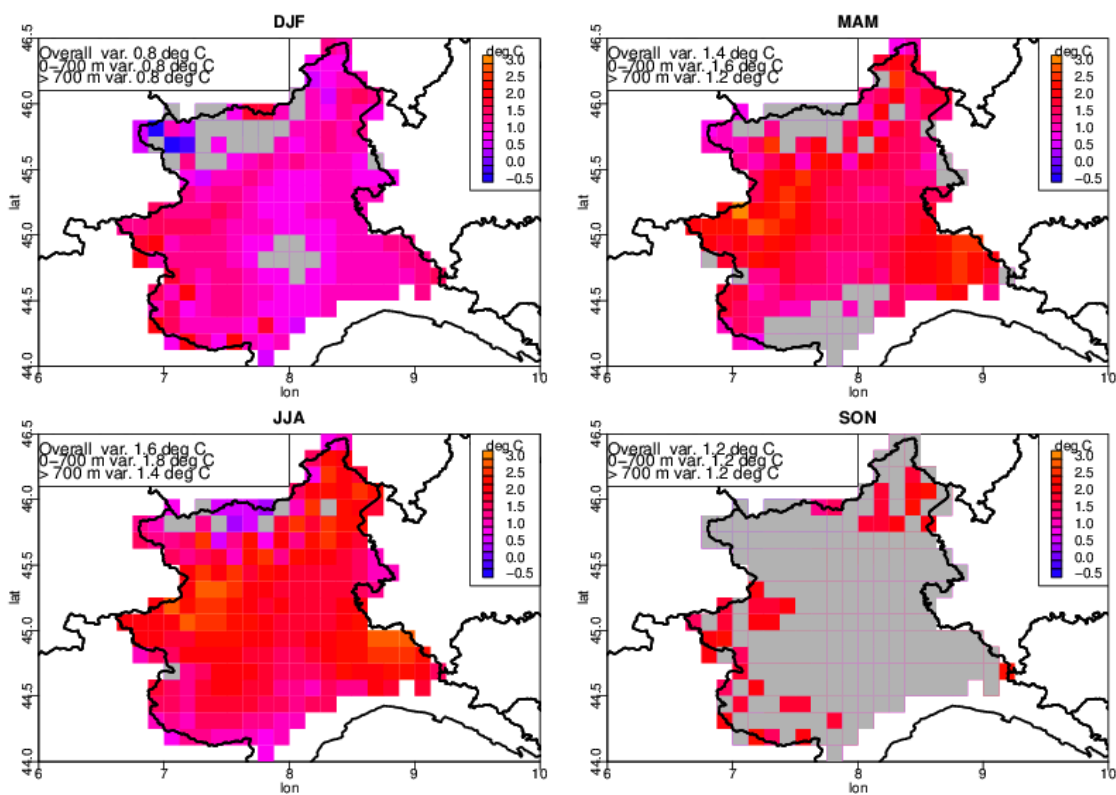


Fig. 3: Difference between the Multimodel SuperEnsemble scenario maximum temperatures averaged over the period 2031-2050 with respect to the period 1981-2000, as a function of the season (T-test conf. level 95%) in Piemonte region. In the upper left boxes overall averages over significant points and altitude bands averages are shown.

In particular, maximum temperatures averaged in the study area show significant increase in winter (+0.8 °C), spring (+1.4 °C), summer (+1.6 °C) and autumn (+1.2 °C limited to the mountains). Maximum temperatures during spring and summer increase more on the plains than in the mountains.

Minimum temperatures show significant increase in winter (+1.1 °C), spring (+1.3 °C), summer (+1.8 °C) and autumn (+1.3 °C limited to the mountains). Minimum temperatures during autumn and winter increase more on the plains than in the mountains (not shown).

4. DOWNSCALING OF PRECIPITATION

A new probabilistic Multimodel SuperEnsemble Dressing, with close description of precipitation Probability Density Functions conditioned to the model outputs was applied to the precipitation fields. This technique allows for a better correction of precipitation biases depending on the value of the forecast precipitation and was already applied on weather forecast models [15].

Here we describe the steps to evaluate the PDFs and the weights for each model:

- we took the ERA40-driven RCMs and compared them with the observed precipitation on all gridpoints
- we considered all the days and points where the model produces a given precipitation;
- we built the distribution of the observed values of that days/points (with bins of width ± 0.5 mm around the central value) and repeated for any reasonable forecast value (up to 300 mm/day)
- we fitted the distributions so obtained with a set of functions, finding that the Weibull function is the best one to represent all of the distributions among a large set of possible candidates
- we interpolated and extrapolated the observed distributions to obtain all possible distributions for all forecast values and we obtain the function PDF(F), where F is the precipitation forecast value
- we calculated the individual RCMs Continuous ranked Probability Scores (CRPS) from ERA40-driven models
- we calculated the weights as the inverse of the CRPSs, normalized to their sum
- we applied the model-specific PDFs and the weights to the GCM-driven models to obtain weighted PDFs.

For any given day a value is extracted randomly from the PDF so-obtained to give a unique time series of precipitation. The use of a random extraction is justified by the large number of the samplings

(~25000 in the considered period) and by the uncorrelation between the scenarios and the observations.

We addressed multimodel uncertainty using a MonteCarlo technique: we simulated 100 realizations of the multimodel precipitation from our empiric PDFs and we evaluated the statistics (average and quantiles) of monthly precipitation and yearly wet/dry periods (defined as the average number of periods with precipitation above/below 1 mm lasting more than 5 days).

The Walter and Lieth [16] diagrams referred to precipitation produced by climate models show very strong biases (up to 200% during winter months) in the Alpine region when compared with observations. In Fig. 4 we compare the Walter and Lieth diagrams after removing each model yearly averaged bias, to obtain a fair comparison with Multimodel which is almost unbiased. Multimodel does not show very large biases in any month and reproduces the precipitation annual distribution quite well, both in time and amount. Only two input models out of seven have quite comparable skill, not taking into account their large average biases.

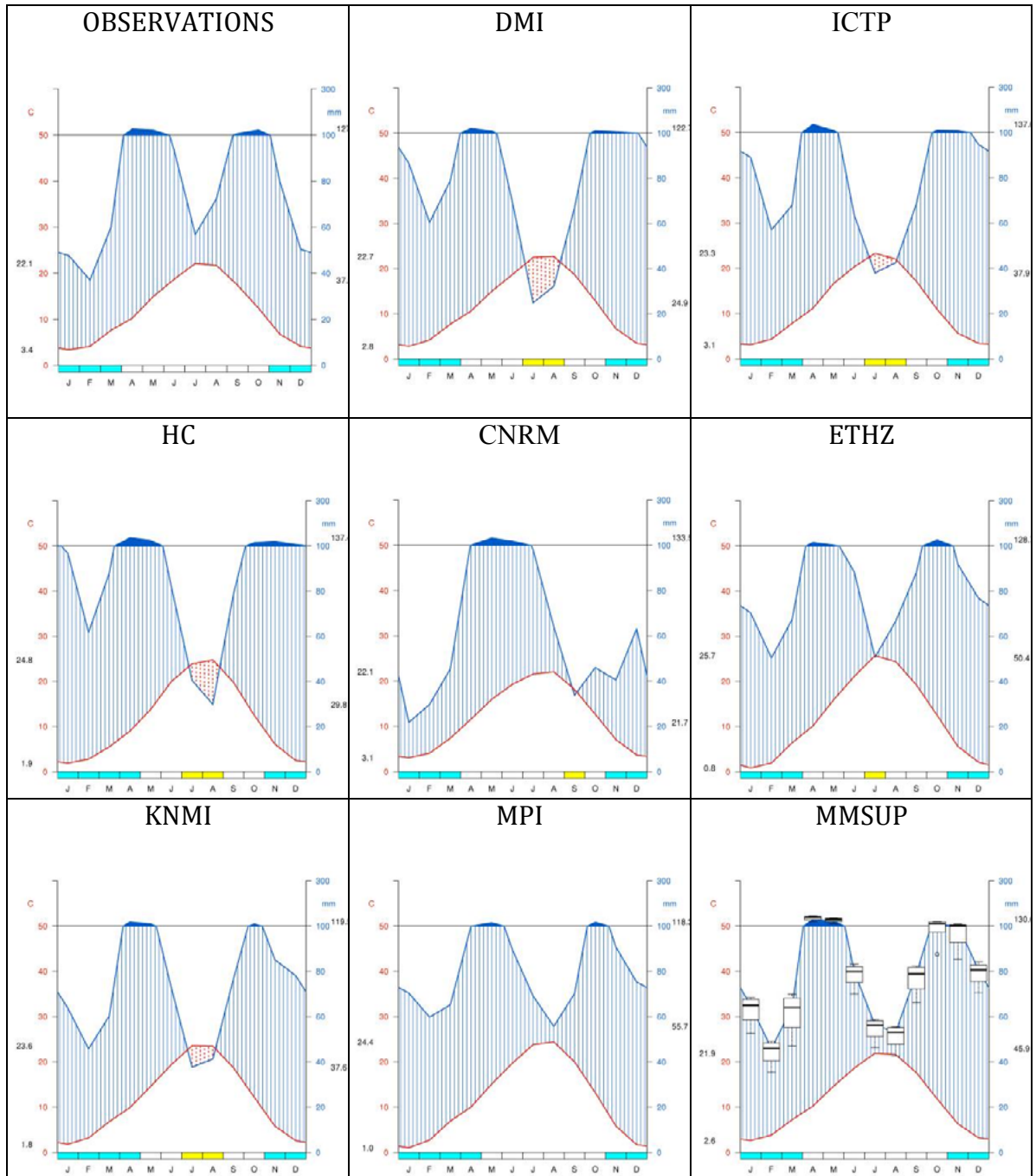


Fig. 4: Walter and Lieth diagrams of the models and Multimodel (MMSUP) for the values averaged over Piedmont OI gridpoints, period 1981-2000. The yearly averaged bias was subtracted from each monthly value. Multimodel uncertainty is represented as boxplots of the precipitation in the MonteCarlo experiment (5th, 25th, 50th, 75th, 95th percentiles are shown).

Nevertheless, the Multimodel post-processing of precipitation allows correcting the statistical properties of the models to reduce the strong models biases, to reproduce the correct precipitation monthly statistics and the average number of consecutive dry periods (more than 5 days without precipitation, namely < 1 mm), Fig. 5.

On the other hand, it is less effective in reproducing the observed average number of consecutive wet periods defined as more than 5 days with precipitation larger than 1 mm. Being that in the Southern Alps the probability of having a dry day (and therefore to extract a dry day and interrupt a wet days series) is much higher than the probability of having a wet day (and then to interrupt a dry day series), the probabilistic sampling from the Multimodel PDF can introduce a gap in a continuous series of wet days.

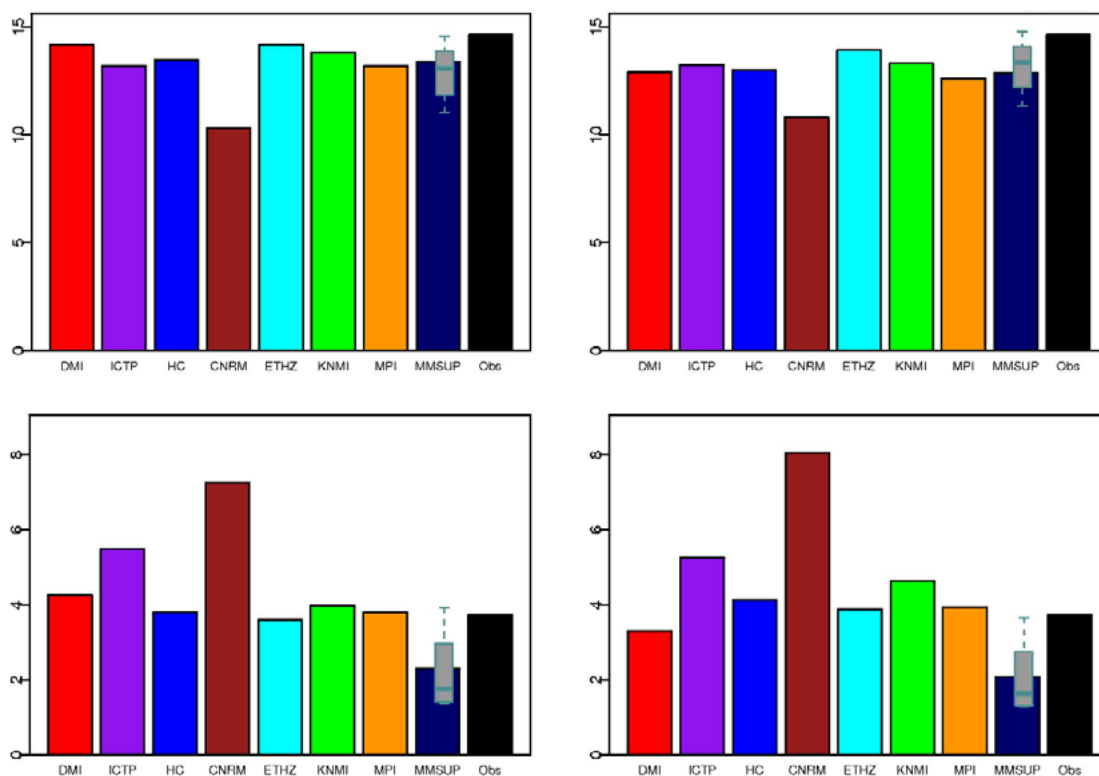


Fig. 5: (top) number of dry periods (5 consecutive days with precipitation < 1 mm) /year for reanalysis (left) and scenario (right); (bottom) number of wet periods (5 consecutive days with precipitation > 1 mm) /year for reanalysis (left) and scenario (right); input models (colours), Multimodel (blue) and observations (black), period 1981-2000. Precipitation is calculated as the average over the Piedmont gridpoints. Multimodel uncertainty is represented as boxplots of the dry/wet mean number of days in the MonteCarlo experiment (5th, 25th, 50th, 75th, 95th percentiles are shown).

In the projected scenario (not shown) precipitation at the annual scale reveal a slight decrease (not statistically significant with 95% confidence level), while on a seasonal basis they show a significant

decrease in spring (-9 mm/month only in the western Alps), summer (-22 mm/month), with few differences among mountains and plains and in autumn, (-26 mm/month limited to the mountains).

5. CONCLUSIONS

Multimodel techniques can be used fruitfully to better evaluate the climatic parameters in complex orography regions. Multimodel SuperEnsemble provides a good estimation of temperature and data in Piedmont, with a very good reduction of the biases and a good reproduction of the monthly variations. We introduced here the application of a new probabilistic Multimodel SuperEnsemble Dressing to precipitation, providing a reasonably good estimation of the precipitation regime in Piedmont.

Temperatures show a general increase in the mid-XXI century scenario, compared with the control period, significant in all the seasons except for autumn and stronger in the higher elevation.

Precipitation is not projected to change significantly at an annual scale, while at a seasonal scale we found a decrease in summer precipitation.

Several impact studies are ongoing with the use of these data, about mountain hydrology, wildfire potential, permafrost, alpine lakes biology, mountain biodiversity, heat waves.

6. ACKNOWLEDGMENTS

This work was partially funded by the the European Union FP7 Integrated Project ACQWA (project reference 212250).

The ENSEMBLES data used in this work was funded by the EU FP6 Integrated Project ENSEMBLES (Contract number 505539) whose support is gratefully acknowledged.

7. REFERENCES

- Ciccarelli N., von Hardenberg J., Provenzale A., Ronchi C., Vargiu A., Pelosini R. (2008), *Climate variability in north-western Italy during the second half of the 20th century*. Global and Planetary Change, 63: 185-195. (1)
- Randall D.A., Wood R.A., Bony S., Colman R., Fichetef T., Fyfe J., Kattsov V., Pitman A., Shukla J., Srinivasan J., Stouffer R.J., Sumi A. and Taylor K.E. (2007), *Climate Models and Their Evaluation*. In:

Climate Change 2007: The Physical Science Basis. Contribution of Working Group I to the Fourth Assessment Report of the Intergovernmental Panel on Climate Change [Solomon, S., D. Qin, M. Manning, Z. Chen, M. Marquis, K.B. Averyt, M. Tignor and H.L. Miller (eds.)]. Cambridge University Press, Cambridge, United Kingdom and New York, NY, USA. (2)

Knutti R., Abramowitz G., Collins M., Eyring V., Gleckler P.J., Hewitson B., and Mearns L. (2010), *Good Practice Guidance Paper on Assessing and Combining Multi Model Climate Projections*. In: Meeting Report of the Intergovernmental Panel on Climate Change Expert Meeting on Assessing and Combining Multi Model Climate Projections [Stocker, T.F., D. Qin, G.-K. Plattner, M. Tignor, and P.M. Midgley (eds.)]. IPCC Working Group I Technical Support Unit, University of Bern, Bern, Switzerland. (3)

Krishnamurti T. N., Kishtawal C. M., LaRow T.E., Bachiochi D. R., Zhang Z., Williford C.E., Gadgil S., and Surendran S. (1999), *Improved weather and seasonal climate forecasts from Multimodel SuperEnsemble*. Science 285, 1548-1550. (4)

Yun W. T., Stefanova L. and Krishnamurti T. N. (2003), *Improvement of the multimodel superensemble technique for seasonal forecasts*. J. Climate, 16, 3834–3840. (5)

Weigel A.P., Knutti R., Liniger M.A., and Appenzeller C. (2010), *Risks of model weighting in multimodel climate projections*. J. Climate, 23, 4175–4191. (6)

Giorgi F., and Mearns L. O. (2002), *Calculation of average, uncertainty range, and reliability of regional climate changes from AOGCM simulations via the "reliability ensemble averaging" (REA) method*. J. Climate, 15, 1141–1158. (7)

Palmer T.N., and Coauthors (2004), *Development of a European Multimodel Ensemble System for Seasonal-to-Interannual Prediction (DEMETER)*. Bull. Amer. Meteor. Soc., 85, 853–872. (8)

Coppola E., Giorgi F., Rauscher S.-A., and Piani C. (2010), *Model weighting based on mesoscale structures in precipitation and temperature in an ensemble of regional climate models*. Climate Res., 44, 121–134. (9)

Christensen J. H., Kjellstro E., Giorgi F., Lenderink G., and Rummukainen M. (2010), *Weight assignment in regional climate models*. Climate Res., 44, 179–194. (10)

Kalnay E. (2003), *Atmospheric modeling, data assimilation and predictability*. Cambridge Univ. Press, 341 pp. (11)

- Cane D., Milelli M. (2006), *Weather forecasts obtained with a Multimodel SuperEnsemble Technique in a complex orography region*. Meteorologische Zeitschrift, Vol. 15, No. 2, 207-214. (12)
- Surendran (2000), *Multi- model superensemble forecasts for weather and seasonal climate*. J. Climate 13, 4196-4216. (13)
- Cleveland R.B., Cleveland W.S., McRae J.E. and Terpenning I. (1990), *STL: A seasonal-trend decomposition procedure based on loess*. Journal of official statistics, Vol. 6, No. 1, 3-73. (14)
- Cane D., Milelli M. (2010), *Can a Multimodel SuperEnsemble technique be used for precipitation forecasts?* Advances in Geoscience, 25, 17-22. (15)
- Walter H. and Lieth H. (1960-1967), *Klimadiagramm-wetatlas*, G.Fisher, Jena. (16)

Implementation and validation of a precipitation downscaling chain for regional climate modelling

D'Onofrio D.^{1,2*}, Palazzi E.¹, von Hardenberg J.¹, Calmanti S.³ and Provenzale A.¹

¹ISAC-CNR, Torino, Italy,

²Università degli Studi di Torino, Italy,

³ENEA, UTMEA-CLIM, Rome, Italy

*Corresponding author: d.donofrio@isac.cnr.it

Abstract

In this work we analyse a precipitation downscaling chain in which ERA40 global reanalyses are downscaled dynamically using the state-of-the-art Protheus Regional Climate Model (RCM). The RCM precipitation is further downscaled using a stochastic downscaling technique, the RainFARM method, which has been adapted for application to climate datasets.

We assess the ability of the complete downscaling chain in reproducing the main statistical properties of the precipitation measured by a dense network of rain gauges located in northwestern Italy, in the time period from 1958 to 2001. We compare the observations also with the precipitation obtained by a direct stochastic downscaling of the ERA40 global reanalyses, in order to assess the possible added value provided by the dynamical downscaling in the chain.

The high-resolution precipitation fields obtained by downscaling stochastically the Protheus RCM output reproduce well the seasonality and the amplitude distributions of observed precipitation during most of the year, including the extreme events. On the other hand, biases introduced by this specific RCM at the large scales, such as an overall overestimation of the total precipitation and underestimation of the number of dry days, particularly during the winter season, cannot be corrected by the stochastic downscaling procedure.

RainFARM produces better results, compared to the observations, when it is applied to Protheus than directly to its large-scale driver (ERA40), highlighting the added value of dynamical downscaling in the chain.

Keywords: *Small-Scale Precipitation, Stochastic downscaling, Regional Climate Models, Impact Studies*



Current global climate models (GCMs) have spatial resolutions that are usually no higher than 70-120 km ([1], [2]), still insufficient to resolve extremes and small-scale variability of precipitation, which are crucial for several applications in climate change impact studies. A step towards higher resolution is provided by dynamical downscaling, by which Regional Climate Models (RCMs) are nested into GCMs or global reanalyses ([3], [4]) to achieve resolutions that are currently of the order of 20-50 km [5].

Even with the use of a RCM nested into a GCM the spatial resolution achieved is frequently too coarse to perform impact studies of climate change at the local scale. Various techniques have been developed to bridge the scale gap between climate change scenarios obtained from the GCMs and RCMs and the small scales needed for specific applications, in particular to obtain high-resolution precipitation useful for hydrological applications and studies of the impact of climate change at the basin scale ([6]). An effective approach for obtaining high-resolution precipitation fields is provided by stochastic downscaling. Stochastic precipitation downscaling ([7]) aims at generating ensembles of possible realizations of synthetic precipitation fields based only on the knowledge of a large-scale precipitation field, as the one produced by a GCM or by global reanalysis systems, or obtained by coarse-scale gridded observations.

Here we use the Rainfall Filtered AutoRegressive Model (RainFARM, [8]), a stochastic downscaling procedure originally devised for the spatiotemporal rainfall downscaling of limited-area meteorological model predictions. RainFARM belongs to the family of “metagaussian models” based on a nonlinear transformation of a linearly correlated stochastic field, obtained by extrapolating to small scales the power spectrum of the large-scale precipitation field.

We discuss the results of the application of RainFARM to the output of the state-of-the-art regional climate model Protheus ([9]) driven by ERA40 global reanalyses. The spatial resolution of the Protheus RCM and of the ERA40 reanalyses is 30 km and ~120 km, respectively.

This is the first application of the RainFARM technique to precipitation fields simulated by a climate model, which required an adaptation of the procedure for a purely spatial (and not temporal) downscaling. Downscaling in time has not been applied here for two main reasons. On the one hand impact studies of climate change require to downscale long-term precipitation scenarios which include a number of isolated rainfall events with different spectral properties, which makes it difficult to downscale in time using spectral methods. On the other hand, the available temporal resolution of the climatic output of state-of-the-art RCMs is often already adequate for impact studies (of the order of 3

or 6 hours in many cases), while the spatial resolution is still too coarse suggesting the application of purely spatial downscaling techniques.

The main focus of this study is to verify the modelling chain by comparing the high-resolution rainfall fields obtained by downscaling the Protheus RCM output with the precipitation data recorded by a network of 122 rain gauges located at different altitudes in Piedmont and Valle D'Aosta regions, north-western Italy [10]. The RainFARM performance is tested also by applying the procedure directly to the large-scale driver of the Protheus system, the ERA40 global reanalyses, in order to highlight the importance of dynamical downscaling in the modelling chain prior to stochastic downscaling to generate climate conditions at the local scale.

a. Upscaling

As a preliminary step of our analysis, we compare the precipitation modeled by the Protheus system with the observed precipitation upscaled to the model resolution. To this end, for each model pixel containing at least one station, we compute the average of all observations in that pixel. Overall we find that, despite the quite good correlation in the interannual fluctuations (the correlation coefficient between the two timeseries is 0.8), Protheus significantly overestimates precipitation with respect to the observations, while the precipitation intensity and the percentage of dry days are lower in the model compared to the observations, as shown in Tab.1 (last two rows). This suggests that during individual events Protheus does not produce more rain than observed, but rain in the model is more frequent than in the observations.

A similar preliminary analysis has been performed for the ERA40 precipitation, compared with observations upscaled to the ERA40 scale. Also in this case precipitation was averaged over all stations contained in each ERA40 grid element. Contrary to what we observe for Protheus, we see that ERA40 precipitation is lower than the observed precipitation evaluated at the ERA40 resolution. The interannual variability is generally well represented in the reanalyses but the correlation coefficient (0.5) is lower than what was found for Protheus. The lower correlation between ERA40 and the observations could be attributed to the coarser resolution of the reanalysis product with respect to that of the RCM. As shown in Tab.1 (first two rows), total precipitation and precipitation intensity are slightly lower in the ERA40 reanalyses than in the observations, while the percentage of dry days is approximately the same.

Fig. 1a shows the probability density functions (PDFs) of total daily precipitation from Protheus and from the observations upscaled to the Protheus resolution. Fig. 1b shows the same of Fig. 1a but for ERA40. Overall we find good agreement between the PDFs produced by Protheus and the observation upscaled to its resolution, whereas ERA40 underestimates the frequency and the amplitudes of observed precipitation events. Figs 1a and 1b also show the precipitation PDFs of individual raingauge observations (red lines) displaying, as expected, longer tails with respect to the PDFs of precipitation at coarser resolution from both Protheus and ERA40.

In order to represent small-scale intense precipitation we have downsampled stochastically the Protheus and ERA40 precipitation output by applying the RainFARM procedure.

b. Downscaling

Since precipitation patterns over the focus region are different in the different seasons, we have calculated seasonal logarithmic slopes of the spatial power spectra of the Protheus precipitation to be used in the downscaling procedure to extrapolate the power spectrum from the resolved to the unresolved model scales. The Protheus data have been downsampled in space from 30 km down to about 1 km spatial resolution, which previous studies have shown to be adequate for a direct comparison with observations [8]. For each rain gauge, the timeseries at the closest downsampled pixel has been chosen and further analysed. The PDFs of total precipitation from the downsampled model and the point-scale observations, represented in Fig. 2a, show a very good agreement. The seasonal precipitation PDFs agree also quite well (not shown here), especially in spring, summer and autumn, the most significant seasons in terms of precipitation in the Piedmont and Valle d'Aosta regions. This demonstrates that the downscaling procedure is capable of generating realistic precipitation amplitude distributions starting from the RCM outputs over the region of interest. There is an overestimation in winter, with the downsampled fields showing more frequent extreme events compared to the observations. Also Protheus at its original resolution presents an overestimation of winter precipitation. This overestimation is simply propagated to small scales by the downscaling procedure.

We verify the skill of the RainFARM procedure in reproducing observed precipitation distributions from raingauges also applying it directly to the ERA40 global reanalyses. The amplitude distribution of downsampled ERA-40 fields is wider than the original one, but still underestimates the amplitudes and the probabilities of occurrence of intense precipitation events, as shown in Fig. 2b.

c. Discussion and Conclusions

We have analysed the precipitation output of one state-of-the-art regional climate model, the Protheus system, and of its large scale driver, the ERA40 reanalyses. Both Protheus and ERA40 have been spatially downscaled using a modified version of the RainFARM procedure and the downscaled fields have been compared to the precipitation measured by a network of rain gauges over northwestern Italy.

We find better results by downscaling Protheus than its driver, ERA40. In the case of the Protheus data, though RainFARM cannot correct large scale biases of the original precipitation fields, there is a very good agreement in terms of PDFs between downscaled model data and the raingauge observations.

We also find that a good agreement of upscaled observations with model data in terms of amplitude distributions represents an important prerequisite for successful application of the downscaling procedure. In other words, since the downscaling procedure acts only at small scales, below a chosen “reliability scale”, it cannot correct for missing model variance at larger scales. In cases when upscaled observations do not agree with the model data, it may be possible to explore larger aggregation scales and to downscale starting directly from those.

The study case considered in this work highlights the added value of nesting an RCM into a large-scale GCM or global reanalyses, in order to produce high-resolution precipitation. Of particular concern with climate change assessments and impact studies, the application of such a modelling chain is fundamental to generate future scenarios of water availability in small basins or catchments, starting from the global coarse-scale resolution projections from the most advanced tools currently in use, the global climate models.

	$\langle \bar{P} \rangle$ (mm day ⁻¹)	$\langle \bar{P} \rangle_{wet}$ (mm day ⁻¹)	Dry days (%)
Obs_ERA40	2.7	8.4	68
ERA40	2.1	5.8	66
Obs_PROTHEUS	2.7	10.0	73
PROTHEUS	3.7	9.3	61

Table 1: Space-time averages over pixels containing raingauges, of total precipitation, precipitation intensity and percentage of dry days for ERA40 and the observation upscaled to the ERA40 resolution (first two rows), and for Protheus and the observation upscaled to the Prothes resolution (last two rows). Dry days are defined by setting to zero all precipitation values < 1 mm day⁻¹

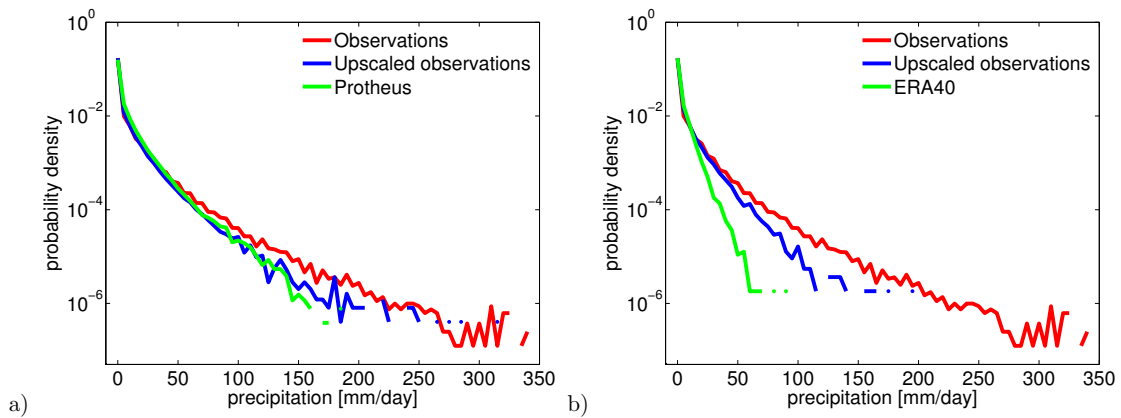


Fig. 1: a) Daily precipitation PDFs of Protheus rainfall (green line), raingauge observations upscaled at Protheus resolution (blue line) and individual observations (red line). b) Daily precipitation PDFs of ERA40 rainfall (green line), raingauge observations upscaled at ERA40 resolution (blue line) and individual observations (red line)

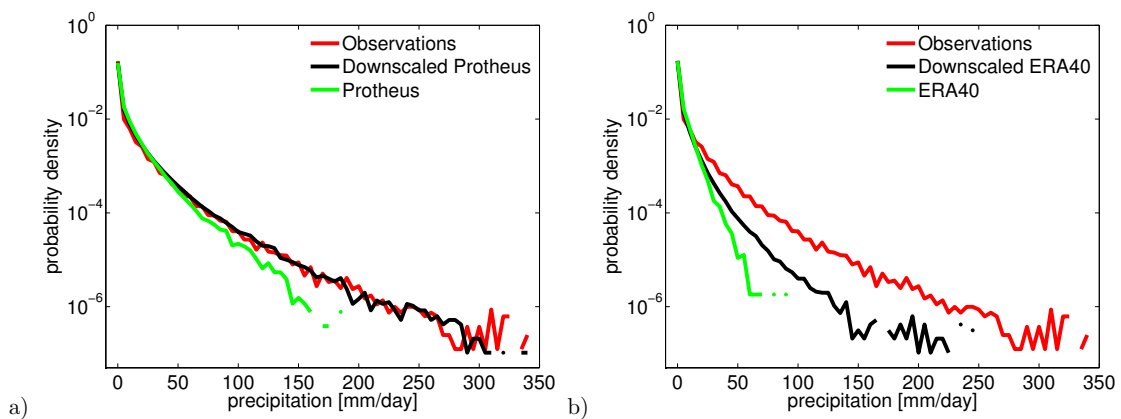


Fig. 2: a) Daily precipitation PDFs of Protheus rainfall (green line), individual observations (red line) and Protheus fields downscaled with RainFARM (black line). b) Daily precipitation PDFs of ERA40 rainfall (green line), individual observations (red line) and ERA40 fields downscaled with RainFARM (black line).

ACKNOWLEDGMENTS

This work has been performed in the framework of the project of national interest NextDATA (<http://www.nextdataproject.it>).

REFERENCES

- Washington W.M. and Parkinson C.L. (2005), *An introduction to three-dimensional climate modeling*. University Science Books, 353 pp. (1)
- Solomon S., Qin D., Manning M., Chen Z., Marquis M., Averyt K. B., Tignor M., and H. L. M. (eds.) (2007), *Climate change 2007: The physical science basis. contribution of working group to the fourth assessment report of the intergovernmental panel on climate change*. Tech. rep., 996 pp. Cambridge University Press, Cambridge, United Kingdom and New York, NY, USA. (2)
- Giorgi F. (1990), *Simulation of regional climate using a limited area model nested in a general circulation model*. J. Clim., 3, 941–964. (3)
- Castro C. L., R. A. P. Sr., and Leoncini G. (2005), *Dynamical downscaling: Assessment of value retained and added using the regional atmospheric modeling system (rams)*. J. Geophys. Res., 110, D05 108. (4)
- Flaounas E., Drobinski P., Vrac M., Bastin S., Lebeaupin-Brossier C., Stéfanon M., Borga M., and Calvet J.-C. (2012), *Precipitation and temperature spacetime variability and extremes in the Mediterranean region: evaluation of dynamical and statistical downscaling methods*. *Climate Dynamics*, doi:10.1007/s00382-012-1558-y, URL <http://www.springerlink.com/index/10.1007/s00382-012-1558-y>. (5)
- Sorooshian S., Hsu K. I., Coppola E., Tomassetti B., Verdecchia M., and G. V. (Eds.) (2008), *Hydrological Modelling and the Water Cycle Coupling the Atmospheric and Hydrological Models*. Water Science and Technology Library, Vol. 63. 138 pp. (6)
- Ferraris L., Gabellani S., Rebora N., and Provenzale A. (2003), *A comparison of stochastic models for spatial rainfall downscaling*. *Water Resour. Res.*, 39, 1368. (7)
- Rebora N., Ferraris L., von Hardenberg J., and Provenzale A. (2006), *Rainfarm: Rainfall downscaling by a filtered autoregressive model*. J. Hydrometeor., 7, 724–738. (8)
- Artale V., et al. (2010), *An atmosphereocean regional climate model for the mediterranean area: assesment of a present climate simulation*. *Climate Dynamics*, 35, 721–740. (9)
- Ciccarelli N., von Hardenberg J., Provenzale A., Ronchi C., Vargiu A., and Pelosini R. (2008), *Climate variability in north-western italy during the second half of the 20th century*. *Global Planet. Change*, 63, 185–195. (10)

Performance evaluation of COSMO-CLM over Italy and climate projections for the XXI century

Bucchignani E.^{1,2*}, Mercogliano P.^{1,2}, Montesarchio M.¹, Manzi M.¹ and Zollo A.¹

¹*Impact on soil and coast – Euro Mediterranean Centre on Climate Change (ISC-CMCC), Capua, Italy*

²*Meteo System & Instrumentation Laboratory - Italian Aerospace Research Center (SUMA-CIRA), Capua, Italy*

*Corresponding author: e.bucchignani@cira.it

Abstract

In this study, we discuss the results of numerical simulations performed with the regional model COSMO-CLM over the entire Italian domain at spatial resolution of 8 km, employing a model configuration optimized at CMCC: an assessment of model capabilities to reproduce the main features of the past Italian climate has been performed using two different simulations: the first is driven by ERA40 Reanalysis and the second is driven by CMCC-MED global model, through a comparison with E-OBS dataset. Then, climate projections over Italy, according with the RCP4.5 emission scenario, have been analysed in terms of change of 2-meter temperature and precipitation.

Keywords: *Regional Simulations, Climate projections*



1. INTRODUCTION

Italy is located in Southern Europe and belongs to the Mediterranean area, affected by the arid climate of North Africa and by the temperate and rainy climate of central Europe [1]. Moreover, it is characterized by a very complex and heterogeneous topography, ranging from high mountain chains, such as Alps and Apennines, to several coastal areas, being Italy almost totally surrounded by Mediterranean Sea. All the numerical simulations performed with General Circulation Models (AOGCM) highlight a general increase of temperature in the Mediterranean basin (both in the average and in the extreme values) [2] especially in summer, combined with a significant reduction of precipitations, making this area a future “hot-spot” of the Earth. For these reasons, a considerable impact on agriculture, tourism and water resources is expected and it is important to provide high resolution climate change projections to decision makers, in order to perform adaptation/mitigation policies. For a better representation of these particular climatic features, a high horizontal spatial resolution is needed [3]. For this purpose, regional climate models are recommended for simulations on the Italian peninsula: in fact, at the resolution of global climate models, Italy is not well delineated or not even captured.

The main aim of this work is the development of very high resolution climate projections over Italy with the regional climate model COSMO-CLM [4]. A simulation for the GHG RCP4.5 emission scenario of IPCC has been performed and analysed, while another one, for GHG RCP8.5 emission scenario, is currently in progress.

2. MODELS AND DATA

The regional model COSMO-CLM is the climate version of the COSMO-LM weather model [5]; it was also used in the PRUDENCE project [6] with competitive results, showing the same range of accuracy as other RCMs. An important feature of COSMO-CLM is the non-hydrostatic formulation, that allows better resolving convective phenomena and using horizontal spatial resolutions lower than 20 km [7]. Higher resolutions than global climate model ones allow a better description of the terrain topography and, consequently, of the phenomena strictly related to the orography, such as precipitation [8,9].

The horizontal resolution adopted in this work is 0.0715° (about 8 km). The area of interest is $3^\circ\text{-}20^\circ\text{E}$ / $36^\circ\text{-}50^\circ\text{N}$. The time step has been set equal to 40 sec, while the convection scheme is the Tiedtke

one. Two simulations have been performed: the first one is forced by ERA40 Reanalysis [10] and covers the time period 1971-2000; the second one is forced by the global climate model CMCC-MED [11] and covers the time period 1971-2100, employing the RCP4.5 emission scenario. ERA40 Reanalysis are characterized by horizontal resolution of 1.125° (about 128 km), 49 vertical levels and 3 soil levels, while ECHAM5 (atmospherical component of CMCC-MED) by horizontal resolution of 0.75° (about 85 km), 31 vertical levels and 4 soil levels.

A sensitivity analysis was conducted in order to adjust the model configuration to better reproduce the past climate over the Italian domain [12]. Then, the selected configuration of COSMO-CLM, optimized at CMCC, has been used to carry on the two simulations.

3. VALIDATION

The validation has been performed on the Italian domain: for a more detailed study, three sub-regions (northern, central and southern areas) have been identified and analysed, following the characteristics of the Italian climate [13]:

1. NORTH : 5.625° to 15.625° E; 43.875° to 47.125° N;
2. CENTRE : 9.625° to 16.875° E; 41.375° to 43.875° N;
3. SOUTH : 7.625° to 19.125° E; 36.125° to 41.375° N.

Model evaluation for both the simulations has been performed by using the E-OBS dataset [14] as reference: it is an European daily high resolution ($0.25^\circ \times 0.25^\circ$) gridded data set for precipitation, minimum, maximum and mean surface temperature and sea level pressure for the period 1950-2010. This dataset has been designed to provide the best estimate of grid box averages rather than point values to enable direct comparison with RCMs.

The analysis of the ERA40 driven simulation bias allows the characterization of the error related only to the regional climate model COSMO-CLM, since “perfect” boundary conditions have been used. From the comparison with the second one, instead, the influence of the global model on the results can be analysed (in this case, the error cannot be traced back to the regional or global model in a specific way).

Fig.1 shows the seasonal spatial values of the 2-meter mean temperature bias (in °C) of COSMO-CLM output with respect to the E-OBS observational dataset for winter (top) and summer (bottom). The analysis reveals a cold bias over the mountainous areas (Alps and Apennines) in all the seasons and for both the simulations. The one driven by the global climate model CMCC-MED has a more pronounced bias in all seasons, with a general underestimation up to 5°C in winter: this high value is partially due to the bias that affects the global model output. Concerning ERA40 driven simulation, the observed bias does not exceed 3°C in absolute value. In winter, a general underestimation of temperature is registered (up to 3°C in the Ligurian Alps), except in the Po Valley and in the northeast part of Italy, where a good agreement is found, with a slight overestimation (at most 0.5°C). In summer, instead, an overestimation occurs (peak of 2.5°C) over the Adriatic coast and in the south of Sicily, while Alps and Apennines are characterized by a slight cold bias (up to 1°C). Concerning the CMCC-MED driven simulation, as said before, it is affected by a cold bias in all seasons, more pronounced in winter, while in summer the bias is lower (at most 0.5°C of difference). Successively the mean values, averaged over the three selected subdomains, have been analysed, in order to study the model ability to represent the seasonal cycles and the time series of the 2-meter mean temperature. The seasonal cycles (Fig.2) are very well captured by both the simulations, in all the regions. The highest error occurs in winter and CMCC-MED driven simulation always underestimates the temperatures, as already highlighted in the seasonal spatial biases.

Fig.3 shows the seasonal spatial biases of precipitation (mm/day) with respect to the E-OBS observational dataset. With respect to temperature, the differences between the simulation driven by ERA40 Reanalysis and the one driven by the global climate model CMCC-MED are less evident. In general, the bias is in the range between -3 and 4 mm/day. For all the seasons, an overestimation over the Alps occurs in both the simulations. A similar bias pattern is observed in winter, but with a stronger overestimation for CMCC-MED driven simulation on the Alps and on the central and southern Italy. In the case of ERA40 driven simulation, the bias does not exceed 2 mm/day in absolute value. In summer, a very good agreement is found, with the exception of the Alps; the bias is between -0.5 mm/day and 0.5 mm/day, while in the case of CMCC-MED forced simulation the differences in central-south regions are close to 0 mm/day. In order to analyse the capability of the model in reproducing seasonal cycles, the mean values over NORTH, CENTRE and SOUTH subdomains have been investigated (Fig.4): in the NORTH region a strong overestimation of the daily precipitation in April, May and June (about 1.5 mm/day) is observed for both the simulations; moreover, in January,

February and March, CMCC-MED driven simulation shows higher differences with respect to the one driven by ERA40. In the other months the agreement is better. In CENTRE and SOUTH regions, instead, the seasonal cycle is very well captured, with a maximum bias of 1 mm/day in some months.

4. CLIMATE PROJECTIONS

Climate projections over the XXI century have been performed using the IPCC-RCP4.5 emission scenario [15]. It is a scenario which includes long term, global emissions of greenhouse gases, short-lived species, and land-use-land-cover in a global economic framework. It is a stabilization scenario and assumes that climate policies, in this instance the introduction of a set of global greenhouse gas emissions prices, are invoked to achieve the goal of limiting emissions and radiative forcing.

Fig. 5 shows the change of 2-meter temperature distribution, averaged on the period 2031-2060, with respect to the period 1971-2000, related to winter (left) and summer (right). A general increase of temperature is expected in all the examined area, more pronounced in winter (up to 3°C), especially in the Piedmont region (north-west Italian area) and in central Italy. The summer warming is always larger than 2.5°C and it reaches 4°C in the northern Italy. In spring (not shown), the temperature increase is of about 2°C, while in autumn (not shown) the temperature increase is homogeneous, being about 2.5°C in the whole domain of interest.

Fig. 6 shows the change of total precipitation distribution, averaged on the period 2031-2060, with respect to the period 1971-2000, related to winter (left) and summer (right). Even if the expected trend is not yet well defined, a decrease of precipitations in both the seasons is projected; in winter, it is more pronounced in the Ligurian region (north coastal area) and in southern Italy (up to -2 mm/day); in summer, a strong decrease of precipitation occurs on the whole Alpine arc (-3 mm/day), with no significant changes in other zones. In spring (not shown), the reduction is higher on the Alps, in the central part of the domain and in Sardinia. In autumn instead (not shown), an increase on the Alps and in other parts of Italian domain is projected (up to 1 mm/day).

Finally, the time series of precipitations (5 years running mean) have been analysed, highlighting a slight decrease in all the three regions (Fig 7).

5. CONCLUSIONS

In this study, an assessment of COSMO-CLM performances over Italy has been carried out, analysing the results of two simulations over the period 1971-2000: one driven by ERA40 Reanalysis and one by the global climate model CMCC-MED. COSMO-CLM is basically able to simulate the spatial and temporal characteristics of the climate of Italy: the temperature seasonal cycles are very well captured; even if COSMO-CLM generally underestimates the temperature in winter and overestimates it in summer, the bias of ERA40 driven simulation does not exceed 3°C, being this value slightly lower than the ones that generally affect regional climate simulations (e.g [2,6]). Concerning precipitations, the bias is generally acceptable, with the exception of mountainous areas, where a strong wet bias occurs (up to 4 mm/day), and of Tuscany region, where an underestimation is registered. It is worth noting that biases are influenced by the difference in resolution between the model and the observational dataset. Moreover, E-OBS is obtained through an interpolation of the station values and this is source of potential uncertainties. For this reason, a comparison with a high resolution observational dataset for Tuscany region (provided by ARPA Tuscany) has been performed, revealing that in this area E-OBS precipitations are over-estimated in winter, so the COSMO-CLM under-estimation is partially justified. Comparisons with other datasets provided by regional Italian authorities (Emilia Romagna, Piedmont, Calabria regions) will be performed in the future, in order to provide a more accurate quantification of the bias [16].

Climate projections over the XXI century, according with RCP4.5 emission scenario have been analysed: the mean temperature increase found is in good agreement with several literature works [17], even it is difficult to make a detailed comparison with other papers, since existing studies have conducted over different observation periods and in different regions. The precipitation reduction is in agreement with results shown in [3]. Also for precipitation, the trend values obtained in this work are not directly comparable with literature papers due to the different time period considered. A numerical simulation for the RCP8.5 emission scenario is currently in progress, in order to perform a multi-scenario ensemble.

6. ACKNOWLEDGMENTS

This paper has been developed within the framework of Work Package 6.2.2 of the GEMINA project, funded by the Italian Ministry of Education, University and Research and the Italian Ministry of Environment, Land and Sea.

7. REFERENCES

- Giorgi F. and Lionello P. (2008), *Climate change projections for the Mediterranean region. Global and Planetary Change*, 63, pp. 90 – 104. (1)
- Van der Linden P., Mitchell J.F.B. (2009), *ENSEMBLES: Climate Change and its impacts: Summary of research and results from the ENSEMBLES project*. Met Office Hadley Centre, UK, pp. 160. (2)
- Coppola E. and Giorgi F. (2010), *An assessment of temperature and precipitation change projections over Italy from recent global and regional climate model simulations*. *Int. J. Climatol.*, 30, pp. 11–32. (3)
- Rockel B., Will A., and Hense A. (2008), *The regional climate model cosmo-clm (cclm)*, *Meteorologische Zeitschrift*, 17(4) pp. 347–348. (4)
- Stappeler J., Doms G., Schattler U., Bitzer H. W., Gassmann A., Damrath U., and Gregoric G. (2003), *Mesogamma scale forecasts using the nonhydrostatic model lm*. *Meteorology and Atmospheric Physics*, 82, pp.75–96. (5)
- Christensen J.H., Hewitson B., Busuioc A., Chen A., Gao X., Held R., Jones R., Kolli R.K., Kwon W. K., Laprise R., and Others (2007), *Regional climate projections*. *Climate Change, The Physical Science Basis*. Contribution of Working group I to the Fourth Assessment Report of the Intergovernmental Panel on Climate Change, University Press, Cambridge, Chapter 11, pp. 847–940. (6)
- Bohm U., Kucken M., Ahrens A., Block A., Hauffe D., Keuler K., Rockel B., and Will A. (2006), *CLM the climate version of LM: Brief description and long term applications*. COSMO Newsletter. (7)
- Montesarchio M., Manzi M., Cattaneo L., Bucchignani E., Mercogliano P. (2012), *Performance evaluation of a regional climate simulation with COSMO-CLM in the Alpine space*. CMCC Research Paper Issue RP0137. (8)
- Bucchignani E., Sanna A., Gualdi S., Castellari S., and Schiano P. (2011), *Simulation of the climate of the XX century in the alpine space*. *Natural Hazards*, DOI 10.1007/s11069-011-9883-8. (9)

- Uppala S.M. et al. (2006), *The ERA40 reanalysis*. Quart. J. Roy. Meteor. Soc., 612, pp. 2961–3012. (10)
- Gualdi S. et al. (2012), *The CIRCE simulations: a new set of regional climate change projections performed with a realistic representation of the Mediterranean Sea*. Bull. Amer. Meteor. Soc. <http://dx.doi.org/10.1175/BAMS-d-11-00136.1> (11)
- Montesarchio M., Mercogliano P., Manzi M., Bucchignani E. (2012), *A sensitivity study with the RCM COSMO CLM over the north and center Italy*. CMCC Research Paper Issue RP0143. (12)
- Zollo A., Montesarchio M., Manzi M., Cattaneo L., Bucchignani E., Mercogliano P. (2012), *Assessment of COSMO-CLM performances in simulating the past climate of Italy*. CMCC Research Paper Issue RP0145. (13)
- Haylock M.R., Hofstra N., Klein Tank A.M.G., Klok E.J., Jones P.D., and New M. (2008), *A European daily high-resolution gridded data set of surface temperature and precipitation for 1950-2006*. Journal of Geophysical Research, 113 (D20). (14)
- IPCC (Intergovernmental Panel on Climate Change). (2008), *Towards New Scenarios for Analysis of Emissions, Climate Change, Impacts, and Response Strategies*. IPCC EXPERT MEETING REPORT (<http://www.aimes.ucar.edu/docs/IPCC.meetingreport.final.pdf>). (15)
- Turco M., Zollo A., Ronchi C., de Luigi C. and Mercogliano P. (2013), *Assessing gridded observations for daily precipitation extremes in the Alps with a focus on northwest Italy*, accepted in Natural Hazards and Earth System Sciences. (16)
- Perini L., Salvati L., Ceccarelli T., Motisi A., Marra F.P., Caruso T. (2007), *Atlante agroclimatico – Scenari di cambiamento climatico*. UCEA, Roma. Collana Climagri n. 52 (Atlante + CD). ISBN 88-901472-8-8, 72 pp. (17)

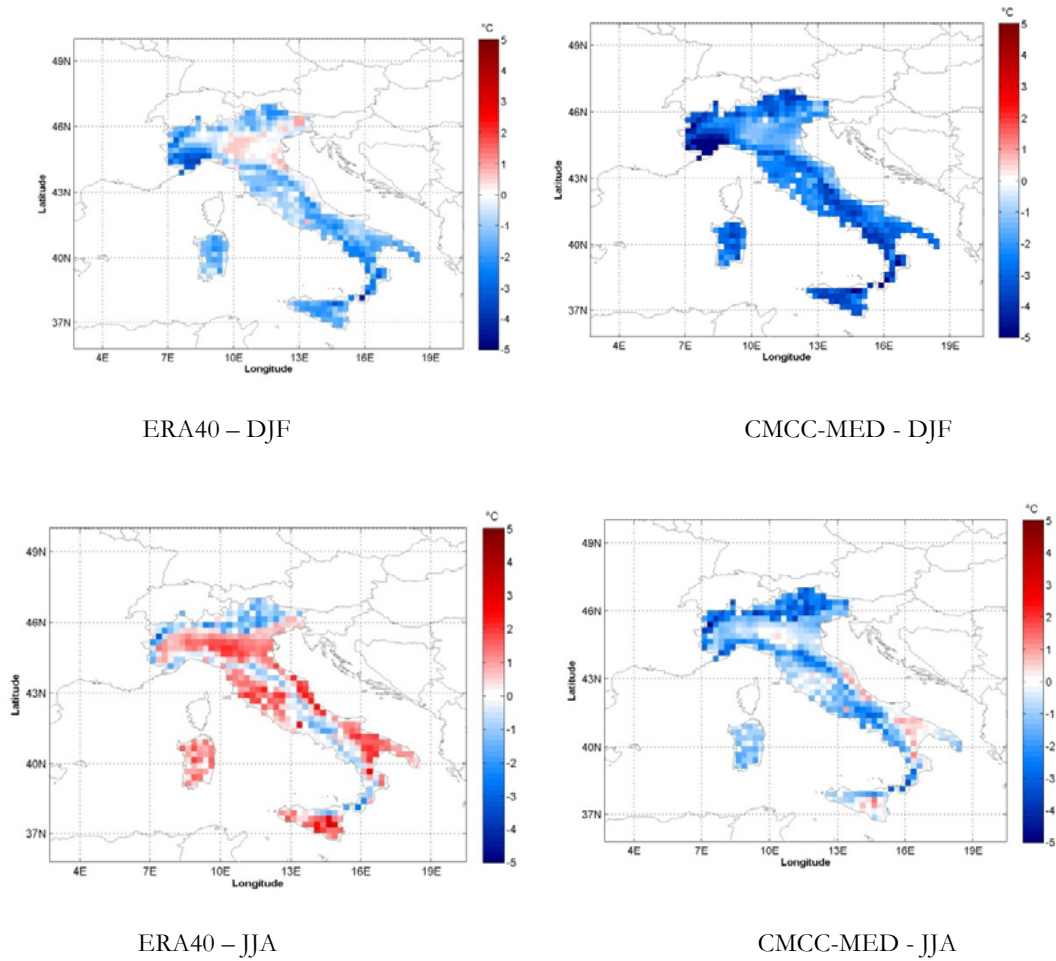


Fig.1: Seasonal differences, in terms of 2-meter mean temperature (°C), between the output of COSMO-CLM and E-OBS dataset, for the simulation forced by ERA40 reanalysis (left) and the simulation forced by CMCC-MED global model (right).

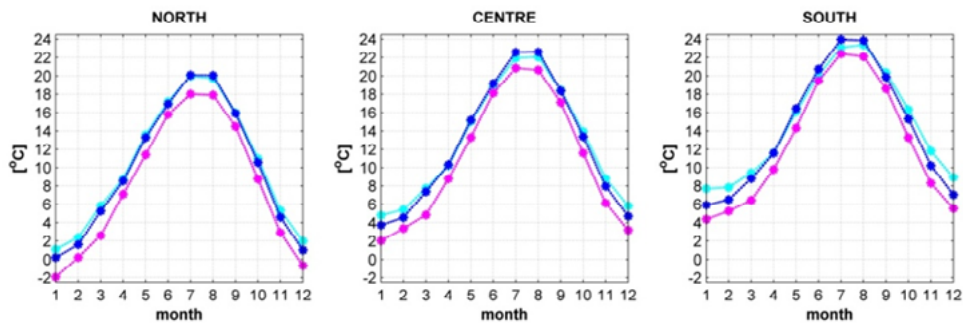


Fig.2: Seasonal cycles of the 2-meter mean temperature, for each subdomain investigated.

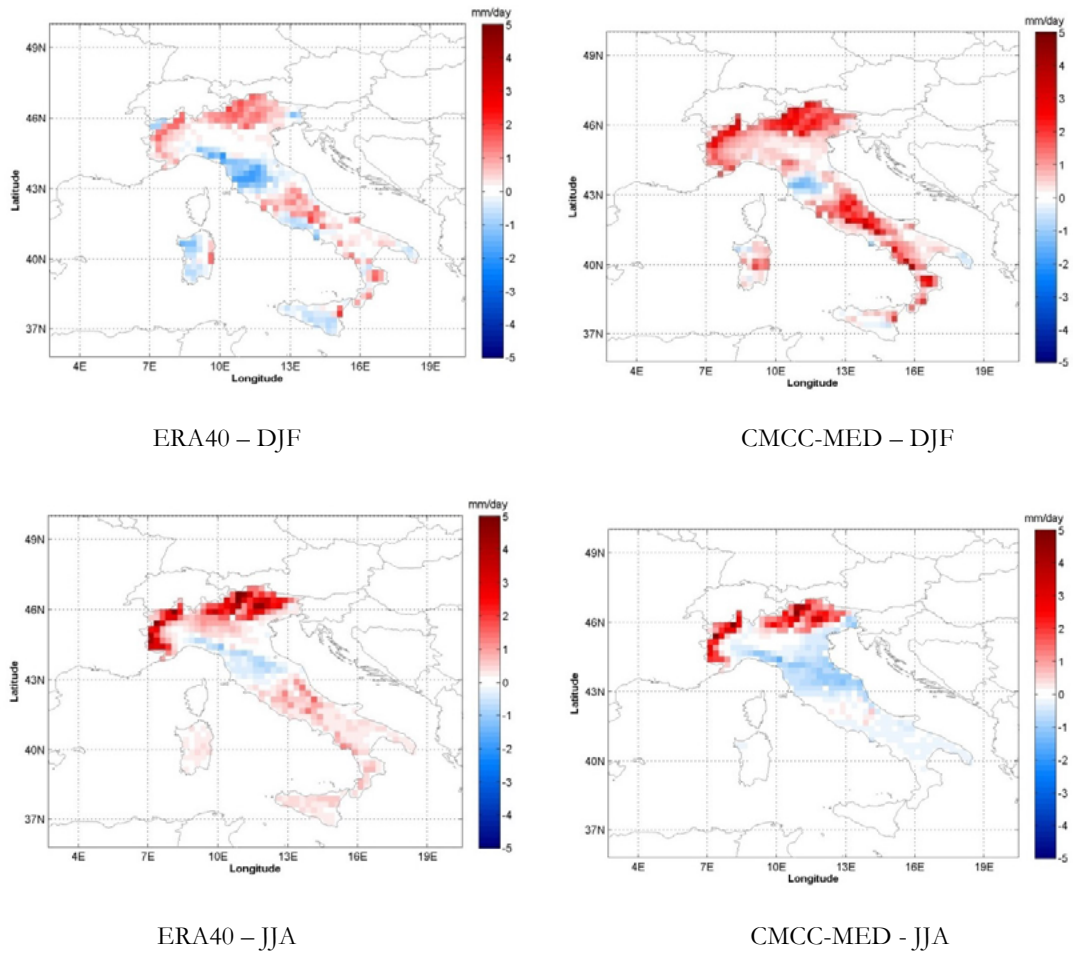


Fig.3: Seasonal differences, in terms of daily precipitation (mm/day), between the output of COSMO-CLM and E-OBS dataset, for the simulation forced by ERA40 Reanalysis (left) and the simulation forced by CMCC-MED global model (right).

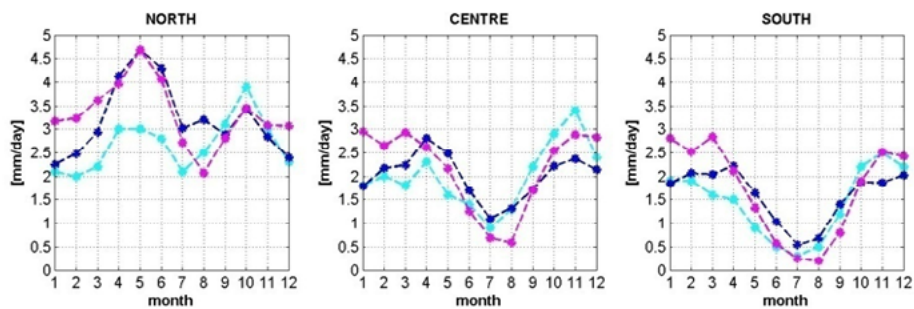


Fig. 4: Seasonal cycles of the daily precipitation, for each subdomain investigated.

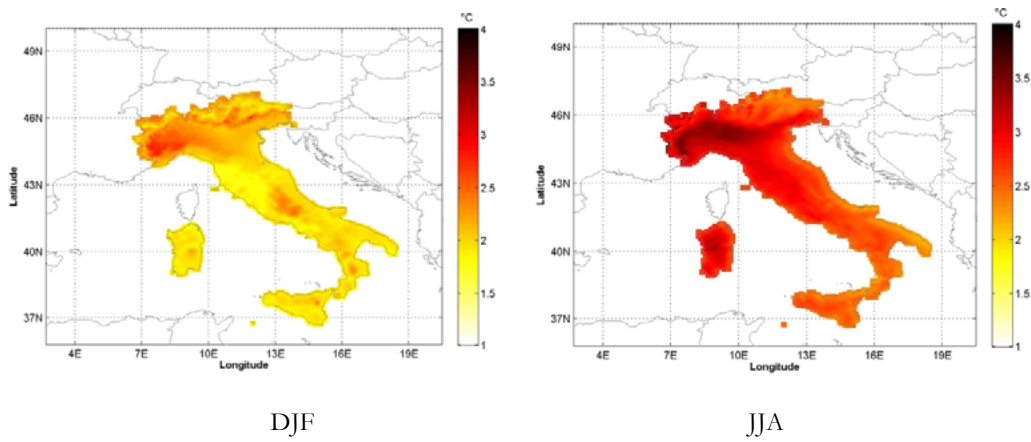


Fig. 5: Temperature climate projections: seasonal differences (°C), between the average value over 2031-2060 and 1971-2000.

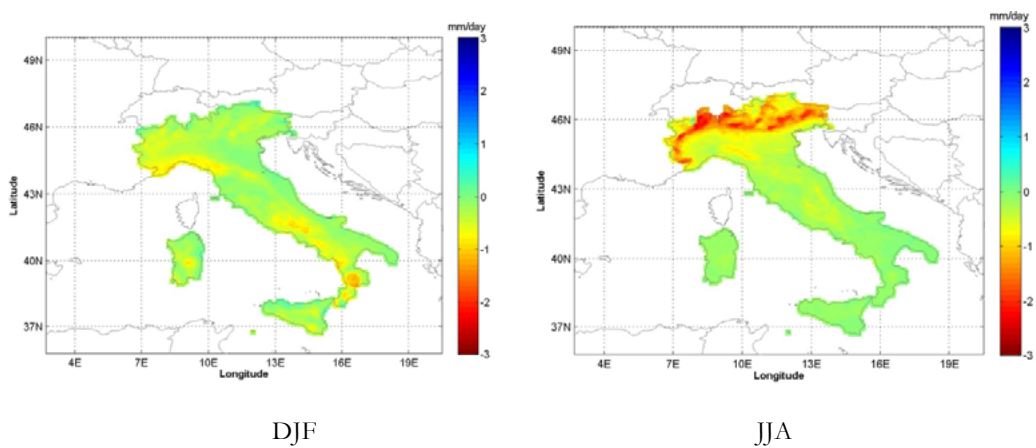


Fig. 6: Precipitation climate projections: seasonal differences (mm/day) between the average value over 2031-2060 vs 1971-2000.

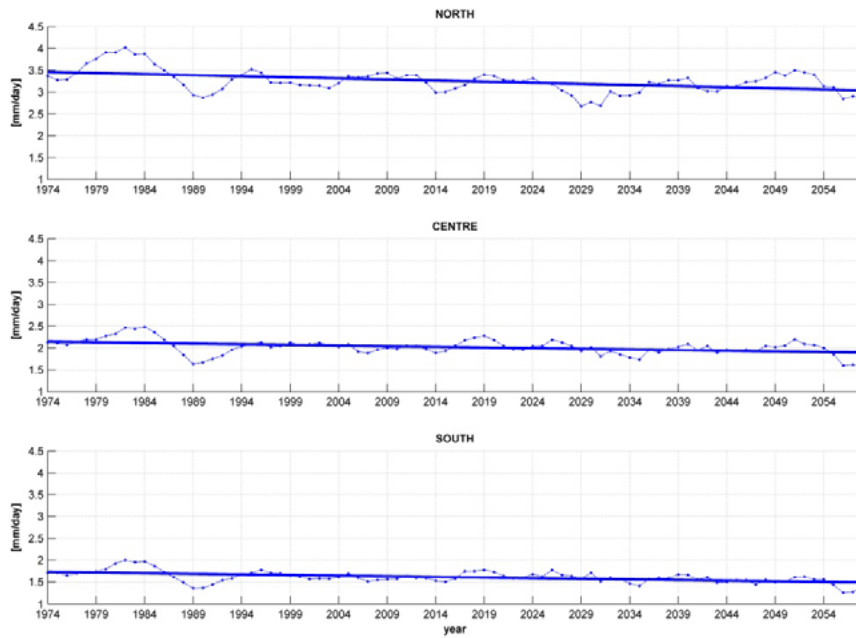


Fig. 7: Precipitation time series (5 years running mean) for each subdomain investigated.

ADVANCES IN CLIMATE SCIENCE

Variability and uncertainties using CMIP5 models

A data-driven causality analysis for the attribution of recent global warming

Pasini A.^{1*}, Triacca U.², and Attanasio A.¹

¹CNR, Institute of Atmospheric Pollution Research, Monterotondo Stazione, Roma, Italy

²Department of Computer Engineering, Computer Science and Mathematics,
University of L'Aquila, Coppito, L'Aquila, Italy

*Corresponding author: pasini@iia.cnr.it

Abstract

Even if the application of dynamical models obviously represents the main road for investigating cause-effect relationships in the climate system, also other analyses can shed light to the problem of attributing recent global warming. In this paper, the concept of Granger causality (well known in econometric studies) is applied to this topic. By considering the direct role of anthropogenic and natural forcings, and the influence of patterns of natural variability, our results confirm the major role of greenhouse-gases radiative forcing in driving temperature and show a clear evidence of a recent causal decoupling between solar irradiance and temperature itself.

Keywords: *Climatic attribution, Granger causality, recent global warming, external forcings, natural variability*



1. INTRODUCTION

The problem of understanding and weighting the main causes of recent climate change is generally faced by runs of Global Climate Models (GCMs). In this framework, cause-effect relationships and feedbacks are described by coupled systems of equations (plus parameterizations) which explicitly simulate the behaviour of the system under the influence of external forcings. As well known, numerical experiments of attribution show that the recent global warming cannot be reconstructed if anthropogenic forcings (mainly due to the increase in greenhouse gases concentrations) are not taken into account [1,2].

Despite this clear evidence of the major role of anthropogenic forcings in driving the global temperature T , in our opinion it is worthwhile to address the problem of attribution by other methods of investigation. In particular, data-driven techniques allow us to avoid a description of the system that could obviously ignore some relevant process or feedback, with possible consequences on the final results of attribution. Furthermore, by adopting a distinct viewpoint of investigation, we can obtain a corroboration or a rebuttal of previous GCMs' results by completely independent models.

In the past, for instance, neural network modelling has been applied to the attribution of T and its results confirm those of GCMs [3]. Further studies show the usefulness of neural investigations for attribution of temperature and precipitation at a regional scale, too [4,5].

Here we adopt a concept of causality by Granger [6], whose analyses were originally developed in the framework of econometric studies, and apply it to the problem of attribution of the recent global warming.

2. THE CONCEPT OF GRANGER CAUSALITY

The concept of Granger causality is quite simple. In a time series approach, we say that a variable x Granger causes another variable y if future values of y can be better predicted (according to standard cost functions) using the past values of x and y rather than only past values of y . In a 1-step ahead forecast, if the prediction which uses x and y is better, then the past of x contains a useful information for forecasting y_{t+1} that is not present in the past of y .

Clearly, the concept of Granger causality is different from correlation or possible instantaneous causality, because it is based on precedence and predictability.

More formally, consider the vector time series $(y_t, x_t)'$ and the following information sets: $I_{yx}(t) = \{y_t, x_t, y_{t-1}, x_{t-1}, \dots\}$ and $I_y(t) = \{y_t, y_{t-1}, \dots\}$. Denote with $P(y_{t+1} | I(t))$ the optimal (minimum mean square error) linear forecast of the variable y_{t+1} based on the information set $I(t)$. We say that x does not Granger cause y , in a bivariate system, if $P(y_{t+1} | I_y(t)) = P(y_{t+1} | I_{yx}(t))$ for any t .

Generally, the causal relationship between the variables x and y is investigated in a bivariate system. Nevertheless, it is well known that in a bivariate framework problems of spurious causality and of non-causality due to omission of some relevant variables can arise. Thus, in this paper also trivariate systems are considered.

Of course, even larger causal structures could be allowed by Granger's formalism, but, as a matter of fact, the non-causality tests require specification of a parametric model and in the case of large causal structures the number of parameters becomes so high that the estimates can lose their reliability. Due to this problem, in this paper we will consider just bivariate and trivariate systems.

In a trivariate system we have that x does not Granger cause y if $P(y_{t+1} | I_{y\tilde{x}}(t)) = P(y_{t+1} | I_{yx\tilde{x}}(t))$ for any t , where $I_{y\tilde{x}}(t) = \{y_t, \tilde{z}_t, y_{t-1}, \tilde{z}_{t-1}, \dots\}$ and $I_{yx\tilde{x}}(t) = \{y_t, x_t, \tilde{z}_t, y_{t-1}, x_{t-1}, \tilde{z}_{t-1}, \dots\}$.

Suppose that the trivariate time series $(y_t, x_t, \tilde{z}_t)'$ follows a vector autoregressive (VAR) model of finite order k :

$$\begin{bmatrix} y_t \\ x_t \\ z_t \end{bmatrix} = \begin{bmatrix} c_1 \\ c_2 \\ c_3 \end{bmatrix} + \sum_{j=1}^k \begin{bmatrix} \phi_{1,j} & \phi_{2,j} & \phi_{3,j} \\ \phi_{21,j} & \phi_{22,j} & \phi_{23,j} \\ \phi_{31,j} & \phi_{32,j} & \phi_{33,j} \end{bmatrix} \cdot \begin{bmatrix} y_{t-j} \\ x_{t-j} \\ z_{t-j} \end{bmatrix} + \begin{bmatrix} u_{yt} \\ u_{xt} \\ u_{zt} \end{bmatrix} \quad (1)$$

where $c = (c_1, c_2, c_3)'$ is a vector of constants, $\phi_{il,j}$ are fixed coefficients and $u_t = (u_{yt}, u_{xt}, u_{zt})'$ is a trivariate white noise process with nonsingular covariance matrix. In this framework, we have that x does not Granger cause y , with respect to the information set $I_{y\tilde{x}}(t)$, if and only if $\phi_{12,j} = 0$ for $j=1,2,\dots,k$. This characterization of the condition of non-causality is often used in literature to perform Granger causality tests.

As a final remark on these Granger causality analyses, it is worthwhile to note that, obviously, the VAR model is a linear one, while it is well known that climate system is highly nonlinear. Thus, considering linear models for investigating causal relationships in this framework could seem inappropriate.

However, in our investigations annual averages are always considered. Therefore, it is quite reasonable that, as a consequence of the central limit theorem [7], averaging can produce near-linear climate relations among variables of the climate system, even if we have to do with highly nonlinear relations at shorter spacetime scales. Thus, we are confident that also a linear model can provide a “first-order” estimate of existence or non-existence of causal links in the climate system. Possible generalizations to nonlinear Granger analyses will be briefly discussed in the last section.

3. APPLICATION TO ATTRIBUTION

At our knowledge, the first paper dealing with Granger causality for attribution of global warming was published by Sun and Wang in 1996 [8]. After that paper, several other papers were published on this topic. All these studies performed in-sample analyses (see [9], for a concise but comprehensive review, and references therein) and their final results were sometimes contrasting.

As a matter of fact, the in-sample approach in statistical analyses could lead to overfitting and, therefore, to not catch realistic relationships among variables involved. Furthermore, significant in-sample Granger causality does not guarantee significant out-of-sample predictability. Moreover, out-of-sample tests are often recommended because they are able to catch the true forecasting ability of one variable for another, and the results are more robust in terms of overfitting [10-12].

In order to overcome the problems that raise in an in-sample approach, according to the analysis of Ashley et al. [13], in recent studies [14,15] we used a technique that relies on the out-of-sample comparison of the forecasting performance of two linear models. This may be more robust in terms of model selection biases and overfitting [11,12]. Furthermore, according to Granger’s definition, Granger causality builds upon the notion of incremental predictability, so that our out-of-sample approach is more keeping the spirit of the original definition by Granger [6]. In what follows we will briefly sketch the method used and the results obtained in our studies.

First of all, one can select several external forcings and test, in a bivariate manner, which of them is Granger causal for global temperature in the last decades. We consider total solar irradiance (TSI), cosmic ray intensity (CRI) and stratospheric aerosol optical thickness (SAOT) as natural forcings. As far as anthropogenic forcings are concerned, CO₂, CH₄ and N₂O concentrations data were taken into account for these major greenhouse gases (GHGs), their single radiative forcings (RFs) were calculated

and considered as effective forcings, and also a GHG-total RF has been estimated. See [14] for details on the sources of data.

If we consider $y = T$ and x_i ($i = 1, \dots, 7$) = one of the external forcings, in our application we can compare the predictive ability one step ahead (in terms of mean square error – MSE) of the two following nested regression models:

$$\text{VAR: } y_t = \delta_1^{(i)} + \sum_{j=1}^k \alpha_j^{(i)} y_{t-j} + \sum_{j=1}^k \beta_j^{(i)} x_{i,t-j} + \varepsilon_t^{(i)} \quad (2)$$

$$\text{AR: } y_t = \delta_2 + \sum_{j=1}^k \gamma_j y_{t-j} + \eta_t \quad (3)$$

Here, $\delta_1^{(i)}$ and δ_2 are constants included as deterministic terms, x_i is the i -th forcing, $\alpha_j^{(i)}$, $\beta_j^{(i)}$ and γ_j are coefficients of our regressions, $\varepsilon_t^{(i)}$ and η_t are univariate white noises. The order k of the models is kept low ($k = 1, \dots, 4$), so that the models are parsimonious and the residuals are uncorrelated, and the models finally selected are those endowed with the best predictive performance on each test set.

We perform Granger out-of-sample tests on five test sets which span the following periods: 1941-2007, 1951-2007, 1961-2007, 1971-2007, 1981-2007. For each test set, the correspondent training set is composed by data patterns since 1850 till the year before the beginning of the test set itself.

We adopt both fixed and recursive schemes for predictions. Under the recursive scheme we use the training set for the first estimate and forecast out-of-sample one step ahead; then we add an annual pattern to our training set, obtain a second estimate and forecast for the next year; and so on, iteratively. Under the fixed scheme the parameters are estimated only once on the original training set and every one-step ahead forecast is obtained using just these fixed parameters.

The statistical significance of results is evaluated by MSE-t and MSE-REG tests, as described in [16]. However, here we are not able to use critical values of these test statistics, as reported in [16], because our series are not stationary. So, we perform a bootstrap procedure to calculate our critical values: see [14] for further details.

The results obtained by this out-of-sample Granger analysis are very clear. If we take TSI, CRI or SAOT as x variable, in every case (any natural forcing, scheme and test set considered) the null hypothesis of non-Granger causality on $y = T$ is never rejected (with only two exceptions), even just at 10% significance level. *Vice versa*, there is a clear general evidence of Granger causality from anthropogenic forcings to global temperature: in Tab.1 we report just the results for GHG-total RF, which show that the null hypothesis of non-Granger causality is always rejected at 1% significance level (see [14] for the complete results and other detailed considerations).

In short, these results show that a genuine Granger out-of-sample predictive approach permits to overcome problems shown by previous in-sample analyses and gives a clear contribution to the assessment of temperature attribution.

Forcing	Test set	Fixed scheme			Recursive scheme		
		VAR order	MSE-t	MSE-REG	VAR order	MSE-t	MSE-REG
Total RF	1941–2007	3	3.36*	3.46*	3	2.36*	2.36*
	1951–2007	1	4.43*	4.91*	3	2.79*	2.86*
	1961–2007	3	4.07*	4.65*	3	2.56*	2.69*
	1971–2007	3	4.13*	4.83*	3	2.57*	2.74*
	1981–2007	3	2.85*	3.18*	3	1.92*	2.01*

Table 1: Results of Granger-causality bivariate analysis for GHG-total RF. Here * indicates that the null hypothesis is rejected at 1% significance level. VAR orders are referred to the models with the best predictive ability.

However, technically speaking, it is possible to find Granger causality from x to y in a bivariate system although x does not Granger cause y when also the information contained in a third “context” variable z is taken into account [17,18].

Furthermore, from a climatic point of view, our system shows an its own internal variability which can contribute to changes in global temperature, at least at decadal scale. Thus, it seems a good idea to insert some index of this climate variability as a context variable z in the information set in order to test the causality relationships from anthropogenic/natural forcings to T even within this extended framework.

For z we consider one of the following indices: Southern Oscillation Index (SOI), related to El Niño Southern Oscillation (ENSO); Pacific Decadal Oscillation (PDO); Atlantic Multidecadal Oscillation

(AMO): see [15] for details on the sources of data. Moreover, the results by the VAR unrestricted model described in Eq. (1) are now compared with those coming from the following restricted model:

$$\begin{bmatrix} y_t \\ x_t \\ z_t \end{bmatrix} = \begin{bmatrix} a_1 \\ a_2 \\ a_3 \end{bmatrix} + \sum_{j=1}^k \begin{bmatrix} \theta_{11,j} & 0 & \theta_{13,j} \\ \theta_{21,j} & \theta_{22,j} & \theta_{23,j} \\ \theta_{31,j} & \theta_{32,j} & \theta_{33,j} \end{bmatrix} \cdot \begin{bmatrix} y_{t-j} \\ x_{t-j} \\ z_{t-j} \end{bmatrix} + \begin{bmatrix} v_{yt} \\ v_{xt} \\ v_{zt} \end{bmatrix}. \quad (4)$$

By adopting the same test sets described before, the one-step-ahead forecast errors were calculated as:

$$\hat{u}_{yt} = y_t - \hat{c}_1 - \sum_{j=1}^k \hat{\phi}_{11,j} y_{t-j} - \sum_{j=1}^k \hat{\phi}_{12,j} x_{t-j} - \sum_{j=1}^k \hat{\phi}_{13,j} z_{t-j}, \quad (5)$$

$$\hat{v}_{yt} = y_t - \hat{a}_1 - \sum_{j=1}^k \hat{\theta}_{11,j} y_{t-j} - \sum_{j=1}^k \hat{\theta}_{13,j} z_{t-j}. \quad (6)$$

As previously done in the bivariate case, also now we evaluate the MSE of these prediction and used the MSE-t and MSE-REG tests in order to test the null hypothesis. Moreover, another bootstrap procedure is performed to calculate the critical values of these tests (see [15] for further details).

The results obtained in this way can be summarized as follows. If we take GHG-total RF as the x variable, in every case (all circulation patterns and test sets considered) – except one – the null hypothesis of Granger non-causality on T is rejected at the 5% significance level, and very often also at 1% significance. Thus, there is clear evidence that a causal link (in the Granger sense) between GHG-total RF and global temperature since 1941 up to the present day can be “detected” even in this extended framework.

On the other hand, if TSI is considered as the x variable, a Granger causal link is significant only in the first test set when AMO is included in the information set, and in the first two sets when PDO and ENSO are considered. In more recent periods this causal link disappears.

The situation becomes even more clear if the p-values of tests are plotted for every test period, as in Fig.1: see [15] for other figures and detailed tables. Here, it is evident that the Granger causal link between TSI and T becomes progressively less marked with time and completely disappears for the last

two periods. In particular, the influences of GHG-total RF and TSI on T appear comparable till the '50s, but, after that decade, a clear causal decoupling between TSI and T is evident and very marked in the data of our Granger analysis. At the same time, the Granger causality from GHG-total RF to T remains robust and, possibly, becomes even more evident: the p-values, which are already very small, decrease further.

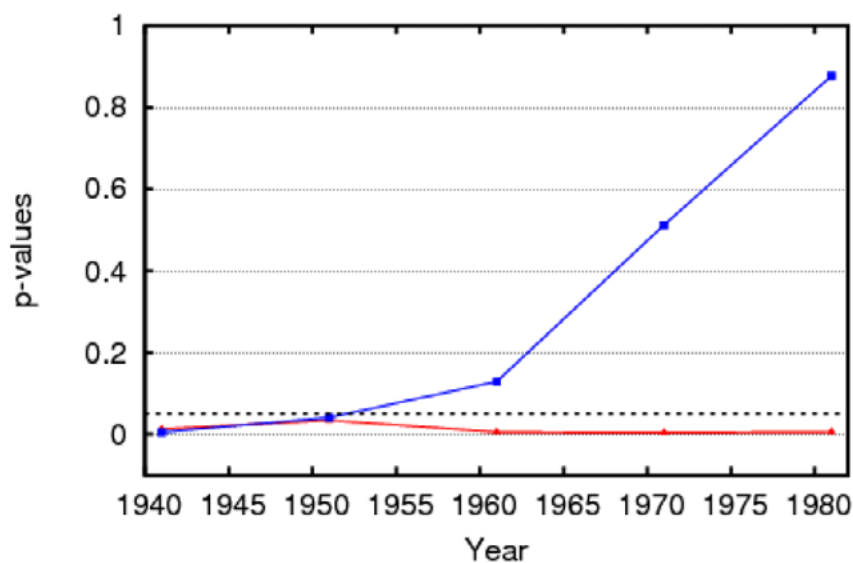


Fig. 1: Plot of the p-values from the MSE-REG test when $x = \text{TSI}$ (blue line) and $x = \text{GHG-total RF}$ (red line) for $z = \text{ENSO}$. The significance threshold of 0.05 is shown (dashed line). The increase in p-values over the recent decades is evident for the performance of the model with TSI.

In particular, in this way we evidenced a causal decoupling between Sun and global temperatures which has been pictured previously just in terms of simple correlations and graphical methods [19,20].

As a final remark, we note that the p-values of the Granger causality tests when AMO is considered in the information set are always higher than the corresponding ones in the cases of $z = \text{PDO}$, ENSO. Thus, when AMO is inserted in the information set, the causal role of external forcings seems to weaken. This indirectly suggests that, among the various patterns of natural variability, AMO plays a more relevant role in driving the global temperature behaviour at decadal time scales.

4. CONCLUSIONS AND PROSPECTS

The results obtained in our investigations are very clear: the radiative forcings of greenhouse gases appear as the main temperature drivers, while natural forcings do not Granger cause T in the last decades, in the case of Sun even if the principal patterns of climate variability are considered in an extended trivariate model. Furthermore, the direct influence of the Sun on T (*via* TSI) shows a recent causal decoupling since the '60s. In particular, our results corroborate those coming from GCMs and neural models.

Some prospects of further investigations are clearly indicated by analyses and results of past studies. In particular, inside a trivariate context we have tested the direct Sun influence *via* TSI. But, what's about the possible joint roles of direct and indirect Sun influences on T, where the indirect forcing could be represented by cosmic rays (modulated by solar wind)?

Another open question is: if we are not able to show linear links between Sun and T, is it possible that a causal link could be found in a nonlinear framework? As far as this problem is concerned, it is worthwhile to note that two of us (AA and UT) developed a nonlinear extension of a Granger causality model based on neural networks and applied it to the classical problem of CO₂ influences on T. Outcomes from a nonlinear in-sample Granger causality analysis are consistent with other results assessing that CO₂ radiative forcing causes recent global temperatures [21]. In future, this extension could be applied to trivariate out-of-sample investigations.

In particular, this nonlinear approach could show its usefulness in analyses of attribution at reduced space-time scales and when the behaviour of other variables of climatic importance, such as precipitation, are considered. It is well known, in fact, that many nonlinear processes are involved in the hydrological cycle and they cannot be easily "averaged away".

5. REFERENCES

- Hegerl G.C. et al. (2007), *Understanding and attributing climate change*. In *Climate Change 2007: The Physical Science Basis*, S. Solomon et al. Eds., Cambridge University Press, pp. 663-745. (1)
- Hegerl G.C. & Zwiers F.W. (2011), *Use of models in detection and attribution of climate change*, WIREs Climate Change, No. 2, pp. 570-591. (2)
- Pasini A., Lorè M. & Ameli F. (2006), *Neural network modelling for the analysis of forcings/temperatures relationships at different scales in the climate system*, Ecological Modelling, No. 191, pp. 58-67. (3)
- Pasini A. & Langone R. (2010), *Attribution of Precipitation Changes on a Regional Scale by Neural Network Modeling: A Case Study*, Water, No. 2, pp. 321-332. (4)
- Pasini A. & Langone R. (2012), *Influence of Circulation Patterns on Temperature Behavior at the Regional Scale: A Case Study Investigated via Neural Network Modeling*, Journal of Climate, No. 25, pp. 2123-2128. (5)
- Granger C.W.J. (1969), *Investigating causal relations by econometric models and cross-spectral methods*, Econometrica, No. 37, pp. 424-438. (6)
- Yuval & Hsieh W.W. (2002), *The impact of time-averaging on the detectability of nonlinear empirical relations*, Quarterly Journal of the Royal Meteorological Society, No. 128, pp. 1609-1622. (7)
- Sun L. & Wang M. (1996), *Global warming and global dioxide emission: An empirical study*, Journal of Environmental Management, No. 46, pp. 327-343. (8)
- Attanasio A., Pasini A. & Triacca U. (2013), *Granger Causality Analyses for Climatic Attribution* (submitted for publication). (9)
- Chao J., Corradi V. & Swanson N. (2001), *Out-of-sample test for Granger causality*, Macroeconomical Dynamics, No. 5, pp. 598-620. (10)
- Clark T. (2004), *Can out-of-sample forecast comparisons help prevent overfitting?*, Journal of Forecasting, No. 23, 115-139. (11)
- Gelper S. & Croux C. (2007), *Multivariate out-of-sample tests for Granger causality*, Computational Statistics & Data Analysis, No. 51, pp. 3319-3329. (12)
- Ashley, R., Granger, C.W.J. & Schmalensee, R. (1980), *Advertising and aggregate consumption: an analysis of causality*, Econometrica, No. 48, 1149-1167. (13)

- Attanasio A., Pasini A. & Triacca U. (2012), *A contribution to attribution of recent global warming by out-of-sample Granger causality analysis*, Atmospheric Science Letters, No. 13, pp. 67-72. (14)
- Pasini A., Triacca U. & Attanasio A. (2012), *Evidence of recent causal decoupling between solar radiation and global temperature*, Environmental Research Letters, No. 7, 034020. (15)
- McCracken M.W. (2007), *Asymptotics for out-of-sample tests of Granger causality*, Journal of Econometrics, No. 140, pp. 719-752. (16)
- Lütkepohl H. (1982), *Non-causality due to omitted variables*, Journal of Econometrics, No. 19, pp. 367-378. (17)
- Hamilton, J.D. (1994), *Time Series Analysis*, Princeton University Press. (18)
- Lockwood M. & Fröhlich C. (2007), *Recent oppositely directed trends in solar climate forcings and the global mean surface air temperature*, Proceedings of the Royal Society A, No. 463, pp. 2447-2460. (19)
- Stauning P. (2011), *Solar activity-climate relations: A different approach*, Journal of Atmospheric Solar-Terrestrial Physics, No. 73, pp. 1999-2012. (20)
- Attanasio A. & Triacca U. (2011), *Detecting human influence on climate using neural networks based Granger causality*, Theoretical and Applied Climatology, No. 103, 103-107. (21)

Reliability and skill of CMIP5 multi-model decadal hindcasts

Corti S.*

ISAC-CNR, Bologna, Italy

*Corresponding author: s.corti@isac.cnr.it

Abstract

The reliability of multi-year predictions of climate is assessed using probabilistic Reliability Diagrams for near-surface air temperature, based on 63 member ensembles of initialised and non-initialised decadal hindcasts using the CMIP5 ten-year decadal climate prediction experiments. It is shown that the reliability from the ensemble system is good for most regions studied, for both initialised and non-initialised hindcasts. Over the North Atlantic the reliability and the resolution of the hindcasts show a substantial improvement for initialised predictions, confirming the importance of the initialisation for this region. Initialisation seems to play a (positive) role in other regions as well, however more experiment are necessary to assess if the improvement is significant.

Keywords: *Near-term climate predictions, Predictability, Probabilistic Measures of Skill, Reliability*



1. INTRODUCTION

Decadal climate predictions exploit both the predictability of the climate system arising from the initial-condition information and from the changes in radiative external forcings [1]. As such they represent the natural extension of seasonal predictions and they must be probabilistic, arising from uncertainties [1] in the knowledge of the initial state, in the computational representation of the underlying equations of motion and in the so-called “forcing” terms, which include greenhouse gases and (natural and anthropogenic) aerosols. Probabilistic predictions are issued as ensembles and they have to be evaluated on the basis of whether they give an accurate estimation of the relative frequency of the predicted outcome. When this happens they are considered “reliable”. The word “reliable” has a specific technical meaning in probability forecasting. Suppose a decadal forecast probability of some event E – say that that temperature lies above the long-term climatological median value – is equal to 0.9. For a reliable forecast system, one could assert that E would actually occur on 90% of occasions where E was forecast with a probability of 0.9.

The decadal prediction system under study here is based on a multi-model dataset from CMIP5 [2]. In this study we assess the reliability and the prediction skill of such a system in simulating the variability of surface and near-surface temperature over multi-year time scales for selected geographical regions.

2. RESULTS

A previous paper [3] showed results from ten sets of ECMWF decadal climate prediction experiments based on four different versions of ECMWF coupled model. Then we assess the reliability and the prediction skill of such a system in simulating the variability of surface and near-surface temperature over multi-year time scales for selected geographical regions. Here we revisit the problem considering a multi-model dataset from CMIP5 [2], which consist of 63 ensemble members of initialised and non-initialised predictions from 13 models. (For each model the same number of initialised and non-initialised ensemble members has been used). Following previous climate prediction studies that highlighted the importance of the initialisation over the North Atlantic Ocean (e.g. [4] [5]), we focus here mainly on this basin and on the Global Ocean.

Near-surface air temperature and sea surface temperature data from ERA Interim [6] and, prior to 1979, from ERA40 [7] are used to evaluate the hindcasts. The reference period is estimated as the average of the entire period from 1960 to 2010. To take into account the model systematic error,

forecast anomalies for each experiment are calculated as: $X'_{j\tau} = X_{j\tau} - \bar{X}_{k\tau}$ where j is the starting year ($j=1,n$), τ is the forecast month ($\tau=1,120$) and $\bar{X}_{k\tau} = \frac{1}{n-1} \sum_{j \neq k} X_{j\tau}$ is the forecast average estimated in cross-validation mode (i.e. estimated removing the model climate for the specific forecast period).

We consider a skill measure, the Brier Skill Score (BSS), based on metrics for categorical probabilistic predictions: (i.e. we want to evaluate the forecasts on the basis of whether they give an accurate estimation of the relative frequency of the predicted outcome). The BSS can be decomposed in two components: Reliability and Resolution. The BSS measures the improvement of the probabilistic forecast relative to a reference forecast (in our case the sample climatology). The reliability measures how close the forecast probabilities are to the observed frequencies. The resolution measures how much the forecast probabilities differ from the climatological probability of the event.

Attributes Diagrams [8,9] are used to illustrate the multi-model CMIP5 decadal hindcast reliability. They measure how closely the forecast probabilities of an event correspond to the actual chance of observing the event. They are based on a discrete binning of many forecast probabilities taken over a given geographical region $\langle x \rangle$. In figure 1 below we will illustrate such Attributes Diagrams for the event $E(x) = \text{''Surface air temperature above the median''}$ for the Global Ocean and the North Atlantic Ocean. For perfect reliability the forecast probability and the frequency of occurrence should be equal, and the plotted points should lie on the diagonal.

Since skill in these decadal hindcasts comes mainly from radiative forcing and the predictive component of natural climate variability, a comparison between initialised and non-initialised hindcasts is the best way to assess the relative importance of initial conditions with respect to forcing.

Figure 1 shows Attributes Diagrams for $E(x)$ for Global and North Atlantic Ocean for Initialised and Non-Initialised predictions at lead time 2-5 year. The BSS for the North Atlantic is higher than for the Global Ocean and it increases when the predictions are initialised. (The moderate skill of the Global Ocean increases as well with initialisation). The Reliability Skill Score of Initialised Predictions over the North Atlantic for this Event is as large as 0.99 (0.95 for Non-Initialised). An improvement in reliability for initialised forecasts for the Global Ocean can be detected as well (0.95 vs. 0.93). The other Ocean basins (not shown) do not present evident changes in reliability when initialised and non-initialised predictions are compared. As far as the BSS is concerned, a summary of the (probabilistic) skill of initialised and non-initialised CMIP5 integrations can be found in tables 1-4. Here we consider cold

(below the lower tercile) and warm (above the upper tercile) events and we list the BSS for sea surface temperature and near surface air temperature over different oceanic and land regions for lead times 2-5 year (tables 1-2) and 6-9 year (tables 2-4). Overall it seems that the CMIP5 multi-model is more skilful in predicting warm events than cold ones (for both initialised and non-initialised predictions).

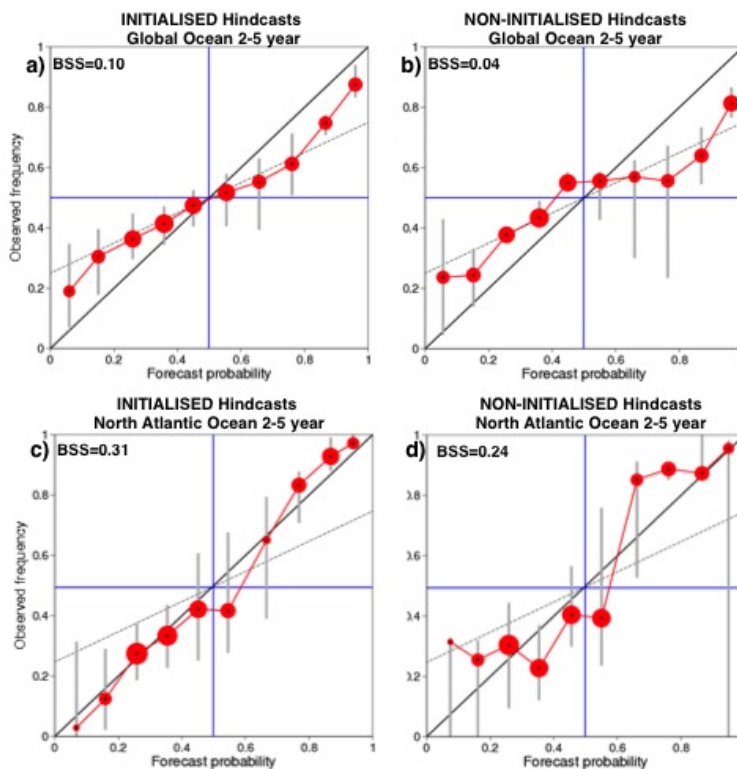


Fig. 1: Attributes diagram for the CMIP5 multi-model decadal initialized (panels a and c) and non-initialized (panels b and d) hindcasts for the event ‘Surface Air Temperature anomalies above the median’ over a) and b) the global oceans (60°N–60°S) and c) and d) the North Atlantic (87.5°N–30°N, 80°W–10°W) for the forecast time 2–5 years. The number of red bullets in the figure corresponds to the number of probability bins (10 in this case) used to estimate forecast probabilities. The size of the bullets represents the number of forecasts in a specific probability category and is a measure of the sharpness of the predictions. The blue horizontal and vertical lines indicate the climatological frequency of the event in the observations and the mean forecast probability, respectively. Grey vertical bars indicate the uncertainty in the observed frequency for each probability category estimated at 95% level of confidence with a bootstrap resampling procedure based on 1000 samples. The longer the bars, the more the vertical position of the bullets may change as new hindcasts become available. The black dashed line separates skilful from unskilled regions in the diagram in the Brier skill score sense. The Brier skill score with respect to the climatological forecast is drawn in the top left corner of each panel.

As pointed out in previous studies (e.g. [10]) the Tropical Indian Ocean stands out as the oceanic basin where multi-year predictions are more skilful both at 2-5 and 6-9 year. However, it appears that the skill is mainly due to the radiative forcing, since there is not much difference between initialised and non-initialised predictions. A negative value of the BSS indicates a very poor forecast (worse than climatology). The only region with a negative BSS is the North Pacific Ocean. Here, despite the potential initial values predictability highlighted by many studies (e.g. [11]) most of CMIP5 models fail in predicting the multi-year natural variability of the SSTs [12]. The initial conditions seem to play a role over the Tropical Atlantic for warm events at lead time 6-9 year. This re-emergence of predictability at longer lead times over the Tropical Atlantic is encouraging because Tropical Atlantic SSTs affect the climate variability over the nearby continental regions [4], such as Central and Western Africa and Southern Europe.

Tables 1-4 show the BSS over some continental areas affected by the Atlantic variability as Europe (here are shown separately Northern and Mediterranean Europe) and Africa. In both continents the skill is considerably high but initialised and non-initialised predictions are equally skilful indicating that (at the moment) it is not evident a positive effect of the initialisation over the continents.

3. CONCLUSIONS

Overall these results are quite consistent with those shown in [3]. This indicates that there is a substantial consistency between different prediction systems. (The study of Corti et al. 2013 [3] was based on different versions of ECMWF coupled system, which are not included in the CMIP5 dataset). Near-term climate predictions appear to be substantially reliable over most of the regions considered (with some important exception though) and they present an encouraging level of skill. However the level of uncertainty associated to these measures of skill (not shown here) is very large. Most of the uncertainty is due to the exiguity of the sample (in terms of number of starting dates) analysed. A better assessment of the skill of decadal predictions will require a better sampling of the climatic attractor, i.e. a larger number of starting points for the hindcasts.

Table 1. Brier Skill Score – Lead Time: 2-5 Year Average

Event: Surface Air Temperature Below The Lower Tercile

	TROP ATL	NORTH ATL	EURO LAND	MED LAND	NORTH EURO LAND	AFRICA	TROP INDIAN	NORTH PACIFIC
CMIP5 INIT	0.04	0.25	0.43	0.48	0.37	0.35	0.50	-0.06
CMIP5 NOINIT	0.01	0.17	0.48	0.50	0.45	0.41	0.56	-0.08

Table 2. Brier Skill Score – Lead Time: 2-5 Year Average

Event: Surface Air Temperature Above The Upper Tercile

	TROP ATL	NORTH ATL	EURO LAND	MED LAND	NORTH EURO LAND	AFRICA	TROP INDIAN	NORTH PACIFIC
CMIP5 INIT	0.24	0.44	0.61	0.63	0.59	0.33	0.57	-0.08
CMIP5 NOINIT	0.18	0.39	0.62	0.61	0.60	0.30	0.54	-0.12

Table 3. Brier Skill Score – Lead Time: 6-9 Year Average

Event: Surface Air Temperature Below The Lower Tercile

	TROP ATL	NORTH ATL	EURO LAND	MED LAND	NORTH EURO LAND	AFRICA	TROP INDIAN	NORTH PACIFIC
CMIP5 INIT	0.04	0.22	0.46	0.46	0.46	0.43	0.59	0.02
CMIP5 NOINIT	0.06	0.17	0.46	0.44	0.49	0.40	0.57	-0.04

Table 4. Brier Skill Score – Lead Time: 6-9 Year Average

Event: Surface Air Temperature Above The Upper Tercile

	TROP ATL	NORTH ATL	EURO LAND	MED LAND	NORTH EURO LAND	AFRICA	TROP INDIAN	NORTH PACIFIC
CMIP5 INIT	0.21	0.38	0.63	0.69	0.54	0.29	0.38	-0.1
CMIP5 NOINIT	0.16	0.38	0.63	0.69	0.55	0.26	0.37	-0.09

4. ACKNOWLEDGMENTS

This work was supported by the EU-funded projects THOR (FP7/2007-2013) under grant agreement 212643, and COMBINE (FP7/2007-2013) under grant agreement 226520.

5. REFERENCES

- Hawkins, E. and R. Sutton (2009) *The potential to narrow uncertainty in regional climate predictions*. Bull. Amer. Meteor. Soc., 90, 1095–1107. (1)
- Taylor Karl E., Stouffer Ronald J., Meehl Gerald A. (2012), *An Overview of CMIP5 and the Experiment Design*. Bull. Amer. Meteor. Soc., 93, 485–498. (2)
- Corti S., Weisheimer A., Palmer T., Doblus-Reyes F., and Magnusson L. (2012), *Reliability of decadal predictions*. Geophys. Res. Lett., doi:10.1029/2012GL053354. (3)
- Keenlyside N.S., Latif M., Junglaus J., Kornblueh L., and Roeckner E. (2008), *Advancing decadal-scale climate prediction in the North Atlantic sector*. Nature. 453, 84–88. (4)
- Pohlmann H., Junglaus J. H., Kohl A., Stammer D., and Marotzke J. (2009), *Initializing Decadal Climate Predictions with the GECCO Oceanic Synthesis: Effects on the North Atlantic*. J. Climate, 22, 3926–3938. (5)
- Dee D.P., and co-authors (2011), *The ERA-Interim reanalysis: configuration and performance of the data assimilation system*. Q. J. R. Met. Soc., 137, 553–597. (6)

- Uppala S. M., and Coauthors (2005), The ERA-40 Re-Analysis. *Quart. J. Roy. Meteor. Soc.*, 131, 2961–3012. (7)
- Hsu W.-R., and Murphy A. H., (1986), *The attributes diagram: A geometrical framework for assessing the quality of probability forecasts*. *Int. J. Forecasting*, 2, 285–293. (8)
- Palmer T. N., Doblas-Reyes F. J., Weisheimer A., Rodwell M. J. (2008), *Toward Seamless Prediction: Calibration of Climate Change Projections Using Seasonal Forecasts*. *Bull. Amer. Meteor. Soc.*, 89, 459–470. (9)
- Guemas V., Corti S., Garcia-Serrano J., Doblas-Reyes F., Balmaseda M. and Magnusson L. (2012), *The Indian Ocean: the region of highest skill worldwide in decadal climate prediction*. *Journal of Climate*. DOI:10.1175/JCLI-D-12-00049.1. (10)
- Deser C., Phillips A., Bourdette V., and Teng H. (2010), *Uncertainty in climate change projections: the role of internal variability*. *Clim. Dyn.*, doi:10.1007/s00382-010-0977-x. (11)
- Doblas-Reyes F.J., Andreu-Burillo I., Chikamoto Y., García-Serrano J., Guemas V., Kimoto M., Mochizuki T., Rodrigues L.R.L. and van Oldenborgh G.J. (2013). *Initialized near-term regional climate change prediction*. *Nature Communications*. 4, 1715, doi:10.1038/ncomms2704. (12)

Snow depth in the “Third Pole”: how do CMIP5 models represent it?

Terzago S.^{*}, Von Hardenberg J., Palazzi E., Provenzale A.

ISAC-Institute of Atmospheric Sciences and Climate, CNR, Torino, Italy

**Corresponding author: s.terzago@isac.cnr.it*

Abstract

The Tibetan Plateau and the Hindu-Kush Karakoram Himalaya mountains, with mean elevation above 4000 m above sea level (a.s.l.), are the world's largest snow and ice reservoir outside the polar regions and they are often referred to as the “Third Pole”. These mountains provide water to about 1.5 billion people in Afghanistan, Bangladesh, Bhutan, China, India, Myanmar, Nepal and Pakistan, and changes in snow dynamics would impact on water availability for downstream populations. Despite its importance, the knowledge on the snow dynamics in the Third Pole region is still incomplete, due to difficult and sporadic surface observations. In this work we investigate how CMIP5 Global Climate Model (GCM) simulations represent the snowpack in the Third Pole environment, we explore the snow seasonal cycle and we compare the results to the ERA-Interim/Land reanalysis.

Keywords: *Snow, CMIP5, Global Climate Models, Third Pole, Hindu-Kush Karakoram Himalaya*



1. INTRODUCTION

With their 5 million Km² extension the Hindu-Kush Karakoram Himalaya and the Tibetan Plateau (Fig.1) are the largest mountain range in the world, including the 14 world's highest peaks above 8,000 m above sea level (a.s.l.). This area hosts the largest reservoir of snow and ice mass outside the polar regions and it is often referred to as the “Third Pole” [1] to point out its relevance in the Earth's cryosphere. The snow melting from the mountains feeds all of Asia's major river systems, providing water to about 1.5 billion people living downstream [2]. The contribution of the snow and glacier melt to the stream flow may vary in the region and it becomes more and more important in the areas that do not receive monsoonal summer precipitation, such as the Hindu-Kush Karakoram and Western Himalaya. Here summer precipitation is relatively scarce and the contribution of meltwater is the major source for the river flow. For example, almost 90% of the mean annual flow of the Indus river system is estimated to originate from the Hindu-Kush Karakoram and Western Himalaya mountains [3]. This feature makes the Third Pole Environment crucial for both local economies and socio-economical activities in the bordering countries.

The scientific community has recently examined this region with increasing interest, recognizing it as particularly vulnerable to climatic change. In fact in high elevation areas a change in the surface air temperature may have an impact on the solid/total precipitation ratio, on the snow cover extension and consequently on the snow/albedo feedback. Changes in the snow amount and duration in the Third Pole might have a direct effect on the availability and seasonal distribution of the water resources, thus on the environment, the ecosystems and all socio-economical activities in the mountains and the surrounding lowlands.

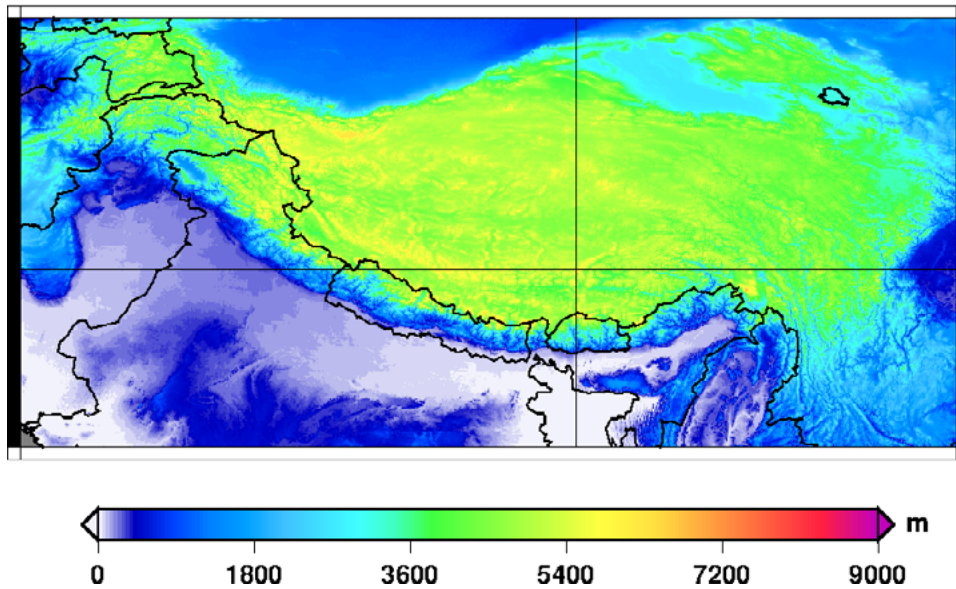


Fig.1: The “Third Pole”: area of study and its elevation in meters above sea level.

Despite its relevance, some current climatic features of the Third Pole, such as precipitation and in particular snow, are still poorly known, mainly due to the difficulties in performing regular meteorological observations in high elevation areas. The highest density of surface snow depth observations is in the Eastern Tibetan Plateau, which currently represents also the most studied area of the Third Pole. For example a recent study [4] used the available data to map the distribution of the mean winter snow depth over the Eastern Tibetan Plateau and explored the relations with the China summer monsoon. Concerning the Karakoram, another study [5] analyzed 10-year time series of snow depth and water equivalent measurements derived from several automatic weather stations at elevation between 1500 and 4700 m a.s.l.: they found that at approximately 5000 m a.s.l. the total annual precipitation ranges between 1500-1800 mm/y and more than 90% of it is deposited as snow. In the valley snow contributes less than 10% to the total annual precipitation. Several studies have been performed on the Hindu-Kush Karakoram Himalaya glaciers (i.e. [6, 7]) and a review is offered in [8]. In that paper the authors draw a picture of the status of the main glaciers of the region and they point out the existing gaps in the present knowledge: the seasonal and spatial variability of mountain snow and ice, along with the annual melting and its contribution to the total discharge are all uncertain mainly owing to the insufficient number of surface observations, only partly balanced by satellite measurements.

Considering the strong limitations associated with scarce availability of observations, in this work we investigate the large-scale features of the snowpack in the Third Pole region using the Global Climate Model simulations included in the CMIP5 experiment [9]. In particular we explore how different GCMs represent the snow climatology over the Third Pole region. The results are compared to the ERA-Interim/Land reanalysis [10], considered here as the best approximation of the ground truth.

2. DATA AND METHODOLOGY

The area of study includes the Tibetan Plateau and the Hindu-Kush Karakoram Himalaya mountains. We considered all CMIP5 GCMs providing the snow depth variable, including the EC-Earth model run at ISAC-CNR [11].

The spatial resolution of CMIP5 models varies in a wide range, from 0.75° up to 2.8125° . We excluded from our analysis the models with too coarse spatial resolution and we considered only those with a maximum gridsize of 1.25° (Tab.1).

For each model we selected the first ensemble member of the historical runs and we generated seasonal maps of the average winter (December-January-February) snow depth. The models climatology has been compared to the ERA-Interim/Land snow depth reanalysis.

Dataset	Spatial Resolution [$^\circ$ longitude]
CMCC-CM	0.75
BCC-CSM1.1m	1.125
MRI-CGCM3	1.125
EC-Earth	1.125
CESM1-BGC	1.25
ERA-Interim/Land	0.75

Tab.1: Datasets used in this study: five high resolution (not coarser than 1.25°) CMIP5 Global Climate Models providing the snow depth variable and ERA-Interim/Land Reanalysis.

We used GCMs and reanalysis data at their original spatial resolution rather than regridding the model data to a common resolution grid in order to not introduce artificial uncertainties related to the spatial interpolation. We calculated the spatial averages of snow depth by weighting the original GCM values

(at the native resolution) by the fraction of each grid cell with elevation greater than 1000 m a.s.l. The GCM snow depth climatologies were compared to the ERA-Interim/Land reanalysis in the overlapping period 1980-2005.

3. RESULTS

Snow depth spatial variability

Fig.2 represents the spatial distribution of the winter (DJF) mean snow depth obtained from the CMIP5 GCM historical simulations averaged over the period 1980-2005. The maps are ordered according to the model grid size, from the highest to the lowest spatial resolution. The ERA-Interim/Land snow field (top left panel) can be considered as an approximation of the ground truth. In correspondence of the Baltoro glacier ERA-Interim/Land presents a fictitious peak of about 10 m of snow water equivalent: since this value is not intended to be representative of the real conditions, the Baltoro area has been excluded from the analysis below.

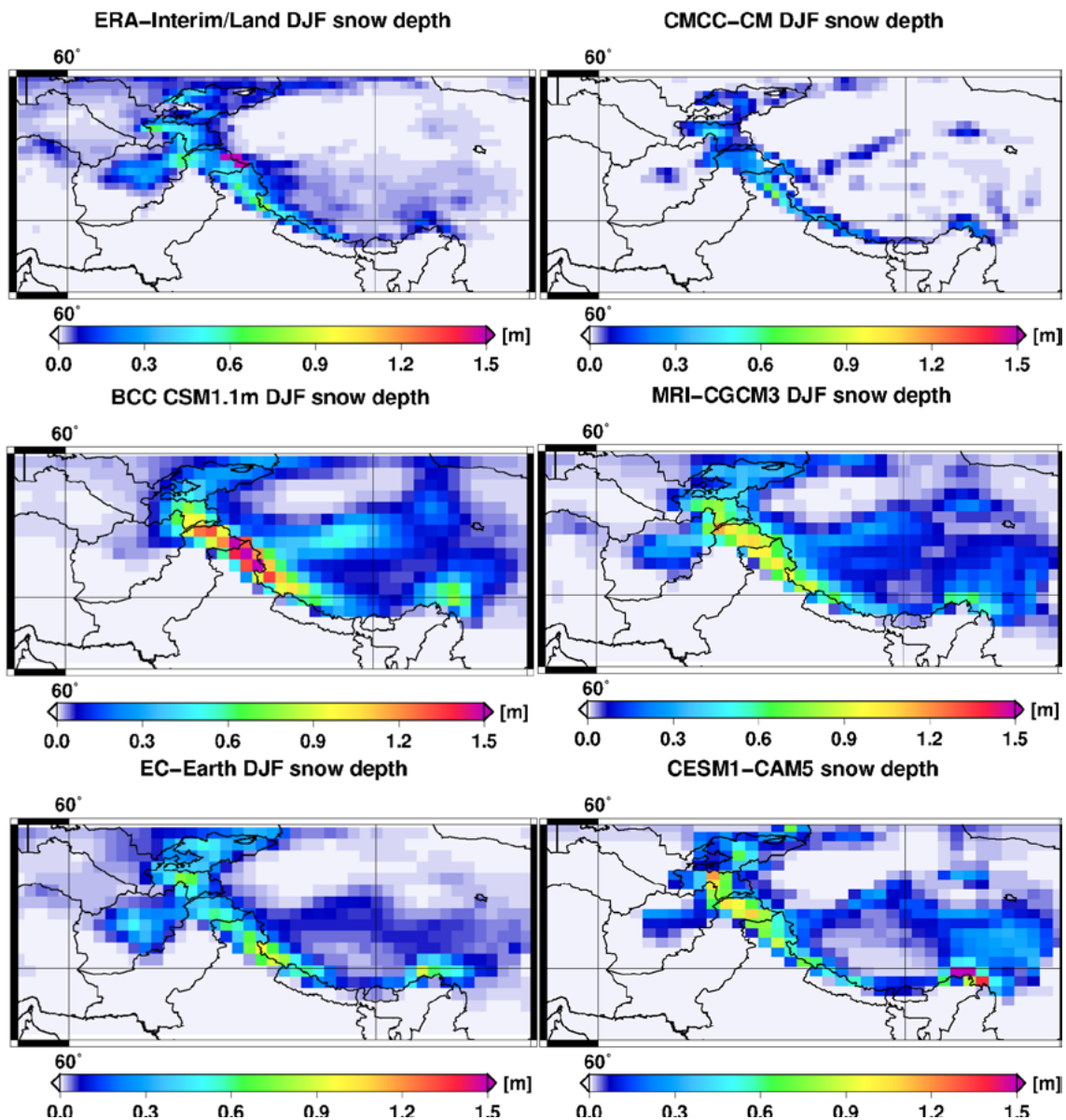


Fig. 2: Spatial distribution of the winter (DJF) snow depth fields obtained from CMIP5 GCM simulations. The maps represent multiannual averages over the period 1980-2005 and they are ordered according to decreasing spatial resolution. The corresponding ERA-Interim/Land snow depth product is reported in the top left panel.

All GCMs identify a similar spatial pattern with a snow depth peak over the Hindu-Kush Karakoram and Western Himalaya mountains and decreasing values moving toward the Himalaya in South-East direction. Another snow depth peak is found in the South-Eastern part of the Tibetan plateau, at the border with India. The models are in fairly good agreement with the ERA-Interim/Land reanalysis, but they generally represent thicker snow depth throughout the region. The main difference among the GCMs is found over the Tibetan plateau: while BCC and MRI models identify continuous and locally

deep winter snowpack, the other models show a shallower (EC-Earth and CESM1) or almost negligible (CMCC-CM) snow depth. The surface observation data available from Chinese stations confirm the presence of thick snowpack in the Eastern and South-Eastern Tibetan Plateau, where winter average snow depth is locally above 20 cm [4]. For the rest of the region it is very difficult to make a comparison with the ground-truth due the lack of surface observations.

Seasonal cycle

We explored how the high resolution GCMs simulate the snow seasonal cycle in the Third Pole. We selected the mountains above 1000 m a.s.l. (excluding Baltoro area) and we calculated for each model the average monthly snow depth in the period 1980-2005 and then the GCMs ensemble mean (Fig.3). All GCMs and ERA-Interim/Land present a unimodal snow regime, with the maximum generally occurring in March. The spread among the models is remarkable, with the CMCC-CM representing the shallowest snowpack and BCC-CSM1.1M the thickest. Compared to ERA-Interim/Land reanalysis, the EC-Earth model provides the closest picture, nevertheless it tends to overestimate snow depth in late autumn and early winter. The ensemble mean shows that the GCMs identify a thicker snowpack with respect to ERA-Interim/Land reanalysis throughout the season.

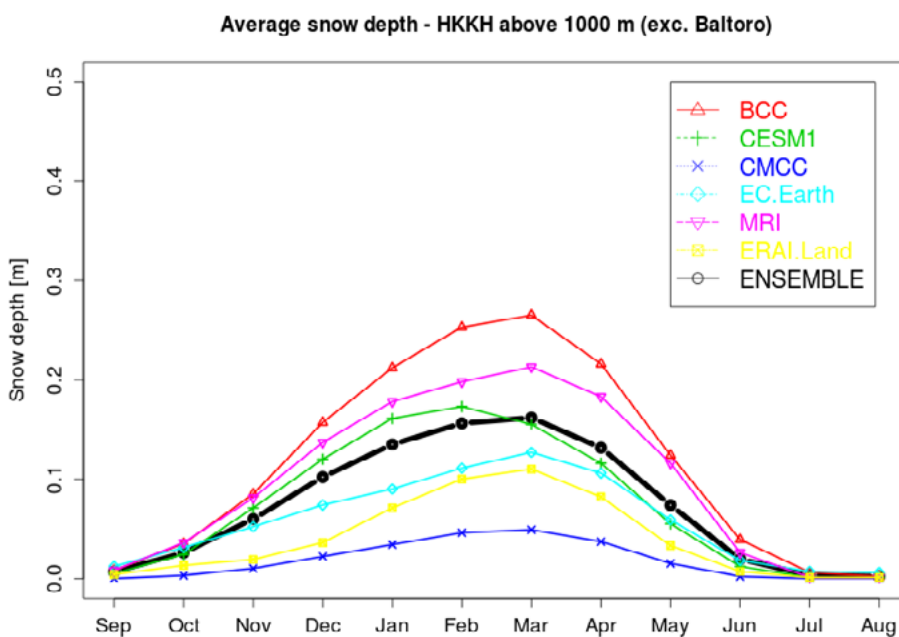


Fig. 3: Seasonal cycle of snow depth in the Third Pole region (area above 1000 m a.s.l.) obtained from the high spatial resolution GCMs. The values refer to the multiannual monthly averages over the period 1980-2005.

4. DISCUSSION AND CONCLUSIONS

The definition of the snow characteristics in the mountains of the Third Pole region is extremely difficult owing to insufficient surface observations. Despite this, we used the simulations of the Global Climate Models to infer information on large-scale snow features. We considered the datasets provided by the CMIP5 GCMs in order to investigate how they represent the winter snowpack distribution and the seasonal cycle. The GCMs intercomparison shows an overall agreement in the reproduction of the spatial patterns of snow depth. Some differences are found when looking at the thickness of the snowpack, that shows a spread among the models. In average the GCMs tend to overestimate snow depth over the Third Pole region in comparison to the ERA-Interim/Land reanalysis, anyway it is difficult to establish what model performs best in such a poorly instrumented area. The results suggest that relying on a single GCM could lead to a biased picture of the snow features in the Third Pole region.

The present study will be extended focusing the attention, separately, on the different climatic subregions of the Third Pole environment (i.e. the Tibetan Plateau, the Hindu-Kush Karakoram and the Himalaya) and exploring the temporal variability of the snowpack in the past 150 years and its expected changes in the future decades.

5. ACKNOWLEDGMENTS

This work was funded by the Ev-K2-CNR SHARE-PAPRIKA-Karakoram project and by the NextData project of the Italian Ministry of Education, University and Research (<http://www.nextdataproject.it>).

6. REFERENCES

- Qiu J. (2008), *China: the Third Pole*. Nature, 454, 393-396. (1)
- Yao T., Thompson L. G., Mosbrugger V., Zhang F., Ma Y., Luo T., & Fayziev R. (2012), *Third Pole Environment (TPE)*. Environmental Development, 3, 52-64. (2)
- Liniger H., Weingartner R. & Grosjean M. (1998), *Mountains of the world: water towers for the 21st century*. Mountain Agenda for the Commission on Sustainable Development (CSD), BO12: Berne; 32. (3)

- Qian Y.F., Zheng Y.Q., Zhang Y. & Miao M.Q. (2003), *Responses of China's summer monsoon climate to snow anomaly over the Tibetan Plateau*. *International Journal of Climatology*, 23, 593–613. (4)
- Winiger M., Gumpert M. & Yamout H. (2005), *Karakorum–Hindukush–western Himalaya: assessing high-altitude water resources*. *Hydrological Processes*, 19, 2329–2338. (5)
- Hewitt K (2005), *The Karakoram Anomaly? Glacier Expansion and the 'Elevation Effect,' Karakoram Himalaya*. *Mountain Research and Development*, 25 (4), 332-340. (6)
- Gardelle J., Berthier E. & Arnaud Y. (2012), *Slight mass gain of Karakoram glaciers in the early 21st century*. *Nature Geoscience* 5, 322–325. (7)
- Bolch T., Kulkarni A., Kääb A., Huggel C., Paul F., Cogley J.G., Frey H., Kargel J.S., Fujita K., Scheel M., Bajracharya S. & Stoel M. (2012), *The State and Fate of Himalayan Glaciers*. *Science*, 336 (6079), 310-314. (8)
- Taylor K.E., Stouffer R.J. & Meehl G.A. (2012), *An Overview of CMIP5 and the Experiment Design*. *Bulletin American Meteorological Society*, 93, 485-498. (9)
- Balsamo G., Albergel C., Beljaars A., Boussetta S., Brun E., Cloke H., Dee D., Dutra E., Pappenberger F., de Rosnay P., Sabater J.M., Stockdale T. & Vitart F. (2012). *ERA-Interim/Land: A global land-surface reanalysis based on ERA-Interim meteorological forcing*. ERA Report Series 13, 25 pp. (10)
- Hazeleger W., et al. (2012), *EC-Earth v2.2: description and validation of a new seamless earth system prediction model*. *Climate Dynamics*, pp. 1–19. (11)

Heavy precipitation events over the Euro-Mediterranean region in a warmer climate: results from CMIP5 models

Scoccimarro E.^{1,2*}, Gualdi S.^{1,2}, Bellucci A.², Zampieri M.² and Navarra A.^{1,2}

¹*Istituto Nazionale di Geofisica e Vulcanologia (INGV), Bologna, Italy*

²*Centro Euro-Mediterraneo sui Cambiamenti Climatici (CMCC), Lecce, Italy*

*Corresponding author: enrico.scoccimarro@bo.ingv.it

Abstract

In this work the authors investigate possible changes in the intensity of heavy precipitation events under a warmer climate, using the results of a set of 20 climate models taking part to the Coupled Model Intercomparison Project phase 5 effort (CMIP5). Future changes are evaluated as the epoch difference between the last four decades of the 21st and the 20th Century assuming the Representative Concentration Pathway RCP8.5 scenario. As a measure of the intensity associated with heavy precipitation events, we use the difference between the 99th and the 90th percentiles. Despite a slight tendency to underestimate the observed heavy precipitation intensity, the considered CMIP5 models well represent the observed patterns during both summer and winter seasons for the 1997-2005 period. Future changes in average precipitation are consistent with previous findings based on CMIP3 models. In addition, we found a projected increase of the width of the right tail of the distribution in a warmer climate, even over regions where nearly the entire precipitation distribution becomes dryer. This is the case of the Euro-Mediterranean domain.

Keywords: *Extreme Events, Precipitation, CMIP5, Europe*



1. INTRODUCTION

Changes in the frequency and intensity of extreme events can affect human health directly through heat waves and cold spells and indirectly through floods or pollution episodes [1, 2, 3]. Because of these large societal and economic impacts, it is of paramount importance to assess potential changes in the upper tail of the rainfall distribution. The availability of a new set of climate simulations for the twenty-first century, carried out with state of the art coupled GCMs produced for the fifth Coupled Model Intercomparison Project (CMIP5 [4]), gives us the possibility to investigate future changes in intense precipitation following one of the Representative Concentration Pathways (RCPs) considered as illustrative of potential future scenarios. The present analysis is performed following the RCP8.5 scenario, the one with the highest rate of increase in greenhouse gas concentrations within the new set of RCPs. The main aim of this work is to inspect changes in the shape of the right tail of the precipitation events distribution under warmer conditions over the Euro-Mediterranean region, comparing the last part of the twenty-first century with the last part of the twentieth century, as simulated by a set of CMIP5 climate models. The paper is organized as follows. Section 2 describes the data and provides an overview of the methodology used, Section 3 presents the results of the analyses, and Section 4 summarizes the main points of the study and concludes the paper.

2. DATA AND METHODOLOGY

For this analysis we use daily precipitation fields from a subset of the CMIP5 multimodel ensemble, consisting of simulations of the twenty and twenty-first century climate performed with 20 coupled ocean-atmosphere climate models (see table 1). CMIP5 simulations are conducted in support of the fifth assessment report of the Intergovernmental Panel on Climate Change (IPCC-AR5). The horizontal resolution of the atmospheric component of the considered models ranges from about 0.75 to about 3.5 degrees with a median of 1.7 degrees. Two periods are analysed: the period 1966-2005 (hereafter PRESENT), corresponding to the last part of the 'historical' CMIP5 simulation and the period 2061-2100 (hereafter FUTURE), run under the high-end RCP8.5 scenario (5,6). The 'historical' simulation is performed forcing CMIP5 models with observed concentrations of greenhouse gasses, aerosols, ozone and solar irradiance, starting from an arbitrary point of a quasi-equilibrium control run. The RCP8.5 scenario follows a rising radiative forcing pathway leading to 8.5 W/m² in 2100.

For this analysis we make use of daily precipitation fields. The capability of the CMIP5 models to simulate the present climate in terms of heavy precipitation events has been assessed using daily data from the Global Precipitation Climatology Project (GPCP, [7]), of the period 1997-2005 (hereafter PRES). In the rest of the paper, for the sake of simplicity we will refer to the GPCP data as ‘observations’. In this work we aim to assess potential changes in precipitation extremes that might have a societal impact, thus we mainly focus on precipitation over land.

To investigate how CMIP5 models represent the right tail of the precipitation distribution compared to observations, we computed the 90th and 99th percentiles (hereafter 90p and 99p) obtained by aggregating daily precipitation values, belonging to the investigated period, over each single grid point. Furthermore, in our analysis, we want also to assess how heavy rainfall, defined as daily events with a precipitation amount greater than the 90p, might change in intensity. To this aim, we use the difference between the 99p and 90p, where the former is representative of very intense precipitation and the latter is the threshold used to define an event as heavy rainfall. This metric has been defined, separately for PRESENT and FUTURE climates, to quantify the width of the right tail of the precipitation distribution. Percentiles are computed for each model, on the corresponding original spatial grid. Individual model results have been then interpolated onto the GPCP regular grid to allow the multi-model averaging.

For abbreviation purposes, we will refer to ‘future changes’ to indicate changes between the FUTURE (2061-2100) and the PRESENT (1966-2005) periods.

3. RESULTS

Previous assessments [8] have shown that at global scale The 90p and 99p are consistently simulated at middle and high latitudes by CMIP5 models, but they tend to underestimate these indices in the Tropics, especially in the northern summer and also at high latitudes in the Northern Hemisphere during northern winter and Southern Hemisphere during northern summer. This tendency is noticeably less pronounced when only models with a horizontal resolution finer than 1.5 degrees are considered (about 50% of the CMIP5 models used in this analysis, see table 1), but the dispersion around the mean does not change (not shown).

Over the Euro-Mediterranean region the 99p-90p model ensemble mean properly captures observed spatial patterns, despite a general tendency to underestimate this metric (Figure 1) during summer and

overestimating it during winter in Northern Europe. Future changes in climatological precipitation patterns (Figure 2 left panels) are overall coherent with previous findings [9] obtained using CMIP3 (the previous phase of the Coupled Model Intercomparison Project) models. During winter a general increase/decrease in precipitation over land is found in Northern/Southern Europe (45N is here used to separate the two mentioned regions). During summer, a similar behaviour is found but with a northward shift of the latitude corresponding to the change of sign (now 55N instead of 45N) if compared to winter results. Future changes in 90p (Figure 2, central panels) follow the described changes in average precipitation. The usage of 99p-90p gives the possibility to better investigate changes in the right tail of the distribution of precipitation events, especially over regions where both 90p and 99p increase/decrease. In fact, despite the very similar patterns found in future changes of climatological precipitation and 90p (Figure 2, left and central panels respectively), the 99p-90p changes, pertaining to heavy precipitation events (Figure 4, right panels), look different: in the FUTURE period the 99p-90p metric increases in almost the entire domain, even over regions where average precipitation and 90p values show a decrease (red patterns in Figure 2). This is the case of southeast Europe during summer, where the width of the right tail of the distribution increases, even if nearly the entire precipitation distribution becomes dryer (i.e., decreases in total, 90p, and 99p precipitation). This positive tendency is then more pronounced for the rightmost part of the rainfall distribution, compared with the leftmost part in the FUTURE period with respect to the PRESENT period are shown.

4. DISCUSSION AND CONCLUSIONS

In this paper we apply the difference between 99th and 90th percentile of the daily precipitation resulting from a set of twenty CMIP5 simulations, with the aim of quantifying potential changes in the width of the right tail of precipitation distribution, thus to the range of values attributable to a heavy (greater than 90p) precipitation event.

Precipitation intensity seems to increase more than mean precipitation under a warmer climate, over a substantial portion of the Euro-Mediterranean domain, confirming previous findings [10, 11, 12]. These changes are consistent with a greater moisture-holding capacity of the warmer air contributing to greater moisture convergence [13] and with the Clausius–Clapeyron dependence which is relevant for heavy precipitation events [14], which are able to empty the atmospheric moisture column [15, 16]. It is

in fact well known that increases in atmospheric water vapour content are generally associated with increases in heavy precipitation in a warmer climate [17, 18]. The width of the right tail of the precipitation event distribution increases almost everywhere over Europe, independently of the direction in which the distribution evolves in a warmer climate, suggesting more heavy precipitation events especially. The increased availability of water in a warmer climate, is confirmed by the water vapour content (WCONT), vertically integrated through the atmospheric column (Figure 3).

To a first approximation, if one considers no changes in precipitation efficiency (here defined as the ratio of total precipitation to total available moisture), we would link the increased width of the right tail of FUTURE precipitation distribution to the increased availability of WCONT: a precipitation event increases its probability to be associated with a column of air with a water content greater than what is available in the PRESENT climate. Regional changes in the atmospheric circulation patterns [19] might also alter the statistics of the heavy rain events. However a conclusive disentangling of the causes underlying the detected changes in the precipitation distribution is beyond the purpose of this work. In summary, despite the fact that model projections of future changes in heavy precipitation events in response to global warming might be underpredicted [16], a picture of a Euro-Mediterranean region with intensifying heavy precipitation events over the majority of land seems confirmed by CMIP5 model projections for the end of the twenty-first century, at least following a future scenario with a continuous rise in radiative forcing during the twenty-first century. This implies increasing risks for natural and human systems that are sensitive to wet extremes [20,14].

5. ACKNOWLEDGMENTS

The research leading to these results has received funding from the Italian Ministry of Education, University and Research and the Italian Ministry of Environment, Land and Sea under the GEMINA project. We also acknowledge the World Climate Research Programme's Working Group on Coupled Modelling, which is responsible for CMIP, and we thank the climate modelling groups for producing and making available their model output. For CMIP the U.S. Department of Energy's Program for Climate Model Diagnosis and Intercomparison provided coordinating support and led development of software infrastructure in partnership with the Global Organization for Earth System Science Portals.

6. REFERENCES

- Zwiers F.W., Kharin V.V. (1998), *Changes in the extremes of the climate simulated by CCC GCM2 under CO2 doubling*. J. Climate 11, 2200–2222. (1)
- Parry M.L., Canziani O.F., Palutikof J.P., van der Linden P.J. and Hanson C.E. (eds Solomon, S. et al.) *Climate Change 2007, 2007: Impacts, Adaptation and Vulnerability* (Cambridge Univ. Press). (2)
- Peterson T. C. et al. (2008), *Weather and Climate Extremes in a Changing Climate. Regions of Focus: North America, Hawaii, Caribbean, and U.S. Pacific Islands* (eds Karl, T. R. et al.) 11–34. Synthesis and Assessment Product 3.3, US Climate Change Science Program, Washington DC. (3)
- Meehl G.A. and Bony S. (2012), *Introduction to CMIP5. WCRP Coupled Model Intercomparison Project – Phase 5: Special Issue of the CLIVAR Exchanges Newsletter, No. 56, Vol. 15, No. 2.* (4)
- Riahi K, Rao S., Krey V., Cho C., Chirkov V., Fischer G., Kindermann G., Nakicenovic N., Rafaj P. (2011), RCP 8.5—A scenario of comparatively high greenhouse gas emissions. Climatic Change. 109:33-57. DOI 10.1007/s10584-011-0149-y. (5)
- Taylor K.E., Stouffer R.J., Meehl G.A. (2012), *An Overview of CMIP5 and the experiment design*. Bull. Amer. Meteor. Soc., 93, 485-498, doi:10.1175/BAMS-D-11-00094.1. (6)
- Bolvin D.T., Adler R.F., Huffman G.J., Nelkin E.J., Poutiainen J.P. (2009), *Comparison of GPCP monthly and daily precipitation estimates with high-latitude gauge observations*. J. Appl. Meteor. Climatol., 48, 1843-1857. (7)
- Scoccimarro E., Gualdi S., Bellucci A., Zampieri M., Navarra A. (2013), *Heavy precipitation events in a warmer climate: results from CMIP5 models*. Journal of Climate. doi: 10.1175/JCLI-D-12-00850.1. (8)
- Giorgi F. and Bi X. (2009), *Time of emergence (TOE) of GHG-forced precipitation change hot-spots*. Geophys. Res. Lett., 36, L06709, doi:10.1029/2009GL037593. (9)
- Trenberth K. E., Dai A., Rasmussen R., and Parsons D. (2003), *The changing character of precipitation*. Bull. Amer. Meteor. Soc., 84, 1205–1217. (10)
- Meehl G.A., Arblaster J.M., and Tebaldi C. (2005), *Understanding future patterns of increased precipitation intensity in climate model simulations*. Geophys. Res. Lett., 32, L18719, doi:10.1029/2005GL023680. (11)
- Chou C., Neelin J.D., Chen C., and Tu J. (2009), *Evaluating the ‘rich-get-richer’ mechanism in tropical precipitation change under global warming*. J. Climate, 22, 1982–2005. (12)

- Tebaldi C., Hayhoe K., ARBLASTER M.J. and MEEHL G.A. (2006), *Going to the Extremes. An Intercomparison of Model-Simulated Historical and Future Changes in Extreme Events*. Climatic Change 79: 185–211 DOI: 10.1007/s10584-006-9051-4. (13)
- Giorgi F., E.-S. Im, Coppola E., Diffenbaugh N.S., Gao X.J., Mariotti L., Shi Y. (2011), *Higher Hydroclimatic Intensity with Global Warming*. J. Climate, 24, 5309–5324. (14)
- Allen M.R., and Ingram W.J. (2002), *Constraints on the future changes in climate and the hydrological cycle*. Nature, 419, 224–232. (15)
- Allan R.P. and Soden B.J (2008), *Atmospheric Warming and the Amplification of Precipitation Extremes*. Science. (321): 1481-1484. (16)
- Pall P., Allen M.R., Stone D.A. (2007), *Testing the Clausius-Clapeyron constraint on changes in extreme precipitation under CO₂ warming*. Clim Dyn 28:351–363. (17)
- O'Gorman P.A. & Schneider T. (2009), *The physical basis for increases in precipitation extremes in simulations of 21st-century climate change*. Proceedings of the National Academy of Sciences 106, 14773-14777. (18)
- Hertig E., Seubert S., Paxian A., Vogt G., Paeth H., Jacobeit J. (2013), *Changes of total versus extreme precipitation and dry periods until the end of the twenty-first century: statistical assessments for the Mediterranean area*. Theoretical and Applied Climatology, 111 (1-2), pg. 1-20. (19)
- Kunkel K.E., Pielke R. Jr. and Changnon, S. A. (1999), *Temporal fluctuations in weather and climate extremes that cause economic and human health impacts: A review*. Bull. Am. Met. Soc. 80,1077–1098. (20)

Model name	Lat x Lon (degrees)	Institute (Institute ID)
BNU-ESM	2.8 x 2.8	College of Global Change and Earth System Science, Beijing Normal University (GCESS)
CCSM4	0.9 x 1.5	National Center for Atmospheric Research (NCAR)
CMCC-CESM	3.7 x 3.7	Centro Euro-Mediterraneo sui Cambiamenti Climatici (CMCC)
CMCC-CMS	1.9 x 1.9	Centro Euro-Mediterraneo sui Cambiamenti Climatici (CMCC)
CMCC-CM	0.8 x 0.8	Centro Euro-Mediterraneo sui Cambiamenti Climatici (CMCC)
CNRM-CM5	1.4 x 1.4	Centre National de Recherches Meteorologiques / Centre Europeen de Recherche et Formation Avancees en Calcul Scientifique (CNRM- CERFACS)
CSIRO-Mk3-6-0	1.9 x 1.9	Commonwealth Scientific and Industrial Research Organization in collaboration with Queensland Climate Change Centre of Excellence (CSIRO-QCCCE)
CanESM2	2.8 x 2.8	Canadian Centre for Climate Modelling and Analysis (CCCMA)
FGOALS-s2	1.6 x 2.8	LASG, Institute of Atmospheric Physics, Chinese Academy of Sciences (LASG-IAP)
GFDL-CM3	2.0 x 2.5	NOAA Geophysical Fluid Dynamics Laboratory (NOAA GFDL)
GFDL-ESM2G	2.0 x 2.5	NOAA Geophysical Fluid Dynamics Laboratory (NOAA GFDL)
GFDL-ESM2M	2.0 x 2.5	NOAA Geophysical Fluid Dynamics Laboratory (NOAA GFDL)
HadGEM2-CC	1.2 x 1.8	Met Office Hadley Centre (MOHC)
HadGEM2-ES	1.2 x 1.8	Met Office Hadley Centre (MOHC)
INM-CM4	1.5 x 2.0	Institute for Numerical Mathematics (INM)
IPSL-CM5A-MR	1.2 x 2.5	IPSL-CM5A-LR Institut Pierre-Simon Laplace (IPSL)
MIROC5	1.4 x 1.4	Atmosphere and Ocean Research Institute (The University of Tokyo), National Institute for Environmental Studies, and Japan Agency for Marine-Earth Science and Technology (MIROC)
MPI-ESM-MR	1.9 x 1.9	Max Planck Institute for Meteorology (MPI-M)
MRI-CGCM3	1.1 x 1.1	Meteorological Research Institute (MRI)
NorESM1-M	1.8 x 2.5	Norwegian Climate Centre (NCC)

Tab. 1: CMIP5 models involved in this study. Bold values in the second column indicate horizontal resolution finer than 1.5°.

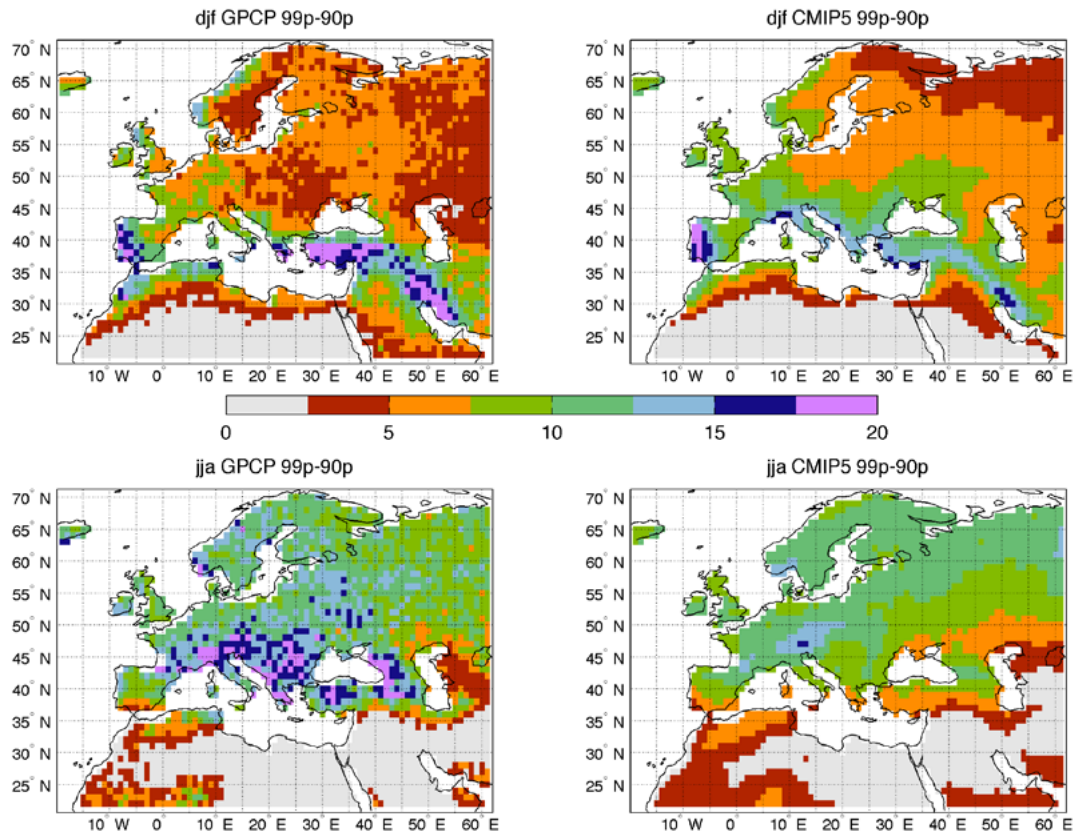


Fig. 1: Measure of the right tail of the precipitation events distribution, represented as 99p-90p during the period 1997-2005 as obtained by the observations (left panels) and CMIP5 (average over the 20 models, right panels). Upper panels refer to boreal winter and lower panels refer to boreal summer. Units are [mm/d].

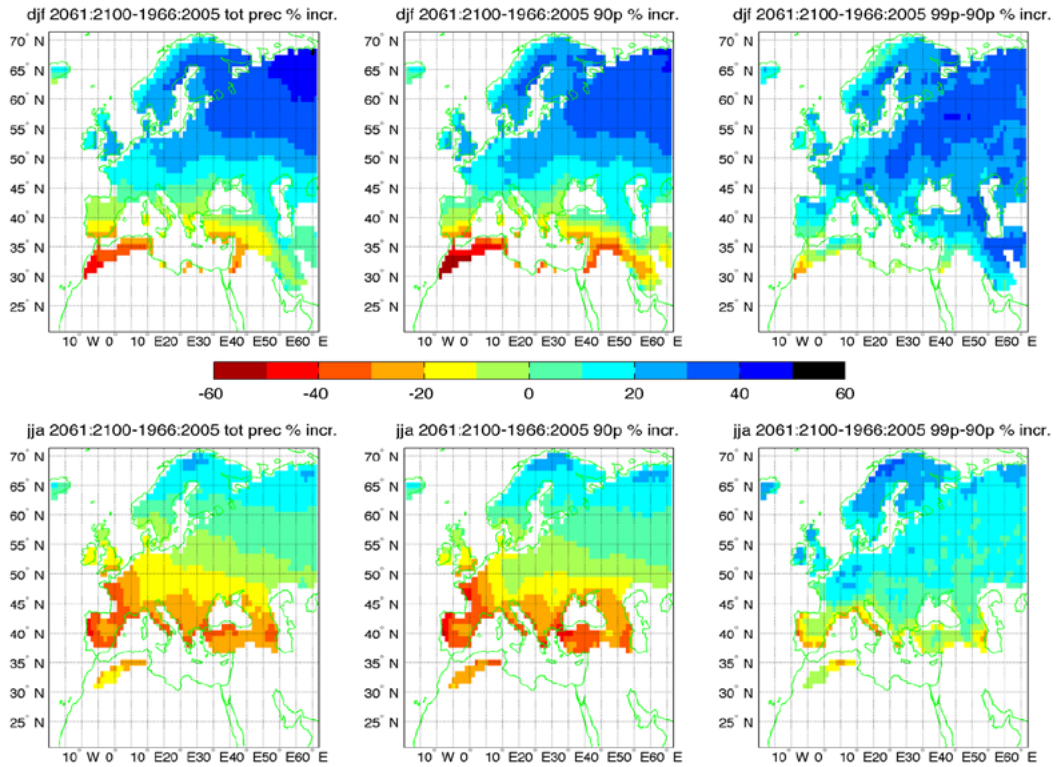


Fig. 2: Future changes (2061-2100 – 1966-2005) in average precipitation (left panels), 90th percentile of precipitation (90p, central panels) and width of the right tail of the precipitation events distribution (99p-90p, right panels) following the RCP8.5 CMIP5 scenario, as averaged over the CMIP5 models. Upper panels refer to boreal winter and lower panels refer to boreal summer. Units are [%]. White patterns over land indicate regions with seasonal precipitation lower than 0.5 mm/d.

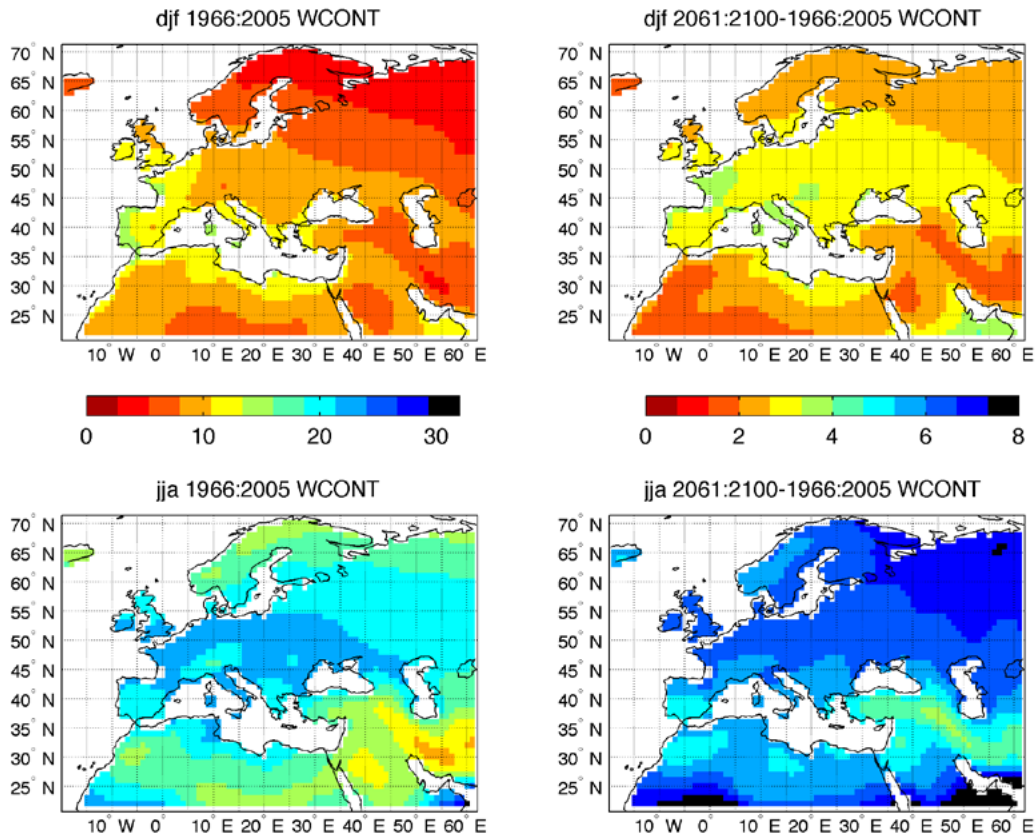


Fig. 3: Water vapour content (WCONT), vertically integrated through the atmospheric column, during the 1966-2005 period (left panels) and increase in 2061-2100 wrt 1966-2005 as averaged over the CMIP5 models. Upper panels refer to boreal winter and lower panel refer to boreal summer. Units are [Kg/m²].

ADVANCES IN CLIMATE SCIENCE

Modes of variability in the atmosphere and ocean

Effects of the North Atlantic Oscillation on winter precipitation in the Hindu-Kush Karakoram

Filippi L.^{1,2*}, Palazzi E.¹, von Hardenberg J.¹ and Provenzale A.¹

¹*Institute of the Atmospheric Sciences and Climate (ISAC)-CNR, Torino, Italy*

²*Dipartimento di Ingegneria Meccanica e Aerospaziale, Politecnico di Torino, Torino, Italy*

*Corresponding author: luca_filippi@polito.it

Abstract

The Hindu-Kush Karakoram (HKK) region, the westernmost part of the Himalayan chain, receives considerable precipitation amounts during winter, mostly associated with the arrival of westerly perturbations (Western Weather Patterns, WWP) that originate from the Mediterranean and the North Atlantic. In this work, we study the effects of the North Atlantic Oscillation (NAO) on winter precipitation over this area, using an ensemble of precipitation datasets and the reanalysis ERA40. We focus on the NAO-induced changes in moisture transport influencing precipitation and we investigate the NAO effects on tropospheric circulation, evaporation, surface wind speed, sea surface temperature and precipitable water from the reanalysis output. An Earth system model (EC-Earth) is tested against the observations/reanalyses to check its skill in reproducing WWP and the mechanisms by which the NAO affects winter precipitation in the HKK. We find that above (below) than normal precipitation occurs in correspondence of the positive (negative) NAO phase. Most of the humidity comes from the Arabian area, where moisture from the Northern Arabian Sea, the Persian Gulf, the Red Sea and even the Mediterranean converges. During the positive NAO phase there is an intensification of moisture transport towards Pakistan and Western India, which is associated with changes in tropospheric circulation and evaporation from these reservoirs. As a result, wetter than normal conditions occur at the foot of the Himalayas and the enhanced available humidity is picked up by WWP that release more precipitation over the HKK slopes. Simulation results from the EC-Earth model are in good agreement with the observations and the reanalysis in the time period from 1957 to 2002. Further investigations will include the possibility to repeat the analysis with EC-Earth using the whole historical simulation (from 1850 to 2005) and for the future (until 2100) under different emission scenarios, in order to evaluate possible changes that occurred in the past and might occur in the WWP activity.

Keywords: *Precipitation, North Atlantic Oscillation, Hindu-Kush Karakoram Himalaya.*



The Hindu-Kush Karakoram (HKK) region constitutes the westernmost part of the Himalayan range, encompassing parts of Afghanistan, Pakistan, India and China. Being the largest mountain region in the world, the whole Himalayan chain feeds some of the major rivers of Southeast Asia (such as the Ganges, the Brahmaputra, the Indus, the Yellow river and the Yang-Tze) bringing water to more than 1.5 billion people [1]. For this reason, the understanding of the hydrological cycle in this area and the study of its possible changes in the next decades are of major importance both from a scientific and a geopolitical point of view and a necessary step to develop adequate adaptation strategies.

There are two main circulation patterns bringing precipitation in the Himalayas: during summer, the Indian monsoon produces high precipitation amounts over the Indian subcontinent and the central and eastern Himalayan range; conversely, during winter, considerable precipitation amounts affect the HKK due to the presence of westerly perturbations, here referred to as Western Weather Patterns (WWP). These systems are low pressure synoptic weather systems that originate from the Mediterranean or even the North Atlantic and move eastward until they reach the HKK. Winter precipitation over this area mostly accumulates in form of snowpack, helping the preservation of glaciers and constituting an important water source for river basins during the whole year [2].

Given the crucial role played by WWP systems in regulating the hydrological cycle of the region, there is an increasing interest into the study of their variability and of teleconnection patterns affecting these circulations (see for example [3] and [4]). In particular, as WWP originate from the Northeastern Atlantic and the Mediterranean regions, strongly influenced by the North Atlantic Oscillation (NAO) especially during winter (see for example [5]), one could expect that the NAO affects also WWP, regulating precipitation over the HKK. Previous works indeed found a correlation between the NAO and precipitation in this area, with above (below) than normal amounts during the positive (negative) NAO phase ([2], [3], [4] and [6]).

It is worth pointing out that the complex orography of the HKK poses a severe constraint to the meteorologic monitoring. Although the efforts made in the recent years to increase the number of stations, the spatial coverage of observations is still sparse and biased by altitude and there are problems in detecting the snow component of precipitation, which is not negligible in this area. All these uncertainties make it difficult to consider any single dataset as a reference “truth” for precipitation [1]. For these reasons, in this work we consider an ensemble of precipitation datasets, including satellite TRMM (Tropical Rainfall Measuring Mission) observations, three rain-gauge-based

datasets - the Asian Precipitation Highly-Resolved Observational Data Integration Towards Evaluation of Water Resources (APHRODITE), the Global Precipitation Climatology Centre (GPCC) and the Climate Research Unit (CRU) - and the ERA40 reanalysis, to study the NAO effects on precipitation in the HKK and, at the same time, to investigate which differences arise when choosing a particular dataset rather than another one. The main features of these datasets are resumed in Tab.1.

The main purpose of this work is to investigate which are the mechanisms that contribute to establish the link between the NAO and precipitation in the HKK. Some authors ([3]) associated the intensification of WWP with the effect of an enhanced sea level pressure and 500 hPa trough which develops over Central-Southwest Asia during the positive NAO phase. Another study ([4]) showed that pressure anomalies associated with the positive NAO phase intensify the Asian jet stream over North Africa and the Middle East, up to Northwestern India, which in turn intensifies WWP. Finally, [3] pointed out that the transport of extra moisture during the positive NAO phase from the Mediterranean, the Caspian Sea and the Arabian Sea contributes to the NAO-precipitation signal in Northern Pakistan.

We perform an analysis of moisture transport towards the HKK to identify the main water sources for humidity and precipitation over this area and to analyze the changes occurring in moisture transport associated with the NAO phase. We investigate the possible causes, by analyzing the NAO effects on evaporation from the identified sources and tropospheric circulation toward the HKK. To this end, evaporation, specific humidity, sea surface temperature and wind data from the ERA40 reanalysis have been used. Moisture transport and precipitable water are calculated following the approach of [9] from 3-dimensional fields of specific humidity and horizontal wind.

Dataset	Type	Period	Spatial coverage	Temporal resolution	Spatial resolution
APHRODITE V1003R1 product	in-situ gridded	1951-2007	60°E-150°E 15°S-55°N	Daily	0.25x0.25°
GPCC	in-situ gridded	1901-2009	Global	Monthly	0.5x0.5°
CRU TS3.10 product	in-situ gridded	1901-2010	Global	Monthly	0.5x0.5°
TRMM 3B42 product	Satellite	1998-2007	global belt 50°S-50°N	3-hour	0.25x0.25°
ERA40	Reanalysis	Sept 1957 Aug 2002	Global	6-hour	1.125x1.125°

Tab. 1: Considered datasets and main features.

In the present work, the winter season is defined to include months from December to March (DJFM) and the NAO is measured with the DJFM station-based NAO index (NAOI) of [8], which is based on the difference between the normalized sea level pressure in Lisbon (Portugal) and in Stykkisholmur/Reykjavik (Iceland). The analysis is based on correlations and composites calculated over the period 1958-2002, which is the overlapping period between the considered datasets (excluding TRMM).

The whole analysis is repeated with the EC-Earth model to assess its ability to reproduce WWP and the associated mechanisms. EC-Earth is an Earth system model based on state-of-the-art models for the atmosphere, the ocean, land, sea ice and the biosphere developed by a consortium of more than 20 European research institutions ([7]). We use the v2.3 release, run at T159 horizontal spectral resolution (corresponding to a grid of about 1.125° latitude-longitude) with 62 vertical levels for the atmosphere. In this work, the output of the historical simulation (from 1850 to 2005) run at ISAC-CNR is analysed. The run is forced by reconstructed solar variability and anthropogenic forcing. Since the oscillation patterns (such as the NAO) in global climate model simulations are not in phase with the observed oscillations, a NAO index for EC-Earth is calculated with the same method as defined in [8] using sea level pressure data from the model output fields.

The study of the NAO effects on winter precipitation shows that all the considered datasets coherently exhibit enhanced precipitation over the HKK during the positive NAO phase. This is particularly evident when considering the difference between the positive and the negative NAO composites of

precipitation, which show the highest absolute values outside the European domain over Northern Pakistan and Northern India. However, differences between the datasets arise in the spatial distribution and in the significance of correlation coefficients. In particular, the three datasets based on the interpolation of in-situ station data (APHRODITE, CRU and GPCC) similarly show significant correlations over a spatially limited area, while ERA40 shows a stronger signal, with significant correlations over a broader area from Northern Afghanistan to Northern India. These differences reflect the difficulty of having reliable precipitation estimates over this region due to the complex orography, problems in detecting snowfall and the sparse coverage of stations. The signal in the EC-Earth model is within the range of the signals observed in the other datasets, showing that the model reliably reproduces the effects of the NAO on precipitation.

The analysis of moisture transport in the ERA40 reanalysis shows that most of the humidity in the HKK region comes from the Arabian area, where moisture from the Northern Arabian Sea, the Persian Gulf, the Red Sea and even the Mediterranean converges. The NAO is found to have a significant effect on moisture transport. During the positive NAO phase, moisture transport over the Mediterranean is strongly reduced, coherently with previous studies showing a more north-eastward oriented transport over the Atlantic, resulting in wet conditions over Northern Europe and reduced moisture transport over the Mediterranean [8]. Conversely, the intensity of moisture transport from the Arabian area towards Pakistan is significantly higher during the positive NAO phase. As a consequence, wetter than normal conditions are found over Northern Pakistan and Northern India, with an accumulation of humidity at the foot of the Himalayan range. The enhanced available humidity is picked up by WWP that release more precipitation as they reach the HKK slopes.

To better understand how the NAO can influence moisture transport and, consequently, precipitation in the HKK, the NAO effects on tropospheric circulation and evaporation from ERA40 are investigated. Since the atmospheric water vapour mainly locates in the lower troposphere, below 500 hPa [9], the main contribution to the total moisture transport is given by circulation in the lower troposphere. During the positive NAO phase, an intensification of lower tropospheric westerly winds from the Arabian area towards Pakistan occurs, allowing for a faster transport of moisture. This anomaly in low level winds is associated with the intensification of the subtropical Asian jet from North Africa to Southwestern Asia in the upper troposphere. Simultaneously, enhanced evaporation occurs from the Red Sea, the Persian Gulf and the Northern Arabian Sea, associated with anomalies of surface wind speed and sea surface temperature and resulting in an increased arrival of humidity in the Arabian

area. Also the Southeastern Mediterranean shows higher evaporation during the positive NAO phase, which is associated to drier conditions of the air, but this anomaly unsuccessfully balances the reduced tropospheric moisture content and transport over this area. As a result, the total moisture transport outgoing the Mediterranean during the positive NAO phase is lower than normal. What can actually cause a higher contribution of moisture from this region to the HKK is the more southward direction of winds, allowing humidity to reach the Arabian area and the main moisture channel from here to the HKK.

The analysis of moisture transport and associated processes in EC-Earth is in a very good agreement with the observations previously made for the reanalysis ERA40. The main difference between the two cases is found for evaporation in the Northern Arabian Sea, where EC-Earth does not show significant changes between the opposite NAO phases. However, the anomaly is of the same sign as in ERA40 and this difference does not affect the intensification of moisture transport towards Pakistan during the positive NAO phase, which is well reproduced by the model. This result has a double implication: on the one hand, it indicates that the model reproduces well not only the NAO effects on precipitation in the HKK, but also the proposed mechanism; on the other hand, it gives robustness to the mechanism itself. These findings give encouraging indications towards the use of the EC-Earth model to investigate the WWP activity in the past decades and to make future projections under different emission scenarios, in order to evaluate possible changes that occurred and might occur and their consequences for precipitation in the Karakoram.

ACKNOWLEDGMENTS

This work was funded by the Ev-K2-CNR SHARE-PAPRIKA-Karakoram project and by the NextData project of the Italian Ministry of Education, University and Research. The numerical simulations with the EC-Earth model used in this study were performed at the CINECA supercomputing center, Rome, grant ext-06-EARTH. We acknowledge the institutions and the teams responsible for the creation and publication of the GPCP, APHRODITE, CRU, TRMM, and ERA40 archives. ERA40 data have been obtained from the ECMWF Data Server.

REFERENCES

- Palazzi E., von Hardenberg J. & Provenzale A. (2013), *Precipitation in the Hindu-Kush Karakoram Himalaya: Observations and future scenarios*. J. Geophys. Res., 118, pp. 85-100. (1)
- Archer D.R. & Fowler H.J. (2004), *Spatial and temporal variations in precipitation in the Upper Indus Basin, global teleconnections and hydrological implications*. Hydrology and Earth System Sciences, 8 (1), pp. 47-61. (2)
- Syed F.S., Giorgi F., Pal J.S. & Keay K. (2010), *Regional climate model simulation of winter climate over Central-Southwest Asia, with emphasis on NAO and ENSO effects*. Int. J. Climatol., 30, pp. 220-235. (3)
- Yadav R.K., Kumar K.R. & Rajeevan M. (2009), *Increasing influence of ENSO and decreasing influence of AO/NAO in the recent decades over northwest India winter precipitation*. J. Geophys. Res., 114. (4)
- Hurrell J.W., Kushnir Y., Ottersen G. & Visbeck M. (2003), *The North Atlantic Oscillation: Climatic Significance and Environmental Impact*. American Geophysical Union, Vol. 134, pp. 1-35. (5)
- Bhutiyani M.R., Kale V.S. and Pawar N.J. (2010), *Climate change and the precipitation variations in the northwestern Himalaya: 1866-2006*. Int. J. Climatol., 30, pp. 535-548. (6)
- Hazeleger W., et al. (2012), *EC-Earth v2.2: description and validation of a new seamless earth system prediction model*, Clim. Dynam. pp. 1-19, doi:10.1007/s00382-011-1228-5. (7)
- Hurrell J.W. (1995), *Decadal trends in the North Atlantic Oscillation: Regional temperatures and precipitation*. Science, 269, pp. 676-679. (8)
- Chen T.C. (1985), *Global water vapor flux and maintenance during FGGE*. Mon. Wea. Rev., 113, pp. 1801-1819. (9)

Atmospheric Blocking and Euro-Atlantic Winter Mid-Latitude Climate Variability

Davini P.^{1*}, Cagnazzo C.², Gualdi S.^{3,4}, and Navarra A.^{3,4}

¹ISAC-CNR, Torino, ²ISAC-CNR, Roma

³CMCC, Bologna, ⁴INGV, Bologna

*Corresponding author: p.davini@isac.cnr.it

Abstract

Atmospheric blocking is a mid-latitude weather pattern characterized by quasi-stationary, long-lasting, high-pressure anticyclonic system that modifies the westerly flow. In this work, Northern Hemisphere winter blocking and its impacts on mid-latitude climate are analysed through the introduction of a new set of bidimensional diagnostics based on the geopotential height. Such diagnostics provide information about the occurrence, the duration, the intensity and the wave breaking associated with the blocking. It is therefore possible to discern among three main categories of blocking: one is detected at high latitude occurring over Greenland and North Pacific, north of the jet stream and dominated by cyclonic wave breaking. A second one is placed at low latitudes over the Pacific and Atlantic oceans, unable to block or divert the flow. Finally a third category is defined as the traditional mid-latitude blocking, and it is only detected over Europe and driven by anticyclonic wave breaking. The relationship among European blocking, the Atlantic eddy-driven jet stream and the North Atlantic Oscillation (NAO) is hence analysed in NCEP/NCAR reanalysis and in a climate model. It is shown that European Blocking is decoupled from the NAO but it is mainly associated with poleward displacements of the jet stream. Moreover, the whole blocking area placed on the equatorward side of the jet stream, broadly ranging from Azores up to Scandinavia, emerges as associated with poleward jet displacements. The diagnostics are finally applied to two different climate model simulations. This analysis highlights large underestimation of European blocking, typical feature of general circulation models. Interestingly, observed blocking and jet biases over the Euro-Atlantic area are consistent with the blocking-jet relationship observed in the reanalysis.

Keywords: *Atmospheric Blocking, North Atlantic Oscillation, Jet Stream, CMIP5 models*



1. INTRODUCTION

The Euro-Atlantic region shows a great amount of natural variability, with weather phenomena acting on different spatial and temporal scales, ranging from synoptic scale cyclones up to large-scale planetary wave oscillations. Renewed interest in the last years has been raising around the role of low-frequency anomalies associated with atmospheric blocking, a mid-latitude weather pattern that describes a quasi-stationary, long-lasting, high-pressure system that modifies the westerly flow, "blocking" (or at least diverting) the eastward movement of the migratory cyclones [1] This usually occurs when a subtropical airmass of low vorticity is advected poleward, developing an anticyclonic circulation. Blocking occurs throughout the year, even if it is more frequent during winter and spring. It typically develops at the end of the Pacific and Atlantic jet streams, and it affects significantly the weather of the underlying regions, sometimes leading to cold spells in winter and heat waves in summer.

Even though largely debated in the literature since the 1950s, a full dynamical understanding of atmospheric blocking is still an open issue: this is confirmed by the large set of theories that has been proposed without achieving a unique conclusion on the dynamics of blocking (e.g [2]) and by the poor skill of weather and climate which is widely documented even for state of the art models [3].

In addition to this, the existence of several objective blocking detection methods makes a clear comparison of different works not straightforward.

In order to face this last issue, a new blocking index based on the bidimensional extension of the [4] is introduced. This index based on the reversal of the meridional gradient of geopotential height, measured at 500 hPa, but it is extended from 30° N to 75° N. This method tries to overcome the traditional fixed-latitude approach, by inferring more details on blocking occurring at different latitudes.

However, this above-presented Instantaneous Blocking (IB) definition does not provide any information about the spatial or temporal extension of the phenomena, which are the main constraints to define a blocking event [1]. In order to introduce spatial persistence, Large Scale Blocking (LSB) events are defined as IB extended for at least 15° of continuous longitude.

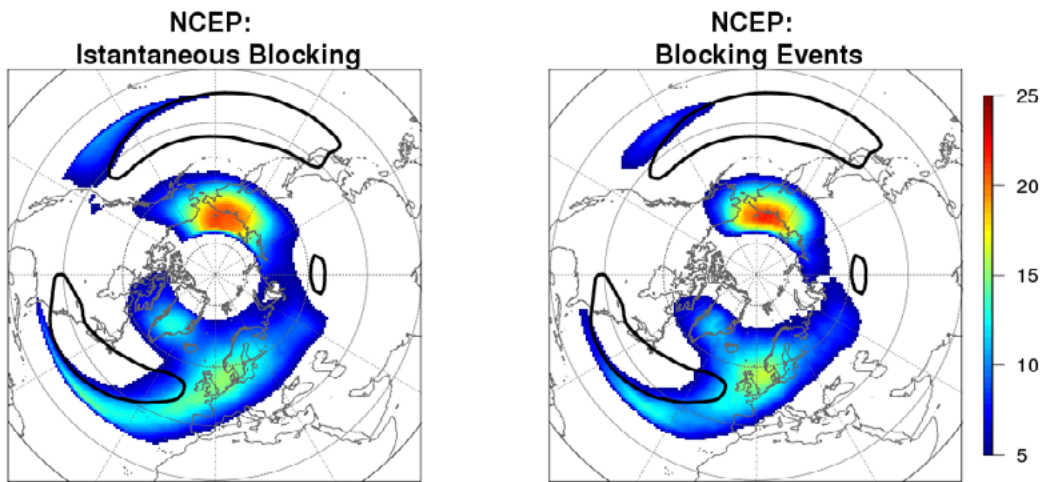


Fig. 1: NCEP/NCAR Reanalysis (DJF 1951-2010) Instantaneous Blocking frequency (left panel) and Blocking Events frequency (right panel). Colours are representative of percentage of blocked days with respect to total days. Contours show the eddy driven jets as climatological zonal wind speed higher than 8 m/s at 850 hPa.

A Blocking Event is finally defined if a LSB occurs within a box of 10° lon x 5° lat centered on that grid point for at least 5 days. Such criteria ensure that the detected episodes have both significant meridional and zonal extension, are quasi-stationary and persist for sufficient time to be considered as real blocking events, fulfilling the criteria defined by [1].

2. A BLOCKING CLIMATOLOGY

The blocking climatology for the NCEP/NCAR Reanalysis (DJF 1951-2010) is reported in Figure 1. Left panel shows the IB frequency, while right panel reports the Blocking Events frequency. The well-known high frequency area present over Europe is evident, with a maximum placed between the British Isles and the North Sea. However, blocking frequency is dominated by high-latitude events occurring over the North Pacific/Eastern Siberia and over Greenland (defined as High-Latitude Blocking, HLB). A strip of high values of blocking frequency develops from the British Isles to the south-west up to Florida at very low latitudes. A similar but less noticeable region of blocking is seen over the Subtropical Eastern Pacific.

The sensitivity of the index to different spatial and temporal constraints has been proved to be negligible, especially concerning the spatial distribution of the preferred regions of blocking occurrence.

Moreover, the agreement among different reanalyses has been tested making use of ECMWF ERA-40 and ERA-INTERIM Reanalysis.

Together with the blocking index, several bidimensional diagnostics have been developed in order to get more physical insight. First of all, the duration of blocking events for each grid point has been computed. Hence, two different indices providing a measure of the intensity of the blocking are computed: the Meridional Gradient Intensity (MGI) and the Blocking Intensity (BI). While the former gives a measure of the intensity of the easterly wind to the south of the blocked point, the latter indicates how the meridional circulation is affected by the presence of blocking.

A measure of the direction of rotation of the Rossby Wave Breaking (RWB) is also obtained. RWB is a large-scale overturning of potential vorticity contours on an isentropic surface. They can be categorized into cyclonic/anticyclonic wave breaking when a Northwest-Southeast/Southwest-Northeast tilted trough-ridge pair is advected cyclonically/anticyclonically and they have been shown to be strongly associated with blocking events [5]. Full details on the blocking detection scheme and the associated diagnostics may be found in [6].

This set of diagnostics provides a large source of information that allowed us to define 3 main categories of blocking events. The first case, blocking occurring on the poleward flank of the jet stream, has been defined as High Latitude Blocking (HLB). HLB events occur mainly over Greenland (Greenland Blocking) and over Eastern Siberia (North Pacific Blocking). A composite of those events can be seen in upper right and left panels of Figure 2 respectively. They are characterized by the fact that they are just able to divert the jet stream equatorward (instead of blocking it) and

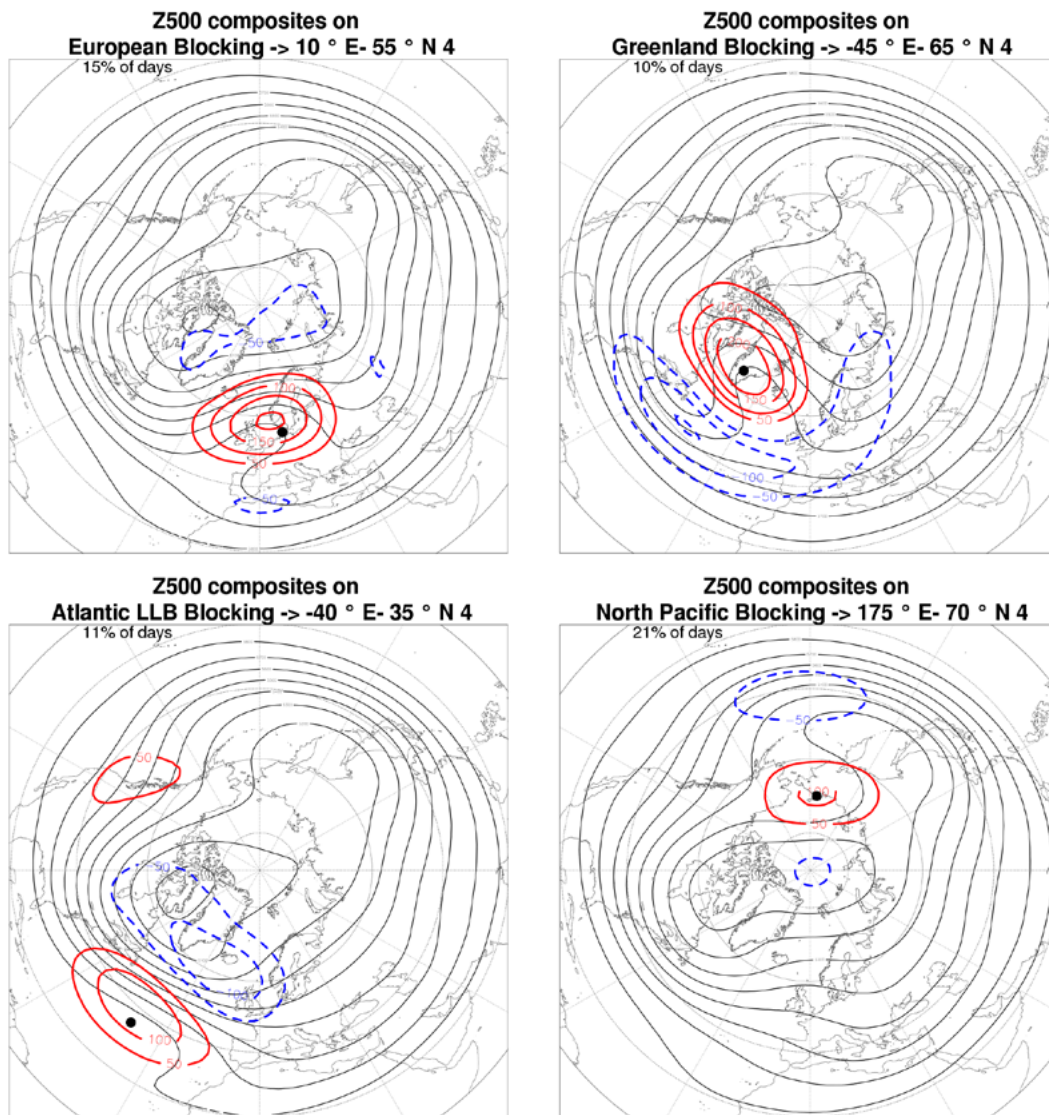


Fig. 2: Composites on blocked days of geopotential height at 500hPa. From upper left, clockwise: European blocking, Greenland Blocking, Atlantic LLB and North Pacific Blocking. Positive anomalies are contoured in red, negative anomalies in blue and are drawn every 50hPa. Dots marks the points on which composites are computed.

able to divert the jet stream equatorward (instead of blocking it) and by the cyclonic Rossby wave breaking associated with them. Moreover, their longitudinal geopotential cross section is tilted showing a baroclinic-like feature.

A second category of blocking-like structure has been defined as Low Latitude Blocking (LLB): this category contains all events detected adjacent to the subtropics, approximately south of 40° N. LLB composite is shown in lower left panel of Figure 2. They are signatures of the oscillations of the

subtropical high and the corresponding flow reversal. These events, occurring mainly over Central Eastern Pacific and Atlantic, are unable to block the flow and they seem also unable to divert it, thus having an almost negligible impact on the weather pattern. They are barotropic, associated with anticyclonic Rossby Wave Breaking, and their signature is an enhanced subtropical ridge.

The last group of blocking events is the one that actually splits the flow and typically occurs at the mid-latitudes. The analysis performed suggests that only events over Central Europe could be defined as "real" mid-latitude blocking events; these events are classified as European Blocking (EB). The composite for these events it is shown in upper left panel of Figure 2. EB shows a signature similar to Atlantic LLB events, with an enhanced barotropic ridge associated with an anticyclonic-wave breaking.

In addition to this, the inter-annual variability and the trends of the blocking frequency and intensity have been analysed. A very marked year-to-year variability emerged as evident, not allowing an easy detection of significant trends in Blocking Events frequency. However, a moderate increase is observed for Atlantic LLB events, while at high latitudes several areas of decreased blocking frequency are identified. The trends reported for the Blocking Intensity are more evident, suggesting an increased impact of Blocking Events over Central Europe and British Columbia. This last feature could potentially have some influence on the extreme events over those regions.

3. BLOCKING AND THE EURO-ATLANTIC VARIABILITY

Once the blocking climatology has been validated, in the second part of the work the attention is focused on the role played by blocking in the context of the Euro-Atlantic variability.

Therefore the analysis has been devoted to the teleconnection patterns of the Euro-Atlantic region. The North Atlantic Oscillation (NAO) and the East Atlantic pattern (EA) has been defined as the first and second Empirical Orthogonal Function (EOFs) of the monthly mean geopotential height at 500hPa over the Atlantic sector. The associated Principal Components (PCs) defines each EOF timeseries.

Four lat-lon sectors, whose coordinates are reported in Table 1, are introduced. Those sectors have been defined as boxes centred on the relative maximum of Blocking Events frequency in the considered area.

The Pearson's Correlation coefficients between the daily blocking timeseries and the daily NAO index (and the second and third EOFs) are reported in Table 2.

Azores (Atlantic LLB)	Europe (EB)	Greenland (GB)	Iberian Breaking (IWB)	Wave
60W-30W	15W-25E	65W-15W	30W-0W	
30N-40N	50N-65N	62.5N-72.5N	37.5N-50N	

Table 1: Sector for blocking analysis

No significant correlation (-0.07/-0.01) is found between the European Blocking and the NAO or EA, suggesting that blocking over Central Europe is independent from the both the main teleconnection pattern. Negative correlation emerges between the NAO and the GB measured (-0.53, significant at 99%) and a smaller but also significant (99%) positive correlation between the NAO and the LLB/IWB sector (0.40/0.36). Correlation values increase if the monthly and yearly timescales are used instead of the daily ones (not shown).

The negative correlation (-0.53) found between GB events and the NAO index is in agreement with the "blocking-dependent" interpretation of the NAO presented by [7].

Telec Pattern	Atlantic LLB	Europe	Greenland	IWB
NAO	0.37	-0.07	-0.53	0.33
EA	0.03	-0.01	0.06	0.13

Table 2: Pearson's correlation values of the entire daily timeseries between blocking occurrence and the PC of the main Atlantic teleconnection pattern

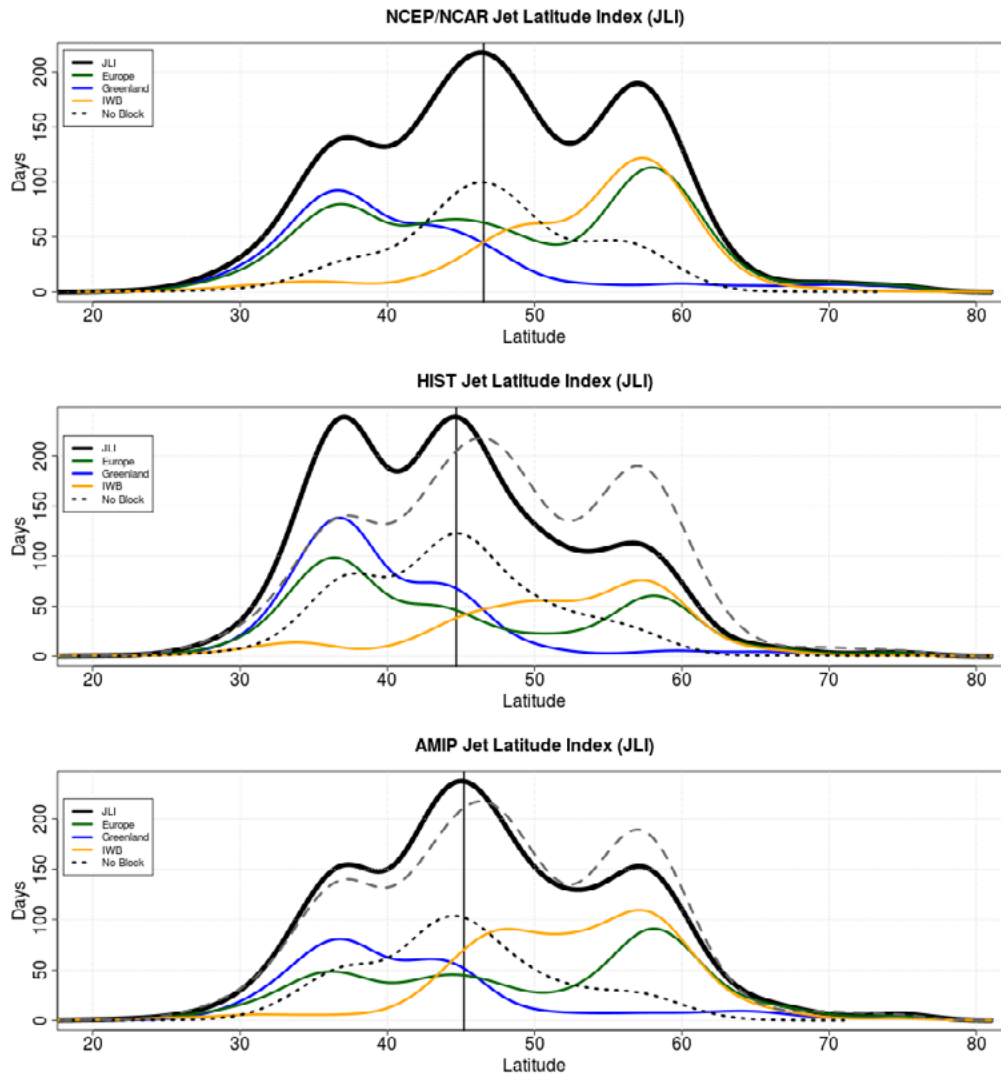


Fig. 3: Upper panel: Jet Latitude Index PDF for NCEP/NCAR Reanalysis, where black line represents the climatological distribution, blue line represents GB days, green line EB days and orange line IWB blocking days. Dotted line represents JLI when no blocking in three sectors are detected. Black vertical line shows the latitude of the central peak. PDFs are multiplied by the number of days of each dataset. Central and lower panel: the same as upper panel but for CMCC-CMS HIST and CMCC-CMS AMIP respectively. Dashed lines are the JLI PDF for the NCEP/NCAR Reanalysis.

In order to provide further insight on the connection between blocking and the Euro-Atlantic climate variability, our attention has been moved on the Atlantic eddy-driven jet stream.

To study the daily changes of the position of the eddy-driven jet stream, the Jet Latitude Index (JLI) is introduced following [8]. The JLI expresses the latitude of the zonally averaged maximum of the zonal wind speed between 60° W and 0° longitude. The wind zonal speed is vertically averaged from 925 hPa

to 700hPa. The daily values of the JLI express a measure of the latitudinal position of the Atlantic eddy-driven jet, each day. A slightly different version of this index is here adopted, based on 5-day running-mean data and on absolute latitude values.

The upper panel of Figure 3 (black line) shows the trimodal distribution of the JLI PDF, consistent with the trimodal behaviour showed by [8]. Blue, green and orange curves show the composites on blocked days for the position of the Atlantic jet-stream for each sector and they are shown in Table 1. The green line shows the well-established relationship linking the occurrence of Greenland Blocking with southward displacement of the jet stream [8]. A clear association between blocking and northward jet displacement is found for blocking events occurring over Eastern Atlantic (IWB, orange)

The PDF for the European Blocking (blue) is also associated with a northernmost occurrence of the jet, even though the jet can still be found in other locations, with a secondary preference for the equatorward position.

Furthermore, excluding the days when a blocking is detected in these three reference regions (EB, GB and IWB), the JLI distribution becomes almost unimodal, as shown by the dotted line in Figure 3. This distribution is very likely representative of the “neutral mean state” of the jet that resembles the “non-perturbed state” proposed by [8]. Moreover, when LLB is occurring the JLI PDF (not shown) is very similar to the “no blocking” situation, confirming that these events are unable to divert the jet. More details can be found in [9].

This frame can be summarized depicting a trimodal blocking-dependent Euro-Atlantic variability: when no blocking is occurring (but also during LLB events, since they cannot affect the jet stream), the Atlantic eddy driven jet is in its central “neutral” position. The equatorward jet position is linked to the occurrence Greenland blocking (and associated cyclonic wave breaking), while poleward jet position is linked to the European blocking (and associated anticyclonic wave breaking). EB is not confined in a small region but is originating from the breaking of the Atlantic ridge, which can occur from 30° E to 20° W (even more to the west if LLB are also considered as a part of EB events).

This trimodal variability partially conflicts with the idea of 4 weather regimes usually detected over the Euro-Atlantic basin. Indeed, the “poleward displaced jet” and “European blocking” modes are substantially indistinguishable under a phenomenological point of view (i.e. vertical cross-section, associated wave-breaking orientation, duration, effects on the jet stream, etc.). Therefore it can be argued that, unlike the first “southward displaced jet / Greenland blocking” and the “central jet / no

blocking” regimes, the “poleward displaced jet” and the “European blocking” regimes have the same physical origin. This hypothesis is also supported by the fact that they are both associated with the Rossby Wave Breaking on the equatorward side of the Atlantic jet.

4. BLOCKING IN THE CMCC-CMS MODEL

In the last part of our work the above-mentioned diagnostics have been applied to two climate simulations from the CMCC-CMS climate model. The oceanic component has a constant resolution of about 2 degrees in horizontal and 31 vertical levels. The atmospheric configuration adopted here is a T63L95.

Data from two different experiments, both performed for the Coupled Model Intercomparison Project Phase 5 (CMIP5), have been used. The first one, hereafter called HIST, is a historical fully-coupled numerical experiment (DJF 1951-2005) of the CMCC-CMS climate model. The second one, hereafter named AMIP, is the corresponding atmosphere-only run (DJF 1951-2005) of the CMCC-CMS with prescribed Sea Surface Temperature (SST). The imposed SST are the HadISST.

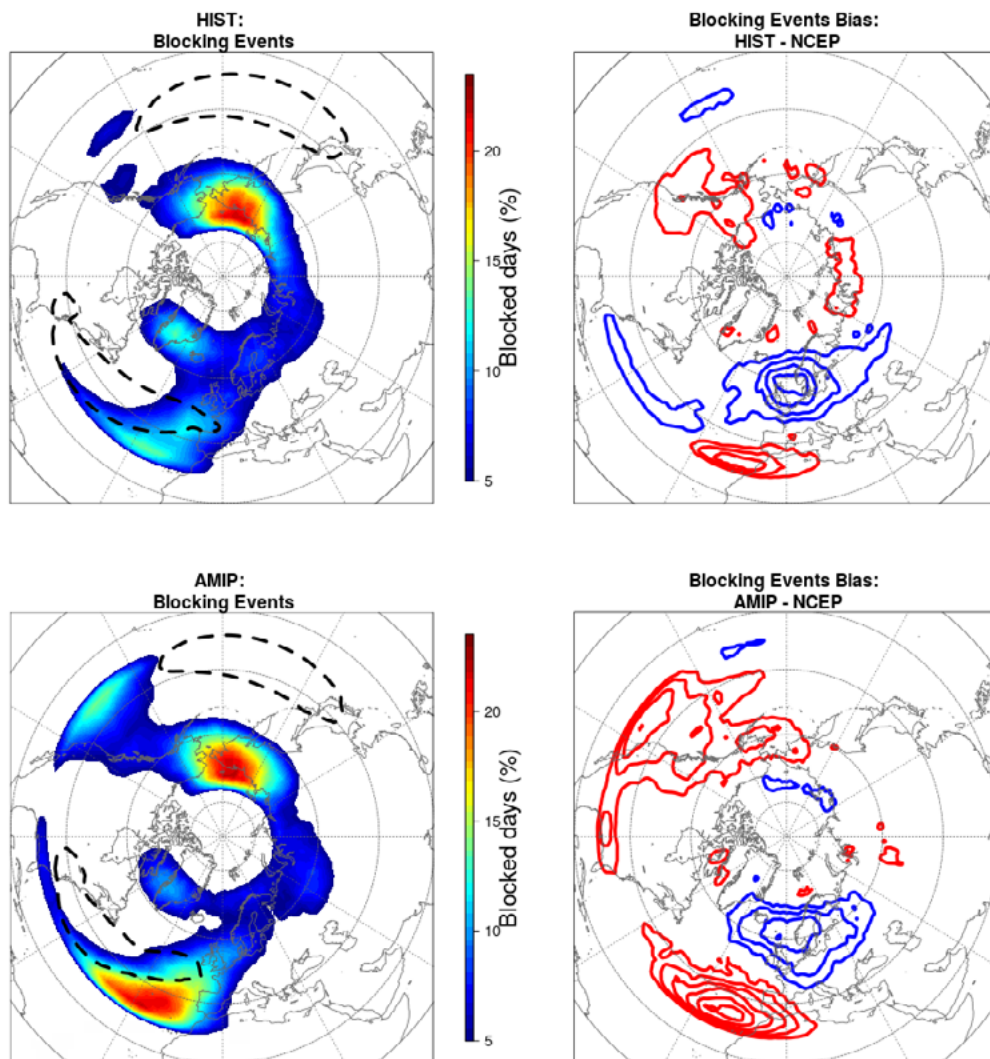


Fig. 4: Left panels: Same as right panel of Fig. 1 but for CMCC-CMS HIST/AMIP runs (upper/lower panel). Right panels: Difference between HIST/AMIP and NCEP-NCAR Reanalysis (upper/lower panel). Blue contours shows negative bias, red contours show positive bias and they are drawn each 2%.

Figure 4 shows the blocking climatology for the HIST simulation (upper left panel) and the difference with respect to the NCEP/NCAR Reanalysis (upper right panel). The simulation exhibits a large underestimation of the European Blocking, associated with an eastward displacement of the blocking on the equatorward side of the jet (blue/red dipole over the Eastern Atlantic). Moreover, the HIST run presents a slight overestimation of the events over Greenland, whereas over the North Pacific the representation of the blocking is more accurate.

Fig. 4 also shows the same diagnostics for the AMIP run (lower panels), showing that with realistic SSTs, a noticeable increase in blocking frequency is obtained almost everywhere. This is especially true at lower latitudes, leading to a marked overestimation of blocking over the Eastern Pacific and the Atlantic LLB area. Conversely, imposed SSTs provide also a small decrease in the bias over Europe. Finally, it is possible to see that the blocking frequency is slightly reduced over Greenland and more generally at high latitudes over the Atlantic.

The main blocking-related diagnostics of the model are in agreement with the NCEP/NCAR Reanalysis. This is especially true for the blocking intensities, the pattern obtained in the composites analysis and the detected region of cyclonic and wave breaking (not shown). Interestingly, both simulations show similar distribution for the blocking duration (not shown) characterized by a weak but significant underestimation (NCEP/NCAR average blocking duration 7.14 days, HIST average duration 6.81 days, AMIP average duration 6.99 days).

Concerning jet variability, CMCC-CMS is doing reasonably well. The HIST simulation (central panel in Figure 3) shows the expected trimodality, with the northward peak smaller and the southward peak notably larger with respect to Reanalysis. These results are consistent with the findings previously reported: the large southern peak of the JLI PDF is associated with the intense simulated GB activity, while the less frequent modelled EB and IWB events are reflected by a smaller northernmost peak of the JLI distribution. Indeed, HIST is characterized by a lack of events over Europe particularly evident in the EB and IWB region (Figure 4). On the poleward side of the jet, a slight overestimation of the blocking frequency is present at high latitudes.

The results shown in the bottom panel of Figure 3 suggest improvements for the AMIP experiment. A small bias is still present in the northernmost peak, but, overall, the PDF is now close to the one obtained from the NCEP/NCAR Reanalysis. However, this improvement may be due to the wrong reason. Indeed, both European Blocking and Iberian Wave Breaking are associated with the poleward displaced jet. Therefore, it is possible that a positive blocking bias (lower right panel in Fig 4) present in the Eastern Atlantic (i.e. broadly over the IWB sector) compensates the negative bias in the EB events. This can be seen in the lower panel of Fig. 3, where the orange line is almost doubled with respect to the HIST. In other words, the right frequency of the northward peak of the JLI PDF is obtained mainly with the overestimated numbers of IWB blocking events.

This point may have an interesting implication: a good representation of the jet variability (measured via the JLI) would not guarantee a good representation of the patterns of variability of the Euro-Atlantic sector.

The SSTs differences between HIST and AMIP (not shown, see [9]) are finally analysed, with a special attention to the characteristics and the position of the mid-latitude SST front. In agreement with previous works performed with aquaplanet models, the stronger and equatorward-displaced jet found in HIST is likely due to a broader and equatorward-displaced SST frontal zone. The consistency of this idea has been also assessed finding higher values for the Eady Growth Rate maximum over the Central Atlantic in the HIST run.

Imposed SSTs over the North Atlantic Ocean lead to improvements in jet stream variability, but only weak improvements in European blocking simulation in our model.

Moreover, the results here presented suggest that, given the clear blocking-jet relationship, blocking can be a more accurate indicator for the Euro-Atlantic variability than the jet stream or the North Atlantic Oscillation alone.

5. REFERENCES

- Rex D. (1950), *Blocking action in the middle troposphere and its effect upon regional climate: I. An aerological study of blocking action*. *Tellus*, 2, 196–211. (1)
- Shutts G. (1983), *The propagation of eddies in diffluent jetstreams: eddy vorticity forcing of blocking flow fields*. *Quarterly Journal of the Royal Meteorological Society*, 109, 737–761. (2)
- Anstey J.A., Davini P., Gray L. J., Woollings T. J., Butchart N., Cagnazzo C., Christiansen B., Hardiman S.C., Osprey S.M., Yang S., *Multi-model analysis of Northern Hemisphere winter blocking, Part I: Model biases and the role of resolution*. *Journal of Geophysical Research - Atmosphere*, 2013, accepted. (3)
- Tibaldi S. and Molteni F. (1990), *On the Operational Predictability of Blocking*. *Tellus*, 42A, 343–365. (4)
- Pelly J. and Hoskins B. (2003), *A New Perspective on Blocking*. *Journal of the Atmospheric Science*, 60, 743–755. (5)
- Davini P., Cagnazzo C., Gualdi S., and Navarra A., *Bidimensional diagnostics, variability and trends of Northern Hemisphere*. *Blocking Journal of Climate*, 2012, 25 (19), 6496-6509, doi:10.1175/JCLI-D-12-00032.1. (6)
- Woollings T., Hoskins B., Blackburn M., and Berrisford P. (2008), *A New Rossby Wave Breaking Interpretation of the North Atlantic Oscillation*. *Journal of Atmospheric Science*, 65, 609–326. (7)
- Woollings T., Hannachi A., and Hoskins B. (2010b), *Variability of the North Atlantic eddy-driven jet stream*. *Quarterly Journal of the Royal Meteorological Society*, 136, 856–868. (8)
- Davini P., Cagnazzo C., Fogli P.G., Manzini E., Gualdi S., Navarra A., *European Blocking and Atlantic Jet Stream Variability in the NCEP/NCAR Reanalysis and the CMCC-CMS climate model Climate Dynamics*, 2013, minor revision. (9)

The temporal variability and associated spectral features of transient-eddy meridional heat transport

Messori G.^{1*} and Czaja A.¹

¹*Space and Atmospheric Physics Group, Department of Physics, Imperial College London*

*Corresponding author: gabriele.messori06@imperial.ac.uk

Abstract

The present study analyses meridional atmospheric heat transport, due to transient eddies, in the European Centre for Medium-Range Weather Forecasts ERA-Interim reanalysis data. Daily, 0.7° latitude and longitude resolution fields at the 850 mb pressure level are used. Probability density functions (PDFs) of meridional transient eddy heat transport display a near-zero most likely value and a very large skewness, highlighting the dominant role played by extreme events. When considering zonal sections, in both the Northern and Southern Hemispheres, events in the top 5 percentiles typically contribute to over half of the net poleward transport. As a result of this sensitivity to extremes, a large fraction of the heat transport by transient eddies, at a given location and season, is realised through randomly spaced bursts (a few per season), rather than through a continuum of events.

Fast growing atmospheric modes are associated with a large heat transport, which would suggest a link between these bursts and growing baroclinic systems (defined here as motions in the 2.5–6 day band). However, by analysing wavelet power spectra of transport extremes, and of the corresponding meridional velocity and moist static energy temporal anomalies, this is found not to be the case. In fact, baroclinic systems provide only a modest contribution to the integrated power of the extreme heat transport event spectrum. The transport extremes are driven by very precise phase and coherence relationships between the velocity and moist static energy anomalies, acting over a broad range of frequencies (2.5–30 days). Motions with periods beyond 6 days play a key role in this framework.

Keywords: *Heat transport, extreme events, transient eddies, wavelet spectrum, arctic climate change*



1. INTRODUCTION

Transient motions drive a major portion of the poleward atmospheric heat transport in the mid-to-high latitudes [1]. This transport has been acknowledged as the key to predicting the time-mean structure of the Earth's climate (e.g. [2]; [3]; [4]), and its variability (e.g. [5]). More recent studies have emphasised the role atmospheric heat transport plays in the response of our climate to anthropogenic forcing, especially at high latitudes (e.g. [6]; [7]). For example, there is evidence that anomalies in atmospheric poleward heat transport might explain the 2007 polar sea-ice minimum [8]. A significant number of studies have also focussed on the timescales driving the transport's variability. Blackmon et al. [9], for example, found that timescales between 2.5 and 6 days and motions with periods beyond 10 days contributed to comparable portions of the transient-eddy heat transport. Following Blackmon's terminology, throughout this study the term 'baroclinic timescales' will be applied to periods between 2.5 and 6 days.

This vast literature has, however, largely overlooked the importance of extreme events in setting the seasonal mean transport by transient motions. A noticeable exception is a study by Swanson and Pierrehumbert [10], who analyzed heat flux probability density functions (PDFs) at three locations in the Pacific storm track. At low levels, the top two percentiles of the distribution were found, surprisingly, to account for 20% of the heat transport.

This article focuses on the contribution of extreme events to transient-eddy atmospheric poleward heat transport, building on the study by Swanson and Pierrehumbert [10]. After robustly establishing the sensitivity of the heat transport to extremes, we demonstrate its sporadic and irregular temporal distribution by showing that a large contribution to the transport arises from a few isolated bursts every season. The focus will be on low levels, at which the heat transport by transient motions is strongest [1].

The outline of this article is as follows. Section 2 describes the data used and outlines the methodology. Section 3 looks at PDFs of the transport and identifies their salient features. Wavelet power spectra of the transport are also presented, and the role of phase and coherence is analysed. Finally, section 4 presents some discussion, and section 5 conclusions and open questions.

2. DATA AND METHODOLOGY

The present study utilises ERA-Interim reanalysis data provided by the European Centre for Medium-range Weather Forecasts (ECMWF) [11]. Daily outputs (1200 UTC) are considered over a period spanning from June 1989 to February 2011, thereby providing twenty-two DJF (December, January and February) and twenty-two JJA (June, July and August) time series. The latitude and longitude resolution is approximately 0.7° , and the analysis focuses on the 850 mb pressure level.

Transient-eddy heat transports are computed as a product of meridional velocity (v) and moist static energy (H , hereafter also referred to as MSE) temporal anomalies, between 30°N and 89°N and 30°S and 89°S . Taking the product $v'H'$ for all data points and repeating the binning process yields the desired PDFs for transient-eddy heat transport. Extreme events are then chosen as values of $v'H'$ which exceed the 95th percentile of the distribution for the full hemisphere and time period considered.

For the wavelet analysis, a Morlet wavelet transform is applied to the selected $v'H'$ and the corresponding v' and H' ([12]; [13]; [14]). The wavelet power spectra for the selected events are then composited, so that a single spectrum for each signal is obtained for every season-hemisphere combination. Neither the exact percentile definition of extreme events nor the type of wavelet applied was found to affect the qualitative results presented here [15].

3. TRANSIENT-EDDY HEAT TRANSPORT EXTREMES

3.1 Probability distribution functions

To investigate the statistical distribution of transient-eddy heat transport, we begin by computing a composite PDF, taking into consideration all available NH latitude bands (30°N – 89°N) and all twenty-two years of the DJF time series. The three panels in Fig. 1 show the results for v' , H' and transport respectively. The key features of the velocity and MSE PDFs are: (i) a very low skewness and a near-symmetrical structure, (ii) significant positive and negative tails, and (iii) a near-zero most likely value when compared to the magnitude of the extreme events. The transport PDF, oppositely, has (i) a very high skewness associated with a highly asymmetric distribution, and (ii) a positive tail which is significantly more extended than the negative one. The most likely value of the distribution is two orders of magnitude smaller than the extremes, and can therefore be considered near-zero in terms of heat transport [15].

The features of the velocity and MSE distributions are not necessarily surprising. Similarly, the strong asymmetry found in the transport PDF is related to the imbalance inherent to meridional heat transport, whereby there must be a net transport from low to high latitudes. Hence, some measure of asymmetry in the transport PDF is to be expected. What is not obvious is that such asymmetry should be related to very pronounced extreme events and a near-zero most likely value [15].

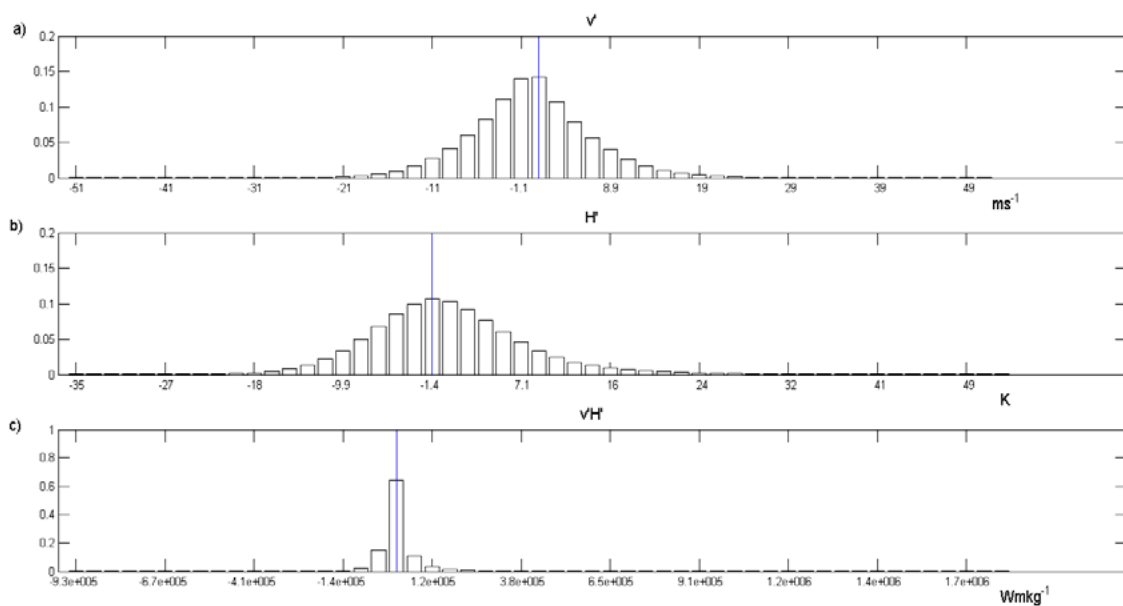


Fig. 1: PDFs of (a) meridional velocity anomalies, (b) moist static energy anomalies and (c) atmospheric heat transport due to transient eddies. The data cover twenty-two Northern Hemisphere DJFs (December 1989 to February 2011). All latitude circles between 30°N and 89°N are taken into account. The skewnesses of the PDFs are (a) 0.24, (b) 0.62 and (c) 3.00 respectively. The corresponding most likely values are (a) 0.87 m s^{-1} , (b) -1.4 K and (c) $1.5 \times 10^4 \text{ W m kg}^{-1}$. The vertical lines show the bins corresponding to the most likely values.

A visual assessment of the heat transport PDF (Fig. 1(c)) suggests that poleward transport is heavily affected by a small number of very large events. Tab. 1, below, displays the contribution of the top 2%, 5% and 10% of events to (i) the overall and (ii) the poleward-only transports. It is immediately clear that, regardless of the percentile used to define extreme events, the higher end of the distribution accounts for a disproportionately large portion of the meridional heat transport. Events in the top five percentiles typically account for over half of the net transient-eddy heat transport, with the exception of SH JJA where the percentage falls just short of 50%. The contribution of the top ten percentiles during NH DJF even approaches 100%, indicating that the transport due to those events is almost as large as the overall net transport. These features are found to be independent of the fact that a single pressure

level is being analysed. Vertical integrals of $v'H'$ over 1000 mb–1 mb, not discussed here, show even higher contributions from the upper percentiles. The anomalous percentage found for NH DJF is due to the seasonal cycle in the net NH transient-eddy transport, whose magnitude is more pronounced in the extreme-event-only integral [15].

The amount of heat carried poleward by transient eddies therefore appears to be largely based on very few, very large events. Obviously, the extremely high contributions found could be due to the overall integral of the distribution being close to zero. The poleward-only contributions, however, show that this is not the case: the same five percentiles still account for 36% to 43% of the poleward-only transport (Tab. 1).

PDFs analogous to those in Fig. 1 have been computed for JJAs and for the SH (not shown). Distributions for individual latitude bands, individual seasons and different pressure levels were also computed. While the magnitude of extreme events and the skewness of the transport PDFs show significant variability, the key features identified above are robust characteristics of the data analysed. Very few events each season therefore seem to account for over half of the poleward heat transport by transient eddies. This is an inherent property of the transport distribution and needs to be satisfactorily explained [15].

Contribution of extreme events to meridional atmospheric heat transport for 30°N–89° N and 30°S–89° S

<i>a) Hemisphere</i>	<i>Percentile</i>	<i>Overall % Weight</i>	<i>Poleward only % weight</i>
<i>N</i>	<i>2</i>	<i>34.5</i>	<i>22.9</i>
	<i>5</i>	<i>61.0</i>	<i>40.5</i>
	<i>10</i>	<i>88.9</i>	<i>59.1</i>
<i>S</i>	<i>2</i>	<i>32.1</i>	<i>24.2</i>
	<i>5</i>	<i>57.0</i>	<i>43.0</i>
	<i>10</i>	<i>82.8</i>	<i>62.4</i>
<i>b) Hemisphere</i>	<i>Percentile</i>	<i>Overall % Weight</i>	<i>Poleward only % weight</i>
<i>N</i>	<i>2</i>	<i>31.7</i>	<i>21.3</i>
	<i>5</i>	<i>57.9</i>	<i>38.9</i>
	<i>10</i>	<i>86.3</i>	<i>57.9</i>
<i>S</i>	<i>2</i>	<i>23.4</i>	<i>19.5</i>
	<i>5</i>	<i>43.7</i>	<i>36.4</i>
	<i>10</i>	<i>66.1</i>	<i>55.2</i>

Tab. 1: Percent contribution of extreme $v \cdot H$ events in (a) DJF and (b) JJA to net and poleward only meridional atmospheric heat transport due to transient eddies. The values displayed are simply (a) the percentage contribution of the selected events to the overall integral of the distribution and (b) the percentage contribution of the selected events to the integral of the positive portion of the distribution. The data cover all longitudes and latitudes, from 30°N to 89°N and from 30°S to 89°S, over twenty-two seasons (June 1989 – February 2011). The percentile column indicates which percentiles of $v \cdot H$ events are classed as extreme.

3.2 The role of phase and coherence

Having ascertained the importance of extreme events in setting the seasonal mean heat transport by transient motions, it is now necessary to relate them to physical processes in the atmosphere. Since fast-growing atmospheric modes are associated with large heat transport, baroclinic perturbations are obvious candidates in this respect. Indeed, a simple analysis of the temporal $v'H'$ signal suggests that the duration, spatial extent and phase speed of extreme events are within the range expected of Eady-type baroclinic growing systems [15].

To identify the origin of the extreme events, it is useful to picture the v' and H' signals as travelling waves, and to reason in terms of phase relationship and magnitude. An anomalously large $v'H'$ event might occur as a result of:

- extremely large velocity and MSE anomalies which, regardless of their phase relationship, yield a very large transport value (magnitude-driven transport);
- non-extreme v' and H' events which occur perfectly in phase (phase-driven transport).

Obviously, a combination of the two, such as near in-phase, large v' and H' events, is entirely possible [15].

To test these hypotheses, we compute a composite wavelet power spectrum, over the full data range as discussed in section 2. Fig. 2 shows the composite power spectra for v' , H' and $v'H'$ (panels (a), (c) and (e) respectively). The white contours indicate the cones of influence, which represent the limit beyond which edge effects become important. Only the data above these lines should therefore be considered. Darker shades indicate higher spectral power. Also displayed are the time averaged spectra for the 5 days centred on the extreme event, and reference slopes (panels (b), (d) and (f) respectively). The key features of the spectra are: i) a clear increase in power with increasing period in v' and H' and, ii) an approximately flat power spectrum in $v'H'$, with a modest peak at periods around 3–5 days. The differences between the spectra are illustrated very clearly in panels (b), (d) and (f) of Fig. 2. The dashed lines in panels (b) and (d) both have positive unit slope, while the ones in panel (f) have zero and negative unit slopes respectively, highlighting the flatness of the spectrum [16].

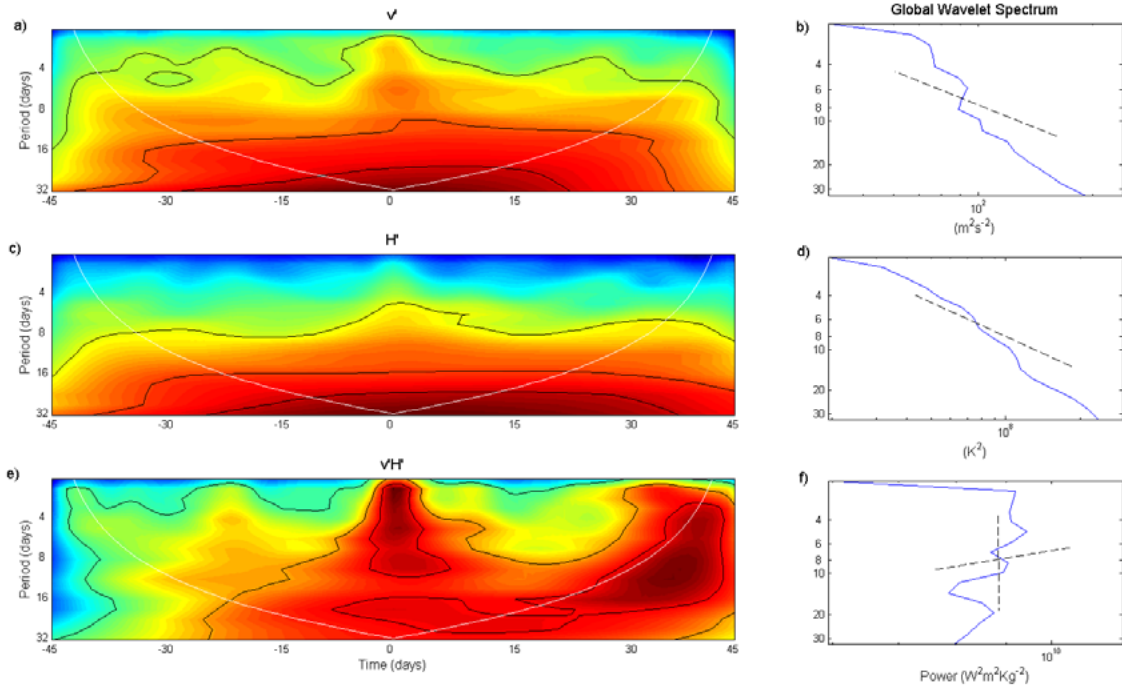


Fig. 2: Composite wavelet power spectra of (a) meridional velocity anomalies, (c) moist static energy anomalies and (e) atmospheric heat transport due to transient eddies. The spectra are centred on local maxima of transport extreme events. Darker colours indicate higher values. The white contours represent the cone of influence. Panels (b), (d), and (f) display the corresponding time-averaged spectra, for the five days centred on the extreme. The dashed lines in panels (b) and (d) are positive unit slope linear fits. Those in panel (f) have slopes 0 and -1 respectively. The data cover all longitudes and latitudes, from 30°N to 89°N and from 30°S to 89°S, over twenty-two seasons (December 1989 – February 2011) [16].

The discrepancy between the $v'H'$ power spectrum and those of v' and H' , suggests that there must be a systematic interaction pattern between v' and H' driving the “flattening” of the transport spectrum. Furthermore, since transport is the result of a product of two signals, a scaling factor must be taken into account. So, for example, periods of 10 days in v' and H' could potentially contribute to the 5 day band in $v'H'$. This suggests that a broad range of frequencies, beyond the 2.5–6 day range, might be contributing to this effect [16].

Fig. 3 shows the composite coherence-phase plot for NH DJF transport extremes. Panel (a) depicts coherence as colours and phase as arrows. The black contour indicates the cone of influence. Since phase for incoherent signals has no meaning, phase arrows are only retained in regions where coherence is greater than 0.5. When the arrows point right, the v' and H' signals are perfectly in phase; when they point upwards, the two signals are in quadrature with v' leading H' . The converse holds for leftward and downward pointing arrows. Panel (b) depicts phase angle in colours for the 10 days

centred on the extreme events. Again, positive values indicate that velocity leads MSE; the black contours bound the regions where coherence exceeds 0.5 [16].

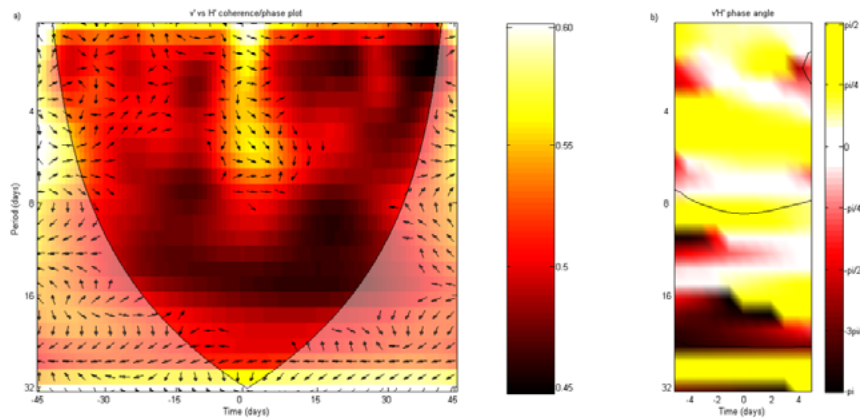


Fig. 3: (a) Composite wavelet coherence/phase spectrum for meridional velocity and moist static energy anomalies. The spectra are centred on local maxima of transport extreme events. The colour map represents coherence values, the arrows the phase relationship. When the arrows point right, the v' and H' signals are perfectly in phase; when they point upwards, the two signals are in quadrature with v' leading H' . The converse holds for leftward and downward pointing arrows. The black contour represents the cone of influence. (b) Depicts phase angle in colours for the 10 days centred on the extreme events. The scale is in radians. Again, positive values indicate that velocity leads MSE; the black contours bound the regions where coherence exceeds 0.5. The data range is the same as in Fig. 2 [16].

For the NH, three features emerge, which explain the patterns seen in Fig. 2: i) the coherence is highest at periods of approximately 2–8 days, ii) the phase angle is smallest at approximately 3 and 7 days, and iii) at longer periods v' and H' approach either quadrature or anti-phase. The “flattening” in the $v'H'$ spectrum is therefore driven by coherent, in phase v' and H' disturbances, while the unfavourable phase relationship at higher periods masks the high power of the two signals there. If not for this “braking” role of phase, there would therefore be significantly more power at long periods in the $v'H'$ spectrum. This effect is evident in both hemispheres [16].

Maps analogous to those in Figs. 2 and 3 have been computed for the remaining seasons and hemispheres (not shown). While the magnitude of the spectra, the coherence and the phase angles show some seasonality, the qualitative features identified above are robust characteristics of the data analysed. It should, however, be noted that the coherence values in NH summer are, perhaps, too small to allow us to make definitive statements using phase, while coherence values in the SH are generally larger [16].

Returning to our initial hypotheses, extreme heat transport events are therefore mainly phase-driven. What is surprising, however, is the secondary role of baroclinic systems. Indeed, if the v' and H' data is high-pass filtered to retain only the baroclinic timescales, the resulting transport composite power spectrum only captures between 22% and 35% of the power found in the original spectrum. If one replicates the analysis selecting events within 5 percentiles of the median of poleward heat transport, rather than extreme events, the ratios are very similar. The contribution from baroclinic periods in v' and H' is therefore comparable for extreme and median events. In both cases, these timescales do not drive the bulk of the transport, which must therefore come from longer periods [16].

4. DISCUSSION

The simplicity of the phase-driven wave view proposed in section 3.2 suggests that: (i) one should not be surprised by the large influence of extreme events on the mean poleward heat transport by transient eddies, and (ii) one should expect to see this statistical signature in very idealized models of the atmosphere and not solely in nature [15].

To test the latter prediction, we have applied the analysis performed in section 3.1 to the output of a coupled ocean-atmosphere model (FORTE: [17]; [18]) run in an aquaplanet geometry (described in [19]). In such geometry, the statistics are only functions of latitude and height, and the circulation is dominated by large-scale waves developing on the midlatitude westerlies. The results of the PDF analysis at 850 mb for FORTE (not shown) were found to be essentially the same as for the ERA-Interim data. This confirms that the sporadic nature of the heat transport, emphasized in this study, has nothing to do with detailed features of the atmosphere's lower boundary, stationary waves and mesoscale features (excluded by the coarse resolution of FORTE but present in the reanalysis through data assimilation). Rather, this must be an intrinsic property of the atmosphere [15].

As a direct consequence of this property, a very large fraction of the transport occurs in a few discrete bursts, each lasting for only a couple of days, as illustrated in Fig. 4. Replicating Fig. 4 for the number of extreme events per day along a full latitude circle (not shown) yields a similar picture, with bursts of extreme events lasting for a few days and typically involving less than 15 % of the grid points at that latitude. This further illustrates the sensitivity of the atmosphere to very few, temporally and spatially localised features [15].

Moreover, the waves driving these bursts cover a wide range of periods and frequencies. As discussed in section 3.2, when focusing specifically on extremes, one would expect the contribution of baroclinic scales to be significantly higher than normal. The present study finds that this is not the case: even though the coherence and phase characteristics of the v' and H' signals favour short period fluctuations, this is not enough for the latter to account for the majority of the power in the $v'H'$ spectrum. It should also be noted that, as mentioned in section 3.2, the longer periods in v' and H' can contribute to shorter ones in the $v'H'$ spectrum [16].

Regardless of hemisphere and season, v' and H' fluctuations therefore combine to produce phase and coherence-driven extreme events in heat transport which, as discussed above, account for over half of the poleward heat transport by transient eddies [15].

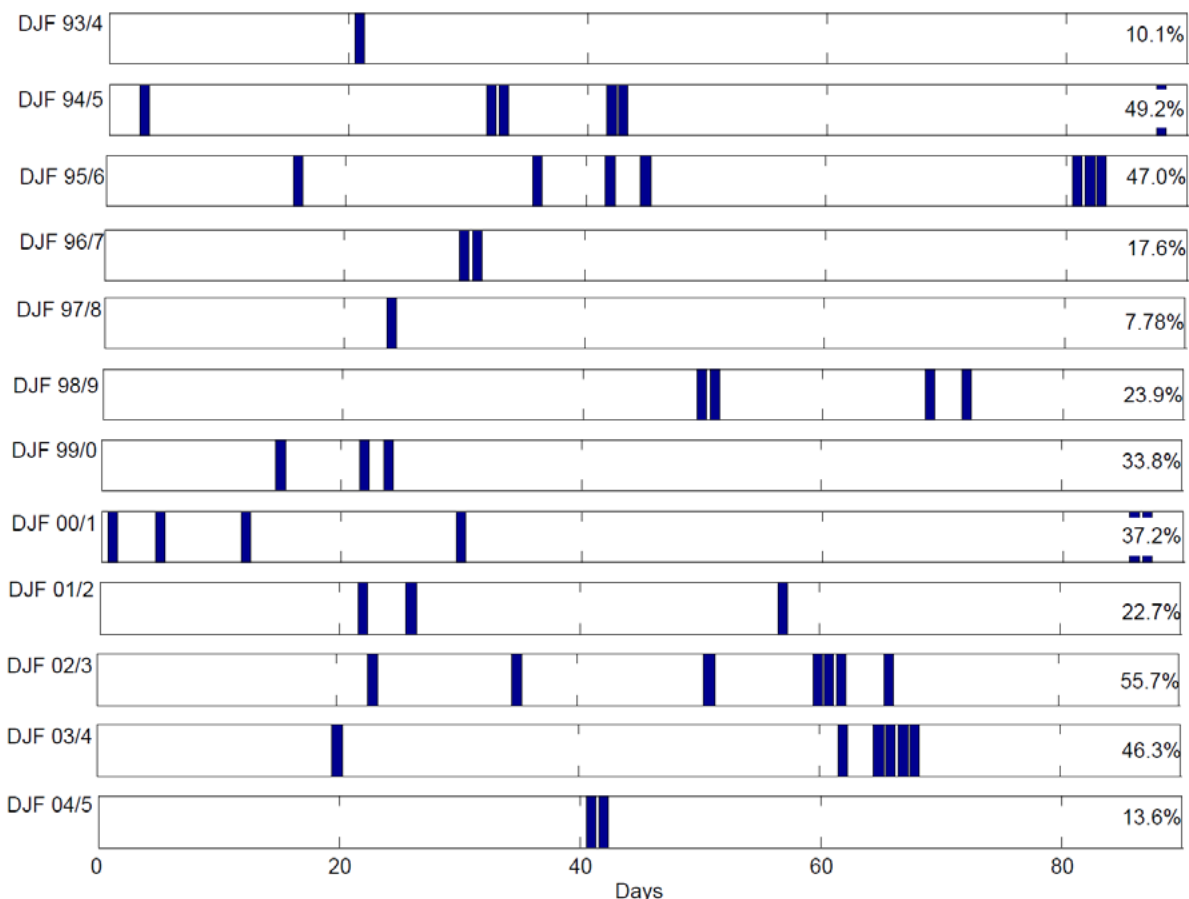


Fig. 4: Bar plot of $v'H'$ extreme events at $50^{\circ}\text{N } 0^{\circ}\text{E}$. Extreme events are defined as events in the top 5 percentiles of the $v'H'$ distribution for the 50°N latitude circle. The twelve panels correspond to DJF seasons from DJF 1993/4 to DJF 2004/5. Bars correspond to an extreme event occurring on a given day; the abscissa indicates the day of the season. The percentages in each panel indicate the contribution of the selected events to the net seasonal meridional transient eddy heat transport across the grid box [15].

This new perspective has an intriguing application to the climate change debate. Polar amplification has traditionally been ascribed to surface-albedo feedback (e.g. [20]), but a number of studies have also highlighted the important contribution of atmospheric heat transport to the phenomenon (e.g. [6]; [21]; [22]). This suggests that there could be a strong link between extreme transport events and the climate of the Arctic (see also [8]) [15]. Graversen et al. [8], for example, argue that the anomalously low Arctic sea-ice extent during the summer of 2007 was linked to an anomalously high atmospheric meridional heat transport and heat transport convergence over the East Siberian Sea. The values measured were unprecedented by any other summer during the 1989–2008 period. Intuitively, this could correspond to a higher frequency of heat transport extremes in that area. To verify this, the number of extreme transport events per JJA season, over the same time period and domain (74°N–82°N and 135°E–165°W) analysed by Graversen, is computed. The mean number of events per season is 33, with a standard deviation of 18. The highest number of extremes is found to occur during the 2007 summer, when 70 distinct events can be identified. This is more than two standard deviations from the mean. These events are always relative to the 850mb level, and a more in-depth analysis would be required to assess the net transport they account for. Nonetheless, the numbers found are suggestive of the potentially crucial importance for the Arctic heat budget of the extremes discussed in this paper.

5. CONCLUSIONS

This article examines meridional atmospheric heat transport due to transient eddies, focusing on low levels in the mid and high latitudes. The analysis is in terms of the probability distribution functions and wavelet spectra of meridional velocity anomaly v' , moist static energy anomaly H' and their product $v'H'$. Two outstanding features of the distribution of $v'H'$ are the near-zero most likely value and the very pronounced positive skewness. These appear to be robust features of the distribution and are only marginally affected by season, hemisphere or latitude. The output from an intermediate complexity climate model, run in an aquaplanet configuration, presents similar characteristics. This suggests that the shape of the $v'H'$ PDFs is not due to mesoscale phenomena, stationary waves or complexities associated with surface boundary conditions. As a direct consequence of the distribution's skewness, the top 5% of $v'H'$ events accounts for over half of the net poleward heat transport by transient eddies [15]. The wavelet spectra further suggest that the extreme events result from the coincidence of ideal

coherence and phase relationships between v' and H' anomalies over a broad range of frequencies, well beyond those expected from pure baroclinic disturbances.

An important consequence of the sensitivity of the heat transport to extreme events is that the transient heat transport process in midlatitudes is fundamentally sporadic in the temporal domain. As discussed above, this new perspective suggests that there could be a strong link between extreme transport events and the climate of the Arctic [15].

Furthermore, one can develop stimulating links to concepts applied in other fields of physics, such as quantum mechanics. Indeed, by comparing particle wave packets and $v'H'$ extremes, these sporadic extremes can be likened to ‘quanta of heat’. This idea is not entirely new, and has been applied to the atmospheric and oceanic sciences by Hogg and Stommel in their Heton model ([23]; [24]). The latter model is currently being used to help interpret the results presented here [16]. Ultimately, only a very few days every season could hold the key to explaining some large-scale features of our climate system [15].

6. ACKNOWLEDGMENTS

G. Messori is funded by a bursary from the National Environment Research Council (RAPID-RAPIT project). ERA-Interim reanalysis data were obtained from the BADC ftp server at <ftp.badc.rl.ac.uk>. The wavelet software was provided by C. Torrence and G. Compo, available at <http://atoc.colorado.edu/research/wavelets/>, and by A. Grinsted, J.C. Moore and S. Jevrejeva, available at: <http://noc.ac.uk/using-science/crosswavelet-wavelet-coherence>. We are grateful to J. Cheung for providing the FORTE data, and to M.O. Archer for discussions on the wavelet analysis. We also thank the anonymous reviewer for his feedback.

7. REFERENCES

- Peixoto JP, Oort AH. (1992), *Physics of Climate*. American Institute of Physics: New York. Pp 317–336. (1)
- Budyko MI. (1969), *The effect of solar radiation variations on the climate of the Earth*. *Tellus* 21: 611-619. (2)
- Stone PH. (1978), *Constraints on Dynamical Transports of Energy on a Spherical Planet*. *Dyn. Atmos. Oceans* 2: 128-139. DOI: [10.1016/0377-0265\(78\)90006-4](https://doi.org/10.1016/0377-0265(78)90006-4) (3)
- Sellers WD., *A Global Climatic Model Based on the Energy Balance of the Earth-Atmosphere System*. *J. Appl. Meteorol.*8: 392-400. DOI: [10.1175/1520-0450\(1969\)008<0392:AGCMBO>2.0.CO;2](https://doi.org/10.1175/1520-0450(1969)008<0392:AGCMBO>2.0.CO;2) (4)
- Bjerknes J. (1964), *Atlantic Air-Sea Interaction*. *Adv. Geophys.* 10: 1-82. DOI:10.1016/S0065-2687(08)60005-9 (5)
- Alexeev VA., Langen PL, Bates JR., (2005), *Polar amplification of surface warming on an aquaplanet in “ghost forcing” experiments without sea ice feedbacks*. *Clim. Dyn.* 24: 655-666. DOI: 10.1007/s00382-005-0018-3 (6)
- Langen PL, Alexeev VA. (2007), *Polar amplification as a preferred response in an idealized aquaplanet GCM*. *Clim. Dyn.* 29: 305-317. DOI: 10.1007/s00382-006-0221-x (7)
- Graversen RG., Mauritsen T., Drijfhout S., Tjernström M., Mårtensson S. (2011), *Warm winds from the Pacific caused extensive Arctic sea-ice melt in summer 2007*. *Clim. Dyn.* 36: 2103-2112. DOI: 10.1007/s00382-010-0809-z (8)
- Blackmon ML., Wallace JM., Lau N-C., Mullen SL. (1977), *An observational study of the Northern Hemisphere Wintertime circulation*. *J. Atmos. Sci.* 34:1040–1053. (9)
- Swanson K., Pierrehumbert R.T. (1997), *Lower-Tropospheric Heat Transport in the Pacific Storm Track*. *J. Atmos. Sci.* 54: 1533–1543. DOI: 10.1175/1520-0469(1997)054 (10)
- Simmons A., Uppala S., Dee D., Kobayashi S. (2006), *ERA-Interim: New ECMWF reanalysis products from 1989 onwards*. *ECMWF Newsletter* 110: 25-35 (11)
- Goupillaud P., Grossmann A., Morlet J. (1984), *Cycle - Octave and Related Transforms in Seismic Signal Analysis*. *Geoexploration* 23: 85-102 (12)
- Grinsted R., Moore JC., Jevrejeva S. (2004), *Applications of the cross wavelet transform and wavelet coherence to geophysical time series*. *Nonlin. Processes Geophys.* 11: 561-566 (13)
- Torrence P., Compo GP. (1998), *A practical guide to wavelet analysis*. *B. Am. Meteorol. Soc.* 79:61-78. (14)

- Messori G., Czaja A. (2013), *On the sporadic nature of meridional heat transport by transient eddies*. *Q.J.R. Meteorol. Soc.*, 139: 999–1008. doi: 10.1002/qj.2011 (15)
- Messori G., Czaja A. (2013), *Some considerations on the spectral features of meridional heat transport by transient eddies*. *Q.J.R. Meteorol. Soc.*, In Press. (16)
- Sinha B., Smith R.S. (2002), *Development of a fast coupled general circulation model (FORTE) for climate studies, implemented using the OASIS couple*. Technical Report 81, 67pp. Southampton Oceanography Centre: Southampton, UK. (17)
- Smith R.S., Gregory J.M. (2009), *A study of the sensitivity of ocean overturning circulation and climate to freshwater input in different regions of the North Atlantic*. *Geophys. Res. Lett.* 36. DOI: 10.1029/2009GL038607 (18)
- Smith R.S., Dubois C., Marotzke J. (2006), *Global climate and ocean circulation on an aquaplanet ocean-atmosphere general circulation model*. *J. Climate* 19: 4719-4737. DOI: 10.1175/JCLI3874.1 (19)
- Hall A. (2004), *The role of surface albedo feedback in climate*. *J. Climate* 17: 1550-1568. DOI: [10.1175/1520-0442\(2004\)017<1550:TROSAF>2.0.CO;2](https://doi.org/10.1175/1520-0442(2004)017<1550:TROSAF>2.0.CO;2) (20)
- Graversen RG. (2006), *Do Changes in the Midlatitude Circulation Have Any Impact on the Arctic Surface Air Temperature Trend?* *J. Climate* 19: 5422-5438. DOI: [10.1175/JCLI3906.1](https://doi.org/10.1175/JCLI3906.1) (21)
- Lee S., Gong T., Johnson N., Feldstein SB., Pollard D. (2011), *On the Possible Link between Tropical Convection and the Northern Hemisphere Arctic Surface Air Temperature Change between 1958 and 2001*. *J. Climate* 24: 4350–4367. DOI: 10.1175/2011JCLI4003.1 (22)
- Hogg N.G., Stommel H.M. (1985), *The beton, an elementary interaction between discrete Baroclinic Geostrophic Vortices, and Its Implications Concerning Eddy Heat-Flow*. *Proc. R. Soc. Lond. A* 397: 1-20 (23)
- Hogg N.G., Stommel H.M. (1985b), *Hetonic explosions: the breakup and spread of warm pools as explained by baroclinic point vortices*. *J. Atmos. Sci.* 42: 1465–1476. (24)

The Antarctic Circumpolar Wave scenario described as a combination of interannual signals

Cerrone D.^{1,2*}, Fusco G.¹, Cotroneo Y.¹, and Budillon G.¹

¹Università degli Studi di Napoli 'Parthenope'

²Università degli Studi di Siena

*Corresponding author: dario.cerrone@unisi.it

Abstract

Several studies have shown the existence of an Antarctic Circumpolar Wave (ACW) constituted by co-varying anomalies that propagate eastward in the high-latitude Southern Hemisphere on inter-annual timescales.

Some speculations on the causal mechanism of the ACW often appear in literature focusing whether it is remotely forced by the tropical El-Niño Southern Oscillation (ENSO) or it is the result of a self-sustained air-sea coupling mechanism propagating eastward around the Antarctic Ocean. In this paper we focus on the Sea Surface Temperatures (SSTs) and Sea Level Pressures (SLPs) interannual variability in Southern Ocean during 1982-2011. The aim is to understand how SST anomalies are caused by atmospheric forcing and vice versa and how the component of the coupled system are connected in space and time. The spatial patterns of the interannual covarying signals through the oceanic and atmospheric wavenumber structures, representing the asymmetric variability in the Southern Ocean, have shown substantial changes during the last three decades implying an unpredictable presence of the ACW. The structures showed by the atmospheric and oceanic systems are characterized by a mixture of wavenumbers, mainly wavenumber-2 and 3, that seem to be strongly linked to the tropical activity of ENSO and to the air-sea coupling mechanism in specific sectors of the Antarctic Ocean. The ACW seems to be the expression of a combination of different interannual covarying signals that interfere each other causing ACW oscillations and conferring to the phenomenon the typical eastward continuous path observed during some periods. The destructive interference between the interannual SLP-SST covarying signals linked to a different intensity of the ENSO fluctuations observed during the last three decades seems to play a key role in determining the interruption of some phases of the waves and in modulating the eastward and global circumpolar behaviour of the phenomenon.

Keywords: *Antarctic Circumpolar Wave (ACW) – Maximum Covariance Analysis (MCA) – Principal Component (PC) – El-Niño Southern Oscillation (ENSO) – Interdecadal Pacific Oscillation (IPO)*



1. INTRODUCTION

In recent years, several studies have shown the existence of an Antarctic Circumpolar Wave (ACW) constituted by co-varying anomalies that appear to propagate eastward in the high-latitude Southern Hemisphere around the Southern Ocean on interannual timescale [1] [2]. This phenomenon has been identified as an eastward phase-locked propagating signal in several parameters (Sea Surface Temperature – SST, Sea Level Pressure - SLP, meridional wind component, sea ice anomalies etc.) characterized by a circumpolar wavenumber-2 spatial structure and by a dominant periodicity of 4-5 years, encircling the Southern Ocean in 8-10 years for individual phases [1]. The SST anomalies originate from low latitudes in the western subtropical South Pacific Ocean then propagate eastward following the Antarctic Circumpolar Current (ACC) path. The entire air-sea coupled system encircles the globe reaching the tropical Atlantic and Indian Oceans about 6-8 years later [2]. Moreover a consistent ACW has also been observed in Sea Surface Height (SSH) anomalies [3].

The ACW has been studied through several oceanic and/or atmospheric global circulation models and through analytical models focusing on planetary waves dynamics coupled to ocean models [4] [5] [6]. Several observational studies investigated the generating mechanisms of the ACW, its persistence, characteristics and existence [7] [8] [9] [10] [11] [12]. In particular, White et al. [13] found the ACW dominating signal at a 3.7-yr period connected to a global zonal wavenumber-2 structure from 1983 to 1992. Venegas [14] found two distinct inter-annual signals interfering constructively or destructively so determining the irregular fluctuations in the spatial structure of the ACW. The first with a periodicity of 3.3 yr and a zonal wavenumber-3 pattern linked to the coupled air-sea interactions and the second with a periodicity of 5 yr and a wavenumber-2 structure presumably related to the tropical ENSO activity. On the other hand Park and Roquet [15] found that the SST, SSH and SLP anomalies in the Southern Ocean represent a quasi-stationary wave train whose modulation is related to ENSO events in the Pacific sector while the anomalies often dissipate prior to encircle the globe contradicting the self-sustained ACW scenario.

In this paper we focused on the Southern Ocean variability analyzing some ACW-related variables over the period 1982-2011. We investigated the importance of the eastward propagating wave component on inter-annual timescales. Moreover we tried to contribute to scientific debate about the zonal wavenumber structure showed by the ACW during the last three decades. We also explored the self-sustained air-sea coupling mechanisms leading the ACWs in order to understand the reason why some

phases of the ACW are interrupted and if these waves are remotely forced by the tropical ENSO variability.

2. DATA AND METHODS

In order to detect the ACW behavior we used monthly means of SLP and 500 mb height (HGT500) from the National Centers for Environmental Prediction/National Center for Atmospheric Research Reanalysis and SST data from International Comprehensive Ocean-Atmosphere Data Set. The reanalysis data have a spatial resolution of $2.5^{\circ} \times 2.5^{\circ}$. The SST data have a spatial resolution of $2^{\circ} \times 2^{\circ}$. The study area extends from 20°S to the South Pole and in some applications we focused on the circumpolar region between 46°S and 66°S , the latitude belt occupied by the ACC. All the records span the 30-yr period from January 1982 to December 2011. We estimated the monthly means anomalies prior to the analysis removing the 30-yr climatological monthly means from the original data. This procedure removes the seasonal cycle from the data set. Then we constructed the frequency spectra for band-passed SLP and SST anomalies (3-7 year) longitudinally and meridionally averaged $46\text{-}66^{\circ}\text{S}$ for identifying the main energy peaks and periodicity on inter-annual timescales. Subsequently, the application of the complex Singular Value Decomposition (SVD) method on the SLP and SST anomalies has permitted to observe the temporal and spatial characteristics and evolution of the covarying patterns also showing the mode of the ACW at different time-frequency bands. The combination of the obtained covarying Principal Components (PCs) at different frequency bands well represents the interference between the inter-annual signals so to give a clear representation of the ACW scenario.

In order to investigate possible relations between the climatic ACW modes and the Antarctic Oscillation (AAO), the ENSO and the Interdecadal Pacific Oscillation (IPO), we used the monthly means of the Southern Annular Mode (SAM) index of Marshall [16], the Southern Oscillation Index (SOI) from the Australian Government–Bureau of Meteorology and IPO index from UK Meteorological Office (UKMO) Hadley Centre for Climate Change respectively.

3. RESULTS

To analyze the inter-annual ACW characteristics and related air-sea interactions, we focused our research on the time frequencies at which the SLP and SST signals show significant energy peaks. We obtained the power spectra (fig. 1) for de-trended and standardized SLP and SST anomalies band-pass filtered (3-7 yr) with a Lanczos filter. SLP anomalies show, at inter-annual timescale, three main energy peaks (significance > 99%) located at frequency of 3.7, 4.3 and 5 yr, and three peaks of energy at 3, 3.3 and 6 yr (significance between 95% and 99%).

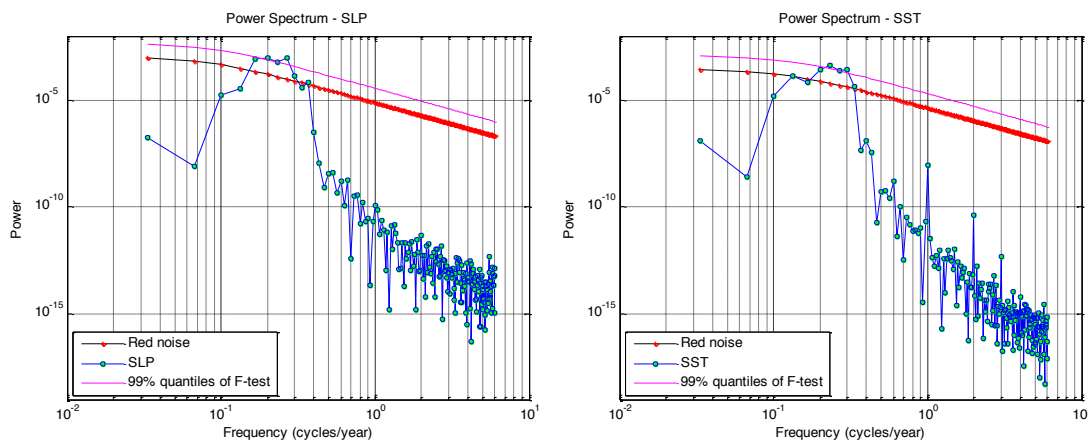


Fig. 1: Power spectra for de-trended and standardized (a) SLP and (b) SST anomalies band-pass filtered (3-7 yr) with a Lanczos filter longitudinally and meridionally averaged (46°-66°S). Solid lines with red asterisks are the 95% confidence level based on the test of red noise. The magenta lines are the 99% quantiles of Fisher test.

The SST anomalies instead show three peaks of significance energy (>99%) located at 3.3, 3.7 and 4.3 year periods and two energy peaks at 3 and 5 yr (significance between 95% and 99%). In order to examine the energy interrelationships of SLP and SST anomalies at inter-annual timescale, cross-spectral analysis was performed. The peaks of covarying significant energy across the ACC belt are located at 3.3, 3.7, 4.3, 5 and 6 yr.

In order to understand how SST anomalies are generated by atmospheric forcing, it is necessary to describe how the components of the coupled system are connected in space and time. We chose to apply the complex SVD, better known as complex Maximum Covariance Analysis (MCA). This method identifies orthogonal patterns maximizing the covariance between two variables by picking out structures in each data set that are best correlated with structures in the other data set [17] [18] [19].

Monthly anomalies are Hilbert-transformed in order to obtain a complex time sequence, then a complex covariance matrix is computed. We consider the inter-annual frequencies at which the SLP and SST anomalies have shown common significant energy peaks: 3.3 yr (hereinafter ACW-3.3), 3.7 yr (ACW-3.7), 4.3 yr (ACW-4.3), 5 yr (ACW-5) and 6 yr (ACW-6).

In our results, as expected, the ACW is represented by a linear combination of different interannual signals with different spatial and temporal characteristics.

The ACW-3.3 (not shown) and ACW-3.7 (fig. 2) signals show similar pattern and evolution (correlation value 0.73) and are characterized by a quasi-standing wavenumber-3 spatial pattern. This wave-3 structure exhibits SLP and SST anomalies that are linked by a self-sustained air-sea interaction mechanism in which the ocean passively responds to the atmospheric forcing (wind stresses and heat fluxes) so reinforcing the SST pattern. The SST anomalies eastward advected by the ACC are responsible for the change of polarity which the atmospheric pattern exhibits respect to the background state of the ocean surface temperatures. The wave-3 structure has many points in common with the known Pacific South America (PSA) pattern across the southern Pacific and Atlantic Oceans and exhibits two standing pressure centers in the Atlantic and Indian sector and, in the Pacific sector, an anomaly moving eastward across the south central Pacific. The correlation value estimated between the composition of the two ACW SST modes and SOI is -0.94 (significance > 95%). This suggests that the associated pattern showed by the combined SLP modes could be linked to the ENSO too. In fact the SLP variability across the southern Pacific and Atlantic sectors is very similar to the PSA, known to be linked to the tropical ENSO events. The correlation with the IPO is 0.90 (significance > 95%) suggesting that the interdecadal low-frequency variability of the SST in the Pacific sector associated to the decadal and interdecadal ENSO fluctuations influences the air-sea feedbacks. On the other hand the correlation with the SAM index is very low and even not significant.

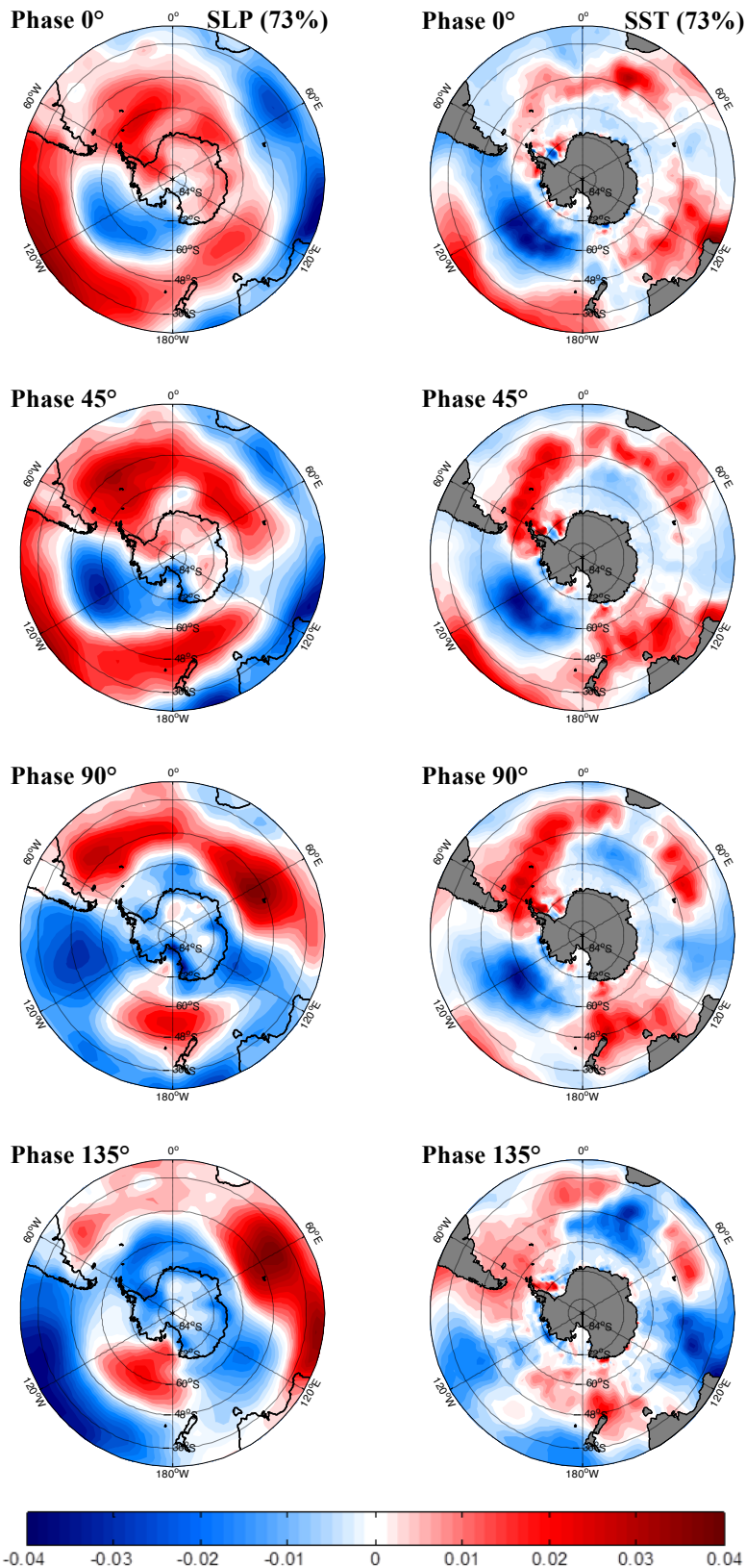


Fig. 2: Phase sequences from the first complex SVD mode of the ACW signal at period 3.7 year displaying the spatial and temporal evolution of covarying SLP and SST variability. Spatial patterns are presented as a sequence of four consecutive snapshots characterizing phases 0°, 45°, 90° and 135° of an average 3-yr period cycle and the time interval between maps is around 4.5 months. Phases 180°, 225°, 270° and 315° correspond to the same patterns with opposite polarity (not shown). SLP and SST normalized weights are color contoured, with blue (red) indicating negative (positive) weights. The covariance fraction explained is indicated.

The ACW-4.3 (not shown), ACW-5 (fig. 3) and ACW-6 (not shown) are characterized by the wavenumber-2 spatial pattern between the Pacific and the Indian sector. The air-sea interaction mechanism observed in the wavenumber-3 does not seem to similarly characterize the wavenumber-2 variability. The SST anomalies are generated by the atmospheric forcing (wind stresses and heat fluxes) principally in the Pacific sector. The wave-2 variability can be observed as a sum of climatic ACW modes with different periodicity that interfere reinforcing or destroying each other conferring to the dynamical ACW mode the characteristics of asymmetry and not continuity along the zonal global path. The correlation coefficient calculated between the sum of the leading SST PCs and SOI is -0.86; this suggests that the wave-2 variability is linked to the global atmospheric and oceanic ENSO mode. The correlation value with the IPO series is 0.81 so the low-frequency variability of the SST in the Pacific also influences the wave-2 variability on inter-annual timescale. The correlation with the SAM index is -0.41 suggesting that the Antarctic Oscillation only partially influences the inter-annual variability of the wave-2 ACW structure.

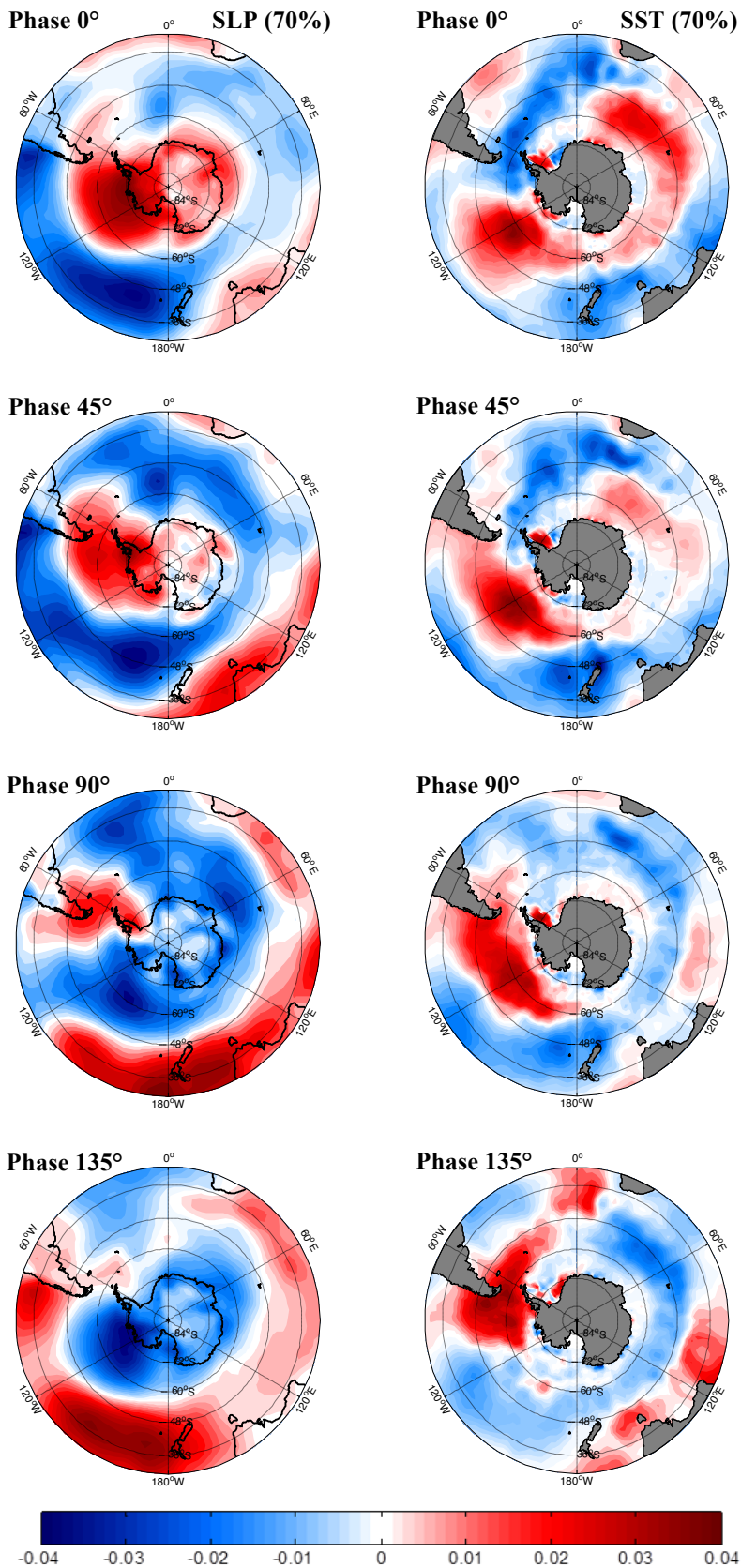


Fig. 3: Phase sequences from the first complex SVD mode of the ACW signal at period 5 year displaying the spatial and temporal evolution of covarying SLP and SST variability. Spatial patterns are presented as a sequence of four consecutive snapshots characterizing phases 0°, 45°, 90° and 135° of an average 5-yr period cycle and the time interval between maps is around 7.5 months. Phases 180°, 225°, 270° and 315° correspond to the same patterns with opposite polarity (not shown). SLP and SST normalized weights are color contoured, with blue (red) indicating negative (positive) weights. The covariance fraction explained is indicated.

The Hovmöller diagrams of the reconstructed ACW SLP (fig.4A) and SST (fig.4B) interannual signals meridionally averaged over 46°S-66°S are realized in order to investigate the reason why some phases of the ACW are missed during the last three decades. The ACW-3.3 signal exhibits larger oscillations during the period 1982-87, 1991-99 and 2005-12. The ACW-3.7 signal shows significant variations during the period 1982-95 and 2005-11. The combination of ACW-3.3 and ACW-3.7 signals (figs.5) exhibits stronger oscillations during the period 1982-98 and 2006-11. The ACW-4.3 signal shows a mixture of wavenumber-2 and 3 and the stronger amplitudes are found during the period 1982-92 and partially during 2009-11 (figs.4). The ACW-5 and ACW-6 signals exhibit a clear and strong zonal phase-related wave-2 structure during 1986-2000 (figs.4). The combination of ACW-4.3, ACW-5 and ACW-6 signals (figs.5) exhibits another more clear and definite wave-2 structure that realizes during 1986-96. This suggests that the ACW-4.3 signal partially interferes destructively with the ACW-5 and ACW-6 signals. It's worth to underline that the greatest positive SST amplitude of the wave-2 structure are observed during the period of the strongest ENSO events (1982-83, 1987-88, 1991-92, 1997-98). Moreover the wave-2 ACW signals seem to disturb each other during the period 2002-11 and the weak ENSO events of the last decade probably have not been able to reinforce the wave-2 structure causing its collapse.

The sum of the all interannual contributions (figs.5) leads to the generation of a clear eastward propagating ACW signal in SLP and SST that results stable and without interruptions during the period 1982-92.

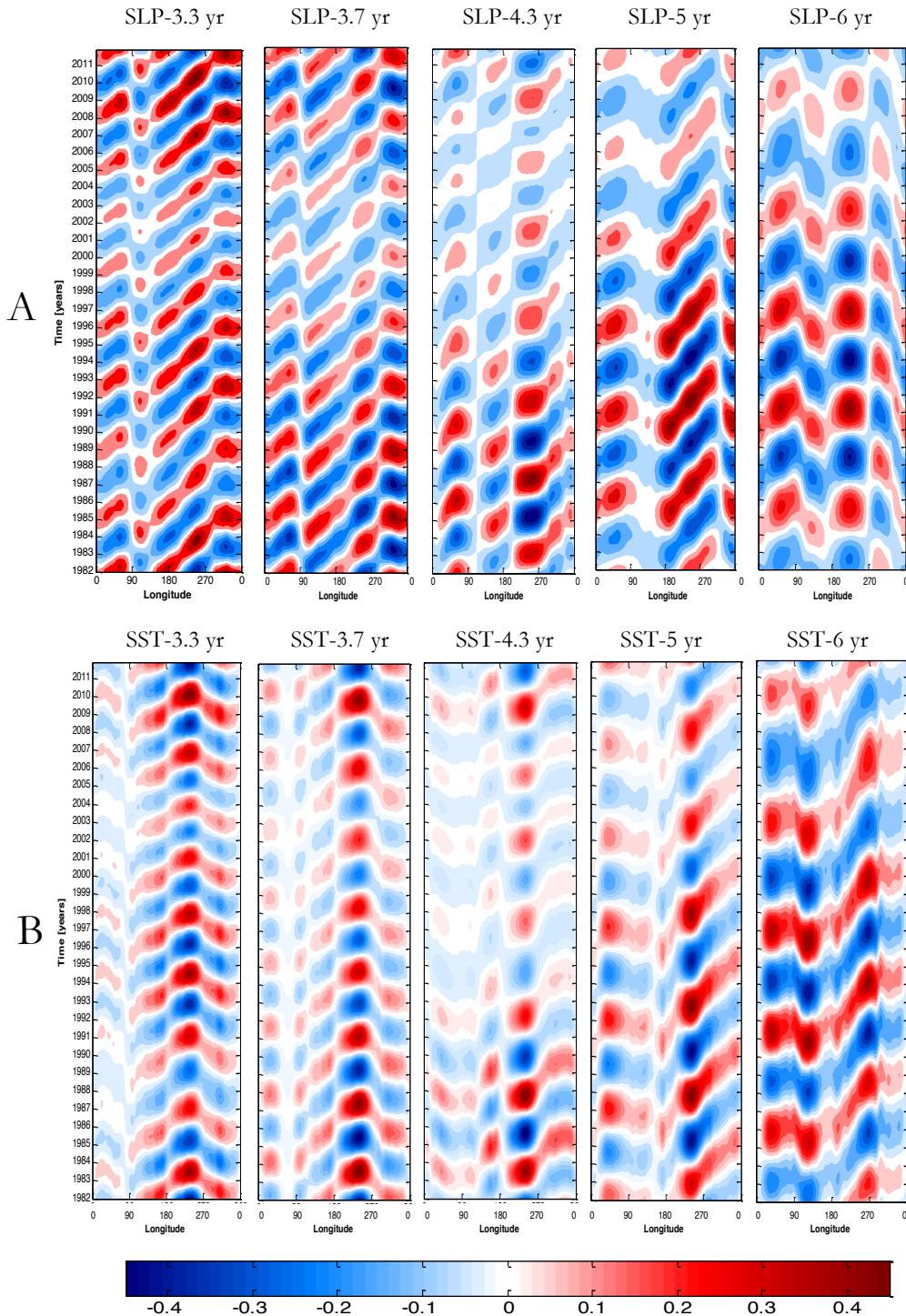


Fig. 4: Hovmöller diagrams (time-longitude) of meridionally averaged (46° - 66° S) (A) SLP and (B) SST anomalies reconstructed from the leading MCA mode associated with the ACW-3.3, ACW-3.7, ACW-4.3, ACW-5 and ACW-6 signals. SST signal is spatially smoothed with a 5 point moving average filter.

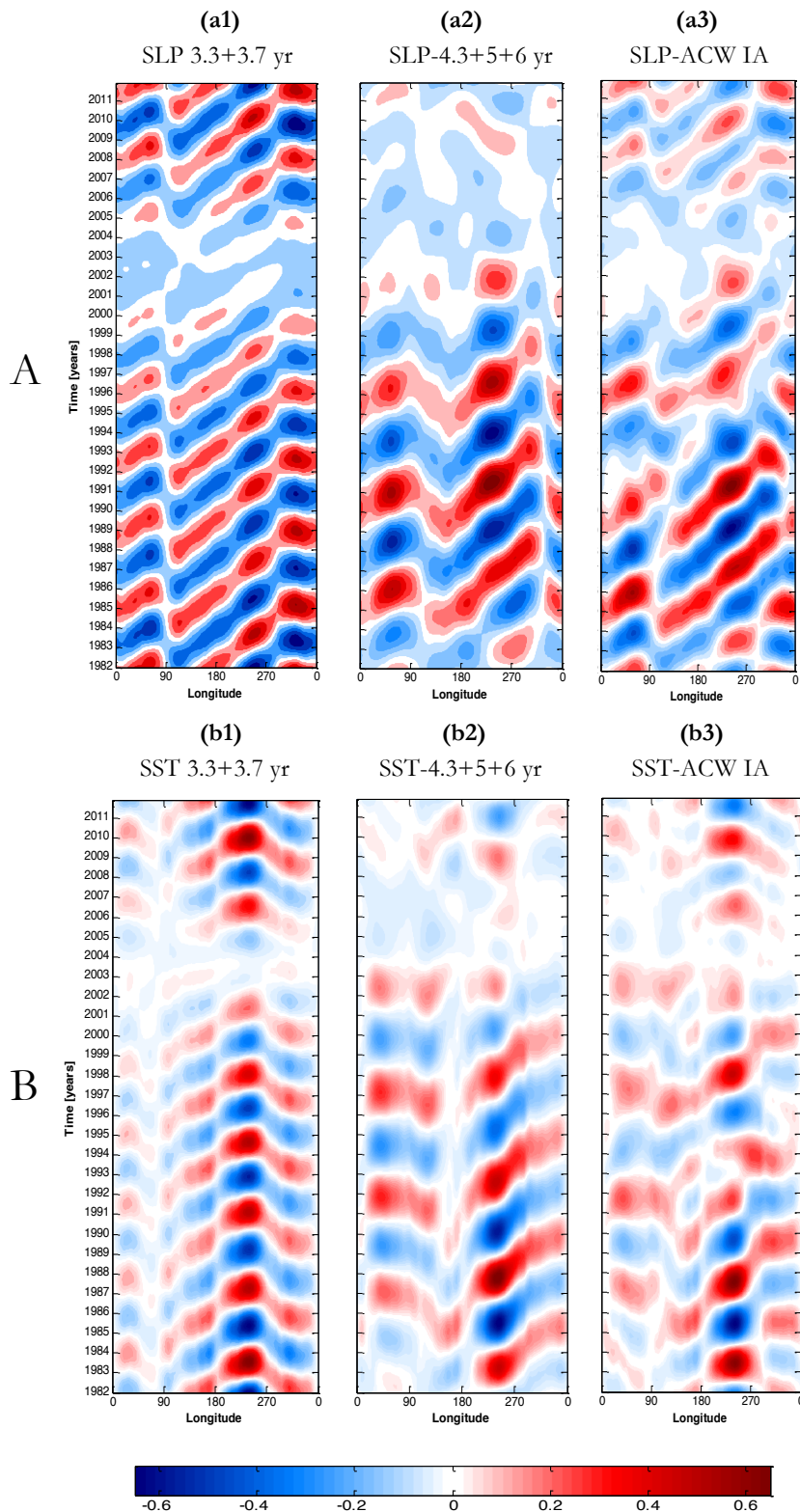


Fig. 5: Hovmöller diagrams (time-longitude) of meridionally averaged (46° - 66° S) (A) SLP and (B) SST anomalies reconstructed from the leading MCA mode associated with the sum of (a1) (b1) ACW-3.3 and ACW-3.7, (a2) (b2) the sum of ACW-4.3, ACW-5 and ACW-6, (a3) (b3) the sum of all interannual ACW signals. SST signal is spatially smoothed with a 5 point moving average filter.

This is the canonical ACW structure observed and described in existent literature [1]. During this period the wave-3 and the wave-2 patterns are phase-related and their sum implies the generation of a well defined ACW signal. On the other hand, during 1995-2002 a new ACW cycle seems to start in the Eastern Indian Ocean but, during its eastward propagation, it presents some interruptions and appears weaker and slower than expected. In fact during this period the wave-2 and wave3 signals disturb each other conferring to the eastward propagation a discontinuous path which interrupts before completing an entire cycle.

In order to obtain an index able to synthesize the interannual ACW signals, we constructed a time series summing all the interannual contributions of the SST-PCs previously observed. We calculated the correlation coefficients between the interannual ACW series and the SOI, the IPO and the SAM indices. The correlation coefficients with the SOI, the IPO and the SAM are -0.88, 0.84 and -0.30 respectively. The correlation with the SOI is higher than that calculated combining only the wave-2 contributions and suggests that the wave-3 variability interacts with the wave-2 influencing the interannual ACW signal. Similar considerations are confirmed by the correlation coefficient obtained with the IPO suggesting that the low-frequency variability of SST affecting the wave-3 dynamics represents an important contribution to the interannual ACW scenario. The correlation obtained with the SAM index indicates that the wave-3 variability seems partially to disturb the wave-2 dynamics that in turn may be influenced by the Antarctic Oscillation. Plotting the interannual SST ACW series against the SOI (fig.6), it is confirmed that positive SST amplitudes occur during major ENSO events (1982-83, 1987-88, 1991-92, 1997-98, 2009-10) and generally the signals appear phase-related even if the SOI seems to be lagging the interannual ACW signal during some periods and leading it during others.

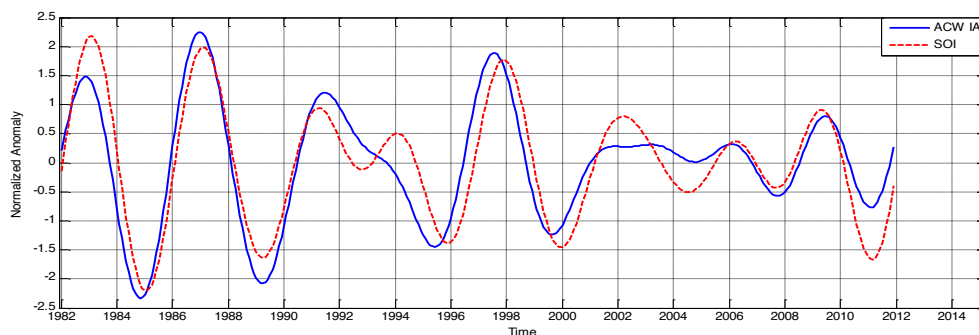


Fig. 6: Time series of the sum (blue line) of the leading PCs of SST for the all interannual ACW signals compared with the SOI (red dashed line) obtained filtering the index at the interannual frequencies considered and summing the contributions.

Combining results (figs.5 and fig.6) we observed that during the period 1982-92 the wave-3 and the wave-2 variability are phase-related and they act together to generate the strongest ACW cycle. After 1992 the relationship partially interrupts. Starting from 1995 the amplitudes of the ACW series rise again but they do not reach the high values observed in the previous period and the constructive interaction between the wave-2 and wave-3 early vanishes. During the period 2001-07 the ACW series tends to zero and this suggests that the wave-2 and the wave-3 variability disturb each other. In order to investigate the origin of the interannual ACW mode we regressed the unfiltered time series of the HGT500 upon the real part of the temporal coefficient of the sum of the leading MCA SST modes for the interannual ACW signals. This analysis reveals a clear PSA pattern extending from the south western Atlantic sector to the western Pacific sector [20] while around the Southern Ocean the atmospheric domain exhibits a clear wave-2 pattern masking the presence of the wave-3 variability. This suggests that the wave-2 variability represents the dominant pattern identifying the climatic signal of the ACW.

Summarizing, our results show that on interannual timescales the wavenumber-3 seems to be the preferred atmospheric and oceanic spatial pattern across the Southern Ocean (figs.4). It is linked to the tropical ENSO activity and shows a PSA-like pattern across the Southern Pacific and Atlantic sectors. On the other hand the wavenumber-2 pattern seems to be the manifestation of only the strongest and long-lasting ENSO fluctuations and partially linked to the SAM oscillations. The multidecadal low-frequency SST variability synthesized by the IPO seems to strongly influence the air-sea interaction mechanisms characterizing the wavenumber-3 and the wavenumber-2 patterns. Moreover the positive phase of the IPO observed during 1978-1998 could have played a key role in modulating ENSO teleconnections in the south west Pacific region reinforcing the SLP and SST anomalies and conditioning the interannual wavenumbers variability of the ACW.

The interannual ACW, described as combination of interannual signals, results to be linked to the tropical ENSO events that act generating the PSA pattern across the southern Pacific and Atlantic sectors. The strong link showed by the combined ACW signal with the IPO variability suggests that the multidecadal SST pattern is crucial in determining the intensity of the tropical ENSO fluctuations and in modulating the teleconnection with the south Pacific sector. The strongest ENSO warm events (1982-83, 1987-88, 1991-92, 1997-98) were phase-related with the positive phase of the IPO implying that the multidecadal SST pattern could have reinforced the ENSO fluctuations conditioning in turn the wave-2 and the wave-3 spatial patterns across the Southern Ocean. Moreover the possible

constructive interference between the wave-3 and the wave-2 modes could have determined the best condition for developing the clear eastward propagating ACW covarying signal during 1982-92. Similar warm ENSO/positive IPO relationship have been observed during the warm ENSO event of 1997-98 even if, in this case, the interannual ACW was only partially observed. This could be explained by the weakness of the IPO signal and its change of phase. Moreover the ACW signal during this period is characterized by numerous interruptions and does not circumvent the globe suggesting that the destructive interference between the interannual ACW signals acted to interrupt the manifestation of the phenomenon. Moreover the variability of the SAM seems to influence the combined interannual ACW signal.

Results suggest that the wave-2 and the wave-3 covariability patterns, both linked to the ENSO fluctuations, interfere reinforcing or weakening each other on the interannual timescale giving the impression of the eastward continuous ACW signal. The wavenumber-3 pattern is the manifestation of the air-sea feedback that continuously is generated around Antarctica and is usually found when the ENSO fluctuations appears weak. On the other hand, when the ENSO variability appears to be strong and its fluctuations persists over time, the wavenumber-2 covariability pattern seems to become the leading mode and sometimes phase-related with the underlying wavenumber-3 pattern especially in the Pacific sector where the anomalies reach the greatest amplitudes.

The multidecadal low-frequency SST signal described by the IPO acts modulating the intensity of the tropical ENSO events and the teleconnection with the south west Pacific sector, especially on the interannual timescales. Hence the constructive interference between the wave-2 and the wave-3 spatial patterns and the phase-relationship between the IPO and the warm ENSO events may have together determined the strong ACW scenario during 1982-92 with a clear eastward continuous path. Since 1992 up to now, the interannual interference between SLP-SST covarying pattern may have generated an asymmetric variability features and caused the presence of only partial phases of the circumpolar waves around Antarctica.

4. REFERENCES

- White W.B. & Peterson R.G. (1996), *An Antarctic circumpolar wave in surface pressure, wind, temperature and sea-ice extent*, *Nature*, Vol. 380, pp. 699-702. (1)
- Peterson R.G. & White W.B. (1998), *Slow oceanic teleconnections linking the Antarctic Circumpolar Wave with the tropical El Niño-Southern Oscillation*, *J. Geophys. Res.*, Vol. 103, pp. 573-583. (2)
- Jacobs G.A. & Mitchell J.L. (1996), *Ocean circulation variations associated with the Antarctic Circumpolar waves*, *Geophys. Res. Lett.*, Vol. 23, pp. 2947-2950. (3)
- Qui B. & Jin F.-F. (1997), *Antarctic circumpolar waves: An indication of ocean-atmosphere coupling in the extratropics*, *Geophys. Res. Lett.*, Vol. 24, pp. 2585-2588. (4)
- Christoph M., Barnett T.P. & Roeckner E. (1998), *The Antarctic Circumpolar Wave in a coupled Ocean-Atmosphere GCM*, *J. Clim.*, Vol. 11, pp. 1659-1672. (5)
- Cai W., Baines P.G. & Gordon H.B. (1999), *Southern mid-to-high latitude variability, a zonal wavenumber 3 pattern and the Antarctic circumpolar wave in the CSIRO coupled model*, *J. Clim.*, Vol. 12, pp. 3087-3104. (6)
- White W.B. & Cayan D.R. (2000), *A global ENSO wave in surface temperature and pressure and its interdecadal modulation from 1900 to 1994*, *J. Geophys. Res.*, Vol. 105, pp. 223-242. (7)
- Cai W. & Baines P.G. (2001), *Forcing of the Antarctic Circumpolar Wave by El Niño-Southern Oscillation teleconnections*, *J. Geophys. Res.*, Vol. 106, pp. 9019-9038. (8)
- Carril A.F. & Navarra A. (2001), *Low-frequency variability of the Antarctic Circumpolar Wave*, *Geophys. Res. Lett.*, Vol. 28, pp. 4623-4626. (9)
- White W.B. & Chen S.-C. (2002), *Thermodynamic mechanisms responsible for the tropospheric response to SST anomalies in the Antarctic Circumpolar Wave*, *J. Clim.*, Vol. 15, pp. 2577-2596. (10)
- White W.B., Chen S.-C., Allan R.J. & Stone R.C. (2002), *Positive feedbacks between the Antarctic Circumpolar Wave and the global El Niño-Southern Oscillation Wave*, *J. Geophys. Res.*, Vol. 107, 3165, doi: 10.1029/2000JC000581. (11)
- Connolley W.M. (2003), *Long-term variation of the Antarctic Circumpolar Wave*, *J. Geophys. Res.*, Vol. 107, 8076, doi: 10.1029/2000JC000380. (12)

- White W.B., Gloersen P. & Simmonds I. (2004), *Tropospheric Response in the Antarctic Circumpolar Wave along the Sea Ice Edge around Antarctica*, J. Clim., Vol. 17, pp. 2765-2779. (13)
- Venegas S.A. (2003), *The Antarctic Circumpolar Wave: A combination of Two Signals?*, J. Clim., Vol. 16, pp. 2509-2525. (14)
- Park Y.-H., Roquet F. & Vivier F. (2004), *Quasi-stationary ENSO wave signals versus the Antarctic Circumpolar Wave scenario*, Geophys. Res. Lett., Vol. 31, L09315, doi: 10.1029/2004GL019806. (15)
- Marshall G.J. (2003), *Trends in the Southern Annular Mode from Observations and Reanalyses*, J. Clim., Vol. 16, pp. 4134-4143. (16)
- Cherry S. (1996), *Singular value decomposition analysis and canonical correlation analysis*, J. Clim., Vol. 9, pp. 2003-2009. (17)
- Cherry S. (1997), *Some comments on singular value decomposition analysis*, J. Clim., Vol. 10, pp. 1759-1761. (18)
- Bretherton C. S., Smith C. & Wallace J. M. (1992), *An intercomparison of methods for finding coupled patterns in climate data sets*, J. Clim., Vol. 5, pp. 541-560. (19)
- Karoly D.J. (1989), *Southern hemisphere circulation features associated with El Niño-Southern Oscillation events*, J. Clim., Vol. 2, pp. 1239-1252. (20)

ADVANCES IN CLIMATE SCIENCE

Climate processes in the Mediterranean region - I

Future Storm Surge Distribution Along The Mediterranean Coast

Conte D.², Lionello P.^{*1,2}

¹ DISTEBA University of Salento, Lecce

² CMCC, Centro Euro-Mediterraneo sui Cambiamenti Climatici

*Corresponding author: piero.lionello@unisalento.it

Abstract

This study investigates the changes in distribution of sea level extremes along the Mediterranean coasts in future climate conditions. This analysis is based on the surface wind and sea level pressure fields of a 7-member model ensemble of regional climate model simulations (covering the period 1951-2050 under the A1B emission scenario), which are used for forcing a hydro-dynamical shallow water model (HYPSE). The regional climate models have been developed and used in the CIRCE fp6 project and include interacting high resolution models of the Mediterranean sea circulation. The climate change signal is computed as the difference between severe storm surge statistics in the 1971-2000 and 2021-2050 period. This analysis does not consider sea level rise and steric effects, but only the contribution due changing marine storminess. Results show that in future climate scenarios large sea level extremes will continue occurring only in the North Adriatic and in the Gulf of Gabes (as they presently do) and that their values are to decrease by the mid of the 21st century.

Keywords: *Climate change, storm surge, Mediterranean coast, extremes*



Several case studies (e.g. Nichols and Hoozemans, 1996) on cities (Venice and Alexandria), deltas (Nile, Po, Rhone and Ebro) and islands (Cyprus) show that storm surges represent hazards with potentially important impacts on many Mediterranean coastal areas. The severity of these hazards depends on sea level rise, vertical land motion and marine storminess. This study describes at basin scale the effect of climate change on this last factor and extend previous studies that have mostly addressed only specific parts of the Mediterranean coastline (e.g. Ullmann et al., 2007 and 2008; Sánchez-Arcilla et al., 2008; Mosso et al. 2009, Snoussi et al. 2008 among others) and in particular the Adriatic Sea (Lionello, 2005; Lionello et al. 2003 and 2012a and 2012b).

In this study an ensemble of recent climate simulations has been used for forcing a barotropic tide-surge model and studying the present distribution and the future evolution of storm surge extremes. The evolution of mean sea level pressure (MSLP) and surface wind fields computed by a set of climate models has been used for computing the corresponding evolution of sea level extremes, as simulated by a barotropic circulation model, which is a robust and well established tool for investigating the effect of wind and atmospheric pressure variations on sea level at various time scales (e.g. Gomis et al., 2008). In this study the Hydrostatic Padua Surface Elevation (HYPSE) model, which is a two-dimensional model based on depth averaged currents (Lionello 2005) has been used. In all simulations sea level values have been saved with hourly resolution and HYPSE has been implemented on a 168 x 82 lon-lat grid, which covers the whole Mediterranean sea with a 0.2degrees steps in latitude and longitude.

Both sea level maxima and minima (that is positive and negative surges) have been considered. Positive surges are produced by pressure minima and wind blowing towards the shore in shallow waters. Negative surges are produced by pressure maxima and offshore winds. The astronomical tide is not included, but it can be separately computed and added to storm surge levels for obtaining the actual sea level. However, it has been shown that the effect of climate change on astronomical tide is not important in the Adriatic basin for realistic climate change scenarios in the 21st century (Lionello et al., 2005). Consequently, it is expected to be negligible in the rest of the basin, where the amplitude of the astronomical tide is smaller than in the Adriatic. This study contributes new information to the existing literature on this subject (e.g. Marcos et al. 2011), because it is based on a new set of climate simulations, which include a high resolution interactive Mediterranean sea as a climate model component and are expected to provide a representation of the air-sea interaction that is more accurate than in previous studies.

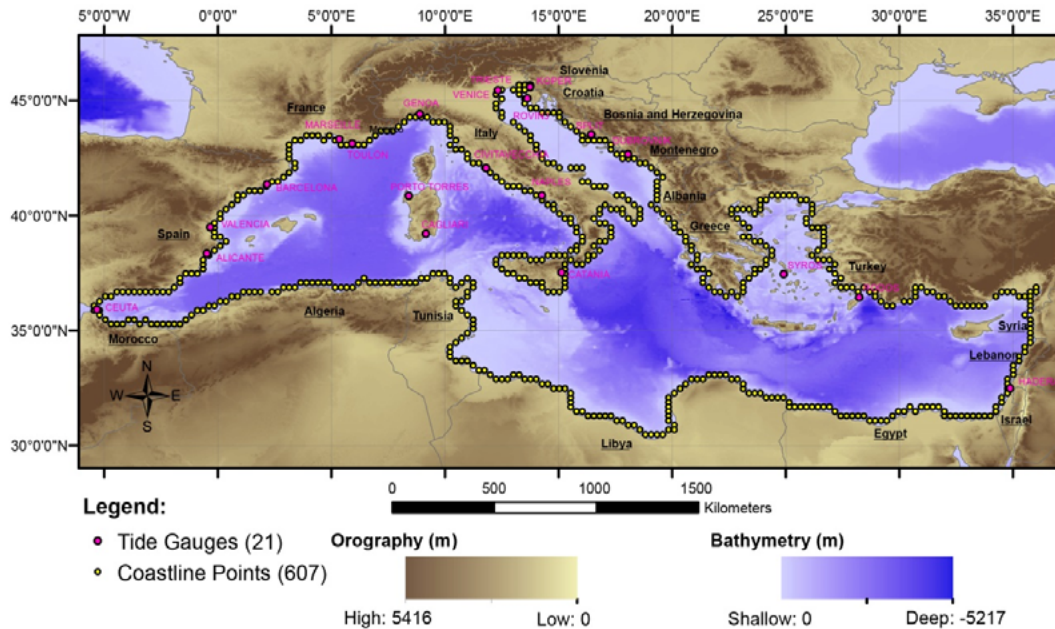


Fig. 1: Bathymetry of the Mediterranean sea. Yellow dots denote the coastal grid points used in the following figure2 for climate change analysis.

Seven scenario datasets, which have been produced in the CIRCE project (Gualdi et al., 2012), are used for the simulation of sea level. Forcing data have been structured as a sequence of 6-hourly meteorological fields covering the period 1951- 2050 under the A1B climate scenario (Nakićenović et al., 2000). They are:

- The CMCC-LR (Euro Mediterranean Centre for Climate Change Low Resolution) datasets produced using the global climate model CMCC-Med with a horizontal resolution of about 0.75 x 0.75 degrees;
- The CMCC-HR (Euro Mediterranean Centre for Climate Change High Resolution) datasets produced using the CMCC-CLM Regional Climate model, which is the climate version of the regional COSMO model with an horizontal grid resolution of 0.12 x 0.12 degrees
- The MPI (Max Plank Institute-Germany) dataset, which is produced using REMO (REgional Model) coupled to the Max-Planck-Institute for Meteorology ocean model (MPI-OM) on a rotated latitude-longitude coordinate system with a spatial resolution of 0.22 x 0.22 degrees.
- The ENEA (Italian National agency for new technologies, Energy and sustainable economic development) dataset with a mean lat/lon resolutions of 0.27 x 0.35 degrees;

- The CNRM (Centre National de Recherches Météorologiques - MeteoFrance) dataset, which is produced using the ARPEGE atmospheric circulation model, whose stretched grid reaches a 50 km resolution over Europe-Mediterranean-North Africa) coupled to NEMO-MED8 (1/8 resolution) for the Mediterranean Sea circulation
- The IPSL-3 (Institute Pierre Simon Laplace) dataset, which is computed by the LMDZ RCM (30km resolution) coupled to MEMO-MED at 1/8° deg resolution in the Mediterranean Sea.
- The IPSL-2 dataset, which uses the same models as IPSL-3, but adopting a two way coupling with the nested regional model.

The MPI, ENEA, CNRM, IPSL-2, IPSL3 and CMCC-LR simulations included a two-way coupling with a high resolution circulation model of the Mediterranean Sea. MPI and CMCC-LR are two different downscaling of CMCC-HR. IPSL-2 and IPSL-3 are two independent simulations, as both initial conditions and model framework are different. Seven HYPSE simulations have been carried out, one for each climate model dataset.

Our analysis considers how the short time scale “storminess” contribution to sea level (SL) variability will change at the coast, which consists of the subset coastal grid points of the model grid (figure 1). Coastal points have been ordered in a clockwise loop around the whole Mediterranean Basin, eastwards along its European northern coast and westwards along its African southern coast (figure 2). Long term oscillations of SL have been eliminated from the time series using a High-Pass Filter with a cutoff frequency of 1/30 days.

The indicators used for describing severe storm surge events are the positive and negative storm surge indexes. They consider the mean of the 3-largest positive and negative, respectively, storm surges in each year. Only events separated by at least 120 hours, which represent an estimate of the maximum duration of a storm in this area, have been considered in order to ensure that statistics include only independent events. These two indicators are meant to describe the largest SL anomalies that occur regularly every year and have been computed for positive/negative storm surge values at each coastal grid point (figure 1) of the model grid and are shown in the upper panel of figure 2. In this contribution the results of the seven simulations are merged in a weighted ensemble mean (see Conte and Lionello 2013 for a detailed discussion) describing their average behaviour.

Figure 2, top panel shows the positive (red line) and negative (black line) storm surge index along the Mediterranean coast. The spatial distribution shows two main features located in the Northern Adriatic

Sea and in the Gulf of Gabes, whose presence is explained by the proportionality of the wind effect to the inverse of the water depth and by the existence of relatively long wind fetch over shallow water in these two areas. Other four much lower maxima are present in figure 2: in the Gulf of Lion (France), at the coast of Tuscany (Italy), in the Aegean sea at the Greece-Turkey boundary and in the Gulf of Alexandretta near the Turkey-Syria boundary. These areas are characterized by shallow water too, even though fetches are much shorter than in the North Adriatic Sea and in the Gulf of Gabes. Note that the spatial distribution of positive and negative surges is virtually identical.

Figure 2 bottom panel shows the climate change index, which is defined at each coastal point as the fraction (actually % is used in Figure 2) of the variation of the storm surge index in the 2021-2050 period with respect to the 1971-2000 period (numerator) to the local mean value (denominator). Positive (negative) values of the climate change index show the fractional amplitude increase (decrease) of positive and negative storm surges. In general changes are small (mostly lower than 5%) and few values are statistically significant in individual simulations. However, the computation of the ensemble mean provides a clear indication of climate change- Both positive and negative surges are projected to slightly decrease their amplitude, which is coherent with the northward shift of the storm track and the decrease of cyclones over the Mediterranean region (Lionello et al. 2007).

The panels of figure 3 show for 4 locations (Marseille, Split, Alessandretta, Gabes) the time series of the largest yearly negative storm surges for the simulations discussed in this contribution. In order to compensate for systematic differences among models, each time series has been reduced to a dimensionless index, subtracting its mean value and dividing by its standard deviation. Also the ensemble mean time series is reported in this figure (thick black line). Negative (positive) values represents deeper (shallower) than average minima. The main feature of the data is their large inter-annual variability, but all these time series show a statistically significant decreasing trend of negative storm surge amplitude

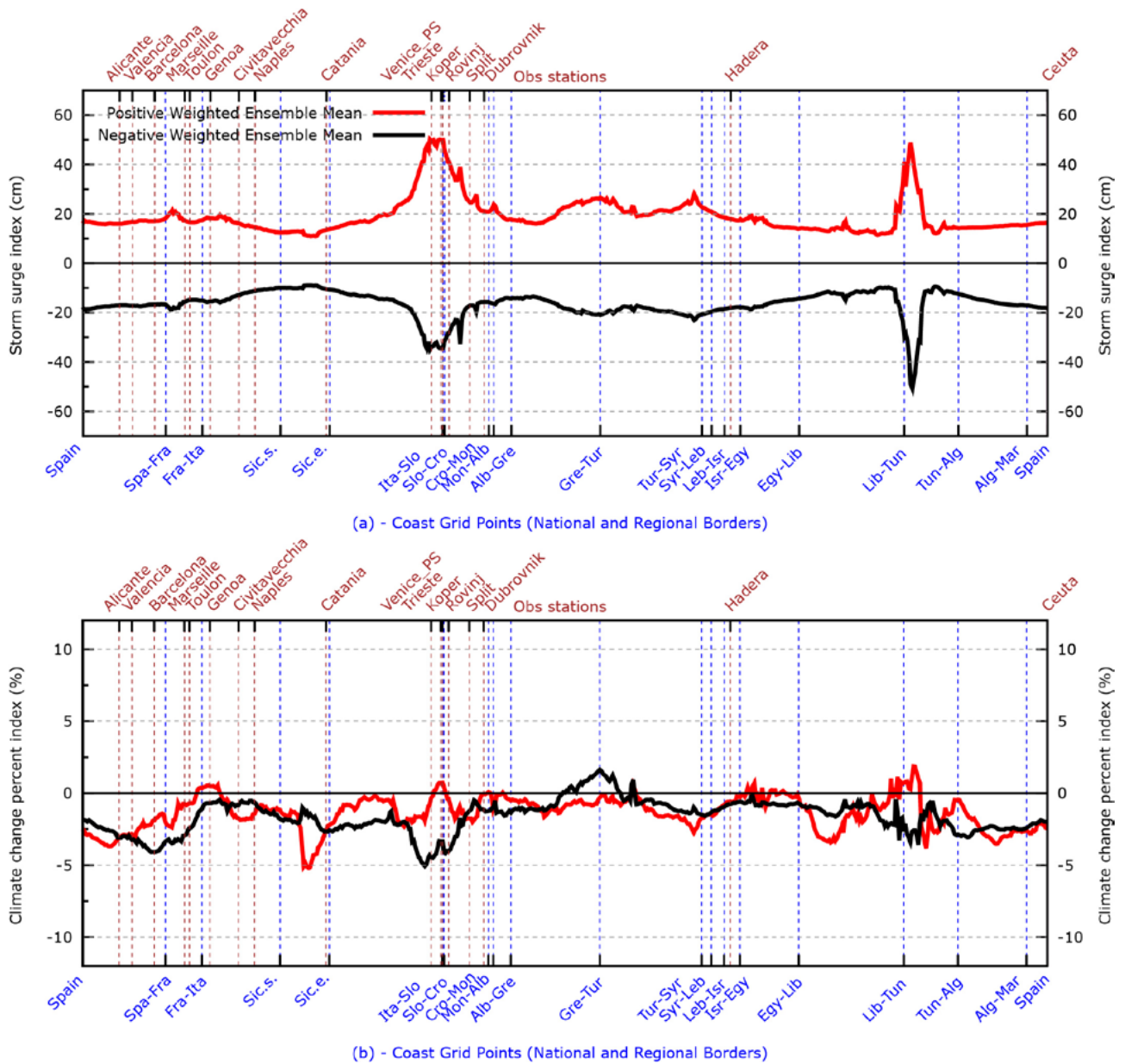


Fig. 2: (a) Ensemble mean storm surge index (cm) for positive (red line, cm) and negative (black line, cm) surges in the present climate (1971-2000) in model simulations (top panel). (b) Climate change percent index (%) for positive (red line) and negative (black line) surges. Negative values denote decreasing amplitude of surges. Coastal points are ordered clockwise starting from Gibraltar. Country national borders and some stations used are marked to help locating the different stretches of the Mediterranean coastline.

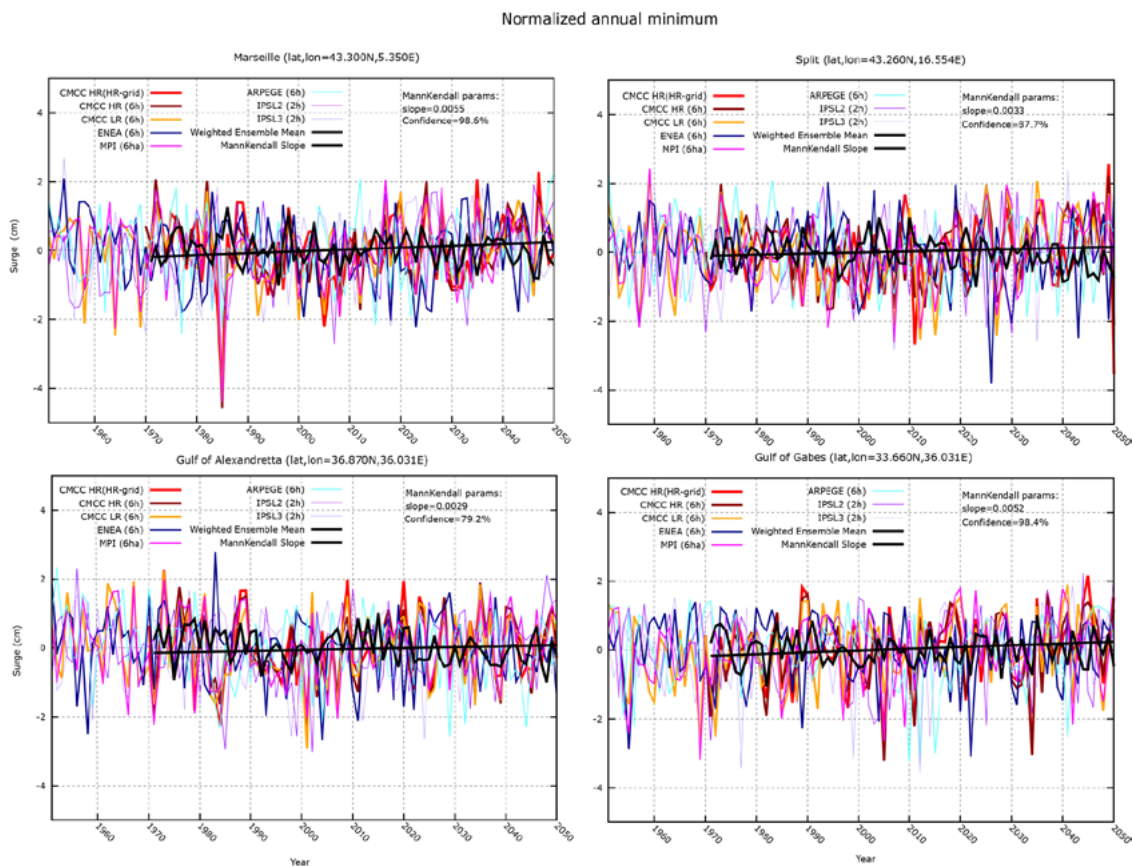


Fig. 3: Time series of the normalized annual largest negative surges at four coastal stations: Marseille, Split, Alessandretta, Gabes. The colored lines refer to the individual model simulation. The weighted ensemble average is the black line. The Sen’s estimate of the linear trend and the confidence level are shown in the figure as well. Annotations shows the trend and the confidence level . The positive trend of negative minima denotes their decreasing amplitude.

The future scenario computations produced in this study show results that have a large spatial variability within individual simulations and large differences among different simulations. However, when all simulations are merged in an ensemble mean, the climate change signal shows a generalized decrease of both positive and negative surges. Though changes are not large (reduction and increase reach 5% only in limited coastal stretches), they are substantially coherent spatially. The time separation between the two slices (1971-2000 and 2021-2050) that have been examined is small and it may prevent the detection of a large climate change signal, which could, and it is likely to, further increase at the end of the 21st century. It appears that managers and policymakers should be aware that significant changes may occur already on the decadal time scale that is addressed by this work. However, for practical applications, besides the effect of storminess, the effect of future sea level rise

and ground subsidence, which might increase significantly the hazard posed by coastal floods, need to be considered for a comprehensive evaluation of future hazards.

REFERENCES

- Climatic Change on Spanish Mediterranean Low-Lying Coasts: The Ebro Delta Case*. Journal of Coastal Research: Volume 24, Issue 2: pp. 306 – 316. (1)
- Gomis D., Ruiz S., Sotillo M.G., Álvarez-Fanjul E., Terradas J., (2008) *Low frequency Mediterranean sea level variability: The contribution of atmospheric pressure and wind*. Global and Planetary Change, Volume 63: 215-229, ISSN 0921-8181, 10.1016/j.gloplacha.2008.06.005. (2)
- Gualdi S., Somot S., Li L., Artale V., Adani M., Bellucci A., Braun A., Calmanti S., Carillo A., Dell'Aquila A., Déqué M., Dubois C., Elizalde A., Harzallah A., Jacob D., L'Hévéder B., May W., Oddo P., Ruti P., Sanna A., Sannino G., Scoccimarro E., Sevault F. and Navarra A. (2012), *The CIRCE simulations: a new set of regional climate change projections performed with a realistic representation of the Mediterranean Sea*, 10.1175/BAMS-D-11-00136. (4)
- Lionello P. (2005), *Extreme surges in the Gulf of Venice*. Present and Future Climate in Fletcher C. and T.Spencer Eds., Venice and its lagoon, State of Knowledge Cambridge University Press, Cambridge UK, 59-65. (5)
- Lionello P., Elvini E., Nizzero A. (2003), *A procedure for estimating wind waves and storm-surge climate scenarios in a regional basin: the Adriatic Sea case*. Clim. Research., 23: 217-231. (6)
- Lionello P., Mufato R., Tomasin A. (2005), *Sensitivity of free and forced oscillations of the Adriatic Sea to sea level rise*. Clim. Res. 29, 23–39. (7)
- Lionello P., Boldrin U., Giorgi F., (2007), *Future changes in cyclone climatology over Europe as inferred from a regional climate simulation*. Clim.Dyn DOI 10.1007/s00382-007-0315-0
- Lionello P., Cavaleri L., Nissen K.M., Pino C., Raicich F., Ulbrich U. (2012a), *Severe marine storms in the Northern Adriatic: Characteristics and trends*. Phys. Chem. Earth, 40-41:93-105, DOI: 10.1016/j.pce.2010.10.002. (8)
- Lionello P., Galati M.B., Elvini E. (2012b), *Extreme storm surge and wind wave climate scenario simulations at the Venetian littoral*. Phys. Chem. Earth 40-41, 86-92, DOI: 10.1016/j.pce.2010.04.001. (9)

- Marcos M., Tsimplis M.N., Shaw A.G.P. (2009), *Sea level extremes in southern Europe*, J. Geophys. Res.- 114, doi- 10.1029/2008JC004912. (10)
- Marcos M., Jordà G., Gomis D., Pérez B. (2011), *Changes in storm surges in southern Europe from a regional model under climate change scenarios*. Global and Planetary Change, 77:116-128, ISSN 0921-8181, 10.1016/j.gloplacha.2011.04.002. (11)
- Mosso C., Mestres M., Sierra J.P., Sanchez-Arcilla A., Goodess C. (2009), *Waves and surges in the Valencia Gulf. Variability rather than climate change*. J Coast Res SI56: 243–24. (12)
- Nakićenović R., Alcamo N.J., Davis G., de Vries B., Fenhann J., Gaffin S., Gregory K., Grübler A., Jung T.Y., Kram T., La Rovere E.L., Michaelis L., Mori S., Morita T., Pepper W., Pitcher H., Price L., Raihi K., Roehrl A., Rogner H.-H., Sankovski A., Schlesinger M., Shukla P., Smith S., Swart R., van Rooijen S., Victor N., Dadi Z. (2000), *IPCC Special Report on Emissions Scenarios*. Cambridge University Press, Cambridge, United Kingdom, New York, NY, USA. p. 599. (13)
- Nicholls R.J and Hoozemans F.M.J. (1996) *The Mediterranean: vulnerability to coastal implications of climate, Ocean Coast. Manage.* - OCEAN COAST MANAGE , 31: 105-132 DOI: 10.1016/S0964-5691(96)00037-3. (14)
- Snoussi M., Ouchani T., Niazi S., (2008), *Vulnerability assessment of the impact of sea-level rise and flooding on the Moroccan coast: The case of the Mediterranean eastern zone*, Estuarine, Coastal and Shelf Science, 77: 206-213, ISSN 0272-7714, 10.1016/j.ecss.2007.09.024. (15)
- Ullmann A., Pirazzoli P.A., Tomasin A., *Sea surges in Camargue: Trends over the 20th century* (2007) Continental Shelf Research, 27: 922-934, ISSN 0278-4343, 10.1016/j.csr.2006.12.001. (16)
- Ullmann A., Pirazzoli P.A., Moron V. (2008), *Sea surges around the Gulf of Lions and atmospheric conditions*, Global and Planetary Change, 63:203-214, ISSN 0921-8181, 10.1016/j.gloplacha.2007.10.002. (17)

Tropical-like cyclones in the Mediterranean sea: from the case study over Salento to a combined satellite-modelling approach

Miglietta M.M.^{1*}, Laviola S.², and Levizzani V.²

¹ISAC-CNR, Lecce, Italy

²ISAC-CNR, Bologna, Italy

*Corresponding author: m.miglietta@isac.cnr.it

Abstract

Vortices with characteristics similar to tropical cyclones have been observed in the last few years in satellite images. The wind energy of these storms is so relevant to be of concern for Mediterranean societies. In the present paper, a case study, which affected Salento peninsula on September 2006, is first analysed. Then, a more systematic approach, based on a combined modelling and satellite analysis, is extended to several tropical-like cyclones. Results show that the most intense convective activity and the largest rainfall rates are generated during the preliminary stage of the cyclone lifetime.

Keywords: *Mediterranean, Tropical-like cyclones, vortices, convective activity*



Cyclones with tropical characteristics have been occasionally observed in the Mediterranean Sea. Compared to tropical vortices, they have a shorter duration, a weaker intensity and a smaller extension. Anyway, they share the same mechanism of development, which is based on intense surface fluxes from the underlying sea and the latent heat released during convection, which cooperate to self-sustain the vortex [1].

Generally, these cyclones spend most of their lifetime over the sea, thus surface observations rarely reported on them. An exception was the case study affecting Salento peninsula on September 26, 2006. The cyclone crossed the region in the morning in about 30 minutes, reaching a maximum intensity of 78 knots and producing a pressure fall of 13 hPa in just one hour [2].

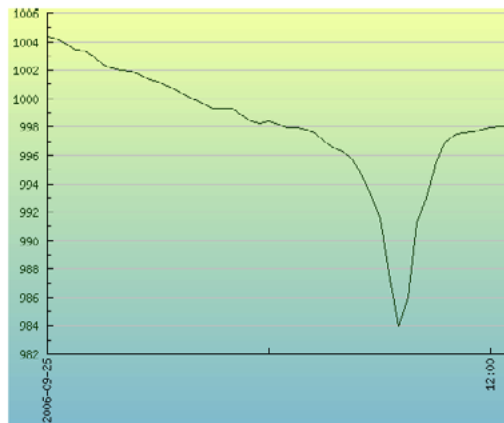


Fig. 1: Mean sea level pressure evolution from 00 UTC to 12 UTC, September 26, 2006, in Monteroni station (lat = 40.33°N, lon = 18.11°E).

Then, the cyclone moved to the Adriatic Sea, and finally landed in Gargano, where it was still very intense. Numerical simulations, performed with the WRF model [3], implemented in a two-way nested configuration over central Mediterranean, were able to correctly reproduce the observed intensity and track of the vortex [4]. Looking at the previous history of the cyclone, numerical simulations revealed that it originated in the lee of the Atlas Mountains, crossed the Strait of Sicily where it gained energy from the sea, and finally interacted with a cold frontal system near Calabria region. Then, all the energy accumulated was released through convection and after a few hours tropical features were apparent [5], i.e. a symmetric structure with a warm low- and upper-level core. The presence of the eye, typical of tropical cyclones, was observed during its transit across the Adriatic Sea.

Tropical-like cyclones, like the one described above, occur occasionally in the Mediterranean, about 1-2 cases a year. Recently, some attempts have been performed in order to identify in a systematic way these cyclones from satellite images [6]. However, this attempt was only partially successful, since only 6 cases were identified in a 20-year dataset when very strict criteria of selection were applied, while a large number of extra-tropical cyclones were also included in case of weaker constraints.

Recently, the authors, in the effort to define an algorithm for the identification of tropical-like cyclones, started to analyse different events, which were considered as potential candidates for showing tropical features [7]. The case studies were selected by considering previous events analysed in literature, identified in dedicated websites, or emerging from satellite images. These 28 cases were first simulated with the WRF model, and their symmetry and temperature vertical structure were analysed using well-established techniques for the identification of tropical cyclones [8]. Only 14 cases showed tropical features. Generally, they showed lifetimes of a few hours to 1 day and extensions from 50 to 150 km. Simulations revealed that the cyclone affecting the western Mediterranean Sea in November 2011 showed an extraordinary persistence of tropical features, as a symmetric warm core was present for more than 60 hours.

After this preliminary screening, the 14 cases were analysed by means of satellite data. Microwave satellite data were used, and in particular the Advanced Microwave Sounding Unit-B (AMSU-B) radiometer on board the NOAA satellites. The water vapour absorption band at 183.31 GHz was used through the precipitation retrieval method Water vapour Strong Lines 183 GHz (183-WSL) [9], which allows to analyse the precipitation at the ground and the cloud type in terms of its precipitation characteristics.

The satellite analysis revealed that in most of the analysed cases, the most intense convective activity, characterised by a deeper vertical extension of convective cells, organized systems and larger rainfall rates, occurred in the earlier stage of the cyclone lifetime. On the opposite, during the mature stage, the clouds were usually located in the middle and lower troposphere, even for the most intense cases, and were characterized by low rainfall intensity, mainly distributed in rainbands. Images relative to the case study of September 2006 are shown in [7, 10]. Figure 2 shows the cloud type analysis for the tropical-like cyclone affecting the western Mediterranean on November 2011.

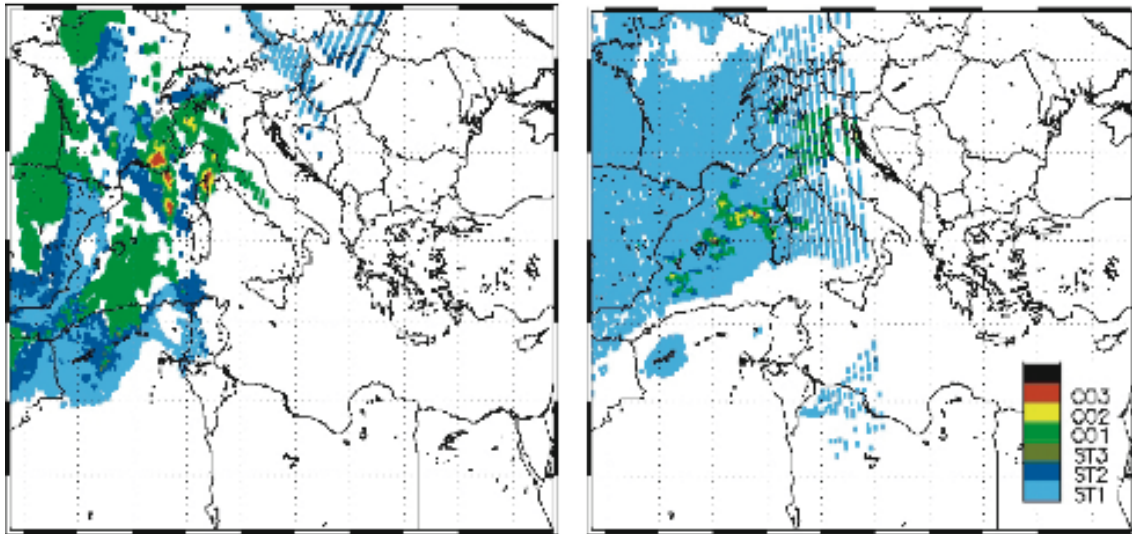


Fig. 2: Cloud type identification [for mid-latitudes, stratiform type: ST1 (cloud top at: 1÷3 km), ST2 (3÷5 km), and ST3 (5÷6 km); convection type: CO1 (6÷7 km), CO2 (7÷9 km), and CO3 (>9 km); left] from the 183-WSL algorithm at 0247 UTC, 05 November 2011 (left), and 1250 UTC, 07 November 2011 (right).

A preliminary analysis of lightning data, although limited to just a few cases, confirm that the maximum convective activity anticipates the phase with tropical characteristics.

ACKNOWLEDGMENTS

Authors SL and VL were funded by EUMETSAT's Satellite Application Facility on Support to Operational Hydrology and Water Management (H-SAF) and by the European Commission 7th Framework Programme FP7-2010-1.1-04 GMES project Global Water Scarcity Information Service (GLOWASIS) GA No. 262255.

REFERENCES

- Rotunno R., and Emanuel K. (1987), *An air–sea interaction theory for tropical cyclones. Part II: Evolutionary study using a nonhydrostatic axisymmetric numerical model*, J. Atmos. Sci., No. 44, pp. 542–561. (1)
- Moscatello A., Miglietta M.M., and Rotunno, R. (2008), *Observational analysis of a Mediterranean “hurricane” over southeastern Italy*, Weather, No. 63, pp. 306–311. (2)
- Skamarock W.C., Klemp J.B., Dudhia J., Gill D.O., Barker D.M., Duda M., Huang X.-Y., Wang W., Powers J.G. (2008), *A description of the Advanced Research WRF Version 3*, NCAR Technical Note. (3)
- Moscatello A., Miglietta M.M., Rotunno R. (2008), *Numerical analysis of a Mediterranean “hurricane” over southeastern Italy*, Mon. Weather Rev., No. 136, pp. 4373–4397. (4)
- Miglietta M.M., Moscatello A., Conte D., Mannarini G., Lacorata G., and Rotunno R. (2011), *Numerical analysis of a Mediterranean “hurricane” over south-eastern Italy: Sensitivity experiments to sea surface temperature*, Atmos. Res., No. 101, pp. 412–426. (5)
- Tous M., and Romero R. (2013), *Meteorological environments associated with medicane development*, Int. J. Climatol., No. 33, pp. 1-14. (6)
- Miglietta M.M., Laviola S., Malvardi D., Conte D., Levizzani V., and Price C. (2013), *Analysis of tropical-like cyclones over the Mediterranean Sea through a combined modelling and satellite approach*, Geophys. Res. Lett., in press. (7)
- Hart R.E. (2003), *A cyclone phase space derived from thermal wind and thermal asymmetry*, Mon. Weather Rev., No. 131, pp. 585–616. (8)
- Laviola S., and Levizzani V. (2011), *The 183-WSL fast rain rate retrieval algorithm Part I: Retrieval design*, Atmos. Res., No. 99, pp. 443–461. (9)
- Laviola S., Moscatello A., Miglietta M.M., Cattani E., and Levizzani V. (2011), *Satellite and numerical model investigation of two heavy rain events over the central Mediterranean*, J. Hydrometeor., No. 12, pp. 634–649. (10)

Sicily monthly high-resolution solar radiation climatologies

Manara V.¹, Brunetti M.², Maugeri M.^{1,2*}, Pasotti L.³, Simolo C.² and Spinoni J.⁴

¹ *Università degli Studi di Milano – Dip. di Fisica, Milano*

² *CNR – ISAC, via Gobetti, 101, I-40129, Bologna*

³ *SLAS- Regione Sicilia, Catania*

⁴ *JRC-IES, TP 280, Ispra, Varese*

*Corresponding author: maurizio.maugeri@unimi.it

Abstract

We present a methodology developed to estimate solar radiation climatologies starting from a network of global radiation and/or sunshine duration records and a digital elevation model. It allows obtaining high-resolution grids of monthly normal values for direct, diffuse and global radiation on an inclined surface. We discuss the application of the methodology to a data set of 41 Sicilian global radiation records and the resulting 2002-2011 monthly radiation climatologies.

Keywords: *Global Radiation, Sunshine Duration, Climatologies, Sicily*



1. INTRODUCTION

High-resolution datasets of monthly climatological normals (i.e. high-resolution climatologies) have proved to be increasingly important in the recent past, and they are likely to become even more important in the future. They are used in a variety of models and decision support tools in a wide spectrum of fields such as, just to cite a few, energy, agriculture, engineering, hydrology, ecology and natural resource conservation [1], [2]. One of the most important variables for a lot of possible applications (e.g. energy production and agriculture) is solar radiation.

It is therefore very important to develop and to apply methodologies that exploit as much as possible the information contained in solar radiation observational records: they consist both of global radiation and sunshine duration records. The latter have the advantage of a much larger data availability, especially when long-term records are considered, the former are more frequently available from present-time station networks.

In this context we set up a methodology for estimating high-resolution solar radiation climatologies from these records. This methodology is an improved version of that presented in [3] and [4]. It consists of the following steps:

- (i) calculating global radiation monthly normals for all station sites or estimating them from sunshine duration normals, when global radiation data are not available;
- (ii) estimating, for all station sites, the bias due to shading and adjusting the normal values in order to make them representative of un-shaded sites;
- (iii) interpolating shading-bias-adjusted global radiation normals on a regular grid and decomposing them into the direct and diffuse components;
- (iv) evaluating atmospheric turbidity over the same grid by means of the direct component obtained from shading-bias-adjusted global radiation;
- (v) calculating direct, diffuse and reflected components of global radiation for any grid-cell, taking into account its slope and aspect and considering shading from the cell itself and from the neighbouring cells.

A preliminary version of the methodology has already been used for estimating global radiation climatologies for Italy from a sparse dataset of sunshine duration records [3],[4]. The aim of this paper

is to discuss the application of the methodology to a network of 41 Sicilian global radiation records covering the 10-year period 2002-2011 and to present the resulting climatologies.

2. STATION DATA, QUALITY AND HOMOGENEITY TESTS AND GAP FILLING

The analyses presented in this paper are based on a network of 41 global radiation records covering the whole Sicilian territory (Fig. 1). The network is managed by SIAS, (www.sias.regione.sicilia.it/), an agrometeorological Service of Sicily regional administration. Global solar radiation is measured by means of thermopile pyranometers. The data have hourly resolution.

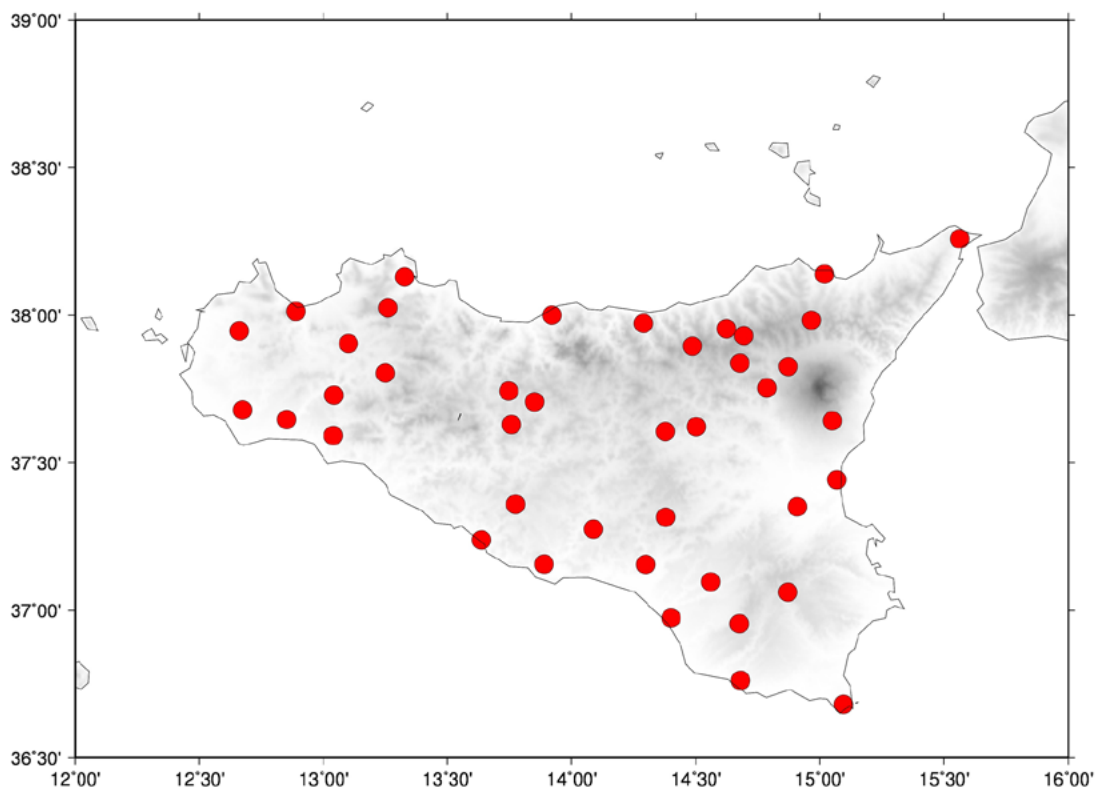


Fig. 1: Network of the SIAS meteorological stations considered in this paper

Before the analyses the hourly data were subjected to a quality check procedure in order to identify and correct gross errors such as negative values; then daily cumulated values were calculated ($Mj/m^2/day$)

and they were used to obtain daily clearness index (i.e. the ratio between measured and eso-atmospheric radiation) records. These records were then averaged for all months in order to obtain monthly records. The monthly clearness index records were then analyzed by means of the Craddock homogeneity test [5]. More precisely, homogeneity testing was performed in sub-groups of 10 series using a revisited version of the HOCLIS procedure [6]. HOCLIS rejects the a priori existence of homogeneous reference series. It consists of testing each series against other series, by means of a multiple application of the Craddock test, in sub-groups of 10 series. The test is based on the hypothesis of the constancy of clearness index differences among nearby sites. The break signals of one series against all others are then collected in a decision matrix and the breaks are assigned to the single series according to probability. This procedure allowed identifying some records with inhomogeneous sub-periods with respect to the remaining part of the record: these sub-periods were deleted from the data.

After the inhomogeneous periods were eliminated, the monthly clearness index records were completed over the 2002-2011 period. Missing data estimation was performed for each month and each station by i) selecting all the records which have at least the same data of the station to be completed; ii) transforming the data of all the stations into anomalies with respect to their averages over the years for which the station to be completed has not missing data; iii) filling the gaps of the station to be completed by a weighted average of the anomalies of the other stations, with weights depending on distance; iv) converting the estimated anomalies into absolute values.

3. ADJUSTING THE STATION NORMALS TO UN-SHADED STATION NORMALS

The completed records were used to calculate monthly clearness index normals referred to the period 2002-2011 for all stations. Most of these stations are located in areas with very limited shading and they are representative of un-shaded sites; there are however also some stations which are located in areas with significant shading, especially in winter. In order to make all stations representative of un-shaded sites we evaluated, by means of the 30 arc-second resolution GTOPO 30 Digital Elevation Model [7] and considering literature values for atmospheric turbidity, the fraction of direct radiation which is lost by the station due to shading, where shading can be caused both by the neighbouring cells and by the cell in which the station is located. Then we performed the same evaluation for diffuse radiation. When at least one of the lost fractions resulted greater than 0.5 %, we corrected the station clearness index normals in order to make them representative of un-shaded measurements.

For this purpose we first estimated the station clearness index by means of the (un-shaded) neighbouring stations and used it to split the global radiation into the direct and diffuse components in order to get the global radiation deficit from both fractions. Then we estimated the contribution of the reflected radiation and finally we estimated the total effect of the slope and orientation of the stations' cell and of the orography of the neighbouring areas on the global radiation measured at the site. This estimation was used to correct the station clearness index normal and to make it representative of an un-shaded situation. Only 13 out of 41 stations required this kind of correction. Moreover corrections were generally rather small as only 4 stations have a maximum monthly correction which exceeds 5 %. The station with the largest correction is indeed Castellamare del Golfo with values ranging from 4.4% (June) to 10.1% (December): it is shaded in the afternoon by rather steep mountains surrounding the bay in which the station is located.

These results highlighted the great care taken by SIAS in selecting the stations' sites.

Fig. 2 shows, as an example, the December clearness index station normals, after the bias due to shading was corrected.

4. GRIDDING THE UN-SHADED STATION NORMALS

Once all station clearness index normals were representative of un-shaded sites, we interpolated these normals onto the GTOPO 30 grid by means of a Multi Linear Regression of the clearness index versus latitude and elevation, followed by an Inverse Distance Weighting of the residuals, with weights depending on distance.

Then, using a decomposition model [8], we estimated the direct and the diffuse fraction of the global radiation which allow us to calculate the direct and diffuse radiation normals of each cell under the hypothesis that the cell is horizontal and that there is no shading from the neighbouring cells. These normals are then independent from the orography: they only depend on the position of the station (latitude), the day of the year and the atmospheric turbidity of the site.

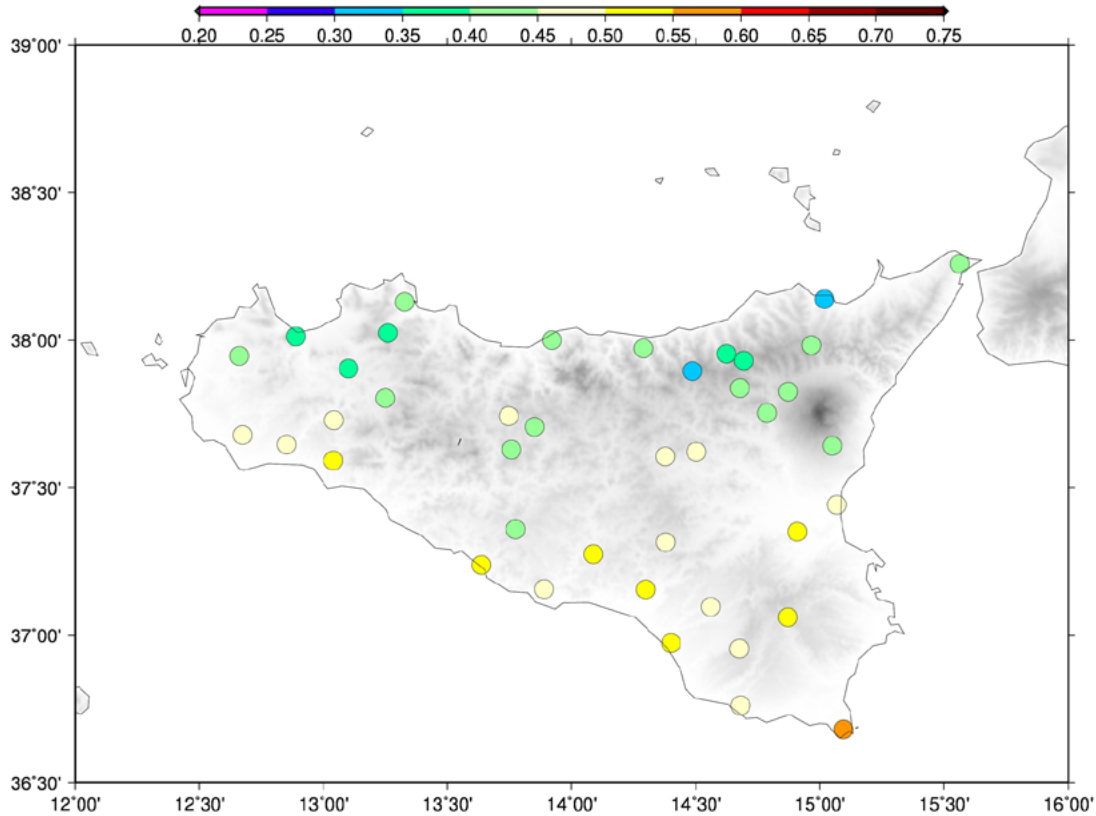


Fig. 2: Spatial distribution of the December shading-bias-adjusted clearness index normals

The direct component of solar radiation was then used to estimate the turbidity of the cell, according to the method described in [4]. This is based on the following relation [8]:

$$H_{dir-flat} = E_0 I_0 \left(\int_{sunrise}^{sunset} \cos(\theta_{inc}) e^{T_F m_A \delta_R(m_A)} dh \right) \quad (1)$$

where $H_{dir-flat}$ is the direct component of global radiation, E_0 is the eccentricity factor (i.e. the correction due to the elliptical orbit of the Earth), I_0 is the solar constant, θ_{inc} is the solar angle of incidence and the exponential part explains the attenuation due to the atmosphere: T_F is the turbidity factor, m_A is the optical air mass, δ_R is the Rayleigh's depth of the atmosphere. T_F represents the turbidity of the vertical column of the atmosphere over the grid cell: clouds, water vapour, pollution, fog, ozone, and many other factors are included in T_F .

For each point and each month we searched for the T_F best matching $H_{dir-flat}$. Details on the calculations can be found in [3].

5. SOLAR RADIATION CLIMATOLOGIES

Once atmospheric turbidity and the direct and diffuse components on an horizontal un-shaded surface were estimated for each cell of the GTOPO30 DEM, we calculated the solar radiation received by the soil taking into account slope and orientation of the surface and shading. More precisely, direct radiation for inclined surfaces ($H_{dir-incl}$) was calculated by means of the following relation:

$$H_{dir-incl} = E_0 I_0 \left(\int_{sunrise}^{sunset} J \cos(\theta_{inc}) e^{T_F m_A \delta_R(m_A)} dh \right) \quad (2)$$

J is a binary factor representing shading: it was obtained by exploring the grid-cells surrounding each node of the GTOPO30 DEM and checking, with a 5-minute temporal resolution, if the path from the node to the sun does or does not intercept the DEM surface. If the grid cell is shadowed in the 5-minute interval that we used in the integration, J was set to 0, otherwise it was set to 1. In this case \mathcal{G}_{inc} is naturally calculated taking into account the slope and the aspect of the surface.

Actually, in spite of the analogies of eqs. (1) and (2), they are used in a completely different way: in fact in eq. (1), we know the direct radiation on an idealized surface (flat and un-shaded) and use it to get T_F ; on the contrary, in eq. (2) we know T_F and use it to get the solar radiation on a real surface.

Diffuse radiation for inclined surfaces ($H_{dif-incl}$) was calculated considering diffuse radiation as isotropic and estimating the fraction of energy lost because the inclination of the cell and the orography of the surrounding areas reduce the sky view factor (V_F), i.e. the visible fraction of the sky from the grid-cell.

Reflected radiation for inclined surfaces ($H_{ref-incl}$) was calculated considering the radiation from the obstructed sky (OS_F), expressed by $OS_F = 1 - V_F$ and considering the albedo of the ground (α). In our procedure we assumed for the albedo the value which we attributed to the grid-cell itself, even though the reflection is due to the surrounding cells. This approach is reasonable since the very small contribution of reflected radiation that we have with a DEM resolution of 30 arc-seconds does not

justify the much greater complexity which would be necessary in order to take into account the slope, aspect and albedo of the surrounding grid-cells.

Albedo was estimated by means of the GLC2000 land cover grid provided by Joint Research Center (<http://bioval.jrc.ec.europa.eu/products/glc2000/glc2000.php>).

Once direct, diffuse and reflected radiation were available, we simply calculated global radiation by their sum. The entire procedure was performed for all the grid-cells of Sicily.

The final results are 2002-2011 monthly global radiation climatologies. The climatologies of December, March, June and September are shown in Fig. 3-6. They show a rather strong North-South gradient in winter, with the lowest values in the Messina area and the highest ones in the Ragusa area. Also in the other seasons the Messina area shows lower radiation than the other parts of Sicily, even though the spatial gradients are lower than in winter.

It is worth noticing that the same procedure we applied to obtain global radiation on a surface inclined as the soil can be applied selecting any combination of slope and aspect. This may be useful for energy applications as solar panels are usually not installed parallel to the ground but in order to collect as much solar radiation as possible.

It is also worth noticing that the global radiation climatologies presented in this paper give much more spatial details than the ones which were available for Sicily: they were produced considering only a few Air Force stations or using satellite measures [9],[10].

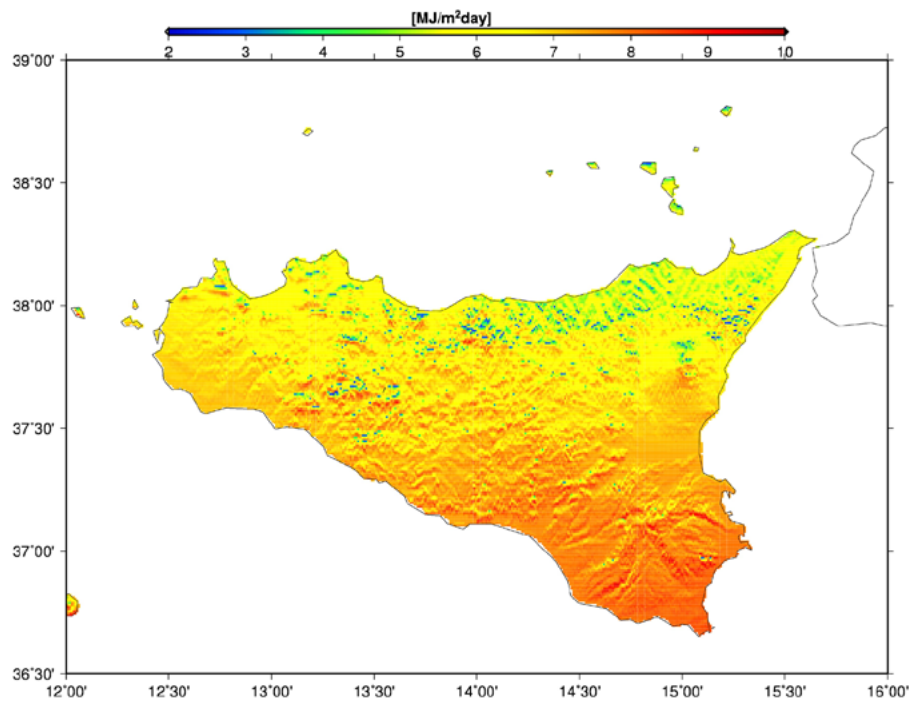


Fig. 3: Global Radiation Climatology for December

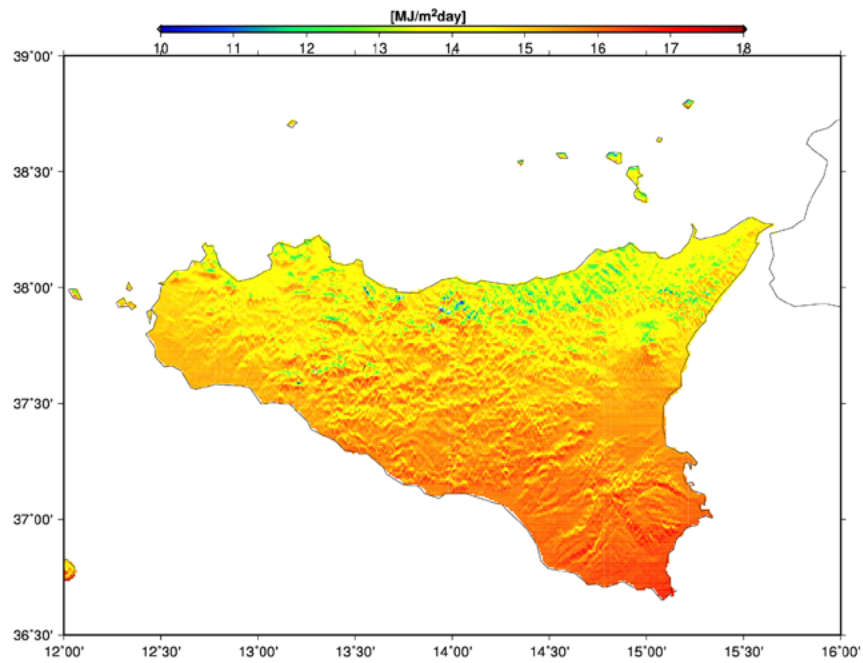


Fig. 4: Global Radiation Climatology for March

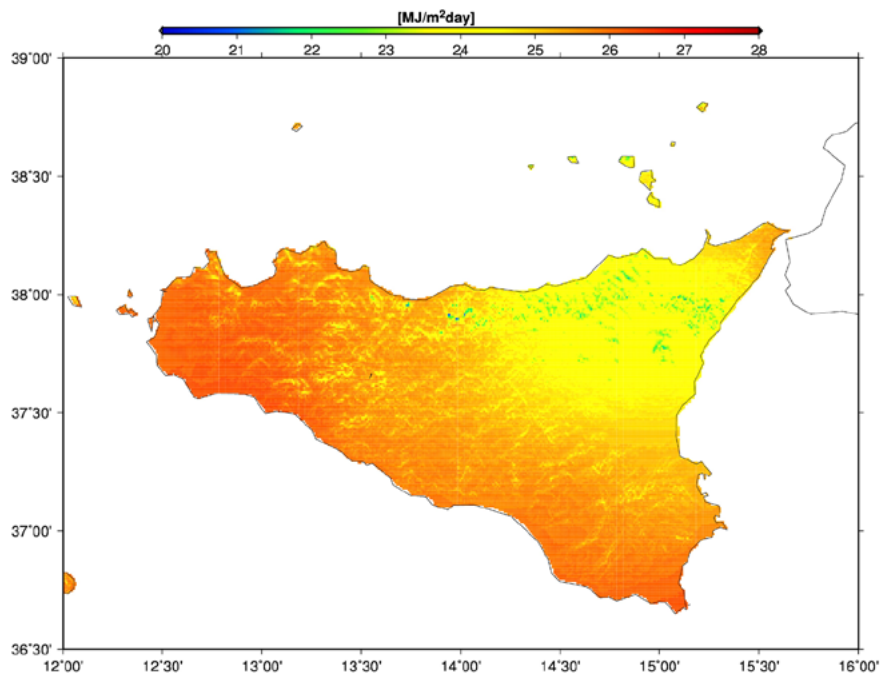


Fig. 5: Global Radiation Climatology for June

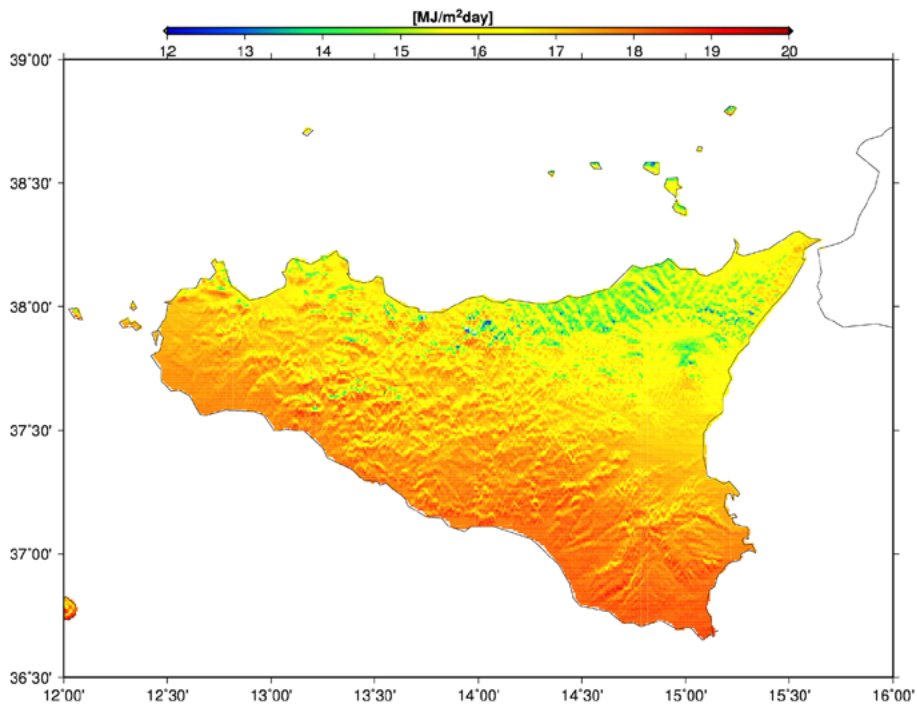


Fig. 6: Global Radiation Climatology for September

6. ACKNOWLEDGMENTS

This study has been carried out in the framework of the EU project ECLISE (265240). We sincerely thank SIAS (Servizio Informativo Agrometeorologico Siciliano) who provided the data used in this paper. We also thank Caterina Bassi, Paolo Bettoni, Diego Bruselli, Alessandro Comolli, Manuela Dell'acqua and Mistral Garzoglio, students at Milan University, for their contribution in the preparation of the data set.

7. REFERENCES

- Daly C., Gibson W.P., Taylor G.H., Johnson G.L. & Pasteris P.A. (2002), *A knowledge-based approach to the statistical mapping of climate*, *Climate Res.*, 22, 99–113. (1)
- Daly C. (2006), *Guidelines for assessing the suitability of spatial climate data sets*, *Int. J. Climatol.*, 26, 707–721. (2)
- Spinoni J. (2010), *1961–90 High-Resolution temperature, precipitation, and solar radiation climatologies for Italy*, Ph.D. thesis, Milan University, available at: http://air.unimi.it/bitstream/2434/155260/2/phd_unimi_R07883_1.pdf. (3)
- Spinoni J., Brunetti M., Maugeri M. & Simolo C. (2012): *1961-1990 monthly high-resolution solar radiation climatologies for Italy*, *Adv. Sci. Res.*, 8, 19-21, available at: www.adv-sci-res.net/8/19/2012. (4)
- Craddock J.M. (1979), *Methods of comparing annual rainfall records for climatic purposes*, *Weather* 34, 332–346. (5)
- Auer I., Böhm R., Schöner W. & Hagen M. (1999), *ALOCLIM - Austrian - Central European Long-term Climate - creation of a multiple homogenized long-term climate data-set*, *Proceedings of the Second Seminar for Homogenisation of Surface Climatological Data*, Budapest, 9-13 Nov. 1998, WCDMP 41, WMO-TD 962, WMO: 47-71. (6)
- U.S. Geological Survey - USGS (1996), *GTOPO30 Digital Elevation Model*, [http://eros.usgs.gov/#/FindData/Products and Data Available/gtopo30 info](http://eros.usgs.gov/#/FindData/ProductsandDataAvailable/gtopo30info). (7)
- Iqbal M. (1983), *An introduction to solar radiation*, Academic Press, Orlando, FL, OSTI ID: 5596615. (8)
- Aeronautica Militare – Centro Nazionale di Meteorologia e Climatologia Aeronautica (1989), *Soleggiamento e radiazione globale in Italia*, Italian Air Force, Meteorological Service. (9)

Petrarca S., Cogliani E., Spinelli F. (2000), *La radiazione solare globale al suolo in Italia, Anni 1998-1999 e media 1994-1999, Valori medi mensili stimati dalle immagini fornite dal satellite Meteosat*, ENEA, Dipartimento Energia, Divisione Sistemi Energetici per la Mobilità e l'Habitat. (10)

Reconstruction of long time series of monthly temperature values by statistical methods: an application to Europe and the Mediterranean region

Scarascia L.^{1*}, Salcedo-Sanz S.²Garcia-Herrera R.^{3,4}, and Lionello P.¹

¹University of Salento DISTEBA - CMCC,

²Escuela Politécnica Superior - Alcalá de Henares - Spain,

³Universidad Complutense de Madrid - Spain,

⁴IGEO (CSIC-UCM)

*Corresponding author: luca.scarascia@unisalento.it

Abstract

This study compares linear and nonlinear statistical techniques applied to the reconstruction of monthly mean temperature time series at European, Mediterranean, Asian, Near and Middle East stations.

The overall goal is exploiting the internal correlations existing in the temperature field for reconstructing the temperature distribution over a relatively large region and since the beginning of the 19th century using the information provided by few long temperature time series. Two techniques are adopted: the Multilinear Regression Model and the Multi Layer Perceptrons Neural Network, representing a linear and non-linear method, respectively.

Data include 209 monthly temperature time series, 11 of which are long time series, starting in the 18th century. These 11 long time series are used as predictors after a preliminary Principal Component Analysis pre-filtering. The remaining 198 short time series are the predictands, whose values are reconstructed for the whole period during which the predictors are available. Results show that for this problem the linear technique is more accurate and reliable than the nonlinear technique. As practical application, the reconstruction of the January monthly mean temperature in the period 1850-2000 over Germany is shown.

Keywords: *Monthly mean temperature, reconstruction, Linear regression, Neural Network.*



The objective of this contribution is mainly methodological. It explores the possibility of reconstructing past monthly temperature time series starting from a small group of long time series, whose data are available since the 18th century by exploiting the internal spatial correlations in the temperature field.

The monthly mean temperature time series have been computed from daily time series extracted by different datasets. The 198 short time series are extracted from ECA&D dataset (European Climate Assessment and Dataset) available at the web page <http://eca.knmi.nl/> and from the CRU dataset available at the web page <http://www.cru.uea.ac.uk/data>. The 11 long time series are from different sources. Stockholm and Vartan are extracted from the ECA&D dataset. Padua and Bologna time series are kindly provided by Dario Camuffo and Chiara Bertolin. Uppsala, Cádiz, Central Belgium, and St. Petersburg are made available by the IMPROVE project.. Prague and Milan are extracted from the CRU dataset. Finally, the Central England monthly time series is extracted from the Metoffice dataset at <http://www.metoffice.gov.uk/hadobs/hadcet/>. This monthly time series is representative of a roughly triangular area of the United Kingdom enclosed by Lancashire, London and Bristol. It begins in 1659 and it is the longest available instrumental record of temperature in the world. Fig.1 shows the position of all stations considered in this study. Colors of dots denote the length of availability period. The green dots with black bold border are the stations that are used as the predictors by the models.

Past temperature series are reconstructed using a set of 11 long temperature series as predictors and 198 time series of single stations as predictands. However, the predictors set is previously filtered by applying a PCA (Principal Component Analysis), which reduces the number of predictors to the 7 first Principal Components of the long time series. The justification for the method is based on the statistical and physical links among temperature time series of different station, which are determined considering the data of the last 50 years of the 20th century when all 209 time series are available.

Pre-filtering consists in decomposing the individual monthly mean temperature time series (after subtracting the mean value) in the product of two factors according the following expression:

$$x_j(t_i) = \sum c_k(t_i) e^k_j$$

where j is the station index, i the temporal index, c_k is the k -th Principal component, and e^k the respective Empirical Orthogonal Function. PCA analysis provides a reorganization of the information contained in a field so that the maximum possible percentage of the total field variance can be explained by the first Principal components in a descendent order. For the 11 long time series that are used in this study, the first 7 Principal components explain the 98% of the total variance and are used as predictors in the two statistical models.

Two types of model are used. The first model is a Multilinear Regression Model (LRM) in which the predictand is expressed as a linear combination of the predictors:

$$y(t) = a_0 + \sum_{n=1}^N a_n x_n(t)$$

where y represents the predictand, N the number of predictors, t the time index, a_n the regression coefficients and x_n the predictors. The regression coefficients are computed using the least square minimization of the target function:

$$X = \sum_{n=1}^N \left(\frac{y_i - a_0 + \sum a_n x_n(t_i)}{\sigma_i} \right)^2$$

where y_i is the observation value, while σ_i is its error (if it is known).

The second regression model is based on a Multi-Layer Perceptrons Neural Network (MLP), which represents the non-linear approach to this reconstruction problem. MLP is implemented defining a Neural Network consisting in a input layer with 7 neurons (the predictors), a hidden layer with 8 neurons and an output layer with a single neuron, which is the reconstructed temperature time series. The hidden layer elaborates the output from the input layer during the training phase in which the weights, w_j , of the model are computed according to the relation:

$$y = \varphi(\sum w_j x_j - \vartheta)$$

where $\varphi(x)$ is called transfer function and ϑ is a threshold value). In the commonly used nonlinear version of the MLP, the transfer function is the logistic function $\varphi(x) = \frac{1}{1+e^{-x}}$. A “linear version” of MLP can be obtained considering a linear transfer function, that is trivially $\varphi(x) = x$. As will be shown later, we have used both versions of MLP.

The objective of this contribution is to compare the results of the LRM and MLP models and to explore their capability to compute the past evolution of temperature time series in periods when very few instrumental data are available. All plots and examples of this paper consider the January monthly mean temperature.

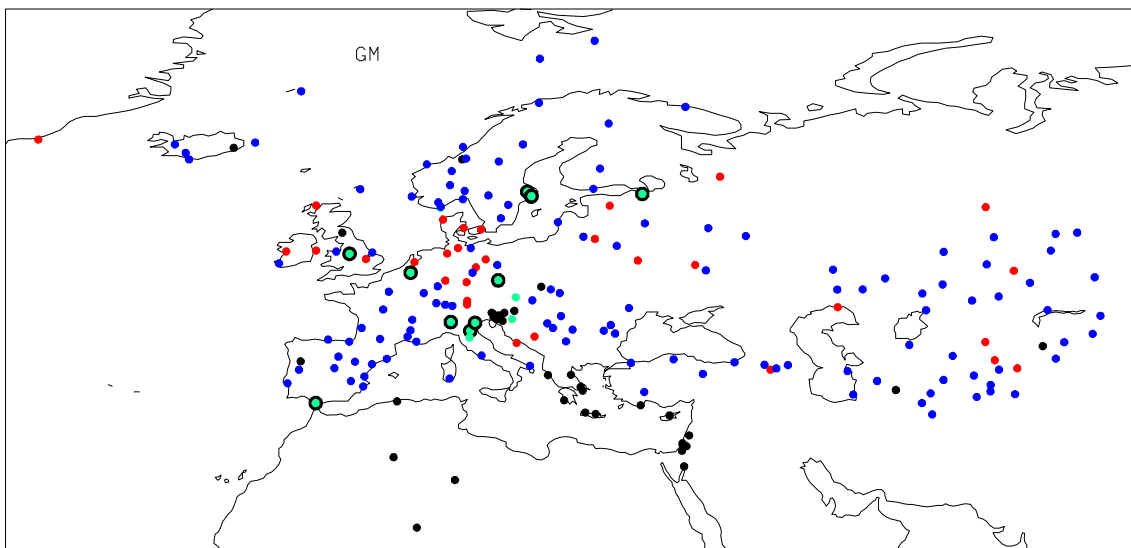


Fig. 1: This map shows all temperature time series considered in this study and the data availability for each of them. Green dots indicate station whose data begin before 1870, red dots between 1871 and 1900, pink dots between 1901 and 1951, black dots indicate time series starting after 1951. Green dots with black circle show the stations from which the first 7 Principal Components have been extracted and used as the predictors of the models

Models are validated and their accuracy evaluated by assessing their capability to reconstruct the temperature against observations. In order to do this the second half of the 20th century is divided in two sub-periods 1951-1975 and 1976-2000. The first sub-period is used for constructing the models and the second sub-period for validating them. Note that the two sub periods have been swapped and it has been checked that the model performance does not depend on the period considered to

construct it. The procedure, the terminology and the construction phase of the model is slightly different for LRM and MLP.

For the LRM, the sub-period 1951-1975 is used to train the model and for computing the regression coefficients that are used for reconstructing the temperature time series in the sub-period 1976-2000. For LRM the first sub-period is called “training period”, the second one “validation period”.

In the case of MLP, data belonging to the 1951-1976 period, in which the model is constructed, are further divided in three groups: training, validation and test. The training data are used for computing and modifying the weights. The error computed on the validation data is used to stop the training phase when it is reduced below a given threshold. Test data don't have any role in the weights determination, but are used to evaluate the reliability of the model against independent data, which are not considered in the training/validation phase. In this study, MLP is implemented so that the 60% of the data included in the interval 1951-1975 are used for training and the 20% for validation and test respectively. The data for each category are randomly distributed in time, so that training, validation and test do not correspond to well defined sub-periods. To facilitate the comparison with the LRM, the statistics describing the MLP accuracy are computed for the sub-period 1976-2000 as well.

The model performance is evaluated through the computation of the rmse (root of mean square error) and the correlation between the original and the reconstructed signal. From these two parameters (and using also the standard deviation of the original and reconstructed signal) the Taylor diagrams is constructed (Fig. 2). In Fig. 2 green dots indicate the stations in central Europe, yellow dots in the Iberian Peninsula, pink dots in Eastern Europe (east of 19 degs of longitude), red dots in the Near and Middle East, blue dots in the Asian countries, black dots, finally, indicate the peripheral stations which are not included in the previous regions. A dot indicates a good reconstruction when its coordinates are closer as possible to the position (1.0, 0.0), meaning that the original and reconstructed time series have the same standard deviation and are very well correlated. In general terms the green stations (central Europe) are those with the best reconstruction quality, the blue stations (Asia) those were quality of reconstruction is very poor.

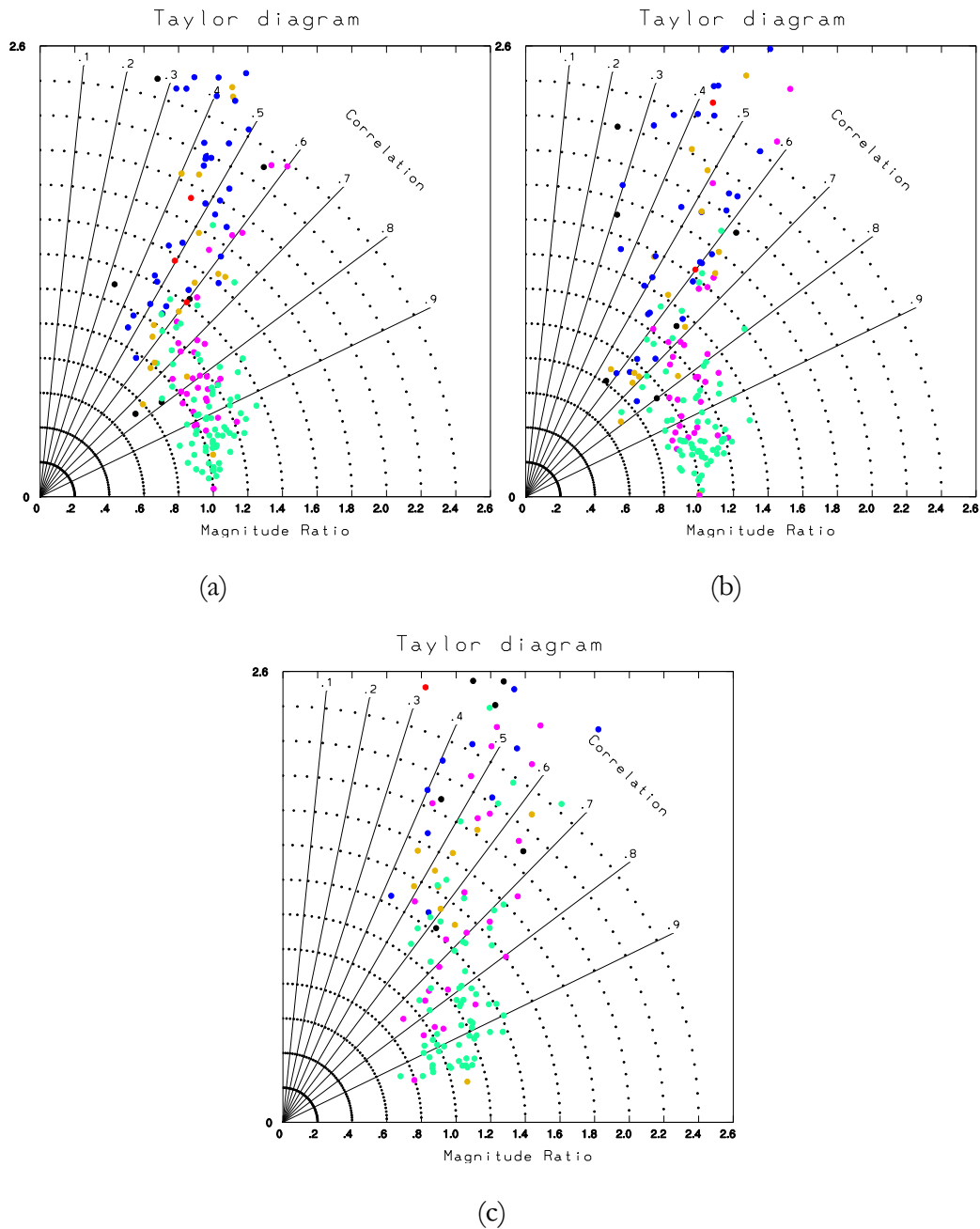
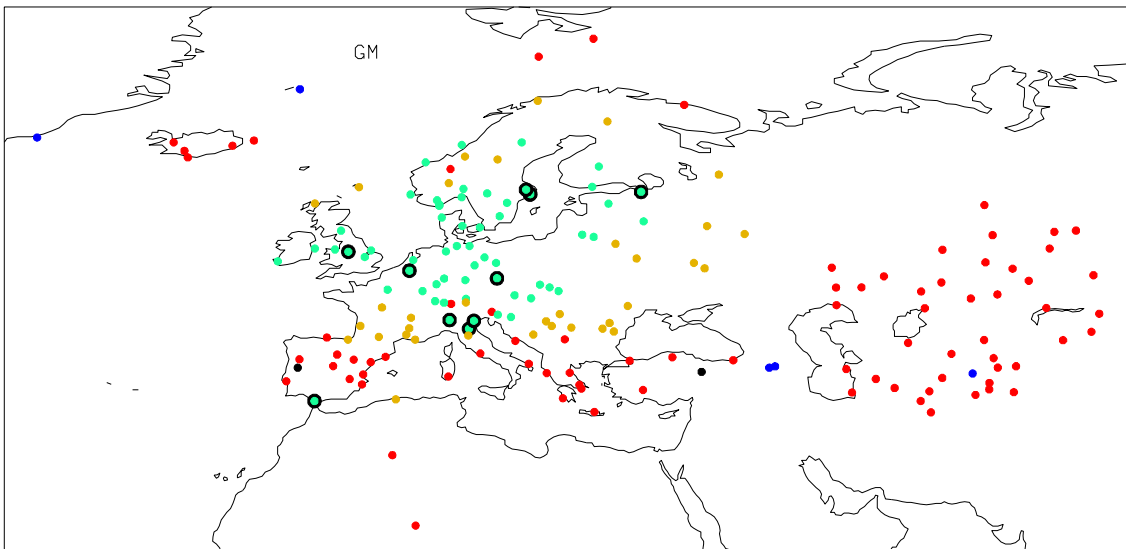


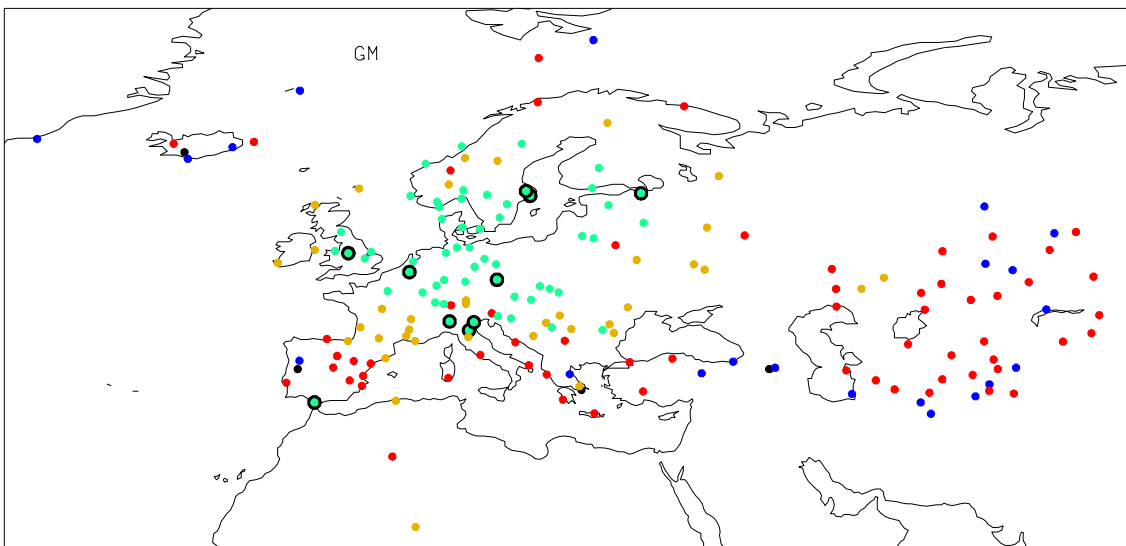
Fig. 2: Taylor diagrams showing, for each station, represented by a dot, the combination Magnitude Ratio – Correlation produced by the LRM (a) , MLP using a linear activation function (b) and MLP with a logistic activation function (c) respectively. The models are built in the sub-period 1951-1975 and applied to the sub-period 1976-2000 to which these results refer. Color references: green dots indicate stations in Central Europe, yellow dots in Iberian Peninsula, pink dots in East Europe, red dots in Near and Middle East, blue dots in Asian countries, black dots remaining peripheral stations

Fig. 3 shows the spatial distribution of the percent error, defined for each station as the ratio of the rmse over the standard deviation of the original time series. Fig. 3 shows, beside the quality of the

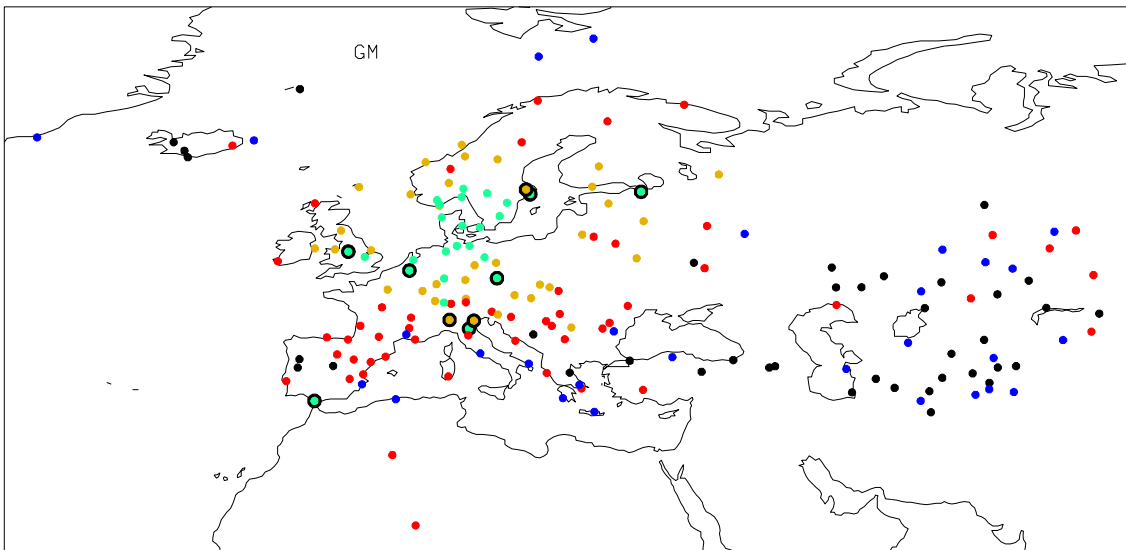
reconstructions, also whether the 11 “predictor” stations are representative of the surrounding stations. The green dots represent the stations that are best reconstructed by the models, with a percent error lower than 0.5 (0.0 is the perfect reconstruction). Yellow, red and blue dots consider ranges until 0.8, 1.2, 1.5 respectively. Black dots are location where the percent error is greater than 1.5. The analysis is performed only for the stations having at least 80% of available data in the interval 1951-2000.



(a)



(b)



(c)

Fig. 3: Plot of the ratio $rmse/standard\ deviation$ produced by the models for the stations having at least the 80% of data available in the period 1951-2000 in the following order: LRM (a), MLP using a linear activation function (b) and MLP with a logistic activation function (c) respectively. The models are constructed in the first sub-period 1951-1975 and applied to the second sub-period 1976-2000 to which the results refer. Color references: green dots indicate the station better reconstructed by the models, with a percent error lower than 0.5 (0.0 is the perfect reconstruction). Yellow, red and blue dots consider ranges until 0.8, 1.2, 1.5 respectively. Black dots are location where the percent error is greater than 1.5

In general the 11 long time series are representative of the stations in the surrounding areas except for Cadiz, which is not representative of the Iberian Peninsula. Results show that the non-linear MLP model performs worse than the LRM. On the other hand, LRM and MLP with a linear activation function appears to be two equivalent and robust methods and there is no clear advantage of adopting one respect to the other.

Fig 4 shows the application of these three methods to the reconstruction of the January mean temperature since 1850 in the area of Central Europe that is included in a box of coordinates 7 – 14 degrees East and 48 -54 degrees North, which approximately coincides with Germany. The corresponding time series is called mean temperature of Germany in this paper. Note that the methods are applied individually to each station and the average of all German stations is considered afterwards and shown in fig.4.

The temperature time series of the German stations are available since 1901. The interval considered for the construction of the statistical models is from 1951 to 1990. The models are applied to the complementary interval 1850-1950 and 1991-2000. The predictors are the first 7 Principal Components

of the 11 long stations from 1850 to 2000. These results visually confirm that LRM and MLP 'linear version' are approximately equivalent, while the performance for the MLP with logistic activation function is slightly worse. Note that the red line showing the LRM results is barely visible only at a very close inspection, because it practically coincides with the green line drawn over it. Same statistic parameters about this reconstruction are reported in the following Table 1. We conclude that there are encouraging results on the capability of these statistical models to reconstruct the past temperature distribution at regional scale. The continuation of this study will investigate the seasonal variability of the models parameters and performance and apply them to other regions.

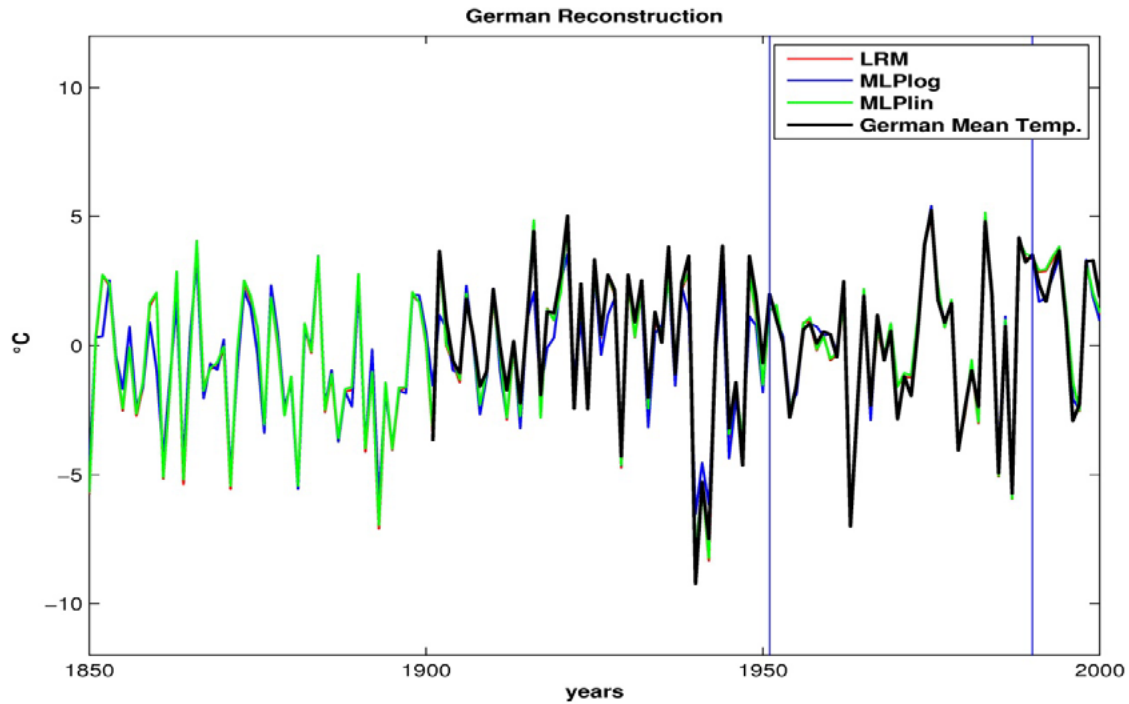


Fig. 4: Reconstruction of January monthly mean temperature of Germany from 1850 to 2000 using as predictors the first 7 PC of the 11 long stations. Black line is the mean temperature of all German stations from 1901 to 2000, red line is the German mean temperature reconstructed by LRM, green line is the signal reconstructed by MLP with a linear activation function and the blue line is the reconstruction by MLP with a logistic activation function. The red line showing the LRM results is visible only at a very close inspection, because it practically coincides with the green line. The interval 1951-1990 (included between blue vertical lines) is the period in which the models are constructed. The mean values for the signals in the interval 1901-2000 are 0.20, 0.08, 0.14,-0.03 for the black, red, green and blue line respectively.

Parameters	LRM	MLP_lin	MLP_log
Corr_tot	0.98	0.98	0.96
Corr_con	0.99	0.99	0.99
Corr_app	0.98	0.98	0.99
Rmse_tot (°C)	0.53	0.55	0.84
Rmse_con (°C)	0.41	0.42	0.25
Rmse_app (°C)	0.59	0.62	1.07

Table 1: Correlation and rmse computed between the reconstructed temperature time series and the January mean monthly temperature of Germany. The subscript “tot” refers to the whole period 1901-2000, the subscript “con” to the period 1951-1990 in which the models are constructed and “app” to the intervals 1901-1950 and 1991-2000 to which the models are applied

ACKNOWLEDGMENTS

We are very grateful to Dario Camuffo and Chiara Bertolin for the Italian temperature long time series and to Fernando Dominguez for the Cadiz data.

REFERENCES

- Bishop C. M. (1995), *Neural networks for pattern recognition*, Oxford University Press.
- Björnsson H. - Venegas S.A. (2000), “*A manual for EOF and SVD analyses of climatic data*” Department of Atmospheric and Oceanic Sciences – Centre for Climate and Global Change Research. McGill University.
- Camuffo D. et al. (2010), *The western Mediterranean climate: how will it respond to global warming?* Climatic Change, 100:137–142 DOI 10.1007/s10584-010-9817-6
- Camuffo et al. (2010), *500-year temperature reconstruction in the Mediterranean Basin by means of documentary data and instrumental observations*. Climatic Change (2010) 101:169–199 DOI 10.1007/s10584-010-9815-8
- Haykin S. (1998), *Neural networks: a comprehensive foundation*, Prentice Hall.
- Manley G. (1953), *The mean temperature of Central England, 1698 to 1952*. Q.J.R. Meteorol. Soc., Vol 79, pp 242-261.
- Manley G. (1974) *Central England Temperatures: monthly means 1659 to 1973*. Q.J.R. Meteorol. Soc., Vol 100, pp 389-405.
- Parker D.E., Legg T.P., and Folland C.K., (1992), *A new daily Central England Temperature Series, 1772-1991*. Int. J. Clim., *Vol 12*, pp 317-342.
- Parker D.E. and Horton E.B. (2005), *Uncertainties in the Central England Temperature series since 1878 and some changes to the maximum and minimum series*. International J. Climatology, Vol 25, pp 1173-1188.
- Press, Teukolsky, Vetterling, Flannery: *Numerical recipes in Fortran 90 second edition*. Cambridge University Press, 1992.
- Von Storch H., Zwiers F.W. (1998), “*Statistical Analysis in Climate Research*” Cambridge University Press.

ADVANCES IN CLIMATE SCIENCE

Climate processes in the Mediterranean region - II

Daily precipitation statistics over the Po Basin: observation and post-processed RCM results

Turco M.^{1*}, Zollo A.L.¹, Vezzoli R.¹, Ronchi C.², and Mercogliano P.^{1,3}

¹*Impacts on Soil and Coasts Division (ISC), Euro-Mediterranean Centre on Climate Change (CMCC), Capua (CE), Italy*

²*Department of Forecasting Systems, Environmental Protection Agency of Piemonte, Turin, Italy*

³*Meteo System & Instrumentation Laboratory, Italian Aerospace Research Center (CIRA), Capua (CE), Italy*

*Corresponding author: marco.turco@cmcc.it

Abstract

In this study we first compare three observed grids of daily precipitation (EMR, EOBS and MAP) over the Po basin, in order to choose the most reliable dataset to develop regional scenarios. The results indicate that although there is generally good temporal agreement between the three datasets, EOBS should be treated with caution since does not provide reliable climatology over this region, especially considering the extremes. The high agreement between MAP and EMR, on the other hand, builds confidence in using these datasets.

Then we compare three different post-processing methods following the MOS (Model Output Statistic) approach: linear-scaling, quantile mapping and MOS analogs, applied to the ERA40-driven COSMO-CLM model. Cross-validation results indicate that the application of MOS techniques generally improves the outputs of the COSMO-CLM model, and, among the MOS methods, better results have been generally obtained with the quantile mapping technique.

Keywords: *Daily precipitation observations, MOS post-processing, regional climate scenarios.*



1. INTRODUCTION

A key problem for climate change impact/adaptation studies is developing regional climate scenarios, especially for geographically complex and heterogeneous regions that are sensible to climate change. The Po river basin is characterized by a great variability of precipitation regimes due to the influences of different climatological regimes, such as the Mediterranean, Continental, Atlantic, and Polar. In addition, precipitation plays a major role in water resources and natural hazards in this area, with high hydrogeological risk and strong human pressure [0]. Due to this climatic variability in a relatively small area with remarkable topographic complexity, this region is a challenging area both to monitor and to simulate the mesoscale characteristics of the precipitation field. Consequently, in order to develop regional climate scenarios, of paramount importance is the assessment of uncertainties, not only of the downscaling methods themselves, but also of the observed datasets.

In this study we compare three high-resolution datasets of interpolated precipitation (EMR, EOBS and MAP) over the Po river basin, in order to choose the most reliable dataset to develop regional scenarios. This analysis extends the recent work of Turco et al. (2013) [0], who compare three observation grids in the Alps, focussing in the northwest Italy. Then we evaluate three different post-processing methods to refine the precipitation output of the regional climate model COSMO-CLM [0]. These methods are of increasing complexity: (i) the simple linear-scaling (LS), (ii) the quantile mapping (QM), and (iii) the MOS Analog method (MA), recently proposed by Turco et al. (2011) [0]. This comparison is performed under “perfect boundary conditions”, that is, the lateral boundary conditions are provided by ERA40 reanalysis data, in order to reduce the influence of the errors relate to the General Circulation Model.

2. OBSERVED DATA

We consider three high-resolution datasets of interpolated observations: (i) EMR, (ii) EOBS [5], and (iii) MAP [6]. These datasets are daily observational grids for precipitation, all produced using data from quality-controlled stations.

EMR is a recently developed gridded dataset covering the Po basin over the period 1971-2000, based on 1128 observed quality controlled precipitation data collected and used for the calibration of the multi-model system FEWS within the project PEDRO over the Po river basin [7]. The rain gauges

network is sufficiently dense (on average around one station per 60 km²) to produce a grid with a horizontal resolution of approximately 8 x 8 km, the same of the COSMO-CLM model.

EOBS (approximately 25 x 25 km) is the state-of-the-art publicly available high- resolution daily dataset for Europe, based on a network of more than two thousand stations. However, compared to MAP, EOBS is based on a lower number of stations, around 750 records over the GAR domain [5].

The MAP dataset, composed of around 6500 stations, covers the GAR area and provides reliable data only over the period 1971-1990. This high-resolution dataset (approximately 25 x 20 km) is considered reliable for reproducing the mesoscale patterns of the present alpine climatology [6].

To compare the three datasets, we focus on the common reliable period, 1971-1990, and the daily outputs of the MAP and EMR are bilinearly interpolated (upscaled) from their original resolution to the grid defined by EOBS (around 25 x 25 km).

3. MODEL DATA AND POST-PROCESSING METHODS

We consider the ERA40-driven COSMO-CLM model [0] for the baseline period 1971-2000. The COSMO-CLM regional climate model is the climate version of the COSMO-LM non-hydrostatic limited area model [0]. A detailed description and evaluation is given in Zollo et al. (2012) [0].

The three MOS methods that we compare are here described: (i) the linear-scaling LS, (ii) the quantile mapping QM, and (iii) the MOS Analog method MA.

The linear-scaling approach consists in correcting the monthly differences between observed and simulated values:

$$P^*(d) = P(d) \cdot \frac{\mu_m(P_{obs}(d))}{\mu_m(P_{rcm}(d))}$$

where, for the day d , $P^*(d)$ is the corrected value, $P(d)$ is the original daily precipitation value from the RCM, $\mu_m(P_{obs}(d))$ is the observed monthly average for the month m , and $\mu_m(P_{rcm}(d))$ is the simulated monthly average.

The quantile mapping correction, instead, tries to adjust all the moments of the probability distribution function (PDF) of the precipitation field. The idea is to calculate the correct variable P^* as a function of the original simulated variable P using a transfer function calculated forcing the equality between the CDF (cumulative distribution function F) of the observed and simulated variables [0]:

$$F_{rcm}(P_{rcm}) = F_{obs}(P_{obs})$$

Where F_{rcm} and F_{obs} are, respectively, the CDF of simulated and observed precipitation. So the corrected value of precipitation is obtained using the following equation:

$$P^*(d) = F_{obs}^{-1}(F_{rcm}(P(d)))$$

We applied the quantile mapping assuming that both observed and simulated distributions are well approximated by a Gamma distribution. This distribution, dependent only on two parameters, is commonly used for representing the PDF of precipitation and several studies have proved that it is effective for modelling rainfall data (see e.g. [0]).

The analog method is based on the hypothesis that "analogue" weather patterns (predictors, e.g. 500 mb geopotential) should cause "analogue" local effects (predictands, e.g. precipitation at a given location). This relatively simple method basically consists in two steps. For the day "A" to be downscaled, in a future or in a test period: (1) The closest historical predictor "B" (the analog) is found; (2) then, the observed local precipitation "b", correspondent to the analog day "B", is used as the downscaled precipitation "a". Then these steps are repeated for each day to downscale. Turco et al. (2011) [0] positively tested over Spain a new implementation of the standard analogs method, in which the predictor is the daily RCM precipitation. This approach is tested here.

4. VALIDATION AND COMPARISON MEASURES

We evaluate the performance of the MOS methods by means of a leave-one-out cross-validation, in which a moving window of 1 year is used as the validation data, and the remaining observations as the training data. For example, the first test year is 1971, and the MOS analog method is calibrated over the period 1972-2000; the second test year is 1972 and is trained with the complementary years, and so on. Also the monthly means for the LS, and the CDF of both observed and simulated precipitation for the

QM, are calculated for every month of the year following this cross-validation approach. Consequently, a total of 30 (equal to the total length of the series) test periods were considered. Finally, we analyse the union of these 30 test periods.

To compare the three datasets and the MOS methods, we apply two main approaches. Firstly, we measure the temporal agreement between the time series comparing the datasets at a gridpoint basis using standard verification measures (e.g. correlation). Specifically, at each gridpoint, the relative mean absolute error (MAEr), relative to the observed mean of the reference dataset, and the Spearman correlation (CORR) is calculated between the datasets.

Secondly, the spatial agreement of the climatologies (spatial patterns averaged over the analyzed period) of a subset of the standard ETCCDI indices (total precipitation amount PRCPTOT, number of precipitation days with precipitation greater than 1 mm R1, maximum precipitation over 1 day RX1DAY; WMO, 2009 [0]) are compared. The comparison between the simulated and observed climatologies are also shown with the Taylor diagram [0], which summarize three metrics of spatial similarity, correlation, standard deviation and root-mean-square-error, in a single bidimensional plot.

5. RESULTS

Comparison of observed datasets

Figure 1 shows the spatial distribution of the accuracy metrics over the Po river basin domain. Both metrics (CORR and MAEr) highlight that generally there is a quite high agreement among the datasets, with greater correspondence between MAP and EMR than between MAP or EMR and EOBS. Generally, the greatest discrepancy between the grids is over the North West Italy, where EOBS has fewer stations, and over mountainous areas. In particular, the greater differences between MAP and EMR on the border could be related to a lack of stations outside the Italian border in the EMR dataset.

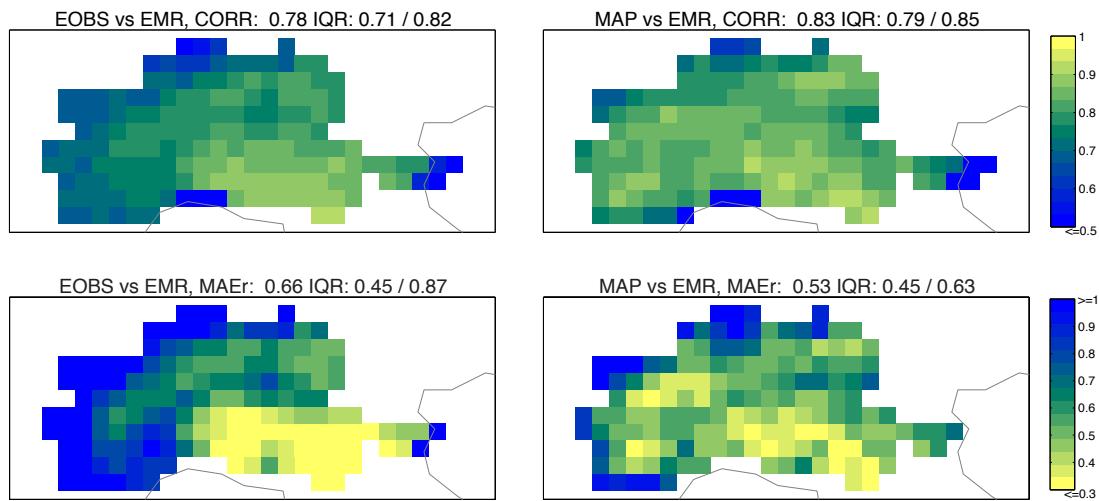


Fig. 1: CORR (top panels) and MAEr (bottom panels) comparing EOBS, MAP and EMR over the Po basin. The values at the top of each map are the median and the interquartile range (IQR) of the spatial distribution of the corresponding score.

Figure 2 shows the annual climatologies (spatial pattern), averaged over the studied period (1971-1990) for three indices and the three datasets: MAP (first column), EOBS (second column) and EMR (third column); the numbers below the figures indicate the calculated similarity scores. There is a quite high agreement between MAP and EMR (e.g. spatial correlation around 75-90%, depending on the index). This is an important result since it builds confidence in using these datasets for climate studies. Instead, the greater differences for the EOBS grid suggest that this dataset, at least for certain studies such as the analysis of the regional alpine climatology, should be treated with caution. In particular, the discrepancies are greater for the extremes indices RX1DAY, with a mean error of -13% and the area with the highest maximum values (the Toce valley, in the north of Piedmont), is not highlighted by EOBS. However, please notice that each dataset has limitations that the users should carefully take into account. For example, it should be noted that common measurement errors, such as undercatch due to wind or evaporation losses and/or snow drift into the rain-gauge, may affect these datasets. So possible systematic underestimation of the amount of precipitation (averaged values of around 10%, **[Errore. L'origine riferimento non è stata trovata.]**) should therefore be taken into account.

Summarizing, the analysis presented here shows that the EMR dataset is the best candidate to apply the MOS techniques, since it is based on hundreds of stations, shows a good agreement with MAP, and covers a longer period (1971-2000).

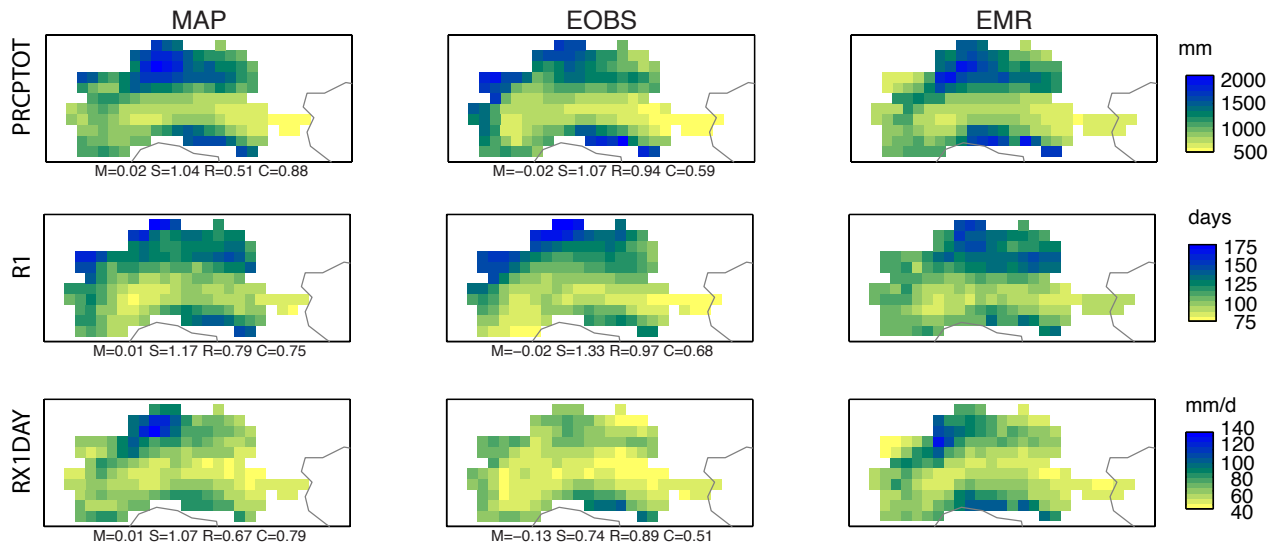


Fig. 2: Spatial distribution of mean values (averaged over the period 1971-1990) of the MAP (left), EOBS (central) and EMR (right), for the annual precipitation indices PRCPTOT, R1 and RX1DAY. The spatial validation scores (Mean error M, Standard deviation S, centred Root-mean-square R, correlation C) for the EOBS and MAP values, with respect to the EMR values, are given below the corresponding panels.

Comparison of MOS methods

The ability of COSMO-CLM and MOS methods to reproduce the seasonal climatology (spatial pattern) for three ETCCDI precipitation indices has been tested. As an illustrative example, and for the sake of conciseness, in Figure 3 we show the comparison maps for the COSMO-CLM model and the corresponding QM values. The panels in this figure show the autumn values of the indices (averaged in the period 1971-2000) for the observed grid EMR (first column), the COSMO-CLM simulation (second column) and the QM values (third column); Each rows is representative of one index, PRCPTOT (top), R1 (middle), and RX1DAY (bottom). The numbers below the figures indicate the bias (or mean error M), the relative standard deviation (S), the correlation (C), and centred root-mean-square (R) values for QM and RCM with regards to the observed ones. These numbers measure the spatial similarity and are plotted in the following Taylor diagram. This figure shows that the QM values clearly outperform the uncalibrated RCM outputs.

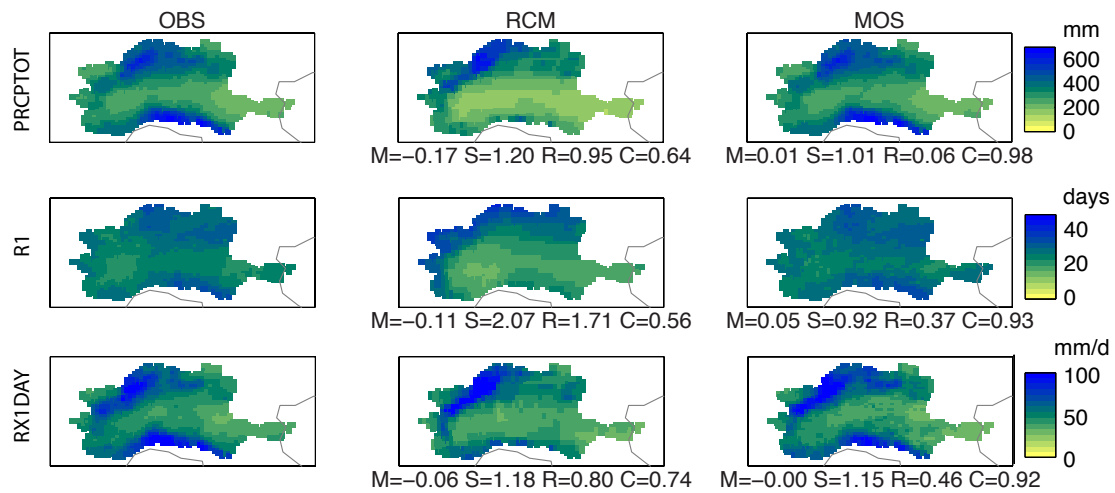


Fig. 3: Spatial distribution of the observed (left), COSMO-CLM (central) and QM (right) mean values (averaged over the control period 1971-2000) for the three ETCCDI precipitation indices considered. The spatial validation scores for the RCM and MOS simulated values are given below the corresponding panels: bias (or mean error M), relative standard deviations (S), correlation (C) and centred root-mean-square (R).

Figure 4 summarizes the verification results for all the MOS methods, seasons, and indices. The MOS methods dramatically improves the RCM result and, among the methods, the quantile mapping generally have the best scores for most indices and seasons, while the linear-scaling shows the worst results in most cases.

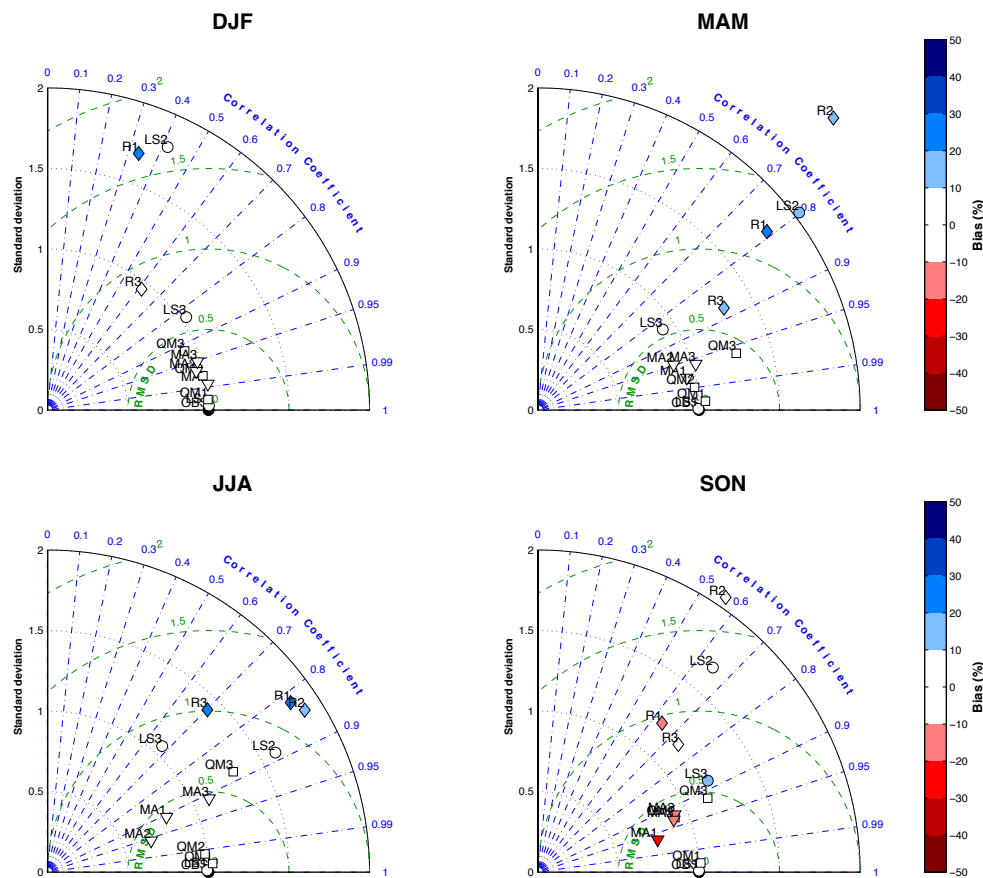


Fig. 4: Taylor diagrams for the seasonal precipitation climatology. Better results are closer to observation (OBS). The circles with LS are used for the linear-scaling method, the squares with QM for the quantile mapping, the triangles with MA for the MOS analogs method while the diamonds with R for the RCM. The colours indicate the bias (in percentage respect to the observed mean). The numbers correspond to the different indices: 1=PRCPTOT; 2=R1; 3=RX1DAY.

Then we test the daily accuracy of RCM simulation and the QM values. Fig. 5 shows the relative mean absolute error and the correlation between the simulated series and the observations, calculated at each grid box. Generally the QM has slightly greater values of CORR and lower of MAEr. These scores highlight the greater difficulties of the RCM to reproduce the precipitation over the Alps.

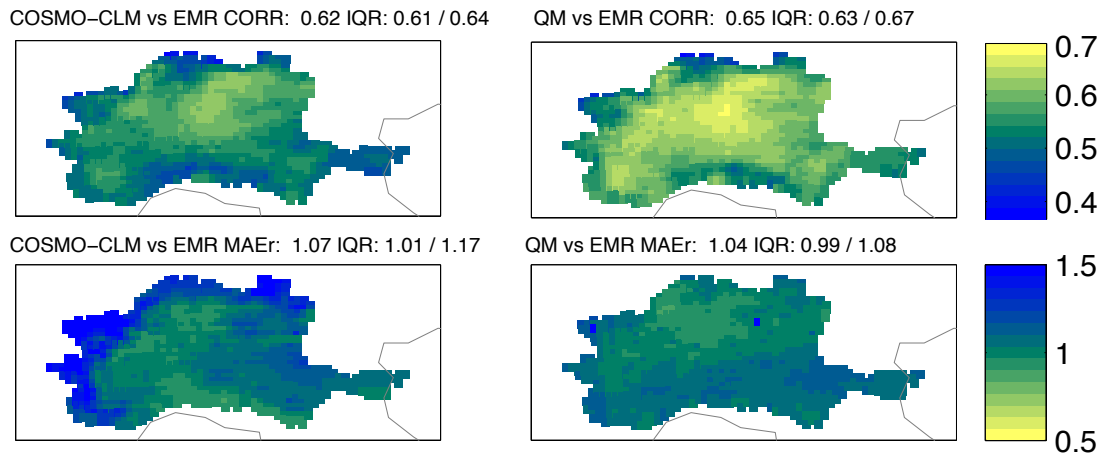


Fig 5.: CORR (top panels) and MAEr (bottom panels) comparing the COSMO-CLM model (left) with the QM (right). The values on the top of each map are the median and the interquartile range (IQR) of the spatial distribution of the corresponding score.

6. CONCLUSIONS

Our overall objective is to generate regional climate scenarios over the Po river basin, to study the impact of climate change on hydrology. To achieve this goal, the following preliminary steps have been identified and addressed in this study:

1. Assessment of the available observed datasets;
2. Comparison of different downscaling techniques to provide regional scenarios for precipitation, at daily scale.

Indeed, in the context of regional climate studies, the analysis of high-resolution daily observation is of the utmost importance. These datasets allow defining the main climatic features of their area and have become increasingly popular to validate regional models or to calibrate the statistical methods. Unfortunately, a number of constraints involving climate data (i.e. availability of the data and their quality) could limit the analysis of daily values, especially in the alpine region, given the complexity of the orography in this area.

These reasons have motivated the first part of this study, in which we have compared three datasets over the Po river basin: (i) EMR, (ii) EOBS and (iii) MAP. Each dataset has limitations that need to be considered. Unfortunately, EOBS, which covers a long period (1950-2012), has shown the greatest discrepancies. Instead, the MAP grid, considered reliable to describe the mesoscale climatology over

the studied area, covers only 20 years. Finally, the high agreement between MAP and EMR, and the availability of the latter for the period 1971-2000, make it the best dataset to be used in order to generate the regional scenario over the Po river basin.

Then, we have tested and compared the performances of three MOS techniques - linear-scaling, quantile mapping, and MOS analogs - to refine the precipitation output of the ERA40-driven COSMO-CLM regional model. The cross-validation results indicate that the MOS downscaled values generally outperform the uncalibrated RCM outputs, and the quantile mapping have often the best scores as it improves the representation of the mean regimes the frequency and the extremes of precipitation, regardless of the season. These results suggest the MOS applicability, especially useful for those users that need high-resolution simulations for climate change impact studies.

Our future research would address the analysis of these methods under "sub-optimal" conditions (using RCM driven by GCM in current climate) and to test their robustness in climate change conditions.

7. ACKNOWLEDGMENTS

This work was funded by the GEMINA and by the NextData projects of the Italian Ministry of Education, University and Research, and the Italian Ministry of Environment, Land and Sea.

8. ACRONYM GLOSSARY

CDF: Cumulative Distribution Function

CORR: Correlation

COSMO-CLM: COSMO model in CLimate Mode (<http://www.clm-community.eu/>)

EMR: Gridded dataset covering the Po basin over the period 1971-2000.

EOBS: High-resolution daily dataset for Europe [5].

ERA40: ECMWF 40 Year Re-analysis (<http://www.ecmwf.int/>)

ETCCDI: Expert Team on Climate Change Detection and Indices

FEWS: hydrological and hydraulic models in Po Flood Early Warning System

GAR: Greater Alpine Region

GCM: Global Climate Model (or General Circulation Model)

IQR: InterQuantile Range

LS: Linear Scaling

MA: Mos Analog method

MAEr: relative Mean Absolute Error

MAP: Precipitation dataset that covers the GAR area [6]

MOS: Model Output Statistics

PDF: Probability Density Function

PRCPTOT: total precipitation amount index

QM: Quantile Mapping

R1: Number of precipitation days with rain rate greater than 1 mm

RCM: Regional Climate Model

RX1DAY: maximum precipitation over 1 day

9. REFERENCES

- Beniston M. (2005), *Mountain Climates and Climatic Change: An Overview of Processes Focusing on the European Alps*, Pure and Applied Geophysics, No. 162, pp. 1587-1606. (1)
- Turco, M., Zollo, A. L., Ronchi, C., De Luigi, C., and Mercogliano, P. (2013), *Assessing gridded observations for daily precipitation extremes in the Alps with a focus on northwest Italy*, Natural Hazards and Earth System Sciences, 13, 1457-1468, doi:10.5194/nhess-13-1457-2013. (2)
- Turco M., Zollo A.L., Rianna G., Cattaneo L., Vezzoli R. and Mercogliano P. (2013), *Post-processing methods for COSMO-CLM precipitation over Italy*, Technical report, CMCC. (3)
- Turco M., Quintana-Seguí P., Llasat M. C., Herrera S., and Gutiérrez J. M. (2011), *Testing MOS precipitation downscaling for ENSEMBLES regional climate models over Spain*, Journal of Geophysical Research, No. 116 (D18), pp. 1-14. (4)

- Haylock M.R., Hofstra N., Klein Tank A.M.G., Klok E.J., Jones P.D., and New M. (2008), *A European daily high-resolution gridded data set of surface temperature and precipitation for 1950-2006*, Journal of Geophysical Research, No. 113 (D20119), pp. 1-12. (5)
- Frei C. and Schär C. (1998), *A precipitation climatology of the Alps from high-resolution rain-gauge observations*, International Journal of Climatology, No. 18, pp. 873-900. (6)
- SIMC ARPA Emilia Romagna (2010). Sistema di modellistica a supporto della gestione delle risorse idriche per la previsione delle magre fluviali dell'asta principale del fiume Po – Stato finale delle attività. (7)
- Rockel B., Will A. and Hense A. (2008), *The regional climate model COSMO-CLM (CCLM)*, Meteorologische Zeitschrift, No. 17(4), pp. 347-348. (8)
- Stappeler J., Doms G., Schättler U., Bitzer H.W., Gassmann A., Damrath U. and Gregoric G. (2003), *Meso-gamma scale forecasts using the nonhydrostatic model LM*, Meteorology and Atmospheric Physics, No. 82, pp. 75-96. (9)
- Zollo A.L., Montesarchio, M., Manzi M. P., Cattaneo L., Bucchignani E. and Mercogliano P. (2012), *Assessment of COSMO-CLM Performances in Simulating the Past Climate of Italy*, Technical report, CMCC. (10)
- Piani C., Weedon G. P., Best M., Gomes S. M., Viterbo P., Hagemann S. and Haerter J. O. (2010), *Statistical bias correction of global simulated daily precipitation and temperature for the application of hydrological models*, Journal of Hydrology, No. 395, pp. 199-215. (11)
- Gutjahr O. and Heinemann G. (2013), *Comparing precipitation bias correction methods for high-resolution regional climate simulations using COSMO-CLM*, Theoretical and Applied Climatology, No. 704, pp. 1-19. (12)
- WMO (2009): *Guidelines on Analysis of extremes in a changing climate in support of informed decisions for adaptation*, Technical Report WCDMP No. 72 WMO/TD-No. 1500. (13)
- Taylor K.E. (2001), *Summarizing multiple aspects of model performance in a single diagram*, Journal of Geophysical Research, No. 106(D7), pp. 7183-7192. (14)

Climatological characterisation of the Ora del Garda wind in the Alps

Giovannini L.^{1,2*}, Laiti L.^{1,2}, Zardi D.^{1,2}, and de Franceschi M.^{1,3}

¹*Atmospheric Physics Group, Department of Civil, Environmental and Mechanical Engineering, University of Trento, Trento, Italy*

²*National Consortium of Universities for Atmospheric and Hydrospheric Physics (CINFAl), Italy*

³*Diocese of Bolzano-Bressanone, Bressanone, Italy*

*Corresponding author: lorenzo.giovannini@unitn.it

Abstract

The “Ora del Garda” is a coupled lake and valley breeze regularly flowing, during warm season clear-sky days, from the northern shorelines of Lake Garda, in the Italian Alps. Climatological characteristics of this wind are investigated through the analysis of observations taken at two surface weather stations – one on the shores of lake Garda, and the other 30 km inland – over a 10-year period. Furthermore the influence of synoptic winds on the lake breeze development is explored by analysing wind speed and direction at 850 hPa level provided by model reanalysis. Lake breeze days are identified by means of a set of objective criteria based on observations of solar radiation, wind speed and direction at the two stations. The analysis shows that the Ora del Garda develops on the shores of the lake in about 70% of the days from April to September, and even more often in the summer months. Moreover, in about 90% of the days in which the lake breeze develops on the lake shores, it also reaches the inland weather station. Its average strength on lake Garda shores is 4-6 m s⁻¹, with maximum intensities reaching frequently around 10 m s⁻¹. It typically starts blowing at 1100-1200 LST, although the onset time is progressively delayed, from spring to summer, and continues until 1700-2000 LST. The lake breeze front takes on average 3.5 h to arrive at the inland weather station, where it lasts until 2000-2100 LST. The analysis of wind speed and direction at 850 hPa from reanalysis highlights that the lake breeze is on average stronger, and its duration is slightly longer, when the synoptic wind blows onshore. Moreover in these situations the lake breeze propagates faster and arrives earlier at the inland weather station.

Keywords: *Mountain meteorology, lake breeze climatology, valley wind*



The present work aims at investigating the climatological characteristics of the so-called Ora del Garda circulation, which is an unusually intense up-valley wind, regularly occurring in the south-eastern Italian Alps. Actually this wind arises as a lake breeze over the northern part of Lake Garda, and extends northward channelling in the valleys nearby, until, on most of the days, it breaks out into the adjacent Adige Valley, north of Trento. Here it interacts with the local up-valley wind, creating a strong and gusty flow in the area (Fig. 1). The first observations of the Ora del Garda wind were carried out in 1908 and 1909 by A. Defant [1, 2], who analysed the pressure gradients associated with the establishment of valley winds between the Po Plain and the Adige and nearby valleys. Later on, the behaviour of diurnal Adige Valley winds at Trento and of the Ora del Garda was the subject of various investigations by German and Austrian meteorologists, which were reported in Wagner's (1938) review on valley winds [3]. The study of this wind has been recently resumed by the Atmospheric Physics Group of the University of Trento. A preliminary characterisation of the Ora del Garda from data collected at surface meteorological stations was performed by Daves et al. (1998) and Baldi et al. (1999) [4,5]. Furthermore various targeted measurement campaigns were carried out, including not only intensive surface observations [6], but also airborne measurements by means of an instrumented motorglider [7,8,9], which explored the upper valley atmosphere and the boundary-layer structure associated to the breeze development.

a) Study area and dataset

As said above, the Ora del Garda starts to blow on Lake Garda shore and then channels into the corridor formed by the lower Sarca Valley and the Lakes Valley, north of it. These valleys represent the northward extension of the basin of Lake Garda, and run almost parallel to the nearby Adige Valley, from which they are separated by the Mount Bondone chain, for approximately 30 km in SSW–NNE direction. On the northern side the Lakes Valley connects to the Adige Valley on its western sidewall, through the elevated saddle of Terlago (Fig. 1).

The lower area of the Sarca Valley, facing Lake Garda, consists in a rather wide and flat region, displaying an altitude slightly higher than the lake's surface (65 m MSL), with the only exception of the isolated relief of Mount Brione (376 m MSL). Up-valley to the town of Arco, the Sarca Valley floor narrows from about 4 km to 0.5 km, and then it widens again farther north into the Lakes Valley: the latter lies between Brenta Dolomites Group (west) and Mount Bondone chain (east), and is flanked on

the eastward side by the elevated Cavedine Valley (valley floor height: 300-580 m MSL) for about 15 km. Farther north, the valley narrows again by Santa Massenza and Toblino lakes (245 m MSL), where it suddenly bends eastward, becoming roughly west–east oriented and broadening out. After an uneven series of bumps and holes, it reaches the elevated saddle of Terlago (minimum height 580 m MSL), incumbent on the adjacent Adige Valley floor (200 m MSL) through a jump of about 400 m, immediately north of the city of Trento.



Fig. 1: Study area along with a schematic representation of the propagation of the Ora del Garda and the weather stations analysed in this work: Riva del Garda (RIV), Arco (ARC), and Gardolo (GAR) (background map from Google Earth)

The climatological characteristics of the Ora del Garda were investigated using data from two surface weather stations, Riva del Garda (RIV), located on the shores of Lake Garda, and Gardolo (GAR), in the Adige Valley (Fig. 1). This allows to evaluate the characteristics of the lake breeze at its onset on the lake’s shore and in the area where it outbreaks into the Adige Valley. The dataset covers the warm semester (April-September) in the period 2003-2012 and is composed of wind speed and direction and air temperature measurements at both weather stations and global radiation at RIV. Moreover radiation data from Arco weather station (ARC), located close to RIV (Fig. 1), were used to fill the gaps of the

record at RIV. Wind speed and direction are measured at 5 m above ground level (AGL) at RIV, and at 3 m AGL at GAR, while temperature is measured at 2 m AGL at both weather stations. All observations are hourly.

b) Selection of lake breeze days

Lake breeze days on the lake's shore were identified by means of objective criteria applied to weather data from RIV station. These criteria were suggested by previous climatological investigations of sea breezes [10,11,12] and take into account both the physical mechanisms leading to the development of the lake breeze and its typical features, especially the wind shift from offshore to onshore in the morning and an the opposite reversal in the evening:

- (I) Global solar radiation until noon is $> 30\%$ of the maximum radiation measured in the same time period in that month. It was noted that the development of the lake breeze is better correlated with the strength of the solar radiation in the morning than with the radiation during the whole day. The threshold of 30% of the maximum radiation was chosen from preliminary investigations.
- (II) Wind direction (WD) reverses from offshore to onshore in the period from 2 h after sunrise to 2 h before sunset.
- (III) WD becomes offshore or wind speed (WS) is $< 1 \text{ m s}^{-1}$ after sunset.
- (IV) WD is offshore or WS is $< 1 \text{ m s}^{-1}$ for most of the hours between midnight and sunrise. This test aims at eliminating days with a strong onshore synoptic wind, which might be wrongly interpreted as lake breeze.
- (V) WD remains onshore consecutively for at least 3 h and at the same time WS is $> 2 \text{ m s}^{-1}$.

An additional test was applied to wind speed and direction data measured at GAR, to identify days in which the lake breeze reaches this weather station.

- (I) WD becomes between $240^\circ\text{N} \pm 30^\circ$ and at the same time WS is $> 2 \text{ m s}^{-1}$ for at least 1 h in the period between the onset of the lake breeze at RIV and two hours after its cessation. 240°N is the typical direction of the Ora del Garda at GAR.

c) Lake breeze climatology on the lake's shore

From the application of the above criteria it results that the lake breeze at RIV occurs in 68% of the days analysed, with higher frequencies in the period May-August (71%, 71%, 75%, and 72% respectively) than in April and September (57% and 63% respectively).

The histograms in Fig. 2 show that the average intensity of the Ora del Garda ranges in 51% of the days between 4 and 6 m s⁻¹, while the maximum hourly velocity reaches 6-9 m s⁻¹ in ~60% of the days.

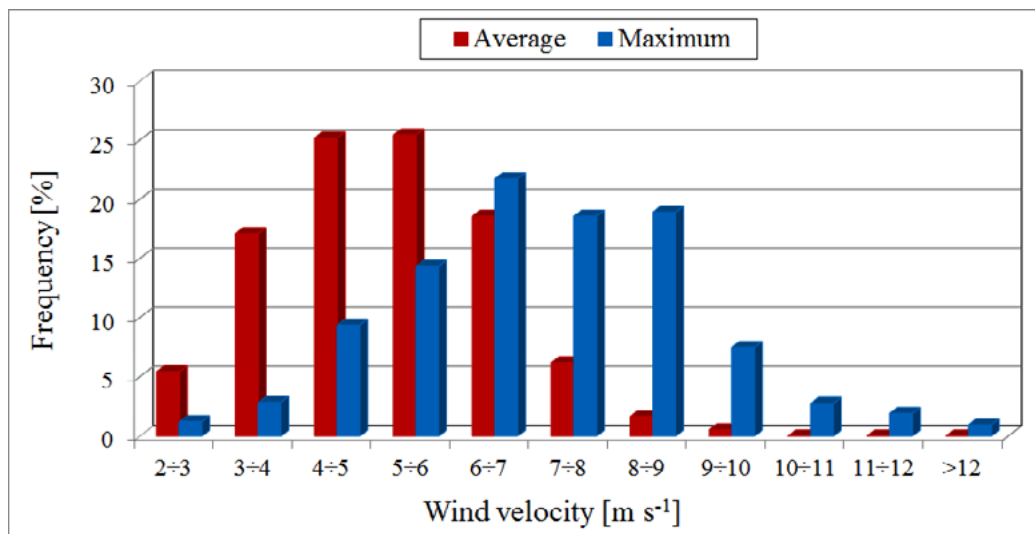


Fig. 2: Frequency distribution of the average and maximum intensity of the lake breeze at RIV

From Fig. 3 it can be seen that the lake breeze starts to blow at RIV in most of the days (65%) between 1100 LST (UTC+1) and 1200 LST, while the variability of the cessation time is higher: frequencies higher than 10% occurs between 1600 LST and 2000 LST. The frequency distribution of the hour of occurrence of the maximum intensity displays a Gaussian shape, centred at 1400 LST.

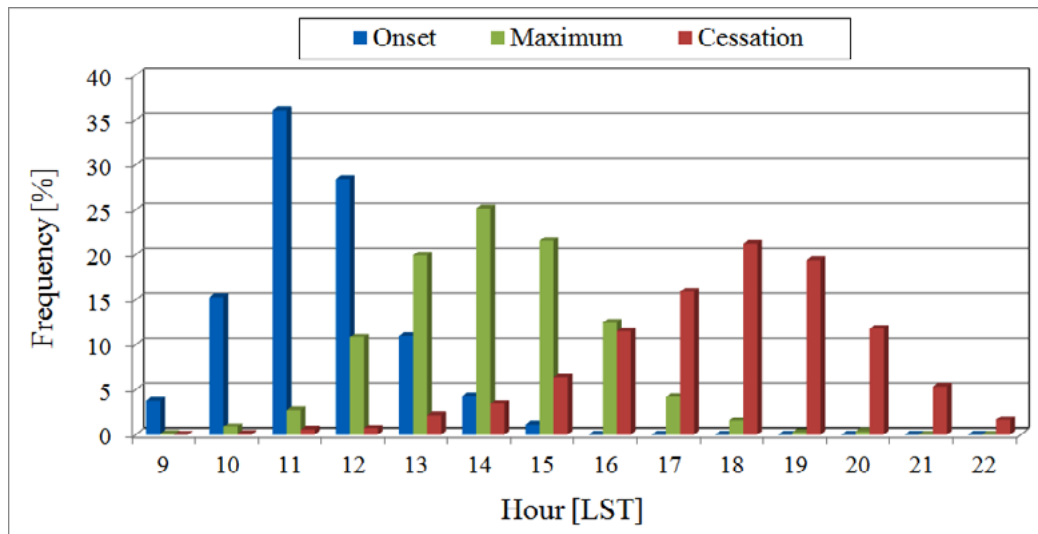


Fig. 3: Frequency distribution of the time of occurrence of the onset, maximum and cessation of the Ora del Garda at RIV

As to the monthly variations, it is found that the onset time of the Ora del Garda progressively delays from April to September. The highest frequency in April is at 1100 LST, while in September it occurs one hour later (Fig. 4). This may be attributed to the progressive warming of the lake during the warm semester and the consequent later development of the thermal contrasts leading to the onset of the lake breeze. The occurrence of the maximum intensity of the lake breeze seems to follow the same behaviour, with earlier occurrences in April, May and June than in July, August and September (not shown). On the other hand the cessation time occurs on average earlier in April and September, probably due to the earlier sunset (not shown).

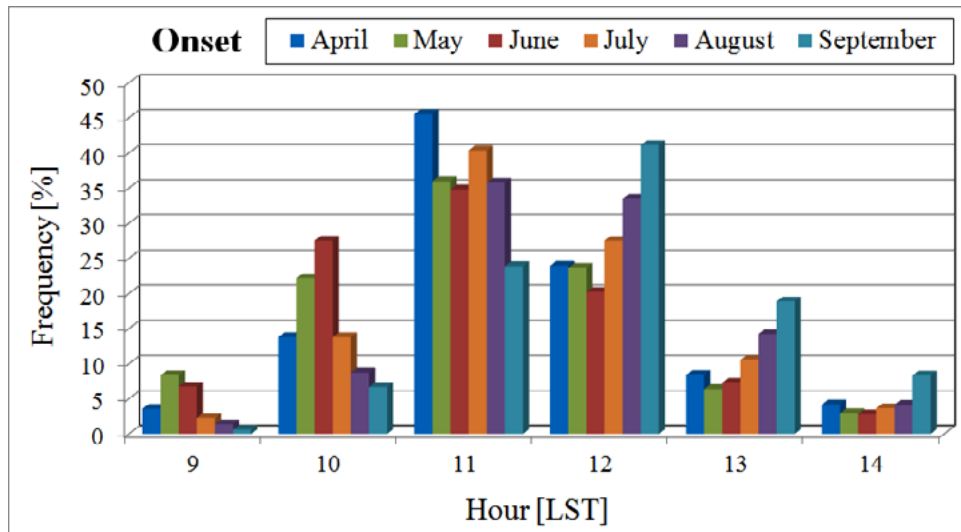


Fig. 4: Frequency distribution of the time of occurrence of the onset of the Ora del Garda at RIV in the six months analysed

d) Lake breeze climatology in the Adige Valley

The Ora del Garda arrives at GAR in 89% of the days in which it occurs at RIV, with rather constant values in the six months analysed. In fact the frequencies range from 85% in May to 92% in July. The lake breeze does not reach GAR especially in the days when it is not well developed at RIV. In fact it is found that the Ora del Garda at RIV is on average weaker ($\sim 0.3 \text{ m s}^{-1}$ in both mean and maximum velocities) and its duration is shorter, with a later onset ($\sim 30 \text{ min}$) and an earlier cessation ($\sim 1\text{h } 15 \text{ min}$), in the days when it does not reach GAR.

The average intensity of the lake breeze is slightly lower than at RIV (in 72% of the days between 2 and 4 m s^{-1}), even though the two results are not completely comparable due to the different measurement heights (Fig. 5).

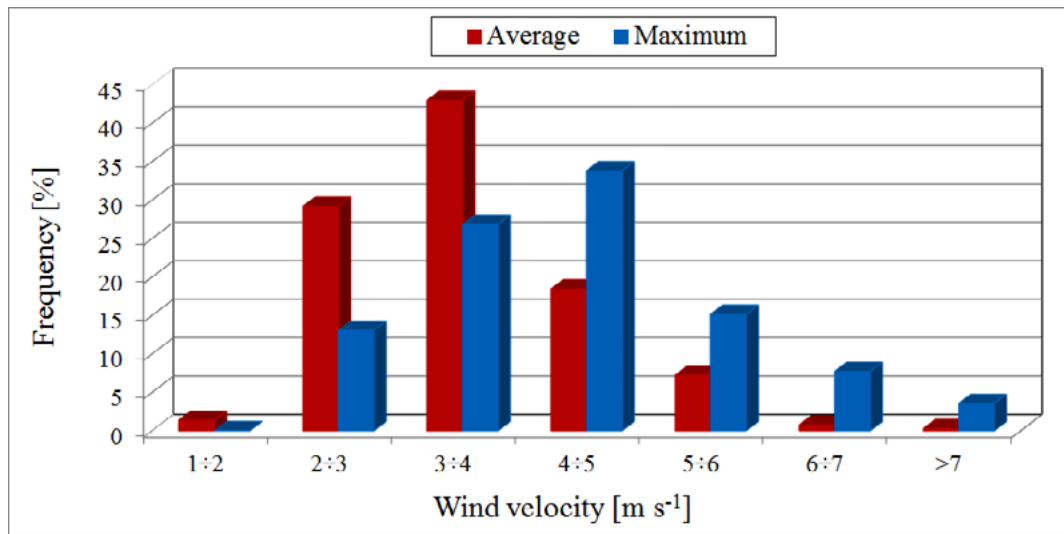


Fig. 5: Frequency distribution of the average and maximum intensity of the lake breeze at GAR

The frequency distributions of the time of occurrence of the onset and of the maximum intensity of the lake breeze present similar shapes to those found at RIV, with a time shift of 3 h. The onset of the lake breeze at GAR occurs in 61% of the days between 1400 LST and 1500 LST, while the frequency distribution of the hour of occurrence of the maximum intensity displays a Gaussian shape centred at 1700 LST (Fig. 6). On the other hand the frequency distribution of the cessation time is more concentrated than at RIV, with maximum frequencies between 2000 LST and 2100 LST (54% of the days). As at RIV, the onset of the lake breeze occurs later and later from April to September, while the cessation occurs earlier in August and September (not shown). No significant monthly trends are found for what concerns the time of occurrence of the maximum intensity.

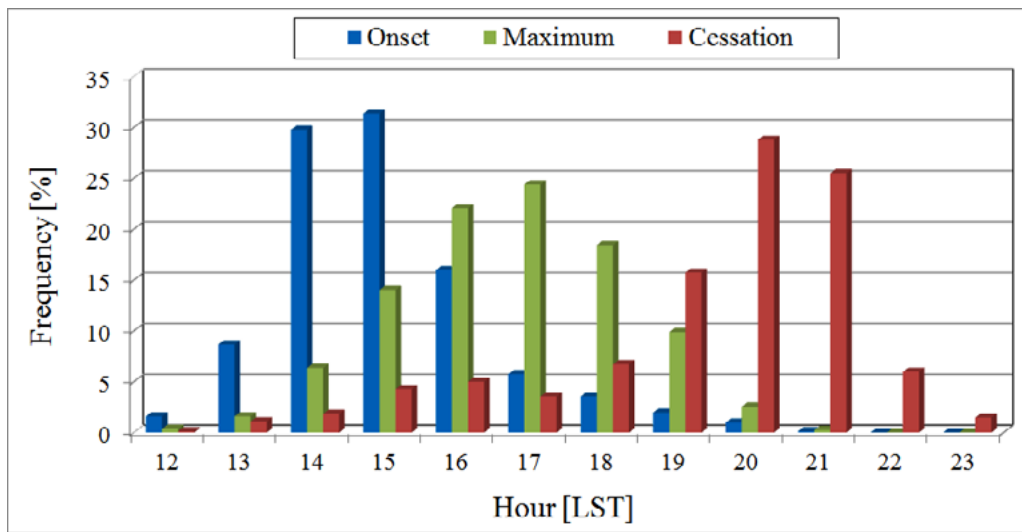


Fig. 6: Frequency distribution of the time of occurrence of the onset, maximum and cessation of the Ora del Garda at GAR

e) Influence of the synoptic wind

In order to investigate the influence of the synoptic-scale flow on the lake breeze, wind speed and direction at 850 hPa from the National Center for Environmental Prediction (NCEP) Operational Global Analysis data on 1.0 x 1.0 degree grids were used. In particular the daily values at 1200 UTC in the grid point where RIV lies were analysed. Similarly to [12], data were first aggregated in classes according to the synoptic wind direction with respect to the lake's shore. Then two subclasses were created from data with onshore and offshore wind direction (see below), including only data with wind speed $> 4 \text{ m s}^{-1}$. The resulting classes are as follows:

- Onshore (On): $135^\circ\text{N} \leq \text{WD} \leq 255^\circ\text{N}$
- Onshore Strong (OnStr): $135^\circ\text{N} \leq \text{WD} \leq 255^\circ\text{N}$ and $\text{WS} > 4 \text{ m s}^{-1}$
- Offshore (Off): $\text{WD} \leq 75^\circ\text{N}$ or $\text{WD} \geq 315^\circ\text{N}$
- Offshore Strong (OffStr): $\text{WD} \leq 75^\circ\text{N}$ or $\text{WD} \geq 315^\circ\text{N}$ and $\text{WS} > 4 \text{ m s}^{-1}$
- Parallel East-West (EW): $75^\circ\text{N} < \text{WD} < 135^\circ\text{N}$
- Parallel West-East (WE): $255^\circ\text{N} < \text{WD} < 315^\circ\text{N}$

Figs. 7 and 8 show that the synoptic wind influences significantly the lake breeze intensity at RIV. Both average and maximum velocities of the lake breeze tend to be stronger when the synoptic wind blows

onshore with respect to the offshore direction. Differences of order $0.7\text{-}0.8\text{ m s}^{-1}$ and 1 m s^{-1} between OnStr and the two offshore classes are found for the average and maximum velocities respectively. Furthermore it can be seen that on average the weakest intensity of the lake breeze occurs in the EW class. It is likely that this is due to the fact that in most cases easterly winds channelling in the low levels are deviated and appear as northerly winds (offshore) [13].

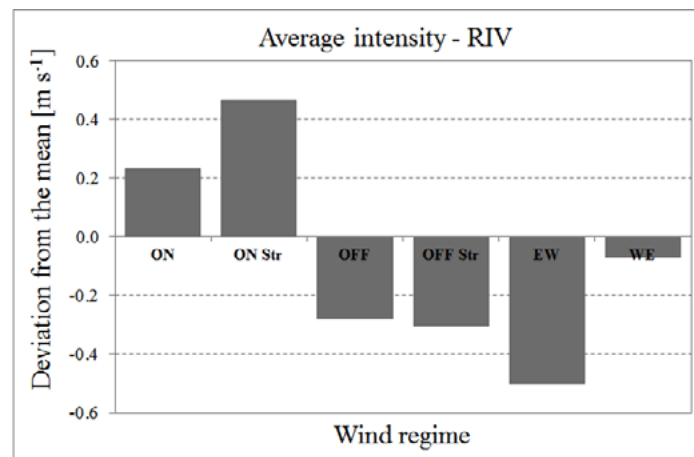


Fig. 7: Deviation from the mean of the average Ora del Garda intensity at RIV for the six synoptic wind classes

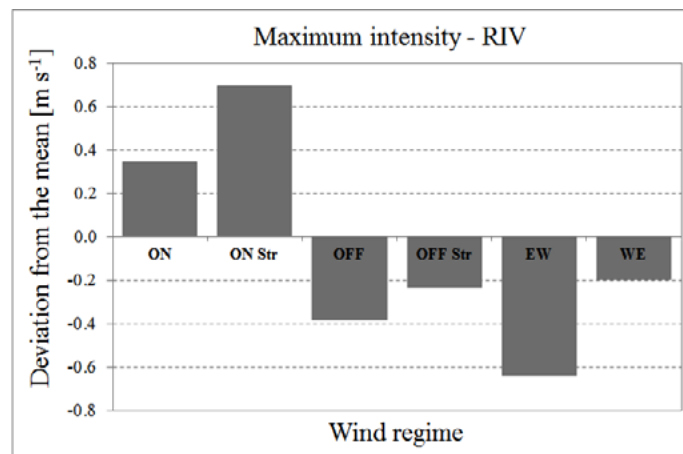


Fig. 8: Deviation from the mean of the maximum Ora del Garda intensity at RIV for the six synoptic wind classes

Fig. 9 shows that the onset of the Ora del Garda at RIV occurs ~ 25 min earlier for OnStr than for offshore and easterly synoptic winds. On the other hand the effects of the synoptic wind on the cessation time is less clear. Low differences are found between onshore and offshore synoptic winds, whereas the cessation time seems to occur significantly earlier with easterly winds (not shown).

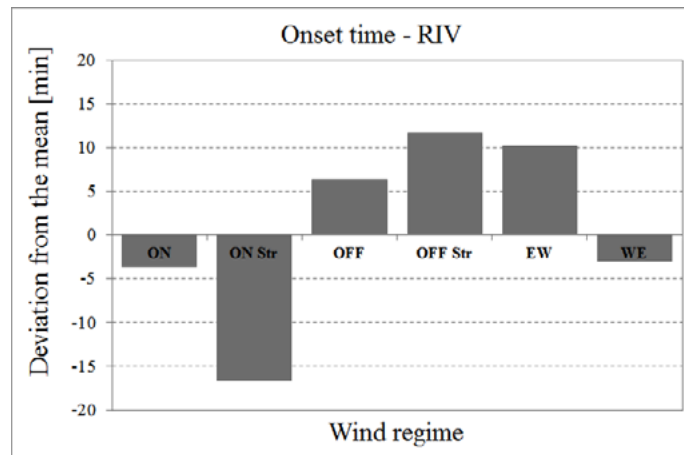


Fig. 9: Deviation from the mean onset time of the Ora del Garda at RIV for the six synoptic wind classes

As to the effects of the synoptic winds on the propagation of the lake breeze, it is found that the Ora del Garda reaches with more difficulties the Adige Valley with offshore and easterly winds, coherently with the above findings that the Ora del Garda at RIV is on average weaker and its duration shorter in the days in which it does not arrive at GAR. In fact the Ora del Garda does not arrive at GAR in 19% and 18% of the days with offshore and easterly synoptic wind respectively, and only in 8% and 7% of the days with onshore and westerly wind respectively.

Differently to what found at RIV, Fig. 10 shows that at GAR the lake breeze is stronger with offshore than with onshore synoptic winds. The differences between OnStr and OffStr reach $\sim 0.5 \text{ m s}^{-1}$ for the average velocity. This is probably connected to the fact that the up-valley wind south of Trento is stronger with onshore (southerly) synoptic winds and, as a consequence, it contrasts the arrival of the Ora del Garda in the Adige Valley [14].

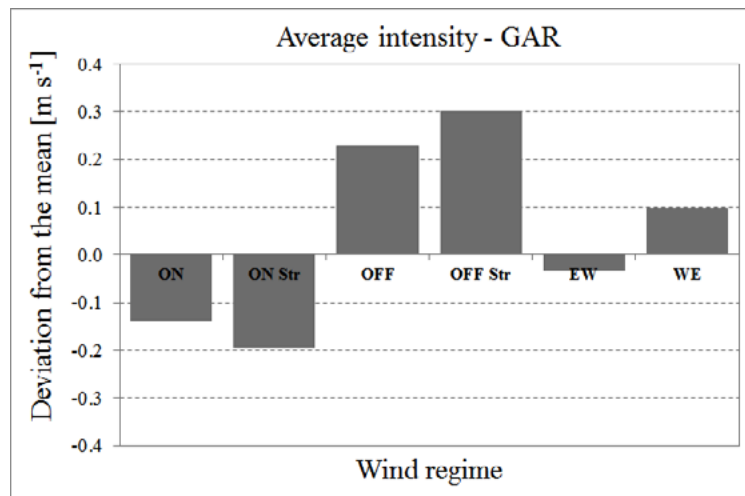


Fig. 10: Deviation from the mean of the average Ora del Garda intensity at GAR for the six synoptic wind classes

Fig. 11 shows that the synoptic wind has a significant influence also on the propagation time of the lake breeze from RIV to GAR. The propagation time is considerably longer for OffStr and EW and differences of ~ 1 h are found between OffStr and OnStr. This is probably due both to the weaker lake breeze occurring on average with these conditions and to the contrasting effect of the synoptic wind to the propagation of the lake breeze along the Sarca and Lakes valleys. It is likely that easterly winds are more effective at slowing down the propagation of the lake breeze in the last part of the Lakes Valley, which is roughly west-east oriented. (Fig.1).

The time of the arrival of the lake breeze at GAR depends both on the onset time at RIV and on the propagation time. As a consequence of the later onset of the lake breeze at RIV and of the slower propagation with offshore and easterly winds, the onset of the Ora del Garda at GAR occurs significantly later in these conditions. In particular the onset time occurs 50 min later than the mean onset time for EW, and the delay reaches 1h 30 min if compared with OnStr (Fig. 12).

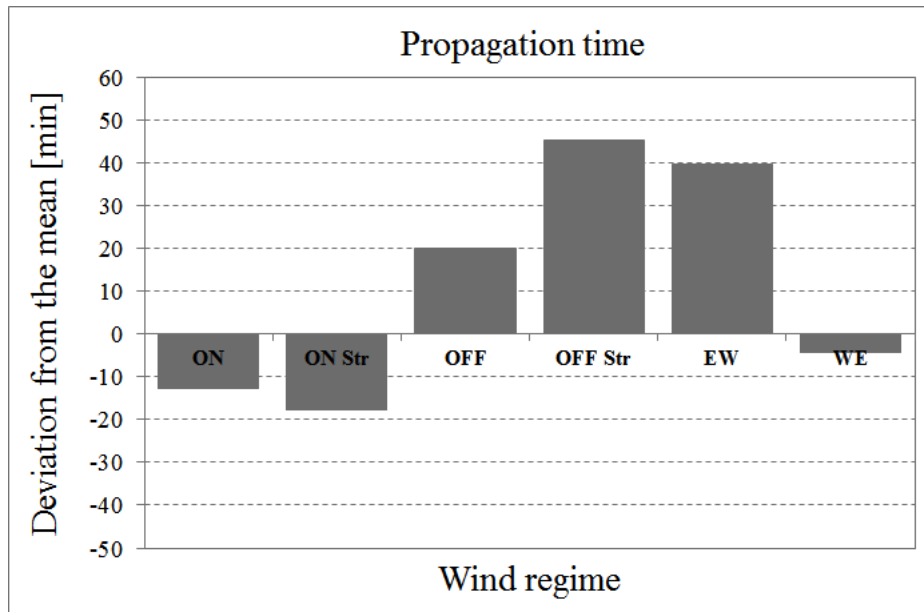


Fig. 11: Deviation from the mean propagation time of the Ora del Garda from RIV to GAR for the six synoptic wind classes

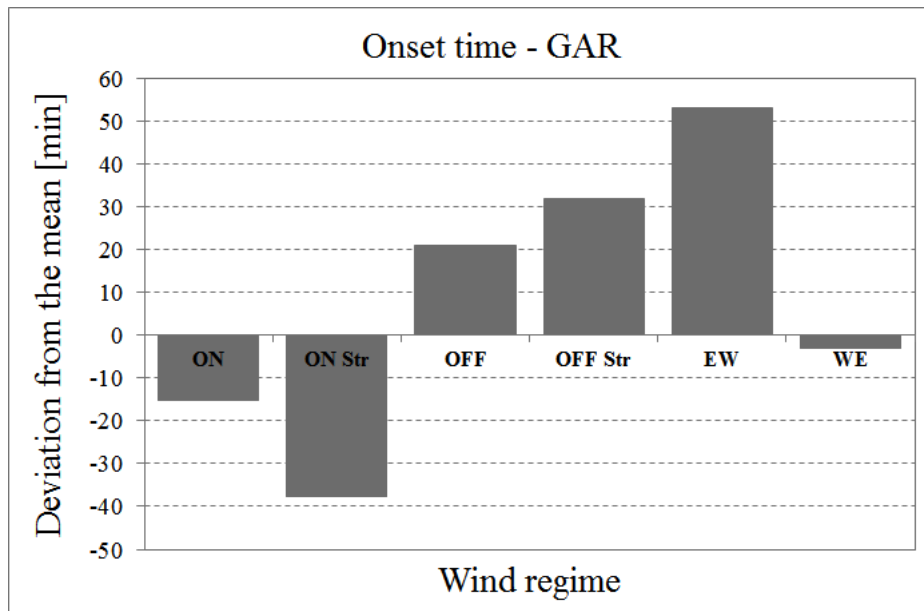


Fig. 12: Deviation from the mean onset time of the Ora del Garda at GAR for the six synoptic wind classes

ACKNOWLEDGMENTS

The Geographic Information System Unit of the Edmund Mach Foundation is kindly acknowledged for data from weather stations.

REFERENCES

- Defant A. (1908), *Über die stehenden Seespiegelschwankungen (Seiches) in Riva am Gardasee [About the stationary fluctuations of lake level (seiches) at Riva del Garda]*. S. B. Akad. Wiss. Wien, 117, Abt. IIa, 697-780. (1)
- Defant A. (1909), *Berg- und Talwinde in Südtirol [Mountain and valley winds in southern Tyrol]*. S. B. Akad. Wiss. Wien, 118, Abt. IIa, 553-604. (2)
- Wagner A. (1938), *Theorie und Beobachtung der periodischen Gebirgswinde [Theory and observation of periodic mountain winds]*. Gerlands Beitr. Geophys., 52, 408-449. English translation: Whiteman C. D., and Dreiseitl E. (1984), *Alpine meteorology: Translations of classic contributions by A. Wagner, E. Ekbart and F. Defant*. PNL-5141/ASCOT-84-3. Pacific Northwest Laboratory, Richland, Washington, 121 pp. (3)
- Daves B., Tampieri F., Tubino M., and Zardi D. (1998), *Exchange processes in a valley system: the effects of local circulation*. Proc. 25th Int. Conf. on Alpine Meteorology, Turin, Italy. (4)
- Baldi M., Cesari R., Tampieri F., Tranquillini M., and Zardi D. (1999), *A study of the valley wind known as Ora del Garda*. University of Trento, Civil and Environmental Engineering Department Tech. Note, IDR 1/1999, 119 pp. (5)
- de Franceschi M., Rampanelli G., and Zardi D. (2002), *Further investigations of the Ora del Garda valley wind*. Preprints, 10th Conf. on Mountain Meteorology and MAP Meeting 2002, Park City, UT, Amer. Meteor. Soc, 3.2. (6)
- de Franceschi M., Rampanelli G., Sguerso D., Zardi D., and Zatelli P. (2003), *Development of a measurement platform on a light airplane and analysis of airborne measurements in the atmospheric boundary layer*. Annali di Geofisica, 46, 269-284. (7)
- Laiti L., Zardi D., de Franceschi M., and Rampanelli G. (2013), *Residual kriging analysis of airborne measurements: application to the mapping of atmospheric boundary-layer thermal structures in a mountain valley*. Atmospheric Science Letters, 14, 79-85. (8)

- Laiti L., Zardi D., de Franceschi M., and Rampanelli G. (2013), *Atmospheric boundary layer structures associated with the Ora del Garda wind in the Alps as revealed from airborne and surface measurements*. Atmospheric Research, 132-133, 473-489. (9)
- Borne K., Chen D., Nunez M. (1998), *A method for finding sea breeze days under stable synoptic conditions and its application to the Swedish west coast*. International Journal of Climatology, 18, 901-914. (10)
- Telišman Prtenjak M., and Grisogono B. (2007), *Sea/land breeze climatological characteristics along the northern Croatian coast*. Theoretical and Applied Climatology, 90, 201-215. (11)
- Azorin-Molina C., and Chen D. (2009), *A climatological study of the influence of synoptic-scale flows on sea breeze evolution in the Bay of Alicante (Spain)*. Theoretical and Applied Climatology, 96, 249-260. (12)
- Gross G., and Wippermann F. (1987), *Channeling and countercurrent in the upper Rhine valley: numerical simulations*. Journal of Climate and Applied Meteorology, 26, 1293-1304. (13)
- Giovannini L., Zardi D., de Franceschi M., and Chen F. (2013), *Numerical simulations of boundary-layer processes and urban-induced alterations in an Alpine valley*. International Journal of Climatology. (14)

Continuous measurements of climate altering halogenated gases at the Italian Climate Observatory O. Vittori (ICO-OV)

Maione M.^{1*}, Giostra U.¹, Furlani F.¹, Arduini J.¹, Graziosi F.¹, Lo Vullo E.¹ and P. Bonasoni²

¹Department of Basic Sciences (DiSBeF), Università degli Studi di Urbino "Carlo Bo", Urbino, Italy.

²ISAC, CNR, Bologna, Italy,

*Corresponding author: michela.maione@uniurb.it

Abstract

Here we present the results of a long term continuous observation (2002-2011) programme conducted at ICO-OV Station, a mountain remote site located on the highest peak of the Italian Northern Apennines (2165 m a.s.l) at the border of two important regions: the Po Valley (and the Alps) to the North and the Mediterranean Basin to the South. Bi-hourly air samples of CFC-12, CFC-11, CFC-114, CFC-115, H-1211, H-1301, Methyl Chloroform, Carbon tetrachloride, HCFC-22, HCFC-142b, HCFC-124, HFC-125, HFC-152a, HFC-134a, HFC-143a, HFC-245fa, HFC-236fa, HFC-365mfc, HFC-32 and Methyl Bromide are collected and analysed using a gas chromatographic-mass spectrometric system, thus providing multi annual time series for a number of halogenated species. Trends, seasonal cycles and pollution episodes are presented.

Keywords: *Climate altering gases, Montreal Protocol, Kyoto Protocol, long term trends, emissions*



1. INTRODUCTION

Long term continuous measurements of halogenated climate altering gases are conducted worldwide with the aim of i) determining the rate of emission and/or chemical destruction of the anthropogenic chemicals that contribute most of the reactive chlorine and bromine released into the stratosphere and/or are strong infrared absorbers; ii) determining optimally the magnitudes and distributions by region of the surface sources of these gases; iii) providing an accurate data base on the rates of accumulation of trace gases over the globe; and iv) determining characteristics of the sources of these gases near the stations.

In particular, direct atmospheric measurements are crucial for the verification of the bottom-up emission inventories of these gases, which are based on statistical data only (Nisbet and Weiss, 2010).

The main monitoring networks for halogenated gases are AGAGE (Advanced Global Atmospheric Gases Experiment), SOGE (System for Observation of Halogenated Greenhouse Gases in Europe) and the NOAA-CMDL (National Oceanic and Atmospheric Administration/Climate Monitoring and Diagnostics Laboratory).

In the Mediterranean area, the only long term measurement programme is carried out, since 2001, at the Italian Climate Observatory “O. Vittori” (ICO-OV).

ICO-OV (WMO-GAW global station) is a research infrastructure managed by the ISAC-CNR, located at the top of Mt. Cimone (2165 m a.s.l.), the highest peak of the northern Italian Apennines, the only high mountain station for atmospheric research located South of the Alps and the Po basin (Bonasoni et al., 2000).

Currently, the ICO-OV observatory is an AGAGE affiliated station, and measurements are linked to the AGAGE calibration scale and the same calibration protocol as the AGAGE stations is used.

Here we report an analysis of data related to a wide range of compounds: CFC-12, CFC-11, CFC-114, CFC-115, H-1211, H-1301, Methyl Chloroform, Carbon tetrachloride, HCFC-22, HCFC-142b, HCFC-124, HFC-125, HFC-152a, HFC-134a, HFC-143a, HFC-245fa, HFC-236fa, HFC-365mfc, HFC-32 and Methyl Bromide, showing how long-term measurement programmes can be effective in deriving long term trends and in assessing compliance of Italy, and other European countries relevant to the site domain, with the international Protocols (Montreal and Kyoto) regulating production and emissions of these gases.

2. LONG TERM CONTINUOUS MEASUREMENTS AT ICO-OV

The gases that are monitored at the site include a wide range of radiatively active compounds: the fully halogenated and solely anthropogenic gases like the chlorofluorocarbons (CFCs) and the halons, the hydrogenated species (HCFCs and HFCs), chlorinated solvents and the methyl halides which are also partially of biogenic origin. Brominated and chlorinated short-lived gases are also monitored. The optimisation of the analytical procedure in terms of efficiency, linearity, and reproducibility is reported in Maione et al., 2004 and 2013. 1 L air is analyzed by gas chromatography–mass spectrometry (GC-MS) every second hour. For calibration purposes, every sample run is bracketed between two working standard runs. Working standards are actual air samples in turn calibrated against the SIO2005 (Scripps Institution of Oceanography)-UB98 (University of Bristol) scales, used within the AGAGE network. The system is fully automated via a GCmanager software developed by Peter Salameh at SIO and adopted from the AGAGE program.

3. RESULTS

The first step of the data analysis consists in the identification of the baseline, through a robust statistical method (Giostra et al., 2011) which is essential both for deriving long term trends . Furthermore, elevations above the baseline are an indication of fresh, not well mixed, emissions from the site domain. Such information is important for ascertaining compliance to the International Protocols.

Long term atmospheric trends of the main species monitored at ICO-OV are reported in Figure 1.

Our data show that the peak in the atmospheric mixing ratios of four CFCs, two halons and two chlorocarbons has been reached and all these species now show a decreasing atmospheric trend, which is consistent with the restriction in the production of these chemicals imposed by the Montreal Protocol. However, pollution episodes are still occurring for species like halon-1211, methyl chloroform and carbon tetrachloride, indicating fresh emissions from the site domain which could be ascribed both to fugitive un-reported uses of the compounds, as in the case of Methyl chloroform, and/or emissions from banks (i.e. halons), thus showing a non-compliance to the Protocol by countries located in the site domain (Maione et al., 2013).

For the hydrofluorocarbons, increases in the baseline are affected by emissions from fast developing Countries in East Asia, meanwhile fresh emissions from the site domain are clearly declining (see also Montzka et al. 2009). However, after 2010, consistent with the 2007 adjustments to the Montreal Protocol calling for an accelerated phaseout of HCFCs starting from 2009, a deceleration in the growth rate has been recorded. Methyl bromide, for which the Mediterranean area is an important source region, shows, in a generally decreasing trend, an emission pattern that is not consistent with the phase-out schedule of this compound, with a renewed increase in the last two years of pollution episodes.

The HFCs, which are strong infrared absorbers, are steadily increasing in the atmosphere. Moreover, for these compounds, during the non-winter periods a rise of the baseline is occurring. An analysis of such phenomenon showed how this is not dominated by the influence of the PBL, but rather is due to an actual and systematic increase of the underlying concentration, as a consequence of an increased use of these chemicals during the warmer periods of the year (Giostra et al., 2011).

To conclude, data from long term continuous measurement programme, are useful not only to appreciate the effectiveness of the regulating Protocols from a regional perspective but, in combination with those from other global programmes, are also useful to derive global emissions and estimate lifetimes of the compounds of interest.

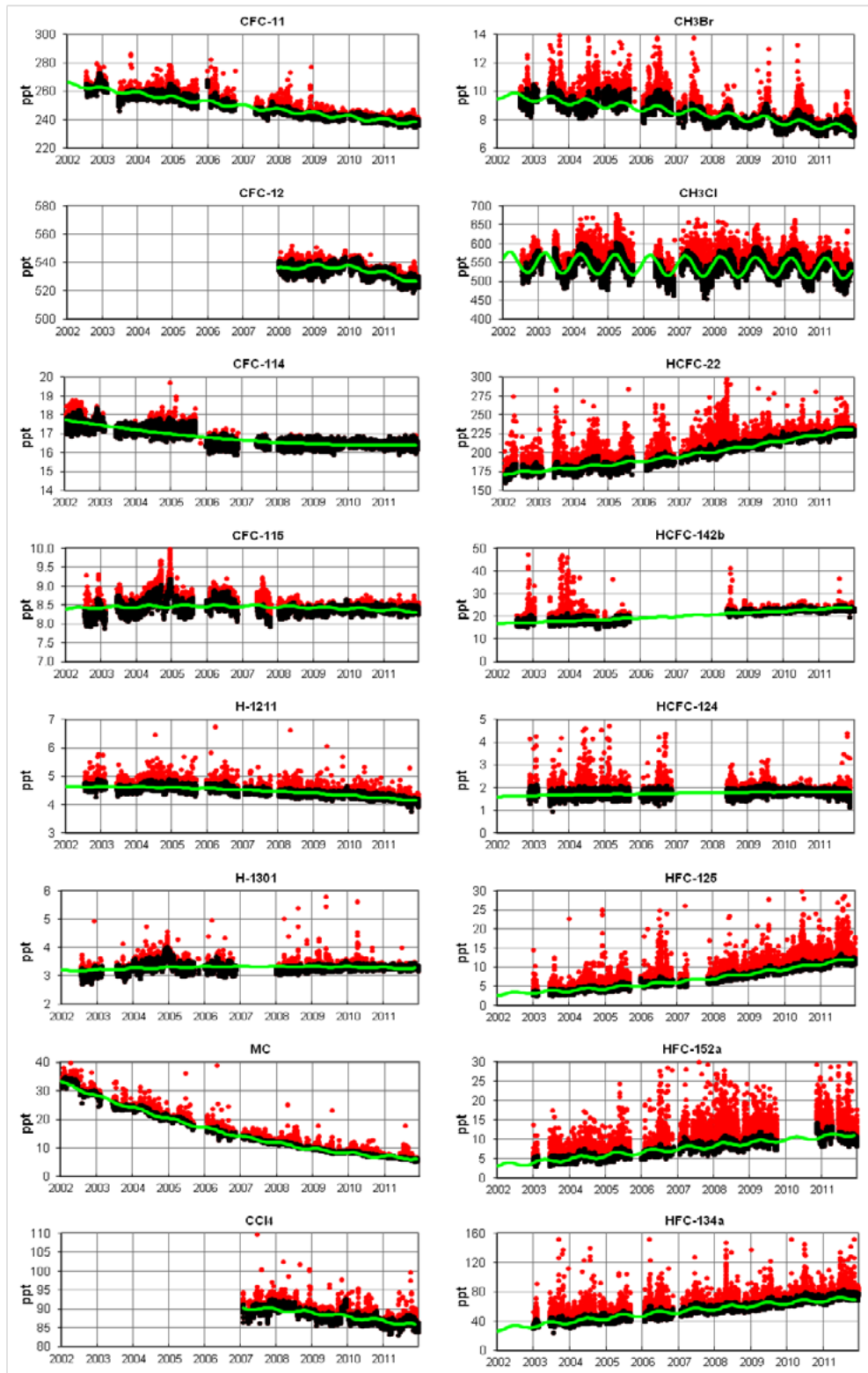


Fig. 1: Time series of gases. Black dots: baseline data; red dots: elevation above the baseline; green lines: best fit of the monthly means of baseline data

4. REFERENCES

- Bonasoni P., Stohl A., Cristofanelli P., Calzolari F., Colombo T., Evangelisti F. (2000), *Background ozone variations at Mt. Cimone station*. Atmos Environ 34.
- Giostra U., Furlani F., Manning A.J., Arduini J., Cava D., Manning A.J., O'Doherty S., Reimann S., Maione M. (2011), *The determination of a "regional" atmospheric background mixing ratio for anthropogenic greenhouse gases: a comparison of two independent methods*. Atmospheric Environment, 45, 7396-7405.
- Maione M., Arduini J., Mangani G., Geniali A. (2004), *Evaluation of an Automated Gas Chromatographic - Mass Spectrometric Instrumentation to be Used for Continuous Monitoring of Trace Anthropogenic Greenhouse Gases*. Intern. J. Environ. Anal. Chem., 84/4, 241-253.
- Maione M., Giostra U., Arduini J., Furlani F., Graziosi F., Lo Vullo E., and Bonasoni P., (2013), *Ten years of continuous observations of stratospheric ozone depleting gases at Monte Cimone (Italy) - Comments on the effectiveness of the Montreal Protocol from a regional perspective*. The Science of the Total Environment, 445–446, 155–164.
- Montzka S.A., Hall B.D., Elkins J.W. (2009), *Accelerated increases observed for hydrochlorofluorocarbons since 2004 in the global atmosphere*. Geophys. Res. Lett., 36, L03804, doi: 10.1029/2008GL036475.
- Nisbet E., Weiss R. (2010), *Top-Down Versus Bottom-Up*. Science 328, 1241 DOI: 10.1126/science.1189936.

The myth of Scylla and Charybdis: a torrent in the Messina Strait

Antonioli F.^{1*}, Sannino G.M.¹

ENEA Casaccia

*Corresponding author: fabrizio.antonioli@enea.it

Abstract

The submerged sill in the Strait of Messina, which is located today at a minimum depth of -81 m m.s.l., represented the only connection between Sicily and mainland Italy (and thus Europe) during the last low-stand, when the sea level locally stood at about -126 m.s.l. The myth has Charybdis lying on one side of a narrow channel of water while on the other side of the strait was Scylla, another dangerous sea-monster surrounded by six dog's head attempting to catch and tear to pieces the sailors. According with the palaeotide-model implemented in this research, the tidal currents reached 15 knots when sea level was 100 m depth, do not allowed the Messina strait crossing for *Homo sapiens* (living in Europe since 40 ka) before Last Glacial Maximum (22 ka).

Keywords: *Palaeotides, Messina strait, Homo sapiens*



In order to calculate the magnitude of palaeotides over the sill in the middle of the Strait of Messina (Fig. 1) when sea level was at about -100 meters we used a numerical model based on the bottom morphology and the present day tidal forcing.

Model bathymetry has been obtained by a bilinear interpolation of very high resolution bathymetric data (1 m resolution). The model used in this work is the Massachusetts Institute of Technology general circulation model (MITgcm). The MITgcm solves the fully nonlinear, nonhydrostatic Navier–Stokes equations under the Boussinesq approximation for an incompressible fluid with a spatial finite-volume discretization on a curvilinear computational grid. The model formulation, which includes implicit free surface and partial step topography, is described in detail by [1,2].

The model domain covers the entire Strait from 37.9N to 38.4N by means of a non-uniform curvilinear orthogonal grid made by 300x840 points. Spatial resolution across the longitudinal axis of the strait, DX, (along the strait axis, DY,) ranges between 15 and 190 m (17–200 m) with the highest resolution reached in the narrowest part of the Strait. To adequately resolve the pycnocline the model has 55 vertical z-levels with a thickness of 7.5 m in the upper 300 m gradually increasing to a maximum of 110 m for the remaining 15 bottom levels.

The very high horizontal resolution adopted, together with the partial cell formulation results in a very detailed description of the bathymetry. No-slip conditions were imposed at the bottom and lateral solid boundaries. The selected tracer advection scheme is a third-order direct space-time flux limited scheme [3], which is unconditionally stable and does not require additional diffusion. As turbulent closure parametrization for vertical viscosity and diffusivity has been used the scheme proposed by [4]. Here we stress that a similar physical configuration for the MITgcm has recently been successfully used to study the dynamics of the Strait of Gibraltar, [5,6].

The model simulation has been start from rest, forced at the north and south open boundaries through the specification of the present-day barotropic tidal currents in particular the principal two semidiurnal and two diurnal harmonics (M2, S2, O1, K1) have been considered. Amplitude and phase of these harmonics have been computed via the OTIS package [7].

Finally, the initial conditions in terms of salinity and temperature have been taken from the present-day Medar-MedAtlas climatological Database [8] for the month of January.

A technique similar to [9] Sannino et al. 2009 has been applied to spin-up the model. The technique consists in initially running the model without tidal forcing in order to achieve a steady circulation. Then the model was forced by tidal components in order to achieve a stable time periodic solution.

After this spin-up phase the model was run for a further tropical month (27.321 days) that represents our reference experiment.

The palaeo simulation performed with the numerical ocean model shows where velocity reaches its maximum on the bottom of the Messina Strait Sill. In particular, due to the combined effects played by the bathymetric constraint and the Coriolis effect, the maximum velocity of about 15 knots is reached on the north-eastern side of the Sill (Fig. 2). Based on the morphology of the present day marine notch carved on stabled limestones coast areas appears evident that the notches width are directly proportional to the local tide. Measurements of Late Holocene and Last Interglacial fossils tidal notches measured in the central Mediterranean sea [10, 11] compared with the present day tidal notch allow us to state that the width remained the same, then we can assume that the Present tide appears fully comparable with the LGM tides.

Effects of tides on the bottom of the Sill but also on the sea surface, with a maximum velocity of about 18 knots (Fig. 3) do not allowed the Messina strait crossing for *Homo sapiens* (living in Europe since 40 ka) before Last Glacial Maximum (22 ka).

Based on this model and results [12] stated: *i*: with 20 m thick sediments eroded, the emersion of the Messina strait Sill was between 27 and 17 ka cal BP; *ii*: without erosion in any case the Sill emerged 1500 yrs between 20 and 21.5 ka cal BP; *iii*: *Homo sapiens* and *E.Hydruntinus*, respectively not arrived in Sicily earlier than 17 and 23-21 ka cal BP.

REFERENCES

- Marshall J., Hill C., Perelman L., and Adcroft A. (1997a), *Hydrostatic, quasi-hydrostatic, and nonhydrostatic ocean modeling*, J. Geophys. Res., 102, 5733–5752. (1)
- Marshall J., Adcroft A., Hill C., Perelman L., and Heisey C. (1997b), *A finite-volume, incompressible Navier Stokes model for studies of the ocean on parallel computers*, J. Geophys. Res., 102, 5753–5766. (2)
- Hundsdorfer W., Koren B., Vanloon M., Verwer J., (1995), *A positive finite-difference advection scheme*. J. Computational Physics 117 (1), 35–46. (3)
- Pacanowski R.C., and Philander S.G.H. (1981), *Parameterisation of vertical mixing in 562 numerical models of tropical oceans*, J. Phys. Oceanogr., 11, 1443–1451. (4)

- Sannino G., Sanchez-Garrido J.C., Liberti L., Pratt L. (2012), *Exchange flow through the Strait of Gibraltar as simulated by a σ -coordinate hydrostatic model and a ξ -coordinate non-hydrostatic mode*. In: Eusebi Borzelli, G.L., Gačić, M., Malanotte-Rizzoli P., Lionello P. (Eds.), *The Mediterranean Sea: Temporal Variability and Spatial Patterns*. AGU Monograph Series, AGU, Washington, D. C. (5)
- Sánchez-Garrido J.C., Sannino G., Liberti L., García Lafuente J., and Pratt L. (2011), *Numerical modelling of three-dimensional stratified tidal flow over Camarinal Sill, Strait of Gibraltar*, *J. Geophys Res*, 116, C12026, doi:10.1029/2011JC007093. (6)
- Egbert G., and Erofeeva L. (2002), *Efficient inverse modeling of barotropic ocean tides*. *J. Atmos. Oceanic Technol.*, 19, 183–204. (7)
- MEDAR Group (2002), *Medatlas 2002: Mediterranean and Black Sea Database of Temperature, Salinity and Bio-Chemical Parameters Climatological Atlas*, Eur. Comm. Mar. Sci. and Technol. Programme, Paris. (8)
- Sannino G., Pratt L., and Carillo A. (2009), *Hydraulic criticality of the exchange flow through the Strait of Gibraltar*, *J. Phys. Oceanogr.*, 39, 2779–2799, doi:10.1175/2009JPO4075.1. (9)
- Ferranti L., Antonioli F., Mauz B., Amorosi A., Dai Pra G., Mastronuzzi G., Monaco C., Orru' P., Pappalardo M., Radtke U., Renda P., Romano P., Sanso' P. & Verrubbi V. 2006. *Last interglacial sea level high stand markers along the coast of the Italian Peninsula: tectonic implications*. *Journal of Quaternary International*, 145-146, 30-54. (10)
- Antonioli F., Kershaw S., Ferranti L. (2006b). *A double MIS 5.5 marine notch ?* *Quaternary International*, 145-146: 19–29. (11)
- Antonioli F., Lo Presti V., Mannino M., Gasparo Morticelli M., Palombo M.R., Ferranti L., Lambeck K., Sannino G.M., Bonfiglio L., Mangano G., Chiocci F.L., Furlani S., Tonielli R., Canese S. Catalano R. (in press. 2013). *Timing of the emergence of the Europe-Sicily bridge (40-17 ka cal BP) and its implications for the spread of modern humans*. *Journal of Geological Society of London*. (12)



Fig 1: The Mediterranean sea and the ubication of the Messina Strait

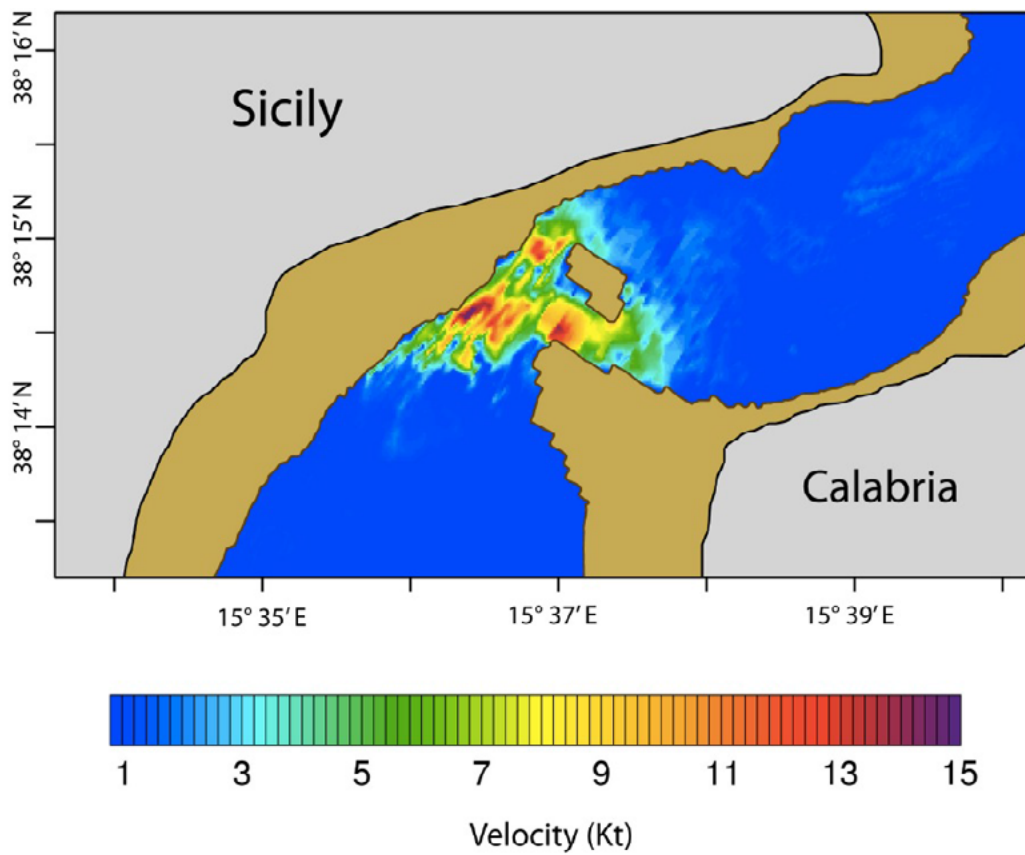


Fig. 2: The Messina strait tides velocity modelled at -100 meters with a 10 m depth water.

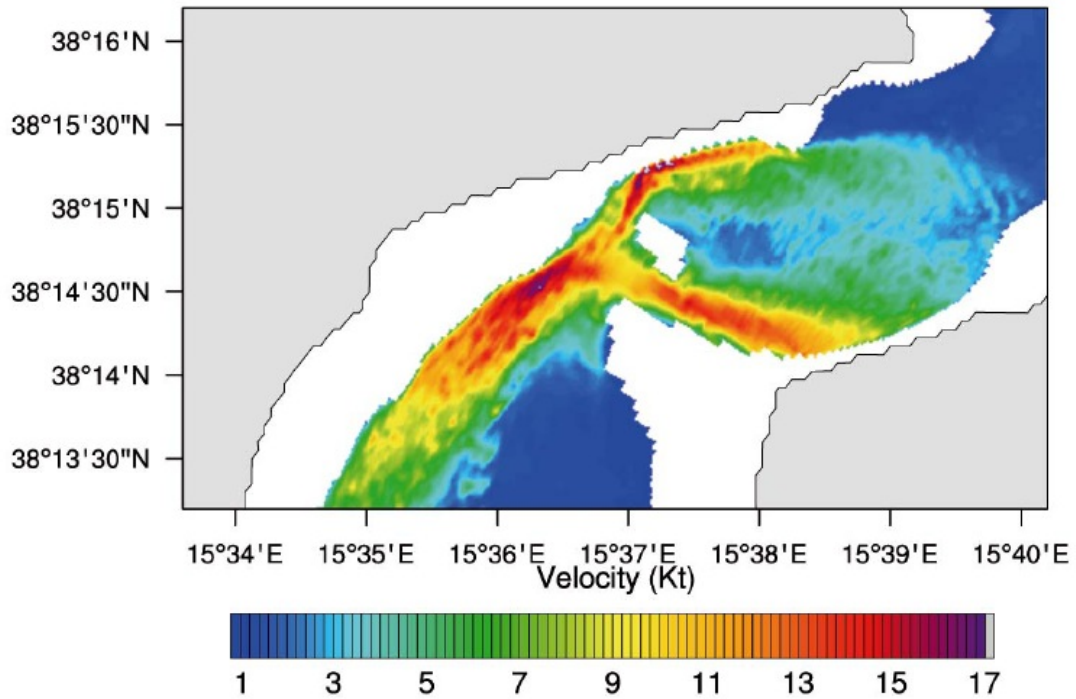


Fig. 3: Maximum surface velocity in the Strait during a complete tidal period (typical month, about 30 days) as simulated by the numerical model. The surface model velocity is representative for the first 3m water column.

ADVANCES IN CLIMATE SCIENCE

Poster Session

Intrinsic variability of the Antarctic Circumpolar Current: low-frequency fluctuations in the Argentine Basin flow

Sgubin G.¹, Pierini S.^{2*}, and Dijkstra H.A.³

¹*Laboratoire des Sciences du Climat et de l'Environnement, Paris*

²*Dipartimento di Scienze e Tecnologia, Università di Napoli Parthenope*

³*Institute for Marine and Atmospheric research Utrecht, Utrecht University*

*Corresponding author: stefano.pierini@uniparthenope.it

Abstract

The dynamics of the Argentine Basin flow is of climatic relevance, as it yields strong mixing between Antarctic water masses (carried by the Malvinas Current) and subtropical water masses (carried by the Brazil Current). Such mixing is regulated by the Zapiola Anticyclone, a counterclockwise current that encircles the Zapiola Rise, the main topographic feature of the Argentine Basin. We investigate the intrinsic variability of the Argentine Basin flow by using a sigma-coordinate ocean model. The periodic domain of integration includes the Pacific/Atlantic sector of the Southern Ocean, which allows us to describe correctly the Antarctic Circumpolar Current and its fronts. The forcing is provided by steady climatological surface heat and momentum fluxes. Results show several phenomena of both high and low-frequency variability which are found to be sensitive to background stratification and the degree of smoothing of the bottom topography. The Argentine Basin circulation is found to be related to fluctuations of the position of the Antarctic Circumpolar Current fronts. Significant agreement is found when comparing our model results with altimeter data.

Keywords: *Argentine Basin flow; Antarctic Circumpolar Current; Zapiola Rise; intrinsic low-frequency variability*



The Argentine Basin (AB), located in the south-western Atlantic Ocean near the South American coasts, is one of the main areas for the meridional exchanges between the Southern Ocean (SO) and sub-tropical water masses. This region is characterized by a deep bottom that is bounded by a very steep continental slope. In the middle of the basin (~45°S, 45°W) the Zapiola Rise (ZR) is an important topographic feature that drives a strong counterclockwise circulation, the so-called Zapiola Anticyclone (ZA). The position of the AB, along with its morphological features, makes the local dynamics rather complex and of great interest in climate. This region is, in fact, characterized by a strong eddy activity, mostly due to the convergence and mixing of the Malvinas Current from the Antarctic Circumpolar Current (ACC) with the relatively warmer Brazil Current from the north. In this context, the ZA is likely to regulate the distribution of the eddy field, thus playing a central role in meridional heat exchanges (Fig. 1).

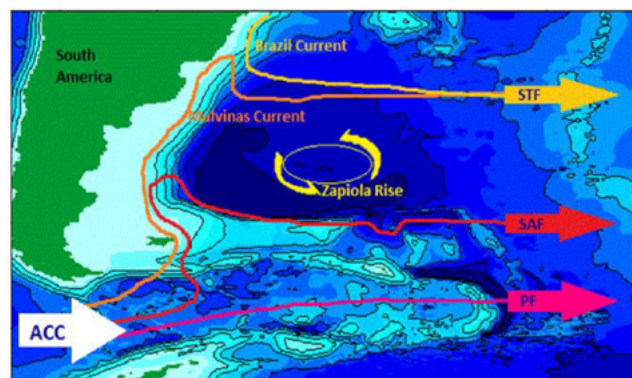


Fig. 1: Sketch of the circulation in the western South Atlantic. The ACC dominates the southern part of the basin, splitting into two major fronts, the Polar Front and the Subantarctic Front. Part of this water turns north forming the Malvinas Current. From the North, the Brazil Current flows southward along the continental shelf, colliding with the Malvinas Current at around 39°S, where it creates the very energetic and turbulent region known as the Malvinas-Brazil Current Confluence.

Recent observations have shown a relevant variability associated with the ZA. Fu et al. [1] found a counterclockwise rotating wave around the ZR with a period close to 25 days. Such a high-frequency variability has been interpreted as a barotropic topographic Rossby mode associated with the basin geometry [2-4]. At lower frequencies, by using satellite altimeter data Saraceno et al. [5] documented for the first time a clear low-frequency variability of the circulation in the AB associated with the acceleration or deceleration of the main anticyclonic flow. Moreover, indications for a possible collapse of the ZA also emerged both from observations and model studies [6].

In this context, Sgubin et al. [7] investigated the role of the intrinsic variability in the AB circulation through an eddy-permitting process-oriented model study, stressing its potential connection with the dynamics of the ACC. By following an approach similar to previous studies of the intrinsic variability of the ACC [8], the Pacific/Atlantic sector of the SO is considered (Fig. 2), in which periodic boundary conditions on the East/West edges of a rectangular channel are imposed. The primitive equation Princeton Ocean Model has been used: its sigma-coordinate vertical discretization makes its implementation ideal in the presence of complex bottom topography.

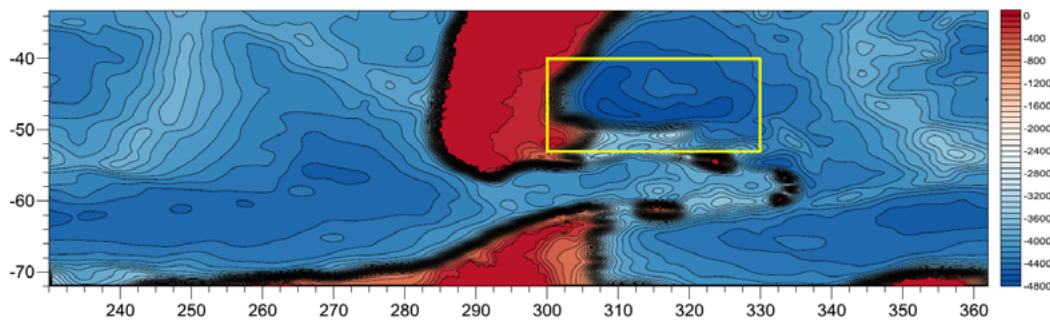


Fig. 2. Domain of integration and bottom topography adopted in [7].

In order to identify intrinsic variability, steady surface heat and momentum fluxes have been imposed. In addition, sensitivity experiments have been performed by varying the initial background stratification and the topographic smoothing. The wind stress and initial temperature profiles used in the reference simulation are shown in Fig. 3.

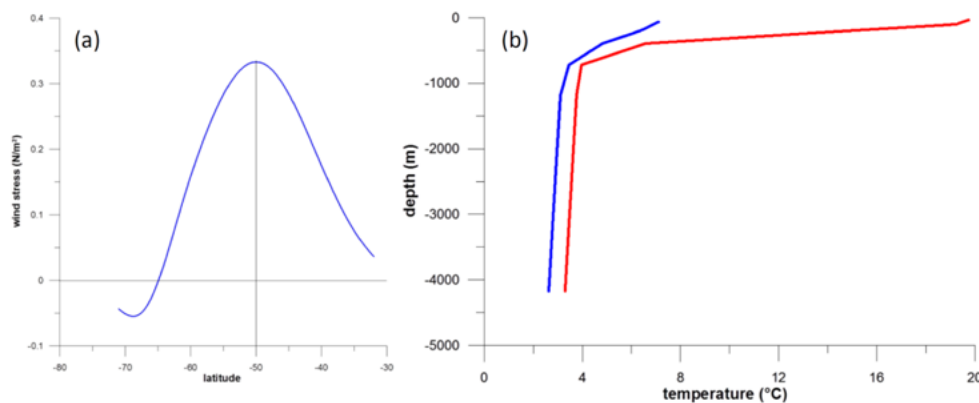


Fig. 3. Left panel: steady zonal wind stress profile used to force the model. Right panel: initial stratifications used in the reference simulation (red/blue line: temperature profile at the northernmost/southernmost latitude). From [7].

Realistic circulation patterns are obtained for the Pacific/Atlantic sector of the SO (Fig. 4). Good agreement with observations in terms of a realistic position of the main ACC fronts, along with a zonal transport across the Drake Passage (of around 120 Sv) are found. The major topographic features play a central role in the dynamical balance of the ACC through the bottom form drag. Moreover, the

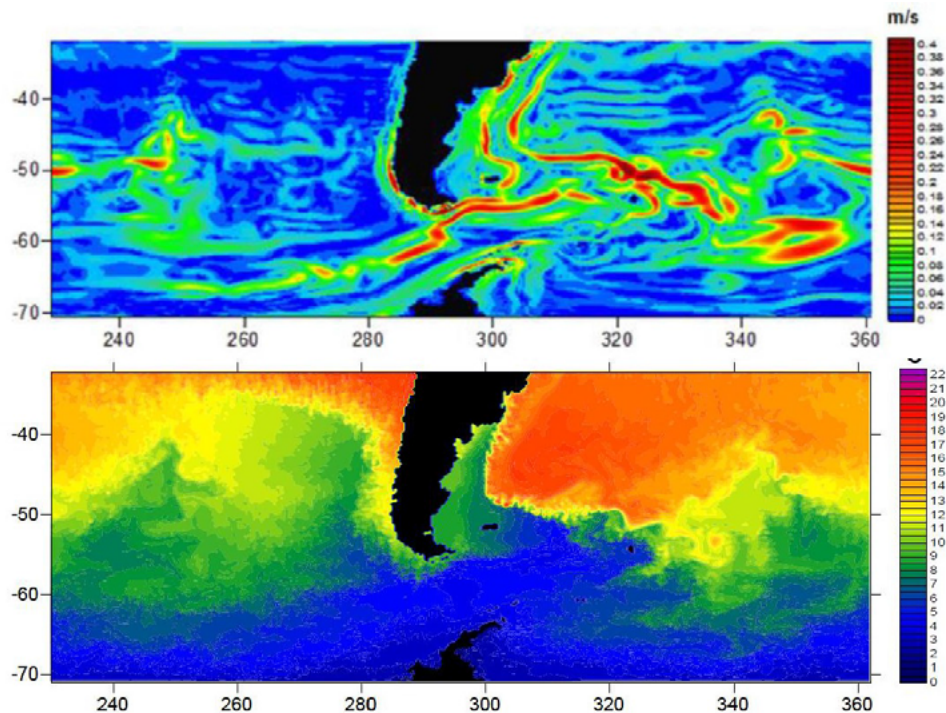


Fig. 4: Snapshots of the vertically averaged velocity (upper panel) and sea surface temperature (lower panel) for the reference simulation. From [7].

particular background stratification prevents total topographic steering.

Maps of the variance computed for different frequency ranges clearly show both high and low-frequency variability, which are significant in the AB, particularly in its southern part over the ZR (Fig. 5a), where the Subantarctic Front is located. The long term variability yields a low-frequency bimodal behaviour connecting two distinct regimes of very different character (Fig. 5b).

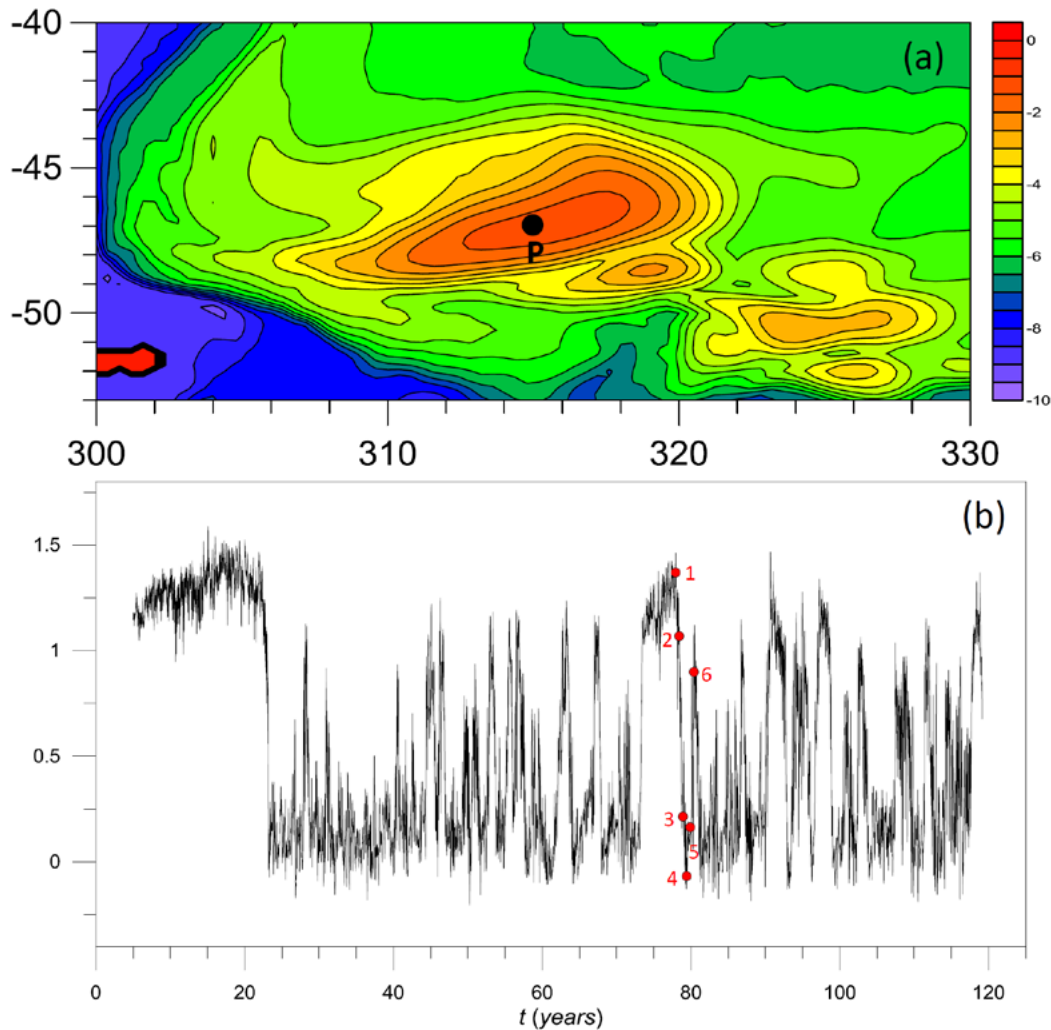


Fig. 5: Map of the logarithm of the SSH variance (a) and SSH time series (in m) in point $P=(47^{\circ}S, 45^{\circ}E)$ (b) for the reference simulation (the red points refer to the snapshots shown in Fig. 6). From [7]. The window shown in (a) is evidenced in the yellow box in Fig. 2.

By selecting a limited period in the time integration, during which the system switches from one regime to the other, it is possible to investigate qualitatively the leading mechanism of the process. The abrupt transition is associated with fluctuations of the flow along the southern part of the AB. This can be identified with the Subantarctic Front, which, due to intrinsic mechanisms, tends to vacillate meridionally, triggering different responses in the AB circulation and, occasionally, the collapse of the ZA (Fig. 6). This behaviour is in basic agreement with altimeter data [5].

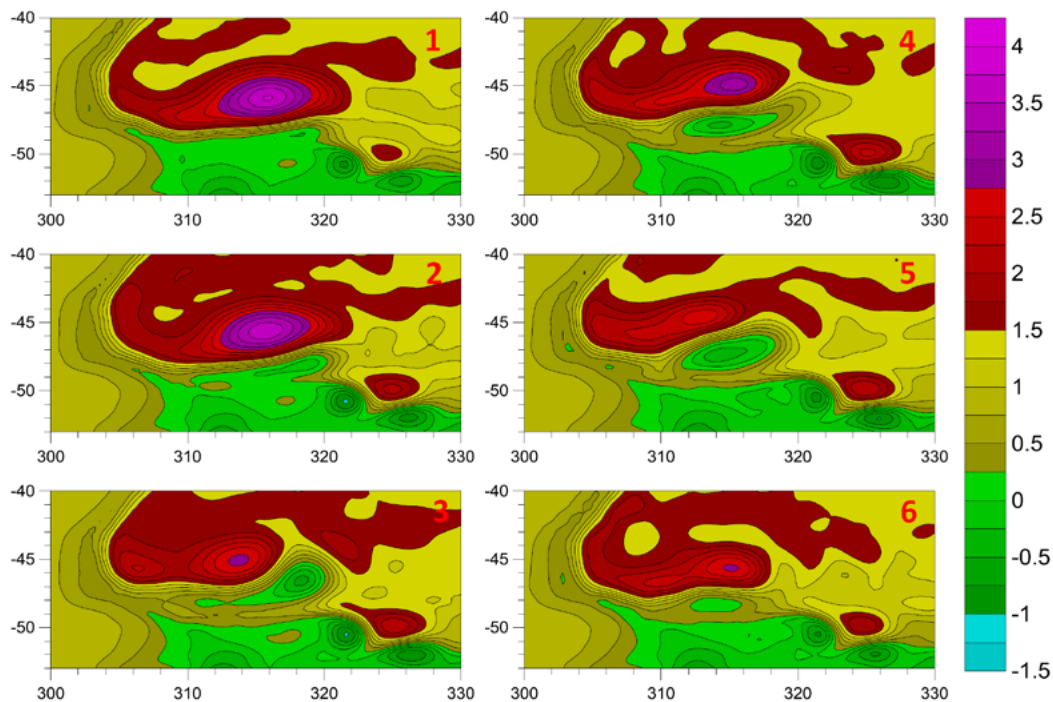


Fig. 6: Snapshots of the streamfunction obtained from 3-month averaged data showing the switch from one regime to the other for the reference simulation (see Fig. 5b for the 6 time instants; the window is evidenced in the yellow box in Fig. 2). From [7].

Several numerical experiments performed by varying the background stratification and topographic smoothing evidence a remarkable sensitivity of the model results. As far as the topography is concerned, the sigma-coordinate vertical discretization is ideal when dealing with flows that interact strongly with topography; however, the pressure gradient error typical of such discretization makes the treatment of bathymetry rather delicate, so in the presence of steep topography an accurate smoothing is needed to reduce such spurious errors. A smoothing method is therefore applied following Barnier et al. [9]. The bimodal behavior is found to be more pronounced (and more realistic) when the ZR features are better retained; in the reference simulation the ZR is well represented.

Finally, the modelled high-frequency variability is characterized by an anticyclonic wave around the ZR, which is interpreted in terms of topographic Rossby normal modes. Such a propagating anomaly has periods in good agreement with observations, and is found to be connected to the lower frequency intrinsic variability described above.

In conclusion, an eddy-permitting sigma-coordinate model for the circulation in the Pacific/Atlantic sector of the SO has been presented. The analysis of the intrinsic variability has evidenced its

dependence upon background stratification and bottom topography. Both high and low-frequency variability could be identified in the AB over the ZR. The low-frequency variability yields two distinct regimes with very different variances. In particular, a more variable regime is associated with fluctuations of the position of the Subantarctic Front, which, in some cases, leads to the collapse of the ZA. These results show the important role played by the ACC variability in the dynamics of the AB, providing an interpretation for the observed occasional collapse of the ZA.

ACKNOWLEDGMENTS

This work has been supported by the Italian "Programma Nazionale di Ricerche in Antartide" (contr. n. 2010/A2.11-2753).

REFERENCES

- Fu L.L., Cheng B. & Qiu B. (2001), *25-day period large-scale oscillations in the Argentine Basin revealed by the TOPEX/Poseidon altimeter*, J. Phys. Oceanogr., No. 31, pp. 506–517. (1)
- Tai C.-K. & Fu L.L. (2005), *25-day period large-scale oscillations in the Argentine Basin revisited*, J. Phys. Oceanogr., No. 35, pp. 1473–1479. (2)
- Weijer W., Vivier F., Gille S.T. & Dijkstra H.A. (2007a), *Multiple oscillatory modes of the Argentine Basin. Part I: statistical analysis*. J. Phys. Oceanogr., No. 37, pp. 2855–2868. (3)
- Weijer W., Vivier F., Gille S.T. & Dijkstra H.A. (2007b), *Multiple oscillatory modes of the Argentine Basin. Part II: the spectral origin of basin modes*. J. Phys. Oceanogr., No. 37, pp. 2869–2881. (4)
- Saraceno M., Provost C. & Zajaczkovski U. (2009), *Long-term variation in the anticyclonic ocean circulation over the Zapiola Rise as observed by satellite altimetry: evidence of possible collapses*, Ocean Mod., No. 29, pp. 176–188. (5)
- Bigorre S. & Dewar W.K. (2009), *Oceanic time variability near a large scale topographic circulation*, Ocean Mod., No. 29, pp. 176–188. (6)
- Sgubin G., Pierini S. & Dijkstra H.A. (2013), *Intrinsic variability of the Antarctic Circumpolar Current System: low- and high-frequency fluctuations of the Argentine Basin flow*, in preparation. (7)

Hogg M.A. & Blundell J.R. (2006), *Interdecadal variability of the Southern Ocean*, J. Phys. Oceanogr., No. 36, pp. 1626–1645. (8)

Barnier B., Marchesiello P., de Miranda A.P., Molines J.-M. & Coulibaly M. (1998), *A sigma coordinate primitive equation model for studying the circulation in the South Atlantic. part I: Model configuration with error estimates*, Deep-Sea Res., No. 45, pp. 543–572. (9)

GNSS Analysis for Meteorological Applications and Climate Monitoring in the Mediterranean Area

Pace B.^{1*}, Pacione R.¹, and Bianco G.²

¹*e-GEOS SpA, ASI/CGS, Matera Italy*

²*ASI/CGS, Matera Italy*

*Corresponding author: brigida.pace@e-geos.it

Abstract

Water vapour is one of the main greenhouse gases of the atmosphere important in weather and climate processes. In the last decade the use of ground-based Global Navigation Satellite System (GNSS) receivers has been developed as an all-weather and low-cost remote sensing system of the atmosphere as compared to conventional techniques such as satellite radiometer sounding, ground-based microwave radiometer and radiosondes.

For more than a decade, the Centro di Geodesia Spaziale (CGS) of the Agenzia Spaziale Italiana (ASI) has supported ground-based GNSS meteorology in Europe participating in various projects such as MAGIC, COST-716, TOUGH, E-GVAP (phase I, II and III), COST Action ES1206 providing Zenith Tropospheric path Delays (ZTD) derived from a European network of GNSS stations covering mainly the central Mediterranean area. Working in close cooperation with the meteorological community, GNSS data are analyzed in order to provide ZTD with different latencies ranging from post-processing, useful for climate studies, to near-real time, for hourly assimilation into Numerical Weather Prediction (NWP) model. However advancements in NWP models (such as the Met Office UKV 1.5km model) with rapid update cycles require observations with improved timeliness and with greater spatial and temporal resolution than is currently available. To fulfil this requirement a sub-hourly Precise Point Positioning (PPP) processing has been set-up, thanks to the availability of the IGS (International GNSS Service) Real Time orbit and clock corrections (<http://rts.igs.org>).

Moreover ZTD estimates are the input data for developing Integrated Water Vapour (IWV) maps which can be useful for nowcasting and severe weather monitoring since they let forecasters to follow IWV time evolution. The existence of more than 15 years of observations from permanent GNSS stations worldwide together with the reprocessing effort in the IGS and EUREF framework will provide an homogeneous database for monitoring trends and variability in atmospheric water vapour.

We present an overview of the developed products and services; the new directions in support of climate monitoring, NWP applications and the nowcasting and forecasting of severe weather events that emerge within E-GVAP phase III and the EU COST Action ES1206 “Advanced Global Navigation Satellite Systems tropospheric products for monitoring Severe Weather Events and Climate” (GNSS4SWEC).

Keywords: *GNSS Meteorology, Climate, Zenith Tropospheric Delays, Integrated Water Vapour Numerical Weather Prediction Models*



1. BACKGROUND

For more than a decade, ASI/CGS has supported ground-based GNSS meteorology in Europe by participating in various projects such as MAGIC, COST-716, TOUGH, E-GVAP (phase I II and III), COST Action ES1206 and providing Zenith Tropospheric path Delays derived from a European network of GNSS stations covering mainly the central Mediterranean area. Working in close cooperation with the meteorological community, GNSS data are analyzed in order to provide ZTD's with different latencies ranging from post-processing, useful for climate studies, to near-real time, for hourly assimilation into Numerical Weather Prediction models. The analysis is carried out by using GPS-Inferred Positioning System and Orbit Analysis Simulation Software (GIPSY-OASIS II) package [3]. However, advancements in NWP models with rapid update cycles require observations with improved timeliness and with greater spatial and temporal resolution than those currently available. To fulfill this requirement, a sub-hourly PPP processing has been set-up thanks to the availability of the IGS RT orbits and clock corrections.

2. USE OF GNSS ZTD IN WEATHER PREDICTIONS: THE E-GVAP PROJECT

E-GVAP (<http://egvap.dmi.dk>) was set up, in April 2005, to provide its EUMETNET members with European GNSS delay and water vapour estimates for operational meteorology in Near Real-Time (NRT).

The NRT GNSS delay data contain information about the amount of water vapour above the GNSS sites. Water vapour plays a key role in some of the most important weather phenomena: it is related to precipitation, but also provides about half the energy to the atmosphere (via latent heat release), contributing to atmospheric dynamics, and it is the dominant greenhouse gas. There is a big lack of humidity observations in the meteorological observing system, usage of ground based GNSS data is one means by which to improve on this. The vast majority of high quality permanent GNSS sites are installed for positioning purposes, by geodetic institutions and private firms. To them the atmospheric delay is a noise term. The core of E-GVAP is a close collaboration between geodesy and meteorology. Raw data from GNSS sites are collected by a number (more than 10) GNSS analysis centres, which process the data to estimate ZTDs (and other parameters). The ZTDs are then forwarded to a data server, for distribution to meteorological institutes, and for quality control and verification. E-GVAP

contributes meteorological data, that can be used to validation GNSS delay estimation, and to improve GNSS positioning in the future.

Presently, the E-GVAP network consists of more than 18500 GNSS sites. Mainly in Europe, but recently processing and distribution of global GNSS data has started, since many E-GVAP members run global NWP models. For the same reason E-GVAP welcomes collaboration with both European and non European institutions, in order to densify the GNSS meteorological observing network.

Usage of ground based GNSS delay data in NWP has proven to improve forecast skill.

3. GNSS-Met PRODUCTS AT ASI/CGS

ZTD solutions with different latency and accuracy are routinely produced at ASI/CGS, using GNSS data from a ground based network in the Mediterranean area, and delivered:

- **ASIP:** Post-Processing solution, for climate studies, 2 week latency;
- **ASI_** hourly update, for NWP model, 90min nominal latency;
- **ASIC:** E-GVAP combined solution [2], hourly update, 2.5 hour latency;
- **ASIS:** sub-hourly update (15min), for rapid-update high-resolution NWP models and nowcasting tools.



Fig. 1 Ground based GPS networks: a) ASIP postprocessed network, b) ASI_ E-GVAP network, c) ASIC combined E-GVAP network.

Besides those products, ASI/CGS has been submitting a postprocessed tropospheric solution to EUREF since 2001 and is partaking to the EPN Repro activities delivering an homogeneous ZTD time series for all the EPN stations covering the period 1996-2012. Such ZTD time series will be a GNSS database for climate monitoring over Europe.

Software / Mode	ASIP GIPSY/ PPP	ASI_ GIPSY/ Net	ASIS GIPSY/ PPP
Network Coverage	Central Mediterranean area	Central Mediterranean area	Europe
# Stations	approx. 250	approx. 200	E-GVAP Super Sites
Orbits, clocks and EOPs	JPL Final	IGS UR	IGS RT
Sat. & Ric. Antenna Model	IGS08.ATX	IGS08.ATX	IGS08.ATX
Tropo. Model	GPT/GMF	exp/NIELL	GPT/GMF
Oceal Tide Loading	FES2004	FES2004	FES2004
Elev. Angle Cutoff	7deg	7deg	7deg
RINEX Type	daily	hourly	RT converted to RNX via BNC
Sliding window	24h	4h, 1h moving forward	24h, 15min moving forward
Estimated trop. param.	ZTD+Grad	ZTD+Grad	ZTD+Grad
Ambiguity Resolution	Fixed	Float	Float

Table 1: Main processing options used in the different ASI/CGS contributions to GNSS meteorology. For more details see [3] and [4]

The postprocessing GNSS data reduction (ASIP) is performed on a daily basis, in a fully automatic way, with 2-week latency. The analysis is carried out by using GIPSY-OASIS II package and precise point positioning approach [4], and fixing Jet Propulsion Laboratory (JPL) fiducial-free satellite orbits, clocks and earth orientation parameters. ZTDs estimated with a sampling rate of 5 min are averaged over 15 min and converted into a standard meteorological data format. The main goal of the postprocessed solution is to provide both ZTD estimates for climate applications and station coordinates, which will be fixed, in the meteorological solutions when enough accuracy is reached. The accuracy of ASIP solution, using the most updated ancillary products and the most complete set of GNSS data, has been assessed during the decadal participation to the GNSS Meteorology projects: cross-comparison with radiosonde and independent measurements (e.g. VLBI ZTD) and consequent parameter fine-tuning in the GNSS processing have been continuously performed to obtain a reference product of the highest accuracy able to support climatology studies [1].

The existence of more than 15 years of observations from permanent GNSS stations worldwide together with reprocessing effort in the IGS and EUREF framework will provide an homogeneous database for monitoring trends and variability in atmospheric water vapour. See for example ZTD time series of PPP solution and RS for CAGL station in the sub-period Jan 2008 – May 2013 (

Fig. 2).

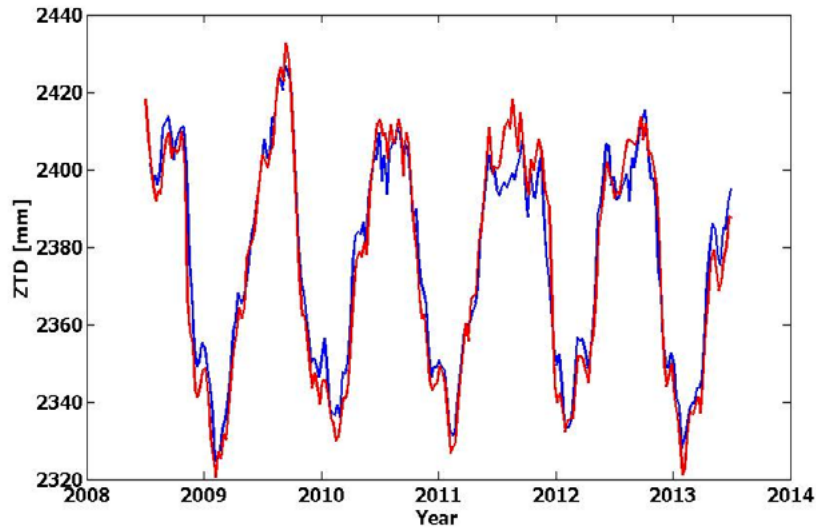


Fig. 2: ZTD time series of PPP solutions (blu) and RS (red) for GAGL station for period Jan2008-May2013

To produce Near Real Time solution, GIPSY-OASIS II software is used for data reduction with a standard technique of network adjustment. The combination of Near Real Time ZTD, instead, is a good tool for detecting problems in data processing and providing a reliable quality indicator for each contributing solution. The accuracy of ASI_ (Near Real Time) and ASIC (Combined Near Real Time) solutions, products designed for weather prediction applications requiring low latency, has been assessed comparing the estimated ZTD values w.r.t. radiosonde data for 4-y period (July 2008-July 2012), Fig. 3.

The combined product compares batter than the individual solution ASI_ upon which the combination is based [2].

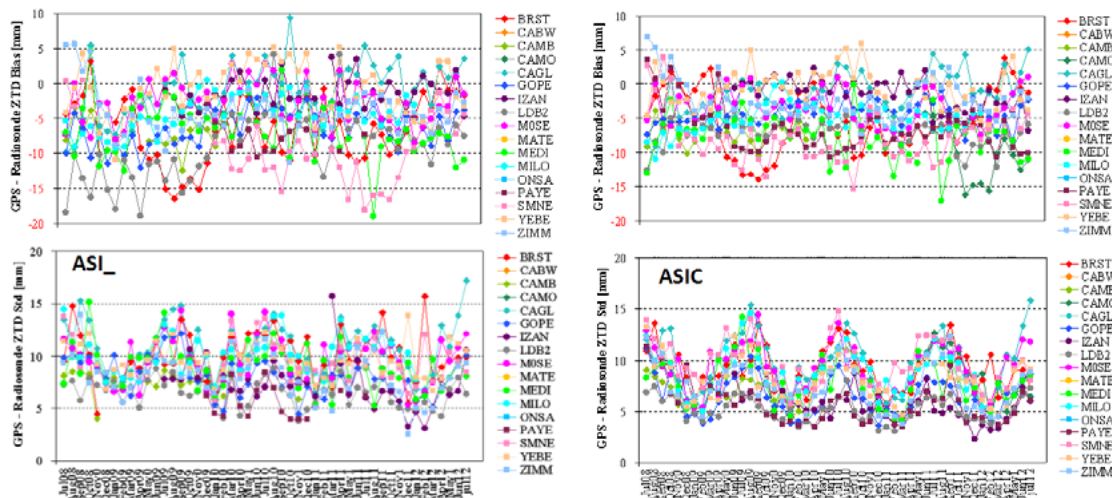


Fig. 3: ASI_ (left) and ASIC (right) comparisons w.r.t. radiosonde data

Sub-hourly PPP solutions are based on IGS Real Time products, available through the IGS Real-Time Service (RTS, <http://rts.igs.org>), and on observations streamed in RT from various NTRIP broadcasters properly converted into RINEX format.

Sub-hourly PPP solutions are assessed against IGS tropospheric solutions (Fig. 4). In the considered period, the overall bias and std are respectively at 1mm and 5mm level. Outliers occur at the same time stamps for all the stations, indicating a potential problem in the RT products used.

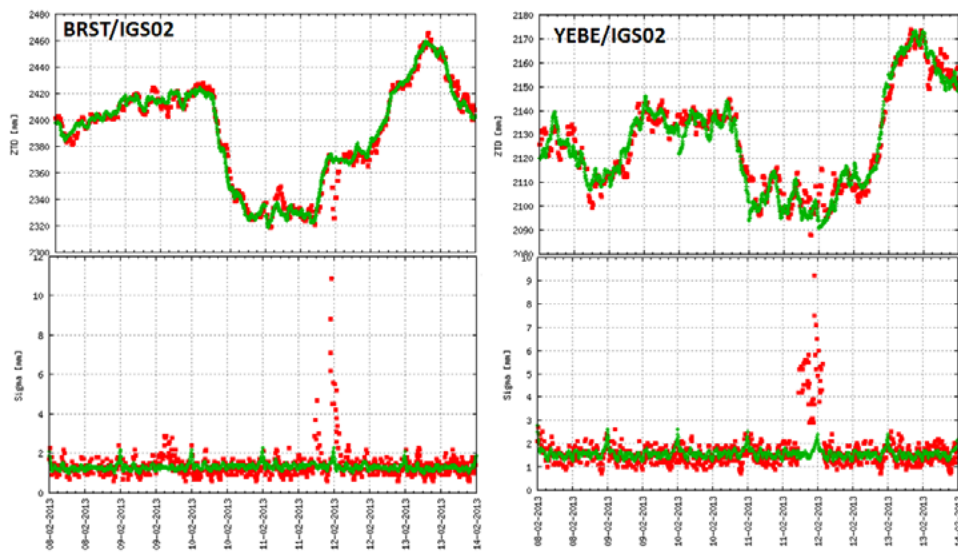


Fig. 4: ZTD time series (top) and related sigmas (bottom) of Sub-hourly PPP solutions (red) and IGS tropospheric solutions (green) for BRST and YEBE for the period February, 08-14, 2013

4. EUROPEAN INTEGRATED WATER VAPOUR FIELD

The GPS-ZTD NRT data stream is used to create a IWV field over Europe, which can be shown as animated time sequences, enabling the forecasters to see IWV time evolution.

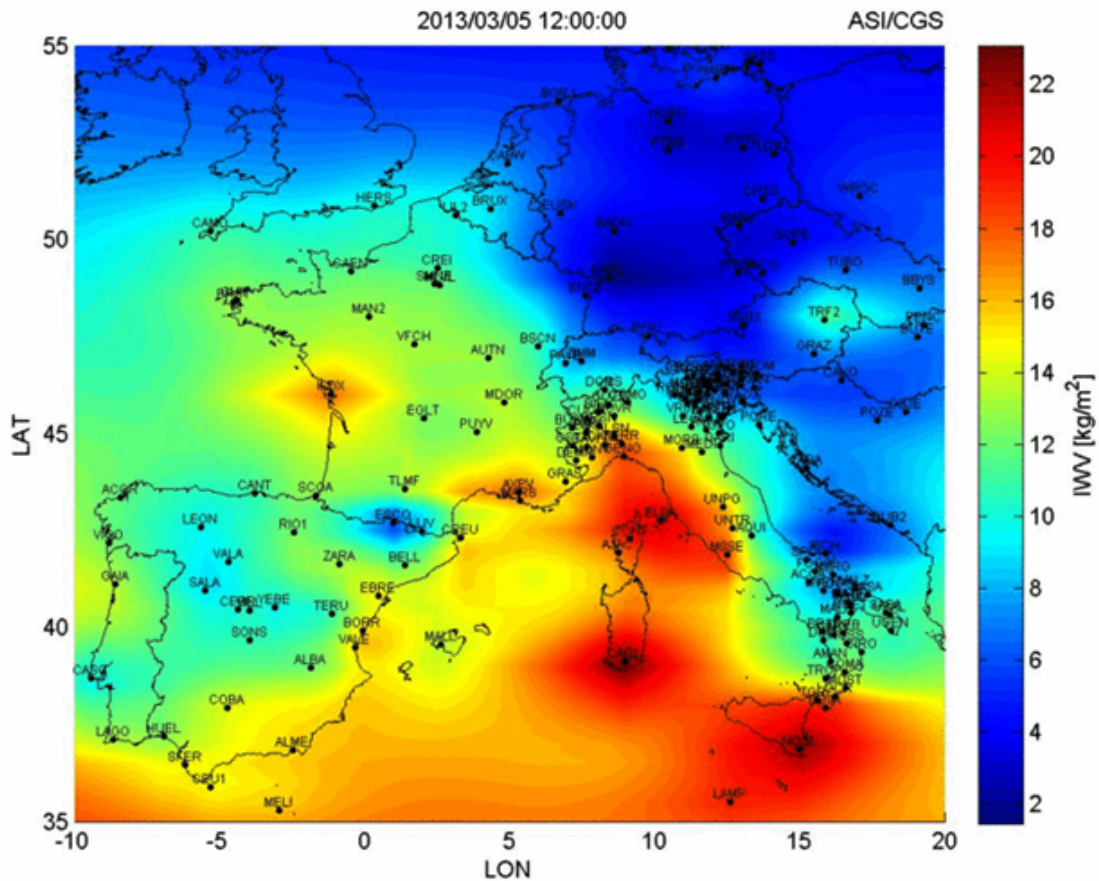


Fig. 5: IWV field Available at http://geodaf.mt.asi.it/ad_ATM_IWV_pub.php

5. FUTURE DIRECTION

ASI/CGS GNSS-Met activities in support of NWP applications, nowcasting and forecasting of severe weather events and climate monitoring will continue in the framework of E-GVAP phase III and of the EU COST Action ES1206 “Advanced Global Navigation Satellite Systems tropospheric products for monitoring Severe Weather Events and Climate” (GNSS4SWEC).

6. ACKNOWLEDGMENTS

This work has been carried out under ASI contract I-014-10-0.

7. REFERENCES

- Pacione R. & Vespe F. (2003), *GPS Zenith Total Delay Estimation in the Mediterranean Area for Climatological and Meteorological Applications*, Journal of Atmospheric and Oceanic Technology, Vol. 20, pp. 1034-1042. (1)
- Pacione R., Pace B., Vedel H., de Haan S., Lanotte R. & Vespe F. (2011), *Combination methods of tropospheric time series*, Advances in Space Research, Vol. 47, pp. 323-335. (2)
- Webb F.H., & Zumberge J.F. (1997), *An introduction to GIPSY/OASIS II*, Jet Propulsion Laboratory Rep. JPL D-11088. (3)
- Zumberge J.F., Heflin, M.B., Jefferson D.C., Watkins M.M. & Webb F.H. (1997), *Precise point positioning for the efficient and robust analysis of GPS data from large networks*, J. Geophys. Res., Vol. 102, pp. 5005-5017. (4)

Study of aerosol - water vapor - clouds interaction at CNR-IMAA Atmospheric Observatory

Madonna F.^{1*}, Rosoldi M.¹, Pappalardo G.¹

*Consiglio Nazionale delle Ricerche, Istituto di Metodologie per l'Analisi Ambientale (CNR-IMAA),
Potenza, Italy*

**Corresponding author: fabio.madonna@imaa.cnr.it*

Abstract

Observations of aerosol and clouds are of crucial importance to understand the weather-climate system. In this work, two examples of the studies related to aerosol - water vapor - clouds interaction carried out at CNR-IMAA Atmospheric Observatory (CIAO), in Potenza, Italy, are briefly discussed. CIAO provides quality controlled vertical profiles of aerosol and cloud properties using active and passive techniques, like multi-wavelength lidar, microwave radiometer and polarimetric radar measurements performed at CIAO. The first example aims at studying the hygroscopic growth of aerosols by means of the aerosol humidification factor; the second shows a possible approach to study the region where droplets are activated below the base of a thin cloud. Both these studies aim at showing the benefit of the use of ground-based measurements to characterize aerosol - water vapor - clouds interaction.

Keywords: *Aerosol, water vapor, clouds, ground-based remote sensing*



1. INTRODUCTION

The study of the hygroscopic growth of aerosols is challenging because of the variety and complexity of the aerosol population to be investigated. This is further complicated because of the mixing process involving different aerosol types. However, several studies have already proven the importance of aerosol hygroscopic growth on the Earth's radiative balance. Nevertheless, the existing parameterizations are still not sufficient to accurately determine the radiative forcing type (positive or negative).

Aerosol processes are strongly linked to water vapor and cloud feedback mechanisms, that is a crucial topic for Global Climate Models (GCMs). Despite the importance of these feedback mechanisms, a comprehensive picture of the impact of water vapor feedback on both externally forced and internally generated climate variations is lacking.

Long term observations of aerosol and clouds are of crucial importance to understand the weather-climate system. Space-based measurements allow us to obtain global spatial coverage but ground-based measurements are necessary for satellite calibration and validation as well as for process study. Ground-based remote sensing techniques are able to provide quality-controlled vertical profiles of atmospheric key variables over the long-term and to monitor parameters or processes that, at present, cannot be studied from space observations. For example, the study of the interactions between aerosol properties and tropospheric water vapor [1] or the study of droplet activation in thin liquid water cloud [2], relevant for both weather and climate studies, are challenging for satellite passive sensors.

2. RESULTS

In this section, two examples of the studies currently carried out at CIAO (the CNR-IMAA Atmospheric Observatory located in Tito Scalo, Potenza, Southern Italy, on the Apennine mountains (40.60 N, 15.72 E, 760ma.s.l.) for the characterization of aerosol - water vapor - clouds interaction are reported.

The first example shows the behavior of the aerosol humidification factor $f(\text{RH})$ during a Saharan dust outbreak over the Mediterranean basin observed at CIAO on 28/05/2008. Though Saharan dusts have a mineral origin, many papers in literature have already described their potential hygroscopic power [3]. In Figure 1 (left panel), the 1064 nm aerosol backscattering coefficient time series observed from 19:19

to 21:30 UTC on 28/05/2008 are reported. These products are obtained with PEARL (Potenza EARlinet Raman Lidar) advanced Raman lidar. The vertical resolution of the 1064 nm aerosol backscattering coefficient is 60 m with a temporal resolution of 10 minutes. In Figure 1 (right panel), the humidification factor $f(\text{RH})$ calculated in terms of the aerosol optical depth is also reported for the layer observed between 3 and 4 km a.g.l. in the period from 19:17 UTC to 21:45 UTC the plot shows that the relative humidity increases from about 22 % to 42 % when the aerosol optical depth increases from 0.09 to 0.12.

The estimation of $f(\text{RH})$ over two years of CIAO data is ongoing. This will allow us to better understand the nucleation mechanisms occurring in the region close to cloud base.

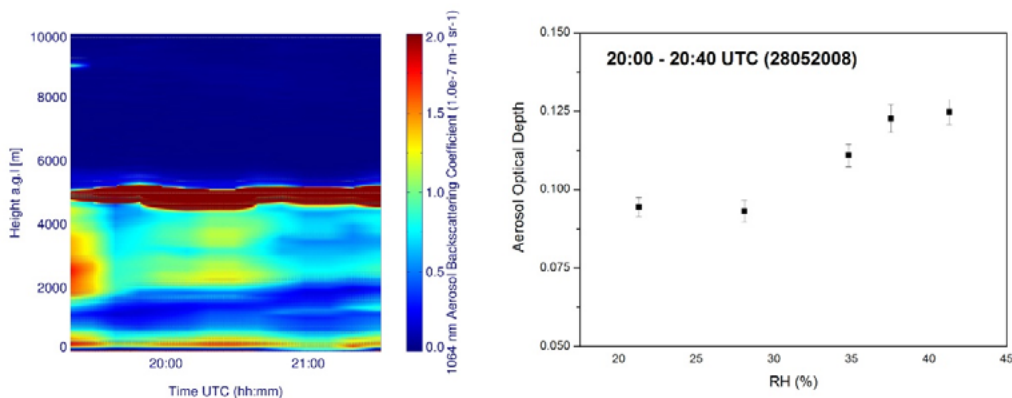


Fig. 1: (left panel) 1064 nm aerosol backscattering coefficient time series observed from 19:19 to 21:30 UTC on 28/05/2008 obtained with PEARL advanced Raman lidar; (right panel) humidification factor $f(\text{RH})$ calculated in terms of the aerosol optical depth related to the layer observed between 3 and 4 km a.g.l. from 19:17 UTC to 21:45 UTC.

At CIAO, an attempt to assess the behavior of thin clouds properties is also ongoing. Particular attention has been devoted to optically thin broken stratocumulus, where it is possible to investigate droplet activation.

Aerosol particles may be activated into droplets when in a rising air mass super-saturation conditions are reached. Cloud droplet activation is a highly complex and nonlinear process: only a fraction of particles can grow beyond the critical sizes to form droplets, depending on several factors [4].

From the ground-based remote sensing point of view the possibility of investigating this process is related to the capability of instruments to provide accurate estimation of aerosol and clouds properties.

Thin clouds are a good target for the study these processes. Measurements performed with the Multi-wavelength System for Aerosol (MUSA), operative at CIAO [5], on 4 August 2011 from 19:22 to 21:15 UTC show the presence of broken clouds between 3 km and 4 km of altitude above sea level (a.s.l.). The presence of broken clouds gives us the opportunity to calculate the vertical profiles of aerosol optical properties in two different ways: “with clouds”, by averaging all lidar signals and “without clouds” by skipping profiles showing the presence of clouds. Fig. 2 shows the vertical profiles of aerosol extinction coefficient at 532 nm with clouds (red line) and without clouds (black line), integrated over 17 minutes, from 19:33 to 19:50 UT (left panel) and over 99 minutes, from 19:33 to 21:16 UTC. The extinction profiles with and without clouds are overlapped up to an altitude of about 3.2 km a.s.l. In this region, aerosol particles do not nucleate. In the region above, the red profile (with clouds) rises significantly compared to the black one (without clouds) due to the formation of droplets. Therefore, the layer above 3.2 km up to 4.5 km a.s.l. may be considered as the region where aerosol particles are activated. These results seem to be confirmed by simultaneous and co-located water vapor profiles retrieved without clouds and with clouds using the Raman technique (not shown here). The discussed example shows how thin liquid water broken clouds allows us to identify the region where aerosol particles are activated and to correlate their properties with the atmospheric thermodynamic variables.

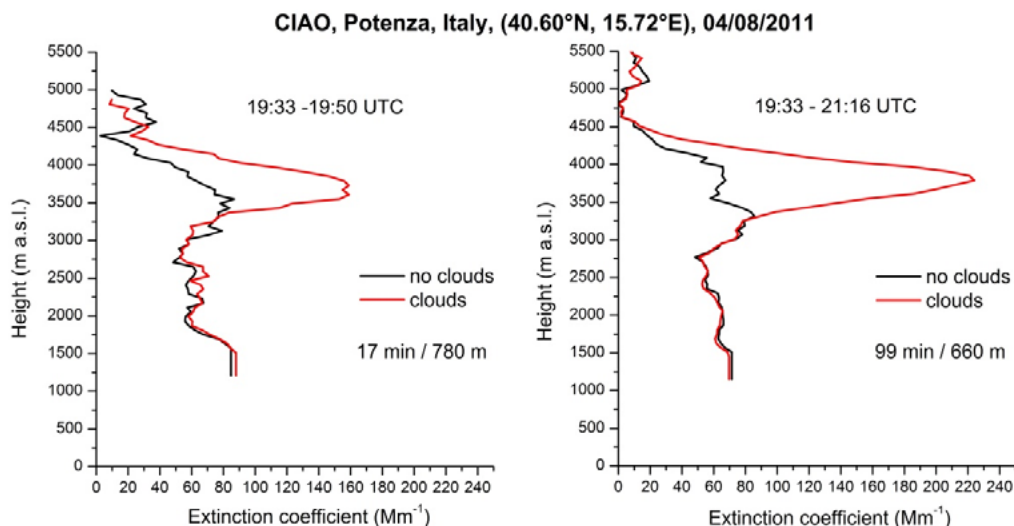


Fig. 2: (left panel) Vertical profiles of aerosol extinction coefficient at 532 nm with clouds (red line) and without clouds (black line) integrated over a time window of about 17 minutes, from 19:33 to 19:50 UTC. The black line indicates the processing over 17 minutes but skipping clouds: 17 files - 5 skipped files = 12 cloud free files. Both the profiles have a vertical resolution of 780m. (right panel) Vertical profiles of aerosol extinction coefficient at 532 nm with clouds (red line) and without clouds (black line) integrated over a time window of about 99 minutes, from 19:33 to 21:16 UT. The black line indicates the processing over 99 minutes but skipping clouds: 99 files - 40 skipped files = 59 cloud free files. Both the profiles have a vertical resolution of 660m.

3. ACKNOWLEDGEMENTS

The financial support for EARLINET by the European Union under grant RICA 025991 in the Sixth Framework Programme is gratefully acknowledged. Since 2011 EARLINET is integrated in the ACTRIS Research Infrastructure Project supported by the European Union Seventh Framework Programme (FP7/2007-2013) under grant agreement n. 262254.

4. REFERENCES

- Pahlow M., Feingold G., Jefferson A., Andrews E., Ogren J.A., Wang J., Lee Y.-N., Ferrare R.A., and Turner D.D. (2006), *Comparison between lidar and nephelometer measurements of aerosol hygroscopicity at the Southern Great Plains Atmospheric Radiation Measurement site*. J. Geophys. Res., 111, D05S15, doi:10.1029/2004JD005646. (1)
- Turner D. D., and Coauthors (2007), *Thin Liquid Water Clouds: Their Importance and Our Challenge*. Bull. Amer. Meteor. Soc., 88, 177–190. doi: <http://dx.doi.org/10.1175/BAMS-88-2-177> (2)
- Müller, D., Heinold B., Tesche M., Tegen I., Althausen D., Amiridis V., Amodeo A., Ansmann A., Arboledas L., Balis D., Comeron A., D'Amico G., Gerasopoulos E., Freudenthaler V., Giannakaki E., Heese B., Iarlori M., Mamouri R.E., Mona L., Papayannis A., Pappalardo G., Perrone R.-M., Pisani G., Rizi V., Sicard M., Spinelli N., Tafuro A. (2009), *EARLINET Observations of the 14–22-May Long-Range Dust Transport Event During SAMUM 2006*. Validation of Results From Dust Transport Modelling –Tellus, 61B, 325–339. (3)
- Ming Yi, Ramaswamy V., Donner Leo J., Phillips Vaughan T.J. (2006), *A New Parameterization of Cloud Droplet Activation Applicable to General Circulation Models*. J. Atmos. Sci., 63, 1348–1356, doi: <http://dx.doi.org/10.1175/JAS3686.1>. (4)
- Madonna F., Amodeo A., Boselli A., Cornacchia C., D'Amico G., Giunta A., Mona L., Pappalardo G., and Cuomo V. (2010), *CLAO: the CNR-IMAA advanced observatory for atmospheric research*, Atmos. Meas. Tech. Discuss., 3, 5253–5293, doi:10.5194/amtd-3-5253-2010. (5)

ACTRIS for coordinated long-term observation of aerosols, cloud-aerosol interactions, and trace gases in Europe

Pappalardo G.

*Consiglio Nazionale delle Ricerche, Istituto di Metodologie per l'Analisi Ambientale
(CNR-IMAA), Potenza, Italy*

**Corresponding author: gelsomina.pappalardo@imaa.cnr.it*

Abstract

Climate change is for a large part governed by atmospheric processes, in particular the interaction between radiation and atmospheric components (e.g. aerosols, clouds, greenhouse and trace gases). Some of these components are also those with adverse health effects influencing air quality. Strengthening the ground-based component of the Earth Observing System for these key atmospheric variables has been unambiguously asserted in the IPCC Fourth Assessment Report and Thematic Strategy on air pollution of the EU. However, a coordinated research infrastructure for these observations is presently lacking.

ACTRIS (Aerosols, Clouds and Trace gases Research InfraStructure Network) aims to fill this observational gap through the coordination of European ground-based network of stations equipped with advanced atmospheric probing instrumentation for aerosols, clouds and short-lived trace gases.

ACTRIS is a coordinated network that contributes: to provide long-term observational data relevant to climate and air quality research produced with standardized or comparable procedures; to support trans-national access to large infrastructures strengthening collaboration in and outside the EU and access to high quality information and services to the user communities; to develop new integration tools to fully exploit the use of atmospheric techniques at ground-based stations, in particular for the calibration/validation/integration of satellite sensors and for the improvement of global and regional-scale climate and air quality models. ACTRIS supports training of new users in particular young scientists in the field of atmospheric observations and promotes development of new technologies for atmospheric observation of aerosols, clouds and trace gases through close partnership with EU SMEs (Small and Medium Enterprises). ACTRIS will have the essential role to support integrated research actions in Europe for building the scientific knowledge required to support policy issues on air quality and climate change. **Keywords:** *Aerosol, clouds, trace gases, climate, observations*



ACTRIS (Aerosols, Clouds and Trace gases Research InfraStructure Network) is an outstanding research infrastructure launched in 2011 and will, for the first time, provide coordinated observations of the major atmospheric variables.

ACTRIS aims at integrating European ground-based stations equipped with advanced atmospheric probing instrumentation for aerosols, clouds and short-lived gas-phase species (Figure 1). ACTRIS will have the essential role to support building of new knowledge as well as policy issues on climate change, air quality and long-range transport of pollutants.

The main objectives of ACTRIS are:

- To provide long-term observational data relevant to climate and air quality research on the regional scale produced with standardized or comparable procedures throughout the network.
- To provide a coordinated framework to support trans-national access to large infrastructures (Figure 2) strengthening high-quality collaboration in and outside the EU and access to high-quality information and services for the user communities (research, environmental protection agencies, etc.).
- To develop new integration tools to fully exploit the use of multiple atmospheric techniques at ground-based stations, in particular for the calibration/validation/integration of satellite sensors and for the improvement of the parameterizations used in global and regional-scale climate and air quality models.
- To enhance training of new scientists and new users in particular students, young scientists, and scientists from eastern European and non-EU developing countries in the field of atmospheric observation.
- To promote development of new technologies for atmospheric observation of aerosols, clouds and trace gases through close partnership with EU SMEs.

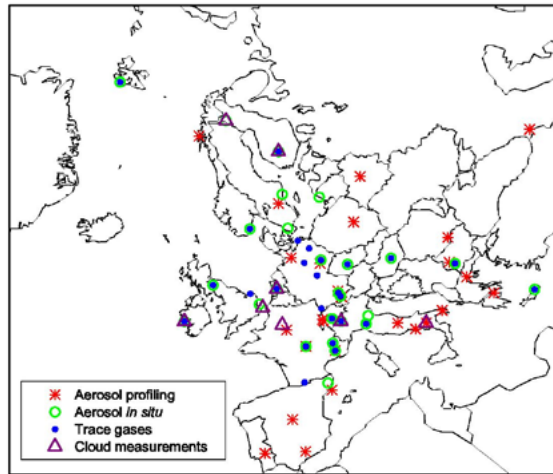


Fig. 1: Map of measurement sites contributing to ACTRIS



Fig. 2: ACTRIS sites offering Transnational Access

A key for ACTRIS success is to build a new research infrastructure on the basis of a consortium joining existing networks/observatories that are already providing consistent datasets of observations and that are performed using state-of-the-art measurement technology and data processing.

In particular the ACTRIS consortium merges two existing research infrastructures funded by the European Commission under FP6: EUSAAR (European Supersites for Atmospheric Aerosol

Research) and EARLINET (European Aerosol Research Lidar Network). ACTRIS also includes the distributed infrastructure on aerosol – cloud interaction existing from a previous EU Research project CLOUDNET and by grouping the existing EU ground-based monitoring capacity for short-lived trace gases which is, at present, not coordinated at any level, besides EMEP (European Monitoring and Evaluation Programme) and GAW (Global Atmosphere Watch) caring for a few specific compounds. Therefore, ACTRIS represents an unprecedented effort towards integration of a distributed network of ground-based stations, covering most climatic regions of Europe, and responding to a strong demand from the atmospheric research community. ACTRIS will be a step towards better integration of aerosol, cloud and trace gases communities in Europe necessary to match the integration of high-quality long-term observations of aerosol, clouds and short-lived gas-phase species and for assessing their impact on climate and environment. ACTRIS outcomes will be used for supporting decisions in a wide range of policy areas, including air quality but also health, international protocols and research requirements.

ACTRIS is organized in WPs (Work Packages) implemented as Networking Activities, Transnational Access and Service Activities, and Joint Research Activities as reported in Figure 3.

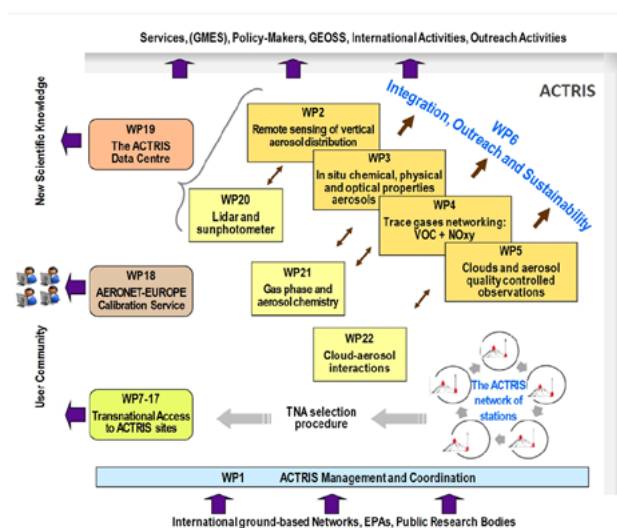


Fig. 3: Interdependence of activities and tasks within ACTRIS

The data provision structure in ACTRIS involves four networking activities (NAs) that will feed the data centre:

WP2: Remote sensing of vertical aerosol distribution

WP3: In-situ chemical, physical and optical properties of aerosols

WP4: Trace gases networking: Volatile organic carbon and nitrogen oxides

WP5: Clouds and aerosol quality-controlled observations

These networking activities are completed by a fifth networking activity aimed at integrating information from WP2-5 into a higher level of products required by users in the modelling and satellite-validation communities: WP6: Integration, outreach, and sustainability. This activity can be considered as the core of the research infrastructure, aiming at:

- technological and conceptual integration of the quality assured products delivered in the frame of the other networking activities,
- dialogue with end-users and dissemination of results,
- sustainability and development of a pan-European long-term monitoring network.

The activities of the research infrastructure will be oriented to a rigorous quality assurance program addressing both instruments and evaluation algorithms, and a standardized data exchange format. ACTRIS will also found and strongly sustain effective partnership between users and data providers and will pursue innovative initiatives to address the need of users. Moreover, standardization of procedures for the different measurement techniques and best practices across all stations and all European climatic regimes are paramount to facilitate the coordinated expansion of the network in a sustainable and efficient way.

Transnational access activities and service activities will enable users to conduct high-quality research by:

- Offering access to infrastructures with an excellent combination of instruments and expertise. This gives the opportunity to perform experiments using the state-of-art equipment in atmospheric research which could be used for measurement campaigns or instrument tests (WP7-17: Trans-National Access).

- Training a new generation of scientists. ACTRIS activities are aimed at enhancing the accessibility to the observatories and the exploitation of technical resources and knowledge. This is organized through WP6 and WP7-17.
- Offering to the whole scientific community the use of a unique sun photometer calibration facility currently operational in the frame of PHOTONS/AERONET. This is performed in WP18: AERONET-EUROPE Calibration Service.
- Enhancing access to information on advanced aerosols, clouds and trace gases high-quality data in Europe through a Service Activity (WP19: The ACTRIS Service Centre: Access to observations and service products of the infrastructure). The data centre integrates measurement data from the ACTRIS infrastructure and other highly relevant networks. In addition to free access to atmospheric high-quality data, the data centre will provide tools and applications for end users to facilitate the use of all measurements for broad user communities, offer a direct interface towards external users (e.g., MACC, GMES in-situ), and take into account the principles outlined in SEIS, INSPIRE, WIS and GEOSS [1, 2].

Joint research activities are:

WP20: Lidar and sunphotometer – Improved instruments, integrated observations and combined algorithms

WP21: Comprehensive gas phase and aerosol chemistry

WP22: A framework for cloud-aerosol interaction studies

These joint research activities are intended to support and promote the ACTRIS infrastructure by taking advantage of the synergistic effects of coordinating different observation capabilities. WP20 and WP22 address novel techniques and algorithms using a multi-sensor approach to improve observation performances and define new data products. WP21 focuses on investigating technological and methodological aspects of simultaneously networking real-time chemical composition of aerosols and trace gases. These JRAs are topically connected with networking activities and in cooperation with WP6 to ensure their results are assimilated for the whole ACTRIS infrastructure benefit.

At international level ACTRIS operates in strong cooperation with the Global Atmospheric Watch Program of the WMO, the ARM Climate Research Program [3] and all the relevant research networks

as (i.e. AERONET, GALION, NDACC, etc.) [4-5] for the establishment of the ground-based component of the Global Earth Observation System of Systems.

ACKNOWLEDGMENTS

The financial support by the European Commission contract no. 262254 is gratefully acknowledged.

REFERENCES

- GEOSS (2005), *Global Earth Observation System of Systems GEOSS*. 10-Year implementation plan reference document. Group on earth observations. Ed. by: B. Battrick. Noordwijk, ESA Publications Division (GEO 1000R). (1)
- WMO (2007a), *WMO Global Atmosphere Watch (GAW) strategic plan (2008–2015)*. Geneva, World Meteorological Organization (GAW report no. 172) (WMO TD No. 1384). (2)
- Report on U.S./European Workshop on Climate Change Challenges and Observations, prepared by the Climate and Environmental Sciences Division within the U.S. Department of Energy Office of Science, Office of Biological and Environmental Research, DOE/SC-0154, 33pp. Online: http://science.energy.gov/~media/ber/pdf/CESD_EUworkshop_report.pdf, 2013. (3)
- WMO (2007b), *Plan for the implementation of the GAW Aerosol Lidar Observation Network GALION* (Hamburg, Germany, 27 - 29 March 2007). Geneva, World Meteorological Organization (GAW Report no. 178) (WMO TD No. 1443). (4)
- WMO (2012), *Recommendations for a Composite Surface-Based Aerosol Network*, Emmetten, Switzerland, 28-29 April 2009, (GAW Report N. 207), November 2012. (5)

Space-borne measurements of carbon dioxide distribution: inverse modelling and data fusion techniques

Cortesi U.^{1*}, Del Bianco S.¹, M. Gai¹, L. Laurenza¹ and B. Carli¹

¹*Istituto di Fisica Applicata "Nello Carrara" del Consiglio Nazionale delle Ricerche (IFAC-CNR)*

*Corresponding author: u.cortesi@ifac.cnr.it

Abstract

Our research group investigated the capabilities of space-borne thermal infrared sounding to provide the accurate measurements of CO₂ distribution that are necessary to better constrain the inversion model of CO₂ surface fluxes and thus improve our knowledge of natural and anthropogenic sources and sinks of carbon dioxide. The study consisted in the implementation of a new wide band and multi-target inversion code for the retrieval of carbon dioxide total column from IASI/ MetOp-A measurements and in the application of the code, named KLIMA, to the analysis of IASI data from the period March 2010 - February 2011. The KLIMA-IASI XCO₂ retrieved values were subsequently compared with the operational XCO₂ products of the GOSAT mission retrieved from the SWIR measurements of the TANSO-FTS instrument.

The paper reports the major steps of the research activities conducted for the KLIMA-IASI study and describes the main outcome from the various phases of development of the retrieval code, processing of the IASI radiances and comparison of the retrieved XCO₂ values with corresponding products from the operational analysis of IASI by EUMETSAT and from TANSO-FTS on-board the GOSAT mission.

Future perspective are discussed in the conclusions for improvements of the KLIMA-IASI retrieval code and for further applications including exploitation of potential synergies between independent and complementary measurements of carbon dioxide in different spectral regions or using passive and active techniques.

Keywords: *Carbon dioxide, climate forcing, space-borne remote sensing, atmospheric radiative transfer modelling*



1. INTRODUCTION

Carbon dioxide is the most important radiative forcing agent among the long-lived greenhouse gases of the terrestrial atmosphere whose increasing concentration is the first driver of climate change [1].

Both natural and anthropogenic processes are responsible for carbon dioxide release into and uptake from the atmosphere, but the growing proportion of human activities since the end of the 18th century shifted the difference between sources and sinks of atmospheric carbon dioxide toward positive values. In the last two centuries, CO₂ concentrations have risen from the pre-industrial value of 280 ppm to the current level already exceeding 390 ppm [2]. Man-made emissions of carbon dioxide - mostly caused by burning of fossil fuel, cement manufacturing, deforestation and land use changes – established a trend of increasing values for the annual growth rate of atmospheric CO₂ [3], [4]. Also due to the weakening of the ocean sink from approximately 32% of anthropogenic emissions in 1960 to the current level of about 26% [5], this rate is now about 2 ppm/year [6].

The combined and integrated policies of adaptation and mitigation measures aimed at addressing the impact of climate change are tightly linked to the need for accurate knowledge of sources and sinks of atmospheric carbon dioxide by inverse modeling of atmospheric transport based on observations of CO₂ distribution on a regional to continental scale. This, in turn, requires the availability of measurements of CO₂ concentration with adequate spatial and temporal coverage provided by ground-based networks and, to a growing extent, by space-borne missions.

In principle, satellite observations of the global distribution of carbon dioxide in the terrestrial atmosphere can be obtained using either active or passive techniques, but at present the only space-borne payload in operation for CO₂ measurements is the one launched in January 2009 on the Japanese mission GOSAT (Greenhouse Gas Observing Satellite). The GOSAT platform embarks the TANSO (Thermal And Near infrared Sensor for carbon Observation) instrument, consisting of two components: a Fourier Transform Spectrometer (TANSO-FTS) and a Cloud and Aerosol Imager (TANSO-CAI). The TANSO-FTS instrument is a passive sounder with capability to observe the total amount and vertical distribution of atmospheric carbon dioxide in nadir viewing geometry, using either CO₂ absorption bands in reflected sunlight at Near Infrared (NIR) wavelengths (1.6 μm and 2.0 μm) or CO₂ emission bands in the Thermal Infrared (TIR) spectral region (4 μm and 15 μm). Reflected infrared measurements provide, in general, the best outcome for observation of CO₂ surface fluxes, due to their sensitivity to the lowermost layers of the atmosphere and to the fact that they are less affected

by temperature and water vapor interferences. Measurements in the TIR, with their best sensitivity to the mid-upper troposphere, do not penetrate the lower altitudes down to the surface, but provide a wider coverage, as they can be performed over water, without depending on the sun glint, and both at day and at night.

A new space-borne instrument, dedicated to monitoring of carbon dioxide in the NIR, the Orbiting Carbon Observatory (OCO-2), is planned to be launched in July 2014, whilst various satellite missions currently in orbit operate thermal infrared sounders that can provide data for the retrieval of CO₂ total column and vertical profile. These include AIRS (Atmospheric InfraRed Sounder) [7] and TES (Tropospheric Emission Spectrometer) [8] on the AURA mission and IASI (Infrared Atmospheric Sounding Interferometer) [9] on the MetOp satellite series. Active CO₂ remote sensing from space, based on the use of lidar systems, has been considered by ESA with the studies for the A-SCOPE (Advanced Space Carbon and Climate Observation of Planet Earth) mission [10] and by NASA that has planned the launch of ASCENDS (Active Sensing of CO₂ Emissions over Nights, Days and Seasons) [11] within 2016. Hungershoefer et al. [12] conducted a comparative evaluation of different observing systems for the global monitoring of CO₂ surface fluxes from space (AIRS, SCIAMACHY, GOSAT, OCO, A-SCOPE) and from ground-based networks, showing the potential of active instruments like A-SCOPE to provide the best information content of the satellite systems considered in the study

In this context, our research group at IFAC-CNR investigated the capabilities of thermal infrared nadir sounding to retrieve accurate information on the total column-averaged dry-air mole fractions of carbon dioxide (XCO₂), relying on the competence and expertise of the team in development and application of atmospheric radiative transfer models and inversion methods. We conducted a dedicated study, focusing on the adaptation and optimization of the KLIMA (Kyoto protocol Informed Management of the Adaptation) line-by-line radiative transfer algorithm into a non-operational retrieval code for inverse processing of IASI/MetOp-A radiances and for the retrieval of XCO₂ total column. The KLIMA-IASI retrieval code, integrated into the ESA-ESRIN Grid-Processing On-Demand system, was applied to bulk processing of a sub-set of IASI data in the year March 2010 – February 2011. We compared the XCO₂ retrieved values to the operational products of TANSO-FTS SWIR measurements from the GOSAT mission for the purpose of cross-validation.

In this paper, we report the activities conducted for the implementation of the retrieval tools and for the analysis of IASI data (Section 4); and we describe the main outcomes derived from the comparison between KLIMA-IASI and TANSO-FTS/GOSAT products (Section 5). In Section 6, as part of our conclusions, we briefly describe the perspectives for further development and application of the KLIMA inversion code and for the potential exploitation of the synergy between independent and complementary measurements of carbon dioxide concentration.

2. CARBON DIOXIDE RETRIEVAL FROM IASI RADIANCES USING THE KLIMA INVERSION CODE

The KLIMA-IASI project was carried out by IFAC-CNR with the contribution of IUP, University of Bremen, and supported by ESA-ESRIN under contract n. 21612/08/I-OL. The activities conducted by the IFAC-CNR team aimed to the adaptation and optimization of the KLIMA algorithm to the retrieval of carbon dioxide vertical distribution and columnar values from thermal infrared spectral radiances observed by the IASI spectrometer, on-board the MetOp-A satellite, and to the integration of this retrieval algorithm into the ESA Grid Processing On-Demand (G-POD).

For the retrieval, we used the KLIMA code, obtained by upgrading the algorithm employed for the analysis of REFIR-PAD (Radiation Explorer in the Far InfraRed-Prototype for Applications and Development) measurements [13], adapted in turn from the MARC (Millimetre-Wave Atmospheric Retrieval Code) code developed for the MARSHALS (Millimetre-wave Airborne Receiver for Spectroscopic CHaracterization of Atmospheric Limb-Sounding) study [14]. The KLIMA retrieval process, which performs an innovative wide band and multi-target analysis, was used in this study. The combination of these two features makes it possible to exploit for the retrieval all the measured spectral channels and to calculate, in a rigorous way, a retrieval error that also accounts for the errors of interfering parameters.

The forward model calculations of the KLIMA code was validated by comparing its synthetic spectra calculations with those of the LBLRTM (Line-By-Line Radiative Transfer Model) code [15]. In order to meet the requirements of the G-POD computing resources, and to operate a bulk processing of IASI data (program size not exceeding 1 Gbyte and running time aimed at processing with one processor the IASI central pixels of one orbit in less than one day), the computing time of the code was reduced by adopting some approximations which provide the best compromise between accuracy and computing

speed. Unfortunately, also considering the maximum program size requirements, a reduction of the analysed spectral range had to be adopted (with the choice of fitted spectral range equal to 645 - 800 cm^{-1}) and, accordingly, the retrieval error of the performed analysis is about twice the retrieval error that is theoretically possible with the analysis of the full spectral range. A large number of simulated retrievals with different spectral noise were performed, in order to verify that the bias caused by the approximations in the averaged retrieved value of XCO_2 is smaller than the accuracy requirement of 0.3%. A bias equal to 0.04% was observed in our tests. This bias can be further reduced using the known spectral errors to determine the Variance Covariance Matrix (VCM) of the forward model and adding this VCM to that of the spectral noise. However, it was decided not to implement this VCM in the first analysis and to postpone its use to when a better experimental understanding of the residuals is obtained. This reduction of the analysed spectral range caused an increasing of the retrieval error, which is about 6 ppm for a single retrieval. In the analysis performed with G-POD about 36 IASI measurements are needed to reach the required performances of an accuracy better than 0.3% (1 ppm out of 370 ppm) on regional scales ($1000 \times 1000 \text{ km}^2$) at monthly intervals (consistent with the required precision established by [16]). Therefore, considering the very large number of IASI measurements, the information that has been extracted from IASI using the new code on G-POD is a significant contribution to CO_2 studies, but remains a fraction (about one half in accuracy) of what can be provided by IASI.

A total of 240 000 IASI spectra, covering the period from March 2010 to February 2011, has been analysed on G-POD computing resources. Selection criteria were adopted that limited the analysis to the best measurements (clear sky, small slant angles, flat topography) and to a maximum of 20 000 spectra each month. To this purpose, only one week was considered each month and a reduced number of measurements were selected over the oceans. The number of analysed spectra is about 1% of the total number of useful spectra. Nevertheless, the collected information is extensive: indeed the G-POD analysis made possible the acquisition of a large amount of data with good geographical and time distributions, which provides a very important starting point for the assessment of problems and capabilities. An example of the attained coverage and quality is given in Figure 1 where the global map of XCO_2 averaged over the full year on a grid of $2^\circ \times 2^\circ$ pixels is shown. Data (even if not yet validated) show a geographical variability that can be reasonably ascribed to the dynamic of the carbon cycle together with some scattered points that seem to be outliers. In the monthly averages, plotted over the same grid (not shown here), we observe rather uniform fields over the oceans and a large variability

with time and location over land, even if the monthly variable sampling makes it difficult to identify any meaningful time variation and the reduced statistics highlights the presence of relatively large errors at high latitudes.

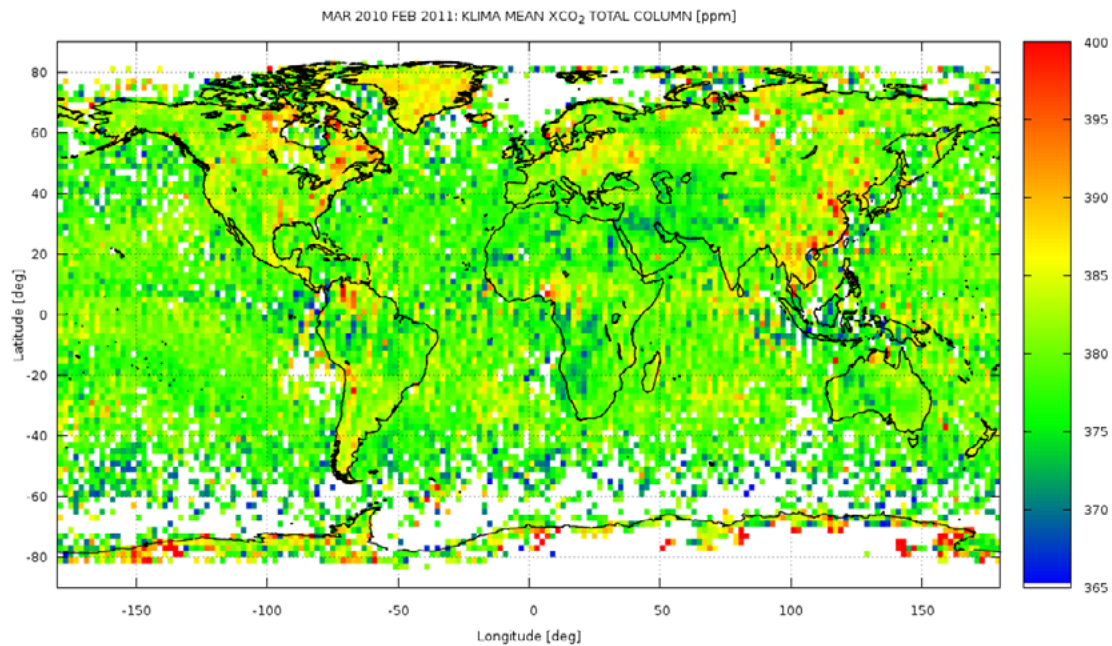


Fig. 1: Global map of XCO₂ retrieved from IASI data using the KLIMA code and yearly averaged over a 2°×2° grid

3. COMPARISON

The comparison of the XCO₂ retrieval performed in the framework of the KLIMA-IASI study with the other existing measurements is made difficult by the small range of the observed values, which is comparable with the measurement error of single observations. On the other hand, averages can be affected by time and space variability that may be present in some locations (especially over land).

A perfect coincidence in time and space exists with respect to data delivered by EUMETSAT together with the other operational products of IASI. However, these measurements, obtained with the retrieval method described by [9], are still experimental. We did not succeed in finding any significant correlation between KLIMA-IASI measurements and EUMETSAT operational products.

The inter-comparison activities of the XCO₂ total column retrieved from KLIMA-IASI with TANSO-FTS/GOSAT L2 SWIR Version 2 (V2) product have been performed in the annual range from March 2010 to February 2011 both for land and water observations. The data set of KLIMA and TANSO-

FTS comparison has a global coverage, but is limited to day observations, because TANSO-FTS does not measure during night.

We mainly focused on three different comparison strategies:

- the first strategy (or *co-located comparison*) consists in the comparison of the XCO₂ total column retrieved from IASI and TANSO-FTS observations made in contiguous locations in time and space;
- the second strategy (or *averaged comparison*) consists in the comparison of the XCO₂ total column averaged on a suitable spatial and time interval;
- the third strategy (or *seasonal variation comparison*) consists in the comparison of the seasonal variations on macro-areas (Northern/Southern Hemispheres and some restricted latitude bands).

Fig. 2 and Fig. 3 report the results in the case of co-located comparison and the comparison of seasonal variation over Northern Hemisphere. Fig. 2 shows the distribution of the differences between KLIMA and TANSO-FTS XCO₂ V2 products evaluated with a coincidence criterion equal to 100 km. Fig. 3 refers to the comparison of different XCO₂ season variations from KLIMA-IASI retrieved product (red points), TANSO-FTS data (blue points) and the EUMETSAT operational product (green points).

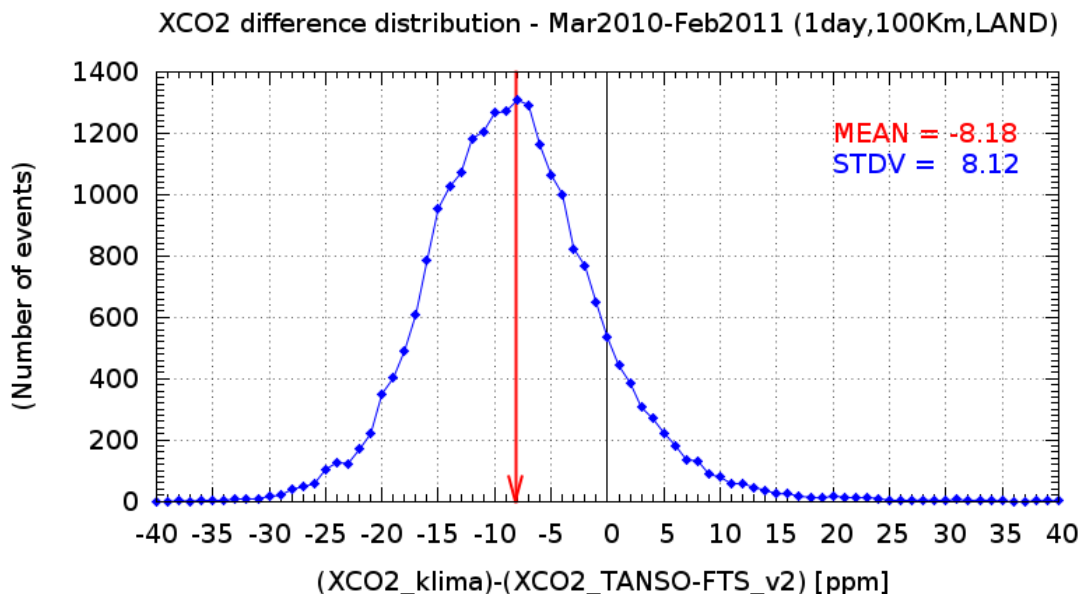


Fig. 2: Distribution of the differences between KLIMA and TANSO-FTS XCO₂ V2 products evaluated with a coincidence criterion equal to 100 km: case observation on land for the period from March 2010 to February 2011

The distribution of the differences between the two dataset shows a negative 8.18 ppm bias of KLIMA-IASI. This spread is much larger than the combined retrieval errors of the two experiments.

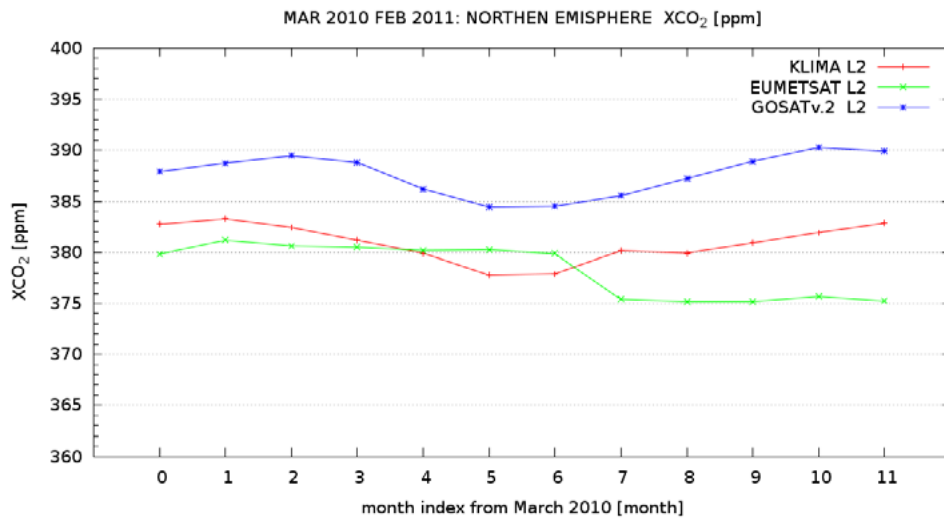


Fig. 3: Northern Hemisphere: seasonal variation of the XCO₂ from March 2010 to February 2011. The average on the Hemispheres of the XCO₂ retrieved by KLIMA-IASI (red points) is compared with the Hemisphere average of TANSO-FTS SWIR XCO₂ products (blue points) and with the seasonal variation of EUMETSAT operational product (green points)

For what concerns the comparison of seasonal trends, we can conclude that there is no evident correlation between KLIMA and EUMETSAT results, even if obtained from the same dataset. In absence of reliable information on the real atmosphere, it is difficult to identify the causes of this inconsistency. However, the larger variability of KLIMA results is often in the direction of the expected differences and seems to be more realistic than the uniform EUMETSAT results.

Afterwards another comparison between KLIMA-IASI and TANSO-FTS products is done by calculating yearly averages in some rather homogeneous geographical areas of $10^{\circ} \times 10^{\circ}$, over land and over ocean. An example of the obtained results is shown in Fig. 4 reporting the annual average related to the selected macro areas obtained from KLIMA-IASI (red) and TANSO-FTS (green). The standard deviation on the mean is also shown. In the bottom of the figure, we added the number of observations for each macro area. Over water the observations are statistically poorer, especially in the case of TANSO-FTS (in some cases the average values are obtained from a few samples and no TANSO-FTS observations are available in two areas). Despite the small number of samples, the behavior over water is consistent with what has been observed for co-located analysis: KLIMA values are significantly lower than TANSO-FTS ones. Apart the South America and over the oceans, the geographical variations agree with TANSO-FTS.

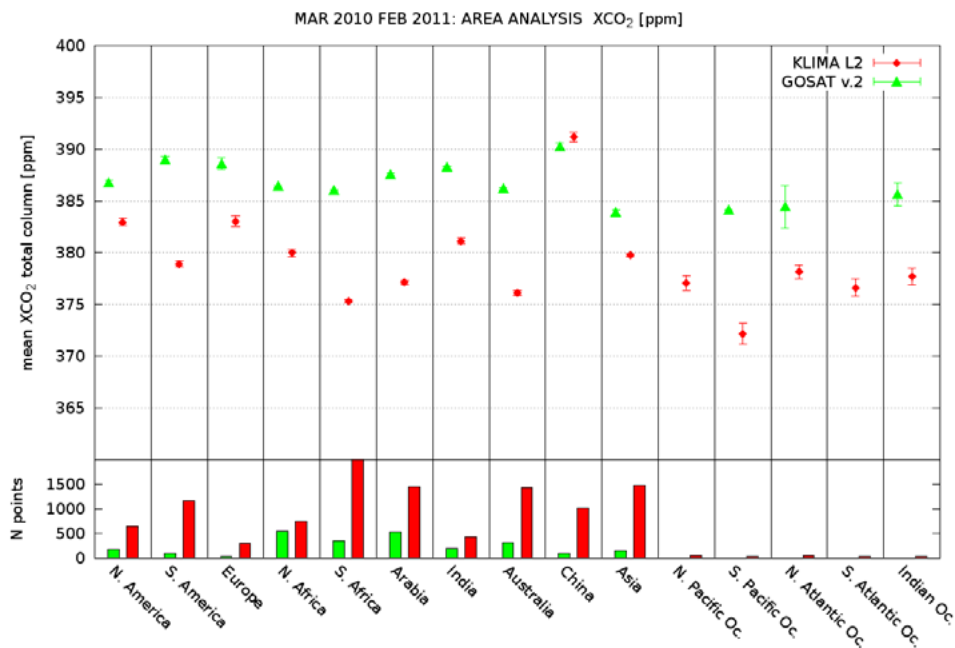


Fig. 4: Top: Average XCO₂ for selected macro areas of 10°×10°. Red points are KLIMA-IASI average XCO₂ while green points are TANSO-FTS products. Bottom: Number of observations for each macro a

4. CONCLUSIONS

We have presented the activities of a research study focusing on the retrieval of accurate information on the distribution of carbon dioxide in the Earth’s atmosphere from observations acquired by the nadir looking thermal infrared sounder IASI on-board the satellite platform MetOp-A. The main outcomes of the study include:

- the development of the KLIMA/ G-POD retrieval code, a wide band, multi-target inversion model capable to retrieve CO₂ total column from IASI radiances;
- the retrieval of total column-averaged dry-air mole fractions of carbon dioxide from the analysis of 240 000 IASI spectra from March 2010 to February 2011.
- the results of the comparison between KLIMA-IASI and GOSAT/TANSO-FTS XCO₂ retrieval products. These indicate that in general KLIMA-IASI and TANSO-FTS products are in a good agreement for land observations, as emerged from the comparison in Northern Hemisphere dominated by land measurements. Differences between the two products are more evident for

measurement on sea, as also confirmed by the co-located comparison. In conclusion, KLIMA-IASI results are quite promising, but further comparisons are necessary for a stringent validation.

Further research work can be envisaged at present for consolidating the outcome of the KLIMA-IASI data analysis and improving the results of the comparison with XCO₂ operational products of EUMETSAT-IASI and of TANSO-FTS/ GOSAT. This is necessary to meet the original objective of the study with cross-validation of KLIMA-IASI and TANSO-FTS XCO₂ measurements.

We also expect to obtain, as a result of the validation effort, an additional improvement in the performance of the KLIMA inversion model. Using G-POD computing resources and the collaboration with the G-POD team, the KLIMA code can become a valuable tool also for other application such as processing the data of the IASI instrument on MetOp-B, or retrieving other atmospheric trarget from IASI observation (e.g. CH₄ that is one of the primary short-lived climate forcers).

Finally, by combining the inverse modelling capabilities of KLIMA with innovative algorithms developed at IFAC-CNR for post-retrieval processing of remote-sounding observations, we plan to investigate the potential synergy of passive measurements of atmospheric carbon dioxide in the NIR and TIR spectral regions or, on a longer term, to test the combination of data acquired using active and passive techniques.

5. ACKNOWLEDGMENTS

This work was performed under the project "Sensitivity Analysis and Application of KLIMA algorithms to GOSAT and OCO validation" (ESA-ESRIN contract N. 21612/08/I-OL). IASI data are received through the EUMETSAT Unified Meteorological Archive and Retrieval Facility (UMARF). The authors wish to thank G-POD Team at ESA/ESRIN for their valuable effort and availability for the bulk processing of IASI data. TANSO-FTS L2 data were obtained from the GOSAT User Interface Gateway GUIG, operated by the National Institute for Environmental Studies (NIES)

6. REFERENCES

- IPCC (2007), *Climate Change 2007, Synthesis Report. Contribution of Working Groups I, II and III to the Fourth Assessment Report of the Intergovernmental Panel on Climate Change*. Geneva, Switzerland, 2007. (1)
- Conway T.P. Tans (2012), *Trends in Atmospheric Carbon Dioxide*, National Oceanic & Atmosphere Administration, Earth System Research Laboratory (NOAA/ESRL), (<http://www.esrl.noaa.gov/gmd/ccgg/trends/>). (2)
- Forster P., Ramaswamy V., Artaxo P., Berntsen T., Betts R., Fahey D.W., Haywood J., Lean J., Lowe D.C., Myhre G., Nganga J., Prinn R., Raga G., Schulz M., Van Dorland R. (2007), *Changes in atmospheric constituents and in radiative forcing. In Climate Change 2007: The Physical Science Basis. Contribution of Working Group I to the Fourth Assessment Report of the Intergovernmental Panel on Climate Change*, Solomon S., Quin D., Manning M., Chen Z., Marquis M., Averyt K.B., Tignor M., Miller H.L., Eds.; IPCC: Cambridge, U.K. and New York. (3)
- NOAA (2011), *The NOAA annual greenhouse gas index (AGGI)*. National Oceanic and Atmospheric Administration (NOAA) Earth System Research Laboratory Boulder, CO. <http://www.esrl.noaa.gov/gmd/aggi/> (accessed April 22, 2012). (4)
- Steffen W. (2010), *Observed trends in Earth System behavior*. WIREs Clim Change 2010, 1: 428-449. doi: 10.1002/wcc.36. (5)
- Blasing T.J. (2012), *Recent Greenhouse Gas Concentrations*. Oak Ridge National Laboratory Carbon Dioxide Information Analysis Center. DOI: 0.3334/CDIAC/atg.032. Oak Ridge, TN. http://cdiac.ornl.gov/pns/current_ghg.html (accessed April 22, 2012). (6)
- Beer R. (2006), *TES on the Aura mission: Scientific objectives, measurements and analysis overview*, IEEE Trans, Geosci. Remote Sens., 44(5), 1102–1105. (7)
- Engelen R.J., Serrar S., and Chevallier F. (2009), *Four-dimensional data assimilation of atmospheric CO₂ using AIRS observations*, J. Geophys. Res., 114, D03303, doi:10.1029/2008JD010739. (8)
- Crevoisier C., Chédin A., Scott N.A., Matsueda H., Machida T., and Armante R. (2009), *First year of upper tropospheric integrated content of CO₂ from LASI hyperspectral infrared observations*, Atmos. Chem. Phys., 9, 4797-4810. (9)

- Ingmann P. (2009), *A-SCOPE, Advanced space carbon and climate observation of planet earth, Report for Assessment, SP-1313/1*, ESA communication production office, Noordwijk, The Netherlands. (10)
- Abshire J. , Riris H., Allan G., Mao J., Wilson E., Stephen M., Sun X., Weaver C., Chen J. (2008), *Laser Sounder for Measurement of CO₂ Concentrations in the Troposphere for the ASCENDS Mission – Progress*, ESTO conference. (11)
- Hungerschofer K., Breon F.-M., Peylin P., Chevallier F., Rayner P., Klonecki A., Houweling S., Marshall J. (2010), *Evaluation of various observing systems for global monitoring of CO₂ surface fluxes*, *Atm. Chem. Phys.*, 10, 10503–10520. (12)
- Bianchini G., Carli B., Cortesi U., Del Bianco S., Gai M., and Palchetti L. (2008), *Test of far-infrared atmospheric spectroscopy using wide-band balloon-borne measurements of the upwelling radiance*, *JQRST*, 109, 6, 1030-1042. (13)
- Carli B., Bazzini G., Castelli E., Cecchi-Pestellini C., Del Bianco S., Dinelli B.M., Gai M., Magnani L., Ridolfi M., and Santurri L. (2007), *MARC: a code for the retrieval of atmospheric parameters from millimetre wave limb measurements*, *J. Quant. Spectrosc. Radiat. Transfer*, 105, 476-491. (14)
- Clough S.A., Shephard M.W., Mlawer E.J., Delamere J.S., Iacono M.J., Cady-Pereira K., Boukabara S., Brown P.D. (2005). *Atmospheric radiative transfer modeling: a summary of the AER codes*, *JQRST*, 91, 233-244. (15)
- Rayner P.J., and O'Brien D.M. (2001) *The utility of remotely sensed CO₂ concentration data in surface source inversions*, *Geophys. Res. Lett.*, 28, 1, 175-178. (16)

Time Series Analysis of Climatological Records from a High Altitude Observatory in Southern Italy (Montevergine, AV)

Capozzi V.¹, Budillon G.^{1*}

*Dipartimento di Scienze per l'Ambiente - Università degli Studi di Napoli "Parthenope"
Centro Direzionale, Napoli, Italy*

**Corresponding author: giorgio.budillon@uniparthenope.it*

Abstract

In this work we show the results obtained from the homogenization and the analysis of a climatic time series (mean temperature and total precipitation) collected in the Southern Italy Apennines (Montevergine, AV). This climatological time series is one of the oldest of Apennines mountains and it's very meaningful for the high altitude region climate study, being located at 1280 m asl (40° 56'N, 14° 43'E). The homogenization of time series is performed using the Standard Normal Homogeneity Test and its non-parametric version. Precipitation time series is characterized only by a discontinuity, occurred on 1950, while temperature time series is affected by multiple inhomogeneities, caused by changing in instruments location, human errors and instruments accuracy degradation. The analysis of homogenized time series is carried out through Wavelet Analysis, in order to investigate about series behavior in time-frequency spectrum, and LOWESS smoothing, aiming to highlight the decadal variability; moreover, we use a linear polynomial model to define trends. The results highlight an increase in annual mean temperature of 0.5°C/100 years and a decrease in annual total precipitation of 32%/100 years (-667 mm/100 years). Positive temperature trend is evident on all seasons, except on autumn, while negative precipitation tendency is particularly sharp on spring. The signals are characterized by a strong oscillation between 1940 and 1950 on 2-4 years period. The opposite trends that characterize temperature and precipitation are very steep from mid-1970s up to early 2000s; in this period the two parameters are strongly anti-correlated, unlike previous decades, in which they show an unstable coupling. Mediterranean Circulation Index (MCI) captures a large portion of precipitation variability, while thermal regime is strongly related to Eastern Mediterranean Pattern (EMP).

Keywords: *Climate Change, Temperature, Precipitation, Historical time series, High Altitude Climate*



1. INTRODUCTION

In recent years climate change issues have taken high resonance, motivating the scientific community to carry out multiple research activities in order to understand the complex mechanisms that regulate atmospheric variability. The Mediterranean area is characterized by a climatic context of great interest, being affected both by atmospheric dynamics typical of Western Europe and by dynamics typical of sub-tropical areas [1]. Therefore, it was decided to restore and enhance the acquired records of Montevergine's Observatory (AV), located at 1280 m asl (40°56'N, 14°43'E) on the western side of Campania Apennines. This climatological time series is one of the oldest of Apennines Mountains and it's very meaningful for the high-altitude regions climate; moreover, it is very representative of Central Mediterranean Climate. Montevergine's Observatory, founded in 1884 at the behest of Padre Francesco Denza, was treated by the alternation of monks, military and government institutions and actually is managed by the Benedictine Community of Montevergine's Abbey. From 1892 to 2007 weather observations were performed in a screen located outside a north-facing window of the highest floor of "meteorological tower", as suggested by Italian Central Office for Meteorology and Climate in 1879. Instead, from 2008 up to date the meteorological parameters are recorded by an Automatic Weather Station (AWS), installed on Observatory terrace. As often happens for this type of data, the original time series was recorded on paper and, consequently, required a huge main time to digitalize it. A sub data set of Montevergine's precipitation time series was examined for the first time in a study concerning the 1884:1987 period [2]. More recently, the seasonal and yearly anomalies and trends in temperature, total precipitation (rain and melted snow), atmospheric pressure and snowfall for the 1884:1960 period were analyzed in [3], that pointed out a slight positive trend in annual-mean temperature (+ 0.2 K/50 years) and a negative tendency for annual precipitation (- 50 mm/50 years). In this work we focus on the homogenization of time series, in order to detect abrupt changes of mean-level of climatic variables due to unnatural causes. After that we describe the variability and trends of mean-temperature and total precipitation (rain and melted snow) of whole time series (1884:2010); moreover, we analyze the relationships between Montevergine's climatological time series and large-scale atmospheric patterns.

2. MATERIAL AND METHODS

The data availability of main meteorological parameters recorded at Montevergine’s observatory is shown in Fig.1. Maximum Temperature, Minimum Temperature and Precipitation are the only parameters characterized by near continuous observations.

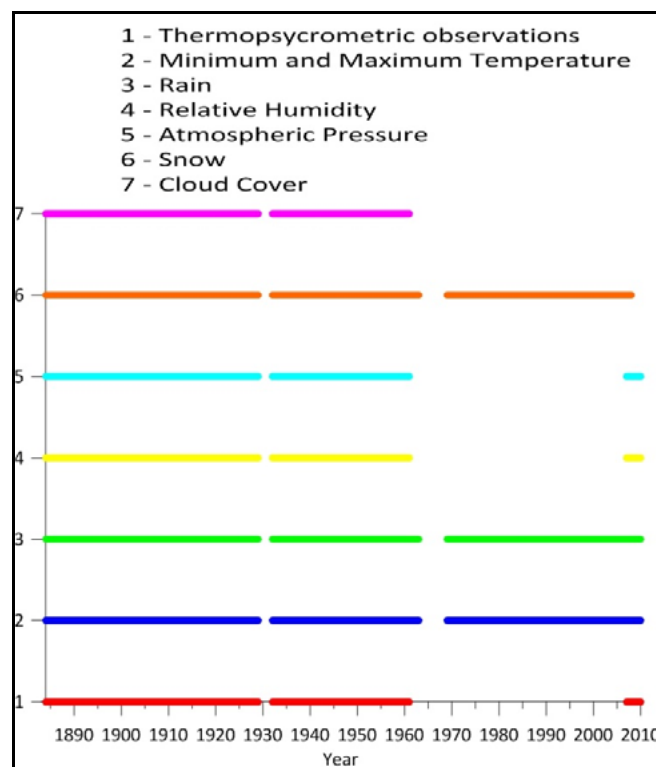


Fig. 1: Annual availability of meteorological parameters recorded at Montevergine’s Observatory in 1884:2010 period.

The homogenization of data-set was carried out adopting the Standard Normal Homogeneity Test [4], which allows to detect single shift in a climatological time series. This methodology requires the construction of a reference time series and the measure of correlation (ρ) between candidate station and reference stations. As suggested in [5], we compute correlation coefficients on the first difference series, dT/dt (where T is the climatological time series and t is time). The degree of likelihood that the candidate time series is homogeneous can be determined by applying a statistical test to the ratio (adopted for precipitation), or difference (adopted for temperature) series $\{Q_t\}$. The size and timing of significant non-homogeneities can also be estimated with statistical test [6]. Given the observed series

$\{z_1\}$ and the year in which the break occurs $\{a\}$, the two levels of the ratio or differences before and after the possible break are:

$$\bar{q}_1 = \sigma_q \bar{x}_1 + \bar{Q}$$

$$\bar{q}_2 = \sigma_q \bar{x}_2 + \bar{Q}$$

The data for the period $\{1 \dots a\}$ should be corrected by $\frac{z_2}{z_1}$ in the case of ratio and by $\bar{q}_2 - \bar{q}_1$ in the case of differences. The Standard Normal Homogeneity Test is based on the assumption that the data set is distributed according to a Gaussian. In some circumstances this assumption fails, so we decided to compare the Alexandersson's SNHT to a non-parametric version of SNHT, described in [7].

In order to investigate about the variability of climatological time series, we decomposed it into three components: trend, decadal and interannual component. The former was evaluated using a first-order polynomial model; we adopt the non-parametric Mann-Kendall method to test the statistical significance of trends. The second was determined from linear polynomial model residuals, using a LOWESS smoothing with a cut-off frequency of 10 years, while the latter is simply the difference between residuals and decadal component.

We used Wavelet Analysis [8] aiming to highlight the behavior of time series and to examine the relationships in time-frequency space between large-scale atmospheric patterns and Montevergine's data set. The Wavelet Analysis was developed as an alternative approach to the short time Fourier transform and it's very useful for geophysical time series examination. Most traditional mathematical methods that analyze periodicities in the frequency domain, such as Fourier analysis, have implicitly assumed that the underlying processes are stationary in time. Wavelet Transform expands time series into time-frequency space and can therefore find localized intermittent periodicities. Continuous Wavelet Transform (CWT) is the most commonly tool used for examining localized intermittent oscillations in a time series.

Moreover, Wavelet Analysis offers the possibility of examine whether regions in time-frequency space with large common power have a significant phase link and therefore are suggestive of cause-effect relationship between the time series. From two CWTs it's possible to construct the Cross Wavelet Transform (XWT), which shows their common power and relative phase in time-frequency space. We used also the Wavelet Coherence (WTC), in order to find significant coherence even though the common power is low.

3. HOMOGENIZATION OF THERMO-PRECIPIATION TIME SERIES

Homogenization of a time series is a fundamental step for a study concerning meteorological observations recovery. However, as remarked in [9], the discontinuity identification can sometimes arise from subjective evaluation and is strongly dependent on the philosophy adopted by researchers. Our approach is based on the comparison between the results derived from SNHT and metadata, which provides a valuable aid in discerning between true and false breaks. Moreover, we gave particular relevance to the comparison with time series collected in a climatic context similar to that in which candidate station is located and with climatological series more correlated with Montevergine one. Metadata were retrieved from meteorological registers and from an old diary called “*Le Cronache dell’Osservatorio*”. The construction of reference time series was performed using historical data-set and reanalysis output [10, 11, 12, 13, 14]. According to metadata and reference time series availability, in order to homogenize precipitation time series, the period we focus on was divided into five temporal segments (1884:1913, 1914:1943, 1944:1973, 1974:1999, 2000:2010). Because of the high spatial variability of rainfall, we used only stations located in a neighborhood of about 100 km. Precipitation time series shows only a discontinuity, which occurred on 1950, as highlighted by Fig.2. According to metadata, the observations seem to suffer of frequent changes of operators and of errors in pluviograph measurements. The results obtained through this analysis are in agreement with those found in [2], in which the precipitation data acquired in 1946-1950 period were considered unreliable. We corrected the data recorded in this period decreasing monthly rainfall amount of 15%.

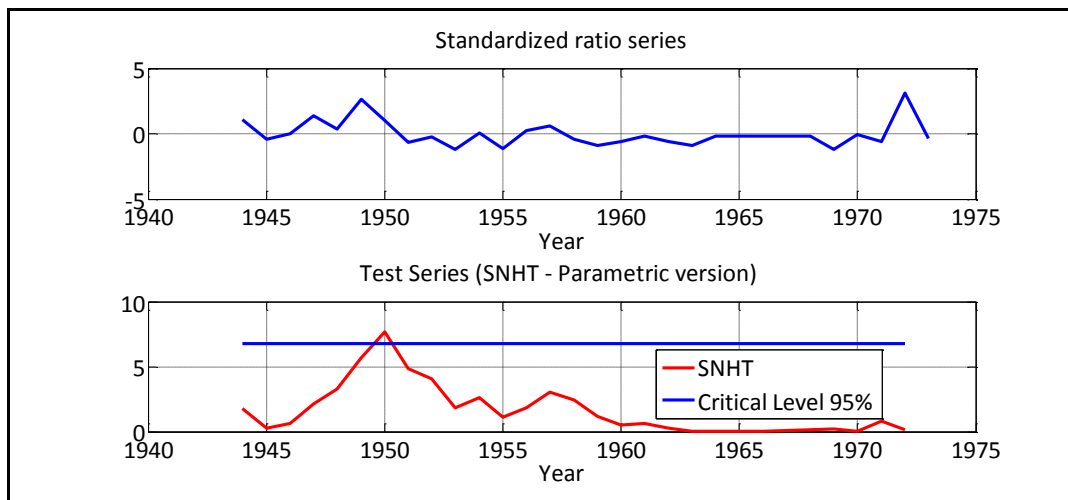


Fig. 2: Homogenization of Montevergine's precipitation time series. Standardized ratio time series and corresponding T-series for the non-parametric SNHT are shown. The 95 per cent critical level is indicated with a blue line.

Mean temperature (evaluated as the arithmetic average of max and min daily values) time series is characterized by several breaks, caused by various factors, such as instruments relocation, changes of observing practices, instruments accuracy degradation and human errors. The homogenization of data recorded in 1884:1961 period was carried out adopting mean temperature time series deriving from thermopshychrometric acquisitions as reference series. This approach required the homogenization of thermopshychrometric time series, which was performed using air-temperature at 850 mb level time series reconstructed by NOAA 20th Century Reanalysis. We constructed the reference series taking account the four grid points closest to the candidate time series, as highlighted by Fig.3a. The analysis shows a discontinuity on 1890 (Fig.3b), which was caused by the initial location of instruments, placed probably slight above the soil-level before the construction of meteorological tower. We correct monthly time series recorded in 1884:1890 period by a factor equal to +0.7°C. In the examined period precipitation time series don't shows any discontinuity and it is in a good agreement with the reference one. Therefore, instruments relocation seems to have affected only the temperature observations.

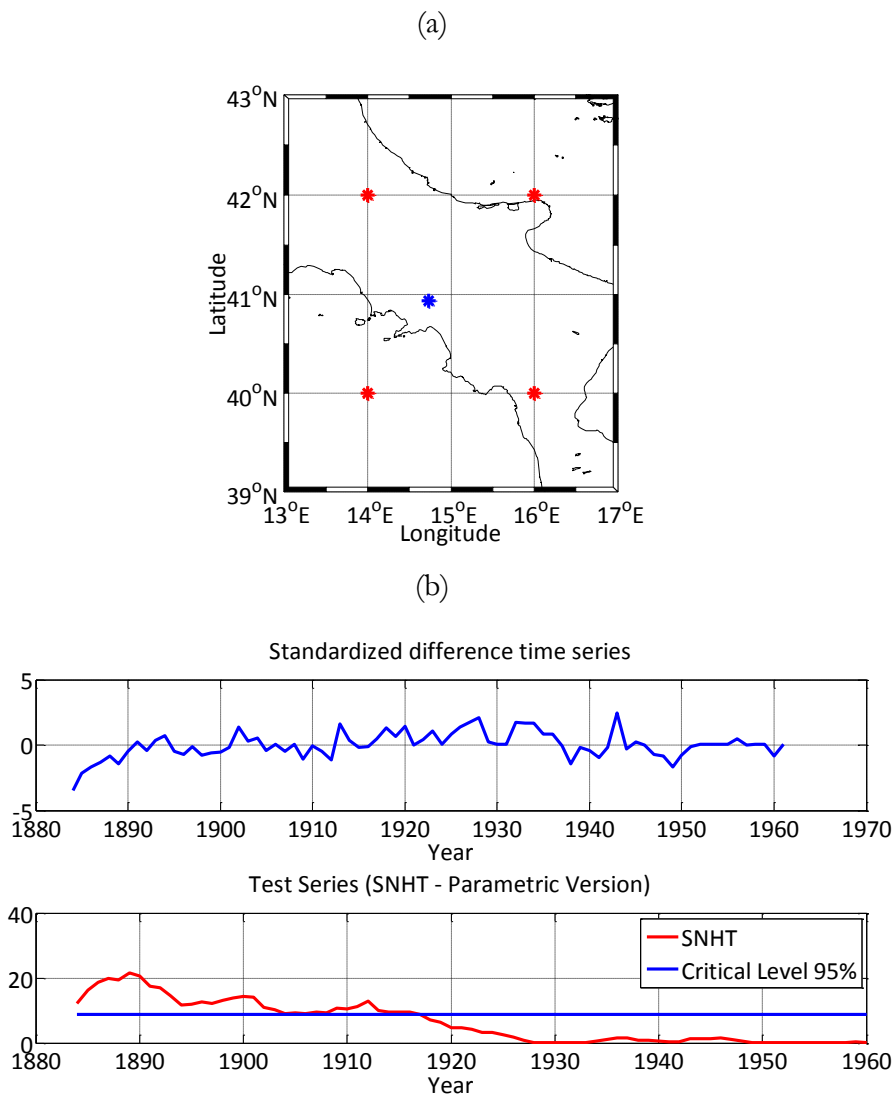


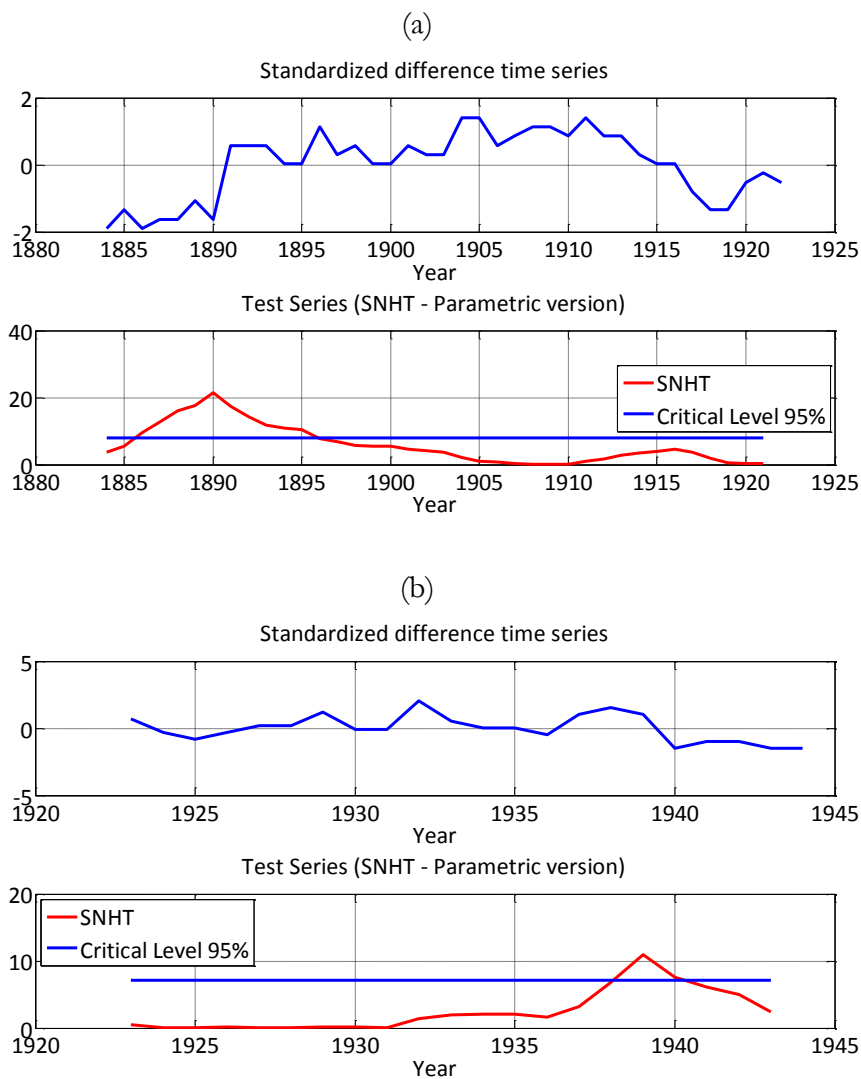
Fig. 3: Spatial location of candidate station (blue star) and of grid points (red stars) adopted for the homogenization of thermopscrometric time series (a). Homogenization of thermopscrometric time series. Standardized difference time series and corresponding T-series for the SNHT are shown. The 95 per cent critical level is indicated with a blue line (b).

The comparison between homogenized thermopscrometric time series and candidate time series showed initially only one significant discontinuity, which occurred on 1890. However, the subsequent subdivision of examined interval in three sub-periods (1884:1922, 1923:1944, 1945:1961) highlighted two further inhomogeneities, one on 1939 and the other on 1951 (Fig.4). The first break was caused by initial instruments location, while the other two, according to metadata, were probably caused by human errors and/or instruments accuracy degradation. The adjustment factors adopted to remove the

discontinuities, which emerged both in parametric and in non-parametric version of SNHT, are reported in Tab. 1.

Period	Correction Factor [°C]	Explanation
1884:1890	+0.7°C	Initial instruments location
1939:1944	+0.3°C	Human errors and/or instruments degradation
1946:1951	-0.8°C	Human errors and/or instruments degradation

Table 1: Correction factors applied for homogenization of 1884:1961 mean-temperature (average of max and min daily values) time series and possible causes of discontinuities.



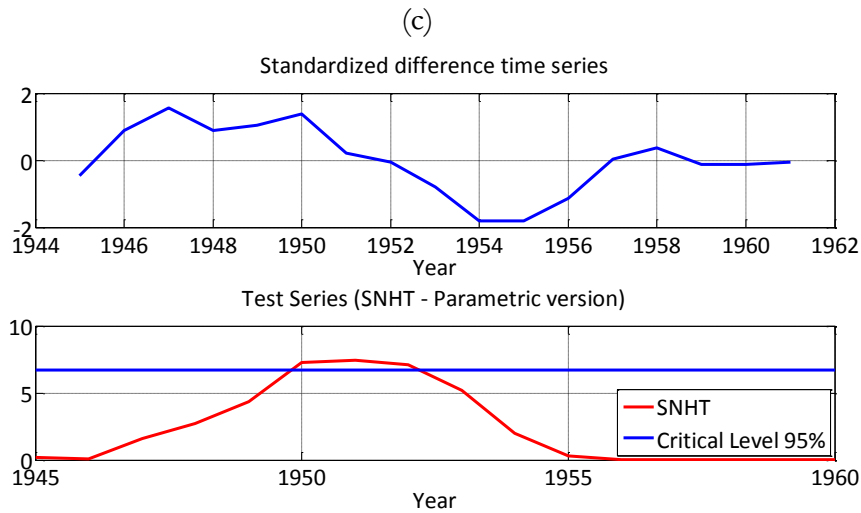


Fig. 4: Standardized difference time series and corresponding T-series for 1884:1922 temperature series homogenization (a), for 1923:1944 temperature time series homogenization (b) and for 1945-1961 temperature time series homogenization (c).

The homogenization of temperature observations acquired in 1974:2010 period was very critical and required additional analytic steps involving minimum and maximum temperature trends examination. As highlighted by Fig.5, average annual maximum temperature is characterized by an anomalous increase in 1999-2001 period, while average annual minimum temperature shows a significant decrease in 1995-1999 period. In the former case, it's reasonable to assume that observations quality was affected by human errors in maximum thermometer readings. In the latter case, the goodness of measurements is likely to have been affected by the accuracy degradation of instrument put into operation in 1989.

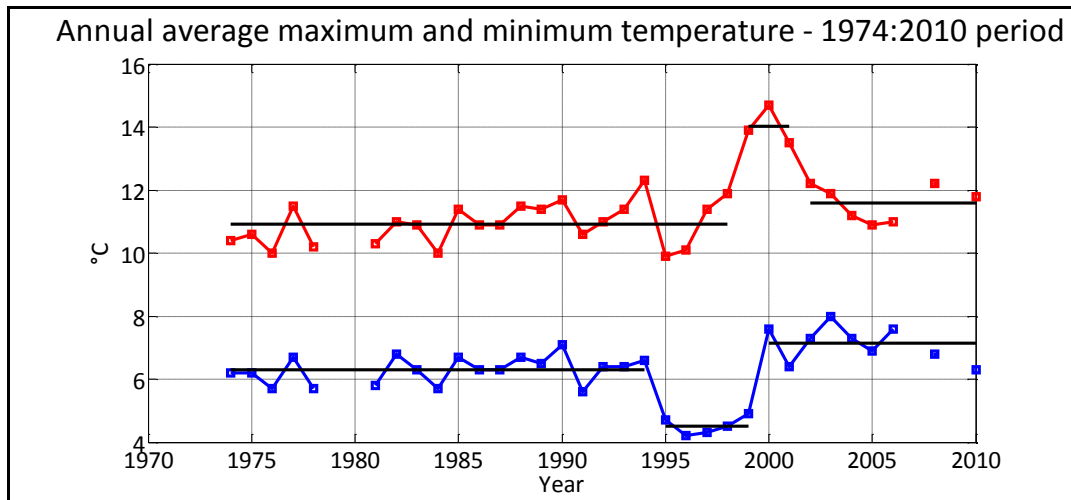


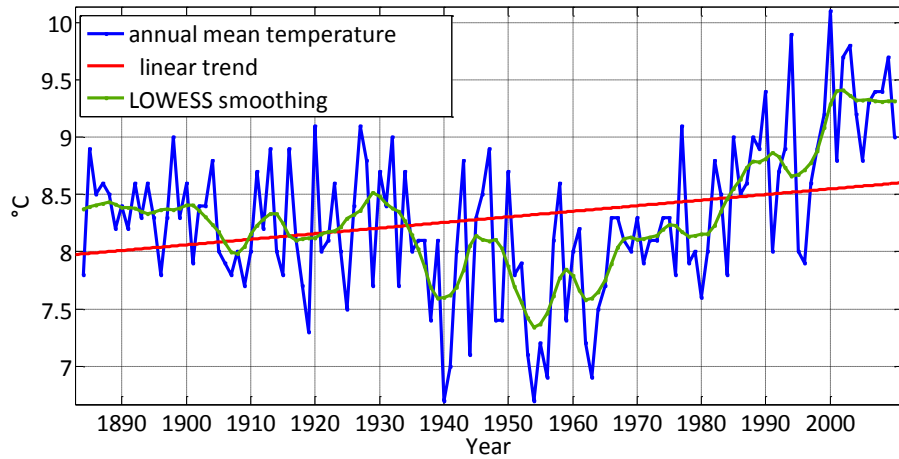
Fig. 5: Annual average of maximum (red) and minimum (blue) temperature in 1974:2010 period. For maximum temperature, black lines define the mean value for 1974-1998 period, for 1999-2001 period and for 2002-2010 period, while for minimum temperature they define the mean value for 1974-1994 period, for 1995-1999 period and for 2000-2010 period.

The different nature of discontinuities suggested us to adopt two distinct approaches for their removal. As regards as maximum temperature, we used a direct approach, correcting the data observed in 1999-2001 period according to the extension of the index of maximum thermometer “SIAP”, corresponding to 3.2°C. We tested subsequently the series homogeneity through the SNHT: the results obtained validated the correction procedure adopted. Regarding minimum temperature, a classical indirect approach was used: the SNHT highlighted a break in 1990, statistically significant only in its non-parametric version. In order to investigate about the presence of other inhomogeneities, we have split the series in two parts, one before (1974 – 1989) and one after (1991 – 2010) the possible break. We have identified a break in 1999 and we corrected the data acquired in the period December 1993 – March 2000 applying a correction factor of +1.1°C. The subsequent application of SNHT to the entire period (1974:2010) did not reveal any discontinuity.

4. YEARLY AND SEASONAL VARIABILITY AND TRENDS

Yearly variability analysis of homogenized climatological time series highlights statistically significant trends: for mean-temperature, we found an increase of $0.5^{\circ}\text{C}/100$ years, while for total precipitation we discovered a drop of $667\text{ mm}/100$ years ($-32\%/100$ years). These results show a partial agreement with those obtained in [9], where for whole Italian Peninsula a rise in mean-temperature of $1.0\text{ K}/100$ years (1863:2003 period) was found, and with those got in [15], where for Southern Italy a decrease in yearly rainfall of about $21\text{ mm}/10$ years (1916:2003 period) was discovered. As shown in Fig.6, mean-temperature is characterized by statistically significant oscillations between 1940 and 1950 and in 1920:1930 time intervals (period of $\approx 2\text{-}5$ years). Wavelet Analysis performed for total precipitation (Fig.7) points out multiple oscillations in high frequency region between 1900 and 1970 (period $\approx 1\text{-}6$ years). Instead in 1975:2010 period time-frequency spectrum shows a strong decrease in high frequencies energy and, therefore, a reduction of the interannual variability.

(a)



(b)

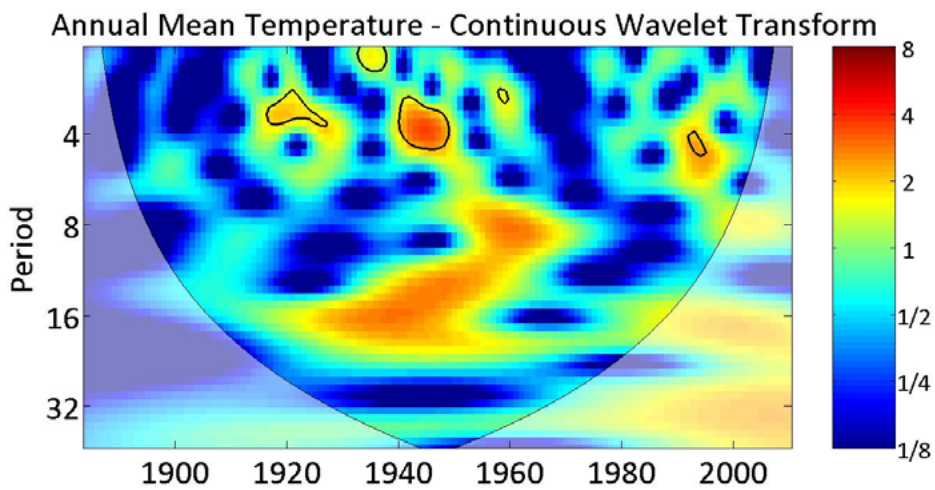


Fig. 6: Annual mean temperature recorded at Montevergine's observatory, with linear trend and LOWESS smoothing (a). Continuous Wavelet Transform of the signal (b).

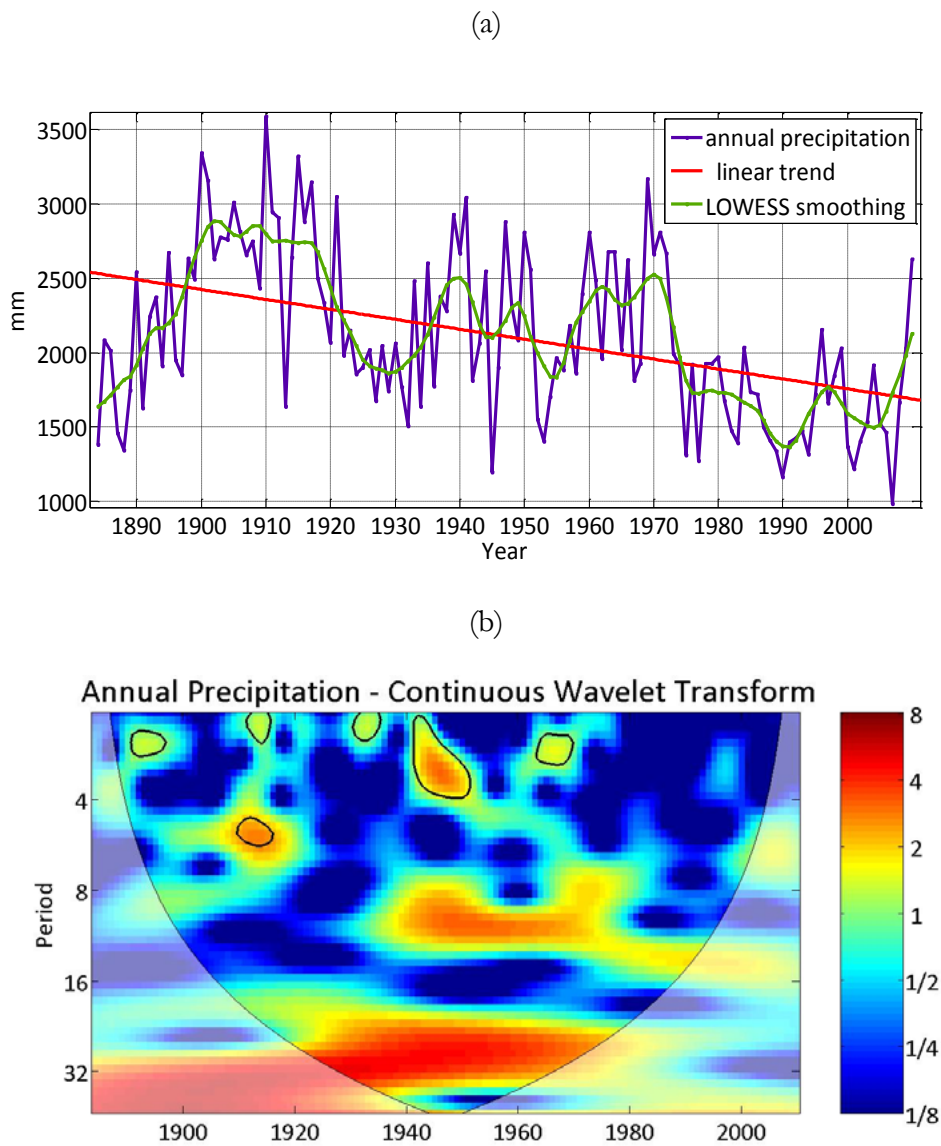


Fig. 7: Annual precipitation recorded at Montevergine’s observatory, with linear trend and LOWESS smoothing (a). Continuous Wavelet Transform of the signal (b).

The discovered trends are strongly influenced by anomalies in temperature and precipitation observed in the last three decades. In order to identify the pattern established between mid-1970s and 2000s, we correlated the first difference of the signals on five years step (Fig.8). During the period just mentioned, mean-temperature and total precipitation show a strong anti-correlation, whose magnitude and persistence have never been observed in previous decades, in which the two variables are characterized by an unstable coupling. As remarked in [16], Western Mediterranean’s climate shows a similar behavior in the last three decades.

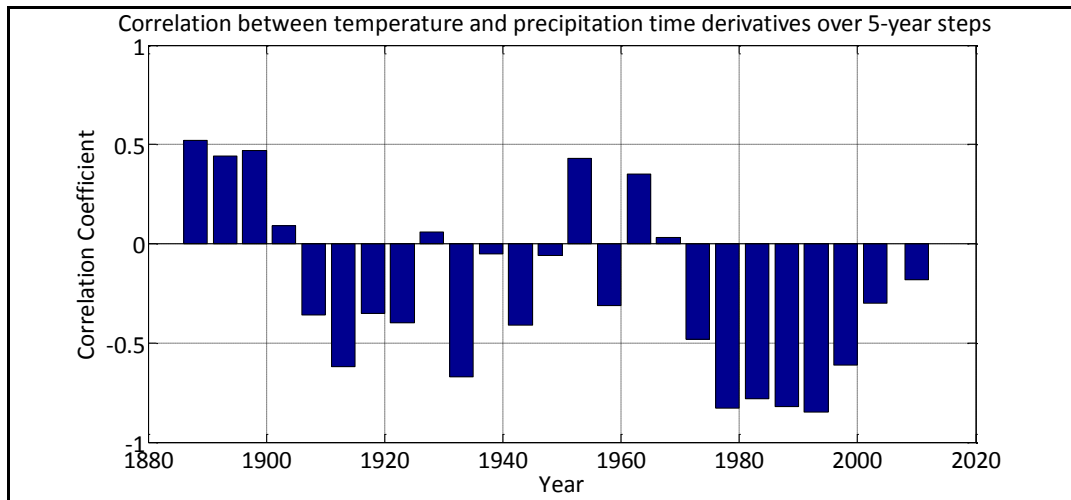


Fig. 8: Correlation between temperature and precipitation first time derivatives over 5-years step.

As regards as mean-temperature, seasonal variability analysis highlights a strong increase on winter, spring and summer, while no trend was detected on fall (Tab.2). Wavelet analysis performed for winter season shows high energy on multiple scales, although statistically significant oscillations were discovered only between 1930 and 1945 and in 1920:1930 periods. Spring CWT highlights a clear energy peak only between 1980 and 1990 (period \approx 1-4 years), while Wavelet Analysis of summer and fall variability points out high energy at high frequencies (period \approx 1-5 years) in 1900:1950 period. Regarding precipitation, we found strong negative trends on all seasons, particularly steep on spring (-41%/100 years) and on autumn (-32%/100 years). Seasonal Wavelet Analysis shows statistically significant oscillations in high frequencies regions (period \approx 1-6 years) between 1890 and 1970, while in the last three decades a strong energy reduction was observed.

Variable	Year	Winter	Spring	Summer	Fall
Temperature	+ 0.5°C/100 years	+ 0.8°C/100 years	+ 0.8°C/100 years	+ 0.7°C/100 years	+ 0.0°C/100 years
Precipitation	- 667mm/100 years	- 185 mm/100 years	- 218 mm/100 years	- 57 mm/100 years	- 217 mm/100 years

Tab. 2: Yearly and seasonal linear trend of temperature and precipitation observed in 1884:2010 period.

5. LARGE SCALE VARIABILITY CONNECTIONS

As remarked in [17], in order to understand local climate variability features, is necessary linking it to large-scale climate atmospheric phenomena. So, we have focused our study on the analysis of links between Montevergine's time series and atmospheric pattern better able to influence Mediterranean and Europe climate. We represent atmospheric circulation by five indices: the North Atlantic Oscillation index (NAO), defined as the difference between Lisbon and Stykkisholmur/Reykjavik normalized sea level pressure, the Mediterranean Circulation index (MCI), defined by the difference between Marseille and Jerusalem sea level pressure, the Western European Zonal Circulation Index (WEZCI), defined by Madrid + Barcelona and Trondheim + Lund surface pressure record, the Eastern Mediterranean Pattern (EMP), defined by the difference in geopotential height at 500 hPa between Northeastern Atlantic (52.5°N, 25°W) and the Eastern Mediterranean (32.5°N, 22.5°E), and the North Sea Caspian Pattern Index (NCPI), proposed by [18], which is calculated from the difference in the normalized 500 hPa geopotential between averages of North Sea (0°E, 55°N and 10°E, 55°N) and North Caspian (50°E, 45°N and 60°E, 45°N) centers of action. For NAO index we used data provided by NCEP/NCAR, while the other indices were reconstructed for the 1884:2010 period means of [14]. Montevergine's precipitation regime is largely influenced by Mediterranean atmospheric circulation, which is represented by Mediterranean Circulation Index (MCI), proposed in [19]. As showed by Fig.9, MCI explains a portion of variance greater than other indexes in the October-April period: the highest correlation values were found on January ($\rho = -0.67$), on December ($\rho = -0.64$) and on February ($\rho = -0.62$).

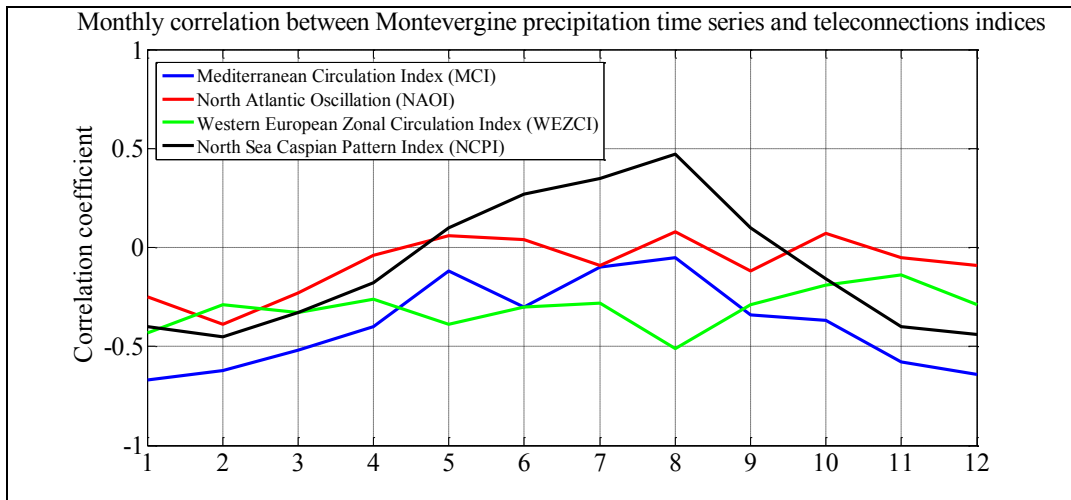
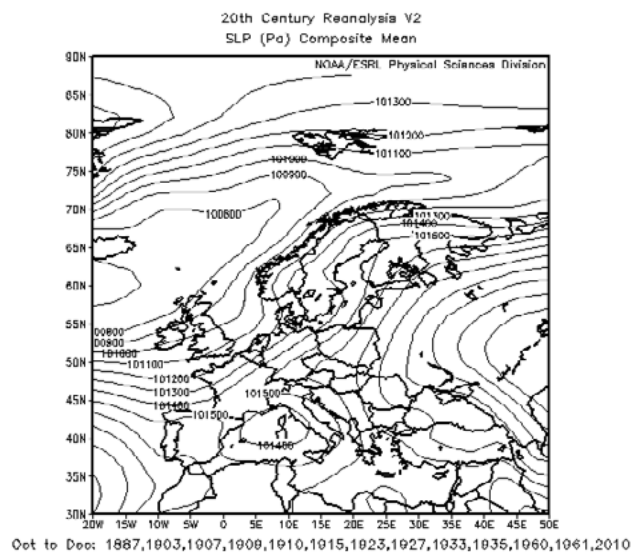


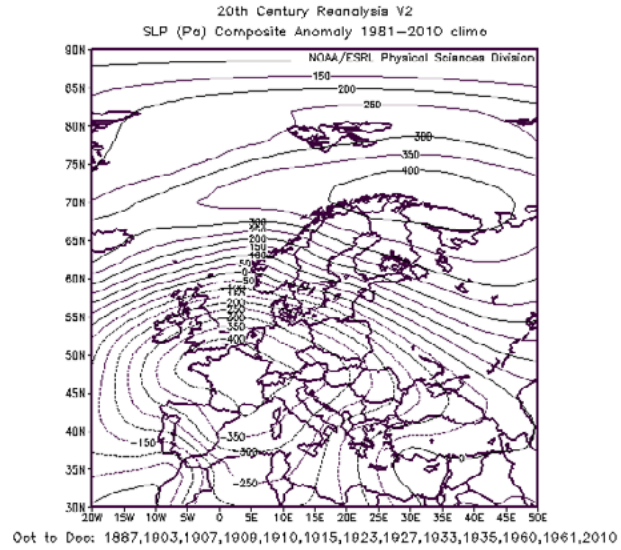
Fig. 9: Monthly correlation between Montevergine’s precipitation time series and teleconnections indices in 1884:2010 period.

In order to identify the atmospheric pattern more favorable to precipitation events in Montevergine during autumn and winter, we selected MCI October-November-December (OND) and January-February-March (MAM) values below the 10th percentiles. The sea-level pressure pattern and the relative anomalies (with respect to 1981-2010 mean) are shown in Figure 10a and 10b (OND) and in Figure 10c and 10d (JFM).

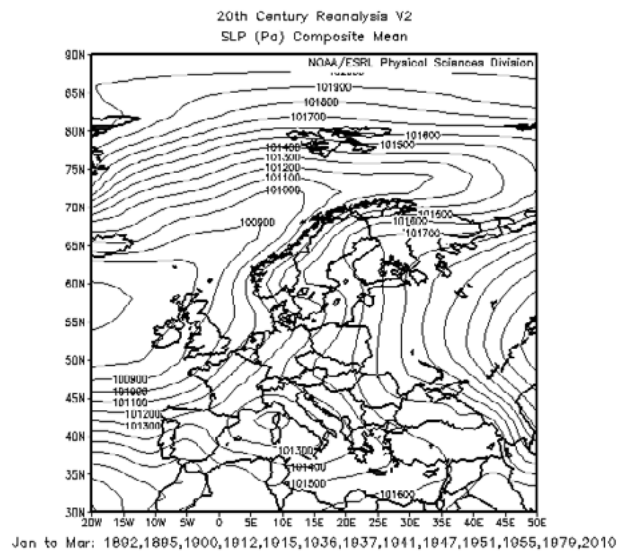
(a)



(b)



(c)



(d)

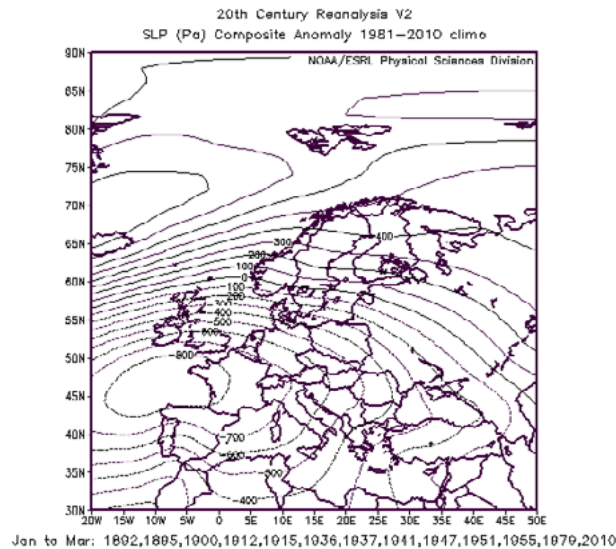


Fig. 10: Sea level pressure pattern and relative departures with respect to the 1981-2010 period for the OND seasons (Fig. 10a and Fig.10b) and JFM season (Fig. 10c and Fig. 10d) characterized by MCI values below the 10th percentiles.

Autumnal and wintery sea-level pressure patterns associated to MCI values below the 10th percentiles show very similar features: they are characterized by a low-pressure center between Corsica and Sardinia, which pumps moist air masses from south-west in the southern Italy, by a weakening of Icelandic low-system and by two strong anomalies centers, one located in the Northern Atlantic, the other situated in the Western European sector.

Wavelet Coherence between MCI and winter precipitation highlights a large area of covariance in 1940-2010 time interval (period \approx 1-8 years), while in 1884-1930 period there is an high covariance only on periods of 1-4 years and of 8-16 years (Fig.11a). The drop in precipitation observed at Montevergine observatory in the last three decades can be related to the significant change in atmospheric circulation, which was caused both by an increase in north-south pressure gradient, represented by the shift into the positive phase of NAO, and by an increase in difference between western and eastern Mediterranean pressure, represented by the shift into the positive phase of MCI. This coupling between NAO and MCI is well captured by the WTC of two signals (Fig.11b), which shows a covariance area in 1970:2010 time over 8-10 years periods.

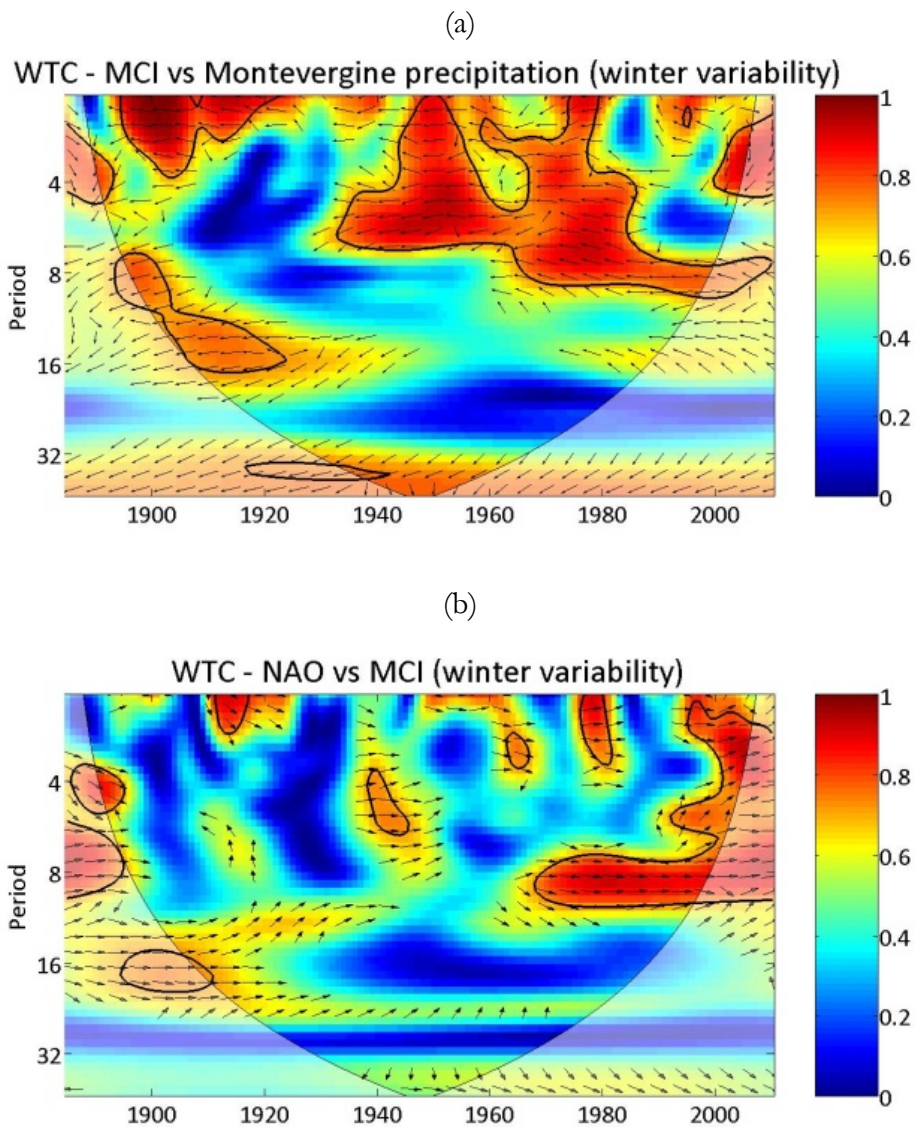
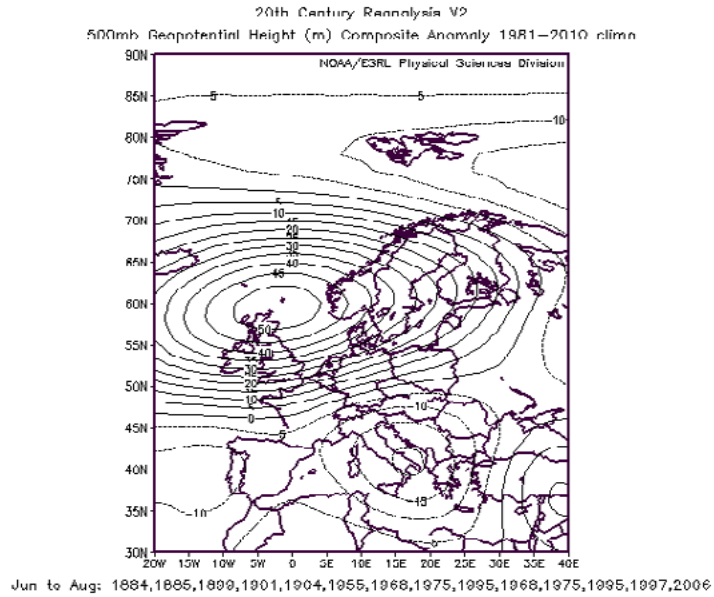


Fig. 11: Wavelet Coherence of MCI and Montevergine's winter precipitation (a) and Wavelet Coherence of NAO and MCI winter variability (b).

Summertime rainfall is partially well captured only by WEZCI and by NCPI: in both cases correlation degree is maximum on August ($\rho = -0.51$ and $\rho = 0.47$, respectively). Summer seasons characterized by NCPI value above the 90th percentile (Fig. 12a) show a pattern in geopotential heights anomalies similar to that observed for those marked by a WEZCI (Fig. 12b) value below the 10th percentile, with strong positive anomalies in North Sea and negative anomalies in Southern Italy.

(a)



(b)

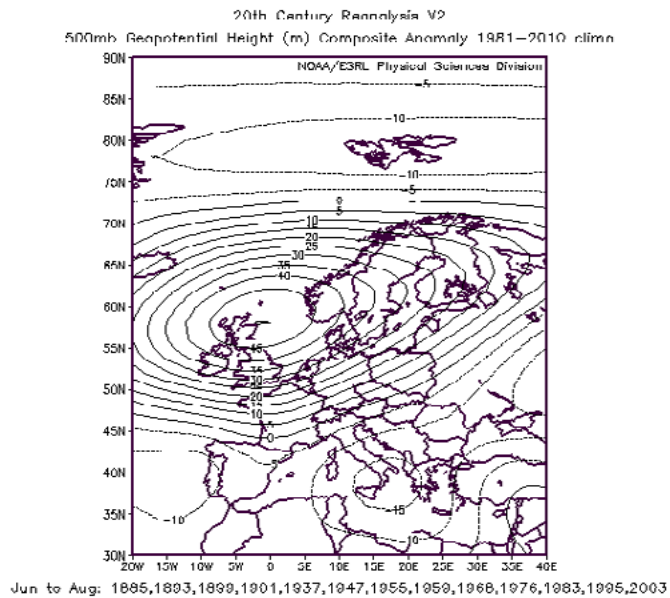


Fig. 12: Geopotential heights anomalies at 500 hPa level (with respect to 1981-2010 mean) for summer season (JJA) characterized by WEZCI values below the 10th percentiles (Fig.12a) and by NCPI values above the 90th percentiles (Fig.12b).

As marked in [19], there is a significant influence of ENSO on rainfall in regions of Euro-Mediterranean sector, especially on spring and on autumn season. Monthly correlation analysis between Montevergine's precipitation time series and Nino3.4, defined as SST anomaly in 5S-5N, 120W-170W, didn't show any perceptible relationship. However, the XWT performed for the autumn season (Fig.13) revealed areas of common power between 1890 and 1895 (period \approx 2-3 years), 1910 and 1920 (period \approx 5-8 years), 1935 and 1940 (period \approx 3-6 years) and between 1970 and 1985 (period \approx 4-6 years). In the latter two areas Nino3.4 seems to lead Montevergine's rainfall variability.

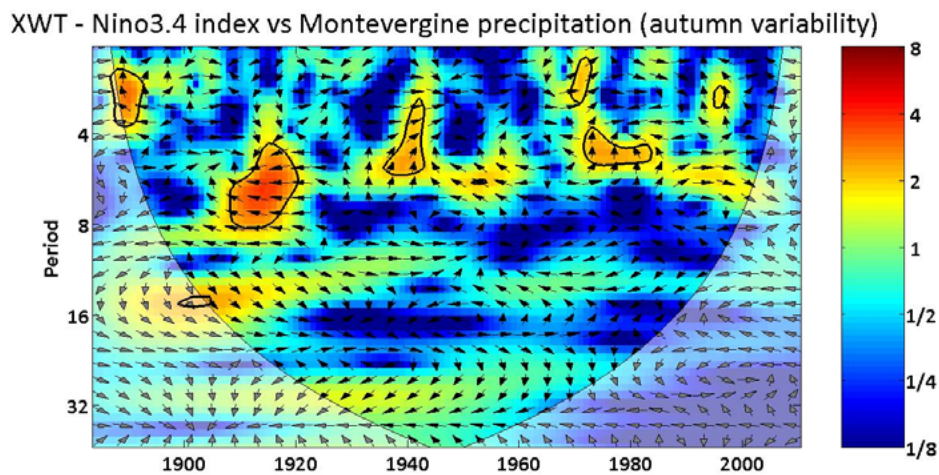
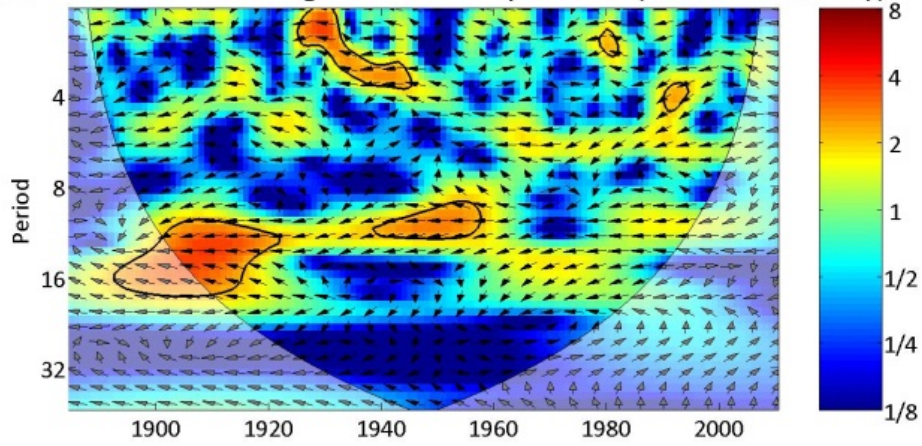


Fig. 13: Cross Wavelet Transform of Nino3.4 index and Montevergine's autumn precipitation.

Montevergine's temperature variability is in a good agreement with EMP, particularly on winter season ($\rho = -0.63$). The strong oscillation of temperature signal between 1940 and 1960 is strongly related to the EMP, as pointed out by the XWT of the two signals performed for winter season (Fig.14a). WTC shows a strong and stable area of covariance on 8-16 years periods on the whole time interval considered (Fig.14b).

(a)

XWT - EMP vs Montevergine mean temperature (winter variability)



(b)

WTC - EMP vs Montevergine mean temperature (winter variability)

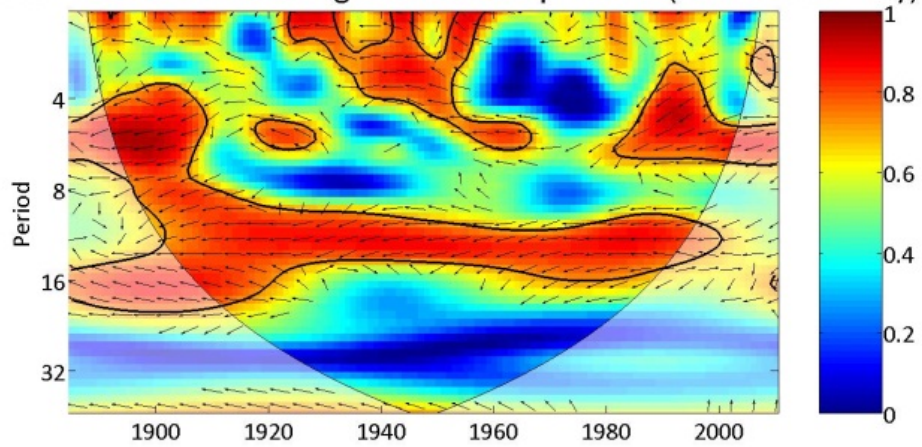


Fig. 14: Cross Wavelet Transform (a) and Wavelet Coherence (b) of EMP and Montevergine's winter temperature time series.

6. CONCLUSIONS

In this study we focused on the homogenization and the analysis of Montevergine's climatological time series for the period 1884:2010. Precipitation data are affected by errors only between 1946 and 1950, while temperature time series is characterized by multiple discontinuities, due to various causes, such as instrument relocation, changing in observers, human errors and instrument accuracy degradation. This study has pointed out an increase of annual mean temperature ($0.5^{\circ}\text{C}/100$ years) and a huge drop in annual total precipitation ($-32\%/100$ years). Positive trend in mean temperature emerges in all seasons, except on fall, while negative trend in total precipitation is particularly strong on spring and autumn. Both signals are characterized by a strong oscillation between 1940 and 1950. The analysis of relationship with large-scale patterns suggested that behind the decrease in precipitation there's an enhancement both of north-south pressure gradient (represented by North Atlantic Oscillation Index) both of eastern-western Mediterranean pressure gradient (synthesized by Mediterranean Circulation Index), which has determined a weakening of the energy associated to atmospheric transients. Montevergine's precipitation time series is in a good agreement with Mediterranean Circulation Index in the October-April period, while summer rainfall variability is partially captured by Western European Zonal Circulation Index and by North Sea Caspian Pattern Index. ENSO irregular oscillations influenced autumn rainfall variability, especially in early 1900s and in 1970-1985 period. Temperature series shows a good correlation degree with Eastern Mediterranean Pattern, particularly on winter season.

There isn't yet a full comprehension of how high-altitude regions have responded to recent change in atmospheric circulation, so in near future our purpose is to extend the study to other mountain stations located in Central-Southern Apennines.

7. ACKNOWLEDGMENTS

The Authors of this work are very grateful to the Benedictine Community of Montevergine's Abbey for the kind collaboration and for the valuable opportunity to use the original archived data.

8. REFERENCES

- Luterbacher J., & Xoplaki E. (2003), *500-Year Winter Temperature and Precipitation Variability over the Mediterranean Area and its Connection to the Large-Scale Atmospheric Circulation*, *Mediterranean Climate: Variability and Trends*, pp. 134-135. (1)
- Diodato N. (1992), *Nota climatica ispirata dalla serie storica delle precipitazioni osservate al Santuario di Montevergine*, *Rivista di Meteorologia Aeronautica*, Vol. LII – N. 3-4 (Luglio-Dicembre 1992), pp. 179-182. (2)
- Budillon G. & Capozzi V. (2011), *Risultati preliminari dell'analisi di una nuova serie di dati climatici nell'Italia meridionale (Osservatorio di Montevergine – AV)*, XXIX Giornata dell'Ambiente: Clima del bacino del Mediterraneo negli ultimi 12 mila anni. In ricordo di Ardito Desio nel decennale della morte, *Atti dei Convegni Lincei*, 267, pp 189-197. (3)
- Alexandersson H. (1986), *A homogeneity test applied to precipitation data*, *Journal of Climate*, Vol. 6, pp. 661-675. (4)
- Peterson T.C. & Easterling D.R. (1994), *Creation of homogeneous composite climatological reference series*, *International Journal of Climatology*, Vol. 14, pp. 671-679. (5)
- Alexandersson H. & Moberg A. (1996), *Homogenization of Swedish temperature data. Part I: Homogeneity test for linear trends*, *International Journal of Climatology*, Vol. 17, pp. 25-34. (6)
- Reeves J., Chen J., Wang Xiaslan L., Lund R. & Lu QiQi (2007), *A Review and comparison of changepoint detection Techniques for Climate Data*, *Journal of Applied Meteorology and Climatology*, Vol. 46, pp. 900-902. (7)
- Grinsted A., Jevrejeva S. & Moore J. (2004), *Application of the Cross Wavelet Transform and Wavelet Coherence to geophysical time series*, *Nonlinear Processes in Geophysics*, Vol. 11, pp. 561-566. (8)
- Brunetti M., Maugeri M., Monti F. & Nanni T. (2006), *Temperature and precipitation variability in Italy in the last two centuries from homogenised instrumental time series*, *International Journal of Climatology*, Vol. 26, pp. 345-381. (9)
- Ufficio Centrale di Meteorologia e Geodinamica, *Annali dell'Ufficio Centrale di Meteorologia e Geodinamica*, 1879-1925. (10)
- Ufficio Centrale di Meteorologia e Geodinamica, *Rivista meteorico-agraia*, 1879-1917. (11)
- Ufficio Idrografico e Mareografico di Napoli, *Annali Idrologici*, 2000. (12)
- www.scia.sinanet.apat.it, *Progetto SCLIA*. (13)
- NOAA Earth System Research Laboratory, *NOAA 20th Century Reanalysis*. (14)

- Caloiero T., Coscarelli R., Ferrari E. & Mancini M. (2011), *Precipitation change in Southern Italy linked to global scale oscillation index*, Natural Hazards and Earth System Sciences, Vol. 11, pp. 1683-1694. (15)
- Camuffo D., Bertolin C., Diodato N., Barriendos M., Dominguez-Castro F., Cocheo C., della Valle A., Garnier E. & Alcoforado M.J. (2010), *The Western Mediterranean climate: how will it respond to global warming?*, Climatic Change, Vol. 100, pp. 137-142. (16)
- De Bellis A., Pavan V. & Levizzani V. (2010), *Climatologia e variabilità della neve sull'Appennino Emiliano-Romagnolo*, Quaderno Tecnico ARPA-SIMC, n°19, pp. 56-87. (17)
- Kutiel H. & Benaroch Y. (2002a), *North Sea-Caspian Pattern (NCP) – an upper level atmospheric teleconnection affecting the Eastern Mediterranean: Identification and definition*, Theor. Appl. Climatol., 71, 17-28. (18)
- Brunetti M., Maugeri M. & Nanni T. (2002), *Atmospheric Circulation and Precipitation in Italy for the last 50 years*, International Journal of Climatology, Vol. 22, pp. 1455-1471. (19)
- Mariotti A., Zeng N. & Lau K.-M. (2002), *Euro-Mediterranean rainfall and ENSO – a seasonally varying relationship*, Geophysical Research Letters, Vol. 29, No. 12, 10.1029/2001GL014248. (20)

Recent trends in daily temperature extremes over the Basilicata Region, Southern Italy (1951 – 2010)

Piccarreta M.¹, Pasini A.^{2*}, and Lazzari M.³

¹Ministero della Pubblica Istruzione

²CNR, Institute of Atmospheric Pollution Research, Monterotondo Stazione, Roma, Italy

³CNR, Institute for Monumental and Archaeological Heritage, Tito Scalco, Potenza, Italy

*Corresponding author: pasini@iia.cnr.it

Abstract

Series of annual and seasonal temperature from 18 stations, distributed all over the Basilicata region (southern Italy), were studied for the period 1951–2010. The analysis is based on high-quality and homogenous daily minimum and maximum temperature. Both minimum (Tmin) and maximum (Tmax) temperatures increased, especially after 1971. The trend is most remarkable for Tmin, with 11 stations showing a positive statistically significant trend. Seasonal results are similar except for autumn where an opposite trend has been recorded. Also Tmax show an overall positive trend, which is statistically significant only for 2 stations. Seasonal results show upward trend in spring and summer, whereas during winter and autumn, Tmax tend to decrease. Six indices were used to assess changes in both the cold and hot tails of the daily temperature distributions. The presence of trends was assessed by means of the Mann-Kendall test. Results reveal a general upward tendency for both warm days (TX90p) and warm nights (TN90p) especially due to the increase in temperature becomes since 1971. This datum is confirmed at seasonal level, with spring and summer the main seasons responsible for the trend. In general both cold days (Tx10) and cold nights (Tn10) showed negative trends. It seems that this negative trend stems from the strong decrease of Tmin during winter, spring and summer. Both annual and seasonal number of frost days (Fd) show an overall negative trend. A few positive trends can also be found in northern Basilicata. The intra-annual extreme temperature range (ETR) index shows a general positive trend. In winter, decreased ETR appears for the majority of the stations examined although the trend has been inverted in the last two normals. During spring, the trend is strongly positive, especially in the last two climate normals. Summer and autumn show a similar predominant negative trend.

Keywords: *Extreme temperature indices; trends; temporal variability; Basilicata; southern Italy*



1. DATA ANALYSIS

Temperature extremes are a major concern with respect to their potential impacts on natural and human systems [1;2]. The semi-arid Mediterranean environment is regarded as a “Hot Spot” of climate change [10], that suffers from more temperature extreme events and an increase of summer heat wave frequency and duration [8]. Several studies indicate that extreme temperature events at daily/multi-daily scales in the Mediterranean have undergone changes in the course of the 20th century whose overall long-term trends are in accordance with the global picture of trends: cold extremes are reduced and warm/hot extremes are increased [9; 11; 13; 14].

Over the last few decades, many studies have put a great deal of effort into exploring the behaviour of temperature in Italy [5;6;7;21;22]. However, little research on the variability of temperature extremes is available for southern Italy at microscale. In this study, the regional character of temperature changes across the Basilicata Region, southern Italy, is examined with emphasis on trends since the mid-20th century in a number of indices of extremes.

The database comprises 18 thermometric stations of the National Hydrographic Service (Servizio Idrografico, 1951 - 2010) (Fig. 1). Thermometers used in the Italian observation network are approved and normalized by the National Hydrographic Service, which provides the instruments and guarantees their uniformity. The data represent observations of daily maximum surface air temperature, T_x , and daily minimum surface air temperature, T_n . To our knowledge, this is the first attempt to gather all the different temperature data sources together over Basilicata.

All the data have been checked and validated before their archiving and any possible error has been deleted. In addition to data availability, the quality and homogeneity of the temperature time series are prerequisites for detailed attribution of extreme events. Therefore, a newly compiled, quality-controlled, and homogeneity-tested dataset was recently developed from the original dataset. Quality control is needed to assure the reliability of climate data. The data were screened for any erroneous data that resulted from archiving, transcription or digitizing processes (e.g. $T_{min} > T_{max}$, non-existent dates). Also, homogenous time series are essential to assess changes in temperature extremes. Accordingly, the temperature series were tested for presence of inhomogeneities by using the Standard Normal Homogeneity Test (SNHT) for a single break [4]. Data gaps were filled using values from the nearest neighbour observatories. At this end, the final dataset was relatively homogenous and free from the

effects of non-climatic factors (e.g. changes in locations, instruments, observers, observing practices, and surrounding environments).

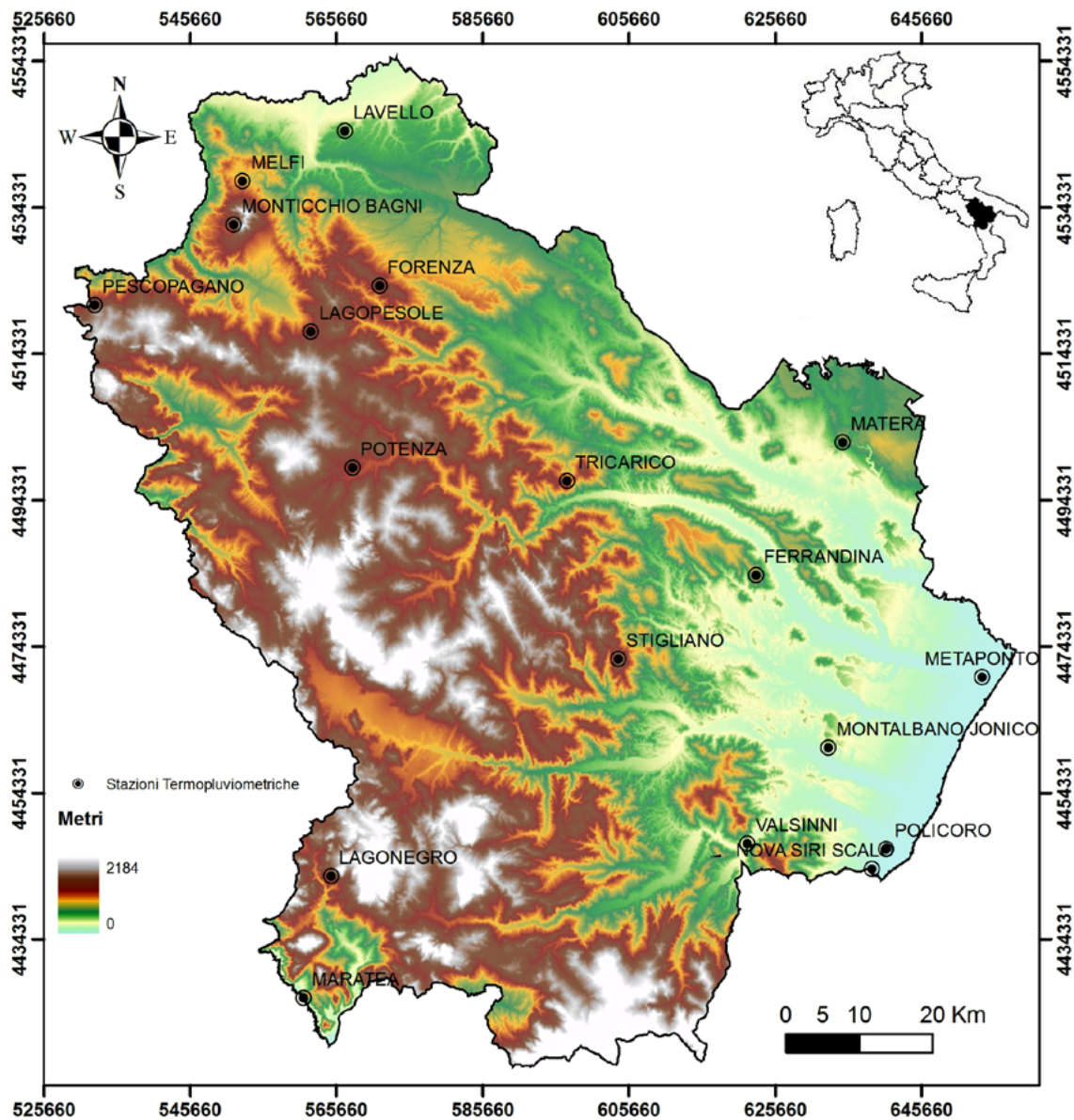


Fig. 1: Location of the study area and spatial distribution of the daily temperature observatories

Index	Definition	Unit
Tx10	Days with Tmax<10th percentile of daily Tmax of the base period (cold days)	%
Tn10	Days with Tmin<10th percentile of daily Tmin of the base period (cold nights)	%
Tx90	Days with Tmax>90th percentile of daily Tmax of the base period (warm days)	%
Tn90	Days with Tmin>90th percentile of daily Tmin of the base period (warm nights)	%
Fd	Total number of frost days (days with absolute Tmin<0 °C)	days
ETR	Extreme temperature range (hottest Tmax in season minus coldest Tmin in season)	°C

Table 1: List of temperature extreme indices used in this study

In this work, firstly we analyzed for each station the temporal behaviour of minimum and maximum temperature at annual and seasonal scale. Then a set of 8 indices were used to examine spatial and temporal variability of temperature extremes (Tab. 1). In order to ensure reasonable sample size and robustness of analysis, the focus is on ‘moderate’ extremes defined by the 10th and 90th percentiles in the distribution of daily observations. The presence of trends in temperature extremes was assessed by means of the Mann-Kendall test [18].

Minimum and maximum temperatures were analyzed and the results are reported in Tab. 2. It emerges that both minimum and maximum temperature increase during the period 1951 – 2010, especially after the 1970 (Fig. 2).

The trend is most remarkable for Tmin, with 11 stations which show a positive statistically significant trend. Only three stations show a negative trend, but never statistically significant. The main normals responsible for the trend are 1971-2000 and 1981-2010 with the last the most determinant. Annual results are fully correspondent for winter, spring and summer, whereas in autumn an opposite trend, especially in the last normal 1981-2010, has been recorded.

Also Tmax show an overall positive trend during the period 1951 - 2010, but it is statistically significant only for 2 stations. Similarly with Tmin, the main normals responsible for the trend are 1971-2000 and 1981-2010. Seasonal results show that the annual trend is the same during spring and summer, whereas during winter and autumn maximum temperatures tend to decrease.

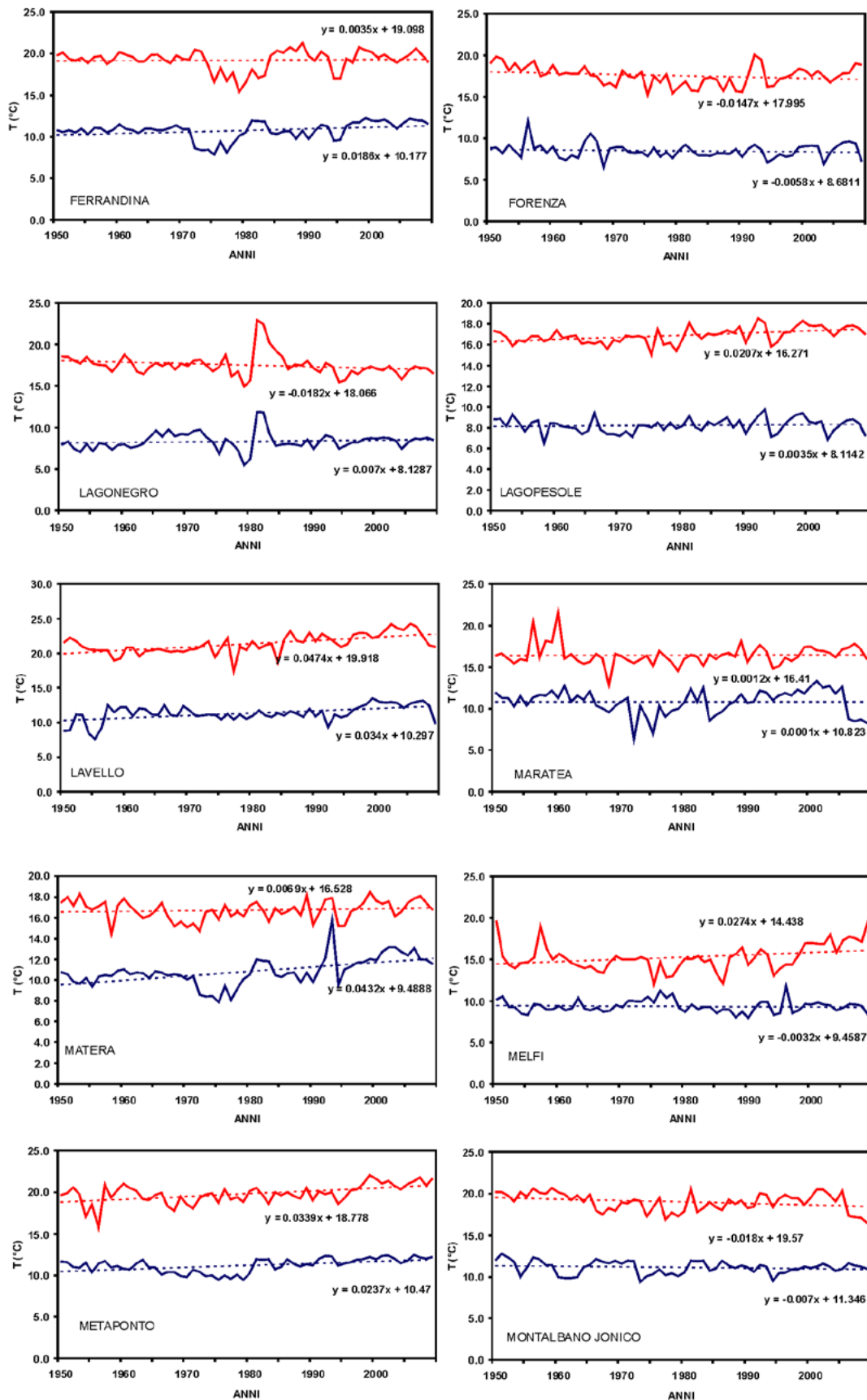
Then the analysis for extremes has been performed.

Index	Trend signal (Sig. = significant)	YEAR					WINTER					SPRING					SUMMER					AUTUMN									
		1951-2010	1951-1980	1961-1990	1971-2000	1981-2010	1951-2010	1951-1980	1961-1990	1971-2000	1981-2010	1951-2010	1951-1980	1961-1990	1971-2000	1981-2010	1951-2010	1951-1980	1961-1990	1971-2000	1981-2010	1951-2010	1951-1980	1961-1990	1971-2000	1981-2010					
		Tmin	Negative Sig.	0	10	0	2	1	3	1	1	5	1	0	1	0	0	1	0	12	0	1	0	2	8	0	0	1	3	5	8
	Negative Non-Sig.	3	5	8	1	4	5	8	8	4	5	1	14	8	5	3	0	5	4	1	2	6	8	11	3	12	11	0	4	11	9
	Positive Sig.	11	0	4	11	9	2	3	4	0	3	10	0	1	2	6	14	0	3	12	10	1	0	0	10	2	4	3	6	4	4
	Positive Non-Sig.	4	3	6	4	4	8	6	5	9	9	7	3	9	11	8	4	1	11	4	6	9	2	7	5	3					
Tmax	Negative Sig.	0	11	0	0	0	4	3	0	2	0	0	2	0	0	0	0	16	2	0	0	1	5	1	0	4	2	7	7	1	5
	Negative Non-Sig.	2	7	7	1	5	7	10	6	10	6	0	14	8	3	1	4	2	3	0	4	10	12	12	1	10	2	0	1	2	4
	Positive Sig.	2	0	1	2	4	0	0	0	1	1	5	0	0	0	2	2	0	0	4	3	0	0	0	2	0	14	0	10	15	9
	Positive Non-Sig.	14	0	10	15	9	7	5	12	5	11	13	2	10	15	15	12	0	13	14	11	7	1	5	15	4					
Tx10	Negative Sig.	7	0	3	6	7	3	2	0	0	9	13	0	0	3	6	6	0	3	9	4	3	0	0	7	5	7	2	9	11	8
	Negative Non-Sig.	7	2	9	11	8	8	11	11	3	9	4	10	14	13	12	10	0	14	9	8	5	0	4	10	3	1	2	0	0	0
	Positive Sig.	1	2	0	0	0	1	0	0	0	0	0	0	0	0	0	0	4	0	0	1	1	1	1	0	2	3	14	6	1	3
	Positive Non-Sig.	3	14	6	1	3	6	5	7	15	0	1	8	4	2	0	2	14	1	0	5	9	17	13	1	8					
Tn10	Negative Sig.	11	1	7	10	5	6	2	4	1	7	16	3	4	3	5	14	0	11	12	6	5	0	2	10	3	6	5	9	4	6
	Negative Non-Sig.	6	5	9	4	6	9	10	7	9	6	2	9	12	10	10	4	4	6	5	7	6	7	10	7	3	0	4	0	0	3
	Positive Sig.	0	4	0	0	3	0	0	1	0	1	0	0	0	0	1	0	6	0	0	1	0	3	0	0	4	1	8	2	4	4
	Positive Non-Sig.	1	8	2	4	4	3	6	6	8	4	0	6	2	5	2	0	6	1	1	4	7	8	6	1	8					
Tx90	Negative Sig.	0	12	1	0	1	2	6	0	1	1	0	5	0	1	0	0	13	1	0	0	0	5	1	0	1	4	5	6	3	5
	Negative Non-Sig.	4	5	6	3	5	4	8	2	6	8	4	11	9	9	3	7	5	10	3	5	8	12	12	6	9	4	0	2	5	4
	Positive Sig.	4	0	2	5	4	1	0	4	2	4	3	1	1	0	2	2	0	1	3	5	1	0	0	3	0	10	1	9	10	8
	Positive Non-Sig.	10	1	9	10	8	11	4	12	9	5	11	1	8	8	13	9	0	6	12	8	9	1	5	9	8					
Tn90	Negative Sig.	0	12	2	1	2	0	1	0	0	2	0	11	0	0	0	0	11	2	1	0	0	9	2	0	2	2	4	8	3	1
	Negative Non-Sig.	2	4	8	3	1	4	13	7	7	1	3	5	10	5	3	2	6	7	0	1	7	8	11	3	6	8	0	1	8	7
	Positive Sig.	8	0	1	8	7	4	1	3	0	5	3	2	0	0	5	6	0	0	5	6	3	0	0	5	4	8	2	7	6	8
	Positive Non-Sig.	8	2	7	6	8	10	3	8	11	10	12	0	8	13	10	10	1	9	12	11	8	1	5	10	6					
Fd	Negative Sig.	4	3	4	0	3	3	3	2	0	5	11	8	11	7	4	18	18	18	18	18	15	11	14	15	9	9	7	9	9	9
	Negative Non-Sig.	9	7	9	9	9	10	9	12	10	9	6	10	7	5	7	0	0	0	0	0	3	7	4	3	9	2	1	0	3	2
	Positive Sig.	2	1	0	3	2	1	0	0	3	0	0	0	0	1	0	0	0	0	0	0	0	0	0	0	0	3	7	5	6	4
	Positive Non-Sig.	3	7	5	6	4	4	6	4	5	4	1	0	0	5	7	0	0	0	0	0	0	0	0	0	0					
ETR	Negative Sig.	0	4	4	0	0	2	1	1	0	0	0	5	0	0	0	0	0	4	0	0	0	1	1	1	0	6	14	10	4	5
	Negative Non-Sig.	6	14	10	4	5	10	16	10	4	8	1	9	11	4	0	11	9	7	12	6	11	12	7	13	8	1	0	1	1	5
	Positive Sig.	1	0	1	1	5	0	0	1	1	2	3	0	0	1	9	1	1	0	0	2	0	0	0	1	1	11	0	3	13	8
	Positive Non-Sig.	11	0	3	13	8	6	1	6	13	8	14	4	7	13	9	6	8	7	6	10	7	5	10	3	9					

Table 2: Results of trend analysis for cold and hot extremes (significance is assessed at the 95% level). Abbreviations of the indices correspond to those in Table 1.

Tab. 2 summarizes the results of the Mann-Kendall test for hot temperature indices, too. The Tx90p index is important to investigations of the temperature regime in the Mediterranean, as it can provide evidence for a tendency towards a warmer climate and/or high summer temperatures leading to unpleasant heatwaves. Results reveal that from 1951 to 2010 there is a general upward tendency for warm days (TX90p) (75% of observatories), which is statistically significant for four thermometric station.

Researchers have connected the rise in the mean global temperature with increases of Tmin. Hence, the index TN90p is considered important to investigate whether changes in the occurrence of Tmin in the Mediterranean contribute to the observed global temperature changes. Again, the annual indices results show a general upward tendency for the warm nights (88.9% of observatories), which is statistically significant for eight stations.



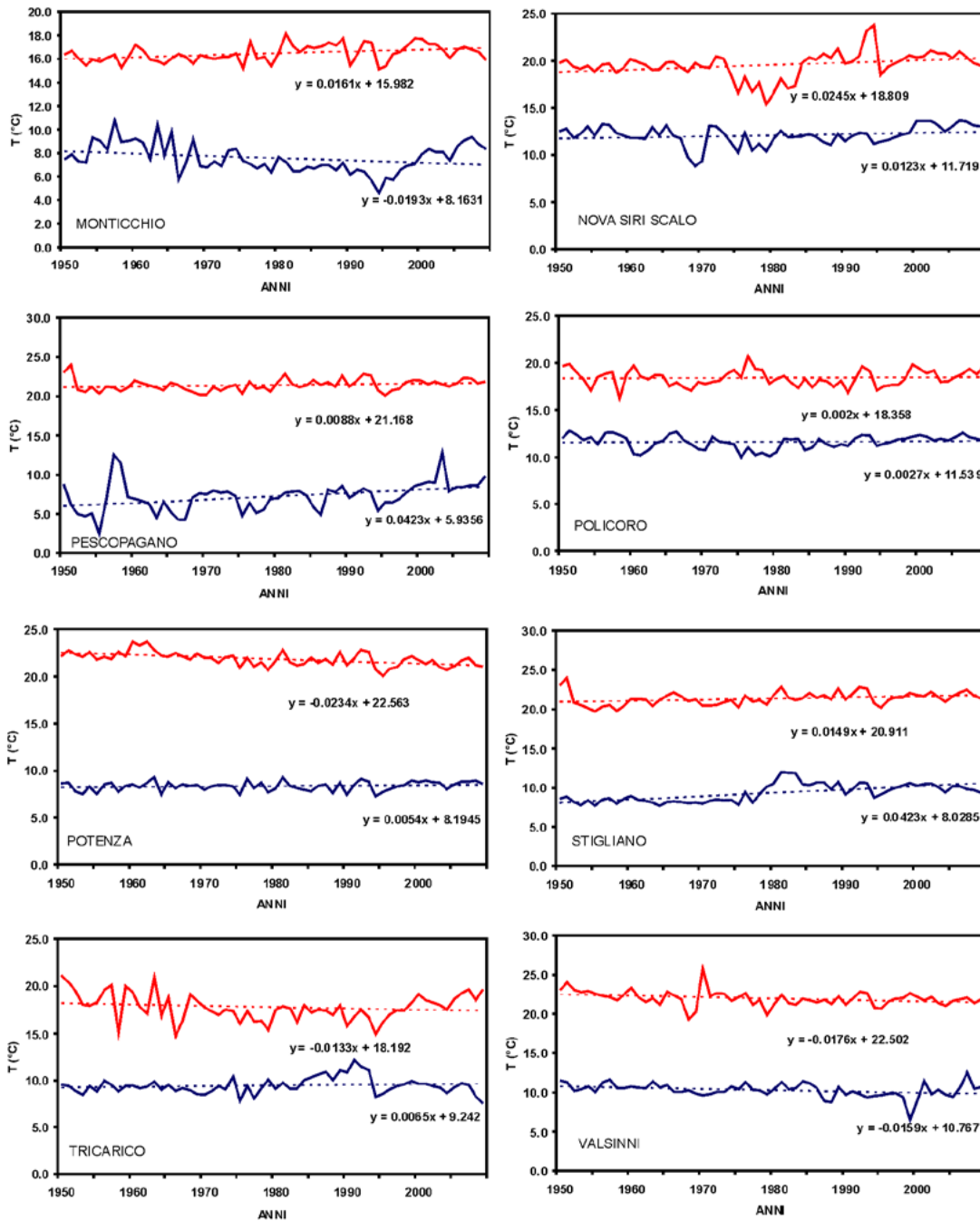


Fig. 2 Temporal trends from 1951 to 2010 of Minimum mean Temperature (blue) and Maximum mean Temperature (red)

From the analysis for normal it emerges that the increase in hot temperature becomes stronger from 1971. This last datum is also confirmed at seasonal level, with spring and summer the main seasons

responsible for the trend. Really interesting is that the increase in hot temperature coincides with a clearly downward trend in precipitation total [15;16].

Table 2 shows the trend results of the cold temperature indices, too. In general, it is evident that both cold days (T_{x10}) and cold nights (T_{n10}) showed negative trends. The cold days (T_{x10}) has decreased throughout the region, with 14 stations being characterized by a negative trend; 7 stations show a statistically significant trend. The remaining four stations indicate a positive trend, which is statistically significant only for the station of Ferrandina. It seems that the widespread negative trend stems from the strong decrease of minimal temperature during winter, spring and summer.

The most significant normal which affected the trend refers to 1961–1990 and 1971–2000. More than half of the stations are characterized by a decrease of the cold nights (T_{n10}), which is statistically significant for eleven stations. It clearly appears that the trend signal is due to the temperature regime change occurred from 1961 in each season.

According to [9], a uniform decrease in the number of frost days has occurred during the second half of the 20th century. Indices for the annual and seasonal number of frost days (F_d) have been calculated (Tab. 2). The datum is fully confirmed for Basilicata region, where more than half of the stations show a negative trend, which is statistically significant only for four stations. A few positive trends can also be found in northern Basilicata, in the area of Vulture Volcano. In this last case, again the climatological normals responsible for the positive trend are the 1971-2000 and 1981-2010. It is worth emphasising the summer and autumn trends which is absolutely negative along all the investigated period.

The intra-annual ETR index is a basic measure of the difference between the extreme maximum and minimum temperature during a certain period of time. The results reported on Tab.2 show a general positive trend (only one statistically significant) which has been clearly defined after 1970, in the last two climate normals 1971-2000 and 1981-2010. Seasonal indices provide clearer results. In winter, decreased intra-seasonal ETR appears for the majority of the stations examined although the trend has been inverted in the last two normals. These reductions in ETR can probably be related to increases in the minimum temperature. During spring, the trend is strongly positive, with three stations characterized by a statistically significant trend.

Again the last two climate normals mainly affected the trend; in particular, during the 1981-2010 period nine stations are characterized by statistically significant trend. Summer and autumn show similar

predominant negative trends; however only one trend is statistically significant in summer and none are statistically significant in autumn.

2. CONCLUSIONS

The results obtained from this study can be summarized as follows:

- both minimum and maximum temperature have increased in the investigated period, especially in the last thirty years.
- warm days (TX90p) and warm nights (TN90p) show a general upward tendency especially due to the increase in temperature becomes after the 1971.
- cold days (Tx10) and cold nights (Tn10) showed negative trends. The most significant normal which affected the trend refers to 1961–1990 and 1971–2010.
- both annual and seasonal number of frost days (Fd) show an overall negative trend.
- the intra-annual extreme temperature range (ETR) index show a general positive trend which has been clearly defined after 1970, in the last two climate normals 1971-2000 and 1981-2010.

3. REFERENCES

Aguilar E., Aziz Barry A., Brunet M., Ekan L., Fernandes A., Massoukina M., Mbah J., Mhanda A., do Nascimento D.J., Peterson T.C., Thamba Umba O., Tomou M. & Zhang X. (2009), *Changes in temperature and precipitation extremes in western central Africa, Guinea Conakry, and Zimbabwe, 1955–2006*, Journal of Geophysical Research, No. 114, D02115, doi:10.1029/2008JD011010. (1)

Aguilar E., Peterson T.C., Ramírez Obando P., Frutos R., Retana J.A., Solera M., Soley J., González García I., Araujo R.M., Rosa Santos A., Valle V.E., Brunet M., Aguilar L., Álvarez L., Bautista M., Castañón C., Herrera L., Ruano E., Sinay J.J., Sánchez E., Hernández Oviedo G.I., Obed F., Salgado J.E., Vázquez J.L., Baca M., Gutiérrez M., Centella C., Espinosa J., Martínez D., Olmedo B., Ojeda Espinoza C.E., Núñez R., Haylock M., Benavides H. & Mayorga R. (2005), *Changes in precipitation and temperature extremes in Central America and northern South America, 1961–2003*, Journal of Geophysical Research, No. 110, D23107, doi:10.1029/2005JD006119. (2)

- Alexander L.V., Zhang X., Peterson T.C., Caesar J., Gleason B., Klein Tank A.M.G., Haylock M., Collins D., Trewin B., Rahimzadeh F., Tagipour A., Rupa Kumar K., Revadekar J., Griffiths G., Vincent L., Stephenson D.B., Burn J., Aguilar E., Brunet M., Taylor M., New M., Zhai P., Rusticucci M. & Vazquez-Aguirre J.L. (2006), *Global observed changes in daily climate extremes of temperature and precipitation*, Journal of Geophysical Research, No. 111, D05109, doi:10.1029/2005JD006290. (3)
- Alexandersson H. & Moberg A. (1997), *Homogenization of Swedish temperature data. Part 1: homogeneity test for linear trends*, International Journal of Climatology, No. 17, pp. 25-34. (4)
- Brunetti M., Buffoni L., Maugeri M. & Nanni T. (2000), *Trend of minimum and maximum daily temperature in Italy from 1865 to 1996*, Theoretical and Applied Climatology, No. 66, pp. 49-60. (5)
- Brunetti M., Buffoni L., Mangianti F., Maugeri M. & Nanni T. (2004), *Temperature, precipitation and extreme events during the last century in Italy*, Global and Planetary Change, No. 40, pp. 141-149. (6)
- Brunetti M., Maugeri M., Monti F. & Nanni T. (2006), *Temperature and precipitation variability in Italy in the last two centuries from homogenized instrumental time series*, International Journal of Climatology, No. 26, pp. 345-381. (7)
- Della-Marta P.M., Haylock M.R., Luterbacher J. & Wanner H. (2007), *Doubled length of Western European summer heat waves since 1880*, Journal of Geophysical Research, No. 112, D15103, doi:10.1029/20007JD008510. (8)
- Frich P., Alexander L.V., Della-Marta P.M., Gleason B., Haylock M., Klein Tank, A.M.G. & Peterson, T. (2002), *Observed coherent changes in climatic extremes during the second half of the twentieth century*, Climate Research, No. 19, pp. 193-212. (9)
- Giorgi F. (2006), *Climate change hot-spots*, Geophysical Research Letters, No. 33, doi:10.1029/2006GL025734. (10)
- Hundecha Y. & Bárdossy A. (2005), *Trends in daily precipitation and temperature extremes across western Germany in the second half of the 20th century*, International Journal of Climatology, No. 25, pp. 1189-1202, doi: 10.1002/joc.1182. (11)
- IPCC (2007), *The AR4 Synthesis Report 2007: Summary for Policy Makers*, Cambridge University Press. (12)

- Klein Tank A.M.G. & Können G.P. (2003), *Trends in Indices of Daily Temperature and Precipitation Extremes in Europe, 1946–99*, Journal of Climate, No. 16, pp. 3655-3680. (13)
- Moberg A., Jones P.D., Lister D., Walther A., Brunet M., Jacobeit J., Alexander L. V., Della-Marta P. M., Luterbacher J., Yiou P., Chen D., Klein Tank A. M. G., et al. (2006), *Indices for daily temperature and precipitation extremes in Europe analyzed for the period 1901–2000*, Journal of Geophysical Research, No. 111, D22106, doi:10.1029/2006JD007103. (14)
- Piccarreta M., Capolongo D. & Boenzi F. (2004), *Trend analysis of precipitation and drought in Basilicata from 1923 to 2000 within a Southern Italy context*, International Journal of Climatology, No. 24, pp. 907-922. (15)
- Piccarreta M., Pasini A., Capolongo D. & Lazzari M. (2013), *Changes in daily precipitation extremes in the Mediterranean from 1951 to 2010: the Basilicata region, southern Italy*. International Journal of Climatology (published online), doi: 10.1002/joc.3670. (16)
- Servizio Idrografico. 1951 – 2010. *Annali*, Istituto Poligrafico dello Stato. (17)
- Sneyers R. (1990), *On the statistical analysis of series of observation*, WMO, Technical Note N. 143, Geneva, 192 pp. (18)
- Toreti A. & Desiato F. (2008), *Changes in temperature extremes over Italy in the last 44 years*, International Journal of Climatology, No. 28, pp. 733-745, doi:10.1002/joc.1576. (19)
- Viola F., Liuzzo L., Noto L.V., Lo Conti F. & La Loggia, G. (2013), *Spatial distribution of temperature trends in Sicily*. International Journal of Climatology (published online), doi: 10.1002/joc.3657. (20)
- WMO (1989), *Calculation of monthly and annual 30-year standard normal*, WCDP, No. 10, WMO-TD/No. 341, Geneva. (21)

Observed long-term trend and low-frequency variability of spring discharge timing in the main Alpine rivers

Zampieri^{1*}, E. Scoccimarro^{1,2}, S. Gualdi^{1,2}, and Navarra A.^{1,2}

¹*Centro Euro-Mediterraneo sui Cambiamenti Climatici (CMCC), Bologna, Italy*

²*Istituto Nazionale di Geofisica e Vulcanologia (INGV), Bologna, Italy*

*Corresponding author: matteo.zampieri@cmcc.it

Abstract

We analyze the observed long-term discharge time-series of the Rhine, the Danube, the Rhone and the Po rivers. These rivers are characterized by different seasonal cycles reflecting the different climates and morphology of the Alpine basins. However, despite the intensive water management in this region, we found common features in the spring discharge timing trend and low-frequency variability in the different basins. All time-series display an anticipating tendency of the spring discharge peaks of more than two weeks per century. These results can be explained in terms of changes in snowmelt timing, in total precipitation and of its liquid portion, which play different roles in the different basins.

Keywords: *Climate, hydrological cycle, Alps, Rivers*



Long term atmosphere-surface transfer studies in Salento Peninsula: a database

Martano P. ^{1*}, Elefante C. ², Grasso F. ¹

¹*Istituto di Scienze dell'Atmosfera e del Clima, U.O.S. di Lecce, ISAC-CNR, Italy,*

²*Università del Salento - Ripartizione Informatica, Lecce, Italy*

**Corresponding Author: p.martano@isac.cnr.it*

Abstract

The micrometeorological base of CNR-ISAC in Lecce, South-East of Italy, is active since 2002, in collecting experimental data about surface-atmosphere transfer of momentum heat and water vapour. It operates in a suburban site inside the Salento University campus and has been improved along the past years to give a quite complete description of the soil-atmosphere vertical transfer. It is composed by a 16 m mast with fast response (eddy correlation) instrumentation and an ancillary automatic meteorological station collecting also soil data at 2 levels depth. Fast response data are pre-processed in half-hour averaged statistics. All collected data are available in a web database (www.basesperimentale.le.isac.cnr.it) and represent a unique long-term daily updated dataset for microclimate and soil use changes studies in southern Italy. Here some preliminary results about the evolution of the surface water budget in the last years are presented. The Lecce data base has been a pilot reference structure for the Climate Change Section of the CNR-DTA GIIDA project (National Research Council - Earth and Environment Department, Interdisciplinary and Interoperative Management of Environmental Data). It is also a data provider for the HYMEX project database (Hydrological Mediterranean Experiment, www.hymex.org).

Keywords: *Database, micrometeorology, microclimate, surface fluxes, water budget*



1. INTRODUCTION

Surface-atmosphere transfer fluxes are the main sources/sinks of atmospheric energy and water vapour, being for this reason strictly connected to larger scale atmospheric motions. Indeed the radiative energy from the solar source transforms into conductive/turbulent vertical fluxes of heat and vapour after impinging on the earth surface, and momentum fluxes are constantly exchanged due to the friction between wind and earth surface [1].

Although directly responsible of the microclimatic conditions in the lower atmosphere, surface fluxes are subject to change due to local changes in land use and water moisture availability at ground level causing in turn changes in larger scale climatic conditions driving atmospheric winds and precipitations [2].

The eddy covariance technique for direct field measurement of the surface turbulent fluxes spread out in the early '80 and in the following years many studies improved its reliability, concerning density, spectral, and vertical velocities corrections for the measured fluxes [3,4,5].

In the decade of '90 this improved know-how led to a general increased technique reliability and applicability [6,7]. This fact, together with the increasing concerns about the climate effects of the global warming with interest in quantify large scale CO₂ and water vapour surface exchanges, led to the creation of several international networks for continuous long term flux monitoring (FLUXNET, EUROFLUX, AMERIFLUX) as well as long lasting regional soil-vegetation-atmosphere transfer experiments (LBA) [<http://fluxnet.ornl.gov>, <http://www.unitus.it/dipartimenti/disafri/progetti/eflux/euro.html>, <http://public.ornl.gov/ameriflux/>, <http://www.lbaeco.org/lbaeco/>]. Nevertheless, together with these great international successfully efforts, some regions are still out of the long term network monitoring, even where routine surface meteorological monitoring is present since long time.

Focusing on Europe, a glance to the site maps for existing networks (Fig.1) shows that the measurement sites concerning the Italian peninsula are located between the north and the centre of the country, with almost no site in the southern regions that have quite different climatic conditions and also different projections for the future climate, compared to the rest of the country. In particular, Salento peninsula has quite characteristic climatic features, due to its position in the Otranto channel, with moderate northern dry winds typically blowing in high pressure conditions, with consequent very clear skies and strong insolation, and scarcity of precipitations due to the lack of relevant orography

and the blocking effect of the Apennines for the incoming Atlantic moisture. This is accompanied however by a relevant low-level nocturnal surface moisture deposition consequent to the anywhere close surrounding seas and the relevant diurnal thermal cycle above the ground [8], that may result in a significant fraction of the surface moisture supply in dry summer periods .

The CNR ISAC micrometeorological base is placed in a suburban area 5 km south-west from Lecce, within the Salento University campus (Lat: 40° 20' 12" Lon: 18° 7' 17") characterized by mixed typical local vegetation (Mediterranean shrubs, pines and olive trees) with an increasing content of buildings and non-natural surfaces, that makes it interesting also from a land-use change study point of view. It is at present a data provider for the HYMEX project long term campaign (Hydrological Mediterranean Experiment, www.hymex.org) and the related data base is a pilot reference for the CNR DTA GIIDA project (National Research Council - Heart and Environment Department Integrated and Interoperative Management of Environmental Data project)

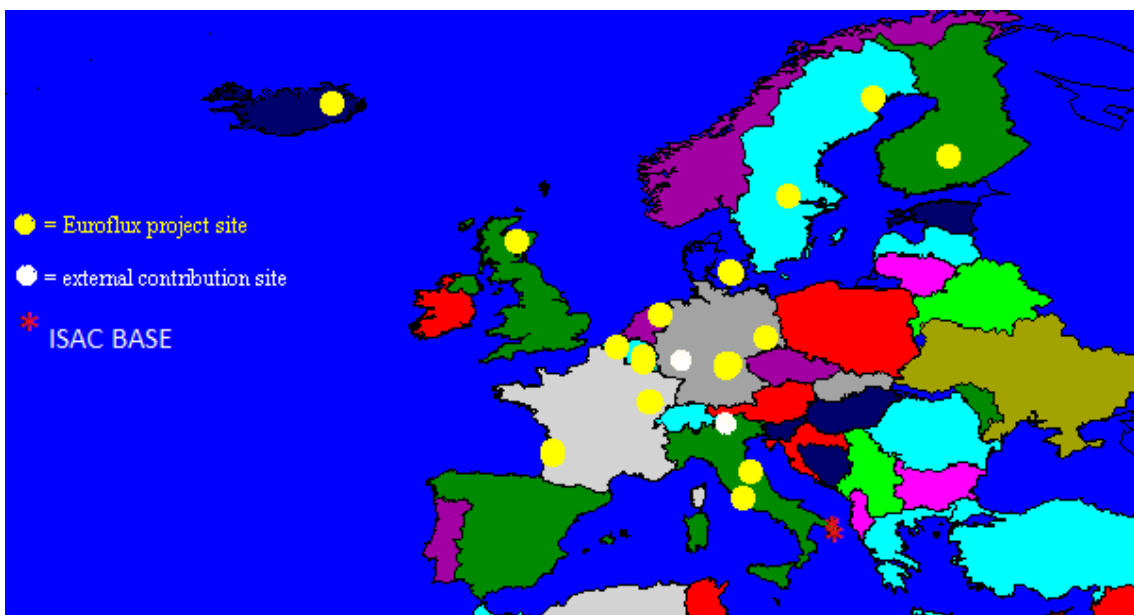


Fig. 1: EUROFLUX site locations and ISAC base

2. METHODOLOGY

At present, the base is mainly devoted to water and energy surface-atmosphere transfer.

It is composed by two complementary systems (Fig.2). A 16 m height mast is equipped with a fast response eddy correlation system and standard meteorological instruments routinely collecting half-hour averaged data. The mast height allows a flux footprint fetch of the order of several hundreds of meters [9,10], thus taking contributions from the campus and some immediately surrounding vegetated areas. Data are collected and processed in a local netbook by a home-made software developed in the LabWindow platform that allows an easy user friendly real time control of measurements as well as of the basic user parameters such as calibration constants and averaging periods. After processing and averaging they are stored in a daily data file. An ancillary Campbell meteorological station collects also standard meteorological and soil surface data in a dedicated data logger. The connection to the web data base is made by an additional local low-power computer interacting with the data logger through a home-made software to collect the ancillary station data and downloading also the eddy correlation daily data file. Both data files are stored in local memory and then transferred to the web data base once per day through UMTS connection system. The whole local system is totally solar energy powered.

The web data base has been developed in by the Opensource Mysql with a logic structure able to catalogue tables of data and information (metadata) for each kind of sensor. Before final storage data pass through a light quality control able to eliminate out of scale data generated by possible problems in the sensors.

Details of the instrumentation are the following.

1) Telescopic mast with fast response instrumentation

It is a 6-elements telescopic mast of 16 m height in full extension, with 3 possible measurements levels. In the upper level there are:

One Solent-Gill 20 Hz ultrasonic anemometer, one Campbell Kh20 Krypton hygrometer for open path optical measurements of water vapour turbulent fluctuations. Both instruments constitute the core of the eddy covariance system.

One surface temperature sensor Everest 4000.GL, measuring the radiative surface temperature by a blackbody-like internal cavity.

One net radiometer (Siap-Micros Radnt), measuring the difference between the total (short and long wavelength) radiation emitted from the sky and from the earth surface.

One slow response thermo-hygrometer for the air temperature and humidity (Rotronic MP100).

Eddy covariance data statistics are output in half hour averages as a compromise between nocturnal and diurnal turbulence time scales, although there are some evidences that longer averaging periods could be required to ensure a better surface energy budget closure especially in diurnal conditions [11]. For the same reason no detrending or filtering are applied to raw time series. The obtained half hour statistics are then rotated in the 'streamline' coordinate system [12] before storage in the daily data file.

2) Automated meteorological station

It is equipped with standard meteorological sensors and soil data sensors.

Standard sensors (2 meters height): Cup anemometer (Campbell A100R) , wind vane (Campbell W200P) thermo-hygrometer (Rotronic MP100), global (Campbell LI200X) and net radiometer (Rebs Q*7.1) , precipitation gauge (EM ARG100), barometer (Campbell PTB101B).

Soil sensors are devoted to collect temperature, moisture and heat flux data at 2 levels underground:

Two thermistor temperature sensors (Campbell107L, 2 and 5 cm depth)

Two thermopile soil heat flux sensor (Hukseflux HFP01, 2 and 5 cm depth)

Two moisture content capacitive sensors (Decagon EC-5, 2 and 30 cm depth)

Data are acquired and half-hour averaged on a dedicated Campbell CR10-X data logger expanded with a multiplexer.

The dataset is available in the web data base: www.basesperimentale.le.isac.cnr.it. A selection of daily data can be visualized online in graphic format. They can be available freely upon request at the address indicated in the staff area. Part of the data set is also available in the Hymex site for subscribed users [www.hymex.org/database/]



Fig. 2a: The ISAC base : particular of the mast top: from left: thermohygrometer, net radiometer, surface temperature sensor, fast krypton hygrometer, ultrasonic anemometer



Fig. 2b: The ISAC base, from left: meteorological automatic station, computer shelter, micrometeorological mast

3. SOME RESULTS AND CONCLUSIONS

At present on-going studies are undertaken about characterizing and modelling evapotranspiration and surface heat flux partition in the warm-arid region of the base area, and about how the surface transfer is affected by increasing surrounding urbanization. Some preliminary results about the annual surface water balance and flux partition are shown in fig. 3, starting from 2006, as precipitation has been recorded only since the late 2005.

Indicating with F_l the latent heat flux, F_s the sensible heat flux, $E(=F_s+F_l)$ the available energy flux, F_e the actual evapotranspiration flux, F_p the potential evapotranspiration flux (calculated by the Penman equation [1]), and P the precipitation (all as annual total amounts), the figure shows the following annual non-dimensional indices: Aridity index (P/F_p , circles), Surface water budget (P/F_e , triangles), Evaporative fraction (F_l/E , squares), Bowen ratio (F_s/F_l , plus signs). Although technical problems in 2007 and logistic problems in 2008 prevented from obtaining significant statistics for these years, data clearly show a decrease of the aridity index after 2010 from semi-arid to arid classification for the surrounding area, together with a decrease of the soil surface water budget from water gain (>1) to water loss (<1).

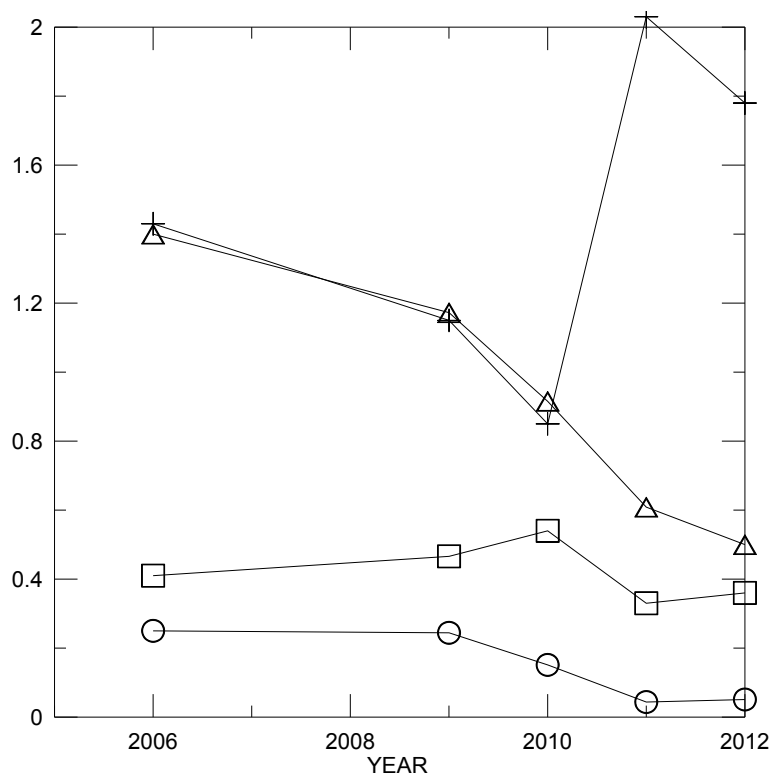


Fig. 3: Aridity index (P/F_p , circles), Surface water budget (P/F_e , triangles), Evaporative fraction (F_l/E , squares), Bowen ratio (F_s/F_l , plus signs). See also text. Lines are to help view only

The strong temperature anomaly in 2010 (the warmest year since 1880) caused an increase of the evaporative fraction in the area with a progressive soil water loss in this year, also documented by a decrease of the Bowen ratio. This fact, together with reduced precipitation amount in 2011 and 2012 (about a half of the previous years) caused the subsequent transition towards aridity conditions: low aridity index and evaporative fraction, soil water loss and a strong increase of the Bowen ratio.

The collected data have also been already used in past years for studies regarding different characteristics of the local atmospheric boundary layer, such as surface roughness and turbulence parameters, mixing height and surface energy budget [11, 13,14,15]. Since the last year measured data are routinely provided to the HYMEX project database.

4. ACKNOWLEDGMENTS.

The authors wish to acknowledge the CNR-DTA GIIDA and PON 2007-2013 I-AMICA projects for supporting the base and database improvement and maintenance.

5. REFERENCES

- Garratt J.R. (1992), *The atmospheric boundary layer*. Cambridge Univ. Press. 316 pp. (1)
- Pielke R.A., Marland G., Betts R.A., Chase T.N., Eastman J.L. Niles, J.O.,m Niyogi D.S., Running S.W. (2002), *The influence of land-use change and landscape dynamics on the climate system: relevance to climate-change policy beyond the radiative effect of greenhouse gases*. Phil. Trans. R. Soc. Lond., 360, 1705-1719. (2)
- Webb E.K, Pearman G.I., Leuning R. (1980), *Correction of flux measurements for density effects due to heat and water vapour transfer*. Quart. J. R. Met. Soc. 106, 85-100. (3)
- Massman W.J. (2000), *A simple method for estimating frequency response corrections for eddy covariance systems*. Agricultural and Forest Meteorol., 104, 185-198. (4)
- Lee X. (1998), *On micrometeorological observations of surface-air exchange over tall vegetation*. Agricultural and Forest Meteorol., 91, 39-50. (5)
- Foken Th, Wichura B. (1995), *Tools for quality assessment of surface-based flux measurements*. Agricultural and Forest Meteorol., 78, 83-105. (6)

- Fuehrer P.L., Friehe C.A. (2002), *Flux corrections revisited*. Boundary-Layer Meteorol. 102, 415-457. (7)
- Mangia C., Martano P., Miglietta M.M., Morabito A., Tanzarella A. (2004), *Modelling local winds over the Salento Peninsula*. Meteorological Applications, 11, 231-244. (8)
- Vesala T., Kljun N., Rannik U., Rinne J., Sogachev A., Markkanen T., Sabefeld K., Foken Th., Leclerc M.Y. (2008), *Flux and concentration footprint modelling: State of the art*. Environmental Pollution 152, 653-666. (9)
- Hsieh C.I., Katul G., Chi T. (2000), *An approximate analytical model for footprint estimation of scalar fluxes in thermally stratified atmospheric flows*. Advances in Water resources 23, 765-772. (10)
- Cava D., Contini D., Donato A., Martano P. (2008), *Analysis of short-term closure of the surface energy balance above short vegetation*. Agric. For. Meteorol., 148, 82-93. (11)
- McMillen R. (1988), *An eddy correlation Technique with extended applicability to non-simple terrain*. Boundary-Layer Meteorol., 43, 231-245. (12)
- Martano P. (2000), *Estimation of Surface Roughness Length and Displacement Height from Single-Level Sonic Anemometer Data*. Journal of Applied Meteorology, 39, 708-715. (13)
- Martano P. (2002), *An algorithm for the calculation of the time-dependent mixing height in coastal sites*. J. of Applied Met., 41, 351-54. (14)
- Martano P. (2008), *Inverse parameter estimation of the turbulent surface layer from single-level data and surface temperature*. J. Applied Met. and Climatol., 47, 1027-1037. (15)

Statistical modelling of sequences of no-rain days

Sirangelo B.¹, Caloiero T.², Coscarelli R.³, and Ferrari E.^{1*}

¹University of Calabria, Dept. of Environmental and Chemical Engineering, Rende (CS)

²National Research Council of Italy, Institute for Agriculture and Forest Systems in the Mediterranean (CNR-ISAFOM), Rende (CS)

³National Research Council of Italy, Research Institute for Geo-hydrological Protection (CNR-IRPI), Rende (CS)

*Corresponding author: ennio.ferrari@unical.it

Abstract

The stochastic models, developed to simulate long-term hydrological data, can be subdivided in “driven data” models, which reproduce the principal characteristics of the available data series, and “physically based” models, which schematize the generating mechanism of atmospheric precipitation. The initial step of a “driven data” stochastic model, able to adequately simulate the sequences of wet and dry days, is the definition of the statistics of the model. In this paper, various statistical models for sequences of no-rain days are firstly presented: the models are based on an approach which considers the arrival of rainfall events as a Poisson process, homogenous or not. Moreover, the first results of an application of one of these models to the daily rainfall series registered at the Cosenza rain gauge (Calabria, Southern Italy) are also shown. In particular, the model applied is a non-homogeneous Poisson model which considers the rainfall as a pulse of random duration.

Keywords: Sequences of no-rain days; Statistical models; Poisson distribution



1. INTRODUCTION

Numerous stochastic models have been developed to simulate long-term hydrological data. All the models can be divided in two main categories: a) the “driven data” models, which reproduce the principal characteristics of the available data series; b) the “physically based” models, which schematize the generating mechanism of atmospheric precipitations.

In the first category the most popular models are the Autoregressive Moving Average (ARMA) ones [1, 2, 3, 4 ,5], used in literature to characterize the correlations within a time series [6]. An ARMA model captures the deterministic components (dominant linear trends) of a time series and leaves behind the stochastic component (residuals). The stochastic component of a time series is defined as persistent if the temporally adjacent values are positively correlated. The persistence may be short-term or long-term depending on the time range over which they are correlated [7].

The physically based models describe the rainfall occurrence (dry–wet) process and the distribution of rainfall amounts on wet days independently [8]. In this category rainfall occurrence can be represented in two ways: as a Markov process [9] or as an Alternating Renewal process for dry and wet sequences [10]. A major limitation of these models is that the adoption of short term memory neglects the existing dependence among different rainfall values separated by longer lags. In absence of such a representation of long term memory, annual sums of the daily simulations exhibit a lower variability than the one observed in reality [11]. Thyer and Kuczera [12] applied a Hidden Markov Model (HMM) for simulating long-term persistence in single site rainfall time series. Their results supported that the HMM provides a conceptually more adequate approach, for simulating long-term persistence in hydrological time series, than the ARMA-type processes. Successively, Thyer and Kuczera [13] presented a Bayesian approach for fully quantifying the parameter uncertainty of a HMM for simulating long-term rainfall time series at multiple sites. This extension showed several advantages over the single site HMM.

Generally, a good “driven data” stochastic model has to adequately simulate the sequences of wet and dry days, thus requiring the definition of the basic statistics of the data series of rainfall measured on ground through rain gauges. To this aim, the no-rain day sequences are strictly embedded to the arrival process of the rainfall events, that can be seen as instantaneous pulses (duration=0) or as pulses of random duration (duration>0).

Usually, the rainfall arrival can be seen as a cluster process, characterized by the variability of both intensity and duration in time and space, which are formulated as Poisson cluster processes [14]. Anyway, for time scale equal to or greater than one day, simple Poisson models characterized by a unique parameter λ (defined as process intensity) can be used. With reference to at-site rainfall measurements, if the λ parameter is constant in time, the model can be defined as temporally homogeneous. More generally, the Poisson model can be not homogeneous in time, thus requiring a time-varying parameter, $\lambda(t)$.

In the following, homogeneous and non-homogeneous Poisson models are presented for explaining no-rain day sequences, considering both instantaneous pulses and pulses of random duration.

Homogeneous Poisson model with instantaneous pulses

Let M be the random variable measuring the number of consecutive intervals of length Δt (equal to 1 day) with zero rainfall, followed by at least one rainy day (Fig. 1).

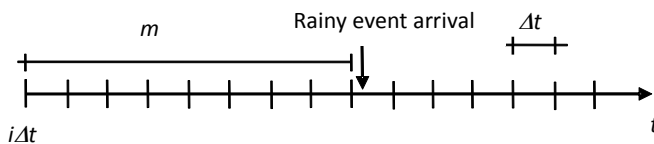


Fig. 1: Schematization of a no-rain day sequence with rainfall as instantaneous pulses.

Under the hypothesis that the arrival process of rainfall is a Poisson model with intensity λ , the probability that at the generic instant $i\Delta t$ a sequence of m no-rain intervals (Δt) will start, followed by the rainy interval $[(i + m)\Delta t, (i + m + 1)\Delta t]$, is given by the following probability density function (pdf):

$$p_M(m) = \begin{cases} \theta^2 (1 - \theta)^m & m = 1, 2, \dots \\ 1 - \theta + \theta^2 & \text{sequence does not start} \end{cases} \quad (1)$$

where:

$$\theta = 1 - \exp(-\lambda\Delta t) \quad (2)$$

The conditional probability of the variable $M | M \geq m_*$, that is the number of m consecutive no-rain intervals equal to, or greater than, a fixed value $m_* > 0$, is given by:

$$P_{M|M \geq m_*}(m) = \theta(1 - \theta)^{m - m_*} \quad m = m_*, m_* + 1, \dots \quad (3)$$

By substituting eq. (2) in eq. (3) it can be obtained:

$$p_{M|M \geq m_*}(m) = [1 - \exp(-\lambda \Delta t)] \exp[-(m - m_*)\lambda \Delta t] \quad m = m_*, m_* + 1, \dots \quad (4)$$

The cumulative distribution function (cdf) of $M | M \geq m_*$ can be obtained as follows:

$$P_{M|M \geq m_*}(m) = 1 - \exp[-(m - m_* + 1)\lambda \Delta t] \quad m = m_*, m_* + 1, \dots \quad (5)$$

The mean and the variance are equal to:

$$\mu_{M|M \geq m_*} = m_* + \frac{\exp(-\lambda \Delta t)}{1 - \exp(-\lambda \Delta t)} \quad \sigma_{M|M \geq m_*}^2 = \frac{\exp(-\lambda \Delta t)}{[1 - \exp(-\lambda \Delta t)]^2} \quad (6)$$

Homogeneous Poisson model with pulses of random duration

With reference to a generic instant $i\Delta t$ within a rainfall event, we define the random variable M' as the number of consecutive intervals of length Δt (equal to 1 day) without arrival of rainfall events, followed by at least one rainy day (Fig. 2).

The probability that, at the generic instant $i\Delta t$, a sequence of m' intervals of length Δt without arrival of rainfall events will start, followed by a rainy event is equal to eq. (1).

Within the sequence of m' intervals, it can be useful to define both the random variable L ($l=0, 1, 2, \dots$) as the number of rainy intervals Δt belonging to a rainfall event started before the instant $i\Delta t$, and the random variable K' ($k'=0, 1, 2, \dots$) as the number of consecutive intervals with no rainfall, where $K' = M' - L$.

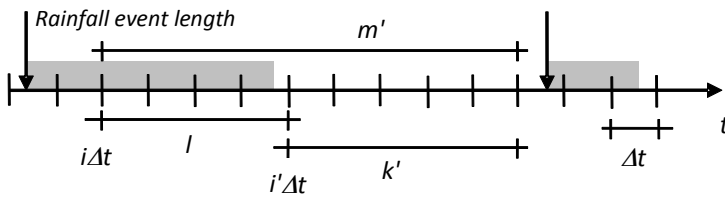


Fig. 2: Schematization of variables m' (sequence of days without arrival of rainfall events), l (sequence of rainy days within m') and k' (difference of the two variables m' and l) with reference to a generic instant $i\Delta t$.

The pdf that at the generic instant $i\Delta t$ a sequence of k' intervals of length Δt without rainfall will start, followed by a rainy interval $[(i'+k')\Delta t, (i'+k'+1)\Delta t]$, can be expressed as:

$$p_{K'}(k') = \begin{cases} r\theta(1-\theta)^{k'} & k' = 1, 2, \dots \\ 1-r(1-\theta) & \text{sequence does not start} \end{cases} \quad (7)$$

where $r = \sum_{l=0}^{\infty} p_L(l)\theta^l$, being $p_L(l)$ the pdf of the variable L .

Given the number of consecutive intervals $K'|K' \geq k_*$ of length Δt with no rainfall equal to, or greater than, $k_* > 0$, the probability that at the generic instant $i\Delta t$ a sequence of k' intervals without rainfall followed by a rainy interval will start, is expressed by the pdf:

$$p_{K'|K' \geq k_*}(k') = \theta(1-\theta)^{k'-k_*} \quad k' = k_*, k_* + 1, \dots \quad (8)$$

By substituting eq. (2) in eq. (8), it yields:

$$p_{K'|K' \geq k_*}(k') = [1 - \exp(-\lambda\Delta t)] \exp[-(k'-k_*)\lambda\Delta t] \quad k' = k_*, k_* + 1, \dots \quad (9)$$

The corresponding cdf is:

$$P_{K'|K' \geq k_*}(k') = 1 - (1-\theta)^{k'-k_*+1} \quad k' = k_*, k_* + 1, \dots \quad (10)$$

By substituting eq. (2) in eq. (10), it yields:

$$P_{K'|K' \geq k_*}(k') = 1 - \exp[-(k'-k_*+1)\lambda\Delta t] \quad k' = k_*, k_* + 1, \dots \quad (11)$$

The mean and the variance are:

$$\mu_{K'|K' \geq k_*} = k_* + \frac{\exp(-\lambda \Delta t)}{1 - \exp(-\lambda \Delta t)} \quad \sigma_{K'|K' \geq k_*}^2 = \frac{\exp(-\lambda \Delta t)}{[1 - \exp(-\lambda \Delta t)]^2} \quad (12)$$

Non-homogeneous Poisson model with instantaneous pulses

The variability of the meteorological conditions triggering rainfall are clearly time dependent [15, 16, 17]. Meteorological phenomena show statistically significant seasonal and daily features due to the revolution of the earth around itself and the sun. Particularly, the storm events in the Mediterranean area show non-stationary behavior with intensity depending on time, $\lambda(t)$, as shown by their marked reduction in summer. Due to this evident periodicity, occurrences of rainfalls can be considered reliably homogeneous only in short temporal intervals. In this case, a stochastic model based on a non-homogeneous Poisson process, characterized by a time-dependent intensity of rainfall occurrence $\lambda(t)$, can be well fitted to explain seasonal variation of no rainfall sequences. Since the probabilistic distribution of $\lambda(t)$ depends on the starting time of the no-rain day sequence, the temporal variation of the intensity parameter $\lambda(t)$ can be statistically developed through a truncated Fourier series. Thus the temporal variation of rainfall intensity $\lambda(t)$ can be expressed as a function of period D:

$$\lambda(t) = \frac{1}{2} a_0 + \sum_{j=1}^{n_h} \left[a_j \cos\left(\frac{2\pi j}{D} t\right) + b_j \sin\left(\frac{2\pi j}{D} t\right) \right] \quad (13)$$

where $a_0, a_j, b_j; j = 1, 2, \dots, n_h$ are the coefficients of the truncated Fourier series, n_h is the number of harmonics and D is the period of the function ($D = 365.25$ for $\Delta t = 1$ day). The integral of the intensity function of non-homogeneous Poisson process is:

$$\Lambda(t) = \frac{1}{2} a_0 t + \frac{D}{2\pi} \sum_{j=1}^{n_h} \left[b_j \cos\left(\frac{2\pi j}{D} t\right) - a_j \sin\left(\frac{2\pi j}{D} t\right) \right] + c \quad (14)$$

where c is an integration constant. The mean value of the arrival number in the generic interval $(t_1, t_2]$ is given by:

$$\Lambda(t_2) - \Lambda(t_1) \quad (15)$$

Considering the random variables M and $M|M \geq m_*$ defined above, the pdf and cdf expressed by equations (4) and (5), respectively, assume the expressions:

$$\begin{aligned}
 p_{M|M \geq m_*}(m) &= \\
 &= \left[1 - \exp(-\Delta\Lambda_{i+m, i+m+1})\right] \exp[-\Delta\Lambda_{i+m_*, i+m+1}] \quad m = m_*, m_* + 1, \dots
 \end{aligned} \tag{16}$$

where $\Delta\Lambda_{j_1, j_2} = \Lambda(j_2\Delta t) - \Lambda(j_1\Delta t)$, and:

$$P_{M|M \geq m_*}(m) = 1 - \exp(-\Delta\Lambda_{i+m_*, i+m+1}) \quad m = m_*, m_* + 1, \dots \tag{17}$$

The mean and the variance of the random variable $M|M \geq m_*$ are:

$$\mu_{M|M \geq m_*} = m_* + \sum_{m=m_*}^{\infty} \exp(-\Delta\Lambda_{i+m_*, i+m+1}) \tag{18}$$

$$\begin{aligned}
 \sigma_{M|M \geq m_*}^2 &= \\
 &= 2 \sum_{m=m_*}^{\infty} m \exp(-\Delta\Lambda_{i+m_*, i+m+1}) - \left(\mu_{M|M \geq m_*} - m_*\right) \left(1 + \mu_{M|M \geq m_*} - m_*\right)
 \end{aligned} \tag{19}$$

Non-homogeneous Poisson model with pulses of random duration

With reference to the random variables M' and K' introduced above, in the case of non-homogeneous Poisson model, it can be verified that the pdf of the random variable K' assumes the following expression:

$$\begin{aligned}
 p_{K'|K' \geq k_*}(k') &= \\
 &= \left[1 - \exp(-\Delta\Lambda_{i'+k', i'+k'+1})\right] \exp[-\Delta\Lambda_{i'+k_*, i'+k'}] \quad k' = k_*, k_* + 1, \dots
 \end{aligned} \tag{20}$$

and the cdf is:

$$P_{K'|K' \geq k_*}(k') = 1 - \exp(-\Delta\Lambda_{i'+k_*, i'+k'+1}) \quad k' = k_*, k_* + 1, \dots \tag{21}$$

The mean and the variance are:

$$\mu_{K'|K' \geq k^*} = k^* + \sum_{k'=k^*}^{\infty} \exp(-\Delta\Lambda_{i'+k^*, i'+k'+1}) \quad (22)$$

$$\begin{aligned} \sigma_{K'|K' \geq k^*}^2 &= \\ &= 2 \sum_{k'=k^*}^{\infty} k' \exp(-\Delta\Lambda_{i'+k^*, i'+k'+1}) - \left(\mu_{K'|K' \geq k^*} - k^* \right) \left(1 + \mu_{K'|K' \geq k^*} - k^* \right) \end{aligned} \quad (23)$$

2. RESULTS AND DISCUSSION

In this paper, in order to analyse no-rain day sequences, the non-homogeneous Poisson model with pulses of random duration has been applied to the Cosenza rain gauge, which has been chosen due to the high quality data. In fact, the observation period of daily rainfall data for this rain gauge spans from 1916 to 2010 and presents missing data only during the Second World War period. Thus, only data from 1951 to 2010 have been selected.

To ensure parsimony of the model, Fourier series has to be limited to the minimum number of harmonics. The estimation of the Fourier coefficients for one harmonic has been obtained through the maximum likelihood method, expressed as:

$$\begin{aligned} \ln L(a_0, a_1, b_1) &= - \sum_{n=1}^{N_d} \Delta\Lambda_{i'_n+k^*, i'_n+k'_n} (a_0, a_1, b_1) + \\ &+ \ln \prod_{n=1}^{N_d} \left[1 - \exp(-\Delta\Lambda_{i'_n+k^*, i'_n+k'_n+1} (a_0, a_1, b_1)) \right] \end{aligned} \quad (24)$$

where N_d is the number of no-rain day sequences. To guarantee stability in the statistical estimation, the sequences used in the application are the ones with duration equal to or greater than 5 days ($k^* = 5$). Moreover, with the aim to analyse temporal change in the sequences, the whole series has been subdivided in two subseries, each composed by 30 years of observation: 1951-1980 and 1981-2010. The estimated Fourier parameters are reported in Tab. 1.

30-year subperiod	N_d	a_0	a_1	b_1
1951-1980	485	0.307	0.0613	0.0280
1981-2010	469	0.279	0.0626	0.0231

Table 1: Statistical features of the different subperiods and estimated values of Fourier coefficients. N_d =number of data of no-rain day sequences; a_0, a_1, b_1 : Fourier coefficients.

In order to analyse the seasonality of the no-rain sequence duration, K' , fig. 3 shows, for each day of the year, the mean value of this variable (in log scale) for both the 30-year periods. The distribution of K' presents maximum values between about the 150th and the 250th day of the year, a time span which roughly corresponds to the summer period, while minimum values are detected in winter. Moreover, by using the estimated Fourier parameters (Tab. 1), the expected values of K' , obtained through a Monte Carlo simulation, have been compared with the corresponding observed values derived by the historical data series.

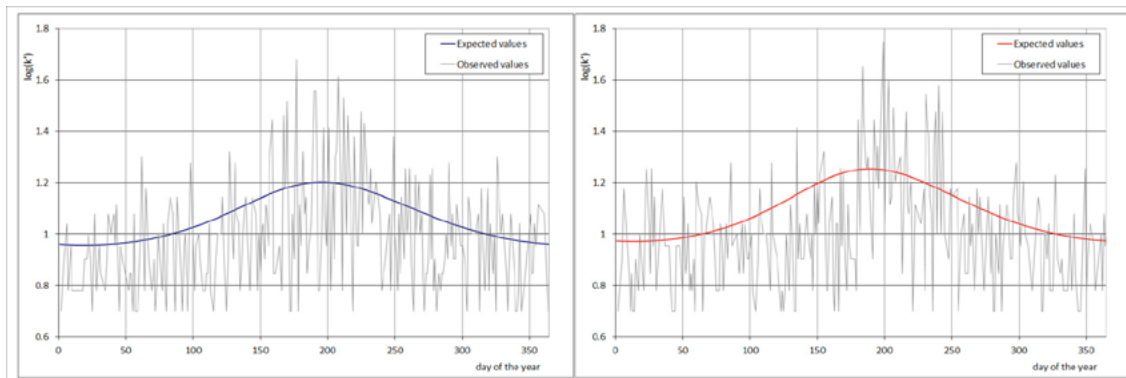


Fig. 3: Comparison between observed and expected values (maximum likelihood method) of K' for the two subperiods (left: 1951-1980; right: 1981-2010).

In Fig. 4 the difference between the daily distributions of the expected values of K' , $E(K')$, estimated for both the subperiods, is shown. For each day of the year, $E(K')$ values estimated in the 1981-2010 subperiod are higher than the ones estimated in the 1951-1980 subperiod, and this difference is more evident during the summer period. Moreover, the maximum value of $E(K')$ for the 1981-2010 subperiod falls few days before the correspondent value of the 1951-1980 subperiod.

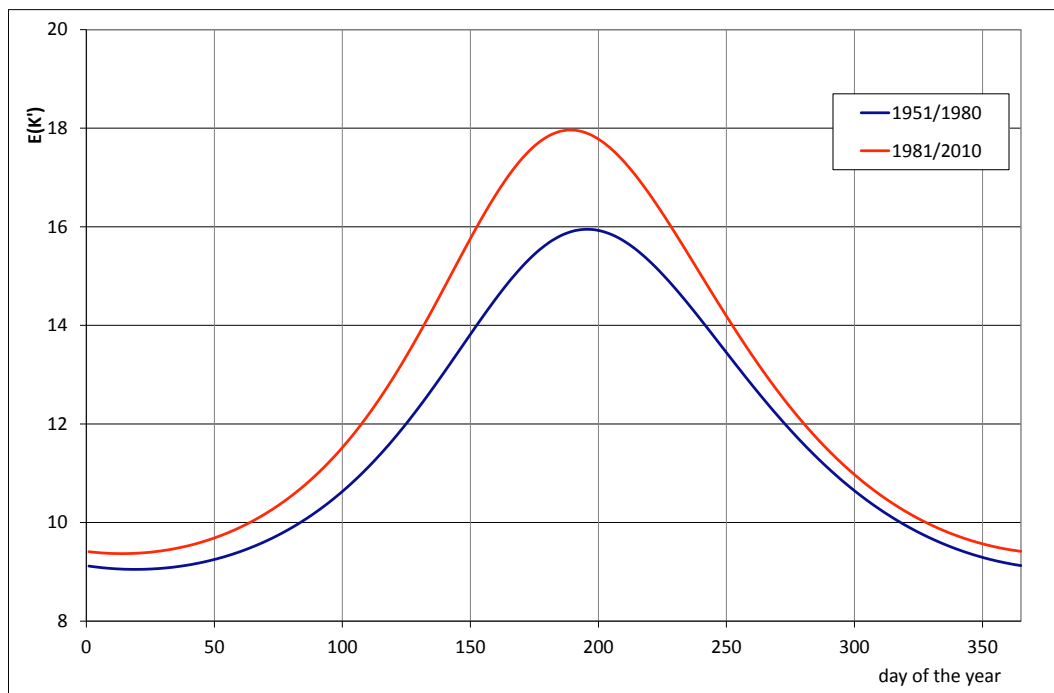


Fig. 4: Comparison between expected values of K' for the two subperiods.

These results show a change in rainfall distribution during the year, with a longer duration of the no-rain day sequences in the last 30-year period, even if the number of sequences (N_d) slowly decreases. The longer duration of the no-rain day sequences matches with the general tendency of increasing frequency of the drought periods, observed in various part of the world [18].

The research is the first step of a wider investigation regarding the probabilistic modelling of both occurrence and intensities of wet and dry rainfall periods, by considering, in particular, the cumulated rainfall lower than fixed thresholds. Anyway, the procedure presented in this work needs an improvement as regards parameters estimation and validation on a larger number of data series, that will be the object of a further application. Moreover, the at-site procedure can be replaced by adopting spatial analysis, taking into account the rainfall variability within a region. The tendency showed in this study, if confirmed by further analyses based on more detailed rainfall stochastic models applied to larger data base, could be very useful in water resources planning and management of specific drainage basins.

3. REFERENCES

- Box G.E.P. & Jenkins G.M. (1970), *Time Series Analysis Forecasting and Control*, Holden-Day, San Francisco, USA. (1)
- Salas J.D. & Smith R.A. (1981), *Physical basis of stochastic models of annual flows*, Water Resources Research, No. 17, pp. 428–430. (2)
- Salas J.D. (1993), *Analysis and modeling of hydrologic time series*, In: Maidment, D. (Ed), Handbook of Hydrology, McGraw-Hill, New York, USA. (3)
- Grayson R.B., Argent R.M., Nathan R.J., McMahon T.A. & Mein R.G. (1996), *Hydrological Recipes: Estimation Techniques in Australian Hydrology*, Cooperative Research Centre for Catchment Hydrology, Melbourne, Australia. (4)
- Srikanthan R. & McMahon T.A. (2000), *Stochastic Generation of Climate Data: A Review*, CRC for Catchment Hydrology, Monash University, Clayton, Victoria, Australia. (5)
- Malamud B.D. & Turcotte D.L. (1999), *Self affine time series: measures of weak and strong persistence*, Journal of Statistical Planning and Inference, No. 80, pp. 173–196. (6)
- Koirala S., Gentry R.W., Mulholland P.J., Perfect E. & Schwartz J.S. (2010), *Time and frequency domain analysis of high-frequency hydrologic and chloride data in an east Tennessee watershed*, Journal of Hydrology, No. 387, pp. 256–264. (7)
- Woolhiser D.A. (1992), *Modeling daily precipitation -progress and problems*, In: Walden, A.T. & Guttorp, P. (Eds), Statistics in the environmental and earth sciences. Edward Arnold, London, UK. (8)
- Gabriel K.R. & Neumann J. (1962), *A Markov chain model for daily rainfall occurrences at Tel Aviv*. Quarterly Journal of the Royal Meteorological Society, No. 88, pp. 90–95. (9)
- Buishand T.A. (1978), *Some remarks on the use of daily rainfall models*, Journal of Hydrology, No. 36, pp. 295–308. (10)
- Srikanthan R. (2005), *Stochastic generation of daily rainfall using a nested transition probability model*. 29th Hydrology and Water Resources Symposium, Engineers Australia, Canberra, Australia. (11)
- Thyer M. & Kuczera G. (2000), *Modelling long-term persistence in hydro-climatic time series using a hidden state Markov model*, Water Resources Research, No. 36, pp. 3301–3310. (12)

- Thyer M. & Kuczera G. (2003), *A hidden Markov model for modelling long-term persistence in multi-site rainfall time series. 2. Real data analysis*, Journal of Hydrology, No. 275, pp. 27–48. (13)
- Daley D.J. & Vere-Jones D. (1988), *An Introduction to the Theory of Point Processes*, Springer-Verlag, New York, USA. (14)
- Waymire E. & Gupta V.K. (1981), *The mathematical structure of rainfall representations 1. A review of the stochastic rainfall models*. Water Resources Research, No. 17, pp. 1261–1272. (15)
- Smith J.A. & Karr A.F. (1983), *A point process model of summer season rainfall occurrences*, Water Resources Research, No. 19, pp. 95–103. (16)
- Chang T.J., Kavvas M.L. & Delleur J.W. (1984), *Daily precipitation modeling by discrete autoregressive moving average processes*, Water Resources Research, No. 20, pp. 565–580. (17)
- IPCC (2007), *Climate change 2007: The Physical Science Basis*. Contribution of Working Group I to the Fourth Assessment Report of the Intergovernmental Panel on Climate Change. Cambridge University Press, Cambridge, UK and New York, USA. (18)

Mesoscale biological-physical interactions in the Sardinian Sea

Bonamano S.^{1*}, Stefani C.¹ and Marcelli M.¹

¹Tuscia University-DEB, Viterbo

*Corresponding author: simo_bonamano@unitus.it

Abstract

In this work the effect of physical processes on the biological variables distribution, with particular attention to phytoplankton primary production, was investigated in four different time periods between 2002 and 2004 in the Sardinian Sea. In order to study the main mesoscale phenomena in the Western Mediterranean Sea, a multidisciplinary approach based on satellite observations, in situ data and numerical simulations was used. In particular MADT (Mediterranean Absolute Dynamic Topography) satellite data and Okubo-Weiss parameter allowed us to detect intense mesoscale activities like the Algerian Eddies (AEs) and the North Balearic Front (NBF). The effects of AEs and NBF on the phytoplankton biomass and primary production distribution were analysed in the Sardinian Sea by in situ data and bio-optical model respectively. To evaluate the biological response associated with mesoscale processes, the phytoplankton primary production (PP) was calculated by the new version of PhytoVFP model. It includes four components: (1) model of superficial and underwater PAR; (2) model of marine phytoplankton photo-physiology; (3) estimation of instantaneous PP and (4) estimation depth integrated and daily PP. The comparison between vertical distributions of potential density and phytoplankton primary production calculated by PhytoVFP model allowed to analyse how the AEs and NBF can modulate the biological response in the Sardinian Sea.

Keywords: *Mesoscale dynamics, phytoplankton primary production, Sardinian Sea, bio-optical model, multidisciplinary approach*



1. INTRODUCTION

The ocean, covering more than 70% of the Earth's surface, can modulate the atmospheric CO₂ concentration by means of the so-called biological pump. This mechanism refers to the sinking of organic matter from the surface productive layers to deep waters in the ocean [1]. Quantifying the carbon flux into the ocean through the marine primary productivity, and understanding the mechanisms that might control it, are of crucial importance for defining the planet's carbon budget. The major player of the oceanic primary production is phytoplankton through photosynthesis. Phytoplankton distribution in the ocean is mainly driven by the availability of light and nutrients [2]. These growth-limiting factors depend in turn on physical processes at different space and time scales.

As revealed by many studies during the last two decades, the Mediterranean Sea is an oceanic region where intermediate scales (mesoscale) play a key role in determining the characteristics of the basin-wide marine circulation, the distribution of water masses, and even ecosystem functioning. A multidisciplinary approach in the study of mesoscale structures and processes is an increasing demand of researchers.

In places where the flow changes in time, and where eddies interact with each other or with the mean flow, frontogenesis or frontolysis results, and the conservation of potential vorticity consequently induces vertical motions. Such upwelling or downwelling events can be strong enough (tens of meters per day) and last long enough (several days) to affect biological processes. The primary production by planktonic algae in particular can be affected, for instance as a result of the displacement of phytoplankton cells along the vertical light profile or as a result of a vertical flux of plant nutrients.

Lewis (2002) [3] provided a review of 50 years of research recognizing and explaining the relationship between scales of biological patchiness and physical mechanisms in the open ocean [see also 4, 5].

The primary producers and herbivores have shorter life time scales (days); time scales that coincide with those of mesoscale eddies and fronts. This suggests that plankton can have either good or bad weather lifetimes associated with just a single cyclonic or anticyclonic eddy system. It also suggests that species or groups may be adapted to rapid acclimation rather than niche exploitation.

2. STUDY AREA

The area investigated in this study includes Sardinian Sea which is part of the Algero-Provencal Basin (APB). This basin represents one of the most dynamic area of the entire Mediterranean Sea, and for this reason, its hydrodynamism was broadly investigated in the past [e.g. 6, 7]. It is divided in two parts, southern and northern, by North Balearic Front (NBF). This is formed by north-south density gradient between saltier water to the north and fresher modified Atlantic water to the south.

The southern part, namely the Algerian Basin (AB), is characterized at the surface by the Atlantic Water (AW) flowing in the Mediterranean Sea through the Gibraltar Strait [8]. AW flows along the Algerian slope, forming the Algerian Current (AC). This current is unstable, meanders and generates Anticyclonic Eddies (AE). Once they reach the Sardinian Channel, they can collapse or, strongly modified, can stay here for several months before collapsing [8]. In some cases, the AEs, can detach from the AC moving eastward and northward. In these cases, the eddies can follow the Sardinian slope northward becoming open-sea eddies. These large “old” and highly energetic AEs can accomplish one or more cyclonic cycle in the AB south of 40°N. Taupier-Letage et al. (2003) [9] depicted complicated relationships depending on the life history, path, and size of the AEs then indicating that further investigations are necessary.

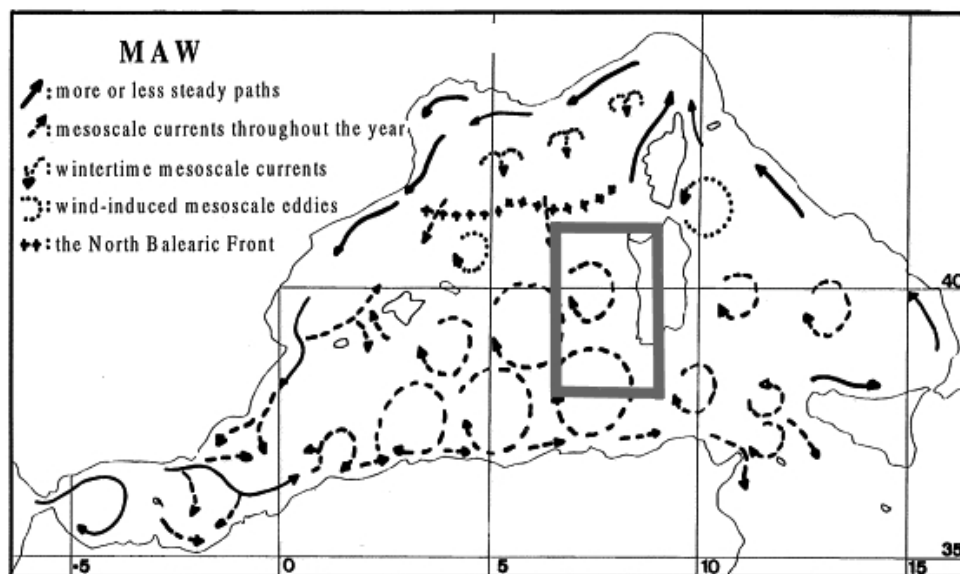


Fig.1: The general circulation of the Atlantic Water (AW) in the western Mediterranean [adapted from 7]. The gray rectangle indicates the Sardinian Sea, the area where MedGOOS cruises was carried out

The northern part of the basin (Provençal Basin, PB) is also a highly dynamic region with strong mesoscale activity, studied as site of deep water formation. The deep water formation and the seasonal bloom occurring in the so-called MEDOC area in spring are strictly related as described in Jacques et al. (1973) [10]. The deep water formation process substantially involves three phases. During the last phase, stable columns of dense waters sink followed by a rapid restratification of the surface waters, also responsible for the onset of an intense algal bloom. The APB was also object of studies for its biophysical relationships, often focusing on the biological signature associated with mesoscale processes but poorly investigated at larger temporal and spatial scales, needing the analysis of consistent and well-structured datasets.

3. MATERIALS AND METHODS

To understand the mesoscale processes a multidisciplinary approach was used. In this case the interactions between physical structures and biological processes were investigated in the Sardinian Sea by satellite observations, numerical simulations and in-situ data. In order to detect the mesoscale activities in-situ biophysical variables, altimeter satellite data and Okubo-Weiss parameter have been described.

Biophysical variables collected

In connection with SIMBIOS-MURST (Sistema per lo studio del Mare con Boa Integrata OffShore) project funded by MedGOOS (Mediterranean Global Ocean Observing System) program, several oceanographic cruises were taken place in Western Mediterranean Sea to study the spatial and seasonal variability of the mesoscale dynamics and their interactions with biogeochemical fluxes. In this work four oceanographic cruises (MedGOOS 4, MedGOOS 5, MedGOOS 6 and MedGOOS 7), carried out in the Sardinian Sea between 2002 and 2004, were considered. In the following table the periods and the number of stations of the four campaigns were reported .

Name	Dates	Stations
MedGOOS 4	10-23 May 2002	64
MedGOOS 5	01-14 November 2002	37
MedGOOS 6	29 March to 14 April 2003	76
MedGOOS 7	08-24 January 2004	72

Table 1: Summary of the cruises

Casts during MedGOOS cruises were performed from the Italian RV *Urania* with a SBE 911 plus CTD profiler and a PrimProd probe.

The first instrument was calibrated within a few months at most from the cruises and was fitted with an in situ SeaTech fluorometer and Seabird dissolved oxygen probe. Acquisition rate for all sensors was 24 scans s⁻¹.

PrimProd is a double-flash pulse fluorometer for measuring temperature, underwater irradiance, chlorophyll concentration and photosynthetic activity by “pump and probe” fluorometric technique. Each measuring cycle involves a consequence of three flashes: probe-actinic-probe. Chlorophyll fluorescence from open reaction centers (F₀) is measured during the first probe flash. Then, after the time interval, the actinic flash of saturating intensity follows. The second probe flash is given 0.05 ms after the pump flash, when all the reaction centres still remain in the closed state. During the second probe flash, chlorophyll fluorescence from closed reaction centres (F_m) is measured. Photosynthetic efficiency (the efficiency of photochemical energy transformation in open reaction centres) is calculated as the ratio (F_m-F₀)/F_m.

During the oceanographic cruises, more than 300 water samples have been collected to estimate chlorophyll-a concentration by spectrophotometric method.

Altimeter satellite data and Okubo-Weiss parameter

In this work MADT (Mediterranean Absolute Dynamic Topography) daily time series provided fundamental information on the mesoscale dynamics in the APB. The altimeter data used here is part of the Ssalto/DUACS products, distributed by AVISO (Archiving Validation and Interpretation of

Satellite Oceanographic Data). To avoid spurious signals related to uneven data coverage, the Mediterranean Absolute Dynamic Topography (MADT) ‘reference’ maps were chosen, built from only two altimeters at any given time, with the addition of a mean dynamic topography (MDT) to the sea level anomalies (SLA), as detailed in Rio et al. (2007) [11] those who estimated an accuracy (RMS error) of the order of 3 cm for the MADT in the Gulf of Lion.

To characterize the spatial structure of the mesoscale features we made use of the Okubo–Weiss parameter [12], which allows to separate the flow into vorticity-dominated and deformation-dominated regions. The application of this parameter to geostrophic velocity fields obtained from MADT maps showed that the observed eddies had a spatial structure in close resemblance to that found in coherent vortices of two-dimensional turbulence. These eddies appeared to have a rather coherent vorticity-dominated core region surrounded by an outer region dominated by deformation with a very complicated and variable in time structure [13].

During the MedGOOS4 cruise, two AEs called M4-1 and M4-2 and one AE (M4-3) that detached from AC (Fig. 2 and 3) were detected; NBF was located above 40° N.

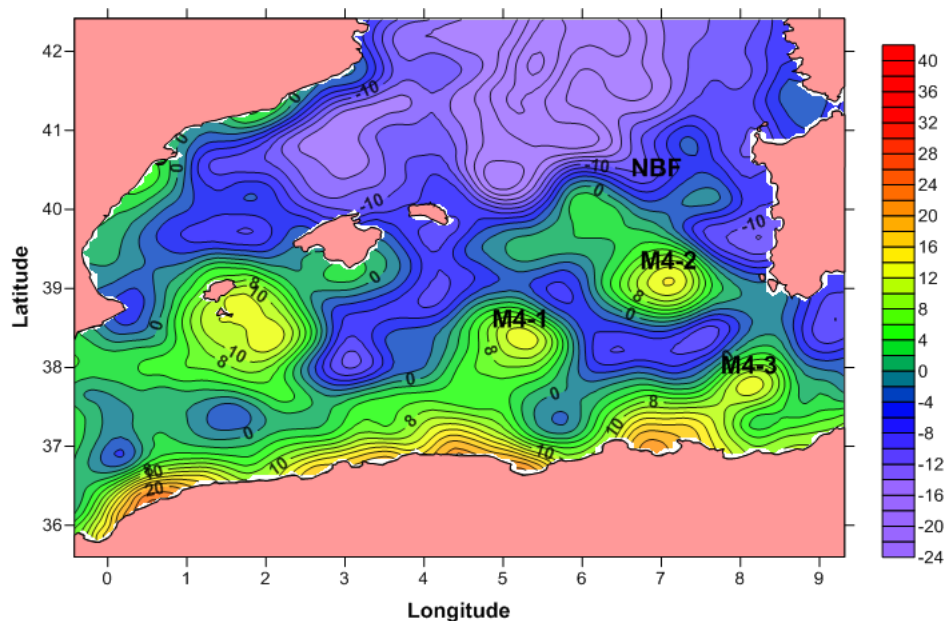


Fig. 2: Distribution of the MADT data in the WMED with the indication of main mesoscale structures during MedGOOS4 cruise

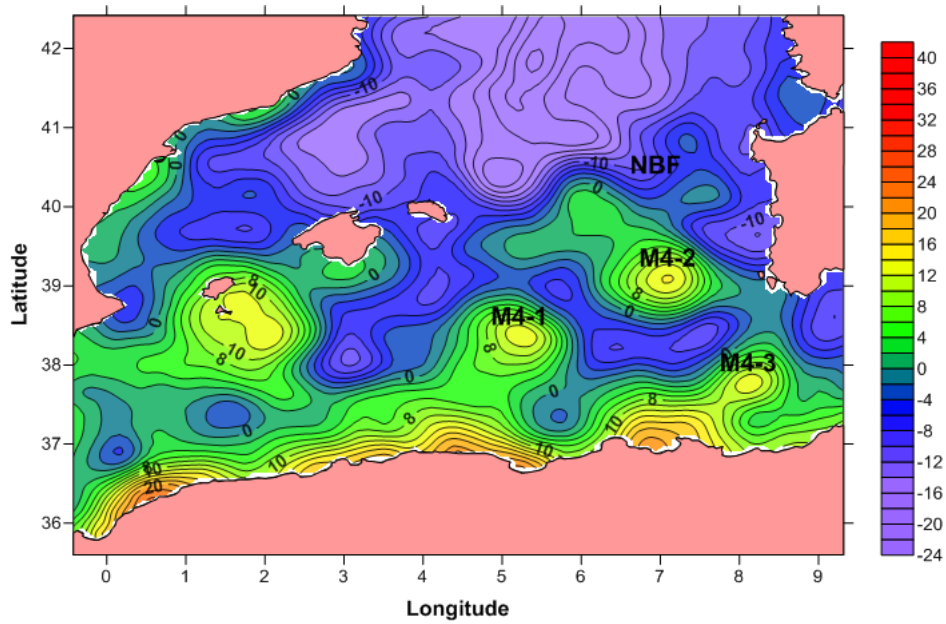


Fig.3: distribution of the Okubo–Weiss parameter in the WMED during MedGOOS4 cruise.

In the MedGOOS5 cruise, MADT data and Okubo-Weiss parameter (Fig. 4 and 5) highlighted the genesis of the “new” AE (M5-1) near Algerian coast.

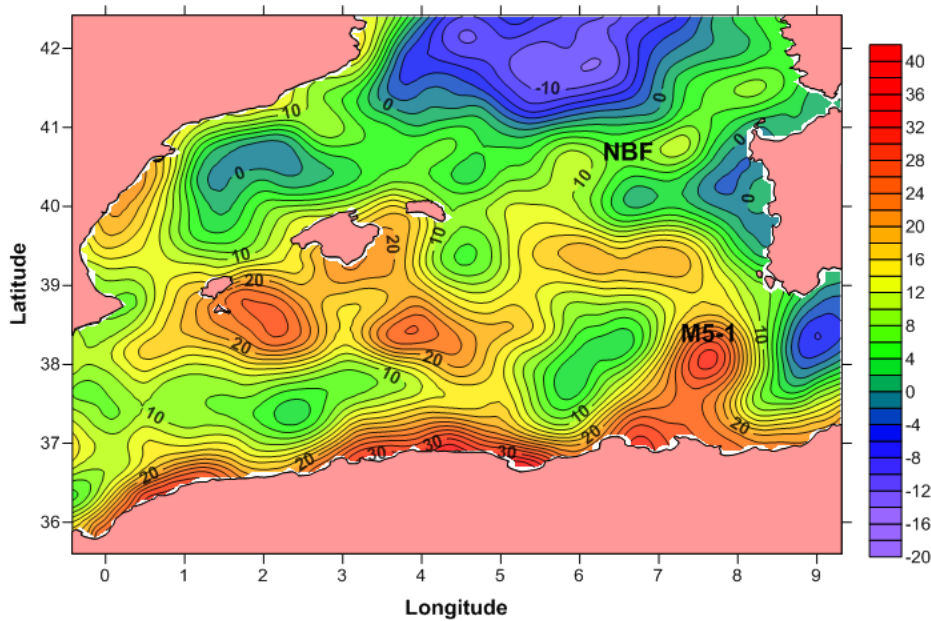


Fig. 4: Distribution of the MADT data in the WMED with the indication of main mesoscale structures during MedGOOS5 cruise

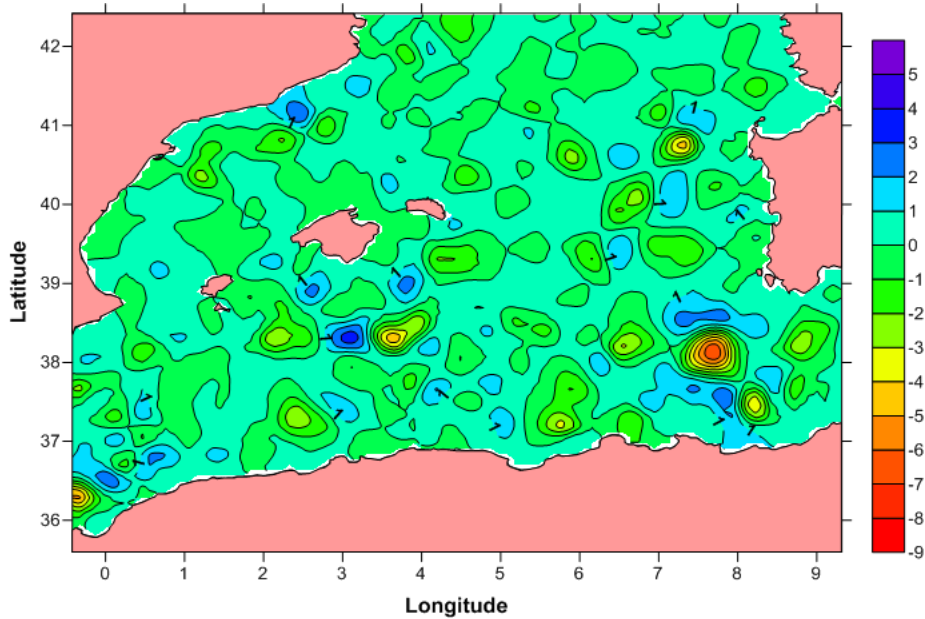


Fig. 5: Distribution of the Okubo–Weiss parameter in the WMED during MedGOOS5 cruise

The MedGOOS6 was characterized by a rapid change of dynamic conditions (Fig.6 and 7): in the first time there was a cyclonic eddy (M6-1) caused by a NBF instability; subsequently, new anticyclonic eddy (M6-2) directed towards Sardinian Sea was observed.

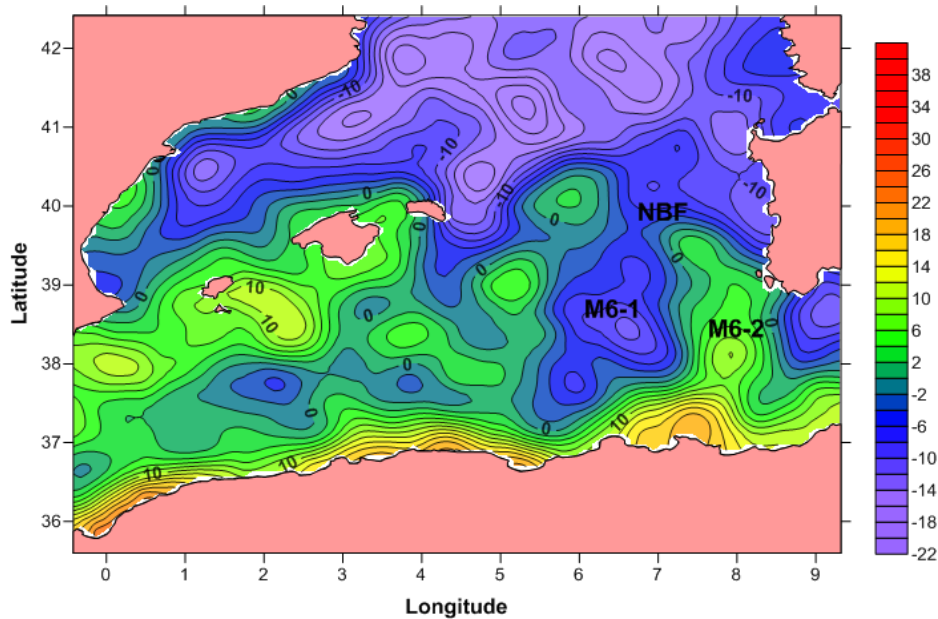


Fig. 6: Distribution of the MADT data in the WMED with the indication of main mesoscale structures during MedGOOS6 cruise

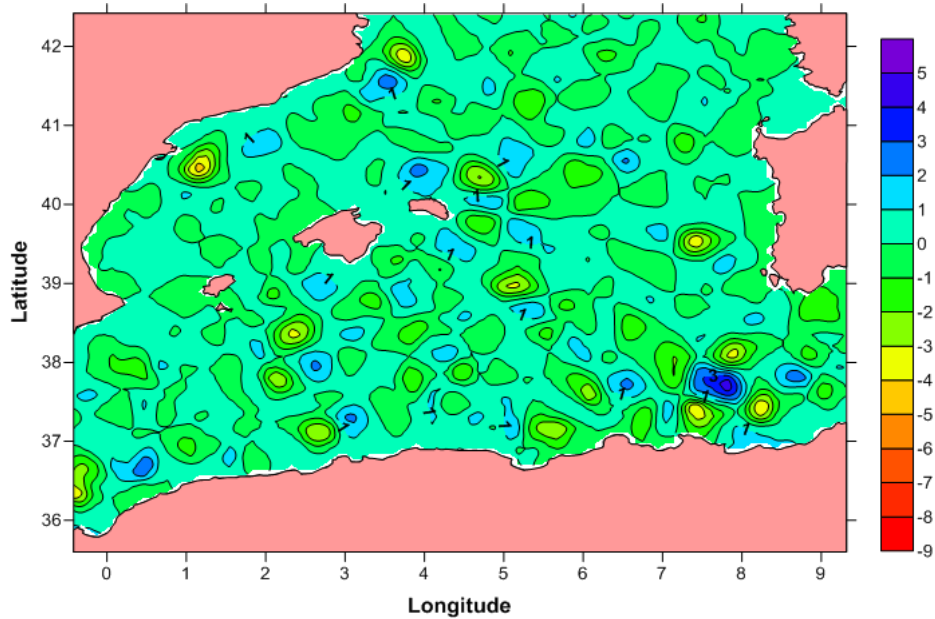


Fig. 7: Distribution of the Okubo-Weiss parameter during MedGOOS6 cruise

Due to the shift of the NBF towards low latitudes (38-39° N), during the MedGOOS7 cruise, the study area was dominated by deformation (Fig. 8 and 9) with a very complicated and variable in time structure.

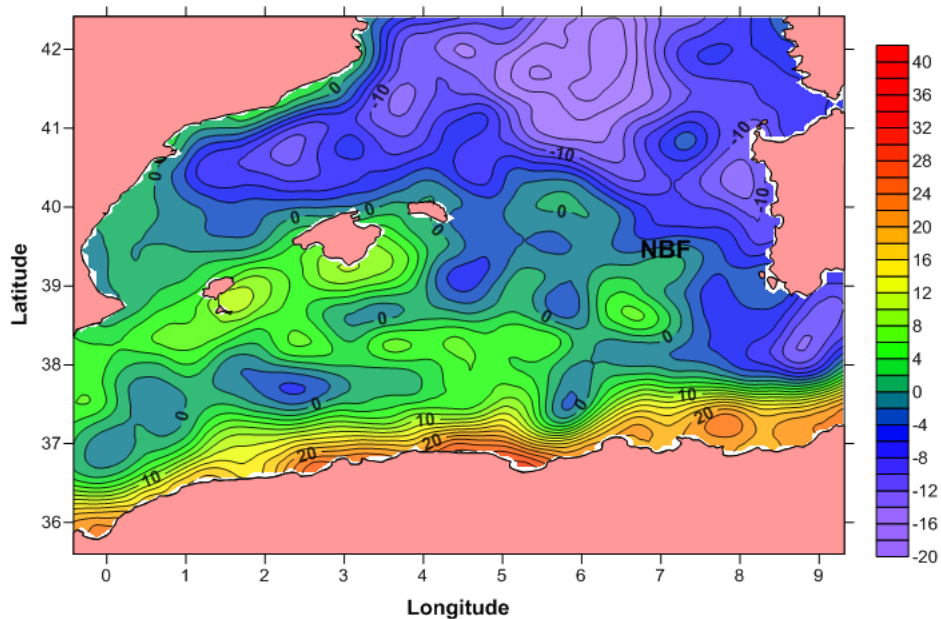


Fig. 8: Distribution of the MADT data in the WMED with the indication of main mesoscale structures during MedGOOS7 cruise

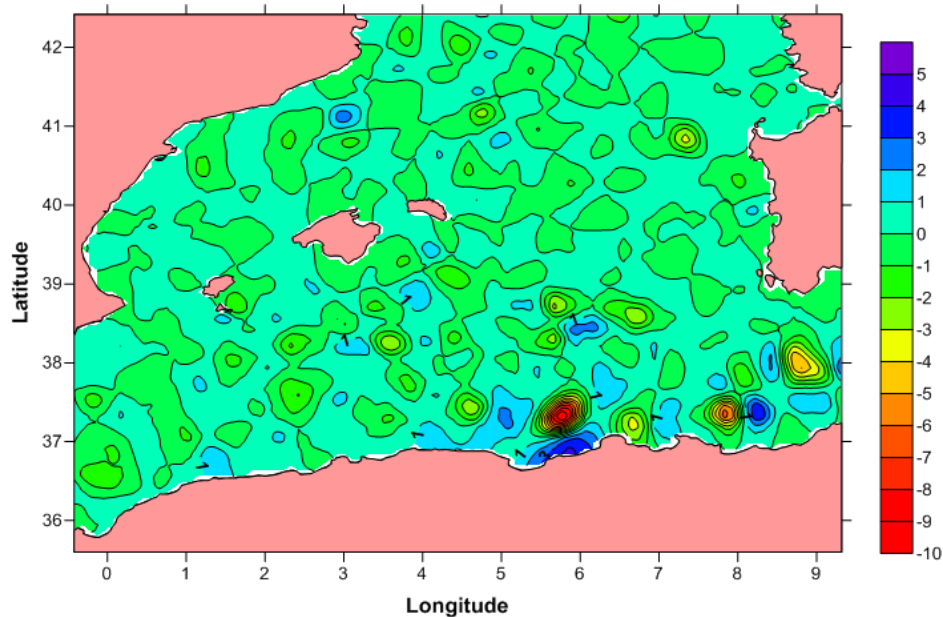


Fig. 9: Distribution of the Okubo–Weiss parameter in the WMED during MedGOOS7 cruise

4. DESCRIPTION OF PhytoVFP MODEL

Phytoplankton primary production was calculated by Phyto-VFP (Phytoplankton Variable Fluorescence Production) model. It was developed, tested and validated by Marcelli et al.(1997) [14] and its architecture was based on four components:

1. model of superficial and underwater PAR;
2. model of marine phytoplankton photo-physiology;
3. estimation of instantaneous PP rates;
4. estimation of depth-integrated and daily PP.

The model of superficial and underwater PAR was obtained taking into account the solar spectral irradiance [15, 16], the direct radiation and the diffuse reflectance [17], the cloud coverage [18] and the effect of chlorophyll biomass depth-profile on the light attenuation.

In the second component we were analysed the effect of photoacclimation on the diel cycles of the photosynthetic response of *Skeletonema costatum* (Greville) Cleve, with the adoption of optical measurements of in vivo chlorophyll-a variable fluorescence. By the laboratory experiments the PE relationship of the organism was parametrized and the variations of the PE parameters (α , P_{max} , E_k) were modelled for three different physiological conditions, as a function of the hour of the day. The superficial and underwater PAR and PE parameters estimated in the first two component, as well as chlorophyll-a and photosynthetic efficiency profiles, were used to calculate instantaneous primary production. The biomass concentration in the water column may be obtained from direct, shipboard observation or from a model; while photosynthetic efficiency can be measured by submersible pump and probe fluorometer.

Instantaneous primary production (PPp) was calculated by the equation:

$$PPp(t, z) = \sigma \cdot FP(t, z) \cdot Eff(z) \cdot Chl(z)$$

where σ is quantum yield; $Eff(z)$ is photosynthetic efficiency; $Chl(z)$ is phytoplankton biomass profile; $FP(t, z)$ is photosynthetic rate (Production Function). In the fourth component of the PhytoVFP model PPI (Integrated Primary Production) and PPg (Daily Primary Production) were computed by the following equations:

$$PPI(t) = \sigma \cdot \int_{-Z_{Euf}}^0 FP(t, z) \cdot Eff(z) \cdot Chl(z) \cdot dz$$

$$PPg = \sigma \cdot \int_{-Z_{Euf}}^0 \int_{t_1}^{t_2} FP(t, z) \cdot Eff(z) \cdot Chl(z) \cdot dz \cdot dt$$

where $-Z_{Euf}$ is euphotic zone and t_1 and t_2 are sunrise and sunset respectively.

The new version of PhytoVFP model contains two main changes:

1. the surface and underwater radiation was estimated integrating the PAR spectrum each 60 intervals and considering the cloud cover;
2. the photosynthetic rate was calculated choosing the Platt expression.

These upgrades were validated by in-situ and modelled data. The comparison between calculated and measured PAR(0+) showed strong correlation in clear sky ($R^2=0.8992$) and in cloudy sky ($R^2=0.8747$) condition; PAR(z) profiles estimated by first component of PhytoVFP model highlighted a close relationship with in situ measurements when the sun is near the zenith. Given the lack of radiocarbon (^{14}C) uptake to measure net photosynthesis during the MedGOOS cruises, the primary production calculated by PhytoVFP model was compared with PP obtained in the same physiological and environmental conditions by Morel model [19]. The analysis on more 300 PP profiles had demonstrated that phytoplankton primary production calculated with PhytoVFP model was very close to PP estimated by the Morel model [20]. However there are some differences between the two bio-optical models: at high depths PP estimated by PhytoVFP was lower than PP estimated by Morel model, while in the surface layers the first model calculated value higher than those computed by second model. The underestimation of the PhytoVFP was mainly due to photosynthetic efficiency effect, while the overestimation at low depth was caused by phytoplankton photo-acclimation to high radiation. In order to obtain a synoptic representation of PP, we assumed that the spatial variation of photosynthetic efficiency and phytoplankton biomass didn't change during cruises periods.

5. RESULTS

The vertical distribution of biophysical variables were described in the stations where the mesoscale phenomena were detected thanks to MDTA data and Okubo-Weiss parameters. These physical processes did not propagate during oceanographic cruises, so that the figures 12-15 are representative of all transects.

In the MedGOOS4 cruise, isopycnals were depressed in correspondence of the the areas where the anticyclonic eddies were detected, accordingly isolines were doming near M4-2 and M4-3 edges. Sigma-t values lower of 28 kg/m^3 were found up to 100 m. Higher chlorophyll-a concentration were in patches between ~ 30 and 70 m reaching $\sim 0.8 \text{ mg/m}^3$ in the central zone. The primary production highest values ($\sim 1.4 \text{ mg C}/(\text{m}^3\cdot\text{h})$ between 30 and 45 m) were found in depths shallower than the DCM (Deep Chlorophyll Maximum), at the peripheral zones of two AEs (M4-2 and M4-3).

In the sigma-t transect (MedGOOS5), isopycnals were depressed by ~60 m in the central zone where M5-1 was individuated. Higher chlorophyll-a concentration was found at eddy edges reaching ~0.85 mg/m³ at station 572 between 30 and 75 m. The primary production showed highest values (~0.35 mg C/(m³*h)) in correspondence of M5-1 at ~15 m. In the MedGOOS6 cruise, isopycnals distributions showed two depressions that were caused by the interaction between M6-2 and M6-1. Higher chlorophyll-a concentration were found in patches between 50 and 70 m reaching a maximum value of ~0.8mg/m³.The maxima primary production reached ~0.275 mg C/(m³*h) at the peripheral zone of M6-2. In the other stations primary production was homogeneously distributed and did not exceed ~0.2 mg C/(m³*h). Potential density values acquired during MedGOOS7 cruise were ranged from 28.5 to 29.1 kg/m³. Chlorophyll concentration was homogeneously distributed, maxima reached ~0.75 mg/m³. Primary production showed similar distribution of phytoplankton biomass with maxima values in the upper layers.

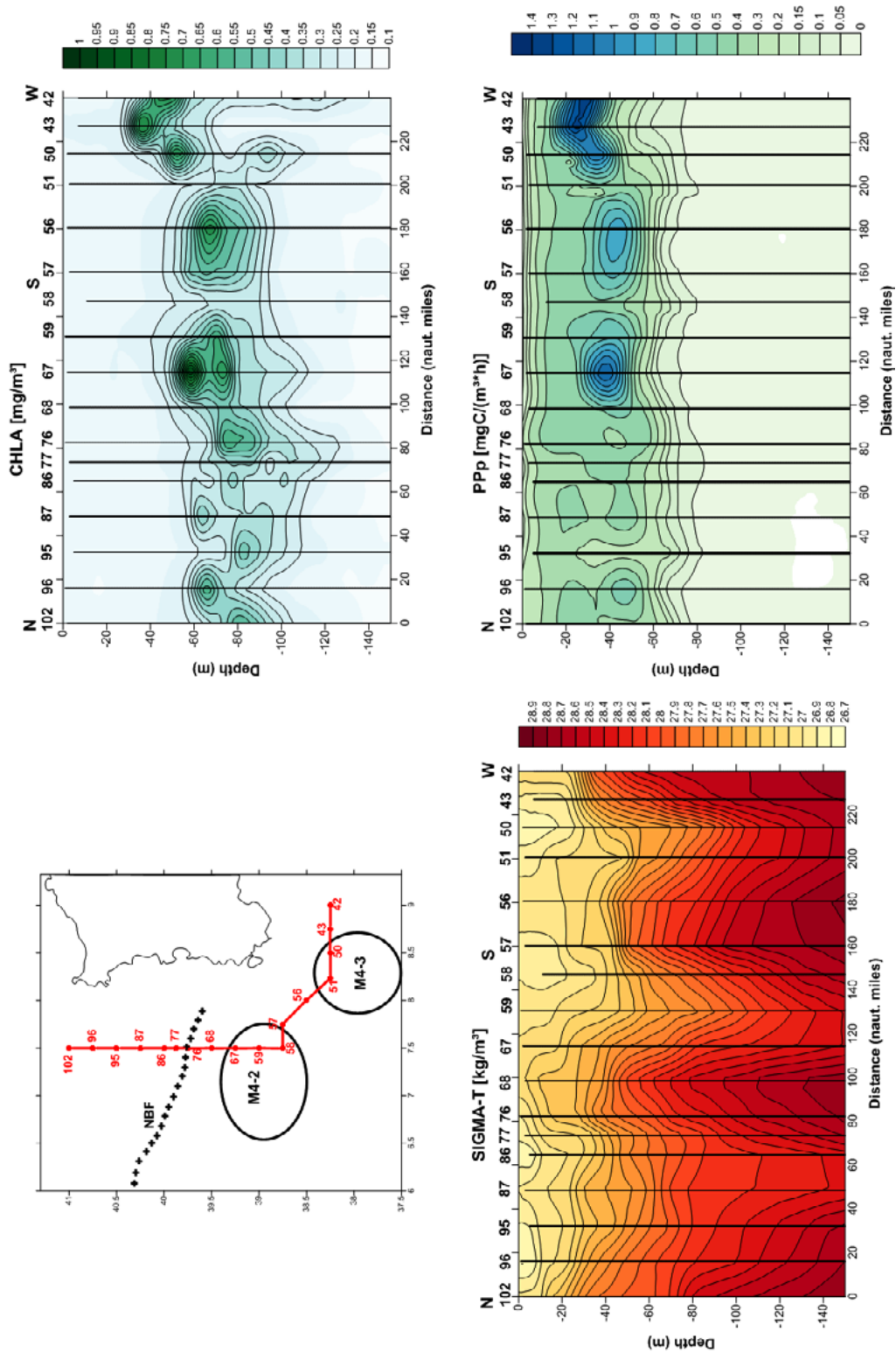


Fig. 12: Transect 102-42 (MedGOOS4): (a) mesoscale structures schematic and stations position, (b) potential density (kg/m^3), (c) chlorophyll concentration (mg/m^3) and (d) primary production ($\text{mg C}/(\text{m}^3\cdot\text{h})$)

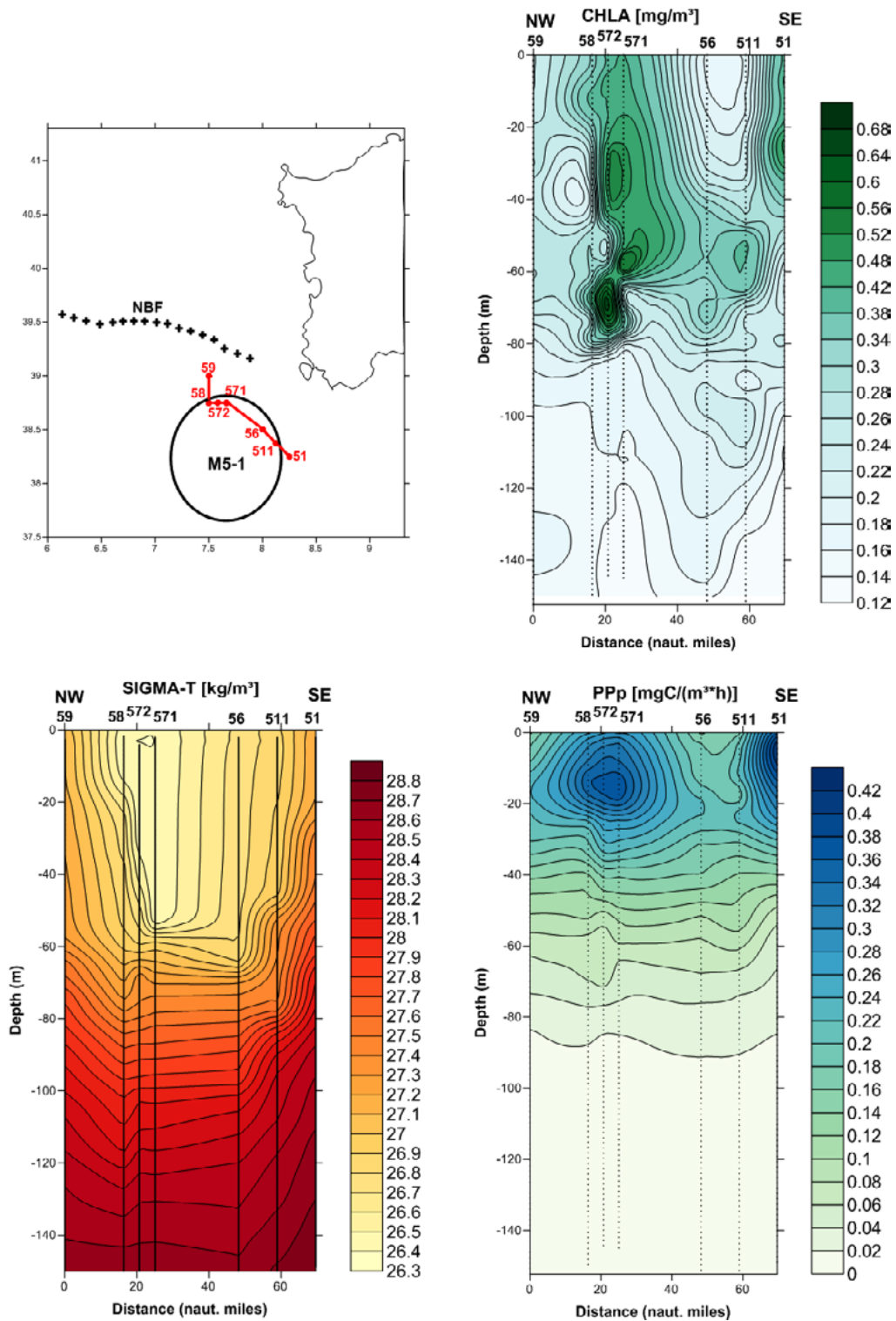


Fig. 13: Transect 59-51 (MedGOOS5): (a) mesoscale structures schematic and stations position, (b) potential density (kg/m^3), (c) chlorophyll concentration (mg/m^3) and (d) primary production ($\text{mg C}/(\text{m}^3\cdot\text{h})$)

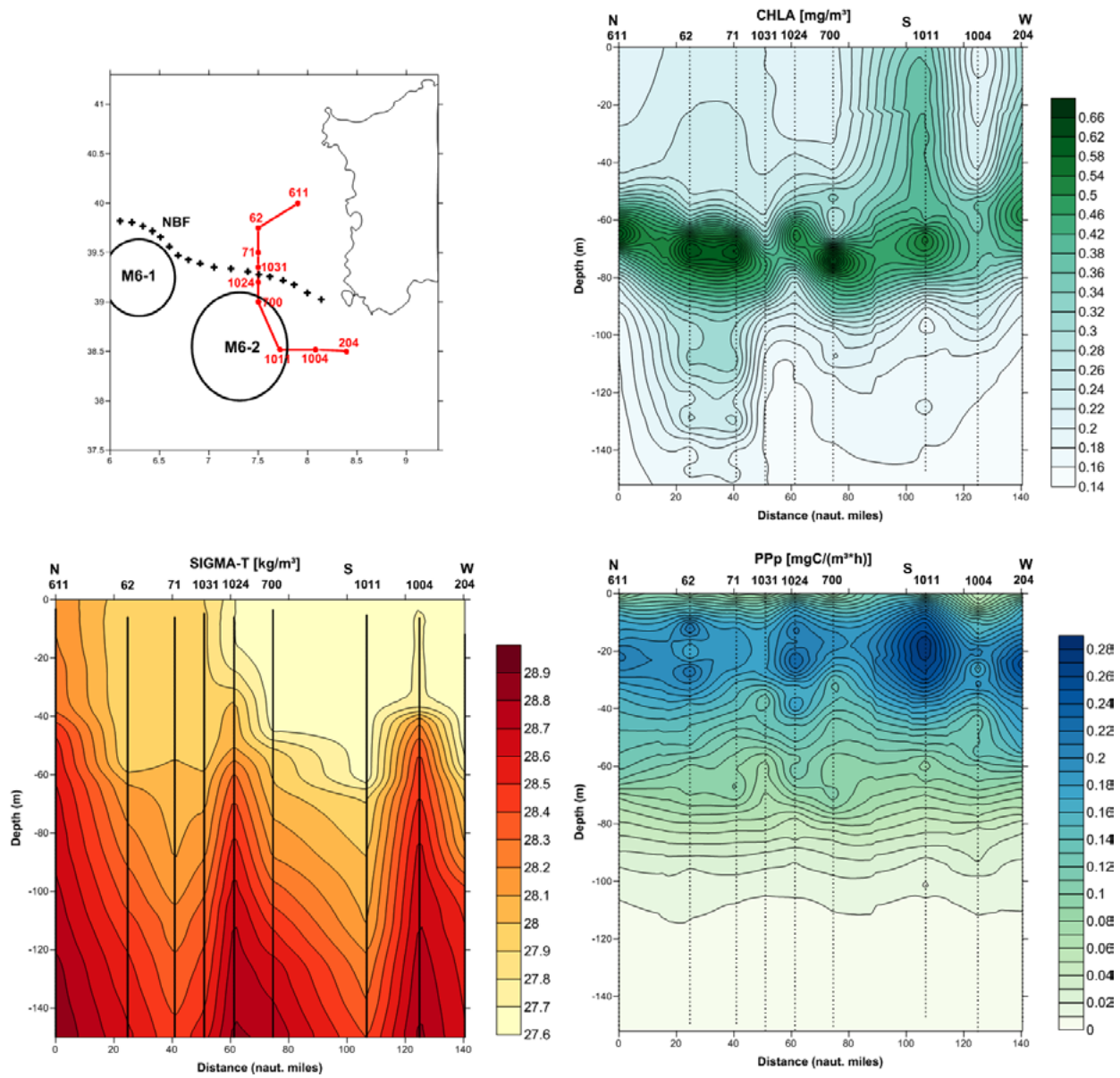


Fig. 14: Transect 611-204 (MedGOOS6): (a) mesoscale structures schematic and stations position, (b) potential density (kg/m^3), (c) chlorophyll concentration (mg/m^3) and (d) primary production ($\text{mg C}/(\text{m}^3 \cdot \text{h})$)

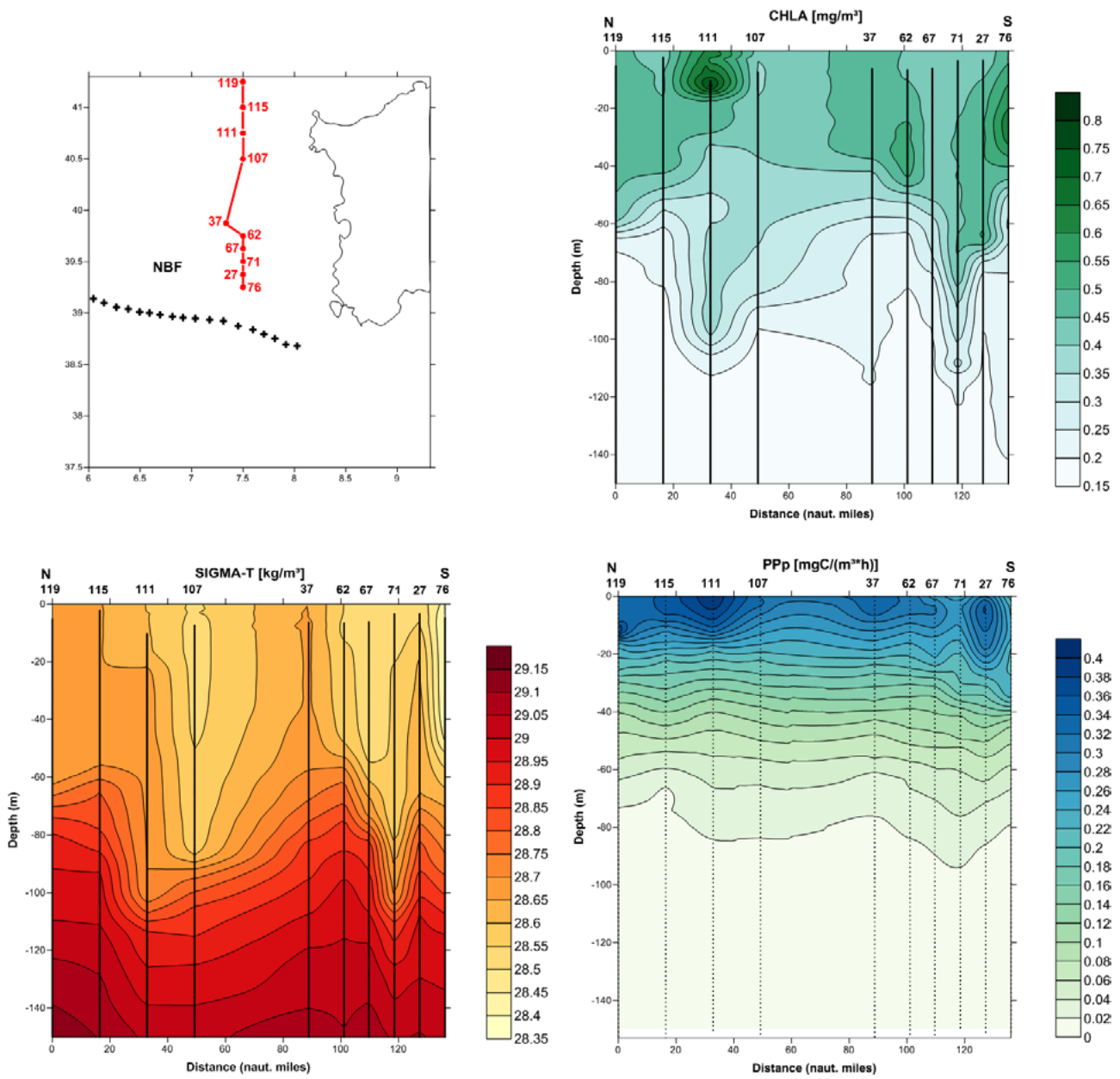


Fig. 15: Transect 119-204 (MedGOOS7): (a) mesoscale structures schematic and stations position, (b) potential density (kg/m^3), (c) chlorophyll concentration (mg/m^3) and (d) primary production ($\text{mg C}/(\text{m}^3\cdot\text{h})$)

6. DISCUSSIONS AND CONCLUSIONS

This work showed as the mesoscale physical processes modulated the phytoplankton primary production in the Sardinian Sea during four different time periods between 2002 and 2004. The satellite observations have highlighted that the MedGOOS4 cruise was influenced by two intense anticyclonic eddies (AE, Algerian Eddies) in the south of Algero-Provencal Basin and by another AE that was detaching from the AC. The Okubo-Weiss parameter confirmed the presence of two AEs off the African coast and deformation-dominated region in the north. These considerations were reflected in the density vertical distribution where two depressions caused by anticyclonic motion were registered. Phytoplankton biomass was found in patches with high concentration in correspondence of isopycnal doming in the south of Sardinian Sea. In the northern zone of the section characterized by small negative values of OW, low chlorophyll concentration at 50 m was found. During the MedGOOS5 the genesis of a "new" AE (M5-1) was highlighted by the distribution of altimeter satellite data and negative values of Okubo Weiss parameter. Even in this situation the AE induced high chlorophyll concentration at its northern edge. In spring 2003 (MedGOOS6) the rapid changes of dynamic conditions in the WMED led to the formation of cyclonic eddy (M6-1) caused by NBF instability and the detach of AE (M6-2) from AC. From the potential density distribution the presence of AE was not well-defined, consequentially DCM was homogeneously distributed between 60 and 80 m of depth. During the MedGOOS7 cruise, according to MDTA distribution and low values of OW parameter, the NBF shifted to the south inhibiting the genesis of new AEs. The high thickness of winter mixed layer depth caused a homogeneous distribution of the physical and biological variables upper to 80 m. The wintertime radiation was able to support high chlorophyll concentration in the upper layer.

Taking into account the phytoplankton photosynthetic efficiency and the effect of photoacclimation, primary production calculated by PhytoVFP model let to separate the total phytoplankton biomass into two components: the "active" fraction, able to produce organic carbon, and the "non active" fraction, constituted by senescent phytoplanktonic cells.

Primary production and chlorophyll-a concentration distribution showed higher values near the eddies edges and lower ones in the AEs central zone. Generally at the AEs peripheral zone, the critical depth exceeds the mixed layer depth supporting the increase of phytoplankton population [21]. Furthermore in the anticyclonic eddies, the eddy-pumping mesoscale process can contribute to the nutrient supply into the mixed layer [22] starting increase of phytoplankton growth. On the contrary, during the

MedGOOS4 and MEDGOOS6 cruises, high chlorophyll concentration located mainly in the northern deformation-dominated regions was associated with low primary production because phytoplankton population, which characterized this area, was principally constituted by senescent cells with low values of photosynthetic efficiency.

Then analysing the primary production distribution estimated by PhytoVFP model we had evaluated better the biological response associated with mesoscale structures than distribution of chlorophyll concentration.

In conclusion, mesoscale anticyclonic eddies are mainly responsible of primary production distribution in the Sardinian Sea.

7. ACKNOWLEDGMENTS

CTD casts of MedGOOS cruises were furnished by IAMC-CNR of Oristano. The altimeter products were produced by Ssalto/Duacs and distributed by Aviso with support from Cnes. A special thank goes to Prof. Angelo Perilli and Prof. Luigi Lazzara for their precious suggestions.

8. REFERENCES

- Lalli C.M. & Parsons T.R. (1997), *Biological oceanography, an Introduction*, Butterworth-Heinemann, Oxford. (1)
- Parsons T. R., Maita Y. & Lalli C. M. (1984), *A Manual of Chemical and Biological Methods for Seawater Analysis*, Pergamon Press. (2)
- Lewis M.R. (2002), *Variability of plankton processes on the mesoscale*. In: Williams PJ le B, Thomas DN, Reynolds CS (eds) *Phytoplankton Productivity: Carbon assimilation in marine and freshwater ecosystems*. Blackwell, pp 141-155. (3)
- Strass V.H. (1992), *Chlorophyll patchiness caused by mesoscale upwelling at fronts*. Deep-Sea Research 39 (1), 75–96. (4)
- Steemann Nielsen E. (1952), *The Use of Radio-active Carbon (C14) for Measuring Organic Production in the Sea*, J. Cons. int. Explor. Mer 18(2): 117-140 doi:10.1093/icesjms/18.2.117. (5)

- Vignudelli S. (1997), *Potential use of ERS-1 and Topex/Poseidon altimeters for resolving oceanographic patterns in the Algerian Basin*. Geophys. Res. Lett. 24 (14), 1787–1790. (6)
- Millot C. (1999), *Circulation in the western Mediterranean Sea*, J. Mar. Syst. 20, 423–442. (7)
- Taupier-Letage I., Puillat I., Raimbault P., & Millot C. (2003), *Biological response to mesoscale eddies in the Algerian Basin*, Journal of Geophysical Research, 108 (C8), 3245. (8)
- Jacques G., Minas H.J., Minas M. and Nival P. (1973), *Influence des conditions hivernales sur les productions phyto et zooplanctoniques en Méditerranée nord-occidentale. II: Biomasse et production phytoplanctonique*. Mar. Biol., 23, 251-265. (9)
- Rio M. H., Poulain P.M., Pascual A, Mauri E, Larnicol G, Santoleri R. (2007), *A Mean Dynamic Topography of the Mediterranean Sea computed from altimetric data, in-situ measurements and a general circulation model*, Journal of Marine Systems 65 484-508. (10)
- Okubo A. (1970), *Horizontal dispersion of floatable particles in the vicinity of velocity singularities such as convergences*, Deep-Sea Research, 17, 445–454. (11)
- Isern-Fontanet J, Font J., Ladona E.G., Emelianov M, Millot C., Taupier-Letage I. (2004), *Spatial structure of anticyclonic eddies in the Algerian basin (Mediterranean Sea) analyzed using the Okubo–Weiss parameter*, Deep-Sea Research II 51 3009–3028. (12)
- Marcelli M., Campana O., Di Maio A., Mangoni O., Ribera D’Acalà M., Saggiamo V., Tozzi S., Fresi E. (1997), *Development of a new operative method to estimate primary production in the pelagic system with a quasi-synoptic space/time scale. International Conference Progress in Oceanography of the Mediterranean Sea*. Roma, Novembre 17-19 1997. Abstract volume pp. 309-310. (13)
- Neckel H. & Labs D. (1984), *The solar radiation between 3300 and 12500 Å A Solar Physics*, (90) 205-258. (14)
- Spencer J. M. (1971), *Fourier series representation of the position of the sun*. Search, (2) 172. (15)
- Tanré D., Herman M., Deschamps P. Y. and De Leffe A. (1979), *Atmospheric modelling for space measurements of ground reflectances, including bidirectional properties*. Applied Optics (18) 3587-3594. (16)
- Alados I., Olmo F.J., Foyo-Moreno I., Alados-Arboledas L. (2000), *Estimation of photosynthetically active radiation under cloudy conditions*. Agricultural and Forest Meteorology,(102) 39-50. (17)
- Morel A. (1991), *Light and marine photosynthesis: a spectral model with geochemical and climatological implications*. Progress in Oceanography, (26) 263-30. (18)

- Puillat I., Taupier-Letage I., & Millot C. (2002), *Algerian eddies lifetime can near 3 years*. Journal of Marine Systems, 31(4), 245-259. (19)
- Morel A., Antoine D., Babin M. and Dandonneau Y. (1996), *Measured and modeled primary production in the northeast Atlantic (EUMELI JGOFS program): the impact of natural variations in photosynthetic parameters on model predictive skill*. Deep Sea Research, 43(8), 1273-1304. (20)
- Sverdrup H.U. (1953), On conditions for the vernal blooming of phytoplankton. J. Cons. Cons. Int. Explor. Mer 18, 145-157. (21)
- Falkowski P., Ziemann D., Kolber Z. and Bienfang P. (1991), Role of eddy pumping in enhancing primary production in the ocean, Nature, (352), 55-58. (22)

Is global warming causing mass mortalities in the Mediterranean Sea upper layer?

Rivetti I.^{*}, Frascchetti S.¹, Lionello P.^{1,2},
Zambianchi E.³, Boero F.^{1,2,4}

¹*DiSTeBA, Università del Salento, CoNISMa, 73100 Lecce, Italy.*

²*CMCC Euro-Mediterranean Center on Climate Change, 73100 Lecce, Italy.*

³*Dipartimento di Scienze per l'Ambiente, Università "Parthenope", CoNISMa, 80143 Napoli, Italy.*

⁴*CNR-ISMAR, 16149 Genova, Italy*

**Corresponding author: irene.rivetti@unisalento.it*

Abstract

Increasing temperatures are often invoked to explain increasingly frequent mass mortalities of marine benthos in the Mediterranean Sea. Here, the thermal structure of the shallow water column is reconstructed from a large dataset of temperature profiles at basin scale. Data identify areas more exposed to thermal anomalies than others but a consistent warming signal at basin scale in the upper layer was not identified. This study shows that, in the Ligurian Sea, the area most frequently subjected to mass mortalities, these events correspond to positive thermal anomalies, suggesting a causal link between increased temperatures and mass mortalities. This local condition, however, is not consistent with the situation at the basin scale.

Keywords: *Mediterranean Sea, Temperature profiles, Mass mortality*



1. INTRODUCTION

Global change threatens marine ecosystems since temperature modifications in the water column influence both biodiversity and the services it provides [1]. Thermal anomalies mainly alter species' distributions, change their phenology, favour the spread of pathogens and invasive species, and cause mass mortalities [2-4] so that the identification of areas particularly exposed to thermal anomalies is crucial to plan monitoring programs, and to propose mitigation strategies and conservation priorities.

Some studies suggest that the Mediterranean Sea reacts faster to global change than the open ocean being affected by important biotic changes, linked to abiotic changes [5]. Since the 1980s, satellite data documented a basin scale increase of Sea Surface Temperature (SST) [6] possibly resulting in events such as mass mortalities of sessile invertebrates [7-9].

For the first time, we combined and compared the thermal structure of the uppermost part of the water column both at basin scale and at the smaller scale of mortality events.

2. MATERIALS AND METHODS

Temperature profiles contained in MEDAR/MEDATLAS [10] are the main source of data used in this study. Thermal anomalies were evaluated by two approaches. First, thermal variations occurring at 20 m depth were assessed considering the summer (Jul-Aug-Sep) average temperature value in the period 1992-2011 minus the period 1945-1982 over a grid of $1^{\circ}\text{lat} \pm 1^{\circ}\text{lon}$. These two periods were chosen because the first documented mass mortality occurred in 1983, and their frequency became almost continuous since 1992, while no event was observed before the 1983. Together with this information, the distribution of the documented cases of mass mortalities across taxa was assessed. Second, thermal profiles in those areas where mass mortalities were observed have been considered. This analysis considers, for each analysed box, average temperature profiles in the periods 1945-1982 and 1992-2011 in the months when mass mortalities were reported at least once. The mean temperature profiles in the months and years when mass mortalities occurred were overlapped to the average temperature profiles of the periods 1945-1982 and 1992-2011.

3. RESULTS

Mass mortalities in the Mediterranean Sea, from 1983 to 2009, were mostly reported for the NW Mediterranean in the first 20 m, in late summer-early fall. The spatial patterns of mass mortalities partially overlap with temperature anomalies in the same time interval (Fig. 1).

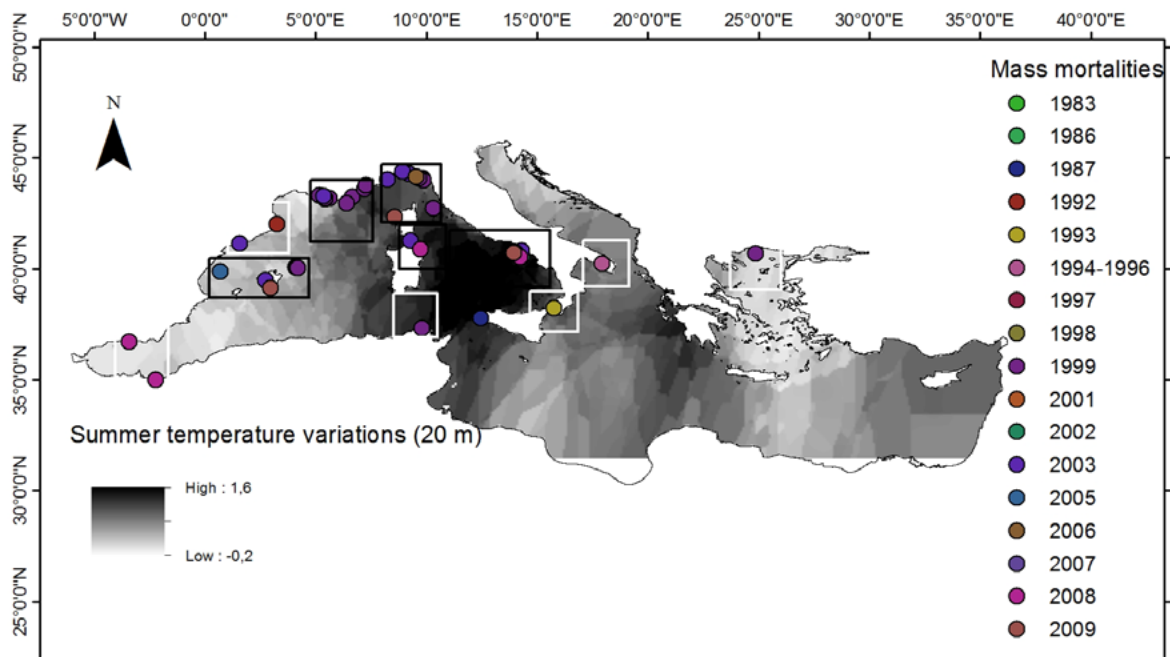


Fig. 1: Temperature variations at 20 m depth in summer months and mass mortalities occurrence. Temperature variations are computed as difference between average temperature values in the period 1992-2011 and those in the period 1945-1982 in 1°lat x 1°lon cell. Dots refers to the locations of documented mass mortalities, each colour represents a single event. In areas marked with black outline an analysis to combine thermal changes and mass mortality events was carried out. In areas marked with a white outline this analysis was not performed because the number of temperature profiles is not sufficient to assess thermal changes during mass mortalities

An analysis combining thermal changes and mass mortality events were carried out at local scale (about 300 km²) in the Ligurian Sea (Fig. 2), the Provence Coast, the Eastern Tyrrhenian, the Western Tyrrhenian, and the Balearic and Columbretes Islands, marked with a black outline in Figure 1.

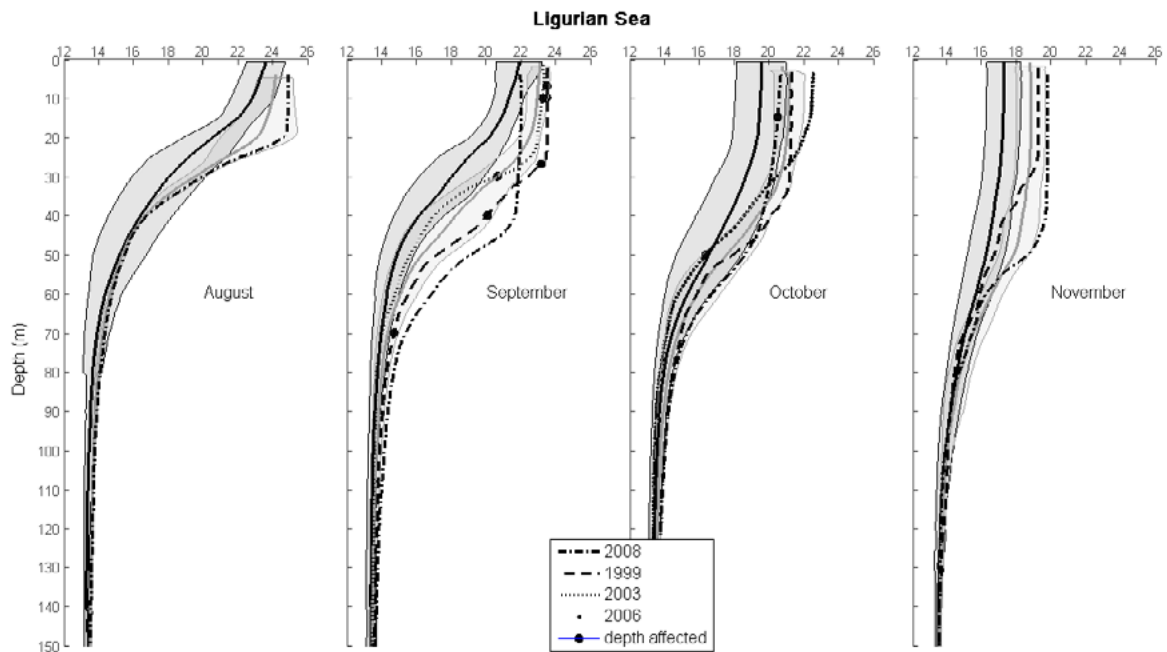


Fig. 2: Monthly average temperature profiles for the periods 1945-1982 (black lines) and 1992-2011 (grey lines) and average temperature profiles for the years and months in which mass mortalities occurred, in the Ligurian Sea

At these locations mean temperature profiles document a systematic warming since the early 1990s. Here, changes of mean monthly temperature caused a rise of the upper limit of interannual temperature fluctuations, sharply associated with mass mortalities.

4. CONCLUSIONS

The available data for the upper layer of the whole Mediterranean Sea show that it is warming up, but with high spatial variability. At locations where at least a mortality event was recorded, mean temperature profiles document a systematic warming since the early 1990s.

The data collected so far cannot exclude that warming was indeed greater, due to lack of strategy in data collection.

The lack of systematic assessment of thermal anomalies can be partly responsible for our results. Implementing monitoring programs to understand the magnitude of this phenomenon, together with specific conservation actions, should be the core of future management strategies for the whole Mediterranean Sea.

5. ACKNOWLEDGMENTS

IR was supported by the CMCC. Financial support from the EU FP7/2007-2013, Grant Agreement No. 287844 for the project "CoCoNet", and the EU integrated projects VECTORS, PERSEUS, and the CIESM "Tropical Signals" project. Special thanks to G. Bavestrello, P. D'Ambrosio, G. Manzella e F. Reseghetti for comments and advice in data analyses.

6. REFERENCES

- Rosenzweig C., et al., in *Climate Change 2007: Impacts, Adaptation and Vulnerability. Contribution of Working Group II to the Fourth Assessment Report of the Intergovernmental Panel on Climate Change*, Parry M.L., Canziani O.F., Palutikof J.P., van der Linden P.J., Hanson C.E., Eds. (Cambridge Univ. Press, UK, 2007), pp.79-131. (1)
- Brierley A. S. & Kingsford M. J. (2009), *Impacts of climate change on marine organisms and ecosystems*. *Curr. Biol.* 19, pp. R602-R614. (2)
- Harvell C. D., et al. (1999), *Emerging marine diseases - Climate links and anthropogenic factors*. *Science* 285, pp. 1505-1510. (3)
- Ward J. R. & Lafferty K.D. (2004), *The elusive baseline of marine disease: Are diseases in ocean ecosystems increasing?* *Plos Biol.* 2, pp. 542-547. (4)
- Lejeusne C., Chevaldonne P., Pergent-Martini C., Boudouresque C. F. & Perez T. (2010), *Climate change effects on a miniature ocean: The highly diverse, highly impacted Mediterranean Sea*. *Trends Ecol. Evol.* 25, pp. 250-260. (5)
- Nykjaer L. (2009), *Mediterranean Sea surface warming 1985-2006*. *Clim. Res.* 39, pp. 11-17. (6)
- Halpern B. S., et al. (2008), *A global map of human impact on marine ecosystems*. *Science* 319, 948-952. (7)
- Coma R., et al. (2009), *Global warming-enhanced stratification and mass mortality events in the Mediterranean*. *P. Natl. Acad. Sci. USA* 106, pp. 6176-6181. (8)
- Crisci C., Bensoussan N., Romano J.-C. & Garrabou J., (2011), *Temperature anomalies and mortality events in marine communities: Insights on factors behind differential mortality impacts in the NW Mediterranean*. *Plos One* 6. (9)

Fichaut M., et al., Eds., in Building the European Capacity in Operational Oceanography: Proceedings
3rd EuroGOOS Conference (Ser. 69 of Elsevier Oceanogr., 2002), pp. 645-648. (10)

High resolution coastal monitoring during the sea breeze event

Martellucci R.^{1*}, Paladini de Mendoza F., Piazzolla D., Pierattini A., Marcelli M.

¹Laboratory of Experimental Oceanology and Marine Ecology (DEB), Tuscia University (Italy)

*Corresponding author: riccardomartellucci@gmail.com

Abstract

This work focuses the interactions between sea breezes and marine coastal dynamic. In this paper we discuss the first results, obtained integrating high resolution oceanographic and meteorological data, concerning the last three years of field experiments.

The seasonal distribution of sea breezes was studied analysing wind data, recorded from 2008 to 2012, by Civitavecchia harbour weather station. In August 2012 water column surveys show local wind effect on marine thermal structure. Summer meteorological data have shown a directional daily wind fluctuation, with a seasonal recur of 37%.

To identify sea breeze regime we utilize Land Sea Breeze Index (LSBI). It was obtained by land-sea thermal gradient and wind direction.

Keywords: *Sea breeze, high-resolution data, Thermal variations, Land Sea breezes Index*



1. INTRODUCTION

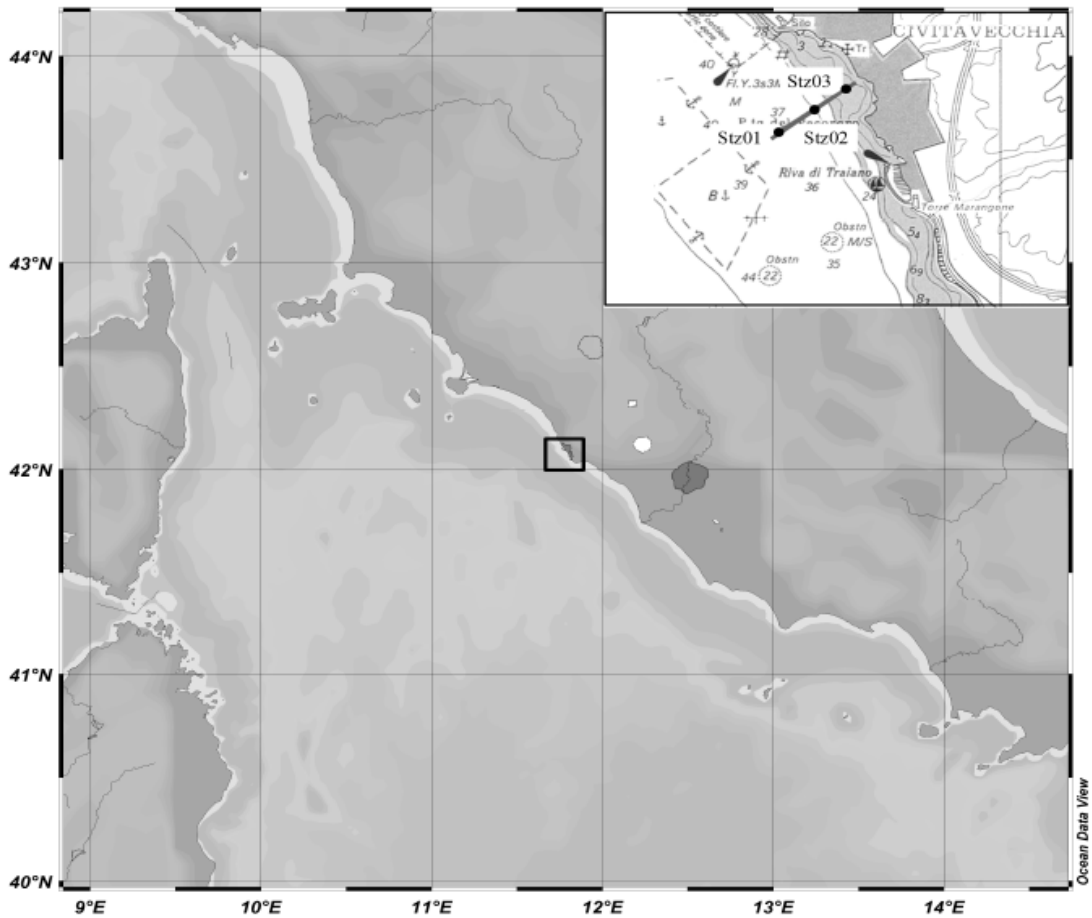
“The dynamics and kinematics of the sea breeze depend greatly on locality” (Haurwitz,1947). At the coast of many hot tropical countries, where the overall thermal gradient is steady from day to day, the sea breeze start regularly every day at the same time. In temperate climates the sea breeze also blows on sunny days, but winds from different directions caused by the movement of depressions and anticyclones often modify its development. “The sea breeze will start to blow when the temperature difference between the land and the sea is large enough to overcome any offshore winds” (Simpson, 1994). However interaction with other local wind systems may complicate the diurnal wind pattern of a particular area making it difficult to extract those atmospheric responses related directly to a sea breeze event (Johnson and O’Brien, 1973).

Coastal weather phenomena such as land-sea breeze have immense impact on issues of health, welfare and economics of coastal regions, where a large part of the world's population lives.

In fact, sea breeze constitutes the atmospheric phenomenon that most determines local weather and climate, not only on the coast but also in adjacent inland areas (Simpson, 1994).

In this paper, we study the characteristics of the sea breeze flow in the coast of Civitavecchia (Latium), in Italy (Picture 1.). The study area is located in the Northern Tyrrhenian sea eastern margin, between 42°01'42"N and 42°09'12"N, and 11°50'10"E and 11°44'20"E. This trait of coast is classified as 'terraces pattern' (Brondi, 1979) and the topography is characterized by the presence of a coastal mountain ranges from the southern to the northern shoreline.

The complex terrain have a strong influence on sea breeze circulation patterns (Johnson and O'Brien, 1973) and cause the deviation of the sea breeze flow from the ideal case (Frenzel, 1962).



Map showing the location of study area, in the northern Latium coast (Italy) included between P. St. Agostino and Capo Linaro (Lazio, Italy), and sampling plan

We focused on the relationship between sea breeze occurrences and local meteorological data, and the behaviour of the local sea breezes. We determined the statistical characteristics of the major sea breeze circulation parameters on Civitavecchia area, and so we computed, according to Frysinger et al (2003), a breeze index (LSBI) used to identify the sea breeze. We have also investigated water column thermal structures related to breeze events by integrating oceanographic and meteorological surveys, in order to observe large variability on phenomena, and to correlate local wind regime with dynamical response of water masses.

2. MATERIALS AND METHODS

The weather data analysed refers to Harbour Authority weather station placed in Civitavecchia harbour at 10 meters high which sampled wind direction ($^{\circ}\text{N}$), wind speed (m/s), atmospheric pressure (hPa) and solar radiation (W/m^2). The water data was collected by a multiparametric probe (Ocean Seven 316 CTD probe IDRONAUT) installed on a oceanographic bouy.

Meteorological data of wind speed and direction were divided in different seasons and then during summer periods, it was carried out the analysis described below.

Coastal orientation of study area allows to identify the directional sectors of offshore and onshore wind. Two directional sectors of eighty degrees were selected, from 20 to 100 degrees for land wind and 200 to 280 for sea wind and the their relative yearly frequencies were computed.

Subsequently, the data were divided in different time intervals of three hours and for each class was computed the seasonal daily frequency.

As the sea breeze is caused by the temperature difference between the air over land and that over water (Haurwits B. 1946), sea breeze index was applied to discriminate these events from large scale weather situations.

Land sea breeze index (*LSBI*) was built considering the wind angle incidence at coast (θ) and the difference in temperature between the ocean surface and overland air (ΔT).

$$LSBI = f(DT, q)$$

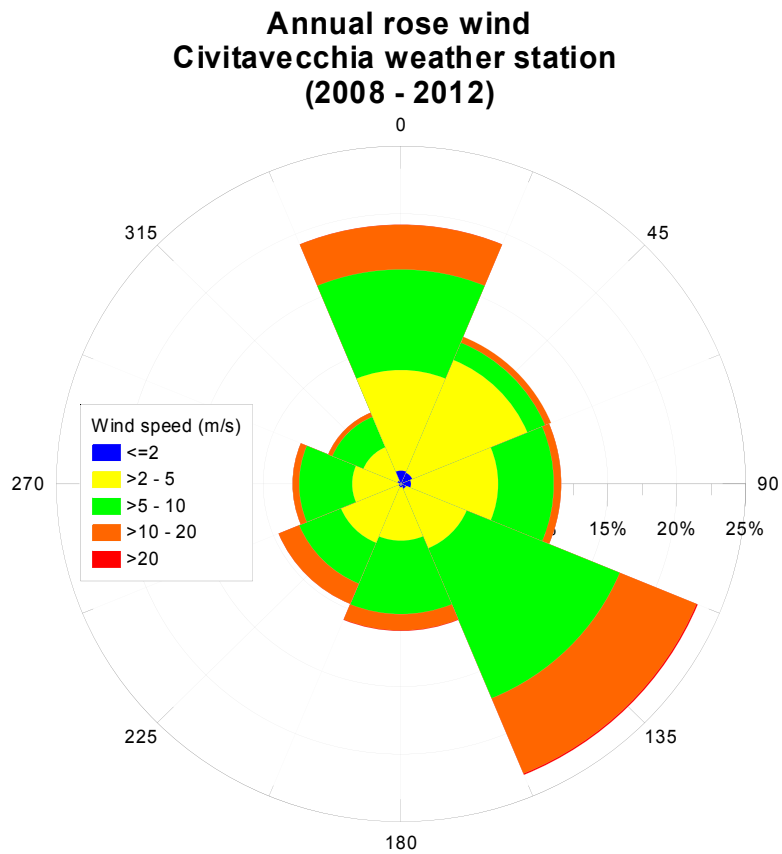
The incidents angle was chosen in 80 degrees range. To give more weight to wind direction perpendicular to the coast, the *LSBI* was computed considering the wind direction angle \sin .

When the *LSBI* is positive there is a sea breeze, when *LSBI* is negative there is land breeze. This index was multiplied for wind speed for quantify the breeze intensity.

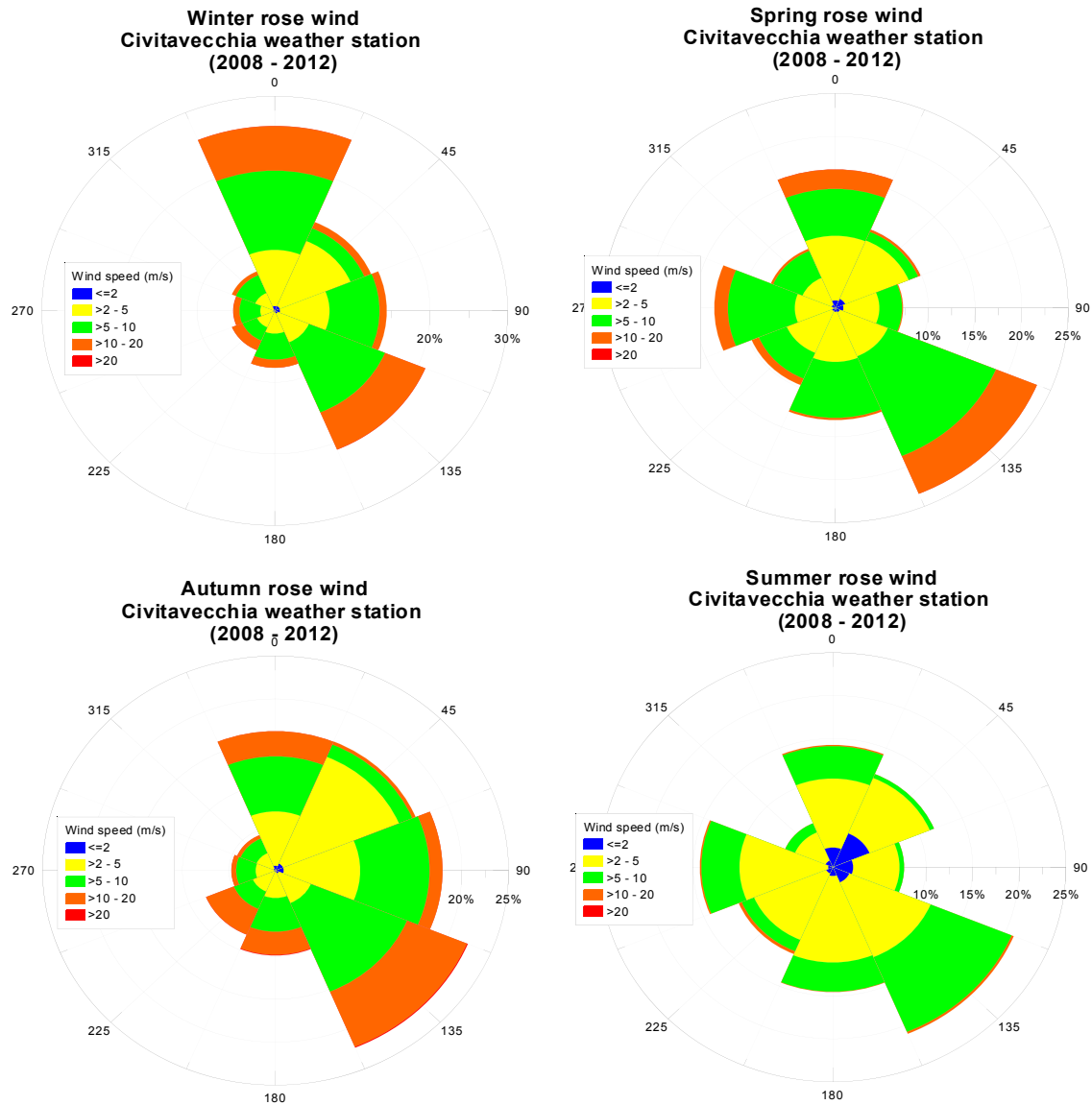
Water column survey was planned on meteorological analysis results and the field experiments was done in three different days (20th, 22nd and 28th August 2012). The survey was carried out by multiparametric probe (Ocean Seven 316 CTD probe IDRONAUT). The sampling plane consists on three stations in proximity of 20, 30 and 40 meters bathymetric contour. In order to obtain high frequency time records, the oceanographic surveys were recorded every 30 minutes. The data were elaborated by *kernel* function smoothing and *kriging* interpolation and were visualized in ODV software.

3. RESULTS

The results of the meteorological and oceanographic data are shown below. Picture 1 shows the wind rose of the sampled data during the period studied. North e South-East are the reignings directions.

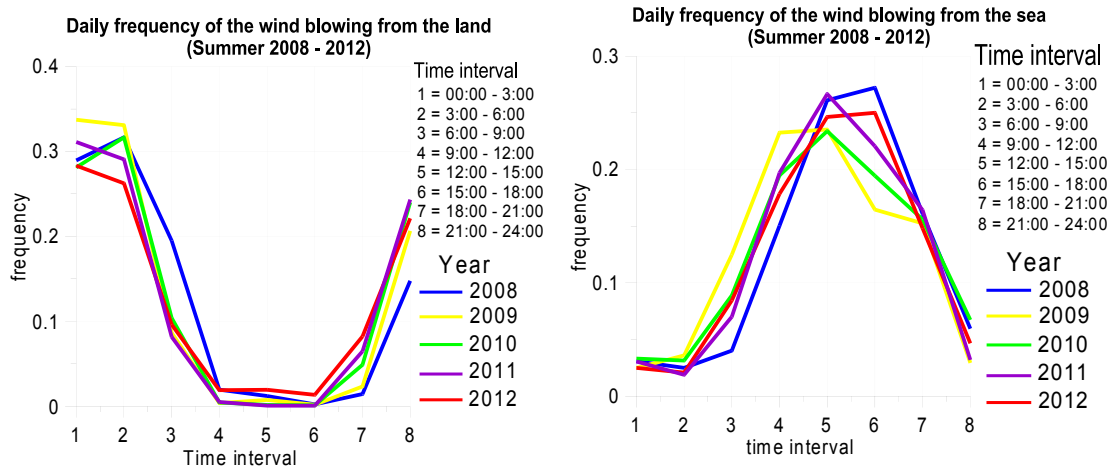


Picture 1



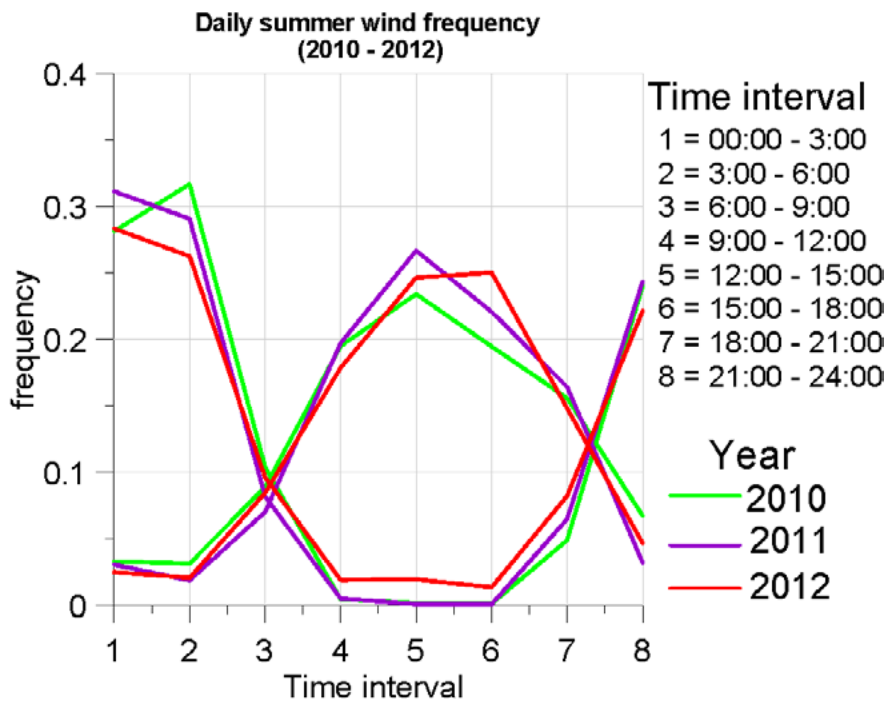
Picture 2: Seasonal rose wind

Picture 2 shows the wind rose of different seasons; in summer the wind speed is lower than other seasons and the events originated from North-East and South-West are more frequent ($> 10\%$) than the others seasons.



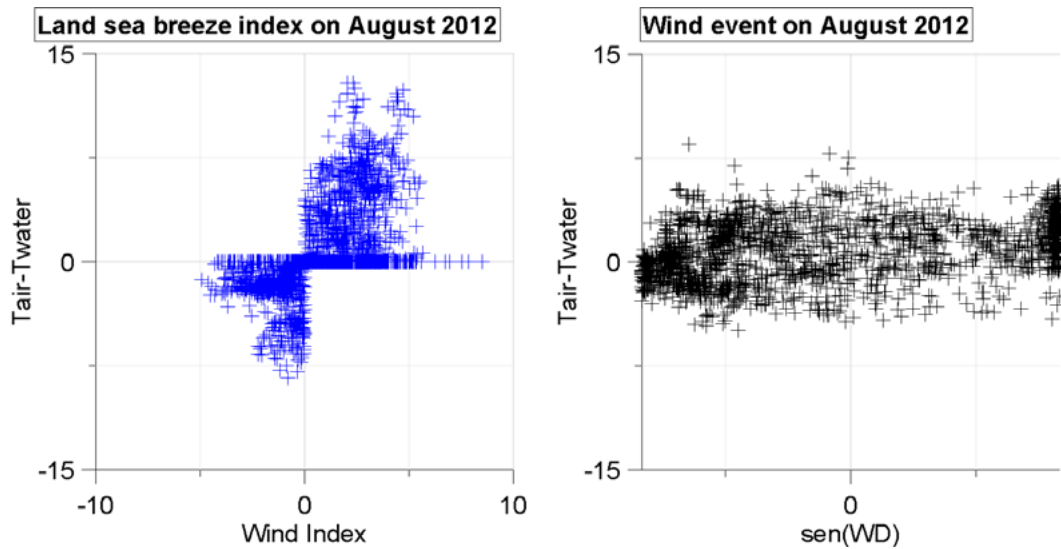
Picture 3: Daily summer frequency of land (right) and sea (left) winds

Picture 3 shows the daily summer wind frequency for land winds and sea wind; The winds coming from the land occurs during the night while the wind from the sea onese during the day.

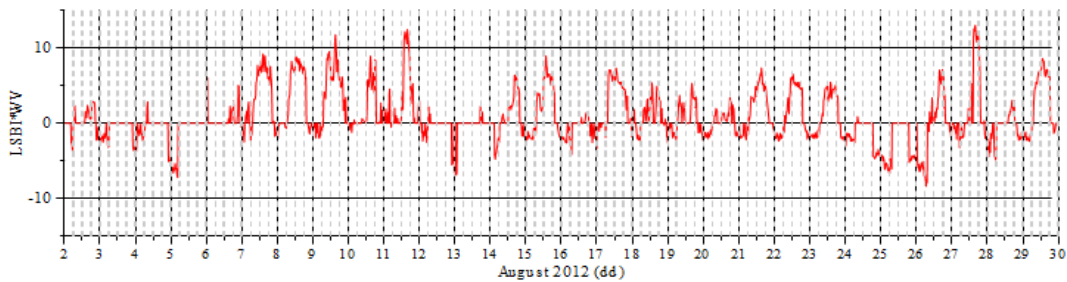


Picture 4: Daily summer frequency of land and sea winds

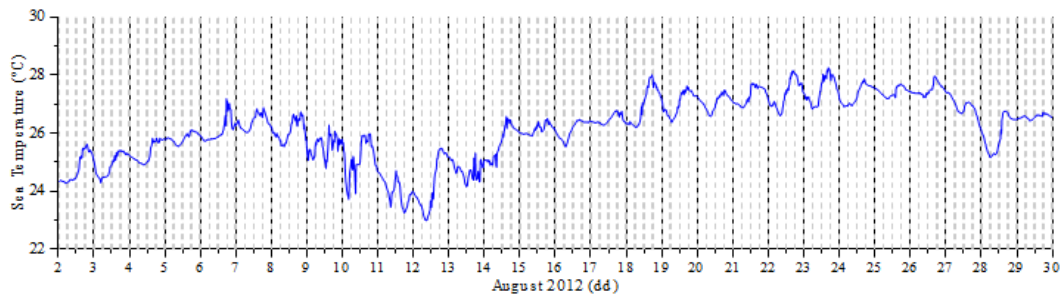
Picture 4 shows the daily summer wind frequency for land and sea winds, and in the graph it's possible to see two different points of wind direction reversal, one between 06:00 at 09:00 a.m. and the other between 08:00 and 10:00 p.m. In according to B.Haurvitz observations.



Picture 5: Scatter plot LSBI (on left) Wind event (on right)



Picture 6: time series of LSBI*WV, from 2nd to 29th August 2012

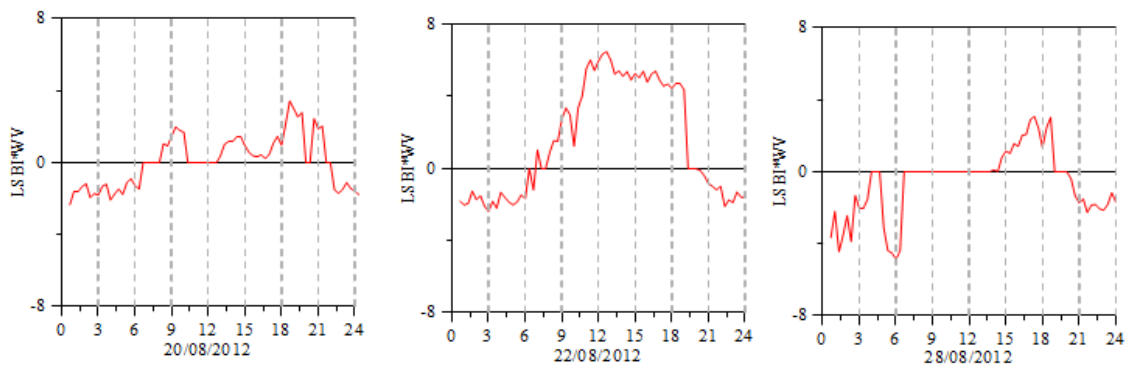


Picture 7: time series of sea temperature, from 2nd to 29th August 2012

Picture 5 shows the scatter plot of LSBI and wind direction on August 2012; these graphs shows how the LSBI sort the breeze events

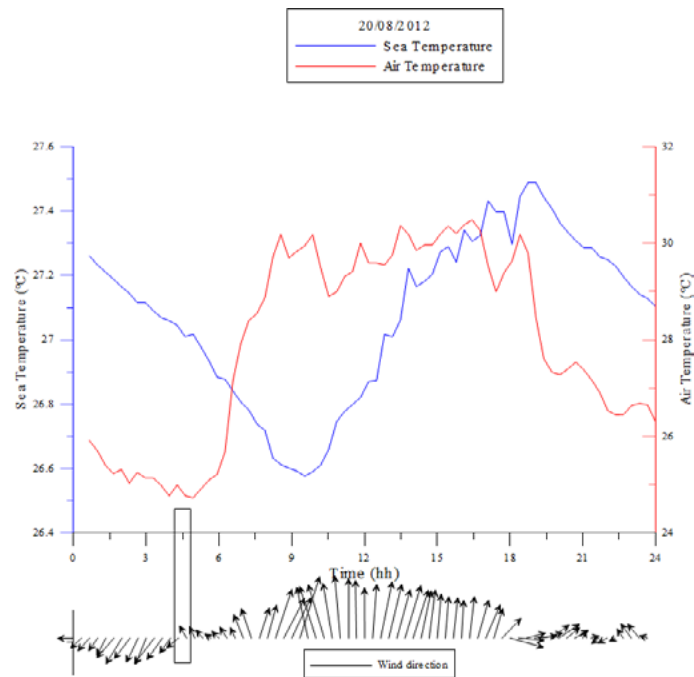
Picture 6 shows the LSBI for August 2012 where it's possible to identify clearly the breeze event. The positive peak represent the sea breeze events while negative peak the land breeze. The peak magnitude show sea breeze intensity greater than land breeze.

Picture 7. The graph show the daily fluctuation and the variation of sea temperature during August 2012. During the first week the temperature rise until 26°C, then decrease until 23°C and in the last part of the month the temperature rise to a costant value of 27°C.

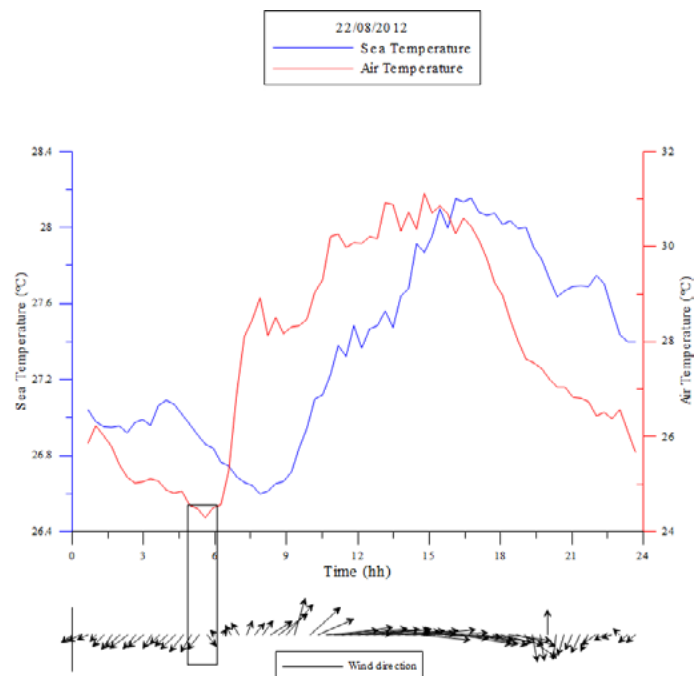


Picture 8: time series of LSBI*WV, 20th, 22nd and 28th August 2012

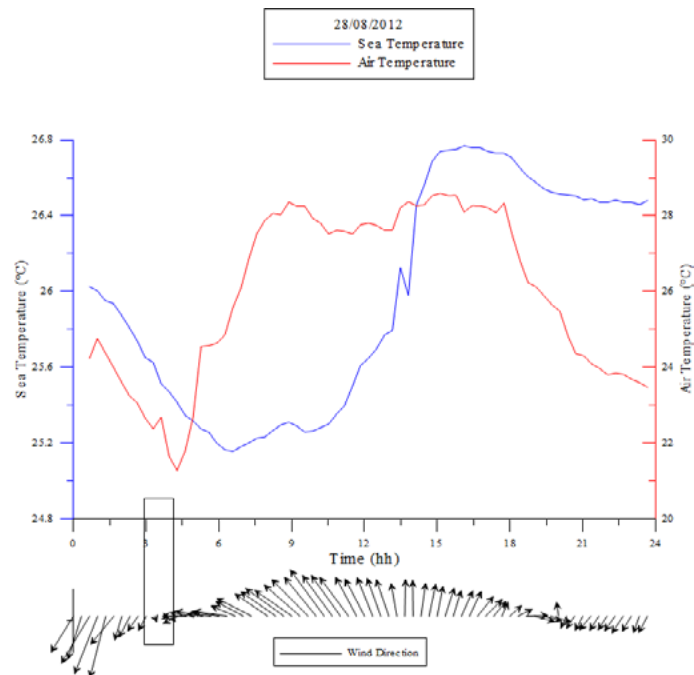
Picture 8 shows the trend of LSBI of 20th, 22nd and 28th August. On 22nd August the breeze events occurs while on 20th the index shows that there isn't a complete breeze event. On 28th August there are only land breezes.



Picture 9a: Time series of air temperature, sea temperature and wind direction, 20/08/2012



Picture 9b: Time series of air temperature, sea temperature and wind direction, 22/08/2012

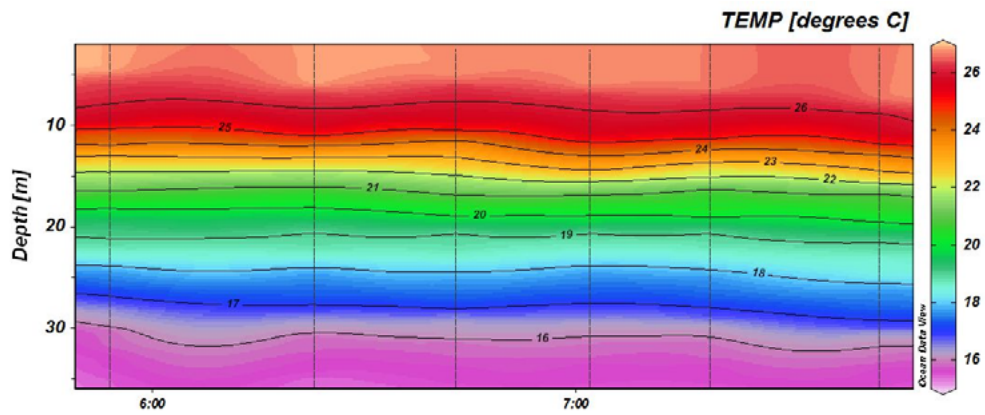


Picture 9c: Time series of air temperature, sea temperature and wind direction, 28/08/2012

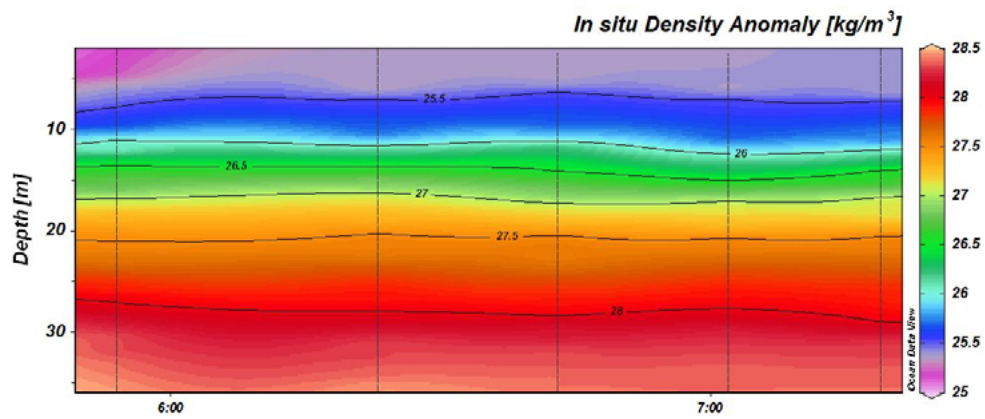
Picture 9 a,b,c, shows air temperature, sea temperature and wind direction of 20th, 22nd and 28th August.

In each graph it's possible to see two point of reversal wind direction. The first (land wind to sea wind) from 04:00 to 06:00 in the morning while the second (sea wind to land wind) occurs from 6:00 to 9:00 in the evening. The air temperature has highest value from nine in the morning until six in the afternoon while in the night decrease. The maximum value of 31°C was recorded the 22th and the minimum value of 21°C was recorded the 28th. The sea temperature has a similar trend of air temperature but the maximum value occurs during the afternoon. The maximum value of 28.1°C was recorded the 22nd while the minimum value of 25.2°C was recorded the 28th morning.

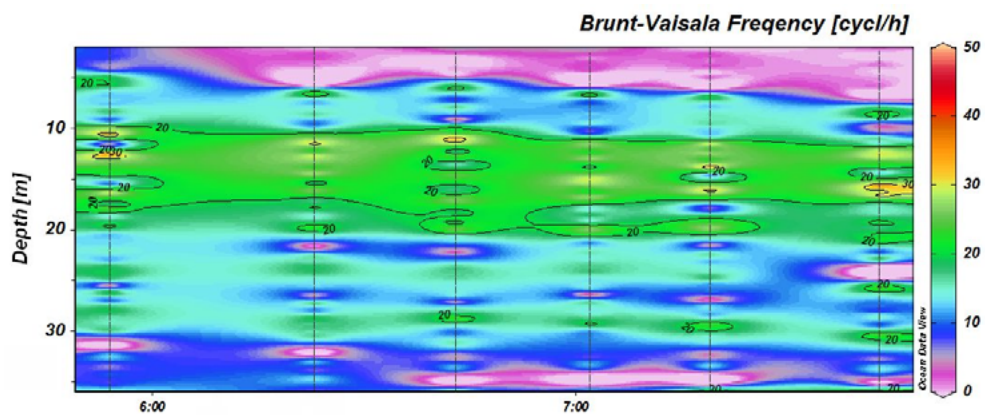
Pictures (10 a,b,c) shows the temperature, density anomaly and Brunt-Vaisala frequency variation with time for station 03 on 20th August. There are not significant variations in the observed variables (Temperature and density anomaly). Brunt-Vaisala frequency graphs shows sinking thermocline of 5 m between first and last station.



Picture 10a: Time series of temperature at station 3, 20/08/2012 from 05:30 to 08:00



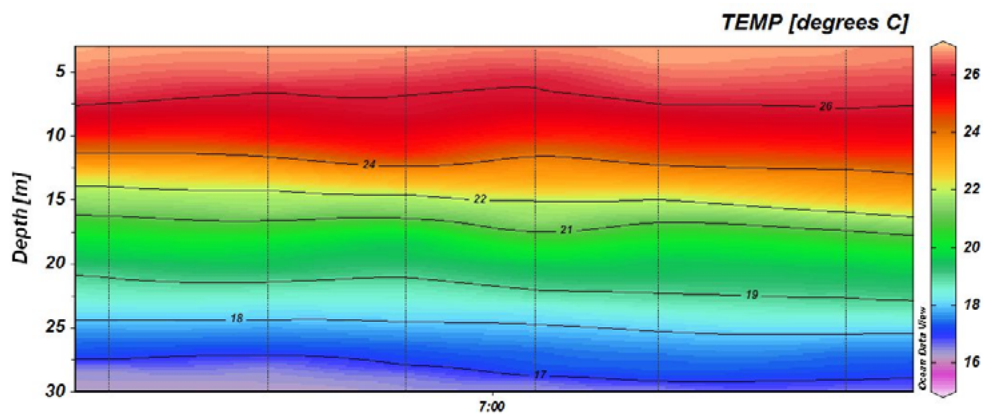
Picture 10b: Time series of density anomaly at station 3, 20/08/2012 from 05:30 to 08:00



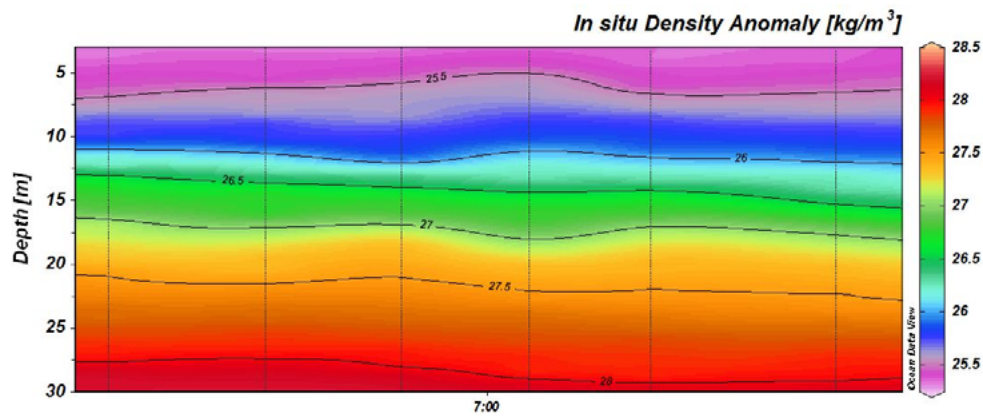
Picture 10c: Time series of Brunt-Vaisala frequency at station 3, 20/08/2012 from 05:30 to 08:00

Pictures 11a,b,c shows the temperature, density anomaly and Brunt-Vaisala frequency variation with time for station 02 on 20th August.

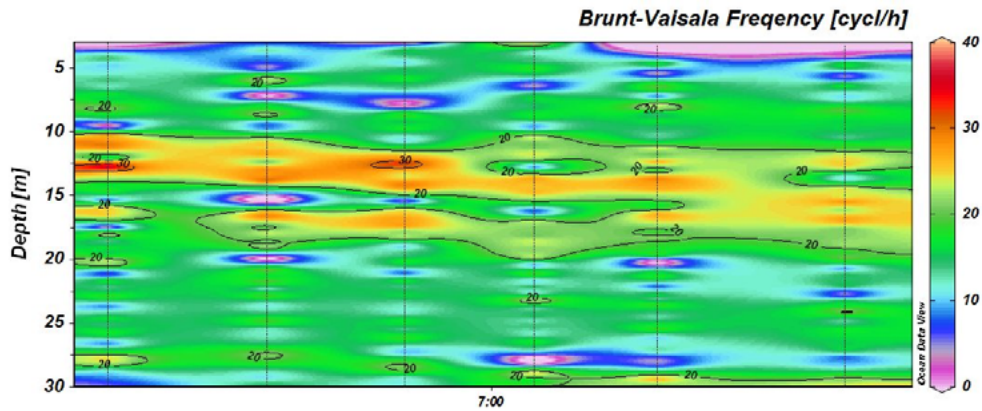
Temperature variation between 06:30 and 07:30 are observed, density anomaly too. Brunt-Vaisala frequency (11c) shows collapsing to 5 m between first and last station.



Picture 11a: Time series of temperature at station 2, 20/08/2012 from 05:30 to 08:00



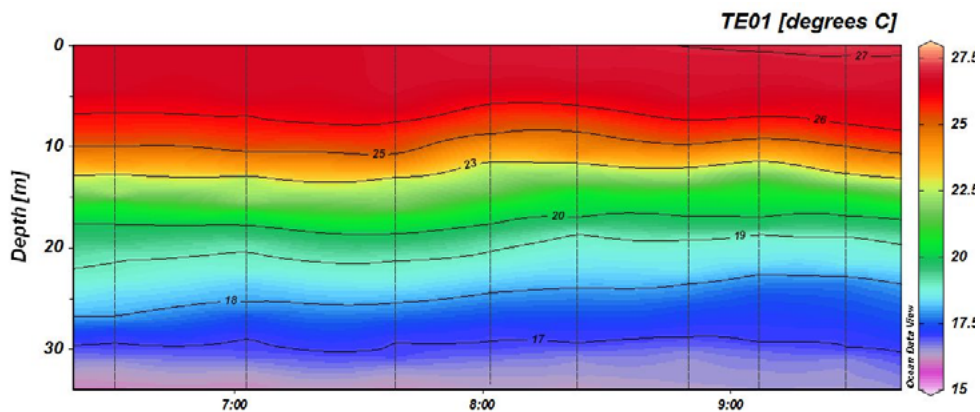
Picture 11b: Time series of density anomaly at station 2, 20/08/2012 from 05:30 to 08:00



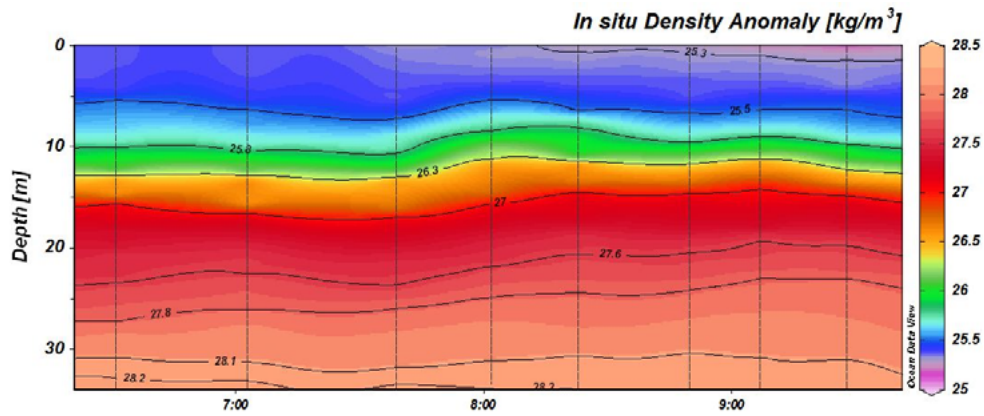
Picture 11c: Time series of Brunt-Vaisala frequency at station 2, 20/08/2012 from 05:30 to 08:00

Picture 12a,b,c shows the temperature, density anomaly and Brunt-Vaisala frequency variation with time for station 03 on 22nd August

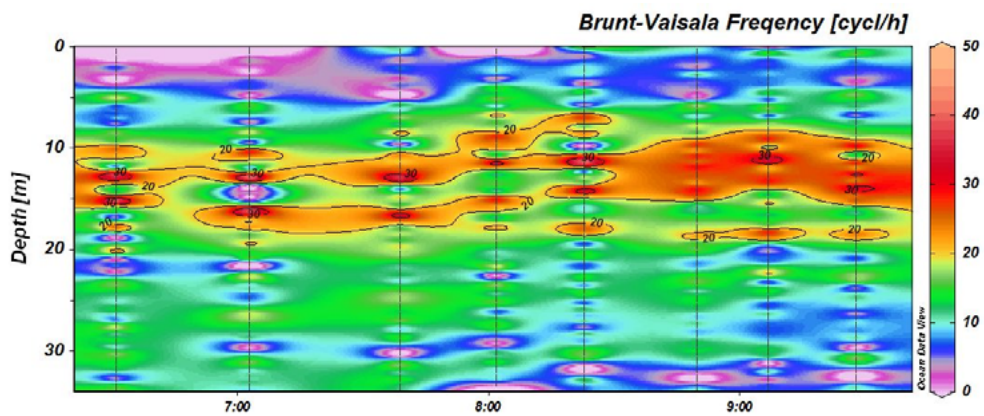
These pictures show a variation that occur between 07:30 and 08:30 am. Data show that the thermal variation (12a) is very intense between 10 m and 25 m depth, with a decrease of about 1 ° C; a similar variation is also present in the density anomaly picture (12b). Brunt-Vaisala frequency (12c) show a rapid variation between 07:30 and 08:30.



Picture 12a: time series of temperature at station 3, 22/08/2012 from 06:00 to 09:30

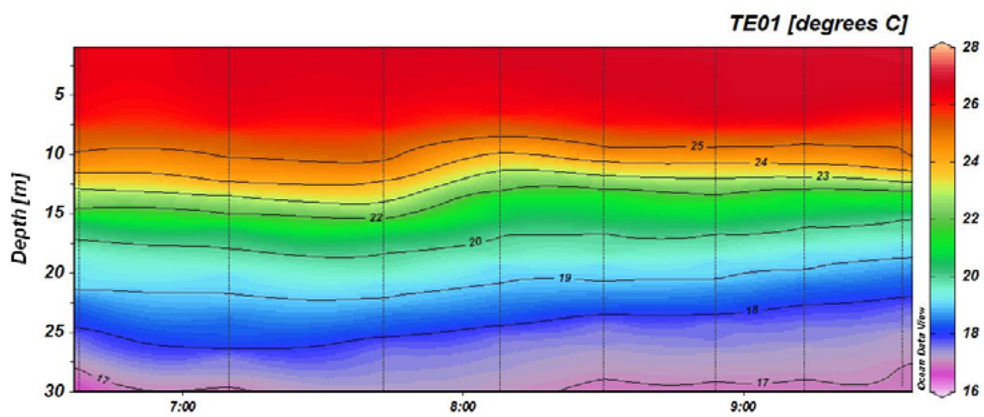


Picture 12b: Time series of density anomaly at station 3, 22/08/2012 from 06:00 to 09:30



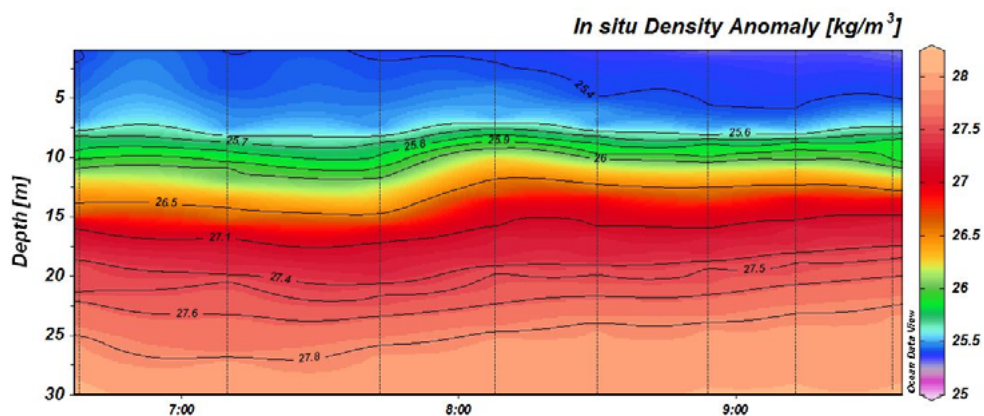
Picture 12c: Time series of Brunt-Vaisala frequency at station 3, 22/08/2012 from 06:00 to 09:30

Picture 13 a,b,c shows the temperature, density anomaly and Brunt-Vaisala frequency variation with time for station 02 on 22nd August

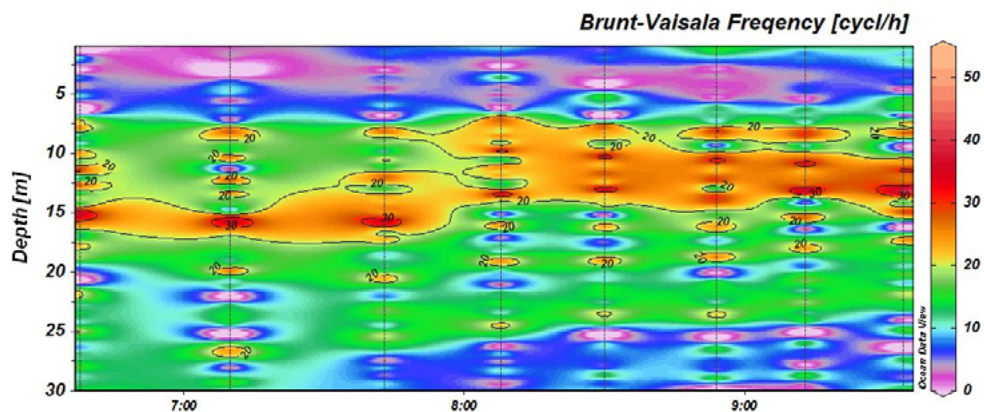


Picture 13: Time series of temperature at station 2, 22/08/2012 from 06:00 to 09:30

These pictures show a variation that occur between 07:30 and 08:30 am. Data show that the thermal variation (13a) is very intense between 10 m and 25 m isobath, with a decrease of about 1 ° C; a similar variation is also present in the density anomaly picture (13b). Brunt-Vaisala frequency (13c) show a rapid variation between 07:30 and 08:30.

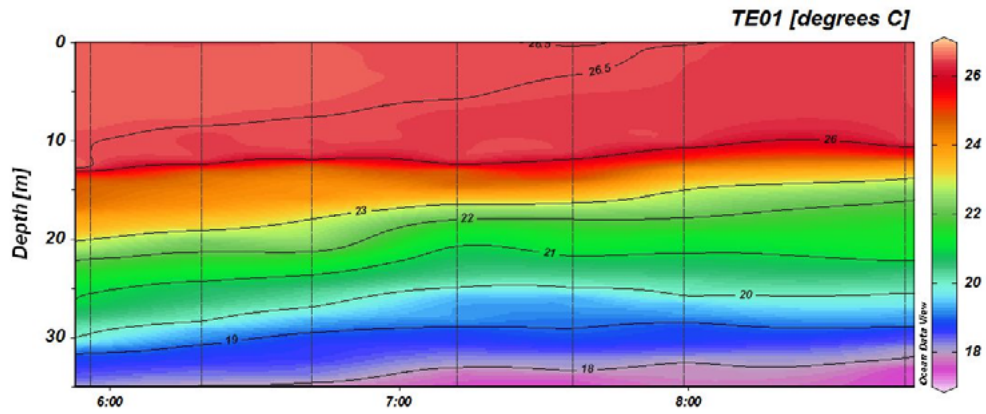


Picture 13b: Time series of density anomaly at station 2, 22/08/2012 from 06:00 to 09:30

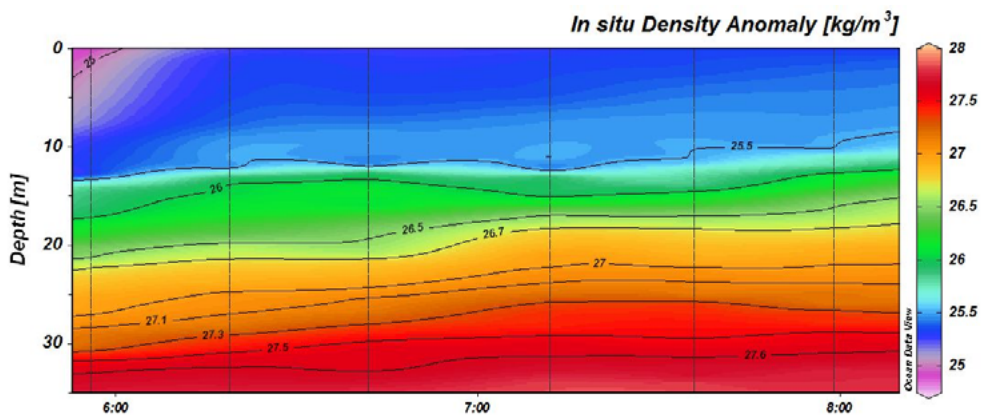


Picture 13c: Time series of Brunt-Vaisala frequency at station 2, 22/08/2012 from 06:00 to 09:30

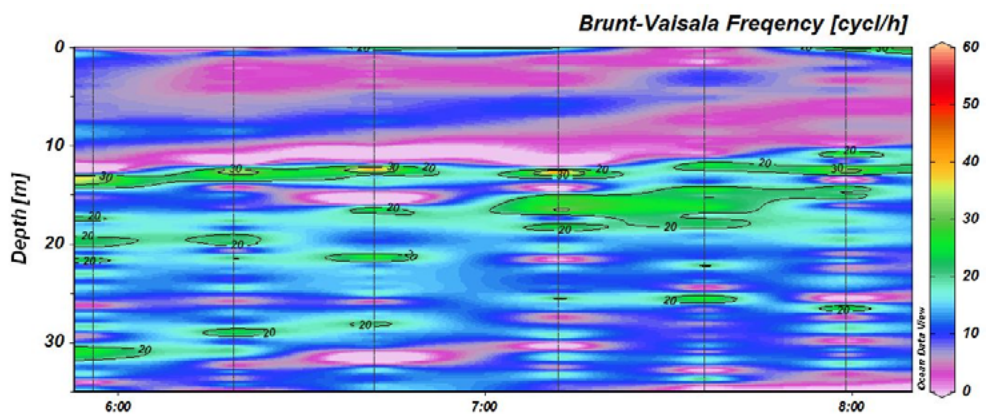
Picture 14 a,b,c shows temperature, density anomaly and Brunt-Vaisala frequency variation with time for station 03 on 28th August.



Picture 14a: Time series of temperature at station 3, 28/08/2012 from 06:00 to 09:00



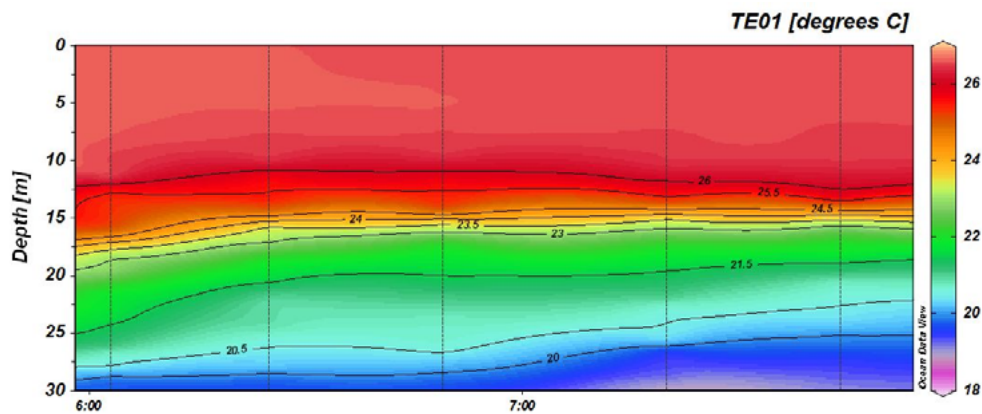
Picture 14b: Time series of temperature at station 3, 28/08/2012 from 06:00 to 09:00



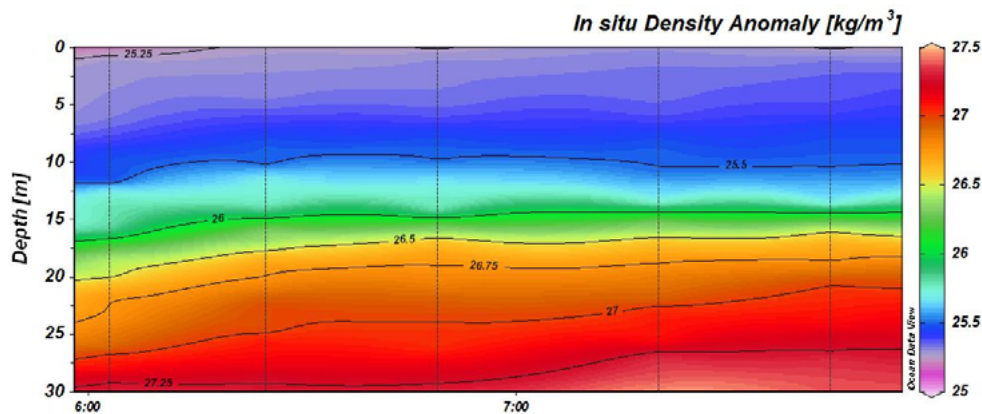
Picture 14c: Time series of temperature at station 3, 28/08/2012 from 06:00 to 09:00

Large temperature and density anomaly (14b) fluctuation is observed within 20 and 30 m, between 6:30 to 8:30. Within surface and 10m, are observed an increment in temperature of -0.5°C .

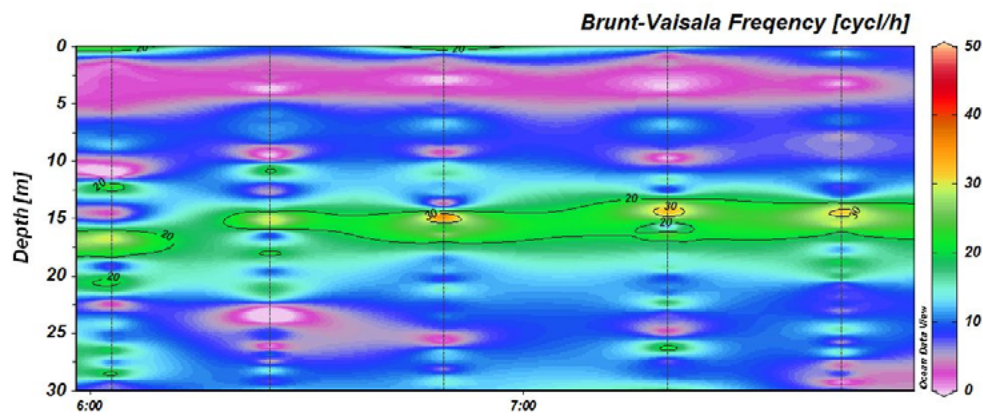
Picture 15 a,b,c shows temperature, density anomaly and Brunt-Vaisala frequency variation with time for station 02 on 28th August.



Picture 15a: Time series of temperature at station 2, 28/08/2012 from 06:00 to 09:00



Picture 15b: time series of density anomaly at station 2, 28/08/2012 from 06:00 to 09:00



Picture 15c: Time series of temperature at station 2, 28/08/2012 from 06:00 to 09:00

Temperature (15a)and density anomaly (15b) graph's show a variation within 20m and 30m approximately -1°C for temperature variable.

Brunt-Vaisala frequency (15c) shows rising termocline approximately to 3m, between 06:00 and 07:00 a.m.

4. DISCUSSION

The analysis of wind data shows two reigning winds from North and South-East during period recorded from 2008 to 2012 (Picture 1). The seasonal wind roses (Picture) show that in summer the events North-East and South-West have more

frequency than the other seasons and the wind speed recorded is lower. The frequency analysis of summer wind show that wind from the land occurs during the night while the wind from the sea ones during the day.

In particular the land wind show a peak frequency approximately from midnight until six in the morning while peak frequency of sea wind occurs from noon to six in the afternoon. It's possible to see reversal wind direction occurs approximately between six and nine in the morning (land wind to sea wind) and between six and nine in the evening (sea wind to land wind) so this trend is probably linked to breeze events.

During the monitoring days the wind record shows the same trend described above. Also it's possible to see a relationship with air and sea temperature measurement (Picture 8 a,b,c). During the night, air temperature is lower than sea temperature and the wind direction is from the land. During the day is opposite and the wind direction is from the sea. Approximately from four to six in the morning air temperature start to increase and the reversal of wind direction (land wind to sea wind) occurs. The same trend appear in the afternoon where air temperature decrease from six.

The variations of physical properties of water column (T and D) show (pictures 11,12,13,14) as a colder water reclimbing of underlying layers occurs and this let us understand that this could be coastal upwelling.

These variations happen during the inversions of wind direction (pictures 5, 6) and this let us believe that the variation of wind direction is related to the variations of water column are related to wind direction, suggesting that breeze regime modulates coastal upwelling.

5. CONCLUSION

The analysis of meteorological data suggests the breeze regime is more suitable in summer season.

LSBI allows to identify breeze days. This scenario is characterized by 180° wind inversion, that occurs from 05:00 to 07:00 a.m and from 08:00 to 10:00.

According to Haurvitz (1947), reversal of the wind is strictly related to reversal of the land-sea thermal gradient, and by these parameters, breeze phenomenon can be recognized.

The use of LSBI on August 22nd shows typical land-breeze regime during night and typical sea-breeze during day. on August 28th, LSBI shows land breeze only, because of large scale perturbation from south-west occurs in the afternoon, dominating the breeze regime.

On August 20nd, conversely, LSBI shows a weak breeze regime.

Oceanographic data show correlation between the water column shifts and the reversal of morning breeze regime. On August 22nd and 28th, during land breeze, large fluctuations in sea water temperature were measured. A decreasing temperature on water column suggests the presence of an upwelling phenomenon driven by land breeze.

This study allowed to analyse the summer distribution and characteristics of land sea breeze.

The field experiment suggesting how this phenomena produce oscillation in water column.

This phenomenon at present is not considered in coastal circulation models.

Further investigations are needed to complete this work. In particular, it's essential to identify how relative humidity influence breeze regime. It's also important study and test LSBI on others scenario, to verify its validity. For this purpose it's desirable a correlation between this index and coastal upwelling in order to model and relate it with coastal ecosystems.

6. ACKNOWLEDGEMENTS

The authors would like to express gratitude to Viviana Piermattei and Umberto Mainardi and to the staff of the Laboratory of Experimental Oceanology and Marine Ecology (DEB), University of Tuscia.

7. REFERENCES

- Anselmi B., Benvegnù F., Brondi A., Ferretti O. (1978), *Classificazione geomorfologica delle coste italiane come base per l'impostazione di studi sulla contaminazione marina*. Atti III° Congresso Associazione Italiana di Oceanologia e Limnologia. (1)
- Frenzel CW. (1962), *Diurnal wind variations in Central California*. Journal of Applied Meteorology (2)
- Haurwitz B. (1947), *Comments on the sea breeze circulation*. Journal of Meteorology. (3)
- Johnson A Jr, O'Brien JJ. (1973), A study of an Oregon sea breeze event. *Journal of Applied Meteorology*. (4)
- Simpson JE. 1994. Sea Breeze and Local Wind. *Cambridge University Press*. (5)
- Azorin-Molina C., Chen D., Tijm S., Baldi M. (2009), *A multi-year study of sea breezes in a Mediterranean coastal site: Alicante (Spain)*. International journal of climatology. (6)
- Frysinger J. R., Lindner B. L., Brueske S. L. (2003), *A statistical sea-breeze prediction algorithm for Charleston, South Carolina*. Weather and Forecasting, Vol. 18. (7)

Relationship Between Sahel Rainfall and Mediterranean Summer Climate

D'Agostino R.^{1*}, Budillon G.², Fusco G.² and Lionello P.¹

¹Università del Salento, Italy and CMCC - Centro Euro-Mediterraneo sui Cambiamenti Climatici, Italy

²Università degli Studi di Napoli "Parthenope", Italy

*Corresponding author: roberta.dagostino@unisalento.it

Abstract

In the last decades the persistence of the North African Anticyclone in the Mediterranean summertime has caused many heat waves, with a large number of deaths and important economic implications in Southern Europe. Changes in the Northern Hemisphere atmosphere circulation patterns and the oscillation of the sea surface temperature of the Atlantic Ocean are connected with the Mediterranean summer climate extremes and also with the Sahel drought/rainfall. The goal of this study is to find evidence of the relationship between the Sahel rainfall and the Mediterranean summer climate and their link to the most important Northern Hemisphere large-scale patterns. In particular this work analyses the correlations in a large domain (0° - 80° N, 80° W - 60° E) between some atmospheric variables (such as surface air temperature - SAT, 500hPa geopotential height - HGT500 and precipitation NCEP/NCAR Reanalysis data) and some climatic indices (such as Sahel Rainfall Index, SRI, Summer North Atlantic Oscillation, SNAO and Atlantic Multidecadal Oscillation, AMO). The analysis, for July and August from 1979 to 2011, shows significant correlations between the Mediterranean and Sahel summer climate, with positive correlation ($R= 0.4$) between the SRI and the Mediterranean HGT500 and SAT, and negative correlation ($R= -0.4$) between the SRI and the Mediterranean precipitation.

In both regions, climate is connected with large-scale patterns. In fact, precipitation in both the Sahel and Mediterranean is linked with the SNAO index ($R= -0.5$ and $R= 0.4$, respectively). On the other hand, the SNAO index is anticorrelated ($R= -0.5$) with the HGT500 and SAT over the Mediterranean and North Africa region. Indeed, the Sahel rainfall is also linked to the AMO index positive phase ($R= 0.5$), meanwhile the AMO index appears to be uncorrelated with SAT, HGT500 and precipitation over the Mediterranean. Therefore results show that the AMO may eventually affects the Mediterranean summer climate, but marginally and indirectly via atmospheric processes involving the Sahel rainfall and/or the sea level pressure (SLP) over the North Atlantic, in turn influencing meridional air fluxes from subtropics to the Mediterranean region.

Keywords: Sahel rainfall – Mediterranean Summer Climate – AMO – SNAO



1. INTRODUCTION

Heat waves are a familiar feature of the Mediterranean summer. They occur for a combination of many different factors, such as low soil moisture [4], warming of lower tropospheric layers [3], and the positive feedback between hot summer temperatures and the absence of the typical summer-afternoon convection [3].

A recent study of Gaetani et al. [11] shows a significant correlation of the West African Monsoon (WAM) action with high upper-layer temperatures and 500hPa geopotential height on the Mediterranean Basin. Indeed a strong action of WAM could be related to intense rainfall to the Sahel and the northward shift of the Libyan or the so called North African Anticyclone, with extremely stable and steady conditions in the Mediterranean. Several anomalous warm summers have occurred in the Mediterranean and in Southern Europe over the last 50 years, with hot events of different intensity and duration [1]. These events have a high cost in terms of damage to agriculture, forest-fire, and also, in terms of human health and victims [1]. In particular, because of the extremely intense and long hot period places, the summer of 2003, the hottest in 500 years in Europe [15], on top of all natural disaster of the year with an estimated economic loss of more than US\$ 12.3 Billion [17] and with an estimated number of heat-related deaths between 22000 and 35000 in Europe [19].

Beniston and Stephenson [2] showed that extreme climatic events in the Mediterranean-European region are due to particular significant changes in the atmospheric circulation and that an increase in the temperature in the last decades is likely to have produced an increase in the frequency of severe heat wave episodes. Many of these anomalous heat waves are due to the long-standing action of the continental subtropical anticyclone, also called North African or Libyan anticyclone, directly connected with the subsiding branch of the African part of Hadley cell. In last decades many studies demonstrated that the Hadley cell, the fundamental regulator of Earth's energy budget, have increased its activity, due strengthening [5] [23] [16] [14] and widening of its circulation which causes a poleward shift of about 2.75 degrees latitude over 1979 – 2003 [10] [20] [14]. What causes the expansion of the Hadley circulation is still an open question.

However, the poleward shift of the subtropical dry zone boundaries could have important implications in ecosystem and human settlements (such as agriculture and water resources) and could present serious hardships in marginal areas (Mediterranean, Southern Australia, Southern Africa and parts of South America) due changes in precipitation patterns. A poleward expansion of the tropics is likely to

bring even drier conditions to these heavily populated regions, but may bring increased moisture to other areas, with an increase of frequency and intensity of tropical storms and tropical cyclones [20]. To estimate the Hadley cell extent, the monthly Sahel Rainfall Index (SRI), calculated by Mitchell (<http://jisao.washington.edu/data/sahel>), has been used. This index is based on the precipitation anomalies in the Sahel region (10° to 20° N and 20° W to 10° E) near the southern boundaries of the Sahara desert and approximately below the Inter Tropical Convergence Zone (ITCZ).

On the other hand, the summer climate in the North-Atlantic-European sector has a principal pattern of year-to-year variability that is the parallel to the well-known North Atlantic Oscillation (NAO) in winter. Folland and Knight [8] showed that SNAO is characterized by a more northerly location and smaller spatial scale than its winter counterpart. The SNAO exerts a strong influence on European rainfall and temperature. It is, therefore, of key importance in generating summer climate extremes, including flooding, drought and heat stress in north-western [8]. In fact the SNAO index negative/positive phase determines dominant meridional/zonal fluxes and change in the direction of the North Atlantic storm-tracks with shallow/deeper Rossby waves modulation in the mid-latitudes. The SNAO index used in this study (<http://climexp.knmi.nl>) is constructed by Folland et al. [8]. and it is defined as the first EOF mode of the NCEP/NCAR SLP field over 40° - 70° N, 90° W - 30° E, for July and August [8].

On interdecadal time scales, Baines and Folland [9] suggest a link between SNAO and the pattern of Atlantic Multidecadal Oscillation (AMO – [6]). In fact the SNAO appears to be related to a quasi-global Sea Surface Temperatures (SSTs) pattern reminiscent of the negative phase of the AMO. The AMO is composed by multidecadal oscillations of the Atlantic SSTs between Greenland and Equator. The AMO index used in this study (<http://www.esrl.noaa.gov>) is computed by Enfield averaging temperatures over the North Atlantic sector (from Kaplan SST dataset), basically since 0° to 70° N. The time series is detrended and smoothed on all months [7]. Many prominent examples of regional multidecadal climate variability have been related to the AMO, such as North Eastern Brazilian and African Sahel rainfall, Atlantic hurricanes and North American and European summer climate [12]. Indeed, the warm phase of AMO is associated to a northward shift of tropical precipitation in the Atlantic sector. Along with consistent changes in the trade winds, this implies northward displacement of the JJA mean ITCZ position, which may cause an increasing in the Sahel rainfall [18] [12].

Moreover Shanahan et al. [21] found that intervals of severe drought in Sahel lasting for periods ranging from decades to centuries are related to the AMO over the past three millennia. Sutton and Hodson [22] showed an effect of AMO on summer climate in North West Europe: in fact a positive phase of AMO anomaly is related to a MSLP decreased, but is associated with lower rainfall over the US and increased rainfall in North West Europe [12]. It is still unclear how AMO might affect hot summer climate in Mediterranean region.

This study relates the Hadley cell northward displacement (throughout positive anomalies of the Sahel rainfall and the AMO positive phase) with the Mediterranean summer climate and the negative phase of the SNAO index. The correlation maps are computed between NCEP/NCAR Reanalysis gridded data, of SAT, precipitation, HGT500 and the SNAO, the AMO and the SRI indices from 1979 and 2011 for July and August.

2. RESULTS

To investigate how the Sahel Rainfall, related to the Hadley cell activity, is linked to the Mediterranean summer climate, the correlation maps between the SAT, precipitation and HGT500 fields and the SRI have been evaluated. The large domain selected between 0° - 80° N, 80° W – 60° E allows to study any possible teleconnection pattern over the Atlantic region.

The results show that the SRI is well correlated with the SAT (Fig. 1 left), with high values of correlation coefficient ($R= 0.5$ – significance $> 95\%$) over the Maghreb and the Aegean area. However, the SAT field may be affected by many different factors, such as sea and land surface temperature, differential heating and winds, so that we have used HGT500 to identify the subtropical anticyclones directly connected to the subsiding branch of Hadley cell.

The SRI is correlated positively ($R= 0.4$ – significance $> 95\%$) with HGT500 (Fig. 1 right) across the West Mediterranean and Mid Atlantic sector, with high values of correlation coefficient also over the West Russia. Moreover, the SRI shows low value of anticorrelation with precipitation over the Mediterranean (Fig. 2). So, when the SRI is positive, the Hadley cell is shifted northerly than normal and the dry sinking motion can subside in the 500hPa troposphere to higher latitudes. These result could implicate that the positive phase of the SRI, linked to the northward displacement of Hadley's cell, determines hot and dry condition over the Mediterranean during summertime.

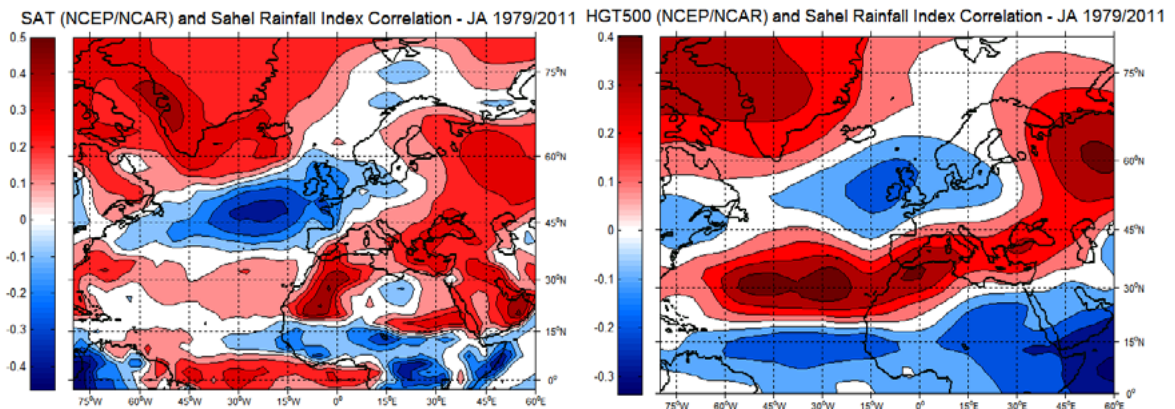


Fig. 1: Correlation between NCEP/NCAR R1 (left) 2m air temperature and (right) 500hPa geopotential height and Sahel Rainfall Index, JA – 1979/2011.

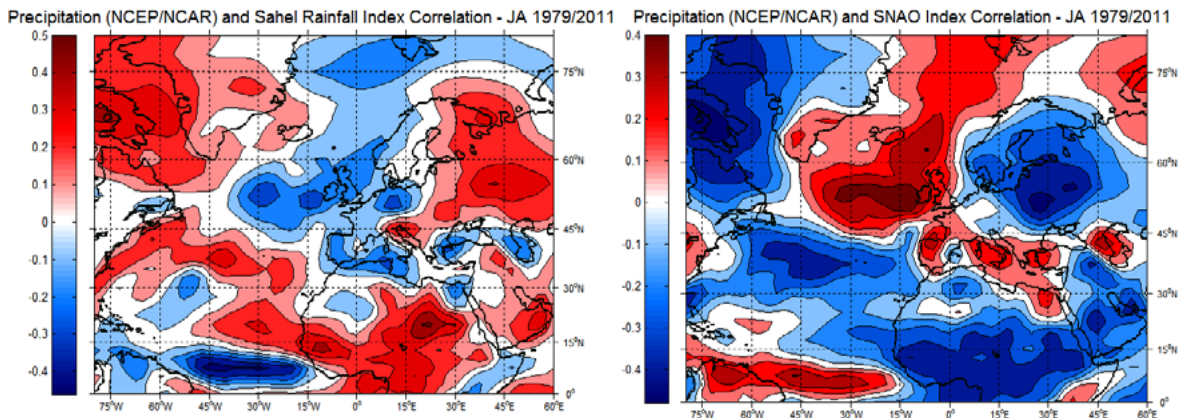


Fig. 1: Correlation between NCEP/NCAR R1 precipitation and Sahel Rainfall Index, JA – 1979/2011.

Fig. 3: Correlation between NCEP/NCAR R1 precipitation and SNAO Index, JA – 1979/2011.

The rainfall over the Sahel and the Mediterranean summer climate are also affected by the baric configuration over the Atlantic, so that it is been used the SNAO index to understand how the sea level pressure field over the Atlantic sector may guide the subtropical fluxes to higher latitudes. When the pressure gradient between the two centres of action in Atlantic is low, the zonal fluxes from the Atlantic to Europe are inhibit while the meridional fluxes are intense. In that case the phase of the SNAO index is negative.

The SNAO index (Fig. 3) is positively correlated with precipitation field over the Mediterranean ($R=0.3 - 0.4$) in according to Folland et al. [8]. So, when the SNAO index is negative, the precipitation over the Mediterranean is low. There is significant negative correlation ($R= -0.5$) over the Sahel region, suggesting more-than-normal rainfall conditions in this zone of the WAM which tend to accompany the negative SNAO index phase (according to Folland et al. [8]). The SNAO index appears to be also

anticorrelated with HGT500 field over the Mediterranean and North Africa, with high temperature in the eastern Mediterranean and North Africa (Fig.4 left and 4 right). Meanwhile, over the Sahel there are not significant correlations.

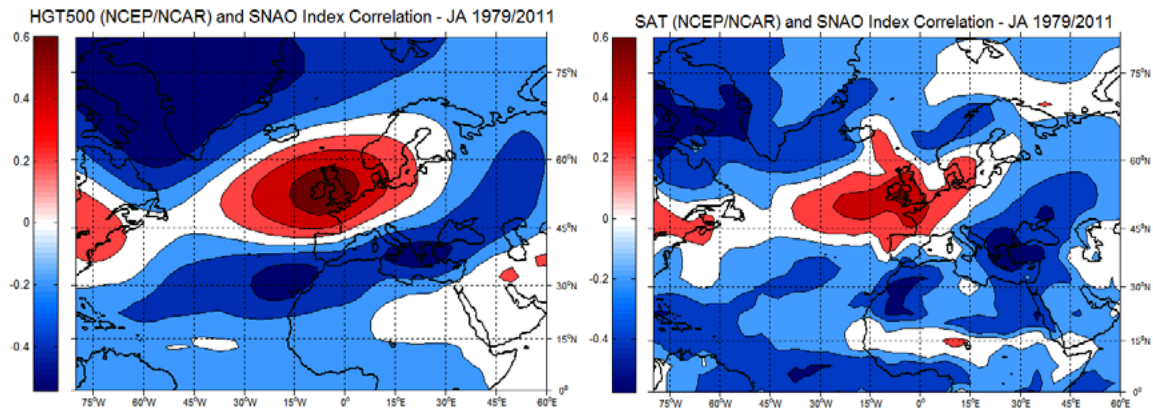


Fig. 4: Correlation between NCEP/NCAR R1 left) HGT500 and right) 2m air temperature data and SNAO Index, JA – 1979/2011

Folland et al. [8] links the positive/negative phase of the SNAO index over multidecadal time scales with natural and cyclic changes of the surface sea temperature over the Atlantic sector and there is a substantial opposite in phase of the SNAO and AMO index. Sutton and Hodson [22] demonstrated that baric field over the north-western Europe is influenced by the Atlantic SSTs, so that SLP field is generically low when AMO index is positive and SNAO is negative. The AMO index is well correlated with multi-variables over the European domain. In particular Knight [12] found a strong positive correlation between AMO and surface temperature in the United Kingdom, but the links between AMO and climate over the Mediterranean is very difficult to analyse.

In this study, the AMO index appear to be uncorrelated with precipitation field over the Mediterranean but it is highly and positively correlated ($R= 0.6$) with rainfall and surface air temperature of the Sahel and West Africa (Fig. 5 left and right). These results suggest that positive phase of the AMO index, with warmer SSTs could enhance the moisture of the tropics throughout more intensive evaporation and then West African Monsoon wind regime transports moist and warm air masses from ocean to lands with an increasing of the precipitation over the Sahel.

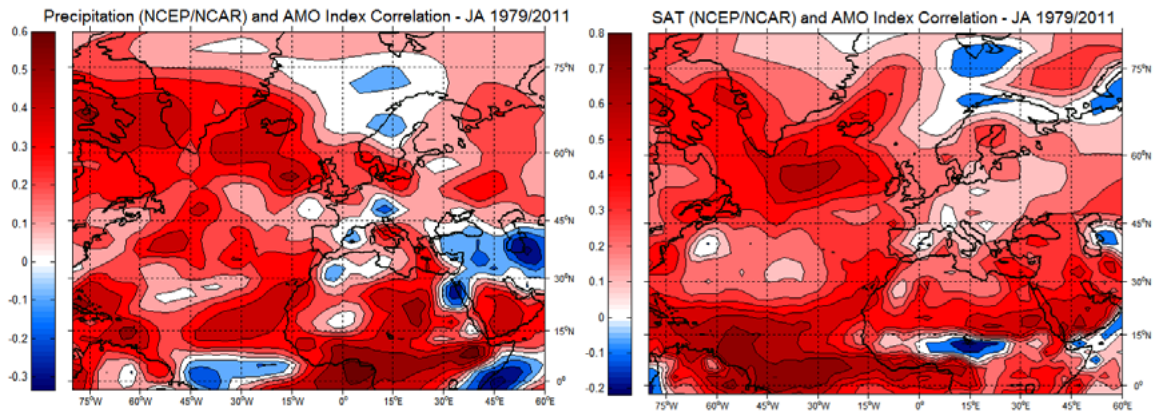


Fig. 5: Correlation between NCEP/NCAR R1 (left) precipitation field and (right) 2m air temperature data and AMO Index, JA – 1979/2011

Warmer SSTs in the central Atlantic and positive phase of the AMO index could affect the Hadley circulation through strong convective events and massive rainfall over the West Africa. Then, the SNAO negative phase guides the subtropical fluxes to higher latitudes, primary affecting the rainfall in the Sahel, and secondary shifting the North African anticyclone over the Mediterranean domain. So, in this way, the AMO could affect indirectly the Mediterranean summer climate via atmospheric forcing of the Hadley Circulation and the Sahel rainfall.

Anyway, this hypothesis requires other studies and further statistical analysis to be confirmed.

3. CONCLUSIONS

Our analysis shows significant correlations between the variables used to describe the climate of the Mediterranean and the Sahel regions. The Sahel Rainfall Index is correlated with the 500hPa geopotential height and surface temperature field ($R = 0.4$, in both cases) and it is anticorrelated ($R = -0.4$) with precipitation field over the Mediterranean. In fact the Mediterranean summer climate and Sahel rainfall are both influenced by the SNAO. During July and August its negative phase determines low precipitation over the Mediterranean and intense precipitation over the Sahel region, with high temperatures and values of the 500hPa geopotential height over the northern Sahara desert and eastern Mediterranean. Moreover, the warm phase of the AMO index forces convective activity over the Guinea Gulf and West Africa, bringing severe rainfall to the Sahel and West Africa region, contributing to reinforcing the Hadley circulation and possibly affecting indirectly and marginally the Mediterranean summer climate via atmospheric processes.

4. REFERENCES

- Baldi M., Dalu G., Maracchi G., Pasqui M., Cesarone F. (2006) *Heat waves in the Mediterranean: a local feature or a larger scale effect?* Int. J. Climatol., 26: 1477–1487. (1)
- Beniston M, Stephenson D.B. (2004), *Extreme climatic events and their evolution under changing climatic conditions*. Global and Planetary Change 44: 1–9. (2)
- Beniston M. (2004) *The 2003 heat wave in Europe. A shape of things to come?* Geophysical Research Letters 31. (3)
- Brabson BB, Lister DH, Jones PD, Palutikof JP. (2005), *Soil moisture and predicted spells of extreme temperatures in Britain*. Journal of Geophysical Research 110. (4)
- Chen J., Carlson B. and Del Genio A. (2002), *Evidence for strengthening of the tropical general circulation in the 1990s*, Science, 295: 838-841. (5)
- Delworth T. L., Mann M. E. (2000), *Observed and simulated multidecadal variability in the Northern Hemisphere*, Climate Dynamics 16: 661–676. (6)
- Enfield D.B., Mestas-Nuñez A.M., Timble P.J. (2001), *The Atlantic multidecadal oscillation and its relation to rainfall and river flows in the continental US*. Geophys. Res. Lett., 28: 2077-2080. (7)
- Folland C.K., Knight J., Hurrell J.W. (2009), *The Summer North Atlantic Oscillation: Past, Present and Future*. Journal of Climate 22 1082-1103. (8)
- Folland C.K., Scaife A.A. (2007), *Climatic impacts of the Atlantic Multidecadal Oscillation*. Geophys. Res. Lett. 33. (9)
- Fu Q., Johanson c., Wallace J. and Reichler T., (2006), *Enhanced midlatitude tropospheric warming in satellite measurements*, Science, 312. (10)
- Gaetani M. et al. (2007), *Connessioni tra il clima della regione mediterranea e l’Africa occidentale attraverso la circolazione meridiana di Hadley*, IBIMET. (11)
- Knight J.R., Folland C.K., Scaife A.A., *Climate impacts of the Atlantic Multidecadal Oscillation*. Geophysical Research Letters, vol.33, L17706, doi:10.1029/2006GL026242, 2006 , Publ. in 2006 by the American Geophysical Union. (12)
- Lionello P., Malanotte-Rizzoli P., Boscolo R., Alpert P., Artale V.Li.L., Luterbacher J., May W., Trigo R., Tsimplis M., Ulbrich U., Xoplaki E. (2006), *The Mediterranean climate: an overview of the main characteristics and issues in Mediterranean variability*, edited by Lionello, P., Malanotte-Rizzoli, R. Boscolo: 1-26. (13)

- Liu J., Song M., Hu Y. and Ren X. (2012), *Changes in the strength and width of the Hadley Circulation since 1971*, *Clim. Past.* (14)
- Luterbacher J., Dietrich D., Xoplaki E., Grosjean M., and Wanner H. (2004), *European seasonal and annual temperature variability, trends, and extremes since 1500*. *SCIENCE*, 303: 1499-1503. (15)
- Mitas C. and Clement A. (2005), *Has the Hadley cell been strengthening in recent decades?* *Geophys. Res. Lett.*, 32. (16)
- Münchener Rückversicherung (2004), *Annual Review: Natural Catastrophes 2003*. *TOPICS Geo*. Munich Re Group: Munich. (17)
- Rowell D.P. (2003), *The impact of Mediterranean SSTs on the Sabelian rainfall season*. *J. Climate* 16: 849-862. (18)
- Schär C, Jendritzky G. (2004), *Hot news from summer 2003*. *Nature*, 432: 559–560. (19)
- Seidel D. and Randel W. (2007), *Recent widening of the tropical belt: evidence from tropopause observations*, *J. Geophys. Res.*, 112.. (20)
- Shanahan T.M., *Atlantic Forcing of Persistent Drought in West Africa*, *Science* 324: 377-380, 2009. (21)
- Sutton R.T., Hodson D.L.R. (2005), *Atlantic Ocean forcing of the North American and European summer climate*. *Science* 309, 115-118. (22)
- Wielicki B., Wong T., Allan R., Slingo A., Kiehl J., Soden B., Gordon C., Miller A., Yang S., Randall D., Robertson F., Susskind J. and Jacobowitz H. (2002), *Evidence for large decadal variability in the tropical mean radiative energy budget*. *Science*, 295: 841-844. (23)

Multivariate analysis for the influence of climate change on maritime structures design

Salvadori G.^{1*}, Tomasicchio G.R.², and D'Alessandro F.²

¹*Dipartimento di Matematica e Fisica, Università del Salento, Lecce, Italy,*

²*Dipartimento di Ingegneria dell'Innovazione, Università del Salento, Lecce, Italy*

*Corresponding author: gianfausto.salvadori@unisalento.it

Abstract

Climate change certainly induces a modification of sea state conditions at a certain site with respect to past observed values. As a consequence, different mutual influences between wave height, wave period, sea storm duration, sea storm direction, and sea storm frequency have to be expected. Therefore, in order to understand and capture the variation of the design conditions for coastal and/or off-shore structures, several dependent variables need to be investigated beyond the traditional wave height. The present manuscript outlines an original approach, exploiting Copulas, in order to provide a consistent framework for the calculation of multivariate design conditions.

Keywords: *Multivariate copula, Multivariate return period, Multivariate design*



Univariate frequency analysis has long been adopted in past decades: see, e.g., [16,17,13,27,19,14,8,28,9,1,7]. However, in practical applications, coastal and off-shore structures typically fail because of the occurrence of a critical combination of the variables which coexist in a sea storm. Then, the lack of knowledge concerning their joint statistics may severely limit the effectiveness of coastal, port, and off-shore structures and / or can lead to expensive and inappropriate decisions [18]. As a consequence, it may be important to consider the joint occurrence of combined conditions.

Recent advances in mathematics show how copulas may represent an efficient tool to investigate the statistical behavior of dependent variables; for a thorough theoretical introduction to copulas see [15,20], for a practical approach see [10,22]. For the sake of simplicity, in the following we shall only investigate the bivariate case. Shortly, a 2-copula \mathbf{C} is the restriction of a bivariate joint distribution with Uniform margins onto the unit square $\mathbf{I}^2 = [0, 1] \times [0, 1]$. The link between a bivariate distribution \mathbf{F} and the associated 2-copula \mathbf{C} is stated by Sklar's Theorem [26], i.e.

$$\mathbf{F}(x_1, x_2) = \mathbf{C}(F_1(x_1), F_2(x_2)) \quad (1)$$

for all $\mathbf{x} \in \mathbf{R}^2$, where the F_i 's are the univariate margins of \mathbf{F} . Below we shall also use the *Kendall's function* $\mathbf{K}: \mathbf{I} \rightarrow \mathbf{I}$ given by [11,12]

$$\mathbf{K}(t) = \mathbf{P}(\mathbf{C}(U_1, U_2) \leq t), \quad (2)$$

where $t \in \mathbf{I}$ is a probability level, and the U_i 's are Uniform r.v.s on \mathbf{I} with copula \mathbf{C} .

Recently, several efforts have been spent on the issues of multivariate design and quantiles: see, e.g., [21,25,24,3,23], and references therein; for coastal and off-shore engineering applications see [6,5,24]. Here we address the following crucial question: "How is it possible to calculate return periods and critical design conditions in a multivariate context?"

Hereinafter, following [23,24], we shall consider as the object of our investigation a sequence $\{\mathbf{X}_1, \mathbf{X}_2, \dots\}$ of i.i.d. sea storms, described in terms of significant wave height H and duration D (but other, and more, variables may be considered): thus, each \mathbf{X}_i has the same bivariate distribution \mathbf{F} as of the random vector $\mathbf{X} = (X_1, X_2) \sim \mathbf{F} = \mathbf{C}(F_1, F_2)$, with suitable marginals F_i 's and 2-copula \mathbf{C} .

Let $\mathcal{R}_t^> = \{\mathbf{z} \in \mathbf{R}^2 : \mathbf{F}(\mathbf{z}) > t\}$, with $t \in \mathbf{I}$, be the "dangerous" region of interest (viz., the one corresponding to the largest, extreme, values of the marginals), and let μ be the average time elapsing between two successive sea storms. The quantity [23]

$$k_x = \mu / (1-\mathbf{K}(t)) \quad (3)$$

is defined as the (multivariate) *Kendall's Return Period* (KRP) of the sea storm \mathbf{x} , where $t = \mathbf{F}(\mathbf{x})$ corresponds to a given “critical” level: k_x provides a consistent estimate of the mean time required for a sea storm to happen in the region $\mathcal{R}_b^>$, and hence to be classified as “dangerous”.

The multivariate case generally fails to provide a solution to the problem of identifying a unique design realization. In fact, there is no natural criterion to select which sea storm lying on the critical isoline $\{\mathbf{x} \in \mathbf{R}^2 : \mathbf{F}(\mathbf{x}) = t\}$, and hence having KRP equal to $\mu / (1-\mathbf{K}(t))$, should be used for design purposes: in a multivariate environment, the sole tool provided by the RP may not be sufficient to identify a design realization, and additional considerations may be required.

Following [23], a possible solution is simply to introduce a suitable function that “weighs” the realizations lying on the critical isoline of interest: then, the practitioner can freely choose the criterion (i.e., the weight function) that best fits the practical needs. For instance, since the density \mathbf{f} of \mathbf{F} over the critical isoline induces a (weak) form of likelihood, it can be used as a weight function, indicating which sea storms are more “likely” than others. For other approaches see [5].

As an illustration, Fig. 1 shows possible bivariate design values of the pair (H,D), for different return periods, according to two different strategies [24] for the sea storm data collected at the Alghero buoy (Sardinia, Italy) from 1989 to 2008.

As a conclusion, the procedures proposed above to calculate the multivariate design conditions for coastal and off-shore structures is innovative. An effort has been made to reduce the troublesome nature of multivariate analysis — which has always limited its practical application — by providing consistent frameworks (the KRP) and techniques (the weight functions on the critical isolines) to address the identification of the critical design events when several dependent variables are involved. The procedure has been tested on several data bases, considering RP's of interest in applications: the preliminary results are valuable, and may provide statistically consistent design values useful in practice.

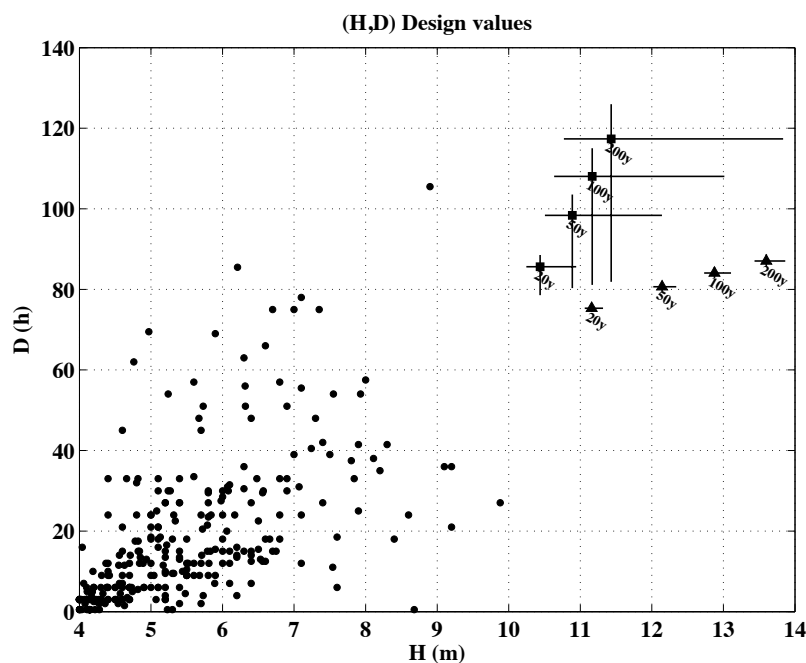


Fig. 1: Possible bivariate design values of the pair (H,D) according to two different strategies (squares and triangles) for the sea storm data collected at the Alghero buoy (circles): shown are the estimates for several return periods, i.e. 20, 50, 100, and 200 years; also indicated are 95% Confidence Intervals

ACKNOWLEDGMENTS

The research was partially supported by the Italian M.I.U.R. via the project “Strumenti operativi per la stima della vulnerabilità dei litorali sabbiosi anche in presenza di strutture costiere” (PRIN 2008) and “Metodi stocastici in finanza matematica” (PRIN 2010).

REFERENCES

- Arena F., Pavone D. (2009), *A generalized approach for the long-term modeling of extreme sea waves*. Ocean Modelling, 26 (4), 217-225. (1)
- Belzunce F., Castano A., Olvera-Cervantes A., Suarez-Llorens A. (2007), *Quantile curves and dependence structure for bivariate distributions*. Computational Statistics & Data Analysis, 51 (10), 5112-5129. (2)
- Chaouch M., Goga C. (2010), *Design-based estimation for geometric quantiles with application to outlier detection*. Computational Statistics & Data Analysis, 54 (10), 2214-2229. (3)

- Chebana F., Ouarda T. B. M. J. (2009), *Index flood-based multivariate regional frequency analysis*. Water Resour. Res., 45, W10435. (4)
- Corbella S., Stretch D. D. (2012), *Multivariate return periods of sea storms for coastal erosion risk assessment*. Nat. Hazards Earth Syst. Sci., 12, 2699-2708. (5)
- De Michele C., Salvadori G., Passoni G., Vezzoli R. (2007), *A multivariate model of sea storms using copulas*. Coastal Engineering, 54, 734-751. (6)
- Fedele F., Arena F. (2010), *The equivalent power storm model for long-term predictions of extreme wave events*. Journal Physical Oceanography, 40, 1106-1117. (7)
- Ferreira J., Soares C. G. (2000), *Modelling distributions of significant wave height*. Coastal Engineering, 40, 361-374. (8)
- Gencarelli R., Tomasicchio G.R., Veltri P. (2006), *Wave height long term prediction based on the use of the spread parameter*. In: Proc. International Conference on Coastal Engineering (San Diego, USA), 701-713. (9)
- Genest C., Favre A. (2007), *Everything you always wanted to know about copula modeling but were afraid to ask*. J. Hydrologic Engineering, 12 (4), 347-368. (10)
- Genest C., Rivest L.-P. (1993), *Statistical inference procedures for bivariate Archimedean copulas*. J. Amer. Statist. Assoc., 88 (423), 1034-1043. (11)
- Genest C., Rivest L.-P. (2001), *On the multivariate probability integral transformation*. Statist. Probab. Lett., 53 (4), 391-399. (12)
- Goda Y. (1988), *On the methodology of selecting design wave height*. In: Proc. 21st International Conference on Coastal Engineering, pp. 899-913. (13)
- Goda Y. (2000), *Random Seas and Design of Maritime Structures*. Advanced Series on Ocean Engineering, vol. 15, World Scientific, Singapore. (14)
- Joe H. (1997), *Multivariate models and dependence concepts*. Chapman & Hall, London. (15)
- Krogstad H. (1985), *Height and period distributions of extreme waves*. Applied Ocean Research, 7 (3), 158-165. (16)

- Kuwashima S., Hogben N. (1986), *The estimation of wave height and wind speed persistence statistics from cumulative probability distributions*. Coastal Engineering, 9, 563–590. (17)
- Li Y., Simmonds D., Reeve D. (2008) *Quantifying uncertainty in extreme values of design parameters with resampling techniques*. Ocean Engineering, 35, 1029-1038. (18)
- Mathiesen M. (1994), *Estimation of wave duration statistics*. Coastal Engineering, 23, 167-181. (19)
- Nelsen R. (2006), *An introduction to copulas*. 2nd Edition. Springer Verlag, New York. (20)
- Salvadori G., De Michele C. (2004), *Frequency analysis via Copulas: theoretical aspects and applications to hydrological events*. Water Resour. Res., 40, W12511. (21)
- Salvadori G., De Michele C., Kottegoda N., Rosso R. (2007), *Extremes in nature. An approach using copulas*. Water Science and Technology Library. Vol. 56, Springer, Dordrecht. (22)
- Salvadori G., De Michele C., Durante F. (2011), *On the return period and design in a multivariate framework*. Hydrol. Earth Syst. Sci., 15, 3293-3305. (23)
- Salvadori G., Tomasicchio G.R., D’Alessandro F. (2013), *Practical guidelines for multivariate analysis and design in coastal and off-shore engineering*. Coastal Engineering. Manuscript submitted, in revision. (24)
- Serfling R. (2002), *Quantile functions for multivariate analysis: approaches and applications*. Statist. Neerlandica, 56 (2), 214-232. (25)
- Sklar A. (1959), *Fonctions de repartition a n dimensions et leurs marges*. Publ. Inst. Statist., Univ. Paris 8, 229-231. (26)
- Smith J. (1988), *Decision Analysis: A Bayesian Approach*. Chapman and Hall. (27)
- Soares C. G., Scotto M.G. (2001), *Modelling uncertainty in long-term predictions of significant wave height*. Ocean Engineering, 28 (3), 329–342. (28)

IMPLICATIONS ON ECOSYSTEM SERVICES

IMPLICATIONS ON ECOSYSTEM SERVICES

Dynamic landscapes: hazard & risk assessment - I

An European HPC Infrastructure and the Climate Challenges

Erbacci G. *, Bassini S., Cavazzoni C.

Supercomputing, Applications and Innovation Department, CINECA, Bologna, Italy

**Corresponding author: g.erbacci@ Cineca.it*

Abstract

Climate change represents a big challenge for scientists and society today. As a consequence, climate sciences are evolving, crossing different scientific disciplines, with the support of advanced computational methods.

Weather and climate models, used to simulate the different earth system processes, grow in complexity and scales to face the climate challenges today. As a consequence, these models require an increasing amount of computational resources that can be offered only by state of the art HPC infrastructures, mainly at European level.

Since his foundation, CINECA has been able to assure to the scientific community a competitive advantage by putting into timely production advanced HPC systems that have proven very wide applicability and success.

In this work we present the evolution of the CINECA HPC infrastructure, outlining its role in the context of the European HPC scene, providing some examples of co-operation with the climate community at Italian and European level.

Keywords: *HPC Infrastructures, Computational sciences, Climate sciences, PRACE*



1. INTRODUCTION

Floods, blizzards, fires, droughts and other natural disasters affect the territory with a growing incidence respect to some decades ago. Climate events which turn into natural disasters have become now worrying situations not confined only to distant lands, but more often also affecting Italy. An example is the tornado that last May caused more than 17 million Euro in damages in the Modena area.

The intensification of these meteorological phenomena, in direct relation with climate change, highlights the vulnerability of the territory with broken infrastructure, urban areas greatly damaged or destroyed.

Climate change is now a new challenge, impacting different human activities in our society from agriculture, to energy, from health to finance. In order to fully understand this phenomena, climate research has become very diffused involving different fields of knowledge and scientific disciplines from meteorology to oceanography, from physics to chemistry to biology to economy.

Climate sciences are focused not only at global scales, but also at regional and local scales, using high-resolution global models, regional models, and observational data sets. Climate sciences make a wide use of computational resources to investigate these models through numerical simulation on domains that range from individual country to global scales. To better investigate the accuracy of the scientific phenomena it is important to increase the numerical resolution of the models, decreasing the mesh size, and increasing the model complexity, adding more processes. All these simulations generate yearly Petabyte of data that must be analyzed, visualized and, in some cases, preserved for further analysis and comparison with other simulated or observed data [1].

In this way, complex models acting on heavy domains require an increasing amount of computational resources and advanced data facilities that can be offered by state of the art HPC and Data-center infrastructures, mainly at National or European level.

CINECA is the Italian supercomputing center, providing state of the art HPC resources to the scientific communities using computational methods to enhance their research activities. CINECA plays a important role also at European level as hosting member of the PRACE HPC Research Infrastructure [2] and it is an active partner in the main European HPC and data Infrastructure projects.

The following sections present the state of the art of the CINECA HPC infrastructure, and the services to the scientific communities, both in terms of HPC and data, outlining its role in the context of the European HPC scene. Then a section outlines some examples of co-operation with the climate community at Italian and European level. Finally some conclusions follow.

2. AN ADVANCED HPC INFRASTRUCTURE

CINECA is the most important Italian supercomputing centre for public and private research activities. Established in 1969, the Consortium actually brings together 56 Italian Universities, the National Institute of Oceanography and experimental Geophysics (OGS), the National Research Council (CNR) and it is directly participated by the Ministry of Instruction, University and Research (MIUR). CINECA statutory aims include the promotion of the use of the most advanced information processing systems to support public and private scientific and technological research. CINECA is an infrastructure at European level offering state of the art HPC resources and services for all the main fields of computational sciences. The first supercomputer was installed in 1984: a vector system CRAY X-MP 12 with a peak performance of 160 MFlop/s and a 16 MByte RAM. As reported in Tab. 1, the actual supercomputing facility is based on two main HPC systems: the FERMI system, an IBM BG/Q system equipped with 163840 cores (see Fig. 1) and the hybrid cluster Linux PLX (3288 cores accelerated with 548 GPUs). FERMI is ranked N. 12 in Top500 list (June 2013) of the 500 most powerful computers in the world, based on the Linpack Benchmark [3].

Logical Name	PLX	FERMI
Model	IBM IDATAPLEX	IBM BG/Q
Architecture	Linux Cluster	MPP System
Processor	Intel Westmere Ec 2.4GHz	IBM PowerA2, 1.6 GHz
# of Cores	3288 + 548 GPU Nvidia M2070	163840
# of Nodes	274	10240
# of Racks	10	10
Total RAM	14 TeraByte	163 TeraByte, 1GByte/core
Interconnection	Qlogiq QDR 4x	NI 11 links => 5D Torus
Disk Space Scratch	100 TeraByte	2PetaByte
O.S.	RedHat	Linux
Total Power	~ 200 KWatts	~ 800 KWatts
Peak Performance	293 TeraFlop/s	2 PetaFlop/s

Tab. 1: CINECA HPC systems for Scientific Research.



Fig. 1: FERMI IBM BG/Q installed in CINECA.

Recently, a prototype cluster system (EURORA), engineered by EUROTECH has been installed in CINECA to test applications with new programming paradigms based on Intel MIC and nVIDIA K20 accelerators. A picture of EURORA is reported in Fig. 2. EURORA is a hybrid cluster composed of 64 nodes Intel Sandy Bridge dual socket, for a total of 1024 cores (32 nodes at 2.1 GHz and 32 nodes at 3.1 GHz). Each node is equipped with 16 GByte DDR3 RAM, 160 GByte SSD and 1 FPGA Altera Stratix V. The nodes are interconnected through both Infiniband QDR and a 3D Torus network. The system is equipped with 64 MIC processors (2 per node on 32 nodes) and 64 NVIDIA K20 accelerators (2 per node on 32 nodes) and is cooled via hot water cooling technology. The peak performance (GPU accelerated) is 175.7 TFlop/s. Eurora is ranked 1st in the [June 2013 Green500 list](#) of the 500 most energy efficient computers in the world [4].

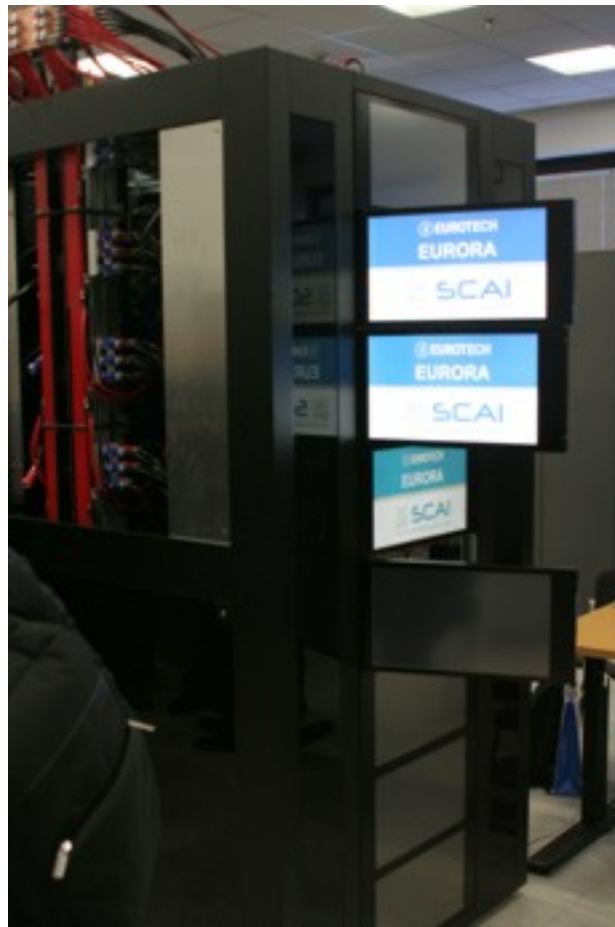


Fig. 2: EURORA hybrid cluster prototype installed in CINECA.

Advanced computational infrastructures must provide powerful HPC systems integrated with efficient data storage systems and innovative instruments to extract all the information from the simulations produced. In line with this aspect, CINECA provides several Petabytes of high performance disk storage integrating the HPC systems, and a service for Remote Visualisation. The CINECA data centre is equipped with technology to provide business continuity. A diagram of the whole CINECA HPC infrastructure, including the HPC Infrastructure for Industry services, is presented in Fig. 3.

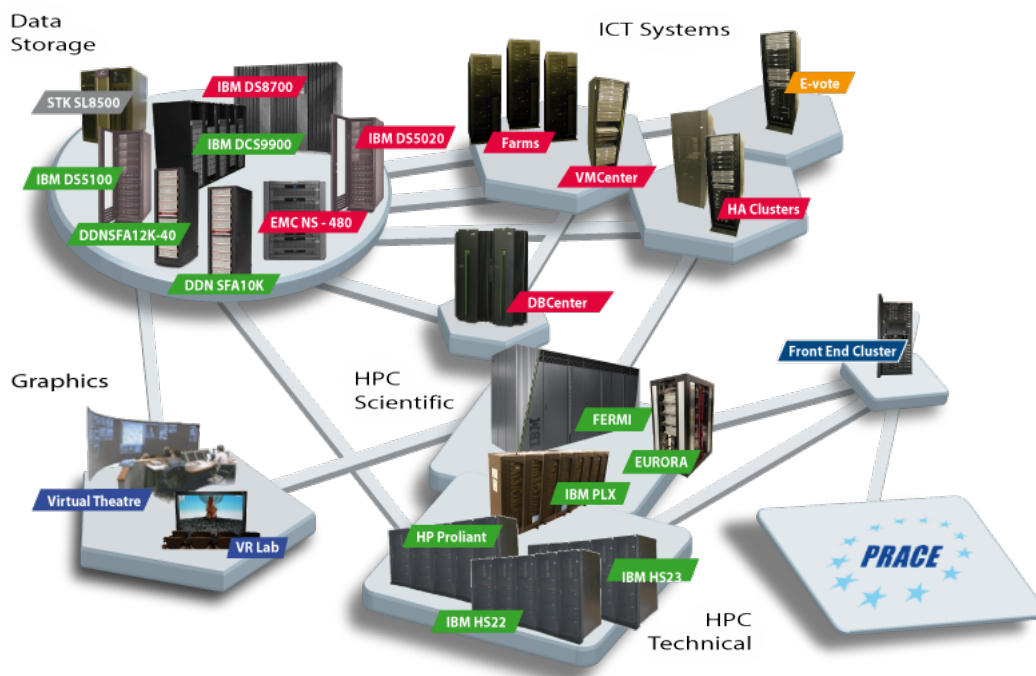


Fig. 3: CINECA HPC Infrastructure.

Specific services for Big Data activity are being implemented. The first step, already in production, is the CINECA Data Repository, a service to store and maintain scientific data sets, with an high level of quality, including reliability and scalability, allowing the users to safely back-up data and at the same time manage them through a variety of clients. The service is implemented through iRODS [5], which relies on plain filesystems as back-end to store data, represented as collections of objects, and on databases for metadata. The service's architecture has been carefully designed to scale to millions of

files and petabytes of data, joining robustness and versatility, and to offer to the scientific communities a complete set of features to manage the data life-cycle.

CINECA has a wide experience in cooperating with the researchers in parallelising, enabling and scaling up their applications in different computational disciplines and in managing big data applications. CINECA has a long tradition in education and training in the different fields of HPC and computational sciences.

3. CINECA AND THE EUROPEAN HPC ECOSYSTEM

From the mandate of Italian Ministry of Education University and Research, CINECA represents Italy in the PRACE Research Infrastructure (Partnership for Advanced Computing in Europe) [2]. The PRACE RI is a pan-European infrastructure seated in Brussels and established as an international non-profit association of European government representative organizations responsible for HPC resources and services for public research. These partners are creating a pan-European world class computing and data management infrastructure, providing access to resources at the highest performance level including sophisticated services for scientific simulations in all fields of research and engineering (Tier-0 Systems). The PRACE RI is open to all European researchers and their collaborators for research with potential for high European and International impact.

With the installation of FERMI, CINECA becomes a Tier-0 hosting site, in the PRACE RI. FERMI is one of the six Tier-0 systems available in PRACE, enabling computational science of scale, allowing Italian and European teams of researchers to perform computationally intensive, large-scale research projects.

CINECA is a member of EUDAT [6], the European project aimed to deliver a Collaborative Data Infrastructure (CDI) with the capacity and capability for meeting future researchers' needs in a sustainable way. Its design reflects a comprehensive picture of the data service requirements of the research communities in Europe and beyond. This will become increasingly important over the next decade as we face the challenges of massive expansion in the volume of data being generated and preserved (the so-called '*data tsunami*') and in the complexity of that data and the systems required to provide access to it. CINECA, with INGV, represent the European Plate Observing System (EPOS) community [7] in EUDAT. EPOS is the integrated solid Earth Sciences research infrastructure,

approved by the ESFRI Roadmap [8] in December 2008. EPOS is a long-term integration plan of national existing RIs.

Furthermore, CINECA is involved in VERCE (Virtual Earthquake and seismology Research Community in Europe e-science environment) [9] a project that addresses the realization of workflows for data-intensive analysis and for HPC modeling by providing tools allowing the scientist to gain simplified interaction with data and modeling results.

4. THE MODEL FOR HPC RESOURCES AT CINECA

All the computational resources available on the HPC systems in CINECA are assigned to the Scientific communities for free, on the basis of scientific excellence, through a blind peer review mechanism.

In particular, the computational resource provided by FERMI are available via both European and national calls for proposals:

- Tier-0 PRACE calls, based on a Peer review process at European level (overseen by the PRACE Scientific Steering Committee comprised of leading European researchers). Two calls per year launched directly by the PRACE-RI.
- National calls, managed by the ISCRA initiative (the Italian Supercomputing Resource Allocation Initiative) established by CINECA. The ISCRA initiative is based on a national peer review process [10].

In this way, each year, CINECA will directly award in excess of 500 millions core processor hours, and indirectly, by mean of the participation of the European PRACE Tier-0 access, in excess of 600 millions core hours, for a total amount in the order of 1.100 millions core hours. Further 8 million core hours are available on EURORA.

5. COLLABORATIONS IN THE FIELD OF CLIMATE SCIENCES

As seen in the previous section, the HPC resources in CINECA are assigned through a peer review process and different scientists, involved in climate sciences, have been granted resources for their research activity, in different projects, ranging from marine to atmospheric models, to modeling of the Adriatic sea ecosystem.

CINECA has issued also some specific collaborations. In the following we mention two of them, by way of example. The first one is a collaboration with the National Institute of Oceanography and experimental Geophysics (OGS) in Trieste and the second one is with ENEA (the Italian national agency for new technologies, energy and sustainable economic development) in Rome.

The collaboration with OGS started some years ago in the context of the European project MyOcean [11] which leads to the implementation of an European service for the Ocean monitoring and forecasting. In MyOcean, OGS was in charge for the production of biogeochemical forecasts for the Mediterranean Sea. OGS provided a fully operational forecasting system in strict collaboration with CINECA which implemented the operational system (operational chain). Actually the service is in full production as a service and runs regularly on the PLX cluster system.

The collaboration with OGS has strengthened and led to the co-design of an application code where OGS built the scientific model and CINECA provided the support for the engineering and the parallelisation of the application. As a consequence, recently a PRACE Tier-0 project, submitted by the research group in OGS, and based on the previous application code, has been granted with 21 Millions core hours and it is currently completing on FERMI. Objective of the project is the implementation of a global sensitivity analysis of a state-of-the-art 3D biogeochemical model of the Mediterranean Sea.

These marine ecosystem models are employed in a wide range of applications, spanning from short-term forecast to climate change studies.

In this project CINECA collaborated with OGS to enable and tune the code and define the environment to run the parallel code using 2048 cores on FERMI.

The second example of cooperation is with the *Energy and Environmental Modeling Division* in ENEA. Here the task is to assist ENEA researchers to integrate ESMF (Earth System Modeling Framework), a parallel open-source framework for building and coupling climate models, with MITgcm, the Massachusetts Institute of Technology general circulation model. At the present MITgcm represents the state-of-the-art for the ocean numerical models.

The objective here is to use the ESMF coupler to couple different instances of MITgcm, at different resolutions, to simulate the whole Mediterranean Thermohaline Circulation from the Strait of Gibraltar to the Black Sea. This activity will represent a challenging simulation that can be faced only with PRACE Tier-0 resources.

Finally, it is worth to mention the activity done in PRACE, in which CINECA is involved, to enable codes of interest for the scientific communities. The objective here is to optimise application codes, to scale-up on the PRACE systems. In the climate domain the enabling activity was done in cooperation with the IS-ENES community, representing the climate community across Europe. The EC-EARTH 3 climate model suite was selected during the initial phase of the activity and specifically the enabling involved NEMO, a modeling framework for oceanographic research, ICON, a general circulation model, OASIS, a software interface (coupler) between different climate models, and Fluidity-ICOM, a three-dimensional non-hydrostatic parallel ocean model [12].

6. CONCLUSIONS

Climate sciences play a growing role in our society, to provide answers to some of the big problems posed by the climate changes directly impacting in our real daily life.

Nowadays, climate science are predominantly multidisciplinary, multisectorial and collaborative ones. Furthermore, the models involved become more and more complex and address huge amount of data, both simulated and observed [13].

As a consequence, state of the art HPC infrastructures are fundamental to support climate research to predict climate variations, identifying possible climate scenarios, impacting different fields in our society, and advance knowledge at European level.

The HPC infrastructures cannot be seen just in terms of power and capacity, but must provide a broad range of services to the scientists, generating new knowledge, crossing the traditional disciplinary boundaries. These aspects will assume more and more importance in the next few years when the HPC systems will evolve in terms of performance but also in terms of complexity and need to be integrated with powerful data facilities to manage the big data deluge coming from real life.

Furthermore, it is very important to cooperate and consolidate the integration between the most important HPC infrastructures at European level, in order to provide a integrated specialized support and service to the computational communities.

CINECA is the most advanced HPC infrastructure in Italy, well integrated in the European HPC Ecosystem. The resources offered by CINECA, integrating both computational and data managements systems, can efficiently support the climate scientists to make progress and innovation in their activity and fostering climate knowledge at the service of the society.

7. REFERENCES

The Scientific Case for High Performance Computing in Europe, PRACE, Guest et al, 2012,
<http://www.prace-ri.eu/PRACE-The-Scientific-Case-for-HPC?lang=en> (1)

<http://www.prace-ri.eu> (2)

<http://www.top500.org> (3)

<http://www.green500.org/> (4)

iRODS, integrated Rule-Oriented Data System , <https://www.irods.org> (5)

<http://www.eudat.eu> (6)

<http://www.epos-eu.org/> (7)

ESFRI *European Roadmap for Research Infrastructures*, Report 2006; European Community, Luxembourg, 2006, ISBN 92-79-02694-1 http://ec.europa.eu/research/infrastructures/index_en.cfm?pg=esfri-roadmap (8)

www.verce-project.eu (9)

<http://iscra.cineca.it> (10)

www.myocean.eu (11)

PRACE-2IP, Deliverable 8.4 " *Re-integration into Community Codes*", ,August 2013. (12)

Synergistic Challenges in Data-Intensive Science and Exascale Computing. *Summary Report of the Advanced Scientific Advisory Committee (ASCAC) Subcommittee*, DOE ASCAC Data Subcommittee, March 2013. (13)

Exploring synergies for disaster risk reduction in Guatemala: the use of cognitive maps.

Giannini V.

Ca' Foscari University of Venice, Department of Economics & CMCC, Venezia-Italy
Corresponding author: valentina.giannini@cmcc.it

a los Guatemaltecos, les deseo un futuro de Paz

Abstract

In this article a method to operationalize climate change adaptation (CCA) is explored to develop tools for knowledge integration and management, based on a participatory process. The result is a Total Cognitive Map useful to collect and analyse visions stakeholders have on risk and disaster risk reduction (DRR), and to identify and improve possible synergies among institutions and organizations dealing with DRR. The case study is identified based upon a knowledge integration process taking place in Guatemala. The idea explored in the case study is to use cognitive maps to define a method to enable synergies and define roles and measures for DRR and CCA. Stakeholders in this research are government organizations (GO), non-governmental organizations (NGO), and civil society organizations (CSO), who have a mandate for -or a stake in- DRR and CCA. Cognitive maps are created through an online questionnaire. The freewares FCMapper and Pajek are used to compare, analyse and synthesize the concept of risk as perceived by a group of stakeholders. Cognitive maps are used to identify DRR measures and relative roles institutions should have to enable the exploitation of synergies. A total cognitive map is then created including all opinions elicited, and then specific cognitive maps are derived from it to exemplify possible uses.

Keywords: *Participation; knowledge integration; climate change adaptation; disaster risk reduction; cognitive map.*



1. INTRODUCTION

There is a strong interconnectedness between the human -or social- and the natural -or ecological- systems [1]. Anthropogenic disturbances are increasing ecosystems vulnerability [2;1]. Increased vulnerability of ecosystems makes them prone to further crisis, such as natural climatic variances like El Niño [3]. Climate change will most likely exacerbate these conditions [4]. Even so, climate change uncertainties may represent a justification for inaction. To overcome this uncertainty experiences in coping with risk derived from climate variability could be implemented: these would decrease risk from climate change as well [5;6]. A possibility to cope with impacts from climate is given by the integration of two paradigms: climate change adaptation (CCA) and disaster risk reduction (DRR) [5;7;8;9].

Including indigenous and local knowledge in CCA and DRR is an added value [5]: on the one hand there is ground to say that scientific and indigenous and local knowledge are both related to the development of research [10]. On the other hand, indigenous and local knowledge can help when research is not available for a specific place: what indigenous and local peoples can provide, in fact, is long term observations [11], which might overcome scientific knowledge gaps. For example, some populations have accurate ways to predict weather based on observations of natural phenomena in their surroundings [12]; some observations led to early action, decreasing risk, and, thus, number of casualties [13]. These studies highlight not only the importance of indigenous knowledge, but also its necessity [14;15].

Since impacts of climate vary at a local scale adaptation measures need to be developed taking into consideration local specificities [16]: populations which have lived in the same areas for a long time have acquired knowledge which can prove very useful to design coping measures [8;17;18;19;20]. There are successful examples in which communities have been able to define and implement plans to cope with climate impacts [21]. To enable this vulnerable communities must not only rely on their traditional knowledge, they must also be empowered and have access to climate information [22]. The commons can be governed when information at the appropriate scale is provided to all, alternative options are analysed and, thus, conflicts decreased, physical and technological infrastructure is provided, and change is taken into account [23].

A variety of institutions and organizations, with mandate on CCA and/or DRR, are to be involved, and the exploitation of synergies among these is necessary. Scientists, policy makers, civil society, practitioners all have their own knowledge and experience, but most lack experience in collaborating

with each other [24]. However, even if many recognize the need and urgency for collaboration there are not many examples of models and methods for this.

The article is organized as follows. First the case used for the methodology test is described. Then, the method section is used to introduce cognitive maps and their use to gather, analyze, and synthesize opinions and visions of stakeholders; also the questionnaire designed to draw cognitive maps is described. In the results paragraph an overview of possible cognitive maps that can be created is given. The discussion paragraph outlines possible uses of the results. Then a paragraph with conclusions indicates further research possibilities and needs.

2. GUATEMALA: CASE STUDY DESCRIPTION

Looking at impacts from climate change we find that Guatemala is among the countries in the world that is most hardly hit [25], and climate change will make precipitations increase significantly [4].

The opportunity for this research is given by a project on knowledge integration in Guatemala for DRR called “La cosmovisión de los pueblos de la humanidad en la construcción social del conocimiento para la Reducción del Riesgo de Desastres y la Adaptación al Cambio Climático”¹ that is implemented by CARE and is financed by PSO, a Dutch non-governmental organization (NGO). Due to its national responsibilities regarding DRR the Secretaría Ejecutiva Coordinadora Nacional Reducción de Desastre² (SE-CONRED) took the responsibility of the process, which led to the creation of the “Comisión para la armonización de los conocimientos y sabidurías de los pueblos Maya, Xinca, Garifuna y Mestizo ante la reducción de riesgo a desastre”³ (hereafter Comisión). The following national institutes integrate the Comisión: SE-CONRED, Ministerio de la Educación⁴, Ministerio de Ambiente y Recursos Naturales⁵, Ministerio de Agricultura, Ganadería y Alimentación⁶, Secretaría de Seguridad Alimentaria y Nutricional⁷.

¹ The vision of peoples for the social construction of knowledge for Disaster Risk Reduction and Climate Change Adaptation

² SE-CONRED, Secretariat of the National Coordinator for Disaster Reduction

³ Commission for the harmonization of knowledge and experiences from Maya, Xinca, Garifuna, Mestizos

⁴ MINEDUC, Ministry of Education

⁵ MARN, Ministry of Environment and Natural Resources

⁶ MAGA, Ministry of Agriculture and Food Security

⁷ SESAN, Secretariat for food security

3. METHOD

This research is not about defining one best practice or comparing methods, but rather, about exploring a possible method to operationalize CCA and DRR, evaluating and exploring the chosen method in a hands-on experience. Available methods and tools appropriate for the acquisition of information on visions, opinions, and knowledge on CCA and DRR, i.e. stakeholders' mental models, were assessed against two criteria: (1) enable organization of information, (2) allow comparison among different visions. Features of the Cognitive Map method make it fit for this research, which is based on stakeholders' participation, and knowledge identification, sharing, and integration, including the development of easy to use tools. Cognitive map as an aid for the description of concepts and causal chains that link them are quite often used for many different scopes [e.g.26; 27]. A cognitive map is a graphical representation where concepts and opinions are represented by nodes, and causal relations between nodes are represented by a link.

However, eliciting a cognitive map can be a challenge [28]. As suggested by Özesmi and Özesmi [27] a questionnaire was designed to gather information from each single stakeholder to be able to draw his/her specific cognitive map. In the frame of climate change and variability, questions were asked for the identification of natural hazards and anthropogenic disasters, of impacts and risks derived from these, of DRR measures needed, and of organizations' mandates. The terminology used for the questionnaire is coherent with that of UNISDR, made available both in English⁸ and in Spanish.⁹

A review of websites on DRR, such as UN-ISDR, was carried out to define questions, to acquire definitions, and to identify risks, hazards, and DRR measures, i.e. all the multiple answers available. The first draft of the questionnaire was written in English, but the definitive one was in Spanish. The questionnaire was tested with the help of native Spanish speakers who work in the field of CCA. Then, using the web platform Qualtrics¹⁰, the questionnaire was made available to stakeholders online. Answers were coded in a matrix, using a spreadsheet¹¹.

Cognitive maps are then drawn with the information derived from the questionnaire using the freewares FCMapper¹² and Pajek¹³. FCMapper is an excel spreadsheet, which enables analysis of

⁸ <http://www.unisdr.org/we/inform/terminology>

⁹ http://unisdr.org/files/7817_UNISDRTerminologySpanish.pdf

¹⁰ <http://www.qualtrics.com>

¹¹ <http://www.openoffice.org/>

¹² <http://www.fcappers.net/joomla/>

¹³ <http://pajek.imfm.si/doku.php?id=pajek>

cognitive maps by means of algorithms defined to calculate descriptive variables according to fuzzy logic. Of all the analyses that can be performed with FCMapper, only one is considered here: centrality, which shows how connected a variable (node) is to other variables (nodes) and what the cumulative strengths of these connections are [27]. The scope of this variable is therefore to determine the relative importance of a node with respect to the other in a cognitive map. Centrality is calculated summing two variables: outdegree, i.e. “the row sum of absolute values of a variable in the adjacency matrix”, and indegree, i.e. “the column sum of absolute values of a variable in the adjacency matrix” [27:pg.51]. FCMapper also creates a net file which can be read by the freeware Pajek, which creates the cognitive map.

Moreover, cognitive maps drawn from information collected from stakeholders can be combined by adding matrices: to combine cognitive maps first an augmented matrix has to be created by listing all nodes in rows (and in columns) then each matrix is coded into the augmented matrix, and finally all matrices are added [27;29;30].

Criteria for stakeholder selection were defined, non-governmental organizations (GO), governmental organizations (NGO), and civil society organizations (CSO) with a mandate, or stake, in CCA and DRR were selected according to the following criteria:

- belonging to the Guatemalan Comisión; these are key informants from the following entities: indigenous and local peoples representatives, national and local government officials, and disaster risk management authorities
- stakeholders involved by the Comisión in their process (roughly 100 stakeholders)
- NGOs which integrate the consortium “Partners for Resilience”.¹⁴

¹⁴ <http://www.climatecentre.org/site/partners-for-resilience>

4. RESULTS

Over 100 stakeholders were contacted by email. After many attempts, only twelve compiled the questionnaire, of these only eight questionnaires were complete: this is about the expected response rate for web surveys, which is 6-15% according to a meta-analysis published [31].

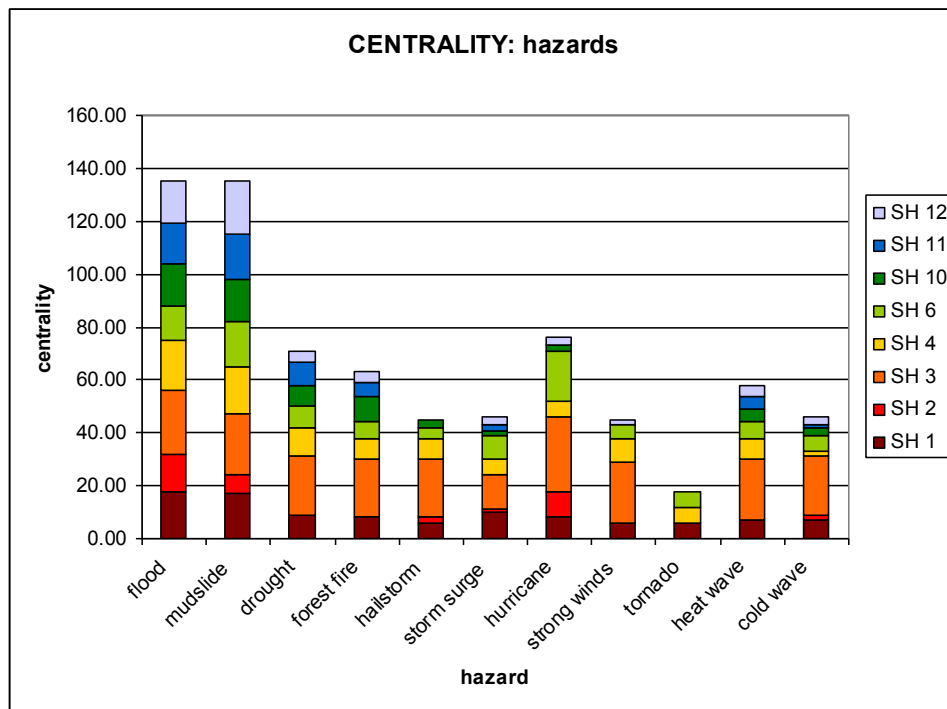


Fig. 1: Centrality: hazards (elaboration made with FCMapper)

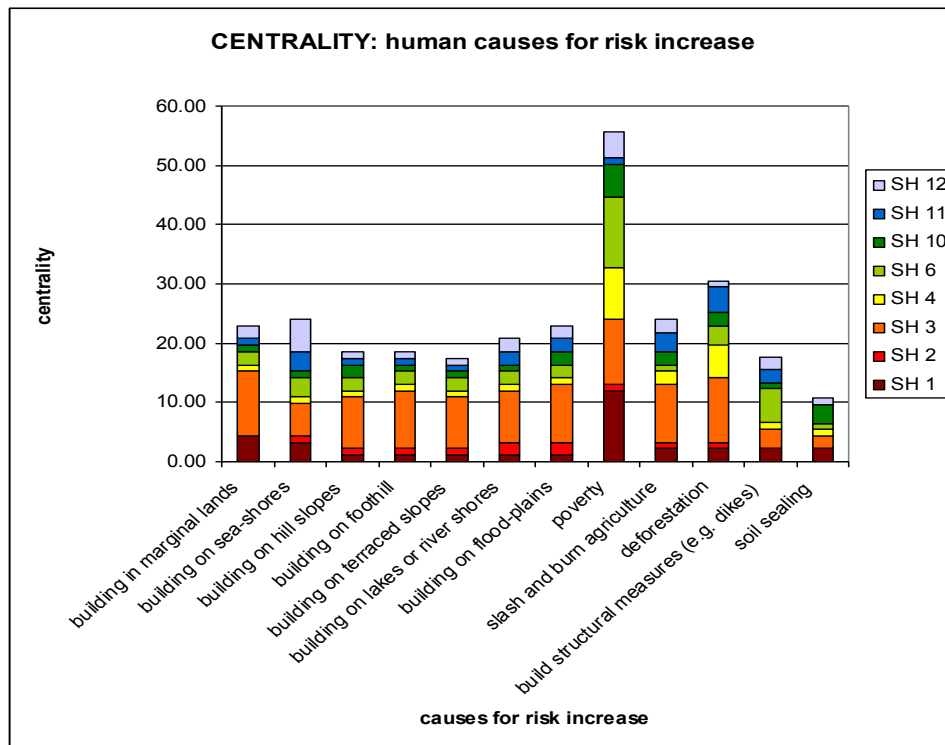


Fig. 2: Centrality: human causes for risk increase (elaboration made with FCMapper)

Answers from questionnaires were coded in a spreadsheet to create the matrix, which was then imported in FCMapper, analysed and then a net file was created and imported in Pajek. This was repeated for each stakeholder, and then a total matrix summing all stakeholders' matrices was created. Results described here validate the method adopted, and give some initial insights. However, more stakeholder would be needed in order for results to be definitive¹⁵.

The variable centrality gives some promising results. First of all in Fig. 1 one can identify which natural hazards are the most relevant for the region: flood and mudslides. This is consistent with the data of PreventionWeb [25]. The other natural hazards are more or less all equally relevant. Risk is not caused only by natural hazards: there are also anthropogenic causes which make risk increase, poverty is twice as important with respect to the rest (Figure 2).

¹⁵ The research described in this article is used to test the methodology proposed, and results are found to have some meaning. However, the research must be based upon a wider stakeholder base, thus the effort to contact the stakeholders who have not yet compiled the questionnaire is ongoing. Opportunities to meet a selected number of stakeholders in person are being sought, and, at the same time, contact by email and telephone is also carried on. A list of stakeholders is kept by the author, it is not published for confidentiality issues.

Looking at the section on DRR measures (Fig. 3) the first issue to note is that the most important ones seem to be those related to general themes, such as <public awareness>, and to all those measures relative to institutions, such as <institutional plans and regulations> and <map risk and no build areas>. The following chart (Figure 4) shows the prominent role of CONRED: its role is only slightly smaller than that of all NGOs taken together.

The over 20 emergency measures identified in open ended questions are linked to each hazard. They include the need for information (how to identify warning signals and on what to do), for zoning laws, for informing communities on climate change, and for a general awareness on environmental issues.

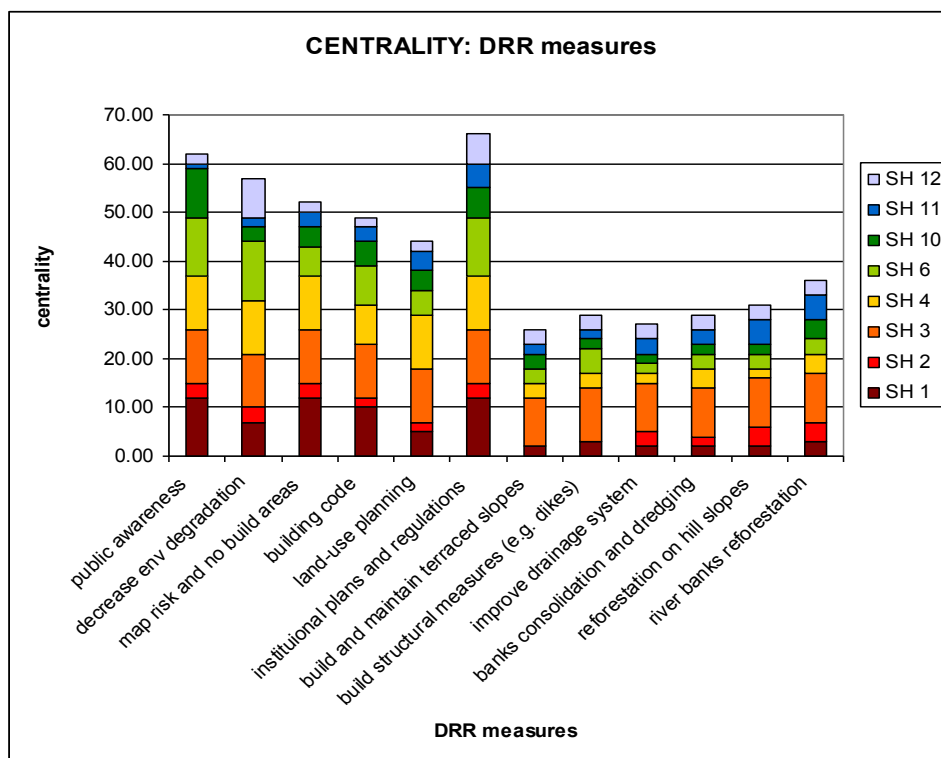


Fig. 3: Centrality: DRR measures (elaboration made with FCMapper)

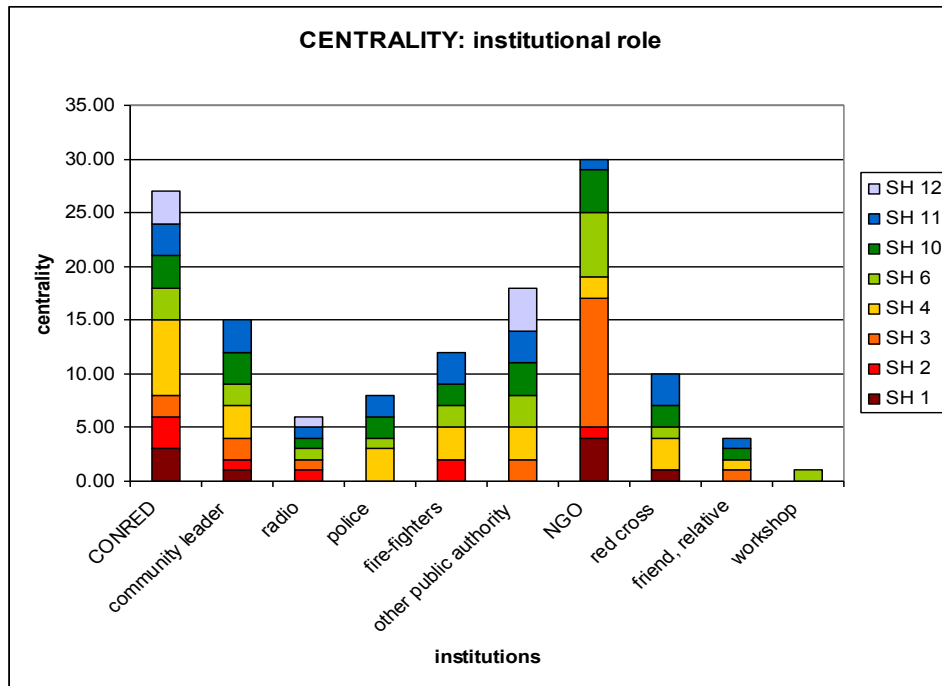


Fig. 4: Centrality: institutional role (elaboration made with FCMapper)

Net files were created with FCMapper and opened with Pajek to create cognitive maps (Figure 5 to Figure 9). A first look at all the maps created for each stakeholder shows the complexity and interconnection of DRR. Many are the hazards and risks identified, and there are multiple measures identified and linked to these. However, the total cognitive map, created integrating all single cognitive maps, is more interesting (Figure 6). A first look at the total cognitive map clarifies the complexity of considering all risks at once, since Guatemala was chosen because globally it ranks high considering multiple risks this is no surprise [25]. Nevertheless, the total cognitive map can be useful to understand several issues:

- roles that institutions and organizations (grey circles) have with respect to DRR measures (yellow squares), including mandates (orange diamonds) they have during an emergency;
- specific measures to address each risk are also identified (orange diamonds on right of total cognitive map), and which of these should be used to address impacts of each hazard;

- DRR measures (yellow squares) are divided in common ones, connected to the specific natural hazard, and ones suggested by stakeholders, connected to the type of institution to which the stakeholder who suggested them belongs.

A cognitive map can be used to identify possible DRR measures needed to cope with one specific hazard, or linked hazards. One should start by selecting hazards to cope with, and from these hazards draw one specific cognitive map, selecting only those nodes connected to the hazards. For instance if we select the hazards <flood> and <mudslide> and delete from a cognitive map all nodes not linked to these, we can draw a cognitive map (Figure 7) that shows what could make risk increase with respect to flood and mudslide (blue diamonds), what DRR measures are needed to cope with these hazards (yellow squares), who is in charge of implementing these DRR measures (grey circles), and other DRR measures suggested (yellow squares).

Another specific cognitive map can be drawn if one considers all hazards, and only one institution (Figure 8). From this cognitive map one could understand what plans can be implemented by the specific institution to cope with all the hazards. Finally, a cognitive map can be drawn with both the restricting conditions described above: one set of hazards, e.g. flood and mudslide, and one institution, e.g. CONRED, see (Figure 9). This cognitive map shows the specific DRR measures that should be implemented by the selected institution to deal with identified hazard.

red triangle	hazard
blue diamond	causes for risk increase
orange diamond	what to do during an emergency
grey circles	GO, NGO, CSO
black square	risk and DRR
yellow square	DRR measures
green circle	both cause for risk increase and DRR measure

Table 1. Legend for all cognitive map

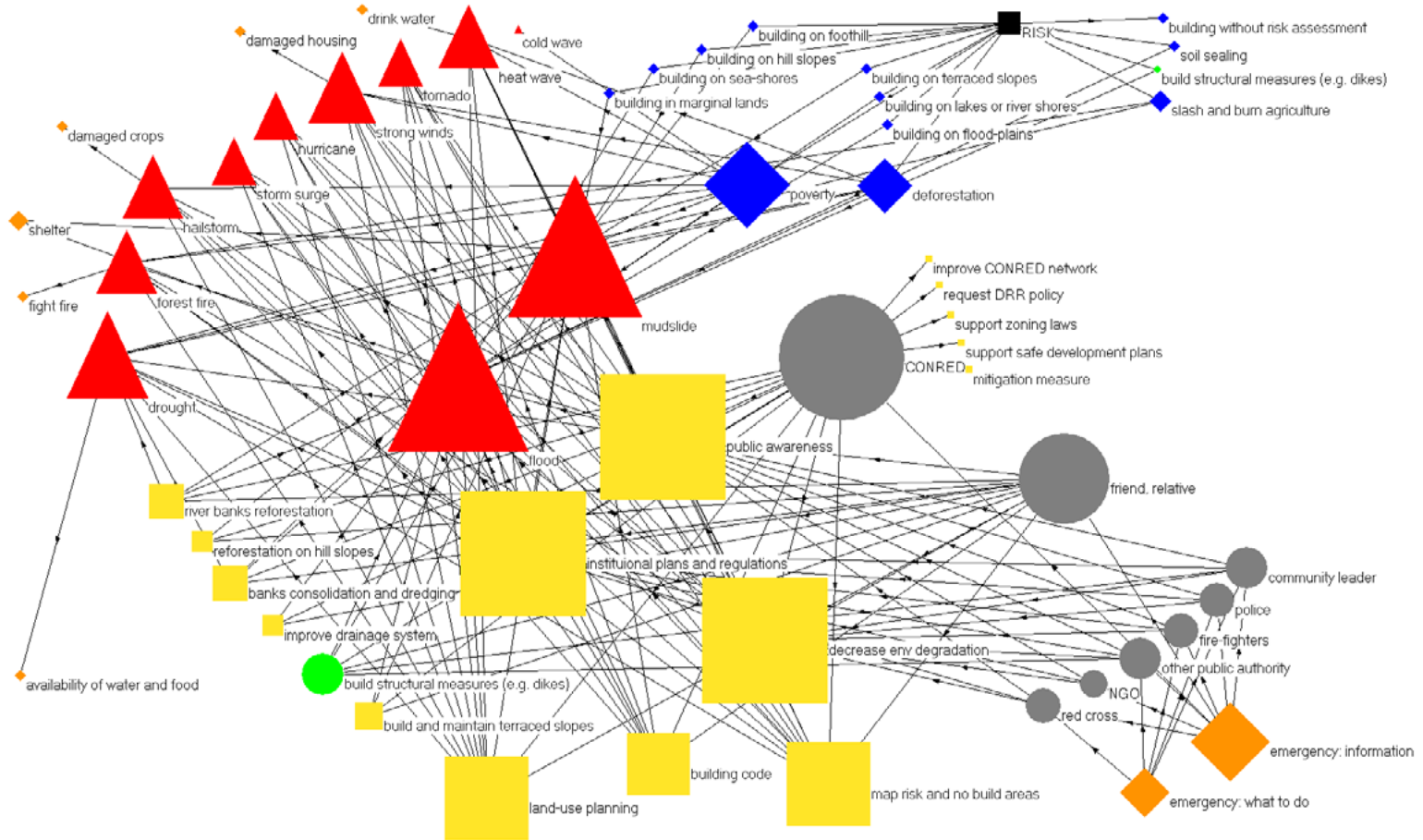


Fig. 5. Cognitive map (stakeholder 4), dimension of nodes represents centrality (elaboration of questionnaires made with FCMapper and Pajek)

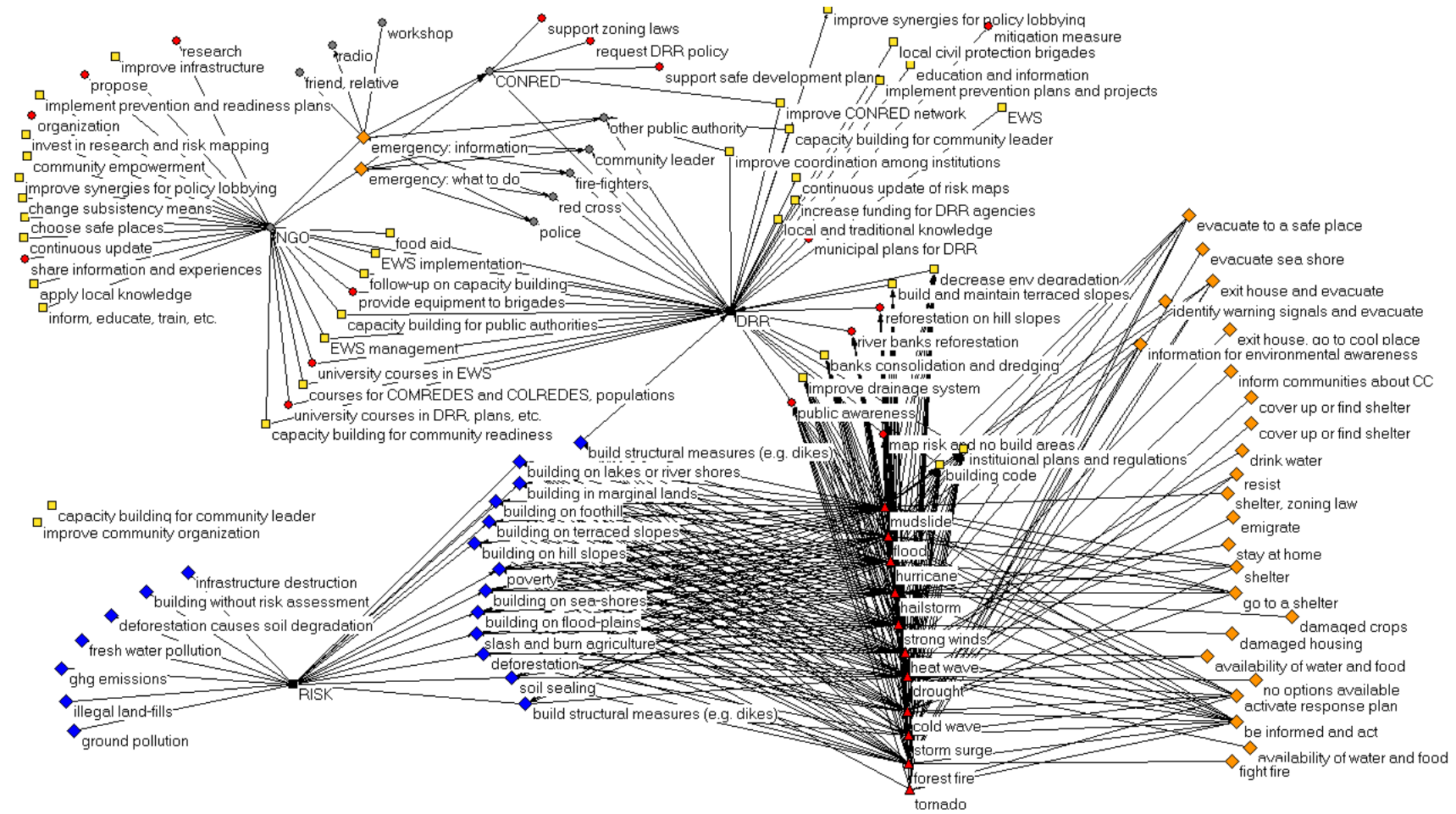


Fig. 6: Total cognitive map (elaboration of questionnaires made with FCMapper and Pajek)

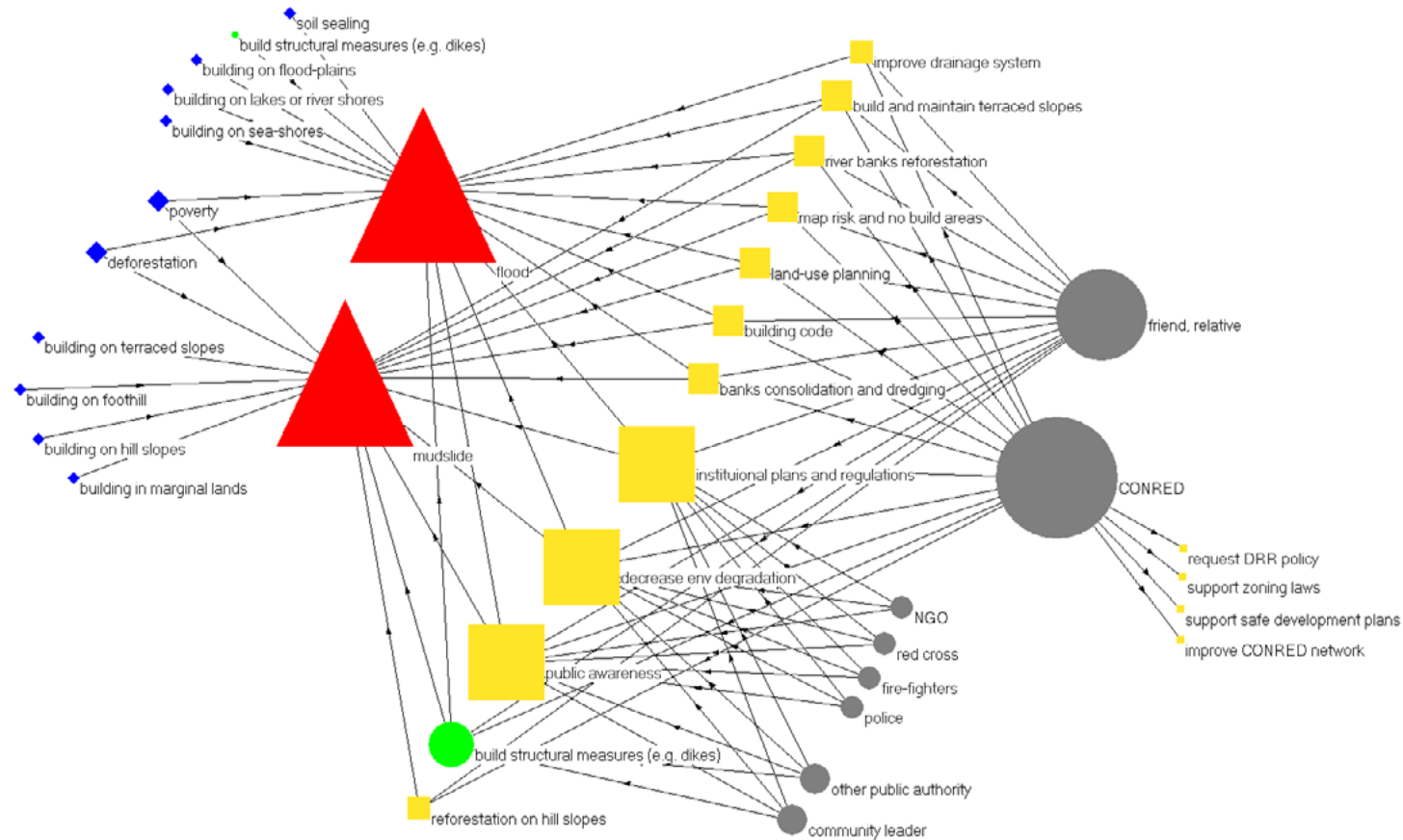


Fig. 7: Cognitive map drawn considering only nodes directly linked to FLOOD and MUDSLIDE (stakeholder 4), dimension of nodes represents centrality (elaboration of questionnaires made with FCMapper and Pajek)

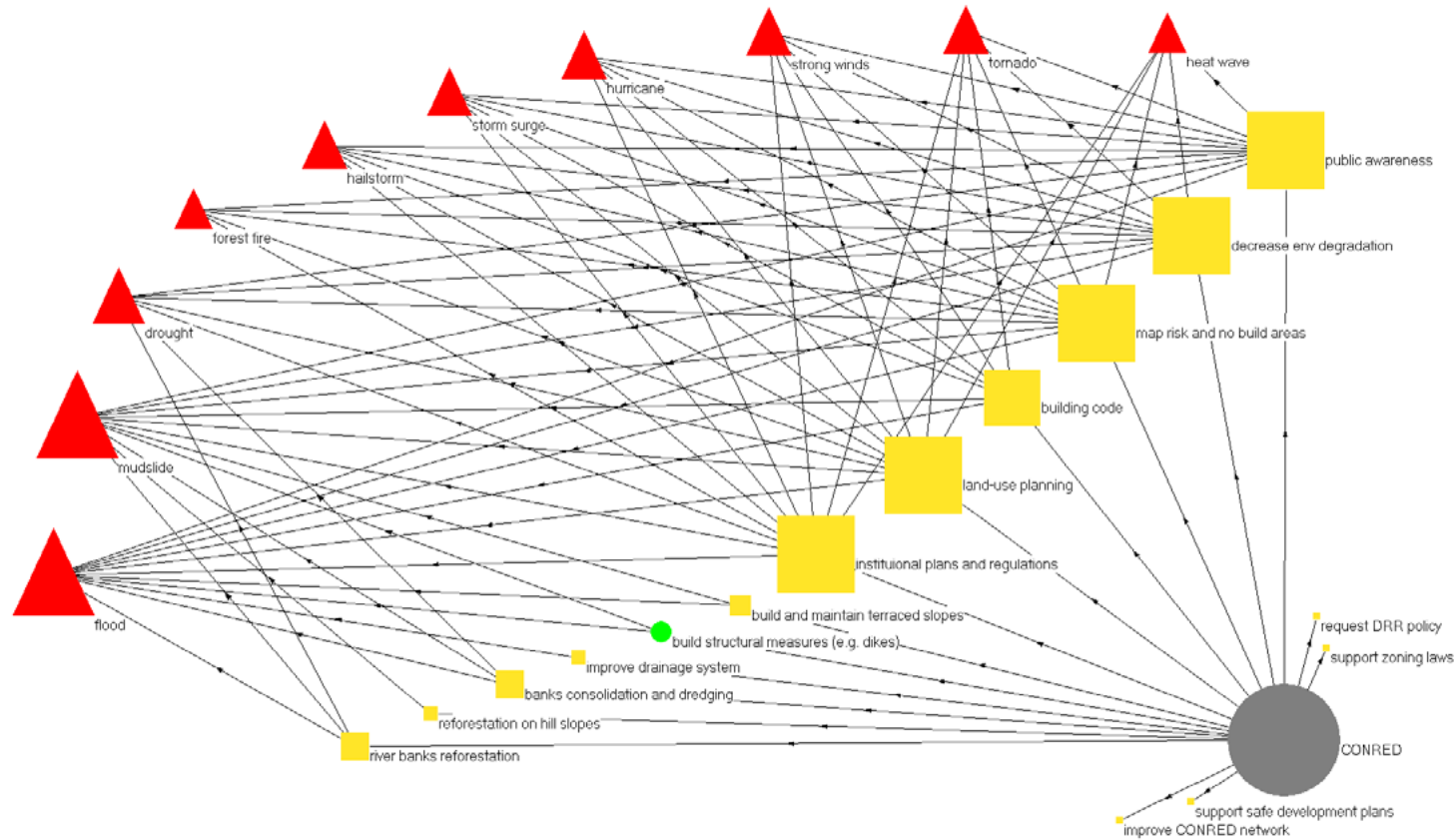


Fig. 8: Cognitive map drawn considering all hazards and only one institution CONRED (stakeholder 4), dimension of nodes represents centrality (elaboration of questionnaires made with FCMapper and Pajek)

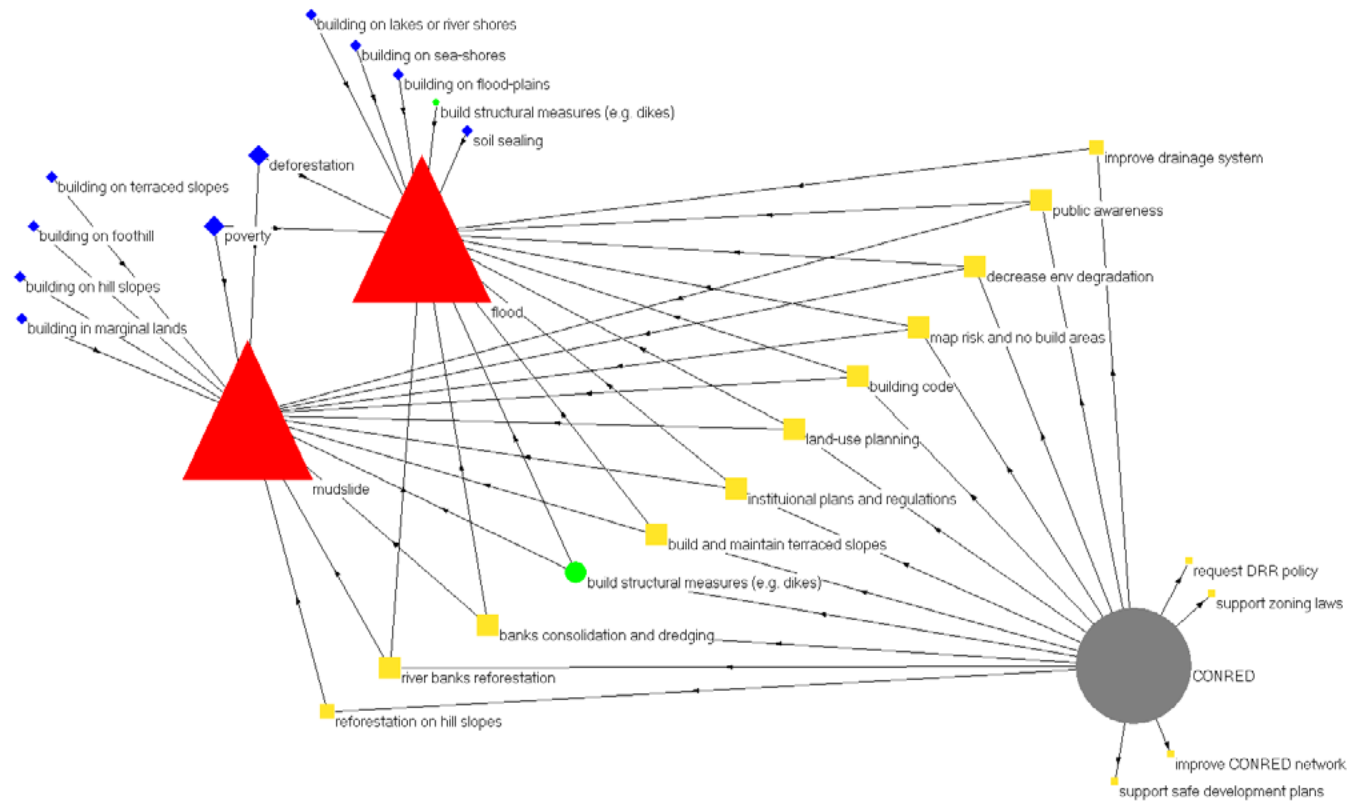


Fig. 9: Cognitive map drawn considering nodes directly linked to FLOOD and MUDSLIDE and only one institution CONRED (stakeholder 4), dimension of nodes represents centrality (elaboration of questionnaires made with FCMapper and Pajek)

5. DISCUSSION

This exercise proves that it is possible to develop cognitive maps to define concepts of risk and DRR from an online questionnaire. The questionnaire should be structured keeping in mind that for the cognitive map to be created the answers should be coded in a matrix, thus, multiple choice questions are well suited for this, while too many open ended questions make it difficult. However, also some possibility to add missing concepts should be given.

The concept of centrality has proven to be well suited to understand relative importance of nodes considered, i.e. natural hazards, anthropogenic causes for risk increase, institutional roles, and DRR measures.

- Outcomes show that the role of CONRED is central, as should be according to the law, which prescribes that CONRED should coordinate actions of local civil institutions, such as police, fire fighters, and red cross; nevertheless, NGOs and other institutions also have a high centrality.
- Looking at natural hazards one can note the higher relevance of floods and mudslides, which is coherent with the country profile [25]. The other hazards are probably less important because specific to some parts of the country.
- Similar interpretation can also be valid for human causes for risk increase. Poverty is certainly one of the most relevant issues in Guatemala, as according to the human poverty index it is ranked 131 out of 187¹⁶.

Reading the list of DRR measures added by stakeholders one can note the importance of knowledge, its dissemination and integration, and capacity building. There is a request for local knowledge integration in the decision making process and for empowerment of local communities.

The single stakeholder's cognitive map and the total cognitive map identify a possible method for the definition of risk and identification of DRR measures. Analysing the total cognitive map one notes the high number of DRR measures linked to the NGO node, as compared to the ones linked to the other ones (25). CONRED with 16 ranks second in this list. However, the ones linked to CONRED are much more general in scope, and, possibly, more effective with respect to general DRR, while those

¹⁶ <http://hdr.undp.org/en/statistics/>

linked to NGOs could prove more effective in specific locations. The other institutions and organizations mentioned are less relevant, thus there is still room for improvement by increasing their agency.

Finally, selecting only specific nodes from the total cognitive map, e.g. one hazard at a time, or a combination of one hazard and multiple organizations, one could understand what needs to be done to decrease a specific risk derived from the hazard, and by whom. In this selection process possible synergies can be enabled: knowing the mandates and roles, and identifying the link with the relevant organizations, the creation of synergies can be fostered.

6. CONCLUSIONS

A tool has been developed to integrate, analyse, and synthesize knowledge, to operationalize CCA and DRR: the total cognitive map. Knowledge was elicited from stakeholders, analysed, and systematized with the help of cognitive maps (FCMapper and Pajek). Opportunities have been sought and created through the involvement in a participatory process run by CARE in Guatemala (see paragraph 2).

This knowledge harmonization process opened the possibility to enable synergies among GOs, NGOs, and CSOs. A methodology was developed to define:

- how risk is identified/perceived by stakeholders belonging to different cultures and/or institutions;
- what the differences and similarities among these perceptions are;
- how these perceptions can be integrated to create a shared understanding and enable synergies among GOs, NGOs, and CSOs who have a mandate for DRR.

Selected stakeholders agreed to share their knowledge and experience answering to an online questionnaire. With the information gathered through the questionnaire with the aid of freewares (FCMapper and Pajek) cognitive maps were created representing each one stakeholder's mental map. More interestingly all the information gathered was summed to create one comprehensive cognitive map: the total cognitive map. Defining criteria several kinds of cognitive maps can be created from this total cognitive map using sub-sets of the rows and columns of the matrix. Examples are shown, which

demonstrate the possibility of using the information collected to understand what to do relative to each hazard, or what roles and mandates GOs, NGOs, or CSOs have.

Lessons can be learned from the experience of each organization to foster synergies and to overcome miscomprehensions and problems. In addition stakeholders from participating might gain:

- GOs could develop a similar framework and establish a participatory and inclusive process;
- NGOs are holders of knowledge, so they could become catalysts for improvement, and could improve their understanding of what their role can be in DRR;
- CSOs, often not taken into consideration as they should¹⁷, could make their voices heard and influence the decision making process by providing information/knowledge, they ask for institutional support and collaboration.

The potential with respect to DRR of each single vision, and/or of the synthesis vision defined in the total cognitive map, could be explored using the links established in the cognitive map. Cognitive maps could, in fact, be used to monitor effectiveness of DRR measures looking at the implementation of identified and designed plans and projects (yellow squares), and the effect these have on risk (blue diamonds) and having established links with natural hazards (red triangles).

In sum the success of this research is due to the identification, organization and creation of relevant knowledge, which enables a shared understanding of the system. This research was guided by the need to develop a methodology based on a hands-on experience. However, this research not only developed a methodology, but also tested it producing results of some significance.

¹⁷ Guatemala has signed the ILO convention 169 on Indigenous Peoples' rights

7. ACKNOWLEDGMENTS

This research was carried out as part of my PhD thesis: I would like to take this opportunity to thank Carlo Giupponi, my advisor, for encouraging me to follow my thoughts. Also I would like to acknowledge the support of researchers at IVM of Vrije Universiteit in Amsterdam where I started developing ideas which led to this research; CARE Nederlands for funding my travel to Guatemala, especially Tialda and Andres for the support in Guatemala; members of Comisión for welcoming me in their activities and meetings; and all who have participated in research by providing insights and sharing their knowledge.

8. REFERENCES

- Janssen M.A., & Ostrom E. (2006), *Resilience, vulnerability, and adaptation: A cross-cutting theme of international human dimensions programme on global environmental change*, Global Environmental Change- Human and Policy Dimensions, No. 16(3), pp. 237-239. (1)
- Du Toit J.T., Walker B.H., & Campbell B.M. (2004), *Conserving tropical nature: current challenges for ecologists*, Trends in Ecology & Evolution, No. 19, pp. 12-17. (2)
- Curran L.M., Trigg S.N., McDonald A.K., Astiani D., Hardiono Y.M., Siregar P., Caniago I., & Kasischke E (2004), *Lowland forest loss in protected areas of Indonesian Borneo*, Science, No. 303, pp. 1000-1003. (3)
- IPCC (2007), *Climate Change 2007: Synthesis Report. Contribution of Working Groups I, II and III to the Fourth Assessment Report of the Intergovernmental Panel on Climate Change* [Core Writing Team, Pachauri R.K and Reisinger A. (eds.)]. IPCC, Geneva, Switzerland, 104 pp. (4)
- IPCC (2011), *Summary for Policymakers. In: Intergovernmental Panel on Climate Change Special Report on Managing the Risks of Extreme Events and Disasters to Advance Climate Change Adaptation* [Field C. B., Barros V., Stocker T.F., Qin D., Dokken D., Ebi K.L., Mastrandrea M. D., Mach K. J., Plattner G.-K., Allen S. K., Tignor M. and P. M. Midgley (eds.)]. Cambridge University Press, Cambridge, United Kingdom and New York, NY, USA. (5)
- Van Aalst M.K. (2006), *The impacts of climate change on the risk of natural disasters*, Disasters, No. 30 (1), pp. 5-18, doi:10.1111/j.1467-9523.2006.00303.x (6)

- Schipper L., & Pelling M. (2006), *Disaster risk, climate change and international development: scope for, and challenges to, integration*, *Disasters*, No. 30 (1), pp. 19-38. doi:10.1111/j.1467-9523.2006.00304.x. (7)
- O'Brien G., O'Keefe P., Rose J., & Wisner B. (2006), *Climate change and disaster management*, *Disasters*, No. 30 (1), pp. 64-80. doi:10.1111/j.1467-9523.2006.00307.x. (8)
- Tadesse T. ; Haile M., Senay G., Wardlow B.D., Knutson C.L. (2008), *The need for integration of drought monitoring tools for proactive food security management in sub-Saharan Africa*, *Natural Resources Forum*, No. 32(4), pp. 265-279. (9)
- Dove M.R. (2006), *Indigenous People and Environmental Politics*, *Annual Review of Anthropology*, No. 35, pp. 191-208. (10)
- Drew J.A. (2005), *Use of traditional ecological knowledge in marine conservation*, *Conservation Biology*, No. 19 (4), pp. 1286-1293. (11)
- Orlove B.S., Chiang J.C.H. & Cane M.A. (2000), *Forecasting Andean rainfall and crop yield from the influence of El Niño on Pleiades visibility*, *Nature*, No. 403(6765), pp. 68-71. (12)
- Baumwolle J. (2008), *The Value of Indigenous Knowledge for Disaster Risk Reduction: A Unique Assessment Tool for Reducing Community Vulnerability to Natural Disasters*, Master Thesis, Webster University. (13)
- Twomlow S. Francis T. Mugabeb F.T., Mwalec M., Delved, R., Nanjae D., Carberry P., & Howdenf M. (2008), *Building adaptive capacity to cope with increasing vulnerability due to climatic change in Africa: A new approach*, *Physics and Chemistry of the Earth, Parts A/B/C*, No. 33(8-13), pp. 780-787. (14)
- Shukla S.R. & Sinclair A.J. (2010), *Strategies for Self-organization: Learning from a Village-level Community-based Conservation Initiative in India*, *Human Ecology*, No. 38, pp. 205-215. (15)
- Smit B. & Wandel J. (2006) *Adaptation, adaptive capacity and vulnerability*, *Global Environmental Change-Human and Policy Dimensions*, No. 16(3), pp. 282-292. (16)
- Allen K.M. (2006), *Community-based disaster preparedness and climate adaptation: local capacity-building in the Philippines*, *Disasters*, No. 30 (1), pp. 81-101. doi:10.1111/j.1467-9523.2006.00308.x. (17)
- Bengtsson J., Angelstam P., Elmqvist T., Emanuelsson U., Folke C., Ihse M., Moberg F., & Nystrom M. (2003), *Reserves, resilience and dynamic landscapes*, *AMBIO*, No. 32(6), pp. 389-396. (18)

- Agrawal A. (2000), *Adaptive management in transboundary protected areas: The Bialowieza National Park and Biosphere Reserve as a case study*, Environmental Conservation, No. 27(4), pp. 326-333. (19)
- Berkes F., Colding J., & Folke C. (2000), *Rediscovery of traditional ecological knowledge as adaptive management*, Ecological Applications, No. 10(5), pp. 1251-1262. (20)
- Van Aalst M.K., Cannon T., & Burton I. (2008), *Community level adaptation to climate change: The potential role of participatory community risk assessment*, Global Environmental Change, No. 18, pp. 165-179, doi:10.1016/j.gloenvcha.2007.06.002. (21)
- Zubair L. (2004), *Empowering the vulnerable*, Tiempo, No. 52, pp. 3-. (22)
- Dietz T., Ostrom, E. & Stern P.C. (2003), *The Struggle to Govern the Commons*, Science, No. 302(5652), pp. 1907-1912. (23)
- Thomalla F., Downing T., Spanger-Siegfried E., Han G., & Rockström J. (2006) *Reducing hazard vulnerability: towards a common approach between disaster risk reduction and climate adaptation*, Disasters, No. 30 (1), pp. 39-48 doi:10.1111/j.1467-9523.2006.00305.x. (24)
- <http://www.preventionweb.net/> last accessed May 2013 (25)
- Kosko B. (1986), *Fuzzy cognitive maps*, International Journal of Man-Machine Studies, No. 24(1), pp. 65-75. (26)
- Ozesmi U. & Ozesmi S.L. (2004), *Ecological models based on people's knowledge: a multi-step fuzzy cognitive mapping approach*, Ecological Modelling, No. 176(1-2), pp.43-64. (27)
- Jones N. A., Ross H., Lynam T., Perez P., & Leitch A. (2011), *Mental models: an interdisciplinary synthesis of theory and methods*, Ecology and Society, No. 16(1), pp. 46. (28)
- Kosko B. (1988), *Hidden patterns in combined and adaptive knowledge networks*, International Journal of Approximate Reasoning, No. 2(4), pp. 377-393. (29)
- Taber R. (1991), *Knowledge processing with Fuzzy Cognitive Maps*, Expert Systems with Applications, No. 2(1), pp. 83-87. (30)
- Manfreda K.L., Bosnjak M., Berzelak J., Haas I., & Vehovar V. (2008), *A meta-analysis comparing response rates*, The Market Research Society, No. 50(1), pp. 79-104. (31)

**Syndromes of land degradation and implications
for ecosystem services in Emilia-Romagna, Italy.
An evaluation framework for the past and
in face of a changing climate**

Ceccarelli T.^{1*}, Bajocco S.¹, Smiraglia D.¹, Salvati L.², and Perini L.¹

¹*Consiglio per la Ricerca e la Sperimentazione in Agricoltura,
Unità di Ricerca per la Climatologia e la Meteorologia applicate all'Agricoltura, Roma, Italy*

²*Consiglio per la Ricerca e la Sperimentazione in Agricoltura,
Centro di Ricerca per lo Studio delle relazioni fra pianta e suolo, Roma, Italy*

**Corresponding author: tomaso.ceccarelli@entecra.it*

Abstract

Land degradation is one of the major forms of environmental degradation all over the world. It entails a reduction in the capacity of providing ecosystem goods and services by cropland, rangeland, and woodlands. Land use/land cover (LULC) patterns often reveals the occurrence of LD and can be analysed and interpreted in terms of change 'trajectories'. The 'syndrome' approach has been used to describe bundles of interactive processes and symptoms which appear repeatedly and in many places in typical combinations and patterns. The notion of syndrome has been extended to LD and desertification processes. LD syndromes can then be evaluated in the past as well as projected in the future, and used as baselines for sustainable land management (SLM) strategies and actions. This will allow for example to assess the effect of climate change on the same individual processes and syndromes of LD. An evaluation conducted in respect to the different ecosystem services is the most appropriate framework for assessing the effects of LD and the basis for identifying measurable outcomes of LD. Within the project AGROSCENARI, this study focussed on the identification of past LULC trajectories further establishing an association with relevant LD syndromes. In the remaining of the project it will also evaluate the possible effects in terms of ecosystem services, and candidate sustainable land management options. Reference is made specifically to the Emilia-Romagna region in Italy, where a diachronic study of the changes occurred over the period from 1954 to 2008 is conducted, and specific trajectories of land use and associated LD syndromes are discussed.

Keywords: *Land degradation, syndromes of change, ecosystem services*



1. INTRODUCTION

Land Degradation (LD) is one of the major forms of environmental degradation all over the world. It is a complex process involving multiple causal factors, among which climate variability, soil quality, and land management play a significant role [1]. LD entails a reduction in the capacity of providing ecosystem goods and services by cropland, rangeland, and woodlands, which becomes irreversible when reaching the last stage of desertification. The European Parliament [2] identified eight main soil degradation processes to which soils in the EU are confronted with: erosion, organic matter decline, contamination, salinisation, compaction, soil biodiversity loss, sealing, landslides and flooding. More processes related not only to soils but to landscapes at large, such as loss of cultural landscapes, should also be taken in consideration.

Land use/land cover (LULC) patterns represent the visible result of human interaction with land [3], reflecting dynamics in both the rural system and settlement arrangement. LULC often reveals the occurrence of LD, either because it bears a direct effect on the processes or because it is associated with unsustainable land uses. It is therefore essential for interpreting past changes that can be associated with LD and for deriving prediction rules. LULC datasets providing comparable classifications in terms of thematic content, spatial resolution and time coverage can be derived from existing cartography, or can be created ad hoc from remote sensing.

LULC changes can be then analysed and interpreted in terms of 'trajectories', as typified for instance by the European Environment Agency (EEA) in its system for Land and Ecosystem Accounts (LEAC) [4].

The concept of 'socio-environmental syndromes' has been proposed as a recent attempt to generalize environmental trajectories: see for instance [5]. The syndrome approach has been used to describe bundles of interactive processes and symptoms which appear repeatedly and in many places in typical combinations and patterns. Syndromes are developed to design a research structure that can help identify interdependencies and subsequently elaborate appropriate response strategies. Geist and Lambin [6] proposed to apply the notion of syndrome to the more specific field of LULC trajectories. They suggest that the apparent complexity in land use change processes can be summarized in a limited number of ways in which these causes interact.

The notion of syndromes has been further extended to LD and desertification processes [7]. Syndromes of LD are described as archetypical combinations of degradation processes reflecting complex patterns of human-nature interactions. Three main syndromes were identified in [5], which are highly significant for the Mediterranean situation: the 'Overexploitation', 'Rural Exodus' and the 'Disaster' syndrome. LD syndromes can then be evaluated in the past as well as projected in the future, in form of scenarios, and used as baselines for sustainable land management (SLM) strategies and actions. This will allow for example to assess the effect of climate change on the same individual processes and syndromes of LD.

An evaluation conducted in respect to the different ecosystem services is nowadays regarded as the most appropriate framework for assessing the effects of LD [8]. As also highlighted in the background document for the 2nd Scientific Conference of the UNCCD, ecosystem services are at the basis for the assessment of measurable outcomes of LD. The evaluation should be possibly not confined to provisioning services (food production in the first place) but encompass other services as well as off-site and indirect effects [9].

Within the framework of the research project AGROSCENARI (Scenarios of agriculture adaptation to climate change) promoted by the Italian ministry of agricultural policies, this study focussed on the identification of past LULC trajectories further establishing an association with relevant LD syndromes. In the remaining of the project it will also evaluate the possible effects in terms of ecosystem services and candidate sustainable land management options, according to the scheme presented in Tab.1.

2. STUDY AREA DESCRIPTION

Reference is made specifically to the Emilia-Romagna region, where the available datasets permit a diachronic study of the changes occurred over the period from 1954 to 2008. In AGROSCENARI this analysis will be further extended to Campania and possibly other regions in Italy. Emilia-Romagna represents a paradigmatic test bed due to the availability of comparable LULC datasets, as well as remarkable changes in land use. A recent pan-European study highlighted areas where urbanisation has been more evident, especially in the last decade (EEA, 2007). These include indeed the northwest of Italy, where Emilia-Romagna is located, Belgium, the Netherlands, southern and western Germany.

It is worth noticing that urban expansion in Emilia-Romagna has taken place at the expenses of the best agricultural soils [10].

Emilia-Romagna is located in north-eastern Italy and covers around 22.120 km². It has a varied morphology and landscapes ranging from the Adriatic coast, to the Po River Valley, and finally to the Apennine Mountain range. After the World War II, the region experienced a remarkable socioeconomic development with a productive structure mainly based on manufacture industry, high-tech services, tourism, and high-income agriculture.

3. MATERIALS AND METHODS

The LULC datasets were produced over the years 1954, 1976, 1994, 2003, and 2008 by the Regional Cartographic and Geographic Information System Service of Emilia-Romagna. Both the geometric and the thematic contents were harmonized and are altogether comparable in terms of spatial resolution and classes.

LULC changes were analyzed comparing 1954 and 2008 datasets as well as intermediate time steps for specific analyses. A mid-point in the 55 years' time horizon was also selected in order to analyze separately periods of comparable length in time (1954-1976 and 1976-2008). This choice is related to the fact that in the late 1970s - early 1980s there has been an expansion of low-density, dispersed settlements with specific effects on land consumption and soil sealing and possibly other ecosystem services. Around the same period, marginal areas in the mountainous and hilly portions of the region have been touched by land abandonment in favor of natural vegetation and especially forest recolonization. LULC changes between 1954 and 2008 are summarized in Tab.2. The interpretation of LULC changes in terms of meaningful land-use trajectories with impact on LD processes was developed according to [7].

4. RESULTS AND DISCUSSION

The main trajectories identified in Emilia-Romagna relate to urban expansion on the one hand and to the abandonment of farmland on the other hand (see also Img.1). In the case of urban expansion, which took place in the form of both dense and dispersed urbanisation, the LD processes which are

more directly associated to this trajectory are land take and soil sealing (we will use, as the syndrome label, the Italian term 'Urbanizzazione'). Apart from the physical take of land, often occurring on the most fertile agricultural areas in the Po river flood plain, the artificialisation has the well-known effect of 'sealing' the soil. In the already mentioned EU guidelines, the process of sealing is seen as exerting a negative off-site effect on the environmental state of the catchments; sealing reduces the amount of rainfall that can be absorbed and stored by the soil, and in extreme cases it can prevent absorption altogether, thus increasing run-off and, indirectly, soil erosion. With soil sealing, topsoil is most often removed during construction activities which is a cause of significant loss of its organic carbon stock. Reduction in evapo-transpiration is, together with others factors, a significant cause for the so called 'urban heat island' effect. While with urban dense growth the mentioned negative effects are clearly exerted on-site, in the case of dispersed expansion and given the generally lower settlement density, the related processes are mainly, although not exclusively, occurring off-site.

In the case of farmland abandonment we will be using the Italian term 'Abbandono' for defining the relevant LD syndrome label. Its effect is directly visible as forest expansion and encroachment of other natural vegetation. What can be observed is a progressive succession from arable land and complex mosaic of cultivations, to protracted fallows, meadows and natural grasslands, to transitional woodland shrub and eventually to forest and woodland creation. In the case of this land use trajectory the association with LD processes is more controversial. In principle abandonment of agriculture in the Emilia-Romagna has been associated to soil erosion, hydrological instability and indirectly, to wild fires. However a number of evidences in similar environments indicated that 'new' forest land, when properly managed, can act as a factor of naturalization, which represents a valuable asset in both economic and biodiversity terms. The final result, i.e. whether the negative impact of LD prevails on the positive effects of the named naturalization processes, very much depends on the climate, morphology and soils of the area, as well as on the initial characteristics of farming (e.g. presence of terraces), the conservation practices adopted in the past and on the type of forest succession. In general terms it is usually recognized that land abandonment is likely to lead to land degradation in cases where vegetation cover is altogether poor.

5. CONCLUSIONS

From the discussion above the diagnostic value of the suggested approach appears evident: spatially explicit LD processes are elicited from LULC trajectories and highlighted as specific syndromes. Ecosystem services can be identified on this basis. This will be a valuable basis for the valuation of the same services as well as for devising possible sustainable land management and restoration actions, hopefully addressing the UNCCD request for identifying measurable outcomes of LD.

6. ACKNOWLEDGMENTS

We would like to acknowledge the Regione Emilia Romagna for the LULC datasets provided.

7. REFERENCES

- Reynolds J.F. and Stafford Smith D.M. (2002), *Global Desertification: Do Humans Cause Deserts?* Dahlem University Press.
- Communication of the Commission to the European Parliament and the Council (2002), *Towards a Thematic Strategy for Soil Protection*, European Commission.
- Conacher A.J. and Sala M. (1998), *Land Degradation in Mediterranean Environments of the World*. Wiley, Chichester.
- Gómez O. and Páramo F. (2005). *Land and Ecosystem Accounts (LEAC). Methodological guidebook. Data processing of land cover flows*. European Topic Centre on Terrestrial Environment. Universitat Antònoma de Barcelona. European Environment Agency.
- Schellnhuber H. J., Block A., Cassel-Gintz M., Kropp J., Lammel,G., Lass W., Lienenkamp R., Loose C., Lüdeke M.K.B., Moldenhauer O., Petschel-Held G., Plöchl M. and Reusswig F. (1997), *Syndromes of Global Change*. GAIA 6 ,1, 19
- Geist H., Lambin E.F. (2006), *Land-Use and Land-Cover Change. Local Processes and Global Impacts Springer Link*.

- Hill J., Stellmes M., Udelhoven T., Roder A., Sommer S. (2008), *Mediterranean desertification and land degradation: Mapping related land use change syndromes based on satellite observations*. *Global Planet Change*, 64, pp. 146-157.
- Nkonya E., Gerber N., von Braun J., and De Pinto A. (2011), *Economics of Land Degradation. The Costs of Action versus Inaction*. International Food Policy Research Institute, IFPRI, Issue Brief 68.
- UNCCD and GRF Davos (2013), *White paper 1. Economic assessment of desertification, sustainable land management and resilience of arid, semi-arid and dry sub-humid areas*. 2nd Scientific Conference of the UNCCD 9-12 April 2013 - Bonn, Germany.
- Salvati L., Ceccarelli T., Bajocco S, Perini L., (in press), *Urbanisation and land take of high quality agricultural soils. Exploring Long-term Land Use Changes and Land Capability in Northern Italy*. *International Journal of Environmental Research*.

**Assessing environmental impacts of climate change
at the regional scale to provide adaptation services:
the DEcision support SYstem for COastal
climate change impact assessment (DESYCO)**

**Torresan S.¹, Rizzi J.^{1,2}, Zabeo A.^{1,2}, Critto A.^{1,2}, Gallina V.^{1,2}, Furlan E.² and
Marcomini A.^{1,2,*}**

¹ *Centro Euro-Mediterraneo sui Cambiamenti Climatici (CMCC), Impacts on Soil and Coast Division (ISC), Lecce, Italy*

² *Department of Environmental Sciences, Informatics and Statistics, University Ca' Foscari Venice, Venice, Italy*

*Corresponding author: marcom@unive.it

Abstract

Climate change is expected to pose a variety of impacts on natural and human systems worldwide. In particular, accelerated sea level rise, increased storminess, changes in water quality and coastal erosion as a consequence of global warming, are projected to pose increasing threats to coastal resources and related surface and ground environments (e.g. river basins, groundwater, marine and terrestrial ecosystems). A major challenge for climate impact research is therefore to develop new methods and tools for the aggregation and synthesis of multiple climate impacts across different regions and sectors. Within the Euro-Mediterranean Centre for Climate Change (CMCC), the Decision support System for Coastal climate change impact assessment (DESYCO) was developed for the assessment and management of multiple climate change impacts on coastal areas and related ecosystems (e.g. beaches, wetlands, forests, protected areas, groundwater, urban and agricultural areas) at the regional/subnational to local scale. DESYCO adopts an ecosystem approach and implements a Regional Risk Assessment (RRA) methodology, based on Multi-Criteria Decision Analysis (MCDA), in order to identify and prioritize areas and targets at risk from climate change, and to support coastal communities in planning appropriate adaptation measures. The RRA methodology integrates climate change hazards analysis - based on the elaboration of output from climate, hydrodynamic, hydrological, hydrogeological and biogeochemical models - with vulnerability analysis of environmental and socio-economic features of the territory. The final output of the tool are GIS-based maps, providing spatially resolved information about downscaled climate change hazard scenarios and regional/local susceptibility, risks and damages. DESYCO was applied to several case studies including the coastal zone of the North Adriatic Sea (Italy) and of the Gulf of Gabès (Tunisia), the groundwater of the Medium-Upper Plain of Veneto and Friuli Venezia Giulia Regions (Italy) and the Esino river basin and groundwater (Marche, Italy). The main components and functionalities of the DSS and examples of the achievable results are here presented and discussed.

Keywords: *Risk Assessment, Climate Change, Decision Support Systems, GIS*



1. INTRODUCTION

Global warming is likely to have profound impacts on coastal communities and ecosystems [1]. Beyond this, coastal zones represent vulnerable environmental, cultural and socio-economic systems highly threatened by the potential impacts of climate-induced hazards such as accelerated coastal erosion, saltwater intrusion, sea-level rise and storm surge flooding events. Coastal areas are also exposed to multiple anthropogenic pressures (e.g. tourism, infrastructures) which can generate further impacts on different natural and human targets. Moreover, climate change impacts and extreme events will not be uniform at the global scale, but will assume specific regional or local characteristics influenced by regional geographical features, climate and socio-economic conditions. Accordingly, it is very important to perform studies at the regional or local scale, taking into account downscaled climate change scenarios and site-specific coastal vulnerability from environmental and socio-economic conditions, in order to provide effective information about climate change impacts and risks to coastal zone managers. Accordingly, there is an increasing need to develop appropriate interdisciplinary scientific methodologies and tools considering multiple natural and anthropogenic impacts on different sectors (e.g. water, forestry, agriculture, urban development, environmental protection) across the land/sea (and freshwater and marine) interface [2] and to provide climate impact and risk information at the regional/subnational to local scale, suitable to guide decision makers in the definition of adaptation strategies in coastal zones.

In order to face these issues and challenges, an environmental spatial DEcision support SYstem for COastal climate change impact assessment (DESYCO) was developed by the Euro-Mediterranean Centre for Climate Change (CMCC, www.cmcc.it).

DESYCO is a Decision Support System (DSS) aimed at the integrated assessment of multiple climate change impacts on vulnerable coastal systems (e.g. beaches, river deltas, estuaries and lagoons, wetlands, agricultural and urban areas). It is an open source software that combines different scenario data (e.g. raster or shapefiles) resulting from climate models (e.g. global and regional climate projections) and high resolution models (e.g. hydrodynamic, hydrological and biogeochemical simulations) with vulnerability analysis of environmental and socio-economic features of the territory, in order to provide GIS-based maps identifying hot-spot areas and receptors at risk from climate change.

After a brief description of the main components and functionalities of DESYCO, projects and case studies will be presented to show how assist regional and local coastal managers in the diagnosis of climate change impacts and in the definition of sustainable adaptation strategies.

2. THE DSS DESYCO AND THE RRA APPROACH

The structure of DESYCO includes four main components: a geodatabase for the storage of biophysical and socio-economic data for the investigated areas; multi-scale scenarios provided by numerical models simulations or time series analysis; a Relative Risk Model (RRM) that integrates Multi-Criteria Decision Analysis [3] techniques for the application of the the RRA methodology; finally, a Graphical User Interface (GUI) that facilitates the interaction of the final user with the system and simplify results understanding.

These integrated four components allow DESYCO to: investigate impacts associated to different climate change scenarios and sensitive targets; identify and prioritize targets and areas susceptible to or at risk from different climate change impacts in the considered study area; produce interactive GIS-based maps (i.e. exposure, susceptibility, risk and damage maps) for different natural and human receptors (e.g. beaches, wetlands, natural environments, urban and agricultural areas); finally, transfer information about potential climate change impacts to support the development of sustainable adaptation actions.

In order to represent potentially significant hazard scenarios at the regional scale and to produce climate change exposure maps to be used in the risk assessment, DESYCO manages different input data (e.g. raster or shapefiles) generated by climate models (e.g. global and regional climate projections) and high resolution models (e.g. hydrodynamic, hydrological and biogeochemical simulations). The individual outputs from the multi-model chain are called hazard metrics, and are then included in the quantitative RRA model [4; 5].

The characterization of the land, land/sea vulnerability, and the construction of susceptibility, risk and damage maps, involve the identification and application of a range of vulnerability indicators and indexes, representing the sensitivity of the coastal communities, systems or assets, to the damaging effects of climate change hazards [6]. Within the RRA, vulnerability indicators are classified in four

main categories of factors: Susceptibility Factors (SF), Value Factors (VF), Pathway Factors (PF) and Attenuation Factors (AF). SF determine the degree to which a receptor is affected, either adversely or beneficially, by climate-related stimuli (e.g. vegetation cover, wetland and urban typologies, river and spring flows). VF identify relevant environmental and socio-economic values of the receptors that need to be preserved for the interest of the community (e.g. land use, fishing areas, crop economic value, population density). PF are physical characteristics of the receptors determining the possibility of contact with climate change hazards and therefore potential exposure areas (e.g. elevation, distance from coastline, soil permeability). AF are factors that can attenuate the intensity of the hazard associated with an impact: for instance, an artificial structure (e.g. a dike) able to reduce the hazard related to a storm surge flooding or to coastal erosion.

In the RRA model, vulnerability factors and hazard metrics are used to estimate risks and damages related to each receptor, using specific MCDA functions. Accordingly, two-dimensional visualization of exposure, susceptibility, risk and damages, based on raster maps and risk indicators, are produced.

Exposure maps, representing climate change hazard scenarios against which a receptor operates (i.e. inundation level, storm surge flooding, erosion and water quality and quantity variations), are presented as a result of the aggregation of hazard metrics, pathway and attenuation factors. The maps highlight areas where the hazard can get in contact with the target (Fig 1a). Susceptibility maps are derived from the aggregation of susceptibility factors and represent the spatial distribution of geo-physical and environmental susceptibility to climate change (Fig. 1b). Moreover, risk maps are obtained from the overlay of exposure and susceptibility maps and enable the identification and ranking of areas and receptors at risk from climate change related impacts in the considered region and according to a selected hazard scenario (Fig 1c). Finally, damage maps derive from the combination of risk and value factors and provide a relative estimation of the potential social, economic and environmental losses (Fig 1d).

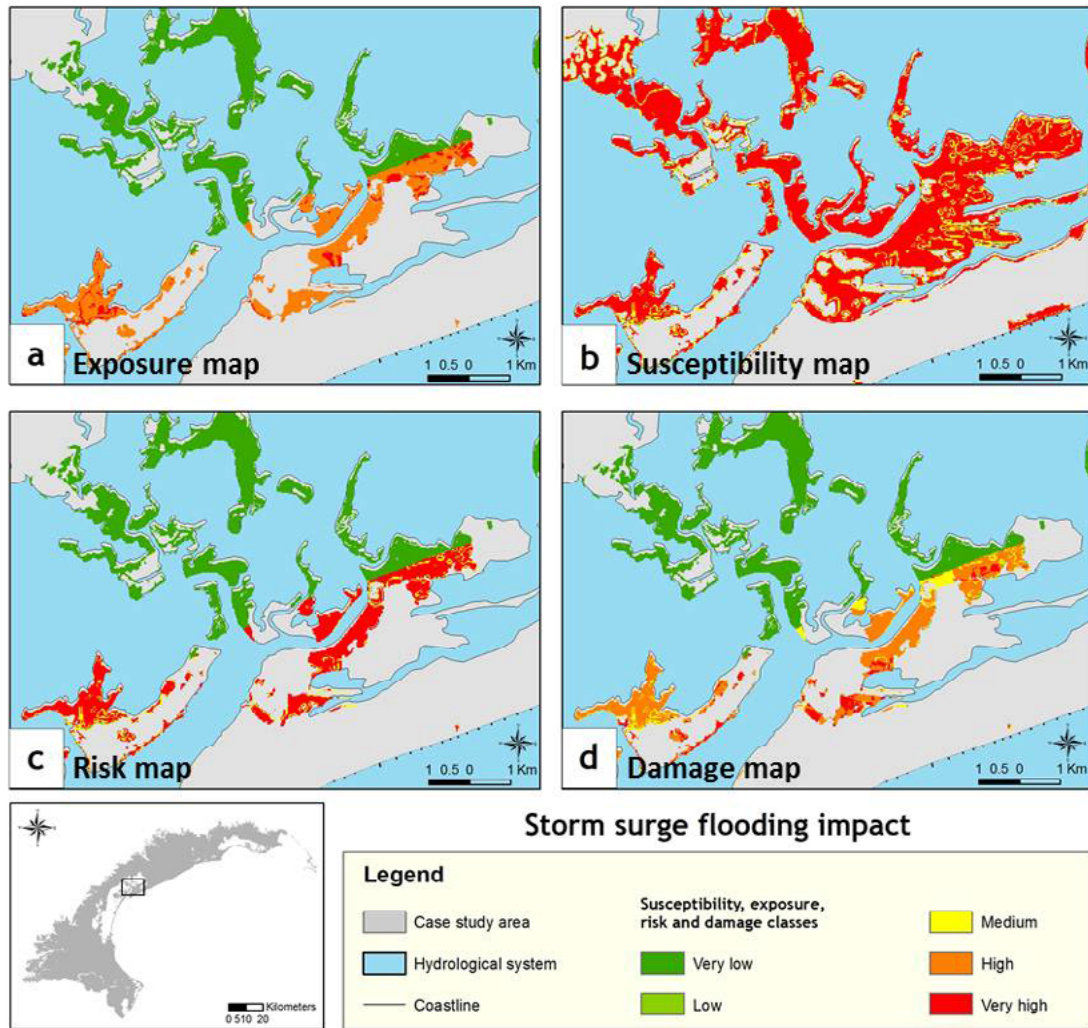


Fig. 1: Example of GIS-based maps produced by DESYCO in the North Adriatic Region (Italy) for the storm surge flooding impact: exposure map for a flooding scenario of 174 cm in 2100 (a), susceptibility (b) risk (c) and damage (d) map for the receptor protected areas.

3. CASE STUDIES

DESYCO and RRA were tested in several national and international projects and case study areas.

The coastal zone of the North Adriatic Sea (Italy) was studied in order to evaluate impacts such as sea level rise inundation, storm surge flooding, coastal erosion and seawater quality variations [7; 8]. Particularly, DESYCO was applied in this region to support ICZM implementation (EU-FP7 PEGASO project) [9] and to provide user-oriented climate impact and adaptation services for coastal stakeholders (EU-FP7 CLIM-RUN project) [10]. Moreover, it was applied in the coastal area of the Gulf of Gabès (Tunisia) within the CANTICO project (ERANET-CIRCLE-MED), with the aim to identify and prioritize the vulnerability of key natural and human receptors to climate change (e.g. beaches, river mouths, wetlands, protected areas, fisheries and aquaculture, urban areas and agricultural areas) [4; 11].

DESYCO and the RRA methodology were also applied to groundwater resources for evaluating climate-related impacts such as decrease of the groundwater level, salt water intrusion and groundwater quality variations [5; 12]. Two case studies were the upper plain of the Veneto and Friuli Venezia Giulia regions (Life+ TRUST project) and the Esino river basin of the Marche region (Life+ SALT project).

DESYCO and the RRA will also be applied to the coastal zone of the Puglia Region (Italy) within the ORIENTGATE project (South East Europe). Finally, the tool and the methodology will be further improved in the GEMINA project (Interministerial Italian Project) in order to tackle multi-hazard issues and consider the cumulative effects of different types of impacts and risks that could potentially affect the same system (e.g. impacts on coasts, agriculture, water resources, biodiversity, forests, human assets).

4. CONCLUSIONS

DESYCO allows to identify and prioritize coastal receptors and areas that could require more urgent adaptation options, in order to avoid risks related to climate change impacts. It supports effectively stakeholders and policy-makers in the definition of more suitable adaptation strategies (e.g. construction of artificial protections, relocation of urban, industrial and tourism infrastructures) and of Integrated Coastal Zone Management (ICZM) plans.

Being based on RRA, DESYCO can be adapted and applied to different geographical contexts and temporal scale of analysis through the application and customization of input data. Moreover, DESYCO supports an open configuration where users can add different receptors and factors focusing the analysis on several targets and critical phenomena, according to specific end-user needs.

Further development of DESYCO will include: the implementation of a multi-risk approach in order to analyze the interactions among different climate change impacts that could affect the same region; the application of a dynamic exposure and vulnerability assessment, taking into account land use and population scenarios; the integration of socio-economic evaluations of damages and losses caused by climate change and natural hazards impacts.

5. ACKNOWLEDGMENTS

The research leading to these results has received funding from the FP7 CLIM-RUN Project (grant agreement 265192).

6. REFERENCES

- IPCC, 2007a. *Climate Change 2007: Impacts, Adaptation and Vulnerability. Summary for Policymakers*. Contribution of Working Group II to the Fourth Assessment Report of the Intergovernmental Panel on Climate Change, Geneva. (1)
- UNEP. *Ecosystem management programme. A new approach to sustainability*. Available online: <http://www.unep.org/ecosystemmanagement/LinkClick.aspx?fileticket=gbPVsoUCp-E%3D&tabid=311&mid=670>; 2009. (2)
- Giove S., Brancia A., Satterstrom F. K., Linkov I., 2009. *Decision Support Systems and Environment: Role of MCDA*. A. Marcomini et al. (eds.), *Decision Support Systems for Risk-Based Management of Contaminated Sites*, DOI 10.1007/978-0-387-09722-0_3. Springer Science+Business Media, LLC 2009. Pp. 53-73. (3)
- Lamon L., Rizzi J., Bonaduce A., Dubois C., Lazzari P., Ghenim L., Gana S., Somot S., Li L., Melaku Canu D., Solidoro C., Pinardi N., Marcomini A. 2013. *An ensemble of models for identifying climate change*

scenarios in the Gulf of Gabes, Tunisia. Regional Environmental Change, doi: 10.1007/s10113-013-0430-x. (4)

Baruffi F., Cisotto A., Cimolino A., Ferri M., Monego M., Norbiato D., Cappelletto M., Bisaglia M., Pretner A., Galli A., Scarinci A., Marsala V., Panelli C., Gualdi S., Bucchignani E., Torresan S., Pasini S., Critto A., Marcomini A., 2012. *Climate change impact assessment in Veneto and Friuli plain groundwater. Part I: an integrate modeling approach for hazard scenario construction*. Sci Total Environ, 440: 154–166. (5)

Torresan S., Critto A., Dalla Valle M., Harvey N. e Marcomini A. *Assessing coastal vulnerability to climate change: comparing segmentation at global and regional scales*. Sustainability Science, 3: 45-65. 2008. (6)

Torresan S., Critto A., Rizzi J., Marcomini A. *Assessment of coastal vulnerability to climate change hazards at the regional scale: the case study of the North Adriatic sea*. Nat Hazard Earth Syst Sci 2012; 12:1-22. <http://dx.doi.org/10.5194/nhess-12-1-2012>. (7)

Torresan S., 2012. *Development of a Regional Risk Assessment methodology for climate change impact assessment and management in coastal zones*. PhD Thesis, University Ca' Foscari Venice, Italy. (8)

Santoro F., Tonino M., Torresan S., Critto A., Marcomini A., in press. *Involve to improve: a participatory approach for a Decision Support System for coastal climate change impacts assessment. The North Adriatic case*, Ocean & Coastal Management, Volume 78, June 2013, Pages 101–111. (9)

Giannini V., Torresan S., Gallina V., Critto A., Giupponi C., Marcomini A., 2012. *Deliverable 8.1 - Workshop report: context and objectives, comparison of data supply and demand, simulation results, feedback and discussion. Integrated case study: Veneto and Friuli Venezia Giulia, Northern Adriatic Sea, Italy*. CLIM-RUN - Project No. 265192. (10)

Rizzi J., Gallina V., Torresan S., Critto A., Marcomini A. *Application of a Regional Risk Assessment addressing the impacts of climate change on the coastal area of the Gulf of Gabès (Tunisia)*, submitted to Regional Environmental Change. (11)

Pasini S., Torresan S., Rizzi J., Zabeo A., Critto A., Marcomini A., 2012. *Climate change impact assessment in Veneto and Friuli Plain groundwater. Part II: A spatially resolved regional risk assessment*, Sci Total Environ, 440: 219-235. (12)

IMPLICATIONS ON ECOSYSTEM SERVICES

Dynamic landscapes: hazard & risk assessment - II

Towards flood risk assessment in a climate change perspective

Ronco P.^{1,2*}, Gallina V.¹, Torresan S.², Critto A.^{1,2}, Zabeo A.¹, Semenzin E.¹ and Marcomini A.^{1,2}

¹Dept. Environmental Sciences, Informatics and Statistics University Ca' Foscari Venice, Venice, Italy

²Centro Euro-Mediterraneo su i Cambiamenti Climatici (CMCC), Impacts on Soil and Coast Division, Lecce, Italy

*Corresponding author: paolo.ronco@unive.it

Abstract

In recent years, the frequency of water-related disasters has increased and recent flood events in Europe caused physical-environmental and socio-economic damages. Specifically, floods are the most threatening water-related disaster that affects humans, their lives and properties. Within the FP7-KULTURisk project (KR_Knowledge-based approach to develop a cULTure of Risk prevention, www.kulturisk.eu) a Regional Risk Assessment (RRA) methodology has been developed to evaluate the benefits of risk prevention in terms of reduced environmental risks due to floods. The methodology is flexible and can be adapted to different case studies (i.e. large rivers, alpine/mountain catchments, urban areas and coastal areas) and spatial scales (i.e. from the large river to the urban scale). It integrates the output of hydrodynamics models with the analysis of site-specific bio-geophysical and socio-economic indicators (e.g. slope, land cover, population density, economic activities) to develop risk maps that identify and prioritize relative hot-spot areas and targets at risk (i.e. people, buildings, infrastructures, agriculture, natural and semi-natural systems, cultural heritages) in the considered region by comparing the baseline scenario with alternative scenarios, where different structural and/or non-structural mitigation measures to cope with the impact of climate change drivers are planned. The risks maps provide crucial information about flood consequences in the considered area to define priorities for prevention measures, for land use planning and management. Moreover, the outputs of the RRA methodology can be used for the economic evaluation of different damages (e.g. tangible costs, intangible costs) and for the social assessment considering the benefits of the human dimension of vulnerability (i.e. adaptive and coping capacity). Finally, the methodology has been applied and validated in several case studies in Europe representative of different hydro-climatic regimes and exposed to different types of water-related risks (from storm surges in coastal areas to debris flows in alpine catchments).

Keywords: *Regional Risk Assessment, Flood Hazards, Flood Risks, Kulturisk*



1. INTRODUCTION

In recent years, the frequency of water-related disasters has increased and recent flood events in Europe (e.g. 2002 in Central Europe, 2007 in UK, 2010 in Italy) caused consistent physical-environmental and socio-economic damages [9]. Specifically, floods are the most threatening water-related disasters that affect humans, their lives and properties [14; 19; 2; 3; 16]. They are growing as a consequence of many factors, both climatic (e.g. climate variability and climate change) and non-climatic (e.g. changing demographics, technological and socio-economic conditions, urban development) [23]. Although there are no evidence that frequency and intensity of water-related hazards has increased due to climate-drivers, as per the last IPCC report, the current increase of such disasters can be mainly attributed to the increase of exposure (i.e. elements located in a flood plain potentially at risk) and vulnerability (i.e. economic, social, geographic, cultural, and physical/environmental characteristics of the exposure) [15]. As a result, a specific legislation regarding flood assessment and management has been established in 2007: the European Floods Directive [11]. It represents a general framework for the assessment and management of flood risks, aiming at the reduction of the adverse consequences for human health, the environment, cultural heritage and economic activities. In this context, research methods and tools are urgently needed to improve the development of adequate prevention, mitigation and preparedness measures. At the European level, available risk-based studies and methodologies are mainly focused on the analysis of the consequences and damages of floods on specific receptors – for instance, population, buildings or agriculture [7; 6; 5; 8] - neglecting the coexistence of multiple receptors living in the same geographical region. Moreover, they address flood hazard mapping and engineering science [9; 10; 21], while multidisciplinary approaches are poorly represented [22]. Finally, current flood risk assessments are also characterized by considerable uncertainty, which needs to be addressed and clearly communicated to decision-makers [18]. Therefore, there is the need to develop a comprehensive risk assessment methodology that could integrate information coming from deterministic and probabilistic flood forecasting, as well as the multi-faceted physical/environmental, social and economic aspects of exposure and vulnerability, in order to evaluate flood risks for different receptors/elements, as required by the EU Directive. The KR project builds upon past and on-going EU research projects and makes a distinctive effort in the development of a culture of risk prevention in Europe, by evaluating the benefits of different risk

prevention initiatives, taking into account different fields of expertise in the flood risk assessment process (i.e. engineering, environmental, and socio-economic sciences).

2. THE KULTURisk PROJECT METHODOLOGY

The main aim of the KR methodology is to evaluate the benefits of risk prevention by adopting a multi-target approach that considers four macro-categories of receptors/elements at risk (i.e. people, economic activities, natural and semi-natural systems, cultural heritage), according to the EU Floods Directive [11]. The method has been developed for analysis at meso-scale level by adopting the land use/land cover classes proposed by CORINE Land Cover dataset, as major spatial units of reference [4]. However, it can also be applied at different spatial scales (i.e. macro or micro) depending on the purposes of the assessment, on the geographical extent of the case study and on the level of detail of input dataset. As depicted in *Img. 1*, the KR methodology is composed of three major tiers of analysis aggregating step by step the physical/environmental, social and economic dimensions of the risk concept.

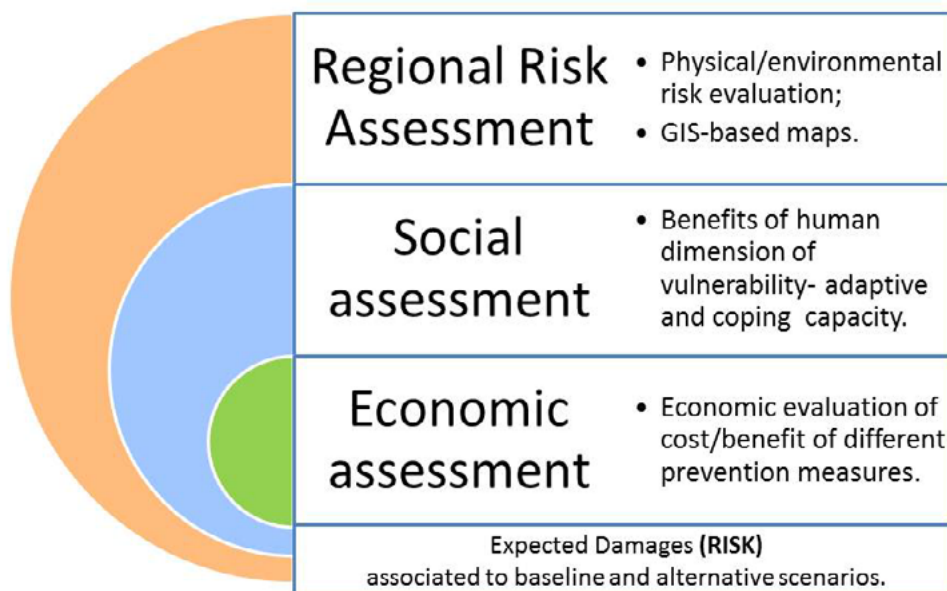


Image 1: Tiers of analysis for the implementation of KR methodology [12]

The first tier implements the Regional Risk Assessment (RRA) approach that deals with problems affecting large geographic areas where multiple habitats, sources, stressors and endpoints are present and their spatial relationships must be evaluated at the regional scale [17]. The RRA approach concerns the use of Multi Criteria Decision Analysis (MCDA) to estimate the relative risks in the considered region at different time scales, to compare different impacts and stressors, to rank targets and exposure units at risk. RRA provides a set of indicators for the different physical/environmental components of the KR framework and a set of methods to normalize and aggregate these indicators in a (spatially resolved) integrated Risk Index. According to Gallina et al.[12], the RRA methodology considers the development of four main steps: 1) Flood hazard assessment; 2) Exposure assessment; 3) Susceptibility assessment; 4) Risk assessment.

The flood hazard assessment aims at identifying flood metrics (e.g. flow velocity, water depth, flood extension) coming from hydraulics models, (e.g. deterministic or probabilistic) according to different scenarios to be investigated (e.g. baseline or alternative), developed on the probabilistic concept of flood return time. The exposure assessment aims at identifying and selecting the receptors that can be prone to potential losses in flooded zones. This step requires the analysis of land use/land cover datasets for the localization of people, environmental resources, infrastructures, social, economic or cultural assets that could be adversely affected by a flood event. As third step, the susceptibility assessment evaluates the degree to which the receptors could be affected by a flood hazard based on physical/environmental site-specific information (e.g. rate of aged-infirm people, vegetation cover, slope, soil type). The risk assessment step is aimed at defining a Relative Risk Index that combines the information about a certain flood hazard scenario with the exposure and susceptibility of the examined receptors. After the normalization of the receptor-related risks, a Total Risk Index is calculated integrating the receptor-related risks using Multi Criteria Decision Analysis (MCDA) functions [13]. Total risk scores are not absolute predictions about the risks related to flood; rather they provide relative classifications about areas and targets that are likely to be affected by floods more severely than others in the same region. The main outputs are GIS-based maps of receptor-Related Risks and of the Total Risk. Finally, the second and third tiers of the KR methodology (not presented in this paper) are the social assessment, that considers the benefits of the human dimension of vulnerability (i.e. adaptive and coping capacity), and the economic assessment, which provides an economic evaluation of costs and benefits of different prevention measures.

3. CASE STUDIES

The mentioned risk-based methodology has currently been applied in different case studies in Europe representative of different hydro-climatic regimes and exposed to different types of water-related risks, as reported in Table 1. Relevant data and information describing the physical-environmental setting of each case studies and requested for the application of the KR methodology are provided by local stakeholders and authorities in form of hydrodynamic models simulations, GIS-based maps and other database.

Name	Country	Typology	Water-related hazard
1. Sihl – Zurich [20]	Switzerland	Urban area	Urban floods
2. Danube	Many countries	Trans-boundary large river	Large-scale inundations
3. Barcelonette	France	Alpine catchment	Landslides and debris flows
4. Carlisle	United Kingdom	Urban area	Urban floods
5. Soča-Isonzo	Slovenia-Italy	Trans-boundary alpine catchment	Floods and landslides
6. Somerset	United Kingdom	Coastal area	Storm surges
7. North-Adriatic Sea(*)	Italy	Coastal area	Storm surges

Table 1: Case studies; (*) not considered in the KR Project

In order to complete the validation of the KR physical-environmental methodology, a summary of the results, (in terms of risk maps) obtained in the project case studies will be sent to the related end-users that will identify strength points, weakness and gaps. The results of this survey will allow to transfer the assessment of prevention benefits and to point out a set of recommendation to improve the overall (final) methodology.

4. CONCLUSIONS

The paper introduces an innovative physical/environmental methodology for the integrated assessment of flood hazards at the regional scale in the framework of the KR Project that focuses on water-related hazards as the likelihood and adverse impacts of water-related catastrophes might increase in the near future because of land-use and/or climate change. A strength of the proposed approach consists in its flexibility as it can be adapted to different case studies (i.e. large rivers, alpine/mountain catchments, urban areas and coastal areas) and spatial scales (i.e. from the large river to the urban scale). Moreover, the use of Geographic Information Systems (GIS) allows a detailed analysis of the results that can be easily communicated to stakeholders and decision/policy makers. The consistency of results provided by the RRA methodology can be properly tested through a sensitivity analysis allowing the ascertainment of how much the output of the assessment could be influenced by its input parameters (i.e. indicators and scores). After application to KR cases studies, the methodology will be further validated through the involvement of end-users of different case studies and its potential generalization to address other types of natural hazards (e.g. seismic risk, forest fires, avalanches, storms, etc.) will be explored.

5. ACKNOWLEDGMENTS

The authors acknowledge KULTURISK financial funding (FP7-ENV.2010.1.3.2-1-265280) and the support of project partners contributing to this work.

6. REFERENCES

- Balbi S., Giupponi C., Gain A., Mojtahed V., Gallina V. , Torresan S., Marcomini A., (2012). *The KULTURisk Framework (KR-FWK): A conceptual framework for comprehensive assessment of risk prevention measures*. Deliverable 1.6. KULTURisk Project 265280. (1)
- Balica S. F., (2007), *Development and application of flood vulnerability indices for various spatial scales*. Master of Science Thesis. (2)
- Bates B.C., Kundzewicz Z.W., Wu S., and Palutikof J.P., Eds., (2008), *Climate Change and Water*. Technical Paper of the Intergovernmental Panel on Climate Change, IPCC Secretariat, Geneva, 210 pp. (3)

- Büttner G., Feranec G., Jaffrain G., (2006), *CORINE Land Cover nomenclature illustrated guide – addendum* 2006. (4)
- Citeau J.M., (2003), *A New Control Concept in the Oise Catchment Area. Definition and Assessment of Flood Compatible Agricultural Activities*, FIG working week, Paris, France. (5)
- Clausen L. and Clark P.B., (1990), *The development of criteria for predicting dambreak flood damages using modelling of historical dam failures*. Proceedings of the International Conference on River Flood Hydraulics, 17-20 September, 1990. John Wiley & Sons Ltd. Hydraulics Research Limited. pp. 369-380. (6)
- Clausen L.K., (1989), *Potential dam failure: estimation of consequences, and implications for planning*. Unpublished Master of Philosophy thesis at the School of Geography and Planning, Middlesex Polytechnic collaborating with Binnie and Partners. Redhill. (7)
- DEFRA, (2006), *Flood Risk to People Phase 2. The Flood Risk to People Methodology*, FD2321/TR1. (8)
- Di Baldassarre G., A. Castellarin, A. Montanari, A. Brath (2009), *Probability weighted hazard maps for comparing different flood risk management strategies: a case study*, Natural Hazards, No.50(3), pp. 479-496. (9)
- Di Baldassarre G., Schumann G., Bates P., Freer J., Beven K., (2010), *Floodplain mapping: a critical discussion on deterministic and probabilistic approaches*, Hydrological Sciences Journal, No. 55(3), pp. 364-376. (10)
- EC, (2007). Council Directive 2007/60/EC of 23 October 2007 on the *Assessment and Management of Flood Risks*. Official Journal of the European Union L 288/27. (11)
- Gallina V., Torresan S., Critto A., Zabeo A., Semenzin E., Marcomini A., Balbi S., Gain A., Giupponi C., Mojtahed V., (2013). *Development of a risk assessment methodology to estimate risk level*. Deliverable 1.7bis. KULTURisk Project 265280. (12)
- Giove S., Brancia A., Satterstrom F.K., Linkov I., (2009), *Decision Support Systems and Environment: Role of MCDA*. In Marcomini A., Suter G.W. II, Critto A. (Eds). *Decision Support Systems for Risk Based Management of Contaminated Sites*. SpringerVerlag, New York. (13)
- Hewitt K., (1997), *Regions of risk. A geographical introduction to disasters*. Longman, Ltd. Essex, U.K. Chorley R.I., 1987. *Introduction to Geographical Hydrology*, Methuen and Company Ltd. New York. (14)

- IPCC, (2012), *Managing the Risks of Extreme Events and Disasters to Advance Climate Change Adaptation*. A Special Report of Working Groups I and II of the Intergovernmental Panel on Climate Change, Cambridge University Press, Cambridge, UK, and New York, NY, USA, 582 pp. (15)
- Kubal C., Haase D., Meyer V., Scheuer S., (2009), *Integrated urban flood risk assessment – adapting a multicriteria approach to a city*. Natural Hazards Earth System Science, No. 9, pp. 1881 – 1895. (16)
- Landis W. G., (2005), *Regional scale ecological risk assessment. Using the relative risk model*. Edited by W. G. Landis. CRC PRESS. (17)
- Pappenberger F., Stephens E., Thielen J., Salamon P., Demeritt D., van Andel S. J., Wetterhall F., Alfieri L., (2012), *Visualising probabilistic flood forecast information: expert preferences and perceptions of best practice in uncertainty communication*, Hydrological Processes, published online. (18)
- Penning-Rowsell E., Floyd P., Ramsbottom D., Surendran S., (2005), *Estimating injury and loss of life in floods: a deterministic framework*. Natural Hazards, No. 36, pp. 43 – 64. (19)
- Rotach M.W., (2009), *MAP D-PHASE: Real-time demonstration of weather forecast quality in the Alpine Region*, Bull. Amer. Meteor. Soc., 90 (9), pp. 1321-1336. (20)
- Rotach M. W., Arpagaus M., Dorninger M., Hegg C., Montani A., Ranzi R., (2012), *Uncertainty propagation for flood forecasting in the Alps: different views and impacts from MAP D-PHASE*, Nat. Hazards Earth Syst. Sci., No.12, pp. 2439–2448. (21)
- Semenzin E., Bonso G., Cirella G. T., Critto A., Marcomini A., (2011), *Review of risk assessment and management methodologies*. Deliverable 1.2. KULTURisk Project 265280. (22)
- UNISDR, (2005), *Hyogo framework for action 2005-2015: Building the resilience of nations and communities to disasters*. Geneva. (23)

A risk-based assessment of impacts affecting groundwater resources and related ecosystems in view of climate change

Torresan S.¹, Pasini S.¹, Rizzi J.^{1,2}, Zabeo A.^{1,2}, Critto A.^{1,2}, Furlan E.² and A. Marcomini^{1,2,*},

¹Centro Euro-Mediterraneo sui Cambiamenti Climatici (CMCC), Impacts on Soil and Coast Division (ISC), Lavezzola, Italy

²Department of Environmental Sciences, Informatics and Statistics, University Ca' Foscari Venice, Venice, Italy

*Corresponding author: marcom@unive.it

Abstract

Climate-related risks for groundwater and related ecosystems pose great concern to scientists and water authorities involved in the protection of these resources. According to the key principles of EU water policy and the expected effects of global climate change, research is needed to understand how develop suitable adaptation options for the sustainable management of groundwater in view of climate change.

In the framework of the European Life+TRUST project (*Tool for Regional-scale assessment of groundwater Storage improvement in adaptation to climate change*), a Regional Risk Assessment (RRA) methodology for the evaluation of climate change impacts on groundwater and associated ecosystems (e.g. surface waters, agricultural areas, natural environments) was developed and applied in order to rank areas and receptors at risk in the case study area represented by the medium/upper plain of Veneto and Friuli Venezia Giulia (Italy).

Based on an integrated analysis of impacts, susceptibility and risks related to climate change at the regional scale, a RRA framework complying with the Sources-Pathway-Receptor-Consequence (SPRC) approach was defined. Through hazard scenario, exposure, susceptibility and risk assessment three relevant impacts on water quantity and quality were analyzed (i.e. groundwater level variations, changes in nitrate infiltration processes, changes in water availability for irrigation).

Relevant outcomes from the described RRA application highlighted that potential climate change impacts will occur with different extension and magnitude in the case study area. Particularly, impacts on groundwater will likely have little direct effects on related ecosystems (croplands, forests and natural environments) while more severe consequences will indirectly occur on natural and anthropic systems through the reduction in quality and quantity of water availability for agricultural and other uses.

Framework and main results of the RRA applied within the Life+TRUST project are here presented and discussed.

Keywords: Regional risk assessment, Groundwater, Climate change, GIS, MCDA



1. INTRODUCTION

National and international studies suggest that climate change is generally responsible for a wide range of impacts that may have significant consequences for environmental and socio-economic systems. In particular, potential impacts of climate change on groundwater would be related to alterations of the hydrological cycle, which could result in decrease of water quality (e.g. salinity, pollution) and water quantity (e.g. decrease and depletion of groundwater resources) with severe consequences for natural and human systems (e.g. loss of habitat and biodiversity, decrease of available water for drinking and agricultural use).

The link between climate change and water resources, particularly groundwater, is therefore widely established even if projections on potential climate change effects at the regional scale are still poorly understood due to uncertainty related both to the reliability of climate projections [1; 2] and to the complexity in modeling of surface and subsurface water resource interactions [3; 4; 5; 6]. A multidisciplinary approach to assess relationships among climate, environment and human pressure is thus required in order to support the definition of effective adaptation measure.

In order to face these issues and challenges, a GIS-based Regional Risk Assessment (RRA) methodology was developed within the European project Life+ TRUST, in order to support water management authorities in the assessment and management of multiple climate change impacts on groundwater and associated ecosystems (e.g. surface waters, agricultural areas, natural environments). The RRA methodology was applied in the medium/upper plain of Veneto and Friuli Venezia Giulia Regions in order to support decision-makers in addressing potential climate change impacts and related adaptation strategies for groundwater resources (e.g. artificial aquifer recharge techniques).

This paper presents the procedure and the main results of the RRA methodology applied within the Life+TRUST project for assessing the impacts affecting groundwater resources and related ecosystems in view of climate change.

2. THE TRUST PROJECT

The TRUST project (*Tool for Regional scale assessment of groUndwater STorage improvement in adaptation to climate change*), co-financed by the European Community's LIFE+ 2007 programme and the Italian Ministry for the Environment, Land and Sea, has addressed the impact of climate change on the future availability of groundwater resources. The project, started in January 2009 and ended in December

2011, was carried out by the Italian Authority of the Northern Adriatic river basins together with the engineering consultant SGI Studio Galli and the Euro-Mediterranean Centre for Climate Change. The main goal of TRUST was to assess the effects of climate change on the recharge of the study aquifer and on groundwater uses. The results of this project have contributed to advance the knowledge base of the groundwater mechanisms in the project area and will aid the management and planning of this precious resource in the coming years. The project is aligned with the implementation of the River Basin Management Plans of Directive 2000/60/EC that establish objectives and measures to improve the status of surface and ground waters. In 2013 the European Commission awarded the TRUST project as one of the 4 “Best of the Best” LIFE Environment projects 2012.

3. THE CASE STUDY AREA

The case study area lies between the Italian pre-alpine and sub-alpine systems and includes the high and middle Veneto and Friuli Plain in North-Eastern Italy, which extends through Friuli-Venezia Giulia and Veneto regions, with a total surface of about 4100 km² (Fig. 1). It is a plain which, in vertical section, is a continual alternation of fine layers (silt-clay, i.e., mainly impermeable) and coarse ones (gravel and sand, sometimes cemented, with various degrees of permeability), crossed by more or less thick water tables. The “phreatic” layer, i.e. the closest to the surface, gradually approaches plain areas richer in impermeable layers, and reaches the surface in the form of springs. The higher and middle plains have important aquifers that provide drinking water supply for most of the two regions: numerous industries abstract groundwater, as well as the agricultural sector which uses substantial amounts of groundwater in addition to the intakes from surface waters. The high plain, also, is the main recharge area for the lower aquifer systems [8], thus the protection and conservation of the unconfined aquifer are essential for assuring future water availability both from the unconfined and the confined aquifers [9; 10].

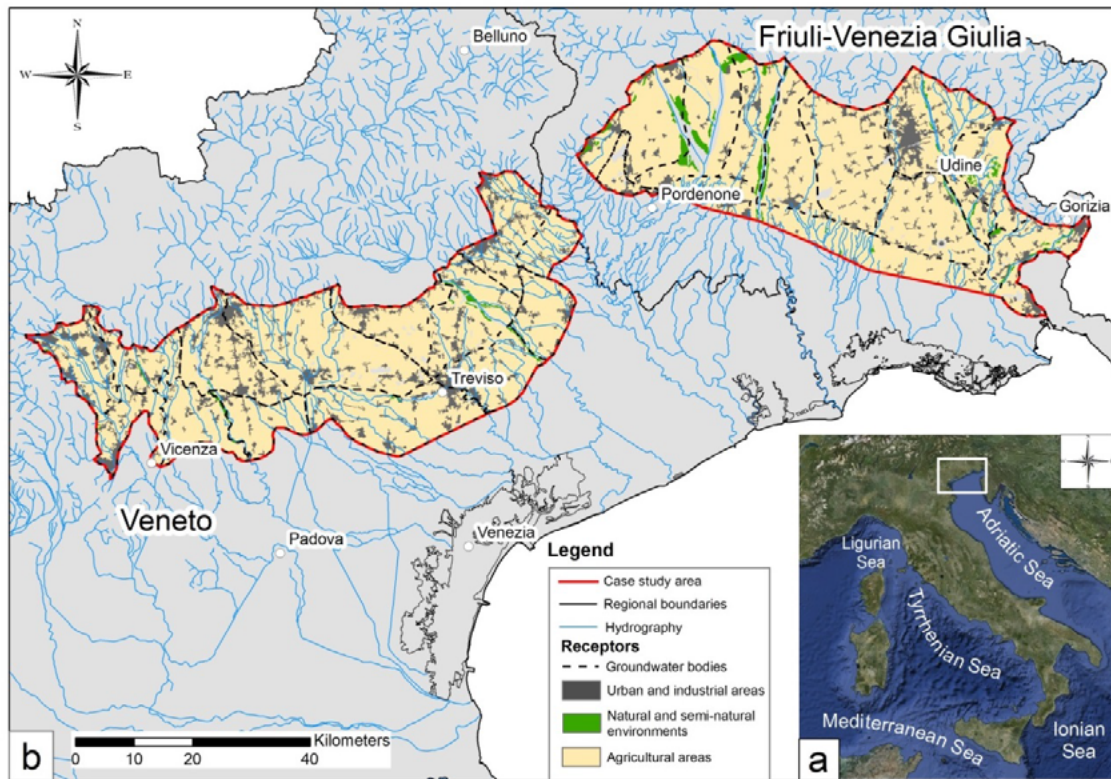


Fig. 1: The case study area: Veneto and Friuli-Venezia Giulia Regions in the North Eastern Italy (a); the investigated high and middle plains zone (b). Adapted from Google Maps: maps.google.it (source 7).

The progressive rise of temperature and the general decrease of annual rainfall recorded in the last 30 years, along with the occurrence of droughts and the increased demands of the irrigation sector, are the main causes of the negative trend of the water table levels [9; 10]. Indeed, this area hosts traditional intensive agriculture for more than 3300 km² (about 80% of the total surface) and few natural or semi-natural zones (94.5 km², about 2.3% of the total surface), mainly located along river beds, including some Natura 2000 network protected sites.

4. REGIONAL RISK ASSESSMENT FOR THE ANALYSIS OF CLIMATE CHANGE IMPACTS ON GROUNDWATER AND ASSOCIATED ECOSYSTEMS

The RRA is an emerging approach at international level aimed to provide a systematic way to estimate and compare the impacts of environmental problems that can affect large geographical areas. In more detail, the RRA is a risk assessment procedure considering the presence of multiple habitats, multiple sources releasing a multiplicity of stressors impacting multiple endpoints [11]. It is therefore a suitable

approach to produce synthetic assessments on the effects of climate change on groundwater at the regional scale.

With the aim to perform an integrated analysis of impacts, vulnerability and risks linked to climate change at the regional scale, the RRA defined within the Trust project integrates GIS tools and Multi-Criteria Decision Analysis (MCDA) techniques resulting in a spatial identification of exposure, susceptibility and relative risk for each considered impact and scenario. Spatial analysis on resulting data was finally applied in order to identify and prioritize areas and receptors at risk and support the decision-makers in addressing potential climate change impacts and related adaptation strategies for groundwater (e.g. artificial aquifer recharge techniques) primarily Managed Artificial Recharge (MAR) techniques.

Figure 2 shows the overall modeling approach applied within the TRUST project, including the RRA methodology. The main models developed by project partners and linked in a model chain are shown in Box 1.a: climatic models (CMCC); geomorphoclimatic model (Alto Adriatico River Basin Authority); hydrogeologic model (SGI Spa). The RRA model developed by CMCC, its input and output data, and its relationships with Box1.a models are depicted in Box1.b.

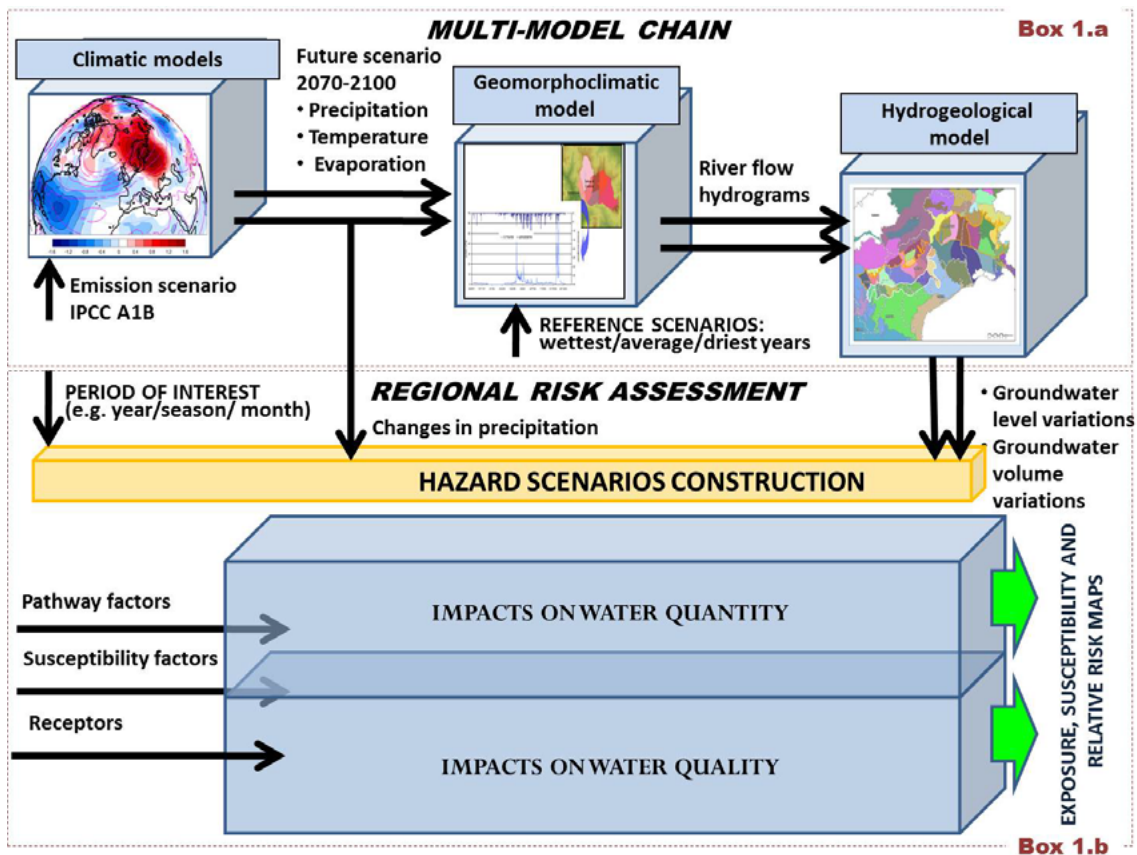


Fig. 2: Modeling approach supporting the Regional Risk Assessment (RRA) in the TRUST project. It includes the models developed by the project partners and linked in a model chain (source: 12)

The first part of the model chain is represented by global and regional climate models and downscaling techniques used to provide future climate scenarios for the 2071-2100 period, according to the IPCC A1B emission scenario (IPCC, 2000). Based on downscaled climate projections, 3 reference scenarios (i.e. the driest, the wettest and the mild year) were constructed through global and high resolution climate models and used to run cascading regional geomorphoclimatic and hydrogeological models. The second part of the model chain, through geomorphoclimatic and hydrogeological model simulation, produced information about the potential variations of the water balance components (e.g. river discharge, groundwater level and volume) in relation to each climate change scenario [12]. The outputs of the model chain are used to develop potential hazard scenarios for the case study area and to apply the regional risk assessment (RRA) methodology for the evaluation of climate change impacts on groundwater and related ecosystems (Box 1.b).

In order to investigate the potential impacts and risks posed by climate change on groundwater resources, the RRA requires also the characterization of the receptors vulnerability. This involves the development and application of a range of vulnerability indicators, representing the sensitivity of the coastal communities, systems or assets to the damaging effects of climate change hazards [13]. Vulnerability indicators, as well as the climate, hydrological and hydrogeological models results at analytical unit scale were used to characterize exposure, analyze susceptibility and rank risk for each considered impact and receptor.

In the present study, the analysis was focused on the following water quantity and quality impacts: a) Groundwater Level Variations (GLV), representing the potential decrease of future water table levels due to climate change, resulting in a worsening of ecological conditions of groundwater-dependant ecosystems on the ground surface; b) Changes in Water Availability for irrigation (CWA), referring to the potential reduction of the river discharge available to be derived for irrigation purposes; and c) Changes in Nitrate Infiltration processes (CNI), related to the potential deterioration of the qualitative status of groundwater bodies due to non-point source pollution and specifically to nitrate leaching from agricultural source into groundwater. These three relevant impacts on groundwater were selected and analysed for key environmental and socio-economic receptors (e.g. agricultural areas, natural environments, wells).

According to Torresan [14], the methodology adopted within the TRUST project, in order to identify key areas and targets at risk from climate change impacts for groundwater and associated ecosystems, includes 5 main phases:

1. Input data collection: vulnerability and hazard matrixes;
2. Hazard Assessment;
3. Exposure Assessment;
4. Susceptibility Assessment;
5. Risk Assessment.

During the first phase (**input data collection**) the definition of hazard and vulnerability matrixes is required in order to define hazard and vulnerability matrixes, useful to identify the components involved in the estimation of risk in the case study area (i.e. impacts, stressors and receptors) and their relationships. The **hazard assessment phase** is aimed at the characterization of climate change hazard scenarios, which describe the future conditions of climate change-related hazard against which a system needs to adapt in order to keep its ecological or socio-economical functions. The following **exposure**

assessment is aimed at identifying and classifying areas where the hazard can be in contact with the target (i.e. potential impacted areas) in the three future timeframe scenario 2071–2100 previously defined. **Susceptibility assessment** is aimed at determining the degree to which each target may be affected, either adversely or beneficially, by the climate-related hazard. This phase employs the definition of a subset of susceptibility indicators representing site-specific bio-geo-physical characteristics of the analyzed targets (e.g. crop water requirement, extension of natural and semi-natural environments), the definition of classes for each selected indicator and then the assignation of scores ranging from 0 (i.e. no susceptibility) to 1 (maximum susceptibility) to each susceptibility class.

The last phase for the application of the RRA methodology, adopted within the TRUST project, is the **risk assessment** aimed to integrate information about the exposure to a given climate change scenario and the receptors susceptibility, in order to provide a relative identification and prioritization of areas and receptors at risk from climate change in the case study area.

Based on this general procedure and on Multi-Criteria Decision Analysis techniques [15], regional risk assessment aims to estimate the degree to which, in each specific future climate scenario (e.g. the summer quarter of the driest year), individual targets (e.g. agricultural areas, groundwater bodies) would be affected by the analyzed impacts.

The main results of the application of the RRA methodology include exposure, susceptibility and risk maps. All the maps are classified in 5 qualitative classes (very low, low, medium, high, very high) allowing the definition of a relative rankings for the case study area. Figure 3 presents an example of exposure, susceptibility and risk maps for the receptor agricultural areas related to the Groundwater Level Variations (GLV) impact. As shown in Fig. 3a, exposure map show areas where a future groundwater level decrease is expected. Exposed areas are located along the area known as “spring band”, due to the presence of resurgence streams which originates from the water table rising to the ground level. Fig 3b presents an example of susceptibility map related to the receptor “agricultural areas” with respect to GLV impact, considering crop typologies and related water requirement according to scientific literature [16; 17]. Risk maps for “agricultural areas” (Fig 3c) are obtained from the overlay of the exposure map - representing the groundwater level decrease - and the susceptibility map of crops in relation to their water needs, and offer the possibility to identify and rank areas at higher risk within the spatial and temporal window selected (i.e. the dry year scenario and the summer season).

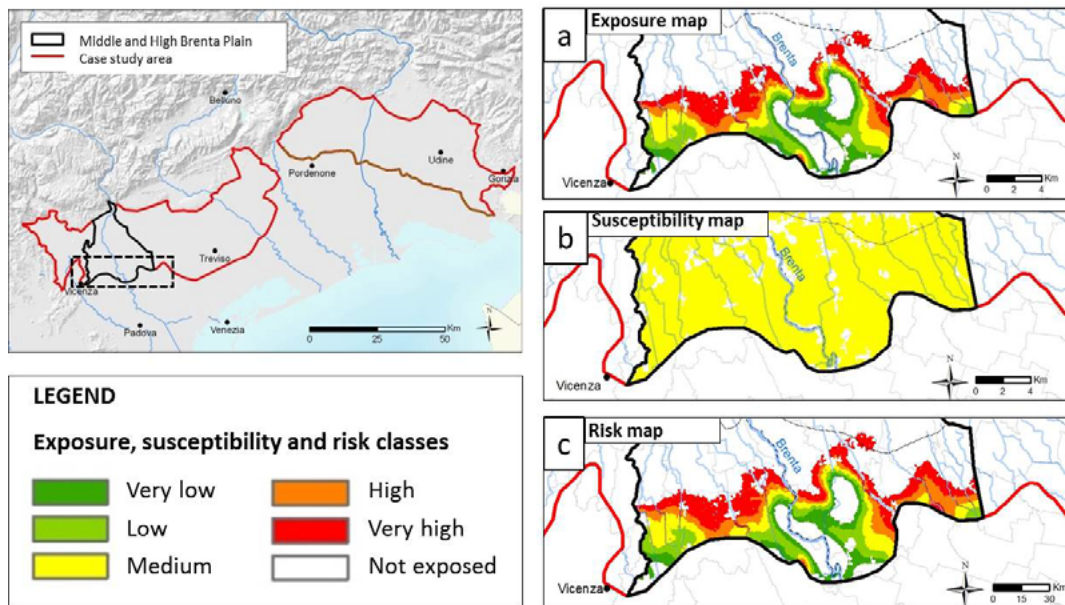


Fig. 3. Regional Risk Assessment maps produced in Veneto and Friuli-Venezia Giulia Regions (North Eastern Italy) for the Groundwater Level Variations (GLV) impact: exposure map (a), susceptibility (b) and risk (c) map for the receptor agricultural areas and related to the quarter June-July-August for the dry year scenario.

5. CONCLUSIONS

The presented spatially-resolved regional risk assessment (RRA) methodology provides a relative estimation of targets and areas at risk from climate change in the high Veneto and Friuli Venezia Giulia plains area and allows to assess potential harms for groundwater resources and dependent ecosystems.

The obtained exposure, susceptibility and risk maps highlighted that potential climate change impacts will potentially cause negative consequences with different spatial distribution and magnitude, depending on examined time frames and scenarios in the case study area. Particularly, impacts on groundwater will likely have little direct effects on related ecosystems (croplands, forests and natural environments) while more severe consequences will indirectly occur on natural and anthropic systems through the reduction in quality and quantity of water availability for agricultural and other uses.

The RRA application provide a preliminary assessment of areas and receptors at risk from climate change and thus is a starting element to be considered in defining priorities for intervention and addressing of groundwater adaptation measures as the identification of suitable areas for the application of Managed Artificial Recharge techniques.

RRA is a flexible and optimizable approach: gives the opportunity to focus the analysis on different receptors and critical issues according to specific end-user needs; gives the chance to integrate expert judgements through the customization of scores, weights and thresholds and can be easily adapted and used with new case studies and specific purposes, including also different spatial and temporal scale of analysis.

6. ACKNOWLEDGMENTS

This paper is a result of European Life+TRUST project, funded by the European Union and the Italian Ministry for the Environment, the Land and the Sea under the Life+ programme.

7. REFERENCES

- Hawkins E., Sutton R. *The potential to narrow uncertainty in regional climate predictions*. Bull Am Meteorol Soc 2009;90:1095–107. (1)
- Randall DA, Wood RA, Bony S, Colman R, Fichefet T, Fyfe J, et al. *Climate models and their evaluation*. In: Solomon S, Qin D, Manning M, Chen Z, Marquis M, Averyt KB, Tignor M, Miller HL, editors. *Climate change 2007: the physical science basis. Contribution of working group I to the fourth assessment report of the intergovernmental panel on climate change*. Cambridge, United Kingdom and New York, NY, USA: Cambridge University Press; 2007. (2)
- Winter TC., *Relation of streams, lakes, and wetlands to groundwater flow systems*. Hydrogeol J 1999;7(1):28–45. (3)
- Sophocleous M. *Interactions between groundwater and surface water: the state of the science*. Hydrogeol J 2002;10:52–67. (4)
- Holman IP., *Climate change impacts on groundwater recharge-uncertainty, shortcomings, and the way forward?* Hydrogeol J 2006;14(5):637–47. (5)
- IPCC (Intergovernmental Panel on Climate Change). *Climate change 2007: impacts, adaptation and vulnerability*. In: Parry ML, Canziani OF, Palutikof JP, van der Linden PJ, Hanson CE, editors. *Contribution of working group II to the fourth assessment report of the intergovernmental panel on climate change*. Cambridge University Press; 2007a. (6)

- Pasini S., Torresan S., Rizzi J., Zabeo A., Critto A., Marcomini A., 2012. *Climate change impact assessment in Veneto and Friuli Plain groundwater. Part II: A spatially resolved regional risk assessment*, *Sci Total Environ*, 440: 219-235. (7)
- Regione del Veneto. *Piano di Tutela delle acque*; 2009. Available online: <http://www.regione.veneto.it/Ambiente+e+Territorio/Ambiente/Acqua+e+difesa+del+suolo/Acqua/Ciclo-Acqua/Pianificazione+Regionale/Piano+di+Tutele+delle+Acque.htm>. (8)
- Autorità di bacino dei fiumi dell'Alto Adriatico. *Salvaguardia del patrimonio idrico sotterraneo del Veneto*. Unpublished report; 1999a. (9)
- Autorità di bacino dei fiumi dell'Alto Adriatico. *Modello idrogeologico delle zone montane e di pianura dei bacini dei fiumi Isonzo, Tagliamento e Livenza*. Unpublished report; 1999b. (10)
- Landis WG., *Regional scale ecological risk assessment*. In: Landis WG, editor. *Using the relative risk model*. CRC Press; 2005. (11)
- Baruffi F., Cisotto A., Cimolino A., Ferri M., Monego M., Norbiato D., Cappelletto M., Bisaglia M., Pretner A., Galli A., Scarinci A., Marsala V., Panelli C., Gualdi S., Bucchignani E., Torresan S., Pasini S., Critto A., Marcomini A., 2012. *Climate change impact assessment in Veneto and Friuli plain groundwater. Part I: an integrate modeling approach for hazard scenario construction*. *Sci Total Environ*, 440: 154–166. (12)
- Torresan S., Critto A., Dalla Valle M., Harvey N. e Marcomini A., *Assessing coastal vulnerability to climate change: comparing segmentation at global and regional scales*. *Sustainability Science*, Springer. 3: 45-65. 2008. (13)
- Torresan S., 2012. *Development of a Regional Risk Assessment methodology for climate change impact assessment and management in coastal zones*. PhD Thesis, University Ca' Foscari Venice, Italy. (14)
- Giove S., A. Brancia, F. K. Satterstrom, I. Linkov, 2009. *Decision Support Systems and Environment: Role of MCDA*. A. Marcomini et al. (eds.), *Decision Support Systems for Risk-Based Management of Contaminated Sites*, DOI 10.1007/978-0-387-09722-0_3. Springer Science+Business Media, LLC 2009. Pp. 53-73. (15)
- Allen RG, Pereira LS, Raes D, Smith M. *Crop evapotranspiration: guidelines for computing crop requirements*. Irrigation and drainage paper no., 56. Rome, Italy: FAO; 1998. (16)
- Giardini L. *Agronomia Generale, ambientale e aziendale*. Bologna: Pàtron Editore; 1992. (17)

Climate change scenarios of minimum, maximum temperature and precipitation over Italian areas, period 2021-2050

Tomozeiu R.^{1*}, Cacciamani C.¹, Botarelli L.¹, Pasqui M.², S.Quaresima³

¹ARPA Emilia-Romagna, Servizio Idro-Meteo-Clima, Bologna, Italy,

²CNR –IBIMET, Roma, Italy,

³CRA –CMA Unità di Ricerca per la Climatologia e la Meteorologia applicate all'Agricoltura, Roma, Italy

*Corresponding author: rtomozeiu@arpa.emr.it

Abstract

Climate change scenarios of seasonal minimum, maximum temperature and precipitation over different Italian areas, during the period 2021-2050 against 1961-1990, are assessed. The areas are those selected in the framework of the AGROSCENARI project and are represented by: Padano-Veneta plain, Marche, Beneventano, Destra Sele, Oristano, Puglia and Sicilia, being areas with an important impact for local agricultural practises. A statistical downscaling technique applied to ENSEMBLES global climate simulations (STREAM1), scenario A1B, is used in order to reach this objective. The statistical scheme consists of a multivariate regression based on Canonical Correlation Analysis (CCAReg). The scheme is constructed using large scale fields (predictors) derived from ERA40 ECMWF reanalysis and seasonal mean minimum, maximum temperature and precipitation (predictands) derived from observed daily gridded data (resolution around 35km) belonging to CRA-CMA. The observed period used to set-up the statistical downscaling scheme is 1958-2002. Once the most skilful model has been selected for each season and variables, this is then applied to the predictors derived from the ENSEMBLES models experiments, A1B scenario, in order to construct climate change scenario at grid point level over the period 2021-2050 with respect to 1961-1990.

The results show that an increase of around 1.5°C could be expected to occur under A1B scenario conditions in all seasons, both in minimum and maximum temperatures. As regards precipitation, the signal is more complex and varies in function of season and region. A reduction of precipitation could be expected to occur especially during summer seasons, more pronounced over areas from the central and southern part of the Italian peninsula.

Keywords: *Climate change projections, grid points, statistical downscaling, seasonal temperature and precipitation*



1. INTRODUCTION

Global Climate Models together with dynamical and statistical downscaling models are the most important tools used by the scientific community in order to simulate climate at different temporal and spatial scale. During the last years a lot of attention has been paid on the increasing of information on future projections at higher resolution, often required by the impact studies. In this way many efforts have been done to increase the spatial resolution and to reduce the uncertainties in the climate projections. This represents also the aim of the present work, namely: construction of climate change scenarios of seasonal temperature and precipitation at local scale, by applying statistical downscaling techniques to large scale fields simulated by several GCMs – ENSEMBLES experiments (<http://www.ensembles-eu.org/>). The availability of high number of models (7GCMs) used in the Ensembles project, allowed the construction of an Ensemble Mean (EM) and evaluation of the variability, that helps to estimate the uncertainties due to GCMs in the climate change projections. Evaluation of climate change scenarios at local scale have been already done over some Italian regions, such as: Apulia and Po valley as concern seasonal precipitation (Palatella et al. 2010) and Emilia-Romagna region and Northern Italy as concerns temperatures (Tomozeiu et al. 2013).

2. METHOD AND DATA

The statistical downscaling technique (SDs) used in the present work is based on the assumption that the local climate is determined by the large-scale fields variability (predictors) linked to the local features (predictands). This link has been detected through the Canonical Correlation Analysis (CCA), constructed using gridded observed temperature/precipitation and ECMWF-ERA40 re-analysis large scale fields (<http://www.ecmwf.int/products/>). Then, the most important patterns provided by the CCA (von Storch, 1995) have been used in a multivariate regression scheme (CCAReg) constructed over the period 1958-1978 and 1996-2002 and validated over the period 1979-1995. This kind of approach is known as Perfect-Prognostic (Wilks 2006). Once the most skilful SD is selected for each season and predictand, this is then applied to the predictors simulated by GCM experiments, in order to evaluate the local future scenarios. A selection of fields such as: mean sea level pressure (MSLP), geopotential height at 500hPa (Z500), temperature at 850hPa (T850), specific humidity, had already been tested as possible predictors in previous works over Northern-Italy and different other Italian regions (Busuioc et al.,2008, Tomozeiu et al.,2013, Villani et al., 2011).

The local data set used in this study is composed from daily minimum, maximum temperature and precipitation defined over different Italian areas (Figure 1), selected in the framework of the national project – AGROSCENARI (www.agroscenari.it). The data are defined at a regular grid with a spatial resolution of 35 km over the period 1951-2009 (source of data: CRA-CMA).

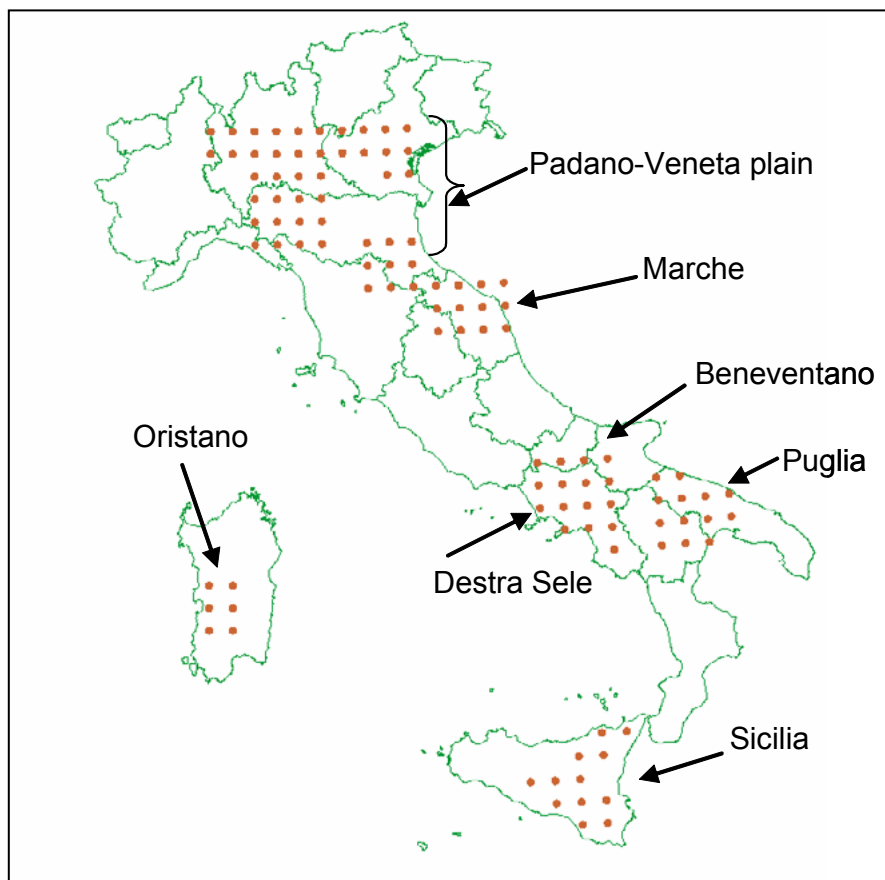


Fig. 1: Map of areas (and grid points) used in the study

The large-scale observed data set (predictors) used in the present work are: mean sea level pressure (MSLP), geopotential height at 500 hPa (Z_{500}) and temperature at 850 hPa (T_{850}). The fields are derived from ERA40 re-analysis (<http://www.ecmwf.int/products/>) and have been used in the set-up phase of the SD scheme. The data cover the window 90°W - 90°E and 0° - 90°N and are referred to the period mid-1957 (September) to mid-2002 (August). Regarding the GCM simulations, the ENSEMBLES model fields, archived in the Climate and Environmental Retrieval and Archive (CERA data base) of the World Data Center System for Climate (WDC), have been obtained by the web site: <http://ensembles.wdc-climate.de>. The STREAM1 simulations, used in the present work, have been

performed with the methodology and the forcing defined for the CMIP3 simulations, contributing to the IPCC AR4 assessment (http://www-pcmdi.llnl.gov/ipcc/about_ipcc.php). In the present work it has been selected the A1B scenario, the control-run is referred to 1961-1990, extracted from the historical simulation 1860-2000, while the future scenario is referred to the period 2021-2050. The simulations produced by the following modelling groups have been taken into account: INGV, NERSC, FUB, IPSL, METOHC (2 runs), MPIMET+DMI.

Analysis of the SDs skill is a crucial element of any downscaling application. This depends on predictors (type, domain, filtering of data) as well as on the predictands (quality of input data, filtering of data). The skill analysis is done most commonly through “cross-validation” or “calibration-validation” with observed data. The second method has been used in the present paper, namely calibration-validation. In order to do this the whole interval was divided into two homogeneous (including positive and negative anomalies) sub-intervals: 1958-1978 together with 1996-2002, and 1979-1995 which alternatively considered as fitting and validation. Then, the most skilful model has been retained in order to construct climate change projections at grid point level. The skill of the downscaling model is quantified in terms of Spearman rank-correlation coefficient, BIAS, root-mean square-error (RMSE).

3. RESULTS

As it was mentioned in the previous paragraph, an important point in the SD scheme is the selection of the predictors. The work done in the present study to select the best predictors, using BIAS, RMSE and rank correlation as indices of performance, reveals that the T850 is the best predictor for minimum and maximum temperature, while MSLP is in general the best predictor for cumulated precipitation. Figure 2 presents the seasonal coefficients of skill of the SDs computed between downscaled and observed time series (mean of the coefficients over all grid points). As it could be noted, good performances are obtained for both minimum and maximum temperatures during all seasons, the values that correspond to a significance level of 0.05 and 0.1 is also represented (dashed lines). Regarding precipitation (figure not shown), good performances are obtained during winter and autumn seasons, while during spring and summer the performance is smaller.

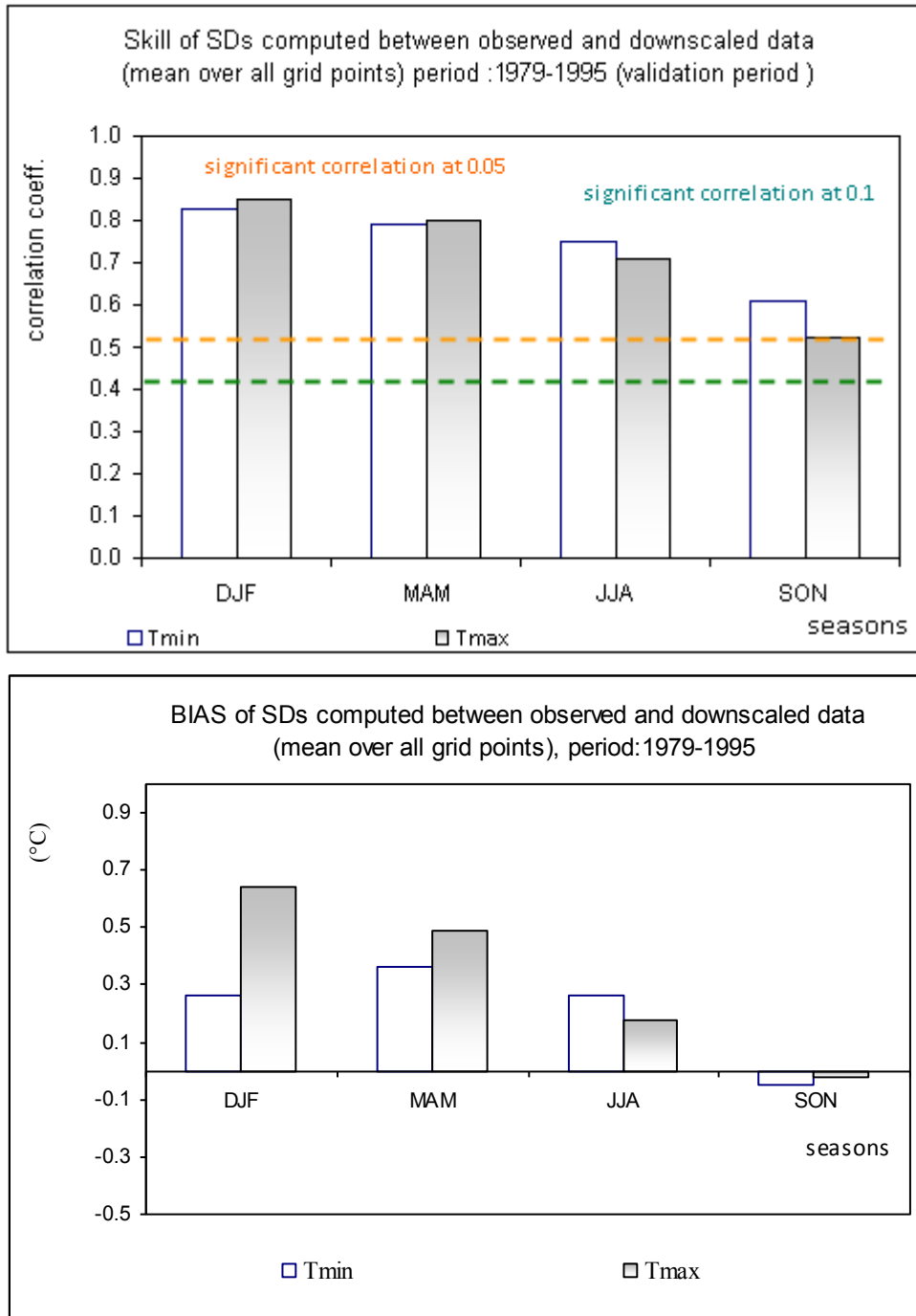


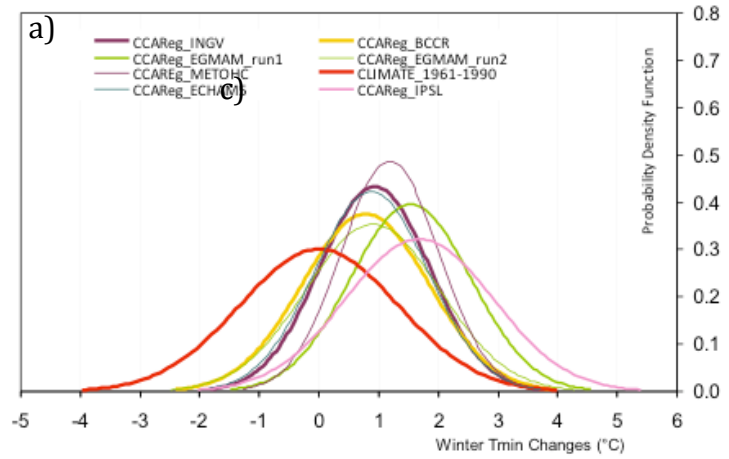
Fig. 2: Skill of the SDs expressed as correlation coefficient and BIAS computed between seasonal observed and downscaled time series (mean over all grid points).

The schemes retained to be the most useful have been then applied to the predictors simulated by the GCMs to construct future projections at local scale. The results are presented in the following as Probability Density Function (PDF) or maps of changes, constructed for each model and for the

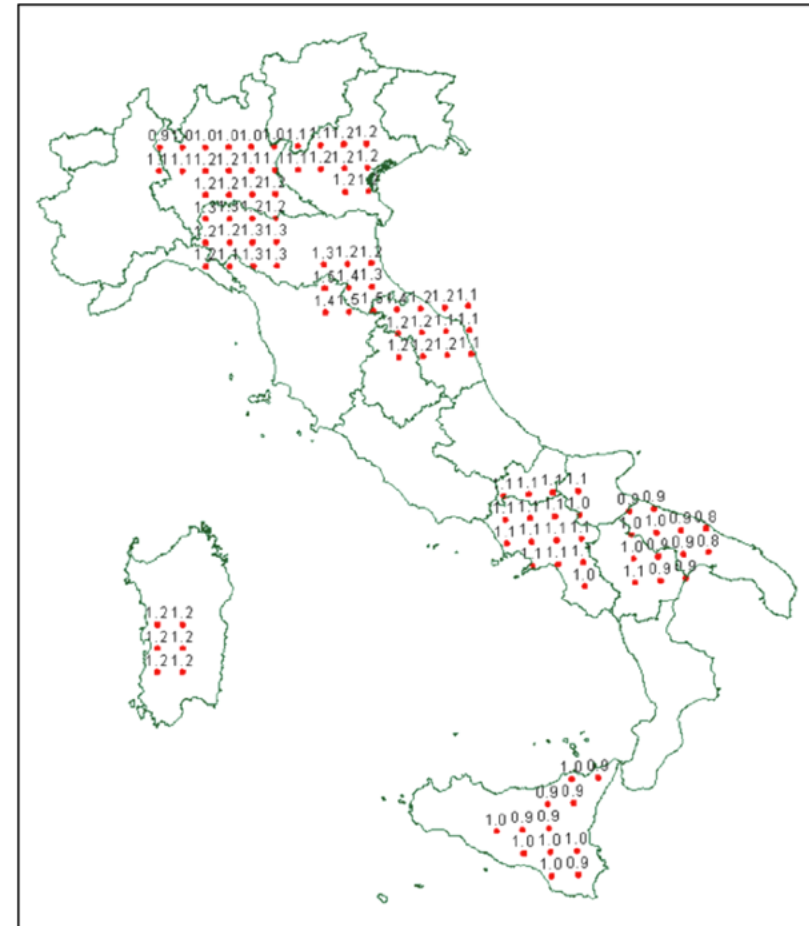
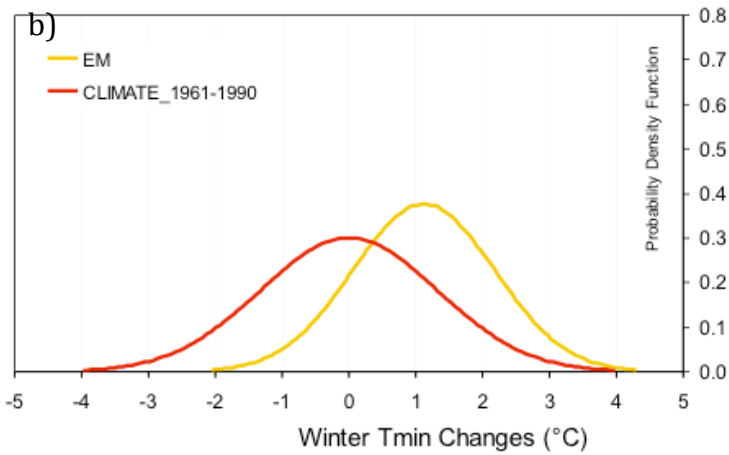
Ensemble Mean (EM). Climate change scenarios of seasonal minimum and maximum temperature, obtained at grid point level, show a possible increase in both minimum and maximum temperature over all analysed areas, in all seasons, during the period 2021-2050 with respect to 1961-1990. Figure 3 presents an example the PDFs of changes in winter Tmin, mean over all grid points (a), the Ensemble Mean of winter Tmin changes (b) and the spatial distribution of changes- Ensemble Mean (c). As it could be noted from Fig.3a, all models show an increase in winter minimum temperature over Italian areas from 0.8°C (e.g. CCAReg applied to ECHAM5, INGV models) to 1.5°C (e.g. CCAReg applied to EGMAM run1 and IPSL models). It is important to underlay that the PDFs show a possible changes not only in the mean values but also in the tails of the distributions, both lower and upper, for the period 2021-2050 with respect to 1961-1990. This could connect to a shift of the distributions to the “warmer values” as could be observed from Fig3b, that shows the Ensemble Mean of changes over all areas, with changes in the upper tail around 3°C. An important change is also projected in the “lower tail” of the distribution, with values up to 2°C Fig.3b). The spatial distribution of winter Tmin changes computed from the Ensemble Mean represented in Fig.3c reveals that the projected warming in winter minimum temperature seems to be a little higher in the Po Valley, Marche and Oristano areas than in the other studied areas.

As regards the other seasons, the projected changes in minimum temperature emphasise a signal of warming more pronounced during summer season, when the increase could reach 2°C (mean value) with respect to 1961-1990 period.

Scenario A1B (2021:2050 - 1961:1990)



Scenario A1B (2021:2050-1961:1990)
Ensemble Mean



A similar signal of changes has been obtained for maximum temperature. Figure 4 displays the projections of seasonal maximum temperature for each analysed region, as a mean of grid points belonging to each region. As it could be noted, the peak of changes is projected during summer (up to 2.3°C) followed by autumn (up to 2°C).

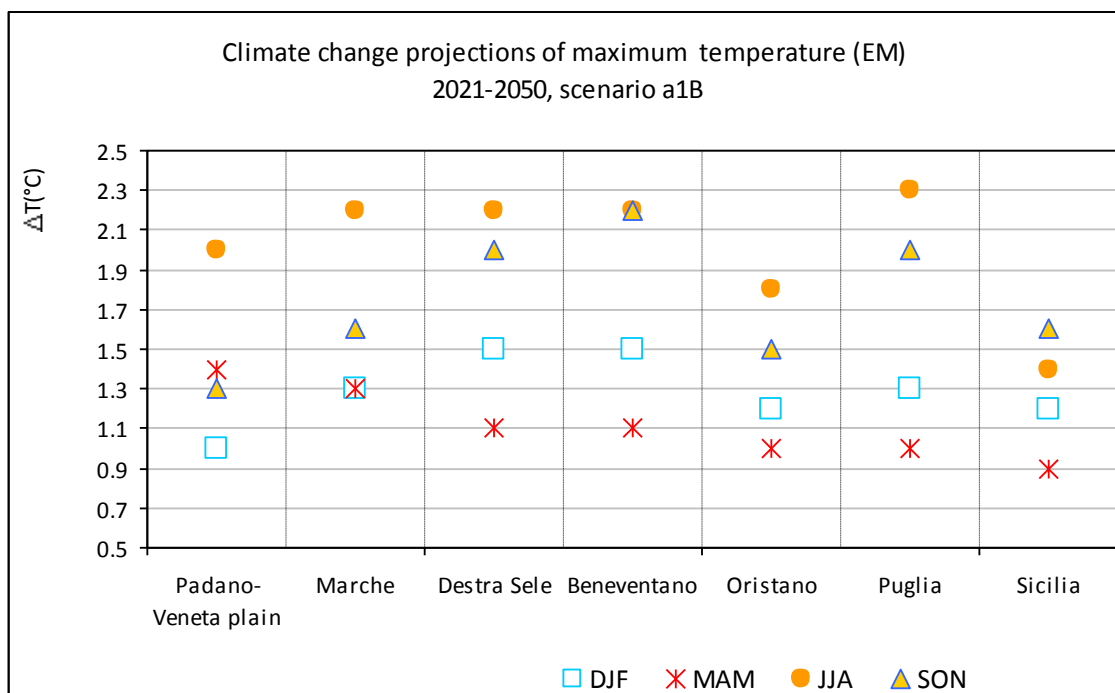


Fig. 4: Climate change scenarios of seasonal maximum temperature, 2021-2050, scenario A1B

As it concerns precipitation, the climate projections obtained through the same technique show a pattern of changes more complex, different from season to season and over the areas. Figure 5 presents the future changes of seasonal precipitation (%), during the period 2021-2050 with respect to 1961-1990, in one grid point that belongs to Po valley (1410 grid points) and another grid point that belong to Oristano (1118 grid point), outputs obtained by applying the CCAReg to : ECAHM5, EGMAM runs, INGV, IPSL and METO_HC models and the Ensemble Mean (EM).

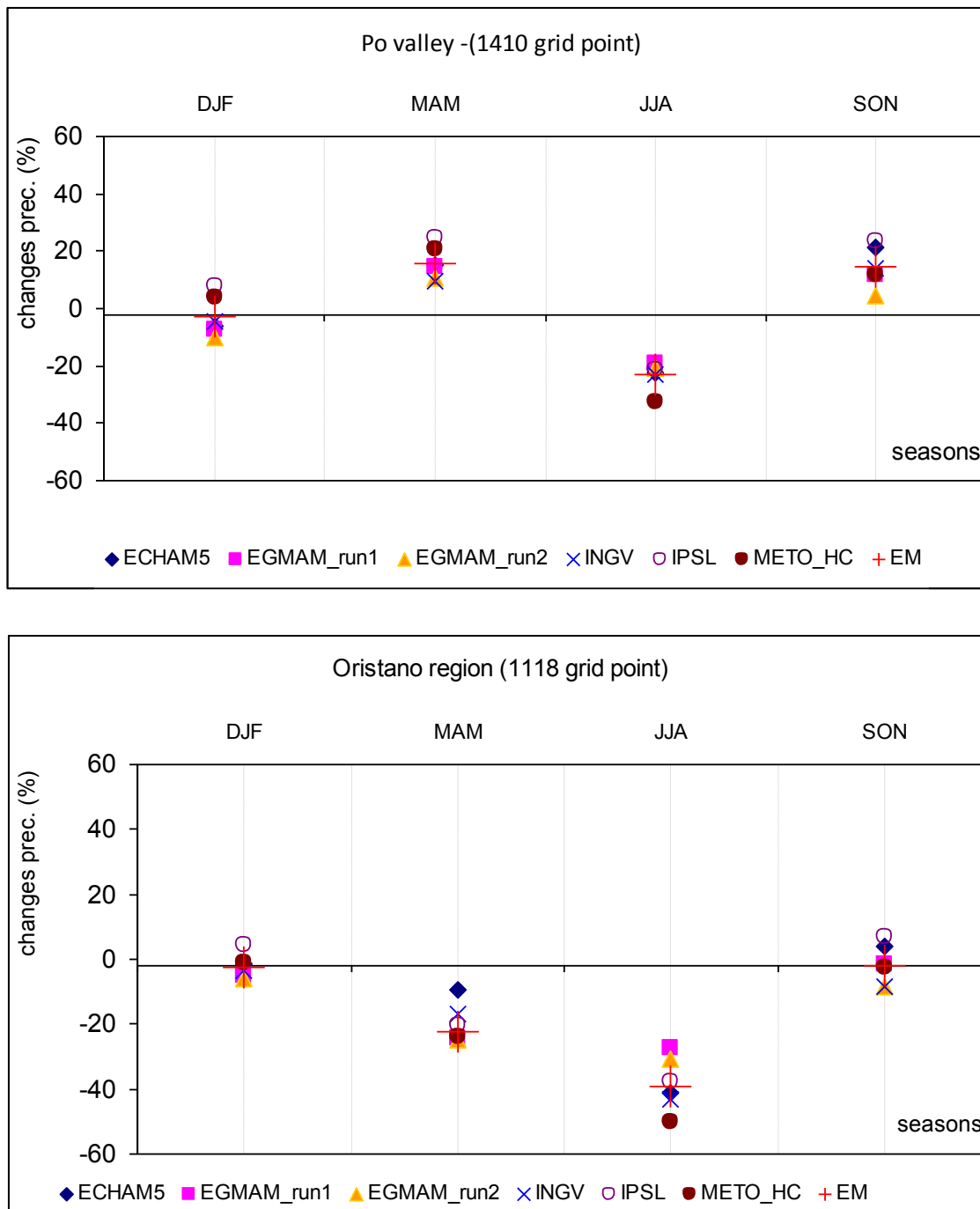


Fig. 5: Climate change scenarios of seasonal precipitation (%) for one grid point from the Po Valley(1410) and one point from Oristano(1118), period 2021-2050, scenario A1B

As it could be observed from Fig. 5, a small decreases of precipitation has been projected in winter (up to 3%). During spring, only the grid point that belong to Po Valley shows a possible increase, around 15%(EM), while for the grid point that belong to Oristano area a possible decrease is projected. Summer is the season when the signal of change goes in the same direction for all grid points, namely a

possible decrease of amount of precipitation, more pronounced for the grid point from Oristano region (up to 40%-EM). As concerns autumn only the grid point from the Po Valley shows a possible increases, up to 15%, while no significant changes have been noted over Oristano grid point (see fig.5).

4. CONCLUSIONS

In the present study, a statistical downscaling scheme is built and applied in order to construct climate projections at grid point level of: minimum, maximum temperature and precipitation over different areas from the Italian peninsula.

The following conclusions could be drawn from the present work:

- significant increases are projected to occur in minimum and maximum temperature over the studied areas in all seasons, for the period 2021-2050 with respect to 1961-1990, A1B scenario;
- the Ensemble Mean computed using all simulations for each season, shows a changes in the mean of the PDFs of minimum and maximum temperature, between 1.5- 2°C. The peak of changes is projected during summer for both, minimum and maximum temperature;
- a shift of the PDFs to warmer value is projected to occur for both, minimum and maximum temperature, in all seasons. This shift is more pronounced in the upper tails and higher magnitude have been detected during summer season (up to 3°C with respect to present climate);
- a reduction of precipitation could be expected to occur during summer season, over the period 2021-2050, more pronounced in the areas situated in the central and southern part of Italian peninsula (up to 40%).

5. ACKNOWLEDGMENTS

The ENSEMBLES data used in this work was funded by the EU FP6 IP Ensembles (Contract nr 505539) whose support is gratefully acknowledged. The results have been obtained in the framework of AGROSCENARI project (www.agroscenari.it).

6. REFERENCES

- Busuioc A., Tomozeiu R., Cacciamani C., (2008) *Statistical downscaling model based on canonical correlation analysis for winter extreme precipitation events in Emilia-Romagna region*. Int J Climatol 28:449–464. (1)
- Palatella L., Miglietta M., Paradisi P., and Lionello P. (2010) *Climate change assessment for Mediterranean agricultural areas by statistical downscaling*. Nat Hazards Earth Syst Sci, 10:1647–1661. doi:10.5194/nhess-10-1647-2010. (2)
- Tomozeiu R., Agrillo G., Cacciamani C., Pavan V. (2013), *Statistically downscaled climate change projections of surface temperature over Northern Italy for the periods 2021-2050 and 2071-2099*, Nat. Hazard, DOI 10.1007/s11069-013-0552-y. (3)
- Villani G, Tomei F, Tomozeiu R, Marletto V (2011) *Climate scenarios and their impacts on irrigated agriculture in Emilia –Romagna, Italy*, Italian J of Agrom, Anno XVI, no.1, Aprile 2011, Patron Editore, Bologna, pag. 5-16. (4)
- Von Storch H (1995), *Spatial Patterns: EOFs and CCA*. In: von Storch H, Navarra A (eds) *Analysis of climate variability. Application of statistical techniques*. Springer pp 227–258. (5)
- Wilks D.S. (2006) *Statistical Methods in the Atmospheric Sciences*, 2nd Ed. International Geophysics Series, Vol. 59, Academic Press, 627 pp. (6)

Preliminary assessment of the effects of climate change on landslide activity of Orvieto clayey slope

Rianna G.^{1*}, Tommasi P.², Comegna L.³ and Mercogliano P.^{1,4}

¹*ISC Impacts on soil and coasts Research Division CMCC Euro-Mediterranean Center on Climate Change, Capua, Italy*

²*National Research Council, Institute for Environmental Geology and Geo-Engineering c/o Engineering Faculty, Sapienza University of Rome, Rome, Italy*

³*DICDEA – Department of Civil Engineering, Design, Construction Industry and Environment Second University of Napoli, Aversa, Italy*

⁴*C.I.R.A. -Italian Aerospace Research Center Onboard Systems & ATM Division Meteo System & Instrumentation Laboratory, Capua, Italy*

*Corresponding author: guido.rianna@cmcc.it

Abstract

The first results of a procedure developed for the evaluation of the effects of climate change on landslide phenomena are shown. The case history is represented by the northern slope of the Orvieto Hill (Central Italy) affected by slow translational movements directly related to soil-atmosphere interaction. The results concern the analysis of available weather observations and a preliminary assessment of the effects of climate changes on landslide activity; the limits of the adopted simplified approaches are identified and the further developments aimed at improving the prediction are so indicated.

Keywords: *Landslide activity, regional climate modelling, earth surface processes, statistical analysis of weather data*



1. INTRODUCTION

Global warming and climate change are some of the most debated issues of the last decade.

The internal variability of the climate system, the intrinsic differences of the response of climate prediction models and the assumptions about the scenario represent significant sources of uncertainty [1,2], nevertheless IPCC Assessment Reports 4 (2007) [3] consider global warming highly likely while the greater capacity of air to hold moisture could induce extreme precipitation events with increased frequency and severity [4,5].

As regards Europe, several studies [6,7] predict an increase of cumulative rainfall over Central and Northern Europe, a possible decrease in the South and a rise of the mean temperature especially during the winter in Northern Europe and in the summer in Southern Europe [8].

Precipitation-induced landslides have a very high socio-economic impact being able to cause huge damages to properties and people: more than U.S. \$ 20 billion/year worldwide [9] and U.S. \$ 2-6 billion for Italy according a rough estimate [10]. A proper understanding of the link between predicted climate change and possible modifications to landslide activity (in terms of magnitude and frequency) at regional and local scale becomes a crucial issue [11].

Even under “steady-state climate conditions”, slope response to weather conditions represents a challenging topic because it depends on numerous factors as mechanical and hydraulic properties of involved soils, stratigraphic conditions, slope geometry. When climate changes are considered, this response becomes extremely complex due to the above mentioned uncertainties of climate modelling, their present low spatial resolution [12], low reliability on daily and sub daily scale [13] and variations in land use/land cover consequent to climate change and/or anthropogenic footprint [14,15].

In general terms, Dixon and Brook [16] state “landslides with a shorter antecedent period, or those that exhibit a strong response to relatively short term rainfall events, could be more vulnerable to the predicted increase variability of winter rainfall and so could experience a shorter return period for slope movements. However, slope instability caused by longer periods of antecedent rainfall may occur less often in response to drier summers with increased evapotranspiration”.

Furthermore, the variety of geomorphological contexts, of data relating weather conditions to landslide phenomena and of the goals to achieve, resulted in the development of different approaches to analyse the impact of climate change on landslide activity. Coe and Godt [11] identify three main research

fields: 1) study of the climate changes and related variations in landslide activity provided that are available datasets over significant temporal scale related to the slope behaviour and weather forcing; 2) investigations about future landslide activity by applying patterns of historical activity to climate projections; [17,18] 3) retrospective approaches aimed at investigating the link between past climate and landslide occurrence e.g. paleo environmental records [4].

Within the GEMINA project, a procedure aimed at integrating the first two approaches has been developed by CMCC Impacts on soil and coasts Division and is currently under testing [19]. Italian landslide case-histories deeply investigated and documented are selected. As first step, an analysis of weather observations directly related to landslide activity is carried out in order to verify their quality, presence and possible significance of the current trends. At the same time, information about the triggering of landslide phenomena, measurements of displacement rate of the landslide body, mechanical and hydraulic properties of involved soils are collected and processed in order to establish a link between slope response and climate conditions. Future climate predictions are provided by regional climate model COSMO-CLM [20] performing dynamical downscaling by global models over the area of interest. The resulting output is then subjected to further statistical downscaling procedures in order to obtain adequate spatial and temporal resolutions. The reliability of the individual rings and of the entire simulation chain is tested over a reference time span. Finally, climate projections for the XXI century are adopted to evaluate the variations of landslide activity.

The present study shows, for the Orvieto case history, the early stages of the ongoing study on the analysis of weather observations and preliminary assessment of the effects of climate changes on landslide activity.

2. CASE-HISTORY

Orvieto is an historical town of Central Italy raising on top of a 50-meters-thick tuff slab (about 700x1500m) delimited by subvertical cliffs. The slab overlies an half cone formed by overconsolidated clays; between the slab and the clay substratum, a formation (Albornoz) of fluvial-lacustrine origin (variable thickness 3-15 meters) is interposed.

The clayey slopes are mantled by an irregular cover of talus and landslide debris. Talus debris originate from the disruption of volcanic and Albornoz materials while landslide debris are caused by landslide movements which have been affecting the slopes [21,22].

Such phenomena include failures (2 events in 110 years, 1900 and 1979) induced by man-made changes to slope geometry or hydraulic conditions and slow movements (translational) directly related to soil-atmosphere interaction. Landslide bodies move along pre-existing slip surfaces located within the softened part of clay formation (displacement rates from 2 to 6 mm/years) and within the debris cover (displacements between 7 and 12 mm/month) [21].

Movement rates are not such to imply loss of human lives but they could induce substantial problems to buildings and linear structures suffering differential displacements, as it was discussed by Mansour et al. [23].

For this reason, since 1982 the Northern slope has been monitored; instrumented boreholes provide displacements values (through inclinometers) and piezometric levels (piezometers).

Daily precipitation and temperature data are available since 1921 thanks to a meteorological station of the Hydrological Office of Regione Umbria located on top of slab (315 m a.s.l.), very close to the investigated slope.

The consistent time series of available data allow understanding if, for the investigated area, modifications in precipitation patterns (and in general for water exchanges at soil surface) are taking place and, in turn, magnitude and frequency of slope movements are varying.

By way of example, a first investigation on the cumulative precipitation over 120 days P_{120} is being carried out. In previous researches [24,21] with reference to displacements measured along a deep slip surface (maximum soil depth about 33m), such parameter exhibited the better correlation between rainfall regime and landslide activity.

A value of P_{120} ranging from 400mm and 500mm is assumed as a reasonable threshold beyond which sliding re-activate or sharply accelerates [21].

The ongoing research is aimed to test validity of the threshold value on the entire available time window and the effectiveness of further indicators, such as the effective precipitation, for interpreting landslide activity.

3. ANALYSIS OF AVAILABLE WEATHER OBSERVATIONS

In Fig. 1, yearly cumulative precipitation data are plotted; the meteorological station has maintained its location in time while in 1991 rainfall data acquisition was switched from manual to automatic. The time series results quite complete: major gaps concern the World War period (1943-1946) when reliable observations are not available even for neighbour stations and years 1966, 1979 and 1980 (partly). For these years, data are replaced by measurements supplied by Acquapendente station (about 20km away from the investigated slope). The choice is carried out verifying the good agreement between the two observation points in term of seasonal cumulated precipitation during the period when both worked (not shown).

Standard Normal Homogeneity Test (SNHT) [25,26,27] is performed to detect possible abrupt homogeneity breaks induced by variation in measurement device/location.

The test returns a maximum value of the indicator lower than the critical value required to assume the existence of a break point, for the tested sample size, with a confidence level of 5% [28].

However, the time series shows a decreasing trend (slope of the regression line -1.29mm/year); its significance is verified via the non-parametric Mann-Kendall test [29,30] which verifies the existence of a preferential order in the observations calculating, for each element x_i , the number n_i for which it is lower/higher than x_j ($j < i$); test quantity is $t = \sum_i n_i$. The test does not reject the null hypothesis, i.e. the absence of trend, with a confidence level of 5%. Similar results are obtained through the Spearman rank test [31].

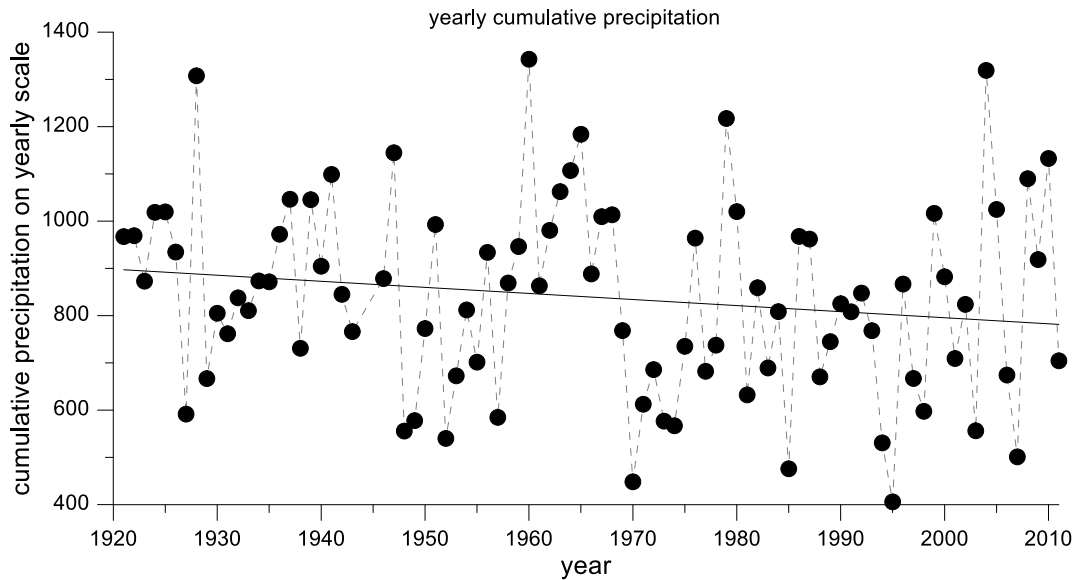


Fig. 1: Yearly cumulative precipitation time series

The result can be also explained by considering interannual variability (IntVar). Following Giorgi et al. [32], it is estimated through the coefficient of variation, first removing the linear trend; returned value, 0.22, indicates a substantial interannual variation probably exceeding the eventual climate signal over the available time series; likewise, error associated (AE) to linear trend (about 200 mm) states its limited ability to reproduce the actual values.

In Fig. 2 [a-d], the time series of cumulative precipitation for the four seasons are shown; in summer (JJA) a slight increase is observed (slope coefficient linear trend, $0.05\text{mm}/\text{year}$) while, for other seasons, a decreasing trend is detected (Tab. 1). Data indicate that the total yearly reduction could be due largely (about 53%) to a decrease of winter precipitation; the intermediate seasons (SON and MAM), despite showing comparable cumulative values, are subjected to lower decreases, respectively 27.3% and 38.8%.

However, for all the seasons, the series are characterized by remarkable interannual variability (up to 52% for the summer season) while the trends result not significant.

Finally, in Fig. 3, maximum cumulated precipitation values over 120 days are reported.

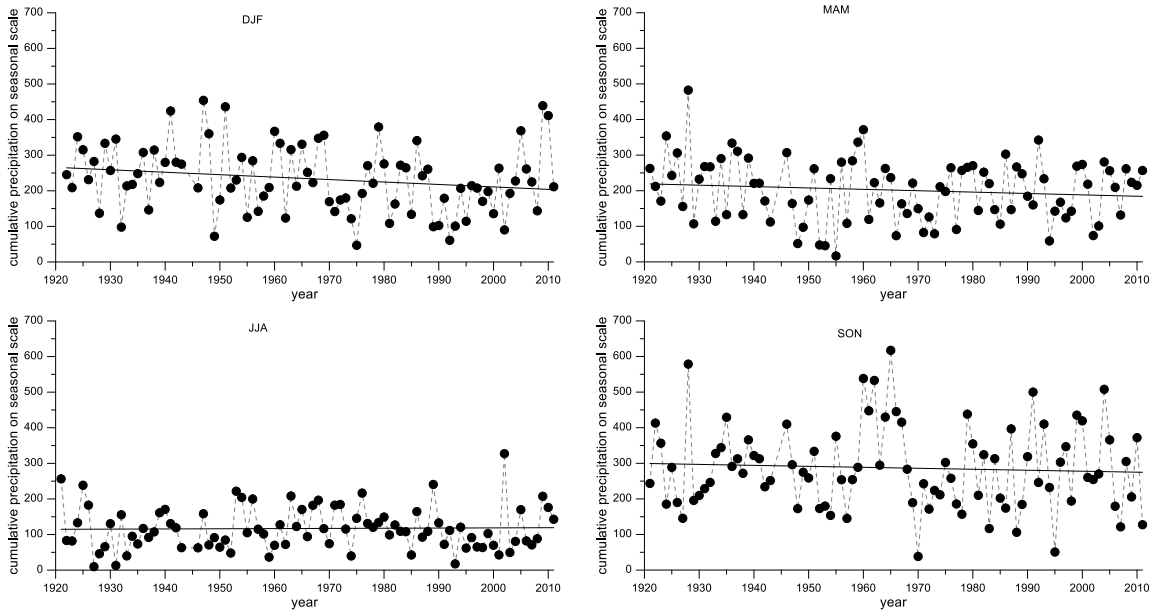


Fig. 2: Seasonal cumulative precipitation time series

The reference year on which every maximum is calculated spans from September 1 to August 31. The choice is driven by the analysis of P_{120} trends which shows, regularly, a minimum between August and September. This condition, enhanced by evapotranspiration, produces the minimum values of soil water pressures within the slope, thus minimizing the effects of previous rainfall history. Thereby, P_{120} values belonging to the same “hydrological year” are compared.

	<i>slope linear trend</i>	<i>associated error</i>	<i>IntVar</i>
yearly cumulative precipitation	-1.28mm/y	199.9mm	0.22
DJF	-0.68mm/y	91.2mm	0.34
MAM	-0.38mm/y	86.15mm	0.39
JJA	+0.05mm/y	59.6mm	0.52
SON	-0.27mm/y	116.0mm	0.39
maximum yearly cumulated precipitation over 120 days	-0.31mm/y	129.3mm	0.27

Table 1: Main synthetic data about yearly and seasonal precipitation trends

Again, the detected decreasing linear trend ($-0.31mm/year$) results not significant according the Mann-Kendall parametric test ($IntVar \approx 0.27$); moreover, frequency distribution of the sample can be well described by Generalized Extreme Value (GEV) model according the main goodness of fit tests

(results not shown). The estimate of the recurrence period T_r of P_{120} according to GEV model is reported in Fig. 4; due to Mann-Kendall test results, model parameters can be assumed to be constant.

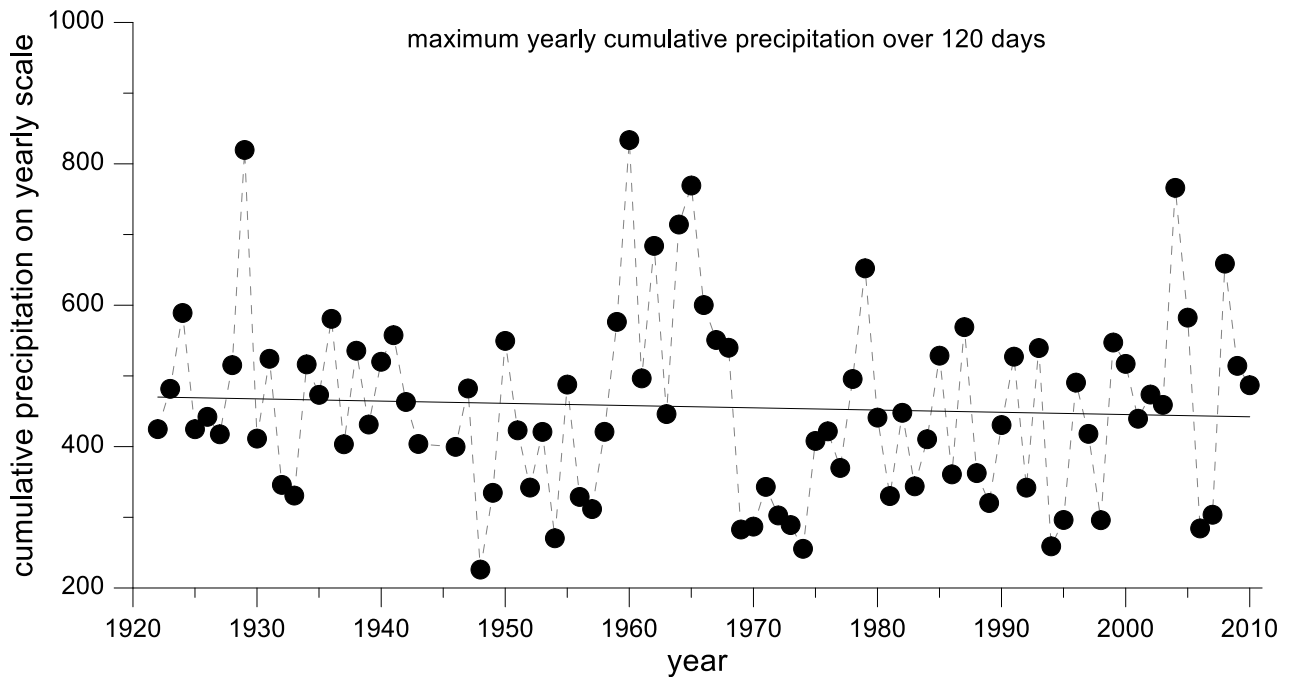


Fig. 3: Maximum yearly cumulative precipitation over 120 days time series

Broadly, T_r values are quite close to those retrieved by [21] adopting as calibration period the subset 1956-2000; for the values corresponding to the extremes of the "threshold" interval above defined, estimated return periods range from 1.5 and 3 years, which are consistent with the average calculated for observed period of landslide reactivation. The trends calculated for the first and the last thirty years of the weather observations window (red lines) are also shown: for the first one (1921-1950), a slight reduction of the return periods is estimated while for 1981-2010 period the opposite is returned. However, considering again reference values of 400-500mm, the corresponding T_r are marked by changes lower than a year.

4. PRELIMINARY ASSESSMENT OF THE EFFECT OF CLIMATE CHANGES ON LANDSLIDE ACTIVITY

A rough estimate of the possible effects of climate changes on the landslide activity is even shown in Fig. 4. “Zero hypothesis” (blue lines) assumes that the present reduction trend of maximum yearly P_{120} values will maintain during the XXI century. Thus, the observed values for the thirty years 1981-2010 are modified by a change factor (CF), which is the ratio between the value found by extrapolating the linear trend in the midpoint of a future time span and the corresponding value for the reference interval (1981-2010). The estimated T_r for upper boundary of “threshold” interval (500 mm), reaches about 4 years for 2021-2050 and about 5 years for 2071-2100, i.e. a substantial increase in the estimated return periods and an actual reduction for the rate of slope movements.

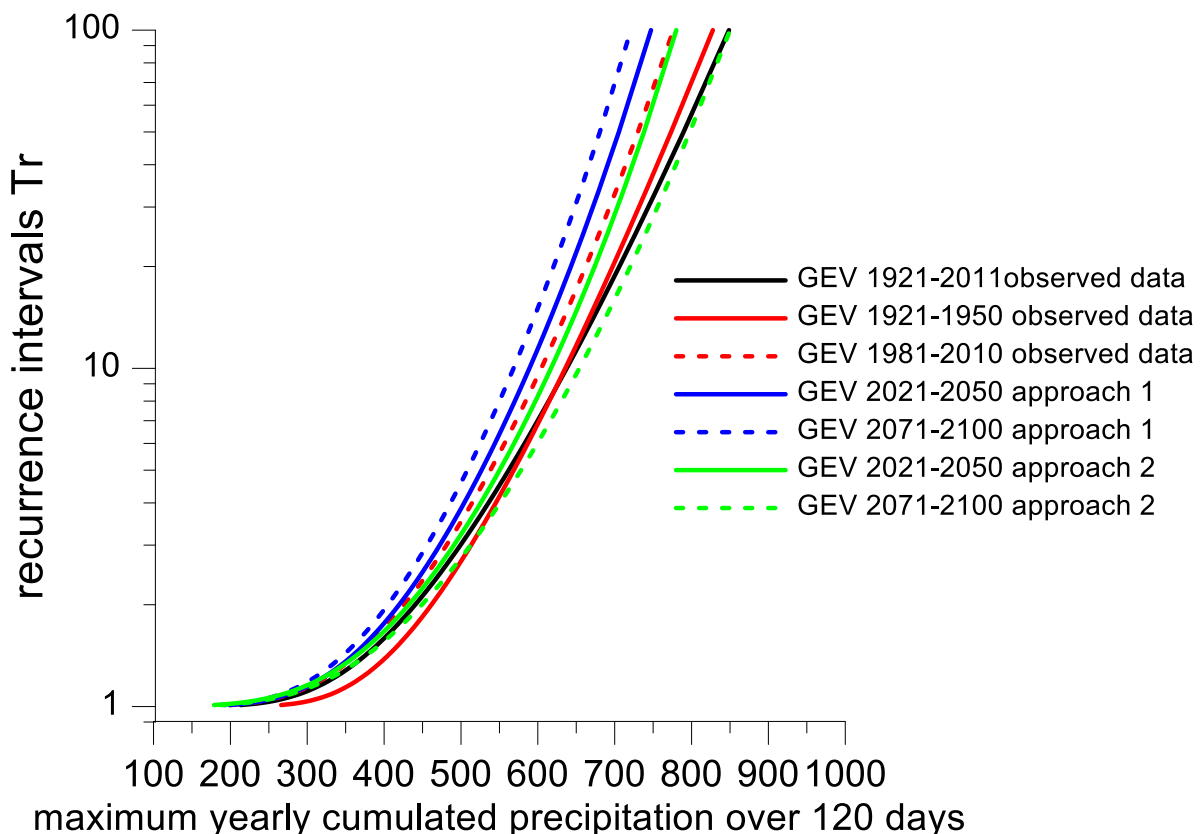


Fig. 4: Estimate of the recurrence period of P120 according to GEV model on observed datasets and for time series modified for taking into account the potential effect of climate change

The main limitations of this approach are: 1) the variation of future precipitation patterns are formulated only in terms of average rainfall value neglecting other features that are believed to be strongly affected by climate change (e.g. reduction of wet days); moreover, predicted future rainfall trend follows a linear law found through regression, which roughly reproduces the observed rainfall variations; 2) the variations of cumulative rainfall are applied under “steady-state” conditions without taking into account changes in future scenarios due to economic development or environmental policies and their effect on the climatic signal.

A first attempt to improve predicted rainfalls is proposed (green lines) again in Fig. 4. Rainfall values were obtained through COSMO-CLM Regional Climate Model. A simulation is performed over the entire Italy with a 8 km horizontal resolution; to this aim, model configuration has been optimized by CMCC [33]. The model is driven by CMCC-CM global model assuming RCP 4.5 emission scenario [34]. Mean monthly cumulated rainfall values are considered for a 5x5 grid (about 40 km x 40 km) within which the investigated slope lies. For each month, the observed values for the 1981-2010 are modified by a coefficient CF corresponding to the ratio between the estimated monthly average value over the future time span (2021-2050 and 2071-2100) and that for the reference interval 1981-2010.

This method provides an unchanged (2021-2050) or reduced (2071-2100) recurrence interval, which is primarily due to a higher estimated future precipitation for the months which mainly contribute to maximum yearly P_{120} values [October-November and February]; conversely, spring and summer months are characterized by CF values much lower than 1.

The results bring out a crucial issue in the prediction of future trends of precipitation during the wet season in the Central Italy; according to regional climate predictions, this region represents the transition zone between the North Europe, for which an increase of cumulative precipitation during the wet season is estimated, and the South where the opposite trend is predicted [35,36].

Also in this approach the effects of limitations stated above are recognizable.

Furthermore, in both approaches, correlating the landslide activity to weather factors simply through cumulative precipitations neglects two elements that could strongly influence the regime of soil water pressures and thus the rate of slope movements: a) possible reduction of the wet days and b) the increase of temperature.

Regarding the item a), over the 1921-2010 time interval, assuming a linear variation of yearly wet days number with time, a reduction slightly higher than 8 days in 100 years is returned (are considered only daily rainfall values higher than 1 mm) [Fig. 5]. Also in this case, the predictive capability of the linear regression is affected by an associated error which is about 13 days. Nevertheless, also if cumulative precipitation remain unaltered in time, the reduction of the wet days number (especially for low intensity events) entails, of course, higher daily rainfall intensity. However, because of the low hydraulic conductivity of cover soils, increased rainfall intensity could lead to a decrease of infiltrated rain and in turn of soil pore water pressure, with the consequent reduction in movement rate.

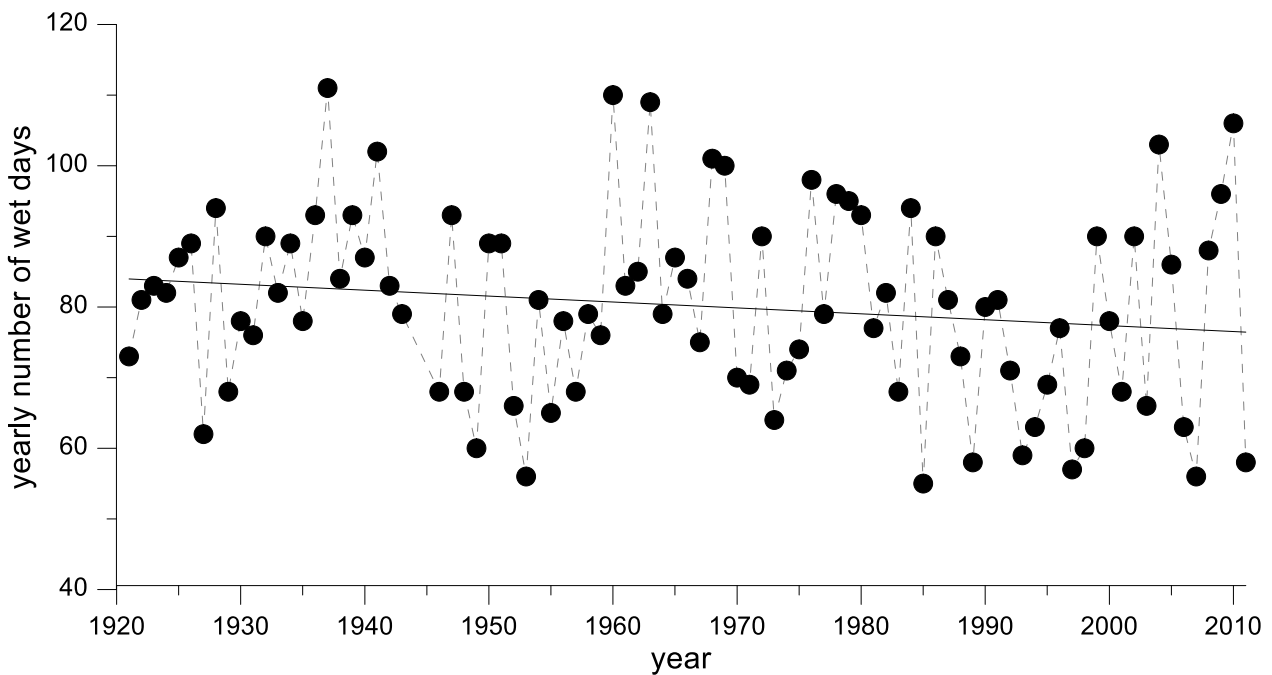


Fig. 5: Yearly number of wet days time series (daily rainfall events higher than 1 mm)

Regarding the item b), (Fig. 6 [a-d]) linear regression of data of mean seasonal temperature predict an increase of about 1°C in 100 years for all seasons except the fall; such an increase enhances evapotranspiration processes and could further contribute to reducing pore pressures.

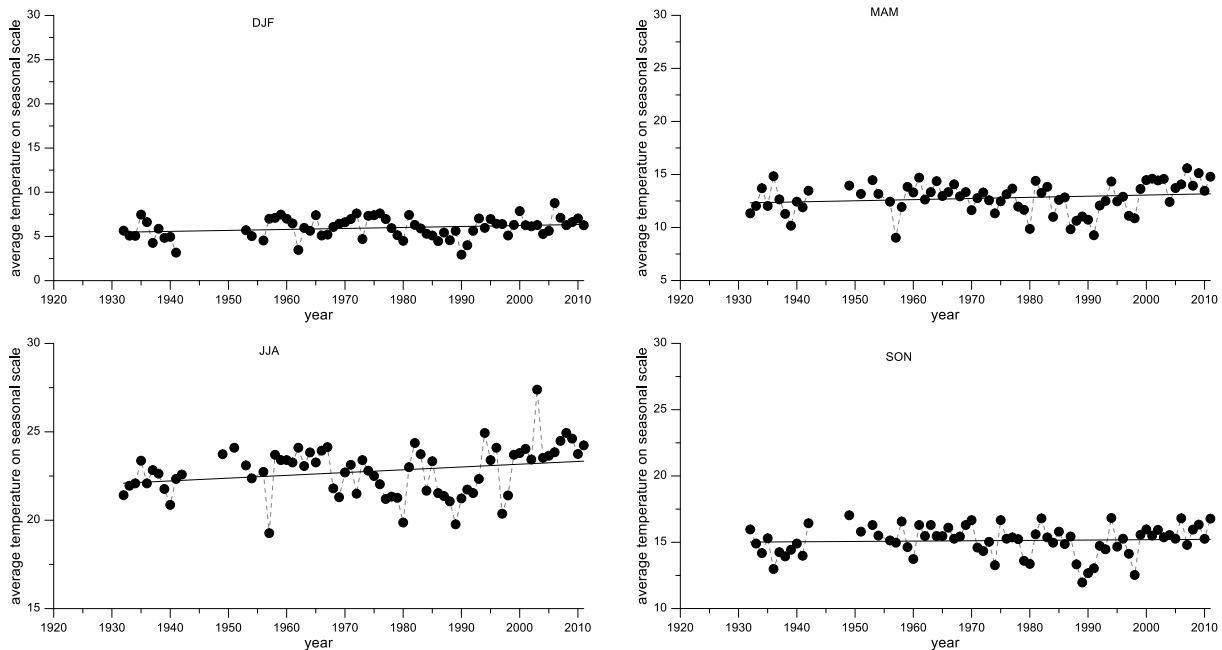


Fig. 6: Seasonal average temperature at 2meters time series

5. CONCLUSIONS

For a proper prediction of the impacts of climate changes on surface earth processes, weather observations and their effects on these processes must be collected over extended time periods. In this respect, retrieving metadata, performing quality controls and analysing the time series to detect possible ongoing trends represent the first essential stages of the study.

These requisites characterize Orvieto landslide case-history; in fact, in addition to a very long series of weather data, long time series of observations directly related to landslide activity (pore water pressures and displacement measurements) are available (and currently under monitoring).

In this study, according to previous researches, slow deep slope movements are assumed to be correlated to rainfall cumulated over 120 days.

The parameter is successively utilized to estimate possible variations of landslide activity induced by climate changes adopting simple assumptions about future precipitation trends: since this procedure yields conflicting results, an improvement of the prediction is currently being pursued following two ways: the available displacement rate values are being correlated to the effective precipitation P_{120eff} cumulated over 120 days thus accounting for surface soil water balance through a simplified way. Moreover, rainfall values predicted by RCM COSMO-CLM model, previously subjected to downscaling approaches and to procedures for estimating uncertainties associated to simulation chain, are directly used to evaluate future possible variations of recurrence period P_{120} or P_{120eff} .

6. ACKNOWLEDGMENTS

This work is developed within the framework of Work Package 6.2.17 of the GEMINA project, funded by the Italian Ministry of Education, University and Research and the Italian Ministry of Environment, Land and Sea.

7. REFERENCES

- Hawkins E.d., Sutton R. (2009), *The Potential to Narrow Uncertainty in Regional Climate Predictions*. Bull. Amer. Meteor. Soc., 90, 1095–1107. (1)
- Meehl G.A., Arblaster J.M., Tebaldi C. (2007), *Contributions of natural and anthropogenic forcing to changes in temperature extremes over the United States*, Geophysical Research Letters, Vol. 34, L19709. (2)
- Intergovernmental Panel on Climate Change (2007) *Climate change 2007: the physical science basis*. In: Solomon S., Qin D., Manning M., Chen Z., Marquis M., Averyt K.B., Tignor M., Miller H.L. (eds) *Contribution of working group 1 to the fourth assessment report of the intergovernmental panel on climate change*. Cambridge University Press, Cambridge, pp 433–498. (3)
- Crozier M.J. (2010), *Deciphering the effect of climate change on landslide activity: A review*, Geomorphology, v. 124, p. 260–267. (4)
- Fowler A.M., Hennessy K.J. (1995), *Potential impacts of global warming on the frequency and magnitude of heavy precipitation*. Natural Hazards 11: 283–303. (5)

- Beniston M., Stephenson D. B., Christensen O. B., Ferro C. A. T., Frei C., Goyette S., Halsnaes K., Holt T., Jylhä K., Koffi B., Palutikoff J., Schöll R., Semmler T., and Woth, K. (2007) *Future extreme events in European climate; an exploration of Regional Climate Model projections* Climatic Change, 81, 71-95. (6)
- Kysely J., Beranová R., 2009 *Climate change effects on extreme precipitation in central Europe: uncertainties of scenarios based on regional climate models*. Theoretical and Applied Climatology, 95, 361-374. (7)
- Christensen J.H., Hewitson B., Busuioc A., Chen A., Gao X., Held I., Jones R., Koli R.K., Kwon W.-T., Laprise R., Rueda V.M., Mearns L., Menéndez C.G., Räisänen J., Rinke A., Sarr A. and P. Whetton, 2007: *Regional climate projections. Climate Change (2007), The Physical Science Basis*. Contribution of Working Group I to the Fourth Assessment Report of the Intergovernmental Panel on Climate Change, S. Solomon, D. Qin, M. Manning, Z. Chen, M. Marquis, K.B.Averyt, M. Tignor and H.L. Miller, Eds., Cambridge University Press, Cambridge, 847-940. (8)
- Leroueil S. (2000), *39th Rankine Lecture – Natural slopes and cuts: movement and failure mechanisms*. Géotechnique Volume 51, Issue 3,01 April 2001 ,pages197 –243. (9)
- Sidle R. C., and Ochiai H. (2006), *Landslides: Processes, Prediction, and Land Use*, Water Resour. Monogr. Ser., vol. 18, 312 pp., AGU, Washington, D. C., doi:10.1029/WM018. (10)
- Coe J.A. and Godt J.W., (2012), *Review of approaches for assessing the impact of climate change on landslide hazards*, In Eberhardt E., Froese C., Turner A.K., and Leroueil S., eds., *Landslides and Engineered Slopes, Protecting Society Through Improved Understanding*, Proceedings of the 11th International and 2nd North American Symposium on Landslides and Engineered Slopes, Banff, Canada, 3-8 June 2012, Taylor & Francis Group, London, v. 1, p. 371-377. (11)
- Dehn M., Burger G., Buma J. & Gasparetto P. (2000), *Impact of climate change on slope stability*. Engineering Geology, 55, 193–204. (12)
- Fowler H.J., Blenkinsop S., Tebaldi C. (2007) *Linking climate change modelling to impacts studies: recent advances in downscaling techniques for hydrological modelling*. Int J Climatol 27:1547–1578. (13)
- Huggel C., Khabarov N., Korup O. and Obersteiner M. (2012) *Physical impacts of climate change on landslide occurrence and related adaptation*. In: Clague, J.J., Stead. D. (eds.), *Landslides, Types, Mechanisms and Modelling*. Cambridge University Press, Cambridge UK, 121-133. (14)

- Lateltin O., Haemmig C., Raetzo H., Bonnard C. *Landslide risk management in Switzerland* Landslides December 2005, Volume 2, Issue 4, pp 313-320. (15)
- Dixon N. and Brook E. (2007) *Impact of predicted climate change on landslide reactivation: case study of Mam Tor, UK in Landslides*, Journal of the International Consortium on Landslides, v. 4 (2) pp. 137-147. (16)
- Comegna L., Picarelli L., Bucchignani E., Mercogliano P. (2012), *Potential effects of incoming climate changes on the behaviour of slow active landslides in clay* LANDSLIDES, Online First™, 14 Giugno 2012. ISSN: 1612-5118 (electronic version). (17)
- Comegna L., Tommasi P., Picarelli L., Bucchignani E., Mercogliano P. (2011), *The impact of climatic changes on the behaviour of active landslides in clay* Putting Science into Practice, Proc. Second World Landslide Forum, Roma, 3–7 October 2011, in press. (18)
- Zollo A.L., Mercogliano P., Turco M., Vezzoli R., Rianna G., Bucchignani E., Manzi M.P., and Montesarchio M. (2012), *Architectures and tools to analyse the impact of climate change on hydrogeological risk on Mediterranean area*. Technical report, CMCC. (19)
- Rockel B., Will A., and Hense A. *The regional climate model Cosmo-clm (cclm)*. Meteorologische Zeitschrift, 17(4):347–348, 2008. (20)
- Tommasi P., Pellegrini P., Boldini D., and Ribacchi R. (2006), *Influence of rainfall regime on hydraulic conditions and movement rates in the overconsolidated clayey slope of the Orvieto hill (Central Italy)*. Canadian Geotechnical Journal, 43:70–86. (21)
- Tommasi P., Boldini D., Caldarini G., Coli N. (2012), *Influence of infiltration on the periodic re-activation of slow movements in an overconsolidated clay slope* Canadian Geotechnical Journal, 2013, 50(1): 54-67, 10.1139/cgj-2012-0121. (22)
- Mansour M.F., Morgenstern N.R., Martin C.D. (2011), *Expected damage from displacement of slow-moving slides*, Landslides 7(1):117–131. (23)
- Tommasi P., Ribacchi R., and Sciotti M. (1997) *Slow movements along the slip surface of the 1900 porta cassia landslide in the clayey slope of the orvieto hill*. Rivista Italiana di Geotecnica, 2:49–58, 1997. (24)
- Vezzoli R., Pecora S., Zenoni E., (2012) *Data analysis to detect inhomogeneity, change points, trends in observations: an application to Po river discharge extremes* Research Papers Issue RP0138 Technical report, CMCC. (25)

- Klein Tank A.M.G., Zwiers F.W., and Zhang X. (2009), *Guidelines on analysis of extremes in a changing climate in support of informed decisions for adaptation*. Technical Report 72, World Meteorological Organization. (26)
- Alexandersson H. (1986), *A homogeneity test applied to precipitation data*. Journal of Climate, 6:661–675. (27)
- Winjngaard J.B., Klein Tank A.M.G., and Konnen G.P. *Homogeneity of 20th century European daily temperature and precipitation series*. Int. J. Climatol., 23:679–692, 2003. (28)
- Brunetti M., Buffoni L., Maugeri M., and Nanni T. (2000), *Precipitation intensity trend in Northern Italy*. International Journal of Climatology, 20:1017–1031. (29)
- Sneyers, R. (1990), *On the Statistical Analysis of Series of Observations*, WMO, Technical Note no.143, Geneva, Switzerland. Original French version, WMO, 1975. (30)
- Gauthier, T.D. (2001) *Detecting trends using spearman's rank correlation coefficient*. Environmental Forensics, 2:359–362, 2001. (31)
- Giorgi F., Bi X., Pal J. (2004), *Mean, interannual variability and trends in a regional climate change experiment over Europe. II: climate change scenarios (2071–2100)* Climate Dynamics (2004) 23: 839–858. (32)
- Zollo A.L., Montesarchio M., Manzi M.P., Cattanel L., Bucchignani E., and Mercogliano P., (2012), *Assessment of COSMO-CLM performances in simulating the past climate of Italy*. RP 145 Technical report, CMCC. (33)
- Meinshausen, M., S. J. Smith, K. V. Calvin, J. S. Daniel, M. L. T. Kainuma, J.-F. Lamarque, K. Matsumoto, S. A. Montzka, S. C. B. Raper, K. Riahi, A. M. Thomson, G. J. M. Velders and D. van Vuuren (2011), *The RCP Greenhouse Gas Concentrations and their Extension from 1765 to 2300*. Climatic Change (Special Issue). (34)
- Giorgi F., Lionello P. (2008), *Climate change projections for the Mediterranean region*, Global and Planetary Change 63 (2008) 90–104. (35)
- Coppola E., Giorgi F. (2010), *An assessment of temperature and precipitation change projections over Italy from recent global and regional climate model simulations*. International Journal of Climatology, 30, 11-32. (36)

IMPLICATIONS ON ECOSYSTEM SERVICES

Impacts on natural ecosystems - I

Distribution of bioclimate zones and their shifting due to climate change

Trabucco A.^{1,2*}, Metzger M.J.³, Zomer R.⁴, Spano D.^{1,5}

¹*Euro-Mediterranean Center for Climate Changes (CMCC), LAFENT Division, Sassari, Italy*

²*KU Leuven, Division of Forest, Nature and Landscape, Leuven, Belgium*

³*The University of Edinburgh, School of GeoSciences, Edinburgh, Scotland, UK*

⁴*Centre for Mountain Ecosystem Studies (CMES), Kunming Institute of Botany, Kunming, China*

⁵*Department of Science for Nature and Environmental Resources (DiPNeT), University of Sassari, Italy*

*Corresponding author: antonio.trabucco@cmcc.it

Abstract

Under climate change and biodiversity decline, there is a growing urgency to develop a consistent numerical stratification of world land surface into relatively homogeneous bioclimate strata. We describe a recently published Global Environmental Stratification (GEnS) based on a statistical approach, which ensures consistency and reproducible stratifications independent of personal bias. Statistical screening produced a subset of relevant bioclimate variables, which were then compacted into fewer independent dimensions using Principal Components Analysis. An ISODATA clustering routine was then used to classify the principal components into relatively homogenous environmental strata. The strata were aggregated into global environmental zones based on the attribute distances between strata to provide structure and support and a consistent nomenclature. The GEnS has a 30 arc-sec resolution and consists of 125 strata, aggregated into 18 global environmental zones. The stratification was compared to nine existing global and national classifications (Kappa statistic 0.54±0.72) indicating good agreement in ecosystem patterns between existing maps and the GEnS.

The impacts of projected future climate on the spatial distribution of Gens zones, and the associated ecoregions and ecosystem productivity, is simulated for the Kailash Sacred Landscape (KSL), in the Himalaya. Projected climate change impact was there modeled by reconstructing the GEnS based upon future climate conditions and identifying the change in spatial distribution of bioclimatic zones. Results indicate that large and significant impacts can be expected in the KSL by the year 2050, within all bioclimatic zones and ecoregions, and with significant consequences for biodiversity, ecosystems, ecosystem services, conservation efforts and sustainable development policies in the region.

Keywords: *Environmental stratification; bioclimate indicators; Climate Change; Himalaya; NPP*



1. INTRODUCTION

Under climate change and biodiversity decline, there is a growing urgency for integration and coordination of environmental data collected across different climate conditions, linking *in situ* observations with earth simulations (Bunce *et al.*, 2008; Scholes *et al.*, 2008), and for assessments relating to the stock and change of global ecosystem resources and biodiversity (Scholes *et al.*, 2008). Climate is the main determinant of environmental patterns at continental and global scale (Odum, 1983; Godron, 1994), where climatically similar areas have similar potentials to support ecosystems (Klijn & de Haes, 1994; Paruelo *et al.*, 1995). A consistent stratification of land based on climate into relatively homogenous strata provides a valuable spatial framework for comparison, aggregation and analysis of environmental data and trends across large heterogeneous areas (Leathwick *et al.*, 2003; Metzger *et al.*, 2005). Most of the available bioclimate classification schemes (von Humboldt, 1867; Köppen, 1900; Holdridge, 1947; Thornthwaite, 1948) provide limited regional detail by distinguishing only 10-30 classes globally. More detailed approaches to distinguish global eco-regions (Bailey, 1998; Olson *et al.*, 2001) rely heavily on expert judgement for interpreting class divisions, making it difficult to ensure reliability across the world (Lugo *et al.*, 1999; Metzger *et al.*, 2005).

This paper presents a recently published Global Environmental Stratification (GENS), distinguishing 125 strata and eighteen zones globally at high spatial resolution (30 arc-sec or ~1 km at equator). The stratification is based on statistical clustering so that subjective choices are explicit, their implications are understood and the strata can be seen in the global context. This is of particular importance where large-scale continuous gradients are involved over thousands of kilometres. Statistical methods ensure consistency and the resulting stratifications are reproducible and, as far as possible, independent of personal bias (Leathwick *et al.*, 2003; Jongman *et al.*, 2006). Multivariate clustering of climate data has already been successfully implemented in several national and sub-continental studies to create detailed stratifications (Jongman *et al.*, 2006, Leathwick *et al.*, 2003, Tappan *et al.*, 2004). These datasets have been used for stratified random sampling of ecological resources (Firbank *et al.*, 2003; Bunce *et al.*, 2008), the selection of representative study sites (Palma *et al.*, 2007), and summary reporting of trends and impacts (Thuiller *et al.*, 2005; Metzger *et al.*, 2008b).

In the second part of this paper, a geospatial modelling approach is used on the Gens bioclimatic stratification to explore the impacts of projected climate change on the spatial distribution of bioclimatic zones and ecosystem productivity within the Kailash Sacred Landscape (KSL), a transboundary area shared among China, India and Nepal.

2. THE GLOBAL ENVIRONMENTAL STRATIFICATION - GENS

2.1 Bioclimate indicators

Climate classifications are implemented on bioclimate indicators, which are directly related to plant physiological processes determining primary productivity and therefore also directly influencing provisional ecosystem services (e.g. food, fibre, and bio-energy production). Several sets of bioclimate indicators have been proposed and implemented in previous climate classifications. In the construction of a statistically-based environmental classification several bioclimate indicators were aggregated from different sources and screened for their statistical and ecological significance.

Global spatial climate data from the WorldClim Global Climate Dataset was used (Hijmans *et al.*, 2005). WorldClim has the greatest spatial resolution (30 arc-sec), enabling representation of regional environmental gradients, which dissolve at coarser resolutions, particularly in mountainous and other areas with steep climate gradients (Hijmans *et al.*, 2005; Hazeu *et al.*, 2011).

The dataset was created by spatial interpolation of climate observations from over 45,000 weather stations obtained from major climate databases. ANUSPLIN software was used to calculate thin plate smoothing splines using the latitude, longitude and elevation as independent variables (Hutchinson, 1998a, b). Variables included are monthly total precipitation, monthly mean, minimum and maximum temperature, and nineteen derived bioclimate variables.

Indicators of moisture availability, crucial determinant for plant growth (Thorntwaite, 1948; Prentice *et al.*, 1992), have been calculated from WorldClim data (Trabucco *et al.*, 2008) and included in the analysis. These include: Potential EvapoTranspiration (PET), calculated using the Hargreaves method; an Aridity Index expressing the ratio between annual precipitation and PET; and Actual EvapoTranspiration (AET) calculated for a fixed Soil Water Holding Capacity and vegetation coefficients (Trabucco *et al.*, 2008).

An additional eighteen bioclimate variables, identified by reviewing earlier studies, have been calculated using the available data, including those reflecting the growing season (Prentice *et al.*, 1992; Sitch *et al.*, 2003), a specific indicator developed for the Mediterranean (Emberger, 1930), and additional indicators used to distinguish isoclimate regions (Sayre *et al.*, 2009).

2.2 Constructing the stratification

The construction of the stratification consisted of three stages. The detailed steps of the complete procedure are summarised in Fig. 1.

Firstly, the initial pool of 42 variables was screened to remove those variables with very high correlations (correlation coefficient > 0.9) and select a subset of easily interpreted ecologically variables that represent the dominant global gradients. The subsequent PCA of the remaining 36 variables revealed that the first three components, explaining 99.9% of the total variation, were determined by only four variables: growing degree-days on a 0 °C base, reflecting latitudinal and altitudinal temperature gradients; the aridity index, an expression of plant available moisture; and temperature and potential evapotranspiration seasonality, which express both seasonality and continentality. These four variables were subsequently used in the statistical clustering algorithm to distinguish 125 strata in the data.

The second stage entailed the actual statistical clustering. The Iterative Self-Organizing Data Analysis Technique (ISODATA) (Tou & Gonzalez, 1974) was used to cluster the Principal Components of the four variables into environmental strata. ISODATA is iterative in that it repeatedly performs an entire classification and recalculates statistics. Self-organizing refers to the way in which it locates clusters with minimum user input. The ISODATA method uses minimum Euclidean distance in the multi-dimensional feature space of the Principal Components to assign a class to each candidate grid cell.

Finally, post-processing has made the dataset more accessible, including the development of a consistent nomenclature, an appropriate map legend and an aggregation scheme (Figure 2).

The PCA of the four clustering variables shows that each component mainly relates to one variable, although the other variables also display some influence. PC1 is mainly determined by the GDD, while

PC2 and PC3 by aridity and seasonality respectively. A global map (Figure 3) was constructed using the mean values per stratum of the first three Principal Components to define the red-green-blue colour scheme. The resulting legend produces a map that clearly distinguishes known climate zones, as more detailed divisions within these zones.

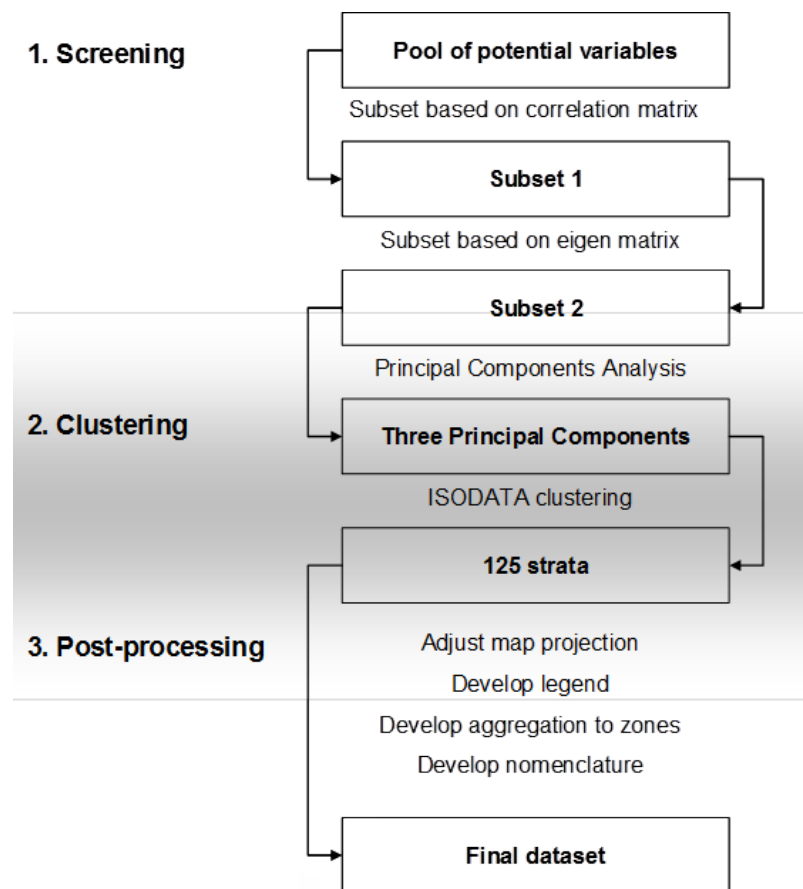


Fig. 1: Flowchart illustrating the procedure for constructing the global environmental stratification

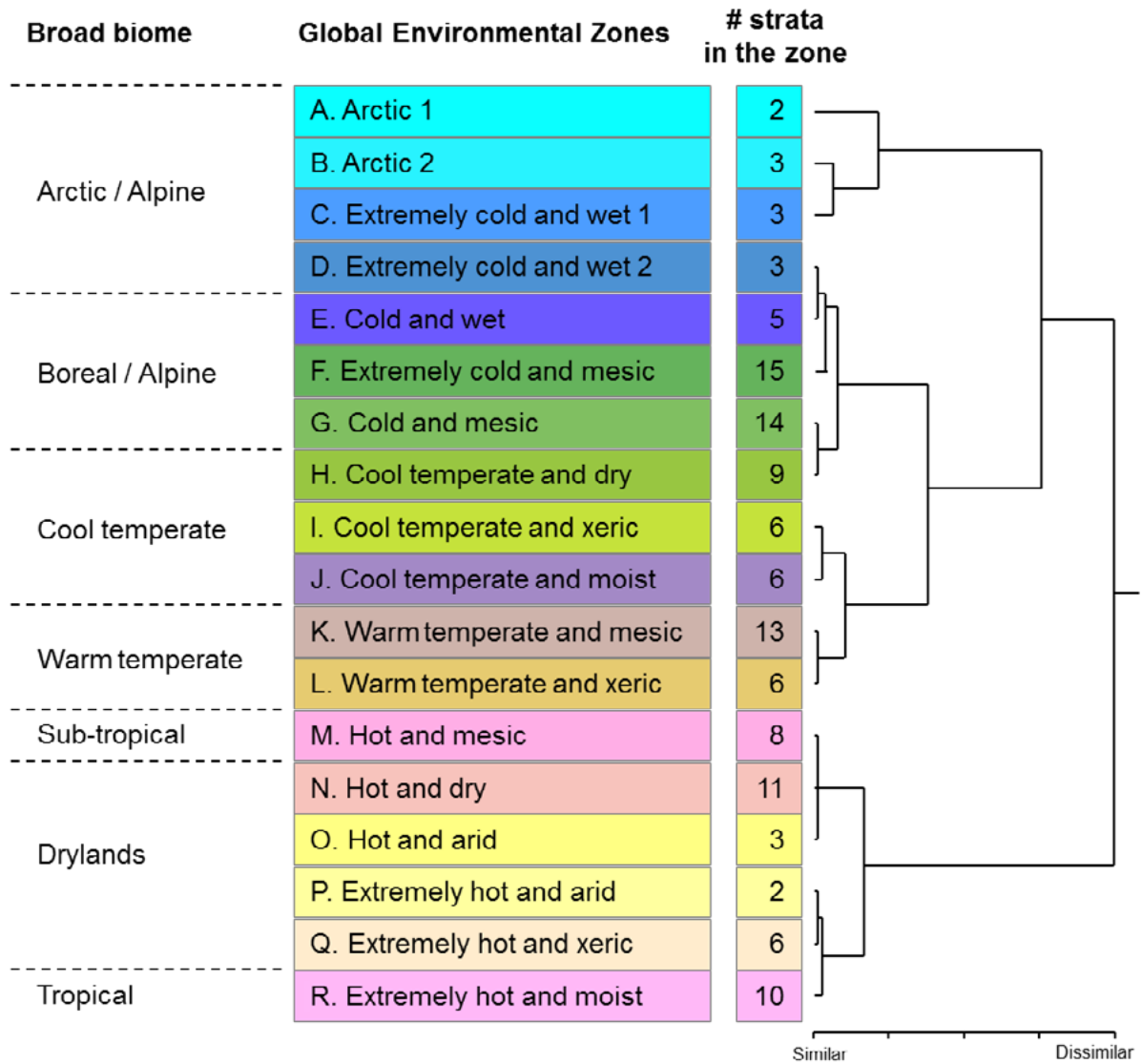


Fig. 2: Dendrogram based on Euclidean distance between cluster means illustrating the relation between the eighteen aggregated Global Environmental Zones and the number of strata per zone

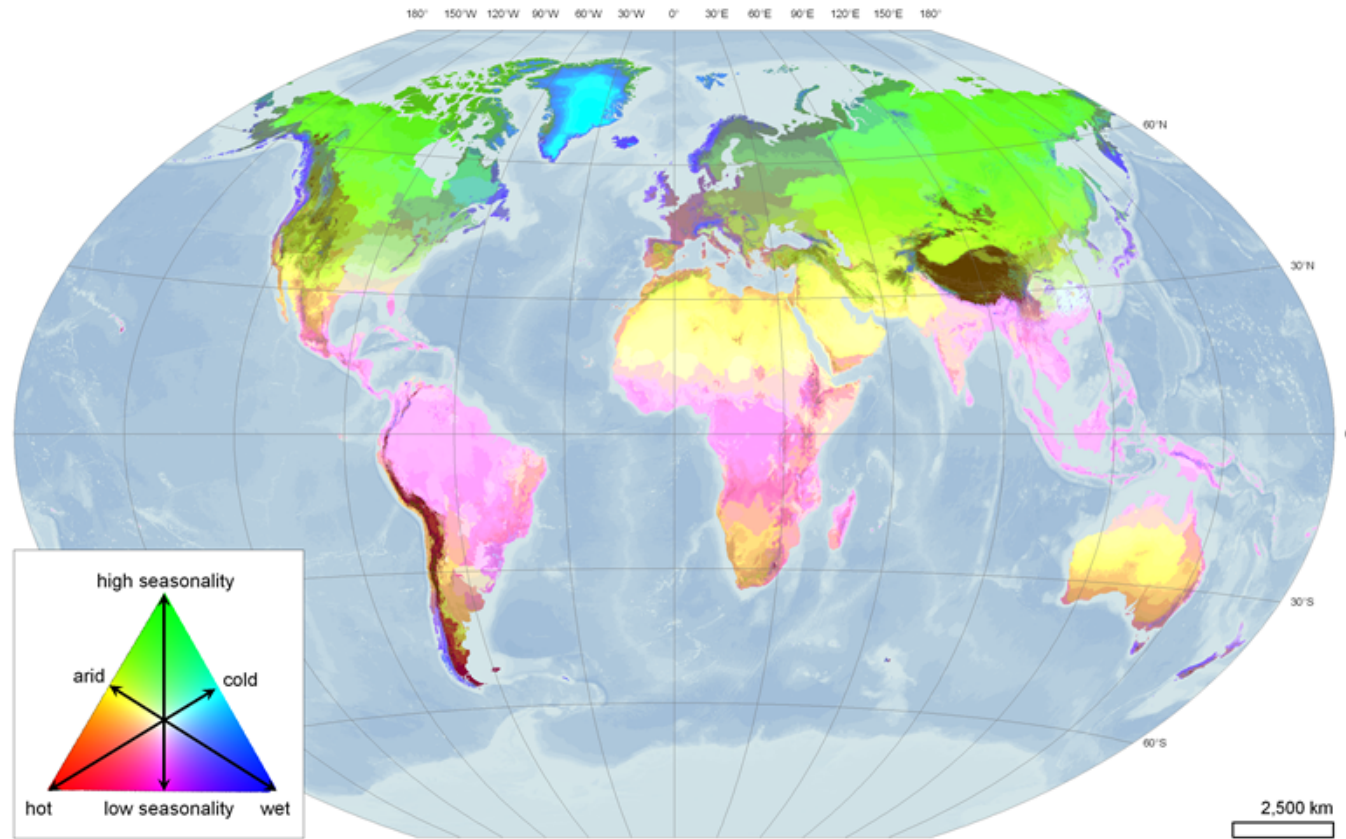


Fig. 3: Map of the global environmental stratification, depicting 125 strata at a 30 arc-sec (~ 1km at equator). PC1 (related to annual temperature gradient) was used to define the amount of red. PC2 (Aridity) the blue coloration and PC3 (Seasonality) the green coloration. The legend provides a visual combination of the three main climate gradients incorporated in the clusteri

2.3 Evaluating the stratification

The reliability of the patterns derived by the statistical clustering can be tested by comparing them to other datasets. The strength of agreement was determined by calculating Kappa statistics (Monserud & Leemans, 1992) between the GEnS and nine climate classifications: WWF ecoregions (Olson *et al.*, 2001); Köppen map of the world (Peel *et al.*, 2007); European Environmental Stratification (Metzger *et al.*, 2005); isoclimate maps for the United States (Sayre *et al.*, 2009), South America (Sayre *et al.*, 2008) and Africa (Sayre *et al.*); ecoregions map of the United States (CEC1997); land classification of Great Britain (Bunce *et al.*, 1996); and a geoclimate stratification of Spain (Regato *et al.*, 1999). Kappa values for the comparison of the GEnS with existing climate classifications range between 0.54 and 0.72 indicating ‘good’ and ‘very good’ comparisons.

At a global scale, climate is the main determinant of environmental patterns (Walter & Lieth, 1964; Odum, 1983; Godron, 1994). However, geomorphology, hydrology, geology, and soils follow climate in the conceptual hierarchy (Klijn & de Haes, 1994; Sayre *et al.*, 2009), but are not included mainly because of the difficulties in obtaining consistent and reliable data. If required, the climate stratification can be integrated with other spatial datasets (e.g. soils) to provide additional thematic detail. There are also limitations to the climate data used to construct the GEnS, which will affect its quality. The high resolution of the climate surface implies spatial variability of data quality, depending on the local climate variability in an area, the quality and density of the observations, and the degree to which a spline can be fitted through it. Locally important climate drivers, e.g. those caused by aspect in mountain areas or the formation of sea fog along coastal ranges are also poorly represented.

2.2 The Kailash Sacred Landscape

The KSL is a recently designated “transboundary landscape”, covering over 31,000 km² across China, India and Nepal (Figure 4). The landscape is rich in biodiversity and culture, with high levels of both natural and agricultural biodiversity, but also high rates of poverty and daunting environmental challenges (Zomer and Oli, 2011).

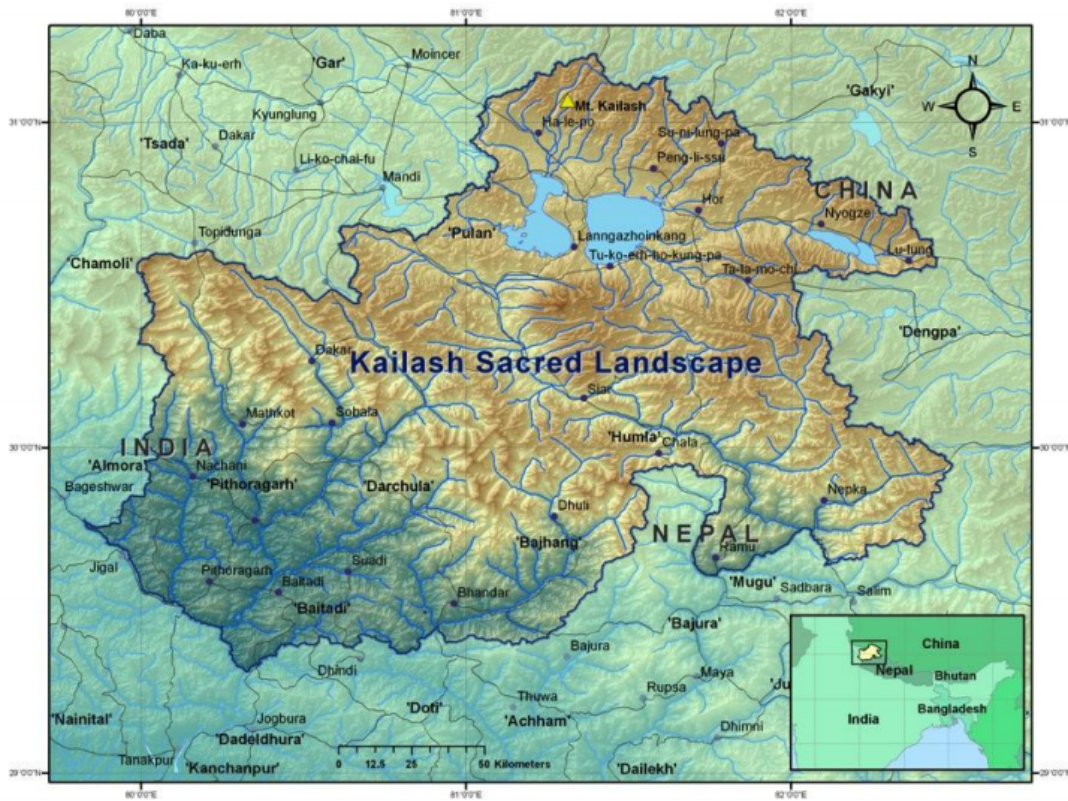


Fig. 4: Map of Kailash Sacred Landscape, a mountainous transboundary region comprised of portions of the Tibet Autonomous Region of China, northern India and northwestern Nepal, including the sacred Mt. Kailash.

A wide range of bio-climatic zones is observed across the steep elevation gradient of KSL ranging from below 500 m to 7,694 m asl. A pronounced Himalayan orographic rainshadow effect creates arid conditions upon the high, cold Tibetan Plateau portions of the KSL, and delineates the major bioclimatic distinction between monsoonal and continental influences. Bioclimatic zones include hot and semiarid regions in the lower hills, lush green and humid valleys in the mid-hills, extensive mountain forests, moist alpine meadows, arid trans-Himalayan valleys, high altitude cold deserts, and permanent snow and ice along the crest of the Himalaya. These habitats support dwindling numbers of threatened wildlife including musk deer, blue sheep, snow leopard, Tibetan antelopes and many other charismatic, endangered and/or rare species (Zomer and Oli, 2011).

2.3 KSL Bioclimate stratification

In this study, the GEnS classification clipped over the KSL (KSL-EnS) is used as a baseline for estimating the actual spatial distribution of bioclimatic zones and ecoregions of the study area. The interpretation of the KSL-EnS zones and strata was based on expert knowledge, secondary sources, and a land cover analysis using remote sensing. A georeferenced photo-survey of the study area was used for ground-truthing. The zones and strata were associated with broad ecological zones (Terrestrial ecoregions of the world (Olson et al., 2001)), FAO Land Cover of Himalaya (FAO, 2010) and Forest and Vegetation Types of Nepal (TISC, 2002)), described in terms of dominant vegetation, and aggregated into ecoregions as per the nomenclature of Olson (2001).

The KSL-EnS identified seven bioclimatic zones (Figure 5a and Table 2) ranging from “Extremely Cold and Wet” to “Extremely Hot and Mesic” at current conditions. Within these seven zones, 34 strata were identified. Each of the 34 strata were characterized by their dominant vegetation types and aggregated into twelve ecoregions (Figure 5c), which were labelled according to Olson (2001). A comparison of the KSL ecoregional classification with Olson (2001) and TISC (2002) shows a good general correspondence, but with greatly improved resolution.

2.4 Projected Impacts of Climate Change on ecosystem distribution by 2050

The KSL-EnS for 2050 was reconstructed based upon the future projected values of the four significant climate variables used in the GEnS classification (growing degree-days on a 0 °C base, aridity index, temperature and PET seasonality). The signature profile that classifies strata as a function of the four significant climate variables was reconstructed for the KSL-EnS using a multivariate analysis. These profiles were used to construct the projected future spatial distribution of KSL-EnS strata for the year 2050, using climate projections (HADCM3 - SERS-A2) downscaled at 1 km resolution (Ramirez and Jarvis, 2010).

Results indicate that a significant and substantial change in the distribution, extent, and productivity of terrestrial ecosystems can be expected by the year 2050. All four of the significant variables used in the statistical analysis show substantial change. Both mean annual temperature and mean annual precipitation increase substantially in the SERS A2 scenario, consistent with current trends (Shrestha et

al., 2012). The standard deviation of the mean monthly temperature across the year, a measure of seasonality, shows a decrease throughout the area, reflecting warmer winters.

Both the distribution and the extent of the zones and strata are substantially shifted by 2050 (Table 1 and Figure 5), with marked expansion of warmer and mesic zones. Based on their average elevation, each of the zones migrates upwards from 285 m to over 600 m along the elevation gradient, except for the highest elevation zone which remains relatively the same. Several strata disappear altogether under future conditions. This change would indicate a significant threat to biodiversity and a high risk of extinction for species endemic to these strata, or adapted to its specific conditions.

KSL-EnS Zone	Ecoregion	KSL-EnS Strata	Mean Elev	Elev Range	Mean Elev	Elev Range	Area	
			(m asl)	(m)	(m asl)	(m)	(km ²)	(km ²)
Year			2000		2050		2000	2050
Extremely cold and wet								
	Nival Zone	(C2 D1 D2 D3)	5431	3184	5653	2819	3478	1355
Extremely cold and mesic								
	West Tibetan Plateau Alpine Steppe	(F4*)	5354	1277	5652	527	3186	163
	Grandise Mountains Alpine Tundra	(F13*)	4690	1095	5043	1064	3309	1250
	Upper Alpine Meadow	(F4** F7 F8 F13** F15)	4728	2540	5007	2748	9385	12878
Cold and mesic								
	Alpine Shrub And Meadow	(G4 G7 G8)	3862	1932	4342	2359	1015	3843
	Subalpine Conifer Forest	(G11 G12 G13)	3609	2518	4014	2368	2031	1467
Cool temperate and moist								
	Subalpine Mixed Forest	(J1 J3 H5 H9)	3041	1945	3573	1881	760	794
	Temperate Conifer Forest	(J4 J5)	2794	1876	3160	2146	758	1341
Warm temperate and mesic								
	Temperate Broadleaf Forest	(K1 K2 K5 K7)	2190	2369	2376	2574	2946	3481
	Subtropical Pine/Mixed Forest	(K10 K13 L3)	1727	2141	2761	844	1895	34
Hot and mesic								
	Subtropical Pine Forest	(N1 N2 N3 N5 N8)	1323	1774	1640	1878	2000	2526
Extremely hot and mesic / moist								
	Tropical Broadleaved Forest	(M2 M8 R3)	922	1304	1225	2317	447	2078

Table 1: Ecoregions and their mean elevation, altitudinal range, and total area in 2000 and 2050

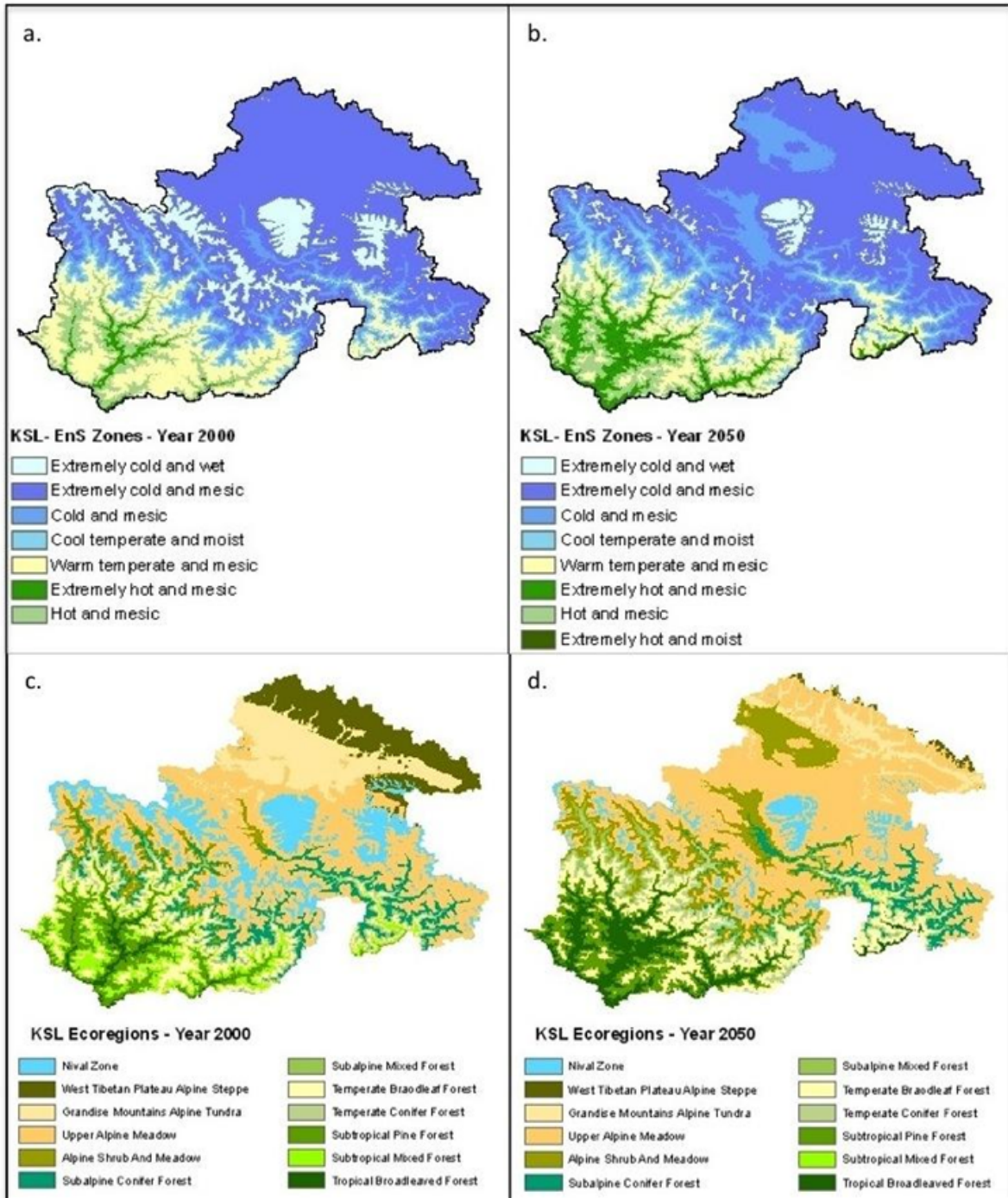


Fig. 5: Distribution of KSL-EnS bioclimatic zones and ecoregions in year 2000 and projected for year 2050

2.5 Modelling changes in productivity

Data from the MODIS Net Primary Production (Running et al., 2004) was used to characterize average ecosystem productivity (tons C/km²) within each of the ecoregions in the KSL. This average NPP value was then multiplied by the area of the respective ecoregion, currently, and as project under future climate. Changes in the areal extent of these ecosystems are used to provide estimates of the potential changes in productivity within the KSL region.

The total annual NPP varies generally across the KSL from fairly high (Table 2) for lower elevation strata (e.g. 9 t C per ha for “Tropical Broadleaved Forest”) to areas of very low productivity at higher elevations. NPP rates were found to be highly correlated with elevation. For the entire KSL area, annual NPP is nearly 10 million tons C per year, with Temperate Broadleaved Forest contributing more than 20% of the total. Increases in both temperature and precipitation are projected to impact the productivity of all the KSL, by the expansion and shifting of higher productivity strata into current lower productivity areas. Overall, the productivity of the entire KSL is projected to increase by nearly 1.9 million tons C, an increase of over 16%.

Ecoregion	Mean NPP	Total NPP	Total NPP	NPP Change
	(tC/km ²)	(tC)	(tC)	(tC)
Year	2000	2000	2050	2050-2000
Nival Zone	68	235,500	91,800	-143,700
West Tibetan Plateau Alpine Steppe	64	202,300	10,400	-191,900
Grandise Mountains Alpine Tundra	75	247,000	93,300	-153,700
Upper Alpine Meadow	128	1,205,000	1,653,600	448,600
Alpine Shrub And Meadow	336	340,900	1,290,800	949,900
Subalpine Conifer Forest	371	754,400	544,900	-209,500
Subalpine Mixed Forest	528	401,000	419,000	18,000
Temperate Conifer Forest	604	457,900	810,100	352,200
Temperate Braodleaf Forest	739	2,176,300	2,571,500	395,200
Subtropical Pine /Mixed Forest	819	1,552,900	27,900	-1,525,000
Subtropical Pine Forest	887	1,773,800	2,240,300	466,500
Tropical Broadleaved Forest	912	407,700	1,895,300	1,487,600
Total		9,754,700	11,648,700	1,894,000

Table 2: Average net primary productivity (NPP), characterized by remote sensing assessments, is associated to each ecoregion in the KSL. The total NPP of the KSL for actual and future conditions (2050) is projected in association with changes of ecoregion distribution.

3. CONCLUSIONS

Since the GEnS method uses a purely quantitative statistical approach to characterize current conditions based upon climate, it can be applied to develop similar stratifications based upon predicted future climate conditions. The change in distribution of bioclimatic strata is used as a surrogate measure of the potential macro-level impacts on terrestrial ecosystems. When combined with other ecosystem or landuse data, these changes can be interpreted in terms of ecosystems services, landuse types, wildlife habitat, or risks and opportunities for agricultural production. The GEnS dataset form a global unifying framework within the Group on Earth Observations Biodiversity Observation Network and is publicly available to support global ecosystem research.

4. REFERENCES

- Bailey R.G. (1998) *Ecoregions: The Ecosystem Geography of Oceans and Continents*. Springer-Verlag, New York.
- Beniston M. (2003) *Climatic change in mountain regions: a review of possible impacts*. *Climatic Change*, 59(1), 5–31.
- Bunce R.G.H., Barr C.J., Clarke R.T., Howard D.C. & Lane A.M.J. (1996) *ITE Merlewood Land Classification of Great Britain*. *Journal of Biogeography*, 23, 625-634.
- Bunce R.G.H., Metzger M.J., Jongman R.H.G., Brandt J., de Blust G., Elena-Rossello R., Groom G.B., Halada, L., Hofer, G., Howard, D., Kovář, P., Múcher, C., Padoa-Schioppa, E., Paelinx, D., Palo, A., Perez-Soba, M., Ramos, I., Roche, P., Skånes, H. & Wrška, T. (2008) *A standardized procedure for surveillance and monitoring European habitats and provision of spatial data*. *Landscape Ecology*, 23, 11-25.
- CEC (1997) *Ecological Regions of North America, toward a Common Perspective*. In, p. 71. Commission for Environmental Cooperation, Montréal, Canada.
- Chen I.-C., Shiu H.-J., Benedick S., Holloway J.D., Chey V.K., Barlow H.S., Hill J.K. and Thomas C.D. (2009) *Elevation increases in moth assemblages over 42 years on a tropical mountain*. *Proceedings of the National Academy of Sciences of the United States of America*, 106(5), 1479–1483.

- Emberger L. (1930) *Sur une formule climatique applicable en géographie botanique*. Comptes Rendus Hebdomadaires des Séances de l'Académie des Sciences, 181, 389-391.
- FAO, (2010) *Land Cover of Himalaya Region*. FAO, Rome.
- Firbank L.G., Barr C.J., Bunce R.G.H., Furse M.T., Haines-Young R.H., Hornung M., Howard D.C., Sheail J., Sier A.R.J. & Smart S.M. (2003) *Assessing stock and change in land cover and biodiversity in GB: an introduction to the Countryside Survey 2000*. Journal of Environmental Management, 67, 207-218.
- Godron M. (1994) *The natural hierarchy of ecological systems*. Ecosystem classification for environmental management (ed. by F. Klijn), pp. 69-83. Kluwer Academic Publisher, Dordrecht.
- Hazeu G.W., Metzger M.J., Mucher C.A., Perez-Soba M., Renetzeder C. & Andersen E. (2011) *European environmental stratifications and typologies: an overview*. Agriculture, Ecosystems & Environment, 142, 29-39.
- Hijmans R.J., Cameron S.E., Parra J.L., Jones P.G. & Jarvis A. (2005) *Very high resolution interpolated climate surfaces for global land areas*. International Journal of Climatology, 25, 1965-1978.
- Holdridge L.R. (1947) *Determination of world plant formations from simple climatic data*. Science, 105, 367-368.
- Hutchinson M.F. (1998a) *Interpolation of rainfall data with thin plate smoothing splines: I two dimensional smoothing of data with short range correlation*. Journal of Geographic Information and Decision Analysis, 2, 152-167.
- Hutchinson M.F. (1998b) *Interpolation of rainfall data with thin plate smoothing splines: II analysis of topographic dependence*. Journal of Geographic Information and Decision Analysis, 2, 168-185.
- Jongman R.H.G., Bunce R.G.H., Metzger M.J., Mucher C.A., Howard D.C. & Mateus V.L. (2006) *Objectives and applications of a statistical environmental stratification of Europe*. Landscape Ecology, 21, 409-419.
- Klijn F. & de Haes H.A.U. (1994) *A hierarchical approach to ecosystems and its implications for ecological land classification*. Landscape Ecology, 9, 89-104.
- Köppen W. (1900) *Versuch einer Klassifikation der Klimat, Versuchsweise nach ihren Beziehungen zur Pflanzenwelt*. Geographische Zeitschrift, 6, 593-611 ; 657-679.

- La Sorte F.A. and Jetz W. (2010) *Projected range contractions of montane biodiversity under global warming*. Proceedings. Biological sciences / The Royal Society, 277(1699), 3401–3410.
- Leathwick J.R., Overton J.M. & McLeod M. (2003) *An environmental domain classification of New Zealand and its use as a tool for biodiversity management*. Conservation Biology, 16, 1612-1623.
- Lugo A.E., Brown S.L., Dodson R., Smith T.S. & Shugart H.H. (1999) *The Holdridge life zones of the conterminous United States in relation to ecosystem mapping*. Journal of Biogeography, 26, 1025-1038.
- Maikhuri R., Rao K. and Semwal R. (2001) *Changing scenario of Himalayan agroecosystems: loss of agrobiodiversity, an indicator of environmental change in Central Himalaya, India*. The Environmentalist, 21(1), 23–39.
- Metzger M.J., Bunce R.G.H., Jongman R.H.G., Múcher C.A. & Watkins J.W. (2005) *A climatic stratification of the environment of Europe*. Global Ecology & Biogeography, 14, 549-563.
- Monserud R.A. & Leemans R. (1992) *Comparing global vegetation maps with the Kappa statistic*. Ecological Modelling, 62, 275-293.
- Myers N., Mittermeier R.A., Mittermeier C.G., da Fonseca G.A. and Kent J., (2000) *Biodiversity hotspots for conservation priorities*. Nature, 403(6772), 853–858.
- Odum H.T. (1983) *Systems ecology, an introduction*. John Wiley and Sons, New York.
- Olson D.M., Dinerstein E., Wikramanayake E.D., Burgess N.D., Powell G.V.N., Underwood E.C., D'Amico J.A., Itoua I., Strand H.E., Morrison J.C., Loucks C.J., Allnutt T.F., Ricketts T.H., Kura Y., Lamoreux, J.F., Wettengel W.W., Hedao P. & Kassem K.R. (2001) *Terrestrial Ecoregions of the World: A New Map of Life on Earth*. BioScience, 51, 933-938.
- Palma J.H.N., Graves A.R., Bunce R.G.H., Burgess P.J., de Filippi R., Keesman K.J., van Keulen H., Liagre F., Mayus M., Moreno G., Reisner Y. & Herzog F. (2007) *Modeling environmental benefits of silvoarable agroforestry in Europe*. Agriculture, Ecosystems & Environment, 119, 320-334.
- Paruelo J.M., Lauenroth W.K., Epstein H.E., Burke I.C., Aguiar M.R. & Sala O.E. (1995) *Regional Climatic Similarities in the Temperate Zones of North and South America*. Journal of Biogeography, 22, 915-925.

- Peel M.C., Finlayson B.L. & McMahon T.A. (2007) *Updated world map of the Koppen-Geiger climate classification*. Hydrology and Earth System Sciences, 11, 1633-1644.
- Prentice I.C., Cramer W., Harrison S.P., Leemans R., Monserud R.A. & Solomon A.M. (1992) *A global biome model based on plant physiology and dominance, soil properties and climate*. Journal of Biogeography, 19, 117-134.
- Ramirez J. and Jarvis A. (2010) *Downscaling global circulation model outputs*, Cali, Colombia: CIAT.
- Regato P., Castejón M., Tella G., Giménez S., Barrera I. & Elena-Rosselló R. (1999) *Cambios recientes en los paisajes de los sistemas forestales de España*. Investigación Agraria. Sistemas y Recursos Forestales, 1, 383-398.
- Running S.W., Nemani R.R., Heinsch F.A., Zhao M., Reeves M. and Hashimoto H. (2004) *A continuous satellite-derived measure of global terrestrial primary production*. Bioscience, 54(6), 547–560.
- Sayre R., Comer P., Warner H. & Cress J. (2009) *A new map of standardized terrestrial ecosystems of the conterminous United States*, U.S. Geological Survey Professional Paper 1768. In, p. 17. U.S. Geological Survey, Reston, Virginia.
- Sayre R., Bow J., Josse C., Sotomayor L. & Touval J. (2008) *Terrestrial Ecosystems of South America*. North America Land Cover Summit-A Special Issue of the Association of American Geographers (ed. by J.C. Campbell, K. Bruce Jones and J.H. Smith).
- Schild A., (2008) *ICIMOD's Position on Climate Change and Mountain Systems*. Mountain research and development.
- Scholes R.J., Mace G.M., Turner W., Geller G.N., Jurgens N., Larigauderie A., Muchoney D., Walther B.A. & Mooney H.A. (2008) *ECOLOGY: Toward a Global Biodiversity Observing System*. Science, 321, 1044-1045.
- Sharma E., Chettri N., Tse-ring K., Shrestha A.B., Jing F., Mool P. and Eriksson M. (2009) *Climate change impacts and vulnerability in the Eastern Himalayas*, Kathmandu: ICIMOD.
- Shrestha U.B., Gautam S. and Bawa K.S. (2012) *Widespread Climate Change in the Himalayas and Associated Changes in Local Ecosystems*. PLoS One, 7(5)

- Sitch S., Smith B., Prentice I.C., Arneth A., Bondeau A., Cramer W., Kaplan J.O., Levis S., Lucht W., Sykes M.T., Thonicke K. & Venevsky S. (2003) *Evaluation of ecosystem dynamics, plant geography and terrestrial carbon cycling in the LPJ Dynamic Vegetation Model*. *Global Change Biology*, 9, 161-185.
- Tappan G.G., Sall M., Wood E.C. & Cushing M. (2004) *Ecoregions and land cover trends in Senegal*. *Journal of Arid Environments*, 59, 427-462.
- Thornthwaite C.W. (1948) *An Approach toward a Rational Classification of Climate*. *Geographical Review*, 38, 55-94.
- Thuiller W., Lavorel S., Arañjo M.B., Sykes M.T. & Prentice I.C. (2005) *Climate change threats to plant diversity in Europe*. *Proceedings of the National Academy of Sciences of the United States of America*, 102, 8245-8250.
- Tingley M.W., Monahan W.B., Beissinger S.R. and Moritz C. (2009) *Birds track their Grinnellian niche through a century of climate change*. *Proceedings of the National Academy of Sciences of the United States of America*, 106(2), 19637–19643.
- Tisc M., (2002) *Forest and Vegetation Types of Nepal*.
- Tou J.T. & Conzalez R.C. (1974) *Pattern Recognition Principles*. Addison-Wesley Publishing Company, Reading, Massachusetts.
- Trabucco A., Zomer R.J., Bossio D.A., van Straaten O. & Verchot L.V. (2008) *Climate change mitigation through afforestation/reforestation: A global analysis of hydrologic impacts with four case studies*. *Agriculture, Ecosystems & Environment*, 126, 81-97.
- von Humboldt A. (1867) *Ideen zu einem Geographie der Pflanzen nebst einem naturgemälde der Tropenländer*. F.G. Cotta, Tübingen.
- Walter H. & Lieth H. (1964) *Klimadiagramm Weltatlas*. In. VEB Gustaf Fischer Verlag, Jena.
- Zomer R.J. and Oli K.P. (2011) *Kailash Sacred Landscape Conservation Initiative*, Kathmandu: ICIMOD.

Influence of population density and climate on the dynamics of the black grouse (*Tetrao tetrix*) populations in the Piedmont region (Italy).

Andrea Mignatti ^{1*}, Renato Casagrandi ¹, Antonello Provenzale ² and Marino Gatto¹.

¹*Dip. di Elettronica e Informazione, Politecnico di Milano, Via Ponzio 34/5, Milano, Italy.*

²*Institute of Atmospheric Sciences and Climate, CNR, Corso Fiume 4, Torino, Italy.*

* Corresponding author: mignatti@elet.polimi.it

Abstract

Because of its particular environmental needs and sensitivity to the human disturbance, *Tetrao tetrix* is a key species in studying the effect of climate change on the Alpine fauna. The majority of the studies on how the climate affects black grouse dynamics are conducted on the “lowland” populations at the northern latitudes, while less is known about Alpine populations, at the Southern edge of the species distribution.

The population abundance of black grouse in Italy constantly declined in the last decades. Here we study the influence of geographical localization, population density and meteorological conditions on the annual growth rate of the black grouse populations in 17 Alpine districts of the Piedmont region (Italy), using census data from 1999 to 2009. We first separately study the linear correlation of the growth rate with the male density and several meteorological variables, then we develop a single multivariate model that includes all the major effects. Using the climatic predictions produced with a regional model, we forecast the future abundance and growth rate of the population. Overall, our results show that in density dependence is in all districts the major driver of population dynamics. Moreover, using the analysis of covariance and an agglomerative clustering algorithm, we identify two different clusters of districts, characterized by the same density dependence parameter, but with different carrying capacities (3.97 and 6.04 Males/100 ha). As for climate, the growth rate decreases as the increasing of the mean temperature measured in the second half of April, just before the critical period of the formation of leks. Using climatic simulations based on the IPCC scenario A1B as forcing of our best multivariate model, we found that climate change should not cause, *per se*, a major risk of extinction for the population.

Keywords: *Italian Alps, tetraonids, clustering, bayesian model averaging, population dynamics.*



1. INTRODUCTION

The black grouse (*Tetrao tetrix*) is a large tetraonid mainly distributed in the northern part of Eurasia but present on the Alps. The mating season occurs between April and May, when the females reach the leks where the males sing. The females that successfully mate, move to areas suitable for nesting to lay eggs, which hatch after 3-4 weeks. The hens and their chicks live together until autumn, when the young males leave their mother. The female juveniles disperse in two different periods, in October and in the subsequent spring [1; 2]. The first days after hatching, in June, are the period characterized by the highest mortality rate for both hens and chicks. Hens are in fact more susceptible to predation [3], while the chicks are sensitive to cold and humidity because of their lack in thermoregulation [4].

The Alpine populations of black grouse show a preference for patchy habitat in which dwarf shrub and rock covers are available [5]. In winter, to reduce the energetic consumption, black grouse stay in holes dug in the snow. These peculiar needs make the species particularly sensitive to human disturbance, such as the land use change, road network in the forests and tourism [6], and winter outdoor activities [7; 8]. Worldwide, the black grouse is not considered as a threatened species, even if its abundance is decreasing at the southern edge of the distribution. On the Italian Alps, the population abundance decreased in the last 30 years to almost 22000 individuals [9].

Viterbi [10] provides an extensive review on the effects of climate on the population dynamics of black grouse, underlining the negative effect of rain and lower temperatures in the brooding and hatching period [11; 12; 13], the importance of snow depth and snow melting [see 14; 15; 16, for other grouse species]. Most of these studies refers to “lowland” populations of black grouse, while less is known about the effect of climate on Alpine populations. According to [10], both density and climate affect the black grouse population in the Orsiera-Rocciavre Park (Piedmont, Italy). In particular, they found that local populations suffer high rainfall in early June (critical post-hatching period) and benefit from high daily temperature range in December.

We study the dynamics of the Piedmont populations of black grouse using censuses performed in 17 Alpine districts, concentrating on growth rate obtained by spring male counts. Before analysing the joint effects of population density and climatic conditions on the growth rate, we study their independent role. Projections of the future climatic conditions given by a regional model are used to assess the future status of the population.

2. MATERIALS

The study area is the Alpine territory of the Piedmont Region, North-Western Italy. This territory is administratively divided into 17 Alpine districts in six provinces: one in Biella (BI1), one in Vercelli (VC1), three in Verbano-Cusio-Ossola (VCO1, ..., VCO3), five in Turin (TO1, ..., TO5) and seven in Cuneo (CN1, ..., CN7). The counts of black grouse populations are performed twice a year in each district, in spring and in late summer. Spring censuses estimate male population density (M_t). Counts are carried out during lek formation, in suitable areas characterized by the presence of important leks. The late summer censuses are carried out using hunting dogs to estimate the number of females, breeding hens and juveniles. Data, available from 1999 to 2010, are aggregated on a district level.

We calculated the instantaneous growth rate (see figure 1) as

$$\text{Log}(\lambda_{t,c}) = \log\left(\frac{M_{t+1,c}}{M_{t,c}}\right) \quad (1)$$

where $M_{t,c}$ is the male density measured in district c . The temporal mean of the growth rate is close to 0 in each district, with a minimum of $-0.045 \text{ years}^{-1}$ (district TO4) and a maximum of 0.069 years^{-1} (CN3).

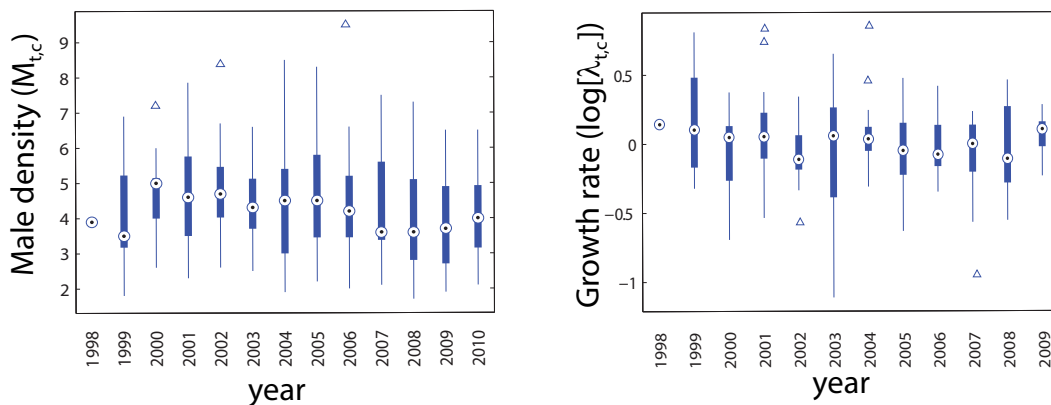


Figure 1: Boxplots of the temporal dynamics of male densities ($M_{t,c}$) and growth rates ($\text{Log}[\lambda_{t,c}]$) measured in the 17 Alpine districts. The median values are plotted as circles with an inner dot, the interquartile ranges with thick lines, the entire range of data with thin lines, excluding outliers (empty triangles).

The historical meteorological data used for model calibration were provided by the Regional Environmental Agency (ARPA) as spatially distributed values referring to cells with a side of 0.125 degrees. For future projections, we used the climatic predictions given by the regional climatic model PROTHEUS [17; 18], based on the IPCC scenario A1B. This model has a spatial resolution of about 0.27 degrees and its predictions are available until 2049.

The available meteorological variables are the daily amount of rainfall ($P_t(\tau)$), the maximum ($T_{Max,t}(\tau)$) and the minimum ($T_{min,t}(\tau)$) temperature. The mean daily temperature and the daily temperature range are calculated, respectively, as $T_{m,t}(\tau) = (T_{Max,t}(\tau) + T_{min,t}(\tau))/2$ and $\Delta T_t(\tau) = T_{Max,t}(\tau) - T_{min,t}(\tau)$. Meteorological data were then standardized using the reference period 1991-2009.

The values assigned to each meteorological variable in a district were calculated by elaborating its values in cells of the meteorological model that overlap with the suitable territory of the district. We define as "suitable" area A_c the portion of a district c where the probability of presence of black grouse is greater than 0.5, according to a suitability map provided by the Institute of Atmospheric Sciences and Climate, CNR, Turin.

Let us call $A_{l,c}$ the fraction of suitable area of the district c that also belongs to the cell l . The value of the generic climatic variable $X_{c,t}(\tau)$, for the day τ of the year t and for the district c , was calculated as:

$$X_{c,t}(\tau) = \sum_{\chi_c} \frac{A_{l,c}}{A_c} X_{t,l}(\tau) \quad (2)$$

where χ_c is the set of climatic cells overlapped with the suitable area of the district c .

To develop our models, we used the semi-month averaged meteorological variables, thus we averaged the meteorological values in the first half (1st-15th day, labelled as 1) and in the second half (16th-last day, labelled as 2) of each month, except for February (two halves: 1st-14th and 15th-last day). Therefore, as an example, with the notation $P_{Apr1,t+1}$ we name the averaged standardized rainfall in the first half of April of year $t + 1$.

We limited the potential semi-months that can influence the growth rate at time t using a specific temporal window: from the first half of January of year t to the second half of April of year $t+1$. The temporal window closes just before the counts of M_{t+1} , thus avoiding the inclusion of anti-casual effects of climate.

3. SEPARATE EFFECT OF METEOROLOGICAL VARIABLES AND POPULATION DENSITY

We studied the separate effect of each meteorological variable on the growth rate using the Pearson coefficient for the linear correlation. Figure 2 summarizes with colours different from white which of the many meteorological variables have a significant (even if weak, $p < 0.20$) correlation with the growth rate. More precisely, red and blue indicate respectively positive or negative correlation while the colour intensity is proportional to the value of the Pearson coefficient. These plots permit to easily check if some specific

period of the year have a clear influence on population fitness and if there is any seasonal pattern. In spite of the huge number of tested meteorological variables, only few of them are significantly correlated with the growth rate. The more significant correlations are with $P_{Oct2,t}$ ($R = 0.19, p = 0.012$), $P_{Jan1,t}$ ($R = 0.19, p = 0.012$), and $Tm_{Apr2,t}$ ($R = -0.18, p = 0.016$).

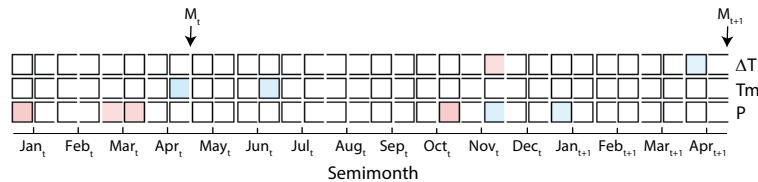


Figure 2: Correlations between the growth rate $\text{Log}(\lambda_{t,c})$ and the semi-monthly meteorological variables: the average of the standardized rainfall P ; the average of the standardized daily temperature range ΔT ; the average of the standardized mean temperature Tm . Every cell in the plot refers to a single correlation between the growth rate and a meteorological variable. For each month label on the x-axis, the left column of cells refers to the first half of the month while the right column of cells to the second half of the month. Red [blue] cells indicate a positive [negative] and significant ($\alpha = 0.20$) correlation, and the intensity of the colours is proportional to the Pearson correlation coefficient. On the top of the figure, we reported the timing of the spring censuses used to calculate $\text{Log}(\lambda_{t,c}) = \text{Log}(M_{t+1,c}/M_{t,c})$.

Studying the influence of population density on growth rate is instead more complex, because of the intrinsic correlations between the two quantities (see eq.1). The correlation between growth rate and population density was therefore tested by (1) pooling data from all districts and (2) leaving them separate.

Growth rate and total male density (case 1) are significantly and negatively correlated ($R = -0.43, p < 0.001$). Yet, the correlation is significant (with $\alpha = 0.05$) also for 11 out of 17 single districts (case 2). We note that p -values of the other 6 districts (BI1, CN6, T01, T03, VC1 and VCO2) are small ($p = 0.12, 0.12, 0.19, 0.13, 0.10$ and 0.11 , respectively).

The slopes of the regression lines between the male density and the growth rate does not significantly differ among the districts ($F = 1.23, p = 0.25$). Interestingly, the analysis of covariance performed under the hypothesis of "same slopes" for all districts shows that intercepts are not identical ($F = 2.92, p = 0.0003$). Thus, we clustered the districts on the basis of the value of their intercepts, using the agglomerative *hierarchical clustering* [19], in which the distance between each pair of Alpine districts is defined as the difference between their intercepts, while the distance between two clusters is calculated using the *furthest neighbour strategy*. For each branch of the resulting tree (3a), we calculated an *inconsistency index* [19, see] using a depth of three links. The final clusters are formed cutting the tree branches where the *inconsistency index* is bigger than 0.95 times the highest *inconsistency index* of the cluster tree.

The described algorithm led us to define two clusters, one including districts CN3, CN4, TO2 and TO5, while the other including all the other districts. For simplicity of notation, we will refer to *cluster 1* for the former cluster (red in figures 3 and 4) and *cluster 2* for the latter (green in the figures). Even if the

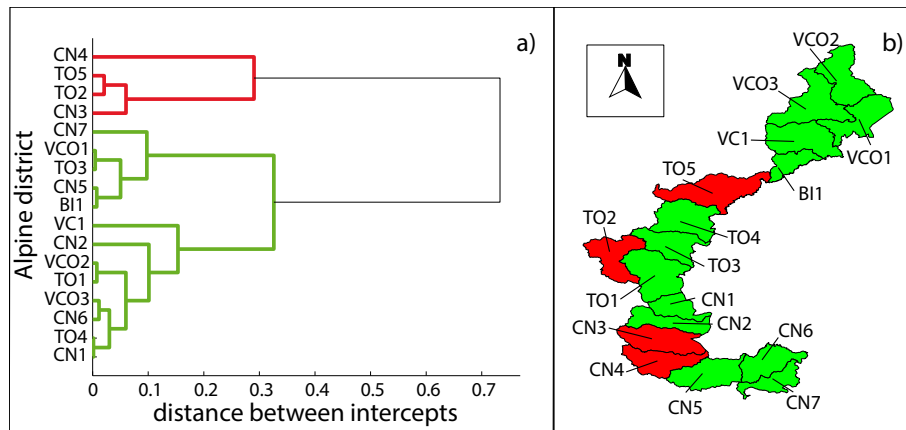


Figure 3: Clusters identified in the univariate growth rate - male density model, obtained using the algorithm explained in the main text. Panel a) the cluster tree; Panel b) map of the Alpine districts. The districts belonging to the same cluster are coloured with the same colour (red or green).

districts CN3 and CN4 are adjacent and the districts TO2 and TO5 belong to the same province, it is not possible to find a clear geographical structure in the two clusters. Since both clusters are characterized by lines with different intercepts but same slope, we can write a Ricker-like model of the form:

$$\text{Log}(\lambda_{t,c}) = \beta_{0,c} + \beta_M M_{t,c} + \varepsilon_{t,c} \quad (3)$$

where c indicates the district, and $\beta_{0,c}$ assumes the same value for all districts belonging to the same cluster. Fitting this model using the least squares method, the coefficient of determination is 0.28, and the correlation between growth rate and density is significant for both clusters ($p < 0.001$). The values of the model parameters are: $\beta_{0,c} = 0.52 \pm 0.065$ for the districts of *cluster 2* and $\beta_{0,c} = 0.798 \pm 0.101$ for the districts of *cluster 1*, and $\beta_M = 0.132 \pm 0.015$. The carrying capacities, measured as the non-trivial equilibrium of the equation 3 ($\bar{M} = -\frac{\beta_{0,c}}{\beta_M}$) solved for each cluster, are 3.97 for *cluster 2* and 6.04 for *cluster 1*. Notice that both the equilibria are stable since $0 < \beta_{0,c} < 2$. In figure 4 we show the growth rate as a function of the male densities, together with the best fit models.

4. THE MULTIVARIATE MODEL

The multivariate models analysed here have a simple linear regression model structure with no interaction terms:

$$\text{Log}(\lambda_{t,c}) = \beta_0 + \sum_{x_j} \beta_j x_{j,t,c} + \varepsilon_{t,c} \quad (4)$$

where $\text{Log}(\lambda_{t,c})$ and $x_{j,t,c}$ are, respectively, the growth rate and the value of the j -th covariate at time t in district c , \mathcal{X}_i is the set of the covariates included in the i -th model (m_i) and $\varepsilon_{t,c}$ a white noise. To

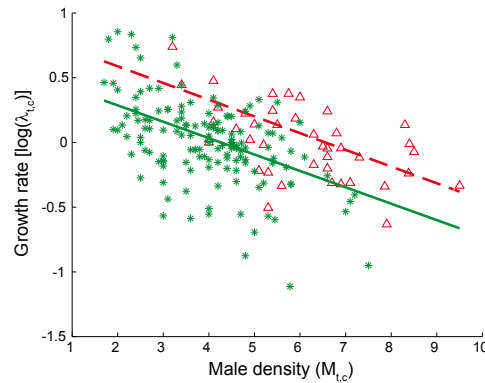


Figure 4: Scatter plot of the growth rate [$\text{Log}(\lambda_{t,c})$] as function of the male density $M_{t,c}$, and regression lines based on the two groups formed using the clustering algorithms described in the text. Using the colour of figure 3, the red triangles and the red dashed line represent, respectively, data and regression line for the group composed by districts CN3, CN4, TO2 and TO5. Green stars and solid green line represent data and regression line for the other cluster of districts.

account for the clustering discussed above, one of the potential covariates to be included in the model is a categorical variable with two categories, named $\Delta Intercept$. The other covariates potentially included in the model are the meteorological variables that significantly (with $\alpha = 0.2$) correlate with the growth rate.

We developed the final model using a multi-model approach. Given a set of k potential covariates to be included in the models, the model selection procedure typically compares, using a selection criteria (e.g Akaike Information Criterion), all the 2^k model structures defined including from 0 to k covariates. The selection of a single best model can be uncertain (model uncertainty) because many models can perform rather similarly for the chosen criterion. Models with similar performances could (i) include only few common covariates, and (ii) lead to drastically different predictions. Effect (i) is critical if the aim is to speculate about the ecological relevance of some climatic covariate, while effect (ii) is a serious drawback for using models as forecast tools.

To overcome these problems, here we used the *Bayesian Model Averaging* [BMA 20], which permits to make predictions using a set of models instead of a single model. Given a dataset D , the final inference for a quantity y (here for $\text{Log}(\lambda_{t,c})$) is produced by suitably weighting the inferences given by different models. The weight of the model m_i is its posterior probability ($P(m_i|D)$). The final prediction is therefore calculated as:

$$E[y|D] = \sum_{i=1}^{2^k} E[y|m_i, D]P(m_i|D) \quad (5)$$

where the posterior probability of a model ($P(m_i|D)$) is calculated with the Bayes formula, using the

prior probability and the marginal likelihood ($P(D|m_i)$) of each model:

$$P(m_i|D) = \frac{P(m_i)P(D|m_i)}{\sum_{j=1}^{2^k} P(m_j)P(D|m_j)} \quad (6)$$

As widely discussed in [21], we set a uniform prior on the model size, using a beta-binomial prior. Moreover, for the prior distribution on the regression parameters, $P(\beta_i|m_i)$, we adopted the Zellner's g -prior with g equal to the number of observations, as in [22].

The number of potential covariate is $k = 12$, thus leading to $2^k = 4096$ possible models, while the number of observations is 169. The model space was exhaustively explored and the expected posterior model dimension, measured as the number of included independent variables, was 3.25.

The posterior probability of inclusion of the single covariates (a measure of variable importance) is summarized in table 1, where the posterior probability of the 5 best models is also reported. The most important variables are: $M_{t,c}$, which negatively affects $\text{Log}(\lambda_{t,c})$; $\Delta Intercept$; $Tm_{Apr2,1}$, included with a negative effect; $P_{Jan1,t+1}$, included with a negative effect. Notice that the ranking of variables changed between the univariate (correlation) and the multivariate (BMA) analysis. For example, the meteorological variables $P_{Oct2,t}$ and $P_{Jan1,t}$, which are the most correlated variables in the univariate analysis, have a posterior probability of inclusion lower than 0.10. On the other hand, the variable $Tm_{Apr2,1}$, which is measured just before the period of lek formation, is the most important meteorological variable in both univariate and multivariate analysis.

Both male density and $\Delta Intercept$ have a posterior inclusion probability close to 1, and are included in the best five models of table 1. This confirms the importance of accounting for density dependence and separating the districts in two clusters. Notice that, following equation 4, the density is included as in the Ricker model. The coefficient of determination obtained on the training set with the BMA model is $R^2 = 0.35$, while it is 0.28 in the pure density-dependent model. Therefore, the inclusion of the climatic conditions significantly improved the predictive ability of our model. Moreover, the values of the model parameters are similar in the univariate analysis and in the BMA. More precisely, in BMA the intercepts are slightly higher ($\beta_{0,c} = 0.53$ for *cluster 2* and $\beta_{0,c} = 0.83$ for *cluster 1*), while the slope is steeper ($\beta_M = -0.136$), as summarized in table 1.

The future projections of the growth rate and the population density were carried out, using the BMA models and the climatic model PROTHEUS, according to the following equations:

$$\begin{aligned} \text{Log}(\hat{\Lambda}_t) &= \hat{\beta}_0 + \hat{X}_t\hat{\beta} + \hat{Z}_t \\ \hat{M}_{t+1} &= \text{log}(\hat{\Lambda}_t)\hat{M}_t \end{aligned} \quad (7)$$

Table 1: Posterior probability of inclusion of the independent variables (covariates) and structure of the best models in BMA. Only the variables with a probability of inclusion greater or equal than 0.1 are shown. x_i is the name of the independent variable, PIP its probability of inclusion, PostMean the posterior mean of the parameter β_i and PostSD its standard deviation. Cond.Pos.Sign. is the probability that β_i is positive, given that it is included in the model. In the last five columns, the structure of the first five best models is shown, labelling with a ``1'' the rows which correspond to the variables included in the model, and with ``0'' the variables that are not included. In the last row, for each of the five best models, we report the posterior probability.

x_i	PIP	PostMean	PostSD	Cond.Pos.Sign	Best models				
<i>Intercept</i>	1.000	0.534	-	-	1	1	1	1	1
$M_{t,c}$	1.000	-0.136	0.016	0.00	1	1	1	1	1
Δ <i>Intercept</i>	0.999	0.296	0.61	1.00	1	1	1	1	1
$P_{Apr2,t}$	0.492	-0.099	0.114	0.00	1	0	0	0	1
$P_{Jan1,t+1}$	0.245	-0.067	0.133	0.00	0	0	1	1	0
$P_{Jun2,t}$	0.100	-0.012	0.044	0.00	0	0	0	1	1
$P_{Oct2,t}$	0.091	0.008	0.035	1.00	0	0	0	0	0
$P_{Nov2,t}$	0.062	-0.003	0.016	0.00	0	0	0	0	0
$P_{Jan1,t}$	0.057	0.005	0.040	0.91	0	0	0	0	0
$P_{Mar2,t}$	0.056	0.008	0.044	0.94	0	0	0	0	0
$\Delta T_{Nov2,t}$	0.053	0.002	0.018	0.93	0	0	0	0	0
$\Delta T_{Apr1,t}$	0.051	-0.002	0.017	0.07	0	0	0	0	0
$P_{Mar1,t}$	0.047	0.004	0.032	1.00	0	0	0	0	0
Posterior model probability: $P(m_i D)$					0.31	0.16	0.11	0.02	0.02

where $Log(\Lambda_t)$ is the vector of the predicted growth rates in different Alpine districts, \hat{X}_t is the matrix of covariates included in the model (each row contains the value, at time t, for a district), $\hat{\beta}$ is the vector of the β parameters calculated using BMA and $\hat{Z}_t \sim (0, \Sigma)$ is a multivariate normal noise where Σ is the variance-covariance matrix of residuals of the BMA model. Therefore, our simulations include a spatial effect *via* the variance-covariance matrix Σ . We initialized the simulation setting $\hat{M}_{2010} = M_{2010}$.

Figure 5 shows the the future projections for the growth rates and the male densities in the two clusters, averaged by districts out of 1000 simulations. Even if the projections of the growth rate show a high uncertainty, the male density never goes below 4 males/100 ha (*cluster 1*) or 3 males/100 ha (*cluster 2*). Demographic simulations on both clusters, have in some years quite unusual behaviours, such as for the growth rate drop in 2006 and the consequent drop of the male density in 2017. Figure 6 reveals why: in 2016, the particular realization of the PROTHEUS model used for the simulations shows a very high value of $Tm_{Apr2,t}$, which is the most important meteorological variable in the model. Although such an effect is not dramatic in the present case, it reveals that climate change might seriously affect the dynamics of black grouse on Alps.

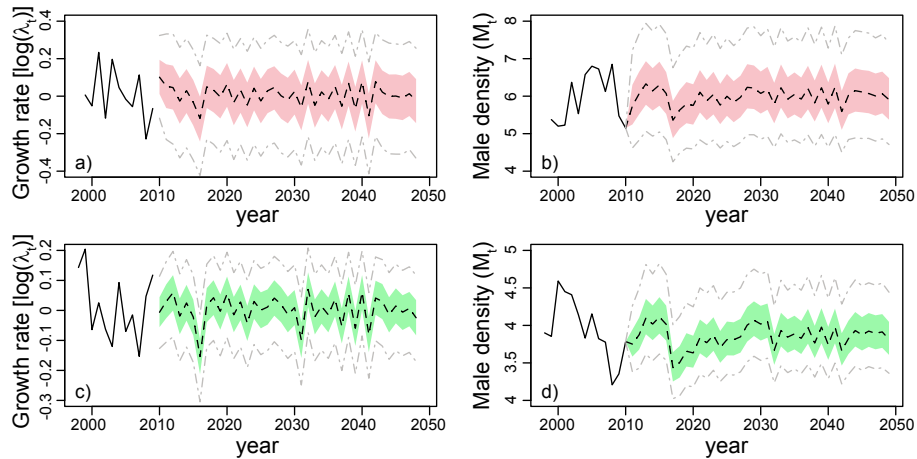


Figure 5: Data and future projections of the male densities (M_t) and the growth rate ($Log[\lambda_t]$) in the two clusters of figure 3, made using the BMA model and the meteorological projections given by the PROTHEUS model. Panel a and b refer to *cluster 1*, while panels c and d to *cluster 2*. Data are shown with a black solid line, median value of the 1000 simulations as black dashed lines, interquartile ranges as coloured areas (following figure 3), the fifth and the 95th percentile as grey dashed lines.

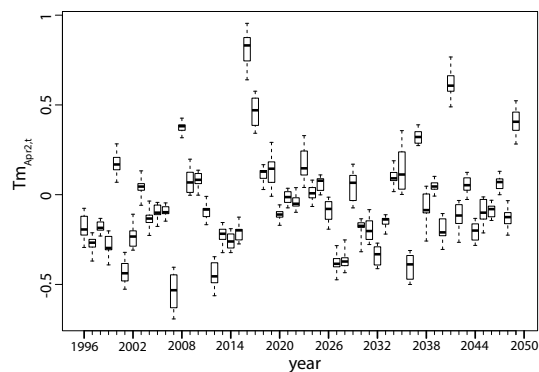


Figure 6: Boxplot of the values of the standardized meteorological variable $Tm_{Apr2,t}$ given by a realization of the PROTHEUS model. The intra-annual variability is given by the variability among districts.

5. CONCLUSIONS

In this work, we studied the influence of density dependence, spatial position and meteorological variables on the growth rate of the black grouse populations in the Piedmont region, measured at the Alpine district level.

Density dependence is clearly detected in all the districts. Moreover, it is not significantly different among districts, showing that it is weakly affected by different environmental conditions of the districts. Conversely, we found two clusters of districts characterized by a different carrying capacity. The cluster with the highest carrying capacity includes only 4 out of 17 districts, which positions does not suggest a clear spatial structure.

The meteorological variable with the greatest influence on the growth rate is the mean temperature measured in late April, both in the univariate and in the multivariate analysis. April is just before spring censuses and the period of lek formation, thus suggesting different possible explanations for the detected effect that we will further discuss in the talk. For example, one of the hypothesis is that an high mean temperature in the first half of April leads to an anticipation of the lek formation, thus to an hatching period occurring when conditions are not optimal for the newborns. A similar effect is described by [13] for a Finnish population. The meteorological ranked 2nd for importance in BMA is the rainfall in early January, which has a negative effect on the growth rate.

The future projections suggest that, although some strong inter-annual variability is clearly visible, the expected climatic conditions for the next 40 years will not directly represent a major danger for the conservation of black grouse. It would be interesting to repeat the simulations including the variability of climate forecast. However, the population growth rate is a variable that includes several aspects of the black grouse life cycle, such as mating probability, fertility, survival of juveniles and adults. Any of these fitness components can be influenced in a different (and potentially contrasting) way by the climate. We thus plan to analyse fertility and breeding rate data of the summer censuses in the near future.

6. ACKNOWLEDGEMENTS

The research has been performed within the project "ALCOTRA IT-FR - Galliformi Alpini" (<http://www.interreg-alcotra.org/>), and during A.M.'s PhD, supported by Fondazione Lombardia per l'Ambiente (project SHARE-Stelvio). We gratefully thank Dr. Simona Imperio and dr. Ramona Viterbi for useful discussion and ongoing collaboration.

7. REFERENCES

- [1] Marjakangas, A. and Kiviniemi, S. (2005), *Dispersal and migration of female Black Grouse Tetrao tetrrix in eastern central Finland*, *Ornis Fennica*, volume 82:pp. 107-116.
- [2] Caizergues, A. and Ellison, L. (2002), *Natal dispersal and its consequences in black grouse Tetrao tetrrix*, *Ibis*, volume 1:pp. 478-487.
- [3] Hannon, S.J. and Martin, K. (2006), *Ecology of juvenile grouse during the transition to adulthood*, *Journal of Zoology*, volume 269:pp. 422-433.
- [4] Boggs, C., Norris, E. and Steen, J. (1977), *Behavioural and physiological temperature regulation in young chicks of the willow grouse (Lagopus lagopus)*, *Comparative Biochemistry and Physiology Part A: Physiology*, volume 58:pp. 371-372.
- [5] Schweiger, A., Nopp-Mayr, U. and Zohmann, M. (2012), *Small-scale habitat use of black grouse (Tetrao tetrrix L.) and rock ptarmigan (Lagopus muta helvetica Thienemann) in the Austrian Alps*, *European Journal of Wildlife Research*, volume 58:pp. 35-45.
- [6] Ranci Ortigosa, G., Antonelli, R. and Gatto, M. (2003), *Influenza dell'ambiente naturale e antropizzato sulla demografia del fagiano di monte (Tetrao tetrrix) in Trentino*, in R. Casagrandi and P. Melià, eds., *Atti del XIII Congresso Nazionale della Società Italiana di Ecologia (Como, 8-10 settembre 2003)*, Aracne, Roma.
- [7] Arlettaz, R. and Patthey, P. (2007), *Spreading free-riding snow sports represent a novel serious threat for wildlife*, *Proceedings of the Royal Society B*, volume 274:pp. 1219-1224.
- [8] Patthey, P., Wirthner, S., Signorell, N. and Arlettaz, R. (2008), *Impact of outdoor winter sports on the abundance of a key indicator species of alpine ecosystems*, *Journal of Applied Ecology*, volume 45:pp. 1704-1711.
- [9] Brichetti, P. and Fracasso, G. (2004), *Ornitologia italiana*, volume 2 - Tetraonidae-Scolopacidae, Alberto Perdisa Editore, Bologna.
- [10] Viterbi, R. (2012), *Climate and animal biodiversity: analysis of risk factors in western Alpine protected areas.*, Tesi di dottorato di ricerca in Monitoraggio dei Sistemi e Gestione dei Rischi Ambientali, XXIII ciclo. Università degli studi di Genova.
- [11] Loneux, M., Lindsey, J. and Vandiepenbeeck, M. (2003), *Climatic influence on Black Grouse population dynamic in Belgian Hautes-Fagnes Nature Reserve: an update.*, *Sylvia*, volume 39 (suppl.):pp. 53-57.

- [12] Summers, R. and Green, R. (2004), *An experimental study of the effects of predation on the breeding productivity of capercaillie and black grouse*, Journal of Applied Ecology, volume 41:pp. 513-525.
- [13] Ludwig, G. and Alatalo, R. (2006), *Short-and long-term population dynamical consequences of asymmetric climate change in black grouse*, Proceedings of the Royal Society B, volume 273:pp. 2009-2016.
- [14] Novoa, C., Besnard, A., Brenot, J. and Ellison, L. (2008), *Effect of weather on the reproductive rate of Rock Ptarmigan Lagopus muta in the eastern Pyrenees*, Ibis, volume 150:pp. 270-278.
- [15] Clarke, J. and Johnson, R. (1992), *The influence of spring snow depth on white-tailed ptarmigan breeding success in the Sierra Nevada*, Condor, volume 94:pp. 622-627.
- [16] Wang, G. and Hobbs, N.T. (2002), *Relationships between climate and population dynamics of white-tailed ptarmigan Lagopus leucurus in Rocky Mountain National Park, Colorado, USA*, Climate Research, volume 23:pp. 81-87.
- [17] Artale, V., Calmanti, S. and Carillo, A. (2010), *An atmosphere-ocean regional climate model for the Mediterranean area: assessment of a present climate simulation*, Climate Dynamics, volume 35:pp. 721-740.
- [18] Dell'Aquila, A. and Calmanti, S. (2012), *Impacts of seasonal cycle fluctuations in an A1B scenario over the Euro-Mediterranean*, Climate Research, volume 52:pp. 135-157.
- [19] Jain, A.K. and Dubes, R.C. (1988), *Algorithms for clustering data*, Prentice Hall PTR.
- [20] Raftery, A.E., Madigan, D. and Hoeting, J.A. (1997), *Bayesian Model Averaging for Linear Regression Models*, Journal of the American Statistical Association, volume 92:pp. 179-191.
- [21] Ley, E. and Steel, M. (2009), *On the effect of prior assumptions in Bayesian model averaging with applications to growth regression*, Journal of Applied Econometrics, volume 24:pp. 651-674.
- [22] Fernandez, C., Ley, E. and Steel, M. (2001), *Benchmark priors for Bayesian model averaging*, Journal of Econometrics, volume 100:pp. 381-427.

Response to climate change of alpine glaciers in North-Western Italian Alps

Bonanno R.^{1*}, Ronchi C.¹, Cagnazzi B.¹, and Provenzale A.²

¹Arpa Piemonte, 10135, Torino, Italy

²Institute of Atmospheric Sciences and Climate - CNR, 10133, Torino,

*Corresponding author: r.bonanno@arpa.piemonte.it

Abstract

In the densely populated Alpine regions, glaciers represent an important source of freshwater and a significant component of tourism economy and hydro-electric power production. The shrinking of glaciers inevitably leads to a reduction of the frozen water supply they are able to store. This is one of the reasons why it is important to model and quantify, over time, the response of Alpine glaciers to different climate change scenarios.

In this work, we analyzed the impact of climate variability on a set of glaciers in the north-western Italian Alps during the last 50 years, considering the fluctuations in glacier terminus position (or snout). The method adopted here involves the development and calibration of a linear empirical stochastic model, in which glacier snout variations depend on temperature and precipitation fluctuations. In the study of Calmanti et al., 2007 [1], it has been shown that linear empirical models are able to reproduce and predict the mean response of glaciers to climate variability.

The model is then used to estimate the average response of Alpine glaciers in different climate change scenarios, assuming that the selected predictors are suitable also for future climate conditions. The SRES A1B and the new RCP4.5 scenario have been considered. For all selected scenarios, the empirical model confirms the observed average retreat of glaciers in the NW Italian Alps during the XXI century. In 2050 the mean estimated retreat for both the scenarios is very similar and approximately about 300 m.

Keywords: *Glacier retreat, climate change, water resources, future scenarios, EC Earth*



1. PURPOSE

The aim of this work is the study of the average response of a set of 14 glaciers in the north-western Italian Alps to climate variability during the last 50 years and to future climate change scenarios.

The method adopted here consists in the use of a lagged-linear empirical stochastic model, in which glacier snout variations depend on the fluctuations in temperature and precipitation.

In this work, we consider a regional viewpoint, trying to assess the overall response of glaciers in a given area to regional-scale climate variations. While this can be less interesting from a glaciological perspective, it is probably even more important in terms of regional climate variability and water resources management. When using a regional perspective, an empirical stochastic modeling approach relating glacier snout fluctuations to climate variability can be of value (e.g., Calmanti et al. 2007 [1]), as a substitute for detailed dynamical models of individual glacier behavior (e.g., Oerlemans 2011 [9], Jouvét et al. 2009 [5]). The study reported here follows this approach, with the aim of estimating the overall glacier response in the north-western Italian Alps to different climate change scenarios in the coming decades.

2. AVAILABLE DATA

One of the dataset used in this work consists in the annual fluctuations of glacier snout positions used as a substitute for the quantitative measurement of glacier mass balance (proxy data).

Secondly we used the records of temperature and precipitation, available in the study area (north-western Italy) in the period: 1958-2009. The observations have been distributed over a predefined regular grid by means of an Optimal Interpolation technique.

Finally we used outputs coming from simulations with global and regional climate models with different climate change scenarios (RCP4.5 and SRES A1B, see IPCC 2007 [4] and Moss et al. 2010 [7].)

3. SNOUT POSITION DATA

We analyze a set of 14 glacier snout fluctuation data in the western sector of the Italian Alps, in the area of Piedmont and Valle d'Aosta.

Glacier snout data are collected by the Comitato Glaciologico Italiano – Consiglio Nazionale delle Ricerche (GCI) and regularly published in the GCI Bulletin (<http://www.glaciologia.it/>).

Climate observed data

In this work, we use temperature and precipitation as proxies of the whole set of climate parameters which can influence glacier dynamics. In past years, Arpa Piemonte developed a dataset of gridded temperature and precipitation records, with spatial resolution 0.125° , by means of a Optimal Interpolation (OI) technique (Kalnay, 2003 [6]) which produces a spatial interpolation of the data provided by an ensemble of meteorological stations in Piedmont and Valle d'Aosta (Ronchi et al. 2008 [10]) for the period 1958-2009.

4. ANALYSIS OF THE DATA

All snout fluctuation data considered here cover the period 1958-2009, while the starting date varies with the individual glaciers.

Almost all values of average snout fluctuation for the glaciers considered here are negative, confirming the overall retreat of Alpine glaciers in this area and the homogeneity of the regional behavior of large glaciers in the northwestern Italian Alps (Calmanti et al. 2007 [1]). This homogeneity allows for averaging the standardized time series of the individual glaciers, to obtain a signal describing the regional glacier behavior in the period 1958-2009. Before averaging the individual glacier data, we tested for the possible presence of outliers and we removed documented anomalies reported in the GCI bulletins, such as a residual snow layer at the time of measurement or glacier breakup.

As regards the temperature and precipitation data, we opted for averaging the meteorological records provided by OI analysis over a large area (the whole Piedmont and Valle d'Aosta region) rather than considering only the single grid point closest to the glacier location itself (see Calmanti et al. 2007 [1] for a detailed discussion about this issue) obtaining a mean regional climatic signal.

5. CONSTRUCTION OF AN EMPIRICAL MODEL FOR THE AVERAGE GLACIER RESPONSE

From the precipitation and temperature data, we calculated the standardized monthly averages over the area that includes Piedmont and Valle d'Aosta. The averages were then grouped in periods of varying duration, resulting in seasonal values. Using precipitation as an example, we considered $P(1-3)$, $P(1-4)$, $P(1-5)$, $P(1-6)$, $P(2-4)$, $P(2-5)$, $P(2-6)$, $P(2-7)$, $P(3-5)$ and so on.

Glacier snout variations respond to climatic fluctuations with a time delay from years to tens of years (Oerlemans 2001 [8]). We estimate the value of the time lag between climatic variables and glacier snout response by systematically examining the lagged cross-correlations between individual climatic variables and snout fluctuations.

For each predictors, we thus calculated the cross-correlation with the series of average snout fluctuations, determining for each variable the time delay (in years) that maximizes the correlation between the glacial snout and the meteorological variables. Snout fluctuations turn out to be positively correlated with precipitation and negatively with temperature.

By screening the predictors with appropriate statistical techniques (such as backward stepwise regression and cross-validation for out of sample prediction), we obtained a simple lagged-linear empirical stochastic model that is able to reproduce past snout fluctuations.

The selected model depends only on four predictors: summer temperature $T_5(6-8)$ and winter precipitation $P_{10}(10-3)$ with time delay of five and ten years respectively, and spring temperature and precipitation $P_0(3-5)$, $T_0(2-5)$ in the year of the snout fluctuation. These predictors are meaningful in terms of glacier physics: summer temperature and winter precipitation correspond to the ablation period and to the accumulation period respectively, whereas spring temperature and precipitation can change the surface glacier albedo in summer ablation period accelerating/slowing down the ice melting.

The parameter values for the model obtained are reported in Tab.1. We want to point out that the variable related to the spring precipitation and temperature of the same year don't give a fundamental contribution to the advance or retreat of the snout position (that is more linked to glacier dynamics and past year mass balance and thus past year meteorological conditions). This is confirmed by the coefficients of the variables $P_0(3-5)$ and $T_0(2-5)$ that are statistically significant but not as important as the winter precipitation and summer temperature.

However we think anyway that these two spring variables may play a non negligible role in the partial preserving of the glacier tongue, for example, in situation when snout retreat is concurrent with abundant snow and low temperature in the spring season. We also noticed that a model without the spring variables is a bit less performant but as acceptable as the complete model from the statistical point of view. The first results reported here consider simulations made with the complete model.

Parameter	Estimated value a	95% prediction bounds	$P(a^r > a)$
a_0	0.1018	(0.0651 , 0.1384)	0.
$a_{P(10-3)}$	0.5714	(0.0651 , 0.7728)	0.
$a_{P(3-5)}$	0.1835	(-0.0035 , 0.3707)	0.002
$a_{T(2-5)}$	-0.2732	(-0.4946 , -0.0518)	0.
$a_{T(6-8)}$	-0.4828	(-0.6633 , -0.3023)	0.
$R^2 = 0.93$	$Adjusted R^2 = 0.93$	AIC=-185	$\sigma_r = RMSE = 0.093$

Table 1: Model parameter estimates obtained from the screening of the precipitation and temperature variables. The first column indicates the predictor, the second column reports the value of the parameter obtained by fitting the linear model to the whole data set, the third column reports the 95% prediction bounds and the fourth column reports the probability that the parameter estimate from a random reordering of the data is larger, in absolute value, than the original parameter. Probabilities have been estimated from a total of 1000 random reorderings of the time series. In the bottom of the table, R^2 , $Adjusted R^2$, AIC and $RMSE = \sigma_r$, are shown.

Fig.1 shows the standardized annual snout fluctuations and the in-sample deterministic reconstruction (hindcast) from the selected lagged-linear model.

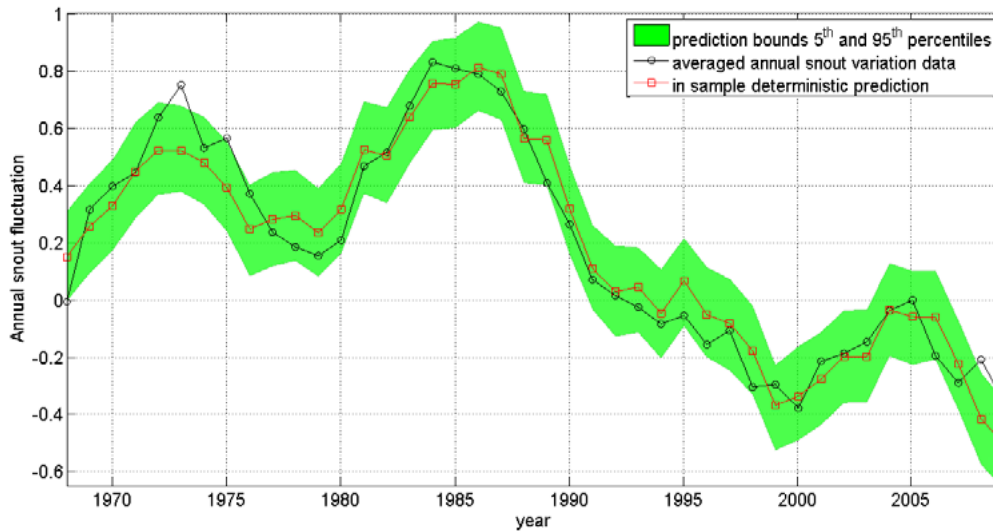


Fig.1: Upper panel: In-sample deterministic reconstruction of the average annual snout variations with the selected empirical lagged-linear model, which parameters are reported in Tab.1. Confidence bounds for the in-sample estimation are computed by including a white noise stochastic component. The procedure is repeated 1000 times and the uncertainty band is defined by the 5th and 95th percentiles.

6. IMPACT OF CLIMATE CHANGE ON THE GLACIERS OF NORTH-WESTERN ALPS: RCPS AND SRES A1B SCENARIOS

The global climate change scenarios considered here are produced by the EC-Earth model, a recent Earth System model developed by a Consortium of European research Institutions (Hazeleger et al. 2012 [3], see also <http://ecearth.knmi.nl/>).

For EC-Earth, climate change scenarios have been simulated using the recently developed Representative Concentration Pathways (RCP), see Moss et al. (2010) [7]. For this work, we considered the RCP4.5 scenario that implies a "stabilization without overshoot", corresponding to 4.5 W/m² total anthropogenic forcing in 2100.

For our study, we also used the outputs of several Regional Climate Models from the ENSEMBLES project for the SRES A1B scenario runs which are individually weighted by an adequate set of weights determined by comparison with observations during a suitably defined training period. For more details about the Multimodel SuperEnsemble technique used to aggregate the RCM outputs see Cane et al., (2012) [2].

For the time series of temperature and precipitation obtained by this technique, bias correction is not necessary as the weights applied to the individual model outputs are determined explicitly to reproduce the observations in the training period 1961-2009 and the model average is imposed to be equal to that of the observations.

In the case of EC Earth runs, bias correction was necessary only for temperature and not for precipitation.

Fig.2 shows an estimate of the cumulated snout positions in the period 1968-2050 for the two scenarios. The snout position is always referred to the value measured in 1968, when we start simulating the glacier length fluctuations.

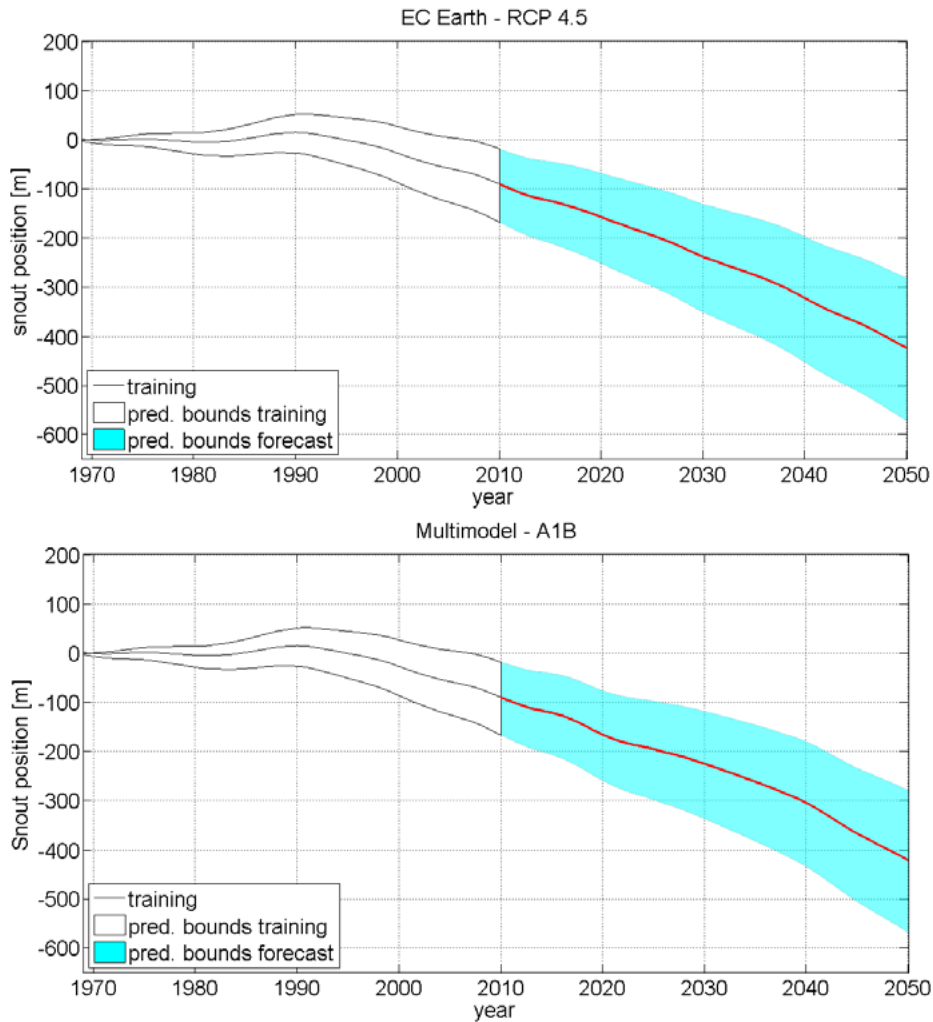


Fig. 2: Snout positions in the period 1968-2050 for the two scenario RCP4.5 and A1B. For each climate run, 1000 realizations of the glacier models were generated to provide an estimate of the uncertainty bands, defined by the 5th and 95th percentiles of the distribution of values produced by the glacier model. The first portion with white uncertainty bounds refers to the training period 1968-2009 used to determine the parameters of the glacier model, the second portion with green uncertainty bounds refers to the simulation of the snout variations over the period 2010-2050 from the climate scenarios. The red curves refer to the average of the glacier model runs.

Both the scenarios considered indicate a continuing retreat of the glacier snout position of about 300 meters in 2050 with respect to the glacier snout position in 2010. This similarity can be explained by the fact that both the A1B and RCP4.5 scenarios are characterized by a stabilization of the CO₂ concentration and of radiative forcing respectively from the middle of the century leading to a similar CO₂ concentration in the 2100 (~760 ppm CO₂ for A1B and 4.5 W/m² equivalent to 650 ppm CO₂ for RCP4.5).

7. DISCUSSION AND CONCLUSIONS

The aim of this work was to study the average behavior of a set of Alpine glaciers in the north-western Italian Alps under different climate change scenarios. We implemented a simple linear-lagged model that can be used to estimate the mean response of Alpine glaciers to basic climate indicators, such as temperature and precipitation. The model is easy manageable as it depends only on four meteorological predictors, which can be justified in terms of glacier physics. The cross-validation shows that the model is reliable for estimating glacier retreat in north-western Italy in into the past and in the near future.

So, using this model, we estimated the behavior of the average glacier snout fluctuations during the next 50 years and under two different and comparable climate forcing scenarios, based both on SRES and on RCP approach. For the SRES family, we selected the A1B scenario and we applied a Multimodel-Super Ensemble technique to the outputs of several Regional Climate Models from the ENSEMBLES project, in order to obtain a common signal. As regard RCP approach, we used the GCM output of EC-EARTH under RCP 4.5 scenario.

The empirical model, show a strong dependence of snout fluctuations by summer temperatures and winter precipitation, with a temporal lag of respectively 5 and 10 years. The model is able to reproduce well the glacier behavior observed in the last 50 years, even under out of sample conditions (not showed here).

Moreover, both scenarios we investigated through our linear model, show a common trend of glacier retreat in the north-western Italian Alps for the next 40 years, at a very similar rate of about 7.5 m/yrs.

As a word of caution, we note that for strong glaciers retreat the assumption of linear response to climate forcing may be invalid and when the glaciers shrink to smaller lengths, the model is not applicable, so it cannot be used to copy glaciers behavior while they are disappearing.

8. ACKNOWLEDGMENTS

We acknowledge useful discussions with Nicola Loglisci and Renata Pelosini of ARPA Piemonte, Marco Turco of CMCC and Sandro Calmanti of ENEA. We are grateful to Jost von Hardenberg of CNR-ISAC for help with the EC-Earth climatic simulations. This work was partially funded by the EU FP7 Integrated Project ACQWA (www.acqwa.ch) and by the Project of Interest NextData (www.nextdataproject.it) of the Italian Ministry for Education, University and Research (MIUR).

9. REFERENCES

- Calmanti S., Motta L., Turco M. and Provenzale A., (2007). *Impact of climate variability on Alpine glaciers in northwestern Italy*. International Journal of Climatology, No. 27: pp. 2041–2053. (1)
- Cane D., Barbarino S., Renier L.A. and Ronchi C. (2012). *Regional climate models downscaling in the Alpine area with Multimodel SuperEnsemble*, Hydrol. Earth Syst. Sci. Discuss., No. 9, pp. 9425-9454. (2)
- Hazeleger W. (2012). *EC-Earth v2.2: description and validation of a new seamless Earth system prediction model*, Climate Dynamics, No. 39, pp. 2611-2629. (3)
- IPCC (2007). *Climate Change 2007: The Physical Science Basis*. Contribution of Working Group I to the Fourth Assessment Report of the Intergovernmental Panel on Climate Change. Cambridge University Press, Cambridge, United Kingdom and New York, USA. (4)
- Jouvet G., Huss M., Blatter H., Picasso M. and Rappaz J. (2009). *Numerical simulation of Rhonegletscher from 1874 to 2100*, J. Comp. Phys, No. 228, pp. 6426–6439. (5)
- Kalnay E. (2003). *Atmospheric modeling, data assimilation and predictability*. Cambridge University Press, Cambridge. (6)

- Moss R.H, et al. (2010). *The next generation of scenarios for climate change research and assessment*, Nature, No. 463, pp. 747–756. (7)
- Oerlemans J. (2001). *Glaciers and climate change*. Balkema Publishers. Lisse. (8)
- Oerlemans J. (2011). *Minimal Glacier Models*. Second print. Igitur, Utrecht Publishing & Archiving Services, Universiteitsbibliotheek Utrecht. (9)
- Ronchi C., De Luigi C., Ciccarelli N. and Loglisci N. (2008). *Development of a daily gridded climatological air temperature dataset based on a optimal interpolation of ERA-40 reanalysis downscaling and a local high resolution thermometers network*. Dissertation, 8th EMS Annual Meeting & 7th European Conference on Applied Climatology, 2008, Amsterdam, The Netherlands. (10)

Has the ocean contributed to the decline of European eel recruitment? Results of a 40-year simulation experiment

Schiavina M.^{1*}, Casagrandi R.^{1,2}, Gatto M.^{1,2}, Bonaventura L.³, Masina S.^{4,5} and Melià P.^{1,2}

¹*Dipartimento di Elettronica, Informazione e Bioingegneria, Politecnico di Milano, Milano, Italy,*

²*Consorzio Interuniversitario per le Scienze del Mare, Roma, Italy,*

³*MOX, Dipartimento di Matematica "F. Brioschi", Politecnico di Milano, Milano, Italy,*

⁴*Centro Euro-Mediterraneo per i Cambiamenti Climatici, Bologna, Italy,*

⁵*Istituto Nazionale di Geofisica e Vulcanologia, Bologna, Italy*

*Corresponding author: m.schiavina@gmail.com

Abstract

The European eel stock is declining since the late 70s. The causes of this decline are still debated, but most likely include habitat loss, water pollution, parasite impact, climate change and overfishing. In particular, climate change is deemed to have affected the larval migration of this catadromous fish from its reproductive area (the Sargasso Sea) to European coasts. Temperature changes might have changed the structure of the plankton community and decreased food availability, while changes in oceanic circulation might have affected migration routes and increased exposure to predation. So far, these (non mutually exclusive) hypotheses have been tested only through correlation analyses among aggregated indices of recruitment, oceanic circulation and environmental features. Attempts to describe eel migration by means of Lagrangian simulations with coupled physical-biological models have been limited to short-term analyses and did not provide any information on possible changes of recruitment success in the long run. In this work, we used a Modular Ocean Model simulating the North Atlantic circulation between 1958 and 2000 to assess if the probability of eel larvae to reach the continental shelf has significantly changed over the second half of the last century. Our main goal is to study the impact of climate change on the geographical distribution of eel larvae and their recruitment success.

Keywords: *European eel collapse, Larval dispersal, Coupled physical-biological models, Lagrangian simulations, Recruitment variability*



1. INTRODUCTION

Understanding the processes that drive the population dynamics of endangered marine species is a preliminary step to devise effective strategies of conservation management. To this end, the analysis of the bio-physical mechanisms determining the spatiotemporal variability of fish recruitment is a crucial source of information. The case of the European eel *Anguilla anguilla* is paradigmatic in this sense. The European eel is a panmictic species reproducing in the Sargasso Sea: eel larvae (also known as leptocephali) migrate across the North Atlantic Ocean following the Gulf Stream towards Europe and Africa, in a journey that lasts 2-3 years, before settling into continental waters. European eel recruitment underwent a dramatic decrease since the end of the 1970s [1], and the species has recently been included in the IUCN Red List as critically endangered. In 2007, the European Council issued the European Regulation EC 1100/2007, aimed to recover the stock by limiting commercial eel fisheries and restoring habitat suitability.

However, assessing the effectiveness of these measures is difficult, because the triggers of the demographic collapse are still poorly understood. A range of human pressures (e.g. overfishing, habitat loss and pollution) have affected the stock directly [1-3], but there are other indirect factors that have likely played a significant role, such as the disease anguillicolosis caused by the invasive nematode worm *Anguillicoloides crassus* [4,5], and climate change [6]. Climate change might have affected the probability to successfully complete the journey of European larvae towards the European continent: changes in oceanic circulation might have prolonged migration routes and increased exposure to predation, while temperature changes might have changed the structure of the plankton community and decreased food availability.

In this work we use a coupled physical-biological model of the migration of European eel larvae [7] to study the impact of climate change on the geographical distribution of eel larvae and their recruitment success. The physical model is based on a Modular Ocean Model [8], which covers the period 1958-2000. The biological model takes into account the major biological processes and was tuned on the basis of the available knowledge on the vital traits of the species and of field data gathered during oceanic surveys. In particular, we investigate, through Lagrangian simulations, how migration duration, migration success, and latitudinal distribution of arrivals have changed during the second half of the last century.

2. MATERIALS & METHODS

The thermohaline circulation of the Atlantic Ocean is described by a long-term (1958-2000) global ocean re-analysis [8]. Current velocity, temperature and salinity fields were obtained by forcing an eddy-permitting version of the Modular Ocean Model covering a near-global domain (78°S-78°N) with the results of an atmospheric re-analysis and by constraining it through data assimilation. The resolution of the model is constant (1/2°) in longitude, while it varies in latitude from 1/3° between 10°S and 10°N to 1/2° at the northern boundary of the domain.

Lagrangian simulations were performed by releasing a cohort of 5×10^6 particles, each one representing a single eel larva, every year from 1961 to 1997. Years from 1958 to 1960 were discarded because they are affected by the initial conditions of the ocean circulation model, which is set at rest at the beginning of the experiment. Particles were released daily within a time window encompassing the spawning season of the species (March to May) and distributed over time according to a Gaussian distribution with mean set to the 1st of April and SD = 20 days. The initial position of larvae was randomly drawn from a trivariate Gaussian distribution centred within the Sargasso Sea to match the available knowledge about the spawning region of the European eel (see [7] for further details). Trajectories were stepped forward via an explicit Euler method with a 3-hour-step and tracked for 4 years.

The physical model describing the transport of eel larvae is coupled with a biological model describing the main biological features that characterize the larval stage of this species: body growth, natural mortality and movement. Vital rates are linked to body size, which, along with temperature, is a primary determinant of all biological processes of the European eel [9-11]. Parameter settings for each sub-model are defined according to the scenario that best reproduces observed field data (see [7] for a full description of each biological component and of the model selection procedure).

Body growth is described by a power function linking body length L to age x ($L(x) = 77 - 73.05 \exp(-0.09x)$, with x in months and L in mm) that was fit to body length data collected at the beginning of the 20th century [12]. The model accounts for plasticity in body growth [13] by describing inter-individual variability through an assignment-at-birth approach ([14], see [7] for details).

The mortality sub-model relies upon the metabolic theory of ecology [15] and is based on a model originally developed for the continental phase of European eel life cycle [11] and adapted to the larval

stage [7]. Mortality rate μ is described as a function of body mass M (through an allometric term) and water temperature T (through a Boltzmann-Arrhenius factor), namely $\mu = a \exp(-E/kT) M^b$, where M is expressed in grams and T in Kelvin, E is the activation energy ($= 1.23$ eV, [7,11]) and k the Boltzmann coefficient ($= 8.62 \times 10^{-5}$ eV K⁻¹), a is a proportionality coefficient ($= 4.26 \times 10^{20}$ [7]) and b is the allometric exponent ($= -0.46$ [11]). Body mass M is calculated from body length L using the morphometric relationship $M = 2.24 \times 10^{-7} L^{3.37}$ [16].

The movement sub-model describes the locomotion and navigation ability of eel larvae. Larval locomotion takes place along both the horizontal and vertical direction. Horizontal locomotion (propulsion) has a crucial role in determining the migration schedule and the migration success [7]. Eel larvae are supposed to swim with a speed proportional to their body length (one body length per second) and to orient their swimming along the direction of the current [7]. Besides their movement on the horizontal plane, eels larvae undergo a diel vertical migration [17] driven by a negative phototaxis, i.e. at daytime they swim at deeper depths than at night-time. Uncertainty associated to the vertical distribution of eel larvae is mimicked by randomly drawing the position of each larva from Gaussian distributions with different means at daytime and night-time. The parameters of the night-time distribution are kept constant (mean \pm SD = 60 \pm 25 m) along the whole journey, while the mean of the daytime distribution increases linearly with body length from 73.5 m at $L = 5$ mm to 470 m at $L = 80$ mm, with a constant SD of 25 m [7].

The arrival of eel larvae to continental waters was monitored along the 15°W meridian. For each cohort, we recorded the number of successful arrivals, the median duration of the migration and the latitudinal distribution of arrivals. Then, we tested for possible changes in these metrics over the study period through a modified Mann-Kendall trend test (MKT) [18], which explicitly accounts for the effect of possible autocorrelation in time series.

3. RESULTS

The results of the Lagrangian simulations show a high inter-annual variability of the metrics monitored along the 15°W meridian. The probability of success (Fig. 1) is, in particular, subject to very wide fluctuations (spanning 3 orders of magnitude) and ranges between a minimum of 0.002% for the 1997 cohort and a maximum of 0.973% for the cohort released in 1982. The average (\pm SD) success rate over the whole study period was 0.132% \pm 0.200%. The MKT test did not detect any significant trend in the series ($P > 0.05$). Therefore, we run a test for the presence of possible discontinuities in the series following the algorithm proposed by [19] and found a discontinuity in the time series in 1972. Tab. 1 reports the basic statistics of migration success for the periods 1961-1972 and 1973-1997, showing a remarkable difference in the mean value and an increase in the standard deviation of migration success. A MKT performed separately on the two time series revealed significant trends in both periods ($P < 0.05$ for 1961-1972 and $P \ll 0.001$ for 1973-1997). Linear regression lines fitting the two sub-samples show a positive trend before 1972 and a negative trend in the second period.

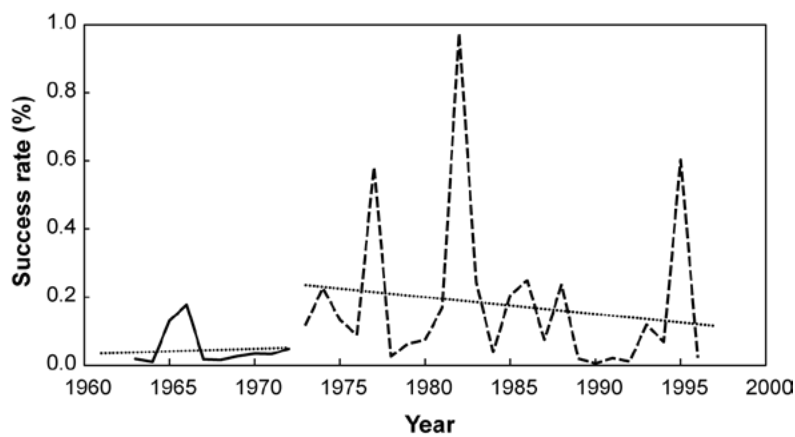


Fig. 1: Migration success recorded along the 15°W meridian between 1961-1972 (solid line) and 1973-1997 (dashed line). The year refers to the date in which the corresponding cohort was released from the Sargasso Sea. The dotted lines indicate the relevant regression lines (1961-1972: $y = 0.00002x + 0.0305$; 1973-1997: $y = -0.00005x + 0.1003$)

Period	Mean \pm S.D.	Median	I – III quartiles
1961-1972	0.043% \pm 0.052%	0.022%	[0.014% - 0.038%]
1973-1997	0.175% \pm 0.224%	0.089%	[0.026% - 0.226%]

Table 1: Basic statistic of migration success for the periods 1961-1972 and 1973-1997

Median migration duration (Fig. 2) ranged between a minimum of 25.0 months for the 1987 cohort and a maximum of 45.3 months for the 1961 cohort, with an average (\pm SD) of 33.5 ± 5.6 months. The MKT test indicated a weakly significant trend in the series ($P < 0.05$). The regression of migration duration on time has a negative coefficient, indicating that the duration of the larval migration is decreasing, on average, by about 6 days per year.

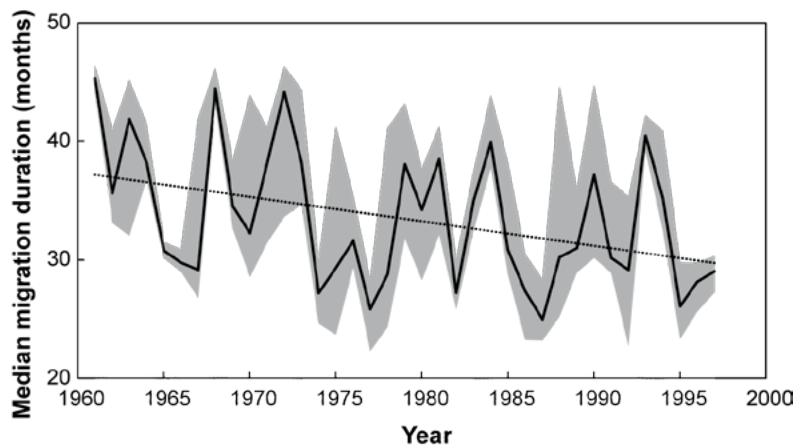


Fig. 2: Median (solid line) and interquartile range (gray area) of migration duration (from the Sargasso Sea to the 15°W meridian) for each cohort released between 1961-1997. The dotted line indicates the regression line ($y = -0.2073x + 443.71$)

The average latitude of arrivals (Fig. 3) ranged between 48.97°N in 1961 and 34.16°N in 1989, with a mean (\pm SD) of $42.06 \pm 4.20^\circ$ N. The MKT test revealed a strongly significant ($P \ll 0.001$) trend in this series, with the mean latitude of arrival that is moving southwards by ca. $1/4^\circ$ per year.

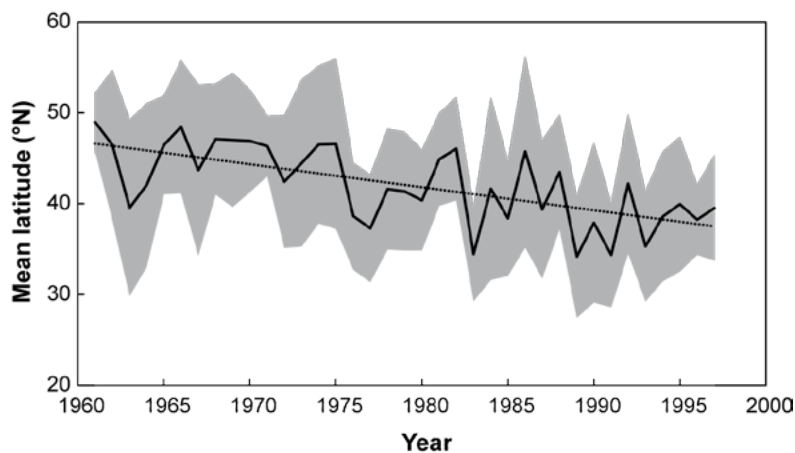


Fig.2: Mean (solid line) \pm standard deviation (gray area) of the latitude of arrival measured along the 15°W meridian for each cohort released between 1961-1997. The dotted line indicates the regression line ($y = -0.2538x + 544.42$)

4. DISCUSSION

Our Lagrangian simulations have been performed on the basis of a number of hypotheses, some of which may not hold in the real world. For instance, Lagrangian particles have been released from a spatio-temporal distribution whose moments are kept constant year after year. Although little is known about the environmental cues followed by European eel spawners to reach their mating grounds, the most recent studies on the oceanic hydrography of the Sargasso Sea region and on the spatial distribution of European eel larvae suggest that the spawning area is delimited by two sharp fronts in the thermocline with a mixing zone in between, where the youngest larvae have been found [20]. Such a structure could be the target of spawner migration and could enhance recruitment success acting as a nursery for eel larvae, offering a suitable habitat and superior feeding conditions [20]. As inter-annual fluctuations in hydrodynamic features may slightly displace the actual spawning location from year to year, releasing larvae from the same location may have biased our results. A correct identification of this structure is crucial to generate realistic simulations and deserves additional investigation.

The results of analysing the time series of migration success suggests that a regime shift has occurred during the 1970s, causing a switch from a positive trend to a negative one. Detecting regime changes in time series is a challenging task, and our analysis provides only preliminary insights about the possible evolution of this metric over the study period. However, it is worth noting that previous work has already put forward the hypothesis that a regime shift (detected from the analysis of time series of glass eel recruitment) has occurred during the 1970s [21]. Understanding the hydrodynamic mechanisms that might have caused this change undoubtedly requires further research effort, but if more comprehensive statistical analyses confirmed the existence of some form of discontinuity in oceanic features affecting the migration success of European eels this would provide an important contribution to the discussion about the causes of the collapse of the species.

Our results indicate also a decreasing, although weakly significant, trend of the migration duration, with a reduction of the median value of this metric of about 6 months in 40 years. If this trend were confirmed by evidence from the field, it might have severe implications for the recruitment schedule of eel leptocephali. Although the actual triggers for metamorphosis from the leptocephalus to the glass eel stage are poorly understood, physical signals such as temperature gradients are likely to have an important regulatory effect on this process [22], and a desynchronization between the periodic temperature fluctuations of the oceanic system and the schedule of the eel journey might have a

dramatic impact of the viability of this endangered species. Also, a change of the season in which leptocephali reach European shelves might change the environmental conditions they encounter at their arrival. The high plasticity in vital traits of catadromous eels makes them likely able to buffer, at least to some degree, the intrinsic inter-annual variability of the oceanic circulation. However, a systematic shift in circulation features affecting their journey may be difficult to face even for a tolerant species such as the European eel. For instance, losing the synchronization between the arrival of leptocephali and the rainy season, when the freshwater lure calls eel larvae into the continental water system, might increase the time they have to wait in the open sea, exposing them to increased risk of predation and reducing their probability to successfully settle into inland waters.

We also identified a significant trend in the average latitude of arrivals. Arrivals of European eel larvae usually have a bimodal distribution, with a major peak in the Biscay bay (historically the region with the highest recruitment) and a minor peak close to the Strait of Gibraltar [7,23]. The observed change in mean (a shift of almost 10 latitude degrees southwards over four decades) suggests that the northernmost peak has reduced its weight while the southernmost one has increased its. Although this has no direct consequences on migration success, it could explain why recruitment time series from the Atlantic coasts (where the glass eel fishery was historically most important) are consistently declining, while the decline is less evident from the few time series available for the Mediterranean Sea (Alain Crivelli, pers. comm., Fabrizio Capoccioni, pers. comm.). A southward shift in the average latitude would displace a larger proportion of the stock towards a region characterized by highly productive coastal waters and higher temperatures, with the probable effect of shortening the duration of the continental phase of the eel's life cycle, but with final consequences on the viability of the species that are difficult to predict.

Our simulation exercise suggests that the ocean has an active role in determining the variability of eel recruitment to continental waters, but it is difficult to definitely confirm whether long-term changes in oceanic circulation have significantly contributed to the collapse of the stock. Further simulation effort and field work are needed to improve our comprehension of the larval migration of the European eel. Although our work is not exempt from limitations, we believe that it provides interesting preliminary insights on how the ocean might have contributed to the observed decline of the recruitment of this mysterious fish.

5. ACKNOWLEDGMENTS

This work has been funded by the Italian Ministry of University and Research (PRIN Project 2008E7KBAE) and the European Commission (FP7 grant agreement 318048).

6. REFERENCES

- Kettle A.J., Vøllestad L.A. & Wibig J. (2011), *Where once the eel and the elephant were together: decline of the European eel because of changing hydrology in southwest Europe and northwest Africa?*, *Fish and Fisheries*, 12, pp. 380-411. (1)
- Feunteun E. (2002), *Management and restoration of European eel population (Anguilla anguilla): an impossible bargain*, *Ecological Engineering*, 18, pp. 575-591. (2)
- Dekker W. (2003), *Did lack of spawners cause the collapse of the European eel, Anguilla anguilla?*, *Fisheries Management and Ecology*, 10, pp. 365-376. (3)
- Lefebvre F. & Crivelli A.J. (2005), *Anguillicolosis: dynamics of the infection over two decades*, *Disease of Aquatic Organisms*, 62(3), pp. 227-232. (4)
- Lefebvre F., Fazio G., Mounaix B. & Crivelli A. J. (2013), *Is the continental life of the European eel Anguilla anguilla affected by the parasitic invader Anguillicoloides crassus?*, *Proceedings of the Royal Society B*, 280, pp. (5)
- Knights B. (2003), *A review of the possible impacts of long-term oceanic and climate changes and fishing mortality on recruitment of anguillid eels of the Northern Hemisphere*, *The Science of the Total Environment*, 310, pp. 237–244. (6)
- Melià P., Schiavina M., Gatto M., Bonaventura L., Masina S. & Casagrandi R. (2013), *Integrating field data into individual-based models for the migration of European eel larvae*, *Marine Ecology Progress Series*, *in press*. (7)
- Masina S., Di Pietro P., Navarra A. (2004), *Interannual-to-decadal variability of the North Atlantic from an ocean data assimilation system*, *Climate Dynamics*, 23, pp. 531-546. (8)
- Melià P., Bevacqua D., Crivelli A.J., Panfili J., De Leo G.A. & Gatto M. (2006b), *Sex differentiation of the European eel in brackish and freshwater environments: a comparative analysis*, *Journal of Fish Biology*, 69, pp. 1228-1235. (9)

- Bevacqua D., Melià P., Crivelli A.J., De Leo G.A. & Gatto M. (2006), *Timing and rate of sexual maturation of European eel in brackish and freshwater environments*, *Journal of Fish Biology*, 69 (Suppl. C), pp. 200-208. (10)
- Bevacqua D., Melià P., De Leo G.A. & Gatto M. (2011), *Intra-specific scaling of natural mortality in fish: the paradigmatic case of the European eel*, *Oecologia*, 165, pp. 333-339. (11)
- Schmidt J. (1923), *The breeding places of the eels*, *Philosophical Transactions of the Royal Society B*, 211, pp. 179-208. (12)
- De Leo G.A. & Gatto M. (1995), *A size and age-structured model of the European eel (Anguilla anguilla L.)*, *Canadian Journal of Fisheries and Aquatic Sciences*, 52, pp. 1351-1367. (13)
- Kirkpatrick M. (1984), *Demographic models based on size, not age, for organisms with indeterminate growth*, *Ecology*, 65, pp. 1874-1884. (14)
- Brown J.H., Gillooly J.F., Allen A.P., Savage V.M. & West G.B. (2004), *Toward a metabolic theory of ecology*, *Ecology*, 85, pp. 1771-1789. (15)
- Melià P., Bevacqua D., Crivelli A.J., De Leo G.A., Panfili J. & Gatto M. (2006a), *Age and growth of Anguilla anguilla in the Camargue lagoons*, *Journal of Fish Biology*, 68, pp. 876-890. (16)
- Castonguay M. & McCleave J.D. (1987), *Vertical distributions, diel and ontogenetic vertical migrations and net avoidance of leptocephali of Anguilla and other common species in the Sargasso Sea*, *Journal of Plankton Research*, 9, pp. 195-214. (17)
- Hamed K.H., Rao A.R. (1998), *A modified Mann-Kendall trend test for autocorrelated data*, *Journal of Hydrology*, 204, pp. 182-196. (18)
- Zeileis A., Kleber C., Krämer W. & Hornik K. (2003), *Testing and dating of structural changes in practice*, *Computational Statistics & Data Analysis*, 44, pp. 109-123. (19)
- Munk P., Hansen M.M., Maes G.E., Nielsen T.G., Castonguay M., Riemann L., Sparholt H., Als T.D., Aarestrup K., Andersen N.G. & Bachler M. (2010), *Oceanic fronts in the Sargasso Sea control the early life and drift of Atlantic eels*, *Proceedings of the Royal Society B*, 277, pp. 3593–3599. (20)
- Bonhommeau S., Chassot E. & Rivot E. (2008), *Fluctuations in European eel (Anguilla anguilla) recruitment resulting from environmental changes in the Sargasso Sea*, *Fisheries Oceanography*, 17, pp. 32-44. (21)

- Kuroki M., Fukuda N., Yamada Y., Okamura A. & Tsukamoto K. (2010), *Morphological changes and otolith growth during metamorphosis of Japanese eel *leptocephali* in captivity*, Coastal Marine Science, 34, pp. 31-38. (22)
- Bonhommeau S., Le Pape O., Gascuel D., Blanke B., Tréguier A.-M., Grima N., Vermard Y., Castonguay M. & Rivot E. (2009), *Estimates of the mortality and the duration of the trans-Atlantic migration of European eel *Anguilla anguilla leptocephali* using a particle tracking model*, Journal of Fish Biology, 74, pp. 1891–1914. (23)

IMPLICATIONS ON ECOSYSTEM SERVICES

Impacts on natural ecosystems - II

Climate change impacts on distribution and composition of the Alpine Natural Pasturelands

Dibari C.^{1*}, Argenti G.¹, Moriondo M.², Stagliano N.¹, Targetti S.³, and Bindi M.¹

¹ Department of Agri-food Production and environment Science (DISPAA), University of Florence, Italy;

² Institute of Biometeorology, National Research Council of Italy, IT;

³ Department of Agricultural Science of the University of Bologna, Italy.

*Corresponding author: camilla.dibari@unifi.it

Abstract

This research simulates the impacts of climate changes on seven main pastoral communities (pasture macro-types) located over the Italian Alps. More specifically, pre-existing spatial databases, namely pastoral cartography, habitat maps, and high resolution soil-topographic-climate datasets (WorldClim and HWSD) were integrated and harmonized within a GIS platform in order to identify seven pasture macro-types characterizing the Italian Alps. The pasture macro-types were those dominated by shrub species (SP), by *Carex curvula* (CC), by *Carex firma* (CF), by *Nardus stricta* (NS), by *Festuca* gr. *rubra* (FR), by *Sesleria varia* (SV), by xeric species (XS). Nine environmental parameters were then extracted from the soil-topographic-climate database and used as model predictors variables. Moreover, a computational framework (BIOMOD), collecting several statistical classification models, was used to select the model resulting with the best prediction accuracy. According to BIOMOD outputs, a machine learning approach (Random Forest, RF) was first calibrated for the present period and then applied to future conditions, as projected by HadCM3 General Circulation Model (GCM), in order to simulate possible spatial variation/shift in potential pastoral areas in three time slices (centred on 2020, 2050 and 2080) under A2 and B2 SRES scenarios. RF simulations showed a moderate reduction (<-16%) of areas potentially suitable to pastoral resource under the future CGM SRES scenarios. Conversely, future climate conditions will have impacts of great concern on pasture macro-types extent and distribution. Specifically, an overall decline, or in some cases complete loss, of lands suitable for the most rare (FR) or high-altitude macro-types (CC, CF, SV) is forecasted by RF simulations at the end of the century for both SRES scenarios. According to these results, the expected climate warming, coupled with an increasing abandonment of the traditional grazing practices over the Alps, will likely threaten the unique and rare herbaceous biodiversity characterizing the Alpine mountain range.

Keywords: Natural pastures, Alps, climate change, statistical models, Random Forest, BIOMOD.



It is evidence based that global warming is affecting the ecological processes of many plant ecosystems especially in marginal areas (e.g. alpine mountain ranges), where climate is one of the major drivers of plants distribution. In particular, in the last century the Alps have been experiencing a climate warming three times higher the global average and, according to climate model projections, changes in temperature, precipitation and extreme events are expected to even higher in the next future. Moreover, natural pastures located in the alpine mountain range are acknowledged as very sensitive and vulnerable ecosystems to climate change [1]. Several studies tried to assess climate effects either on single alpine grassland species [2, 3] or on very locally [4], but a comprehensive assessment of climate changes impacts on the alpine pastoral communities is still lacking at a territorial scale. To fill this gap, in this study we applied ground breaking techniques (classification models integrated with spatial data through GIS techniques) in order to define and environmentally characterize the main pasture macro-types over the Italian Alps. Potential impacts of future climate conditions on the identified pastoral communities distribution were analysed as well.

Current distribution and composition of the Italian alpine pastures were retrieved by integrating local pastoral cartographies, CORINE Land Cover Map, and Habitats Natura2000 Map within a GIS platform. By means of GIS techniques, legend harmonization and a heuristics based approach, the main pasture macro-types characterizing the Italian alpine chain were thus identified. The environmental parameters of the study area were acquired from a high-resolution soil-topographic-climate gridded database. The topographic variables (altitude, slope and aspect), present and future climate parameters (monthly maximum and minimum temperature and seasonal precipitation) were extracted from the WorldClim database [5], which is a set of global topographic and climate georeferenced layers (grids) with approximately 1 km x 1 km spatial resolution. WorldClim parameters referred to present period derive from the interpolation, through a thin-plate smoothing spline algorithm, of 150 thousand meteorological stations spread over the world, referenced to 1950-2000 baseline period. Conversely, WorldClim data referred to future climate derive from a statistical downscaling that has been performed by means of a correction factor, as simulated by the Global Circulation Model (GCM) HadCM3 [6], which was applied to the baseline climatology over the climatic variation of mean temperature and precipitation for each grid cells. More specifically, WorldClim future climate data refer to A2 and B2 SRES scenarios, both referenced to three time slices (short, medium and long-term period), 30 years long each, centred on 2020, 2050 and 2080, respectively. Soil features

(i.e. pH) were extracted from HWSO (Harmonized World Soil Database) [7], a relational grid spatial dataset having the same grid spatial resolution as WorldClim (1 km x 1 km). According to what reported in literature, seven predictive environmental variables were identified and calculated in order to characterize pasturelands. These variables comprise the mean maximum temperature of the warmest month (July) (TMAX_Jul), the mean minimum temperature of the coldest month (January) (TMIN_Jan), seasonal precipitation (Prec_DJF, Prec_MAM, Prec_JJA, Prec_SON) - respectively referred to Winter, Spring, Summer and Autumn seasons - and soil pH (pH). Pasture macro-types map was then spatially integrated into the soil-topographic-climatic dataset within a unique 1 km x 1 km gridded database within a GIS platform.

BIOMOD software (BIODiversity MODelling, [8]), which ensembles a range of statistical classification models widely used for environmental modelling (*Generalised Linear Models, Generalised Additive Models, Classification Tree Analysis, Artificial Neural Networks, Surface Range Envelops, Generalised Boosting Models, RandomForest*), was used to select the classification model maximizing the prediction accuracy amongst all models included in it. According to BIOMOD outputs, *RandomForest* – RF [9] was the model showing the lowest prediction error. RF, a machine-learning algorithm based on decision tree classifiers, has been widely used in many ecological studies, especially for predicting climate changes effects on species distribution [10, 11]. RF consists of a combination of decision trees where each classifier is generated using a bootstrap sample which is randomly split into two subsets, one used for training (66%) and one for internal testing (33%, Out-Of-Bag sample, OOB). RF was first trained to simulate pasturelands and pasture macro-types distribution for the present period. Considering that RF training performs at its best with balanced response variables [12] and being the integrated dataset highly unbalanced towards areas not covered by pastures (or pasture macro-types), the training dataset to feed RF was obtained using a five time reiterative one side sub-sampling, which included all the test cases where pastures (or pasture macro-type) occurred. Accordingly, the same number of test cases from those pixels not belonging to areas covered by pastures (or pasture macro-type) were also randomly sub sampled. The five random sub-sample RF models were comprehensively combined into a final model and thus applied over the whole dataset. RF calibration was performed on randomly selected 80% of pastures and pasture macro-types dataset, while the 20% was used for validation. RF model resulting from this procedure provided information on the Out Of Bag errors (OOB), the relative importance of each predictor, the partial dependence plot of probability of pastures and pasture

macro-types presence. The accuracy of RF simulation was evaluated on the validation dataset by the OOB sample, and calculated for each tree over the data split of the corresponding random bootstrap sample. Since OOB observations are not used in RF trees training, these represent cross-validated accuracy estimates. The probability scores outputs derived from RF application, were converted into presence/absence prediction maps by computing the True Skill Statistic index – TSS [13] that minimized the prediction error. Finally, the calibrated RF model was then applied to the spatial datasets to predict potential expansion/reduction and/or altitudinal shifts of pasturelands and of the identified pasture macro-types according to the three future time slices (2020, 2050 and 2080), as expected by A2 and B2 emission scenarios.

By a methodological approach, which relied on GIS data integration, legend harmonization and an heuristics based approach, seven pastoral macro-types were identified according to their extent over the Italian Alpine mountain range, their ecological importance and pastoral relevance: i) pastures encroached by shrub species (SP) (mainly belonging to *Vaccinium*, *Rhododendron* and *Calluna* genus); ii) pastures dominated by *Carex curvula* (CC); iii) by *Carex firma* (CF); iv) by *Nardus stricta* (NS); v) by *Festuca gr. rubra* (FR); vi) by *Sesleria varia* (SV); vii) by xeric species (XS). For all these macro-types, representing in terms of coverage the 83.5% out of the total pastures mapped by the background maps (about 202,000 ha), the main environmental, botanical and pastoral characteristics were defined and briefly described (data not shown).

The spatial resolution of soil, topography and climate baseline datasets used in this study (1 km x 1 km) may represent a wide area (hundred hectares) in mountain ranges where a high variety of heterogeneous environmental and landscape features are often combined. Nevertheless, dataset resolution was constrained by the availability of baseline maps over the whole study area. However, the environmental characteristics of the seven pastoral macro-types showed a high correspondence with respect to what reported in scientific literature [14, 15].

According to BIOMOD outputs, RF provided the best prediction accuracy amongst the seven models included in the computational framework. The summer climate predictive variables (i.e. TMAX_Jul and Prec_JJA) resulted the most determinant for pasturelands classification; whilst TMAX_Jul and pH for pasture macro-types classification.

With regards to present period, the application of RF classification model proved to be robust and very efficient to predict both lands suited to pastures (OOB = 12.7%) and to the seven pasture macro-types

(OOB = 14.3%). According to RF simulation, within the 2.08 million hectares currently covered by pastoral resources (data from Corine Land Cover, 2000), NS are the mostly common and wide spread macro-types over the Italian Alps (48%); whereas CF and FR the rarest and most restricted (1.8% and 1.1%, respectively). The rest of the areas are mainly eligible to CC, SP, SV and XS with a similar coverage ranging from 11.9% to 12.7%. Both current altitude distribution and pH attitudes referred to the seven pastoral macro types examined were also correctly predicted.

Concerning future climate impacts, the range of lands suited to pastures denoted a slight contraction over the three time slices examined. Particularly, the maximum reduction of pastures cover (-16%) coupled with a slight rise in the average altitude (+54 meters) is projected by 2070-2099 of B2 SRES scenario, with respect to present period (data not shown). Conversely, pastures composition is of great concern at the end of the century since a high decline in grassland biodiversity was predicted. Specifically, climatic conditions as projected in both A2 and B2 SRES scenarios by the middle of the century, will likely determinate, with respect to the baseline period, a general reduction of areas potentially suitable for the high-altitude macro-types. In particular, an evident decline of lands suitable for the rarest macro types (i.e. FR) or pastures currently restricted at the highest altitudes of the alpine range (i.e. CC, CF and SV) was predicted. Conversely, pastures dominated by XS showed wide expansion (+356% and +294%, for A2 and B2 scenarios respectively), whereas NS displayed the slightest reduction (< -30% in A2) (Tab. 1). At the end of the century the 97.7% (A2 scenario) and the 94.6% (B2 scenario) of pasturelands are expected to be suitable only for two main pastoral macro types, namely XS and NS with a 60.2% and 37.3% of coverage (in A2) and 39.7% and 54.8% (in B2), respectively (data not shown). By a cross tabulation analysis, at the end of the century out of the 95.8% of pastures currently suitable for SP are expected to be occupied by NS (39.4%) and XS (56.4%) in A2 scenario (the 63.0% of SP will turn into NS in B2). At the latest time slice, more the 80% of lands currently suited to the highest altitudes macro-types (i.e. CC, SV and CF) or rare pasture macro-types (i.e. FR) will be likely environmentally eligible only to NS and XS, under both A2 and B2 scenarios (Tab. 1).

Table 1: Percentage of expansion (+) or reduction (-) of pasture macro-types with respect to present period; cross tabulation (in percentage out of total) of pasture macro-types

			% of Cross tabulation out of total							
			Exp./red. (%)	SP	CC	CF	NS	FR	XS	SV
A2	2020	SP	+16	53.1	7.6	2.2	21.9		7.0	8.2
		CC	-17	6.8	49.1	1.5	24.0	0.2	0.6	17.8
		CF	-12	42.6	13.3	29.5	6.7		2.1	5.9
		NS	-19	7.4	5.3	0.1	63.4	0.2	15.0	8.7
		FR	-72	18.6	5.7	0.7	18.6	21.4	18.6	16.4
		XS	+88	0.6			4.8	0.1	93.6	0.9
		SV	22	9.5	10.3	2.5	10.9	0.4	6.4	59.9
	2050	SP	-95	1.7	2.9		66.3		26.2	2.9
		CC	-83	0.9	7.2		81.4		4.1	6.4
		CF	-100	2.1	0.1		80.8		16.9	0.1
		NS	-5	0.3	1.1		52.8		45	0.8
		FR	-100				19.8		77.8	2.5
		XS	+200				2.1		97.6	0.3
		SV	-81	1.9	4.1		51.6		33.9	8.6
	2080	SP	-96	2.2	0.5		39.4		56.4	1.5
		CC	-97	1.1	1.2		75		20.6	2
		CF	-100				90.5		9.5	
		NS	-30	0.1	0.2		25.8		73.4	0.5
		FR	-100				5.2		94.8	
		XS	+356	0.2	0		2.6		97.2	
		SV	-90	0.7	1		46.9		43.3	8.2
B2	2020	SP	-10	26.6	7	0.1	46		14.7	5.5
		CC	-33	13.4	30.8		40.1	0.1	0.4	15.1
		CF	-98	38.9	17.8	0.2	30		8.2	4.8
		NS	-4	5.2	3.3		64.3	0.2	21.2	5.8
		FR	-81	7.7	3.8		33.1	7.7	23.8	23.8
		XS	+115	0.1			4.7		95.1	0.2
		SV	-20	14.2	11.5	0.1	24.7	0.1	15.6	33.8

			% of Cross tabulation out of total							
B2		Exp./red. (%)	SP	CC	CF	NS	FR	XS	SV	
			2050	SP	-87	2.4	3.2		66.2	
CC	-77	1.1		11.6		79.2		2.6	5.5	
CF	-100	7.4		0.4		79.8		12.3	0.1	
NS	-3	0.4		0.7		50.3		47.9	0.7	
FR	-100					20.7		78	1.3	
XS	+294					2.4		97.5	0.1	
SV	-76	6.7		5.2		37		37	14.2	
2080	SP	-97	0.9	0.9		63		31.9	3.2	
	CC	-87	0.3	5.7		84		5.4	4.6	
	CF	-100	0.1			86.3		13.6	0	
	NS	-5	0.4	0.7		55.4		41.9	1.6	
	FR	-100		0.5		50.5		48.5	0.5	
	XS	+179				10.2		89.6	0.3	
	SV	-79	0.9	4.2		48.7		32.2	14	

In conclusion, ground-breaking tools, namely classification models coupled with spatial data integration by GIS techniques, proved to be reliable to predict potentially suitable areas for pasturelands and pasture macro-types under A2 and B2 climate change scenarios. This approach, though not considering vegetation successions nor species inter-actions, intrinsically incorporates the long lasting influence of species competition, through fitting pasture response to the environmental predictors. Very likely, the abandonment of alpine grasslands, which is the main current trend, will promote the substitution of NS and XS macro-types with SP and, therefore, will exacerbate the effects of climate warming on biological diversity and ecosystem services of the alpine permanent grasslands. However, the effects of pastures management/abandonment and their interactions with climate factors would need a separate *ad-hoc* analysis, which goes beyond the objectives of the present paper. The implemented methodology, resulting robust and very reliable in this study, could be easily applied over the entire Alpine chain. According to RF simulations, a moderate reduction of areas potentially suited to pastoral resources is expected under the future climatic conditions as predicted at the end of the century by the two SRES scenarios. Specifically, pasture composition is of great concern especially if we consider that pastoral resources significantly contribute, with their unique flora, to the alpine biodiversity. The distribution of the seven pastoral macro-types examined in this study is predicted to severely vary as a consequence of

global warming and reduction in precipitation. Nevertheless, an overall decline, or in some cases complete loss, of lands suitable for the most endangered macro-types is simulated by RF under future climate. Finally, as also confirmed by Dirnböck et al. [16], Gottfried et al. [17] and Pauli et al. [18], the permanent grassland dominating the highest belt of the Alps will likely cope with relevant contractions, threatening the typical and unique herbaceous biodiversity of the alpine ecosystems.

ACKNOWLEDGMENTS

The authors are gratefully to the Italian Institute for Environmental Protection and Research of Italy (ISPRA) and to the colleagues of the Department of Agriculture, Forest and Food science of the University of Turin for providing us with the dataset of Habitats Natura2000 Map and the pastoral cartography, respectively.

REFERENCES

- IPCC (2007), *Climate Change 2007: The Physical Science*. Contribution of Working Group I and II to the Fourth Assessment Report of the Intergovernmental Panel on Climate Change. (1)
- Gottfried M., Pauli H., Reiter K. & Grabher G. (1999), *A fine-scaled predictive model for changes in species distribution patterns of high mountain plants induced by climate warming*. Diversity Distributions, No. 5, pp. 241-251. (2)
- Cannone N., Sgorbati S. & Guglielmin, M. (2007), *Unexpected impacts of climate change on alpine vegetation*. Frontiers in Ecology and the Environment No. 5, pp. 360–364. (3)
- Guisan A. & Thuiller W. (2005), *Predicting species distribution: offering more than simple habitat models*. Ecology letters No. 8, pp. 993-1009. (4)
- Hijmans R.J., Cameron S.E., Parra, J.L., Jones P.G. & Jarvis A. (2005), *Very high resolution interpolated climate surfaces for global land areas*. International Journal of Climatology No. 25, pp. 1965-1978. (5)
- Pope V.D., Gallani M.L., Rowntree P.R. & Stratton R.A. (2000), *The impact of new physical parameterizations in the Hadley Centre climate model — HadAM3*. Climate Dynamics No. 16, pp. 123–146. (6)
- Nachtergaele F., Van Velthuizen H., Verelst L., Batjes N., Dijkshoorn K., Van Engelen V., Fischer G., Jones A., Montanarella L. & Petri, M. (2008), *Harmonized World Soil Database*. Rome, FAO and Laxenburg, IIASA. (7)

- Thuiller W., Lafourcade B., Engler R. & Araùjo M.B. (2009), *BIOMOD - a platform for ensemble forecasting of species distributions*. *Ecography* No. 32, pp. 369-373. (8)
- Breiman L. (2001) *Random Forests*, *Machine Learning* No. 45(1), pp. 5-32. (9)
- Moriondo M., Stefanini F.M. & Bindi M. (2008), *Reproduction of olive tree habitat suitability for global change impact assessment*. *Ecological modelling* No. 218, pp. 95–109. (10)
- Evans J.S. & Cushman S.A. (2009), *Gradient modeling of conifer species using random forests*. *Landscape and Ecology* No. 24, pp. 673–683. (11)
- Evans J.S., Murphy M.A., Holden Z.A., Drew C.A., Wiersma Y.F. & Huettmann F., (2011), *Modelling Species Distribution and Change Using Random Forest*. In *Predictive Species and Habitat Modelling in Landscape Ecology*, Drew C. A. et al. (eds). Cap. 8: 139-159. Springer Science+Business Media. DOI 10.1007/978-1-4419-7390-0_8. (12)
- Allouche O., Tsoar A & Kadmon R. (2006), *Assessing the accuracy of species distribution models: prevalence, kappa and the true skill statistic (TSS)*. *Journal of Applied Ecology*, No. 43, pp. 1223-1232. (13)
- Ellenberg H. (1988), *Vegetation ecology of central Europe*. Cambridge University Press, Cambridge, UK (<http://www.efnecp.org/download/Grasslands-in-Europe-brochure.pdf>). (14)
- Veen P., Jefferson R., De Smidt J. & van der Straaten J. (2009), *Grasslands in Europe of high nature value*. Zeist, The Netherlands: KNNV Publishing. (15)
- Dirnböck T., Essl F. & Rabitsch W. (2011), *Disproportional risk for habitat loss of high-altitude endemic species under climate change*. *Global Change Biology*, No. 17, pp. 990-996. (16)
- Gottfried M., Pauli H., Futschik A., Akhalkatsi M., Barančok P., Benito Alonso J.L., Coldea G., Dick J., Erschbamer B., Fernández Calzado M.R., Kazakis G., Krajči J., Larsson P., Mallaun M., Michelsen O., Moiseev D., Moiseev P., Molau U., Merzouki A., Nagy L., Nakhutsrishvili G., Pedersen B., Pelino G., Puscas M., Rossi G., Stanisci A., Theurillat J.P., Tomaselli M., Villar L., Vittoz P., Vogiatzakis I. & Grabherr G. (2012), *Continent-wide response of mountain vegetation to climate change*. *Nature Climate Change* 10.01.2012. (17)
- Pauli H., Gottfried M., Dullinger S., Abdaladze O., Akhalkatsi M., Benito J.L., Coldea G., Dick J., Erschbamer B., Fernández M.R., Goshn D., Holten J.I., Kanka R., Kazakis G., Kollár J., Larsson P., Moiseev P., Moiseev D., Molau U., Molero-Mesa J., Nagy L., Pelino G., Puscas M., Rossi G., Stanisci A., Syverhuset A.O., Theurillat J.P., Tomaselli M., Unterluggauer P., Villar L., Vittoz P. & Grabherr G. (2012), *Recent Plant Diversity Changes on Europe's Mountain Summits*. *Science* No. 336, pp. 353-355. (18)

Larval connectivity in the Central Pacific Ocean: lagrangian simulations in the Northern Line Islands

Mari L.^{1,2}, Melià P.¹, Gatto M.¹, Storto A.³, Vichi M.^{3,4}, Masina S.³ and Casagrandi R.^{1*}

¹*Dipartimento di Elettronica, Informazione e Bioingegneria, Politecnico di Milano,*

²*Laboratory of Ecohydrology, Ecole Polytechnique Fédérale de Lausanne,*

³*Dept. of Numerical Applications and Scenarios, CMCC, Bologna,*

⁴*Istituto Nazionale di Geofisica e Vulcanologia, Bologna,*

*Corresponding author: renato.casagrandi@polimi.it

Abstract

By influencing flows and currents in the oceans, climate change might seriously affect the connectivity of coral reefs, one of the most diversified ecosystem of our planet. Assessing if and to what extent larval dispersal could be altered is an important challenge. This is particularly true for remote Pacific Islands, very small states whose survival is by all means based on the protection of their natural resources. Here we use Lagrangian simulations to study the present and the future connectivities of the five Northern Line Islands, in the Central Pacific Ocean. In particular, we focus our attention on the Palmyra Atoll (US) because it is a natural reserve and therefore it can play a major role in conservation. We discuss how connectivity from and to Palmyra Atoll changes through the months of the year and how it is influenced by the Pelagic Larval Duration (PLD) of dispersing species. Despite the long distances involved (on the order of thousands of kilometers), we find non negligible connections even between islands that are far apart, and for reasonable PLDs (from few weeks to three months). As for the long term scenarios, our simulations over the time horizon 1970-2098 do not reveal (at present) any clear trend, although some peaks in connectivities seem to emerge out of erratic patterns.

Keywords: *Pelagic Larval Duration, Coral Reefs, Metacommunities*



The extraordinary variety of organisms that inhabit our Earth results from the never-ending action of natural selection. For billions of years, the perennial change of environmental conditions has played a crucial role in causing the diversification of (i) individuals within populations (genetic diversity), (ii) species within ecosystems (species diversity), and (iii) ecosystems within biomes (ecosystem diversity). The importance of biodiversity at all the biological levels is not only restricted to aesthetics or pure science. Much empirical evidence [1] shows that there is a positive correlation between species diversity and ecosystem productivity and stability. This means that more diversified ecosystems are characterized by a larger biomass production per unit time, thus generating more resources. Also, more diversified ecosystems generally support more trophic levels and are less prone to invasion from alien species. In addition to food and fiber production, ecosystems also provide other services such as natural protection from catastrophic events.

The diversity of life on Earth is very unevenly distributed in space. Extensive reviews of available data in both terrestrial and marine ecosystems [2,3] have revealed that biodiversity is concentrated in some regions of the planet, called the “hotspots” of biodiversity. The Small Island Developing States of South Pacific are actually one of the richest hotspots of biodiversity, thus being of paramount importance for ecological conservation at the global scale. Also, this network of small islands consists of small archipelagos in which local populations of animals and plants are weakly connected by dispersal. Thus these fragmented habitats are prototypical examples of metapopulations and metacommunities [4].

In particular, coral reefs are among the most diversified ecosystems of our planet and have high aesthetic, recreational and resource value. They act as nurseries for many marine species of commercial value, thus sustaining many fisheries. Rapid climate change is expected to impact on population connectivity in coral reef ecosystems [5]. Higher ocean temperatures may accelerate larval development thus reducing pelagic larval duration and earlier reef-seeking behavior. Changes to oceanic currents can alter the dynamics of larval supply to the islands. Reduction of dispersal distances might lead to patch isolation thus increasing the extinction risk, especially if the species are also subject to fishing pressure.

Coral reefs constitute a unique natural environment endowed at the same time with very complex and peculiar hydrodynamic features [6]. These structures can play a significant role in protecting the coastal areas from tropical storms or tsunami waves [7,8], which in turn have an important impact on the ecology of the reefs [9]. Studying their hydrodynamic features is essential for the full understanding of

their response to changes in sea temperature, sea level, nutrient load and storm frequency, and for providing information on the dispersal pathways of marine organism between different islands.

In this preliminary work we aim to assess the patterns of potential connectivity of coral reef ecosystems, with specific reference to a class of organisms of ecological and conservation interest, namely the reef builder corals. For these organisms, the connectivity network is largely determined by passive dispersal of coral propagules transported by oceanic currents. Our study area is represented by the Line Islands (Fig.1, Republic of Kiribati), a chain of eleven atolls and low coral islands in the central Pacific Ocean, south of the Hawaiian Islands, that stretches for 2,350 km in a northwest-southeast direction, making it one of the longest islands chains of the world. Eight of the islands form part of Kiribati, while the remaining three are United States territories grouped with the United States Minor Outlying Islands. The group is geographically divided into three subgroups: Northern, Central, and Southern Line Islands. Here we specifically focus on the Northern Line Islands, which represent an ideal setting to analyze connectivity patterns and the effects of anthropic pressure because, despite their similar biogeography (they are all located in the Intertropical Convergence Zone, an area influenced by the equatorial countercurrent), they have recently diverged along a trajectory from virtually un-impacted (e.g. Palmyra Atoll in the north) to heavily impacted (Christmas Island-Kiritimati), following a gradient of fishing pressure and human impact increasing from North to South [10].

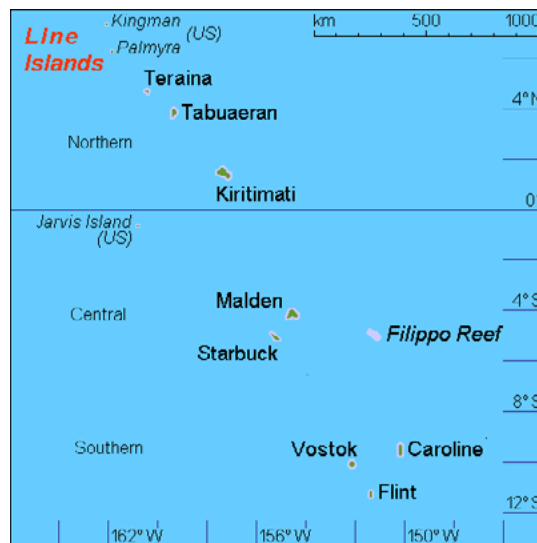


Fig. 1: Map of the study area. From North to South, the five Northern Line Islands are (1) Kingman reef, (2) Palmyra Atoll, (3) *Teraina* or Washington Island, (4) *Tabuaeran* or Fanning Island, and (5) *Kiritimati* or Christmas Island.

We investigate dispersal patterns via individual-based simulations, in which coral gametes/larvae are described as passive Lagrangian particles [e.g. 11,12,13] subject to advection operated by oceanic currents. Particles are released from 5 round patches whose positions and sizes match those of the Northern Line Islands, and subsequently tracked for a timespan corresponding to their Pelagic Larval Duration (PLD), assumed as a fixed parameter. The geographical representation of islands is simplified because they are approximated as circles. The hydrodynamic engine for the individual-based simulations is the ocean circulation code OPA9 [14] coupled to the multilayered sea-ice code LIM2 [15] in the ORCA-R025 configuration [16], i.e. a ζ -coordinate, global eddy-permitting ($1/4^\circ$) model simulating 3D thermohaline circulation. The outputs of the hydrodynamic model are reanalyzed and corrected by means of a data assimilation system [CIGODAS, see 17, 18, 19] to ensure consistency with observed temperature, salinity and circulation fields. Particle tracking is performed via the standard Euler explicit scheme, with a time step of 6 hours. Linear interpolation of the velocity fields (monthly averages) is performed in the x , y and z directions. Note that we do not consider the vertical component of the velocity field, i.e. a particle released at initial depth z_0 will remain at the same depth throughout the simulation. Also, particles are no longer tracked as soon as they exit the spatial domain (165° - 155° W, 0° - 10° N).

The results of Lagrangian simulations can also be used to derive the topology of the connectivity network (*sensu* [20]) among the different islands of the Northern Line Island archipelago. Specifically, we quantify connectivity between any two of the Northern Line Islands (say i and j) as the fraction of particles released at island i whose trajectories cross (at any time) the 'influence zone' of island j . Here we define an island's influence zone as a round patch centered on the island with a surface α times larger than that of the island itself. Once a particle reaches the influence zone of another island it is assumed that it is able to colonize the patch. Self-connectivity is produced by particles that either remain confined within the influence zone of their originating island or cross it again after having left it. As differences in reproductive strategies (e.g. broadcast spawners vs. brooders, characterized by long and short PLDs, respectively) and the temporal variability of oceanic currents are expected to have a remarkable impact on dispersal distances and connectivity, here we study broad ranges of both PLDs (from one week to 4 months) and spawning seasons (12 release dates have been considered, from January 1st to December 1st). At the present stage of our work, we do not use water temperatures to model their potential effects on pelagic larval durations (PLD).

As an example, Fig.2 reports a Lagrangian simulation where larvae/particles are released on March 1st, 2000, and tracked over a two-month period. More specifically, 10^4 particles are released from each of the Northern Line Islands with an initial depth randomly extracted from a uniform distribution with support 0-50 m. The daily velocities of ocean currents in each spatial position is obtained by linearly interpolating in space (not in time) the monthly averaged values reported for grid points. The individual trajectories (panel A) show that currents predominantly flow from SE to NW during the considered timespan, thus favoring a remarkable connectivity along that direction. Because of the inner anisotropy of ocean currents, between-island connectivity is expected to be highly heterogeneous, with northmost/southmost islands representing sinks/sources for propagule dispersal. These results are clearly visible in the connectivity matrix (evaluated for $\alpha = 3$) displayed in panel B which shows, for instance, that no particles leaving from Kingman Reef land in any of the Northern Line Islands, while more than 35% of the particles released at Palmyra Atoll reach Kingman Reef. The other (positive) values of connectivity fall in the between of these two extremes. Quite interestingly, Kingman Reef is expected to receive a significant amount of particles (from 7 to 8% in this simulation) also from Washington and Fanning Islands, which are located about 300 and 450 km away, respectively. In this model run self-connectivity is in contrast negligible for all islands.

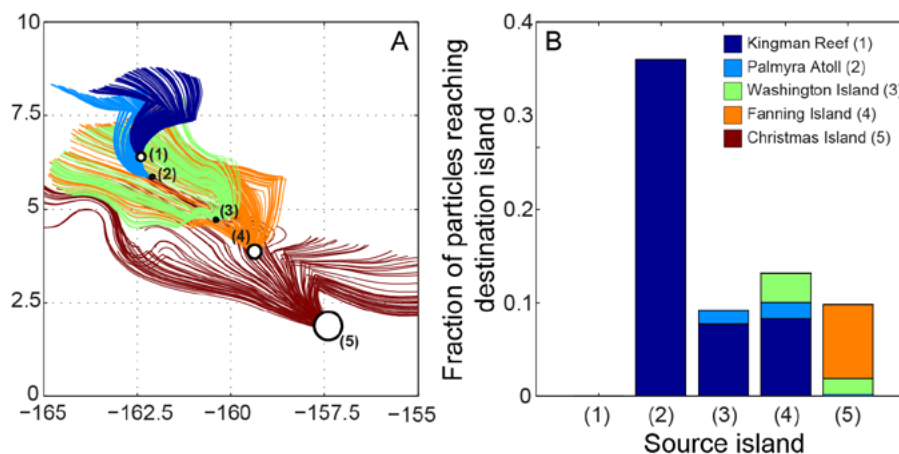


Fig. 2: Simulation of particle/larval dispersal. A) Sample trajectories of Lagrangian particles released from each of the Northern Line Islands; circles indicate the influence zone of each island (see text for details). B) Histogram visualization of the between-island connectivity matrix; bars represent the fraction of particles that leave from the source island i (horizontal axis) and cross the influence zone of island j (color coded, see legend).

All these results do obviously depend on the length of the PLD and the timing of spawning – as well as on the year considered in the simulation, as not only intra- but also inter-annual variability of the seascape plays a major role in determining connectivity patterns and overall metapopulation dynamics [21]. Fig.3 reports how connectivity from and to Palmyra Atoll (home to some of the best preserved reefs in the Line Island archipelago, thus of paramount importance for conservation) varies with different PLDs and spawning seasons in year 2000. As expected, increasing PLD lengths favor both out- and in-bound connectivity (bottom panels in Fig. 3). Interestingly, as documented in the top panels of Fig. 3, Palmyra atoll acts as a propagule source not only for Kingman Reef (in March, June and December) but also for Washington and Fanning Islands (during late Spring/early Summer months), while no outbound connectivity to Christmas Island is observed (the distance between the two islands is more than 9 thousands kilometers). As a sink, see the bottom panels of Fig.3, Palmyra Atoll receives propagules from the southmost islands (although some connectivity is observed also from Kingman Reef in June for $PLD \geq 60$ days), especially during Winter and Spring. Self-connectivity (not shown in Fig.3) is present only in June for $PLD \geq 60$ days, with $\sim 2\%$ of the particles released at Palmyra being trapped in the atoll's influence zone).

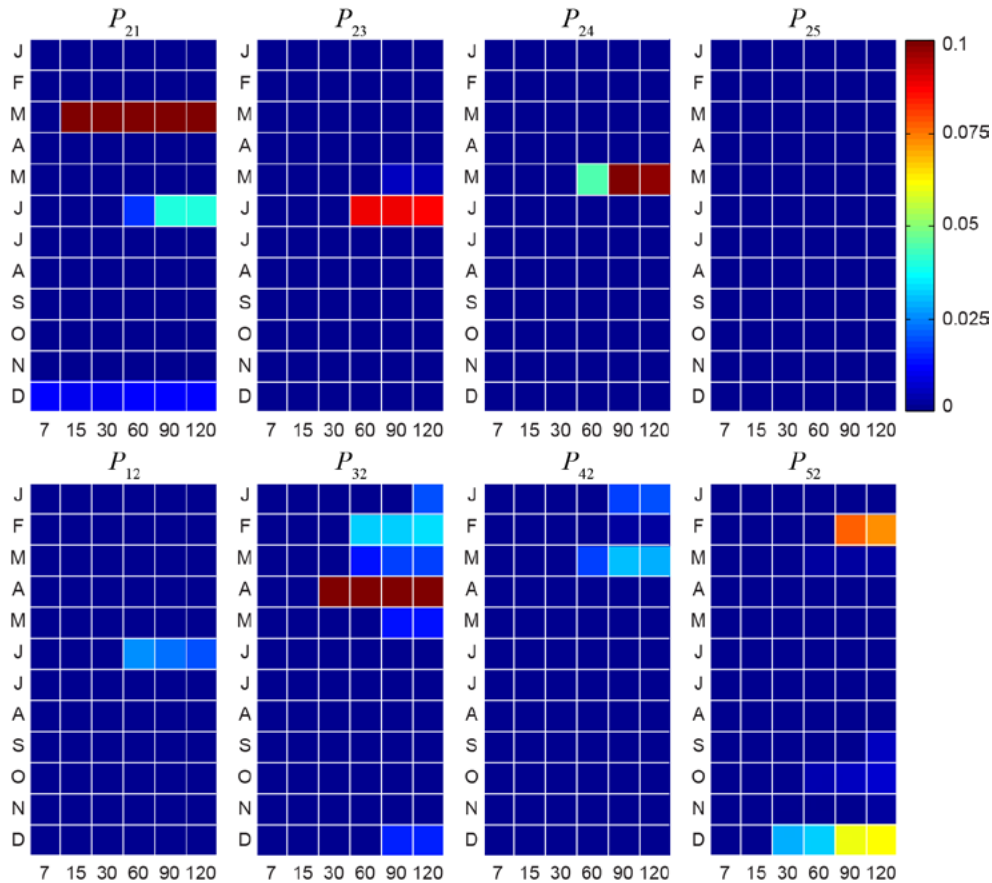


Fig. 3: Out- (top row of panels) and in-bound connectivity (bottom row) for Palmyra Atoll as a function of PLD (horizontal axis) and spawning season (vertical axis). P_{ij} represents connectivity (defined as in Fig. 2) from island i to island j ($i, j = 1, 2, \dots, 5$; 1: Kingman Reef, 2: Palmyra Atoll, 3: Washington Island, 4: Fanning Island, 5: Christmas Island) for some PLDs and all release months. Note that self-connectivity (P_{22}) is not shown.

Potential connectivity can change significantly between different years, following variations of the relevant circulation fields. Fig.4 displays how connectivity patterns within the Northern Line Islands archipelago have changed over a twenty-year timespan, namely from 1990 to 2009 (average values over the spawning seasons considered in Fig.3). The comparison between the panel reporting P_{21} with its counterpart reporting the sum of all other P_{2i} 's clearly reveals that the connectivity from Palmyra Atoll to Kingman Reef (as already discussed in the two months simulation of year 2000 in Fig. 2) was not exceptional. Rather, it has been significantly increasing in recent years. However, our numerical simulations show that the intensity of connectivity patterns is overall fairly erratic, with higher connectivity loosely associated with El Niño years.

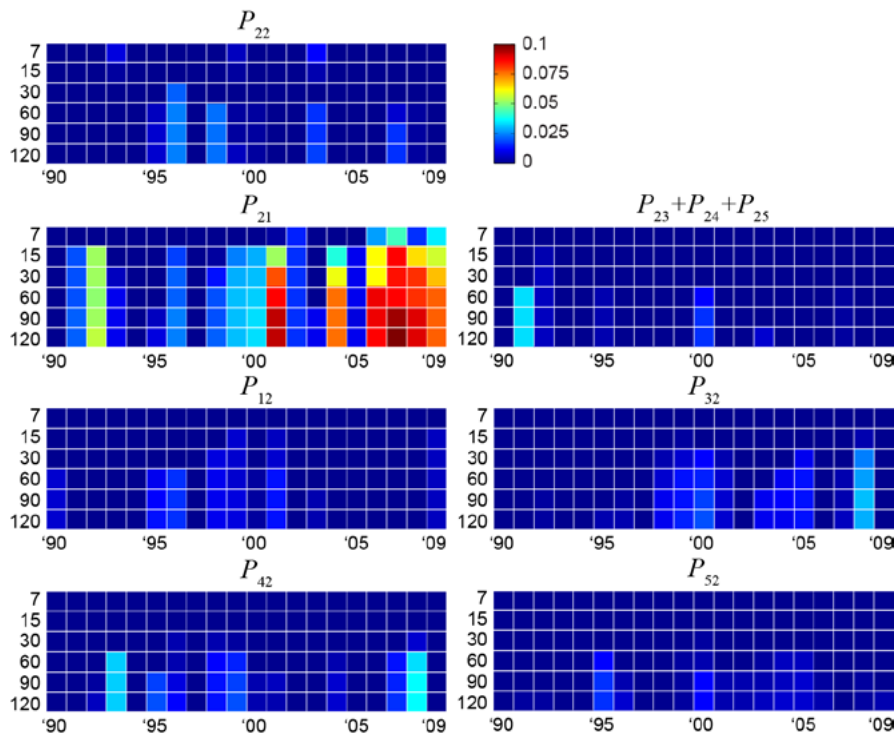


Fig. 4: Connectivity patterns for the period 1990-2009. Connectivity levels P_{ij} have been averaged over the release months considered in Fig.3

Understanding the potential effects of climate change on the connectivity of coral reefs, say over a time horizon of a century, cannot yet be done with oceanographic reanalyses at the fine scale such as those used above. In order to proceed, therefore, we used currents projected at a fine (daily) temporal resolution via a model that is (1) at a coarser spatial scale (from $1/2^\circ$ to about 2°), and (2) simulated with current climate by using as data only the observed CO_2 concentrations. The connectivities from and to Palmyra Atoll during the period 1970 to 2009 are shown in Fig.5. Although no clear trend is visible in the self-connectivity of Palmyra Atoll in the long run, we must notice that the auto-connectivity peaks seems to be higher in intensity and more frequent starting from mid century. This somehow suggests that larval retention in Palmyra Atoll might increased in the future.

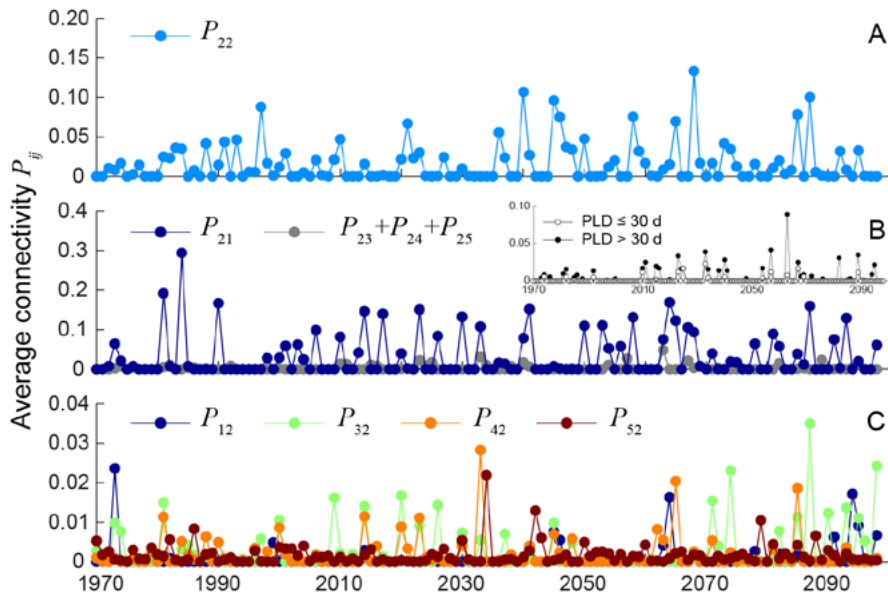


Fig. 5: Connectivity patterns for the period 1970-2098. The values P_{ij} have been averaged over both (1) the release months and (2) the PLDs considered in Fig.3, except for the inset of panel B where values of $P_{23} + P_{24} + P_{25}$ have been grouped by PLD (either short or long) before averaging. Note that here connectivity has been evaluated with Lagrangian simulations based on a hydrodynamical model with a coarser spatial resolution than the one used for Figs.2-4 (see text for details).

If the connection between Palmyra Atoll and Kingman reef (blue dots in panel 5B) seems to remain high in the next decades, the connectivity from Palmyra toward Southern islands is quite low. It must be noticed, however, that the averaged values plotted as gray dots are averages that accounts for particles/larvae with short (<30 days) and long PLDs (>30 days), which contributions to connectivity is quite different (see inset to panel 5B). The presence of relatively high connectivity peaks between Palmyra and Washington Island also appear by the end of the century, although the pattern is quite erratic. Definitely, further analysis is needed and will be done in these months, perhaps with an assimilated model at finer resolution, which is in preparation by some of the authors.

As a caveat to our analyses, we emphasize that the actual connectivity level between two or more populations will depend also upon the chemo-physical characteristics of the water column (temperature, pH, salinity), the health and abundance of the source populations, the larval characteristic affecting larval survival, behaviour and developmental time, and the availability and suitability of downstream habitat. For these reasons, climate change is predicted to possibly alter connectivity structures for ecosystem-building corals and other reef organisms in a variety of ways, including:

- direct changes in the directions and intensities of oceanic currents (as also shown in Figs. 4 and 5);
- changes in PLDs and/or larval survival and or metabolic functions driven by increasing water temperature;
- changes in primary productivity driven by temperature, which may also affect prey abundance and distribution, thus altering entire community food chains;
- changes in pH potentially affecting coral growth.

In sum, the effects of climate change are likely to rearrange processes at both the top and the bottom of coral reef ecosystems – and thus require serious consideration.

ACKNOWLEDGMENTS

Financial support came from Comune di Milano, Project “Climate Change Assessment in Small Pacific Islands States”. We acknowledge Dr. Giulia Galluccio (CMCC) for her continuous and encouraging help.

REFERENCES

- Hooper D.U., Chapin F.S., Ewel J.J., Hector A., Inchausti P., Lavorel S., Lawton J.H., Lodge, D.M., Loreau M., Naeem S., Schmid B., Setälä H., Symstad A.J., Vandermeer J. & Wardle D.A. (2005), *Effects of biodiversity on ecosystem functioning: A consensus of current knowledge*, Ecological Monographs, No. 75, pp. 3-35. (1)
- Myers N., Mittermeier R.A., Mittermeier C.G., da Fonseca G.A.B. & Kent J. (2000), *Biodiversity hotspots for conservation priorities*, Nature, No. 403, pp. 853-858. (2)
- Halpern B.S., Walbridge S., Selkoe K.A., Kappel C.V., Micheli F., D'Agrosa C., Bruno J.F., Casey K.S., Ebert C., Fox H.E., Fujita R., Heinemann D., Lenihan H.S., Madin E.M.P., Perry M.T., Selig E.R., Spalding M., Steneck R. & Watson R.A. (2008), *Global map of human impact on marine ecosystems*, Science, No. 319, pp. 948-952. (3)

- Levins R. (1969), *Some demographic and genetic consequences of environmental heterogeneity for biological control*, Bulletin of the Entomological Society of America, No. 15, pp. 237-240. (4)
- Munday P.L., Leis J.M., Lough J.M., Paris C.B., Kingsford M.J., Berumen M.L. & Lambrechts J. (2009), *Climate change and coral reef connectivity*, Coral Reefs, No. 28, pp. 379-395. (5)
- Monismith S.G. (2007), *Hydrodynamics of Coral Reefs*, Annual Review of Fluid Mechanics, No. 39, pp. 37-55. (6)
- Fernando H.S.J., McCulley J.L, Mendis S.G. & Perera K. (2005), *Coral poaching worsens tsunami destruction in Sri Lanka*, Eos, No. 86, pp. 301-304. (7)
- Kunkel C.M., Hallberg R.W. & Oppenheimer M. (2006), *Coral reefs reduce tsunami impact in model simulations*, Geophysical Research Letters, No. 33, pp. L23612. (8)
- Madin J.S. & Connolly S.R. (2006), *Ecological consequences of major hydrodynamic disturbances on coral reefs*, Nature, No. 444, pp. 477-480. (9)
- Sandin S.A., Smith J.E., DeMartini E.E., Dinsdale E.A., Donner S.D., Friedlander A.M., Konotchick T., Malay M., Maragos J.E., Obura D., Pantos O., Paulay G., Richie M., Rohwer F., Schroeder R.E., Walsh S., Jackson J.B.C., Knowlton N. & Sala E. (2008), *Baselines and degradation of coral reefs in the Northern Line Islands*, PloS ONE, No. 3, pp. e1548. (10)
- Siegel D.A., Kinlan B.P., Gaylord B. & Gaines S.D. (2003), *Lagrangian descriptions of marine larval dispersion*, Marine Ecology Progress Series, No. 260, pp. 83-96. (11)
- Pineda J., Hare J.H. & Sponaugle S. (2007), *Larval transport and dispersal in the coastal ocean and consequences for population connectivity*, Oceanography, No. 20, pp. 22-39. (12)
- Cowen R.K. & Sponaugle S. (2008), *Larval dispersal and marine population connectivity*, Annual Review of Marine Science, No. 1, pp.443-466. (13)
- Roullet G. & Madec G. (2000), *Salt conservation, free surface and varying volume: a new formulation for ocean GCMs*. Journal of Geophysical Research, No. 105, pp. 23927-23942. (14)
- Fichefet T. & Morales Maqueda M.A. (1997), *Sensitivity of a global sea ice model to the treatment of ice thermodynamics and dynamics*. Journal of Geophysical Research, No. 102, pp. 12609–12646. (15)

- Bernard B., Madec G., Penduff T., Molines J.M., Treguier A.M., Le Sommer J., Beckmann A., Biastoch A., Böning C., Dengg J., Derval C., Durand E., Gulev S., Remy E., Talandier C., Theetten S., Maltrud M., McClean J. & De Cuevas B. (2006), *Impact of partial steps and momentum advection schemes in a global ocean circulation model at eddy-permitting resolution*, *Ocean Dynamics*, No. 56, pp. 543-567. (16)
- Masina S., Pinardi N. & Navarra A. (2001), *A global ocean temperature and altimeter data assimilation system for studies of climate variability*, *Climate Dynamics*, No. 17, pp. 687-700. (17)
- Masina S., Di Pietro P. & Navarra A. (2004), *Interannual-to-decadal variability of the North Atlantic from an ocean data assimilation system*, *Climate Dynamics*, No. 23, pp. 531-546. (18)
- Bellucci A., Masina S., Di Pietro P. & Navarra A. (2007), *Using temperature–salinity relations in a global ocean implementation of a multivariate data assimilation scheme*, *Monthly Weather Review*, No. 135, pp. 3785-3807. (19)
- Treml E.A., Halpin P.N., Urban D. & Pratson L.F. (2008), *Modeling population connectivity by ocean currents, a graph-theoretic approach for marine conservation*. *Landscape Ecology*, No. 23, pp. 19-36. (20)
- Watson J.R., Kendall B.E., Siegel D.A. & Mitarai S. (2012), *Changing seascapes, stochastic connectivity, and marine metapopulation dynamics*, *The American Naturalist*, No. 180, pp. 99-112. (21)

The effects of climate change on Cuatro Ciénegas aquatic ecosystem in the desert environment of Northern Mexico

Herrera-Pantoja M.

Queretaro Water Commission, Queretaro, Qro
**Corresponding author: hpmarina@yahoo.com*

Abstract

In many arid and semiarid regions of the world, freshwater aquatic ecosystems are facing increasing pressures as populations and economies grow, and it is expected that during the 21st century climate change will impose new pressures on these regions. Cuatro Ciénegas Basin is a UNESCO World Biosphere Reserve located in the state of Coahuila, in the northern desert of Mexico. This groundwater-dependent ecosystem is of special interest because of the presence of more than 70 endemic species. During the last decades it has been heavily degraded mainly by over-exploitation of groundwater in adjacent valleys. In order to conserve the wildlife, the plant populations and the functions of this unique ecosystem in a changing climate, it is important to investigate how climate change is likely to impact the groundwater recharge so that integrated water management strategies can be implemented. To investigate the future impacts of climate change the downscale output of six global circulation models were used to produce future simulations of groundwater recharge for the B1 and A1B emissions scenarios. Overall, the results presented in this study, have demonstrated that future climatic changes are likely to significantly influence the nature of groundwater recharge in the semi-arid zone of northern Mexico. Projected temperature increase and precipitation decrease will imply a decrease in groundwater recharge between -10% to -18% over the 21st century. The drier conditions will increase pressures on water resources putting at risk ecological sustainability.

Keywords: *Climate change, endemic species, groundwater, desert environment*



1. INTRODUCTION

Desert ecosystems play an important role in supporting biodiversity, providing cultural and recreational services, aesthetic value, and dust control [1]. Desert ecosystems are highly vulnerable to climate change, since changes in temperature and precipitation regimes could modify the specific habitat requirements; disrupt the species interactions and alter the distribution and composition of natural communities [2,3,4].

Cuatro Ciénegas Basin (CCB) is a UNESCO World Biosphere Reserve located in the state of Coahuila, in the northern desert of Mexico (Fig. 1). It is a complex ecosystem formed by hundreds of geothermal springs, wetlands, ponds and lakes fed by a karstic underground water system. Over 60 mammal species, 145 birds, 60 reptiles, 8 amphibians, 17 fishes, 28 mollusks, 19 scorpions and 883 species of vascular plants have been identified in this unique ecosystem. This groundwater-dependent ecosystem is of special interest because of the presence of more than 70 endemic species and early Cambrian endemic species, such as stromatolites [5,6].

During the last decades Cuatro Cienegas has been heavily degraded, primarily by over-exploitation of groundwater for agricultural use in adjacent valleys, increasing population growth and the invasion of exotic species [6,7].

In 1970 groundwater level was close to the ground surface in the north Ocampo Valley and South Hundido Valley [8]. Since 1980, development of groundwater for agricultural development started to cause a decline in water levels of about one meter per year and the dryness of the Río Cañon spring, which flowed from the Ocampo Valley to the Cuatro Cienegas, reducing the size of the groundwater-dependent ecosystem [9]. There is a concern that the unrelenting extraction of groundwater in the Hundido Valley and changes in climate will be the major challenge for maintaining adequate supplies of water for the ecosystem's survival. Therefore, in order to conserve wildlife, plant populations and ecosystem functions in a changing climate, it is important to investigate how climate change is likely to impact the groundwater recharge so that integrated water management strategies can be implemented.

2. SITE DESCRIPTIONS

Cuatro Cienegas Basin (CCB) is located in the Chihuahuan Desert, Coahuila (Fig. 1). The basin is located at 740 m above sea level, surrounded by high mountains with an elevation of around 3000 m. La Madera to the North West, La Fragua to the South West, San Marcos to the South, La Purisima to the South East, San Vicente to the East and La Menchaca to the North East. Cuatro Cienegas is hydrologically interconnected with four adjacent basins: to the West with El Hundido, to the North with the Ocampo, to the South with San Marco and to the South West with the Sobaco. The highlands are dominated by Cretaceous carbonates and the intermountain basins are filled with alluvial and lacustrine sediments. Both mountains surrounding the CCB and the valleys display a high degree of karstification [7].

The CCB is a semiarid region with a mean annual temperature of 19.3 °C, maximum temperature of 44°C and minimum temperature of 0 °C. Mean annual precipitation is 268 mm and falls between May and October (Tab. 1) .

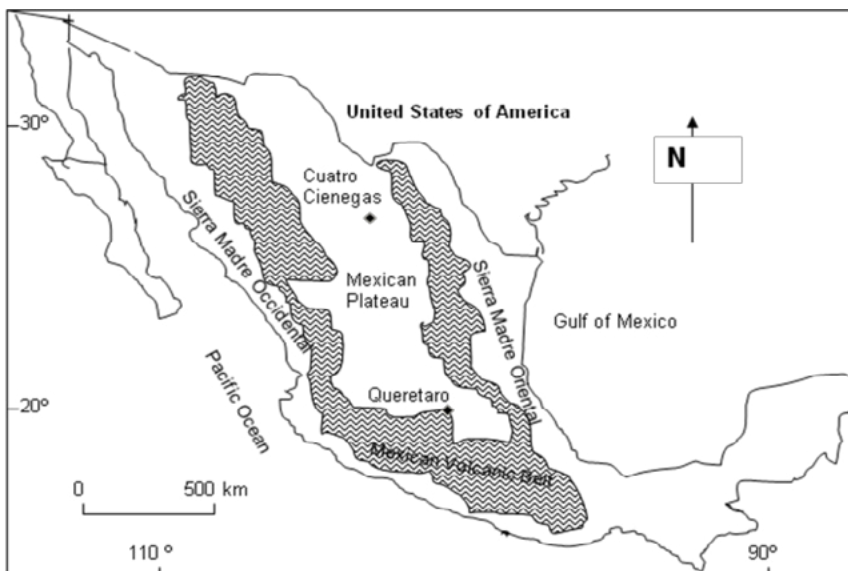


Fig. 1: Location of the Cuatro Cienegas Basin.

Date	P	Tmax	Tmin
Jan	12.8	19.3	2.3
Feb	6.8	22.4	3.7
Mar	6.3	26.4	7.2
Apr	15.7	30.5	11.6
May	36.3	32.8	15.3
Jun	37	34	17.8
Jul	34.4	33.5	18.2
Aug	34.9	32.8	18
Sep	37.6	30.8	15.9
Oct	21.8	28.2	11.5
Nov	11.3	23.7	6.3
Dec	13.3	19.8	3

Table 1: Long-term mean annual precipitation (P), maximum temperature (Tmax) and minimum temperature (Tmin) for Cuatro Ciénegas Basin for the historic period.

The primary recharge mechanism in the CCB is direct recharge on fractured carbonate mountains, recharge from mountain front runoff, low recharge in valley floors and interbasin flow created by high transmissivity carbonate rocks of about $4 \times 10^2 \text{ m}^2 \text{ day}^{-1}$ [10, 11,12]. The groundwater system flows from the mountain highland recharge areas surrounding the Sobaco, Hundido, Ocampo, and San Marcos Valleys to the springs discharge areas in Cuatro Ciénegas valley. Annual spring discharge at the CCB is around $35 \text{ Mm}^3 \text{ a}^{-1}$ [7]. Chloride-balance recharge estimates carried out by Wolaver [7] suggest local flows and regional interbasin flows from the surrounding valleys to the CCB. Discharge areas are characterized by high concentrations of salts by evaporation processes, total dissolved solids ranging from 900 to $300,00 \text{ mg} \cdot \text{l}^{-1}$ and temperatures ranging from $23.7 \text{ }^\circ\text{C}$ to $34.7 \text{ }^\circ\text{C}$ [13].

3. METHODS AND DATA

In order to assess the impact of climate change a review of the existing historical data was carried out using historical daily records of temperature and precipitation obtained from the National Weather Service of Mexico. The World Meteorological Organization recommends using the period of 1961-1990 as a standard period against which to compare the effects of climate change. However, since most of the weather stations included in the database present data until 1988 the 30-year period used in this study spanned the period from 1959 to 1988.

In semiarid areas, characterized by low precipitation and high evapotranspiration, direct recharge from precipitation through the soil profile is very low, while mountain system recharge is frequently the dominant source of recharge [14,15]. Quantification of mountain system recharge has been carried out by several authors in different arid and semiarid regions. For example, Winograd et al., [16] estimated MSR in the Spring Mountains in Nevada, USA; Cunningham et al., [17] in the Tucson basin in Arizona, USA; Wahi [15] in the Upper San Pedro Basin, Arizona and Tyler et al., [18] calculated recharge as a percentage of precipitation In Nevada, USA. Wolaver [7] found that groundwater recharge in the valley floor is very close to zero percent of precipitation while potential groundwater recharge in mountains could range from three to seven percent and concluding that overall recharge rate at Cuatro Cienegas may range around one percent of precipitation. In this study, groundwater recharge was estimated to occur at this rate.

In order to investigate the future impacts of climate change on the water balance, six global circulation models (Tab. 2) from the WCRP CMIP3 multi-model were used to produce the future simulations for two emission scenarios: the B1 (low emissions) and A1B (medium high emissions) [19]. GCMs outputs were downscaled to catchment-scale using the scaling factor technique used by Yusoff et al., [20]. The adjusted series were used to simulate groundwater recharge time series for the Cuatro Cienegas study area in northern Mexico for the historic baseline 1960-1990 and for a low and medium high emissions scenarios for the 2011-2100 time period.

Model	Country Sponsor
GISS_AOM	New York, USA
BCCR_BCM2_0	Bergen, Norway
MIROC3_2_MEDRES	Tokyo, Japan
CSIRO_MK3_0	Melbourne, Australia
NCAR_CCSM3_0	CO, USA
MIROC3_2_HIRES	Tokyo, Japan

Table 2: Global circulation models used in this study.

4. RESULTS

In general the scenarios of climate change under the low and medium high emissions scenarios indicate an increase in long-term average annual temperature and a decrease of long-term average annual precipitation for Cuatro Ciénegas by the end of the 21st century (Tab.3). The increases in temperature could range from 1.6 °C, to 3.6 °C under the B1 scenario and from 1.5 °C to 4.9 °C under the A1B scenario by the end of the 21st century. The lowest temperature scenarios were given by the NCAR and CSIRO models for both emissions scenarios. The highest temperatures scenarios were given by the MIROCh and MIROcm for the B1 emissions scenario and the BCCR and MIROCh for the A1B scenario.

Precipitation scenarios produced for four of the models predict a decrease in long-term mean annual rainfall for both emissions scenarios. For the B1 scenario decreases could range from -10% to -13% compared with the baseline. For the A1B scenario decreases could range from -12.7% to -18.4%. According to the CSIRO and NCAR models the long-term mean annual rainfall could increase between 8.1% and 8.9% under the B1 scenario and between 2.1% and 13.0% under A1B emissions for the CSIRO and NCAR models respectively.

	Temperature (° C)		Precipitation (%)	
	B1	A1B	B1	A1B
BCCR	3.0	4.9	-10.0	-18.4
CSIRO	1.7	1.5	8.9	2.1
GISS	1.9	3.4	-11.8	-15.2
MIROCh	3.6	4.9	-11.0	-12.7
MIROcm	3.5	3.3	-13.1	-12.8
NCAR	1.6	2.8	8.1	13.0

Table 3: Changes in long-term mean annual precipitation for the three time periods of the B1 and A1B emissions scenarios projected by six GCMs

An analysis of wet and dry season revealed that during the wet season four out of the six models presented a decrease in groundwater recharge (Fig. 2). Under the B1 emission scenarios, the decreases ranged between -10% for the BCCR model to -13% for the MIROcm model. Under the A1B emissions scenario the decreases ranged between -12.7% to -18% according to the MIROCh and

BCCR models respectively. Both the CSIRO and NCAR models presented increases in groundwater recharge that range from around 8% under the B1 scenario and from 2% to 13% for the A1B scenario. During the dry season almost all scenarios presented a decrease in groundwater recharge. The decreases ranged between -8% to -20% for the B1 scenario and from -9.8% to -30% for the A1B scenario. The GISS model simulated an increase of 2.4% and 2.9% for the B1 and A1B emissions scenarios respectively.

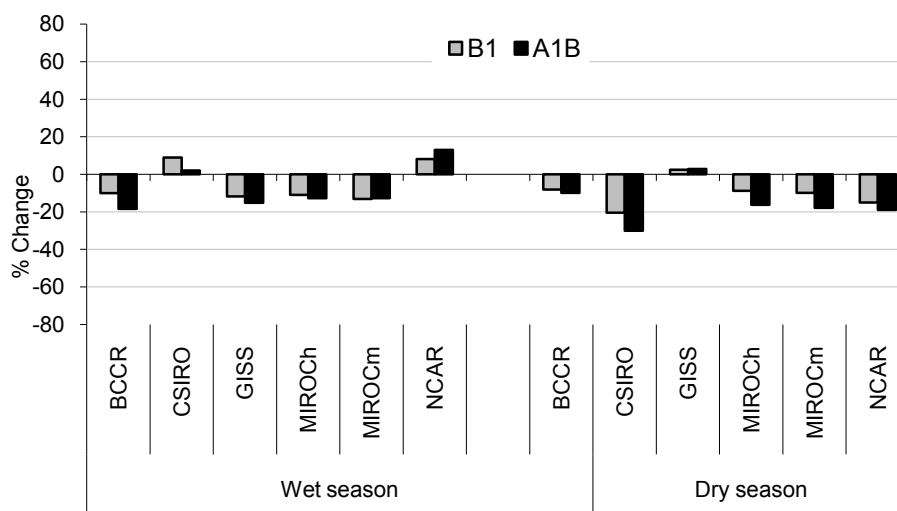


Fig. 2: Percentage change in potential groundwater recharge during the wet and dry season in the Cuatro Ciénegas Basin under six GCM models simulated for A1B and B1 scenarios.

5. DISCUSSION AND CONCLUSIONS

Over the last decades, there have been great interests in understanding the impacts of climate change on natural resources and the communities that depend on them. In this study, using a simple methodology some general conclusions have been reached over the magnitude of the effects of climate change on a desert environment. In general, future simulations projected less precipitation and continued warming which in turn will influence groundwater recharge in the semi-arid zone of northern Mexico. The likely decrease of -10% to -18% in groundwater recharge during the 21st century will potentially produce a decline in water levels.

Local and regional lowering of groundwater heads has occurred in several areas of Cuatro Ciénegas as a consequence of groundwater abstraction to meet agricultural and domestic water supply demands. This situation could be exacerbated in the future by climate change resulting in significant changes in water levels. Consequently, the groundwater-aquatic ecosystem of Cuatro Ciénegas could undergo varying degrees of alteration. On the one hand, prolonged exposure to lower water levels could lead to a loss of springs, ponds and shallow wetland on the other hand changes in water levels could also alter soil fertility, pH, oxidation-reduction potential, nutrient availability and chemical compositions with important repercussions for distribution patterns, competitive abilities and survival of species.

The projections of future changes in climate entail major challenges for conserving and supporting wildlife, plant populations and ecosystem functions in this desert ecosystem. Climate change is already affecting biodiversity and if the vulnerability of species is increased by human activities negatively modifying their habitat it is very possible that many species will become extinct.

Future work may consider quantifying the effects of projected climate change on threatened and endangered species to produce specific conservation and protection approaches to minimize species loss. Groundwater managers and conservationists need to work together to have a program in place to properly maintain adequate supplies of water for ecosystem persistence in the long term, since many plants and animals in the desert ecosystem are already facing water stress. In order to preserve this unique ecosystem, effective water resource management policies must be extended outside of the Cuatro Ciénegas Basin to include the surrounding areas to reduce drawdowns. A regional action plan for the conservation of the desert ecosystem that mitigates ecosystem degradation from anthropogenic sources has to be drawn.

Local and regional land-use planners must work together to identify conflicting interests and missed opportunity areas to develop strategies to preserve the ecosystem. Managers need to categorize the most suitable protection approaches and adaptive actions for effectively protecting wildlife, plants and ecosystem functions and provide sustainable recreational and commercial use in a changing climate.

6. ACKNOWLEDGMENTS

The author is grateful to the Mexican National Council for Science and Technology (CONACYT) for its financial support of this research and to Justin Paul Radcliffe for his valuable comments that improved the manuscript.

7. REFERENCES

- Fernandes J., Flynn N., Gibbes S., Griffis M., Isshiki T., Killian S., Palombi L., Rujanavech N., Tonsky S., and Tondro M. (2010), *Renewable energy in the California desert, mechanisms for evaluating solar development on public lands*. School of Natural Resources and Environment, University of Michigan, M.S. Thesis, S. Yaffee, Advisor. (1)
- Archer S.R. and Predick K.I. (2008), *Climate change and ecosystems of the Southwest United States*. Society of Range Management 30:23-28. (2)
- Barrows C.W., Rotenberry J.T., and Allen M.F. (2010), *Assessing sensitivity to climate change and drought variability of a sand dune endemic lizard*. Biological Conservation 143:731-736. (3)
- Hernández H.M., Gómez-Hinostrosa C., and Hoffmann G. (2010), *Is geographical rarity frequent among the cacti of the Chihuahuan Desert?*. Revista mexicana de biodiversidad 81:163-175. (4)
- Stein, Bruce A., Lynn S. Kutner, Jonathan S. Adams (2000) *Precious Heritage: The Status of Biodiversity in the United States*. Oxford University Press, Oxford. (5)
- Souza V., Espinoza-Asuar L., Escalante A.E., Eguarte L.E., Farmer J., Forney L., Lloret L., Rodríguez-Martínez J.M., Soberón X., Dirzo R., Elser J.J. (2006), *An endangered oasis of aquatic microbial biodiversity in the Chihuahuan desert*. PNAS, v. 103: 6565-6570. (6)
- Wolaver B. D., Sharp J. M., Rodriguez J. M. and Ibarra Flores J. C. (2008), *Delineation of Regional Arid Karstic Aquifers: An Integrative Data Approach*. Ground Water, 46: 396–413. (7)
- Instituto Mexicano de Tecnología del Agua (IMTA) (2005), *Estudio hidrogeológico de los acuíferos el Hundido y Cuatrociénegas*. Coahuila, 292 p. (8)
- Minckley W.L. (1992), *Three decades near Cuatro Ciénegas, Mexico: photographic documentation and a plea for area conservation*. Proceedings of the Arizona-Nevada Academy of Science. 26: 89–119. (9)

- Rodríguez A.A., Mijares F.J.A., Ojeda C.G., Morales M.M., Hita L.G., Zamarron G.H., Arellano I.M., González M.A.M., Flores G.O., Almanza P.G., Sánchez R.L., López J.L.P., Arzate G.R., Fritz P., and Espinoza J.R. (2005), *Estudio hidrogeológico de los acuíferos el Hundido y Cuatrociénegas, Coahuila*. Secretaría de Medio Ambiente y Recursos Naturales, Instituto Mexicano de Tecnología del Agua, Comisión Nacional del Agua, Instituto Nacional de Ecología. Mexico. (10)
- Van Broekhoven N.G., (2002), *Recharge in a semi-arid basin aquifer: Ryan Flat and Lobo Flat, Trans-Pecos, Texas*. M.S. thesis. The University of Texas at Austin. (11)
- Johannesson K.H., Cortés A., and Kilroy K.C. (2004), *Reconnaissance isotopic and hydrochemical study of Cuatro Ciénegas groundwater, Coahuila, México*. Journal of South American Earth Sciences. 17: 171–180. (12)
- Evans S.B. (2005), *Using geochemical data to define flow systems in Cuatrociénegas, Coahuila, Mexico*. M.S. thesis. The University of Texas at Austin. (13)
- Massuel S., Favreau G., Descloitres M., Le Troquer Y., Albouy Y., Bernard C. (2006), *Deep infiltration through a sandy alluvial fan in semiarid Niger inferred from electrical conductivity survey, vadose zone chemistry and hydrological modelling*. CATENA 67: 105 – 118. (14)
- Wahi A.K., Hogan J.F., Ekwurzel B., Baillie M.N., Eastoe C.J. (2008), *Geochemical quantification of semiarid mountain recharge*. Ground water. 53: 1-12. (15)
- Winograd I.J., Riggs A.C., Coplen T.B. (1998), *The relative contribution of summer and cool-season precipitation to groundwater recharge, Spring Mountains, Nevada, USA*. Hydrogeology Journal. 6: 77-93. (16)
- Cunningham E.B., Long A., Eastoe C., Bassett R.L. (1998), *Migration of recharge waters downgradient from the Santa Catalina Mountains into the Tucson basin aquifer, Arizona, USA*. Hydrogeology Journal 6: 94-103. (17)
- Tyler S.W., Chapman J.B., Conrad S.H., Hammermeister D.P., Blout D.O., Miller J.J., Sully M.J. and Gianni J.M. (1996), *Soil-water flux in the southern Great Basin, United States; temporal and spatial variations over the last 120,000 years*. Water Resources Research. 32: 1481–1499. (18)
- IPCC (2007) *Technical Summary*. In: *Climate Change 2007: The Physical Science Basis Conference. Contribution of Working Group 1 to the Fourth Assessment Report of the Intergovernmental Panel on Climate Change*. Solomon S., Qin D., Manning M., Chen Z., Marquis M., Averyt K.B., Tignor M., Miller H.L. (eds), Cambridge University Press: United Kingdom. (19)

Yusoff I., Hiscock K.M., Conway D. (2002), *Simulation of the impacts of climate change on groundwater resources in eastern England*. In: Sustainable Groundwater Development. Hiscock K.M., Rivett M.O., Davison R.M. (eds). Geological Society Special Publication 193, Geological Society: London. (20)

IMPLICATIONS ON ECOSYSTEM SERVICES

Impacts on forest and agricultural ecosystems - I

The impact of selective logging on Forest structure, Plant Diversity and above-ground biomass of African tropical forests

Gatti Cazzolla R.^{*}, Castaldi S.[§], Lindsell J. A.^{**},
Coomes D. A.[†], Marchetti M.^{§§}, Maesano M.^{§§}, Di Paola A.[#],
Paparella F.[°], Valentini R.^{**}

^{}DIBAF, University of Tuscia, Viterbo, Italy,*

[§]Dipartimento di Scienze Ambientali, Seconda Università di Napoli, Caserta, Italy

*^{**}The Royal Society for the Protection of Birds (RSPB), Sandy, Bedfordshire, United Kingdom.*

[†]Department of Plant Sciences, University of Cambridge, Cambridge, United Kingdom.

^{§§}STAT, EcoGeoFor Lab, University of Molise, Pesche (IS), Italy

[#]Euro-Mediterranean Centre on Climate Change (CMCC), Lecce, Italy

[°]Department of Mathematics and Physics "Ennio De Giorgi", University of Salento, Lecce, Italy.

Corresponding author: francesco.paparella@unisalento.it

Abstract

Emissions Tropical deforestation for timber market is well known to have serious negative consequences on local biodiversity, terrestrial carbon sink and the balance of atmospheric greenhouse gases. In contrast, selective logging of tropical forests is often regarded as a management practice that has less dangerous effects on the ecosystem, even though the available scientific literature is scanty and somewhat contradictory on this issue. We compared field data that we collected in Africa (Cameroon, Gabon, Sierra Leone and Ghana) from plots of tropical forest subject to different forest management practices (old-growth primary forests, selectively logged and secondary forests). Our findings suggests that the vertical structure and plant diversity of the logged forest are not largely different from those of a primary forest, while are able to show a remarkable difference in forest density, together with a concomitant invasion by vines, climbers and other infestants. A simple mathematical model may explain these data.



In recent decades, many tropical countries have changed forest resource extraction management from clear cutting to selective logging [1, 2, 3], in response to the scientifically recognized role of deforestation activity in the increase of CO₂ atmospheric concentration [4, 5] and following the concept that the close relationship between biodiversity and productivity makes policies which support preservation of forest integrity a win-win approach for both carbon sequestration and biodiversity protection [6, 7, 8].

Selective logging is defined as the harvest of valuable timber trees above a threshold trunk diameter with methods designed to maintain the forest cover, including a significant understock of living biomass. Currently, selective logging is considered to be a “sustainable forest management” (SFM) practice and it is increasingly embraced as an approach to protect forest integrity while allowing an appropriate use of resources. Overall, there appears to be a consensus on viewing selective logging as causing only minor disturbance [9, 11, 10, 12], and thus acceptable within the requirements of certification schemes such as the Forest Stewardship Council (FSC), a highly regarded SFM standard established in 1993 and now included in REDD programs [13]. However, at the moment, we lack an extensive knowledge on the short and long-term effects of selective logging on carbon sequestration and biodiversity, as well as the trade-off between these two ecosystem variables as functions of the intensity of timber harvesting, despite its increasingly wide adoption.

Some of the few available studies quantified the disturbance caused by selective logging solely in terms of diversity of the logged forest [14, 15, 16] with results that were encouraging for that practice. Other studies documented significant changes in species composition, genetic diversity, variations in forest structure, nutrient cycling and aboveground carbon stocks [17, 18, 19, 20, 21, 22, 23, 24, 25, 26, 27], showing that selective logging definitely has non-negligible impacts.

An important aspect in evaluating forest damage is the assessing of the extension of canopy gaps by selective timber harvests. One of the main effects of canopy gaps discontinuities appears to be the creation of spaces readily invaded by weeds, vines and climbers at the expense of the late-successional state cenosis [28]. Conversely, natural gaps (e.g. due to big broken branches or naturally died trees) are usually smaller than logging gaps, and tree saplings seems to be prepared to grow fast enough to fill the canopy opening [29]. This reduces the likelihood of vines, weeds and climbers invasion [30]. Here we argue that changes in native cenosis caused by the selective removal of the tallest trees induce a local variation of forest structure with relative consequences on biodiversity and carbon stocks.

To support our thesis we compare three different types of forest management (old-growth/untouched, clearcut and subject to selective logging) of tropical forests in Western and Central Africa looking for statistically significant differences. The clearcut and selectively logged plots were selected in places where the logging activity was performed between 15 to 30 years ago, according to the avail-

able documentation. For this purpose we collected data of tree heights, diameter at breast height (dbh), surface covered by vines and infestants, and species composition from 33 forest plots, each one of 500 m² located in Ghana, Gabon and Cameroon (Dataset₁). All trees larger than 5cm dbh were sampled in these plots. From the height and diameter data, together with the wood density of each species taken from the Global Wood Density Database we compute the aboveground biomass of each tree, using allometric equations [31].

We computed 12 indices for each plot. The first group of four indices contains the average tree height, diameter and biomass, and the height of the 80th percentile in each plot. The second group of four indices contains measures of density, that is the sum of height, diameter, biomass and number of individuals normalized by the area of the plot. The third group contains three indices of biodiversity (richness, entropy and evenness *i*) and a measure of the abundance of vines in each plot. For each index, we compare the values scored by primary forest plots with those scored by secondary forest plots, and, separately, by selectively logged forest plots. The null hypothesis, namely that the index shows no difference between primary forest and either secondary or selectively logged forest, is tested with a Mann-Whitney U test, which is appropriate because it does not require a normal distribution of data, and is applicable to samples of small size. We report the probability value *P* of the null-hypothesis any time that it is lower than 0.05.

We also processed 478 plots of 1250 m² each, located in Sierra Leone (Dataset₂). The plots are divided into three categories: “unlogged”, “well-managed” and “logged”. The “unlogged” plots should be taken as primary forest, although there is some uncertainty about the extent and the location of disturbances due to indigenous farmers during the last century; the “well-managed” plots were subject to careful selective logging in the eighties, with minimal crown damage; the “logged” plots were subject to less careful selective logging, with extensive crown damage in the seventies, eighties and nineties.

The only quantity considered in these plots was the diameters of trees larger than 30 cm dbh. However, the very large number of plots, all from the same location, allows us to study the distribution of tree diameters (for trees larger than 30 cm dbh) of the entire forest, rather than just plot-by-plot averages (or percentiles). For this purpose we form three large samples of diameter data by grouping together the diameter measurements from all the unlogged, all the well-managed and all the logged forest plots. We then perform pairwise comparisons between the unlogged and well-managed samples, and between the unlogged and logged samples by means of a two-sided, two-sample Kolmogorov-Smirnov test. We also compute the tree density and the normalized diameter. In this case we have to revert to a plot-by-plot analysis, because we need the plot’s area to compute these quantities.

Figure 1 shows the first group of indices, namely the average values of tree height, diameter, biomass

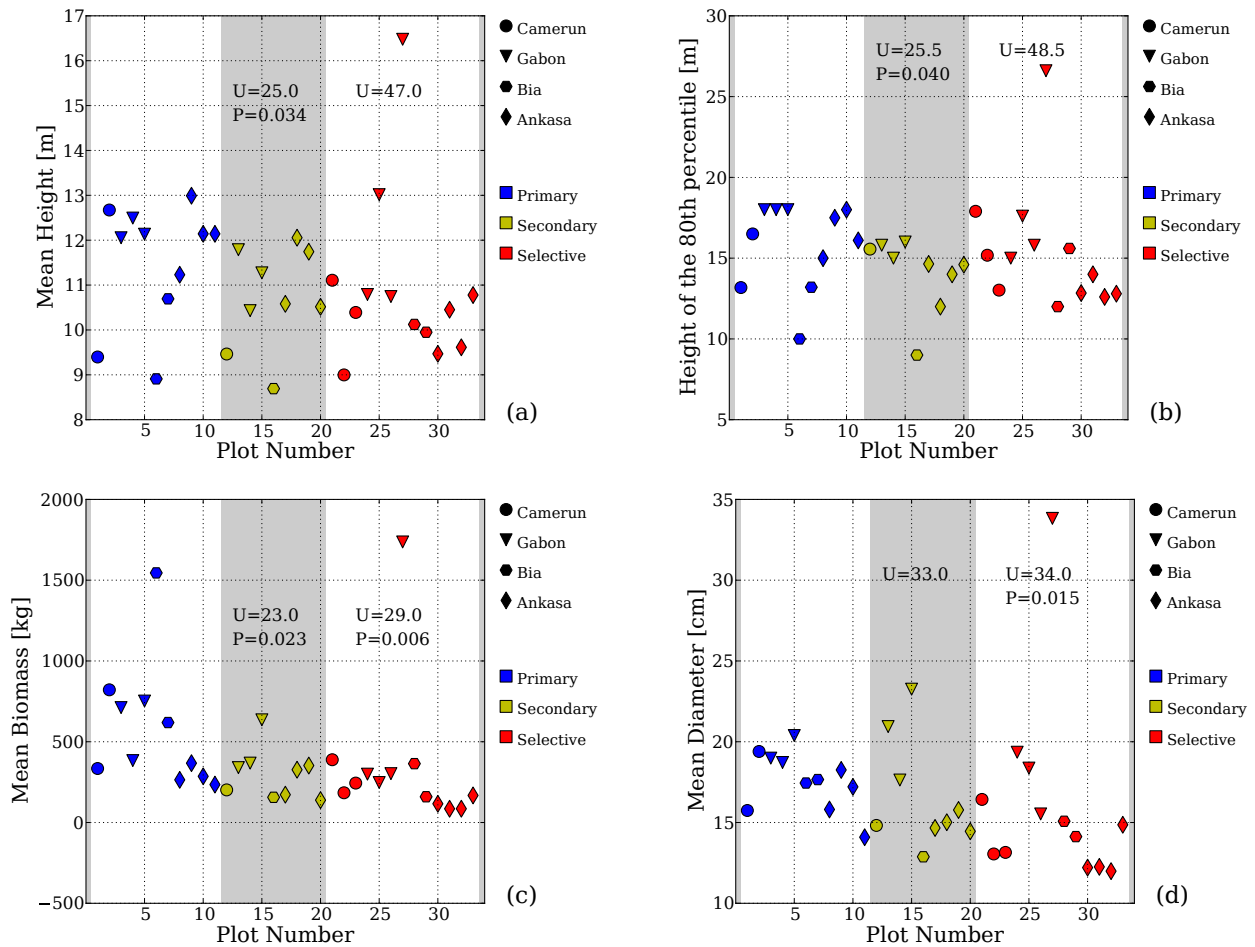


Figure 1: Indices characterizing the distribution of tree height, biomass and diameter in each plot. (a) mean tree height, (b) height of the 80th percentile, (c) mean biomass, (d) Mean diameter. The abscissa shows a serial number attributed to each plot (which is held the same in all the figures). The marker shape identifies the geographical location of the plot (circles: Cameroon; triangles: Gabon; hexagons: Ghana - Bia; diamonds: Ghana - Ankasa). The marker color identifies the type of forest management (blue: primary, yellow: secondary, red: selectively cut). We show the values of the Mann-Whitney U statistics, above the yellow symbols when comparing primary vs selectively cut forest plots. If the probability P of the null hypothesis is lower than 0.05 we report it under the value of U.

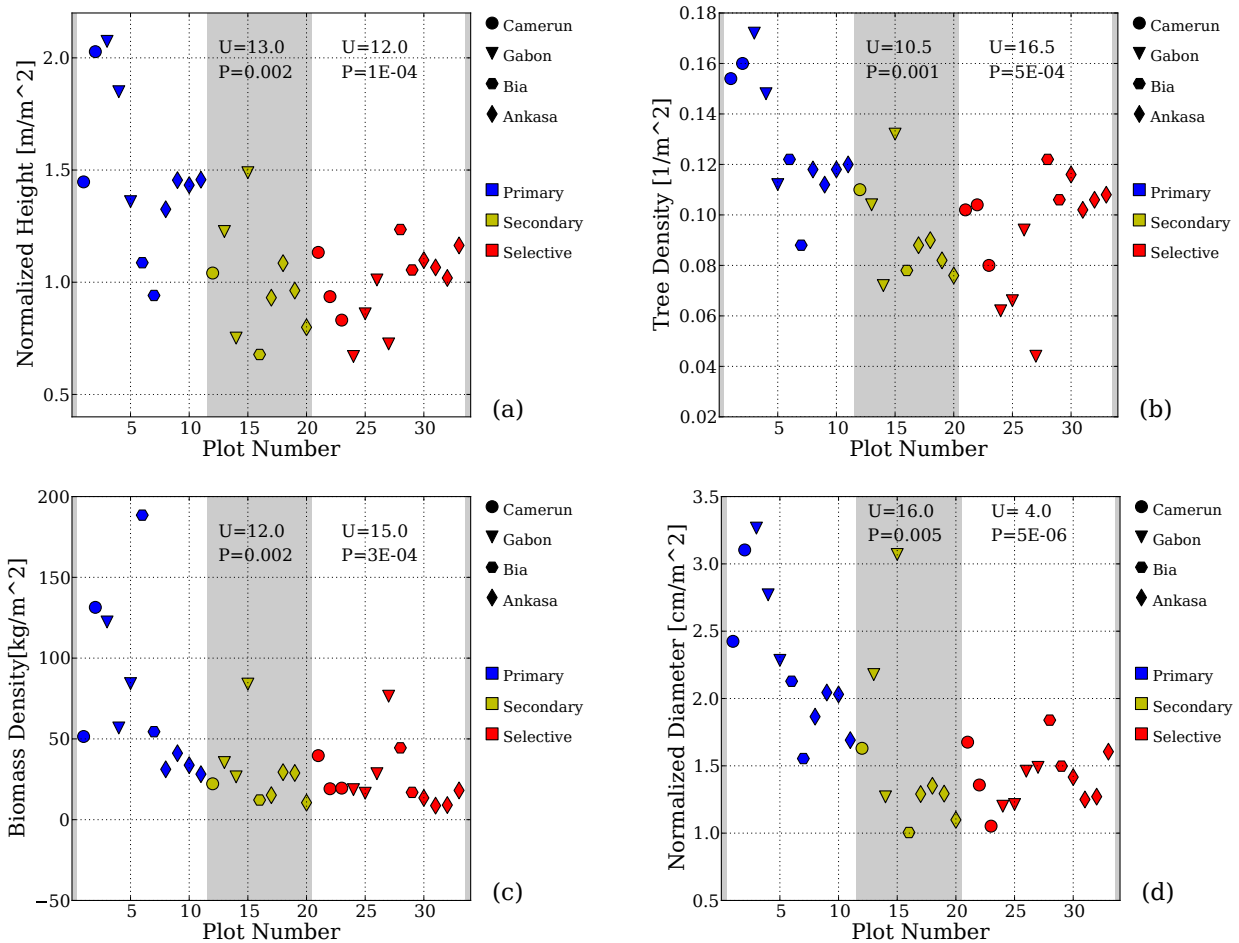


Figure 2: Indices characterizing the forest density in each plot. (a) normalized height, (b) tree density, (c) biomass density, (d) normalized diameter. Symbols, colors and legends as in Figure 1.

and the 80th percentile of height, for each plot. It is quite evident that these indices do not show striking differences between plots of primary forest and plots of either secondary or selectively cut forest. Although visually the values of selectively logged forest (red symbols) appear to be generally lower than those of primary forests (blue symbols), the probability of the null hypothesis is not as low as to allow for its outright dismissal, except possibly in the case of the mean biomass. In addition, we must observe that one selectively logged plot in Gabon scores the highest value in all these four indices, reflecting the fact that selective logging does not always remove all the big trees in a given area.

Figure 2 shows the four density indices, namely the sum of the height, biomass, diameter of each tree, and the number of trees in each plot, divided by the area of the plot. The Mann-Whitney U tests let us conclude, with a very high confidence, that all four densities are systematically higher in primary forests. Therefore, these indices are sensitive to differences between primary forests and the other two types of forest.

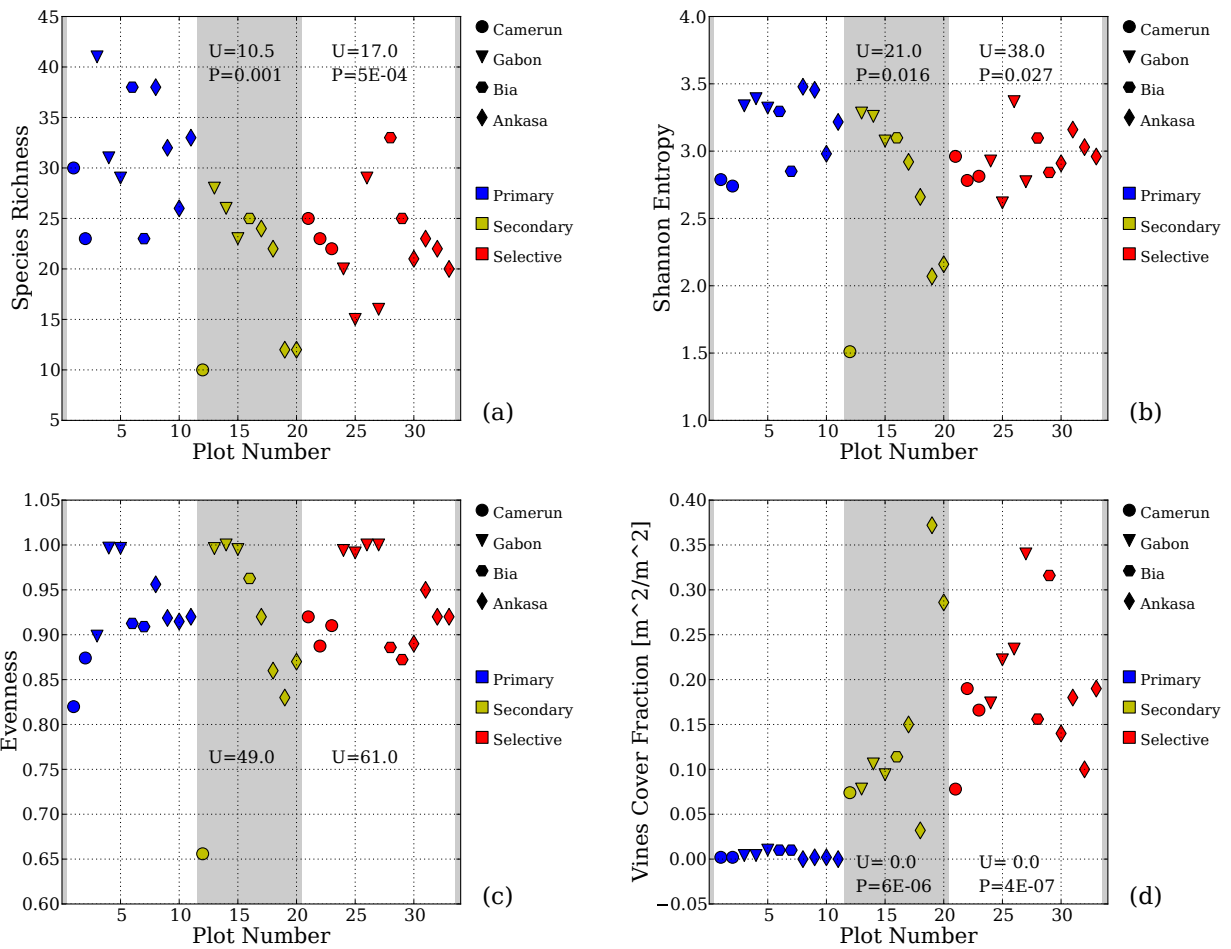


Figure 3: Indices characterizing the diversity and vine coverage in the plots. (a) species richness, (b) Shannon's entropy, (c) evenness, (d) Vines cover fraction. Symbols, colors and legend as in Figure 1.

Figure 3 shows the diversity and vines coverage indices. In all cases, with the sole exception of a plot of secondary forest in Cameroon, entropy and evenness of the plots have very high values, signalling that most of the species appear only once in each plot, regardless of the forest management type. Evenness is unable to distinguish between primary and the other two forest types, and entropy does so with a relatively low statistical confidence. This result is consistent with previous studies that did not record large losses of diversity in selectively logged forests [16]. Not surprisingly, the species richness is instead significantly lower in plots of secondary and selectively logged forest than in plots of primary forest: this is the expected consequence of the fact that the number of individuals per plot is less in selectively logged than in primary forests (Figure 2b), and that most species are represented by just one individual. Finally, the fraction of plot surface covered by vines is the index that most reliably singles out the primary forest plots from the other two types: in each primary forest plot the vine coverage is less (usually by a factor larger than ten) than in all non-primary forest plots.

Figure 4 shows the results of Sierra Leone. Panel (a) shows the probability density function of the diameter of the trees for the “Unlogged”, “Well-Managed” and “Logged” plot types, obtained with a kernel density estimation. The three curves appear very similar to each other, and a Kolmogorov-Smirnov test on the data gives *P*-values that confirm that any difference is just marginally significant. The curves, however, do show slight differences for trees above 75 cm dbh, that is in the range of the commercially interesting sizes. This result is coherent with those of the indices of Figure 1, that also showed just marginally significant differences between primary and the other two forest types. Panels (b) and (c) show the tree density and the normalized diameter indices. Because of the large number of plots, showing the values scored by each plot with individual markers, as in Figure 2, would be rather confusing and not very informative. We then opt for showing a kernel density estimate of the probability density function of each index as a function of the index value. It is then visually obvious that the “Logged” plots score systematically lower values than the “Unlogged” and the “Well-managed” plots. This is confirmed by the Mann-Whitney U test, which gives vanishingly low values to the null-hypothesis for the pair “Unlogged” vs “Logged”. However, it does not show significant differences for the pair “Unlogged” vs “Well-managed”.

Our results show that the distribution of heights, diameters and biomasses, and the diversity of trees in a logged forest are not largely different from those of a primary forest, while all indices of density show a marked rarefaction of the logged forest together with the concomitant invasion by vines, climbers and other weeds. In other words, the forest subjected to selective logging does not seem to have any effect on its vertical structure but rather shows a well-markable arboreal thinning. The single exception to these findings are the “well-managed” plots of Sierra Leone (Dataset 2), where the density indices appear to have roughly the same values than in the “unlogged” plots. On

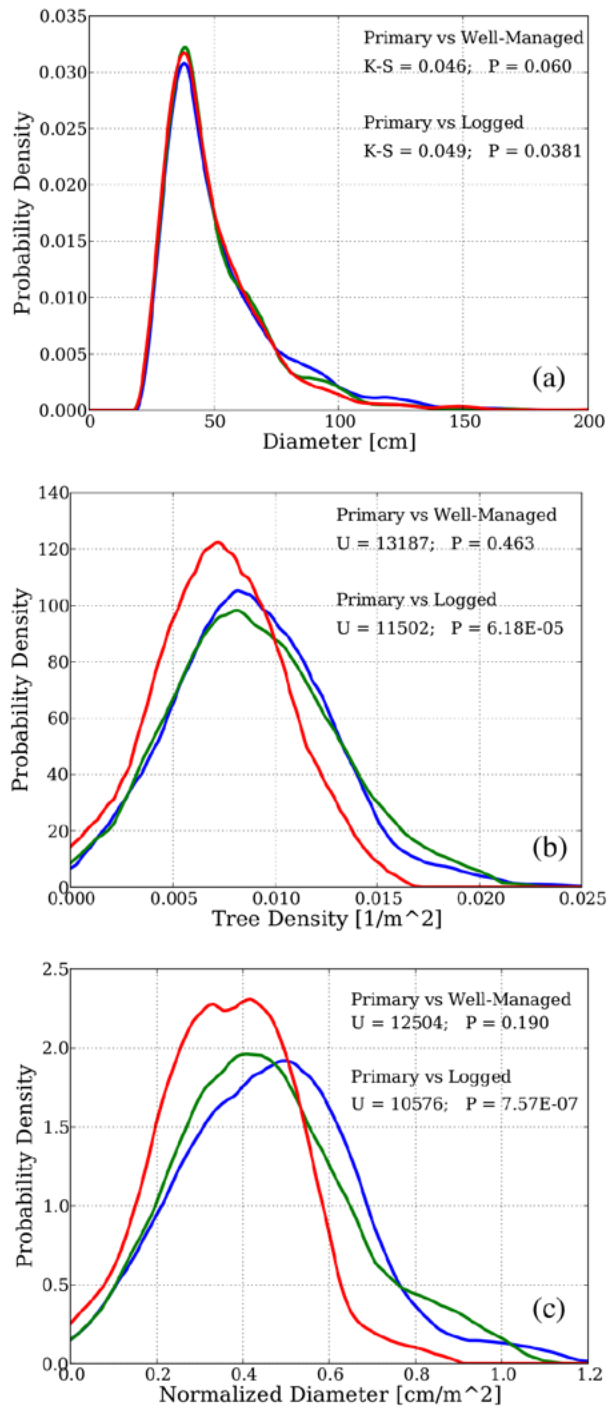


Figure 4: Probability density function (pdf) of data collected in Sierra Leone. a) pdf of trees diameter; b) pdf of tree density; c) pdf of normalized diameter. Blue line: unlogged plots; green line: well-managed plots; red line: logged plots.

the other hand, the “logged” plots of Gola show a drop in the density indices even though they were logged several decades ago. This result suggests the key that allows for an understanding of the observed data. In the “well-managed” plots of Gola the harvesters took care to minimize as much as possible the amount of canopy damage exerted by the logging activities. No such care was taken in the “logged” plots. This, in turn, implies that the amount of extra light filtering to the lower forest layers, and to the ground, was limited for “well-managed” plots, and more abundant and spread out for “logged” plots. It is reasonable to assume that the extra light caused by canopy openings larger than some threshold, triggers a complex chain of effects on the plant community, that eventually results in the death of some of the shade-intolerant species of the secondary or tertiary layer, and their replacement by patches of vines, climbers and shrubs that become dense enough to suppress the growth of seedlings of typical primary forest species.

A very simple model that catches the dynamics suggested by the data is the following

$$\begin{cases} \dot{\rho} &= (g(\rho) - \alpha q) \rho \\ \dot{q} &= \beta \left(1 - \frac{q}{K(\rho)}\right) q \end{cases} \quad (1)$$

where ρ is an index of arboreal density; q is the density of vines, climbers and shrubs (the infestants); g is the growth rate of the arboreal density, with $g'(\rho) < 0$, and there exists a value ρ^* such that $g(\rho^*) = 0$; K is the carrying capacity of the infestants, and it is a growing functions of ρ at low arboreal densities, and a decreasing function of ρ at high arboreal densities; α is a coupling coefficient between the infestants and the arboreal density, modeling the growth suppression of the seedlings; β is the maximum growth rate of the infestants. Note that, in the absence of infestants, the forest experiences a logistic-like growth, up to the equilibrium value ρ^* . If the density of the forest were kept constant, the vines would be subject to a logistic growth, too, but their carrying capacity is not fixed *a priori*, but is a function of the arboreal density. Very high forest densities correspond to low infestant carrying capacities, because not enough light filters to the lower forest levels. Very low forest densities also correspond to low infestant carrying capacities, because the soil fertility drops, and the infestants are unable to withstand the direct competition of pioneer species that colonize bare land (e.g. after a fire or a clear cut). Under rather mild conditions (to be discussed elsewhere), the system (5) shows two stable equilibria, with basins of attraction separated by a manifold containing an unstable equilibrium (Figure (5)).

One of the two equilibria corresponds to a “healthy forest” state, characterized by high arboreal density and low infestant density. The other stable equilibrium corresponds to a “sick forest” state, with intermediate arboreal and infestant density. A selective cut that thins the forest too much may bring the system from the “healthy forest” state to a state belonging to the basin of attraction

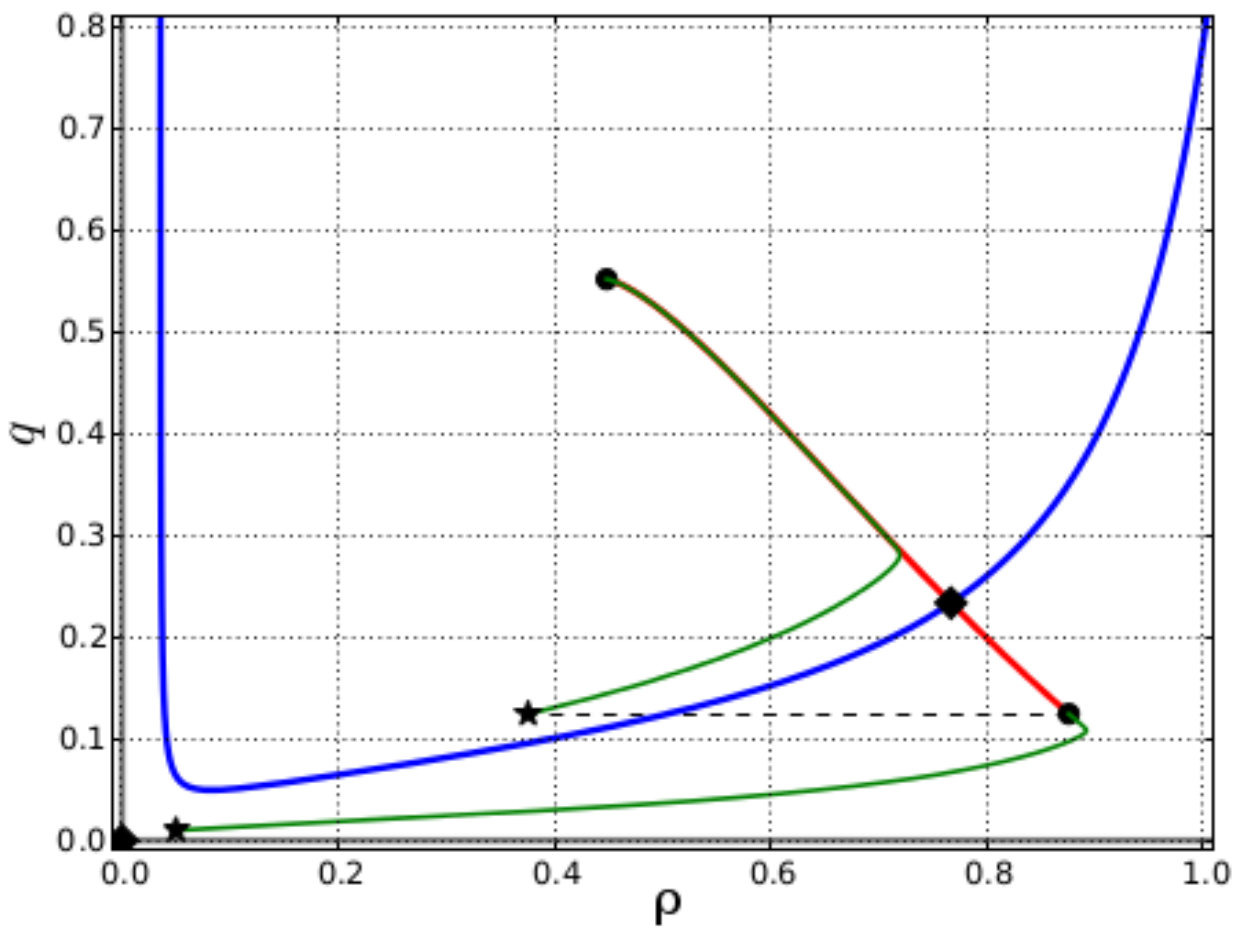


Figure 5: Phase space of model (1) for reasonable choices of the functions g , K and of the constants α , β . The black dots are stable equilibria; the black square is a saddle equilibrium. The red line shows the unstable manifold of the saddle. The blue line is the stable manifold of the saddle, and acts as boundary of the basins of attractions of the two stable equilibria. Stars are hypothetical initial conditions, representing, respectively, the state of the system after a damaging selective cut (the star at the left end of the dashed line), and the system after a clear cut or fire.

of the “sick forest” state (dashed line in Figure (5)). This results in a system that becomes locked in a low density state.

Therefore we conclude that the practice of selective cut, unless it is practiced very carefully at very low harvest intensities, may significantly reduce the biomass density of a tropical forest for time scales spanning decades, and possibly longer, seriously diminishing the aboveground carbon storage of the forest.

REFERENCES

- [1] De Wasseige C., Defourny P. 2004 Remote sensing of selective logging impact for tropical forest management. *Forest Ecology and Management* 188: 161–173.
- [2] Gascon C., Mesquita R., Higuchi N. 1998 Logging On in the Rain Forests, *Science* Vol. 281 no. 5382 p. 1453, DOI: 10.1126/science.281.5382.1453b
- [3] Drigo R., Lasserre B., Marchetti M. 2009 Tropical land cover change: patterns, trends and impacts. *Plant Biosystems* 143 (2), pp. 311–327.
- [4] Houghton R. A., Skole D. L., Nobre Carlos A., Hackler J. L., Lawrence K. T., Chomentowski W H. 2000 Annual fluxes of carbon from deforestation and regrowth in the Brazilian Amazon, *Nature* 403, 301–304
- [5] DeFries R. S., Houghton R. A., Hansen M. C., Field C. B., Skole D., and Townshend J.. 2002 Carbon emissions from tropical deforestation and regrowth based on satellite observations for the 1980s and 90s. *Proceedings of the National Academy of Sciences* 99:14256–14261, 2002.
- [6] Food and Agriculture Organization of the United Nations. 2010 Global Forest Resources Assessment 2010: Main Report. Food and Agriculture Organization of the United Nations.
- [7] Pan, Y., Birdsey, R. A., Fang, J., Houghton, R., Kauppi, P. E., Kurz, W. A., and Hayes, D. 2011 A large and persistent carbon sink in the world’s forests. *Science*, 333(6045), 988–993.
- [8] Thompson, I., Mackey, B., McNulty, S., Mosseler, A. 2009 Forest Resilience, Biodiversity, and Climate Change. A synthesis of the biodiversity/resilience/stability relationship in forest ecosystems. Secretariat of the Convention on Biological Diversity, Montreal. Technical Series no. 43, 67 pages.
- [9] Medjibe V. P., Putz F. E., Starkey M. P., Ndouna A. A., Memiaghe H. R. 2011 Impacts of selective logging on above-ground forest biomass in the Monts de Cristal in Gabon, *Forest Ecology and Management* 262,1799–1806.

- [10] Deckker, M. & de Graaf, N.R. 2003 Pioneer and climax tree regeneration following selective logging with silviculture in Suriname. *Forest Ecology and Management*, 172, 183–190.
- [11] Schleuning M., Farwig N., Peters M.K., Bergsdorf T., Bleher B., et al. 2011 Forest Fragmentation and Selective Logging Have Inconsistent Effects on Multiple Animal-Mediated Ecosystem Processes in a Tropical Forest. *PLoS ONE* 6(11): e27785. doi:10.1371/journal.pone.0027785.
- [12] Picard N., Gourlet-Fleury S., Forni ÁL. 2012 Estimating damage from selective logging and implications for tropical forest management, *Canadian Journal of Forest Research*, 42(3): 605–613, 10.1139/X2012-018.
- [13] Rametsteiner, E., Simula, M. 2003 Forest certification - an instrument to promote sustainable forest management? *Journal of Environmental Management*. 67 (1), 87 – 98.
- [14] Imai, N., Seino, T., Aiba, S. I., Takyu, M., Titin, J., & Kitayama, K. (2012). Effects of selective logging on tree species diversity and composition of Bornean tropical rain forests at different spatial scales. *Plant Ecology*, 213(9), 1413–1424.
- [15] Johns, A. D. 1988 Effects of " selective" timber extraction on rain forest structure and composition and some consequences for frugivores and folivores. *Biotropica*, 31-37.
- [16] Cannon, C. H., Peart, D. R., & Leighton, M. 1998 Tree species diversity in commercially logged Bornean rainforest. *Science*, 281(5381), 1366–1368.
- [17] Silva, J.N.M., Carvalho, J.O.P., Lopes, J.do.C.A., Costa, D.H., Oliveira, L.C., Vanclay, J.K. & Skovsgaard, J.P. 1995 Growth and yield of a tropical rain Forest in the Brazilian Amazon 13 years after logging. *Forest Ecology and Management*, 71, 267–274.
- [18] Magnusson, W.E., de Lima, O.P., Reis, F.Q., Higuchi, N. & Ramos, J.K. 1999 Logging activity and tree regeneration in an Amazonian forest. *Forest Ecology and Management*, 113, 67–74.
- [19] Luna, A.C., Osumi, K., Gascon, A.F., Lasco, R.D., Palijon, A.M. & Castillo, M.L. 1999 The community structure of caged over tropical rain forest in Mt. Makiling Forest Reserve, Philippines. *Journal of Tropical Forest Science*, 11, 446–458.
- [20] Ganzhorn, J. U., Ganzhorn, A. W., Abraham, J. P., Andriamanarivo, L., & Ramananjato, A. 1990 The impact of selective logging on forest structure and tenrec populations in western Madagascar. *Oecologia*, 84(1), 126–133.
- [21] Jennings, S.B., Brown, N.D., Boshier, D.H., Whitmore, T.C. & Lopes, J.do.C.A. 2001 Ecology provides a pragmatic solution to the maintenance of genetic diversity in sustainably managed tropical rain forest. *Forest Ecology and Management*, 154, 1–10.

- [22] Hall, J., Harris, D.J., Medjibe, V. & Asthon, P.M. 2003 The effects of selective logging on forest structure and tree species composition in a Central African forest: implications for management of conservation areas. *Forest Ecology and Management*, 183, 249–264.
- [23] Okuda, T., Suzuki, M., Adachi, N., Quah, E.S., Hussein, N. & Manokaran, N. 2003 Effect of selective logging on canopy and stand structure and tree species composition in a lowland dipterocarp forest in Peninsular Malaysia. *Forest Ecology and Management*, 175, 297–320.
- [24] Cannon C.H., Peart D.R., Leighton M., Kartawinata K. 1994 The structure of lowland rain-forest after selective logging in West Kalimantan, Indonesia, *Forest Ecology and Management*, 67:49-68.
- [25] Herbohn, J.L. & Congdon, R.A. 1993 Ecosystem dynamics of disturbed and undisturbed sites in North Queensland wet tropical rain forest. II. Litterfall. *Journal of Tropical Ecology*, 9, 365–380.
- [26] Asner, G. P., Knapp, D. E., Broadbent, E. N., Oliveira, P. J., Keller, M., & Silva, J. N. 2005 Selective logging in the Brazilian Amazon. *Science*, 310(5747), 480-482.
- [27] Lindsell, J. A., & Klop, E. 2013 Spatial and temporal variation of carbon stocks in a lowland tropical forest in West Africa. *Forest Ecology and Management*, 289, 10-17.
- [28] Schnitzer, S. A., Dalling J. W., and Carson W. P. 2000 The impact of lianas on tree regeneration in tropical forest canopy gaps: evidence for an alternative pathway of gap-phase regeneration. *Journal of Ecology* 88:655–666.
- [29] Callaway, R. M., & Mahall, B. E. 2007 Plant ecology: family roots. *Nature*, 448(7150), 145-147.
- [30] Asner G.P., Keller M., Silva J.M., 2004 Spatial and temporal dynamics of forest canopy gaps following selective logging in the eastern Amazon. *Global Change Biology* 10, 765–783.
- [31] Chave, J., Andalo, C., Brown, S., Cairns, M. A., Chambers, J. Q., Eamus, D., and Yamakura, T. 2005 Tree allometry and improved estimation of carbon stocks and balance in tropical forests. *Oecologia*, 145(1), 87-99.

Assessing the resilience of Mediterranean trees diversity to climate change projections

Di Paola A.^{1*}, Valentini R.², Paparella F.³

¹*Euro-Mediterranean Center for Climate Change (CMCC), LAFENT Division, Viterbo–Italy*

²*Director of Division of Climate Change Impacts on agriculture, forests and natural ecosystems.*

Euro-Mediterranean Center for Climate Change. Viterbo, Italy

³*Department of Mathematics and Physics “Ennio De Giorgi”, University of Salento, Lecce, Italy*

**Corresponding author: arianna.dipaola@cmcc.it*

Abstract

The Mediterranean region is one of the hot spots of climate change. This study evaluates whether the actual and future climate conditions allow for a stable coexistence of typical endemism of deciduous and evergreen oak species in the Mediterranean Region. In this work, Deciduous and Evergreen oak species are broadly distinct according to their distinct adaptive strategies of trees against water stress of summer drought and prolonged wet periods in winter, respectively. We suggest that at intermediate levels of actual evapotranspiration, of which we outline a map, the coexistence remain stable. By comparing our findings with a quantile ensemble analysis based on projections from 16 General Circulation Models (GCMs) for 2070–2099 [14], we point out that climate change highly threatens Mediterranean diversity, since the lower threshold (315 mmYr^{-1}) of evapotranspiration could be reached in the second half of the current century due to an overall decline in soil moisture.

Keywords: *Coexistence, tree diversity, Climate Change, Dynamic Model, Mediterranean*



The Mediterranean region has been identified as a highly vulnerable area to climate change. In the past this region has experienced large climate shifts [1] and recent study identify the Mediterranean area as a prominent hot-spots in future climate change projections [2, 3]. The potential vulnerability of the Mediterranean basin to climate changes has been linked to its transitional location between the rainy temperate climate of North Europe and the arid climate of North Africa. Such position allows to even a little change of general circulation pattern to have a substantial consequences on the Mediterranean climate [2].

The particular features of such a climate enable the establishment of a unique Mediterranean biome, characterized by plant species usually adapted to survive long, hot summer droughts and prolonged wet periods in winter. [4]. This region holds an extraordinary diversity of species because of the great multitude of different habitats that characterize it [5]. All these kind of habitat, of which the most common are forests, woodlands, savannas, grasslands and wetlands, are highly distinctive, collectively harbouring 10% of the Earth's plant species with high numbers of rare and locally endemic plants [5,6].

The native arboreal vegetation of the warmest zones of the Mediterranean climate is typically sclerophyllous and ever-green, adapted to water stress during the dry summer period, and able to grow on infertile soils [7]. Where the climate is characterized by relative higher precipitation and lower winter temperature the characteristic vegetation become that of deciduous trees. Few deciduous species may be also relatively xeric and thus have a similar distribution area of those of evergreen species (e.g. *Quercus pubescens*, *Q. faginea*). Overall, this two broadly kinds of vegetations, having different *hygrophilia*, share a wide distribution areas giving rise to many case of broad-leaved deciduous and evergreen trees co-occurrence. Ecologists are generally agreed that long-lived, evergreen leaves offer a potentially longer photosynthetic season than deciduous leaves, promotes water savings and enhances tolerance during dry periods. Deciduous trees generally compensate for a shorter growing season by producing leaves that have higher photosynthetic and transpiration rates per unit mass than do evergreen trees [8]. These respective advantages and disadvantages explain, at least in qualitative terms, why in the Mediterranean basin the two kind of species coexist (adaptive significance). For an exhaustive discussion about the adaptive significance of co-presence deciduous and evergreen species in Mediterranean climate see the work of [8].

The native copresence of evergreen oaks species with deciduous ones around the Mediterranean basin is one of the distinctive features of Mediterranean diversity and was subjected to numerous

discussions[8,9,10]. For this reason we focus on Mediterranean mixed oaks forests characterized by typical endemism of oaks species having both of leaf habit, thus hygrophilia, extending the coexistence model [9] to point out where climate changes threatens trees diversity within the Mediterranean region. Note that in the present work we use the word *copresence* when we refer to the evidences while we use the term *coexistence* when we refer to the homonymous equilibrium allowed by the coexistence model.

1. MODEL OVERVIEW

The coexistence model about Mediterranean plain forests reproduces the minimum set of factors that should be accounted to explain the observed coexistence of trees having different hygrophilia(1-3). The fixed point of coexistence is easily determinable as the triplet of the state variables (X_0, Y_0, W_0) corresponding to zeros of the expression on the right-hand side of equations (1-3):

$$\dot{X} = F(W)X - k(X + Y)X \tag{1}$$

$$\dot{Y} = H(W)Y - k(X + Y)Y \tag{2}$$

$$\dot{W} = -T_X(W)X - T_Y(W)Y + S(W) \tag{3}$$

Assuming a same death rate k for both the species, it is rather straightforward to observe that if (X_0, Y_0, W_0) is a coexistence equilibrium, then W_0 is a solution of:

$$F(W_0) = H(W_0) \tag{4}$$

This is one of the most relevant result of the local stability analysis on the state of coexistence [9] which points out that the equality of the net growth rate of the two species modelled is a necessary condition in order to have coexistence.

Eq(4) shows also that at the equilibrium point of coexistence the soil water content does not depend on biomass-independent water term S , which encloses climate conditions. The same equilibrium point

neither depends on the transpiration rates T_x and T_y . A similar observation can be made for the total biomass density since the equality of eq.s (1) and (2) leads to

$$X + Y = F_0/k = H_0/k \quad (5)$$

Therefore, the model predicts that a forest in which hygrophilous and non-hygrophilous coexist, the species are able to maintain a homeostatic equilibrium of total biomass density and soil water content. The local stability analysis showed that there are other necessary conditions for a stable coexistence. These can be summarized as follow: *i)* the transpiration rate of the hygrophilous species is higher than those of non-hygrophilous species; *ii)* it must be $dH_0/dW \geq 0$, assumption that can be reasonably assumed as valid at the equilibrium of coexistence (otherwise the growth of non-hygrophilous species should be in decline).

Finally, the stability condition for a stable coexistence may be reduced to the meaningful imposition of a positive biomass, that is:

$$\frac{T_{y0}F_0}{k} < S_0 < \frac{T_{x0}F_0}{k} \quad \text{with } T_{x0} > T_{y0} \quad (6)$$

Where T_{x0} and T_{y0} are the transpiration rates of deciduos and evergreen species, respectively [$\text{Kg m}^{-2} \text{Yr}^{-1}$]; F_0/k is the total forest ($X + Y$) biomass density [Kgm^{-2}] and S_0 is the amount of water lost through forest traspiration [$\text{Kgm}^{-2}\text{Yr}^{-1}$].

More specifically S_0 can be also expressed as

$$S_0 = T_{0x}X + T_{y0}Y = p - e - qW \quad (7)$$

where X and Y are the biomass density of the Deciduos and Evergreen species [Kgm^{-2}], respectively; p is the input of water through precipitation [$\text{Kgm}^{-2}\text{Yr}^{-1}$], e the soil evaporation [$\text{Kgm}^{-2}\text{Yr}^{-1}$] and qW is

the flux of water lost through shallow and deep percolation [$\text{Kgm}^{-2}\text{Yr}^{-1}$]. All these terms refer to the equilibrium point of coexistence, marked with subscript "0".

Eq. (6) incorporates a very simple set of assumptions and impositions that if met can show where environmental and climatic conditions allows, at least theoretically, the coexistence of Deciduous and Evergreen species. The bifurcation analysis carried out in the previous work [9] showed that the mechanism of coexistence appears to be robust, but that coexistence is possible only within a somewhat narrow interval of *water supply*, namely the difference between precipitation and evaporation $p - e$.

From an practical point of view, it is convenient to express condition (6) as follows:

$$\frac{T_{y0}F_0}{k} + e < p - qW < \frac{T_{x0}F_0}{k} + e \quad (8)$$

In this way, the condition of stability can easily be interpreted as a function of the forest evapotranspiration, data widely available. Now, equation (8) shows that to have a stable coexistence between the two species, the evapotranspiration at the equilibrium point $p - qW_0$, must range between the hypothetical evapotranspiration that would occur in the cases of forests composed only by the *Y* species, i.e. $\frac{T_{y0}F_0}{k} + e$, and only by the *X* species, i.e. $\frac{T_{x0}F_0}{k} + e$.

For the purpose of our work, we regard the mean annual evapotranspiration (ET) as the evapotranspiration at the equilibrium point. The evaluation of the extremes of condition(8), become possible by knowing the distribution of the main deciduous and evergreen Mediterranean species, by which we can select the data of ET corresponding to sites with a single category of species (e.g. forest covered only by *X* or *Y* species), namely the *characteristic evapotranspiration*.

2. DATA SOURCES

We use the MODIS Evapotranspiration (ET) global maps to evaluate where condition (8) is satisfied. The ET dataset defines the mean annual water flux lost through evapotranspiration [mmYr^{-1}] and covers the time period 2000-2011. Data consist of matrices of values distributed on a rectangular grid of geographical coordinates (latitude-longitude), referring to the WGS84 geoid. The first dimension of

the grid (longitude) increases from west (-180°) to the east ($+180^{\circ}$) more rapidly than the second (latitude) which in turn increases from the south (-90) to the north ($+90$), both with a constant angular step of 0.0083° degree. Data are provide in Tagged Image File Format (.tif), for more information see [11].

The Joint Researcher Center provides a database of tree species distributions (TSD) [12], expressed as percentage of coverage, for 115 different species of Europe. The data set consists of 115 georeferred maps giving the distribution of 115 tree species in 30 European countries. Data are arranged into a grid of square mesh at constant footsteps of 1 km. The data has the following projection (Sphere Lambert Equal Area) parameters: latitude of projection center: 48°N ; Longitude of projection center: 9°E ; false easting: 0; flase northing: 0; The sum of the percentages of the individual trees returns the percentage of land covered by forest (up to 100% in totally forested areas). The data are provided in ARC / INFO grid format. The values of tree coverage should be considered as a rough estimate with higher discrepancy for small countries and for countries with a low or scattered forest cover or with a high species diversity [12]. The dataset does not contain the complete European distribution of all the species entered but only the distribution of species in areas where it was possible to record their presence and classification. However we believe that such data are sufficient and very useful for the estimates of the single category-characteristics evapotranspiration.

3. OUTLINING THE MEDITERRANEAN AREAS OF STABLE COEXISTENCE

The annual data of ET have been averaged to obtain a single estimate of the mean ET for the whole available period 2000-2011 (Fig. 1), taken to be the total forest evapotranspiration at the equilibrium point ($p - qW$). Since the model was devised to explain the observed coexistence in the Mediterranean forests, the study area selected for the model extension range between 30° and 48° North and from -12° to 45° East.

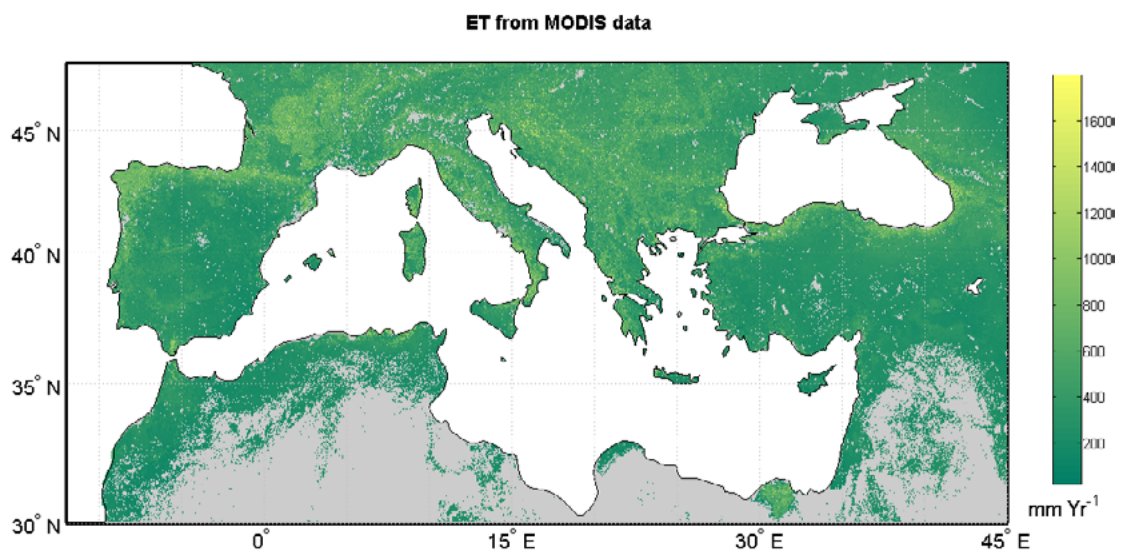


Fig. 1: Mean Annual Evapotranspiration (2000-2011) from MODIS data. The gray areas are those of missing data

From the dataset of forest tree species distribution (TSD) we select those of interest, i.e. 4 matrices of evergreen tree species (*Q. ilex*, *Q. coccifera*, *Q. suber* and *Q. Rotundifolia*) and 5 matrices of deciduous ones (*Q. cerris*, *Q. frainetto*, *Q. pyreaica*, *Q. faginea* and *Q. Pubescens*).

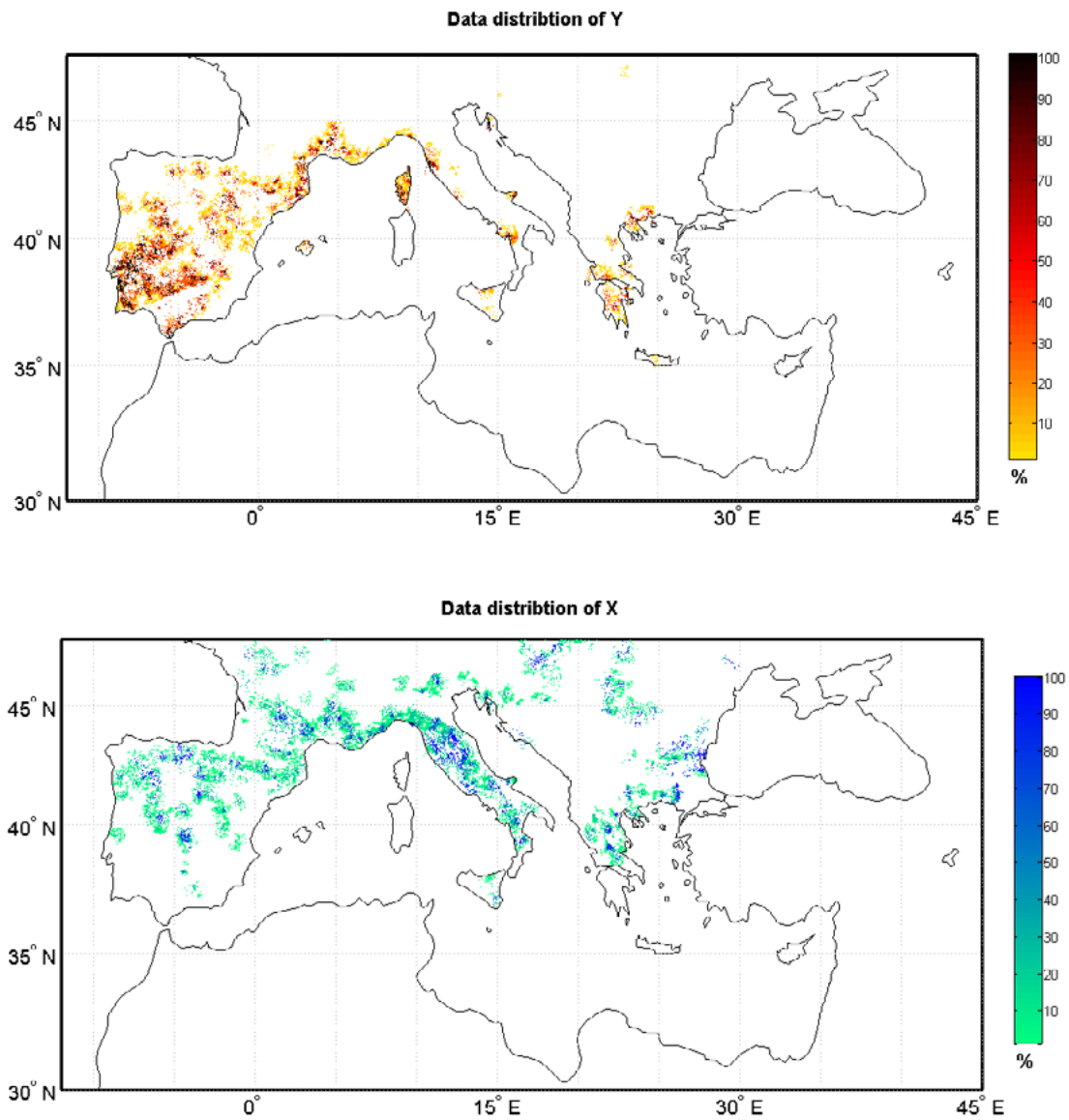


Fig. 2: Distribution of the selected Mediterranean oak species. Red scale: Evergreen oak species (*Q. ilex*, *Q. coccifera*, *Q. suber* and *Q. Rotundifolia*). Blue scale: Deciduous oak species (*Q. cerris*, *Q. frainetto*, *Q. pyraica*, *Q. faginea* and *Q. Pubescens*). The distribution is expressed as percentage of land cover.

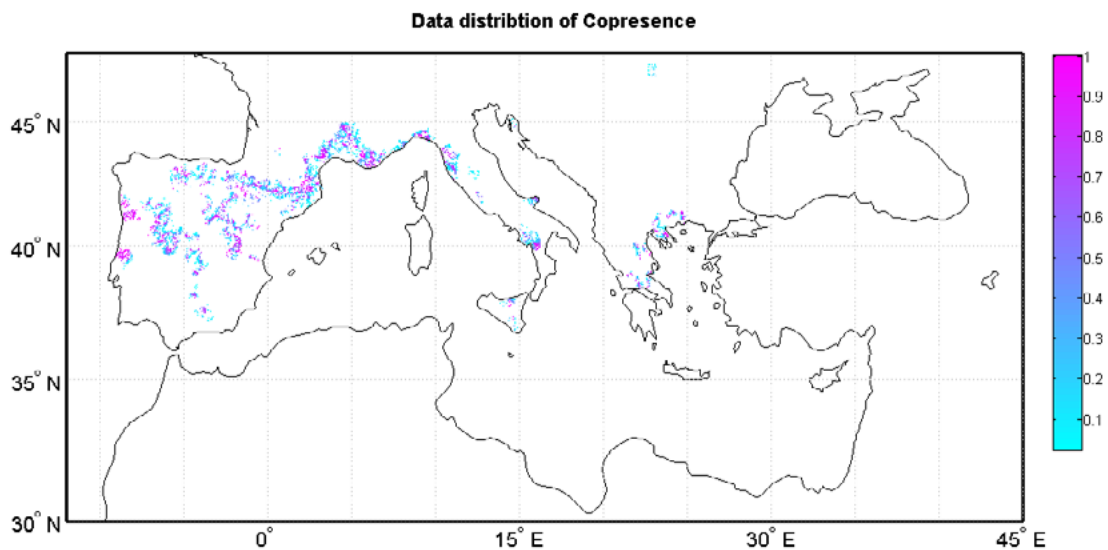


Fig. 3: Area of Co-presence of the selected Mediterranean Evergreen oak species with Deciduous ones

Their aggregation, obtained through a simple sum of them, in the broad categories X (Deciduous) and Y (evergreen) reflect their general behavior of being wet tolerant and drought resistant respectively. Such process allows us to identify the forested areas covered by a single category (Fig. 2) as well as the areas of copresence (Fig. 3). After the combination of the selected forest species, the spatial reference of the X and Y species distribution has been converted into the same of ET, i.e. in geographical coordinates (Latitude and Longitude) referring to the WGS84 geoid with a constant angular resolution of 0.0083 degree.

At this point, quantifying the extremes of condition (8) is quite simple. We select three group of ET, namely ET data occurring only in the monospecific presence of species X (ET_x), ET data occurring only in the monospecific presence of species Y (ET_y) and ET data occurring only in the case of copresence (ET_{co}). The relative abundance of data of each groups (always more than $1 \cdot 10^5$ pixel for each subset of ET) allow us to perform a kernel density estimation of the probability density function (pdf) for each subset (Fig. 4), based on the gaussian kernel and using Silverman's rule for bandwidth selection[13].

The curves of pdf show different distributions of habitat between the two species X and Y. This first result represents a considerable proof of consistency about the assumptions made by the model: from an independent dataset we observe that the X species (blue line of the Fig. 4) tend to evapotranspire more than Y species. From an ecological point of view, the curves of probability density function show

that both the species share the same climate areal (from 100mm/Yr to 1300 mm/Yr approximately) even though with discernible preferences of occurrence (namely, the mode of the red and blues curves differs by about 200 mm/Yr).

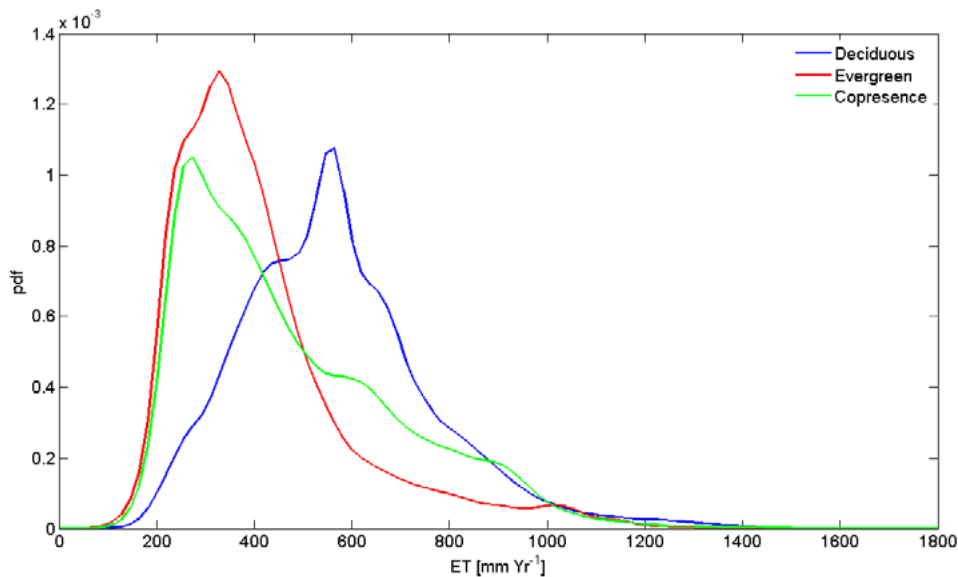


Fig. 4: Probability density function of tree subset of ET. Blue line: evapotranspiration of forest covered only by X species (ET_x); red line: evapotranspiration of forest covered only by Y species (ET_y); green line: evapotranspiration of forest covered by the copresence of both the species (ET_{co}).

Even the curve of probability density function of the case of copresence is a proof of the model validity: the green curve (obtained from an independent subset of ET) could have been shifted with respect to the monospecific curves (i.e. blue and red). Conversely it falls well within the climate areal of the X and Y.

We assume that the mode of the pdf of the monospecific cases (blue and red lines of Fig. 4), is a reasonable quantitative estimate of the extremes of condition (8). Now, we can outlining the geographical area characterized by an average evapotranspiration that ranges between the extremes of condition (8), that is, at least theoretically, the area characterized by a climate condition which ensure a stable coexistence (Fig. 5).

The fraction of the cases of copresence within the range of evapotranspiration that insure for a stable coexistence (306-587 mm/Yr) is 0.46. Such performance is not very high, however it must be considered that the quantitative estimation of the extremes of condition (8) through the mode (the

median as well as the median could be just as valid) of the monospecific distributions is a very simplistic assumption that inevitably excludes much of the data that are on the outer side of the distribution of copresence.

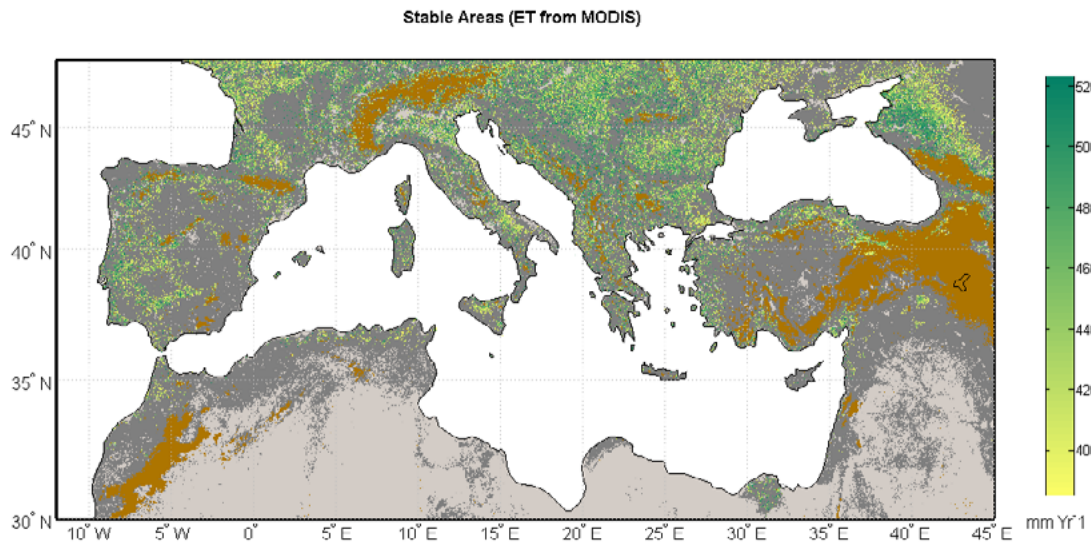


Fig. 5: Area of stable coexistence. Areas that are yellow to green have a climate condition (mean annual ET from 306 to 587 mmYr⁻¹) that ensure a stable coexistence of evergreen oak species with deciduous ones. Areas that are brown represent where the altitude is more than 1400 m.a.s.l. The gray areas are those of missing data.

The bifurcation analysis carried out in the previous work [9] showed that the mechanism of coexistence appears to be robust, but that coexistence is possible only within a somewhat narrow interval of *water supply*, namely the difference between precipitation and evaporation $p - e$. In this subsequent work we have shown an equivalent form of the condition of stability, in which the coexistence of evergreen oak species with deciduous ones is preserved by an intermediate level of actual evapotranspiration rather than a water supply. This allowed us to extend the model on a regional scale in the Mediterranean basin through the MODIS dataset of Evapotranspiration. By comparing our findings with a quantile ensemble analysis based on projections from 16 General Circulation Models (GCMs) for 2070–2099 [14], we may point out where climate change mainly threatens Mediterranean diversity.

For example, Girvets et al. [14] showed that under the A1B scenario, the Mediterranean region is projected to decrease in precipitation by approximately 10–30% in the 80th percentile ensemble map, which means that 80% of the models (13 out of 16) agree that precipitation is projected to decrease by at least this amount. Moreover, the mean temperature in this region is projected to increase under the

“Maximum” ensemble of at least 2°C, showing that all Global Climatic Models project agree with a increasing mean temperature . According to such as expected climate scenarios, the lower threshold (315mmYr⁻¹) of evapotranspiration could be reached in in the second half of the current century due to an overall decline in soil moisture.

4. CONCLUSION

Climate change implies a potential dramatic shift towards evergreen species communities that would result in a loss of biodiversity in the Mediterranean mixed oak forests, exacerbated by the strong local endemism of such Region. Our work confirms the importance of using dynamic, deterministic models for identifying vulnerabilities and thresholds while assessing the impacts of climate change. We believe that in the future approaches like this model will have a wider use because they provide simple and clear instruments to policy makers and planning institutions for decision making.

5. ACKNOWLEDGMENTS

The authors gratefully acknowledge Dario Papale (UNITUS), Goffredo Filibeck (UNITUS), Roberto Cazzola Gatti (CMCC) and Francesco Di Paola (IMAA-CNR) for many constructive suggestions.

6. REFERENCES

Luterbacher J., Xoplaki E., Casty C., Wanner H., Pauling A., et al. (2006), *Mediterranean climate variability over the last centuries. A review*. In: Lionello P., Malanotte-Rizzoli P., Boscolo R., eds. *Mediterranean Climate Variability*. Elsevier, Amsterdam, pp. 27–148. (1)

Giorgi F., Lionello P., (2008), *Climate change projections for the Mediterranean region*. *Global and Planetary Change* 63:90-104. (2)

Sala O.S., Chapin III F.S., Armesto F., Berlow J.J., Bloomfield E., et al. (2000), *Global biodiversity scenarios for the year 2100*. *Science*, 287: 1770–1774. (3)

Huston M.A. (1994), *Biological diversity: the coexistence of species on changing landscapes*. Cambridge University Press. 681 p. (4)

- Cody M.L. (1986), *Diversity, rarity, and conservation in Mediterranean-climate regions*. In Soulé, M.E.. *Conservation biology: the science of scarcity and diversity*. Sunderland, Massachusetts, USA. Sinauer. pp. 122–152. (5)
- Cowling R.M., Rundel P.W., Lamont B.B., Arroyo M.K. and Arianoutsou M. (1996), *Plant diversity in Mediterranean-climate regions*. *Tree*, 11:362-366. (6)
- Gasith A., Vincent H.R. (1999), *Streams in Mediterranean climate regions: abiotic influences and biotic responses to predictable seasonal events*. *Annual review of ecology and systematics*. 30:51-81. (7)
- Baldocchi D.D., Ma S., Rambal S., Misson L., Ourcival J.M. et al (2010), *On the differential advantages of evergreenness and deciduousness in Mediterranean oak woodlands: a flux perspective*. *Ecological Applications*, 20:1583–1597. (8)
- Di Paola A., Valentini R., Paparella F. (2012), *Climate Change Threatens Coexistence within Communities of Mediterranean Forested Wetlands*. *PLoS ONE* 7(10): e44727. doi:10.1371/journal.pone.0044727. (9)
- Givnish T.J. (2002), *Adaptive significance of evergreen vs. deciduous leaves: solving the triple paradox*. *Silva Fennica*, 36(3), 703-743. (10)
- Mu Q., Zhao M., & Running S.W. (2011), *Improvements to a MODIS global terrestrial evapotranspiration algorithm*. *Remote Sensing of Environment*, 115(8), 1781-1800. (11)
- Köble R. and Seufert G. (2001), *Novel maps for forest tree species in Europe*. *Proceedings of the 8th European Symposium on the Physico-Chemical Behaviour of Air Pollutants: "A Changing Atmosphere!"*, Torino (It) 17-20 September 2001. Data set available online at:
- <http://afoludata.jrc.ec.europa.eu/index.php/dataset/detail/66> (12)
- Wand M.P., & Jones M.C. (1995), *Kernel smoothing* (Vol. 60). Chap. 2,3. Chapman & Hall/CRC. (13)
- Girvetz E. H., Zganjar C., Raber G. T., Maurer E.P., Kareiva P., & Lawler J. J. (2009), *Applied climate-change analysis: the Climate Wizard tool*. *PLoS One*, 4(12), e8320. (14)

Projected climate change impacts on staple food crops in Nigeria

Mereu V.^{1,2*}, Gallo A.², Carboni G.³, Cervigni R.⁴, and Spano D.^{1,2}

¹Department of Science for Nature and Environmental Resources DipNET, Sassari, Italy

²Euro-Mediterranean Center on Climate Changes (CMCC), LAFENT Division, Sassari, Italy

³AGRIS - Agricultural Research Agency of Sardinia, Department of Crop Production, Cagliari, Italy

⁴Climate Change Sustainable Development Sector Department Environment and Natural Resources (AFTEN), Africa Region The World Bank, N.W. Washington D.C., USA.

*Corresponding author: vmereu@uniss.it

Abstract

The projected impacts of future climate change on agriculture are expected to be significant and extensive in the Sub-Saharan Africa Countries due to the shortening of the growing seasons and the increasing risk of water stress.

In this context, there is an urgent need to identify specific agricultural sectors and Agro-Ecological Zones (AEZs) that will be more vulnerable to changes in climatic conditions, in order to provide indications on the most appropriate policies to cope with these threats.

The agricultural sector is strategic for Nigerian economy and its vulnerability to climate change may be exacerbated by population increase, the widespread poverty and other social factors.

In this study, a multi-model approach was used to explore uncertainties related to climate change projections for the most important crops in Nigeria.

Crop models implemented in the DSSAT-CSM software were used, after a parameterization phase, to evaluate climate change impacts on crop production. Multiple combinations of soils and climate conditions, crop management and varieties were considered for each Agro-Ecological Zone. The climate impact assessment was made using an ensemble of future climate projections. Crop yields are expected to decrease, especially for cereals in the medium term period (2050). Even if precipitation increases in several parts of the country, this is not likely to offset the negative effects of rising temperatures on yields of most rain-fed crops, particularly over the long term. The shorter-term effects are more uncertain: by 2020, according to more than half of the climate models, yields for cassava and perhaps other crops might actually increase. The wide variability of simulated yields, especially in the northern AEZs, reflects the wide variability of climate model projections.

Keywords: *Simulation models, crop production, multi-model analysis, uncertainty*



1. INTRODUCTION

The agriculture sector in Nigeria contributes more than 40 percent of gross domestic product (GDP) and accounts for about 60 percent of employment [1].

The principal food crops cultivated in Nigeria are cereals, mainly millet, sorghum, maize and rice, and root crops as cassava and yam [2]. Together they account for 80 percent of the total agricultural production [3].

Millet and sorghum are produced in the drier savanna North, which experiences a dry season of five to seven months. Maize, yam and cassava are commonly grown in the middle and southern part of the country, where rainfall is more abundant. Rice is cultivated in virtually all of Nigeria's AEZs, from the mangrove and swamp ecologies of the Niger Delta in the coastal areas to the dry zones of the Sahel in the north.

Sorghum is the most widely cultivated cereal in Nigeria, accounting for more than 40 percent of the total area devoted to cereals, with more than 7.6 million ha under cultivation in 2008 [4]. Millet is the second most important cereal, with a cultivated area of about 5 million ha and total production of more than 9 million tons in 2008 [4]. Rice is cultivated in 2.4 million ha of harvested land with low yields, averaging 1.7 tons per hectare. Other production systems make up the remaining 4 percent [5]. Cassava and yams are the lead crops for the Nigerian economy, with a production of over 45 million tons per year for both cassava and yam [4].

National crop production has been adversely affected by recent climate patterns [6] as a consequence of an increase in crop failure or a decrease in yields due to the false start of the rains, frequent drought during the growing seasons, and early cessation of rains that limit the growing season ([7], [8]). Storms, flooding, rising temperatures, and pest infestations could also determine crop damage and reduce crop production.

These damages could be aggravated in the future years by climate change and the entity depending on the Agro-Ecological Zones, production systems, and sociocultural conditions.

The vulnerability of Nigeria to Climate is aggravated by the heavy dependence of the economy and food security on rain-fed agriculture, and by the rapid population growth coupled with widespread poverty, which reduces its resilience to climate risks.

In this context, the aim of this study was the assessment of climate change impacts for key crops in Nigeria, using a multi-model analysis, in order to explore the uncertainties related to climate projections and indicate suitable adaptation strategies, focused on local needs.

2. MATERIALS AND METHODS

The DSSAT-CSM (Decision Support System for Agrotechnology Transfer— Cropping System Model) software [9], based on the modular approach described by Jones, Keating, and Porter [10] and Porter, Jones, and Braga [11], was used to simulate physiological process of crop growth, development and production, by combining genetic crop characteristics and environmental (soil and weather) conditions. Crop models included into DSSAT-CSM allow to simulate growth, development, and yield of a crop growing on a uniform area of land under prescribed or simulated management. This software is also able to take into account changes in soil water, carbon, and nitrogen that take place in a cropping system over time. Improved application programs included into DSSAT permit seasonal and sequence analyses for assessment of environmental impacts of irrigation management, climate change and variability, and precision management [12]. Moreover, it is possible to evaluate the effect of change in the air CO₂ concentration, which is very important in climate change impact studies because it has effects (in particular for C3 crops) on photosynthesis (biomass accumulation) and water use efficiency (stomatal conductance).

“Minimum data set” (MDS), which is the minimum data required to run the crop models and validate the outputs, includes: (i) site daily weather data for the entire growing season; (ii) site soil data; (iii) management and observed data from experiments and or bibliography: information on planting date, planting density, row spacing, planting depth, crop variety, irrigation, tillage and fertilizer practices.

The methodology applied for crop modelling analysis (fig. 1) includes: (a) model set-up (collection of the MDS required by the models and preparation of crop, soil, and weather databases); (b) calibration and validation of crop simulation models and (c) assessment of impact of projected climate change conditions. Finally, adaptation strategies were suggested to cope with the projected climate changes conditions.

Analyses were made for Sorghum, Maize, Millet, Rice, and Cassava. A first attempt was made to simulate growth and development of Yam crop, the model of which is not included into DSSAT.

Numerous combinations of soil and climate conditions were considered for each Nigerian Agro-Ecological SubZone (AESZ) (fig. 2), in which specific crop management, such as growing periods, plant density, fertilization, crop calendar, and/or crop varieties cultivated (long or medium growing season), were set based primarily on USAID MARKET ([5], [14], [15]).

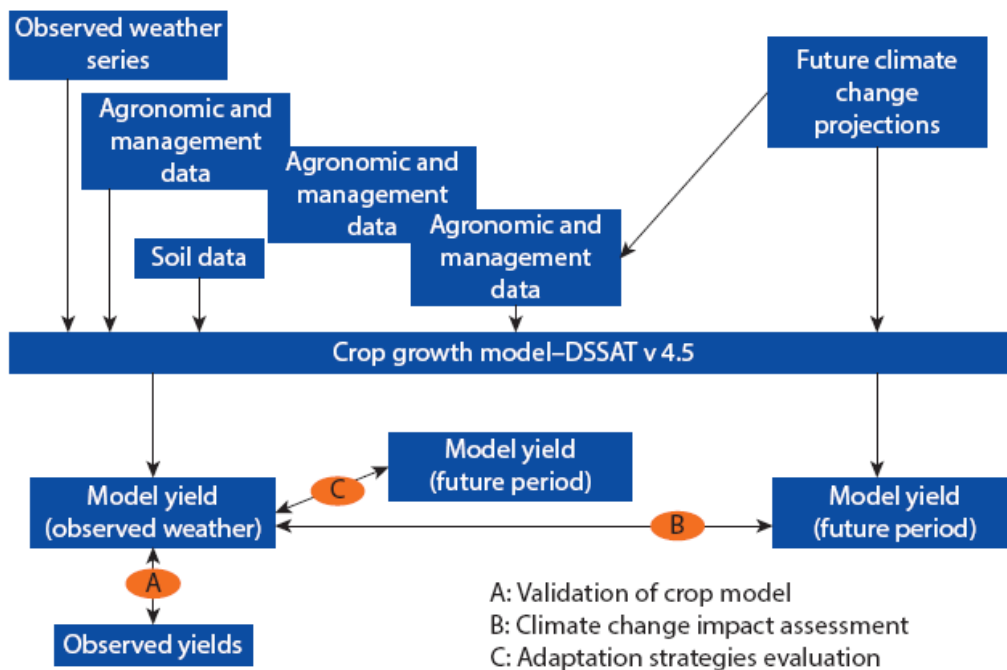


Fig. 1: Scheme of Methodology (Source: Dubrovsky [13], modified)

For each crop, simulations were performed in the AESZs where the crops are most diffused. Model calibration and validation were performed in representative geographical locations to enable extrapolation of the results to the entire national territory. Climate impact was assessed by comparing yields obtained with the weather for the present period and projected yields obtainable under changed climate conditions. Land use change were not considered. Climate data used in impact analysis are obtained from the unperturbed regional climate model (RCM), COSMO-CLM, and five of its perturbations. The climate projections used to perturb the RCM were derived by CMCC-MED, Geophysical Fluid Dynamics Laboratory (GFDL), Institute of Atmospheric Physics (IAP), MIROC, and National Center for Atmospheric Research (NCAR). These selected

perturbations were used to explore a wide range of uncertainties in climate projections because they allow to estimate the most extreme impacts due the changes in temperature and precipitation. Climate change impacts were calculated for the baseline period 1976–2005 (centered on 1990) and for the 30-year climatic periods centered on 2020 (2006–35) and 2050 (2036–65).

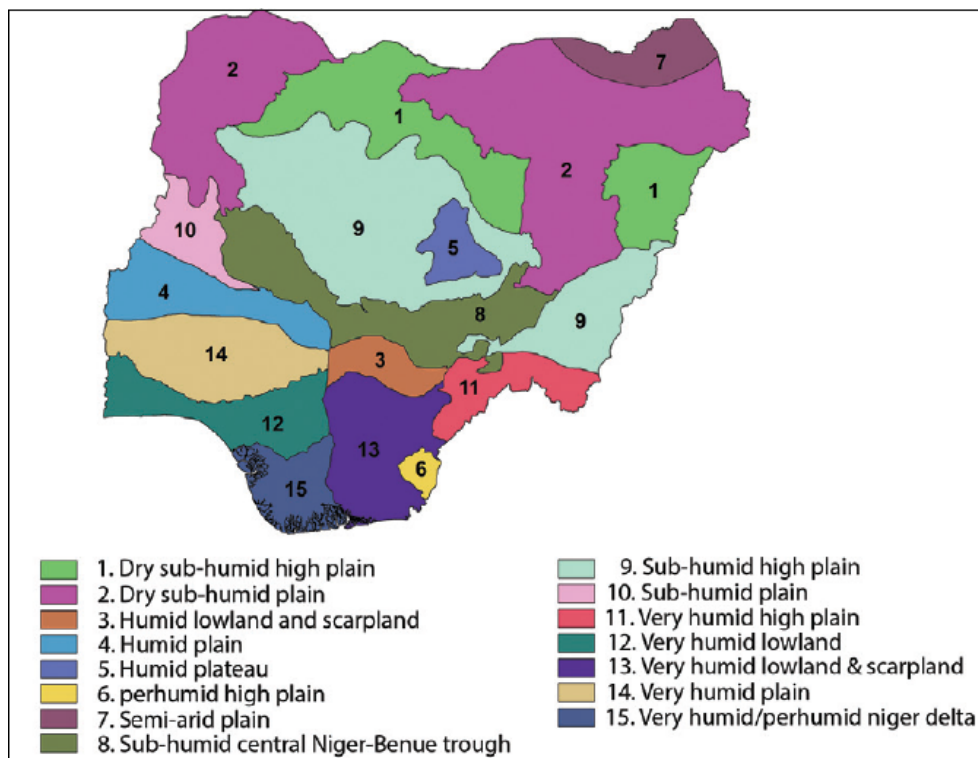


Fig. 2: Agro-Ecological SubZones (AESZ)

Simulations were performed assuming both a fixed CO₂ concentration (380 ppm) and a higher concentration (from 380 to 582 ppm, consistent with the A1B emission scenario), to examine combined direct and indirect effects.

Thanks to the higher resolution of the RCM, simulations were performed in all areas where crops are normally cultivated and the simulated yields were aggregated for any AESZ. Yields obtained with weather data for the reference period 1976–2005 (baseline) were compared with those obtained under climate conditions over the short (2020) and medium term (2050).

Impacts on crop yields were analyzed considering the aggregation of simulation results of a sub-ensemble consisting of the RCM simulation and its five most extreme and significant GCM perturbations in terms of climate change projections.

The results were aggregated across Agro-Ecological SubZones to identify impacts at the level of individual crops and across crops to produce results at the AESZ level, using base-year information on production shares and value added to define weights used for aggregating. Clearly, these weights will vary over time, since farms will respond to evolving biophysical, climatic, and economic drivers by modifying cropping patterns (subject to constraints in terms of technology, resource endowments, and local suitability of crops).

3. RESULTS

Climate change impacts on crops proved to vary considerably by Agro-Ecological Zones and crop type. The differences in impacts on yields depend on the sensitivity of the specific crop to changed climate conditions, on crop distribution and crop calendar. The impacts tend to increase between the short (2020) and the medium term (2050).

The estimated crop yields in the medium-term (2050) show higher impacts, with negative median values for all crops (fig. 4), when compared to the yield changes expected for the 2020 period (fig.3).

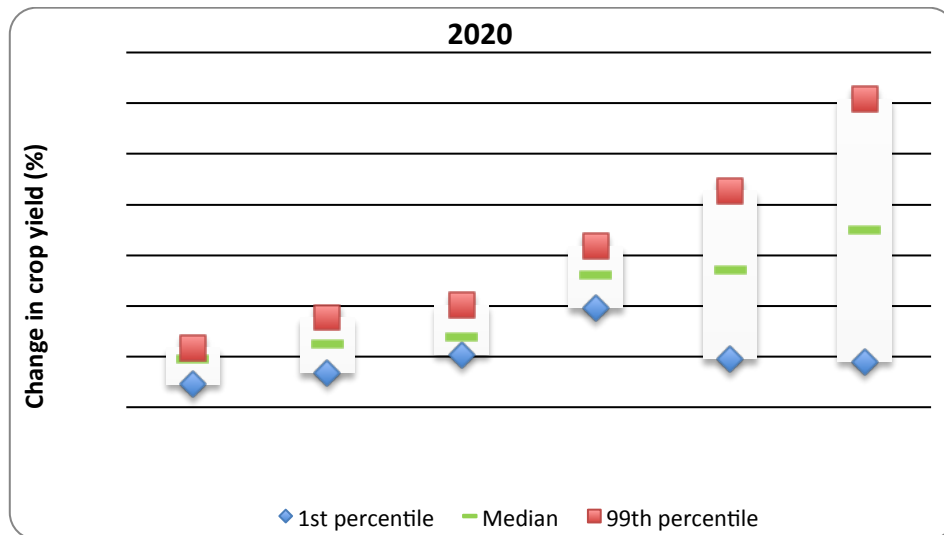


Fig. 3: Changes in crop yield aggregated across Nigeria for 2020, compared to the baseline (1975-2005)

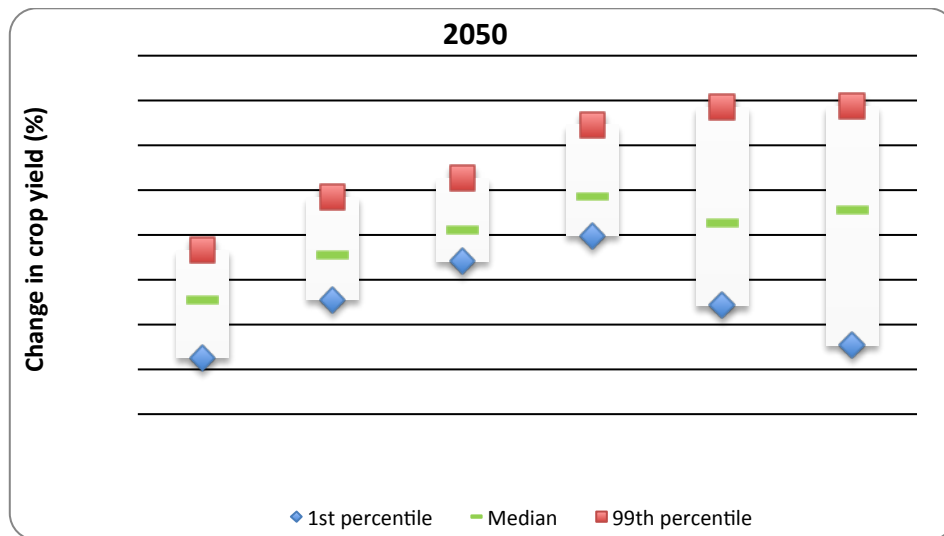


Fig. 4: Changes in crop yield aggregated across Nigeria for 2050, compared to the baseline (1975-2005)

However, the obtained results have great variability and uncertainties, especially for cassava and millet, both in 2020 and 2050. In 2050 the negative trend of crop production estimated by crop models is clearer when compared to the short term (2020).

Rather than precipitations, temperature changes are likely to be the major drivers of changes in yields: this behaviour is consistent with several recent studies ([16], [17]). While rainfall variability is certainly the main driver for the year-to-year crop yield, there is widespread recognition of the fact that a significant and strong signal of temperature increase above the historical range (that is consistent across climate models) is likely to be the main driver of yield changes, particularly when the signals related to precipitation change are less clear and evident. The effect of temperature increase consists in the acceleration of development causing a shorter crop-growing period and therefore reduces the amount of biomass accumulated by crops. The reduction of crop-growing period decreases crop yields even if crops are not stressed by water conditions (droughts or drier seasons). Furthermore it has been shown that there is no linear correlation between yield and water ([18], [19]) or with other nonclimatic factors affecting crop production (e.g., soil characteristics, management options).

Specific yields and productions at both the levels of crops and AESZ are reported in the study of Mereu et al., (under submission).

Aggregate percent change in yield at the AESZ level (figs. 5 and 6), show that there are large uncertainties in most of AESZ (especially in 10, 2, and 12).

Despite the significant amount of variability, especially in the Northern AESZ, a decline in crop yield is likely to be expected in all AESZ, particularly for the medium term period, as indicated by the negative median values observed in figure 6.

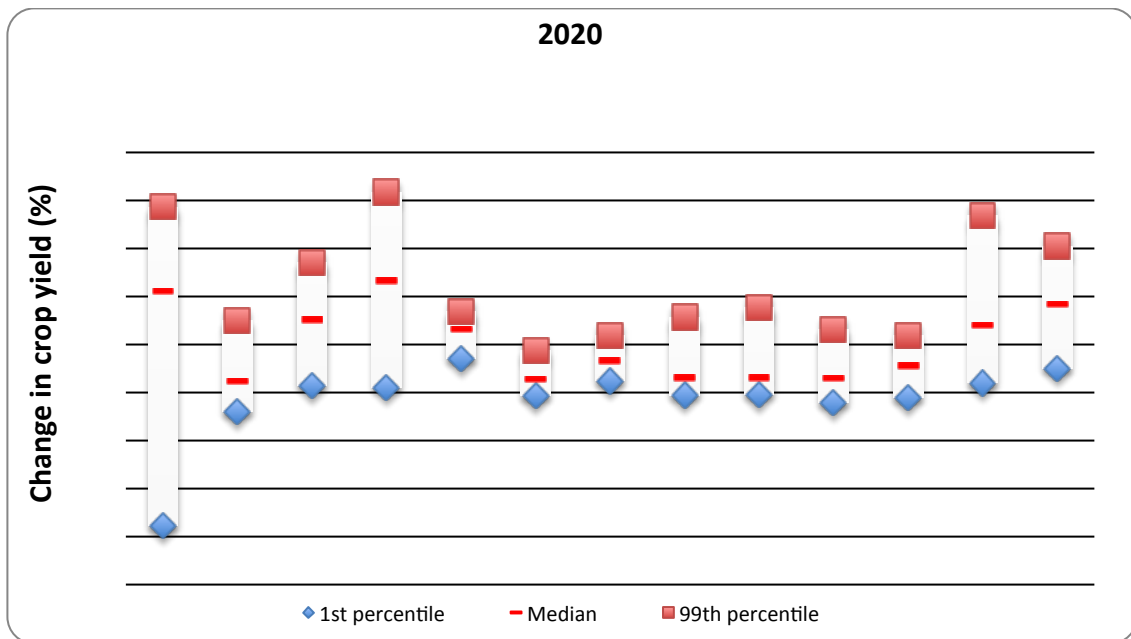


Fig. 5: Changes in crop yield aggregated across agro-ecological zones (AEZs) for 2020, compared to the baseline (1975-2005).

The key findings of these analyses are that (i) in the short term (2020) cereals (without considering millet) show higher yield reductions than cassava and yam; (ii) these reductions are higher in the medium term (2050) than in the short term (2020); (iii) results obtained for cassava and millet show higher variability in yield impacts than for other crops: the more pessimistic models suggest yield decline in both 2020 and 2050, while more optimistic models show increases both in cassava and millet yields.

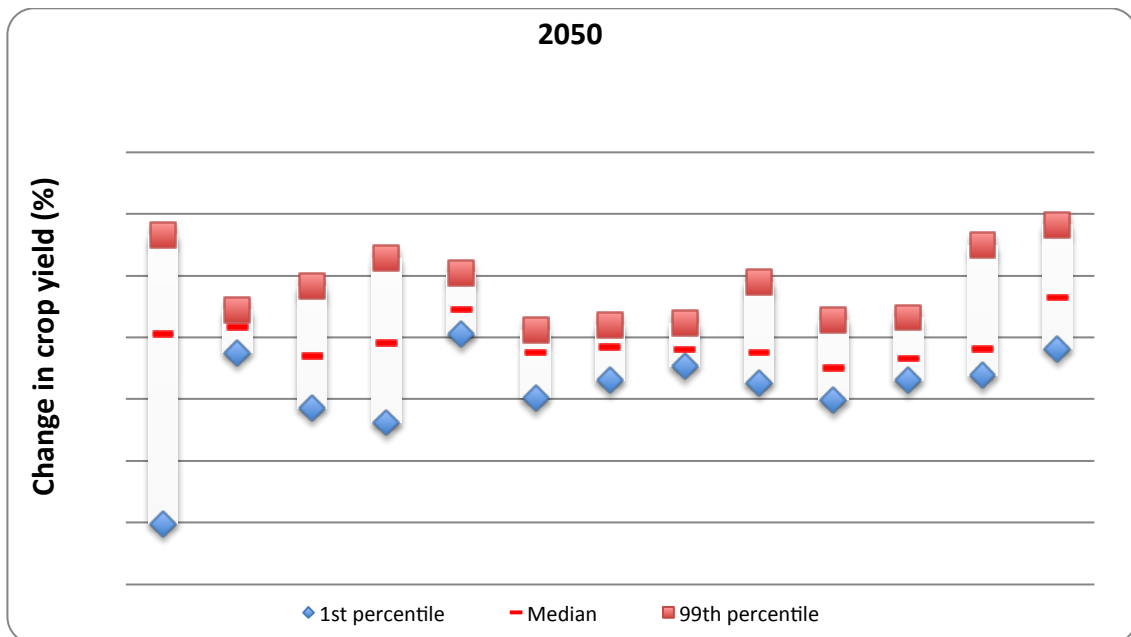


Fig. 6: Changes in crop yield aggregated across agro-ecological zones (AEZs) for 2050, compared to the baseline (1975-2005).

The impacts on crop yields for 2020 and 2050 shown in this study without considering increasing in atmospheric CO₂ values could be partially, and in some case totally, reduced by the increasing in atmospheric CO₂ concentration. As an example of this issue, maps of changes in yield for maize and cassava in the medium term period considering the regional climate model COSMO-CLM, are represented in figures 7 and 8. The maps show the positive effect of the CO₂ air enrichment, particularly for Cassava crop.

The positive effect is particularly evident in C3 crops, whose physiology better responds to higher CO₂, improving photosynthesis rates. Another important effect, for both C3 and C4 species, is stomata closure, which improves water use efficiency especially in areas with low precipitation, like the northern AESZs.

However, the negative effects of changed climate conditions are confirmed especially for sorghum, millet, and rice (*data not shown*).

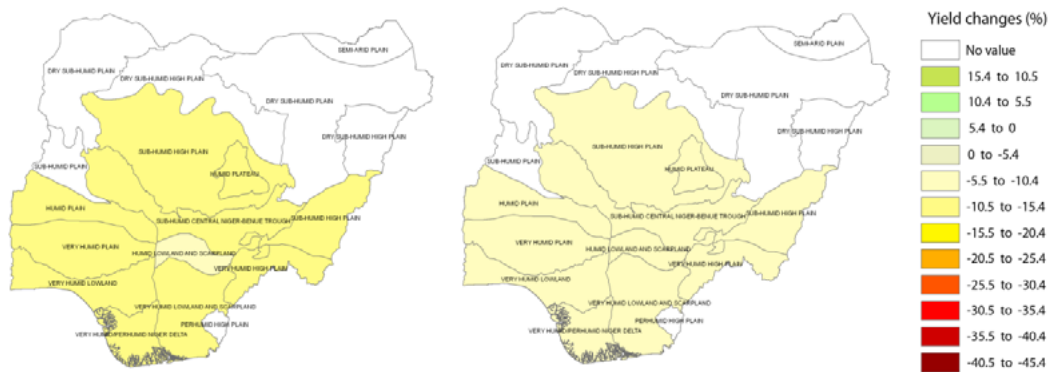


Fig. 7: Changes in crop yield for maize, projected for 2050 with COSMO-CLM, compared to the baseline (1975-2005), with (map on the right) and without (map on the left) considering increases in CO₂ atmosphere concentration.

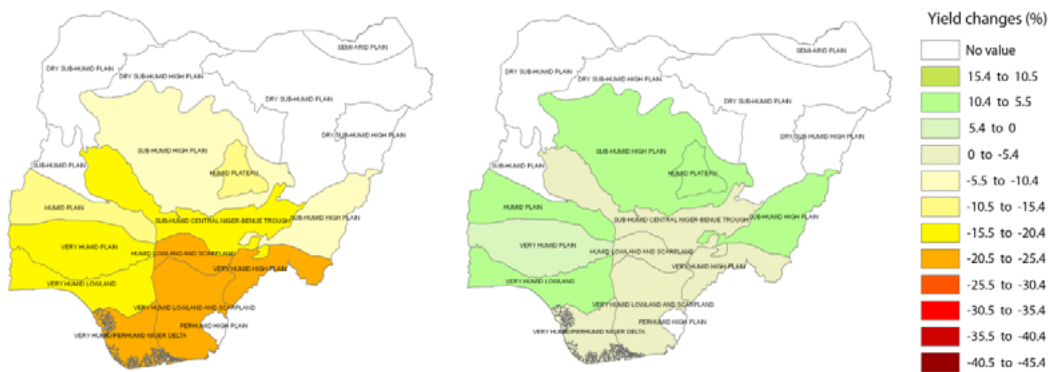


Fig. 8: Changes in crop yield for cassava, projected for 2050 with COSMO-CLM, compared to the baseline (1975-2005), with (map on the right) and without (map on the left) considering increases in CO₂ atmosphere concentration.

4. CONCLUSIONS

Reductions in crop yields, especially for cereals, are expected in Nigeria particularly for the medium term period (2050). Large differences between crops and between AESZs are recognizable. Crop yields reductions could be mainly due because of higher temperature shortening the crop growing cycle and consequently resulting in lower biomass accumulation.

Although crop yields could also be affected by changes in precipitation patterns, these are not a remarkable driver in this area. The negative effects due to changed climate conditions could be partially, or in some cases totally, mitigated by increases in atmospheric CO₂ concentration. The extent of this

mechanism is still debated ([20], [21], [22]), since this effect could be overestimated for many reasons and has not yet been fully proven experimentally.

The positive effect of CO₂ air enrichment is more evident in C3 crops, whose physiology better responds to higher CO₂ air concentration. Another important effect, for both C3 and C4 species, is the stomata closure, which improves water use efficiency, especially where precipitation is low, as in the northern AEZs.

Cereals, and especially rice, are more affected by changes in climate with respect to cassava and yam.

Improving cropping systems, by employing a range of farming practices consistent with principles of sustainable land management (SLM) can be applied to cope negative effect of climate change. Conservation/organic agriculture practices, including manure and residues management, shift of the ordinary sowing/planting date, introduction of irrigation, and improving use of inorganic fertilizers are the main strategies that can be applied to cope with climate change.

5. ACKNOWLEDGMENTS

This work was made in the framework of a World Bank funded project. Results reported in: Raffaello Cervigni, Riccardo Valentini, and Monia Santini, eds. 2013. *Toward Climate-Resilient Development in Nigeria*. Directions in Development. Washington, DC: World Bank. doi:10.1596/978-0-8213-9923-1. License: Creative Commons Attribution CC BY 3.0.

6. REFERENCES

NBS (Nigeria National Bureau of Statistics) (2010), *“The Review of the Nigerian Economy”*. <http://www.nigerianstat.gov.ng/>. (1)

USDA data, available at: <http://www.pecad.fas.usda.gov/>. (2)

NPAFS (2010), *Report of the 2009 agricultural production survey (APS)*. National Programme for Agriculture and Food Security, Federal Ministry of Agriculture and Rural Development, Abuja, Nigeria. (3)

FAOSTAT database available at: <http://faostat.fao.org/>. (4)

USAID MARKETS (2009a), *“Package of Practices for Rice Production”* <http://www.nigeriamarkets.org/>. (5)

- Lebel T., and Ali A. (2009), *Recent Trends in the Central and Western Sabel Rainfall. Regime (1990–2007)*. Journal of Hydrology 375: 52–64. (6)
- Adejuwon J. D. (2008), *Vulnerability in Nigeria: A National-Level Assessment*. In Climate Change and Vulnerability, edited by Neil Leary, Cecilia Conde, Jyoti Kulkarni, Anthony Nyong, Juan Pulhin, 198–217. London: Earthscan. (7)
- Odekunle T.O. (2004), *Rainfall and the Length of the Growing Season in Nigeria*. International Journal of Climatology 2: 467–79. (8)
- Jones J.W., Hoogenboom G., Porter C.H., Boote K.J., Batchelor W.D., Hunt L.A., Wilkens P.W., Singh U., Gijsman A.J., and Ritchie J.T. (2003), *DSSAT Cropping System Model*. European Journal of Agronomy 18:235-265. (9)
- Jones J.W., Keating B.A., Porter C.H. (2001), *Approaches to modular model development*. Agricultural Systems 70: 421–443. (10)
- Porter, C., J. W. Jones, and R. Braga R. 1999. “An Approach for Modular Crop Model Development.” Agricultural and Biological Engineering Department Research Report No 99-0701 University of Florida, Gainesville, Florida 13. <http://www.icasa.net/modular/pdf/modular.pdf>. (11)
- Jones J.W., Hoogemboom G., Porter C.H., Boote K.J., Batchelor W.D., Hunt L.A., Wilkens P.W., Singh U., Gijsman A.J., and Ritchie J.T. (2003), *The DSSAT Cropping System Model*. European Journal of Agronomy 18: 235–65. (12)
- Dubrovský M. (2009), *Linking the Climate Change Scenarios and Weather Generators with Agroclimatological Models*. Paper presented at a seminar in Sassari, May 25–June 5 <http://www.ufa.cas.cz/dub/crop/2009-sassari-martin-seminar-part3.pdf>. (13)
- USAID MARKETS (2009b), *Package of Practices for Sorghum Production*. <http://www.nigeriamarkets.org/>. (14)
- USAID MARKETS (2010), *Package of Practices for Maize Production*. <http://www.nigeriamarkets.org/>. (15)
- Lobell D.B., and Burke M.B. (2010), *On the Use of Statistical Models to Predict Crop Yield Responses to Climate Change*. Agricultural Forest Meteorology 150: 1443–52. (16)
- Lobell D.B., Burke M.B., Tebaldi C., Mastrandrea M.D., Falcon W.P., and Naylor R.L. (2008), *Prioritizing Climate Change Adaptation Needs for Food Security in 2030*. Science 319: 607–10. (17)

- Jones P.G., and Thornton P.K. (2003), *The Potential Impacts of Climate Change in Tropical Agriculture: The Case of Maize in Africa and Latin America in 2055*. *Global Environmental Change* 13: 51–59. (18)
- Thornton P.K., Jones P.G., Alagarswamy G., and Andresen J. (2009), *Spatial Variation of Crop Yield Response to Climate Change in East Africa*. *Global Environmental Change* 19 (1): 54–65. (19)
- Long S.P., Ainsworth E.A., Leakey A.D.B., Nosberger J., and Ort D.R. (2006), *Food for Thought: Lower-than-Expected Crop Yield Stimulation with Rising CO₂ Concentrations*. *Science* 312: 1918–21. (20)
- Tubiello F.N., Amthor J.S., Boot K.J., Donatelli M., Easterling W., Fischer G., Giord R.M., Howden M., Reilly J., and Rosenzweig C. (2007), *Crop Response to Elevated CO₂ and World Food Supply: A Comment on 'Food for Thought'*, edited by Long et al. *Science* 312: 1918–1921, 2006.” *European Journal of Agronomy* 26: 215–23. (21)
- Tubiello F.N., Soussana J.F., and Howden S.M. (2007), “*Crop and Pasture Response to Climate Change*.” *Proceedings of the National Academy of Sciences of the United States of America* 104 (50): 19686–90. (22)

Evaluation of the potential of genomic tools and plant genes to mitigate the climate change impact and extremes on natural ecosystems and agriculture

Ricciardi L.^{1*}, Pavan S.¹, Lotti C.² and De Pace C.³

¹University of Bari "Aldo Moro", Faculty of Agriculture, Department of Soil, Plant and Food Science (DiSSPA), Plant Genetics and Breeding Unit, Bari, Italy.

²University of Foggia, Department of Agro-Environmental Science, Chemistry and Crop Protection, Foggia, Italy.

³Department of Agriculture, Forests, Nature and Energy, University of Tuscia, Viterbo, Italy.

*Corresponding author: luigi.ricciardi@uniba.it

Abstract

Breeding programs to release varieties needed for agroforestry and modern agriculture, are continually confronted with the need to find genetic solutions to the ever changing problems posed by diseases and pests (e.g. viruses, fungi, insects) and environmental stresses (e.g. drought, global warming, cold temperatures, flooding) as consequences of climate change.

Domestication of crop and forest tree species has demonstrated that genes for traits of agronomic significance can be selected from extant populations in forests and wild-crop relatives (WCR). Therefore, native forest tree populations and WCR, which have been exposed to thousands years of natural selection under climate changes, are the primary source of the genes needed to accelerate breeding for adaptation to stressful climatic conditions or to threats related to climate modification over times. However, the pace of the breeding achievement will depend also on the efficiency of the methods used for selecting the genotypes endowed of the proper traits and genes for adaptation. It is still possible to find in natural populations and WCR the candidate genes for improving important traits related to disease resistance, plant-architecture, phenology, drought, flooding and submergence tolerance, higher nutrient and water use efficiency, etc.. The current and forthcoming genomic strategies offer insight into the innovative methodologies for the highest benefit from the breeding efforts to introgress those genes in selected forest trees for plantations and crop varieties to increase resilience in the plant communities and mitigate the impact of climate changes and extremes in lands used for agriculture, agroforestry, and afforestation.

Keywords: *Genes, Genome, Resilience, Plant Breeding, Plant domestication*



1. GENOMIC APPROACHES TO IDENTIFY AND SELECT GENES FOR RESILIENCE TO MITIGATE THE CLIMATE CHANGE IMPACT AND EXTREMES ON NATURAL AND DISTURBED ECOSYSTEMS

Domestication of the wild forest genetic resources for the development of climate resilient forest tree populations

Forests represent one of the largest natural ecosystem covering 30% (about 3.8 billion ha) of Earth's terrestrial surface. The genetic diversity within and between the biota components of forest habitats are of particular ecological relevance not only for the biosphere but also for the ecosystem services they provide such as mitigation of hydrological processes, reduced erosion, increased wildlife habitat, wood and other forest products, CO₂ sequestration, and support to agricultural productivity (i. e. windbreak; stabilization of hillslopes, and abundant source of wild pollen for crops such as the autoincompatible hazelnut and chestnut orchards). Current understanding of the genetic basis of adaptation in long-lived populations is based largely on temperate forest trees that have been evolving in response to selection pressures such as diseases, drought, and cold; examples include the management, domestication and breeding of the forest wild 'primary gene-pool' (GP1_w) [1] in genera from the northern hemisphere (*Populus*, *Castanea*, *Picea*, *Pinus*, *Alnus*, *Ulmus*,) and some from the southern hemisphere (*Eucalyptus*, *Podocarpus* pines, evergreen southern beech *Nothofagus*, etc.) [2]. Anthropogenic intervention along the natural biological path to increase plant adaptation to disturbance may improve forest resilience through restoration and afforestation practices. One or two cycles of selection within the GP1_w using the criteria of 'increased fitness', 'tolerance to stresses', and 'successful intergenotypic competition', will lead to a domesticated subgene pool (GP1_d) enriched of those target alleles underlying the adaptive performance of the extracted genotypes. Nursery materials can be prepared from the GP1_d for agroforestry efforts and establishment of plantation forests to compensate the ever-increasing demand for timber, wood products, and bioenergy feedstocks, and to reduce pressure on native forests. However, invasive pathogens and insects now entering Europe [3] could narrow the choice of plantation species for agroforestry and reforestation, and undermine proposals to use tree planting as a means of mitigating climate change through carbon sequestration [4]. Fortunately, in most cases the forest degradation or threats posed by those events can be mitigated by using resistance genes still present in the GP1_w and introgressed in the derived resistant or tolerant GP1_d. Examples are the efforts going on to: (1) restore the American chestnut to its former status by backcross breeding program designed to transfer the blight resistance genes from the GP1_w of Chinese chestnuts (*Castanea mollissima*)

to *C. dentata* [5]; (2) counteract the recent establishment in Italy of the oriental chestnut gall wasp *Dryocosmus kuriphilus* in *C. sativa* fruit orchards by introgressing the gene for resistance to the wasp from *C. crenata* and the Italian *C. sativa* coppiced plantations; (3) breeding for the development of clones resistant to the Dutch Elm Disease (DED) in the European species *Ulmus glabra* Huds., *Ulmus laevis* Pall., and *Ulmus minor* Mill., by transferring, through hybridization, genes for DED resistance from the elm species *U. parvifolia*, *U. pumila*, and *U. wallichiana* growing in Central-Eastern Asia [6; 7]; (4) explore the feasibility of using the phloem content of the phenolic tyrosol hexoside pentoside and ellagic acid, associated to resistance to *Phytophthora ramorum* expressed by coast live oak (*Quercus agrifolia*) in stands of high infection and mortality, as biomarkers of resistance in other oak trees (<http://ucanr.org/sites/sod5/files/147556.pdf>). Breeding for resistance to local pests of native forests was also possible using the GP1_w of WCR, as occurred in *Eucalyptus camaldulensis* for increasing the resistance to the defoliating fungus *Cylindrocladium quinqueseptatum*, in accessions of black poplar (*Populus nigra*) for enhancing the resistance to the Asian longhorned beetle (*Anoplophora glabripennis*), in Monterey pine (*Pinus radiata*) and western white pine (*Pinus monticola*) to resist infection by *Mycosphaerella pini* and white pine blister rust (*Cronartium ribicola*), respectively [8].

Genetics and genomics of forest trees

The mentioned breeding efforts can be greatly accelerated using the genetics and genomics toolbox (i.e. molecular genetic markers, MGM) for identifying the proper genes or DNA tags associated to the desired plant phenotype for resilience to environmental and biotic stresses in the GP1_w, and assist the transfer of those genes to the GP1_d by intercrossing and recurrent backcrossing selection.

Currently, there are many approaches for discovering molecular determinants of forest tree phenotypes expressed at the individual, population, community, or ecosystem level [9; 10], including: (1) Two-point linkage analysis between a marker and a qualitatively inherited trait such as a disease resistance gene; (2) Quantitative trait locus (QTL) mapping; (3) Association genetics of single nucleotide polymorphism (SNP) to candidate gene identified by gene expression analysis, mutation or modulation of gene function (gene silencing or promoter activation), and genome wide association; and (4) Genome selection and phenotypic evaluation.

Sequencing and annotation of genes in overlapping bacterial artificial chromosome BAC provide information on candidate genes surrounding the marker locus associated to the trait phenotype and has been carried out for Aspen (*Populus tremuloides*) [11], Eucalyptus (EUCAGEN, www.eucagen.org), and Pedunculate oak (*Quercus robur*) [12]. In forestry, the search of SNPs has been focused largely on “candidate genes” associated to quantitative variation using approaches similar to the ‘case vs control’ studies in humans [13].

Discovery of candidate genes involved in the appearance of a trait phenotype may be achieved also by the analysis of ‘gene expression’ and ‘gene function’. Gene function can be assessed by point mutations altering the encoded protein or by modulating the production of the functional protein using gene silencing or promoter activation. Mutagenic treatments with chemical agents (i. e. Ethyl Methan Sulfonate) induce SNPs which can be identified in a target gene by TILLING (Targeted Induced Local Lesions in Genomes). A variant of that methodology called Ecotilling display spontaneous SNPs underlying phenotypic variation in natural populations, and it has been used as an efficient SNP discovery tool in *Populus trichocarpa* [14].

Gene silencing induced by RNA interference (RNAi) has been shown to provide resistance against insects (*Diabrotica*, *Helicoverpa*), bacteria (*Agrobacterium*, *Staphylococcus*), nematodes (*Heterodera*, *Meloidogyne*) and parasitic plants (*Orobanche*, *Striga*, *Triphysaria*), and should provide effective, durable resistance to insect parasites of plant tree such as the red palm weevil *Rhynchophorus ferrugineus* [15].

Genome-wide association study (GWAS) for SNPs in candidate genes associated with wood property traits, disease resistance, drought tolerance, and metabolome has been focused on loblolly pine (*Pinus taeda*) [16] (http://dendrome.ucdavis.edu/NealeLab/pdf/Eckert_AssocGen_NP_2012.pdf) and *Populus* [9]. Rare functional variants, usually missed by GWAS, can be discovered by combining genome sequencing for *de novo* assembly in non model species and restriction associated DNA (RAD)-tag sequences in genotypes of the same population [17].

The sum of the effects of genome-wide markers capturing most QTLs for the target trait gives a measure of the tree breeding value and is used as a predictor of performance for genomic selection (GS). GS is being developed for application in Eucalyptus [18; 19].

Several procedures have been developed for the high-throughput DNA genotyping and genome-wide marker identification in forest trees. The DArT (Diversity Arrays Technology) procedure for genome

complexity reduction [20] and whole-exome capture using in-solution target enrichment [18], have successfully been tested for genome-wide markers identification needed for GS in *Pinus taeda*.

A sequenced genomes is an important reference for genetic marker detection in both GWAS and GS. On the basis of the genomic knowledge accumulated so far, species of Conifers (i.e. pines and spruce trees), Eucalyptus, Birch family (i.e., oaks and chestnuts), and Poplars have been chosen as nonclassical model eukaryotes for forest tree genome wide sequencing projects. The Conifer Genome Project (<http://www.pinegenome.org/cgp/>) aims to advance genome research in loblolly pine (*Pinus taeda*; 21,658Mbp; n=12), and white pines (*Pinus* subgenus *strobus*), as well as *Sequoia sempervirens* (31.4 Gbp/1C; n=33), and Douglas fir (*Pseudotsuga menziesii*, 18.6 Gbp/1C; n=13). Extensive genetic resources and a gene catalog were developed for *P. taeda* and *Picea glauca* (white spruce; 19.7Gbp/1C; n=12) (<http://www.pinegenome.org/cgp/>). The GENOAK project (<http://urgi.versailles.inra.fr/Projects/GenOak>) aims to establish a high quality reference genome sequence for pedunculate oak (*Quercus robur*) (905Mb/1C; n=12). *Eucalyptus grandis* (640 Mbp/C n = 11) tree genome has been deciphered (<http://www.phytozome.net/eucalyptus.php>) and will benefit agroforesters utilizing this fast-growing hardwood tree to support industries based on eucalypt fibre (pulp, paper, cellulose, etc) and hardwood products (poles, construction, furniture, etc), and the production of Eucalypt feedstocks for cellulosic biofuels.

Examples of other genes discovered in forestry germplasm using molecular genetics approaches and transgenics to elucidate which gene may be deployed to accelerate forest tree breeding for fast response to the need of adapted populations facing environmental modification induced by climate changes, are given in [21; 22; 23; 24; 25; 26].

The discovered MGM will be exceedingly useful for marker assisted selection (MAS) during the early growth stages of the seedlings possessing the putative genetic factors of interests, even when the target phenotype of the trait will be expressed years later, after the transition from the juvenile to the reproductive stage. MAS will be valuable also for: *in vitro* selection of somaclones surviving to stressors included in growth medium or growing environment, fingerprinting new clones, tracing wooden artifact, and certification of the improved nursery materials for plantations in agroforestry intervention to mitigate the effects of climate changes. MGM are also effective to develop proper candidate genes for elucidating the biological mechanisms of adaptation and for identifying the underlying genetic factors and interactions for forest tree domestication.

The mentioned whole genome sequencing, GWAS and GS approaches, help finding genes for important functions in forest plants, and when coupled with comparative genomics it is possible to discover orthologous genes in other species, while transgenics will facilitate the verification of hypothesis on the function of the orthologous gene in mutants or in different growth stages of the host species. A transgenic American chestnut variety with a wheat gene for the enzyme oxalate oxidase, which disarms the fungus *Cryphonectria parasitica*, has already shown resistance in the field; researchers are also developing a genetically modified (GM) version of an American chestnut accession with resistance based on genes from Asian chestnuts, and because the resulting GM plants are ‘cisgenic’ trees containing only chestnut genes, researchers hope that the trees won’t provoke strong public objection [5].

2. GENE NETWORKS TO MITIGATE THE CLIMATE CHANGE IMPACT AND EXTREMES ON AGRICULTURAL VARIETIES OF ANNUAL AND FRUIT TREE CROPS

It has been ascertained that global warming may greatly influence yield in agricultural species [27]. The most prominent effects of the climate change on agriculture varieties of annual and fruit tree crops are physiological disorders associated to variation in plant phenology, decrease in nutrient and water use efficiency, decrease in CO₂ sequestration, increase in the occurrence of biotic and abiotic stresses [28].

Important achievements have been made in the functional characterization of genes and gene networks underlying many aspects related to plant phenology, as well as to response to abiotic and biotic stresses (Tab. 1). As mentioned above, such a knowledge together with the availability of powerful genomic tools (i.e. the sequenced genomes reported in Tab. 2), can today greatly improve the efficiency of germplasm screening for alleles involved in resilience to climate change.

Recently, specific genes involved in phenology and seasonal traits have been described [29], such as those controlling flowering time. These have been characterized through complementary approaches that include identifying of QTLs through positional cloning as well as the identification and characterization of orthologues of known genes from model species, particularly *Arabidopsis thaliana*. A nondormant peach genotype (‘Evergrowing’) was identified in southern Mexico which fails to enter dormancy under dormancy-inducing conditions and exhibits a persistent shoot growth. A deletion of four out of six MADS-box genes (*DAM* genes) responsible for ‘Evergrowing’ phenotype was identified

and characterized [30]. A similar Mendelian trait has been discovered in hazelnut [31; 32] which allows the plant to escape the water stress effect on nut yield by anticipating of three months the nut maturity (nut harvest in June instead then in September).

Quantitative genetic studies also allowed to identify, in cultivated species such as rice, barley, and wheat, several photoperiod genes orthologous to others characterized in the photoperiod pathway of *Arabidopsis*. For example, the *CONSTANS* (CO) gene family is involved in photoperiodic response in all the above mentioned species [33], and its expression has different effects on phenology depending on the downstream targets. In more detail, *A. thaliana* CO and its rice orthologue *Hd1* combine signals from the diurnal clock oscillator with the outputs of photoreceptors to measure day length as the external coincidence model [34]. However, whereas high levels of CO upregulate the floral integrator *FT* in *A. thaliana*, expression of rice *Hd1* represses the *FT* rice orthologue *Hd3a*, thus producing a short-day flowering response [35].

Concerning abiotic stresses, it is important to point out that, for breeding purposes, stress tolerance cannot be uncoupled from elevated yield capacity in both stressed and non stressed conditions. Molecular mechanisms underlying the perception of abiotic stresses remain elusive, although it is thought that they might be related to changes in membrane fluidity, turgor pressure and redox potential, and cytoskeletal rearrangements. Instead, downstream events leading to physiological adaptation to major abiotic stresses have been at least partly elucidated, mostly thanks to system biology and –omics studies [36]. Key players in such signal transduction pathways are second messengers such as intracellular calcium, reactive oxygen and nitrogen species (ROS and RNS), phytohormones, protein kinases and transcription factors [37].

Changes in gene expression during plant stress start within minutes of the plant stress signal perception. The early responsive genes are those that do not require synthesis of new proteins and whose signaling components are already primed. Transcription factors (TFs) fall into this category, and a diverse array of TFs regulate the activity of various stress-responsive promoters through their cis-regulatory elements such as the C-repeat dehydration-responsive element (CRT/DRE), that imparts responsiveness to low temperature and dehydration [38], ABA-responsive element (ABRE), that induces abscisic acid expression [39], and the myelocytomatosis (MYC) and myeloblastosis (MYB) oncogene regulon-recognition sequences (MYCRS/MYBRS), that induce abscisic acid during drought [40]. Other important TFs that have been well characterized include the soybean zinc-finger protein

(SCOF-1), that is involved in cold tolerance and ABA-response [41], dehydration-responsive (DRE) elements DREB2A and DREB2B, that become activated for cold tolerance and help maintain osmotic equilibrium [42; 43], and the basic leucine zipper (bZip) transcription factors that bind to ABRE elements [44].

Other abiotic stress responsive genes that are expressed due to a sustained late response include the responsive to dehydration (RD), cold responsive (COR), and kinetin-induced (KIN) genes that are involved in protein synthesis modulation of crucial plant molecular elements such as late embryogenesis abundant (LEA)-like proteins, antioxidants, membrane stabilizing proteins, and osmolyte synthesizers [45; 46; 47; 39; 48; 49].

Notably, approaches based on the overexpression/silencing of some of key genes involved in the abiotic stress signalling network have resulted in extremely tolerant/phenotypes, strongly suggesting targets where to address breeding activities (including non-transgenic ones) based on reverse genetics.

In plant–pathogen interactions, a defense responses may follow the recognition event between plant transmembrane pattern recognition receptors (PRRs) and conserved molecular signatures associated with pathogenesis. These can be either slowly evolving pathogen-associated molecular patterns (PAMPs), like that displayed against the carriers of bacterial flagellin and fungal chitin, or damage-associated molecular patterns (DAMPs), such as oligogalacturonides produced by the pathogen-mediated degradation of the plant cell wall [50]. Corresponding induced immunities, referred to as PAMP-triggered immunity (PTI) and DAMP-triggered immunity (DTI), have been associated to both nonhost and host resistance, the latter being the immunity exhibited, towards a given pathogen species, by particular genotypes of an other-wise susceptible plant species [51].

It is now clear that the process of adaptation of pathogens to cognate host species involves the differentiation of proteins, known as effectors, which establish susceptibility through the suppression of PTI and DTI. Subsequently, plant–pathogen co-evolution might proceed through a zig-zag model, in which plants differentiate receptors (R) enabling the recognition of effectors and the onset of a second kind of induced immunity (referred to as effector-triggered immunity or ETI), and pathogens evolve new effectors which re-establish susceptibility [51].

Recognition events associated with induced immunity towards insects are less understood. However, they are thought to derive from the recognition of DAMPs, oviposition-related compounds, or putative herbivore-associated molecular patterns [52].

Striking similarities are shared by the signaling pathways underlying the response to biotic and abiotic stresses. Indeed, in biotic stress responses a pivotal role is played by intracellular calcium influxes, which act as second messengers once the stress stimulus is perceived. Next, proteins transducing calcium signaling, such as calmodulin, calcium-dependent protein kinases (CDPKs), and other calcium-binding proteins, activate cascades of reactions, which primarily involve phosphorylation events (by means of CDPKs or other kinases, mainly MAPKs), the activation of hormonal pathways, and transcriptional reprogramming.

Biotic stress signalling ultimately leads to the adoption of a vast array of defence measures, including localized cell-death (referred to as hypersensitive response), the formation of cell wall appositions at plant-pathogen interaction sites, and the *de novo* synthesis of pathogenesis-related proteins and secondary metabolites (referred to as phytoalexins).

After the local activation of defense responses at the interaction sites, systemic defense can be induced or primed, thus protecting undamaged tissues by subsequent invasion. Systemic acquired resistance (SAR) may follow PTI or ETI and is characterized by the activation, dependent on the hormone salicylic acid (SA), of pathogenesis-related proteins. Induced systemic resistance (ISR) commonly follows plant interaction with beneficial microorganisms like plant-growth-promoting rhizobacteria and consists in a systemic primed state for the activation of defense responses, mediated by the hormones jasmonic acid (JA) and ethylene (ET) [53].

Several genes involved in pathogen/pest recognition and in defence signalling pathways have been characterized at the functional level. Genes which might be used in breeding against biotic stresses can be broadly divided in resistance genes, encoding for proteins having a role in activating or enhancing defense responses, and susceptibility genes, which are required for the biotic stress to occur. In particular, a breeding strategy based on the selective inactivation of plant susceptibility genes has been recently proposed and has led to important results related to the control of pathogens causing the powdery mildew disease in several cultivated species [54; 55; 56].

In general, plant breeding for adaptation to major stresses, and thus breeding for resilience too, might greatly benefit from the exploitation of natural genetic variation residing in areas that are repeatedly affected by selection pressure, leading to the identification of valuable ecotypes and landraces tolerant and “pre-adapted” to one or multiple stresses. However, while ecotypes of forest species can be used directly for agroforestry practices, ecotypes and landraces of crop species generally need intense breeding efforts aimed to improve yield potential, input responsiveness, and quality [57; 58; 59; 60]. It is therefore suggested that progenies derived from crosses from tolerant landraces and high-yielding popular varieties are screened for tolerance as well as yield and quality attributes applying either classical breeding methodologies coupled with marker assisted selection or genomic selection.

3. ACKNOWLEDGMENTS

This paper was realized within the framework of the “ATI MONDO NOCCIOLA, Azione 1” and “GenHort PON R&C” projects, funded by the Italian Ministry of Agriculture (MIPAF) and the Italian Ministry of University and Research, respectively.

4. REFERENCES

- Harlan J.R. & de Wet J.M.T. (1971), *Toward a rational classification of cultivated plants*, *Taxon*, Vol. 20, pp. 509-517. (1)
- Kole C. (ed.) (2011), *Wild Crop Relatives: Genomic and Breeding Resources: Forest Trees*, Springer, Berlin. 1st Edition. (2)
- Santini A., Ghelardini L., De Pace C., Desprez-Loustau M.L., Capretti P. et al. (2012), *Biogeographical patterns and determinants of invasion by forest pathogens in Europe*, *New Phytologist*. Article first published online: 11 OCT 2012. DOI: 10.1111/j.1469-8137.2012.04364.x. (3)
- Brasier C. & Webber J. (2010), *Sudden larch death*, *Nature*, Vol. 466, pp. 824-825. (4)
- Thompson H. (2012), *The chestnut resurrection*, *Nature*, Vol. 490, pp. 22-23. (5)
- Ghelardini L. & Santini A. (2009), *Avoidance by early flushing: a new perspective on Dutch elm disease research*, *iForest*, Vol. 2, pp. 143-153. doi: 10.3832/ifor0508-002. (6)
- Santini A., Pecori F., Pepori A.L., Ferrini F. & Ghelardini L. (2010), *Genotypexenvironment interaction and growth stability of several elm clones resistant to Dutch elm disease*, *Forest Ecology and Management*, Vol. 260, pp. 1017–1025. (7)

- FAO (2009), *Global review of forest pests and diseases*, FAO Forestry Paper, 156, FAO, Rome. (8)
- Stanton B.J., Neale D.B. & Li S. (2010), *Populus breeding: from the classical to the genomic approach*. In: S. Jansson et al. (eds.), *Genetics and Genomics of Populus*, *Plant Genetics and Genomics: Crops and Models*, 8, pp. 309-348. Springer Publ. DOI 10.1007/978-1-4419-1541-2_14. (9)
- Whitham T.G., Difazio S.P., Schweitzer J.A., Shuster S.M., Allan G.J., Bailey J.K. & Woolbright S.A. (2008), *Extending genomics to natural communities and ecosystems*, *Science*, Vol. 320, No. 5875, pp. 492-495. (10)
- Fladungh M., Kaufmann H., Markussen T. & Hoenicka H. (2008), *Construction of a Populus tremuloides Michx. BAC library*, *Silvae Genetica*, Vol. 57, No. 2, pp. 65-69. (11)
- Rampant P.F., Lesur I., Boussardon C., Bitton F., Martin-Magniette M.-L., Bodénès C., Le Provost G., Bergès H., Fluch S., Kremer A. & Plomion C. (2011), *Analysis of BAC end sequences in oak, a keystone forest tree species, providing insight into the composition of its genome*, *BMC Genomics*, Vol. 12, pp. 292., doi: 10.1186/1471-2164-12-292. (12)
- Grattapaglia D., Plomion C., Kirst M. & Sederoff R.R. (2009), *Genomics of growth traits in forest trees*, *Current Opinion in Plant Biology*, Vol. 12, No. 2, pp. 148–156, <http://dx.doi.org/10.1016/j.pbi.2008.12.008>. (13)
- Gilchrist E.J., Haughn G.W., Ying C.C., Otto S.P., Zhuang J., Cheung D., Hamberger B., Aboutorabi F., Kalynyak T., Johnson L., Bohlmann J., Ellis B.E., Douglas C.J. & Cronk Q.C. (2006), *Use of Ecotilling as an efficient SNP discovery tool to survey genetic variation in wild populations of Populus trichocarpa*, *Mol Ecol*, Vol. 15, No. 5, pp. 1367-1378. (14)
- Niblett C.L. & Bailey A.M. (2012), *Potential applications of gene silencing or RNA interference (RNAi) to control disease and insect pests of date palm*, *Emir J Food Agric*, Vol. 24, No. 5, pp. 462-469. (15)
- Neves L., Davis J., Barbazuk B. & Kirst M. (2011), *Targeted sequencing in the loblolly pine (Pinus taeda) megagenome by exome capture*, *BMC Proceedings*, Vol. 5, Suppl. 7, pp. 48, doi:10.1186/1753-6561-5-S7-O48. (16)
- Amores A., Catchen J., Ferrara A., Fontenot Q. & Postlethwait J.H. (2011), *Genome evolution and meiotic maps by massively parallel DNA sequencing: spotted gar, an outgroup for the teleost genome duplication*, *Genetics*, Vol. 188, pp. 73-84. (17)
- Resende M.D., Resende M.F. Jr, Sansaloni C.P., Petroli C.D., Missiaggia A.A., Aguiar A.M., Abad J.M., Takahashi E.K., Rosado A.M., Faria D.A., Pappas G.J. Jr, Kilian A. & Grattapaglia D. (2012a), *Genomic selection for growth and wood quality in Eucalyptus: capturing the missing heritability and accelerating*

- breeding for complex traits in forest trees*, New Phytol., Vol. 194, No. 1, pp. 116-28, doi: 10.1111/j.1469-8137.2011.04038.x. (18)
- Resende M.F. Jr, Muñoz P., Acosta J.J., Peter G.F., Davis J.M., Grattapaglia D., Resende M.D. & Kirst M. (2012b), *Accelerating the domestication of trees using genomic selection: accuracy of prediction models across ages and environments*, New Phytol., vol 193, N. 3, pp. 617-24, doi: 10.1111/j.1469-8137.2011.03895.x. Epub 2011 Oct 5. Erratum in: New Phytol., Vol. 193, No. 4, pp. 1099. (19)
- Alves-Freitas D.M.T., Kilian A. & Grattapaglia D. (2011), *Development of DArT (Diversity Arrays Technology) for high-throughput genotyping of Pinus taeda and closely related species*, BMC Proceedings, Vol. 5, Suppl. 7, p. 22. (20)
- Merkle S. & Dean J.F.D. (2000), *Forest tree biotechnology*, Curr. Opin. Biotechnol., Vol. 11, pp. 298–302. (21)
- Boerjan W. (2005), *Biotechnology and the domestication of forest trees*, Curr Opin in Biotech, Vol. 16, pp. 159–166. (22)
- González-Martínez S.C., Krutovsky K.V. & Neale D.B. (2006), *Forest-tree population genomics and adaptive evolution*, New Phytologist, Vol. 170, pp. 227–238. (23)
- Flachowsky H., Hanke M.-V., Peil A., Strauss S.H. & Fladung M. (2009), *A review on transgenic approaches to accelerate breeding of woody plants*, Plant Breeding, Vol. 128, pp. 217-226. (24)
- Neale D. & Kremer A. (2011), *Forest tree genomics: growing resources and applications*, Nature Review Genetics, Vol. 12, pp. 111-122. (25)
- Harfouche A., Meilan R., Kirst M., Morgante M, Boerjan W., Sabatti M. & Scarascia Mugnozza G. (2012), *Accelerating the domestication of forest trees in a changing world*, Trends Plant Sci, Vol. 17, No. 2, pp. 64-72. (26)
- Lobell D.B., Schlenker W., Costa-Roberts J. (2011), *Climate trends and global crop production since 1980*. Science, Vol. 333(6042), pp. 616–620. (27)
- De Pace C., Ricciardi L., Kumar A., Pavan S., Lotti C., Dixit S., & Emani C. (2013), Identification of Traits, Genes, and Crops of the Future. In: Kole C. (ed.), *Genomics and breeding for climate-resilient crops*, Springer-Verlag Berlin Heidelberg, Vol. 1, doi 10.1007/978-3-642-37045-8_3. (28)
- Alonso-Blanco C., Aarts M.G.M., Bentsink L., Keurentjes J.J.B., Reymond M., Vreugdenhil D. & Koornneef M. (2009), *What has natural variation taught us about plant development, physiology, and adaptation?* Plant Cell, Vol 21, pp. 1877–1896. (29)

- Bielenberg D.G., Wang Y.(E.), Li Z., Zhebentyayeva T., Fan S. et al. (2008), *Sequencing and annotation of the evergrowing locus in peach [Prunus persica (L) Batsch] reveals a cluster of six MADS-box transcription factors as candidate genes for regulation of terminal bud formation*. Tree Genet Genomes 10.1007/s 11295-007-0126-9. (30)
- Thompson M.M., Smith D.C. and Burgess J.E. (1985), *Non dormant mutants in a temperate tree species, Corylus avellana L.* Theor Appl Gen, vol. 70, pp. 687-692. (31)
- Catarcione G., Vittori D., Ciaffi M., Rugini E., De Pace C. (2009), *The 'Evergrowing' genotype of Corylus avellana is expressed in the offspring of 'Tonda Gentile Romana', 'Nocchione' and 'Tonda di Giffoni'*. Acta Hort (ISHS), vol. 845, pp. 195-200. (32)
- Griffiths S., Dunford R.P., Coupland G., & Laurie D.A. (2003), *The evolution of CONSTANS-Like gene families in Barley, Rice and Arabidopsis*. Plant Physiology, Vol. 131, pp. 1855-1867. (33)
- Hayama R. & Coupland G. (2004), *The molecular basis of diversity in the photoperiodic flowering responses of Arabidopsis and rice*. Plant Physiology, Vol. 135, pp. 677–684. (34)
- Hayama R., Yokoi S., Tamaki S., Yano M. & Shimamoto K. (2003), *Adaptation of photoperiodic control pathways produces short-day flowering in rice*. Nature, Vol. 422, pp. 719–722. (35)
- Wang W., Vinocur B. & Altman A. (2003), *Plant responses to drought, salinity and extreme temperatures: towards genetic engineering for stress tolerance*. Planta, Vol. 218, pp. 1–14. (36)
- Cramer G.R., Urano K., Derrot S., Pezzotti M. & Shinozaki K. (2011), *Effects of abiotic stress on plants: a systems biology perspective*. BMC Plant Biology, Vol.11, pp. 163. (37)
- Thomashow, M.F. (2001), *So what's new in the field of plant cold acclimation? Lots!* Plant Physiol., Vol. 125, pp. 89–93. (38)
- Thomashow M.F. (1999), *Plant cold acclimatization: freezing tolerance genes and regulatory mechanism*. Annu. Rev. Plant Physiol. Plant Mol. Biol., Vol. 50, pp. 571–599. (39)
- Abe H., Urao T., Ito T., Seki M., Shinozaki K., Yamaguchi-Shinozaki K. (2003), *Arabidopsis AtMYC2 (bHLH) and AtMYB2 (MYB) function as transcriptional activators in abscisic acid signaling*. Plant Cell, 15, pp. 63–78. (40)
- Kim J.C., Lee S.H., Cheong Y.H., Yoo C.M., Lee S.I. et al (2001), *A novel cold-inducible zinc-finger protein from soybean, SCOF-1, enhances cold tolerance in transgenic plants*. Plant J, Vol. 25, pp. 247–259. (41)
- Liu D.J., Liu J.Y., Tao W.J., Chen P.D. (1998a), *Molecular markers and breeding wheat for powdery mildew resistance*. In: Slinkard AE (ed), Proceedings of 9th international wheat genetics symposium, University Extension Press, University of Saskatchewan, Saskatoon, Vol 3, pp. 128–131. (42)

- Liu Q., Kasuga M., Sakuma Y., Abe H., Miura S., Yamaguchi-Shinozaki K., & Shinozaki K. (1998b), *Two transcription factors, DREB1 and DREB2, with an EREBP/AP2 DNA binding domain separate two cellular signal transduction pathways in drought and low-temperature-responsive gene expression, respectively, in Arabidopsis*. *Plant Cell*, 10, pp. 1391–1406. (43)
- Uno Y., Furihata T., Abe H, Yoshida R., Shinozaki K., Yamaguchi-Shinozaki K. (2000), *Novel Arabidopsis bZIP transcription factors involved in an abscisic-acid-dependent signal transduction pathway under drought and high salinity conditions*. *Proc Natl Acad Sci USA*, Vol. 97, pp. 11632–11637. (44)
- Vierling E. (1991), *The roles of heat-shock proteins in plants*. *Annu Rev Plant Biol*, Vol. 42, pp. 579–620. (45)
- Ingram J.n & Bartels D. (1996), *The molecular basis of dehydration tolerance in plants*. *Annu Rev Plant Biol*, Vol. 47, pp. 377–403. (46)
- Thomashow M.F. (1998), *Role of cold-responsive genes in plant freezing tolerance*. *Plant Physiol.*, Vol. 118, pp. 1–7. (47)
- Bray E.A., Bailey-Serres J. & Weretilnyk E. (2000), *Responses to abiotic stresses*. In: Grissem, W., Buchannan, B., Jones, R. (eds), *Biochemistry and molecular biology of plants*. American Society of Plant Physiologists, Rockville, MD, pp. 1158–1249. (48)
- Vranova E., Atichartpongkul S., Villaroel R. et al (2002),. *Proc Natl Acad Sci USA*, Vol. 99, pp. 10870–10875. (49)
- Zipfel C. & Robatzek S. (2010), *Comprehensive analysis of gene expression in Nicotiana tabacum leaves acclimated to oxidative stress. Pathogen-associated molecular pattern-triggered immunity: Veni, Vidi Vici?* *Plant Physiol*, Vol. 154, pp. 551–554. (50)
- Jones J.D.G. & Dangl J.L. (2006), *The plant immune system*. *Nature*, Vol. 444, pp. 323–329. (51)
- Erb M., Meldau S., Howe G.A. (2012), *Role of phytohormones in insect-specific plant reactions*. *Trends Plant Sci*, Vol. 17, pp. 250–259. (52)
- Pieterse C.M.J., Leon-Reyes A., Van der Ent S., Van Wees S.C.M. (2009), *Networking by small-molecule hormones in plant immunity*. *Nat Chem Biol*, Vol. 5, pp. 308–316. (53)
- Bay Y., Pavan S., Zheng Z., Zappel N.F., Reinstadler A., Lotti C., De Giovanni C., Ricciardi L., Lindhout P., Visser R., Theres K. & Panstruga R. (2008), *Naturally occurring broad spectrum powdery mildew resistance in a Central American tomato accession is caused by loss of mlo function*. *Molecular Plant Microbe Interaction*, Vol. 21, pp. 30–39. (54)
- Pavan S., Lotti C., Resta P. & Ricciardi L. (2011a), *Geni di suscettibilità agli stress biotici e metodiche innovative per la loro valorizzazione nel miglioramento genetico vegetale. Italus Hortus*, Vol. 18 (1), Review n. 13, pp. 3–12. (55)

- Pavan S., Schiavulli A., Appiano M., Marcotrigiano A.R., Cillo F., Visser R.G.F, Bay Y., Lotti C. & Ricciardi L. (2011b), *Pea powdery mildew er1 resistance is associated to loss-of-function mutations at a MLO homologous locus*. Theoretical and Applied Genetics, Vol. 123, pp. 1425-1431. (56)
- Ricciardi L., Lotti C., Marzano C.F., Albo M., Marcotrigiano, A.R. (2005), *Confronto tra linee di frumento duro selezionate per la durogranicoltura sostenibile*. Atti del VI Convegno AISTEC: “Cereali: biotecnologie e processi innovativi. Una sfida per un mondo in cambiamento”. Valenzano (Bari), 16-18 giugno 2005, pp. 126-137. (57)
- Ricciardi L., Lotti C., Pavan S., Bai Y., Lindhout P., De Giovanni C. (2007), *Further isolation of AFLP and LMS markers for the mapping of the Ol-2 locus related to powdery mildew (Oidium neolycopersici) resistance in tomato (Solanum lycopersicum L.)*. Plant Science, 172, pp. 746-755. (58)
- Lotti C., Panstruga R., Theres K., Ciccarese F., De Giovanni C., Ricciardi L. (2008), *Comparison between ol-2 and mlo loci conferring resistance to Oidium in tomato and barley, respectively*. In: Proceedings of the XV Meeting of the Eucarpia Tomato Working Group, Bari (Italy) 20-23 September 2005, Acta Hort., 789, pp. 95-100. (59)
- Resta P., Lotti C., De Giovanni C., Ricciardi A., Zonno V., Marcotrigiano A.R., Fanizza G., Ricciardi L. (2009), *Amygdalus webbii Spach e Pyrus amygdaliformis Vill. in Puglia: collezionamento e ricerche in corso*. Italian Journal of Agronomy, vol. 4, n.4 suppl., pp. 461-467. (60)

Table 1. Examples of some genes which will play an important role in breeding new genotypes with enhanced response to the main biotic and abiotic pressures driven by climate changes or expressing resilience and adaptation to stressful climate factors (i.e. air temperature increase, drought, scarcity of water or salty water, excess of water in the soil).

Adaptation to abiotic stress	Mechanism	Genes	Species
Cold, Drought, Salinity	Transcription factor	<i>CBF.1, CBF.3, CBF.4, CBF.s</i>	<i>Arabidopsis thaliana, Solanum lycopersicum, Brassica napus</i>
		<i>ZmNF-YB2</i>	<i>Zea mays</i>
		<i>AtNF-YB1</i>	<i>A. thaliana</i>
		<i>DREB1A</i>	<i>A. thaliana</i>
		<i>AtMYC2, AtMYB2</i>	<i>A. thaliana</i>
		<i>ABF3 or ABF4</i>	<i>A. thaliana</i>
		<i>HSF1, HSF3, HSFA1</i>	<i>A. thaliana, S.lycopersicum</i>
High Temperature, Cold, Drought, Salinity	Heat shock protein	<i>spl7</i>	<i>Oryza sativa</i>
		<i>Hsp17.7</i>	<i>Daucus carota</i>
		<i>Hsp21</i>	<i>A. thaliana</i>
		<i>AtHSP17.6A</i>	<i>A. thaliana</i>
		<i>DnaK1</i>	<i>Nicotiana tabacum</i>
Cold, Drought, Salinity	Lea protein	<i>SP1</i>	<i>Populus tremula</i>
		<i>COR15a</i>	<i>A.thaliana</i>
		<i>HVA1</i>	<i>O. sativa</i> <i>Triticum aestivum</i>
Drought, Salinity	<i>WCS19 ss</i>	Cereals	
	Na ⁺ -H ⁺ exchanger that facilitates efflux of Na ⁺ across the plasma membrane	<i>SOS1</i>	<i>A. thaliana, O. sativa, Z. mays</i> ³
	Vacuolar Na ⁺ -H ⁺ antiporter for transport of cytosolic Na ⁺ into vacuoles	<i>NHX1</i>	
	H ⁺ -pyrophosphatase	<i>AVP1</i>	
	HKT-type transporter regulating shoot K ⁺ content and is a selective transporter for Na ⁺ inducing higher K ⁺ content and lower Na ⁺ content in the shoot	<i>Skc1</i>	<i>O. sativa</i> ³
lower Na ⁺ /K ⁺ ratio	<i>Kna1</i>	<i>T. aestivum</i> ³	

Drought, Salinity	Lower Na ⁺ and higher K ⁺ concentrations in the leaf blade	<i>Nax1</i>	<i>Triticum turgidum</i> and <i>Triticum monococcum</i> ³
Drought	QTLs for stay-green, one form of drought resistance mechanism	<i>Stg1, Stg2, Stg3, and Stg4</i> (53.5% of the phenotypic variance for the stay-green trait)	<i>Sorghum bicolor</i> ³
	QTL affecting root traits and leaf ABA concentration	(-) <i>root-ABA1</i> allele maintain yield under drought	<i>Z. mays</i> ³
Submergence tolerance	A QTL containing a cluster of three genes that encode putative ethylene response factors (ERFs)	<i>Sub1A, Sub1B, and Sub1C</i>	<i>O. sativa</i> ³
Chilling and heat requirement of the floral buds and in the blooming date	Two QTL explained much of the phenotypic variance for these three characters, one in G1 for chilling requirement and blooming date, and the other in G7 for blooming date.	<i>Evg</i> (in G1)	<i>Prunus persica</i>
Resistance to biotic stress	Mechanism	Genes	Species
<i>Blumeria graminis</i> f.sp. <i>Hordei</i> ; <i>Oidium neolycopersici</i> , <i>Erisiphe pisi</i>	Transmembrane protein	<i>Mlo</i> orthologs	<i>Hordeum vulgare</i> , <i>S. Lycopersicum</i> , <i>Pisum sativum</i>
<i>Potyviridae</i>	Translation initiation factor	<i>eIF4E</i> orthologs	Several species
<i>Xanthomonas oryzae</i>	Transcription factor IIA-γ	<i>Xa5</i>	<i>O. sativa</i>
<i>Xanthomonas oryzae</i>	Membrane localized protein	<i>Xa13</i>	<i>O. sativa</i>
<i>Venturia inaequalis</i>	R-gene	<i>Rvi2, Rvi4, Rvi5, Rvi10; Rvi11, Rvi12, Rvi13, and Rvi15</i>	<i>Malus domestica</i> ⁴
Root-knot nematode resistance		<i>Mi</i>	<i>S. lycopersicum</i>

	Key R genes that encode the nucleotide-binding site (NBS) domain showing similarity to eukaryotic cell death effectors and the leucine-rich repeat (LRR) domains. They are grouped according to the presence of either a coiled-coil (CC-NBS-LRR) or a <i>Drosophila</i> Toll/mammalian Interleukin-1 Receptor (TIR-NBS-LRR) motif in the N-terminal domain. Variant types with different domains or truncated structures also exist (others).	Number of genes with one of the following encoding motif:			
		CC-NBS-LRR	TIR-NBS-LRR	Others	
Several plant pathogens		58	110	39	<i>A. thaliana</i> ¹
		17	42	33	<i>Brassica rapa</i> ¹
		152	94	87	<i>Medicago truncatula</i> ¹
		77	112	203	<i>Glycine max</i> ²
		125	0	120	<i>S. bicolor</i> ²
		392	0	81	<i>O. sativa</i> ¹
		62	0	67	<i>Z. mays</i> ²
		136	0	102	<i>Brachypodium dystachyon</i> ²
		278	121	3	<i>Populus trichocarpa</i> ¹
		203	97	159	<i>Vitis vinifera</i> ¹
		4	6	44	<i>Carica papaya</i> ¹
		181	224	587	<i>M. domestica</i> ²

(1) Mun J-H, H-J Yu, S Park, and B-S Park (2009) Genome-wide identification of NBS-encoding resistance genes in *Brassica rapa*. *Mol Genet Genomics* 282(6): 617–631.

(2) Velasco R, Zharkikh A, Affourtit J, et al (2010) The genome of the domesticated apple (*Malus x domestica* Borkh.). *Nature Genetics*, 42(10):833-841.

(3) Takeda S., M. Matsuoka (2008) Genetic approaches to crop improvement: responding to environmental and population changes. *Nature Reviews Genetics* 9, 444-457.

(4) Patocchi A., A. Frei, J.E. Frey and M. Kellerhals (2009) Towards improvement of marker assisted selection of apple scab resistant cultivars: *Venturia inaequalis* virulence surveys and standardization of molecular marker alleles associated with resistance genes. *Molecular Breeding* 24 (4), 337-347.

Table 2. Examples of species with sequenced (complete or partial) genome

Species	Common name	Genes/gene density ^a	Haploid chromosome number (n)	Haploid genome size (Mbp/1C)
Annual-Eudicots				
<i>A. thaliana</i>	<i>Arabidopsis</i>	27,228/2.2	5	~160
<i>Citrullus lanatus</i>	Watermelon	23340/0.73	11	425
<i>Glycine max</i>	Soybean	46,430/0.42	20	1000-2000
Annual-Monocot				
<i>Brachypodium distachyon</i>	<i>Brachypodium</i>	25,532/0.94	5	355
<i>Sorghum bicolor</i>	Sorghum	34,496/0.47	10	760
<i>Zea mays</i>	Maize	32,540/0.15	10	2.066
<i>Oryza sativa</i>	Rice	40,577/0.97	12	374
Perennial tree-Eudicot				
<i>Prunus persica</i>	Peach	27852/1.22	8	227
<i>Eucalyptus grandis</i>	Eucalyptus		11	611
<i>Malus domestica</i>	Apple	57,386/0.78	17	742,3
<i>Populus tremula</i>	Poplar	45,654/0.94	19	403
<i>Vitis vinifera</i>	Grape	33,514/0.66	38	500
Perennial tree-Conifers				
<i>Picea abies</i>	Spruce	28354/0.014	12	19600

^a Gene density= Numb. of genes every 10 Kb

IMPLICATIONS ON ECOSYSTEM SERVICES

Impacts on forest and agricultural ecosystems - II

Local impact assessment of climate change on fire season length

Pellizzaro G.^{1*}, Arca B.¹, Dubrovsky M.², Ventura A.¹, Bortolu S.¹, Duce P.¹

¹*Institute of Biometeorology, National Research Council, CNR IBIMET, Sassari, Italy,*

²*Institute of Atmospheric Physics, Praha, Czech Republic*

*Corresponding author: p.duce@ibimet.cnr.it

Abstract

Wildland fires represent an important disturbance for ecosystems in the Mediterranean Basin. Evergreen sclerophyll shrubland is an important component of Mediterranean vegetation community and constitutes the surface fuels primarily responsible for the ignition and the spread of wildland fires in the Mediterranean area. Several works highlighted the importance of vegetation moisture content in relation to ignition and rate of spread in shrubs. Critical threshold values of fuel moisture for fire occurrence and spread were also proposed. The main aim of this work was to present a methodology for evaluating possible impacts of future climate change on moisture dynamic and length of fire danger period at local scale. Measurements of seasonal pattern of live fuel moisture content (LFMC) of three Mediterranean shrub species were performed in North Western Sardinia (Italy). Seasonal patterns of LFMC were also compared with the Drought Code (DC) of the Canadian Forest Fire Weather Index System. A threshold value of DC useful to determine the end of the potential fire season due to fuel status was identified. In addition, impacts of future climate change on fire season length were simulated at 4 experimental sites located in Northern Sardinia, Italy. A weather generator linked to climate change scenarios derived from 17 available General Circulation Models (GCMs) was used to produce synthetic weather series, representing future climates, and then the expected changes of the fire season length was determined. Results confirmed that the projected climate scenarios over the Mediterranean area will determine a general increase (up to 1 month) of the fire season length.

Keywords: *Wildfires, Mediterranean shrubland, fuel status, fire danger season*



1. INTRODUCTION

Wildland fires represent an important disturbance for ecosystems in the Mediterranean Basin. The Mediterranean area is characterized by an elevated frequency of wildland fires, and large fires can also occur. Evergreen sclerophyll shrubland represents an important component of Mediterranean vegetation community, which is characterized by high specific and structural heterogeneity and complexity. Shrublands constitute also the surface fuels primarily responsible for the ignition and the spread of wildland fires in the Mediterranean area.

Several conditions are required for fire ignition and spread such as source of ignition, fuel availability, fuel horizontal continuity, weather, slope, etc. The different conditions that allow fire to spread “can be regarded as hypothetical switches that must be simultaneously activated for large fire to occur” [3].

Vegetation flammability is influenced by several factors including structural properties, chemical properties and moisture content. However, it is well known that moisture content is an essential factor influencing the fire ignition and spread in vegetation. Depending on the moisture content and the heat flux from a fire, living vegetation may act as a heat source or a heat sink, either contributing to fire energy or retarding fire propagation and intensity [22; 17; 25]. Several authors have found relationships between vegetation water content and ignitability in several Mediterranean species [16; 12; 19]. Some works highlighted the importance of vegetation moisture content in relation to crown fire potential, ignition and rate of spread in shrubs [26; 5; 1; 10]. Studies carried out in Mediterranean areas have shown that area burned tends to increase as live fuel moisture decreases [9; 24; 8; 11].

Critical threshold values of fuel moisture for fire occurrence and spread have been also proposed in past studies. Van Wagner [26] reported that crown fire potential in pine forests increases when the tree crown moisture drops below 100%. Chandler *et al.* [5] suggested critical live fuel moisture content (LFMC) values for fire spread equal to 100% and 75% for coniferous and Mediterranean shrubs, respectively. Weise *et al.* [31] assumed that high fire danger occurs for Mediterranean species when LFMC is below 80%. Chuvieco *et al.* [7] suggested LFMC values below 105% as a relative threshold to ignition for shrubs. Dennison *et al.* [11] found that LFMC values ranging from 70 to 80% can be considered as critical thresholds for potential occurrence of large fires in chaparral.

Moisture exchange in dead materials is mainly affected by weather factors and controlled by physical processes [30]. Water content variations of live plants depend on both environmental conditions (e.g.

meteorological variables, soil water availability) and ecophysiological characteristics of plant species [23; 4, 20; 2]. It can therefore vary within and among species.

According to recent projections of future climate in Southern Europe, changes in temperature, precipitation and extreme events are expected [14; 13]. The largest warming is likely to occur in the Mediterranean area during the summer season when the highest temperatures occur. In addition, the annual number of rainy days is very likely to decrease in the Mediterranean area with a general decrease of annual precipitation in most of the Mediterranean Basin, and an increase of risk of summer drought in both Central and Southern Europe [6].

The relationship between fire occurrence and drought is well known; forest fires mainly occur during dry summer periods when air temperature is high, air humidity is low and fuel moisture reduced [21]. More prolonged drought seasons induced by climatic changes is likely to have major consequences on both fuel water status and length of critical periods of high ignition danger for Mediterranean ecosystems.

Therefore, seasonal monitoring of vegetation moisture content, relative to the whole vegetation and the single species, in conjunction to a better knowledge of the relationships between weather (i.e. air temperature, rainfall, drought) and LFMC pattern can contribute to better understand the potential effects of prolonged drought season and extreme events on live fuel water status. In addition, considering the observed climatic variations and foreseen future scenarios, an evaluation of the impact of these variations on fire danger seems essential. For these reasons, LFMC variations need to be simulated using models or codes based on meteorological data. In general, weather-based fire danger indices are commonly used to modeling the moisture dynamics of dead fuel whereas little research has been carried out on live fuel. Therefore, it seems essential to test empirical drought indices and to evaluate their performances in estimating moisture dynamics of live fuel under Mediterranean conditions.

The main aim of this work was to propose a novel methodology for evaluating the possible impacts of future climate changes on moisture dynamic and length of fire danger period at local scale. Specific objectives were: i) evaluating performances of drought indices in describing seasonal pattern of LFMC, ii) identify threshold values for drought indices that indicate the end of fire season due to fuel status in Mediterranean shrubland, and iii) simulate the potential impacts of future climate changes on the duration of fire danger period.

2. MATERIAL AND METHODS

The study was carried out in a nature reserve located in North Western Sardinia, Italy (40° 36' N; 8° 09' E, 30 m a.s.l.). The climate is Mediterranean with water deficit conditions occurring from May through September and precipitation mainly concentrated in autumn and winter. The mean annual rainfall is 640 mm and the mean annual air temperature is 16.8 °C. The soils are Luvi and Litosols, neutral, with depth rarely exceeding 0.2-0.3 m. Mediterranean maquis and garigue, grown after a fire event occurred in the middle 1970s, cover the study area. The prevailing species of the vegetation community are: *Chamaerops humilis* L., *Cistus monspeliensis* L., *Genista acanthoclada* DC, *Helichrysum italicum* Roth, *Juniperus phoenicea* L., *Phillyrea angustifolia* L., *Pistacia lentiscus* L., and *Rosmarinus officinalis* L.

LFMC values were measured on three dominant species of the study area: *Cistus monspeliensis* L., *Juniperus phoenicea* L., and *Rosmarinus officinalis* L., very common in the Western Mediterranean Basin. Samples of live fine fuel, consisting of terminal twigs with diameter not greater than 6 mm, were collected from each species. Phenological observations were also made on sampling dates. Samples were collected twice a month or weekly from March to November for six years (2005, 2007, 2008, 2009, 2010 and 2011). For each sampling date, individuals were chosen randomly in an area of approximately 200 m × 200 m close to a weather station.

To determine the live fuel moisture, three samples of each species were weighed, dried and reweighed. Live fine moisture content was expressed as a percentage of dry weight. Meteorological data were also collected from an automated weather station located in the study site.

Drought conditions that occurred during the LFMC sampling period were assessed by calculating the Drought Code (DC) of the Canadian Forest Fire Weather Index System [28]. DC is widely used worldwide in wildfire danger assessment as an indicator of the moisture content of very slow drying fuels and its values have been shown to be associated with occurrence of drought [15; 32]. It is calculated from daily rainfall and air temperature and it similar to other drought models such as the Keetch–Byram Drought Index and the Palmer Drought Index [18]. Some authors have attempted to evaluate DC performance based on the correlation with real fuel moisture data and have shown that DC is well related to LFMC of shrub species [29; 20]. In the current FWI System, a DC value equal to 0 corresponds to a saturation moisture content, with increasing values indicating drier conditions without a specific maximum value [28]. In this work the DC code was calculated using the equations given by Van Wagner and Pickett [27].

Correlation analysis was performed to test the significance of linear relationships between (i) LFMC and precipitation cumulated over 30 days before sampling, and (ii) LFMC and the mean value of daily maximum air temperature calculated over 10 days before sampling. In addition, correlation analysis between LFMC and the Drought code was performed.

Analysis of cumulative distribution curves of DC values for only those days characterized by LFMC values over the critical threshold for fire ignition and spread was performed in order to identify the DC values that indicate the end of the fire danger season. Based on available literature, LFMC values below 95% were used as threshold values for indicating ignition and fire spread danger over Mediterranean shrubs.

The M&Rfi weather generator linked to climate change scenarios derived from 17 available General Circulation Models (GCMs) (see Table 1 for details) was used to produce synthetic weather series, representing present and future climates, for four selected sites located in North Sardinia, Italy. The projected future climates were then used to determine the expected changes of the fire season length.

3. RESULTS

Different ranges and trends of LFMC were observed for the three studied species (Figure 1). *Cistus*, and *Rosmarinus* showed the highest seasonal variability of LFMC, whereas *Juniperus phoenicea* showed a narrower range throughout the observation period. For all species the highest values of moisture content were observed in spring when plants were resprouting and/or flowering. A continuous decrease in LFMC values was observed during the drought period. LFMC values increased in early autumn when the first rainfall events after the drought period occurred, and the air temperature started to decrease.

The moisture content values of *Cistus*, *Rosmarinus* and *Juniperus* were negatively correlated with the mean value of maximum air temperature calculated over 10 days before sampling (Table 2). *Cistus*, *Rosmarinus* and *Juniperus* were also positively correlated at different significance levels with cumulated values of daily precipitation over 30 days before the sampling date (Table 2).

In general, LFMC values of all species were correlated with the Drought Code values (Table 3). The analysis showed significant and negative correlation between LFMC and DC for all species. High correlation coefficients were obtained for *Cistus* and *Rosmarinus* throughout the entire study period.

LFMC and DC patterns were also compared with the purpose of evaluating whether or not DC values could be useful to describe the seasonal changes of LFMC.

DC pattern was very close to LFMC during rising phase of moisture content (from mid-summer to autumn). During the moisture falling phase, even if DC is correlated to LFMC values, the code is not able to follow the peaks of LFMC due to resprouting and flowering phases of plants. Therefore, it seems more appropriate the use of DC to identify the end of fire danger season rather than the date of starting.

Analysis of cumulative distribution curves of DC (LFMC rising phase) for only those days characterized by LFMC values above the critical moisture threshold showed that when LFMC values are above 95%, the 95% of DC values are below 700 (Figure 2). Therefore, a DC threshold of 700 was used to estimate the end of fire danger season due to LFMC of Mediterranean shrubs.

Figure 3 shows the actual and projected average dates of end of fire season for 4 experimental sites located in Northern Sardinia, Italy. Projected dates were calculated using synthetic weather data from M&Rfi weather generator linked to 17 climate change scenarios derived from a subset of available GCMs. The average actual ending date of the fire season danger ranges from September 20 (day of the year, DOY = 264) to October 14 (DOY = 287). The calculation of the DC values using the synthetic weather series derived from 17 climate change scenarios resulted in a general increase of the duration of the fire danger season ranging in average from 2.3 days (best-case scenario) to 25.4 days (worst-case scenario).

One of the expected global impact of climate change on fire danger is the prolongation of the fire danger season. Our study confirms that the projected climate scenarios over the Mediterranean area will determine a general increase (up to 1 month) of the fire season length. The results reported in this paper are based on local data and information and on the calibration of the commonly used DC code. Our findings allow to better and accurately understand the impacts of the predicted future climate on fire danger at local scale, and also to plan appropriate adaptation and mitigation strategies and measures.

BCM2	Bjerknes Centre for Climate Research, Norway
CGMR	Canadian Center for Climate Modelling and Analysis, Canada
CNCM3	Centre National de Recherches Meteorologiques, France
CSMK3	Commonwealth Scientific and Industrial Res. Organisation, Australia
ECHOG	Met. Inst. Univ. Bonn + Met. Res. Inst., Korea + Model and Data Groupe at MPI-M, Germany
GFCM20	Geophysical Fluid Dynamics Laboratory, USA
HADCM3	UK Met. Office, UK
HADGEM	UK Met. Office, UK
INCM3	Institute for Numerical Mathematics, Russia
MIMR	National Institute for Environmental Studies, Japan
MPEH5	Max Planck Institute for Meteorology, Germany
MRCGCM	Meteorological Research institute, Japan
NCCCSM	National Centre for Atmospheric Research, USA
NCPCM	National Centre for Atmospheric Research, USA
GFCM21	Geophysical Fluid Dynamics Laboratory, USA
GIER	Geophysical Fluid Dynamics Laboratory, USA. Model E20/Russel
IPCM4	Institute Pierre Simon Laplace, France

Table 1: General Circulation Models (GCMs) used in conjunction with the M&Rfi weather generator to produce synthetic weather series representing present and future climates at four location in North Sardinia, Italy.

Species	2005		2007		2008		2009		2010		2011	
	ΣP 30	Tmax										
	(mm)	(°C)										
<i>Cistus m.</i>	***	***	***	***	***	***	***	***	***	***	***	***
<i>Rosmarinus.</i>	***	***	***	**	*	***	**	***	***	***	***	***
<i>Juniperus</i>	***	***	***	***	***	**	***	n.s.	***	n.s.	***	***

Table 2: Significance of Spearman correlation coefficients between cumulative precipitation cumulated 30 days before sampling (ΣP 30), mean value of daily maximum air temperature (Tmax) calculated over ten days before samplings and live fine fuel moisture content (LFMC) by species.

<i>Species</i>	<i>2005</i>	<i>2007</i>	<i>2008</i>	<i>2009</i>	<i>2010</i>	<i>2011</i>
<i>Cistus m.</i>	***	***	**	***	***	***
<i>Rosmarinus o.</i>	***	***	***	***	***	***
<i>Juniperus</i>	***	***	***	*	***	***

Significant probabilities: *, $P \leq 0.05$; **, $P \leq 0.01$; ***, $P \leq 0.001$

Table 3: Significance of Spearman correlation coefficients between Drought Code (DC) and live fine fuel moisture content (LFMC) by species

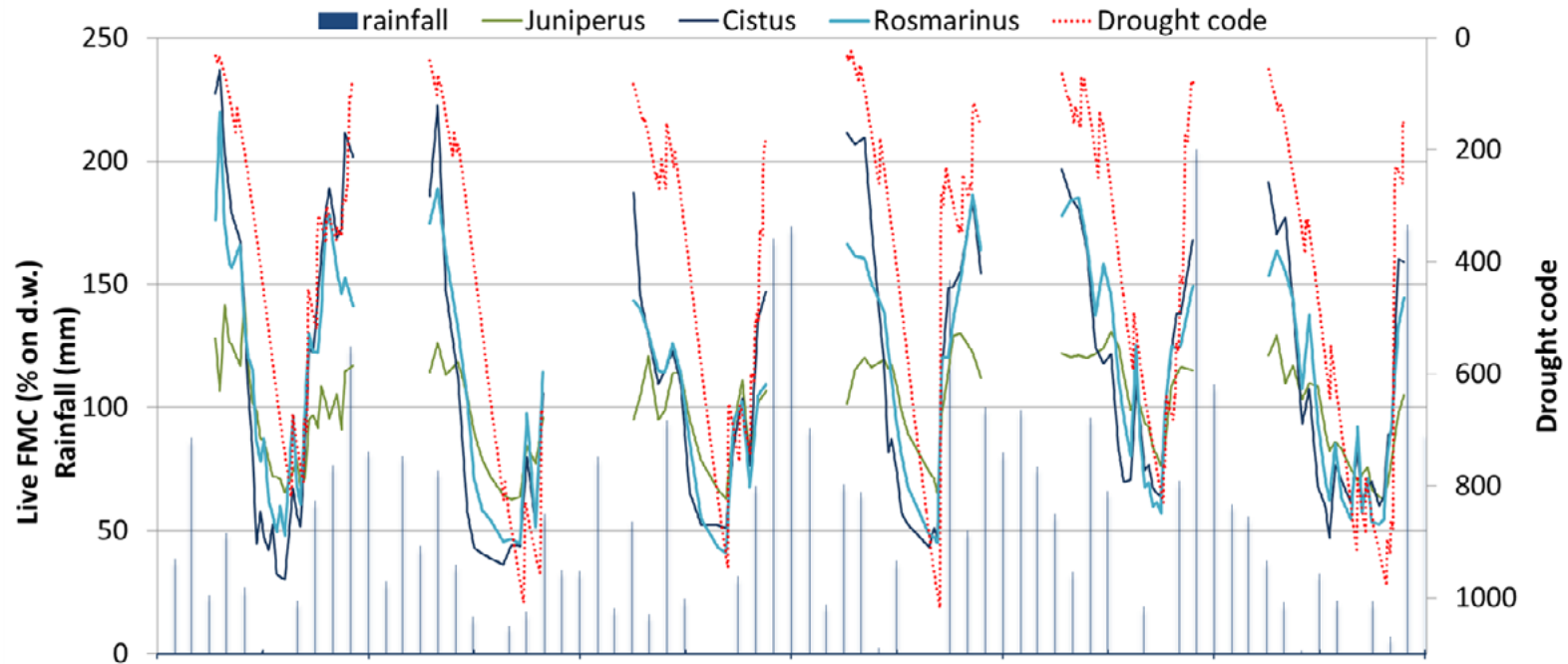


Fig. 1: Seasonal trends of Drought Code (DC) and live fuel moisture content (LFMC) values observed for *Cistus monspeliensis*, *Juniperus phoenicea* and *Rosmarinus officinalis* at the experimental site during the periods April-November 2005, and 2007-2011.

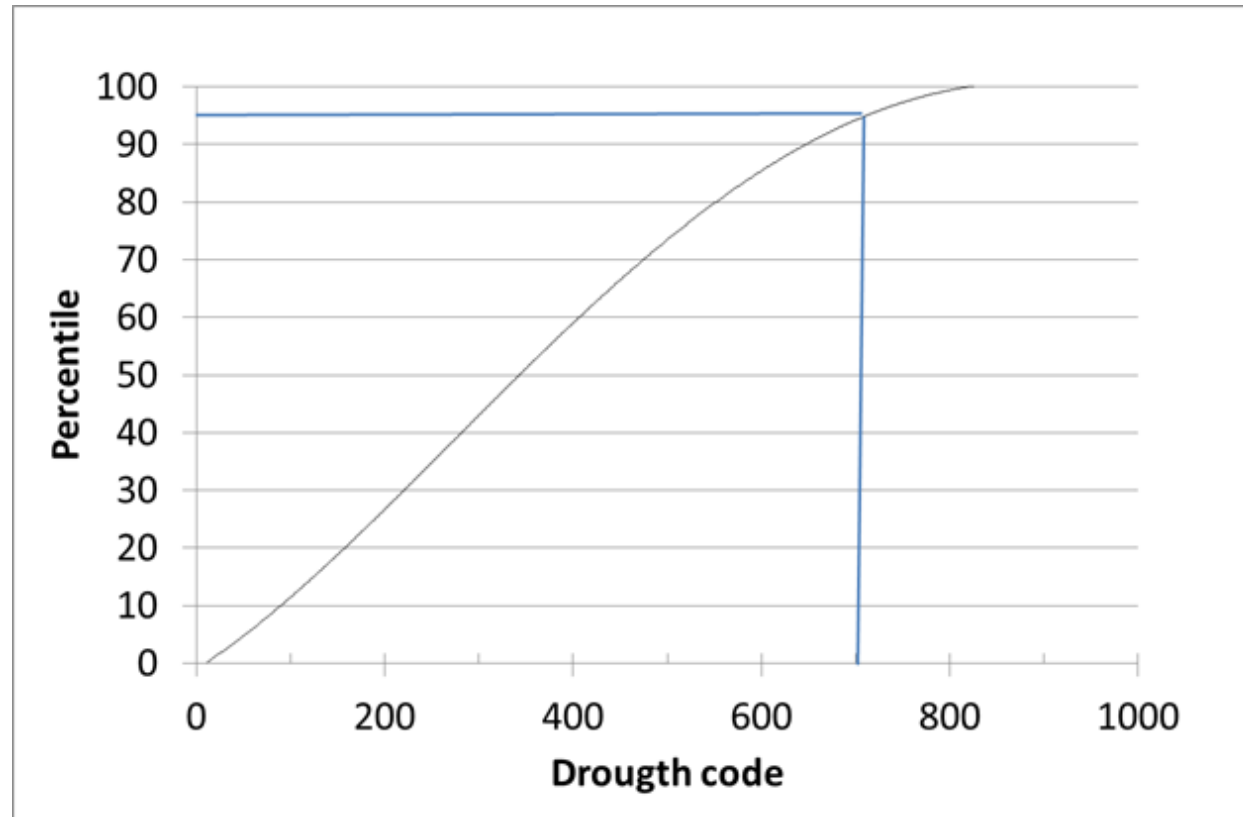


Fig. 2: Cumulative distribution of Drought Code values observed during days with LFMCI values above 95% (rising phase of LFMCI).

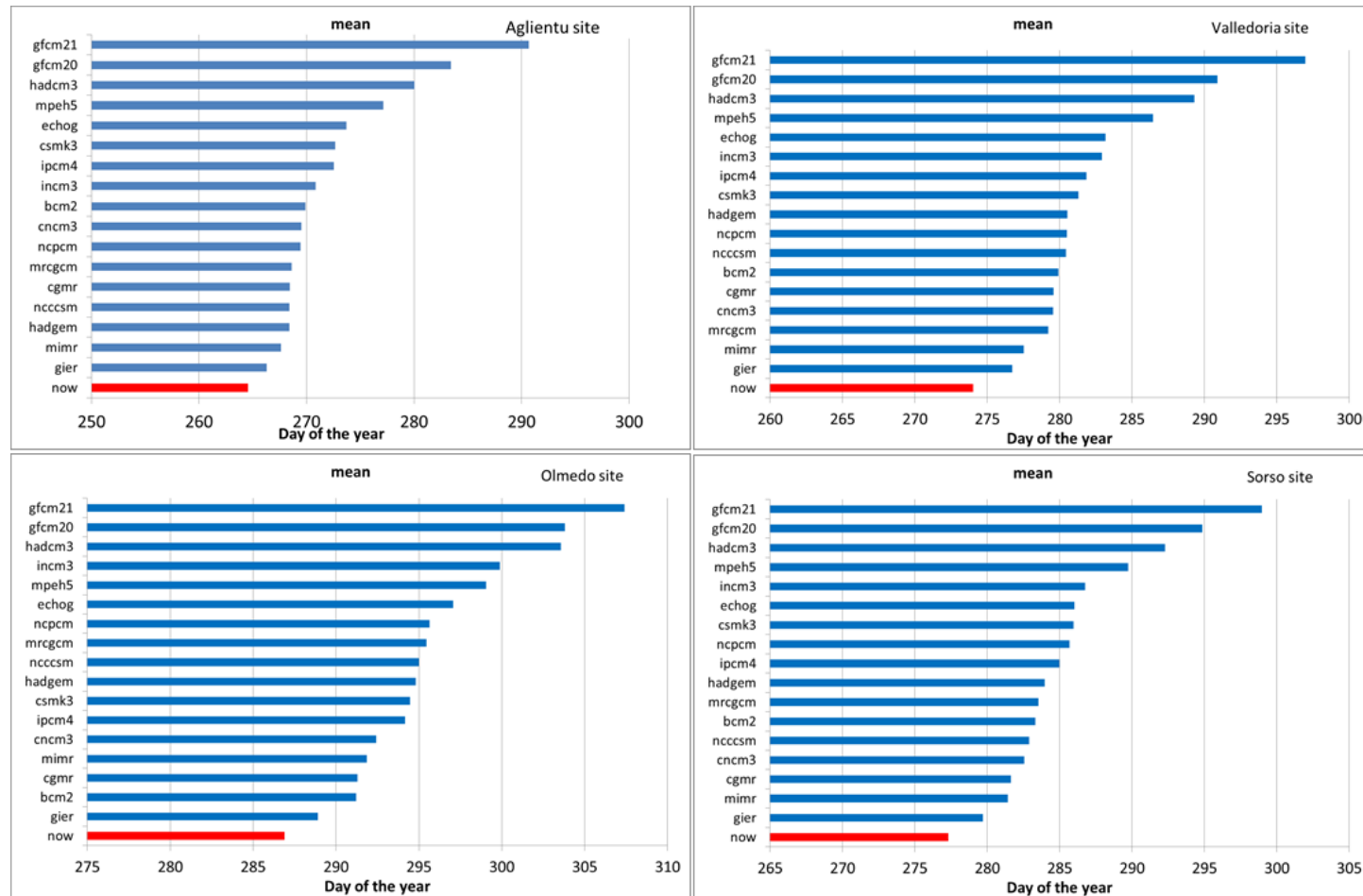


Fig. 3: Actual (red) and projected (blue) average dates of end of fire season for 4 experimental sites located in Northern Sardinia, Italy.

4. ACKNOWLEDGMENTS

This study was funded by (i) CNR (Italy) – ASCR (Czech Republic) bilateral project (Climate change impacts on crop production and fire danger in selected Mediterranean areas), (ii) FUME project (“Forest fire under climate, social and economic changes...”; 7FP, Theme ENV.1.3.1.1, Grant Agreement 243888), and (iii) The Ministry of Education, Youth and Sports of the Czech Republic (project LD12029 - "Downscaling the Global Climate Models with use of the Stochastic Weather Generator").

5. REFERENCES

- Agee J.K., Wright C.S., Williamson N. & Huff M.H. (2002), *Foliar moisture content of Pacific Northwest vegetation and its relation to wildland fire behaviour*. Forest Ecology and Management 167, pp. 57–66. (1)
- Alexander M. (2010), *Foliar moisture content input in the Canadian Forest Fire Behavior Prediction System for areas outside of Canada*. Proceedings of VI International Conference on Forest Fire Research D. X. Viegas (Ed.) Coimbra, 2010. (2)
- Bradstock R.A. (2010), *A biogeographic model of fire regimes in Australia: current and future implications*, Global Ecology and Biogeography, 19, pp. 145-158. (3)
- Castro F.X., Tudela A., Sebastià M.T. (2003), *Modeling moisture content in shrubs to predict fire risk in Catalonia (Spain)*. Agricultural and Forest Meteorology 116, pp. 49-59. (4)
- Chandler P., Cheney P., Thomas L., Trabaud L. & Williams D. (1983) *Fire in forestry*. Vol. 1. John Wiley & Sons, New York, USA. (5)
- Christensen J.H., Hewitson B., Busuioc A., Chen A., Gao X., Held I., Jones R., Kolli R.K., W.-T. Kwon, Laprise R., Magaña Rueda V., Mearns L., Menéndez C.G., Räisänen J., Rinke A., Sarr A. & Whetton P. (2007), *Regional Climate Projections*. In: Climate Change 2007: The Physical Science Basis. Contribution of Working Group I to the Fourth Assessment Report of the Intergovernmental Panel on Climate Change [Solomon, S., D. Qin, M. Manning, Z. Chen, M. Marquis, K.B. Averyt, M. Tignor and H.L. Miller (eds.)]. Cambridge University Press, Cambridge, United Kingdom and New York, NY, USA. (6)
- Chuvieco E., Aguado I. & Dimitrakopoulos A. (2004), *Conversion of fuel moisture content values to ignition potential for integrated fire danger assessment*. Canadian Journal of Forest Research 34, pp. 2284-2293. (7)
- Chuvieco E., González I., Verdú F., Aguado I. & Yebra M. (2009), *Prediction of fire occurrence from live fuel moisture content measurements in a Mediterranean ecosystem*. International Journal of Wildland Fire, 18, pp. 430–441. (8)

- Davis F.W. & Michaelsen J. (1995), *Sensitivity of fire regime in chaparral ecosystems to climate change*. In Global Change and Mediterranean-Type Ecosystems. (Eds JM Moreno, WC Oechel) pp. 435–456. (Springer: NewYork). (9)
- Davis F.W., Legg C.J., Smith A.A. & MacDonald A.J. (2009), *Rate of spread of fires in Calluna vulgaris-dominated moorlands*. Journal of Applied Ecology 46, pp.1054–1063. (10)
- Dennison P.E., Moritz M.A. & Taylor R.S. (2008), *Evaluating predictive models of chamise critical live fuel moisture in the Santa Monica Mountains, California*. International Journal of Wildland Fire 17, pp. 18–27. (11)
- Dimitrakopoulos A.P. & Papaioannou K.K. (2001), *Flammability Assessment of Mediterranean Forest Fuels*. Fire Technology 37 pp. 143-152. (12)
- Giannakopoulos C., Le Sager P., Bindi M., Moriondo M., Kostopoulou E., & Goodess C.M. (2009), *Climatic changes and associated impacts in the Mediterranean resulting from a 2 °C global warming*. Global and Planetary Change, 68, pp. 209-224. (13)
- Giorgi F., Bi X.Q. & Pal J. (2004), *Mean, interannual variability and trends in a regional climate change experiment over Europe. II: climate change scenarios (2071- 2100)*. Climate Dynamics, 23, pp. 839-858. (14)
- Girardin M.P., Tardif J., Flannigan M.D., Wotton B.M. & Bergeron Y. (2004), *Trends and periodicities in the Canadian Drought Code and their relationships with atmospheric circulation for the southern Canadian boreal forest*. Canadian Journal Forest Research 34(1), pp. 103–119. (15)
- Hernando Lara C., Moro C., Valette J.C. (1994), *Flammability parameters and calorific values of Erica arborea and Arbutus unedo*. In Proceedings of the 2nd International Conference on Forest Fire Research, Vol. II, 481-489, Coimbra, Portugal. (16)
- Nelson R.M. Jr. (2001), *Water relations of forest fuels*. In: “Forest Fires – behavior and ecological effects.” (Eds Johnson E.A. and Miyanishi K.) pp. 79-149. Academic Press, San Diego, CA, USA. (17)
- Palmer W.C. (1965), *Meteorological drought*. Research Paper No. 45. Washington DC: U.S. Department of Commerce Weather Bureau. (18)
- Pellizzaro G., Duce P., Ventura A. & Zara P., (2007 a), *Seasonal variations of live moisture content and ignitability in shrubs of Mediterranean Basin*. International Journal of Wildland Fire, 2007, 16 pp. 633–641. (19)
- Pellizzaro G., Cesaraccio C., Duce P., Ventura A. & Zara P., (2007 b). *Relationships between seasonal patterns of live fuel moisture and meteorological drought indices for Mediterranean shrubland species*. Int. J. Wildland Fire 16 pp. 232–241. (20)

- Piñol J., Filella I., Ogaya R. & Peñuelas J. (1998), *Ground-based spectroradiometric estimation of live fine fuel moisture of Mediterranean plants*. Agricultural and Forest Meteorology 90, pp. 73-186. (21)
- Pyne S.J., Andrews P.L., & Laven R.D. (1996) *Introduction to Wildland Fire*, 2nd ed., 769 pp. John Wiley & Sons, Toronto, Canada. (22)
- Rothermel R.C. (1972), *A mathematical model for predicting fire spread in wild and fuels*. USDA Forest Service Research Paper INT-115. (23)
- Schoenberg F.P., Peng R., Huang Z. & Rundel P. (2003), *Detection of nonlinearities in the dependence of burn area on fuel age and climatic variables*. International Journal of Wildland Fire 12, pp. 1–6. (24)
- Sun L., Zhou X., Mahalingama S. & Weise D.R. (2006), *Comparison of burning characteristics of live and dead chaparral fuels*. Combustion and Flame 144 pp. 349–359. (25)
- Van Wagner C.E. (1977), *Conditions for the start and spread of crown fires*. Canadian Journal of Forest Research 7, pp. 23-34. (26)
- Van Wagner C.E. & Pickett T.L. (1985), *Equation and FORTRAN program for the Canadian Forest Fire Weather Index System*. Canadian Forestry Service, Forestry Technical Report 33, Ottawa, ON, Canada. (27)
- VanWagner C.E. (1987), *The development and structure of the Canadian Forest FireWeather Index System*. Canadian Forest Service, Petawawa National Forestry Institute. Chalk River, Ont. FTR-35. (28)
- Viegas D.X., Pinol J., Viegas M.T. & Ogaya R. (2001), *Estimating live fine fuels moisture content using meteorologically-based indices*. International Journal of Wildland Fires, 10, pp. 223-240. (29)
- Viney N.R., (1991), *A review of fine fuel moisture modelling*. International Journal of Wildland Fire 1, pp. 215-234. (30)
- Weise D.R., Hartford R.A. & Mahaffey L. (1998), *Assessing live fuel moisture for fire, management applications*. In: Fire in ecosystem management: shifting the paradigm from suppression to prescription (Eds TL Pruden and LA Brennan Eds.) pp. 49-55. Tall Timbers Fire Ecology Conference Proceedings, No. 20. Tall Timbers Research Station, Tallahassee, FL. (31)
- Wotton M. (2009), *Interpreting and using outputs from the Canadian Forest Fire Danger Rating System in research applications*. Environmental and Ecological Statistics 16, pp. 107–131. (32)

Analyzing changes in wildfire likelihood and intensity in Mediterranean areas: a case study from central Sardinia, Italy

Salis M.^{1,2*}, Alcasena F.², Ager A.A.³, Casula F.², Arca B.⁴, Bacciu V.², and Spano D.^{1,2}

¹University of Sassari, Department of Science for Nature and Environmental Resources (DIPNET), Sassari, Italy,

²Euro-Mediterranean Center for Climate Changes (CMCC), LAFENT Division Sassari, Italy.

³USDA Forest Service, Pacific Northwest Research Station,

Western Wildland Environmental Threat Assessment Center, USA.

⁴National Research Council (CNR), Institute of Biometeorology (IBIMET), Sassari, Italy.

*Corresponding author: miksalis@uniss.it

Abstract

In this work, we used mechanistic wildfire simulation to examine how ignition patterns, land use, weather, and fuels affect wildfire likelihood and intensity. The study area was located in central Sardinia, Italy and encompassed about 680 km². We simulated 10,000 wildfires for each combination of the input variables using the MTT algorithm as implemented in FlamMap and Randig. The range of values for the input variables was chosen from historical weather data to represent realistic conditions within the study area. Wildfire outputs analyzed included flame length, burn probability, and fire size. The results suggested that the most important role in influencing burn probability and flame length for the conditions studied was fuel moisture. Land use change was also responsible for increases in burn probability and flame length, and resulted from the expansion of unmanaged *Quercus* spp. forests and Mediterranean shrubs into areas that were traditionally managed grasslands and crops. Wind direction and ignition locations had a substantial influence on spatial patterns in fire size and burn probability, with a relatively minor effect on fire intensity. Wind speed had a notable effect on the shape of fire perimeters, and also resulted in increased burn probability.

Keywords: *Historical changes, fire modeling, wildfire likelihood and intensity, Mediterranean areas*



1. INTRODUCTION

Forest fires are a growing problem in the Mediterranean area, and cause substantial losses to vegetation, housing, infrastructures, and human lives. Wildfire spread and behavior are affected by complex and non-linear relationships among many factors including weather, fuels, topography, and ignition patterns (24, 5, 21). The role of humans in Mediterranean forest fires is an important factor, since more than 90% of fire ignitions are caused by anthropogenic factors (arson, negligence, power lines, etc.) (12, 17). Socio-economic changes have led to an increase of the anthropic pressure in urban and coastal areas and to a progressive abandonment of farming and agro-forestry activities (19, 22). This has favored substantial increases in fuel loading and continuity (10), especially where agricultural areas and pastures have converted to shrublands and woodlands (9, 26). In addition, a number of studies have suggested that in the last decades climate change was responsible for the rise in potential fire risk, due to the increase of temperature, heat waves frequency and duration, and to the reduction of rainfall (3, 20). All these changes triggered an escalation in the incidence of mega-fires and a lengthening of the fire seasons broadly observed in recent years in in Mediterranean areas (Sardinia, 1983, 1993, and 2009; Portugal, 2003 and 2005; Spain, 2006 and 2009; Italy and Greece, 2007 and 2011) and all over the world (Russia, 2010; Australia, 1991 and 2009; USA, 2000, 2006, 2007 and 2012; Canada, 2004) (8, 32, 16, 27). In fact, these critical fire seasons were characterized by the occurrence of one or more days with extreme environmental conditions (strong winds, low relative humidity, and very dry fuels).

Despite the large number of studies on fires and climate changes, a relatively small number of papers analyzed the impacts of the combined variation of environmental components and ignition patterns on fire behavior and burn probability. For instance, we know little how wind, landscape fragmentation, fuel characteristics, fire suppression, ignition points, and topography ultimately affect the likelihood and intensity of wildfires (5). Landscape fire behavior modeling offers a method to simulate, map and analyze fire spread and behavior at landscape scales and to test the effects of different factors on spatio-temporal patterns of fire propagation, fire intensity, fire size, and spread direction (30). The MTT fire spread algorithm (13) as implemented into FlamMap (14) or Randig (15) has been extensively used for this purpose, and is routinely applied to fire management, hazard and exposure analysis in the US and elsewhere (1, 2, 31, 25).

In this work, we used wildfire simulation to examine how different combinations of ignition patterns, land use and fuel type changes, fuel moisture and wind scenarios, affect fire likelihood and intensity.

The analysis was performed in a large fire-prone landscape of about 680 km² located in central Sardinia, Italy. We examined a number of factors that determine fire behavior including ignition patterns, land use changes, fuel moisture and weather. The results provided a number of insights into potential fire behavior that will be useful to fire managers tasked with managing wildfire risk on the island of Sardinia.

2. MATERIAL AND METHODS

a) Study area

The study area is located in the province of Nuoro, in the central part of Sardinia (Italy), and covers approximately 680 km² (Figure 1). This area represents one of the most important fire-prone areas of the island, and was historically affected by a large number of fires that exceeded 100 hectares.

The topography is characterized by slightly defined NW-SE hilly reliefs, with open and flat valleys between. The average elevation of the area is about 470 m above sea level, with ranges from 48 m in the lowest plains to 1,344 meters (Figure 1). Many secondary narrow watersheds lead from the mountains perpendicularly to the open valleys; the steepest zones are located in the hillsides of the narrowest watersheds. The climate is typically Mediterranean, with moderately cold and wet winters and hot and dry summers. The mean accumulated annual rainfall ranges between 650 and 750 mm, with no relevant precipitation in the summer season. The coldest months are January and February, while the highest temperatures are recorded in July and August, with peaks of more than 35°C in the hottest days of the season.

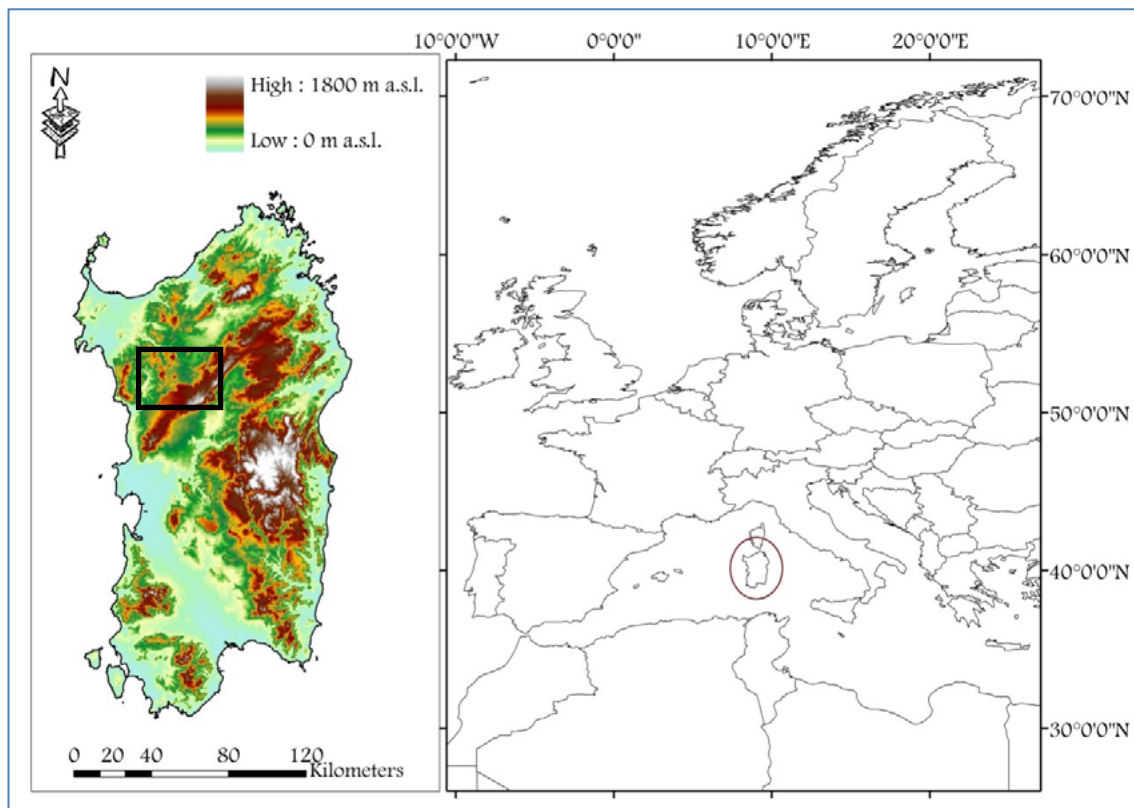


Fig. 1: Location of the island of Sardinia (Italy) in the Euro-Mediterranean area. The study area is framed by the black rectangle, in the left.

The vegetation is nowadays represented by grasslands and pastures in the open and flat areas, while the Mediterranean maquis occupies the less productive and the previous natural pastures (Figure 2). Basically, *Quercus ilex* L. and *Quercus suber* L. woods are located in the hilly areas, also in association with *Quercus pubescens* Mill., which is more abundant in humid and north facing slopes. Despite the fact that herbaceous fuel types are still the most relevant land use in the study area (about 50%), the incidence of forests and Mediterranean maquis increased significantly in the last decades, rising from 25% to as much as 40% (Figure 2). This shift was mainly due to land abandonment and to the reduction of livestock pressure in the less productive pastures. The urban areas have also increased their incidence.

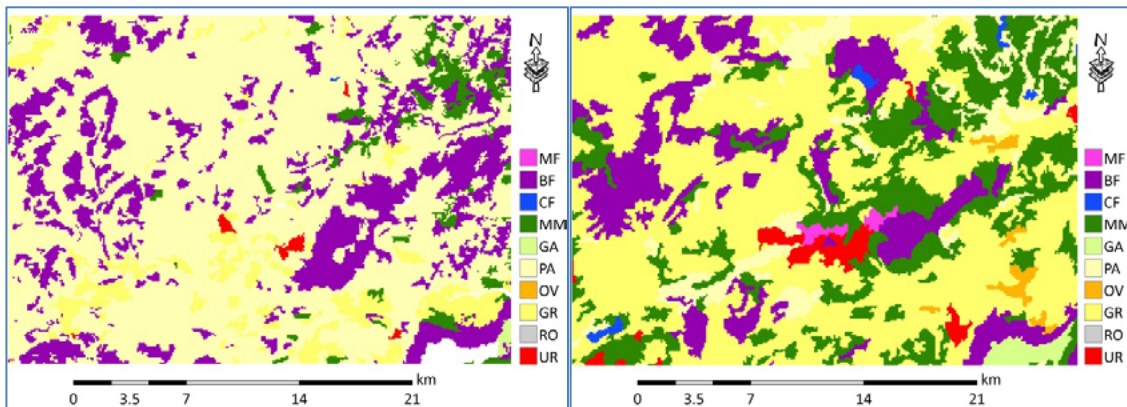


Fig. 2: Fuel model maps of 1954 (left) and 2000 (right). UR = urban areas; RO = rocky areas; GR = grasslands; OV = olives and vineyards; PA = herbaceous pastures; GA = garrigue; MM = Mediterranean maquis; CF = conifer forest; BF = broadleaf forest; MF = mixed forest.

b) Input data

Fuel model and topography data were assembled in a landscape file, as required by the FlamMap model, with a 50 m cell size resolution. Topography layers were derived from the Sardinia digital elevation model (10 m of resolution, <http://www.sardegnaoportale.it/>). Fuel and canopy cover layers were obtained by supervised classification of aerial photographs (1:10,000) of the study area. The supervised classification of aerial photographs allowed for discriminating different fuel types (Figure 2, and Table 1); for each of them, a custom or standard fuel model and a canopy cover value was assigned (4, 28, 25). The canopy cover characteristics set for the runs were representative of *Quercus* spp. stands in the study area. We created three different fuel and canopy cover layers, in correspondence of the years 1954, 1977, and 2000, in order to analyze how the observed changes in the main fuel types affected wildfire likelihood and intensity. The information on fuel moisture was obtained combining literature data (18, 6, 11) with sampling campaigns conducted in Sardinia in recent years (23). The FlamMap simulations were performed considering two moisture scenarios (extreme and very dry fuel moisture conditions), to evaluate how moisture could affect fire behavior and burn probability. For each fuel model, the values of 1h, 10h and 100h dead fuels, and live fuels are presented in Table 1.

Fuel Type	DFM1h	DFM10h	DFM100h	LHFM	LWFM
Rocky areas	9/7	11/9	13/11	80/70	80/70
Grasslands	9/7	11/9	13/11	80/70	80/70
Olive groves and vineyards	9/7	11/9	13/11	80/70	80/70
Herbaceous pastures	9/7	11/9	13/11	80/70	80/70
Garrigue	9/7	11/9	13/11	80/70	50/40
Mediterranean maquis	9/7	11/9	13/11	80/70	80/70
Conifer forests	11/9	13/11	15/13	80/85	100/85
Broadleaved forests	11/9	13/11	15/13	80/85	100/85
Other forests	11/9	13/11	15/13	80/85	100/85

Table 1: Very dry / extreme fuel moisture content used for the simulations. DFM1h = 1 hour dead fuel moisture (%); DFM10h = 10 hour dead fuel moisture (%); DFM100h = 100 hour dead fuel moisture (%); LHFM = live herbaceous fuel moisture (%); LWFM = live woody fuel moisture (%).

Wind speed and direction for the modeling were determined based on the observed data series from meteorological stations close to the study area, focusing on days with fire events. Two dominant wind directions were mainly associated to the largest fires in the study area: south-west (225°) and north-west (315°). For each wind direction, wind speeds of 35 km h⁻¹ and 25 km h⁻¹ (corresponding to the 95th and 75th percentile of average daily wind speed, respectively) were used to run the simulations. Finally, we defined 10,000 ignition points within the study area. To assess the effect of ignition location on the outputs, we defined two different datasets of ignition points, using observed probability grids and random locations. Therefore, the first dataset was created taking into account the observed spatial distribution of ignitions, while the second one was obtained by randomizing 10,000 fire ignitions in the study area. The observed ignition points were mainly concentrated in areas where anthropic activity was more relevant, close to pastures, agricultural lands, urban areas, and roads (7, 28).

c) Wildfire simulations

Overall, we ran 48 simulations, considering several combinations of land uses, fire ignition distributions, and environmental conditions as inputs for the modeling. In particular, we considered: a) three fuel types maps, corresponding to the years 1954, 1977 and 2000; b) two fuel moisture scenarios, corresponding to very dry and extreme moisture conditions; c) two ignition points scenarios, historically based and random; d) two wind speed, 25 and 35 km h⁻¹; e) two wind directions, south-west and north-west.

Each fire was simulated to reproduce 10 hours of active spread. The resolution of calculation and the interval for minimum travel time were set to 50 m. For each simulation, the outputs (burn probability, fire size, conditional flame length) were produced at 50 m of resolution, and then analyzed using ArcGIS 9.3.1 (Esri Inc.). The conditional burn probability (BP) output defines the probability each pixel burns for twenty 0.5 m intervals of flame length. So, BP is the chance that a pixel will burn at a given flame length interval considering one ignition in the whole study area under the assumed fuel moisture and weather conditions (2, 25). Conditional flame length (CFL) is a weighted probability of flame length given a fire occurrence. Fire size (FS) output reports the coordinates of the 10,000 ignition points and the area burned by each fire. The 10,000 fire perimeters were also exported in shapefile format.

3. RESULTS

Wildfire likelihood and intensity were analyzed for each simulation. We mapped the main outputs of FlamMap and analyzed the mean, minimum and maximum values obtained. A detailed overview of BP, CFL and FS is reported in Tables 2, 3, 4 and 5, and in Figures 3, 4 and 5. To summarize the results obtained, we mainly focused on the mean values of BP, CFL, and FS

INPUT DATA					FIRE SIZE (ha)				BURN PROBABILITY				FLAME LENGTH (m)			
FT	WD	WS	FM	IP	min	max	mean	SD	min	max	mean	SD	min	max	mean	SD
1954	225	35	EXT	RND	0	4555.6	1591.1	664.5	0	0.0276	0.0096	0.0041	0	6.2	0.6	0.7
	225	35	VD	RND	0	2595.5	495.5	241.0	0	0.0157	0.0030	0.0015	0	5.6	0.5	0.6
	225	25	EXT	RND	0	4579.4	1957.4	859.7	0	0.0292	0.0119	0.0051	0	5.6	0.7	0.7
	225	25	VD	RND	0	3335.5	602.4	332.6	0	0.0188	0.0036	0.0020	0	5.1	0.5	0.7
	315	35	EXT	RND	0	4959.9	1564.5	695.3	0	0.0281	0.0095	0.0043	0	6.4	0.6	0.7
	315	35	VD	RND	0	3289.7	500.3	283.5	0	0.0180	0.0030	0.0018	0	6.3	0.5	0.6
	315	25	EXT	RND	0	5096.3	1948.9	882.3	0	0.0291	0.0118	0.0053	0	5.8	0.7	0.7
	315	25	VD	RND	0	3905.0	605.2	376.2	0	0.0203	0.0036	0.0022	0	5.8	0.5	0.7
1954	225	35	EXT	OBS	0	4540.2	1612.6	656.6	0	0.0620	0.0104	0.0121	0	6.8	0.6	0.8
	225	35	VD	OBS	0	2569.3	501.9	242.7	0	0.0156	0.0030	0.0034	0	6.0	0.5	0.6
	225	25	EXT	OBS	0	4684.8	2004.4	849.4	0	0.0790	0.0131	0.0155	0	5.8	0.6	0.7
	225	25	VD	OBS	0	3221.2	613.4	336.6	0	0.0197	0.0036	0.0042	0	5.4	0.5	0.7
	315	35	EXT	OBS	0	5151.6	1576.1	690.4	0	0.0602	0.0095	0.0122	0	6.8	0.6	0.7
	315	35	VD	OBS	0	3150.5	506.0	283.2	0	0.0155	0.0029	0.0034	0	5.7	0.5	0.6
	315	25	EXT	OBS	0	4952.2	1963.1	874.3	0	0.0753	0.0122	0.0157	0	5.8	0.6	0.7
	315	25	VD	OBS	0	3787.6	614.0	379.2	0	0.0202	0.0035	0.0042	0	5.9	0.5	0.7

Table 2: Fire size, burn probability and flame length outputs for the simulations related to fuel types maps of 1954. FT = fuel types; WD = wind direction (degrees); WS = wind speed (km h⁻¹); FM = fuel moisture (EXT = extreme; VD = very dry); IP = ignition point patterns (RND = random; OBS = based on observed ignitions); SD = standard deviation.

INPUT DATA					FIRE SIZE (ha)				BURN PROBABILITY				FLAME LENGTH (m)			
FT	WD	WS	FM	IP	min	max	mean	SD	min	max	mean	SD	min	max	mean	SD
1977	225	35	EXT	RND	0	4367.7	1790.6	714.8	0	0.0286	0.0108	0.0044	0	6.9	0.7	0.9
	225	35	VD	RND	0	2281.2	555.3	267.8	0	0.0138	0.0034	0.0017	0	6.6	0.5	0.8
	225	25	EXT	RND	0	4796.2	2215.7	867.5	0	0.0310	0.0134	0.0052	0	6.1	0.7	0.9
	225	25	VD	RND	0	3058.0	697.0	365.2	0	0.0176	0.0042	0.0023	0	5.6	0.6	0.8
	315	35	EXT	RND	0	4964.6	1777.0	717.7	0	0.0254	0.0108	0.0045	0	6.2	0.7	0.9
	315	35	VD	RND	0	2240.0	561.6	279.8	0	0.0132	0.0034	0.0019	0	5.6	0.5	0.8
	315	25	EXT	RND	0	5336.4	2209.4	871.9	0	0.0292	0.0134	0.0054	0	5.9	0.7	0.9
	315	25	VD	RND	0	2736.2	705.2	380.8	0	0.0178	0.0043	0.0024	0	5.7	0.6	0.8
1977	225	35	EXT	OBS	0	4657.5	1809.1	697.2	0	0.0582	0.0116	0.0125	0	7.3	0.7	0.9
	225	35	VD	OBS	0	2289.3	562.8	266.9	0	0.0311	0.0034	0.0042	0	6.4	0.5	0.8
	225	25	EXT	OBS	0	4797.6	2236.8	845.8	0	0.0732	0.0142	0.0154	0	6.2	0.7	0.9
	225	25	VD	OBS	0	3051.6	707.2	358.7	0	0.0353	0.0043	0.0052	0	6.0	0.5	0.8
	315	35	EXT	OBS	0	4824.1	1792.6	716.1	0	0.0723	0.0110	0.0136	0	7.9	0.7	0.9
	315	35	VD	OBS	0	2272.5	564.6	279.4	0	0.0336	0.0034	0.0045	0	6.5	0.5	0.8
	315	25	EXT	OBS	0	5333.0	2215.5	868.0	0	0.0879	0.0138	0.0169	0	6.2	0.7	0.9
	315	25	VD	OBS	0	2746.7	708.9	379.2	0	0.0383	0.0043	0.0057	0	5.8	0.5	0.8

Table 3: Fire size, burn probability and flame length outputs for the simulations related to fuel types maps of 1977. FT = fuel types; WD = wind direction (degrees); WS = wind speed (km h⁻¹); FM = fuel moisture (EXT = extreme; VD = very dry); IP = ignition point patterns (RND = random; OBS = based on observed ignitions); SD = standard deviation.

INPUT DATA					FIRE SIZE (ha)				BURN PROBABILITY				FLAME LENGTH (m)			
FT	WD	WS	FM	IP	min	max	mean	SD	min	max	mean	SD	min	max	mean	SD
2000	225	35	EXT	RND	0	12948.1	2951.9	2243.3	0	0.0889	0.0181	0.0152	0	7.8	1.4	1.6
	225	35	VD	RND	0	9095.7	1221.4	1280.1	0	0.0529	0.0075	0.0081	0	6.0	1.1	1.4
	225	25	EXT	RND	0	13714.4	3243.3	2230.7	0	0.0809	0.0199	0.0147	0	6.8	1.3	1.5
	225	25	VD	RND	0	10589.9	1676.2	1671.6	0	0.0574	0.0102	0.0103	0	5.7	1.2	1.5
	315	35	EXT	RND	0	13390.8	2854.5	2405.4	0	0.0807	0.0174	0.0139	0	7.6	1.4	1.6
	315	35	VD	RND	0	7570.8	1126.9	1110.2	0	0.0421	0.0069	0.0067	0	5.9	1.1	1.4
	315	25	EXT	RND	0	12511.6	3139.4	2309.4	0	0.0769	0.0191	0.0135	0	6.4	1.3	1.5
	315	25	VD	RND	0	9017.1	1550.1	1482.1	0	0.0518	0.0094	0.0090	0	5.8	1.2	1.5
2000	225	35	EXT	OBS	0	13036.0	3034.2	2274.1	0	0.1296	0.0213	0.0264	0	8.1	1.4	1.7
	225	35	VD	OBS	0	8850.0	1261.8	1303.0	0	0.0631	0.0085	0.0120	0	6.5	1.1	1.4
	225	25	EXT	OBS	0	13555.4	3324.2	2249.0	0	0.1209	0.0226	0.0270	0	7.0	1.3	1.5
	225	25	VD	OBS	0	10422.0	1729.4	1695.5	0	0.0716	0.0116	0.0159	0	5.9	1.1	1.5
	315	35	EXT	OBS	0	13403.0	2900.0	2409.7	0	0.1161	0.0174	0.0237	0	7.8	1.3	1.6
	315	35	VD	OBS	0	7541.6	1144.0	1101.5	0	0.0596	0.0067	0.0098	0	6.3	1.0	1.3
	315	25	EXT	OBS	0	12498.2	3192.1	2310.5	0	0.1229	0.0196	0.0261	0	6.7	1.3	1.5
	315	25	VD	OBS	0	8920.4	1586.6	1480.1	0	0.0742	0.0096	0.0137	0	5.7	1.1	1.4

Table 4: Fire size, burn probability and flame length outputs for the simulations related to fuel types maps of 2000. FT = fuel types; WD = wind direction (degrees); WS = wind speed (km h⁻¹); FM = fuel moisture (EXT = extreme; VD = very dry); IP = ignition point patterns (RND = random; OBS = based on observed ignitions); SD = standard deviation.

The mean BP values of the simulations ranged between 0.0029 ± 0.0034 and 0.0226 ± 0.0269 (Tables 2 and 4). Hence, the range of variation of mean BP among the 48 simulations was relevant, with the minimum BP averaging 10-fold less than the maximum mean BP. As far as mean CFL of the simulations is concerned, the values varied between a minimum of 0.462 ± 0.677 m, and a maximum of 1.369 ± 1.633 m (Tables 2 and 4). Regarding fire size, the lowest mean was observed for the fuel types of 1954, which had 495.55 ± 240.95 ha, and a mean FS growth of about 50 ha h^{-1} (Table 2). On the other hand, the maximum mean FS was obtained for the fuel types of 2000, with $3,324.17 \pm 2,249.02$ ha, and a mean FS growth of about 330 ha h^{-1} (Table 4).

We then investigated how the differences in fuel types affected wildfire potential and burn probability for the 48 simulations, by holding constant all the other input data. We also did the same analysis for wind speed, wind direction, fuel moisture, and ignition locations (Table 5).

Regarding land use changes, overall, we observed a rise in the mean values of FS, BP and CFL, and the increase was particularly relevant from 1977 to 2000. As showed in Table 5, the mean values of BP, CFL and FS outputs increased of about 12-13% from 1954 to 1977, while from 1977 to 2000 BP and FS raised as much as 45% and CFL increased 49%. The same trends were observed for minimum and maximum values of FS, BP, and CFL. The highest increases of maximum BP, CFL and FS, from 1977 to 2000 reached 63%, 52% and 59%, respectively (Table 5).

INPUTS	COMPARISON	DIFFERENCE IN FIRE SIZE (%)				DIFFERENCE IN BURN PROBABILITY (%)				DIFFERENCE IN FLAME LENGHT (%)			
		mean	SD	max	min	mean	SD	max	min	mean	SD	max	min
Fuel moisture	VD - EXTR	-186.5	48.9	-92.2	-226.8	-193.9	53.4	-94.2	-261.0	-28.9	6.8	-14.6	-37.7
Wind direction	315 -225	2.4	3.4	10.3	-1.7	5.8	7.7	25.4	-1.5	1.3	1.5	5.0	-1.3
Wind speed	25 - 35	18.8	5.5	27.9	8.7	19.2	5.8	30.0	5.8	1.9	2.8	7.3	-2.5
Ignitions	RND - OBS	1.5	8.1	3.2	0.3	3.5	5.3	15.2	-5.2	-2.4	1.9	0.9	-6.0
Fuel types	1977 - 1954	11.8	1.2	14.2	10.4	12.8	2.7	18.7	7.7	11.9	1.7	14.9	9.5
	2000 - 1977	44.9	10.8	59.1	29.6	45.9	11.2	63.1	29.5	48.6	2.5	52.2	45.2

Table 5: Influence of the variation of input data on fire size, burn probability, and flame length. This analysis was performed holding constant the other four input data. Values represent the variation in percentage.

Fuel moisture greatly affected the outputs of FlamMap, particularly when considering FS and BP. As expected, the extreme fuel moisture scenario resulted in higher values of BP, CFL and FS as compared to the outputs obtained with the very dry moisture scenario. The increase of mean BP and FS changing from one scenario to the other was about 190%, while a less relevant difference (about +29%) was observed as far as CFL is concerned. Moreover, maximum and minimum BP and FS showed strong and similar increases (respectively about +90% and +240%) from very dry to extreme fuel moisture values, while the variation in maximum and minimum CFL was more limited (approximately +15% and +38%) (Table 5).

The wind directions from SW and NW played a key role in changing the spatial distribution of BP and also of large fires (Figure 5), but the differences in mean BP, CFL and FS were very slight. The same result was obtained for maximum and minimum values, which did not present relevant variations.

Regarding wind speed, the effect of different intensities (25 or 35 km h⁻¹) on wildfire intensity and burn probabilities was limited, although not as slight as the wind direction. Wind speeds of 25 km h⁻¹ were responsible for higher mean BP and FS values (about +19%) than wind speeds of 35 km h⁻¹. No significant differences were observed for mean CFL (Table 5).

Finally, we evaluated how ignition patterns, random and historical ones, affected FS, CFL, and BP. As expected, the outputs clearly showed differences between the fire hazard and burn probability maps obtained with the random ignitions and those obtained using historical ignitions grids (Figure 5). Yet, no significant differences were observed in mean CFL, BP, and FS between the two ignition scenarios. Furthermore, maximum and minimum values of fire behavior and burn probability did not present relevant differences between historical and random ignitions, even though in some limited areas the concentration of fires lead to very high BP in the simulations ran with historical ignitions grid.

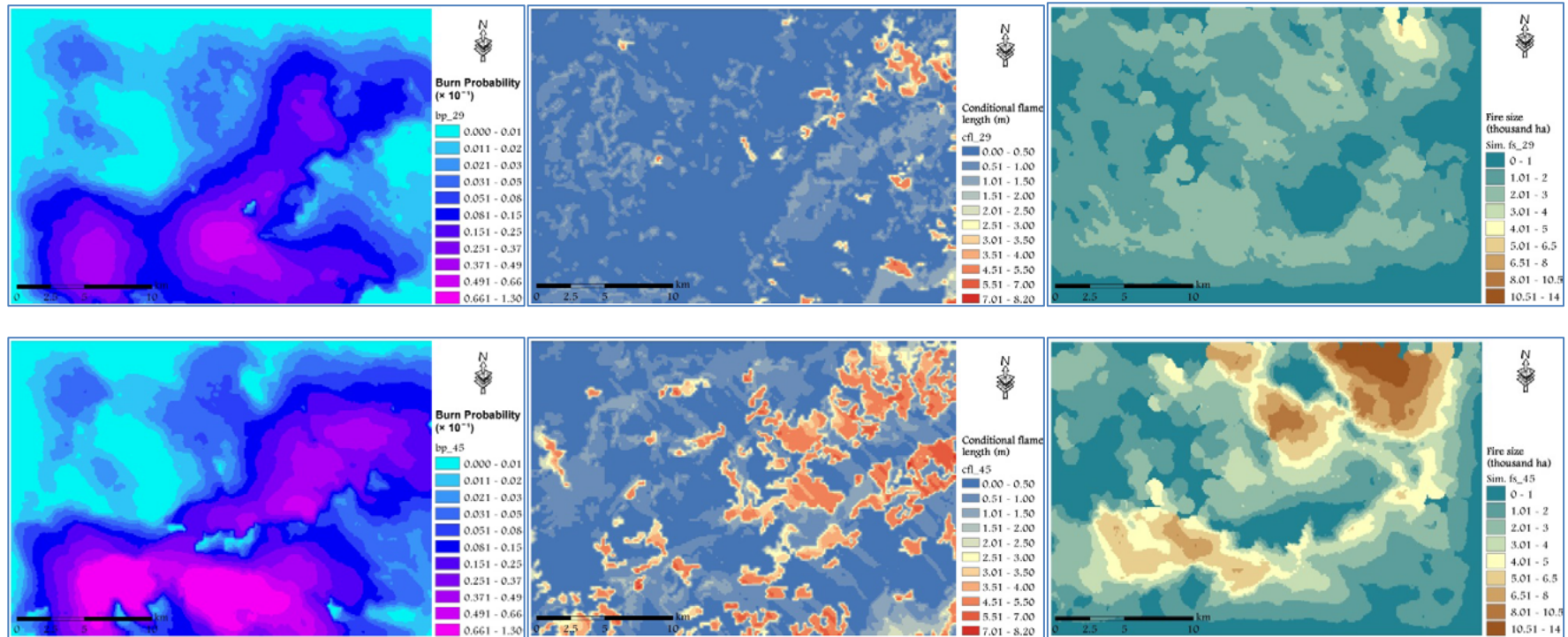


Fig. 3: Maps of burn probability (left), flame length (center), and fire size (right) considering fuel model maps of 1954 (top) and 2000 (bottom). These simulations were run holding constant wind speed (35 km h^{-1}) and direction (315°), fuel moisture (extreme), and using historical ignitions pattern.

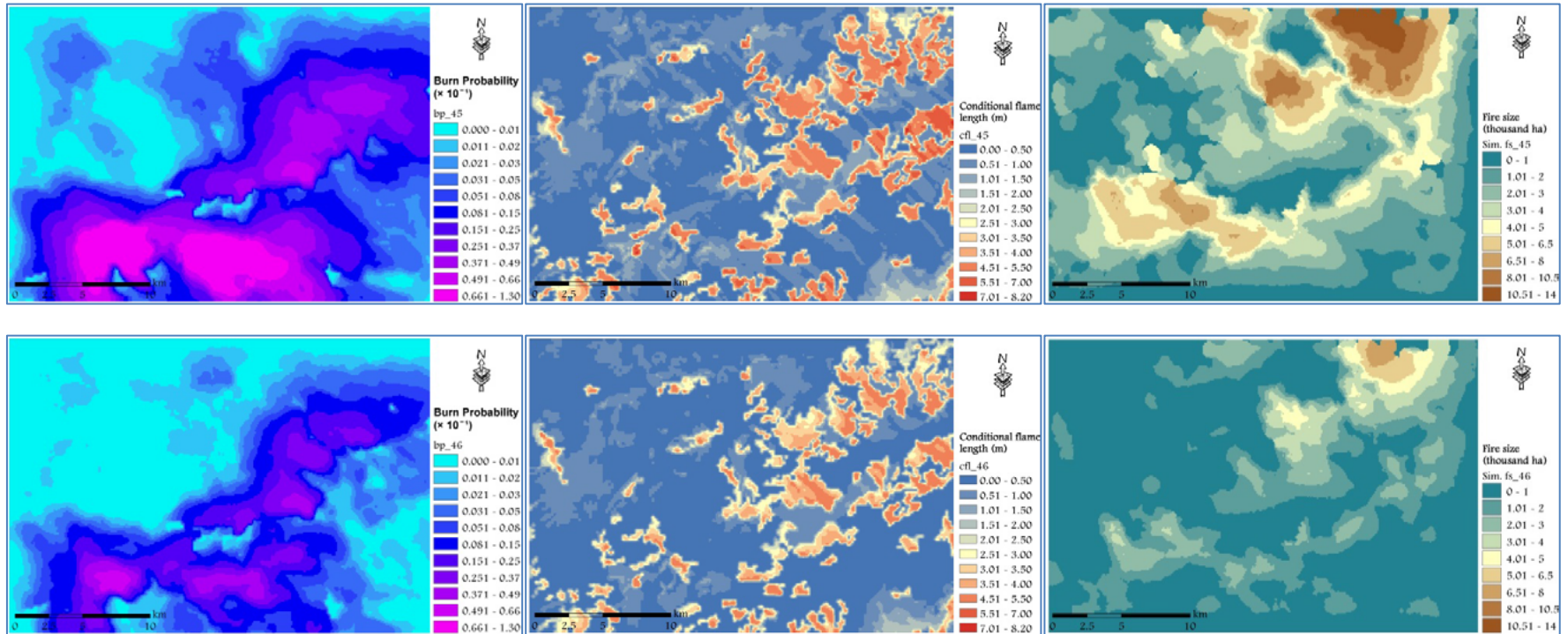


Fig. 4: Maps of burn probability (left), flame length (center), and fire size (right) considering fuel moisture conditions extreme (top) and very dry (bottom). These simulations were run holding constant wind speed (35 km h^{-1}) and direction (315°), fuel model maps of 2000, and using historical ignitions pattern.

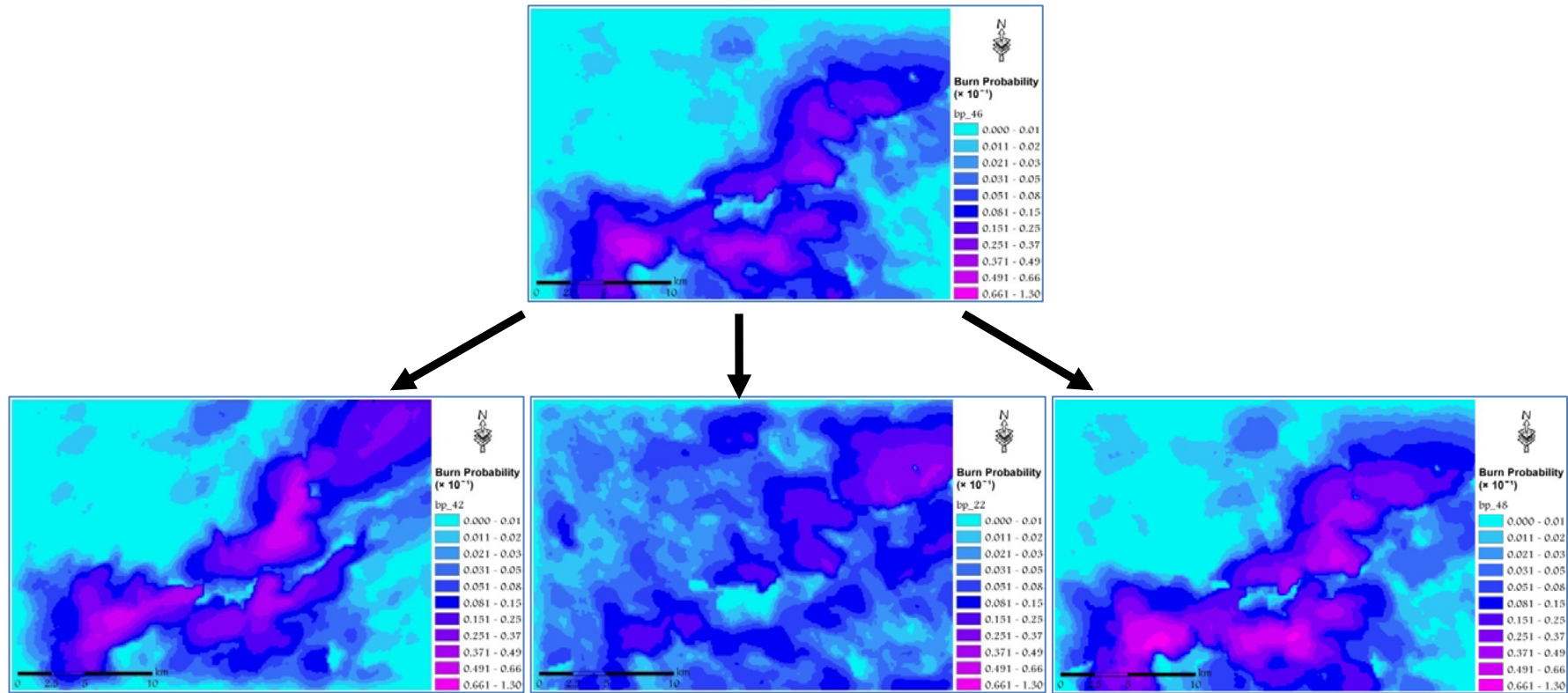


Fig. 5: Map of burn probability (top) considering wind speed 35 km h⁻¹ and direction 315°, fuel model maps of 2000, fuel moisture extreme, and using historical ignitions pattern. The burn probabilities obtained varying, from the reference output (top), single input data (wind direction, from 315° to 225° (left); ignition patterns, from historically based to random (middle); wind speed, from 35 to 25 km h⁻¹ (right) are showed in the bottom maps

4. DISCUSSION

This work investigated how different combinations of ignition patterns, land use changes, fuel moisture and wind fields can affect potential fire likelihood and intensity at landscape scale, using a fire modeling approach based on the MTT algorithm (13).

Our analysis revealed that a key role is played by fuel moisture, which can greatly influence fire spread and behavior in the simulations. The shift from very dry to extreme fuel moisture conditions resulted in strong increases in BP and FS, although CFL did not change so relevantly. This important finding should be taken into consideration in a climate change context, since an increase of temperatures and a reduction of summer rainfall, together with increasing frequency and duration of heat waves, would inevitably lead to greater likelihood of having strongly dehydrated live and dead fuels, capable of sustaining active fire spread. Another interesting outcome resulted from the analysis of the influence of land use changes on BP and fire behavior. In our study area, there was a net increase in forest areas (mainly of Mediterranean maquis and broadleaf forests) at the expense of agricultural areas and pastures, in particular from 1977 to 2000. This change was mostly due to land abandonment, exodus towards urban and coastal areas, and reduction of livestock pressure in the less productive pastures. The observed increase in forest areas affected the wildfire potential by increasing mean BP, FS and CFL of about 50%. This was expected, since the forest types of the study area are characterized by high fuel load, with an important fine dead fuel component, and live fuels highly flammable (particularly for several species of the maquis). In addition, the fact that the broadleaf crown architecture is characterized by low base height increases the probability of transition from surface to crown fires, which inevitably leads to a rise in fire intensity and in the difficulty of suppression for fire fight teams. This result highlighted the need to properly manage forest fuels, particularly by giving more attention to tree crowns architecture and surface fuel load, in order to limit wildfire potential; this becomes crucial in the Mediterranean Basin where socio-economic changes are resulting in exodus from rural areas and forests to urban and coastal areas. Besides, such migrations lead to a progressive reduction of cattle and grazing (which had contributed to ensure a reduction of surface fuel load in the past), and to an increased incidence of ladder fuels and of forest types with low height and crown base height. An important result concerns the use of different ignition patterns, which led to variations in fire distribution and spatial concentration outputs, but to limited differences in BP, FS and CFL. In fact, the ignition point distribution is a key element that determines the actual fire exposure of values and

ecosystems at landscape scale. On the other hand, since in the Mediterranean area fires are basically human-caused, the prediction and forecasting of spatio-temporal distribution of fire occurrence becomes a very complex task. Finally, the wind direction and intensity had a remarkable effect on burn probability and wildfire behavior. With regard to wind direction, the effect was mainly the production of preferential fire spread directions, as expected. In our work, the fires simulated with wind direction from 225° presented the main propagation axis oriented SW-NE, and wind from 315° led to a main propagation axis oriented NW-SE. These two directions led to significantly different spatial distribution of BP and FS, although the mean values did not present significant differences between the two scenarios. Wind speed played a more significant role, since the perimeter and the area burned were related to wind speed, with higher BP and FS being observed for the scenario with 25 km h^{-1} than with 35 km h^{-1} . This result was not surprising since fires spreading with very strong winds (e.g. 35 km h^{-1}) tend to propagate with a clear predominance of the heading, and follow the main wind direction; so fire flanks are not able to widen, and the final fire perimeters are very stretched. Conversely, with lower wind speed (e.g. 25 km h^{-1}), the fire shape tends to be less elongated and less eccentric, since the flanking propagation assumes greater importance. This study provides important guidelines and relevant information to evaluate how different scenarios can affect burn probability, fire intensity, fire size, and fire rate of spread. Such analysis can allow for strengthening awareness of risks related to wildfires, and can help defining the best strategies and policies to be adopted to mitigate fire risk. The results should be taken into account for fire management activities also in the light of future changes, since well-defined adaptation and mitigation strategies are needed to face the worst combinations of environmental conditions that might lead to very large and intense fires. Also, the combination of the results obtained for the tested scenarios represent an important and objective tool for prioritizing fuel management in specific areas and for assessing fire hazard and exposure in fire management and operative phases.

5. ACKNOWLEDGMENTS

This work was partially funded by the GEMINA Project - MIUR/MATTM n. 232/2011, by the Extreme Project (Sardinia Regional Project, CRP-25405, L.R. 7/2007), and by the FUME Project - FP7/2007-2013, Grant Agreement 243888.

6. REFERENCES

- Ager A.A., Finney M.A., Kerns B.K. & Maffei H. (2007), *Modeling wildfire risk to northern spotted owl (*Strix occidentalis caurina*) habitat in Central Oregon, USA*. Forest Ecology and Management, No. 246, pp. 45–56. doi:10.1016/J.FORECO.2007.03.070. (1)
- Ager A.A., Vaillant N.M. & Finney M.A. (2010), *A comparison of landscape fuel treatment strategies to mitigate wildland fire risk in the urban interface and preserve old forest structure*. Forest Ecology and Management, No 259, pp. 1556–1570. doi:10.1016/J.FORECO.2010.01.032. (2)
- Alcamo J., Moreno J.M., Novaky B., Bindi M., Corobov R., Devoy R.J.N., Giannakopoulos C., Martin E., Olesen J.E. & Shvidenko A. (2007), *Europe. Climate Change 2007: Impacts, Adaptation and Vulnerability*. Contribution of Working Group II to the Fourth Assessment Report of the Intergovernmental Panel on Climate Change. C. U. Press. Cambridge, United Kingdom, pp. 541–580. (3)
- Anderson H.E., (1982), *Aids to determining fuel models for estimating fire behaviour*. USDA Forest Service, Intermountain Forest and Range Experiment Station, General Technical Report INT-GTR-122, Ogden, UT. (4)
- Arca B., Salis M., Pellizzaro G., Bacciu V., Spano D., Duce P., Ager A.A. & Finney M.A. (2010), *Climate change impact on fire probability and severity in Mediterranean areas*. In ‘VI International Conference on Forest Fire Research’, 5–18 November 2010, Coimbra, Portugal, Ed. Viegas, D.X., University of Coimbra: Coimbra, Portugal. Available at <http://www.treesearch.fs.fed.us/pubs/39345>. (5)
- Baeza M.J., De Luis M., Raventos J. & Escarré A. (2002), *Factors influencing fire behaviour in shrublands of different stand ages and the implications for using prescribed burning to reduce wildfire risk*. Journal of Environmental Management, No 65, pp. 199–208. doi:10.1006/JEMA.2002.0545. (6)
- Bajocco S. & Ricotta C. (2008), *Evidence of selective burning in Sardinia (Italy): which land cover classes do wildfires prefer?*, Landscape Ecology, No 23, pp. 241–248. doi:10.1007/S10980-007-9176-5. (7)
- Brown T.J., Hall B.L. & Westerling A.L., (2004), *The impact of twenty-first century climate change on wildland fire danger in the western United States: an applications perspective*, Climatic Change, No 62, pp. 365–388. (8)

- Castellnou M., Kraus D. & Miralles M. (2010), *Prescribed 464 Burning and Suppression Fire Techniques: from Fuel to Landscape Management*, In Montiel C and Kraus D (ed.), *Best Practices of Fire Use-Prescribed Burning and Suppression Fire Programmes in Selected Case-Study Regions in Europe*. (9)
- Castellnou M. & Miralles M. (2009), *The great fire changes in the Mediterranean – the example of Catalonia, Spain*, *Crisis Response*, No 5, pp. 56–57. (10)
- De Luis M., Baeza M.J., Raventos J. & Gonzales-Hidalgo J.C. (2004), *Fuel characteristics and fire behaviour in mature Mediterranean gorse shrublands*, *International Journal of Wildland Fire*, No 13, pp. 79–87. doi:10.1071/WF03005. (11)
- FAO (2007), *Fire management – Global assessment 2006*, Food and Agriculture Organization of the United Nations, Forestry Paper No 151, Rome, Available at <ftp://ftp.fao.org/docrep/fao/009/a0969e/a0969e00.pdf>. (12)
- Finney M.A. (2002), *Fire growth using minimum travel time methods*, *Canadian Journal of Forest Research*, No 32, pp. 1420–1424. (13)
- Finney M.A. (2006), *An overview of FlamMap fire modeling capabilities*, in "Fuels Management – How to Measure Success: Conference Proceedings", 28–30 March, Portland, OR, Eds PL Andrews, BW Butler, USDA Forest Service, Rocky Mountain Research Station, Proceedings RMRS-P-41, pp. 213–220, Fort Collins, CO. (14)
- Finney M.A., Seli R.C., McHugh C.W., Ager A.A., Bahro B. & Agee J.K. (2006), *Simulation of long-term landscape-level fuel treatment effects on large wildfires*, in "Fuels Management – How to Measure Success: Conference Proceedings", 28–30 March, Portland, OR., Eds PL Andrews, BW Butler, USDA Forest Service, Rocky Mountain Research Station, Proceedings RMRS-P-41, pp. 125–148. (Fort Collins, CO). (15)
- Koutsias N., Arianoutsou M., Kallimanis A.S., Mallinis G., Halley J.M. & Dimopoulos P. (2012). *Where did the fires burn in Peloponnisos, Greece the summer of 2007? Evidence for a synergy of fuel and weather*, *Agricultural and Forest Meteorology*, No 156 (1), pp. 41-53. - doi: 10.1016/j.agrformet.2011.12.006. (16)
- Martinez J., Vega-Garcia C. & Chuvieco E. (2009), *Human-caused wildfire risk rating for prevention planning in Spain*. *Journal of Environmental Management*, No 90, pp. 1241–1252. doi:10.1016/J.JENVMAN.2008.07.005. (17)

- Martins Fernandes P.A. (2001), *Fire spread prediction in shrub fuels in Portugal*, Forest Ecology and Management, No 144, pp. 67–74. doi:10.1016/S0378-1127(00)00363-7. (18)
- Moreira F., Viedma O., Arianoutsou M., Curt T., Koutsias N., Rigolot E., Barbati A., Corona P., Vaz P., Xanthopoulos G., Mouillot F. & Bilgili E. (2011) *Landscape – wildfire interactions in Southern Europe: implications for landscape management*, Journal of Environmental Management, No 92, pp. 2389-2402. (19)
- Moritz M.A., Parisien M.A., Batllori E., Krawchuk M.A., Van Dorn J., Ganz D.J. & Hayhoe K. (2012), *Climate change and disruptions to global fire activity*. Ecosphere, No 3(6), art. 49. <http://dx.doi.org/10.1890/ES11-00345.1>. (20)
- Parisien M.A., Snetsinger S., Greenberg J.A., Nelson C.R., Schoennagel T., Dobrowski S.Z. & Moritz M.A. (2012), *Spatial variability in wildfire probability across the western United States*. International Journal of Wildland Fire. <http://dx.doi.org/10.1071/WF11044>. (21)
- Pausas J.G. & Fernández-Muñoz S. (2012), *Fire regime changes in the Western Mediterranean Basin: from fuel-limited to drought-driven fire regime*, Climatic Change, No 110, pp. 215-226. (22)
- Pellizzaro G., Ceseraccio C., Duce P., Ventura A. & Zara P. (2007), *Relationships between seasonal patterns of live fuel moisture and meteorological drought indices for Mediterranean shrubland species*, International Journal of Wildland Fire, No 16(2), pp. 232–241. (23)
- Pyne S.J., Andrews P. & Laven R.D. (1996), *Introduction to Wildland Fire (Second Edition)*, John Wiley and Sons, New York. (24)
- Salis M., Ager A.A., Arca B., Finney M.A., Bacciu V., Duce P. & Spano D. (2012a), *Assessing exposure of human and ecological values to wildfire in Sardinia, Italy*, International Journal of Wildland Fire, DOI: 10.1071/WF11060. (25)
- Salis M., Diana G., Casula F., Farris G., Farris O., Licheri F., Musina G., Orotelli S., Peluffo L., Pirisi A.M., Bacciu V., Fois C., Sirca C. & Spano D. (2012b), *Potential effects of prescribed burning and tactical fires on fire risk mitigation*, In Spano, D., Bacciu, V., Salis, M. & Sirca, C. (eds.), Modelling Fire Behaviour and Risk, pp. 174-180, ISBN 978-88-904409-7-7. Nuova Stampa Color, Muros (SS) – Italy. (26)
- Salis M., Mavuli S., Falchi S., Piga A., Desole G., Montesu G.P. & Spano D. (2012c), *Extreme wildfire spread and behavior: a case study from North Sardinia*, In Spano, D., Bacciu V., Salis M. & Sirca C. (eds.),

Modelling Fire Behaviour and Risk, pp. 138-144, ISBN 978-88-904409-7-7. Nuova Stampa Color, Muros (SS) – Italy. (27)

Sardinia Forest Service, (2009), *Piano Regionale di Previsione, Prevenzione e lotta attiva contro gli incendi boschivi 2008-2010*, Available at: http://www.sardegnaambiente.it/documenti/1_73_20090612104212.pdf, [Verified 18 September 2012; in Italian]. (28)

Scott J.H. & Burgan R. (2005), *Standard fire behavior fuel models: a comprehensive set for use with Rothermel's Surface Fire Spread Model*, USDA Forest Service, Rocky Mountain Research Station, General Technical Report RMRS-GTR-153. (Fort Collins, CO). (29)

Thompson M.P., Ager A.A., Finney M.A., Calkin D.E. & Vaillant N.M. (2012), *The Science and Opportunity of Wildfire Risk Assessment*, Novel Approaches and Their Applications in Risk Assessment, Dr. YuzhouLuo (Ed.), ISBN: 978-953-51-0519-0, InTech, Available from: <http://www.intechopen.com/books/novel-approaches-and-their-applications-in-risk-assessment/advancementsin-integrated-wildfire-risk-assessment>. (30)

Thompson M.P., Calkin D.E., Finney M.A., Ager A.A. & Gilbertson-Day J.W. (2011), *Integrated national-scale assessment of wildfire risk to human and ecological values*. Stochastic Environmental Research and Risk Assessment, No 25, pp. 761–780. doi:10.1007/S00477-011-0461-0. (31)

Trigo R.M., Pereira J.M.C., Pereira M.G., Mota B., Calado M.T., Da Camara C.C. & Santo F.E. (2006), *Atmospheric conditions associated with the exceptional fire season of summer 2003 in Portugal*, International Journal of Climatology, No 26, pp. 1741–1757. doi:10.1002/JOC.1333. (32)

Skill assessment of the global model EC-Earth in fire danger indices evaluation over the Greater Alpine Region: a comparison with the corresponding ERA-Interim Reanalysis parameters

Barbarino S.^{1,2*}, Cane D.², von Hardenberg J.¹, Pelosini R.², Provenzale A.¹

¹ ISAC-CNR, Torino, Italy

² Arpa Piemonte (Regional Agency for Environmental Protection), Torino, Italy

*Corresponding author: s.barbarino@arpa.piemonte.it

Abstract

Wildfires represent a very relevant phenomenon in Europe: besides the heavily involved Mediterranean area, the alpine region also experiences an increasing summer fire occurrence. First resource for fire fighting and prevention is the fire danger assessment evaluated by fire danger indices, which require local weather information to be computed.

In this study we investigate the application of the global climate model EC-Earth to mesoscale impact studies as wildfires over such area. The preliminary aim is the skill assessment of fire danger indices produced by such model on a region characterized by specific forest fire regimes. A prospective study could be addressed to the application of EC-Earth scenario runs, which exploit the new Representative Concentration Pathways, to have future fire potential scenarios in this region, as it is likely to be particularly prone to a strong warming in the future according to current projections.

We focused our analysis on the Canadian Fire Weather Index and its component, the Fine Fuel Moisture Code, related to daily weather variability. The analysis focuses on the Greater Alpine Region over the period 1979-2003.

The study compares both the input weather parameters and fire danger indices obtained from EC-Earth runs with the corresponding ERA-INTERIM data. The results indicate that EC-Earth variables are generally representative of the ERA-INTERIM climate although a slight cold bias turns out in temperature and a weaker spatial correlation occurs along the vegetative season, mainly over the Alps. The comparison of fire indices with their input parameters shows a reasonable agreement: EC-Earth FFMC reproduces also the highest percentiles, corresponding to extreme fire events, whereas FWI results have a slight poorer skill in representing extreme distribution values. The results are therefore encouraging in the application of EC-Earth scenarios to evaluate climate change impacts on forest fire potential over the Greater Alpine Region.

Keywords: EC-EARTH, forest fire danger, Fire Weather Indices



1. INTRODUCTION

In Europe wildfires represent a very relevant phenomenon. The regions around the Mediterranean Sea are commonly recognized to be the most prone to forest fires: besides changes of farm-land use, droughts and higher temperature also contributed to a raise of fire occurrence [1]. The Alpine chain is usually not considered to be strongly affected by wildfires; nevertheless it is experiencing an increasing fire occurrence during summer, with growing number of events and severity. In addition, a recent analysis showed a change in fire seasonality [3] and current climate scenarios predict a particularly strong warming over such area [4], thus favouring the meteorological conditions suitable for forest fire ignition.

Wildfires give rise to a huge effect on lives, natural heritage and ecosystem services and require a strong employment of human and economic resources for fire fighting and suppression. The targeted prevention, through forest management and collective preparedness, is the only sustainable action to preserve the forest resource. That outlook highlights the importance to achieve reliable forest fire potential assessment techniques aimed to properly evaluate future fire potential projections.

In this study we investigate the application of the global climate model EC-Earth [5], [6] to mesoscale impact studies as wildfires over this region.

The preliminary aim is the skill assessment of fire potential evaluation computed from EC-Earth historical runs by a comparison with the corresponding ERA-Interim Reanalysis parameters.

A prospective study could be addressed to the application of EC-Earth scenario runs in order to have future fire potential projections.

Tools usually employed to assess fire potential are represented by a variety of fire weather indices that are used by the operational fire prevention systems worldwide: they are calculated from local daily weather conditions with the aim to provide alert levels related to forest fire danger. One of the most applied fire danger indices in the world is the Canadian Fire Weather Index (hereafter, FWI), based on the Canadian Forest Fire Danger Rating System [7]. Conceived and initially used in Canada, it is currently employed in many countries worldwide and adopted by the European Joint research Centre to produce fire danger index maps (effis-viewer.jrc.ec.europa.eu/). The Fire Weather Index System consists of six components, three fuel moisture codes and three fire behaviour indices. The three fuel moisture codes refer to daily variations of the moisture content of classes of fuel with different drying

rates, other two components represent rate of spread of propagation and burning fuel availability. The last index FWI is the combination of such components and expresses the expected intensity of the flame front. The FWI System is calculated using four input variables taken each day at noon local standard time: temperature, relative humidity, wind speed and previous 24 hourly accumulated precipitation [7].

In order to have a wide overview on the skill of the model, we focused our study on the evaluation both of FWI and the Fine Fuel Moisture Code (hereafter, FFMC), the FWI component referring to the moisture content of the superficial layer of litter and fine dead fuels. The FFMC is an indicator of the relative ease of ignition and flammability of fine fuels and it has the fastest response time in weather conditions changes [7]. Moreover FFMC is strongly correlated with temperature, which is one of the parameters most representative of the future climate changes.

2. DATA AND METHODS

EC-Earth model

EC-Earth is a fully coupled AOGCM [5] based on the concept of “seamless predictions”: climate and weather forecasting are based on the same physical principles, in spite of their different purposes and the introduction of the concept 'seamless prediction' intends to address the predictability of the Earth's climate system within one common framework (<http://www.knmi.nl/cms/content/93093/>), “blurring of the distinction between shorter-term predictions and longer-term climate projections” [8]. Numerical weather prediction (NWP) models are indeed state-of-the art models which actually can provide advanced atmospheric components for climate models (<http://www.to.isac.cnr.it/ecearth/>).

EC-Earth is a recent earth-system model developed by a consortium of European research institutions and researchers, based on state of-the-art models for the atmosphere, the ocean, sea ice and the biosphere (<http://www.to.isac.cnr.it/ecearth/>). The development of EC-Earth within the EC-Earth consortium started with the operational seasonal forecast system ECMWF's Integrated Forecast System (hereafter, IFS) as a well-tested atmospheric module, with different components being added over time (<http://www.knmi.nl/cms/content/93093/>).

EC-Earth currently consists of two main components: an atmosphere, chemistry, land and vegetation model and an ocean and sea-ice model. Each of these two main elements respectively comprise various

sub-components for the representation of physical processes and properties related to the biological and geochemical parts of the climate [9]. The ocean model is the Nucleus for European Modelling of the Ocean NEMO [10]. The land surface component in IFS is modelled using the Hydrological extension of the Tiled ECMWF Surface Scheme for Exchanges processes over Land HTESSEL [11], whereas the sea-ice module The Louvain-la-Neuve sea-Ice Model LIM2 [12] ends the set of modules being coupled with IFS.

The version of EC-Earth used in this study is the V2.2 and it consists of a fully coupled AOGCM, with oceanic (NEMO), sea ice (LIM2) and land surface (HTESSEL) components having been coupled to the IFS through the OASIS3 coupler [9], [13]

(<http://www.knmi.nl/cms/content/93093/>). The model can be run at different resolutions. Here, we use a horizontal spectral resolution of T159 (which corresponds to a 1.125 degrees spacing) and 62 vertical levels for the atmosphere and about 1° horizontal resolution and 42 vertical levels for the ocean [5]. The reasons that led to choose a global model to deal with a higher resolution phenomenon as forest fires are suggested by some considerations: in spite of the coarse resolution and the shortcomings of using a global model, EC-Earth represents the most recent next generation earth system model, as just explained. Moreover, the climate change scenario simulations run by this model are obtained by applying the recently developed Representative Concentration Pathways RCPs [14], the new emission scenarios adopted by the IPCC for its fifth Assessment Report AR5 [15], (IPCC 2007). The EC-Earth dataset selected to represent the required variables for the FWI calculation comprises temperature, wind speed and relative humidity taken at 12:00UTC and the previous 24 hourly accumulated precipitation.

ERA-Interim Reanalysis

The benchmark dataset for our analysis is represented by the ERA-Interim Reanalysis, the latest global atmospheric reanalysis produced by the European Centre for Medium-Range Weather Forecasts (ECMWF). The ERA-Interim project is conducted in preparation for the next-generation extended reanalysis to replace ERA-40 Reanalysis dataset, which will extend back to the early part of the twentieth century. It is considered as an 'interim' reanalysis and it covers the period 1979-present [16].

The ERA-Interim input weather variables taken into account are the instantaneous 2m. temperature and 10m. wind speed at 12:00UTC, relative humidity is obtained from 12:00UTC instantaneous 2m.

temperature and 2m. dew point temperature. As concerns precipitation, it is important to highlight that it is a forecast variable: ERA-Interim reanalysis outputs provide accumulated precipitation data at 3-hourly forecast time basis for the analysis time: we used previous 24 hourly accumulated precipitation.

ERA-Interim fields have been retrieved on the EC-Earth grid directly (resolution 1.125°).

Statistical analysis

The domain considered in our study is the Greater Alpine Region (fig.1), (GAR, 4–19°E, 43–49°N 0–3500m a.s.l.) [17], divided in three areas according to the specific forest fire regimes: North of Alps, Alps and Mediterranean area (fig.2). The analysis covers the period 1979-2003, looked at a sort of control period, in the aforementioned perspective of the EC-Earth scenario runs application.

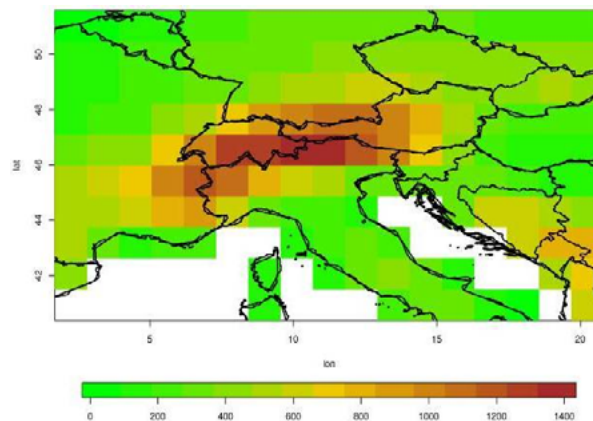


Fig. 1: The Greater Alpine Region (GAR) orography on the EC-Earth grid



Fig. 2: Areas of analysis: North of Alps (2a), Alps (2b), South of Alps (2c)

We conducted the whole statistical analysis both on the meteorological variables and on the selected fire danger indices: time span was split into vegetative and non vegetative season, due to proper fire seasons.

In order to assess the skill of EC-Earth historical simulations in reproducing extreme distribution values, a percentile analysis was considered. For each grid point the 50^o, 90^o, 95^o percentile values were extracted from the temporal distribution and depicted on maps.

The spatial correlation between EC-Earth and ERA-Interim data was performed through temperature, precipitation, wind speed and relative humidity scatterplots displaying the mean of grid point temporal distributions over the whole period 1979-2003. A further check was carried on taking into account precipitation/non precipitation days and the length on dry periods, both being key drivers for forest fire potential. These comparisons allowed to verify the EC-Earth simulations reliability and to get a confidence level degree on capability to reproduce past condition affecting forest fire regimes. Then we tested the correlation between the input weather variables and the corresponding resulting fire indices FWI and FFMFC. The validation between the EC-Earth and ERA-Interim outputs was done by applying the Pearson product-moment correlation test.

Same kind of information, shown in a different manner, was expressed by correlation maps. Correlation maps provided, in addition to a spatial pattern, an indication about temporal correlation between grid point distributions, instead of the mean on temporal distributions as derived by scatterplots.

Considerations about shapes and general features of distributions were revealed by boxplots and frequency distribution histograms. Such figures indicate the different variable characteristics, regardless any spatial distinction.

3. DISCUSSION AND CONCLUSIONS

Percentile maps show that EC-Earth variables are generally slightly underestimated in comparison with ERA-INTERIM dataset. Differences increase from median to extreme values and are more pronounced during the vegetative season, as general overview. As concern the fire danger indices, FFMC maps provide a quite reasonable agreement: the values obtained from EC-Earth historical runs result similar to ERA-Interim ones, except across North of Alps. FWI maps depict spatial difference patterns quite pronounced, above all regarding high percentile values and during the vegetative season (fig.3a-b-d-e). In summary, it is very important to highlight that, even if absolute values of the entire set of variables calculated from EC-Earth and ERA-Interim are somehow different, however maps indicate that the spatial variations inside the region are in agreement for the most of time domains considered.

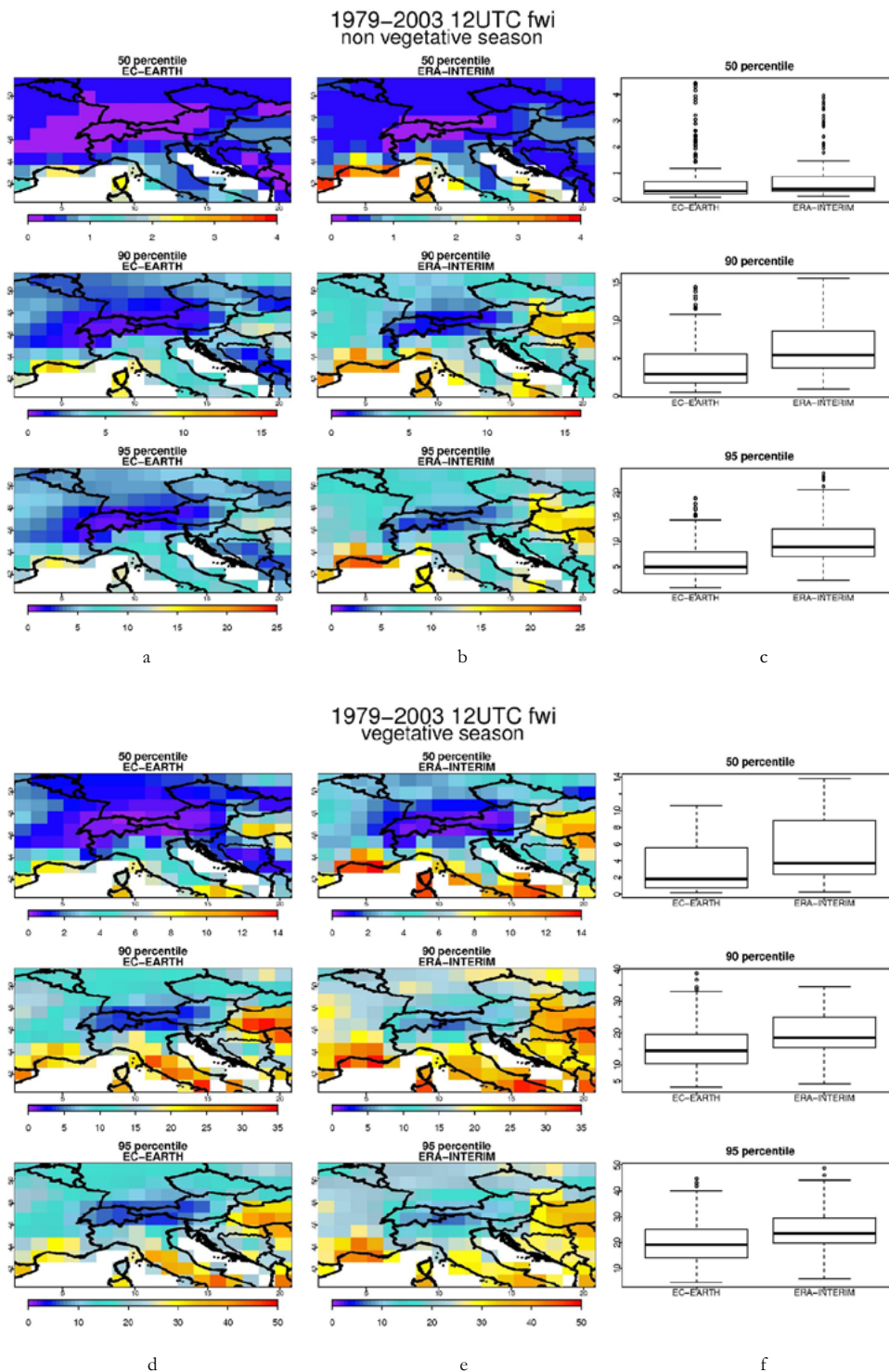


Fig.3: FWI maps. Top panel: non vegetative season (Dec to April), bottom panel: vegetative season (May to Nov). FWI values corresponding to 50°, 90° and 95° percentile of temporal distributions at each grid point are depicted. Left column (2a,2d): EC- Earth; middle column (2b,2e): ERA-Interim; right column (3c,3f): EC-Earth and ERA-Interim boxplots. In order to clearly detect the whole range of differences between EC-Earth and ERA-Interim percentile values, for each percentile map a scale fitting with the degree of differences was used, both for vegetative and non vegetative season.

Frequency distributions and boxplots confirm a slight underestimation regarding the EC-Earth simulations, in particular temperature shows a general cold bias (fig.4). As concerns the fire danger indices evaluation, FWI and FFMC frequency distributions show a general good agreement, although slight differences result for the highest frequency values (fig.5).

1979-2003 Alps temperature distribution

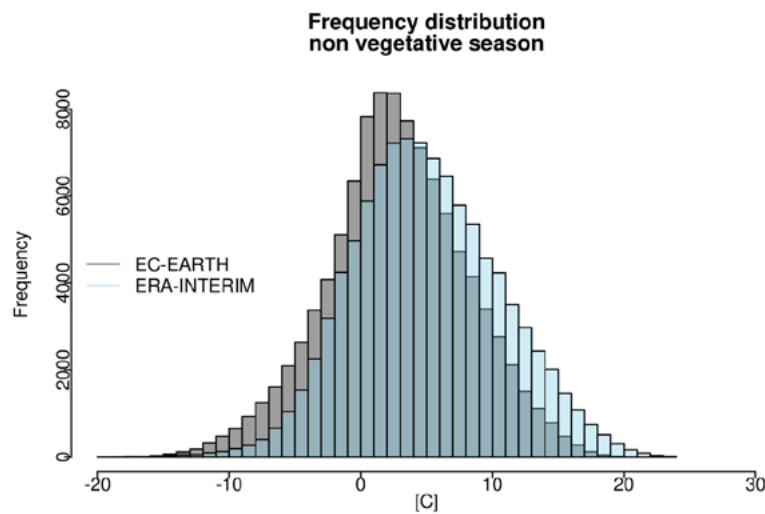


Fig.4: Histogram of temperature frequency distribution over the Alps for EC-Earth outputs (grey) and Era-Interim (sky blue) data. Figure shows a cold bias which affects the whole range of EC-Earth temperature during the non vegetative season.

1979-2003 ffmc distribution

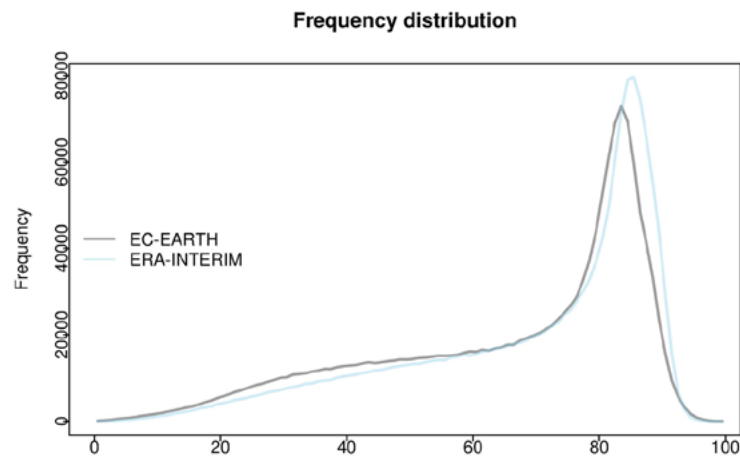


Fig.5: Curve of frequency distribution of Fine Fuel Moisture Code (FFMC) over the GAR. The curves reveal a general good agreement. In particular, they overlap along the median and the highest percentiles values (greater than 90°), usually regarded as thresholds for moderate and extreme fire danger conditions.

Scatterplots provide information not only regarding the agreement between model simulations and reanalysis runs, but also about the consistency among the weather variables and the corresponding fire indices. The latter case is interesting as we can also test the coherency of the ERA-Interim outputs. Scatterplots show a quite good agreement among variables when compared with each other, if considered into a general overview: deviations occur over Alps and North of Alps in both seasons, referring in particular to precipitation scatterplots over the Alps during vegetative season, probably due to the high spatial and temporal variability of summer precipitation pattern (fig.6). FWI scatterplots show a better agreement during non vegetative season and, to a small degree, also FFMC scatterplots provide quite good results. The scatterplots displaying the correlation among input parameters and fire indices show a general quite good agreement, for both model and reanalysis outputs: to be stressed the agreement referring to EC-Earth input-output variables is reasonably comparable with ERA-Interim input-output variables. This confirms the capability of the fire weather indices selected to carry over changes in weather parameters into the forest fire potential framework .

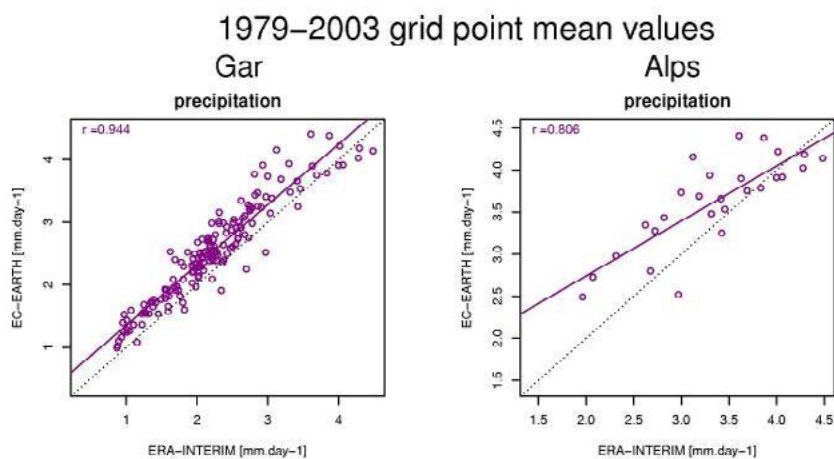


Fig. 6: Scatterplots of precipitation over the vegetative season. Points in the graph represent the mean value of temporal precipitation distributions at each grid point. Left panel: whole GAR grid points; right panel: Alps grid points. Scatterplots on the left display the skill of EC-Earth model in reproducing precipitation over the GAR domain; on the right side, they highlight the shortcomings arising out of the employment of a global climate model to describe properly physical processes that influence precipitation over a region characterized by a complex orography like the Alps.

The purpose of this study was to verify the application of the state-of-the-art earth system model EC-Earth to mesoscale impact studies as wildfires over the Greater Alpine Region. The preliminary aim was the skill assessment of FWI and FFMC fire danger indices by a comparison with the benchmark

ERA-Interim Reanalysis dataset in the control period 1979-2003, in the perspective to apply the EC-Earth scenario runs produced by the recent developed Representative Concentration Patterns (RCPs) to have future projections of fire potential in this region.

Results show that EC-Earth variables are generally representative of the ERA-INTERIM climate although a slight cold bias turns out in temperature and a weaker spatial correlation occurs along the vegetative season, mainly over the Alps. The comparison of fire indices with their input parameters shows a reasonable good agreement. Moreover, FFMC obtained from the EC-Earth model reproduces properly the median and the highest percentile values (greater than 90th percentile), corresponding to moderate and extreme fire events. FWI results have a slight poorer skill in describing extreme distribution values, probably due to the strong sensitivity to the wind field, which is hard to reproduce over a region characterized by a complex orography mainly.

As a whole, results can be considered encouraging for the application of EC-Earth scenario runs to evaluate climate change impacts on forest fire potential both over the Greater Alpine Region and, adopting a proper downscaling technique, over the Alps.

4. ACKNOWLEDGMENTS

This work was conducted with the support of NEXTDATA project (<http://www.nextdataproject.it/>).

5. REFERENCES

- Moriondo M., Good P., Durao R., Bindi M., Giannakopoulos C., & Corte-Real J. (2006), *Potential impact of climate change on fire risk in the Mediterranean area*. *Climate Research*, 31(1), 85-95. (1)
- Reinhard M., Rebetez M., & Schlaepfer R. (2005), *Recent climate change: Rethinking drought in the context of Forest Fire Research in Ticino, South of Switzerland*, *Theoretical and Applied Climatology*, 82(1-2), 17-25. (2)
- Valese E., Conedera M., Vacik H., Japelj A., Beck A., Cocca G., & Wastl C. (2011), *Wildfires in the Alpine region: first results from the ALP FFIRS project*. In *Proceedings of the V International Conference on Forest Fire Research*, Millpress, Rotterdam, The Netherlands. (3)

- Ruosteenoja K., Tuomenvirta H., & Jylhä K. (2007), *GCM-based regional temperature and precipitation change estimates for Europe under four SRES scenarios applying a super-ensemble pattern-scaling method*, *Climatic Change*, 81(1), 193-208. (4)
- Hazeleger W., Severijns C., Semmler T., Stefanescu S., Yang S., Wang X.,... & Willén U. (2010), *EC-earth: a seamless earth-system prediction approach in action*, *Bulletin of the American Meteorological Society*, 91(10), 1357-1363. (5)
- Hazeleger W., Wang X., Severijns C., Ștefănescu S., Bintanja R., Sterl A.,... & van der Wiel, K. (2012), *EC-Earth V2. 2: description and validation of a new seamless earth system prediction model*, *Climate dynamics*, 39(11), 2611-2629. (6)
- Van Wagner, C.E. (1987), *Development and Structure of the Canadian Forest Fire Weather Index System*, No.Canadian Forestry Service Forestry Technical Report 35, Ottawa (7)
- Shukla J., Palmer T.N. , Hagedorn R. , Hoskins B. , J. Kinter J. , Marotzke J. ,...& Slingo J., (2010), *Climate Prediction from Weeks to Decades in the 21st Century: Towards a New Generation of World Climate Research and Computing Facilities*, *Bull. Amer. Meteor. Soc.*, 91(10), 1407-1412. (8)
- Martijn Brandt, *EC-Earth documentation*, (2010),
http://eearth.knmi.nl/ECEarth_model_documentation.pdf. (9)
- Madec G. (2008), *NEMO ocean engine. Note du Pole de modelisation*. Institut Pierre-Simon Laplace (IPSL), France, No 27 ISSN No 1288-1619. (10)
- Dutra E., Balsamo G., Viterbo P., Miranda P.M., Beljaars A., Schär C., & Elder, K. (2010), *An improved snow scheme for the ECMWF land surface model: description and offline validation*. *Journal of Hydrometeorology*, 11(4), 899-916. (11)
- Fichefet T., & Maqueda M. M. (1997), *Sensitivity of a global sea ice model to the treatment of ice thermodynamics and dynamics*. *Journal of Geophysical Research*, 102(C6), 12609-12. (12)
- Valcke S. (2006), *OASIS3 user guide (prism_2-5)*. PRISM support initiative report, 3, 64. (13)
- Moss R.H., Edmonds J.A., Hibbard K.A., Manning M.R., Rose S.K., van Vuuren D.P., ... & Wilbanks T.J. (2010). *The next generation of scenarios for climate change research and assessment*. *Nature*, 463(7282), 747-756. (14)

- Van Vuuren D.P., Edmonds J., Kainuma M., Riahi K., Thomson A., Hibbard K., ... & Rose, S. K. (2011), *The representative concentration pathways: an overview*. *Climatic Change*, 109(1-2), 5-31. (15)
- Dee D. P., Uppala S.M., Simmons A.J., Berrisford P., Poli P., Kobayashi S., ... & Vitart F. (2011), *The ERA-Interim reanalysis: Configuration and performance of the data assimilation system*. *Quarterly Journal of the Royal Meteorological Society*, 137(656), 553-597. (16)
- Auer I., Böhm R., Jurkovic A., Lipa W., Orlik A., Potzmann R., ... & Nieplova, E. (2007), *HISTALP—historical instrumental climatological surface time series of the Greater Alpine Region*. *International Journal of Climatology*, 27(1), 17-46. (17)

Historical trends and future trajectories of fire emission in Italy

Bacciu V.^{1,2*}, Salis M.^{2,1}, Spano D.^{2,1}

¹CMCC-LAFENT Division, Sassari, Italy,

²Dipartimento di Scienze della Natura e del Territorio, University of Sassari, Sassari, Italy

*Corresponding author: valentina.bacciu@cmcc.it

Abstract

Emissions from forest fires are recognized to be an important health and environment issue. Fire emissions include a wide range of gaseous compounds and particles that contribute significantly to the atmospheric budgets at local, regional, and even global scale. This paper aims to present the state of the art of the research concerning forest fire emission inventories, illustrating the principal methodologies and related uncertainties. To this end, this work analyzes historical trends [1970-2010] of fire emissions in Italy through the comparison of several publicly available inventories of biomass burning emissions, highlighting that fire emission estimates are still affected by large uncertainties. Finally, the paper presents an overview of the 21st century fire emissions provided by the new RCPs scenarios.

Keywords: *biomass burning emission, emission inventory, RCP.*



1. INTRODUCTION

Forest fires play a crucial role within the natural ecosystems, with both negative and positive impacts on all biosphere components and with reverberations on different scales, from local to global. Among the primary effects of forest fires, the production of a remarkable amount of greenhouse gases and solid particulate matter is one of the most important [61, 35, 28]. CO₂ and CO, being responsible for about 90–95% of the total carbon emitted [1], are the dominant fractions released by fires. In addition, according to the IPCC [28], fires contributed up to the 40% of the total CO annual budget. The remaining carbon emitted is represented by carbonaceous aerosol [35%], nitrogen oxides [20%], and CH₄ [6%] [IPCC, 2001]. Less than 5% of the carbon is emitted as particulate matter [45]. The remaining fire emissions include other volatile organic carbon compounds.

Fire emissions interfere with local, regional and global phenomena in the biosphere [15, 54] and influence climate [44, 59]. The smoke aerosols can scatter and absorb solar radiation, affecting the atmospheric radiation budget [25, 42, 43] and the terrestrial heat budget [27]. This could influence local wind circulation patterns [27] and cloud dynamics [e.g. cloud formation and microphysical processes, 33, 2, 13]. Neaher et al. [40] highlighted that hydrocarbons and nitrogen oxides can lead to the formation of ozone in smoke plumes, acting as short-lived climate forcing [59]. In addition, recent publications highlighted that fire can be a source of extremely toxic products [e.g. mercury, 17; dioxins, 12].

Due to the consequent increase of primary pollutant emission, fire emissions contribute to air quality degradation [37, 6, 50, 26]. Air pollution episodes caused by fires [e.g. Indonesia and Philippines in 1997/98, California, Russia, Portugal in 2003 and 2005, Italy and Greece in 2007] have brought attention to these issues. The most relevant contribution to air pollution is given by particulate [34, 38, 47, 53], which is also responsible for significant respiratory health problems [11] and reduced visibility effects associated with high ambient concentrations [38]. Other gaseous component such as SO₂, CO, NO_x, O₃ can also cause health problems, such as chronic bronchitis, irritation to respiratory tracts [5], enhanced by exposure to ultra-fine particles [68].

The demand for quantification of fire emission, and the definition of emission inventory, is then growing due to the increased need of governments and companies to account for greenhouse gas emissions [5] and to identify the source of air pollution affecting human health.

Over the past decades, a number of inventories, both at global and regional scale, addressed the above needs. Earlier studies [e.g. 9, 23, 20] made use of biome-averaged fuel load and fire return times, while the latest inventories use satellite remote-sensing data, often combined with biogeochemical models [e.g. 60].

A crucial point to support emissions inventories and modelling of air quality has been recognized in up-to-date, accurate, and consistent fire emission estimates [4, 22]. Although the quality of the inventories is difficult to assess, since the methodology, input data, and assumptions vary strongly between the inventories [22], a helpful method to identify uncertainties in inventory data is the comparison between emission estimates from many inventories [e.g. 22, 56, 33, 30].

From this context, this paper firstly presents the contemporary state of the art on the forest fire emission inventory, and then analyzes historical trends [1970-2010] of fire emission in Italy through the comparison of several publicly available inventories of biomass burning emissions. Finally, the paper presents an overview of the 21st century fire emission provided by the new RCPs scenarios.

2. FIRE EMISSION INVENTORIES

Two main approaches can be recognised for the estimation on GHG and particulates from forest fires. The *bottom-up* approach, as provided by Seiler and Crutzen [49], relies on the equation that converts the burned area into emitted gases taking into account the amount of burnable biomass and the emission factors of a chemical species [g kg^{-1}], which translates biomass burned into trace species emissions. Conversely, the *top-down* approach is based on inversion models, developed in the late 90s, that estimate emissions from atmospheric concentrations [e.g., NASA-MOPITT instrument, 7]. In this paper, we will mainly focus our attention on inventories developed through the *bottom-up* approach and on the different available products used to estimate fire emissions, principally in terms of fire activity and land cover type.

The **RETRO** inventory [48] was the first attempt to produce long period biomass burning estimates. This product is based on the analysis of available literature and datasets, estimates from different satellite products, and a numerical model with semi-physical approach to simulate fire occurrence and spread.

GICC [Global Inventory for Chemistry-Climate studies] inventory [36] was built in two steps. For the recent period [1997-2005] fire emissions were estimated using satellite products [GBA2000 burnt areas and ATSR fire hotspots], whereas the historical period, covering from 1900 to 2000 on a decadal basis, is derived from the historical reconstruction of burned areas from Mouillot and Field [39]. The historical emission estimates are forced, for each main ecosystem, to agree with the 1997-2005 estimates, ensuring consistency between past and recent emissions.

GFED2 and **GFED3** inventories [60, 61] provide emissions on a monthly basis for the period 1997-2004 and 1997-2010, respectively. The datasets were built combining burned area data from MODIS direct broadcast algorithms with a biogeochemical model [CASA-GFED] that estimates fuel loads and combustion completeness for each monthly time step. GFED3 differs from GFED2 in the restricted use of active fire counts, and in several changes applied to the algorithm for the vegetation parameterization [56].

EDGAR4.2 [30] provides global biomass burning emissions of greenhouse gases and air pollutants for a broad period [1970-2008]. For the period 1997-2005, EDGAR4.2 depends on GFED2 inventory, whereas from 1970 to 1996 EDGARv4.2 is based on the GFED2 inventory scaled back with regional biomass burning trend from RETRO.

GUESS-ES [31] is computed using the LPJ-GUESS ecosystem model [50] with burned area based on the GFED3 database [21], at a monthly time step, using biome-specific emission factors by Andreae and Merlet [1] updated 2008.

ACCIMIP historical dataset [33] provides decadal monthly mean biomass burning emissions for the period 1850-2000. The best guess estimate for biomass burning emissions was established from a combination of three datasets (GICC, RETRO, and GFEDv2) [33]. Carbon emission fluxes from the these three datasets were first harmonized, taking the 2000 estimate from GFEDv2; the vegetation cover map is derived from the MODIS predominant vegetation cover map as provided with the GFEDv2 inventory [60]. The ACCIMIP inventory was extended at monthly base for the 1997–2008 period as part of the MACC and CityZen projects [we will use the **MACCity** acronym to represent this inventory] [10].

Inventory	Time coverage	Time Resolution	Grid Size	Species						
				CO ₂	CH ₄	CO	NO _x	SO ₂	BC	PM _{2.5}
MACCity	1960-2010	M	0.5°		●	●	●	●	●	
ACCMIP	1850-2000	D	0.5°	●	●	●	●	●	●	
RETRO	1960-2000	M	0.5°	●	●	●	●	●	●	●
EDGARv4.2	1970-2000	Y	0.5°	●	●	●	●	●		
GICC	1900-2005	D/M	0.5°	●	●	●		●	●	
GFED3	1997-2010	M	0.5°	●	●	●	●	●	●	●
GFED2	1997-2005	M	1.0°	●	●	●	●		●	●
GUESS-ES	1997-2009	M	1.0°	●	●	●	●	●	●	●

Tab. 1. Basic characteristics of the biomass burning inventories reviewed and used in this study [other information can be found at the web site www.eccad.sedoo.fr]

3. COMPARISONS OF BIOMASS BURNING EMISSIONS

In this section, we present the comparison of CO₂, CO, and BC [black carbon] fire emissions for the 1970-2010 period deriving from the height inventories illustrated in the previous section and in Tab. 1. The first two species were selected due to the fact that together are responsible for the 97% of the total carbon emitted by fires, and due to the CO precursor role of ozone [O₃] [56]. The BC was selected because its deposition results in a decrease of surface albedo [e.g. 55] inducing a positive radiative forcing.

The analyzed emission datasets seemed to capture well the inter-annual variability showed by the Italian burned areas from 1970 to 2010 [Fig. 1, A]. However, there are some evident differences in the magnitude of the estimates among the considered inventories. Overall, MACCity, ACCMIP, and RETRO inventories showed the lowest emissions, whereas EDGAR4.2 and GICC [after 2000] emissions are the highest.

Until the 1997, for CO₂, only two long term emission inventories were available at monthly base [EDGAR4.2 and RETRO], and other two were accessible on a decadal base [ACCIMIP and GICC]. In the 1970s, ACCIMIP, RETRO, and GICC inventories agreed returning a mean value of 1.2 Tg decade⁻¹, while EDGAR4.2 showed an average of 4.2 Tg decade⁻¹, with a difference of a factor of 3.3. In 1980s and 1990s, the mean difference was of a factor of 3. During 2000s, GICC inventory showed the higher estimate [on average 5.2 Tg year⁻¹] in comparison with the other datasets.

CO and BC emissions showed a similar pattern [Fig.1, C and D]. During the 1970s, the highest values were given in 1970 by EDGAR4.2 dataset [0.25 Tg CO] and RETRO [5.8E⁻⁰⁴ Tg BC], while the lowest values were given in 1976 by MACCity, at 0.03 Tg CO and 1.9E⁻⁰⁴ Tg BC. ACCIMIP and GICC provided decadal mean of 0.06 and 0.078 Tg CO. Overall, the mean difference between the lowest and highest total CO emissions was about a factor of 3 in both the 1970s and the 1980s. The mean difference among inventories was of a factor of 1.6 and 1.9 for BC respectively in 1970s and 1980s. During the 1990s, EDGAR4.2 dataset showed a convergence with the other datasets, while on the other hand GICC showed the highest values among inventories.

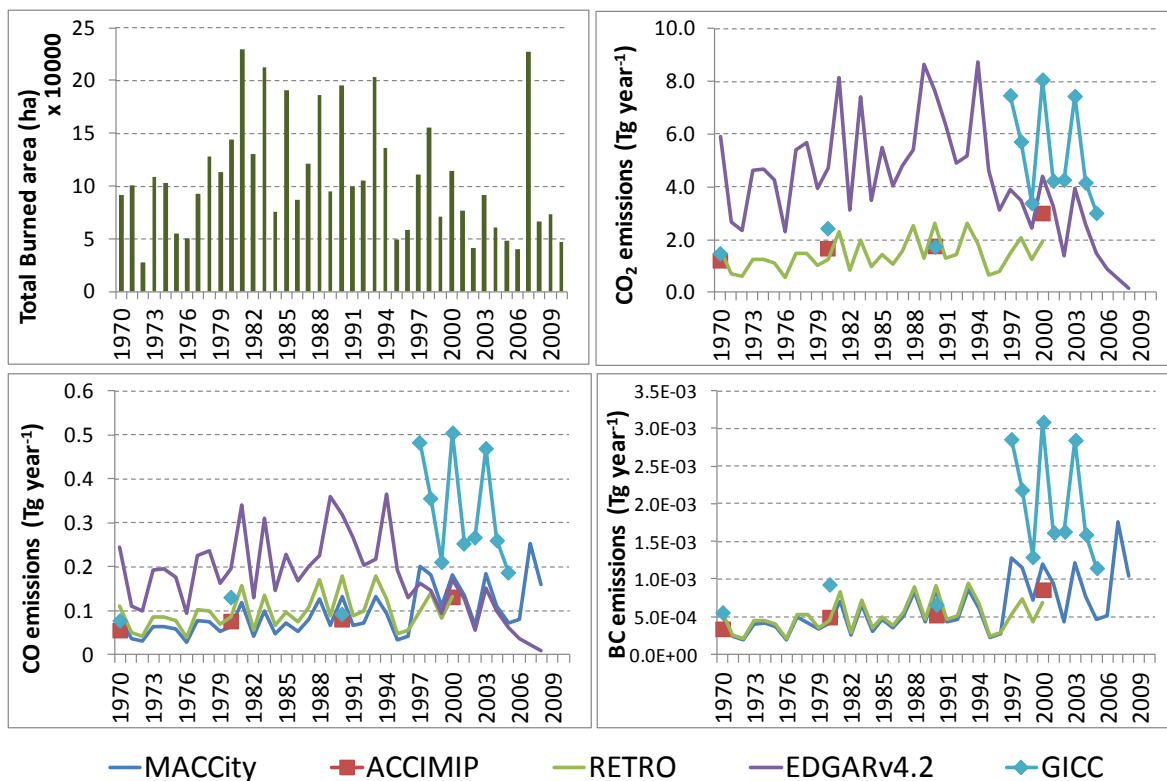


Fig. 1: Total burned area [A] and comparison of fire emissions for the 1970-2010 period in Italy: [B] emissions of CO₂, [C] CO, and [D] BC .

We also compared the CO and CO₂ emission from Italian National Inventory Report [NIR, 2011] with the mean of five datasets [EDGARv4.2, GICC, GFED3, GFED2, GUESS-ES] for the common period 1997-2005. The NIR inventory collected the greenhouse gas for the 1990-2009 period in accordance with the United Nation Framework Convention on Climate Change guidelines [58]. The NIR methodology estimated the CO₂ amount released by forest fires assuming combustion completeness equal to 1 [all stocks completely oxidized by fire] and assigning forest typologies burned based on their respective weight on total national forest area, considering the total value of burned forest area from national statistics.

CO₂ data from NIR were well above the mean of the six datasets, and in few cases [1997, 1998, and 2001] above the range [Fig. 2]. In general, the NIR average for the analyzed period was higher than the five data sets mean by a factor of 1.7. CO data from NIR showed a different trend, being under the mean of the six data sets and very close to the minimum values of the range. In that case, the NIR average for the analyzed period was lower than the five data sets mean by a factor of 0.7 [Fig. 2].

The evidenced differences are likely to derive from different methods of burned area estimates [different satellite sensors *vs* national statistics], as well as from discrepancy between biomass estimation methods and emission factors [56]. For example, the emissions provided by GFED3 are lower than the GFED2 estimates, mainly due to the use of a new burned area data set, as well as upgraded emission factors for woodland burning [61].

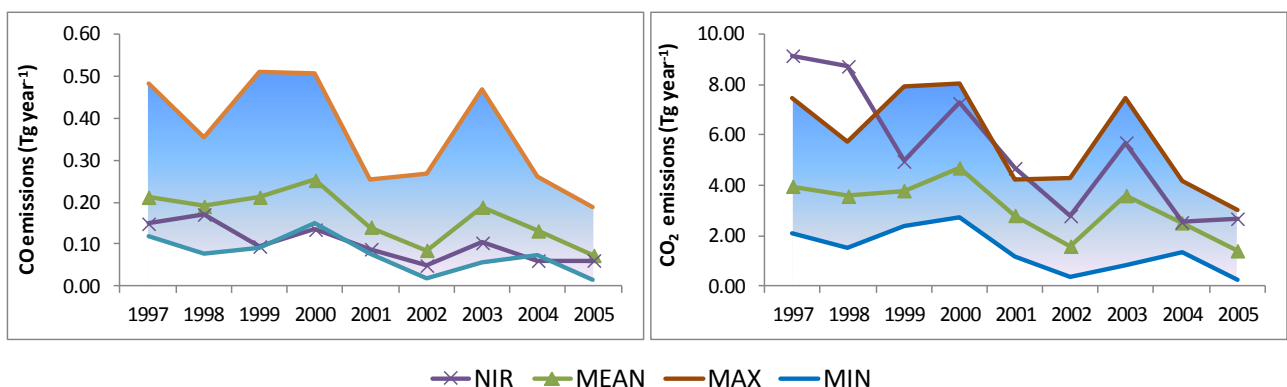


Fig. 2: Comparison of five dataset [EDGARv4.2, GICC, GFED3, GFED2, GUESS-ES] average (green line) and Italian National Inventory Report [NIR, 2011] (purple line). Blue area indicates the range of listed inventories

4. 21ST CENTURY TRAJECTORIES

Within this paragraph we will investigate how fire emissions may change during the 21st century, starting from the Representative Concentration Pathways [RCPs], a set of four new pathways developed for the climate modelling community as a basis for long-term and near-term modelling experiments [64], covering the literature range of year 2100 radiative forcing values [from 2.6 to 8.5 W m⁻²]. The four RCPs include one mitigation scenario leading to a very low forcing level [RCP3PD], two medium stabilization scenarios [RCP4.5/RCP6] and one very high baseline emission scenarios [RCP8.5] [Tab. 2].

Fig. 3 shows the trends of CO and BC emitted by forest fires as estimated by the four RCPs in Italy. In general, RCP3PD showed a peak around 2030, a modest decline to around 2050 and then a rapid increase in 2060 followed by stabilization. RCP6 and RCP8.5 showed more-or-less stable patterns throughout the century. Finally, RCP4.5 showed the opposite trends with respect to RCP3PD, slightly decreasing around 2030 followed by a sudden change in 2050 and then as much rapid reduction in 2080.

Name	Description	Source	Model name
RCP3PD	Peak in radiative forcing at ~3 W m ⁻² [~490 ppm CO ₂ eq] before 2100 and then decline [the selected pathway declines to 2.6 W m ⁻² by 2100].	62; 65	IMAGE
RCP4.5	Stabilization without overshoot pathway to 4.5 W m ⁻² [~650 ppm CO ₂ eq] at stabilization after 2100	8; 52; 67	GCAM
RCP6	Stabilization without overshoot pathway to 6 W m ⁻² [~850 ppm CO ₂ eq] at stabilization after 2100	19; 24	AIM
RCP8.5	Rising radiative forcing pathway leading to 8.5 W m ⁻² [~1370 ppm CO ₂ eq] by 2100.	46	MESSAGE

Tab. 2: Overview of representative concentration pathways [RCPs] [modified from 65]

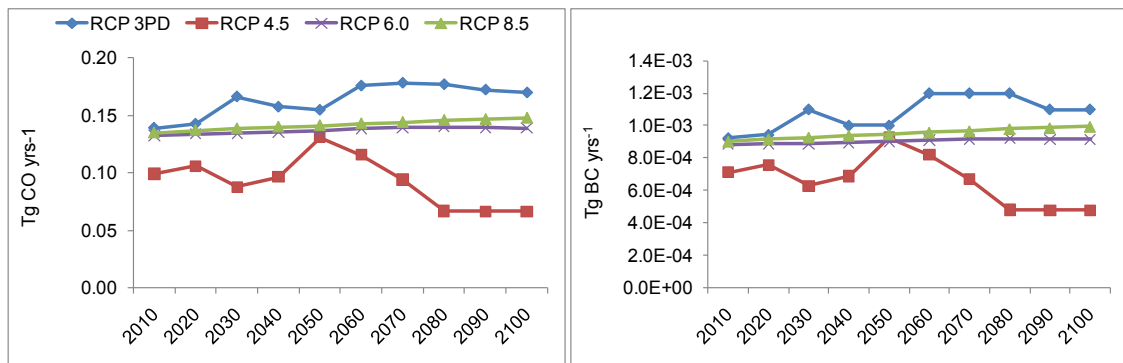


Fig. 3: CO [top left] and BC [top right] projections of the four scenarios underlying the RCPs

As highlighted by van Vuren et al. [64], the emissions are largely due to differences in the assumed climate policy, along with differences in land-use assumptions. Regarding land-use, RCP8.5 captures an increased use of cropland and grasslands, principally due to population increase. Similarly, RCP3PD shows an increase in cropland, mainly as a result of bio-energy production. On the other hand, vegetation land-use shows a clear increasing trend for RCP4.5 and RCP6 [Fig. 4]. The low emission estimates of RCP4.5, in comparison with the other scenarios, are likely due to the policies underlying this pathway, assuming that carbon in natural vegetation will be valued as part of global climate policy [64].

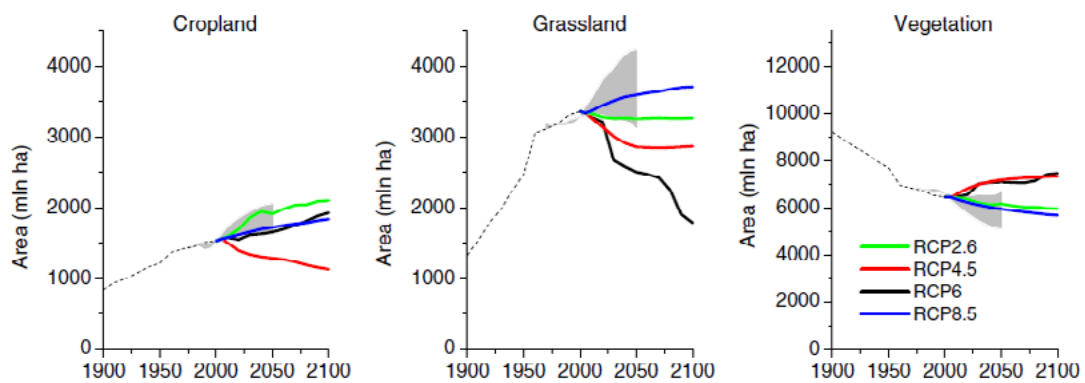


Fig. 4: From van Vuren et al. [64]: Land use [crop land and use of grass land] across the RCPs. Grey area indicates the 90th percentile of scenarios reported in the literature [51]. Vegetation is defined as the part not covered by cropland or anthropogenically used grassland.

5. CONCLUDING REMARKS

The complex interactions between fire emissions and climate [the first influencing the second contributing to greenhouse gases and aerosol particles, and the second affecting length and intensity of fire season] have been emphasized in the last years [e.g. 34], and there is an increasing interest on the establishment of fire emission inventories and the regulation of regional fire emissions to the atmosphere [e.g 66]. Still, there is a significant uncertainty regarding the magnitude, timing, and variability of fire emissions[66].

As pointed out by Langmann et al. [34] and Stroppiana et al. [56] fire emission estimates are affected by large uncertainties mainly due to the differences in capturing the burned area, despite the improvements achieved by remote sensing. In addition, large inconsistencies derive from the assessment of fuel characteristics [56] and combustion estimation [41]. Recently, numerical biogeochemical models have been used to better simulate spatial variability in fuel loads [e.g. 60, 61].

Another point of open discussion is the role of fire in climate policy development. Changing climate may lead to fire emissions that increasingly diverge from historical means, as highlighted for the Italian country. So that, while the long-term impacts of fire emissions differ undoubtedly from fossil fuel emissions, especially due to the vegetation recovery and the consequent carbon storage, the fire impacts over shorter time periods are highly considerable. This point has been recalled also during the Durban conference in 2011: the countries, when accounting for forest management, “may exclude from the accounting emissions from natural disturbances that in any single year exceed the forest management background level” [57]. This is of particular importance especially considering that the occurrence of extremely severe fire weather may increase as a consequence of global warming [14, 16, 3].

6. ACKNOWLEDGMENTS

The research leading to these results has received funding from the Italian Ministry of Education, University and Research and the Italian Ministry of Environment, Land and Sea under the GEMINA project. The Authors wish to thank the ECCAD-GEIA database [Emissions of atmospheric Compounds & Compilation of Ancillary Data] for freely provide emission data.

7. REFERENCES

- Andreae MO, Merlet P [2001] *Emission of trace gases and aerosols from biomass burning*. Global Biogeochem. Cy. 15:955–966. (1)
- Andreae MO, Rosenfeld D, Artaxo P, Costa AA, Frank GP, Longo KM, Silva-Dias MAF [2004] *Smoking rain clouds over the Amazon*. Science 303, 1337–1342. (2)
- Arca B, Bacciu V, Duce P, Pellizzaro G, Salis M, Spano D [2009] *Maps of the likelihood of spread and severity of fire in a report different scenarios of fuel moisture and weather*. ITALIAN JOURNAL OF AGROMETEOROLOGY, VOL. 14, P. 16-17, <http://www.scopus.com/inward/record.url?eid=2-s2.0-79954493172&partnerID=40&md5=f3676815b79cc2565b5c46afe23d24ab>. (3)
- Battye W, Battye R [2002] *Development of Emission Inventory Methods for Wildland Fire*. Final Report to US EPA. Contract # D205-01. Available at: <http://www.epa.gov/ttn/chief/ap42/ch13/related/c13s01.html>. (4)
- Bell T, Adams M [2009] *Smoke from Wildfires and Prescribed Burning in Australia: Effects on Human Health and Ecosystems*. In: Bytnerowicz A, Arbaugh M, Riebau A, Andersen C [eds] *Wildland Fires and Air Pollution*. Elsevier, Amsterdam. (5)
- Borrego C, Miranda AI, Carvalho AC, Carvalho A [1999] *Forest fires and air pollution: A local and global perspective*. In: Brebbia, C., Jacobson, M., and Power, H., eds. *Proceedings of the 7th International Conference on Air Pollution*. WIT Press, Southampton, Boston, 741–750. (6)
- Chevallier F, Fortems A, Bousquet P, Pison I, Szopa S, Devaux M, Hauglustaine DA [2009] *African CO emissions between years 2000 and 2006 as estimated from MOPITT observations*. Biogeosciences, 6, 103–111. (7)
- Clarke LE, Edmonds JA, Jacoby HD, Pitcher H, Reilly JM, Richels R [2007] *Scenarios of greenhouse gas emissions and atmospheric concentrations*. Sub-report 2.1a of Synthesis and Assessment Product 2.1. Climate Change Science Program and the Subcommittee on Global Change Research, Washington DC. (8)
- Crutzen PJ, Andreae MO [1990] *Biomass burning in the tropics: Impact on atmospheric chemistry and biogeochemical cycles*. Science 250:1669–1677. (9)

- Diehl T, Heil A, Chin M, Pan X, Streets D, Schultz M, Kinne S [2012] *Anthropogenic, biomass burning, and volcanic emissions of black carbon, organic carbon, and SO₂ from 1980 to 2010 for hindcast model experiments*. Atmospheric Chemistry and Physics Discussion 12 : 24895-24954. (10)
- Dost FN [1991] *Acute toxicology of components of vegetation smoke*. Reviews of Environmental Contamination and Toxicology, 119: 1-46. (11)
- EFSA [2012] *Update of the monitoring of levels of dioxins and PCBs in food and feed*. EFSA Journal, 10[7]:2832. doi:10.2903/j.efsa.2012.2832. (12)
- Feingold G, Jiang H, Harrington JY [2005] *On smoke suppression of clouds in Amazonia*. Geophys. Res. Lett., 32, L02804, doi:10.1029/2004GL021369. (13)
- Flannigan MD, Campbell I, Wotton BM, Carcaillet C, Richard P, Bergeron Y [2001] *Future fire in Canada's boreal forest: paleoecology results and general circulation model – regional climate model simulations*. Canadian Journal of Forest Research 31:854–864. (14)
- Forster C, Wandinger U, Wotawa G, James P, Mattis I, Althausen D, Simmonds P, O'Doherty S, Jennings G, Kleefeld C, Schneider J, Trickl T, Kreipl S, Jäger H, Stohl A [2001] *Transport of boreal forest fire emissions from Canada to Europe*. J. Geophys. Res., 106:22,887 – 22,906. (15)
- Fried JS, Torn MS, Mills E [2004] *The impact of climate change on wildfire severity: a regional forecast for northern California*. Clim Change 64:169–191. (16)
- Friedli H, Arellano A, Cinnirella S, Pirrone N [2009b] *Initial Estimates of Mercury Emissions to the Atmosphere from Global Biomass Burning*. Environ/ Sci. Technol., 43, 3507–3513. (17)
- Friedli HR, Arellano AF, Cinnirella S, Pirrone N [2009a] *Mercury emissions from global biomass burning: spatial and temporal distribution*. Springer, New York, USA, chap. 8, 193–220. (18)
- Fujino J, Nair R, Kainuma M, Masui T, Matsuoka Y [2006] *Multigas mitigation analysis on stabilization scenarios using aim global model*. The Energy Journal Special issue #3:343–354. (19)
- Galanter M., Levy H., and Carmichael G. R. [2000] *Impacts of biomass burning on tropospheric CO, NO_x, and O₃*. J. Geophys. Res.-Atmos., 105, 6633–6653. (20)
- Giglio L., Randerson J. T., van der Werf G. R., Kasibhatla P. S., Collatz G. J., Morton D. C., and DeFries R. S. [2010] *Assessing variability and long-term trends in burned area by merging multiple satellite fire products*. Biogeosciences, 7, 1171–1186, doi:10.5194/bg-7-1171-2010. (21)

- Granier C, Bessagnet B, Bond T, D'Angiola A, van der Gon HG, Frost G, Heil A, Kainuma M, Kaiser J, Kinne S et al [2011] *Evolution of anthropogenic and biomass burning emissions at global and regional scales during the 1980–2010 period*. Climatic Change. doi: 10.1007/s10584-011-0154-1. (22)
- Hao WM, Liu MH, Crutzen PJ [1990] *Estimates of Annual and Regional Release of CO₂ and Other Trace Gases to the Atmosphere from Fires in the Tropics*. In Goldammer, J. G. (ed.), *Fire in the Tropical Biota*, Springer-Verlag, Berlin, pp. 440–462. (23)
- Hijioka Y, Matsuoka Y, Nishimoto H, Masui T, Kainuma M [2008] *Global GHG emission scenarios under GHG concentration stabilization targets*. J Glob Environ Eng 13:97–108. (24)
- Hobbs PV, Reid JS, Kotchenruther RA, Ferek RJ, Weiss R [1997] *Direct radiative forcing by smoke from biomass burning*. Science 275, 1776–1778. (25)
- Hodzic A, Madronich S, Bohn B, Massie S, Menut L, Wiedinmyer C [2007] *Wildfire particulate matter in Europe during summer 2003: meso-scale modeling of smoke emissions, transport and radiative effects*. Atmos. Chem. Phys. 7, 4043–4064. (26)
- IPCC [Intergovernmental Panel on Climate Change], 2001. The Scientific Basis. Available from: <http://www.ipcc.ch/ipccreports/tar/wg1/index.htm>. (27)
- Ito A. and Penner J. E. [2004] *Global estimates of biomass burning emissions based on satellite imagery for the year 2000*, J. Geophys. Res.-Atmos., 109, D14S05, doi:10.1029/2003JD004423. (28)
- Jain AK [2007] *Global estimation of CO emissions using three sets of satellite data for burned area*. Atmos. Environ., 41, 6931–6940, doi:10.1016/j.atmosenv.2006.10.021. (29)
- Janssens-Maenhout G, Petrescu A, Muntean M, Blujdea V [2010] *Verifying Greenhouse Gas Emissions: Methods to Support International Climate Agreements*. Greenhouse Gas Measurement and Management 1 [2]:132-133. JRC67524. (30)
- Knorr W, Lehsten V, Arneth A [2011] *Determinants and predictability of global wildfire emissions*. Atmospheric Chemistry & Physics Discussions, submitted to The Pan European Gas-Aerosols Climate Interaction Study [PEGASOS] Special Issue. (31)
- Koren I.L., Kaufman Y.J., Remer L.A., Martins J.V., 2004. *Measurement of the effect of Amazon smoke on inhibition of cloud formation*. Science 303, 1342–1345. (32)

- Lamarque J.-F., Bond T. C., Eyring V., Granier C., Heil A., Klimont Z., Lee D., Liousse C., Mieville A., Owen B., Schultz M. G., Shindell D., Smith S. J., Stehfest E., Van Aardenne J., Cooper O. R., Kainuma M., Mahowald N., McConnell J. R., Naik V., Riahi K., and van Vuuren D. P.: *Historical [1850–2000] gridded anthropogenic and biomass burning emissions of reactive gases and aerosols: methodology and application*. *Atmos. Chem. Phys. Discuss.*, 10, 4963–5019, doi:10.5194/acpd-10-4963-2010, 2010. (33)
- Langmann B., Duncan B., Textor C., Trentmann J., and vander Werf G. R. [2009] *Vegetation fire emissions and their impact on air pollution and climate*, *Atmos. Environ.*, 43, 107–116, doi:10.1016/j.atmosenv.2008.09.047. (34)
- Michel C, Liousse C, Grégoire J-M, Tansey K, Carmichael GR, Woo J-H [2005] *Biomass burning emission inventory from burnt area data given by the SPOT-VEGETATION system in the frame of TRACE-P and ACE-Asia campaigns*. *J. Geophys. Res.*, 110, D09304, doi:10.1029/2004JD005461. (35)
- Mieville A, Granier C, Liousse C, Guillaume B, Mouillot F, Lamarque J-F, Grégoire J-M, Pétron G [2010] *Emissions of gases and particles from biomass burning using satellite data and an historical reconstruction*. *Atmos. Environ.*, 44, 1469–1477, doi:10.1016/j.atmosenv.2010.01.011. (36)
- Miranda AI, Coutinho M, Borrego C [1994] *Forest fire emissions in Portugal: A contribution to global warming?* *Environ. Pollut.*, 83[1–2], 121–123. (37)
- Miranda J, Barrera VA, Espinosa AA, Galindo OS, Nunez-Orosco A, Montesinos RC, Leal-Castro A, Meinguer J [2004] *PIXE analysis of atmospheric aerosols from three sites in Mexico City*. *Instruments and Methods in Physics Research, Section B: Beam Interactions with Materials and Atoms*, pp. 157–160. (38)
- Mouillot F, Field CB [2005]. *Fire history and the global carbon budget: a 1°x1° fire history reconstruction for the 20th century*. *Global Change Biology* 11[3]: 398–420. (39)
- Naeher LP, Brauer M, Lipsett M, Zelikoff JT, Simpson CD, Koenig JQ, Smith KR [2007] *Woodsmoke health effects: A review*. *Inhal Toxicol* 19[1]:67–106. (40)
- Ottmar RD, Miranda AI, Sandberg DV [2009] *Characterizing Sources of Emissions from Wildland Fires*. In: Bytnerowicz A, Arbaugh M, Riebau A, Andersen C [eds] *Wildland Fires and Air Pollution*. *Wildland Fires and Air Pollution*. Elsevier, Amsterdam. (41)

- Penner JE, Andreae M, Annegarn H, Barrie L, Feichter J, Hegg D, Jayaraman A, Leaitch R, Murphy D, Nganga J, Pitari G [2001] *Aerosols, their direct and indirect effects*. In: Houghton JT, Ding Y, Griggs DJ, Noguer M, van der Linden PJ, Dai X, Maskell K, Johnson CA (eds) *Climate change 2001. The scientific basis*. Contribution of Working Group I to the Third Assessment Report of the Intergovernmental Panel on Climate Change. Cambridge University Press, Cambridge, UK, pp 881. (42)
- Podgorny IA, Li F, Ramanathan V [2003] *Large aerosol radiative forcing due to the 1997 Indonesian forest fire*. Geophys. Res. Lett., 30(1), 1028, doi:10.1029/2002GL015979. (43)
- Randerson JT, Liu H, Flanner MG, Chambers SD, Jin Y, Hess PG, Pfister G, Mack MC, Treseder KK, Welp LR, Chapin FS, Harden JW, Goulden ML, Lyons E, Neff JC, Schuur EAG, Zender CS [2006] *The impact of boreal forest fire on climate warming*. Science 314:1130-1132. (44)
- Reid JS, Eck TF, Christopher SA, Koppmann R, Dubovik O, Eleuterio DP, Holben BN, Reid EA, Zhang J [2005] *A review of biomass burning emissions part III: intensive optical properties of biomass burning particles*. Atmos. Chem. Phys., 5, 827–849. (45)
- Riahi K, Grübler A, Nakicenovic N [2007] *Scenarios of long-term socio-economic and environmental development under climate stabilization*. Technol Forecast Soc Chang 74:887–935. (46)
- Schollnberger H, Aden H, Scott BR [2002] *Respiratory tract deposition efficiencies: Evaluation of effects from smoke released in the Cerro Grande forest fire*. J. Aerosol Med. 15, 387–399. (47)
- Schultz M. G., Heil A., Hoelzemann J. J., Spessa A., Thonicke K., Goldammer J. G., Held A. C., Pereira J. M. C., and van het Bolscher M. [2008], *Global wildland fire emissions from 1960 to 2000*. Global Biogeochem. Cycles, 22, GB2002, doi:10.1029/2007GB003031. (48)
- Seiler W, Crutzen P [1980] *Estimates of gross and net fluxes of carbon between the biosphere and the atmosphere from biomass burning*. Climatic Change, 2, 207–247. (49)
- Simmonds PG, Manning AJ, Derwent RG, Ciais P, Ramonet M, Kazan V, Ryall D [2005] *A burning question. Can recent growth rate anomalies in the greenhouse gases be attributed to large-scale biomass burning events?* Atmos. Environ. 39, 2513–2517. (50)
- Smith SJ, van Aardenne J, Klimont Z, Andres R, Volke A, Delgado Arias S [2010] *Anthropogenic sulfur dioxide emissions: 1850-2005*, Atmos. Chem. Phys. Discuss., 10, 16111–16151, doi:10.5194/acpd-10-16111-2010. (51)

- Smith SJ, Wigley TML [2006] *MultiGas forcing stabilization with minicam*. The Energy Journal Special issue #3:373–392. (52)
- Spengler J, Wilson R [1996] *Emissions, dispersion, and concentration of particles*. In R. Wilson and J. Spengler, (eds.), *Particles in Our Air: Concentrations and Health Effects*, Cambridge, MA, Harvard University Press. (53)
- Spichtinger N, Wenig M, James P, Wagner T, Platt U, Stohl A [2001] *Satellite detection of a continental-scale plume of nitrogen oxides from boreal forest fires*. Geophys. Res. Lett., 28, 4579 – 4582. (54)
- Stohl A, Andrews E, Burkhardt JF, Forster C, Herber A, Hoch SW, Kowal D, Lunder, C, Mefford T, Ogren JA, Sharma S, Spichtinger N, Stebel K, Stone R, Strm J, Trseth K, Wehrli C, Yttri KE [2006] *Pan-Arctic enhancements of light absorbing aerosol concentrations due to North American boreal forest fires during summer 2004*, J. Geophys. Res., 111, 148–227, doi:10.1029/2006JD007216. (55)
- Stroppiana D, Brivio PA, Grégoire J-M, Liousse C, Guillaume B, Granier C, Mieville A, Chin M, Pétron G [2010] *Comparison of global inventories of CO emissions from biomass burning derived from remotely sensed data*. Atmos. Chem. Phys., 10, 12173–12189, doi:10.5194/acp-10-12173-2010. (56)
- UNFCCC [2012] *Report of the Conference of the Parties serving as the meeting of the Parties to the Kyoto Protocol on its seventh session, held in Durban from 28 November to 11 December 2011*. Part Two: Action taken by the Conference of the Parties serving as the meeting of the Parties to the Kyoto Protocol at its seventh session FCCC/KP/CMP/2011/10/Add.1. (57)
- UNFCCC [2006] *United Nations Framework Convention on Climate Change: Handbook*. Bonn, Germany: Climate Change Secretariat. (58)
- Urbanski SP, Hao WM, Nordgren B [2011] *The wildland fire emission inventory: western United States emission estimates and an evaluation of uncertainty*. Atmos. Chem. Phys., 11, 12973-13000, doi:10.5194/acp-11-12973-2011, 2011. (59)
- van der Werf GR, Randerson JT, Giglio L, Collatz GJ, Kasibhatla PS, Arellano A F [2006] *Interannual variability in global biomass burning emissions from 1997 to 2004*. Atmos. Chem. Phys., 6, 3423–3441, doi:10.5194/acp-6-3523-2006. (60)
- van der Werf GR, Randerson JT, Giglio L, Collatz GJ, Mu M, Kasibhatla PS, Morton DC, DeFries RS, Jin Y, van Leeuwen TT [2010] *Global fire emissions and the contribution of deforestation savanna forest*

- agricultural and peat fires [1997-2009]*. Atmospheric Chemistry and Physics 10 11707-11735 doi:105194/acp-10-11707-2010. (61)
- van Vuuren DP, Den Elzen MGJ, Lucas PL, Eickhout B, Strengers BJ, Van Ruijven B, Wonink S, Van Houdt R [2007a] *Stabilizing greenhouse gas concentrations at low levels: an assessment of reduction strategies and costs*. Clim Chang 81:119–159. (62)
- van Vuuren DP, Lucas PL, Hilderink H [2007b] *Downscaling drivers of global environmental change: enabling use of global SRES scenarios at the national and grid levels*. Glob Environ Chang 17:114–130. (63)
- van Vuuren DP, Edmonds JA, Kainuma M, Riahi K, Thomson AM, Hibbard K, Hurtt GC, Kram T, Krey V, Lamarque J-F, Masui T, Meinshausen M, Nakicenovic N, Smith SJ, Rose S [2011] *The representative concentration pathways: an overview Climatic Change*. 109: 5-31. DOI: 10.1007/s10584-011-0148-z. (64)
- van Vuuren DP, Eickhout B, Lucas PL, den ElzenMGJ [2006] *Long-term multi-gas scenarios to stabilise radiative forcing—exploring costs and benefits within an integrated assessment framework*. Energ J 27:201–233. (65)
- Wiedinmyer C, Neff JC [2007] *Estimates of CO₂ from fires in the United States: implications for carbon management*. Carbon Balance and Management 2007, 2:10 doi:10.1186/1750-0680-2-10. (66)
- Wise M, Calvin K, Thomson A, Clarke L, Bond-Lamberty B, Sands R, Smith SJ, Janetos A, Edmonds J [2009] *Implications of limiting CO₂ concentrations for land use and energy*. Science 324:1183–1186. (67)
- World Health Organization [2002] *Reducing Risks, Promoting Healthy Life*. (68)

IMPLICATIONS ON ECOSYSTEM SERVICES

Poster Session

Fluctuation in spatial patterns in semi-arid ecosystems under pressure

Corrado R.^{1,2}, Cherubini A. M.¹, and Pennetta C.^{1,2*}

¹Dipartimento di Matematica e Fisica "Ennio De Giorgi", Università del Salento, 73100 Lecce, Italy

²INFN, Istituto Nazionale di Fisica Nucleare, Sezione di Lecce, Via Arnesano, Lecce, Italy

*Corresponding author: cecilia.pennetta@unisalento.it

Abstract

The identification of reliable early-warning signals of critical transitions is crucial in fragile ecosystems such as arid or semi-arid ones strongly exposed to desertification risks. Previous studies in this field suggested that some indicators of an approaching transition to desertification could be related to the evolution of vegetation patchiness [1,5]. These studies mainly focused on the analysis of the spatial fluctuations of the vegetation patterns and they indicated the deviation from power laws in vegetation patch size distributions as a reliable signal of approaching desertification [1,5]. We have analyzed some ecological models for semi-arid ecosystems based on stochastic cellular automata (CA) [1,2,3,4]. These models depend on a number of relevant parameters describing, beside soil and vegetation properties, external stresses, etc. In particular, we have studied the time fluctuations properties of some global and local quantities associated with the steady states of two CA models [1,3,4]. We have found other possible and earlier signals related to the time fluctuations distribution of the biggest cluster size.

Keywords: *Desertification, critical transitions, early-warning signals, cellular automata*



METHOD AND RESULTS

The identification of early warning signals of regime shifts in ecosystems is a crucial issue since these shifts can imply severe losses of ecological and economic resources. In particular, environmental stresses induced either by an excess of anthropic load or by an increased frequency of meteorological extreme events, can give rise in arid or semi-arid ecosystems to desertification transitions. Many recent studies highlighted the interest in vegetation patchiness analyses as a tool to provide indicators of desertification risk. Recently, Kefi et al. [1] investigated the influence of external stress on the spatial organization of the vegetation, by combining modelling and field data from three Mediterranean arid grazed ecosystems. The model is based on a stochastic cellular automaton (CA); the ecological landscape is determined by parameters, in particular, the mortality parameter m associated with the external stress (grazing pressure) and the facilitation parameter f controlling the strength of local cooperative interactions among plants. The main result in [1] is that far from a transition the vegetation patch-size distribution follows a power law while at increasing m or at decreasing f it significantly deviates from it, showing an exponential cut-off. These deviations from a power-law in patch-size distribution were proposed as warning signals for the onset of desertification [1]. The Pareto-like behaviour of the spatial distributions in ecosystems has been explained in [2].

So far, the greatest part of literature on desertification risk mainly focuses on the analysis of the spatial fluctuations of the vegetation pattern. We took a different approach and investigated the *time* fluctuations properties of some global and local quantities associated with the steady states of the CA model in [1]. In particular, we have analyzed the distributions of the time fluctuations of three relevant quantities (the total vegetation mass fraction, the degraded cells fraction and the size of the biggest living cell cluster) by calculating the probability density function (PDF) and the first three moments of the distributions as a function of m and of the system size N . We have found that the system undergoes a critical transition for a given value m_c of the mortality parameter, associated with the desertification transition, as proved by the scaling behavior of both the average and the variance of the living cell density as a function of the difference $m - m_c$. Consistently with this statement, the time fluctuations of the biggest cluster size S_B strongly deviate from Gaussianity when m approaches m_c , displaying a positive skewness persistent at increasing N . The fluctuations of S_B follow the universal Bramwell-Holdsworth-Pinton (BHP) distribution [5,6], independently of N [3,4]. Moreover, variance of S_B exhibits a sharp peak at a given value $m^* \ll m_c$, percolation threshold for the living cells and

corresponding to the emergence of the exponential cut-off observed in [1]. We have also found that a strong non-Gaussianity of the S_B fluctuations, now with negative skewness, weakly dependent on N , occurs $m < m^*$. We propose that this change of skewness, from negative to positive values, and in particular this strong non-Gaussianity as a "very" early warning of the onset of desertification transitions.

REFERENCES

- Kefi S. et al., *Nature*, 449(13), 213 (2007) and Kéfi S., Rietkerk M., van Baalen M. and Loreau M., *Theor. Popul. Biol.*, 71, 267 (2007). (1)
- Manor A., Shnerb N. M., *Phys. Rev. Lett.*, 101(26), 8104 (2008). (2)
- Corrado R., Cherubini A. M. and Pennetta C., *Signals of Critical Transitions in Ecosystems Associated with Fluctuations of Spatial Patterns*, Proceedings of the IEEE 22st International Conference on Noise and Fluctuations, ICNF 2013, Montpellier, France, June 24-28, 2013, in print. (4)
- Corrado R., *Desertification transition in semiarid ecosystems: models analysis and study of early warning signals*, PhD Thesis, 2013. (4)
- Bramwell S.T., *Nature Physics*, 5(6), 443 (2009). (5)
- Clusel M., Fortin J.F., Holdsworth P.C., *Phys. Rev. E*, 70(4), 046112, 2004. (6)

Application of the 3D-CMCC FEM (Three Dimension Forest Ecosystem Model) on multi-temporal NDVI satellite imagery and future scenarios

Collalti A.^{1,2*}, Santini M.¹, Marconi S.², Mattiuzzi M.³,
Candini A.⁴, Natali S.⁵, Nolè A.⁶ and Valentini R.^{1,2}

¹*Euro-Mediterranean Centre on Climate Changes – Impacts on Agriculture, Forest and Natural Ecosystem division (LAFENT), Lecce, Italy;*

²*University of Tuscia - Department for innovation in biological, agro-food and forest systems (DIBAF), Viterbo, Italy*

³*Institute of Surveying, Remote Sensing and Land Information, University of Natural Resources and Life Sciences, Vienna, Austria,*

⁴*MEEO s.r.l., Via Saragat 9, 44122 Ferrara, Italy*

⁵*Sistema GmbH Waehringerstrasse 61, 1090 Vienna, Austria*

⁶*School of Agricultural, Forestry, Food and Environmental Sciences, University of Basilicata, Italy*

*Corresponding author: alessio.collalti@cmcc.it

Abstract

With the suspect of CO₂ influences on global climate dynamics, scientists, decision makers and stakeholders have increasingly been interested in developing methods to assess Carbon balance dynamics and predict changing climate impacts on vegetation. Among others, yield and productivity models seem to return consistent descriptions of vegetation gross carbon assimilation and net ecosystem exchange. Unfortunately they need several input data; information which would be both difficult and very expensive to be collected for wide areas of investigation and/or short time intervals. For this reason several scientists developed methodologies to couple ecosystem models to remotely-sensed data to be inputted in. This work aims to present consistency of a technique we developed, in the framework of KLAUS project, to be used with 3D-CMCC-FEM model, a hybrid forest ecosystem model. Hence we have compared two case studies, the former running the model with a prognostic phenology approach, the latter, using satellite data, with a diagnostic one. Results show 3D-CMCC-FEM's good capability to simulate GPP, NPP and carbon allocation in stem and root compartments. Moreover the model seems to be able to simulate the reduction in rates of productivity for hygrophilous species in dry years. Even though 3D-CMCC-FEM in some cases produces slight overestimation, its results may be anyway considered statistically meaningful. Therefore, coupling high resolution satellite data with field information as input can successfully be used to simulate at regional scale physiological processes in forest ecosystems.

Keywords: *model; 3D-CMCC-FEM; remote-sensing; climate change*



1. INTRODUCTION

The increase of atmospheric carbon dioxide due to anthropogenic emissions and the associated global warming are partly counterbalanced by active carbon sequestration by terrestrial vegetation and forests [1]. In terrestrial plant communities photosynthesis, respiration and litter decomposition processes involve large amounts of carbon dioxide, contributing to the overall balance of the predominant greenhouse gases in global warming [2]. The assessment of forest productivity on wide areas is crucial for both scientific and practical purposes[3]. Satellite images have massively been used for wide areas of investigation over the last two decades, especially because of the high spatial variability of productivity controlling factors, and the strong expenses and time consumption related to field-based measurement techniques [4]. Thus, a procedure mostly independent to field measurements, and driven by remote sensing data, would be extremely useful to routinely produce spatially extended estimates of forest productivity [5]. Satellite images were commonly coupled with forest ecosystem models (FEMs) to produce qualitative and quantitative information of the forests trend of productivity and thus of carbon sinks. The lack of information about forests status such as composition and structure, have led to consider the remote sensing techniques as an important tool providing model inputs [6]. This is especially the case for the variables describing forest composition and structure, such as tree species, density and leaf area index (LAI); these variables are generally highly changing in space and/or time, and difficult to measure with conventional methods [7].

In the framework of the European Space Agency (ESA)-funded KEO Demonstrator with Models for Land Use Management (KLAUS) project, was carried out the design and implementation of so-called KEO Demonstration Applications (KDAs); it aimed at creating new software modules to provide advanced environmental monitoring maps, making use of satellite and in-situ measurements.

This paper aims at describing the design and implementation of the software modules (KEO modules) that we developed, coupled with 3D-CMCC FEM (Three Dimension Forest Ecosystem Model of Mediterranean Center on Climate Change, [8]), and to present two application use cases.

2. MATERIALS AND METHOD

Model description

The 3D-CMCC FEM is a generic, dynamic, hybrid model, developed to predict forest growth, carbon allocation for un-managed and managed forests on variable spatial (from 10 x 10 meters to 1Km x 1Km) and temporal (from daily to monthly time scale) resolutions. The model incorporates the key elements of empirical and process-based approaches into an hybrid modeling approach, leading to a tool that can predict forest growth, production and dynamics in both short and medium temporal scale. The model combines empirical and mechanistic components that can be used for: (a) give a support to forest management (i.e. growth and yield prediction) to pursue the best management practices (BMP), (b) quantify forest carbon budgets and (c) assess the effects of climate change on forests. The 3D-CMCC FEM can be applied not only to plantations, even-aged, or homogeneous forests but also to natural forests, defined as multi-species (mixed stand), multi-age (uneven aged stand), multi-layered. The model is based on the main approaches of well-established process models as 3-PG [9], BIOME-BGC [10], TREEDYN 3 [11], FORMIX [12], TRIPLEX [13] and LPJ[14]. The 3D-CMCC FEM model is a generic stand model, which means that its structure is not site or species-specific. It only needs to be parameterized for the site modelled, and for individual species or forest macro-class. The model is able to run both using a prognostic phenology (version “un-spatial”), e.g. the model computes itself the monthly phenological trends of Leaf Area Index, and a diagnostic phenology, (version “spatial”); where it uses external data through satellite. The 3D-CMCC FEM is provided by the euroMediterranean Center on Climate Change (CMCC), and works on a single pixel basis; in order to be able to apply the module over regions, it was necessary to develop input and output interfaces to the module itself. The scope of the interfaces is to transform the input maps/images into single point information to be processed by the forest model, and to build the output images/maps joining the single point results of the model. The input/output interfaces of the 3D-CMCC FEM are provided as a single processing module wrapped by a shell script. Interfaces have been developed by SISTEMA GmbH in the framework of the KLAUS project and the module is available through the KEO system (<http://rssportal.esa.int/deepenandlearn/tiki-index.php?page=KEO+Project>) for registered user.

Simulations and study area

The 3D-CMCC FEM (4.0), was tested on a monthly time step in two study cases. The former was for the National Park of Monti Sibillini (Marche region) (case study 1) mainly composed by beech forests (*Fagus sylvatica* L.), the latter was for the National Park of Madonie (Sicily region) and the Comunità Montana del Titerno ed Alto Tammaro (Campania region) (case study 2), grouped into three macro forests classes i.e.: deciduous temperate oak (*Quercus cerris* L. and *Q. pubescens* L.), sweet chestnut (*Castanea sativa* M.) and beech (*Fagus sylvatica* L.).

In the case study 1 the model was set to be fully diagnostic, using satellite images (see below) and was run from 2007 to 2010. In the case study 2 the model was set to run with a diagnostic phenology from 2002 up to 2009 switching to fully prognostic from 2010 up to 2020.

3. INPUT DATA

Ancillary data

For its initialization (the first year of simulation), the 3D-CMCC FEM requires information on forest structure for each cell. In detail the required information are: species, number of trees, height and diameter at breast height. Concerning the case study 1 the information on forest biomass needed for the model were computed using the data reported in the local forest management plans elaborated by D.R.E.Am. ITALIA company and the Regional Forest Inventory of Marche Region. The Regional Forest Inventory provides the mean values of biomass volume and the number of trees per hectare of each forest typology for different areas belonging to the 'Comunità Montane' of Marche Region. Starting from these data we have downscaled them to the spatial resolution of ALOS-AVNIR2 LB2G satellite images (10 m x 10 m resolution). Concerning about the National Park of Madonie (Sicily region) and the Comunità Montana del Titerno ed Alto Tammaro (Campania region), the data for model initialization were obtained by the National Forest Inventory and the Regional Forest Cover of Sicily Region; those data were correlated with the National Corine Land Cover (CLC) and downscaled to the spatial resolution of LANDSAT 5-7 satellite images at 30 m x 30 m.

Meteorological input data

For case study 1 input meteorological data i.e.: average temperature, precipitations, solar radiation and relative humidity (see Tab 1.), were obtained from the meteorological sites of Montefortino and Visso, from several textual files downloaded from the Italian National Environmental Information System (SINAnet) (<http://www.scia.sinanet.apat.it>). Meteorological input dataset was finally organized on a monthly basis for the years covered by this study (2007, 2008, 2009 and 2010), by producing monthly climatologic images.

For average temperature, precipitations and relative humidity images, it was used a linear interpolation [15] on the area of interest of data taken by control units of Montefortino and Visso. For case study 2 as much data as possible have been retrieved from satellite-based information, trying to avoid point measurements. Precipitation data were derived from images obtained from the Tropical Rainfall Measuring Mission (TRMM), product 3B-43, monthly time, global coverage, $0.25^\circ \times 0.25^\circ$ ortorectangular gridding, produced by the National Oceanic and Atmospheric Administration (NOAA) Climate Prediction Center and from the Global Precipitation Climatology Center (GPCC, ftp://meso-a.gsfc.nasa.gov/pub/trmmdocs/3B42_3B43_doc.pdf). The temperature data were collected from images obtained by the MODIS sensor (level 3 product, MOD08_M3, monthly data, global coverage, $1^\circ \times 1^\circ$ ortorectangular gridding, http://modis-atmos.gsfc.nasa.gov/MOD08_M3): from this product the monthly average temperature (Retrieved Mean Temperature), the monthly average temperature maximum (Max Retrieved Mean Temperature) and the monthly average temperature minimum (Min Retrieved Mean Temperature), were retrieved. These data have been further scaled using DTM (Digital Terrain Model) obtained from ASTER images (Advanced Spaceborne Thermal Emission and Reflection Radiometer) at 30 meters resolution (<http://asterweb.jpl.nasa.gov/gdem.asp>) through the techniques defined in Flores et al. [16]. The solar radiation data were obtained from re-processed products from satellite imagery on a global scale MERRA301 (Modern Era Retrospective-Analysis for Research and Applications) (<http://disc.sci.gsfc.nasa.gov/mdisc/documentation/data-re-processing>).

For both cases, vapour pressure deficit values (mBar) were retrieved from relative humidity and maximum/minimum temperature through the relation proposed by [17].

For case study 2, in order to perform future scenarios of forest resource and the carbon storage capacity we forced the model using future meteo-climatic scenarios datasets derived from global forecasting models with time range of 8-10 years. In particular we used the climatic data provided by

the HadCM3 global climatic model associated with the B1 emission scenario[18], which stands in an intermediate position between the temperature forecast future scenarios.

Satellite data

Multi-temporal NDVI information from satellite imagery has been used to determine Leaf Area Index variable. The derived multi-temporal profiles were reflecting the photosynthetic activity and the amount of active green biomass over the entire period and test site. Due to noise in the original data, caused mainly by clouds, cloud shadows and different view angles, it was not possible to directly extract reliable plant related information. For case study 1 Leaf Area Index (LAI) images were created starting from 13 ALOS-AVNIR2 LB2G satellite images, with UTM georeference and 10 meters of spatial resolution, covering the area of interest through years 2007-2010. These images were covering the area with different percentages, from 18% to 97%. Where data were missing a mix of interpolation and merging techniques were used to obtain complete information. For case study 2 LAI images were created starting from Landsat TM 5 and ETMp 7 imagery with a ground resolution of 30 x 30m to produce the multi-temporal NDVI information to determine the condition of the forest area between 2002 and 2009. Therefore the dataset was filtered with the “modified Whittaker smoother” [19] approach using the software package “MODIS” [20] [21]. But the scarce availability of Landsat data within the test sites did not allow a reliable filtering. Therefore the forced alternative MODIS-13Q1 was used, reducing the effective ground resolution to 230 x 230 m and, compared to the profiles derived from Landsat, increasing the temporal profile reliability for the sample area.

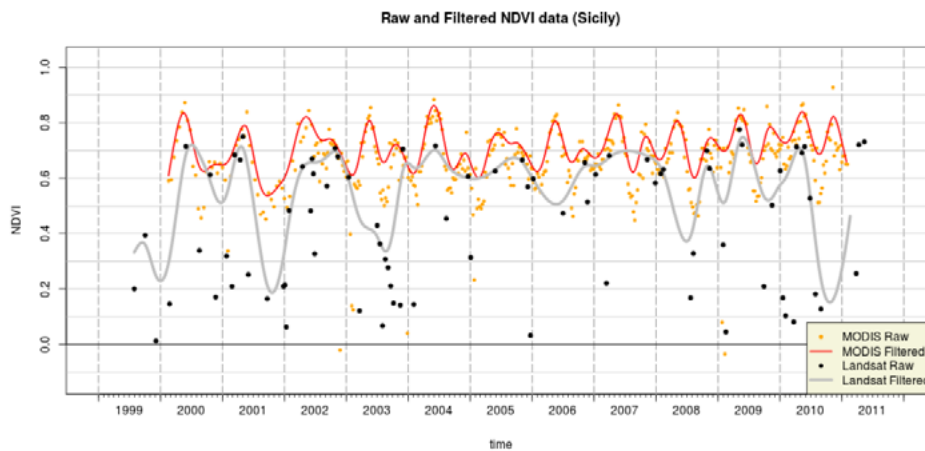


Fig 1: Example of NDVI curve before and after filtering for the same location with Landsat and MODIS data

Every image was radiometric calibrated and georeference was adjusted if needed. Considering only Red and Near Infra Red calibrated bands, the following relations were used to obtain Normalized Difference Vegetation Index and subsequently LAI, applying the well established exponential relationship [23], using the approach of Nolè et al. [24].

Final LAI images for every year were created with 12 layers, each one representing a month of data, with resolution of 100x100, 30x 30 and 10x10 meters.

Finally we run the 3D-CMCC FEM to produce outputs, on monthly and yearly basis, for the state variables such as gross primary productivity (GPP, $gC\ m^{-2}yr^{-1}$) and net primary productivity (NPP, $tDM\ ha^{-1}yr^{-1}$). Other model outputs directly or indirectly related with carbon and soil water balance such as evapotranspiration (ET, $mm\ yr^{-1}$), leaf area index, rain interception all at class-level (species, age or height), layer-level and stand level were computed. Moreover other model outputs, useful for forest management decision such as the current and mean annual increment of volume (CAI, $m^3\ ha^{-1}yr^{-1}$ and MAI, $m^3\ ha^{-1}yr^{-1}$ respectively) and mean diameter at breast height (DBH) were provided.

4. RESULTS

The model results related to W_s (stem biomass) and W_r (root biomass), for case study 1 (see Fig. 2 and 3), were validated for all the years of simulation (2007 to 2010, 4 years) against data obtained using the stereometric and allometric tables for *Fagus sylvatica* L.. We assumed a linearly biomass increment, from January 2007 (first year of run) to December 2010, considered the year in which the data are measured as for the values of stem biomass. From the stem biomass and root biomass values estimated for the year 2010, we computed the root/shoot ratio; that ratio, combined with the 2007 stem biomass value, was used to compute the root biomass of 2007. The model validation showed a strong correlation between the simulated data and the measured data. In the case of stem biomass (W_s) the small values obtained for RMSE (0.0016 tonnes of DryMatter a^{-1}) and the high value of the coefficient of determination ($R^2 = 0.9439$), show a good agreement with observed values. Nevertheless the model tends to underestimate for 0.04 tDM a^{-1} the stem biomass for the 4 years of simulation. In the same way, the results for root biomass (W_r) simulation show a good ability of the model to predict this variable with a high coefficient of determination ($R^2 = 0.9263$) and low RMSE (0.0001 tDM a^{-1}). Differently to the stem biomass, the model tends to overestimate the root biomass of about 0.002 tDM a^{-1} at the end of the four years of simulation. For the simulation of GPP and NPP the output of the model are in reasonable agreement with the literature data with average values of 992.41 gC $m^{-2} year^{-1}$ of GPP and 0.061 tDM $a^{-1} year^{-1}$ of NPP. For the case study 2 for the years 2002-2009 the model showed a good ability in estimating both the gross (see Fig. 4) and the net productivity rates for different forestry classes in line with the values reported in the literature for Italian forests [25], [4], [26]. The output values for the period 2002-2009 of GPP for beech (1330 gC $m^{-2} year^{-1}$), for chestnut (1258 gC $m^{-2} year^{-1}$) and for temperate deciduous oak (1265 gC $m^{-2} year^{-1}$) were comparable with the literature data of 1318, 1393, 1355 gC $m^{-2} year^{-1}$ respectively. For the period 2010-2020 through the use of future meteorological scenarios the model shows for beech forests an average reduction in GPP of about 70%, for chestnut of about 40% and for temperate deciduous oak of about 20%.with a really strong decrement both for GPP and NPP in the last years of simulation.

5. DISCUSSION AND CONCLUSIONS

The results of the model implementation for both case study show good capability of the model to simulate GPP, NPP and carbon allocation in the stem and root compartments. Slightly differences between measured and simulated data can be considered acceptable and physiological. These inaccuracies to estimate the values are probably solvable with a better model calibration in the future especially in the model partitioning-allocation routine. For the case study 2 the slight overestimation for the period 2002-2009 produced by the model against literature values, is mainly related to the juvenile age of the stand (about 22 years). The model also showed a high sensitivity to environmental variables disclosing to capture the years of 2003 and 2007, particularly unfavorable for forest productivity, characterized by abnormal heat waves on a continental European scale and very intense in the Mediterranean basin. In particular, for the years 2007, the rates of gross productivity experienced a strong decrease due to the high temperatures and the strong reduction in precipitation especially during the vegetative phase on which the deciduous species are particularly sensitive. The strong reduction for GPP and NPP rates for the years 2010-2020 are clearly overestimated by the model. The causes of these overestimations are partially due to the lack in the model routine of a physiological based simulation of the species adaptability to the changes of environmental conditions. Nevertheless a strong contribution to this overestimation may also be attributed to the low spatial resolution of climate data. This is especially the case of the Madonie Park, which is located in a mountainous area (about 1000 meters a.s.l.) but very close to the coastline (about 20 kilometers). As a matter of fact a single climatic cell included a very large area, considering as a unit both mountain and coastal areas, and not highlighting the topographic and thus climatic differences within the extremely various territory. So this strong reduction in productivity may be the product of the overestimation of predicted temperatures and a strong underestimation of precipitations on a wide portion of coast land, level land and sea areas.

It is however important to note that the model was able to simulate the reduction in rates of productivity for those species that are more hygrophilous and temperate (e.g. beech), while reductions were lower for those species most adaptable (e.g. temperate deciduous oak). In conclusion, the high correlation showed between observed and computed data for the two cases study can be considered statistically meaningful and hence the model can be considered a good predictor both for high resolution (10 m x 10 m or 30 m x 30 m) and for short period of simulation. However it is very important to run the model, in order to improve the overall accuracy of estimates, using a more

accurate calibration and parameterization. Nevertheless the coupling of satellite data at high resolution and field information as input data generally improved the 3D-CMCC FEM model reliability. These data can be also successfully used to simulate at regional scale the main physiological processes and to produce reliable output to better investigate forest growth and dynamics.



Image 1: Map of Landsat images in south-central Italy overlapped on the study areas

Variable	Units	Description	Optional/Mandatory
Tmax	C°	Mean monthly maximum temperature	M
Tmin	C°	Mean monthly minimum temperature	M
Tav	C°	Mean monthly temperature	M
Solar Rad	MJ m ⁻² day ⁻¹	Solar radiation	M
Rh	%	Relative humidity	M
Frost days	days month ⁻¹	Frost days	O
Rain	mm month ⁻¹	Cumulated monthly precipitation	M
Swc	% vol	Soil water content	M
LAI	m ² m ⁻²	Leaf area index	O

Tab. 1. Meteorological monthly input data.

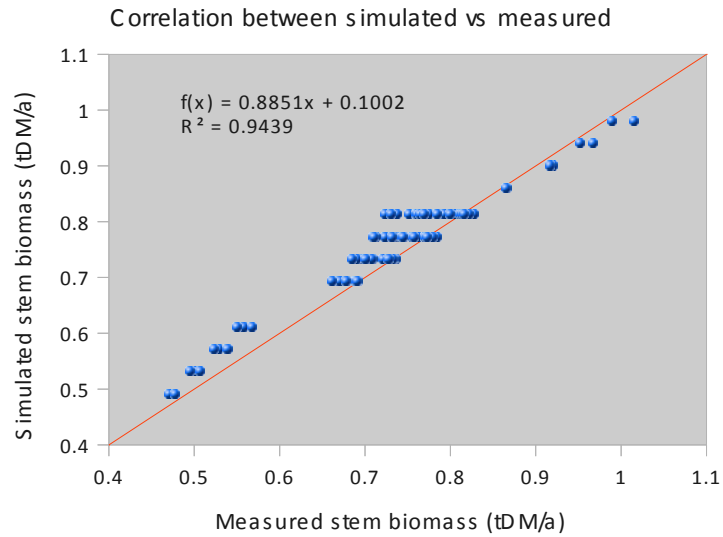


Fig. 2: Relationship between measured and simulated stem biomass for case study 1

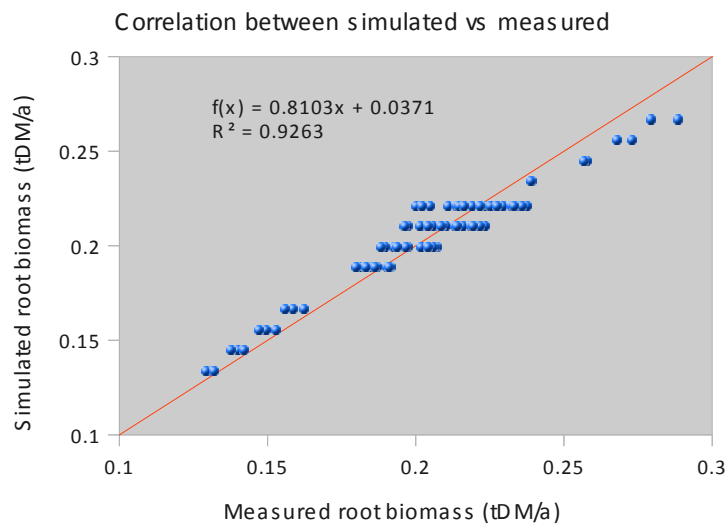


Fig.3: Relationship between measured and simulated root biomass for case study 1

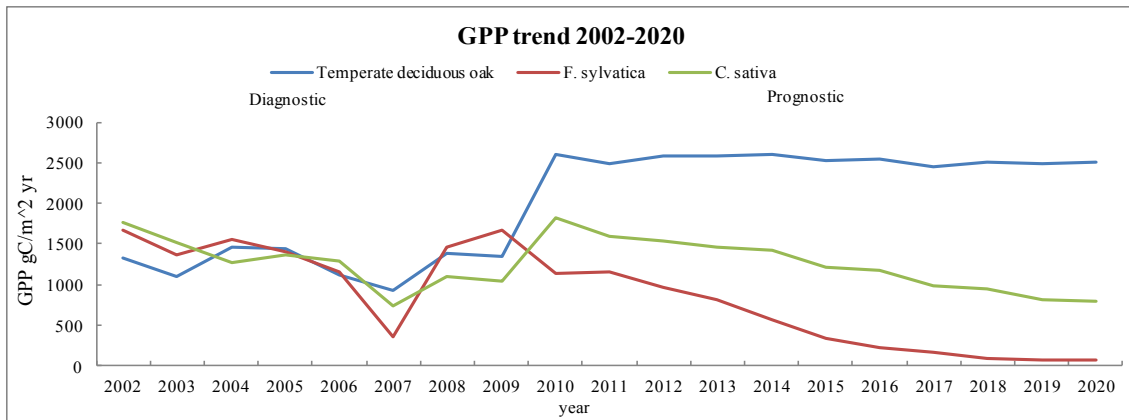


Fig.4: Gross primary production (GPP) for the simulation period 2002-2020 for case study 2

6. ACKNOWLEDGMENTS

Authors acknowledge the European Space Agency (ESA) for partially funding the development of the spatial version of the system in the framework of the KLAUS project (<http://rssportal.esa.int/deepenandlearn/tiki-index.php?page=KLAUS+Project>)

7. REFERENCES

- Magnani F., Mencuccini M., Borghetti M., Berbigier P., Berninger F., Delzon S., Grelle A., Hari P., Jarvis P.J., Kolari P., Kowalsky A., Lankreijer H., Law B. E., Lindroth A., Loustau D., Manca G., Moncrieff J., Raymet M., Tedeschi V., Valentini R., Grace J. (2007). *The human footprint in the carbon cycle of temperate and boreal forests*. Nature, 447 (7146), p. 849-851. (1)
- Veroustraete F., Sabbe H., Eerens H., (2002). *Estimation of carbon mass fluxes over Europe using the C-Fix model and Euroflux data*. Remote Sensing and Environment, vol 83, p. 376-399. (2)
- Waring R., Running S. (1998). *Forest ecosystems. Analysis at multiple scales (2nd edition)*. San Diego, USA: Academic Press. (3)
- Maselli F., Barbati A., Chiesi M., Chirici G., Corona P. (2006). *Use of remotely sensed and ancillary data for estimating forest gross primary productivity in Italy*. Remote Sensing and Environment, vol. 100, p. 563-575. (4)

- Running S.W., Baldocchi D.D., Bakwin P.S., Hibbard K.A. (1999). *A global terrestrial monitoring network integrating tower fluxes, flask sampling, ecosystem modeling and EOS satellite data*. Remote Sensing of Environment, vol. 70, p. 108–127. (5)
- Chiesi M., Maselli F., Bindi L., Fibbi L., Cherubini P., Arlotta E., Tirone G., Matteucci G., Seufert G. (2005). *Modelling carbon budget of Mediterranean forests using ground and remote sensing measurements*. Agricultural and Forest Meteorology, vol. 135, 22-34. (6)
- Caselles V., Hill J., Lacaze B. (1996). *Integrated approaches to desertification mapping and monitoring in the Mediterranean basin*. Final report of De-Mon I Project. Ispra (VA), Italy: Joint Research Centre of European Commission. (7)
- Collalti A., Perugini L., Santini M., Chiti T., Nolè A., Matteucci G., Valentini R. (2013). *A process-based model to simulate growth in forests with complex structure: evaluation and use of 3D-CMCC Forest Ecosystem Model in a deciduous forest in Central Italy*. Submitted to Ecological Modelling. (8)
- Landsberg J.J., Waring R.H. (1997). *A generalised model of forest productivity using simplified concepts of radiation-use efficiency, carbon balance and partitioning*. Forest Ecology and Management. vol. 95, p. 209-228. (9)
- Thorton, P. (2010). *Biome BGC version 4.2: Theoretical Framework of Biome-BGC*. Technical documentation. (10)
- Bossel H. (1996). *TREEDYN3 forest simulation model*. Ecological Modelling. Vol. 90, p. 187-227. (11)
- Huth A., Ditzer T. (2000). *Simulation of the growth of a lowland Dipterocarp rain forest with FORMIX3*. Ecological Modelling. vol. 134, p. 1-25. (12)
- Peng C., Liu J., Dang Q., Apps M.J., Jiang H. (2002). *TRIPLEX: a generic hybrid model for predicting forest growth and carbon and nitrogen dynamics*. Ecological Modelling. vol. 153, p. 109-130. (13)
- Sitch S., Smith B., Prentice I.C., Arneth A., Bondeau A., Cramer W., et al., 2003. *Evaluation of ecosystem dynamics, plant geography and terrestrial carbon cycling in the LPJ dynamic global vegetation model*. Global Change Biology. vol. 9, p. 161-185. (14)
- F. Attorre, F. Francesconi, R. Valentini, A. Collalti, F. Bruno (2008). *Production of climatic and bioclimatic maps by Universal Kriging with external drift: theory and examples for Italy*. Forest@, 5. (15)

- Flores F. P., Lillo M. S. (2010). *Simple Air Temperature Estimation Method from MODIS Satellite Images on a Regional Scale*. Chilean J. Agric. Res. vol.70, no.3, p.436-445. (16)
- FAO *Penman-Monteith equation: calculations and options for substitutions for missing data IPCC, 2001: Climate Change 2001: Impacts, Adaptation and Vulnerability*. CUP, Cambridge, UK. (17)
- Atzberger C. and Eilers P.H.C., September 2011. *A time series for monitoring vegetation activity and phenology at 10-daily time steps covering large parts of South America*. International Journal of Digital Earth, Vol. 4, No. 5, 365-386. (18)
- MattiuZZi M., Verbesselt J., Stevens F., Mosher S., Hengl T., Klisch A., Evans B. and Lobo A. (2013). *MODIS: MODIS download and processing package. Processing functionalities for (multi-temporal) MODIS grid data. R package version 0.8-14*. <http://r-forge.r-project.org/projects/modis/> (19)
- R Core Team (2013). *R: A language and environment for statistical computing*. R. Foundation for Statistical Computing, Vienna, Austria. ISBN 3-900051-07-0, URL. <http://www.R-project.org/> (20)
- Myneni R.B., Keeling C.D., Tucker C.J., Asrar G., Nemani R.R. (1997). *Increased plant growth in the northern high latitudes from 1981 to 1991*. Nature. vol. 386, p. 698-702. (21)
- Nolè A., Law B.E., Magnani F., Matteucci G., Ferrara A., Ripullione F., et al. (2009). *Application of the 3-PGS model to assess carbon accumulation in forest ecosystems at a regional level*. Canadian Journal of Forest Research. vol. 39, p. 1647-1661. (22)
- Chiesi M., Maselli F., Moriondo M., Fibbi L., Bindi M., Running S. (2007). *Application of BIOME-BGC to simulate Mediterranean forest processes*. Ecological Modelling. vol. 206, p. 179-190. (23)
- Maselli F., Chiesi M., Moriondo M., Fibbi L., Bindi M., Running S.W. (2009). *Modelling the forest carbon budget of a Mediterranean region through the integration of ground and satellite data*. Ecological Modelling. vol. 220, p. 330-342. (24)

Are cereals globally in trouble?

De Cian E.^{1*}, Sue Wing I.²

¹*Fondazione Eni Enrico Mattei, Dep. of Earth and Environment, Boston University*

²*Dep. of Earth and Environment, Boston University*

*Corresponding author: enrica.decian@feem.it

Abstract

This paper estimates the impacts of climate change on the productivity of four major grains across the world, rice, maize, wheat, and sorghum. High-resolution data on agricultural maps, crop calendar, and geospatially referenced dams for irrigation are paired with fine-scale weather data to estimate the response of crop productivity to temperature and precipitation variations between 1961 and 2010. The paper characterizes the pattern of temperature and precipitation impacts on crop yields and total cereal production around 2050 by climatic areas (temperate versus tropical and sub-tropical regions), distinguishing between irrigated and rain-fed areas.

If we consider the gap between the short-term reaction to weather shocks and the long-term response as an indicator of the adaptation potential, our results suggest that adaptation does not significantly reduce impacts over time, especially in rain-fed tropical areas. A change in temperature or precipitation distribution would have long-lasting effects, which would take between six and twenty years to disappear. Our differentiated results for irrigated and rain-fed areas suggest that irrigation can be effective in tropical areas to deal with high temperature levels. It would be not effective at dealing with low precipitation and heavy rainfall.

Cereals will be in trouble, globally and regionally, as the total amount of calories produced by the top producers will decline. To some extent irrigation will be able to mitigate these losses, but the efficacy of this adaptation strategy will be conditioned on the climate itself and future precipitation patterns could actually exacerbate impacts in largely irrigated regions.

Keywords: Climate change, adaptation, agriculture, global impacts



Cereals are the major source of calories to most world population but the composition differs regionally and different part of the world rely on different diets. Developing countries depend more on cereals for direct consumption than the developed ones, where the indirect use of cereals (feed livestock, food industry) can exceed direct consumption. The type of grains produced and consumed varies across regions due to social, economic, and environmental factors. The three major cereals are maize, rice and wheat. Sorghum production is globally ten times smaller than average production of any of the big three grains, but it is an important contributor to calories intake in various countries in South Asia and Africa. While rice and maize are highly traded, rice and sorghum are produced mostly for domestic consumption ([1]). Climate change will affect different cereals in a different way. The question is whether a specific cereal will be hit more where it is mostly consumed, whether substitution across cereals will allow us to maintain diets with an equivalent calorific content. Prior studies, especially those using more precise climate data, focused on maize. In order to formulate general conclusions regarding the agricultural risk to climate and the implications for food security we examine how climate could affect the portfolio of the main cereals consumed.

Temperature and precipitation are the major environmental factors that influence crop productivity. The mode of climate variation that is relevant to each crop varies over crops, over the growing season, and across regions. Fine-scale, gridded climate data enable us to identify the relevant climate variability over the growing season. Recently, a number of assessments have exploited the greater variability of daily climate data to account for the full distribution of climate indicator, but mostly with a regional focus on the United States. [13] and [3] infer physical responses to climate from the daily distribution of temperature. [13] use daily climate data to study climate change impacts on agriculture in the United States. [3] use daily climate data to study climate change impacts on mortality rates in the United States. Since the majority of crop studies have focused on the United States, a lot of emphasis has been put on the corn and on the role of temperature. The few studies that considered the whole portfolio of cereals, globally, relied on coarser data. [5] and [6], the most recent assessments to characterize the heterogeneity in the climate response functions across the world, use monthly weather data. A quadratic terms of growing season average precipitation and average temperature data is meant to capture the particularly harmful effects of extreme cold and hot weather.

Our study improves over prior global assessments in a number of ways. First, while existing global studies rely on monthly climate data ([5], [6]), we provide more precise estimates of yield responses by

considering the distribution of daily mean temperature and precipitation. Methodologically, our study follows the approach recently introduced in the field of climate change impacts and health in the United States by [3] and we model the effect of daily temperature and precipitation semi-parametrically, using a number of separate bins. Inter-annual variation is used to infer the impacts of climate change. Future impacts are then assessed using more updated climate scenarios from the GFDL-CM3 climate model¹, both for tropical and temperate regions. Daily data on precipitation and temperature up to 2010, paired with more updated climate scenarios, give us an improved evaluation of climate shocks to yield around 2050. The finer spatial and temporal resolution of data allows better accounting for the distribution of precipitation and temperature across world regions, differentiating the response between tropical and temperate regions.

Second, we differentiate the immediate response to weather shocks from long-term response that includes adjustment to expected weather and thus, to some extent adaptation, whereas most published studies delivered static or short-term effects. Short-term estimates capture the responses to inter-annual variation, or weather, while long-term semi-elasticities might give a better indicator of the response to expected changes in climate. As discussed in [2], long-term impacts can be larger or smaller than short-run ones. Farmers might have more adaptation options in the long-term, but at the same time some adaptation strategies are only sustainable for a short period of time. We describe the relationship between log yield and climate as an error correction model (ECM), which is a reformulation of an autoregressive distributed lag model where the crop log yield depends on lagged yield as well as contemporaneous and lagged temperature and precipitation variables. Farmers decide about crop varieties and planting based on expectations about land quality and weather. This yields the long-run equilibrium between yields and weather patterns. At any time, a change in weather compared to the expectations would cause yields to be different from the expected long-run equilibrium. An ECM model describes the long-term relationship, as well as any short-term deviation from that. The error-correction speed of adjustment parameter informs about the movement towards the long-run equilibrium and is expected to be negative and significant in the presence of a long-run relationship.

Third, we evaluate the contribution of historical adaptation to climate impacts on yields. In addition to using the difference between short- and long-run elasticities to identify the effectiveness of adaptation, we separate the climate effect from that of other variables that account for the role of irrigation,

¹ <http://www.gfdl.noaa.gov/coupled-physical-model-cm3>

fertilizers, technology, and machinery. Not controlling for these variables would bias the impact estimates upward (they would be less negative), as they would confound the effect of climate with that of technology.

Our results (Table A1, A2, A3) indicate that short- and long-term responses can be very different, in both directions, with results that are crop-specific. In the case of maize, the negative impacts of an additional day with high mean temperature is persistent in both temperate and tropical regions. If we consider the gap between the short-term response to a weather shock and the long-term response as an indicator of the adaptation potential, results for rain-fed crops indicate low adaptation potentials for rain-fed maize worldwide. This implies that prior studies that rely on static estimates are likely to have underestimated the impacts on corn. In the case of wheat, static or short-term semi-elasticities underestimate the impacts in tropical regions, where adaptation potentials are lower, but overestimated them in temperate regions, where there appears to be a great potential for adaptation. Regarding tropical rice, high precipitation levels damage crop productivity only in the long-run (Table A1).

Adaptation does not significantly reduce impacts over time, especially in rain-fed, tropical areas where the negative effects of temperature on rice, maize, and wheat remain significant also in the long-run. A change in the temperature or precipitation distribution would have a long-lasting effects, which would take between six and twenty years to disappear. Our differentiated results for irrigated and rain-fed areas suggest that irrigation can be effective in tropical areas to deal with high temperature levels. It appears less effective at dealing with low precipitation or heavy rainfall.

Figure 1 summarizes the qualitative pattern of the estimated impacts for the rain-fed and irrigated crops in tropical and temperate regions. Estimated coefficients are reported in the tables in the appendix. By considering the full distribution of both temperature and precipitation we are able to identify the effect of extreme climate outcomes not only in terms of heat, but also in term of drought and flooding. It shows that irrigated areas remain exposed to the risk of drought and flood, whereas the potential damage caused by extreme heat mostly occurs in rain-fed areas.

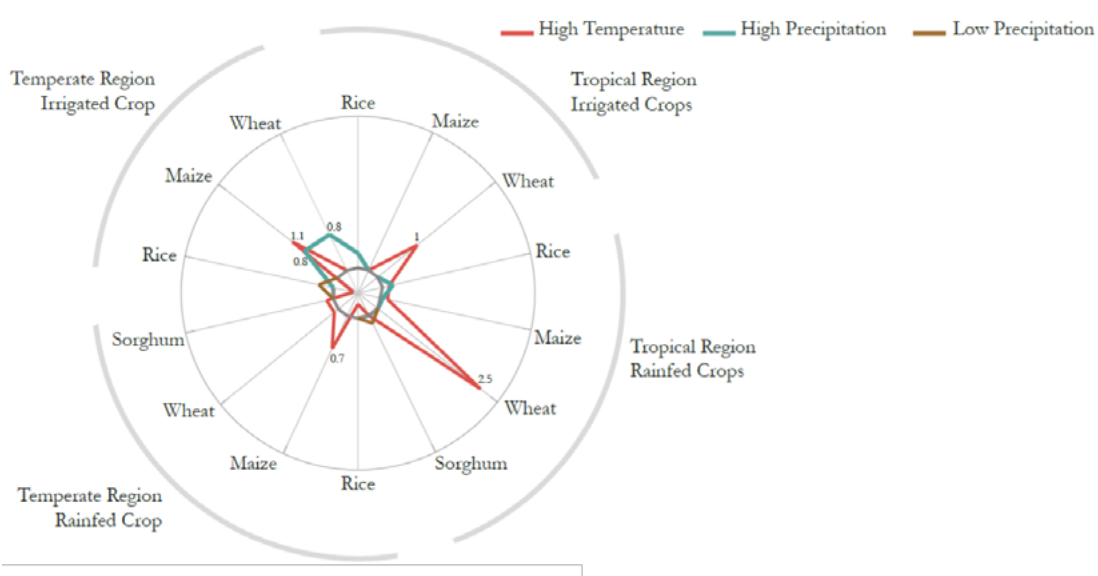


Fig. 1: Estimated vulnerability of different cereals to high temperature, high and low precipitation levels. Numbers represent long-term effects. Positive numbers denotes reductions, negative numbers denote increases in crop productivity.

The long-term elasticities of crop productivity to the historical variation in the distribution of daily precipitation and temperature are combined with future climate scenarios to compute the future impacts of climate change on crop productivity.

We considered two climate scenarios, the Representative Concentration Pathway RCP 8.5 and 2.6 ([9]) as simulated by the GFDL-CM3 climate model². Using model's results, we define the current and future distribution of daily temperature and precipitation during the growing season of each cereal, weighting the frequencies counted in each cell with the normalized harvested area for that specific crop. Future climate (henceforth 2050) is defined as the decadal mean between 2046 and 2055, current climate as the average precipitation and temperature daily conditions between 2006 and 2015 (henceforth present). Predicted yields are obtained by applying the long-term semi-elasticities to the difference in the frequency distribution between future and current daily temperature and precipitation. Summing over bins and exponentiating crop yields we obtain the ratio of future to current yield in each

² <http://www.gfdl.noaa.gov/coupled-physical-model-cm3>. We are currently calculating the impacts for an ensemble of models used in CMIP5.

country and for each crop. The calculation assumes that crop productivity changes are only driven by changes in production while the harvest area is held constant. By comparing the future impacts in high (8.5) and low (2.6) emission scenarios, we can make some considerations regarding the expected impact of mitigation around 2050.

Future impacts will be driven by the estimated semi-elasticities and the future distribution of daily mean temperature and precipitation. Figure 2 and 3 illustrates the exposure of the four cereals to extreme climate change outcomes in the RCP 8.5 and 2.6, respectively³. It focuses on the tail of the temperature and precipitation distributions, extreme heat (days with mean temperature $>30^{\circ}\text{C}$), extreme precipitation ($>15\text{mm/day}$), and drought ($<5\text{mm/day}$).

In the high emission scenario (RCP 8.5), regions where extreme heat will become particularly more frequent include Sub-Saharan Africa, South East Asia, Central America, and selected places in the US and Australia. Mitigation (Figure 3) could reduce the frequency of hot days especially in African and South-East Asian countries. Panels (a) and (b) suggest that some places will become drier even if they will not get extremely warmer. Consider for example South Africa. The frequency of hot days will increase less than in other places, but the number of days with scarce precipitation will increase more than in other places. The effect of mitigation on precipitation patterns is more uncertain, and what can change is also the spatial distribution. The maps also point at the significant heterogeneity within the boundaries of the same country. Since the estimated yield response functions differentiate the semi-elasticities by temperature and precipitation bin, when projecting climate change impacts into the future we partly preserve the observed spatial heterogeneity⁴.

³ Cell-weighted frequencies counted within the extreme temperature and precipitation bins have been summed over crops.

⁴ Our ability to capture the spatial heterogeneity is limited by the fact that production and harvested area time series data is available at the country level.

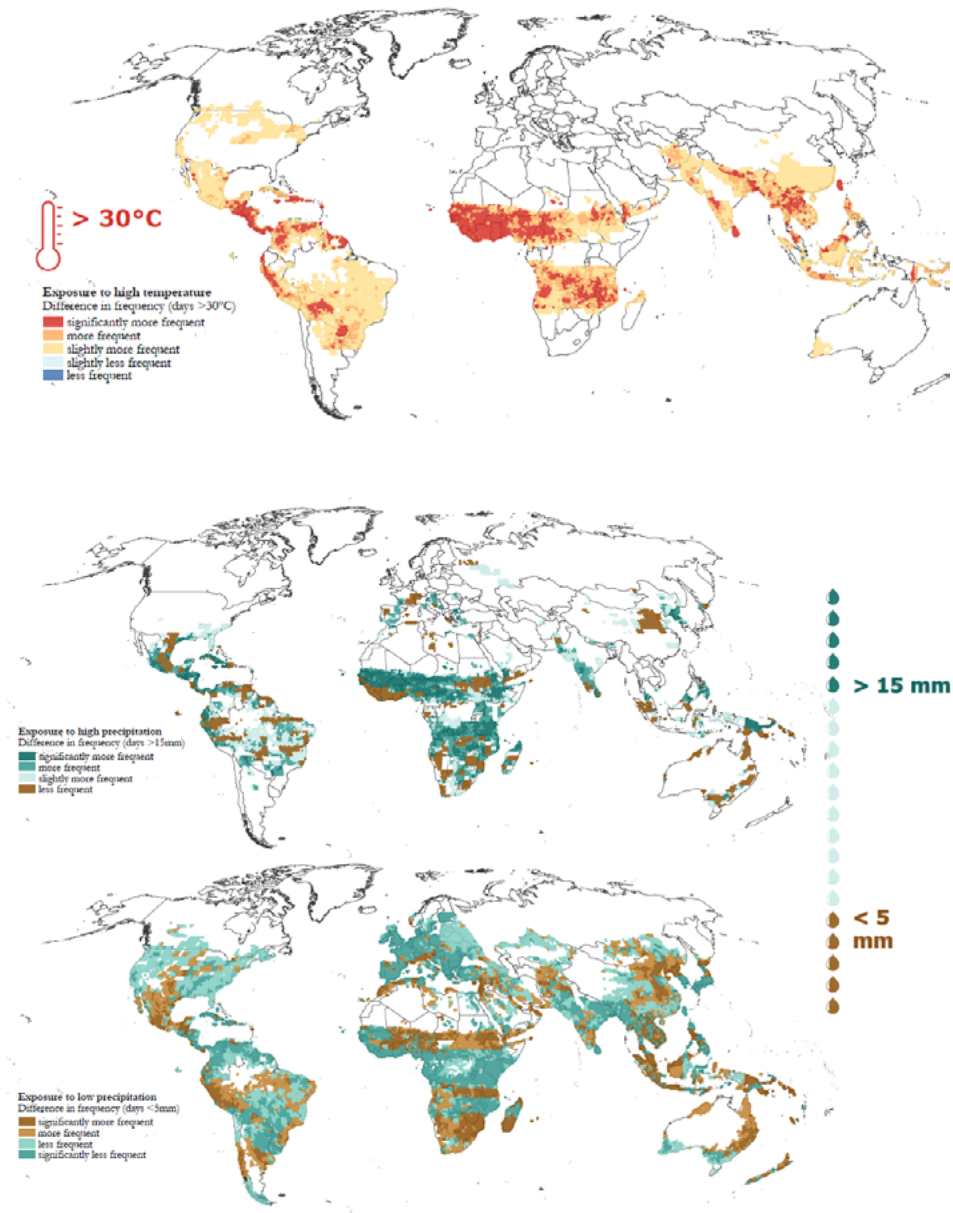


Fig. 2: Future exposure of wheat, rice, sorghum, and maize to extreme heat (a), heavy precipitation (b), and scarce precipitation (c). Maps show the frequency of additional cell-weighted days with daily mean temperature above 30°C (a), with daily mean precipitation above 15mm/day (b), with daily mean precipitation below 5mm/day (c) in 2050 (2055-2046) vs. Present (2015-2006) during the growing season in the RCP8.5 scenario simulated by the GFDL-CM3 climate model. Dark yellow/brown color indicates more days with high temperature (>30°C) in panel (a), with low precipitation (<5mm/day) in panel (b), and with precipitation less than 15mm/day in panel (c). Blue indicates more days with precipitation levels above 5mm/day in panel (b) and above 15mm/day in panel (c).

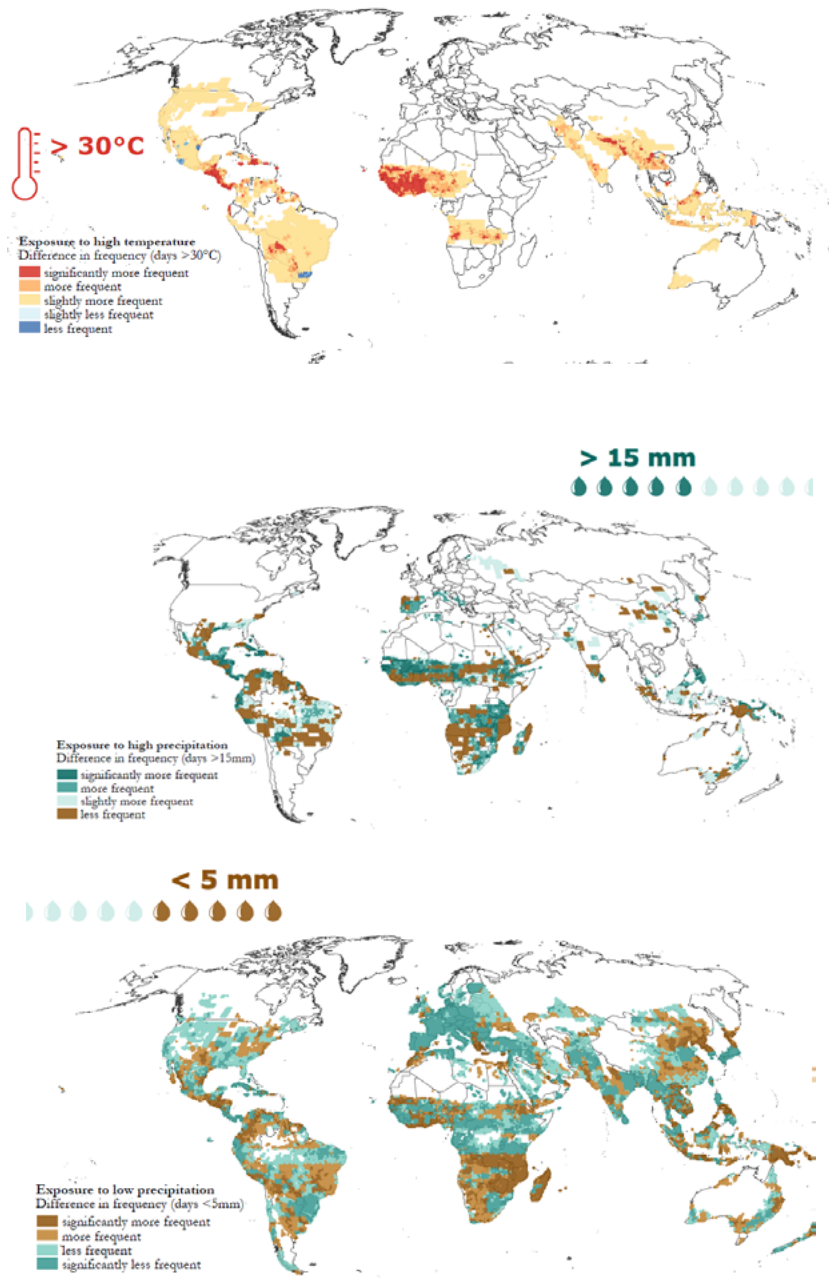


Fig. 3: Future exposure of wheat, rice, sorghum, and maize to extreme heat (a), heavy precipitation (b), and scarce precipitation (c). Maps show the frequency of additional cell-weighted days with daily mean temperature above 30°C (a), with daily mean precipitation above 15mm/day (b), with daily mean precipitation below 5mm/day (c) in 2050 (2055-2046) vs. Present (2015-2006) during the growing season in the RCP2.6 scenario simulated by the GFDL-CM3 climate model.

Figure 4 shows the future impacts of climate change on crop productivity. The range of estimated impacts tends to become less negative and shifts toward the positive quadrant when considering irrigated crops, especially in the case of wheat and rice. Major producers experience losses also in irrigated areas, especially in the case of maize and wheat. Previous studies based on crop model ([10]) also suggested that irrigated grains are generally more negatively affected by climate change. Although irrigated areas can deal with temporary droughts and heat, this adaptation strategy is less effective at coping with extreme precipitation levels, on both tails of the distribution. At the same time, irrigated areas might more vulnerable. Mitigation could reduce climate change impact in some crops and some regions (e.g. wheat in Brazil, maize in China), but the general pattern of estimated vulnerability is not expected to change significantly. The main reason is that even the extreme scenario RCP 2.6 starts to diverge from the high emission case when it is too late to have an effect on 2050 impacts.

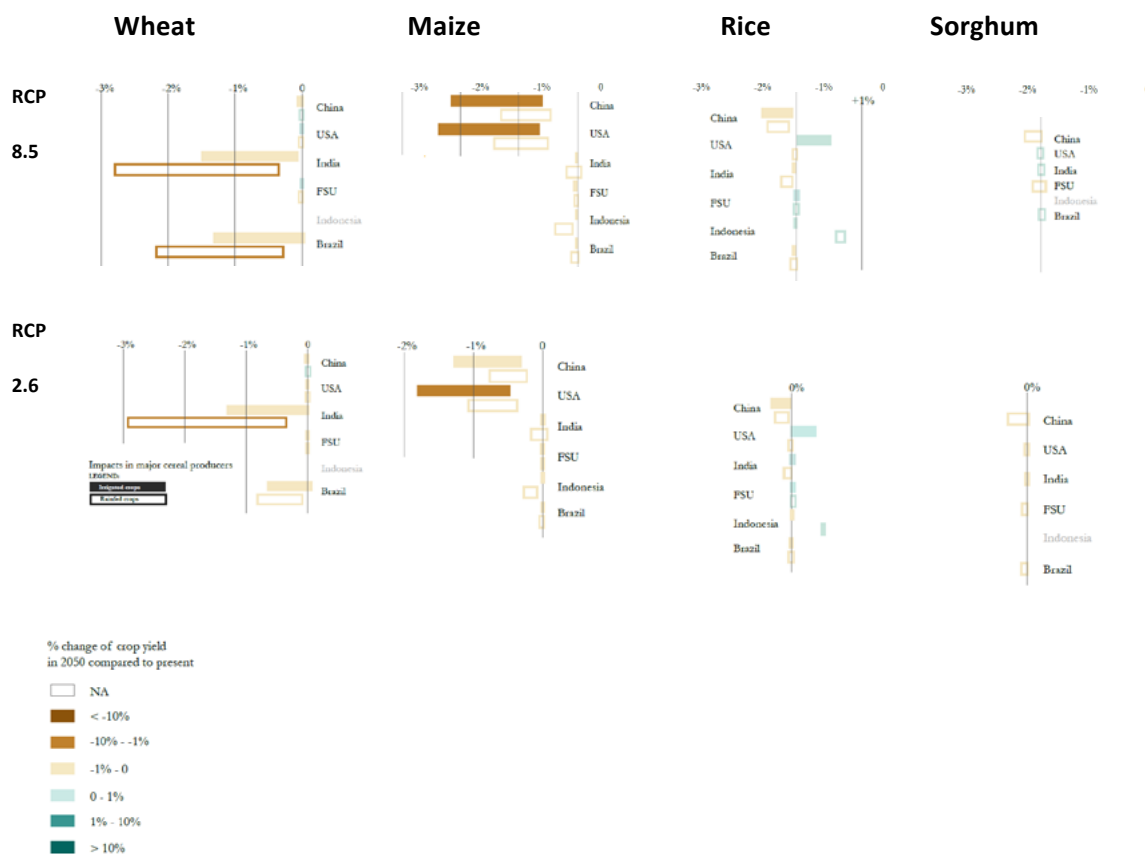


Fig. 4: Future climate impacts on cereal productivity in major producers around 2050 relative to present, 90% confidence intervals. Brown denotes negative impacts, blue represents positive impacts. Filled boxes refer to irrigated crops, empty boxes to rain-fed crops. If a crop is not available, country name appears in light grey.

Figure 5 suggests that the distribution of temperature and precipitation simulated for 2050 will lead to lower cereal production in the major producers. The USA, China, India, which are the top producers, would reduce the calories produced the most. Their production losses could range between 13 and 32 billion kcal, which is comparable to the current production of Paraguay (12 bn kcal) or Venezuela (14 bn kcal) and Spain (35 bn kcal). Table 1 summarizes the effects on future global production as share of current production. Overall, cereal production could decline by 0.25%, but a global increase equal to 0.21% cannot be ruled out. Gains in rice and sorghum productivity would account for such increase, whereas the global negative figures are driven by the vulnerability of maize and wheat, a result already found in previous studies (e.g. Hertel et al. 2010).

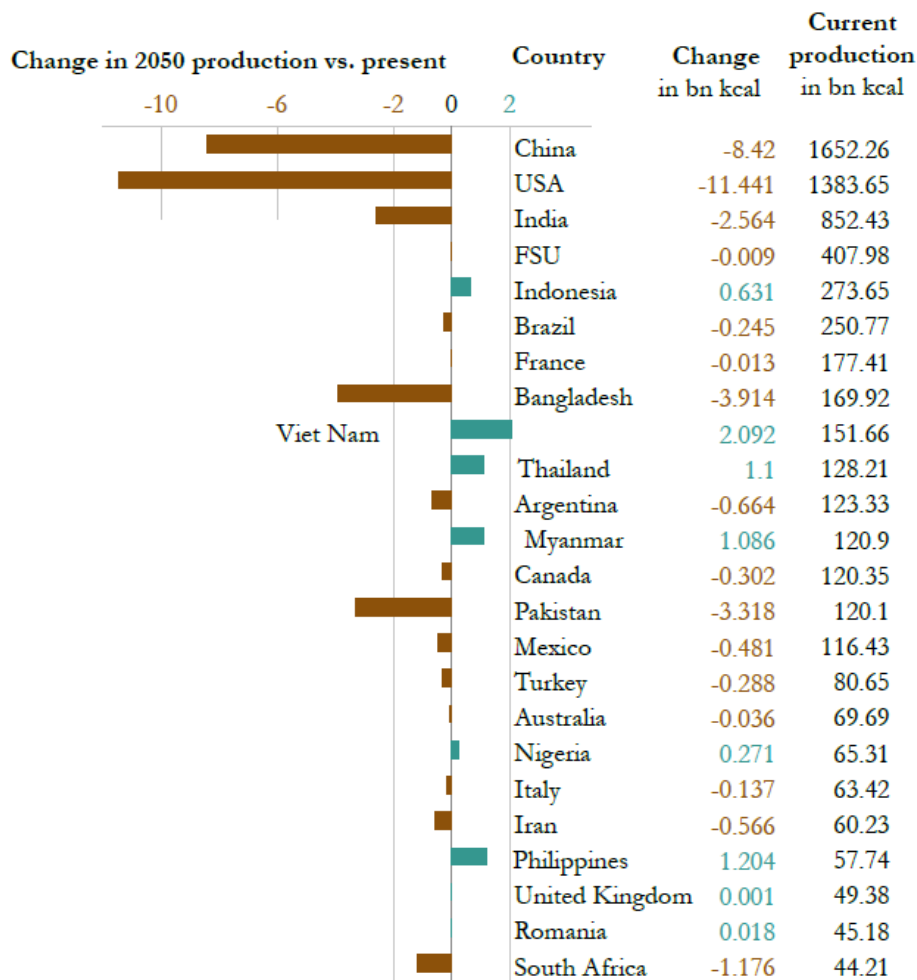


Fig. 5: Calorie production change in 2050 vs. present in selected major producers of cereals. Production has been computed as the product of current harvested area (average values between 2006 and 2010) and the estimated gap in crop yields, using point estimates – high emission scenario (RCP 8.5). Current production levels refer to the annual average production between 2006 and 2010 as in the FAOStat Database.

		Maize	Wheat	Rice	Sorghum	Cereals
(Bn kcal)	Point est.	-23.22	-12.3	16.26	0.39	-18.87
(Bn kcal)	Lower	-39.45	-21.47	10.54	0.79	-49.59
(Bn kcal)	Upper	-5.79	-1.84	23.29	0.05	15.7
Prod. (Bn kcal)		2805	2138	2340	205	7489
%	Point est.	-0.83%	-0.58%	0.69%	0.19%	-0.25%
%	Lower	-1.41%	-1.00%	0.45%	0.39%	-0.66%
%	Upper	-0.21%	-0.09%	1.00%	0.02%	0.21%

Table 1: Future climate impacts on global cereal production. Percentage change compared to current production levels (2010-2006 average) in rain-fed and irrigated areas under the high emission scenario (RCP 8.5).

Future impacts on cereal production suggest that cereals will probably be in trouble, both globally and regionally, as the total amount of calories produced by top producers countries will decline. Irrigation could attenuate this effect, though the efficacy of this adaptation strategy is conditioned on the climate itself and future precipitation patterns could exacerbate impacts in largely irrigated regions.

The estimated elasticity with respect to per capita GDP (see tables A1, A2, A3) suggests that crop productivity will increase anyway, but because of climate change it will increase by less than otherwise. Our analysis identifies a number of hot spots where economic growth will not compensate the potential impacts of climate change. These places are located in areas already characterized by unfavorable conditions to agriculture and where vulnerability to days with high mean temperature or too low/high precipitation levels is expected to increase under the RCP 8.5 scenario. They include Bhutan, Ecuador, Israel, Jamaica, Jordan, Kuwait, Lebanon, Lesotho, Malawi, Paraguay, Rwanda, and Swaziland. These countries are among the minor producers of food. If they cannot compensate the

almost entire expected production loss with food imports, climate change impacts on crop productivity can have dire repercussions on the entire economy. A general equilibrium analysis could help to better understand the role of crop substitutability within and across countries and inform about food security and nutritional issues, e.g. will a given cereal will be hit more where it is mostly consumed? Will substitution across cereals and with other sources of calories allow maintaining diets with similar calorific content?

Two major caveats apply to our research. First, our results rely on the distinction between rain-fed and irrigated areas as observed around the year 2000 to derive the crop-specific distributions of past and future temperature and precipitation. In order to obtain more precise estimates, the potential future distribution of irrigation infrastructure and groundwater irrigation, especially in developing countries, should be taken into account. Second, our calculations of future impacts do not account for potential changes in the harvested area. Changes in crop productivity determine changes in total production. This might be a minor issue globally, as the historical expansion of agricultural output has been mostly driven by yield improvements, but it might lead to some bias in some regions that are expected to expand cropland significantly, such as Sub-Saharan Africa, Latin America and Caribbean countries. Ongoing research is testing the sensitivity of impacts to future scenarios from different climate models.

ACKNOWLEDGMENTS

The research leading to these results has received funding from the People Program (Marie Curie Actions) of the European Union's Seventh Framework Program(FP7/2007-2013) under the REA grant agreement n° 298436.

REFERENCES

- Awika J.M. (2011). *Major Cereal Grains Production and Use around the World*. In *Advances in Cereal Science: Implications to Food Processing and Health Promotion*; Awika et al. ACS Symposium Series; American Chemical Society; Washington, DC. (1)
- Burke M. and Emerick K. (2012). *Adaptation to Climate Change: Evidence from US Agriculture*. (2)
- Deschenes O., Greenstone M. (2011). *Climate Change, Mortality, and Adaptation: Evidence from Annual Fluctuations in Weather in the US*. American Economic Journal: Applied Economics 3 (October 2011): 152–185. (3)
- Lehner B., R-Liermann C., Revenga C., Vörösmarty C., Fekete B., Crouzet P., Döll P. et al.: *High resolution mapping of the world's reservoirs and dams for sustainable river flow management*. *Frontiers in Ecology and the Environment*. Source: GWSP Digital Water Atlas (2008). Map 81: GRanD Database (Dataset) (V1.0). Available online at <http://atlas.gwsp.org>. (4)
- Lobell D. B., Schlenker W., and Costa-Roberts J. (2011). *Climate trends and global crop production since 1980*. Science (New York, N.Y.), 333(6042), 616–20. (5)
- Lobell D. B., and Field C. B. (2007). *Global scale climate–crop yield relationships and the impacts of recent warming*. Environmental Research Letters, 2(1), 014002. (6)
- Masseti E. and Mendelsohn R. (2011). *Estimating Ricardian Functions with Panel Data*. Climate Change Economics, 2(4): 301-319. (7)
- Mendelsohn R. and Dinar A. (2009). *Climate Change and Agriculture: An Economic Analysis of Global Impacts, Adaptation, and Distributional Effects*. Cheltenham, UK: Edward Elgar Publishing. (8)
- Moss R. H., Edmonds J. A., Hibbard K. A., Manning M. R., Rose S. K., van Vuuren D. P., Carter T. R., et al. (2010). *The next generation of scenarios for climate change research and assessment*, Nature 463, n. 7282, pp 747-756. (9)
- Nelson G.C., Rosegrant M. W., Koo J., Robertson R., Sulser T., Zhu T., Ringler C., Msangi S., Palazzo A., Batka M., Magalhaes M., Valmonte-Santos R., Ewing M., and Lee D. (2009). *Climate Change Impact on Agriculture and Costs of Adaptation*. International Food Policy Research Institute, Washington, D.C. (10)

- Ortiz-Bobea A. (2012). *Is it only heat affecting crop yields?* Paper prepared for the Association of Environmental and Resource Economists (AERE), Asheville, North Carolina, June 2012. (11)
- Portmann F. T., Siebert S., and Döll P. (2010). *MIRCA2000—Global monthly irrigated and rainfed crop areas around the year 2000: A new high-resolution data set for agricultural and hydrological modeling*. *Global Biogeochemical Cycles*, 24(1). (12)
- Sacks W. J., Deryng D., Foley J. a., and Ramankutty N. (2010). *Crop planting dates: an analysis of global patterns*. *Global Ecology and Biogeography*. (13)
- Schlenker W., Hanemann W.M. and Fisher A.C. (2006). *The Impact of Global Warming on U.S. Agriculture: An Econometric Analysis of Optimal Growing Conditions*. *Review of Economics and Statistics* 88(1): 113-125. (14)
- Schlenker W., and Roberts M. J. (2009). *Nonlinear temperature effects indicate severe damages to U . S . crop yields under climate change*. *PNAS* 106 (37), 15594-15598. (15)

APPENDIX

This appendix summarizes the regression results. A more detailed version of the paper is available upon request from the author.

	Δ log rice yield	Δ log maize yield	Δ log wheat yield	Δ log sorghum yield
$\Delta(<5)$	0.027*** (-0.008)	0.011** (-0.006)	0.253*** (-0.077)	-0.058* (0.034)
$\Delta(5_15)$	0.019(-0.015)	0.012(-0.008)	0.259*** (-0.077)	-0.042 (0.035)
$\Delta(15_30)$	0.006(-0.007)	-0.002(-0.006)		-0.036 (0.027)
$\Delta(>30)$	-0.002(-0.026)	0.031*** (-0.011)		-0.061 (0.054)
$\Delta(17.5_20)$	-0.026* (-0.016)	0.001(-0.007)	1.26** (-0.521)	-0.147 (0.771)
$\Delta(20_22.5)$	-0.039*** (-0.006)	-0.028*** (-0.005)	0.374* (-0.22)	-0.124 (0.632)
$\Delta(22.5_25)$	-0.116*** (-0.014)	-0.022*** (-0.008)	0.678(-0.5)	-0.115 (0.585)
$\Delta(25_27.5)$	-0.100*** (-0.012)	-0.028*** (-0.009)	0.18(-0.31)	-0.218 (0.696)
$\Delta(27.5_30)$	-0.029***			-0.009 (0.007)
$\Delta(>27.5)$	-0.088*** (-0.014)		0.166 (0.318)	-0.216 (0.694)
$\Delta(>30)$		-0.026** (-0.012)		
Δ lgdppc	0.003(-0.068)	0.053(-0.095)	0.061(-0.11)	0.165 (0.130)
EC	-0.267*** (-0.028)	-0.360*** (-0.083)	-0.296*** (-0.041)	-0.441*** (0.101)
lag (<5)	-0.001(-0.011)	0.019*** (-0.004)	0.12(-0.09)	-0.072** (0.032)
lag (5_15)	-0.014(-0.018)	0.012** (-0.006)	-0.09(-0.112)	-0.069** (0.030)
lag (15_30)	-0.063*** (-0.014)	0.023(-0.014)		-0.014 (0.041)
lag (>30)	-0.050** (-0.022)	0.017(-0.014)		-0.051 (0.050)
lag (17.5_20)	0.01(-0.021)	-0.006(-0.011)	0.24(-0.629)	-0.303 (1.259)
lag (20_22.5)	-0.001(-0.008)	-0.039*** (-0.006)	-0.428(-0.276)	-0.627 (0.975)
lag (22.5_25)	-0.030*** (-0.011)	-0.034*** (-0.013)	0.022-0.34	-0.19 (0.946)
lag (25_27.5)	-0.041*** (-0.009)	-0.034*** (-0.011)	-0.751** -0.0382	-0.214 (0.971)
lag (27.5_30)	-0.042*** (-0.011)			-0.215 (0.971)
lag (>27.5)	-0.029*** (-0.009)		-0.772** (0.382)	
lag (>30)		-0.037** (-0.014)		
lag lgdppc	0.058** (-0.023)	0.105*** (-0.029)	0.075** (-0.037)	0.043 (0.029)
Intercept	2.413*** (-0.245)	2.698*** (-0.662)	2.063*** -0.563	4.883 (4.108)
Regional sample	Trstr	Trstr	Trstr	Trstr
N	1665	2106	1253	1677
R²	0.181	0.193	0.199	0.209

* 10%, **5%, *** 1%

Table A1. Estimated coefficients in rain-fed tropical and subtropical (Trstr) areas.

Point estimates and robust standard errors. EC is the error correction coefficient. Covariates include temperature bins (from 17-5_20°C to >30 or >27.5°C), precipitation bins (from >5mm/day to >15 or 30mm/day), per capita gdp (lgdppc). The regressions also include trade variables use to proxy for the role of technology, fertilizers, machinery and an irrigation variable that interacts large dams with cumulative precipitation over the growing season.

	$\Delta \log$ rice yield	$\Delta \log$ maize yield	$\Delta \log$ wheat yield	$\Delta \log$ sorghum yield
$\Delta(<5)$	-0.068* (-0.036)	0.008 (-0.037)		-0.038(-0.051)
$\Delta(5_15)$	-0.027 (-0.033)	0.072 (-0.045)		0.057(-0.056)
$\Delta(15_30)$	0.078 (-0.119)	0.031 (-0.068)		-0.089(-0.131)
$\Delta(>30)$	-0.584 (-0.467)	-0.148 (-0.215)		-0.375* (-0.207)
$\Delta(17.5_20)$	0.076 (-0.07)	-0.005 (-0.011)	0.034 (0.025)	-0.031** (-0.012)
$\Delta(20_22.5)$	0.073 (-0.068)	-0.009 (-0.016)	-0.059 (-0.045)	0.019(-0.029)
$\Delta(22.5_25)$	0.144 (-0.123)	-0.029 (-0.021)	-0.085** (-0.039)	0.014(-0.027)
$\Delta(25_27.5)$	0.062 (-0.069)	-0.033 (-0.025)	-0.021 (-0.099)	0.042(-0.025)
$\Delta(>27.5)$	0.001 (-0.072)	-0.166*** (-0.044)	-0.156 (0.109)	-1.432*** (-0.141)
$\Delta \lg dppc$	0.101 (-0.142)	0.285 (-0.28)	0.381** -0.155	-0.048(-0.148)
EC	-0.486*** (-0.024)	-0.309*** (-0.061)	-0.698*** (-0.068)	-0.329*** (-0.107)
lag (<5)	-0.116 (-0.074)	-0.006 (-0.066)		0.053(-0.042)
lag (5_15)	-0.124 (-0.105)	0.068 (-0.063)		0.198* (-0.115)
lag (15_30)	0.05 (-0.143)	-0.098 (-0.147)		-0.037(-0.155)
lag (>30)	-0.535 (-0.532)	-0.125 (-0.288)		0.508(-0.327)
lag (17.5_20)	0.089 (-0.111)	-0.031 (-0.028)	0.056 (0.038)	-0.045** (-0.02)
lag (20_22.5)	0.109 (-0.077)	-0.014 (-0.025)	-0.0151 (-0.06)	0.048(-0.031)
lag (22.5_25)	0.117 (-0.108)	-0.036 (-0.046)	-0.072** (-0.035)	0.03(-0.029)
lag (25_27.5)	0.137** (0.055)	-0.077* (-0.042)	0.020 (0.151)3	0.11(-0.088)
lag (>27.5)	0.007 (-0.085)	-0.369*** (-0.076)	0.019 (0.238)	-0.048(-0.165)
lag $\lg dppc$	0.015 (-0.033)	0.07 (-0.078)	0.229*** -0.044	-0.074(-0.055)
Intercept	4.513*** (-0.296)	2.109** (-0.84)	5.96*** (0.592)	2.116** (-1.013)
Regional sample	Temp	Temp	Temp	Temp
N	799	1401	1725	883
R²	0.29	0.178	0.373	0.181

* 10%, **5%, *** 1%

Table A2. Estimated coefficients in rain-fed temperate (Temp) areas. Point estimates and robust standard errors. EC is the error correction coefficient.

	Δ log rice yield	Δ log maize yield	Δ log wheat yield	Δ log rice yield	Δ log maize yield	Δ log wheat yield
$\Delta(<5)$	0 (-0.015)	0.002 (-0.012)	-0.027 (-0.02)	-0.100* (-0.05)	0.004 (-0.066)	-0.007 (0.045)
$\Delta(5_15)$	0.015 (-0.026)	0.005 (-0.012)	0.154 (-0.144)	-0.11 (-0.072)	0.073 (-0.071)	0.233*** (0.056)
$\Delta(15_30)$	-0.075*** (-0.018)	-0.017 (-0.016)		0.209 (-0.146)	0.045 (-0.065)	
$\Delta(>30)$	-0.004 (-0.072)	0.033** (-0.014)		-0.424 (-0.537)	0.127 (-0.246)	
$\Delta(>15)$			-0.405* (0.239)			-0.258(0.167)
$\Delta(17.5_20)$	0.938*** (-0.347)	-0.002 (-0.007)	-0.018 (-0.028)	0.098 (-0.085)	0.029 (-0.022)	-0.034** (0.019)
$\Delta(20_22.5)$	0.559** (-0.233)	0 (-0.005)	-0.007 (-0.014)	0.055 (-0.053)	-0.023 (-0.038)	-0.074** (0.032)
$\Delta(22.5_25)$	0.272 (-0.24)	-0.006 (-0.007)	-0.115*** (-0.023)	-0.002 (-0.072)	0.007 (-0.011)	-0.085** (0.033)
$\Delta(25_27.5)$	0.328 (-0.214)	-0.038 (-0.025)	-0.156 (0.116)	0.071 (-0.058)	-0.085** (-0.034)	-0.125 (0.107)
$\Delta(27.5_30)$		-0.043* (-0.025)				
$\Delta(>27.5)$	0.334 (-0.213)		-0.235** (0.117)	-0.034 (-0.072)	-0.149** (-0.066)	-0.639 (0.774)
$\Delta(>30)$		-0.038* (-0.021)				
Δ lgdppc	-0.002 (-0.069)	0.067 (-0.096)	0.125 (-0.124)	0.122 (-0.149)	0.272 (-0.274)	0.371** (0.154)\
EC	-0.260*** (-0.027)	-0.358*** (-0.083)	-0.298*** (0.042)	-0.494*** (-0.025)	-0.309*** (-0.064)	-0.698*** (-0.067)
lag irr	-1.42e-07 (7.93e-07)	-9.02e-07 (9.98e-07)		-3.16e-07 (1.21e-06)	1.73e-06 (1.66e-06)	5.76e06 (5.06e-06)
lag (<5)	-0.012 (-0.011)	0.004 (-0.006)	-0.018* (0.011)	-0.145* (-0.071)	-0.131 (-0.091)	-0.041 (0.093)
lag (5_15)	0.002 (-0.027)	-0.002 (-0.008)	0.185 (0.200)	-0.1 (-0.106)	-0.07 (-0.073)	0.271** (0.104)
lag (15_30)	-0.060*** (-0.018)	0.008 (-0.016)		-0.038 (-0.137)	-0.261** (-0.117)	
lag (>30)	-0.090*** (-0.029)	0.007 (-0.017)		-0.098 (-0.774)	0.084 (-0.341)	
lag (>15)			-0.210 (0.291)			-0.547* (0.309)
lag (17.5_20)	0.142 (-0.475)	0.002 (-0.019)	0.021 (0.032)	0.238* (-0.13)	0.039 (-0.047)	-0.095 (0.081)
lag (20_22.5)	0.245 (-0.531)	-0.002 (-0.008)	0.005 (0.020)	0.121 (-0.073)	-0.012 (-0.034)	-0.036 (0.060)
lag (22.5_25)	-0.097 (-0.406)	0.007 (-0.016)	-0.200*** (0.033)	0.026 (-0.069)	0.036 (-0.025)	-0.066 (0.048)
lag (25_27.5)	-0.037 (-0.42)	0.011 (-0.021)	-0.144 (0.174)	0.161** (-0.076)	-0.127** (-0.059)	0.114 (0.206)
lag (27.5_30)		0.006 (-0.021)				
lag (>27.5)	-0.039 (-0.43)		-0.359* (0.209)	0.049 (-0.087)	-0.584*** (-0.145)	-0.72 (1.33)
lag (>30)		0.011 (-0.023)				
lag lgdppc	0.058*** (-0.022)	0.103*** (-0.029)	0.081** (-0.0244)	0.018 (-0.03)	0.071 (-0.079)	0.223** (0.045)
Intercept	2.294 (-1.759)	2.550*** (-0.679)	2.40*** (0.323)	4.604*** (-0.316)	2.531*** (-0.902)	6.03*** (0.64)
Regional sample	Trstr	Trstr	Trstr	Temp	Temp	Temp
N	1665	2106	1245	799	1401	1725
R2	0.155	0.191	0.192	0.302	0.182	0.404
* 10%, **5%, *** 1%						

Table A3. Estimated coefficients in irrigated temperate (Temp) and tropical and subtropical (Trstr) areas. Point estimates and robust standard errors. EC is the error correction coefficient.

Assessing future land suitability of winter wheat crop

Mereu V.^{1,2}, Trabucco A.¹, Daccache A.^{1,3} and Spano D.^{1,2}

¹Euro-Mediterranean Center on Climate Changes (CMCC), LAFENT Division, Sassari, Italy

²Department of Science for Nature and Environmental Resources DipNET, Sassari, Italy

³Cranfield University, Bedfordshire, UK

*Corresponding author: vmereu@uniss.it

Abstract

To meet the food demand of a rapidly growing population, the world must raise its food production for 2030 by 50%. This has to be achieved with less water resources available and under changing climate. In this paper, large datasets of global climatic, pedological and land cover were extracted and manipulated to assess the current and future land suitability for winter wheat, one of the most important staple crop for the world. Using an intensive literature search, the main climatic limitation for winter wheat were identified as growing degree days, temperature for vernalization, water stress and soil wetness. Soil depth, water holding capacity in the root zone, drainage capacity and soil pH instead were used as the main pedological limitations. Accordingly, the global arable lands were classified into suitable, moderate, marginal and unsuitable for winter wheat. The outputs of three GCM were used to perturb the baseline climate (1961-1990) under low (SRES B1) and high (SRES A1FI) emissions scenarios. Results have shown that droughts induced by global warming will affect noticeably the two major wheat producing countries, China and the US. Some lands that are currently classified as highly suitable are likely to become moderately or marginally suitable in the future and hence their wheat production capacity will become more vulnerable and less stable. Under these conditions, current lands growing wheat under rain-fed will need to shift toward irrigated production or to the adoption of more drought tolerant varieties. In other regions such as the Middle East and North Africa, the global circulation models are predicting an increase in the winter rainfall with positive consequences on winter wheat especially those located in dry areas. This can be true if the future rain follow the same pattern as the current climate. However, there is a high confidence that large part of the rainfall increase will be in the form of extreme events causing more damage than benefit to winter crop.

Keywords: *climate change, multi-model analysis, production, adaptation, irrigation.*



1. INTRODUCTION

Wheat together with rice and maize provide two-third of human food consumption and make the staples for more than 4 billion people [7]. Currently, wheat is grown on more lands than any other crop in the world [1] and its cultivation ranges from 67° N in Scandinavia and Russia to 45° S in Argentina, including elevated regions in the tropics and sub-tropics [5]. China and India are currently the two largest wheat producing countries and combined they cover almost 30% of the global wheat production (Figure 1)).

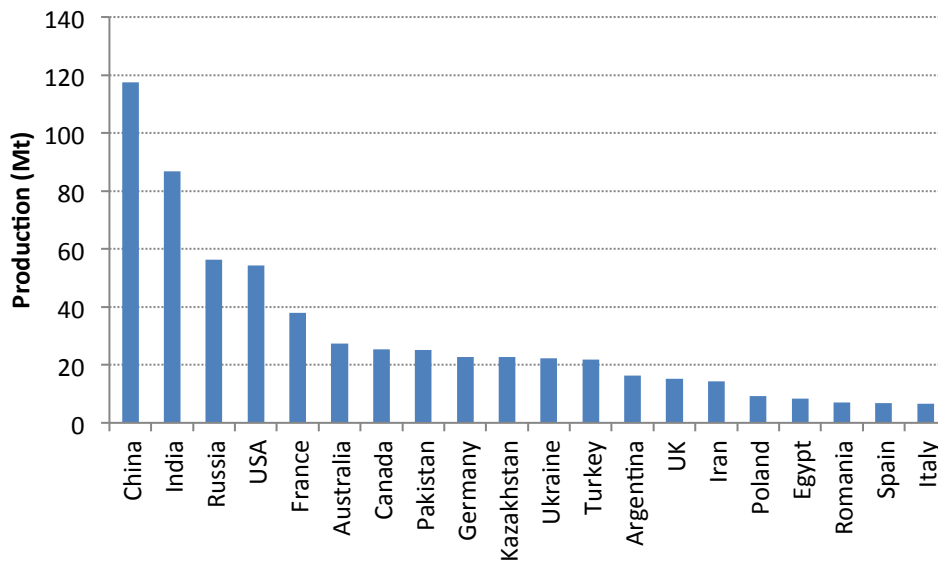


Fig. 1: List of the largest wheat producing countries (FAOStat, 2011)

The rapid population growth and water scarcity are posing a real challenge to maintain sustainability, accessibility and affordability of our current food supply system. This latter is critically dependent on temperature and precipitation and hence climate change will add further pressure on the system where farmers will be forced to change their practices and adapt to the new climatic conditions. For certain vulnerable regions, such changes will have large implications on the future food security as it will largely affect the production cost and the environmental sustainability.

The aim of this work is to assess the impact of climate change on the land suitability for winter wheat one of the most important staple crop for the world. A land suitability model based on the use of several pedo-climatic indicators was developed to assess the current (1961-1990) and the 2050's future land suitability. Using the outputs of three Global Circulation Models (GCM) with 2 emissions

scenarios (SRAS A1FI and SRES B1), a multi-model analysis approach was used to reduce the level of modelling uncertainty. This work will identify areas where global warming will pose new challenges and threats to the winter wheat production and those where climate change will provide new opportunities. Adaptation and mitigation options will also be discussed.

2. METHODOLOGY

2.1 Current land suitability

Long term observed climate datasets were collected from meteorological stations across the globe and used to produce the 0.5 degree grid of CRU (Climate Research Unit) database as described by Harris et al. [9]. This database consists of high resolution of global monthly climate grids for nine climate variables (temperature, diurnal temperature range, daily minimum and maximum temperatures, precipitation, wet-day frequency, frost-day frequency, vapour pressure, and cloud cover) and cover the time period from 1901–2011. In this work, the baseline period (1961-1990) was chosen to coincide with the baseline of the Global Circulation Models (GCM). Global monthly minimum temperature (T_{min}), maximum temperature (T_{max}) and precipitation for each year from 1961-1990 are then extracted from CRU database to calculate the climatic indicators used in the land suitability model as described hereafter (Figure 2).

The soil parameters were extracted from the Harmonized World Soil Database [4]. The HWSD is a 30 arc-second raster database with over 16000 different soil mapping units that combines existing regional and national updates of soil information worldwide. The crop calendar (planting and harvesting date) used in this work was generated from CRU datasets as described by Sacks et al., [23]. At the end, the land suitability model was validated against the current grown areas of winter wheat-maps produced and described by Monfreda et al., [17].

Soil and climate are the main factors affecting wheat productivity and hence land suitability. A brief description of the main pedo-climatic indicators used in for the winter wheat land suitability assessment is presented hereafter (Figure 3).

2.1.1 Soil limitations

The main soil properties which affect the crop establishment suitability are texture, structure, depth, stoniness and chemical fertility. These may act alone as limiting factor for crop development or management requirement or in combination.

Soil texture and structure influence the soil water retention capacity and hence can play a major role in alleviating the drought effect or increase the water logging risks. Clay soils tend to form large and hard clods when dry and are plastic when wet. These soils can be cultivated under narrow climatic conditions. On the other hand, plants grown on sandy soils are more susceptible to drought than those cultivated on fine textured soils. Shallow soils also can restrict the root development and hence nutrient and water uptake.

A steep slope (higher than 25%) can limit the trafficability of the combine harvester. High stone contents instead can increase the production cost by causing extra wear and tear to the machinery involved.

Soil reaction (pH) affects a wide variety of chemical and biological phenomena in soil.

The effect of soil pH is great on the solubility of minerals or nutrients. If the soil pH declines below a critical level, the solubility of aluminium and manganese ions increases, resulting in toxicity and lower yields. When soil pH is higher than 8.5 this will make some essential nutrients such as magnesium (Mg) and Calcium (Ca) to be unavailable. For wheat, the optimal soil pH should range between 5 and 7 [15].

2.1.2 Climatic limitations

Temperature and rainfall are the main climatic parameters affecting agricultural productivity. Areas that are too cold or too wet are not favourable for production and at the same time; areas that are too dry or too hot can also limit the crop establishment regardless the soil characteristics. Using climatic parameters, the following indicators were used to identify the climatic limitations for winter wheat production:

2.1.2.1 *Wettness*

To assess climate variability across the globe a simple water balance model was used to estimate the potential soil moisture deficit (PSMD) using monthly rainfall (P) and reference evapotranspiration (ET_o) for each of the 30 years historical climate data (1961-1990) as following:

$$PSMD_i = PSMD_{i-1} + ET_i - P_i$$

where PSMD_{*i*} is the potential soil moisture deficit in month *i*, mm, P_{*i*} is rainfall in month *i*, mm, and ET_{*i*} is reference evapotranspiration of short grass in month *i*, mm, calculated using the empirical formula of Hargreaves-Samani [8]. The PSMD calculation starts in the wettest months of the year (depends on the location) with zero deficit and builds up as ET exceeds the precipitation. The maximum PSMD of the 12 months is the PSMD_{max} value at that given site.

The maximum Potential soil moisture deficit (PSMD_{max}) has been applied to quantify the irrigation needs at national scales in different countries due to the strong correlation between PSMD_{max} and crop water needs ([14], [2], [22]). For the same crop and soil type, higher value of PSMD_{max} indicates drier climate and hence higher water need and vice versa (Figure 2).

Wet areas are characterized by high rainfall and/or low evapotranspiration during the crop growing season of winter wheat. Therefore, the period of potential soil moisture deficit (PSMD_{max}) in these areas is short and restricted to few months. Under these conditions (PSMD_{max} < 50 mm) the workability and the trafficability of the field can be restricted especially on heavy and poorly draining soils. These conditions will be considered the wet limit for winter wheat production.

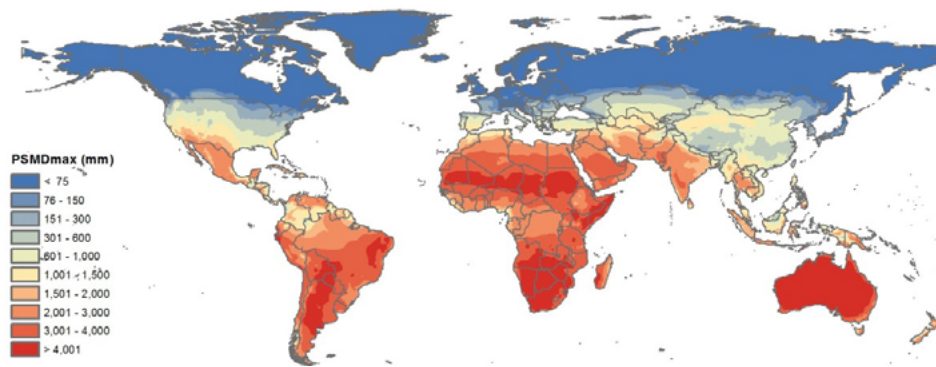


Figure 2: Long term average (1961-1990) maximum potential soil moisture deficit (PSMDmax)

2.1.2.2 Droughtiness

To assess droughtiness, average soil moisture balance (SMB) at a given location was calculated taking into account soil characteristics, canopy development timing and rooting depth of winter wheat as described hereafter [25].

$$SMB = AWC_{wheat} - SMD_{wheat}$$

Where AWC_{wheat} and SMD_{wheat} are the available soil water holding capacity (mm) and the soil moisture deficit (mm) adjusted to winter wheat crop, respectively. AWC_{wheat} is highly dependent not only on soil characteristics (texture, structure, organic matter and stoniness) but also on the crop root depth.

Deficits under grass are greater than under wheat which does not attain full ground cover early in the growing season. Under the UK conditions for example, winter wheat the full leaf cover is normally achieved at the end of April while the deficit attains its maximum in July and August. Therefore, Jones and Thomasson [13] developed the following equation to derive the SMD_{wheat} from the monthly accumulated values of PSMD:

$$SMD_{wheat} = PSMD_{July} - 1/3PSMD_{April}$$

Using this equation, the SMD for winter wheat used by Jones and Thomasson [13] was adapted for each site taking into consideration the deficit in the months of full canopy cover and that at the end of the growing season where normally the moisture deficit is at its peak.

2.1.2.3 Growing degree days

Since the plant development is temperature dependent, the concept of cumulative growing degree days (GDD) or “heat units” has been introduced to track and predict the phenological development [18]. The GDD is a measure of the heat energy accumulated by the plant above a certain threshold called base temperature, below which the crop ceases its development. Many authors reckoned that wheat ceases growth at the freezing point while the total growing degree days (GDD) to reach full maturity ranges between 1500 and 2500 depending on the variety ([21], [19], [24]).

2.1.2.4 Vernalization

Germinating winter wheat seeds or seedlings must be exposed to cool temperatures to trigger its reproductive development. These cool temperatures must be continuous and not interrupted with warm temperatures. This process is called vernalization.

Although the exact temperature and time period required varies by variety, the winter wheat vernalization normally occurs between -4 and 17°C with an optimum temperature ranging between 3 and 10° [10].

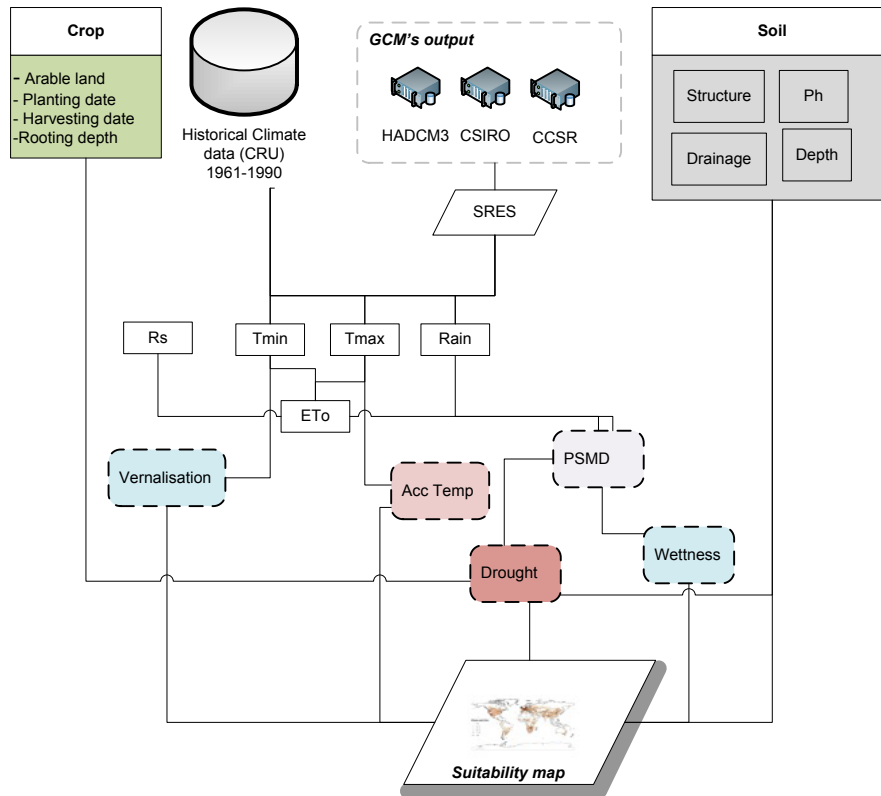


Fig. 3: Flow chart of winter wheat land suitability model

2.2 Future land suitability

Predicting the future is difficult, especially when it is related to a complex system such as climate that is largely affected by human activities but also by natural processes as the volcanic eruptions and solar activities.

Uncertainties in climate projections are also the result of our incomplete understanding of the climate and the difficulty to represent a complex system such as climate in a single computer model.

To reduce the modelling uncertainty, three general circulation models (HADCM3, CSIRO [11] and CCSR [3]) were selected from the GCM list used in the IPCC Fourth Assessment Report (AR4). This sort of multi-model ensemble approach is more informative than the single projection as it provides a valuable range of possible future changes and reflects more openly the state of the science (e.g. [6], [16]).

In this study, the high (A1F1) and low (B1) emission scenarios for the 2050s were used. The emission scenarios used are those developed by the IPCC [20] and best known as SRES (Special Report on

Emission Scenarios) where each represents a different storyline combining two sets of divergent tendencies; one set varying between strong economic values and strong environmental values, the other set varying between increasing globalisation and increasing regionalisation [12]. The A1 scenarios characterise alternative developments of energy technologies, with A1FI being fossil fuel intensive while B1 is the scenario with the lowest atmospheric CO₂ concentration and reflects efforts to control CO₂ emissions principally through the introduction of clean and resource-efficient technologies.

The 2050's period was chosen because it is far enough to detect the impact of climate change and close enough to react and to implement adaptation and mitigation measures.

The future change of climate variables were extracted from the GCM' s outputs and applied to the baseline (1961-1990) grid of CRU datasets- adding the changes in temperature to the observed temperature, and multiplying ratio changes for precipitation.

Once the 2050's climate for each GCM and with the two divergent emission scenarios are produced, the land suitability model for the six equiprobable future climate ensembles was assessed and analysed.

3. RESULTS AND DISCUSSION

3.1 Baseline land suitability of winter wheat

Under the current climatic conditions (1961-1990), the model shows that suitable lands for wheat production are mainly located in the United States, East of China, Europe (Central and most of the South) and Central Asia (Figure 5). The potential production of these lands is high and sustainable from year to year. In an average year, planting and harvesting are rarely restricted by weather and poor ground conditions. The working conditions in a wet year remain acceptable for crop establishment. The growing season is long enough to allow the crop to accumulate the needed heat to reach maturity. The soil water reserves are also sufficient to meet the crop water demand and as a rainfed crop, winter wheat is highly productive in these areas.

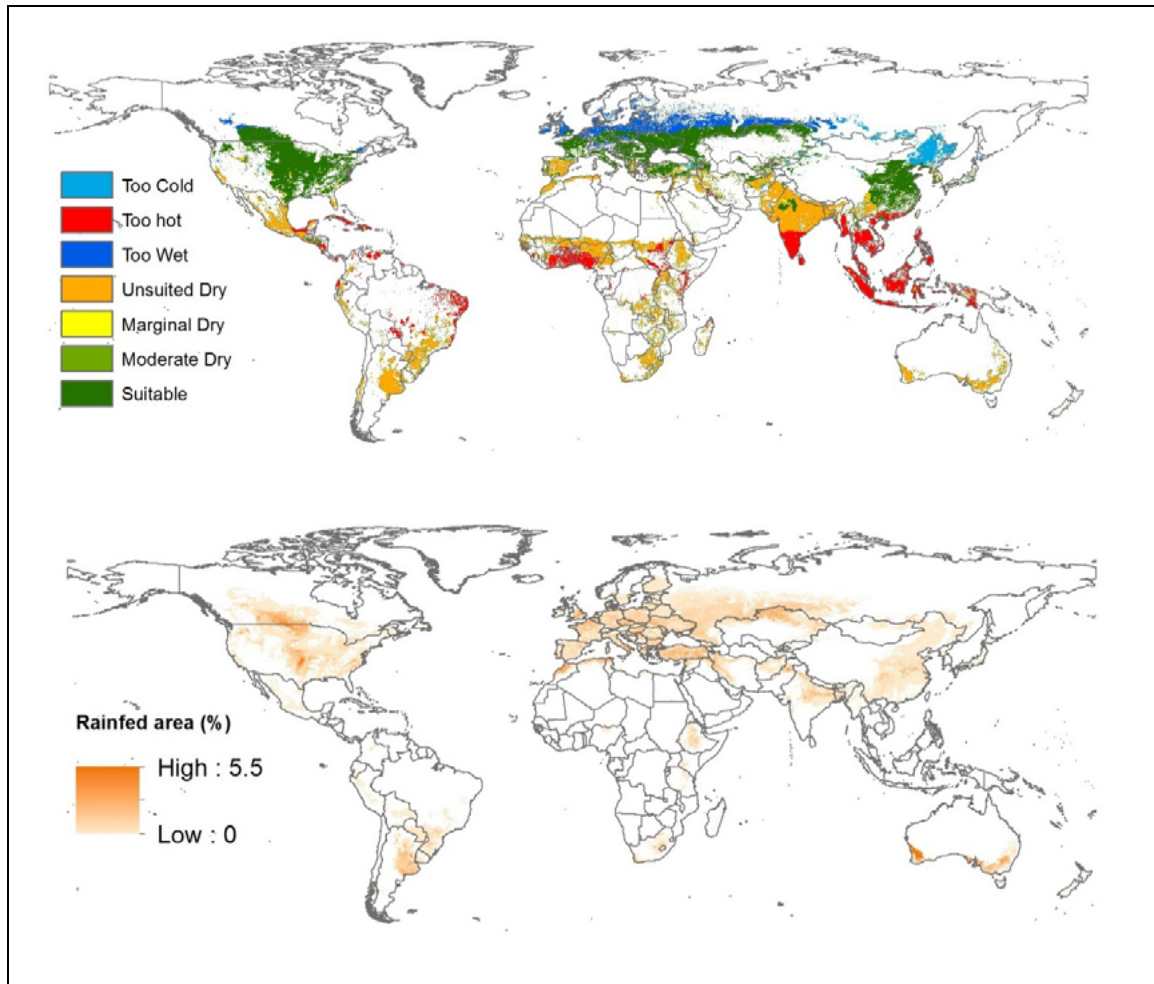


Fig. 4: Current (1961-1990) land suitability of rainfed winter wheat compared to the production area of rainfed wheat according to GAEZ (2013).

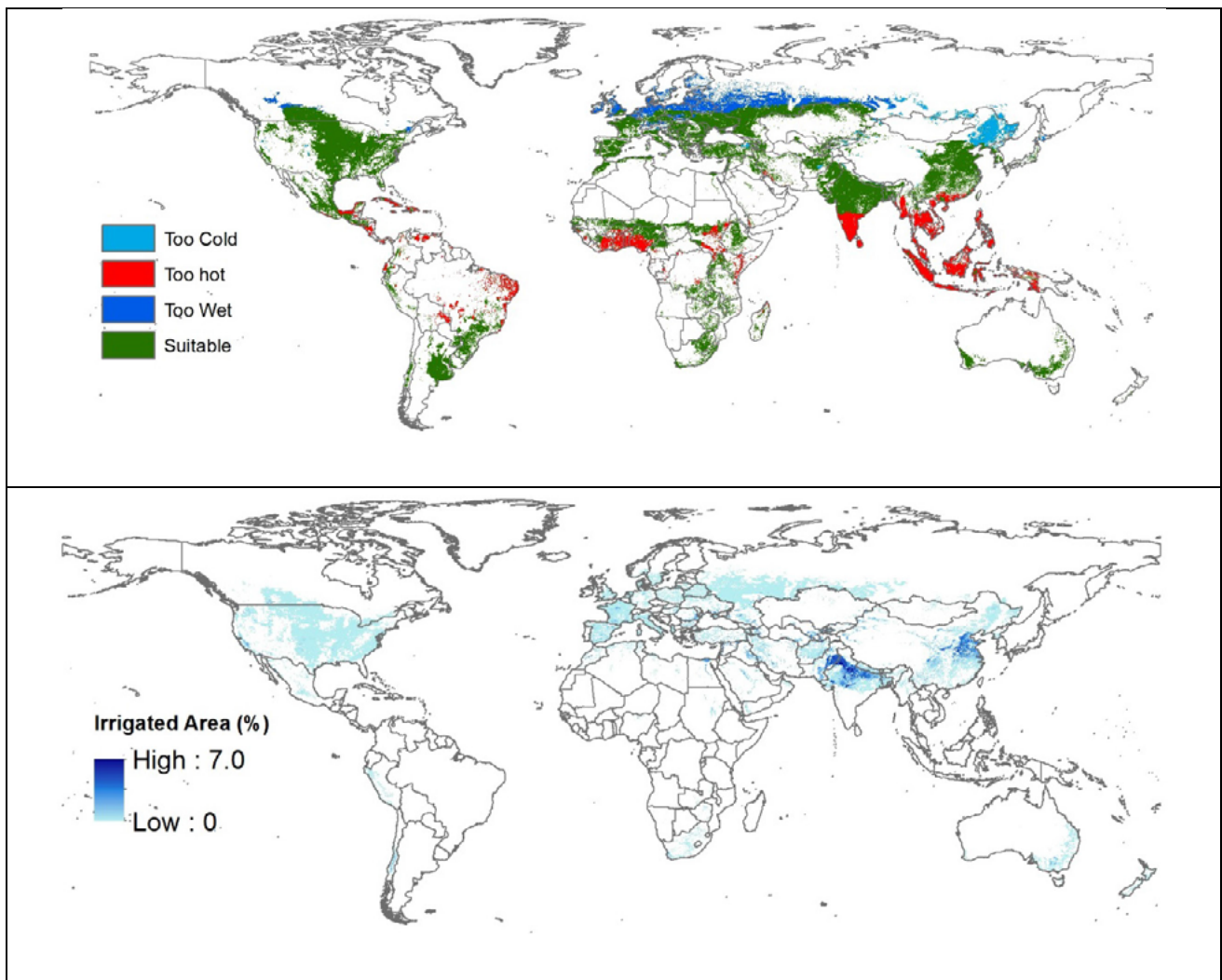


Fig. 5: Current (1961-1990) land suitability of irrigated winter wheat under the baseline climate (1961-1990) and their production area (GAEZ, 2013).

Moderately suited areas have a potential production that is variable (moderate to high) from year to year due to either temperature, poor soil conditions affecting sowing or harvesting time, or due to shortage in soil water to sustain the full crop development. In favourable years which could be dry years in a wet climate or wet years in dry climate, acceptable yields can be achieved. The potential production of marginal lands is variable from year to year. There are difficulties in maintaining continuity of output and in some years the weather can be too cold or too dry for winter wheat establishment.

On lands classified as unsuited for climate, occasionally there will be favourable years with favourable weather for production but generally the climatic conditions are too wet (Northern Europe and Central Russia), too cold (Northern China) or too warm for vernalization (Equator and South India). When the climate is too dry for winter wheat (Africa, Australia, Spain and South America) artificial water application (supplemental or full irrigation) can transform vast area of unsuitable lands to highly suitable for winter wheat production; hence the importance of irrigated agriculture in food production and continuous supply regardless weather change. The suitability criteria for soils are irreversible instead and are totally independent of the climate conditions. However, a deep and heavy soil can better tolerate dry climate but is more likely to limit productivity in the Northern Europe as result of excessive wetness.

The main cropped area of winter wheat is located in Europe and Central Asia (40%), followed by North America (19%) and South Asia (17%) (Figure 6). In Europe and Central Asia, soil wetness mainly in the Northern part of the continent is the major limiting factor for winter wheat. In North America, 14% of winter wheat are grown on moderately suited land, most of which limited by temperature ($GDD < 1750^{\circ}C$). Drought is by far the major problem for wheat production in large part of the world and especially in the Southern Asia (83%), Sub Saharan Africa (97%), Middle East and North Africa (80%). In these areas, supplemental or full irrigation of winter wheat is a normal practice and is needed to boost productivity and maintain continuous supply.

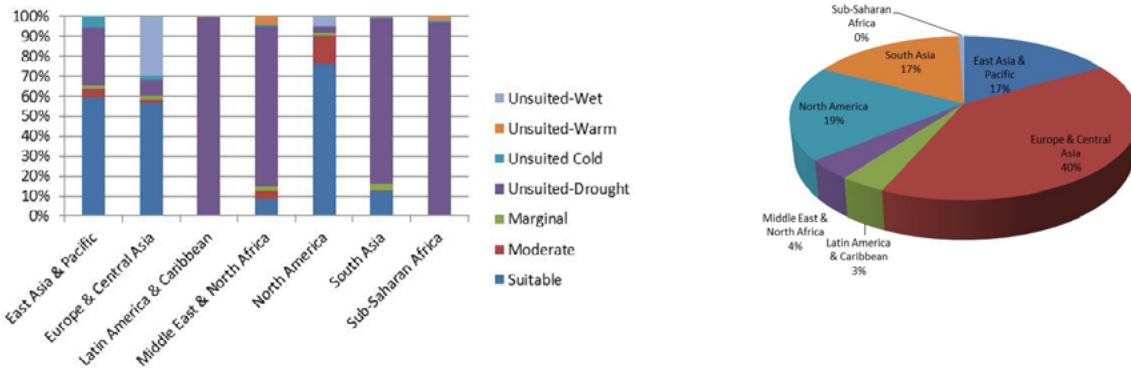


Fig. 6: Production areas of winter wheat and percentage of production area per land class suitability.

3.2 Future land suitability of winter wheat

According to the multi-model results, climate change will impact wheat production areas differently based on their geographical location. In some areas, climate change may present an opportunity for winter wheat and in others, global warming is likely to threaten the production system (Figure 7).

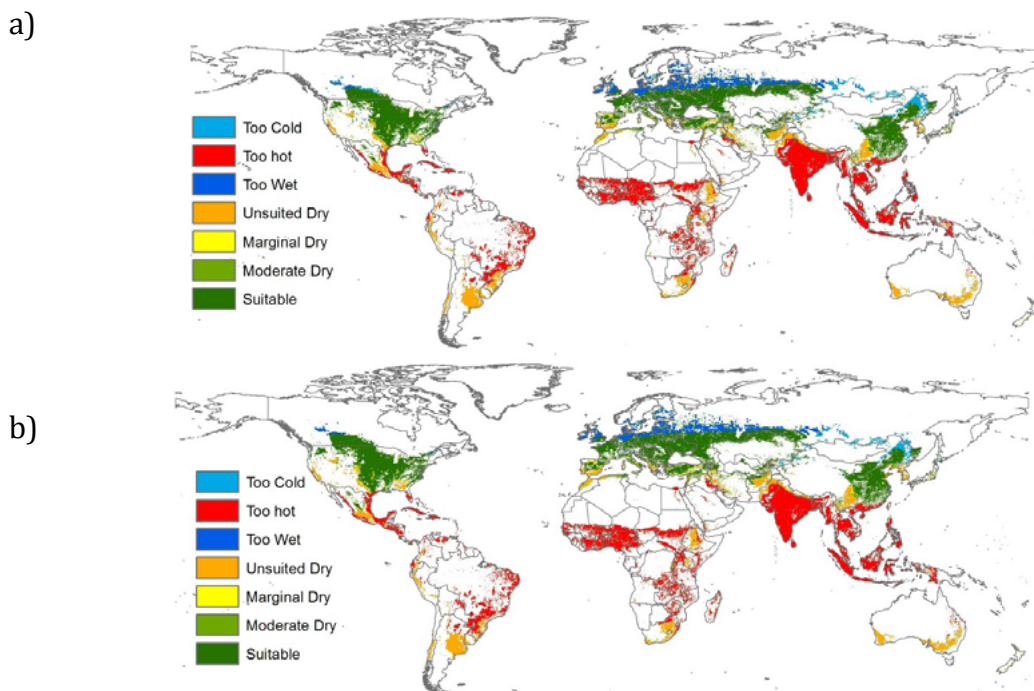


Fig. 7: Land suitability of Winter wheat under a) SRES B1 and b) A1FI emissions scenario.

The results of the 30 years of future climate data for each of the three GCM outputs and emissions scenarios (SRES A1FI and SRES B1) were analysed assuming that there is no GCM that is better than the other and all the projections are equiprobable.

The future (2050) land suitability of the current production area is presented in Figure 8 for both low and high emissions scenarios. Accordingly, South Asia appears to be the region that will be hardly hit by climate change with almost half of the current lands considered to be unsuitable if not irrigated will become very warm for winter wheat (Table 1 Annex). Under these conditions, new heat tolerant varieties are needed.

In Europe, areas currently restricted by soil moisture excess are likely to become drier and hence more suitable for winter wheat production. In these regions, climate change could provide new opportunities for winter wheat cropping. For Middle East and North Africa, climate change appears to have a beneficial effect as the drought limiting factor is likely to become less intensive with the projected increase of winter rainfall.

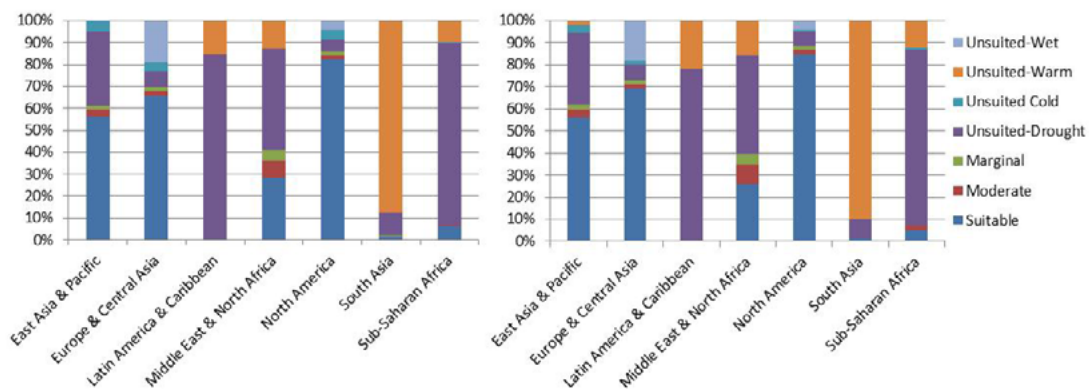


Fig. 8: Classification by suitability of the future winter wheat area under SRES B1 and SRESA1FI emissions scenario.

4. CONCLUSION

This work highlighted the major climatic limitations of winter wheat and the future trends using a multi-GCM outputs analysis to reduce climate modelling uncertainties. In terms of winter wheat suitability, South Asia and East Asia will be negatively affected by climate change where the implication of drought is very likely to become much more relevant. Limitations from low temperature will be eased in North America while the Southern regions will suffer more from drought. The projected increase in winter rainfall over the Middle East and North Africa is instead likely to improve land suitability for winter wheat, if these increases do not occur in the form of extreme events. In North Europe and Russia instead, the drier future climate will improve field trafficability and hence the winter wheat land suitability.

This work also has many limitations, such as the assumption that the future weather will have the same pattern as current. This is not necessarily true, especially that extreme weather events are expected to become more intense and more frequent. Under these conditions, the damage that can be caused by intense rain can be more harmful than the benefit caused by the average rainfall increase. This could be the case of the Middle East and North Africa. The same is also applied to the extreme temperatures. In this work, the pest infestations and diseases occurrences that are likely to change with climate are not assessed.

Drought appeared to be the main challenge to the winter wheat growers in large part of the world. In front of such challenge, farmers already irrigating wheat must make an additional investment to secure more water or to increase their irrigation system capacity. In many regions, irrigating wheat is not beneficial but with the continuous increase in cereal prices, irrigating wheat might become one day profitable. More pressure on the already stressed resources is likely to occur as well as the production cost with energy cost continuously increasing thus raising concern for production sustainability and food security.

5. REFERENCES

- Curtis B.C., Rajaram S. And Macpherson H.G. (2002). *Bread Wheat- Improvement and production*. FAO Plant Production and Protection Series N° 30. (1)
- De Silva C. S., Weatherhead, E. K., Knox, J. W. and Rodriguez-Diaz, J. A. (2007). *Predicting the impacts of climate change - A case study of paddy irrigation water requirements in Sri Lanka*. Agricultural Water Management: 93: 19-29. (2)
- Emori S., Nozawa T., Abe-Ouchi A., Numaguti A., Kimoto M., and Nakajima T. (1999). *Coupled ocean-atmosphere model experiments of future climate change with an explicit representation of sulfate aerosol scattering*. J.Meteor. Soc. Japan. (3)
- FAO/IIASA/ISRIC/ISSCAS/JRC, 2009. *Harmonized World Soil Database (version 1.1)*. FAO, Rome, Italy and IIASA, Laxenburg, Austria. (4)
- Feldman M (1995). *Wheats*. In: Smartt J, Simmonds NW, editors. *Evolution of crop plants*. Harlow, UK: Longman Scientific and Technical; 1995. p. 185-192. (5)
- Fischer, G., Shah M., Tubiello F.N. and van Velhuizen H. (2005). *Socio-economic and climate change impacts on agriculture: an integrated assessment, 1990–2080*. Philos. Trans. R. Soc. B 360: 2067–2083. (6)
- Food and Agriculture Organization of the United Nations (1995) .*Dimensions of Need: An atlas of food and agriculture"*. (7)
- Hargreaves G.H., Samani Z.A. (1982). *Estimating potential evapotranspiration*. Tech. Note. ASCE Journal of Irrigation and Drainage Engineering 108 (3), 225-230. (8)
- Harris I., Jones P.D., Osborn T.J., and Lister D.H.(2013). *Updated high-resolution grids of monthly climatic observations*. In press, Int. J. Climatol., Doi: 10.1002/joc.3711. (9)
- Harrison P.A. and Buterrfield R.E. (1996). *Effects of climate change on Europe-wide winter wheat and sunflower productivity*. Climate Research. 7: 225-241. (10)
- Hirst, A. C., Gordon H. B., and O'Farrell S. P. (1996). *Global warming in a coupled climate model including oceanic eddy-induced advection*. Geophysical Research Letters, 23 : 3361-3364. (11)

- IPCC-TGCI (1999). *Guidelines on the use of Scenario Data for Climate Impact and Adaptation Assessment, Version 1*. Prepared by Carter T.R., Hulme M., Lal M. Intergovernmental Panel on Climate Change, Task Group on Scenarios for Climate Impact Assessment. (12)
- Jones R. J. A. and Thomasson A. J. (1987). *Land suitability classification for temperate arable crops*. In *Quantified Land Evaluation Procedures* (Eds K. J. Beek, P. A. Burrough & D. E. McCormack), pp. 29-35. Enschede: ITC Publication. (13)
- Knox J.W., Rodríguez Díaz J.A., Nixon D.J., and Mkhwanazi M. (2010). *A preliminary assessment of climate change impacts on sugarcane in Swaziland*. *Agricultural Systems* 103: 63–72. (14)
- Landon (1984) *Booker Tropical Soil Manual*. New York: Booker Agriculture International Limited. (15)
- Lobell D. B., Burke M.B., Tebaldi C., Mastrandrea M.D., Falcon W.P. and Naylor R.L. (2008). *Prioritizing Climate Change Adaptation Needs for Food Security in 2030*, *Science* 319. (16)
- Monfreda et al. (2008), *Farming the planet: 2. Geographic distribution of crop areas, yields, physiological types, and net primary production in the year 2000*, *Global Biogeochemical Cycles*, Vol.22, GB1022, doi:10.1029/2007GB002947. (17)
- Monteith J. L. (1977). *Climate and the efficiency of crop production in Britain*. *Philosophical Transactions of the Royal Society of London, Series B*, 281: 277–294. (18)
- Motzo R., Giunta F. and Deidda M. (1996). *Relationship between grain-filling parameters, fertility, earliness and grain protein of durum wheat in a Mediterranean environment*. *Field crops research*. 47(2-3): 129—142. (19)
- Nakicenovic N., Alcamo J., Davis G., de Vries B., Fenhann J., Gaffin S., Gregory K., Grübler A., Jung T.Y., Kram T., La Rovere E.L., Michaelis L., Mori S., Morita T., Pepper W., Pitcher H., Price L., Raihi K., Roehrl A., Rogner H., Sankovski A., Schlesinger M., Shukla P., Smith S., Swart R., van Rooijen S., Victor N. and Dadi Z. (2000). *IPCC Special Report on Emissions Scenarios*. Cambridge University Press, Netherlands. (20)
- Pala M., Stockle C.O. and Harris H.C. (1996). *Simulation of durum wheat (*Triticum turgidum* ssp. *Durum*) growth under different water and nitrogen regimes in a Mediterranean environment using CropSyst*. *Agricultural systems*. 51(2): 147—163. (21)
- Rodríguez Diaz J.A., Knox J.W., & Weatherhead E.K. 2007. *Competing Demands for Irrigation Water: Golf and Agriculture in Spain*. *Irrigation and Drainage*, 56, 541-549. (22)

- Sacks W.J., Deryng D., Foley J.A., and Ramankutty N. (2010). *Crop planting dates: an analysis of global patterns*. *Global Ecology and Biogeography* 19, 607-620. (23)
- Santiveri F., Royo C. and Romagosa I. (2004). *Growth and yield responses of spring and winter triticale cultivated under Mediterranean conditions*. *European journal of agronomy*. 20(3): 281—292. (24)
- Thomasson A. J. (1979) *Assessment of soil droughtiness*. In: *Soil Survey Applications* (ed. M G Jarvis and D Mackney). *Soil Survey Technical Monograph No. 13*, 43-50. (25)

ANNEX

	<i>East Asia & Pacific</i>	<i>Europe & Central Asia</i>	<i>Latin America & Caribbean</i>	<i>Middle East & North Africa</i>	<i>North America</i>	<i>South Asia</i>	<i>Sub-Saharan Africa</i>	<i>Total</i>
Suitable	26,798,568	60,802,543	0	883,355	38,240,615	5,598,046	0	132,323,127
Moderate	1,957,238	1,558,862	0	398,376	7,098,018	325,629	0	11,338,122
Marginal	689,363	2,092,339	0	221,705	859,106	1,316,372	0	5,178,886
Unsuited-Drought	13,267,647	8,390,141	9,824,294	8,144,187	1,496,507	37,260,264	1,520,756	79,903,797
Unsuited Cold	2,494,179	2,217,048	10,392	65,819	72,747	124,709	13,857	4,998,751
Unsuited-Warm	31,177	0	45,034	450,338	0	412,232	38,106	976,887
Unsuited-Wet	20,785	31,821,568	0	0	2,577,318	0	0	34,419,671
Total	45,258,957	106,882,500	9,879,720	10,163,780	50,344,311	45,037,253	1,572,718	269,139,240

Table 1: Production area (ha) of total wheat crop classified by their suitability for winter wheat (elaborated from [Monfreda et al. \(2008\)](#))

		<i>East Asia & Pacific</i>	<i>Europe & Central Asia</i>	<i>Latin America & Caribbean</i>	<i>Middle East & North Africa</i>	<i>North America</i>	<i>South Asia</i>	<i>Sub-Saharan Africa</i>	<i>Total</i>
<i>Baseline</i>	Suitable	10	23	0	0	14	2	0	49
	Moderate	1	1	0	0	3	0	0	4
	Marginal	0	1	0	0	0	0	0	2
	Unsuited-Drought	5	3	4	3	1	14	1	30
	Unsuited Cold	1	1	0	0	0	0	0	2
	Unsuited-Warm	0	0	0	0	0	0	0	0
	Unsuited-Wet	0	12	0	0	1	0	0	13
<i>2050L</i>	Suitable	9	26	0	1	15	0	0	52
	Moderate	0	1	0	0	0	0	0	2
	Marginal	0	1	0	0	0	0	0	2
	Unsuited-Drought	6	3	3	2	1	2	0	17
	Unsuited Cold	1	2	0	0	1	0	0	3
	Unsuited-Warm	0	0	1	0	0	15	0	16
	Unsuited-Wet	0	8	0	0	1	0	0	8
<i>2050H</i>	Suitable	9	27	0	1	16	0	0	54
	Moderate	1	1	0	0	0	0	0	2
	Marginal	0	1	0	0	0	0	0	2
	Unsuited-Drought	5	3	3	2	1	1	0	16
	Unsuited Cold	1	1	0	0	0	0	0	2
	Unsuited-Warm	0	0	1	1	0	15	0	17
	Unsuited-Wet	0	7	0	0	1	0	0	8

Table 2: Wheat harvested area (% of total wheat area) classified by suitability for winter wheat under current (1961-1990) and future climate with low (2050L) and high (2050H) emissions scenarios.

Water scarcity, climate change, and food security: challenges for the future

Mancosu N.^{*1,2}, Snyder R.L.³, Spano D.^{1,2}

¹*Dept. of Science for Nature and Environmental Resources (DipNET), University of Sassari, Sassari, Italy.*

²*Euro-Mediterranean Center on Climate Changes (CMCC), LAFENT Division, Sassari, Italy.*

³*Dept. of Land, Air and Water Resources, University of California, Davis, USA.*

**Corresponding author: nmancosu@uniss.it*

Abstract

Water scarcity is nowadays one of main world issues, and according to climate change projections, it will be more important in future. Since water availability is the most significant limiting factor for crop yields, addressing this issue is essential for countries affected by water scarcity. As a result of the increased of water scarcity and drought, due to climate change, an extensive water use for irrigation is expected to happen in a context of increasing competition between agriculture and other sectors of the economy. Moreover, the projected increase of the world population growth rate suggests that a higher food demand shall be expected in the future, with a direct effect on agricultural water usage. In agriculture, assessing the irrigation requirement is indispensable for water resource planning. Thus, this paper reviews current and future issues related to “water scarcity” in order to denote the necessity of a more sustainable approach to water resource management. The application of adaptation strategies may reduce water usage, and help avoiding excessive water consumption.

Keywords: *water for food; irrigation demand; sustainable water management; virtual water; adaptation strategies*



1. THE WATER RESOURCES

1.1 Basic concepts

Water is the most important resource for life. It has been the main issue on the international agenda for the last 30 years, starting with the first International Conference on Water (Mar de la Plata, 1977), and, since then, this topic has been considered increasingly important. The concept of water resources is multidimensional, and it goes over the physical connotation. In fact, not only the quantity, measured in flows and stocks, is considered important, but also the quality. Water is a natural and environmental resource that acquires a socio-economic connotation.

Water is divided in two types of resources:

- renewable water resources: the long-term average annual flow of rivers (surface water) and groundwater;
- non-renewable water resources: groundwater bodies (deep aquifers) that have a negligible rate of recharge on the human time scale, and for this reason can be considered non-renewable.

Water is also defined as blue water, the liquid water above and below the ground (rivers, lakes, groundwater), and green water as the soil water in the unsaturated zone derived from precipitation [14]. The portion of water that is directly used and evaporated by non-irrigated agriculture, pastures, and forests, is defined as green water. Thus, green-water flow has two components: the productive part, or transpiration involved in biomass production in terrestrial ecosystems, and the non-productive part, or evaporation [14]. Blue and green water are both considered renewable resources in the broad sense, but only blue water is evaluated in the strict sense.

The method used to assess the renewable water resources by country was first described in FAO/BRGM [18]. The method computes the total renewable water resources (TRWR) of a country and assesses the dependency ratio from neighboring countries. The TRWR are the sum of both renewable water resources: internal (IRWR) and external (ERWR). IRWR are the volume of the water resources (surface water and groundwater) generated from precipitation within a country or catchments. Surface water and groundwater are usually studied separately, even if the two concepts often overlap. In fact, surface water flows can contribute to groundwater replenishment through seepage in the riverbed. On the other hand, aquifers can discharge into rivers and contribute to their base flow, the sole source of river flow during dry periods. ERWR are considered resources that enter

from upstream countries through rivers or aquifers. ERWR are separated into two categories: natural and actual ERWR. The natural ERWR are equal to the volume of average annual flow of rivers and groundwater that enter into a country from neighbouring countries. The actual ERWR take into account the quantity of flow reserved by upstream (incoming flow) and/or downstream (outflow) countries through formal or informal agreements or treaties. Therefore, the actual resource is related to resources shared with neighbouring countries (geopolitical country constraints).

All these parameters facilitate the analysis of how different countries depend on the water resources of their neighbours. The dependency ratio of a country is an indicator that expresses the part of the water resources originated outside the country, and it is computed as the ratio between the ERWR and TRWRA country with a dependency ratio equal to zero does not receive any water from neighbouring countries. While a country that possesses a dependency ratio equal to 100% receives all its water from outside without producing any.

The total freshwater water resources in the world are estimated in the order of $43,750 \text{ km}^3 \text{ yr}^{-1}$ distributed throughout the world; at the continental level, America has the largest share of the world's total freshwater resources with 45%, followed by Asia with 28%, Europe with 15.5 %, and Africa with 9% [15]. In terms of resources per inhabitant in each continent, America has $24,000 \text{ m}^3 \text{ yr}^{-1}$, Europe $9,300 \text{ m}^3 \text{ yr}^{-1}$, Africa $5,000 \text{ m}^3 \text{ yr}^{-1}$, and Asia $3,400 \text{ m}^3 \text{ yr}^{-1}$ [15]. However, at a country level, there is an extreme variability in terms of TRWR. For 19 countries or territories (e.g., Morocco, Algeria, Bahrain, Jordan, Kuwait, Libyan Arab Jamahiriya, Maldives, Malta, Qatar, Saudi Arabia, United Arab Emirates, Yemen) the TRWR per inhabitant are less than 500 m^3 [15], the threshold that correspond to the water scarcity levels proposed by Falkenmark [13], where Kuwait is probably the worst case (10 m^3 per inhabitant) [15].

The most critical situations in terms of IRWR is recorded all over the Middle East and in large part of Africa, with values that range from 0 to $1,000 \text{ m}^3 \text{ yr}^{-1}$ per person (Fig. 1), where the threshold of $1,000 \text{ m}^3$ per inhabitant corresponds to the water stress level [13].

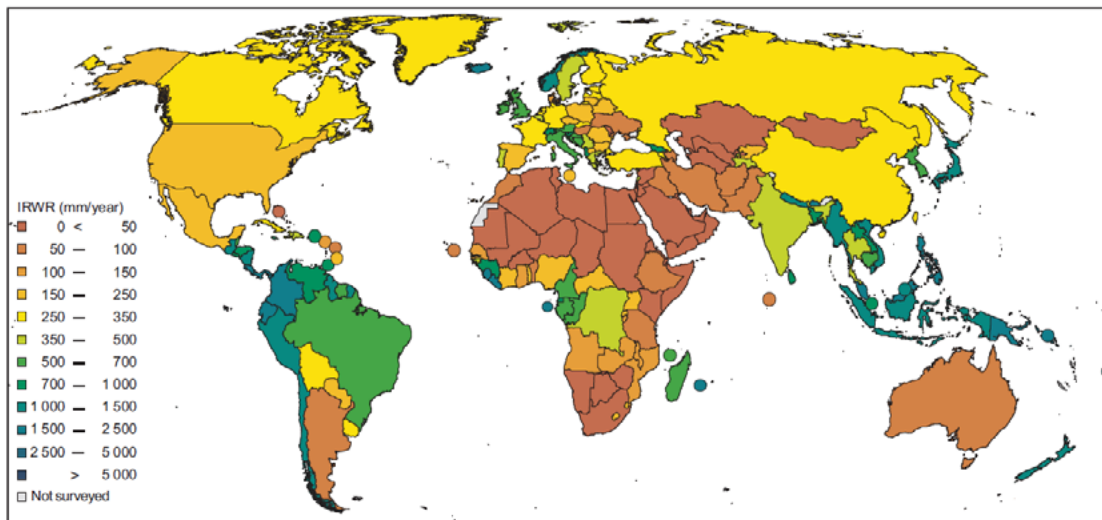


Fig. 1: World map of internal renewable water resources (IRWR) per country [15].

1.2 Water needs from the present to future projections

Nowadays, the term “water” is linked to the water scarcity concept, and there are many ongoing studies and projects to assess the world water demand and its availability. In fact, despite the vast amount of water on the planet, the balance between water demand and water availability has reached a critical level in many areas of the world. This is due to a misuse of the water resources, but also to the impact of climate change. The Intergovernmental Panel on Climate Change (IPCC) Fourth Assessment Report declares that climate change is expected to exacerbate the current stress on water resources due to population growth, economic and land-use change, including urbanization. According to the scenarios described in the IPCC Special Report on Emissions Scenarios [42], changes in precipitation and temperature may lead to changes in runoff and water availability, which in turn could affect crop productivity [24]. The physical, chemical, and biological properties of freshwater lakes and rivers will be affected by the increase in temperature [24]. This change is predicted to negatively affect many individual freshwater species, community composition, and water quality. Moreover, the sea level rise affects low-lying coastal areas, and the intrusion of saline water influences the quality of freshwater aquifers.

The rising atmospheric CO₂ concentration, associated with higher temperature, changes with precipitation patterns. As pointed out by Bates et al. [8], climate model simulations for the 21st century are consistent in projecting precipitation increases at high latitudes and parts of the tropics, and

decreases in some subtropical and lower mid-latitude regions. Altered frequencies of extreme events associated with melting of winter snow and reduced storage of precipitation as snow causes a reduction in water availability will have significant effects on crop production (Fig. 2). An increase of evaporative demand from crops, as result of higher temperature, and the reduction of water availability in regions affected by falling annual or seasonal precipitation, means a reduction in crop yield and agricultural productivity where temperature constrains crop [17]. On the other hand, current research confirms that crops would respond positively to elevated levels of CO₂ in the absence of climate change [27; 25; 1]. The direct effect of CO₂ enrichment on plant growth and development, also called the CO₂ fertilization effect, has generally a positive effect on crop yield [23]. In fact, the increase of CO₂ concentration reduces the stomatal conductance and transpiration rates [30]. Moreover, the combination of increased water use efficiency and root water uptake capacity modifies the relative crop yield response to elevated CO₂ [43].

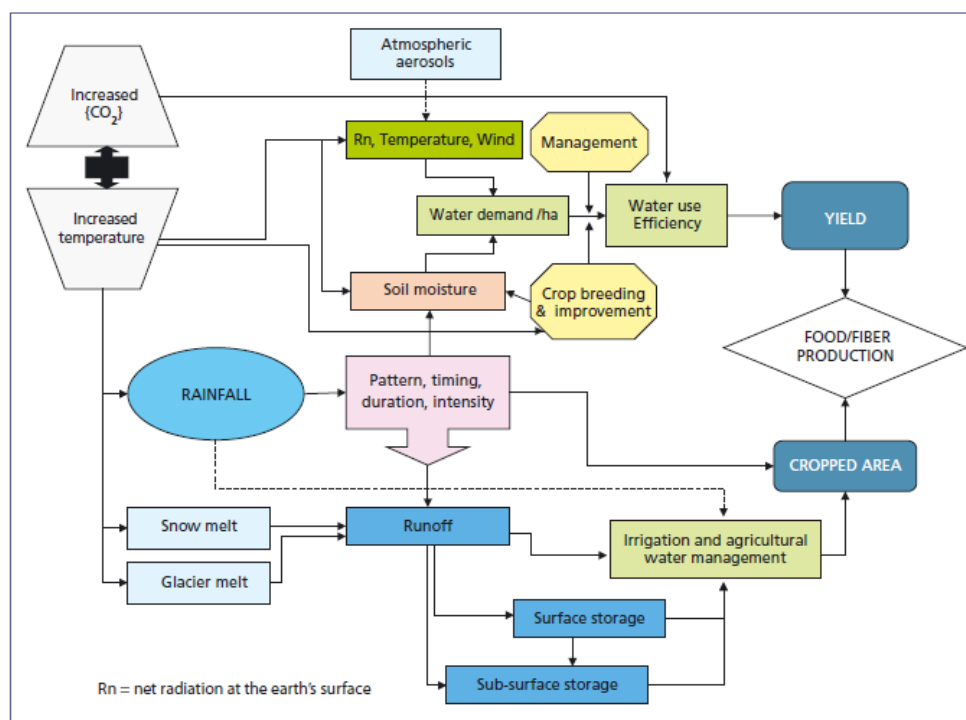


Fig. 2: The agricultural production cycle as impacted by climate change [17].

Precipitation and soil moisture are important factors that hinder crop production, even though the increase in atmospheric CO₂ concentration counteracts the negative effect, potentially causing the crops to be less water stress sensitive [9; 40]. Changes in precipitation patterns, intensity and frequency of extreme events, soil moisture, runoff, and evapotranspiration fluxes have already been observed, and

more important changes are expected for the future [8]. Sillmann and Roeckner [39] estimated that extreme precipitation is projected to increase significantly in most regions of the world, especially in those regions that are already relatively wet under present climate conditions. Analogously, dry spells are expected to increase, particularly in those regions that are characterized by dry conditions in the present-day climate, such as European regions [39].

Nowadays, 12% of the land surface is used for cultivation, and another 22% is used for pastures and rangelands [28]. Shiklomanov [37] estimated that the agricultural sector uses two-thirds of the world water withdrawals, which accounts for 90% of the total water consumption in the world in the period from 1961 to 2004. On the world average, agriculture is the largest water user sector, accounting for approximately 70% of the total water withdrawals [26]. FAO [16] reported that more than 80% of global agricultural land is rain-fed; irrigated land, representing only 18% of global agricultural land, produces 1 billion tonnes of grain annually, or about half the world's total supply. This is because yields of irrigated crops are on average 2–3 times more than their rain-fed counterparts. As pointed out by Shiklomanov [38], the smallest values for specific water withdrawals are observed in northern Europe, and they are between 300-5,000 m³ ha⁻¹, while in southern and eastern European countries they amount to 7,000-11,000 m³ ha⁻¹. In the USA, the specific water withdrawal for irrigation is estimated to be between 8,000-10,000 m³ ha⁻¹. In the countries of Asia, Africa, Central and South America, where there is a great variety of climatic conditions, crop composition, and watering techniques, the values for specific water withdrawal range from 5,000 - 6,000 m³ ha⁻¹ to 15,000 - 17,000 m³ ha⁻¹ [38]; the highest values for specific water withdrawal are observed in regions of Africa (20,000-25,000 m³ ha⁻¹).

Nowadays, such water-stressed basins are located in northern Africa, the Mediterranean region, the Middle East, the Near East, southern Asia, northern China, Australia, the USA, Mexico, northeastern Brazil, and the west coast of South America [2]. An increase in irrigation water demand, particularly in the aforementioned countries, is projected because of climate change [24]. Fischer et al. [20] estimated that irrigation water requirements are expected to increase over 50% in developing regions, and by about 16% in developed regions. In this study, estimations of irrigation water requirements were computed from 2000 to 2080, with the largest relative increases occurring in Africa (+300%) and Latin America (+119%). Furthermore, Africa and the Middle East possess the most critical values of annual renewable freshwater resources. In fact, as shown in Fig. 3, populations in the North-Africa belt (from Morocco to Egypt, including Sudan) had less than 1,000 m³ of water per person per year in 2000,

whereas populations in the Middle East and Southern Africa had between 1,000 to 2,000 m³ per year. The estimates made by Wallace [45] determines that the available water per capita will drop below 1,000 m³ per capita per year before 2050 for North, East, and South Africa, and the Middle East.

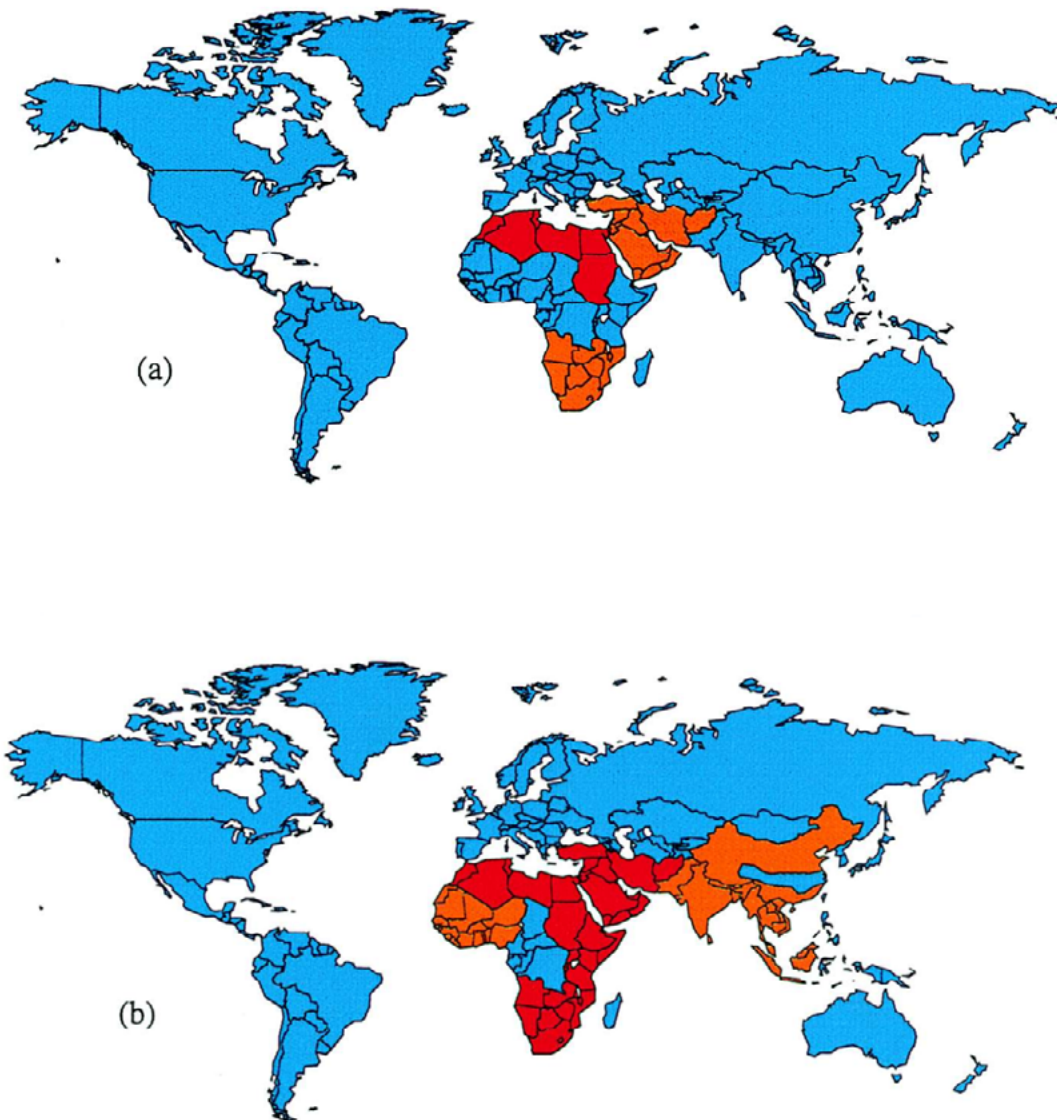


Fig. 3: Global water scarcity now (a) and in 2050 (b). Red is used for regions that present less than 1,000 m³ per person per year, orange between 1,000 and 2,000 m³ per person per year and blue for value greater than 2,000 m³ per person per year. Data from [19], source: [45].

The future population growth is another factor to consider. As estimated by Roetter and Van Keulen [34], the median population growth projection for 2025 is 7.8 billion, compared with the present 6.4 billion; the highest projection is 8.3 billion, while the lowest projected population is 7.3 billion. For the year 2050, the average projection is around 9 billion. In Asia, the population will grow by 650 million people between now and 2025, indicating an annual growth rate of approximately 1%. Population estimates for such water-stressed basins range between 1.4 billion and 2.1 billion [44; 4; 29; 7]. At present, about 7% of the world's population lives in areas affected by water scarcity and this is predicted to rise to a staggering 67% by 2050 [45]. The increase of world population has an impact on water usages for food. Rijsberman [33] reports that the International Water Management Institute (IWMI) estimated that a 29% increase in the amount of irrigated land will be required by the year 2025 under a base scenario that included optimistic assumptions on productivity growth and efficiency. From such a growth rate, it can be assumed that a higher food demand shall be expected in the future, resulting in a direct effect on water usage in agriculture, particularly in areas affected by water scarcity.

1.3 Virtual water

A significant relationship exists between renewable water resources of a country and the capacity for food production. In order to have a consumption-based indicator of water use that could provide useful information in addition to the traditional production-sector-based indicators of water use, the “water footprint” concept was introduced. It is defined as the total volume of freshwater that is used to produce the goods and services consumed by the people of the nation [22]. The water footprint consists of two parts: use of domestic water resources and use of water outside the borders of the country, since not all goods consumed in a particular country are produced locally. This can be related to the concept of “virtual water”. Virtual water is defined as the volume of water consumption required to produce commodities traded to an importing or exporting nation (or any region, company, individual, etc.). Countries affected by water scarcity, could alleviate problems related to agricultural and livestock production by importing food and certain commodities that would otherwise consume great quantities of water [5]. Virtual water takes into account both blue and green water. Allan [6] termed such food imports as “virtual water imports” due to the fact that they are equivalent to a transfer of water to an importing country. Hanasaki et al. [21] showed that the global virtual water export of five crops (barley, maize, rice, soybean, and wheat) and three livestock products (beef, pork, and chicken) is

545 km³ yr⁻¹. Of the total virtual water exports, 61 km³ yr⁻¹ (11%) were blue water, and 26 km³ yr⁻¹ (5%) were nonrenewable and nonlocal blue water. North and South America are the major regions from which virtual water export flows originate, while East Asia, Europe, Central America, North Africa, and West Asia are the major destinations for all water sources (Fig. 4).

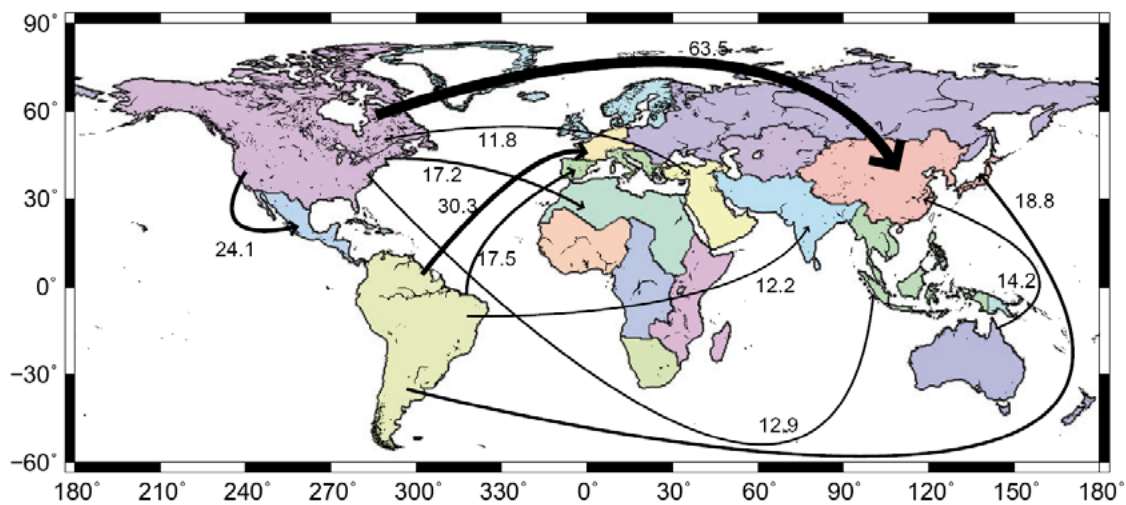


Fig. 4: World map of virtual water exports, total virtual water exports (flows exceeding 10 km³ yr⁻¹ are shown). Source: [21]

Africa and Asia are considered water-scarce continents because of the high concentration of countries affected by this problem [11; 41]. Many countries in these two continents are net importers of cereal grains. Cereal imports have played a crucial role in compensating local water deficits. Yang et al. [48] estimated the water resources threshold with respect to cereal imports for Africa and Asia. Below the threshold, the demand for cereal import increases exponentially with decreasing water resources. This means that in the next 30 years, many poor and populous countries will drop below the threshold due to their rapid population growth and the depletion of fossil groundwater.

During the past two decades, irrigated areas expanded relatively rapidly in various countries, e.g. Egypt, Algeria, Libya, Israel, Morocco and Tunisia, while at the same time a significant import of cereals was observed. Yang and Zehnder [47] reported that in 1998–99, cereal imports accounted for 52% of the total supply in the six countries combined. Under the baseline scenario, cereal demand in the six countries as a whole will increase above the 1998-99 level by 38% in 2020. Under a scenario of

increased consumption, cereal demand will rise above the 1998-99 level by 47% in 2020. This means that the international trade in food grains and other agricultural products has played and will continue to play a critical role in water-scarce countries. Therefore, it will be not easy for some countries to meet food demands without importing.

The import of virtual water poses various questions in relation to the concept of “Food Security”. The World Food Summit of 1996 established that “Food security exists when all people, at all times, have physical and economic access to sufficient, safe, and nutritious food to meet their dietary needs and food preferences for an active and healthy life”. Three core concepts are at the base of the food security theory:

- 1) food availability: the amount of food constantly available;
- 2) food access: the ability to have sufficient resources to obtain appropriate foods for a healthy diet;
- 3) food utilization: the use of appropriate products based on basic knowledge of nutrition, water, and adequate sanitary conditions.

Nevertheless, the necessity of other countries to meet the food requirements of their populations creates uncertainties mostly related to the policies of importing countries. In fact, water scarcity related to the food import demand can have an adverse impact on the stability of the world food economy. On the other hand, “virtual water” food imports are a valid way to create economic growth in water-scarce countries, and to maximize the value of their limited water supplies.

1.4 Conclusions

The overall conclusion is that a large share of the world’s population, up to two-thirds, will be affected by water scarcity over the next several decades [36; 32; 35; 2; 3; 44; 45; 46]. In many countries the quantity of water that is available and the uneven distribution of these resources in time and space are pressing issues [10].

Climate change impacts on water pose questions not only about the amount of future water reduction, but also on water quality. In fact, excessive abstraction from coastal aquifers can cause the intrusion of saltwater, diminishing the quality of the groundwater and preventing its subsequent use [12]. In addition, taking into account that in some countries (e.g. the Mediterranean region) irrigation is applied

during the summer season, which also coincides with the main tourism season, a consequential competition between these two sectors is expected. As pointed out by Qadir et al. [31], this underlines the necessity of the sustainable management of available water resources at the global, regional, and site-specific level is necessary.

In order to achieve this objective, the first step is to compute how much water is needed by crops with regards to climate conditions. The monitoring and modeling approach are two ways to achieve this goal. Once the crop water requirement is assessed, the application of some easy water management strategies may be valuable for the sustainable utilization of water resources. Scheduling irrigation management strategies, modifying agricultural practices, and improving irrigation systems are just a few practices that can lead to a more efficient agricultural water management. Moreover, the implementation of policy measures, followed by the establishment of farmer advisory schemes, could be the key for a future agricultural and economic growth in countries affected by water shortages.

2. ACKNOWLEDGMENTS

The research leading to these results has received funding from the Italian Ministry of Education, University and Research and the Italian Ministry of Environment, Land and Sea under the GEMINA project, and the European Community's Seventh Framework Program (FP7/2007-2013) under grant agreement 244255 (WASSERMed project).

3. REFERENCES

- Ainsworth E.A., Long S.P. (2005). *What have we learned from 15 years of free-air CO₂ enrichment (FACE)? A meta-analysis of the responses of photosynthesis, canopy properties and plant production to rising CO₂*. *New Phytologist*, 165, 351-372. (1)
- Alcamo J., Döll P., Kaspar F., Siebert S. (1997). *Global change and global scenarios of water use and availability: an application of WaterGAP 1.0*. University of Kassel, CESR, Kassel, Germany. (2)
- Alcamo J., Henrichs T., Rosch T. (2000). *World water in 2025: global modeling and scenario analysis*. In: Rijsberman F.R. (Ed.), *World water scenarios analyses*. World Water Council, Marseille, France. (3)
- Alcamo J., Döll P., Henrichs T., Kaspar F., Lehner B., Rösch T., Siebert S. (2003). *Global estimates of water withdrawals and availability under current and future “business-as-usual” conditions*. *Hydrological Sciences Journal*, 48, 339-348. (4)
- Allan J.A. (1996). *Policy responses to the closure of water resources: regional and global issues*. In: Howsam P. (Ed.), *Water Policy: Allocation and Management in Practice*. Taylor and Francis, London, UK, pp. 3–12. (5)
- Allan J.A. (1997). *Virtual water: a long-term solution for water short Middle Eastern economies?* Paper presented at the 1997 British Association Festival of Science, University of Leeds, 9 September 1997, UK. (6)
- Arnell N.W. (2004). *Climate change and global water resources: SRES scenarios and socio-economic scenarios*. *Global Environmental Change*, 14, 31–52. (7)
- Bates B.C., Kundzewicz Z.W., Wu S., Palutikof J.P. (2008). *Climate Change and Water*. Eds. IPCC Secretariat, Geneva. (8)
- Brown R.A., Rosenberg N.J. (1997). *Sensitivity of crop yield and water use to change in a range of climatic factors and CO₂ concentrations: a simulation study applying EPIC to the central USA*. *Agricultural Forest Meteorology*, 83, 171–203. (9)
- Correia F.N. (1999). *Water Resources in the Mediterranean region*. *Water International*, 24 (1), 22-30. (10)
- Cosgrove W., Rijsberman F. (2000). *Making water everybody’s business, World Water Vision*. The World Water Council, Earthscan Publications Ltd., London, UK. (11)
- European Environment Agency (EEA). (2009). *Report No 2/2009: Water resources across Europe — confronting water scarcity and drought*. European Environment Agency, Copenhagen, Denmark. (12)

- Falkenmark M. (1986). *Freshwater - time for a modified approach*. *Ambio*, 15(4), 192-200. (13)
- Falkenmark M., Rockström J. (2006). *The new blue and green water paradigm: breaking new ground for water resources planning and management*. *Journal of Water Resources Planning and Management*, 132(3), 129–132. (14)
- FAO. (2003). *Review of world water resources by country*. Water Report No. 23. Rome, Italy. <ftp://ftp.fao.org/agl/aglw/docs/wr23e.pdf> (15)
- FAO. (2003). *World agriculture towards 2015/2030*.
http://www.fao.org/documents/show_cdr.asp?url_file=/docrep/004/y3557e/y3557e00.htm. (16)
- FAO. (2011). *Climate change, water and food security*. FAO water reports No. 36. Rome, Italy. <http://www.fao.org>. (17)
- FAO/BRGM. (1996). *Les ressources en eau*. Rome. (18)
- Fischer G., Heilig G.K. (1997). *Population momentum and the demand on land and water resources*. *Philosophical Transactions of Royal Society, B: Biological Sciences*, 352, 869–889. (19)
- Fischer G., Tubiello F.N., Van Velthuis H., Wiberg D.A. (2007). *Climate change impacts on irrigation water requirements: effects of mitigation, 1990–2080*. *Technological Forecasting & Social Change*, 74, 1083–1107. (20)
- Hanasaki N., Inuzuka T., Kanae S., Oki T. (2010). *An estimation of global virtual water flow and sources of water withdrawal for major crops and livestock products using a global hydrological model*. *Journal of Hydrology*, 384, (3–4), 232–244. (21)
- Hoekstra A.Y, Hung P.Q. (2002). *Virtual water trade: A quantification of virtual water flows between nations in relation to international crop trade*. Value of Water Research Report Series No. 11, UNESCO-IHE Institute for Water Education, Delft, The Netherlands.
<http://www.waterfootprint.org/Reports/Report11.pdf> (22)
- Idso K.E., Idso S.B. (1994). *Plant responses to atmospheric CO₂ enrichment in the face of environmental constraint: a review of the past 10 years' research*. *Agricultural and Forest Meteorology*, 69, 153–203. (23)
- Intergovernmental Panel on Climate Change (IPCC). (2007). *Fourth IPCC Assessment Report (AR4): Climate Change 2007*. Cambridge University Press, Cambridge, UK. (24)

- Jablonski L.M., Wang X., Curtis, P.S. (2002). *Plant reproduction under elevated CO₂ conditions: A meta-analysis of reports on 79 crop and wild species*. *New Phytologist*, 156 (1), 9-26. (25)
- Johnson N., Revenga C., Echeverria J. (2001). *Managing Water for People and Nature*. *Science*, 292 (5519), 1071-1072. (26)
- Kimball B.A., Kobayashi K., Bindi M. (2002). *Responses of agricultural crops to free-air CO₂ enrichment*. *Advances in Agronomy*, 77, 293-368. (27)
- Leff B., Ramankutty N., Foley J.A. (2004). *Geographic distribution of major crops across the world*. *Global Biogeochemical Cycles*, 18, GB1009. (28)
- Oki T., Sato M., Kawamura A., Miyake M., Kanae S., Musiake K. (2003). *Virtual water trade to Japan and in the world*. In: Hoekstra A.Y. (Ed.), *Virtual Water Trade: Proceedings of the International Expert Meeting on Virtual Water Trade*. Value of Water Research Report Series 12, Delft, The Netherlands, pp. 221–235. (29)
- Olesen J.E., Bindi M. (2002). *Consequences of climate change for European agricultural productivity, land use and policy*. *European Journal of Agronomy*, 16, 239–262. (30)
- Qadir M., Boers Th.M., Schubert S., Ghafoor A., Murtaza G. (2003). *Agricultural water management in water-starved countries: challenges and opportunities*. *Agricultural Water Management*, 62, 165–185. (31)
- Raskin P., Gleick P., Kirshen P., Pontius G., Strzepek K. (1997). *Water futures: assessment of long-range patterns and prospects*. Stockholm Environment Institute, Stockholm, Sweden. (32)
- Rijsberman F.R. (2006). *Water scarcity: Fact or fiction?* *Agricultural Water Management*, 80, 5–22. (33)
- Roetter R.P., Van Keulen H. (2008). *Food security*. In: Roetter R.P, Van Keulen H., Kuiper M., Verhagen J., Van Laar H.H. (Eds.), *Science for agriculture and rural development in low-income countries*. Springer, Dordrecht, The Netherlands, pp 27–56. (34)
- Seckler D., Amarasinghe U., Molden D.J., De Silva R., Barker R. (1998). *World water demand and supply, 1990 to 2025: scenarios and issues*. IWMI Research Report 19. IWMI, Colombo, Sri Lanka. (35)
- Shiklomanov I.A. (1991). *The world's water resources*. In: Proceedings of the International Symposium to Commemorate 25 Years of the IHP, UNESCO/IHP, Paris, France, pp. 93–126. (36)

- Shiklomanov I.A. (1997). *Assessment of water resources and water availability in the world*. World Meteorological Organization/Stockholm Environment Institute, Geneva, Switzerland. (37)
- Shiklomanov I.A. (1998). *World Water Resources: An appraisal for the 21st century*. IHP Report. UNESCO, Paris, France. (38)
- Sillmann J., Roeckner E. (2008). *Indices for extreme events in projections of anthropogenic climate change*. Climatic Change, 86, 83–104. (39)
- Singh B., El Maayar M., André P., Bryant C., Thouez J.P. (1998). *Impacts of a GHG-induced climate change on crop yields: effects of acceleration in maturation, moisture stress and optimal temperature*. Climatic Change, 38, 51–86. (40)
- Smith L., Obeid A., Jensen H. (2000). *The geography and causes of food insecurity in developing countries*. Agricultural Economics, 22, 199-215. (41)
- SRES. 2000. *Emission Scenarios. A Special Report of IPCC, WG III. Summary for Policymakers*. (42)
- Tubiello F.N., Ewert F. (2002). *Modeling the effects of elevated CO₂ on crop growth and yield: a review*. European Journal of Agronomy, 18(1–2), 57-74. (43)
- Vörösmarty C.J., Green P.J., Salisbury J., Lammers R.B. (2000). *Global water resources: vulnerability from climate change and population growth*. Science, 289, 284–288. (44)
- Wallace J.S. (2000). *Increasing agricultural water use efficiency to meet future food production*. Agriculture, Ecosystems and Environment, 82, 105–119. (45)
- Wallace J.S., Gregory P.J. (2002). *Water resources and their use in food production*. Aquatic Sciences-Research Across Boundaries, 64, 363–375. (46)
- Yang H., Zehnder A.J.B. (2002). *Water Scarcity and Food Import: A Case Study for Southern Mediterranean Countries*. World Development, 30 (8), 1413–1430. (47)
- Yang H., Reichert P., Abbaspour K., Zehnder A.J.B. (2003). *Water Resources threshold and its implications for food security*. Environmental Science & Technology, 37, 3048-3054. (48)

An analysis of the fire danger regime in Italy

Masala F.^{1*}, Sirca C.^{1,2}, Bacciu V.^{1,2}, and Spano D.^{1,2}

¹ Euro Mediterranean Center on Climate Change (CMCC LAFENT), Sassari, Italy,

² Department of Science for Nature and Environmental Resources (DipNeT), University of Sassari, Italy

*Corresponding author: framasala@uniss.it

Abstract

The main aim of this work was to improve our understanding in relation to the fire regime and its relationships with wildfires in Italy.

The study was conducted at national and regional scale for the period 1985-2008. A preliminary hierarchical cluster analysis, based on the fire occurrence and weather data has allowed to identify six homogeneous areas in terms of fire regime and climate. Then, two worldwide fire danger indexes (the Canadian Fire Weather Index - FWI, and the Keetch-Byram Drought Index - KBDI) have been used to characterize the fire danger trends and patterns across Italy and the indexes potential to reproduce the fire occurrence.

The results have showed an increasing trend of fire danger in Italy during the study period and a good correlation between FWI and fire occurrence in southern Italy during summer. The results improve our knowledge of the usefulness of fire danger indexes in Italy. In addition, the analysis of the relationships between fire occurrence and fire danger can be profitably applied to assess the impacts of climate changes on fire regimes in Italy.

Keywords: FWI, KBDI, MARS, wildfire



There are several and heterogeneous definitions of fire danger. Following Chuvieco et al. [1] fire danger can be defined as the probability of fire occurrence in case of favorable conditions for ignition and propagation. On the other hand, fire risk is the danger with respect to the vulnerability of the area [2]. The fire risk also depends from the value of goods and from the possibility of casualties [3, 4].

Several studies highlight that the main determinants for fire danger are climate and weather conditions [5, 6, 7]. In particular, the relationship between weather and fire danger has led to the development of several models or indexes to estimate fire danger. These indexes are widely used both for scientific and operational purposes. Several papers report analysis related to fire danger patterns of specific areas and, in view of a climate change scenario, fire danger projections for the next decades [8, 9, 10]. Fire danger indexes are also often used for operational purposes due to their relationship with fire occurrence. Nevertheless, most of papers report results related to a relatively wide areas (national scale or wider) [8] and low spatial resolutions or analysis at very local scale [11]. In the first case it is often difficult to link the results with operational actions; in the second case the results are rarely comparable with analysis carried out in other areas due to the difference in the adopted methodologies.

In this work an analysis of fire danger patterns across Italy is showed. Fire danger regime was firstly analyzed in order to establish significant trends in the recent past through its characterized at both national and regional scale, and then we investigate the relationships between fire occurrence and fire danger.

The analyses were carried out at annual and seasonal scale for the period 1985-2008. Two indexes were selected. The first is the FWI – the Canadian Fire Weather Index [12, 13]. This index is part of the CFFDRS - Canadian Forest Fire Danger Rating System and is often used as a stand-alone fire danger index. Probably the FWI is the most diffuse fire danger index due to its performances to represent fire danger in different climate and vegetation conditions and because the input data are easily available from the standard weather station networks [14, 15, 16]. The second index is the KBDI-Keetch-Byram Drought Index [17]. This index is a simplified soil water balance model and roughly estimates the water status of the soil and vegetation. Basing on its formulation, this index is used, stand alone or integrated in fire danger systems, as indicator of the potential fire danger. In this study, a modified version of KBDI [18] has been used.

The input data for the indexes calculation, at daily scale and 25 km resolution (maximum and minimum temperature, vapor pressure, rainfall and wind speed) were extracted from the MARS (Monitoring

Agricultural ResourceS) database, available online at <http://www.marsop.info/ExtractGrid/RegistrationForm.php>. The MARS project was set up in 2007 and one of its components is the AGR4CAST, which represents the system for yield forecasting. The core of AGR4CAST is represented by the Crop Growth Monitoring System (CGMS). Among the main outputs of the CGMS are interpolated weather data, created by using different weather data sources such as direct observations from meteorological stations, products derived from ECMWF (European Centre for Medium-Range Weather Forecasts), modelling of weather and meteorological observations from remote sensing platforms. Fire data for peninsular Italy and Sicily (fire number and burned area) were supplied from the European Fire Database (managed by the JRC-European Union Joint Research Center) while, for Sardinia island, they were obtained from the CFVA-Corpo Forestale e di Vigilanza Ambientale (Sardinian Forestry Corp).

In the first part of the analysis, the national territory was classified into homogeneous areas with respect to climate and fire occurrence. A hierarchical cluster analysis was performed based on maximum and minimum temperature, rainfall, and burned area. The homogeneous regions, called “piro climatic” areas, are showed in the Fig. 1.

To characterize the fire danger patterns, the mean and maximum FWI and KBDI value were calculated at monthly scale. In addition, the number of the days in which indexes exceed a defined threshold (corresponding to high fire danger conditions) were also calculated. For the FWI, a threshold value of 19.9 was chosen [11, 19, 20, 21, 22, 23, 24]. The KBDI threshold was arbitrarily defined as the 75th percentile of its distribution, corresponding to a value of 150.

The Fig. 2 and 3 showed the mean annual value and the number of days above the threshold for the FWI and KBDI, respectively. The analysis indicated that the areas with the higher fire danger are localized in Southern Italy (particularly in the two main islands), and in the south-east part of the Italian peninsula. The piro climatic areas with the highest fire danger are the number 5 and 6, localized in Southern Italy; the piro climatic areas with the lower fire danger are the number 1 and 2, localized in the Alpine area.

The presence of fire danger trends during the examined period was also investigated at national scale and for each piro climatic area. In order to identify annual variations of fire danger during the study period, parametric (linear regression) and non-parametric (Mann-Kendall test) statistics were applied. Tabs. 2 and 3 presented two examples of this analysis. In particular, the characterisation of the FWI

days (number) >19.9 and of the mean annual KBDI trends is showed. The FWI trend analysis revealed a general positive trend with the exception of the piro-climatic area 1, while KBDI showed a negative (decreasing) trend only for its mean value and only for the piro-climatic area 1.

In the last part of the analysis, the fire danger dynamics were compared with the fire occurrence to evaluate the skills of the fire danger indexes to represent the occurred fire conditions. With this aim, data related to fire occurrence (burned area BA and fire number FN) were converted in a GIS (Geographic Information System) format. Descriptive statistics were initially calculated for each piro-climatic area. Then, the relationships between fire occurrence (FN and BA) and fire danger indexes value were analyzed at seasonal and annual scale through a stepwise multiple regression. BA and FN values were normalized (by expressing them in a natural logarithm scale) to avoid effects induced by the non-normal distribution of raw data [6]. For the FWI, the index and all its five sub codes were evaluated:

FFMC	Fine Fuel Moisture Code;
DMC	Duff Moisture Code;
DC	Drought Code;
ISI	Initial Spread Index;
BUI	Build Up Index.

Tab. 3 illustrates the results obtained from the linear multiple regression calculated for all Italy and for all clusters between FWI and KBDI mean values and fire occurrence (only the results with a R^2 over 40% are reported).

At national scale the FFMC and the BUI explained over 70% and 60% of variance for FN and BA, respectively. The piro-climatic areas 1 and 2 showed that any index is able to explain the variance of fire. In the piro-climatic area 3, a combination of indexes that explains the 58% of variance for FN and 50% for BA was found. In the piro-climatic area 4, the linear multiple regression analysis did not reveal any significant result. Finally, the piro-climatic areas 5 and 6 showed the best results with the FFMC and BUI for both FN and BA. In the area 5, the explained variance was 83% and 78% for FN and BA, respectively; in the area 6 it is 75% and 74% for FN and BA, respectively.

The multiple regression analysis showed that the FWI index is a good predictor for the areas with summer fires. Similar results were found in Portugal [6].

The relationship between fire danger and fire occurrence, assessed in this analysis, showed complex and not linear connections in function of the piro-climatic area. From our analysis, the fire danger models gave a better response in reproducing fire regime in regions with marked summer season. This is a limitation of both FWI and KBDI that are typical weather indexes, and then are not able to modeling some effects of the weather on the vegetation (e.g. frost damages and desiccation during the winter season, that make the vegetation prone to fire [7]).

In conclusion, this work provides a perspective of the complexity of fire danger in Italy, identifying patterns of the variation of dangerous in the country, and showing that a multiple approach analysis greatly improves our knowledge of fire science.

ACKNOWLEDGMENTS

The research leading to these results has received funding from the Italian Ministry of Education, University and Research and the Italian Ministry of Environment, Land and Sea under the GEMINA project, and from the European Community's Seventh Framework Program (FP7/2007-2013) under grant agreement 243888 (FUME project).

REFERENCES

- Chuvieco E., Pilar M., Chris J., 2003. *Proceedings of the 4th International Workshop on Remote Sensing and GIS applications to Forest Fire Management: Innovative concepts and methods in fire danger estimation*. Ghent University –EARSel, 233 pages, ISBN: 2-908885-25-5. (1)
- Hardy C.C., 2005. *Wildland fire hazard and risk: Problems, definitions, and context*. *Forest Ecology and Management* 211: 73–82. (2)

- Bachman A. and Allgower B., 1998. *Framework for wildfire risk analysis*. In '3III International Conference on Forest Fire Research'. Luso, 16-29 November 1998. . (Eds X. Viegas) pp. 2177-2190. (University of Coimbra: ADAI). (3)
- Bachmann A., and Allgower B., 2001. *A consistent wildland fire risk terminology is needed!* Fire Management Today 61 (4): 28-33. (4)
- Pausas J.G. 2004. *Changes in Fire and Climate in the Eastern Iberian Peninsula (Mediterranean Basin)*. CLIMATIC CHANGE Volume 63, Number 3, 337-350. (5)
- Carvalho A., Flannigan M.D., Logan K., Miranda A.I., Borrego C., 2008. *Fire activity in Portugal and its relationship to weather and the Canadian Fire Weather Index System*. International Journal of Wildland Fire 17: 328-338. (6)
- Turco M., Llasat M.C., von Hardenberg J., Provenzale A., 2010. *Impact of climate variability on summer fires in a Mediterranean environment (northeastern Iberian peninsula)*. Climatic Change. (7)
- Moriondo M., Good P., Durao R., Bindi M., Giannakopoulos, C. and Corte-Real J. 2006. *Potential impact of climate change on fire risk in the Mediterranean area*. Climate Research 31: 85–95. (8)
- Brown T. J., Hall B. L., and Westerling A. L., 2004. *The impact of twenty-first century climate change on wildland fire danger in the western united states: an applications perspective*. Climatic Change 62: 365–388. (9)
- M. D. Flannigan, B. D. Amiro, K. A. Logan, B. J. Stocks, B. M. Wotton. *Forest Fires and Climate Change in the 21st Century*. Mitigation and Adaptation Strategies for Global Change July 2006, Volume 11, Issue 4, pp 847-859. (10)
- Valese E., 2008. *Applicazione del Canadian Forest Fire Weather Index System nel contesto della Grande Regione Alpina (GAR): potenzialità e problematiche*. (11)
- Van Wagner C.E., 1987: *Development and Structure of the Canadian Forest Fire Weather Index System*. Canadian Forest Service, Forestry Technical Report 35, Ottawa, Canada. (12)
- Van Wagner C.E., Pickett T.L., 1987. *Equation for Fortran program for the Canadian Forest Fire Index System*. Canadian Forestry Service, Forestry Technical Report 33, Ottawa, Canada. (13)
- Lawson B.D., Armitage O.B., 2008. *Weather guide for the Canadian Forest Fire Danger Rating System*. Natural Resources Canada, Canadian Forestry Service, Northern Forestry Centre, Edmonton, AB. (14)

- De Groot W.J., Field R.D., Brady M.A., Roswintarti O., Mohamad M., 2006. *Development of the Indonesian and Malaysian Fire Danger Rating Systems*. Mitig. Adapt. Strategies Global Change, 12: 165-180. (15)
- Dymond C.C., Field R.D., Roswintarti O., Guswanto. 2005. *Using satellite fire detection to calibrate components of the Fire Weather Index System in Malaysia and Indonesia*. [Environmental Management](#) 35:426–440. (16)
- Keetch J.J., and Byram G., 1968. *A drought index for forest fire control*. Res. Paper SE-38. U.S. Department of Agriculture, Forest Service, Southeastern Forest Experiment Station, Asheville, NC, 32 pp. (17)
- Snyder R.L., Spano D., Duce P., Baldocchi D., Xu L., Paw U K.T., 2006. *A fuel dryness index for grassland fire-danger assessment*. Agricultural and Forest Meteorology 139: 1–11. (18)
- Turner J. A., 1972. *The Drought Code component of the Canadian Forest Fire Behavior System*. Environment Canada., Canadian Forestry Service., Ottawa, ON. Publ. 1316. (19)
- Stocks B.J., Lawson B.D., Alexander M.E., Van Wagner C.E., McAlpine R.S., Lynham T.J., Dube D.E., 1989. *The Canadian Forest Fire Danger Rating System: an overview*. Forestry Chronicle 65:450–457. (20)
- Camia A., and Bovio G., 2000. *Description of the indices implemented in Eudic software for the European meteorological forest fire risk mapping*. European Forest Fire Information System (EFFIS). (21)
- Abbott K.N., Alexander M.E., MacLean D.A., Leblon B., Beck J.A., Staples G.C. 2007. *Predicting forest floor moisture for burned and unburned Pinus banksiana forest in the Canadian Northwest Territories*. International Journal of Wildland Fire 16(1):71–80. (22)
- Otway S.G., Bork E.W., Anderson K.R., Alexander M.E. 2007. *Relating changes in duff moisture to the Canadian Forest Fire Weather Index System in Populus tremuloides stands in Elk Island National Park*. Canadian Journal of Forest Research. 37:1987–1998. (23)
- Lawson B.D., Armitage, O.B., 2008. *Weather guide for the Canadian Forest Fire Danger Rating System*. Natural Resources Canada, Canadian Forestry Service, Northern Forestry Centre, Edmonton, AB. (24)

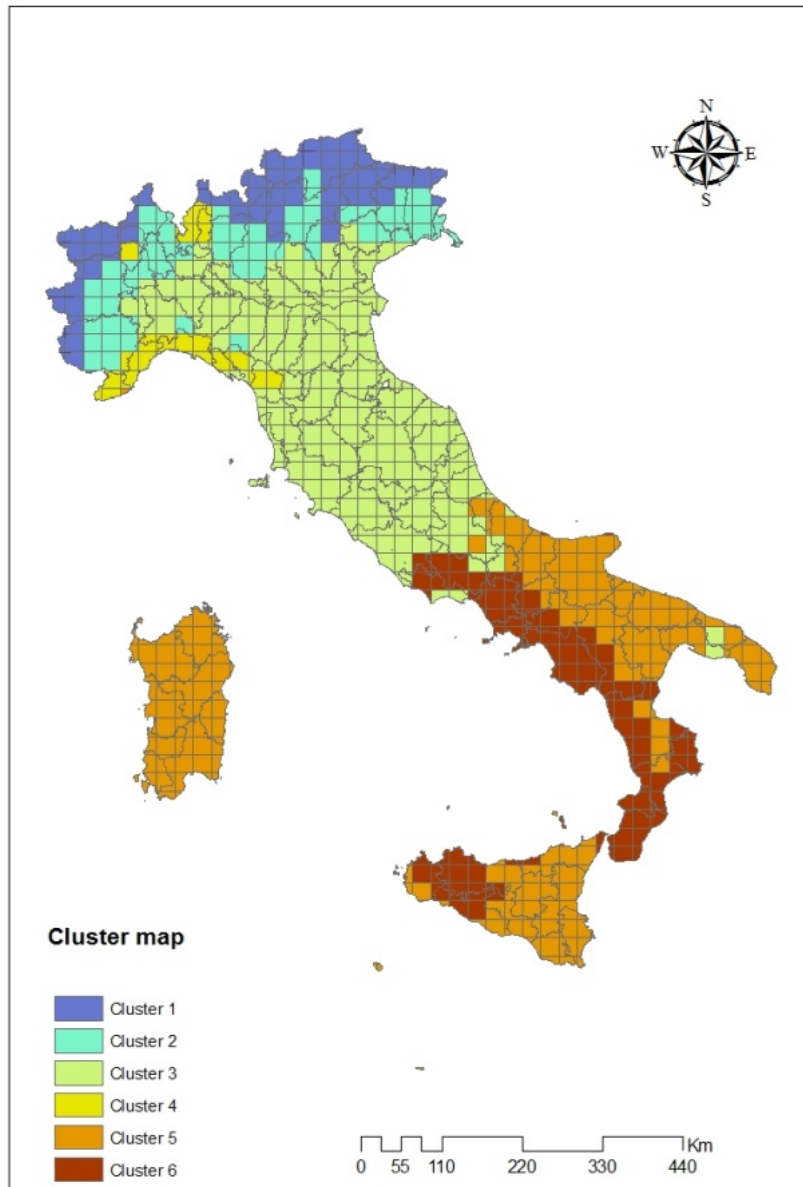


Fig. 1: Piro-climatic areas identified in Italy by the cluster analysis

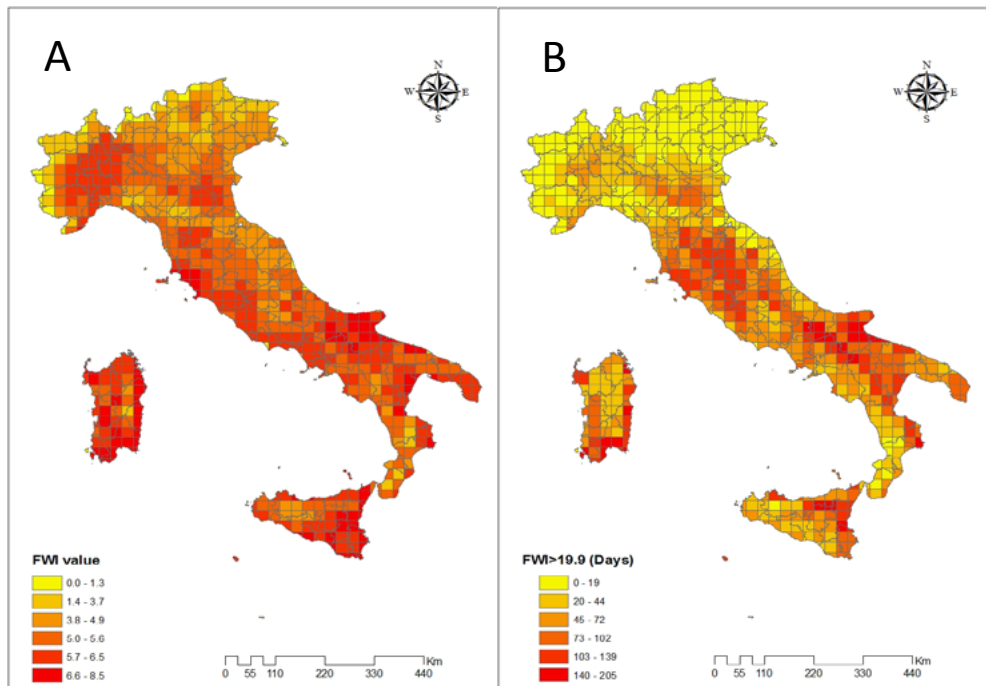


Fig. 2: A: Mean annual value of FWI; B: Number of days above the value of 19.9. Data are referred to the 1985-2008 period

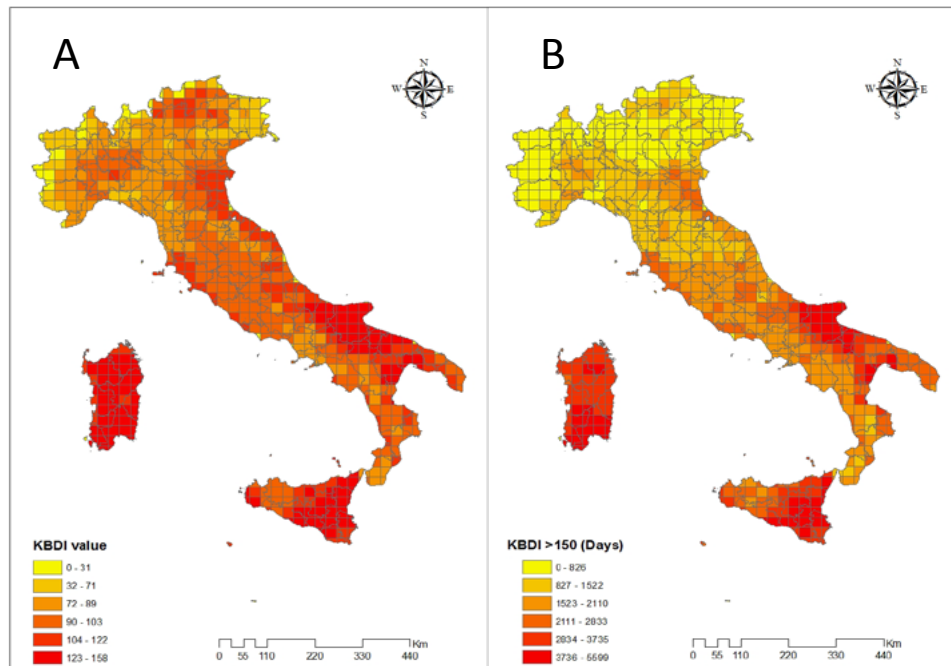


Fig. 3: A: Mean annual value of KBDI; B: Number of days above the value of 150. Data are referred to the 1985-2008 period

Area	Slope	Standard error	F	ρ	Sign.	Test Z	Sig.	Q
Cluster 1	0.08	0.13	0.45	0.51	n.s.	0.39	n.s.	0.00
Cluster 2	4.26	1.23	12.02	0.00	**	2.81	**	2.04
Cluster 3	41.52	10.64	15.24	0.00	***	2.90	**	29.41
Cluster 4	1.68	0.54	9.58	0.01	**	2.78	**	1.00
Cluster 5	40.07	10.05	15.89	0.00	***	3.40	***	39.69
Cluster 6	11.08	4.37	6.43	0.02	*	1.94	+	8.63
Italy	98.70	23.69	17.35	0.00	***	3.18	**	91.61

n.s.= not significative; + p= 0.10; * p= 0.05; ** p= 0.01; ***p= 0.001

Tab. 1 Least square linear fitting and Mann-Kendall results for the number of days above the value of 19.9 of FWI trend for Italy and for each piro climatic area

Area	Slope	Standard error	F	ρ	Sign.	Test Z*	Sig.	Q
Cluster 1	-1.97	0.46	18.39	0.00	***	-3.35	***	-1.82
Cluster 2	-0.88	0.50	3.04	0.09	+	-1.66	+	-1.08
Cluster 3	0.13	0.47	0.07	0.79	n.s.	-0.07	n.s.	-0.05
Cluster 4	0.23	0.52	0.19	0.66	n.s.	0.42	n.s.	0.31
Cluster 5	-0.78	0.39	4.14	0.05	+	-1.76	+	-0.83
Cluster 6	0.22	0.43	0.25	0.62	n.s.	0.17	n.s.	0.06
Italy	-0.40	0.33	1.44	0.24	n.s.	-1.76	+	-0.57

n.s.= not significative; + p= 0.10; * p= 0.05; ** p= 0.01; ***p= 0.001

Tab. 2 Least square linear fitting and Mann-Kendall results of the KBDI mean values trend for Italy and for each piro climatic area

*The presence of a statistically significant trend has been evaluated by using the Z standardized values. A positive (negative) value of Z indicates an upward (downward) trend

Cluster	Fire Number			Burned Area		
	R ²	<i>p</i>	Equation	R ²	<i>p</i>	Predictors
Cluster 1	-	-	-	-	-	-
Cluster 2	-	-	-	-	-	-
Cluster 3	0.58	***	FFMC; DMC	0.50	***	FFMC, DMC
Cluster 4						
Cluster 5	0.83	***	FWI; FFMC; DC	0.79	***	FWI
Cluster 6	0.75	***	FFMC; BUI	0.73	***	FFMC; BUI; ISI
Italy	0.71	***	FFMC; BUI	0.62	***	FFMC; BUI

Tab. 3 Multiple regression between the FWI and its subcodes, fire number FN and burned area BA for all Italy and for each cluster (monthly mean values)

A modelling framework to estimate CO₂ fluxes under urban development scenarios

Marras S.^{1,2*}, Blečić I.³, Trunfio G.A.³, Falk M.^{2,4}, Pyles R.D.^{2,4}, Cecchini A.³, and Spano D.^{1,2}

¹*University of Sassari, DipNET-Department of Science for Nature and Environmental Resources, Sassari, Italy,*

²*Euro-Mediterranean Centre on Climate Change (CMCC), Sassari, Italy,*

³*University of Sassari, DADU-Dipartimento di Architettura, Design e Urbanistica, Alghero, Italy,*

⁴*University of California, LAWR-Department of Land, Air and Water Resources, Davis, CA, USA*

**Corresponding author: serenam@uniss.it*

Abstract

It is known that urban development has an influence on the so-called urban metabolism, which represents the flow of material and energy within urban settlements and between a city and its surroundings. It is important to quantitatively estimate the exchange of energy, water, and in particular carbon exchanges to evaluate their impact on human liveability under different urban development scenarios. To contribute to this effort we developed a modelling framework for estimating carbon exchanges in relation to alternative land-use scenarios. The framework includes three components: (i) a Cellular Automata model for the simulation of the urban land-use dynamics; (ii) a transportation model for estimating the variation of the transportation network load and (iii) the ACASA (Advanced Canopy-Atmosphere-Soil Algorithm) model tightly coupled with the mesoscale weather forecasting model WRF. We present and discuss the results of an example application on the City of Florence.

Keywords: *urban metabolism, climate change, land-use dynamics, CO₂, urban planning*



1. INTRODUCTION

Cities and human settlements in general are a primary source of emissions responsible for human-induced climate change. So, it is crucial to understand how different patterns of urbanisation and land use influence flows of energy and materials responsible for climate change. For example, sprawled, low-density cities usually have higher per capita energy consumption for transportation than compact cities and, thus, higher carbon emissions. Human activities in the city, such as heating, the characteristics of buildings, the distribution of urban green areas, etc., play an important role in the dynamics of carbon and heat fluxes. But the climate itself influences urban matter and energy fluxes. On the most obvious account, a city with continental climate consumes more energy for heating and cooling than does a city with a more temperate climate. Urban fluxes then interact in a complex way with the local climate and weather conditions.

Several advanced models, operating at different spatial and temporal scales, have been developed to quantitatively estimate the urban metabolism components, such as fluxes of energy, water, and carbon dioxide (CO₂). Also, quantitative indicators have been developed to support urban planning and management for a more sustainable metabolism in future cities.

In this work, we present a modelling framework composed by three main components (Figure 1): (i) a Cellular Automata model of urban land-use dynamics [17, 18, 2]; (ii) a transportation model for estimating the impact of different land-use scenarios on the transportation network load [15, 16]; (iii) a Soil-Vegetation-Atmosphere Transfer model (SVAT) [11, 12, 14, 7, 8, 5] tightly coupled with the mesoscale weather forecasting model WRF [13] for simulating interactions related to carbon fluxes between the city, environment, and local weather.

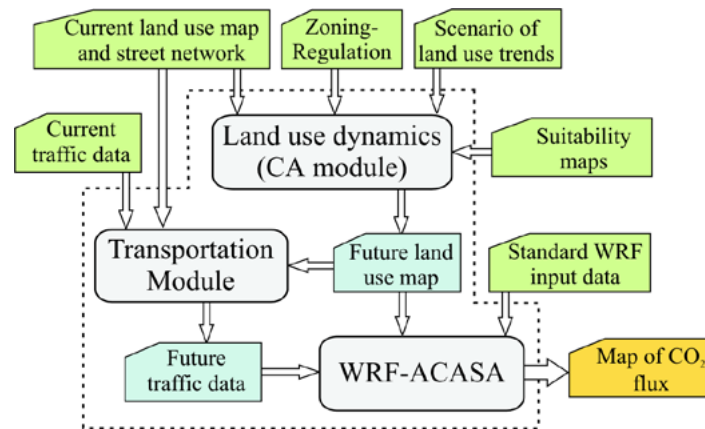


Fig. 1: Outline of the modelling framework with the most relevant data exchanges between the components

2. METHODS

The land-use dynamics CA module generates future land-use scenarios, that is, maps of possible future land uses by using information on the current land uses and street network, the zoning regulations, the physical suitability of the cells to develop into specific land uses, and a set of alternative projections of the aggregate demand for different land uses.

In a second step, the maps of future land uses generated by the CA module, together with the street network, are fed into the transportation module to estimate future road traffic. The current road traffic data are used for its calibration.

Finally, the SVAT model ACASA, in the coupled version with the mesoscale model WRF, uses both future land uses and road traffic to simulate the carbon exchanges between the urban surface and the atmosphere, and their interaction with local weather. WRF-ACASA outputs are then future maps of CO₂ fluxes in the urban area under consideration.

2.1 The CA-based land-use model

The Constrained Cellular Automata (CCA) modelling approach [17, 18] was used to simulate the land-use dynamics. We set three design objectives before our CA module: (i) the ability to operate at a reasonably high spatial resolution; (ii) the possibility to adequately simulate spatial processes which

determine land-use patterns; and (iii) the capability to process suitable representations of relevant landscape features as well as legal and planning restrictions on land uses.

Given an aggregate demand for different land uses, the CCA model allocates land uses in space based on local CA transition rules and on cells' characteristics. The aggregate demand is assumed to depend on large-scale processes (demography, development of specific economic sectors, and so on) and can be determined by a-spatial demographic and economic dynamic models or by projections based on historical data [17, 18].

The CCA can, hence, be viewed as a procedure to estimate a spatial distribution of an aggregate land-use demand by taking into account local interactions between different land uses as well as the physical, environmental, and institutional characteristics of each cell.

In a CCA model, each cell is defined by a set of properties representing relevant physical, environmental, social and economical characteristics, its distance from the transportation network, and the regulatory constraints imposed upon it (like land-use zoning). This underlying data structure can both conceptually and practically be represented in a GIS [17, 1, 3], and the cellular space on which the CA model operates can indeed easily be obtained from the layers of a raster GIS.

The CA model includes both dynamic (which change during the simulation) and static land uses (which do not change but still influence other dynamic cells in their neighbourhoods in terms of attractive or repulsive effects). We derived the current land uses from the CORINE land-cover data. Static land uses include road and rail networks, subways, airports, water bodies, agricultural and natural areas not available for development, and so on. The actively modelled dynamic land uses in the present application include: continuous urban fabric, discontinuous urban fabric, industrial areas, and commercial areas.

The final outputs of the CCA model are maps of the predicted evolution of land uses in the area of interest over a predefined period of time. By varying the inputs of the CCA model (zoning status, transport networks, distribution of facilities and services), the model can be used to explore future urban development scenarios of the area under alternative planning policies.

2.2 The Transportation Model

The aim of the transportation module is to capture the long-term average vehicle load on the road network. In particular, the model provides an estimate of the load variation related to the future scenarios of land uses. For this purpose, we adapted a dynamic formulation of the gravity model of trips distribution [16, 4]. It uses an origin-destination (OD) trip matrix, expressing the distribution of trip demand, which is computed on the basis of relevant land uses (that is, the ones modelled by the CA module described above) considered as trip sources and attractors. Running the model for both the current land-use map and future land-use scenarios provides thus estimates about possible future street network load variations.

Thanks to its simplicity, this approach allows for the simulation of real road networks using reasonable computational resources. In addition, it requires a relatively small amount of parameters to be calibrated.

2.3 The WRF-ACASA Coupled Model

SVAT (Soil-Vegetation-Atmosphere Transfer) models describe how atmospheric processes (transfer of heat, moisture, and momentum due to turbulent motion) affect the exchanges of energy (heat), moisture, and trace gases between soil, vegetation, water bodies, urban surface, and the atmosphere itself. To simulate the processes of CO₂ exchanges and fluxes shaped by future scenarios of urbanisation generated by the land-use and transportation model, we used the SVAT model ACASA (Advanced Canopy-Atmosphere-Soil Algorithm), a multilayer model originally developed by the University of California (Davis). It simulates the exchange of heat, water vapour, and CO₂ within and above the canopy of the urbanised area [11, 12]. ACASA has been widely applied over natural and agricultural ecosystems [14, 8], and it was recently modified to account for the anthropogenic contribution to heat exchange and carbon production in urban environments [7].

In addition, to produce regional estimates of urban metabolism components, ACASA has been coupled with the Weather Research and Forecasting model (WRF) [5]. WRF [13] is a mesoscale numerical weather prediction system, which is widely used for both operational forecasting and atmospheric research. According to recent validated results [5], WRF-ACASA produces reliable patterns of heat and

CO₂ fluxes at high spatial resolutions over urban areas. In Figure 2 is represented the scheme of processes, interactions, and exchange fluxes modelled by the coupled model WRF-ACASA.

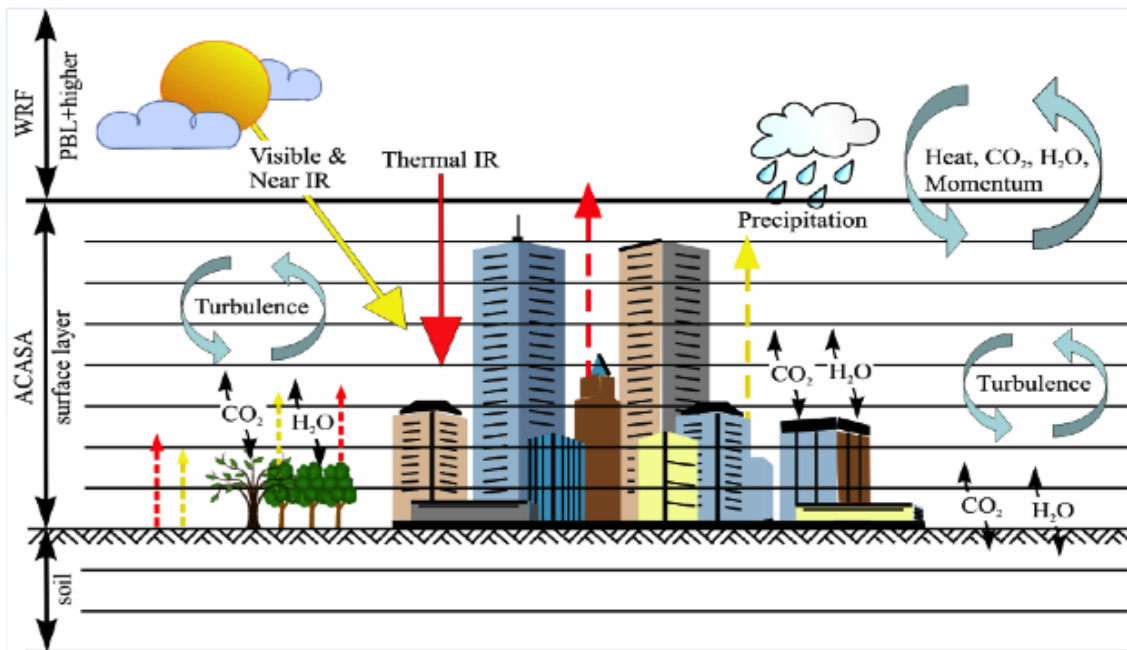


Fig. 2: Scheme of the processes modelled by the coupled model WRF-ACASA

The WRF model, driven by North American Regional Reanalysis data (NCAR-NCEP), was run down to its planetary boundary layer, which is the lowest part of the atmosphere directly influenced by its contact with a surface, characterised by a rapid fluctuations (turbulence) of physical quantities such as flow velocity, temperature, moisture etc., where ACASA is called (see Figure 2 above).

In ACASA, the canopy is represented as a horizontally homogeneous medium with all leaves and branches arranged with spherical symmetry. This includes both plant and urban (building) canopies. Twenty equally spaced atmospheric layers extend to twice the canopy height [9, 10], with the canopy occupying the lowermost 10 layers. All sources of heat and mass turbulent exchanges, calculated using third-order turbulence equations, occur within the canopy and at the soil – (or snowpack) – atmosphere interface, while constant-flux assumptions prevail in the 10 layers above the canopy. Surface temperatures, terrestrial-infrared radiative transfer, physiological conditions, and associated fluxes

needed for the turbulence calculations are produced after iterative numerical convergence, and provided to WRF.

The required meteorological data from the lowest WRF atmospheric layer, applied to ACASA on a half-hourly basis, are: precipitation rate and form ($\text{kg m}^{-2} \text{ timestep}^{-1}$), specific humidity (kg kg^{-1}), wind speed (m s^{-1}), downwelling short-wave radiation (W m^{-2}), downwelling long-wave radiation (W m^{-2}), air temperature (K), air pressure (hPa), and carbon dioxide concentration (ppm). Furthermore, initial soil temperature (K) and moisture (volumetric) profiles for the first model timestep are provided by the WRF initialisation routines. Surface morphological parameters that drive the physiological responses also have to be specified, which vary by WRF land use type (including CCA and/or satellite-derived data wherever possible). The set of key morphological parameters includes: total (green) leaf area index ($\text{m}^2 \text{ m}^{-2}$), maximum canopy height (m), leaf-scale ideal photosynthetic potential ($\mu\text{mol m}^{-2} \text{ s}^{-1}$), human population density ($\# \text{ people km}^{-2}$, currently keyed in by WRF urban land use type), and eventually vehicle flux density ($\# \text{ vehicles m}^{-2}$). Morphological parameters not represented in the WRF land-use parameter suite, quantities such as mean leaf diameter and basal respiration rates for plant tissues, are specified with constant near-cardinal values for all land points.

The ACASA model output, which feed information back to the WRF-simulated atmosphere, include half-hourly vertical fluxes of heat (W m^{-2}), water vapour ($\text{kg m}^{-2} \text{ s}^{-1}$), CO_2 ($\mu\text{mol m}^{-2} \text{ s}^{-1}$), momentum (as friction velocity, m s^{-1}), and turbulence kinetic energy ($\text{m}^2 \text{ s}^{-2}$). In addition, snowpack and/or soil and canopy thermal and hydrological states, needed for adequate simulation of the surface-layer, are updated at all land points and are stored between timesteps.

The initial conditions for a WRF run are pre-processed through a separate package called the WRF Preprocessing System (WPS). Among others, the input to WRF-ACASA from WPS contains the vegetation/land-use type coded according to the U.S. Geological Survey (USGS) standard and to the Urban Canopy Model (UCM) [6]. Other relevant input are represented by the CO_2 anthropogenic emissions, which can be directly related to the estimated traffic load of the road network, to the prevalent land use of each cell, and to the local population density.

To simulate carbon fluxes in urban environment under alternative future scenarios, the coupled WRF-ACASA model uses the land-use and traffic scenarios produced respectively by the CA and transportation modules. For this purpose, the CA module is able to export future land-use projections

into the binary format accepted by the WRF Preprocessing System (WPS). The coupling was based on a suitable table of conversion between CORINE codes, which are used by the CA module, and the USGS+UCM codes used by WRF.

3. RESULTS

Florence case study application

The key objective of this work was to evaluate the impact of future planning alternatives on carbon emissions. In this context, we present an application of the modelling framework on the City of Florence, for which the WRF-ACASA model has been calibrated through measured fluxes collected in the city centre.

The 100 m-resolution CORINE land cover (CLC) was used as the input land-use layer, and Figure 3 shows the masterplan prescriptions reduced to land-uses permissions and prohibitions relevant for the CA simulation, both in terms of land-use types simulated by the CA (continuous urban fabric, discontinuous urban fabric, industrial, commercial, agriculture), and in terms of its spatial scale of operation (pixel lattice representing 100×100 meters square).

The transportation module was designed to import XML data from the OpenStreetMap collaborative project, which provides free street network data with notable level of detail and geographic coverage. A pre-processing phase for the calculation of the cells accessibilities was carried out using the current street network. During the same phase, we used a simple formula to derive the suitability factors from a Digital Elevation Model of the urban area under consideration. In addition, we calibrated CCA parameters using the CLC1990 dataset, the map of Florence provided by the Urban ATLAS EU project, and additional spatial data provided by the Municipality of Florence.

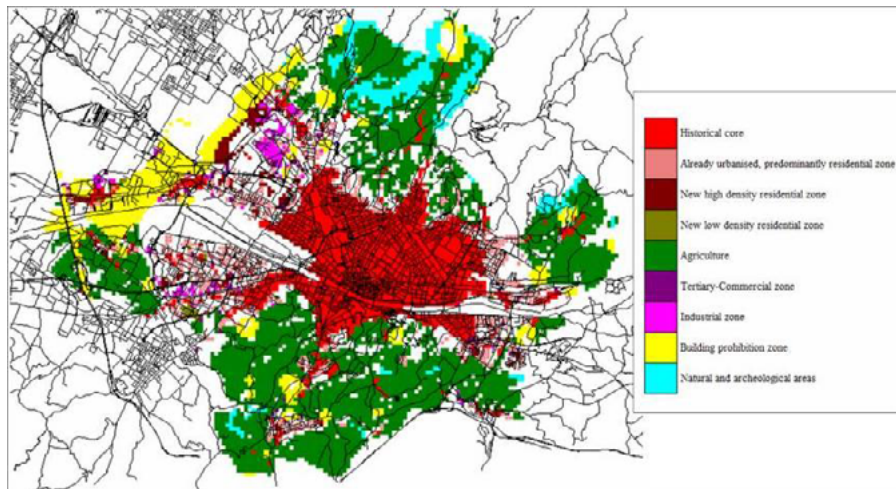


Fig. 3: Schematic zoning regulation for Florence derived from the urban master plan

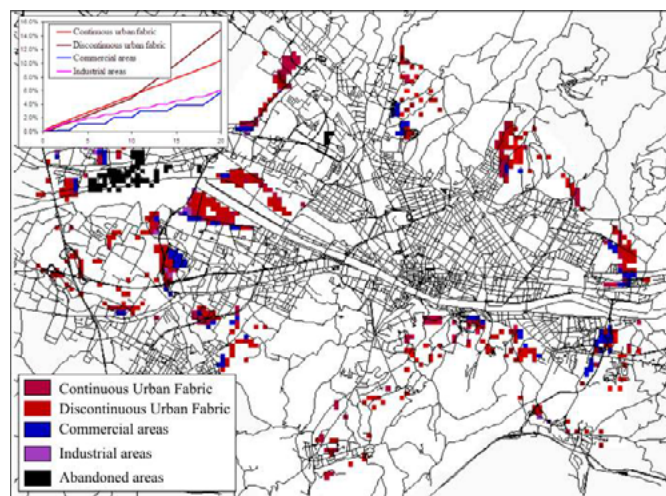


Fig. 4: A future land-use scenario obtained by the CCA module in 20 simulation steps. Only the cells where the land use was changed by the simulation are depicted. The embedded graph shows the extensions evolution of the actively modelled land uses.

Then, using the land cover and the planning regulation map (Figure 3) as inputs for the CCA model, we were able to generate several future land-use scenarios. For example, the future land use projection represented in Figure 4 corresponds to a 20-year evolution of the urban area, while the transportation model was able to estimate the variation of the load of vehicles on the road network.

Finally, the WRF-ACASA model generated maps of CO₂ fluxes by using the land-use scenario and traffic load information as input. In Figure 5 are reported the simulation results of CO₂ fluxes for March and April for the current land uses (based on Corine 2000) and the 2020 future land-use scenario, which showed a 10% increase continuous urban fabric, 20% increase in discontinuous urban fabric, and 10% increase in commercial/industrial land uses (Figure 4). Results show that most of the investigated area changed from being a net sink to becoming a net source of CO₂, and points with values passing from -2 μmol m⁻² s⁻¹ to 2 μmol m⁻² s⁻¹.

Green areas have become urbanised under the land-use scenario (therefore emitting rather than contributing to the absorption of the local CO₂ fluxes), and the impact on the net variation of emissions is nonetheless wider than that strictly due to the newly urbanised zones from 2000 to 2020 (Figure 5). So, it seems that, according to our model, the relation between the extension of urbanisation and CO₂ emissions is not linear, and that increases in urbanisation, depending on its pattern and effect on transportation, could have amplified impacts on CO₂ emissions.

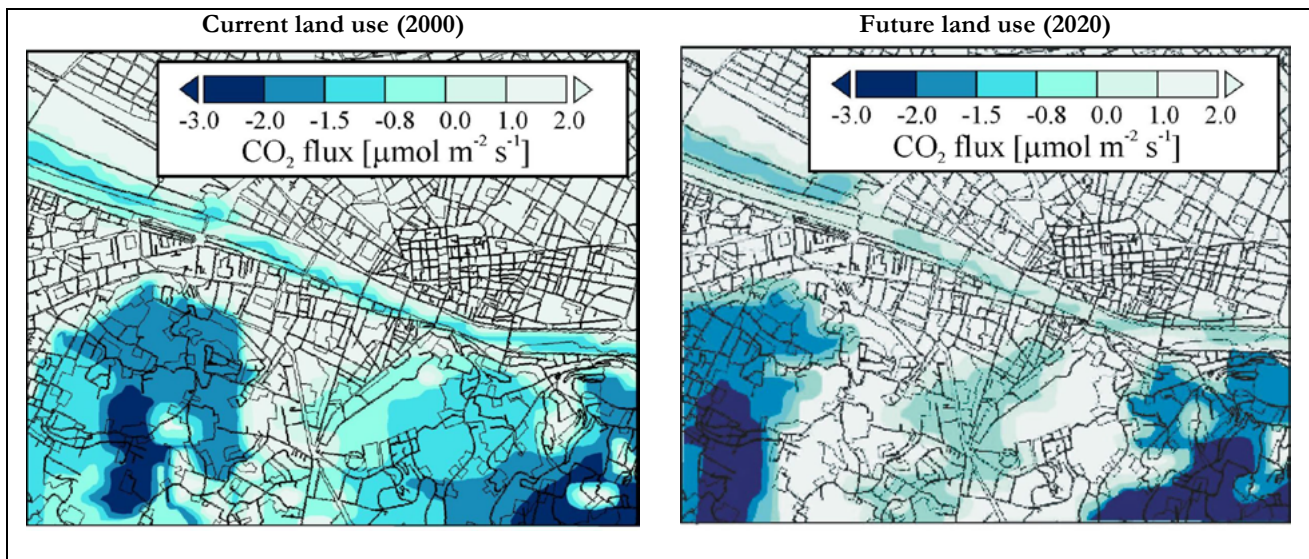


Fig. 5: WRF-ACASA simulated CO₂ fluxes for current (left panel) and future 2020 (right panel) land-use scenario.

The complexities of urban systems and the interaction of carbon emissions with the environment and local meteorology make it a non-trivial task to support urban planning and management for a more sustainable metabolism of future cities. In this contest, we have presented an off-line coupling between

different models with the purpose to link urban planning decisions to the estimates of their impact on the CO₂ emissions in the atmosphere.

Results represent the first application of this integrated modelling framework, and even if many aspects of the methodology and of the application protocol require further testing, we believe it has proven to be a promising perspective for developing decision support tools for sustainable urban planning.

4. ACKNOWLEDGMENTS

This research was funded by the EU FP7/2007-2013 Program under grant agreement 211345, and by the Italian MIUR and MATTM (Gemina project) under grant agreement 232/2011. Authors wish to thank the CNR-IBIMET Institute of Florence for providing the measured data of urban fluxes.

5. REFERENCES

- Batty M., Xie Y. (1994), *From cells to cities*, Environment and Planning B, pp. 31-48. (1)
- Blecic I., Cecchini A., Trunfio G.A. (2009), *A General-Purpose Geosimulation Infrastructure for Spatial Decision Support*, Transactions on Computational Science No 6, pp. 200-218. (2)
- Clarke K.C., Gaydos L.J. (1998), *Loose-coupling a cellular automaton model and GIS: long-term urban growth predictions for San Francisco and Baltimore*, International Journal of Geographic Information Science, pp. 699-714. (3)
- Erlander S., Stewart N.F. (1990), *The Gravity Model in Transportation Analysis: Theory and Extensions*, VSP, Utrecht. (4)
- Falk M., Pyles R.D., Marras S., Spano D., Snyder R.L., Paw U K.T. (2010), *A Regional Study of Urban Fluxes from a Coupled WRF-ACASA Model*, American Geosciences Union Fall Meeting, San Francisco, California, USA. (5)
- Kusaka H., Kondo H., Kikegawa Y., Kimura F. (2001), *A simple single-layer urban canopy model for atmospheric models: Comparison with multi-layer and slab models*, Boundary Layer Meteorology, No. 101, pp. 329-358. (6)

- Marras S., Spano D., Pyles R.D., Falk M., Snyder R.L., Paw U, K.T. (2010), *Application of the ACASA model in urban environments: two case studies*, AMS Conference on Ninth Symposium on the Urban Environment, Keystone, Colorado, USA. (7)
- Marras S., Pyles R.D., Sirca C., Paw U K.T., Snyder R.L., Duce P., Spano D. (2011), *Evaluation of the Advanced Canopy-Atmosphere-Soil Algorithm (ACASA) model performance over Mediterranean maquis ecosystem*, Agriculture and Forest Meteorology, No. 151, pp. 730-745. (8)
- Meyers T.P., Paw U K.T. (1986), *Testing of a higher-order closure model for modelling airflow within and above plant canopies*, Boundary Layer Meteorology, No. 31, pp. 297-311. (9)
- Meyers T.P., Paw U K.T. (1987), *Modelling the plant canopy micrometeorology with higher-order closure principles*, Agriculture and Forest Meteorology, No. 41, pp. 143-163. (10)
- Pyles R.D., Weare B.C., Paw U K.T. (2000), *The UCD Advanced Canopy-Atmosphere-Soil Algorithm: Comparison with observations from different climate and vegetation regimes*, Q.J.R. Meteorol. Soc., No. 126, pp. 2951-2980. (11)
- Pyles R.D., Weare B.C., Paw U K.T., Gustafson W. (2003), *Coupling between the University of California, Davis, Advanced Canopy-Atmosphere-Soil Algorithm (ACASA) and MM5: Preliminary Results for July 1998 for Western –North America*, Journal of Applied Meteorology, No. 42, pp. 557-569. (12)
- Skamarock W.C., Klemp J.B., Dudhia J., Gill D.O., Barker D.M., Duda M.G., Huang X.Y., Wang W., Powers J.G. (2008), *A Description of the Advanced Research WRF Version 3*, NCAR/TN-475 + STR - NCAR TECHNICAL NOTE. (13)
- Staudt K., Falge E., Pyles R.D., Paw U K.T., Foken T. (2010), *Sensitivity and predictive uncertainty of the ACASA model at a spruce forest site*, Biogeosciences, No. 7, pp. 3685-3705. (14)
- Tsekeris T., Stathopoulos A. (2003), *Real-time dynamic Origin-Destination matrix adjustment with simulated and actual link flows in urban networks*, Transportation Research Record–Journal of the Transportation Research Board, No. 1857, pp. 117-127. (15)
- Tsekeris T., Stathopoulos A. (2006), *Gravity models for dynamic transport planning: Development and implementation in urban networks*, Journal of Transport Geography, No. 14:2, pp. 152-160. (16)
- White R., Engelen G., Uljee I. (1997), *The use of constrained cellular automata for high resolution modelling of urban land use dynamics*, Environment and Planning B, No. 24, pp. 323-343. (17)

White R., Engelen G. (2000), *High-resolution integrated modelling of the spatial dynamics of urban and regional systems*, Computers, Environment and Urban Systems, No. 2824, pp. 383-400. (18)

CLIMATE POLICY AND ECONOMIC ASSESSMENT

CLIMATE POLICY AND ECONOMIC ASSESSMENT

Economic analysis of climate change impacts: methods and approaches

Probabilistic economic impacts of climate change in an integrated assessment model framework

Bosetti V.^{1,2}, Drouet L.^{1,2*}, and Tavoni M.^{1,2}

¹*Euro-Mediterranean Center on Climate Change - CIP Division, Italy*

²*Fondazione Eni Enrico Mattei, Italy*

*Corresponding author: laurent.drouet@feem.it

Abstract

The uncertainties are present in many parts of the integrated assessment of long-term climate mitigation policies. In this work, we show how to build a probabilistic chain in an integrated assessment framework to capture the uncertainties in the economy and in the climate. First, a sequence of contrasted socio-economic scenarios are generated to cover the range of uncertainties of the challenges of mitigation and adaptation. Then, the integrated assessment model, WITCH, is used to produce cost-efficient future emission paths. Secondly, the simple climate model SNEASY, calibrated with past observations using a Monte-Carlo Markov chain approach, computes probabilistic temperatures projections. And, finally, we produce the distribution of the economic impacts of climate change, by combining the temperatures with the impact estimates coming from previous studies. Preliminary results shows that, in 2050, climate change tends to benefit to the economy in the majority of the scenarios, while in 2100, the range of the economic impacts is much larger, but with a negatively skewed distribution.

Keywords: *Integrated assessment, cost-risk management, probabilistic approaches*



1. INTRODUCTION

The Integrated Assessment Models (IAMs), for climate change, combines the knowledge from climate sciences and social sciences to inform the policymakers. To assess global long-term climate mitigation strategies, the IAMs must explore the space of the possible futures. This space encompasses the current and the future uncertainties, i.e. the uncertainties about the future human decisions, about the physical phenomenon and about the interaction human-nature.

In practice, an IAM can only apprehend a subspace of the space of possible futures because of its inherent limitations. This subspace is circumscribed by model parameters and by imposed constraints to the socio-economic and the geophysical representation in the model.

In this study, we give a weight to each of the anticipated world that lie in the exploration space. This weight is equivalent to the scenario's likelihood in view of current knowledge. To do so, we take into account the uncertainties subsequently at the socio-economic level, at the geophysical level and at the level of the calculation of the economic impact. Then, by gathering all this information, we compute the distribution of the global economic impacts of climate change.

2. SOCIO-ECONOMIC SCENARIOS

The socio-economic scenarios specify the IAM assumptions on the GDP growth, the demography, the technological progress, etc. We produce five socio-economic scenarios corresponding to an implementation of the Shared Socioeconomic reference Pathways (SSPs) defined in [2], namely SSP1, SPP2,.., SSP5. The SSPs follow contrasted but plausible socio-economic storylines, which span a two-dimensional space defined by the levels of effort required by the challenges of mitigation on one side and by the challenges of adaptation on the other side. These scenarios aim at covering the range of uncertainty suitable to tackle these challenges and their direct consequences.

The scenarios drive the WITCH integrated model, which is an economic growth model designed to study optimal economic and climate change policies [7]. The WITCH energy-economic system covers the world, split in 12 regions sharing identical economic, energetic and/or geographical characteristics. The energy sector is well represented and includes electric and non-electric use, six types of fuels and seven electricity generation technologies. The model accounts for acquired technological knowledge due to experience and also for research and development investments to increase energy efficiency and

reduce costs of biofuels. This model has been used in several economic and climate change policy studies [8,9]. For our work purpose, the climate and the damage existing modules have been deactivated, as they are replaced by a climate model (Section 5) and a probabilistic damage function (Section 6).

Our implementation of the SSPs redraws three drivers of the WITCH model for each region over the 21st century and for the 5 SSPs scenarios: the total-factor productivity on labour, the total-factor productivity on energy and the population.

In [4], the authors have shown that the cumulative greenhouse gases (GHG) emissions provide a robust indicator of the warming which will occur throughout the 21st century, especially for stringent scenarios. The WITCH integrated model is able to find the optimal policy strategies, in which the world regions act cooperatively to respect a given carbon budget. We then constrain the WITCH model with carbon budgets varying between 1115 GtCO₂, the minimum possible for the model, to the Business as usual levels (3447-3791 GtCO₂ across the SSPs). As a result, we obtain a bit more than 400 emissions scenarios corresponding to as many mitigation policies. Fig. 1 displays the carbon dioxide emissions trajectories from these scenarios.

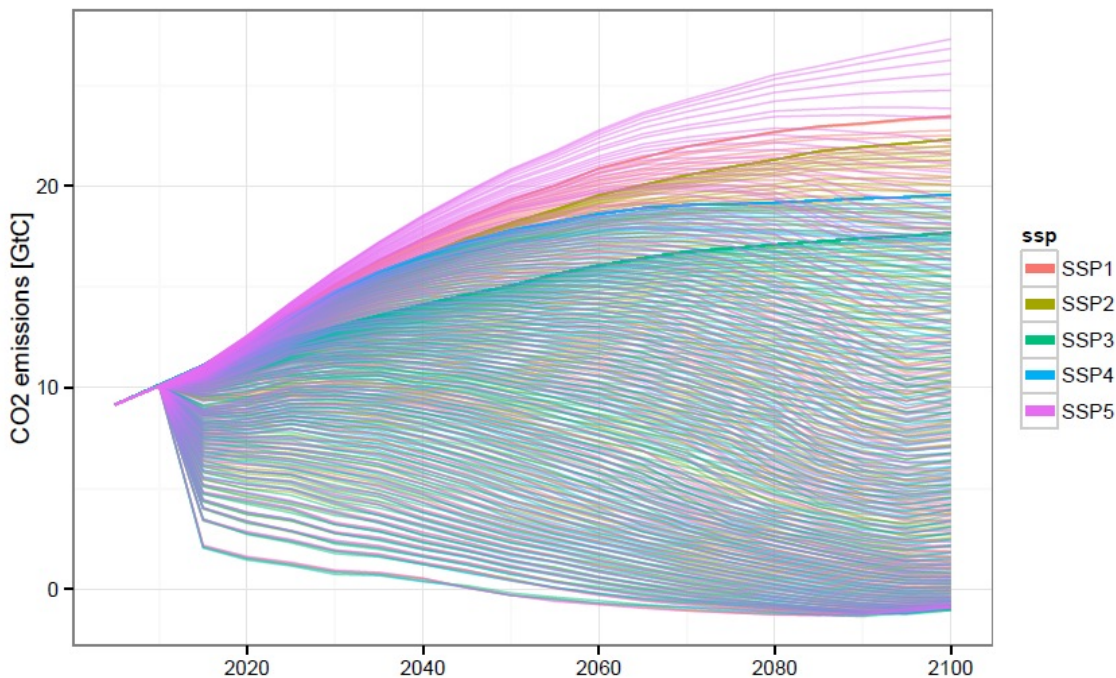


Fig. 1: Optimal CO₂ emission profiles from a cost-effective analysis with about 400 carbon budgets. The colours distinguish the emission scenarios obtained from each SSP.

For now, no studies have been performed to assess the likelihood of the SSPs scenarios, so we arbitrarily decide that the SSPs scenarios are equiprobable. Within each SSPs, the likelihood of the generated trajectories is trickier to evaluate, as it would make sense to say that the more stringent carbon budget and the more costly is the effort, the less likely is the scenario. However, we don't have any information to weigh the scenario. So, for the sake of simplicity, we equally weight the socio-economic scenarios.

3. A SIMPLE CLIMATE MODEL

The carbon dioxide and the other greenhouse gases emitted by the anthropogenic activities go to the atmosphere and impact the climate system. We use the simple climate model SNEASY, which is composed of a climate module, a carbon cycle model which includes feedbacks from the atmospheric CO₂ concentration and temperature, and an Atlantic meridional overturning circulation (AMOC) box model [1]. In this study, we don't assess any tipping points, thus the slowdowns of the AMOC are not explored.

The key geophysical model parameters are estimated from a hindcast calibration period of 1850-2009 using a Bayesian inversion technique based on the Markov Chain Monte Carlo (MCMC) algorithm. This procedure has been previously applied to an older version of the model in [1].

Precisely, the estimated climate parameters are the climate sensitivity, the vertical diffusivity of heat in the ocean and the aerosol scaling factor to the radiative forcing. The carbon-cycle estimated parameters are the carbon fertilization from living plants, the respiration sensitivity related to temperature and the thermocline carbon transfer rate in the ocean. Additionally, initial conditions of atmospheric temperature and CO₂ concentration are also estimated. Fig. 2 presents the marginal a posteriori distributions of the model parameters.

The Markov chain obtained by the MCMC procedure is used to obtain the probabilistic temperature projection from carbon dioxide emissions and radiative forcing of other greenhouse gases until 2100, which are computed by the WITCH model.

The probability distribution function values associated to temperature increase are calculated from a Monte Carlo ensemble, varying the model parameters coming from the generated Markov chain. We retain 3'333 parameters' combinations out of the 100'000 generated, which are equally distant in the chain, to avoid cross-correlation.

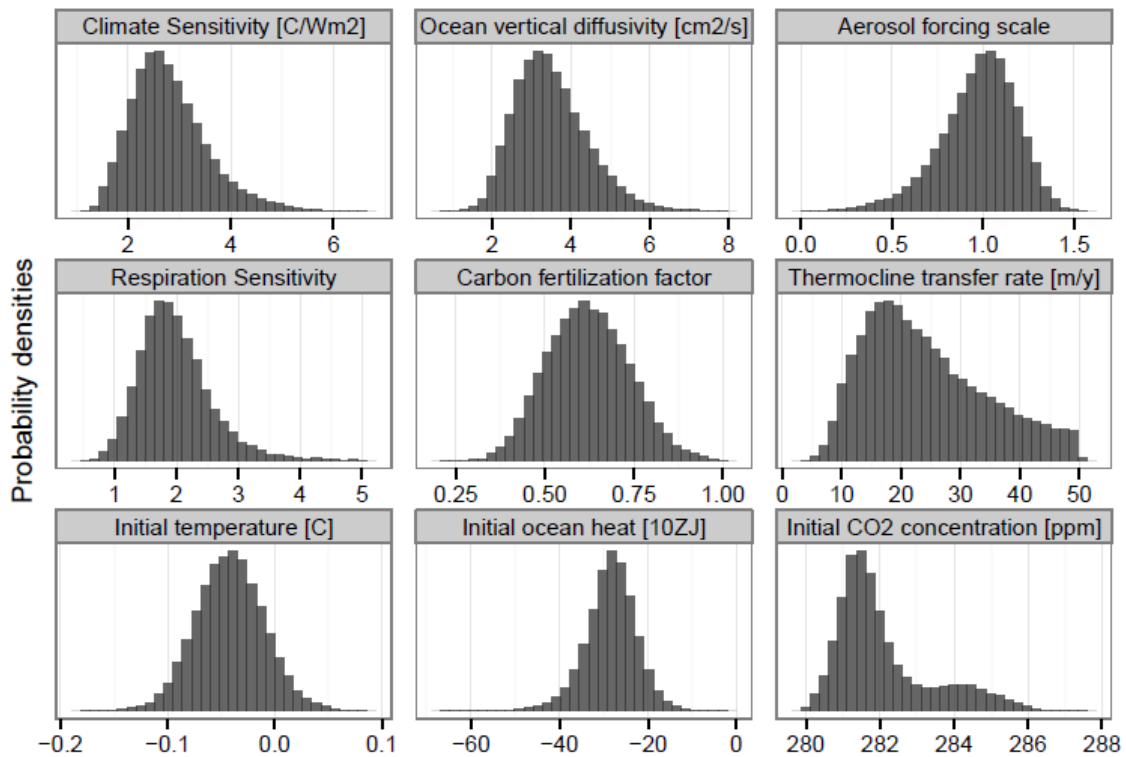


Fig. 2: Marginal probability densities of the estimated parameters of the simple climate model SNEASY.

4. GLOBAL DAMAGE FUNCTION

A damage function translates the temperature increase into global economic impacts. [3] reviews from the literature 14 mean estimates of total economic effects of climate change. Five of them also include a measure of uncertainty under the form of standard deviation or a confidence interval. These estimates have been calculated using various methods, but they usually aggregates one by one the economic costs of individual global and local impacts [3]. We adopt a damage function of the form:

$$D = \beta_1 T + \beta_2 T^2, \quad (1)$$

where D is the economic impact expressed in % of GDP, T is the temperature increase and β_i are the regression coefficients.

We compute the distribution of the coefficients of the quadratic damage function, by carrying out least square fits of 1'000 random samples of the estimates (Fig. 3). The R^2 of the regressions have a median of 0.56, a minimum of 0.22 and a maximum of 0.72.

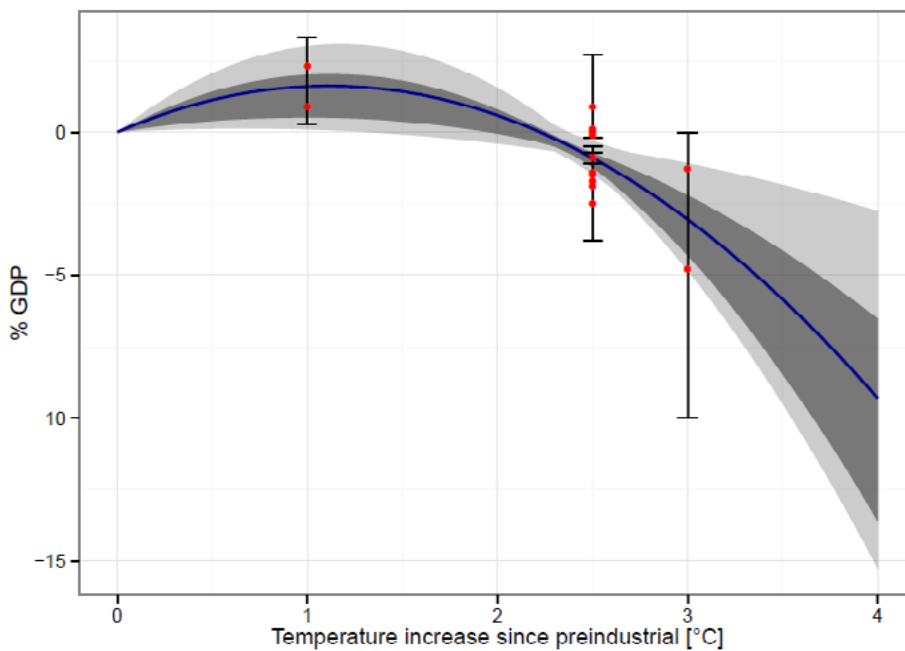


Fig. 3: Global impact of climate change (% of GDP) as a function of temperature increase since preindustrial levels. Red dots are mean estimates. The blue thick line is the quadratic regression fit of the mean estimates. The dark and light grey areas delineate the 95% confidence interval and the range of the regression coefficients, respectively. The confidence interval estimates are displayed by error bars. Original data are taken from [3].

For a temperature increase lower than 2°C, the warming is likely to benefit while, for higher warming, the effects will impact negatively on the economy. However, the range of uncertainty become larger for high warming.

5. PRELIMINARY RESULTS

As a first approach, we build up the joint probability distribution of the socio- economic scenarios distribution, the temperature projection distribution and the damage function coefficients distributions. Fig. 4 presents the probabilistic economic impact of climate change for every decade. The median of the distributions remains positive until 2070, and becomes negative afterwards. In 2050, the major part of the economic impacts distribution is positive. These results are in line with the fact that low

emissions scenarios have the same likelihood than high emissions scenarios. The picture shows the whole coverage of economic impacts from the integrated model, which can be very large. So, in 2100, the impacts vary in a range starting from a loss of 24% of GDP to a benefit of 6% of GDP.

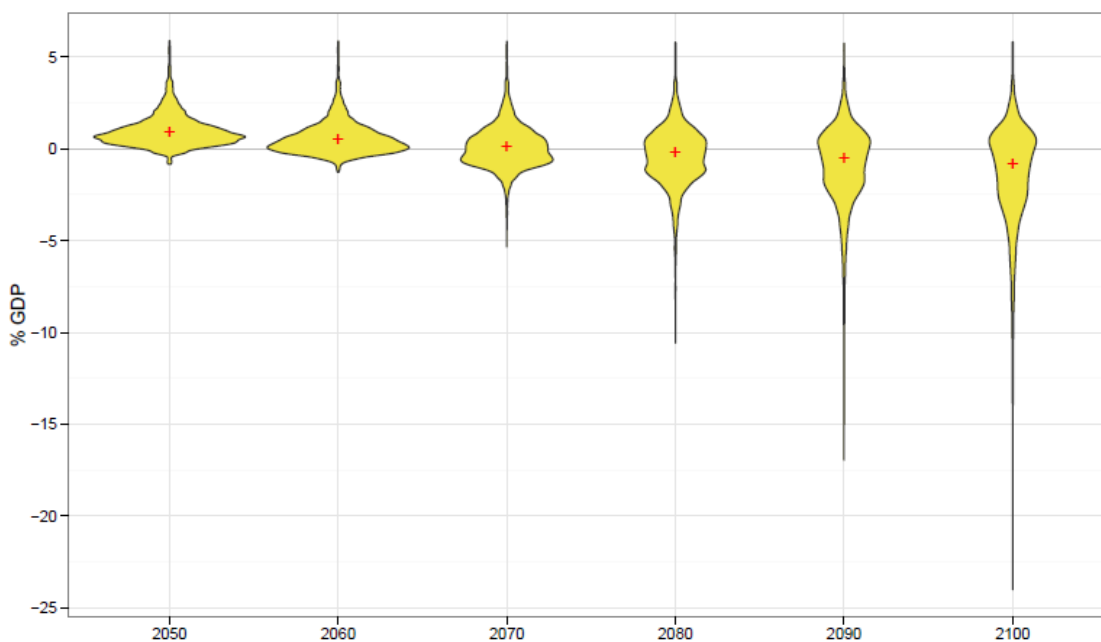


Fig. 4: Probabilistic global economic impacts for climate change in terms of % of GDP through the second part of the 21st century. Red cross shows the median of the distributions.

6. CONCLUSION

In this short paper, we have used a probabilistic information chain in an integrated assessment framework to capture the uncertainties in the economy and in the climate and to compute the distribution of the economic impact of climate change.

Some new developments have to be carried out to improve this new framework:

- A measure of likelihood for the socio-economic scenarios has to be investigated. For example, the likelihoods of the SSPs can be asked from experts, some criterion, as the acceptability from the society, can also be introduced.
- New estimates of economic impact of climate change at global level should be considered. The regional scale should also be taken into account. In fact, if a global benefit is observed for low

warming, the regional impacts are more diverse, and the regions the more vulnerable undergo negative impacts on the economy.

- The assessment and the selection of policies can be carried out using the probabilistic information. The first criteria would be to choose the policy which maximizes the expected utility by incorporating the expected level of damages in the output function. It can be also used to manage the risk of high damage, by taking into account the risk incurred in the tail of the economic impact distribution.

7. ACKNOWLEDGMENTS

The authors thank Klaus Keller for providing the SNEASY climate model and his support in the calibration phase. Moreover, the research leading to these results has received funding from the Italian Ministry of Education, University and Research and the Italian Ministry of Environment, Land and Sea under the GEMINA project.

8. REFERENCES

- Urban N. M., and Keller K. (2010), *Probabilistic Hindcasts and Projections of the Coupled Climate, Carbon Cycle and Atlantic Meridional Overturning Circulation System: a Bayesian Fusion of Century-scale Observations with a Simple Model*. Tellus A.
- Kriegler E., O'Neill B.C., Hallegatte S., Kram, T., Lempert R.J., Moss R.H., and Wilbanks T. (2012), *The need for and use of socio-economic scenarios for climate change analysis: A new approach based on shared socio-economic pathways*, Global Environmental Change, No. 22, pp. 807–822.
- Tol R.S., (2009), *The economic effects of climate change*. The Journal of Economic Perspectives No. 23, pp. 29–51.
- Meinshausen M., Meinshausen, Hare N., W., Raper S.C.B., Frieler K., Knutti, R., Frame D.J., and Allen M.R. (2009), *Greenhouse-gas emission targets for limiting global warming to 2 °C*. Nature No. 458, pp. 1158–1162.
- Rogelj J., McCollum D.L., Reisinger A., Meinshausen M., and Riahi K. (2013), *Probabilistic cost estimates for climate change mitigation*. Nature No. 493, pp. 79–83.

- Heal G., Millner A., (2013) *Uncertainty and Decision in Climate Change Economics* (Working Paper No. 18929), National Bureau of Economic Research Working Paper Series. NBER.
- Bosetti V., Carraro C., Massetti E., Sgobbi A., Tavoni, M. (2009), *Optimal energy investment and R&D strategies to stabilize atmospheric greenhouse gas concentrations*. Resource and Energy Economics No. 31, pp. 123–137.
- Bosetti V., Carraro C., Tavoni M. (2012). *Timing of Mitigation and Technology Availability in Achieving a Low-Carbon World*. Environmental and Resource Economics No. 51, pp. 353–369.
- Bosetti V., Carraro C., De Cian E., Massetti E., Tavoni M., 2013. *Incentives and stability of international climate coalitions: An integrated assesment*. Energy Policy No. 55, pp. 44–56.

A Ricardian analysis of the impact of climate change on European agriculture

Van Passel S.^{1,2}, Massetti E.^{2,3}, Mendelsohn R.²

¹ Hasselt University, Faculty of Business Economics,
Centre for Environmental Sciences, Agoralaan, Diepenbeek, Belgium

² Yale University, School of Forestry and Environmental Studies, New Haven, USA

³ Fondazione Eni Enrico Mattei (FEEM) and Euro-Mediterranean Center for Climate Change, Italy

Corresponding author: steven.vanpassel@uhasselt.be

Abstract

Although there have been several economic analyses of the impact of climate change on American agriculture [1-4], there have been few studies in Europe. European Ricardian studies have been limited to single country analyses such as in Germany [5, 6] and Great Britain [7]. The primary tool to study agriculture in Europe is crop modeling, which has very limited economic sophistication. This study addresses this shortcoming in the economic literature by analyzing farm level data that has never been analyzed before. The data set is collected by the European Union (EU) to administer farm policies. This data set resembles the US Census Public Use sample available for Housing and Population. It contains individual data about farms in small geographic units (similar to US counties) across Europe. The study relies on a sample of over 37,000 farms from all the countries in the EU-15 (Western Europe).

The paper relies on a Ricardian analysis of this data [1]. There is now a rich literature describing the strengths and weaknesses of the Ricardian technique. The strength of the approach is its ability to measure long run impacts from climate change incorporating the adaptation that farmers have already demonstrated they can do. But there are limitations. The technique does not capture future technical change to either crops or new farming methods. As with all uncontrolled experiments, if there are unmeasured factors correlated with climate, they can bias the results. It is consequently important that analyses measure likely factors that might influence crop productivity such as soils and market access. Especially, as emphasized by Fisher, Hanemann, Roberts and Schlenker [8], it is critical that climate is measured carefully. The Ricardian method does not measure either price sensitivity [9] or carbon fertilization since both prices and the level of carbon dioxide remain the same across the entire sample. The absence of price effects cause the Ricardian method to overestimate large global damages or global



benefits of warming [10]. The absence of direct carbon dioxide effects causes the technique to underestimate the beneficial effects of carbon dioxide fertilization [11]. The Ricardian approach is a comparative static analysis of long run equilibriums. It does not capture the dynamic transition costs of moving from one equilibrium to another [12]. Short run dynamics such as farmer responses to weather changes are much better captured by intertemporal analyses such as Deschênes and Greenstone [4] and Fisher, Hanemann, Roberts and Schlenker [8].

In addition to the concerns above, there has been an extensive debate concerning whether the Ricardian technique properly accounts for irrigation [3]. American Census data cannot address this problem because there is no separate data for rainfed and irrigated farms. However, studies done in other countries have compared the climate sensitivity of irrigated versus rainfed farms. Irrigated farms are less sensitive to warming than rainfed farms in Africa [13, 14] and China [15]. In fact, in China, moderate warming is beneficial to irrigated farms though harmful to rainfed farms. However, in Latin America, the climate sensitivity of both irrigated and rainfed farms are similar [16]. We reexamine this question in this paper by estimating separate Ricardian functions for rainfed and irrigated farms.

Our empirical results show that the seasonal climatic variables have a strong influence on current farmland values across Europe. In all cases, increasing spring temperature is beneficial while increasing summer temperature is detrimental for agricultural land value. Also important to mention is the beneficial impact of more precipitation in summer. The results are consistent with the results found in other studies using different approaches. Our study shows that quantile regressions offer a much richer and focused view. It provides a way to explore sources of heterogeneity in the response to climate change.

Our results show that the climate sensitivity of irrigated farms is not the same as the climate sensitivity of rainfed farms. Rainfed farms cannot be used to predict the climate outcome of irrigated farms (and vice-versa). The analysis also suggests that the climate sensitivity of cropland and grazing land is different. In order to measure the climate sensitivity of the entire agricultural sector, it is important to estimate a Ricardian model with both samples included. Analyzing the impact of climatic variables on just crops or just livestock does not allow substitution between crops and livestock.

The climate coefficients suggest that climate change is going to have a strong influence on future farmland values in Europe. The results suggest that climate change will be harmful to European agriculture by 2100. European agriculture is harmed in every tested climate scenario. The impacts are very different, however, for each climate scenario. With the milder climate scenario (NCAR PCM),

European farms lose an average 8% of their value. With the more intermediate climate scenario (ECHO-G), European farms lose 28% of their value by 2100. Finally, with the more severe Hadley CM3 climate scenario, farms lose 44% of their value by 2100.

The impact of climate change is not uniform across Europe. With all three climate scenarios, the impact is more severe in southern Europe which is harmed in all cases. In contrast, with the two milder climate scenarios, several northern European countries benefit from climate change. Only Ireland, however, appears to benefit in all three climate scenarios.

The Ricardian model captures adaptations that farmers can make with current crops, livestock, and technology. The analysis does not take into account adaptations that can be made through new breeds, varieties, and technologies. One important role of government is to conduct research and technology that might provide farmers with new opportunities to adapt to new climates. Another important role of government is to manage surface and ground water supplies to increase their overall efficiency. Finally, governments have an important role to play in reforming agricultural policy to facilitate farm adaptation. They must be careful to avoid creating incentives that inadvertently discourage farmers from making efficient responses to climate change.

Note that we use the estimated Ricardian functional form to predict how future climate change might affect future agricultural land value, assuming that all other conditions are kept constant. In other words, we simply isolate the effect of climate change and we do not make a forecast of how farmland values actually change. It is a comparative analysis and hence we do not take into account other likely changes such as in technology, prices, and investment. A major advantage of the Ricardian approach is that structural changes and farm responses are implicitly taken into account. Our study also takes into account all current major farming activities in Europe such as crop and livestock farms. There remain several interesting topics for future research. It is important to explicitly capture adaptation within the Ricardian framework and estimate structural Ricardian models (e.g. Seo and Mendelsohn [27]). It is also interesting to expand the analysis to include the new European member states of Eastern Europe and it is important to include changes in water supply especially in the regions of Europe that will depend on irrigation.

A full version of the paper is available at:

<http://www.feem.it/userfiles/attach/201345151394NDL2012-083.pdf>

Chaos in, chaos out: the effect of deterministic chaos in GCM scenarios on estimates of climate change impacts

Massetti E.

FEEM and CMCC

emanuele.massetti@feem.it

Abstract

GCMs incorporate *deterministic chaos* to reflect real-world chaotic dynamics of weather. This implies that small changes in external forcing can generate very different weather patterns, especially at local level. By using the Coupled Model Intercomparison Project phase 3 (CMIP3) multi-model dataset I show that small variations in Greenhouse Gas Emissions (GHG) and other forcing agents across the SRES scenarios generate substantial different climate scenarios in the US. By using a Ricardian model of climate change impacts on agriculture I show that the “noise” in the climate scenarios generates a “noisy” relationship between global GHG concentrations and local impacts. This implies that climate change scenarios from the CMIP3 dataset - used for the IPCC AR4 - should be used with caution. This problem might be limited by providing model ensemble runs that use same initial conditions but introduce small perturbations around the central exogenous forcing scenario.

Keywords: *climate change impacts, deterministic chaos, general circulation models*



General Circulation Models incorporate *deterministic chaos* to reflect real-world chaotic dynamics of weather. This means that two runs of the same model that use the same starting conditions and the same external forcing generate the same identical climate change scenario. However, the models also embed chaotic dynamics. This means that apparently small changes in initial conditions and/or in external forcing may result in very different predictions of weather patterns. Since there is large uncertainty on the initial conditions that should be used in GCM runs climate modelers have traditionally run “ensembles” of scenarios. A “model ensemble” is a set of runs that use the same GCM but different initial conditions. For example, one ensemble run is initialized using weather and other observations on January 1st 1870. Another ensemble run uses weather observations on January 1st 1880 and so on. By averaging over different runs it is possible to predict an average weather pattern by computing the average of all runs. If the number of runs (i.e.) of alternative initial conditions is sufficiently large, the “model ensemble” mean will provide an accurate characterization of climate for that model. When climatologists simulate future climate change they make assumptions on the initial conditions for their GCMs and on the pattern of exogenous forcing. For example, the AR4 climate change scenarios were generated by imposing different patterns of Greenhouse Gases (GHGs) and of other forcing agents starting from the year 2000. Two SRES scenarios that share the same initial conditions have identical weather patterns until January 1st 2000. After that date the weather patterns start to diverge because the forcing conditions are different. Climatologists have provided several “ensemble” runs for each SRES scenario using different initial conditions. For the AR4 it is not rare to find only one or at most three “model ensemble” runs available. This shortcoming seems to be addressed in the most recent set of runs that will be used in the AR5 IPCC report. However, “model ensemble” runs on different initial conditions do not control for all possible sources of noise in climate scenarios. In fact, small perturbations of external forcing in the year 2000 may cause surprisingly sharp weather changes. Unfortunately, runs in which the same GCM is run using the same initial condition with small changes in a given emission trajectory are not available. It is therefore not possible to determine the average response of the model to the change in emission trajectories. The chaos embedded in the GCM scenarios cannot be resolved.

In this paper I show that the noise in the GCM scenarios generated for the AR4 report is surprisingly large. Small differences in GHG concentrations are responsible for abnormally high differences in local weather patterns. The noise remains significant even if weather patterns are averaged over longer term

periods to build climatologies of weather variables. The noise tend to diminish as the external signal becomes stronger, but it never vanishes. This implies that the GCM output is typically a random draw from the true distribution of weather change for that GCM. In this model I use a Ricardian model of impacts of climate change on US agriculture to show that the noise in the SRES climate change scenarios used for the AR4 translates into noisy climate change impact estimates on agriculture. I compare the uncertainty that arises from chaotic dynamics within each single GCM – the within models uncertainty – to the uncertainty that arises when all GCMs climate scenarios are used – the between models uncertainty.

CLIMATE POLICY AND ECONOMIC ASSESSMENT

Strategies for adaptation and mitigation policies - I

Putting climate change adaptation into action: an operational approach to implement the European Guidelines on developing adaptation strategies

Giupponi C.^{1,2}

¹ *Università Ca' Foscari di Venezia, Venezia, Italia*

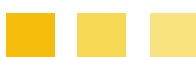
² *Centro Euro-Mediterraneo sui Cambiamenti Climatici, Venezia, Italia*

carlo.giupponi@unive.it

Abstract

The European Commission recently released the Communication “An EU Strategy on adaptation to climate change” (COM(2013) 216 final) and a series of related documents, including the Guidelines on developing adaptation strategies (SWD(2013) 134 final). In parallel to those documents, a significant effort is ongoing at the EU level through the European Environmental Agency (EEA) and the European Topic Centre for Climate Change adaptation (ETC-CCA) for the development of the European Climate Adaptation Platform (Climate-ADAPT) as the 'one-stop shop' for adaptation information in Europe, including the Adaptation Support Tool, coherent with the contents of the Guidelines, and intended to move further towards supporting Member States in operational implementations. This paper shows how a pre-existing methodological framework and suite of tools for supporting participatory decision processes can be easily adapted to provide the operational solutions to the principles enunciated in the EU Strategy and the prescriptions of the related Guidelines.

Keywords: Climate change adaptation strategies, assessment, decision making process



1. GUIDING AND SUPPORTING THE IMPLEMENTATION OF CLIMATE CHANGE ADAPTATION (CCA) STRATEGIES IN EUROPE

The European Commission has recently released the Communication “An EU Strategy on adaptation to climate change” (COM(2013) 216 final) and a series of related documents, including the Guidelines on developing adaptation strategies (SWD(2013) 134 final). The EU Strategy calls Member States (MSs) for remarkable efforts in terms of developing new adaptation instruments (National Adaptation Strategies and Plans) and revising those already produced. The Guidelines are aimed to contribute to achieving the objectives of the EU Adaptation Strategy, and in particular promoting action on CCA by MSs, but also contributing to climate-proofing actions and increasing resilience in Europe through CCA efforts in key sectors (agriculture, fisheries, etc.), and facilitating the implementation of better informed decision-making by addressing gaps in knowledge. In parallel to the documents mentioned above, a significant effort is in place at the EU level through the European Environmental Agency (EEA) and the European Topic Centre for Climate Change adaptation (ETC-CCA) for the development of the European climate adaptation platform (Climate-ADAPTI) as the “one-stop shop” for adaptation information in Europe, including the “Adaptation Support Tool”, coherent with the contents of the Guidelines, and intended to move further towards supporting MSs in operational implementations. The cyclic flow-chart depicted in Fig. 1 reports the six steps foreseen for the implementation CCA strategies in Europe.

Over the last two decades, a series of research projects under my scientific responsibility brought to the developments of a methodological framework called NetSyMod (Network Analysis – Creative System Modelling – Decision Support), aimed at providing a flexible but comprehensive and operational contribution to decision support through a suite of methods and tools for facilitating participatory decision making processes (DMPs) dealing with socio-ecosystems, including CCA. Decision is here intended in a broad sense, including any process in which a choice has to be taken by examining the available information on a given problem. The problem itself, the information, and the choice are defined with the contribution of different actors. The implementation field of NetSyMod is in general the management of natural resources, with two typical application cases, which may be also encountered together in the same case, depending on institutional and legislative contexts: (i) the involvement of experts in a decision or an evaluation of an environmental problem requiring multiple

fields of expertise, and (ii) the involvement of interested actors in a participatory process dealing with the management of environmental resources.

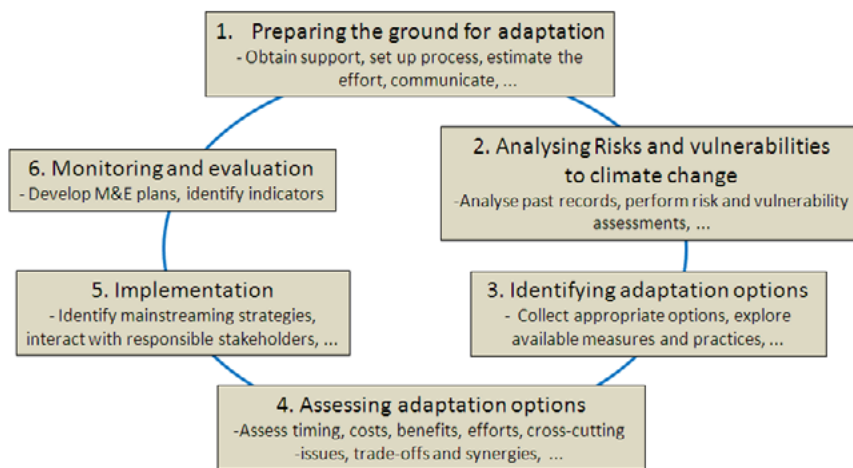


Fig. 1: The sequence of steps for the implementation of climate change adaptation strategies proposed by the EU Guidelines (SWD(2013) 134 final) and the Adaptation Support Tool (<http://climate-adapt.eea.europa.eu/en/web/guest/adaptation-support-tool/step-1>).

The proposed approach is aimed in particular at facilitating the integration of environmental, social and economic knowledge and the involvement of interested parties in the formulation of strategies and decisions. This appears to be perfectly in line with the EU approach for the identification and implementation of CCA strategies, typically characterised by choices to be made between alternative plausible options (strategies and measures) with the involvement of multiple actors. As the EU Guidelines, the NetSyMoD approach foresees the implementation of a cyclic sequence steps (see Fig. 2), which are in general consistent with those proposed by the EU documents cited above. The similarities between the two approaches are evident from the comparison of Fig. 1 and 2: step 1 is in both cases focused on setting up the process and defining the problem, thus providing the ground for adaptation. NetSyMoD emphasises more the need for an effective participatory approach since the early stages of the process and thus its step 2 is specifically focused on the identification of the main actors to be involved (experts, policy makers, and stakeholders in general) and the design of scientifically sound and robust participatory activities. Step 2 in the Adaptation Tool and in the Guidelines corresponds to the third one in NetSyMoD, and they are focused on the analysis of the problem, i.e. the assessment of risks and vulnerabilities to climate change. The outcomes of those steps

allow for the identification of the adaptation options (Step 3 of the Guidelines) and their description, with the support of various data processing, modelling and preliminary evaluations as proposed in Step 4 of NetSyMoD. In parallel, the assessment of adaptation options is approached in NetSyMoD through the “Analysis of Response Options”. Finally, steps 5 and 6 of the Guidelines are approached in NetSyMoD through the sixth step, which includes both action taking (Implementation) and Monitoring of the effects of the strategies adopted. NetSyMoD is presented in more details in the two following sections, with focus on steps 3 to 5.

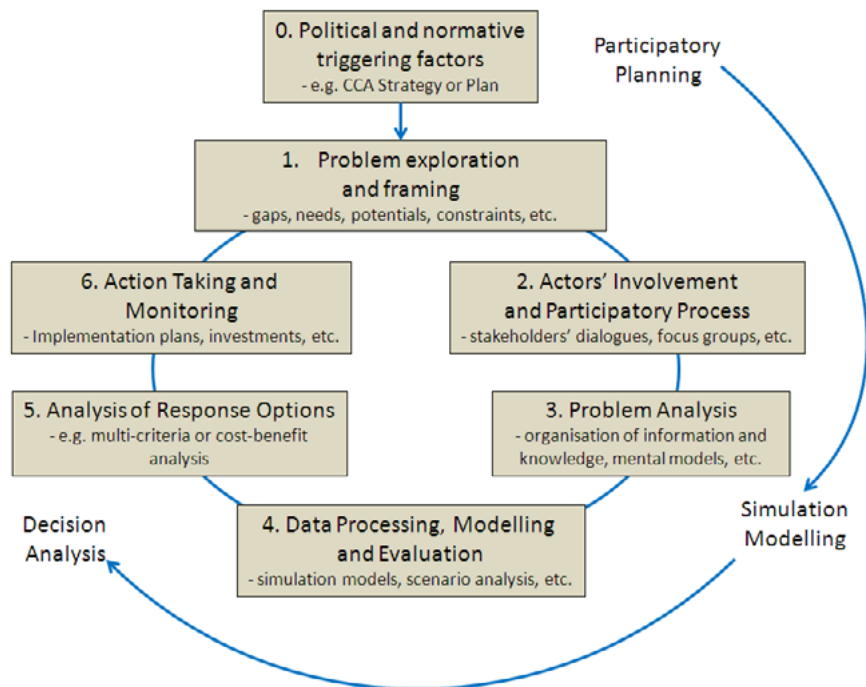


Fig. 2: The sequence of steps for the implementation of climate change adaptation strategies proposed by the NetSyMoD approach.

2. PROBLEM ANALYSIS AND DATA PROCESSING, MODELLING AND EVALUATION

As depicted in Figure 2, we propose two initial steps in which a substantial role is played by participatory approaches: problems and decision are first explored in the Problem Exploration and Framing Phase and then the participatory activities are designed and launched in the Actors’

Involvement and Participatory Process Phase. Having identified the decision context (i.e. the specific CCA case), the actors to be involved and how to deal with such issues, ideas are further elaborated and formalised in dedicated workshop activities, which facilitate collective learning and the building of a shared conceptual model. The latter - usually developed through Cognitive Maps, Causal Loop Diagrams or similar - provides the common communication basis, together with the frame for the design of data processing, modelling and evaluation procedures. As proposed in NetSyMoD, these initial steps are also intended to provide solid bases for the development of a dedicated Decision Support System (DSS). The DSS here plays a fundamental role as a means to facilitating the integration of scientific knowledge and participatory approaches, and for providing end users with efficient methods and tools for the management of the process leading to the implementation of CCA measures.

A few very important rules for effective DSS design can be extracted from Giupponi et al. [1]: (i) adapt existing or new DSS tools to the needs and not vice-versa; (ii) refine mutual understanding of users' requirements throughout the development phase and ensure flexibility; and (iii) develop effective analytical tools for the assessment of uncertainty and interfaces for its effective communication.

The main outcomes of the Problem Exploration and Framing Phase are the identification of the most relevant aspects of the decision, including legal and institutional ones, and, in particular:

- a list of most relevant exogenous and endogenous drivers governing the system and the problem considered;
- a preliminary list of options to be assessed (i.e. plausible approaches for adaptation);
- a preliminary set of scenarios regarding the future development of the main drivers and cause-effect relations;
- a list of decision criteria and possibly quantitative indicators against which the performance of the possible solutions (alternative options) can be measured.

The degree of, and the approach for, actors' involvement should be defined case by case. We propose the organisation of one or two workshops, depending on the number of issues to discuss (e.g. needs for future scenarios; potentials for quantitative assessment to follow a preliminary qualitative analysis), the complexity and uncertainty of the problem, and the number of stakeholders to be involved and their availability. In order to minimise the time required for the preparation and briefing of participants, the questionnaires used for stakeholders' analyses in the initial phases can also be used to collect their views

and opinion on one or several of the information typologies listed above. This is to facilitate the participation of key stakeholders by limiting the duration of workshops that should be possibly organised to last less than one day. These workshops aimed at problem analysis and development of shared cognitive models of the problems at stake are called Creative System Modelling (CSM) Workshops. By CSM workshops we intend a form of participatory modelling in which cognitive mapping techniques are used to design and later on develop a formal dynamic model aimed at the analysis of the of the socio-ecosystem considered in the specific case, with the contribution of the involved actors. CSM provides not only a common ground for the mutual understanding among the parties involved, but also a sound basis for the development or tailoring of the DSS tool and for easier communication with the general public.

A revised version of the DPSIR framework (Driving Forces, Pressures, State, Impacts, Responses; proposed by [2]) is the preferred reference for building a shared model of the adaptation problem at hand, by formalising the relevant cause-effects chains within a conceptual model based upon an easily understandable language. Such a scheme, proposes an extremely simplified causal model of a social-ecological system and, in particular of the relationships between human activities as Driving forces, exerting Pressures on the State of the environment, which in turns may result in Impacts requiring interventions by policy/decision makers (Responses) – in this case adaptation strategies and measures. In order to make it more suitable for dealing with climate change purposes, we have further developed the DPSIR framework into DPSIRS by including a new category of elements (Exogenous Drivers), to represent all the forcing variables acting from outside the system boundaries (climate change phenomena, higher level policies, international agreements, etc.), which should be considered when analysing alternative Scenarios, as it should in the assessment of CCA options.

In order to build a shared causal model of a given problem through a participatory process, by exploring viewpoints, beliefs, values, and knowledge, several approaches are available. The cognitive mapping (CM) approach is our preferred option [3], since it emphasises surfacing deeply held beliefs in form of mental models, which can be easily communicated with simplified symbolic languages, such as the DPSIRS framework. Very importantly, CM can also provide an effective basis for further developments towards simulation modelling. Our preferred sequence is to make the CM evolve into Causal Loop Diagrams, and further into Stock&Flow Relational Diagrams with a final formalisation step by means of system dynamic modelling tools in order to develop the system of differential

equations required for the modelling needs. Loos of full coupling of modelling outcomes are then implemented within the DSS tool.

Exploration of plausible future scenarios, on the basis of previously developed reference storylines (e.g. the SRES scenarios developed by the Intergovernmental Panel for Climate Change at the global level; [4]) is also of great potential in these phases, because it allows for defining possible boundary conditions which could determine the effectiveness and the robustness of current decisions.

The Data Processing, Modelling and Evaluation Phase builds upon the knowledge developed in the CSM workshop. The identified cause-effect relations and the screening of adaptation options, scenarios and indicators helps to articulate questions the simulation models have to answer. Very importantly in this phase all the decisional criteria to be considered are identified, thus indentifying also the information needs and the elaboration procedures to be implemented in the DSS.

3. ANALYSIS OF ALTERNATIVE RESPONSE OPTIONS

The analysis of alternative options is carried out during an ad hoc workshop, which could be merged with the CSM one, in particular in those case in which the assessment of options is carried out by means of qualitative assessment provided by the stakeholders/experts involved in the CSM. Otherwise, the ideal situation is that a quantitative assessment follows the preliminary qualitative analyses, once the quantitative results are available to provide an assessment of the expected performances of the alternative response options, usually through model simulations.

An original piece of software developed throughout a sequence of research grants, mDSS (from MULINO-DSS) is usually adopted in NetSyMoD applications to manage the crucial steps of the assessment of alternative options, from the formalisation of the problem at hand within the DPSIRS framework, to the analysis of multidisciplinary outcomes by means of Multi-Criteria Decision Methods (MCDMs).

Typically, an Analysis Matrix (AM) is built by processing qualitative and/or quantitative data (spatio-temporal indicators) representing the performances of the alternative options (e.g. alternative option, strategies, or projects) according to the selected criteria. The AM thus stores the performances of the alternative options, evaluated individually against each decision criterion. In some cases some of the criteria cannot be assessed by means of quantitative indicators provided by model simulations, and

thus actors can be asked to provide their own qualitative evaluations, and their preferences are integrated with the quantitative indicators in order to complete the filling of the AM.

At this stage MCDMs provide a framework for decision analysis, and a set of techniques aiming at the elicitation and aggregation of decision preferences [5]. Preference analysed by MCDM can be imagined as a choice or ranking of alternative options assessed through their performances according to a series of criteria [6]. All multi-criteria decision rules aggregate partial preferences describing individual criteria into a global preference index/score and rank the alternatives. Examples of techniques implemented in the mDSS software¹ are (i) Simple Additive Weighting (SAW); (ii) Order Weighting Average (OWA) [7]; (iii) the Technique for Order Preference by Similarity to Ideal Solution (TOPSIS) [8]; and (v) ELECTRE [9, 10, 11, 12, 13]. In addition, several techniques for elicitation of weights are available such as pair-wise comparison, swing weighting, direct rating and hierarchical weighting. Moreover, as far as the DSS considers – as it should – the subjective preferences of the involved actors, their different views and preferences (e.g. through the expression of different weighting), divergences are to be expected after the problem analysis, and thus also conflict mitigation/resolution must be performed. This can be implemented in different ways such as using inter-personal preference aggregation, or, simply, by performing parallel evaluation procedures to assess whether or not the diversity of opinions would lead to different results in terms of suggested choice, i.e. ranking of alternatives.

The results of the assessment of adaptation options should be adequately documented, and assumptions, subjective choices and uncertainties of various kinds should be transparently communicated with charts, tables, and statistical annexes. Such documentation should allow interested people to go step-by-step deeply in the understanding of all the details of the decision process. On the other hand, also effective concise means should be adopted for communicating the results to a broad public. An example being the interpretation of results in terms of sustainability of the decision, expressed in terms of balanced environmental, economic, social and institutional performances of the options analysed. Following the MCA approach proposed above, criteria can be allocated to the pillars of sustainable development, and effective graphical means can be used to explore their balancing in a chart in which the various options are allocated in a space (see Fig. 3 for examples of sensitivity and sustainability of decisions).

¹ www.netsymod.eu/mDSS/

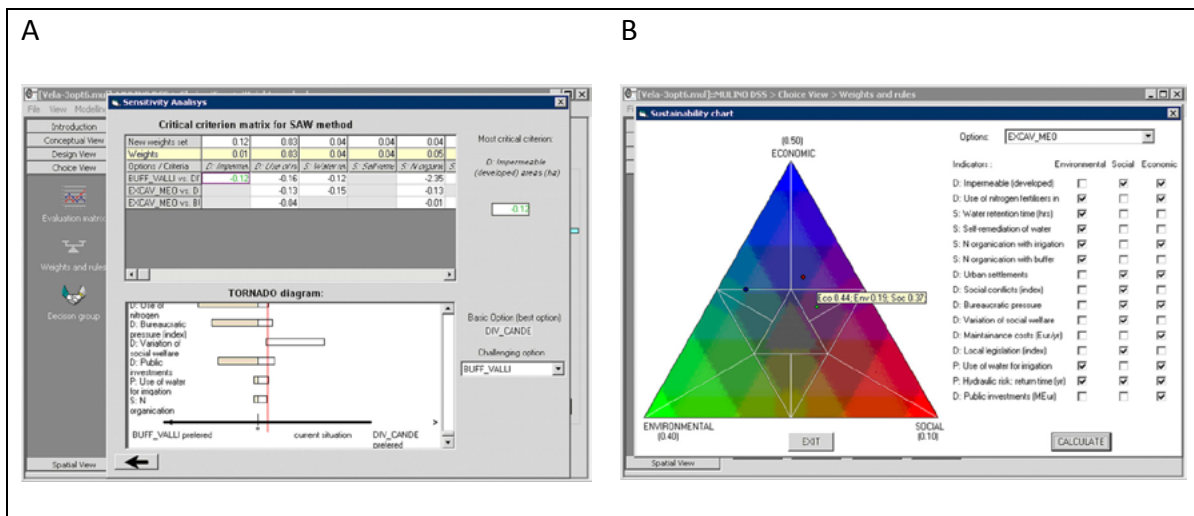


Fig. 3: Sensitivity analysis (a) and sustainability chart with performances of the preferred options (b) (from [14]).

In Practice, depending on the resources available, the relevance of the problem to be analysed, the availability of information, etc. two main application context can be foreseen: (i) qualitative analyses based only on expert judgement, or (ii) quantitative analyses carried out making use of simulation routines to estimate the expected performances of the proposed options, for each selected criterion/indicator. Case (ii) typically follows (i), and in that case a first exploratory and qualitative workshop is followed by the Data processing Modelling and Elaboration phase, which produces the outputs to be presented at a second workshop.

4. CONCLUDING REMARK

The European Commission has recently released a comprehensive set of policy documents which will guide Member States in the process of implementing or revising climate change adaptation strategies. Operational solutions are needed in particular in those countries such as Italy, where the process of developing national and local strategies for CCA has only recently started. The NetSyMoD approach, already tested in various CCA contexts, can be one of them. The development of the Italian National Adaptation Strategy and Plan can be an opportunity for capitalising the experiences developed over two decades of research projects in the field of decision support and made available through a coordinated package of methods, tools guidelines and tutorial documentation. It could also be an important

opportunity to go beyond state of the art of the approaches adopted elsewhere. At this regard, at least two directions emerge as of particular interest for research developments:

- 1) integration of methods and space and temporal scales between disciplines and between the science and policy spheres;
- 2) management of the various sources of uncertainty intrinsically inherent in decision processes such as those related to sustainability and climate change adaptation, in which decisions are to be taken today in consideration of the current – limited – understanding of the evolving dynamics of social and ecological systems.

5. REFERENCES

- Giupponi C., Mysiak J., Depietri Y., Tamaro M. *Decision Support Systems for water resources management: current state and guidelines for tool development*. In “Decision Support for Water Framework Directive Implementation”; Vanrolleghem, P. A., Ed. IWA Publishing: London (UK), 2011; Vol. 3, pp. 107-202. [1]
- EEA, E.E.A. *Environmental indicators: Typology and Overview*; European Environmental Agency: Copenhagen, 1999; Vol. 25, 25 pp. [2]
- Axelrod, R. *The structure of decision: The cognitive maps of political elite*; Princeton University Press: Princeton, NJ, 1976; p.^pp. [3]
- Nakićenović N., Alcamo J., Davis G., Vries B.d., Fenhann J., Gaffin S., Gregory K., Grübler A., Jung T.Y., Kram T., Emilio la Rovere E., Michaelis L., Mori S., Morita T., Pepper W., Pitcher H., Price L., Riahi K., Roehrl A., Rogner H.-H., Sankovski A., Schlesinger M.E., Shukla P.R., Smith S., Swart R.J., Rooyen S.v., Victor N., Dadi., Z. *Special report on emissions scenarios*; Cambridge University Press, Cambridge.: 2000; p.^pp. [4]
- Figueira J., Greco S., Ehrgott M., *Multiple criteria decision analysis: State of the art survey*; Springer: New York, 2005; p. 1040. [5]
- Hwang C.L., Yoon K., *Multiple Attribute Decision Making: Methods and Applications*; Springer Verlag: Berlin, 1981; p.^pp. [6]
- Jiang H., Eastman, J.R. *Application of fuzzy measures in multi-criteria evaluation in GIS*, Int. Journal of Geographic Information Science 2000, 14 173-184. [7]

- Belton V., Stewart T.J., *Multiple criteria decision analysis: An integrated approach*; Kluwer Academic Publishers: Boston, Dordrecht, London, 2002; 370 pp. [8]
- Figueira J., Mousseau V., Roy B., *ELECTRE methods*. In “Multiple criteria decision analysis: state of the art survey”; Springer: 2005; pp. 133-162. [9]
- Bella A., Duckstein L., Szidarovszky F., *A multicriterion analysis of the water allocation conflict in the Upper Rio Grande basin*. Applied Mathematics and Computation 1996, 77, 245-265. [10]
- Mahmoud M.R., Garcia L.A., *Comparison of different multicriteria evaluation methods for the Red Bluff diversion dam*. Environmental Modelling and Software 2000, 15, 471-478. [11]
- Salminen P., Hokkanen J., Lahdelma R., *Comparing multicriteria methods in the context of environmental problems*. European Journal of Operational Research 1998, 104, 485-496. [12]
- van Huylenbroeck G., *The conflict analysis method: bridging the gap between ELECTRE, PROMETHEE and ORESTE*. European Journal of Operational Research 1995, 82, 490. [13]
- Giupponi C., *Decision Support Systems for Implementing the European Water Framework Directive: the MULINO approach*. Environmental Modelling and Software 2007, 22, 248-258. [14]

The dynamic feedback of climate change impacts and catastrophic risk on mitigation and adaptation investments

Francesco Bosello^{1,2,3*}, Enrica De Cian^{2,3}, Licia Ferranna^{2,3}

¹University of Milan,

²Fondazione Eni Enrico Mattei,

³Centro Euro-Mediterraneo sui Cambiamenti Climatici

*Corresponding author: francesco.bosello@feem.it

Abstract

This paper contributes to the normative literature on mitigation and adaptation by framing the question of the optimal policy balance in the context of climate catastrophic risk. The analysis uses an integrated assessment model and it accounts for the endogenous link between the probability of experiencing a climate-change related catastrophic event and the temperature increase caused by GHG emissions. Results indicate that the presence of catastrophic risk induces substantial mitigation effort even in a non-cooperative setting where global cooperation on climate does not succeed. The policy balance is realigned from adaptation toward more mitigation, and the responsiveness of mitigation to changes in adaptation decreases. Compared to a world without climate catastrophes, risk reduces the substitutability between adaptation and mitigation because only mitigation can manage the catastrophic probability. In this setting, our analysis shows that adaptation funds and strategic unilateral commitments to adaptation are not the most efficient ways of buying emission reduction in less developed countries, though they could create some welfare gains and induce abatement in the recipient countries.

Keywords: *Climate change, mitigation, adaptation, climate risk, integrated assessment.*

JEL Classification: C61, D58, Q5



1. INTRODUCTION AND BACKGROUND

As recently emphasised by strategic documents such as the 2009 EU White Paper on Adaptation and the 2010 Cancun Adaptation Framework, adaptation is recognised as an unavoidable complement to mitigation. Moreover, the recent Durban talks confirmed the difficulty to negotiate emission reduction and achieve the 2°C temperature stabilization target. In this context, the role of adaptation as a strategy coping with climate change can become even more important.¹ Nonetheless, mitigation is the only instrument capable of tackling not only the smooth and continuous consequences of climate change, but also its potential catastrophic and irreversible outcomes. Adapting to a catastrophe would be extremely costly, meaning that mitigation should keep a key role in climate change strategy (Wright and Erikson, 2003). Indeed research has identified a number of climate related discontinuous, irreversible, and low-probability occurrences that could bring a sudden and sharp decline in economic growth and social welfare, for instance, the collapse of North Atlantic thermohaline circulation, the runaway greenhouse effect, and the melting of West Antarctic or of Greenland ice sheets, (Pearce et al., 1996; Posner, 2004; Guillerminet and Tol, 2008; Lenton et al. 2008).

The first contribution of this paper is to study with an applied model how climate catastrophic risk can shape the optimal mix between mitigation and adaptation. This research brings together different streams of applied and theoretical literature.

A first line of applied research is that investigating the role of uncertainty and irreversibility on mitigation choices. This presents mixed results. According to a group of studies, acquiring better information on future climate change damages warrants postponing costly abatement investments until uncertainty is resolved (Nordhaus and Popp, 1999, Ulph and Ulph 2007, Karp and Zhang, 2006). In contrast, a second group of works suggest that hedging might be a preferable response. Keller et al. (2004) show that climate threshold can render significant abatement a utility-maximizing choice. Other studies show that the risk of irreversible changes in the climate system induce anticipated precautionary abatement (Gjerde et al. 1998, Roughgarden and Schneider 1999, Yohe et al. 2004). These analyses did not include adaptation as a possible climate change strategy though.

The second line of research refers to the effect of catastrophic risk on the mix between adaptation and mitigation, but mainly with a theoretical perspective. In this vein Kane and Shogren (2000) and Ingham

¹ <http://climateactiontracker.org/news/>

et al. (2005, 2007). They developed an analytical model for the relation between mitigation and adaptation in the presence of uncertainty. Uncertainty is not explicitly defined as an irreversible catastrophic event, but as a risk of a climatic damage that can be endogenously controlled by agents. In Kane and Shogren (2000) both adaptation and mitigation reduce the risk of adverse effects of climate change. Their results are also mixed. Whether adaptation, mitigation, or both, grow in response to an increased climate change risk depends on a complex interaction between direct and indirect effects of risk on the marginal productivity of both strategies and their complementarity or substitutability. In general² the direct effect of a higher risk implies more mitigation or more adaptation. However, the final balance between the two strategies is determined by the indirect effect. This can both strengthen or counteract the direct effect. At the end Kane and Shogren (2000) conclude that what can be effectively observed is an empirical matter.

Ingham et al. (2007) assume that the climate risk can be reduced only by mitigation and the climate damage only by adaptation. In this set-up they find that an increase in risk always implies more adaptation and more mitigation. Still, the two strategies are economic substitutes: an increase in adaptation costs reduces adaptation and increases mitigation. Economic complementarity arises only when there is a strong cross effect of mitigation on adaptation costs. In this case increasing mitigation costs will reduce both mitigation and adaptation and *vice versa*. This can arise for instance when the costs of adaptation depend on the stock of greenhouse gases because more mitigation slows the rate of change of climate or avoids a potential catastrophe and hence makes adaptation easier (Ingham et al., 2005).

The third stream of modelling literature is that investigating the relation between mitigation and adaptation, applying Integrated Assessment Models (IAMs). So far, it assumes neither uncertainty nor irreversibility. Those studies tend to emphasize how, in a non-cooperative setting, mitigation remains negligible because of its public good nature. On the contrary, since adaptation entails almost fully appropriable benefits, it is basically the only climate change strategy pursued (Agrawala et al., 2010; de Bruin et al., 2009; Bahn et al., 2009; Bosello et al., 2011).

Substantive mitigation becomes optimal only when emission externalities are fully internalised. Alternatively, it had to be imposed exogenously to replicate given climate policy targets. When this is the case, the adaptation effort is crowded out. On the one hand, more mitigation reduces the climate

² The authors discuss examples where this is not the case.

change damage it is necessary to adapt to. On the other hand, scarce budgetary resources have to be allocated between two strategies instead of one. Nonetheless, the optimal climate policy always consists of a mixture of the two. The inertia of the climatic system and the path-dependency of investments in the energy system play also a role: adaptation remains an important strategy even if policies aimed at stabilising CO₂ are successful, and mitigation expenditure needs to be anticipated even in the presence of early adaptation (Hof, 2009, 2010; Agrawala et al., 2011). Anyway, especially in cost-benefit analyses, the crowding out of mitigation on adaptation is considerably weaker than that of adaptation on mitigation.

A second research field this paper addresses empirically relates to the feedback that international adaptation support from a group of donor countries exerts on mitigation or adaptation efforts of the receivers. This is partly related to the recent theoretical literature analyzing the implications of the joint presence of adaptation and mitigation in international environmental agreements. It shows that the presence of adaptation can indeed influence the incentive to be part of the environmental agreement. Barrett (2010) demonstrates that if more adaptation implies less mitigation, adaptation can enlarge participation to a mitigation agreement in a non-cooperative game theoretical set-up. Enlargement occurs because adaptation, by reducing the need to mitigate, pushes the environmental effectiveness of the agreement closer to the non-cooperative effort. In conclusion, adaptation enhances participation by making the agreement empty of its mitigation content. In a non-cooperative setting, Buob and Stephan (2011) show that, in principle, developed countries could use adaptation funding to developing countries to foster their abatement effort as well as global mitigation, if and only if mitigation and adaptation are complements. They also show however, that under strict complementarity it would be economically rational for developed countries to fund adaptation in developing regions only if this came in the exchange of lower abatement by developed regions. But realistically, developing countries will not be willing to accept such an agreement. Auerswald et al., (2011) show that in a leader follower game, early adaptation commitment from a group of countries can be used as a credible signal of low willingness to mitigate. This would induce other countries to increase their abatement effort. Total abatement effort can then increase or decrease depending on the shape of the respective reaction functions. Marrouch and Chauduri (2011) offer an interesting perspective which links Barrett (2010) and Auerswald et al. (2011). They show that, at given conditions, the presence of adaptation can enlarge participation to an abating coalition. Moreover, if the coalition acts as a Stackelberg leader, total

emissions can decrease. The intuition is the following: if a country can also adapt to climate damages, it may respond to higher emissions from another country with higher adaptation and lower abatement (thus higher emissions). On the one hand, this lowers the incentive to free ride on a mitigation agreement and consequently could enlarge participation. On the other hand, as now emission reaction curves are no more orthogonal, the abating coalition may increase its abatement effort to lower the emissions in non-participatory countries. In this paper we investigate whether financial transfers directed at supporting adaptation needs in developing countries can be used as a leverage to increase their abatement effort, and under which conditions.

The remainder of the paper is organized as follows. Section 2 introduces the improved AD-WITCH model and the design of climate change-related risk set-up. Section 3 presents the major model results and section 4 concludes.

2. ADAPTATION AND CATASTROPHIC RISK MODELLING

The AD-WITCH model

This paper uses an improved version of the AD-WITCH model as described in Bosello et al. (2011), Agrawala et al. (2010) and Agrawala et al. (2011). AD-WITCH builds on the WITCH model (Bosetti et al. 2006, Bosetti et al. 2009), of which it shares the main characteristics. It is an intertemporal, optimal growth model in which forward-looking agents choose the path of investments to maximise a social welfare function subject to a budget constraint. It can be solved in two alternative game theoretical settings. In the non-cooperative one, the one chosen in this study, the twelve model regions behave strategically with respect to all major economic decision variables – including adaptation and emission abatement levels. This yields a Nash equilibrium, which does not internalise the environmental externality. The cooperative setting describes a first-best world, in which all externalities are internalised, because a benevolent social planner maximises a global welfare function³.

Adaptation consists of a set of control variables that are chosen optimally with all the other controls, namely investments in physical capital, R&D, and energy technologies. The large number of potential adaptive responses has been aggregated into four macro categories: generic and specific adaptive capacity-building, anticipatory and reactive adaptation. Generic adaptive capacity building captures the link between the status of the development of a region and the final impact of climate change on its economic system (Parry et al. 2007, Parry 2009). Specific adaptive capacity building accounts for all investments dedicated to facilitate adaptation activities (e.g. improvement of meteorological services, of early warning systems, the development of climate modelling and impact assessment). Anticipatory adaptation gathers all the measures where a stock of defensive capital must already be operational when the damage materialises (e.g. dike building). Reactive adaptation gathers all actions that are put in place when the climatic impact effectively materialises (e.g. use of air conditioning) to accommodate the damages not avoided by anticipatory adaptation or mitigation.

The different adaptation strategies are linked into a CES (Constant elasticity of substitution) form. A first node distinguishes adaptive capacity building from adaptation activities *strictu sensu*. In the first nest, generic adaptive capacity building is represented by an exogenous trend increasing at the rate of total

³ AD-WITCH, as well as the WITCH model, features technology externalities due to the presence of Learning-By-Researching and Learning-By-Doing effects. The cooperative scenario internalises all externalities. The non-cooperative scenario does not internalise the technology externalities. For more insights on the treatment of technical change in the WITCH model see Bosetti et al. (2009).

factor productivity. Specific adaptive capacity building is modelled as a stock, which accumulates over time with adaptation-specific investments. In the second nest, anticipatory adaptation is also modelled as a stock of defensive capital. It is subject to some economic inertia (investments in adaptation takes one period - five years - to accrue to the defensive stock), and must be planned in advance. Once built, defensive capital remains effective over time subject to a depreciation rate. Reactive adaptation is modelled as a flow expenditure: it represents an instantaneous response to the damage faced in each period. Adaptive capacity building and adaptation activities, and similarly reactive and anticipatory adaptation are modelled as mild substitutes (substitution elasticity is 1.2 in both cases) to reflect the current debate supporting both substitutability and complementarity. On the contrary, general and specific adaptive capacity are modelled as gross complements (elasticity of substitution equal to 0.2)⁴ as we consider basic socio-economic development (generic capacity), an essential prerequisite for facilitating any form of adaptation. The analysis that follows assumes a cost-benefit, non-cooperative setting. Environmental externalities are not internalised globally, but only within the boundary of each given region.

Modelling non-catastrophic damages

For this study, the climate change damages of the AD-WITCH model, significantly based on Nordhaus (2001), have been recalibrated using new studies. Both market and non-market impacts are partly considered.

The market component of climate change damages has been revised using the recent estimates provided by the interdisciplinary work carried out within the ClimateCost project (Bosello et al. 2012). That project has quantified the physical and economic impacts of climate change on sea-level rise, energy demand, agricultural productivity, tourism flows, net primary productivity of forests, floods, and reduced work capacity because of thermal discomfort. The economic impacts have been estimated using a recursive-dynamic computable general equilibrium (CGE) model, ICES (Intertemporal General Equilibrium System). The estimated impacts incorporate the effect of market adjustments induced by price changes (e.g market driven adaptation). This is a first novelty compared to the DICE/RICE99

⁴ In a sequence of sensitivity tests we verify the robustness of our results to many different assumptions on the degree of substitutability among adaptive options. Results are robust to different parameterisation. They are available upon request.

and AD-WITCH models described in Agrawala et al. (2010), as they do not account for the role of market-driven adaptation.

The non-market component, refers to potential ecosystem losses and non-market health impacts, assessed using a willingness to pay approach.

Figure 1 summarises the outcome of the calibration procedure⁵. Global climate change damages are mildly convex in temperature, reaching a 4% loss of world GDP when there is a 3.6°C warming above pre-industrial levels. The largest discrepancy with the older data relates to South Asia and South East Asia, which are both expected to lose 12% of their GDP while in the previous estimate the loss was 10% and 5%. The EU loses roughly 0.5% of GDP in 2100. Eastern European countries are expected to gain until 2050. Economies in Transitions will have benefits until the end of the century, though at a decreasing rate, due to positive non-market effects on health.

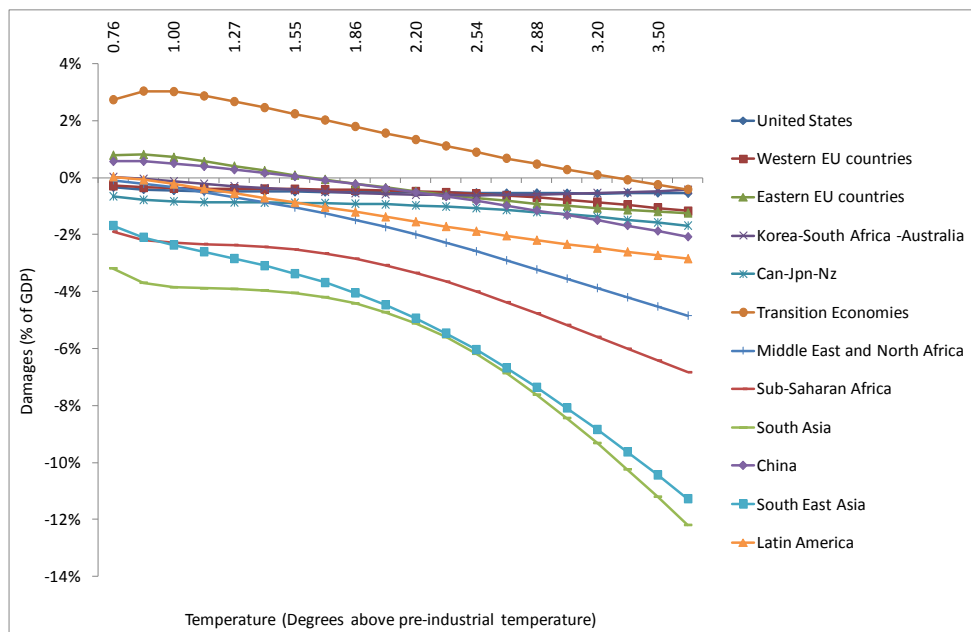


Fig. 1: Regional climate change damages in the AD-WITCH model without catastrophic risk

⁵ Detailed results are available in Bosello, De Cian, Ferranna (2012)

Modelling and Calibrating Climate Catastrophic Risk

Following Gjerde et al (1998), Bosello and Moretto (1999), Bosello and Chen (2010) catastrophic risk is implemented through a failure distribution function characterising the probability of a catastrophic event. It is denoted by a hazard rate, which assumes a Weibull form:

$$p(T_t) = \frac{1}{e^{\varphi\eta(T_t - T_0)^{1.5}}} \quad (1)$$

$T_t - T_0$ is the temperature increase relative to the pre-industrial level, T_0 . According to eq. (1), keeping the atmospheric temperature at the level T_0 would eliminate the possibility of catastrophic events. The probability of a catastrophe grows when temperature increases above T_0 . The social planner of each given region can control the probability of the catastrophic event by choosing her investment in technology portfolio, which will ultimately affect temperature and hence the probability through GHG emissions and concentrations. However, the benefit of this endogenous control on temperature has to be compared with its costs (see below).

In (1) the relationship between temperature increase and catastrophic probability depends on the two parameters φ and η . The parameter η is assigned the value of 2.5 to maintain the convexity of the hazard rate function. The parameter φ is calibrated such that the probability of a catastrophic occurrence for a temperature increase of 3°C above the pre-industrial period is 16%, ($\varphi=0.021$). In the model this happens at the end of the century. The 16% probability is relatively higher than the 4.8% value used by Nordhaus (1994). It accounts for the more recent studies on the likelihood of catastrophic outcomes or the trespassing of tipping points (Lenton et al., 2008, Kriegler et al., 2009). Catastrophic risk affects decision-making as the planner now faces an inter-temporal expected damage, which she can partially control⁶ (eq. 2).

$$CCDA_{n,t} = p(T_t) \cdot \frac{1}{1 + ADAPT_{n,t}} \cdot CCD_{n,t} + (1 - p(T_t)) \cdot CCR_{n,t} \quad (2)$$

In (2) damage ($CCDA_{n,t}$) is a weighted sum of its non-catastrophic ($CCD_{n,t}$) and catastrophic ($CCR_{n,t}$) realisation. Weights are given by the probability of the catastrophic occurrence, $p(T_t)$, and its

⁶ In fact, as noticed, the catastrophic probability could be eliminated if the temperature was blocked at its pre-industrial level, but in practice this would entail negative emissions.

complement to one. In (2) the component $CCR_{n,t}$ has been calibrated such that the catastrophic damage equals 25% of GDP in each given region at the calibration point. According to equations (2) and (3) adaptation ($ADAPT_{n,t}$) does not play any direct role in decreasing the catastrophic probability. Nor does it play a role in decreasing the post-catastrophic penalty. This was motivated by the assumption that, by definition, a catastrophe is outside the system coping range. The relationship between damage and economic activity is described in eq. (3):

$$YNET_{n,t} = \frac{1}{1 + CCD A_{n,t}} YGROSS_{n,t} \quad (3)$$

3. RESULTS

Mitigation and adaptation under climate risk: global results

In a world without catastrophic risk and with no global cooperation on climate, our numerical results confirm the findings from the existing theoretical and empirical literature. Mitigation is negligible due to free-riding incentives (Figure 2). In contrast, adaptation contributes almost entirely to damage reduction especially after 2050⁷ (Figure 3). The introduction of catastrophic risk changes the picture. Despite the non-cooperative set-up, substantive abatement becomes optimal, indicating that the risk of a catastrophe mitigates the free-riding incentive. The optimal Nash abatement almost stabilises CO₂ emissions, which in 2100 are 58 instead of 84 GtCO₂. Accordingly, in contrast with the no risk case, an increased amount of resources is devoted to mitigation. At the world level these are now primarily allocated to abatement (investment in energy saving R&D and renewable energy sources) until 2085 while, without risk, adaptation expenditure would overtake mitigation already in 2050.

The effect on temperature and risk is small though. Temperature increases to 3.3°C rather than 3.6°C in 2100, and the probability of the catastrophic outcome declines from 24% to 21%. It is worth noticing that the emission path under risk is still much higher than that implied by a temperature stabilisation policy at 2°C that would require declining emissions after 2020.

⁷ In addition, the presence of adaptation reduces the mitigation effort compared to when only mitigation is viable, and vice versa. The crowding out of adaptation on mitigation is stronger than the opposite.

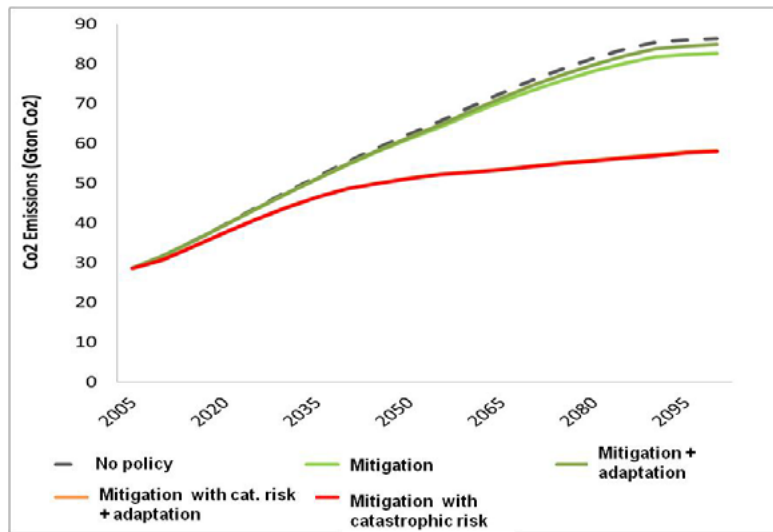


Fig. 2: CO₂ emissions with and without catastrophic risk with and without adaptation

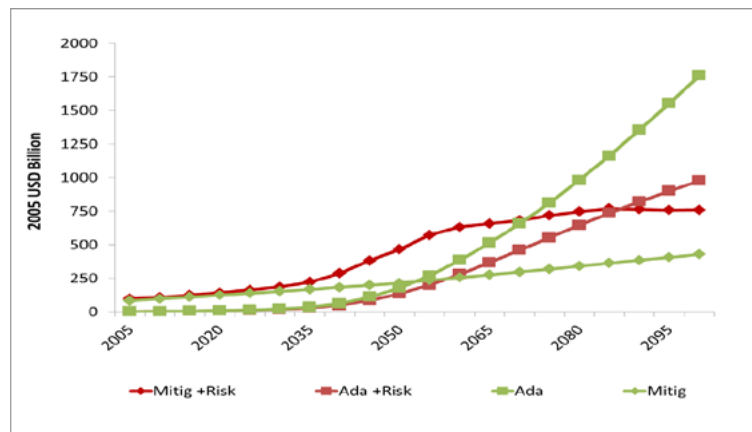


Fig. 3: Global investments in clean energy technologies* (mitigation) and adaptation expenditure (US \$ Billion) with and without catastrophic risk

*Includes wind, solar, nuclear, and coal IGCC with CCS power, energy efficiency R&D, radical R&D (reducing the cost of advanced mitigation options)

The introduction of catastrophic risk also changes the size of the crowding out effect between mitigation and adaptation (Table 1). Thus, throughout the century, the possibility to adapt would reduce cumulative abatement by 48% without risk, but by less than 1% when risk is considered. On the contrary, mitigation reduces cumulative adaptation expenditure by 1% without risk, and by 4.5% when risk is accounted for.

	Impact of mitigation on cumulative adaptation investments		Impact of adaptation on cumulative emission reduction*	
	With risk	W/o risk	With risk	W/o risk
World	-4.53%	-1.02%	-0.64%	-47.84%
Western Europe	-2.53%	-0.74%	-0.064%	-68.58%
Eastern Europe	-3.41%	-0.42%	-10.39%	-15.38%
Middle East and North Africa	-2.34%	-0.57%	-11.17%	-65.78%

Table 1: Crowding out between adaptation and mitigation

*Percentages are large numbers because the absolute values are small

Nonetheless, some reciprocal degree of crowding out between the two strategies remains since part of the mitigation effort still responds to the smooth climate-change damage component and continues to be influenced by adaptation measures and vice versa.

Different regions react differently to the introduction of the same risk. Abatement is driven by the effective ability of a country to reduce overall temperature and thus catastrophic risk. Therefore, emissions are reduced especially by major emitters. At the same time, emissions reductions also tend to be higher in the regions where abatement costs are lower. Accordingly, strong reductions are observed in China, United States, Western Europe, Canada-Japan-New Zealand, South Asia, whereas moderate reductions occur in Middle East and North Africa and Latin America. As said, the free riding incentive is weakened, but does not disappear completely. Some regions (Korea-South Africa-Australia, Sub-Saharan Africa, Eastern Europe) even increase their emissions compared to the no risk case. Figure 4 shows the different reaction in terms of CO₂ emissions in the Mediterranean regions (Europe and MENA).

When the catastrophic risk increases mitigation, adaptation decreases responding to the reduced country specific damage. For instance (Figure 5), all over the century, Europe increases its cumulated mitigation expenditure by roughly the 57% and reduces its cumulated adaptation expenditure by the 34%, while Middle East and North Africa increase mitigation expenditure by the 5.8%, but still reduce adaptation expenditure the 28%. This also explains why Eastern EU decreases its adaptation effort even though its mitigation also declines. Figure 5 finally shows that risk does not significantly change the adaptation basket. Throughout the century, most adaptation in the EU is of proactive nature, followed by reactive expenditure and investment in adaptive capacity building. The situation is similar in MENA, with just a higher importance of investment in adaptive capacity building. The different mix reflects the priority of less developed areas to build a suitable environment for successful adaptation.

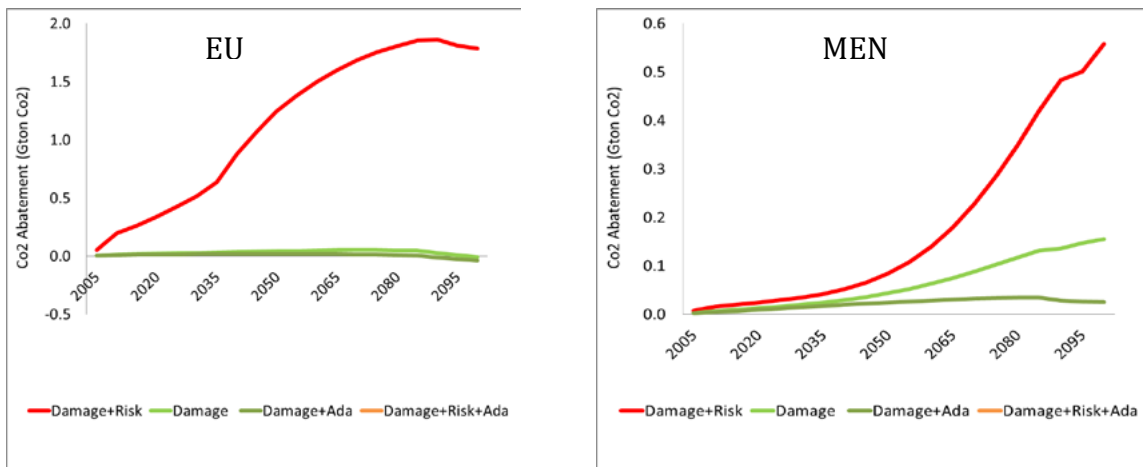


Fig. 4: CO₂ abatement in Europe (left) and Middle East and North Africa (right)

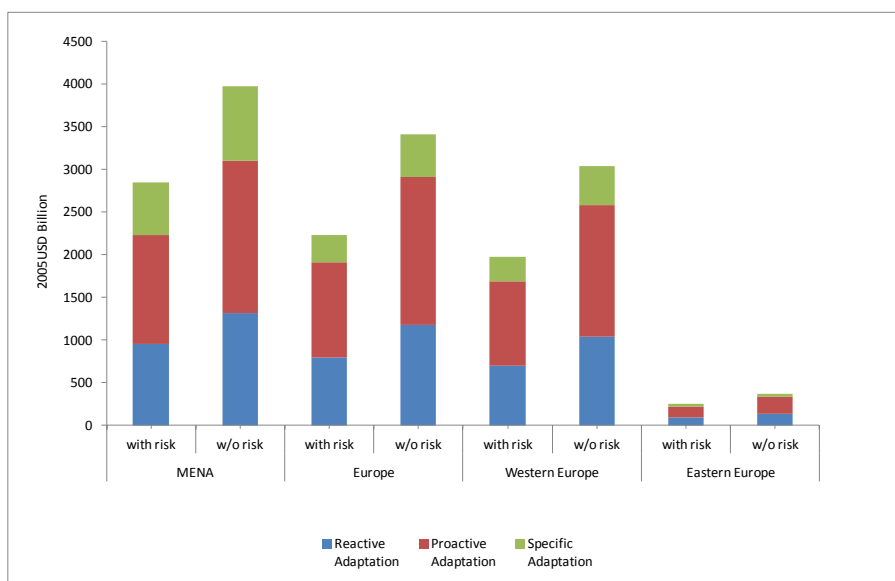


Fig. 5: Cumulated expenditure in different adaptation forms, 2005-2100

The results discussed in this section have important policy implications. In a world characterised by smooth and reversible climate damages, mitigation is a marginal option. Although viable and welfare improving if coupled with adaptation, mitigation would be less effective than adaptation. On the contrary, in a world with catastrophic risk, mitigation is the only strategy capable of reducing the probability of the catastrophic outcome. Therefore, it becomes a key policy variable, irrespectively of its ability to reduce the non-catastrophic damage. This clearly indicates that mitigation choices should be

driven mainly by precautionary considerations and to some extent independently from adaptation. On the contrary, adaptation should tackle the residual damage not accommodated by mitigation.

We examine the sensitivity of our results⁸, and in particular of the trade-off between adaptation and mitigation when the discount rate, the catastrophic risk, and the catastrophic penalty change. We find that, once catastrophic risk is introduced, lower discounting unambiguously implies more abatement and also an increase in adaptation. The higher probability associated with the catastrophic event has the effect of increasing abatement while adaptation is crowded out. When the risk of a catastrophic event increases, the crowding out of abatement induced by adaptation is reduced basically to zero.

Mitigation and adaptation: a strategic analysis

In this section we analyse the use of adaptation transfer and of adaptation expenditure by a group of countries as a strategic leverage to foster mitigation outside the group. More specifically, maintaining a non-cooperative and cost-benefit setting, we assume that the OECD, perceive and react to catastrophic risk, whereas the non-OECD, react only to the non-catastrophic damage component⁹.

We therefore assume that, the OECD are not only inclined to strong domestic abatement, but are also willing to foster abatement in non-OECD. Indeed risk can be better curbed by an enlarged abatement effort since it depends on global temperature. Non-OECD, on their turn, need to find their additional abatement profitable. That is they need to receive a compensation at least equal to the additional abatement cost. The leverage used to get the desired result by the OECD is through financing adaptation needs in non-OECD.

In a first experiment we assume that the OECD would finance all adaptation needs of non-OECD to a ceiling of \$ 100 billion per year. This is just an indicative figure inspired by the annual transfers from developed to developing countries proposed during COP 15 at Copenhagen. Transfers are divided across donors proportionally to the respective GDP share of the group total. When the total adaptation expenditure of the recipients exceeds \$ 100 billion, these are shared among receivers proportionally to

⁸ Available upon request.

⁹ To highlight clearer results, the risk setting chosen is different from that used in section 2. Namely both the probability and the catastrophic penalties have been increased respectively to the 50% and 99% of GDP for a temperature increase of 3.6°C.

the respective adaptation need share of the group total. In this simulation, (Transf A in Figure 7), the major donors are the USA and Western Europe while the larger recipients are the Middle East and North Africa, South East Asia, Sub Saharan Africa. The ceiling of \$ 100 billion is reached in 2060. As adaptation needs in developing countries rapidly increase after 2040, the \$ 100 billion amount covers roughly 19% of the total adaptation needs in 2100.

Adaptation funds almost completely replace domestic adaptation in receiving countries, which in fact only slightly increases. Investment in physical capital and in mitigation activities (energy saving R&D and renewable technologies) is basically unaffected. The additional available budget is almost totally used for consumption. Discounted consumption throughout the century increases by 0.046% (or by US \$ 265 Billions) compared with the case with no transfers. In other words, mitigation behaves quasi-linearly in non-OECD preferences. After optimal adaptation is reached, consistent with the countries damage/risk perception, adaptation becomes insensitive to further shifts of the budget line. In our particular setting, when countries start from a non-cooperative optimum, the adaptation fund does not crowd out domestic mitigation, but domestic adaptation, even when adaptation and mitigation are substitutes¹⁰. At the same time, even though mitigation investment in the non-OECD does not shrink, higher consumption and production implies slightly higher emissions.

Accordingly, adaptation funds can only foster mitigation if a conditionality clause is included, stating that the adaptation fund will be delivered only in the presence of a binding-detectable mitigation commitment from the non-OECD. We consider the same adaptation transfer as in the case Transf A, but now non-OECD are required to invest in either energy saving R&D or renewable energy. We design this deal to be welfare improving for the non-OECD by identifying the mitigation threshold that leaves non-OECD indifferent between accepting adaptation funds and engage in additional mitigation or giving up the adaptation funds and avoid further abatement effort. This is done by imposing different levels of additional mitigation investment in either energy saving R&D (1/10 or 1/5 of the transferred resources for adaptation, Transf A+1/10R&D, Transf A+1/5R&D in Figure 7 left panel respectively) or renewable energy (1/10 of the transferred resources for adaptation in Transf A+1/10 Ren in Figure 7 left panel).

¹⁰ A potentially different situation would be one in which, because of an adaptive capacity deficit and a resource constraint, developing countries implement sub-optimal (lower than needed) adaptation levels. In this case foreign and domestic adaptation can be expected to be additional. This issue, which will imply a change in the model setting, will be explored in future research.

In terms of welfare, which in AD-WITCH is a function of consumption, non-OECD would benefit from this exchange, and therefore would be willing to accept, as long as the required investments in energy saving R&D or renewable energy is not greater than 1/5 of the adaptation funds received¹¹ (see Table 2). One dollar received in adaptation funds weights 1/5th of one dollar spent in mitigation. This happens because every additional abatement effort in non-OECD is strategically balanced by an increase in emissions in the OECD (Figure 7), which therefore erodes part of the benefit of the non-OECD mitigation.

Does this conditional transfer succeed in cutting emissions? The overall impact of the transfer on non-OECD emissions is almost negligible, though it moves in the expected direction (Figure 7). Despite the small magnitude of the effect, it can be noticed that allocating the same resources to renewable energy entails higher emission reductions than when allocated to energy saving R&D. AD-WITCH nicely captures the well-known rebound effect: more efficient energy input implies also as a secondary effect a higher energy use. If the funds allocated to energy saving R&D are low enough (1/10 of the adaptation fund received), emissions in non-OECD, can in fact increase. At the world level, emissions decrease only when adaptation funds are coupled with investment in renewable energy. In AD-WITCH the cost of renewables declines endogenously with installed capacity (Learning-By-Doing). Therefore, the additional capacity installed in the non-OECD reduces the technology cost in the OECD as well.

As a further experiment (Figure 7 right panel) we examine the effect of adaptation implemented in OECD countries on mitigation and adaptation in non-OECD. The aim, following the ideas put forward by Auerswald et al. (2011) and Marrouch and Chaudury (2011) is to test whether adaptation can be used as strategic signal or leverage by a group of countries to induce more abatement in other countries. Specifically, we assume that OECD unilaterally decide a 10% increase of adaptation expenditure. As adaptation and mitigation are substitutes, abatement in OECD regions decreases (cumulated OECD emissions increase by 18.38%). As a reaction, abatement in non-OECD regions slightly increases (cumulated emissions decline by 0.55%) while adaptation remains basically unchanged (-0.009%). More precisely, the mild increase in reactive adaptation, +0.074% is compensated by a reduction in proactive adaptation and capacity building, (-0.059% and -0.072%). This seems to confirm

¹¹ Indeed when the investment in mitigation is 1/3rd of the adaptation transfers, non-OECD would be worse off than in the case of no transfers.

Auerswald et al., (2011) intuition and to confute Marrouch and Chauduri (2011) point. The reaction to decreased mitigation in one country or group is always contrasted with an increase in mitigation outside the group, notwithstanding the possibility to adapt. However, the effect on overall abatement is negative, as world cumulated emissions increase by 3% (Figure 7, right panel). This raises some caution regarding the practical possibility to use adaptation as a credible signal of low mitigation commitment in a country to induce mitigation in other countries.

Summarising, the results presented so far seem to suggest that using adaptation, through international financing or as a strategic device, are not the most efficient and effective way of buying emission reduction in non-OECD countries. A legitimate question then is whether OECD countries could achieve better results by directly financing abatement in the non-OECD. Let us assume this would be possible, neglecting for experimental sake all the transaction costs potentially involved. In a last simulation (Trans M in Figure 7 left panel) we assume that what is available to adaptation is directly invested by OECD to support investment in renewable energy in the non-OECD. The region thus experiences an increase in its investments in renewables from \$ 12 to 55 Billion in 2050, from \$ 47 to 100 Billion in 2100. Emission reduction in Non-OECD is effectively higher (-0.4%) and, because of the technical change effect - the global cost of renewable energy is 10% lower compared to the case with no transfer - also OECD's emission reduction is higher (-1%).

In terms of discounted consumption, although developing countries would still be better off with a mitigation transfer than without, they would slightly prefer a support to adaptation (Table 2 third vs. first column). Indeed, the benefit from additional abatement is a public good, whereas the benefit from adaptation is fully appropriable. Moreover, adaptation funding is replacing what developing countries would have done anyway, while mitigation funding is financing something additional with respect to what is optimal for them. Contrary to OECD countries, which perceive the risk of a catastrophe, non-OECD lacks this perception and therefore under-evaluates the benefit of mitigation.

This suggests two partly countervailing messages. On the one hand, albeit in principle adaptation funding can be used by developed countries as a leverage to induce more mitigation in developing countries, the effectiveness of this strategy is very limited. The resources needed by developing countries to de-carbonise their production and energy system are much higher than \$100 billion yearly. When also non-OECD perceive the risk of a catastrophe and global emissions are stabilised, their

additional investments in clean energy would reach 100 USD Billion in 2035 and climb to 300 USD Billion in 2080 just to stabilise emission levels.

On the other hand, although the transfer would reduce consumption possibilities in the OECD, in terms of GDP they could experience small gains, especially when the transfer goes to financing renewables (see Table 3, case Trans M and Trans A+1/10 Ren). The mechanism behind this is the technological change effect that is induced by the transfer. This is quite a powerful insight. Even though a financial support to adaptation from developed countries would be insufficient to spur significant mitigation in developing countries, it could be beneficial for the donor countries. This happens if the transfer is specifically designed to foster investments in those technologies that, because of other market failures, are sub-optimal in the receiving countries.

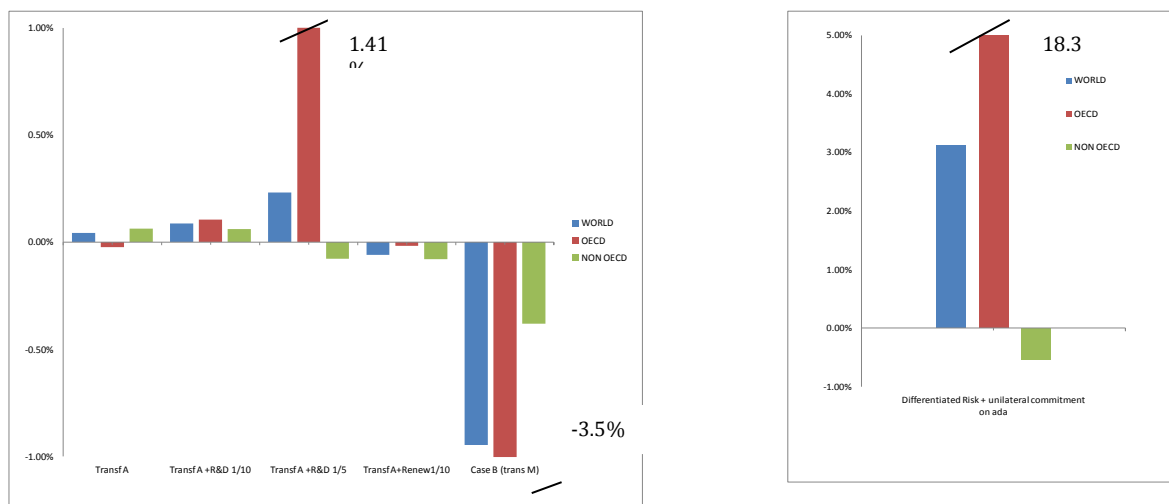


Fig. 7: CO₂ cumulated emissions 2005-2100, percentage change compared to the case without transfer

% change (USD Billion)	Transf A	Transf A+Renew1/10	Transf M	Transf A +R&D 1/10	Transf A +R&D 1/5	+10% adaptation in OECD
WORLD	0.001% (7.78)	0.002% (29.22)	-0.001% (-21.12)	-0.001% (-22.55)	-0.003% (-48.93)	-0.020% (-303.80)
OECD	-0.026% (-257.42)	-0.024% (-232.28)	-0.028% (-278.29)	-0.027% (-263.38)	-0.016% (-155.80)	0.030% (293.09)
NON-OECD	0.046% (265.20)	0.045% (261.50)	0.045% (257.17)	0.042% (240.83)	0.018% (106.87)	-0.103% (-596.89)
Europe	-0.025% (-97.76)	-0.022% (-88.11)	-0.056% (-220.46)	-0.017% (-68.31)	-0.057% (-223.66)	-0.012% (-48.24)
MENA	0.086% (52.42)	0.086% (51.93)	0.078% (47.34)	0.081% (49.34)	0.048% (29.27)	-0.141% (-85.32)

Table 2: Consumption: difference compared to the case with no transfer. Percentage point difference (discounted over the century)

Note: World and non-OECD figures do not include Transition Economies as in the simulation they neither receive nor give adaptation funds, being positively affected by climate change.

% change (USD Billion)	Transf A	Transf A+Renew1/10	Transf M	Transf A +R&D 1/10	Transf A +R&D 1/5	+10% adaptation in OECD
WORLD	0.001% (18.99)	0.004% (73.53)	0.026% (501.88)	-0.001% (-21.74)	-0.007% (-142.42)	-0.087% (-1698.61)
OECD	0.003% (35.69)	0.005% (63.62)	0.022% (277.23)	-0.002% (-30.95)	-0.004% (-49.40)	-0.077% (-952.10)
NON-OECD	-0.002% (-16.70)	0.001% (9.91)	0.032% (224.65)	0.001% (9.21)	-0.013% (-93.02)	-0.105% (-746.51)
Europe	0.004% (17.78)	0.006% (28.17)	-0.013% (-63.97)	-0.005% (-22.70)	-0.033% (-163.43)	-0.090% (-449.29)
MENA	-0.004% (-3.17)	0.004% (2.77)	0.066% (50.36)	0.008% (5.76)	-0.008% (-6.38)	-0.135% (-102.77)

Table 3: GDP difference compared to the case with no transfer. Percentage point difference

Note: World and non-OECD figures do not include Transition Economies as in the simulation they neither receive nor give adaptation funds, being positively affected by climate change.

4. CONCLUSIONS

Various official documents, such as the 2009 EU White Paper on Adaptation or the 2010 Cancún Adaptation Framework, acknowledge mitigation and adaptation as necessary strategies to combat climate change. A rapidly expanding scientific literature has provided normative indications regarding the optimal combination of the two. This paper contributes to the normative literature on mitigation and adaptation by framing the question of the optimal policy balance in the context of climate catastrophic risk. The analysis uses an integrated assessment model and it accounts for the endogenous link between the probability of experiencing a climate-change related catastrophic event and the temperature increase caused by GHG emissions.

The presence of catastrophic risk induces substantial mitigation effort even in a non-cooperative setting where global cooperation on climate does not succeed, as the incentive to free ride is greatly weakened. The policy balance is realigned from adaptation toward more mitigation, and the responsiveness of mitigation to changes in adaptation decreases. Compared to a world without climate catastrophes, risk reduces the substitutability between adaptation and mitigation because only mitigation can manage the catastrophic probability.

Nonetheless, the strategic complementarity between mitigation and adaptation does not vanish. Even though adaptation does not influence the catastrophic probability, it is still a necessary complement to mitigation to address the residual damage not accommodated by mitigation. By the same token, a trade-off between mitigation and adaptation persists: when adaptation increases, the need to mitigate the smooth part of climate change damages decreases. Therefore even though greatly reduced, a minimal crowding out of adaptation on mitigation remains.

These findings suggest that in a world characterised by catastrophic risk, mitigation is a key policy variable, as it is the only strategy able to reduce the catastrophic probability. Mitigation should be justified on the basis of precautionary considerations and only marginally considering its capacity to reduce the smooth component of climate change damages. Adaptation should be deployed to tackle that part of the climate damage that mitigation fails to accommodate because of time lag between mitigation action and mitigation benefits.

Given these results, we then investigate whether unilateral or partial commitment to adaptation can be used as a leverage to increase abatement effort outside the group in a non-cooperative setting. We find

that if the OECD countries financed all adaptation needs of non-OECD up to a ceiling of \$ 100 billion, such adaptation funding *per se* would not affect neither abatement nor adaptation. Domestic adaptation expenditure is displaced almost perfectly by the international adaptation aid and mitigation remains unchanged. If the adaptation fund were conditional on additional mitigation, than the adaptation funding can foster additional mitigation in developing countries, though the effectiveness of this strategy is very limited. On the one hand, the resources needed by developing countries to significantly de-carbonise their production and energy system are much higher than \$100 billion yearly. On the other hand, in the chosen non-cooperative setting any additional abatement effort in non-OECD is strategically balanced by an increase in emissions in the OECD, which therefore erodes part of the benefit of the non-OECD mitigation. Even though a financial support to adaptation from developed countries would be insufficient to spur significant mitigation in developing countries, it could be beneficial for the donor countries. This happens if the transfer is specifically designed to foster investments in those technologies that, because of other market failures, are sub-optimal in the receiving countries.

We also evaluate whether a unilateral commitment to adapt by the OECD countries can induce more abatement in other countries. As a reaction, abatement in non-OECD regions effectively increases. However, the effect on overall abatement is negative, as world cumulated emissions increase.

Summarising, adaptation funds and strategic commitments to adaptation do appear efficient and effective ways of buying emission reduction in non-OECD countries. Needless to say that adaptation funding remains important, but for other purposes, such as addressing the adverse distributional implications of climate change impacts. Two important qualifications of these results are necessary. First, the outcomes are based on a situation in which both adaptation and mitigation are at their non-cooperative optimum. Welfare implication of and reaction to adaptation transfers can be different in a second-best condition assuming for instance that resource or capacity constraints would impose sub optimal adaptation levels in the non-OECD. Second , the overall setting is non-cooperation. Although we strongly believe that this framework is the most realistic, and therefore also the most interesting to study, a cooperative optimum could offer partly different insights.

5. DISCLAIMER

The estimation of the market damage component of the AD-WITCH reduced-form damage function heavily builds on the interdisciplinary work undertaken by the CLIMATECOST FP7 project. We are highly indebted with the project coordinator, Tom Downing and the project technical coordinator, Paul Watkiss for data disclosure and availability. All imprecisions and potential mistakes are our own responsibility.

6. REFERENCES

- Agrawala S., Fankhauser S. (eds) (2008), *Economic aspects of adaptation to climate change: costs, benefits and policy instruments*. OECD, Paris.
- Agrawala S., Bosello F., Carraro C., De Cian E., Lanzi E., De Bruin K., Dellink R. (2010), “*PLAN or REACT? Analysis of adaptation costs and benefits Using Integrated Assessment Models*”. OECD Environment Working Papers, No. 23, OECD Publishing. doi: 10.1787/5km975m3d5hb-en
- Agrawala S., Bosello F., Carraro C., De Cian E., Lanzi E., De Bruin K. and Dellink R. (2011), “*PLAN or REACT? Analysis of adaptation costs and benefits Using Integrated Assessment Models*, *Climate Change Economics*, Vol.2 (3), 1-36.
- Aldy J.E. and Viscusi W.K (2003), *The Value of a Statistical Life: A Critical Review of Market Estimates Throughout the World*, *Journal of Risk and Uncertainty*, Volume 27, Number 1, 5-76,
- Arrow K. and Fisher A.C. (1974), *Environmental Preservation, Uncertainty, and Irreversibility*, *The Quarterly Journal of Economics*, Vol. 88, No. 2: 312-319
- Auerswald, Heike, Konrad, Kai A. and Thum, Marcel P., *Adaptation, Mitigation and Risk-Taking in Climate Policy* (January 31, 2011). CESifo Working Paper Series No. 3320.
- Bahn O., Chesney M., and Gheysens J. (2010), *The Effect of Adaptation Measures on the Adoption of Clean Technologies*. Paper presented at the WCERE Congress, Montr´eal, 2010. Viewed on December 22, 2010
- Barrett S. (2010), *Climate Change and International Trade: Lessons on their Linkage from International Environmental Agreements,* “prepared for Conference on Climate Change, Trade and Competitiveness: Issues for the WTO, World Trade Organization, Geneva, 16-18 June 2010.
- Balmford A., Gravestock P., Hockley N., McClean Colin J., and Callum M. Roberts (2004), *The worldwide costs of marine protected areas*, *PNAS* Vol. 101, no. 26.
- Bigano A., Hamilton J.M. and Tol R.S.J. (2007), *The Impact of Climate Change on Domestic and International Tourism: A Simulation Study*, *Integrated Assessment Journal* 7, 25-49.
- Bondeau A., Smith P.C., Zaehle S.O.N., Schaphoff S., Lucht W., Cramer W., Gerten D., Lotze-Campen H., Muller C. and Reichstein M., (2007). *Modelling the role of agriculture for the 20th century global terrestrial carbon balance*. *Global Change Biology*, 13, 679-706.

- Bosello F. and Chen C. (2011), *Adapting and Mitigating to Climate Change: Balancing the Choice under Uncertainty*, FEEM Note di Lavoro 550.2011.
- Bosello F., Eboli F., Pierfederici R. (2012), *Assessing the Economic Impacts of Climate Change. An Updated CGE Point of View*, FEEM Note di Lavoro, No. 2.2012
- Bosello F. and Moretto M. (1999), *Dynamic Uncertainty and Global Warming Risk*. FEEM Note di Lavoro. 80.99
- Bosello F., Carraro C., and De Cian E. (2011), *Adaptation can help mitigation: an integrated approach in post-2012 climate change policy*, FEEM Working paper No. 69.2011, Sept 2011.
- Bosello F., Carraro C., and De Cian E. (2010), *Climate Policy and the Optimal Balance between Mitigation, Adaptation and Unavoided Damage*, *Climate Change Economics*, Vol. 1, No. 2, 71–92.
- Bosetti V., Carraro C., Galeotti M., Massetti E. and Tavoni M. (2006), *WITCH: A World Induced Technical Change Hybrid Model*, *The Energy Journal*. Special Issue on Hybrid Modeling of Energy-Environment Policies: Reconciling Bottom-up and Top-down 13-38
- Bosetti V., Carraro C., Duval R., Sgobbi A. and Tavoni M. (2009), *The Role of R&D and Technology Diffusion in Climate Change Mitigation: New Perspectives using the WITCH Model*, OECD Working Paper No. 664
- Bosetti V., Carraro C., De Cian E., Massetti E., Tavoni M. (2011), *Incentives and Stability of International Climate Coalitions: An Integrated Assessment*, FEEM Working Paper No.97.
- Buob S. and Stephan G. (2011), *On the incentive compatibility of funding adaptation*, NCCR Climate, Research Paper 2011/02.
- Ciscar J.-C. (Ed.) (2009), *Climate change impacts in Europe: final report of the PESETA research project*. JRC Scientific and Technical Research series, EUR 24093 EN. Office for Official Publications of the European Communities: Luxembourg. ISBN 978-92-79-14272-7. 131 pp.
- Criqui P. (2001), *POLES: Prospective Outlook on Long-term Energy Systems*, Institut d'Economie et de Politique de l'Énergie, 2001, available on line at: http://webu2.upmf-grenoble.fr/iepe/textes/POLES8p_01.pdf

- Criqui P., Mima S. and Menanteau P. (2009), *Trajectories of new energy technologies in carbon constraint cases with the POLES Model*, IARU International Scientific Congress on Climate Change, p. 16.
- de Bruin K.C., Dellink R.B. and Tol R.S.J. (2009), *AD-DICE: An Implementation of Adaptation in the DICE Model*, *Climatic Change*, Vol. 95: 63-81
- De Cian E, Bosetti V. and Tavoni M. (2011), *Technology innovation and diffusion in less than ideal climate policies. An assessment with the WITCH model*, *Climatic Change*, Special Issue, DOI 10.1007/s10584-011-0320-5.
- James A., Gaston K.J., and Balmford A. (2001), *Can we afford to conserve biodiversity?*, *BioScience*, Vol. 51 No. 1
- Emerton L., Bishop J. and Thomas L. (2006), *Sustainable Financing of Protected Areas. A global review of challenges and options*. The World Conservation Union (IUCN), Gland, Switzerland
- Feyen L. (2009), *Review of Literature on Impacts of Climate Change Infrastructure and Extremes*, Deliverable D2D.1, ClimateCost project.
- Gjerde J., Sverre Grepperud, Snorre Kverndokk (1999), *Optimal climate policy under the possibility of a catastrophe*. *Resource and Energy Economics*, Volume 21, Issues 3–4.
- Guillerminet M.L. and Tol R. S. J. (2008), *Decision making under catastrophic risk and learning: the case of the possible collapse of the West Antarctic Ice Sheet*. *Climatic Change*, Volume 91, Numbers 1-2, 193-209.
- Hanemann W.M. (2008), *What is the Cost of Climate Change?*, CUDARE Working Paper No. 1027, University of California, Berkeley
- Hof AF, de Bruin KC, Dellink RB, den Elzen MGJ, van Vuuren DP (2009), *The effect of different mitigation strategies on international financing of adaptation*, *Environmental Science and Policy* 12: 832–843
- Hof AF, den Elzen MGJ, van Vuuren DP (2010), *Including adaptation costs and climate change damages in evaluating post-2012 burden-sharing regimes*, *Mitigation and Adaptation Strategies Global Change* 15:19–40
- Iglesias A., Garrote L., Quiroga S. and Moneo M., (2009), *Impacts of climate change in agriculture in Europe*. PESETA FP6 project, available on line at: <http://ipts.jrc.ec.europa.eu/publications/pub.cfm?id=2900>

- Iglesias A., Quiroga S. and Garrote L. (2010), *Report Analysis for Europe*, Deliverable D2B.2, *ClimateCost* project.
- Ingham A., Ma J. and Ulph A.M. (2005), *Can Adaptation and Mitigation be Complements?*, Working Paper 79, Tyndall Centre for Climate Change Research, University of East Anglia
- Ingham A., Ma J. and Ulph A.M. (2007), *Climate Change, Mitigation and Adaptation with Uncertainty and Learning*, *Energy Policy* 35 (11): 5354-5369
- Kane S. and Shogren J. (2000), *Linking Adaptation and Mitigation in Climate Change Policy*, *Climatic Change* 45: 75-102
- Keller K., Bolker B. M., & Bradford D. F. (2004), *Uncertain climate thresholds and optimal economic growth*. *Journal of Environmental Economics and Management*, 48, 723–741.
- Kjellstrom T., Kovats R.S., Lloyd S.J., Holt T., Tol R.S.J. (2009), *The Direct Impact of Climate Change on Regional Labor Productivity*, *Archives of Environmental & Occupational Health*, Vol. 64(4), 217-227.
- Kovats R.S. and Lloyd S.J., (2011), *Climate Change Impacts on Health in Europe*, Deliverable D2E.2, *ClimateCost* project.
- Kriegler E., Hall J.W., Held H., Dawson R., Schellnhuber H.J. (2009), *Imprecise probability assessment of tipping points in the climate system*, *Proceedings of the National Academy of Sciences USA* 1-6.
- Lenton T.M., et al. (2008), *Tipping elements in the earth's climate system*. *Proceedings of the National Academy of Sciences USA* 105:1786–1793.
- Manne A. and Richels R. (2005), *Merge: An Integrated Assessment Model for Global Climate Change, Energy and Environment*, 175-189.
- Marrouch W. and Ray Chaudhuri A. (2011), *International Environmental Agreements in the Presence of Adaptation*, Working Papers 2011.35, Fondazione Eni Enrico Mattei.
- Nordhaus W.D. 1994. *Managing the Global Commons: The economics of the greenhouse effect*. The MIT Press
- Nordhaus W.D. and J.G. Boyer 2000. *Warming the World: the Economics of the Greenhouse Effect*. The MIT Press
- Nordhaus W. (2007), *Accompanying Notes and Documentation on Development of DICE-2007 Model: Notes on DICE-2007.delta.v8 as of September 21, 2007*

- Nordhaus W. (2007) *A Review of the Stern Review on the Economics of Climate Change*, Journal of Economic Literature, Vol. 45, No. 3.
- Parry M., Canziani O., Palutikof J., van der Linden P., Hanson C. (eds.) (2007), *Climate Change 2007: Impacts, Adaptation and Vulnerability. Contribution of Working Group II to the Fourth Assessment Report on Climate Change*. Cambridge University Press
- Parry M. (2009), *Closing the loop between mitigation, impacts and adaptation*, Climatic Change, 96: 23–27
- Pearce D.W., Cline W.R., Achanta A.N., Fankhauser S., Pachauri R.K., Tol R.S.J. and Vellinga P.: (1996), *The Social Costs of Climate Change: Greenhouse Damage and the Benefits of Control*, in Bruce, J.P. Lee H. and Haites E.F. (eds.), *Climate Change 1995: Economic and Social Dimensions - Contribution of Working Group III to the Second Assessment Report of the Intergovernmental Panel on Climate Change*, Cambridge University Press, Cambridge.
- Roughgarden T., & Schneider S. H. (1999). *Climate change policy: Quantifying uncertainties for damages and optimal carbon taxes*. Energy Policy, 27, 415–429.
- Stern N. (2006), *The Economics of Climate Change: The Stern Review*, Cambridge University Press, Cambridge.
- Tol R.S.J. (2002), *Estimates of the Damage Costs of Climate Change*. Environmental and Resource Economics, 1(21) 47-73.
- Vafeidis A.T., Nicholss R.J., McFadden L., Tol R.S.J., Hinkel J., Spencer T., Grashoff P.S., Boot G. and Klein R.J.T., (2008) *A new global coastal database for impact and vulnerability analysis to sea-level rise*, Journal of Coastal Research, 24, 917-924.
- Van der Knijf J.M., Younis J. and de Roo A.D.P. (2010), *LISFLOOD: A GIS-based distributed model for river-basin scale water balance and flood simulation*, International Journal of Geographical Information Science, 24(2), 189-212.
- Warren et al. (2006), *Spotlighting impacts functions in integrated assessment*, WP 91, Tyndall Centre for Climate Change Research.
- Weitzman M.L. (2009), *On Modelling and Interpreting the Economics of Catastrophic Climate Change*, Review of Economics and Statistics 91, (1), 1-19.

Weitzman M. (2001), *Gamma Discounting*. American Economic Review, Vol. 91, No. 1.

Wright E.L. and Jon D. Erickson (2003), *Incorporating Catastrophes into Integrated Assessment: Science, Impacts, and Adaptation*, Climatic Change, 3(57), 265-286.

Yohe G., Andronova N., & Schlesinger M. (2004). *To hedge or not against an uncertain climate future*. Science, 306, 416–417.

Zickfeld K, et al. (2007), *Expert judgements on the response of the Atlantic meridional overturning circulation to climate change*. Climatic Change 82, 235–265

Is Geoengineering a viable option for dealing with climate change?

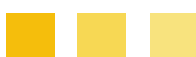
Emmerling J., Tavoni M.

Euro-Mediterranean Center on Climate Change - CIP Division, Italy

Abstract

The difficulty in implementing comprehensive policies aimed at reducing greenhouse gas emissions has led analysts and researchers to wonder about alternative strategies for dealing with climate change. Geoengineering – that is the deliberate reduction of the incoming solar radiation - has received increased interest in recent years as an alternative or complementary climate strategy to abatement of greenhouse gas emissions. In particular, the uncertainties about the magnitude and impact of climate change contributed to the vision of geoengineering as a last resort type of climate policy, which could render abatement in the short term dispensable. In recent research, we analyse the interaction between both types of climate policies and find that under uncertainty, substantial abatement in the medium and short term remains optimal under fairly general conditions due to the time lag until geoengineering options might be available.

Keywords: *Geo-engineering, climate policy, mitigation*



1. INTRODUCTION

The slow progress in climate change mitigation policies aimed at reducing greenhouse gas emissions has fuelled the discussion about alternative policy options in order to cope with the impacts from climate change. The better known one is adaptation, but most recently ‘climate geo-engineering’ has begun to attract increasing attention. In particular, geoengineering options which either remove carbon dioxide from the atmosphere (carbon dioxide removal or CDR) or counteract the temperature increase by deliberately managing incoming solar radiation (Solar Radiation Management or SRM) have been proposed and increasingly debated over recent years. These two geoengineering options differ fundamentally in terms of costs and effectiveness. While CDR strategies tend to be costly and slow in terms of temperature response, SRM has been argued to be a much more cost-effective solution since it can reduce the effects of global warming relatively fast (Matthews and Caldeira 2007).

The most widely discussed strategy for reducing solar radiation is through stratospheric aerosols. The reduction in solar radiation after volcanic eruptions has provided natural “experiments” as a basis for this strategy. In 1991, the eruption of Mount Pinatubo led to the injection of around 20 megatons of sulphur dioxide into the stratosphere leading to a decrease of global temperature of about 0.5°C in the years after the eruption (Soden et al. 2002). Based on these experiences, a large scale Solar Radiation Management scheme could offset global warming at a fraction of costs of abatement of greenhouse gas emissions (McClellan et al. 2012). It provides thus a potential game-changer for climate policy which has led to a polarizing debate, focussing on the cost-efficient potential to offset climate change and the political difficulties in climate policy negotiations on the one hand, or on the potentially severe consequences such as increased ozone depletion and continued damages from a higher CO₂ concentration on the other. Economists have contributed to the debate about risks and virtues of geoengineering, unsurprisingly finding mixed results and mostly relying on numerical simulations, see (Klepper and Rickels 2012) for an overview. The fundamental driver of the divergence of opinion in this debate resides in the assumptions about relative costs, damages, and the uncertainty about the parameters characterising geoengineering (Sterck 2011).

2. UNCERTAINTY OF GEOENGINEERING

Very few papers though have provided an explicit modelling of the uncertainty of geoengineering, with the exception of (Moreno-Cruz and Keith 2012). In recent research (Emmerling and Tavoni 2013), we use standard economic models of dynamic decision theory under uncertainty in order to assess the optimal climate policy under uncertainty with geoengineering. We deliberately take an optimistic view about the costs of geoengineering vis à vis abatement to study how much abatement should still be implemented even with a geoengineering option available in the future.

We analyse the optimal climate policy by means of abatement and geoengineering, where the latter is only available in the future and with uncertainty characterizing both the uncertainty of geoengineering as well as the climate. Our results suggest that under fairly general conditions, today's mitigation effort is decreasing but concave in the probability of success of geoengineering under a fairly general condition. Geoengineering does provide an alternative to abatement, but the uncertainty around its effectiveness makes abatement today respond slowly to the probability of success of geoengineering. The following graph illustrates the results for a reasonable calibration. If geoengineering were a certain option in the future, optimal abatement in the short run would be very low as soon as the effectiveness of geoengineering is slightly above zero as shown by the green curve. Under uncertainty (brown curve), however, the curve is concave in the probability of geoengineering showing a rather 'flat' relation as long as the probability of geoengineering being implemented and effective is not close to one. This shows that significant abatement reductions are optimal only if SRM is very likely to be effective.

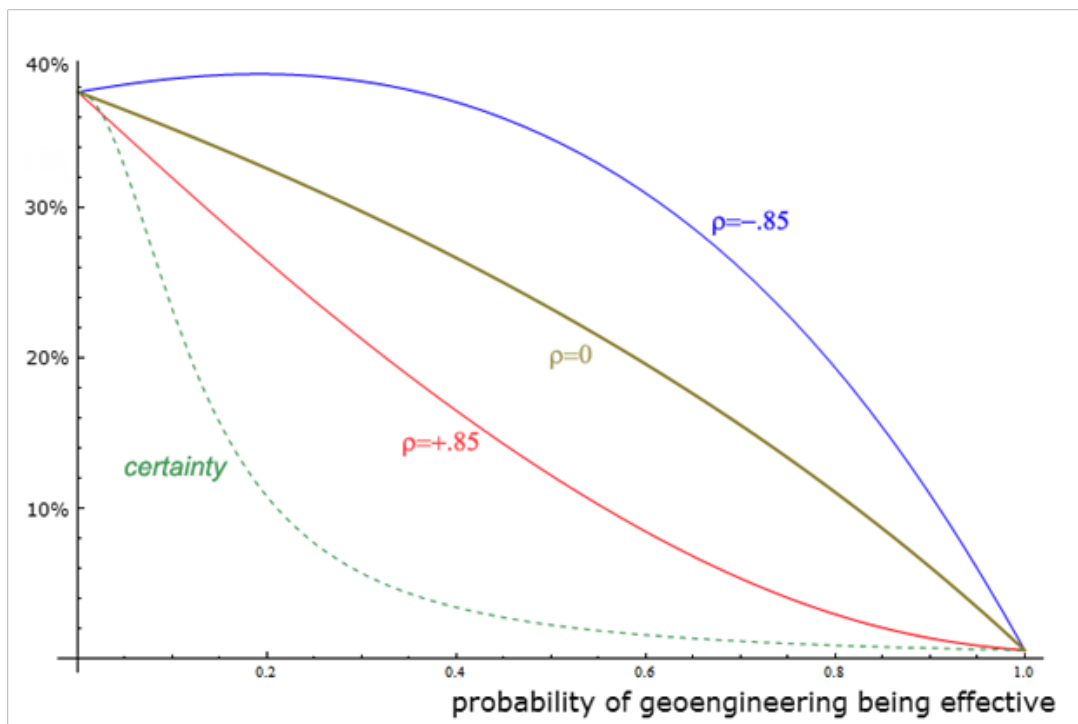


Fig. 1: Optimal abatement 2005-2050 in per cent of BaU emissions

We also investigate the potential insurance effect of geoengineering using a copula approach to model the relationship between the uncertainty about climate response and geoengineering, and are able to confirm the results for reasonable correlation structures between the climate and the effect of geoengineering. An “insurance” effect arises only if the relatedness between geoengineering becoming effective and severe impacts from climate change is very high and moreover if the probability of SRM becoming a viable option is large enough.

Figure 1 shows the results for different degrees of correlation (ρ) between the effectiveness of geoengineering and the climate sensitivity. It reveals that even for a considerable “optimistic” correlation structure that still a significant amount of abatement is optimal to implement.

3. NUMERICAL RESULTS WITH AN INTEGRATED ASSESSMENT MODEL

We confirm the results using a fully-fledged Integrated Assessment Model (WITCH) and find that the results carry over to a much more detailed set up. To assess the quantitative magnitude of the effect of uncertain geoengineering on the optimal abatement path, we integrate geoengineering as an option to reduce solar radiation through stratospheric aerosols. Specifically, we model million tons of sulphur (MtS) injected into the stratosphere to lead –if successful– to a negative radiative forcing of -1.75W/m^2 (Gramstad and Tjøtta 2010) per MtS. Moreover, we assume a stratospheric residence time of two years and consider a linear cost function at a cost of 10 billion USD per MtS, which lies within the broad range of estimated costs (Robock et al. 2009). Maintaining the optimistic viewpoint on geoengineering, we abstract from side-effects and damages associated with the deployment of geoengineering and do not consider damages linked to the CO₂ concentration such as ocean acidification.

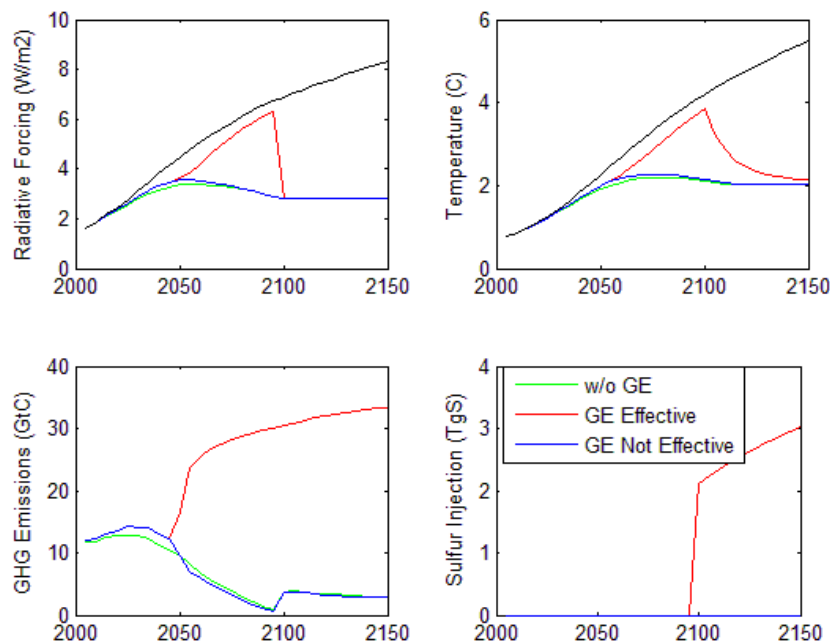


Fig. 2: IAM results with and without geoengineering, CEA policy

Considering a climate policy with limit of global warming to 2°C by the year 2100 and where geoengineering becomes available in 2050 with 50% chance, abatement goes to zero after that date in the case where geoengineering “works”. However, before 2050, the differences are rather small. The

optimal abatement path in the WITCH optimization under uncertainty is only slightly below the one without the geoengineering option. In both cases, significant abatement is carried out, both via energy efficiency measures as well as by deploying mitigation technologies such as CCS, renewables, nuclear power and low carbon fuels. The social cost of carbon in 2010 decreases only from 28.9 \$/tCO₂ to 19.4 \$/tCO₂ if geoengineering is possible. Thus, as in the case of the analytical model, hedging against the risk of geoengineering not being effective provides a strong rationale for carrying out abatement prior to uncertainty being resolved.

Running the model with different probabilities of geoengineering, we also confirm the theoretical findings of our analytical model that the relation between optimal abatement prior to resolution of uncertainty and the probability of success of geoengineering is concave. With respect to the magnitude, the level of abatement declines to almost zero only if the probability becomes very high: at a 80% probability of success of geoengineering, optimal abatement is approximately 60% of what would be carried in the absence of geoengineering.

Summing up, our research provides a strong argument for maintaining mitigation policies even when considering a very optimistic viewpoint on the potential of Geoengineering. This is due to the dynamic nature of the decision problem. We also show that our results hold even when we explore the relation between the uncertainty about geoengineering and the climate, as a way to assess the insurance value of geoengineering. While further research is a prerequisite to assess whether there will be a viable geoengineering option at some point in the future, the results suggest that for the time being, geoengineering does not warrant to be taken as a reason to significantly delay abatement effort from an economic point of view, even under optimistic scenarios about its feasibility and acceptability.

4. REFERENCES

- Emmerling J. and Tavoni M., 2013. *Geoengineering and abatement: a “flat” relationship under uncertainty*, FEEM Nota di lavoro No. 2013/31, Milan: Fondazione ENI Enrico Mattei.
- Gramstad K. and Tjøtta S., 2010. *Geoengineering - a part of climate change policies*, MPRA Working Paper No.27302, Munich.
- Klepper G. and Rickels W., 2012. *The Real Economics of Climate Engineering*. Economics Research International, 2012, pp.1–20.

- Matthews H.D. and Caldeira, K., 2007. *Transient climate-carbon simulations of planetary geoengineering*. Proceedings of the National Academy of Sciences, 104(24), pp.9949–9954.
- McClellan J., Keith D.W. and Apt, J., 2012. *Cost analysis of stratospheric albedo modification delivery systems*. Environmental Research Letters, 7(3), p.034019.
- Moreno-Cruz J.B. and Keith D.W., 2012. *Climate policy under uncertainty: a case for solar geoengineering*. Climatic Change, forthcoming.
- Robock A. et al., 2009. *Benefits, risks, and costs of stratospheric geoengineering*. Geophysical Research Letters, 36(19), p.L19703.
- Soden B.J. et al., 2002. *Global Cooling After the Eruption of Mount Pinatubo: A Test of Climate Feedback by Water Vapor*. Science, 296(5568), pp.727–730.
- Sterck O., 2011. *Geoengineering as an alternative to mitigation: specification and dynamic implications*, IRES Discussion papers – 2011035, Louvain.

Insurance and climate change adaptation: field experiments in Chilika Lagoon, India

Sharma A.^{1*}, Siva Chaudhry B.²

¹*Department of Economics and Statistics, University of Siena, Italy*

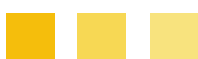
**Corresponding author: xsharma@gmail.com*

Abstract

In the context of adaptation to climate change, we shed light on two sociocultural aspects of fishing communities warrant attention. One, although economic theory regards human beings as risk averse, recent literature suggests that fishing communities may be less risk averse than individuals in other communities. Two, fishing communities in developing countries are often marked by social divisions on the basis of religion, ethnicity, tribe, clan etc. The implications of these two characteristics are of some concern, for risk-seeking persons are less likely to adapt, and social divisions can act as a barrier to community focused adaptation initiatives.

In a series of field experiments conducted at Chilika Lagoon, India, we examine fishers' (fishermen) attitude towards risk (measurable risk as well as uncertainty) under various levels of climatic vulnerability, and explore the implications of such attitudes in fishers' willingness to adapt through the purchase insurance protecting against climate change induced losses. We further examine whether social interactions in the socially divided region can lead to enhanced total insurance coverage under economies of scope.

Keywords: *Climate Change, Fisheries, Adaptation, Risk*



1. INTRODUCTION

Recent studies suggest that individuals in the fishing industry may be more drawn to risky propositions than most other populations. A stated-choice experiment by [1] in Sweden found evidence of risk-aversion in only 52% of studied fishers. [2], in a field study conducted in Tanzanian fisheries, classified only 32% of their subjects as risk-averse. We were interested in examining whether fishers approach decisions pertaining to climate change adaptation with similar attitudes towards risk. In the context of climate change adaptation, low levels of risk aversion are of obvious concern.

Other than their propensity for risk, other facets of fishing populations make adaptation initiatives particularly complex, and act as potential barriers to adaptation. We focus here on one such facet- the divisive and heterogeneous nature of fisheries in developing countries that make community driven adaptation measures especially challenging. These social divisions may appear in a number of forms. The Batticaloa fisheries of Sri Lanka, for example, serve as a common pool resource to members of three ethnic groups- the *Sinhalese*, the *Tamils*, and the *Moor*. In the artisanal fisheries off the coast of Cameroon such divisions are instead determined by tribe membership, with the *Yassa*, *Batanga*, *Babimbi*, *Douala* and *Bakuerians* tribes constituting the majority of traditional fishing settlements. We were interested in studying whether these divisions act as a barrier to adaptation. In particular, we were interested in assessing whether social interactions and economies of scope can increase adaptation rates in fisheries given the pervasive communal antagonisms that seem to define fishing communities worldwide.

Historically, India has been affected by a number of natural calamities. Climate change is likely to bring about an increase in both the number of adverse weather events as well as the extremity of damaging events. Consequently, the purchase of income insurance becomes a realistic option for vulnerable groups seeking to limit crippling income loss induced by adverse weather.

The purchase of this type of insurance is intervention that fits the very definition of an adaptation strategy. The temporal and geographical spread of losses makes the economic repercussions of adverse weather manageable for vulnerable populations in the risk pool. Insurance can thus be thought of as a community level adaptation initiative that curtails heavy economic damages at the individual level.

Using a framed field experiment [3], this article draws from a previous study examining the effect of ambiguous risk and coordination on climate change adaptation decisions of coffee farmers in Costa Rica [4].

In light of the conceptual framework presented here, we define the following four research questions: (1) Are Chilika fishers less risk averse than vulnerable communities in other regions of the world? (2) Are fishers in low income regions like Chilika uncertainty averse, and does uncertainty aversion has any bearing on the willingness to pay for income-insurance; (3) To what extent do economies of scope enhance community wide insurance coverage?; (4) Do the social divisions in regions like Chilika act as a barrier to adaptation?

2. CHILIKA REGION

Sprawling over an area of more than 1100 sq. km, the brackish water lake provides fishing resources to 68,128 adults and 54,211 children [5]. The majority of fishers belong to one of the six traditional fishing communities (subcastes)- *Khatia*, *Kandara*, *Tiara*, *Nolia*, *Niary* and *Gokha* [6]. Relationships between the subcastes are poor, and marked by frequent conflicts.

A mutual agreement between the region's subcastes dictates where in the lagoon each community is allowed to fish, what kind of fish species they are permitted to catch, and what kind of fishing gear they may use. Since climate change is one of the common threats facing Chilika, the readiness of fishers to participate in a cooperative response will determine the effectiveness of adaptation. The mutual agreement between fishing subcastes also specifies how many days each community is allowed access to the lagoon. The number of fishing days in the typical Chilika fisher's year is 238 (approximately 20 days per month). The number is fairly constant across all communities in the region. With worsening climatic conditions, it would seem reasonable to expect a decline in wellbeing of fishers as a consequence of a reduction of fishing days.

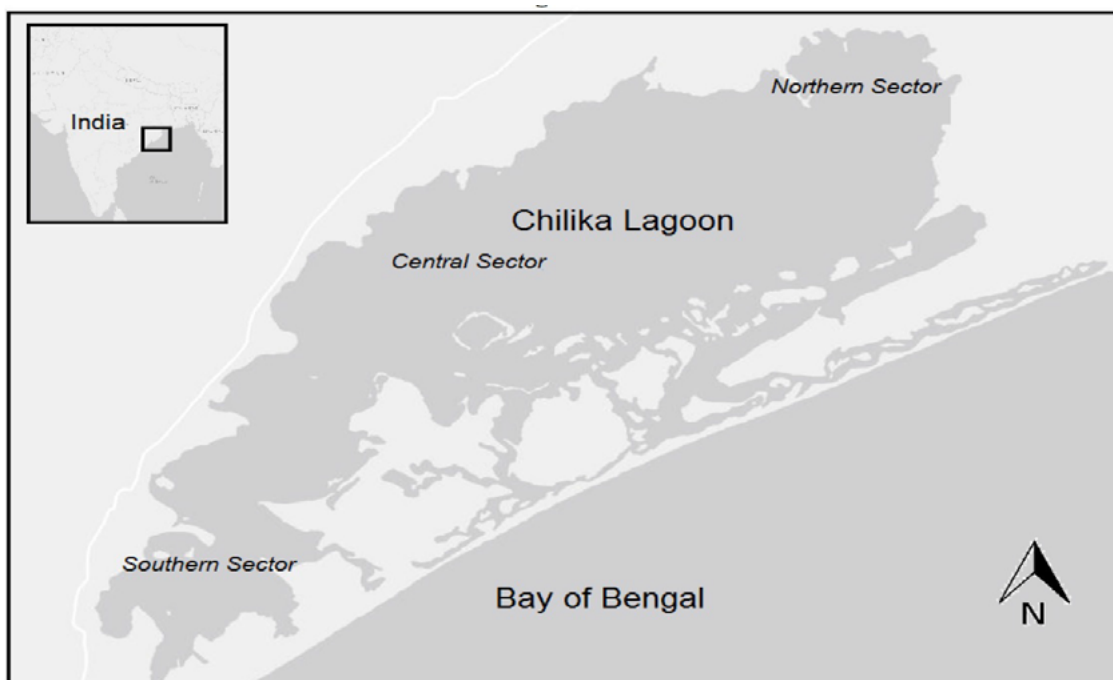


Fig.1 : Chilika Region

Variable	Population	Sample	Population	Variable	Category	Population	Sample
Community	Khatia	55%	68%	Age (Yrs)	All	43.5	42.1
	Nolia	4 %	7 %	Gender	Male	54%	54%
	Niary	6%	2%		Female	46%	46%
	Kandara	24%	14%	Education (Yrs)	All	6	7
	Tiara	3%	7 %				
	Gokha	3%	1%				
	Outsider	5%	1%				

Tab.1

3. EXPERIMENTAL DESIGN

Tab.2 summarizes the design of all the experiment. Subjects were randomly assigned into two person groups, with the letter A or B identifying each group member. The experiment was conducted over 9 rounds- the first four rounds constitute the baseline.

Rnd	Fisher A <i>Lost Fishing Days Faced Under Bad Outcome</i>	Fisher B	NI	ES	SI
Baseline Rounds					
1	5 days (Mildly Vulnerable)	20 days (Completely Vulnerable)	No	No	No
2	10 days (Moderately Vulnerable)	15 days (Severely Vulnerable)	No	No	No
3	15 days (Severely Vulnerable)	10 days (Moderately Vulnerable)	No	No	No
4	20 days (Completely Vulnerable)	5 days (Mildly Vulnerable)	No	No	No
Treatment: Uncertainty					
5	<i>Unknown Vulnerability</i>	<i>Unknown Vulnerability</i>	No	No	No
Treatment: Social Interactions					
6	10 days (Moderately Vulnerable)	15 days (Severely Vulnerable)	Yes	No	Yes
7	10 days (Moderately Vulnerable)	15 days (Severely Vulnerable)	Yes	Yes	Yes
8	10 days (Moderately Vulnerable)	15 days (Severely Vulnerable)	Yes	Yes	No
9	10 days (Moderately Vulnerable)	15 days (Severely Vulnerable)	Yes	No	No

Note: The probability of a bad outcome (an adverse weather event) is always 10%.

NI: Neighbor Information. Yes if subjects are informed of their partner's vulnerability level.

ES: Yes if economies of scope available, SI: Yes if social interactions permitted

Tab.2

In addition to a participation fee of INR 25, a random round was selected to make actual payments to subjects based on the choices they made. However, due to constraints in our budget, payments were made using a scale of 20:1.

All rounds followed the same basic structure- a certain scenario with a constant risk level, but varying vulnerability level was presented to the fishers, and they were asked to either purchase, or decline income-insurance at the specified cost. The occurrence/absence of adverse weather was simulated by drawing pieces of paper, marked and folded, from a bucket. The income of fishers was assumed to be 100 INR per day if fishing- an approximation of actual income in the region. Those who declined insurance risked losing income because of lost fishing days if an adverse weather event were to occur. In the absence of adverse weather, however, those that declined insurance received their full 20 day

fishing income. On the other hand, those that chose to purchase insurance were assured of their 20 fishing day income, regardless of weather outcome. They did, of course, incur the cost of insurance (200 INR, i.e, two days worth of wages)- a cost that would dissuade some fishers from purchasing insurance.

Subjects were not permitted to talk unless explicitly allowed to do so in a particular round. This was important because social interactions was one of the treatments of the experiment. In order to isolate the effect of social interactions, it was necessary to permit social interactions only in certain rounds.

4. EXPERIMENTAL BASELINE

In each of the first four rounds, fishers were asked to make a choice between purchasing or declining income-insurance given possible outcomes under two possible status of nature: good (no adverse weather event) and bad (an adverse weather event occurs), at a given probability level of of 0.10 of climate change induced adverse weather event. For simplicity, we held the probability level of an adverse weather event constant in all rounds (10%). We did, however, vary the individual vulnerability level of the subjects (as determined by number of days lost from the adverse weather event) throughout the experiment. We believe this to be a reflection of the reality- although the residents of a particular region face the same probability of experiencing adverse weather, the vulnerability level of each resident of is not the same.

Potential Days Lost From 20 Available	Net Days	Declines (in INR)		Purchases (in INR)		σ
		Good	Bad	Good	Bad	
5 days (Mild Vulnerability)	15 days	2000	1500	1800	1800	11.75
10 days (Moderate Vulnerability)	10 days	2000	1000	1800	1800	2.30
15 days (Severe Vulnerability)	5 days	2000	500	1800	1800	0.53
20 days (Complete Vulnerability)	0 days	2000	0	1800	1800	0
0-20 (Unknown Vulnerability)	Unknown	2000	Unknown	1800	1800	N/A

Notes: σ Coefficient of risk aversion if indifferent between declining and purchasing insurance

Tab.3

Fishers were told that if they were to decline income insurance, they would be able to continue fishing at the current rate of 20 days per month under good outcomes. However, in the case of a bad outcome, they faced a loss of fishing days. In Round 1, they faced a loss of 5 fishing days per month if the adverse weather event were to occur at the probability level. For our analysis, we classify a fisher who faces a loss of 5 fishing days as *mildly* vulnerable.

In Rounds 2,3 and 4 we progressively increased vulnerability levels- subjects faced a loss of 10 days, 15 days and 20 days respectively in each of these rounds in the event of adverse weather. We shall classify a fisher who may lose 10 fishing days as *moderately* vulnerable, a fisher who may lose 15 fishing days as *severely* vulnerable, and a fisher who may lose 20 fishing days as *completely* vulnerable.

Note that the completely vulnerable fisher has a coefficient of risk aversion 0, if indifferent between purchasing and declining income insurance (Round 4). This indicates risk neutrality. Therefore, subjects who decline insurance under complete vulnerability have a coefficient a of coefficient of risk aversion of less than zero, and can be considered risk seekers.

5. UNCERTAINTY AVERSION

Several studies have examined the role of uncertainty in insurance markets. [7] found that ambiguity aversion increases the demand for self-insurance, and raises the optimal insurance coverage. Round 5 was designed to test whether uncertainty in vulnerability levels can affect decisions to purchase insurance. In our baseline rounds, fishers knew exactly how many days they would lose in the event of bad weather- they knew how vulnerable they were. But what if they did not whether they were mildly, moderately, severely or completely vulnerable?

In the context of climate change, understanding general attitudes towards uncertainty (as opposed to known risk) is important in assessing the community's willingness to adapt. The question in this round was asked in a format identical to previous rounds- with the exception being that subjects were told that if an adverse weather event were to occur, they could lose 5,10, 15 or 20 days if the case of the bad outcome at the same probability level of 10%.

6. ROUNDS 6 – 10: SOCIAL INTERACTIONS

Subjects played the last four rounds of the experiment in groups. These rounds were designed to test our remaining hypotheses- that economies of scope, social interactions, and social divisions have an impact on fishing communities' adaptation decisions. The independent and joint effect of social interactions and economies of scope were studied using a 2x2 design. The impact of social divisions was studied by comparing insurance purchase decisions of groups where both members belonged to the same subcaste, with insurance purchase decisions of groups where both members belonged to different subcastes within the 2x2 framework.

Although subjects were aware of who they were partnered with in previous rounds, those rounds were administered on subjects independently. Our focus in rounds 6-9 moved away from individual decisions to group purchasing behavior. In Round 6, in addition to being informed of their own vulnerability, subjects were also made aware of the vulnerability of the subject with whom they were partnered. For all groups, Fisher-A was given a moderate level of vulnerability, while Fisher-B was assigned a severe level of vulnerability/ Interactions between group members was still not permitted, and the possibility of economies of had not been yet introduced.

Round 7 was identical to Round 6 except that economies of scope were now present. This was done by allowing group members the possibility of sharing the cost of insurance. In other words, if both chose to purchase coverage, the cost of insurance to each fisher was reduced to INR 100. If only one fisher chose to purchase insurance, the cost to her remained at INR 200. While both fishers were aware of each other's vulnerability, the absence of social interactions between fishers meant that they had no knowledge of the insurance purchase decision of their partner. As a result, a fisher considering coverage was forced to consider the prospect of paying the entire cost out of her own pocket.

In Round 8, we allowed for both social interactions as well as economies of scope. By allowing fishers to communicate, we were essentially giving subjects an opportunity to coordinate adaptation decisions to their advantage.

Finally, in Round 9, we still allowed subjects to interact but withdrew the possibility of economies of scope. This was necessary to isolate the effect of social interactions on insurance purchase decisions, and to complete the 2x2 experimental design.

7. RESULTS

181 subjects participated in the experiments. Out of these, results for 15 were inconsistent, and not included in analysis.

8. HOW RISK AVERSE ARE CHILIKA FISHERS?

Table 4 summarizes our sample's insurance decisions under the four levels of vulnerability. When mildly vulnerable, only 7 (4.2%) of the 166 subjects with consistent responses chose to purchase income insurance. Even at complete vulnerability, a mere 93(56%) purchased coverage. Using these numbers we can estimate the median level of risk aversion for our subjects to be between 0 and 0.53- a range that is close to risk neutrality. 44% of subjects declined insurance even under complete vulnerability, would be characterized by a degree of risk aversion < 0 , and may be described as risk-seeking.

Potential Days Lost From 20 Available	Declines	Purchases
5 days (Mildly Vulnerable)	159 (95.8%)	7 (4.2%)
10 days (Moderately Vulnerable)	132 (79.5%)	34 (20.5%)
15 days (Severely Vulnerable)	103 (62%)	63 (38%)
20 days (Completely Vulnerable)	73 (44%)	93 (56%)

Tab.4

We also conducted a logistic regression using the subjects' insurance purchase decision under complete vulnerability level as the dependent variable. An assortment of subject characteristics compiled during a pre-experimental survey were used as independent variables in the model.

Characteristic	Description	Mean	$\partial y / \partial x$	P-val
Majority	1 if belonging to majority community, 0 otherwise	0.572	0.602	0.174
Marital status	1 if married, 0 otherwise	0.861	0.507	0.360
# of Dependents***	Total number of dependents	1.373	0.583	0.005
Boat Owner***	1 if household at least partially owns boat, 0 otherwise	0.681	1.369	0.008
Age*	0 if under 35 , 1 if between 35 and 55, 2 if over 55	1.000	0.752	0.055
Gender**	1 if female	0.446	-0.849	0.036
Supercyclone	1 if affected by 1999 Super Cyclone	0.602	0.774	0.104
Income Level*	0 if under 37250 INR (quartile 1) 1 if > INR 3725 & < 4500 (quartile 2) 2 if > INR 4500 & < 6000 (quartile 3) 3 if > INR 6000 (quartile 4)	1.548	0.400	0.099
Education Level	Number of years of formal education	5.843	0.053	0.580
Pseudo R-square	0.279			
# of Subjects	166 (consistent responses only)			

Note: (i) Dependent variable is 1 if subject purchases insurance when "completely vulnerable". 0 if she declines coverage (ii) * denotes significance at 10% level, ** at 5%, and *** at 1% .

Tab.5

9. ARE CHILIKA FISHERS UNCERTAINTY AVERSE?

One of our objectives was to test whether our subjects are averse to uncertainty and if their insurance purchase decisions are altered when they're unaware of their vulnerability. According to the design of the experiment, a fisher facing uncertainty in vulnerability levels may lose 5, 10, 15 or 20 (if the extreme weather event were to occur) days she enjoys in a typical month in the absence of extreme weather events. For such a fisher, an expected vulnerability can be computed based on the standard expected value approach (12.5 fishing days). Our assessments of a subject's attitude towards uncertainty involves a comparison of this expected value under unknown vulnerability with the subject's vulnerability when levels of vulnerability are known.

Insurance purchase decisions under known vulnerability for those who purchase insurance under unknown vulnerability:

Mildly Vulnerable	Moderately Vulnerable	Severely Vulnerable	Completely Vulnerable	Risk Attitude	Number of Subjects
	Declines			Inconsistent	2
	Declines		Purchases	Uncertainty Averse	10
Declines		Purchases		Uncertainty Averse to Neutral	11
Declines		Purchases		Not Classifiable	21
	Purchases			Not Classifiable	7

Insurance purchase decisions under known vulnerability for those who decline insurance under unknown vulnerability:

Mildly Vulnerable	Moderately Vulnerable	Severely Vulnerable	Completely Vulnerable	Risk Attitude	Number of Subjects
	Declines			Not Classifiable	71
	Declines		Purchases	Not Classifiable	20
Declines		Purchases		Not Classifiable	18
Declines		Purchases		Uncertainty Loving	6
	Purchases			Inconsistent	0

Tab .6

An uncertainty averse fisher is more likely to purchase income insurance when there is uncertainty in the number of fishing days she may lose from an adverse weather event, than the corresponding situation where she knows how many days she may lose from such an event. Then, subjects who only purchase insurance at a known vulnerability level of severe or higher, but accept the offer to purchase insurance when faced with an uncertain level of vulnerability exhibit risk aversion. Of the 51 fishers that chose to purchase insurance when facing unknown levels of vulnerability, 11 chose to purchase insurance only when facing (known) severe vulnerability, and declined coverage at lower levels. An additional 10 chose to purchase insurance only when facing (known) total vulnerability, but declined coverage at lower levels. Therefore, 21 of the 51 fishers adapting under unknown vulnerability may be classified as uncertainty averse.

10. DO SOCIAL INTERACTIONS AND ECONOMIES OF SCOPE INCREASE REGIONWIDE COVERAGE?

In rounds 6-9, pairings resulted in 83 two person groups. Previously, we were concerned solely with individual adaptation decisions. We now focus on group purchase decisions. Graph 7 summarizes the group level purchase decisions for rounds 6-9.

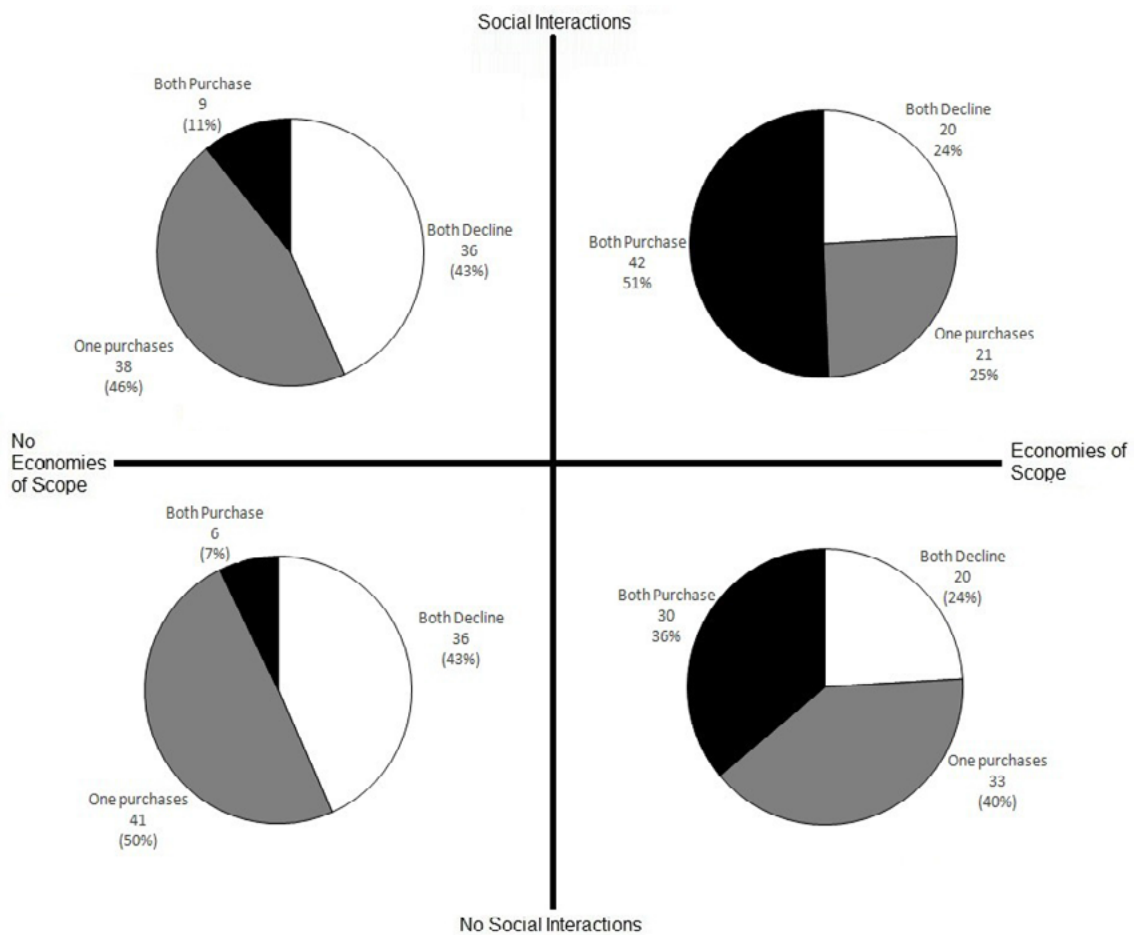


Fig.2

Round 7 was identical to Round 6, with the only exception being that economies of scope were made available. Social interactions, however, were still permitted. The results in this round were more encouraging - the number of groups in which both subjects chose to purchase insurance

increased to 30 (out of the 83 groups). This increase is statistically extremely significant (McNemar Test p -value < 0.01) compared with Round 6, when neither economies of scope nor social interactions were permitted.

In comparison, in Round 9, when social interactions were permitted, but economies of scope were not possible, the number of groups where both subjects chose to purchase insurance increased only by 3 from Round 6. Using the same McNemar Test, this increase is not statistically significant (p -value = 0.25).

Until now, we've presented the individual effects of social interactions and economies of scope on fishers' insurance purchase decisions. We've observed that while economies of scope have a significant effect on insurance purchase decisions, social interactions do not. But what if both social interactions and economies of scope were offered simultaneously? In other words, do social interactions offer any benefit when economies of scope are available? This was the objective of Round 8, and a question best answered by comparing the results of Round 8 (both economies of scope and social interactions available) with those of Round 7 (economies of scope not possible, but social interactions permitted). Once again we use the McNemar test and this time, find a statistically significant increase (p -value > 0.01) when both economies of scope and social interactions are available. Our results therefore indicate social interactions alone do not expand community wide adaptation initiatives. However if incentives are available- such as the realization of economies of scope, social interactions can greatly enhance overall adaptation.

11. SOCIAL DIVISION: A BARRIER TO ADAPTATION?

We compare the treatment responses of groups that are homogeneous (both group members belonged to the same subcaste), with the responses for groups that are heterogeneous (both members belong to a different subcaste). Out of the 83 total groups in the study, 33 were homogeneous, while the remaining 50 were heterogeneous. Figure 6.4 summarizes the number of groups in which both subjects purchase insurance under the four different experimental treatments for both group types- homogeneous and heterogeneous.

We've determined already that overall adaptation levels increase when social interactions are permitted given that an incentive, like economies of scope exists. But is this finding true for both homogeneous

and heterogeneous groups? We must once again compare the results of Round 8 with those of Round 7, but this time do so separately for heterogeneous and homogeneous groups. In 15 of the 33 homogeneous groups (45.45%), both group members chose to purchase insurance in Round 7, when economies of scope were available but social interactions were not permitted. When social interactions were permitted (Round 8), the number of homogeneous groups where both group members chose to purchase insurance increased to 21 (64.64%). The McNemar Test confirms the difference between the results of the two rounds to be significant (p-value).

Next, we turn our attention to the 50 heterogeneous groups. In 15 of these groups, both group members chose to purchase insurance in Round 7, whereas 21 of the 50 groups chose to purchase insurance in Round 8. The McNemar Test finds the difference between the two rounds for the heterogeneous groups, to be statistically significant (p-value = 0.04). We may therefore conclude that if incentives such as economies of scope are possible, social interactions have a definite role in increasing adaptation levels in both homogeneous and heterogeneous communities. We are, however, intrigued, by what appears to be seemingly very different adaptation rates between the homogeneous and heterogeneous groups in Round 8, when both economies of scope are available, and social interactions permitted. In 63.64% of homogeneous groups, both group members chose to purchase insurance. The corresponding figure in heterogeneous groups was only 42%. Fisher's Exact Test finds this difference to be significant at the 10% level, but not at the 5% level (p-value = 0.07).

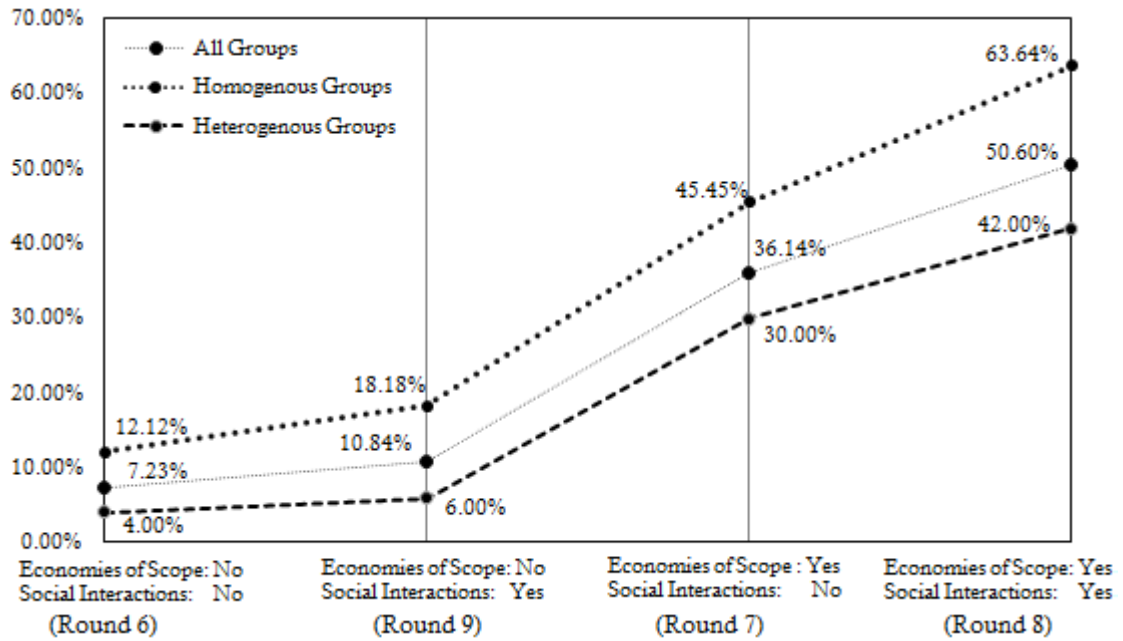


Fig.3

12. ACKNOWLEDGEMENTS

We would like to thank the invaluable research assistance provided by graduate students Subhranshu, Preet, Vishu and Suraj. Funding was through the University of Siena grants for academic visits for PhD students.

13. REFERENCES

- Eggert H. and Martinsson P. (2004) *Are Commercial Fishers Risk-Lovers?* Land Economics, Vol. 80, No. 4, pp. 550–560. (1)
- Eggert H. and Lokina R.B. (2007) *Small-scale fishermen and risk preferences*, Marine Resource Economics, Vol. 22, No. 1, p. 49. (2)
- Harrison G.W. and List J. (2004) *Field experiments*, Journal of Economic Literature, Vol. 42, No. 4, pp. 1009–1055. (3)
- Francisco A. , Carlsson F., and Naranjo M.A. (2011) *The effect of ambiguous risk, and coordination on farmers' adaptation to climate change A framed field experiment*, Ecological Economics, Vol. 70, No. 12, pp. 2317 – 2326. (4)
- Pattanaik S. (2007) *Conservation of Environment and Protection of Marginalized Fishing Communities of Lake Chilika in Orissa, India*, Journal of Human Ecology, Vol. 22, No. 4, pp. 291–302. (5)
- Sekhar N. (2007) *Social Capital and Fisheries Management: The Case of Chilika Lake in India*, Environmental Management, Vol. 39, pp. 497–505. (6)
- Alary D., Gollier C. and Treich N. (2010) *The effect of ambiguity aversion on insurance demand*, in “World Risk and Insurance Economics Congress”, Singapore. (7)

CLIMATE POLICY AND ECONOMIC ASSESSMENT

Strategies for adaptation and mitigation policies - II

Guidelines for the implementation of the Regional Adaptation Strategy in Lombardy (RAS)

Terradez Mas J.^{1*}, Rossetto M.², Ballarin Denti A.^{1,3}, Lapi M.¹, De Leo G. A.⁴

¹Fondazione Lombardia per l'Ambiente, ²Politecnico di Milano,

³Università Cattolica del Sacro Cuore, ⁴Stanford University (CA, USA)

*Corresponding author: jutemas@hotmail.com

Abstract

The present study is the result of one-year working experience on the definition of the guidelines towards the Regional Adaptation Strategy (RAS) in Lombardy, North of Italy. In particular, this research has the goal of I. providing a general overview of the vulnerability of the Lombardy region to the impacts of global climate change (GCC) with a list of preliminary possible adaptation measures; II. reviewing the strategic factors that should be taken into account in the definition of a comprehensive and effective adaptation strategy of Lombardy region. The present research shows that a number of socioeconomic sectors in Lombardy face multiple and often interacting impacts due to change in climatic conditions. In addition, we suggest that filling knowledge gap, ensuring quantitative impact assessment, guarantee a high level of stakeholder involvement and appropriate financing are all critical key factors to be taken into account to ensure a successful RAS in Lombardy.

Keywords: *climate change, adaptation strategy, regional, Lombardy*



1. INTRODUCTION

Lombardy, for its particular regional position and for its geographical, territorial and socioeconomic features, presents a high vulnerability to GCC impacts. Past trends and future scenarios suggest for the coming decades a marked increase in mean temperatures and in the frequency and intensity of heat waves events, a decrease in snow and ice cover, and changes in seasonal precipitation patterns such as a rainfall decrease in summer season (Table 1).

Table 1. Projections of future climate variability in Lombardy in the short (2021-2050 time period) and long term (2071-2100 time period).

DRIVER	Short term: 2021-2050 respect to 1961-1990		Long term: 2071-2100 respect to 1961-1990			
	Ref	A1B Change	Ref	B2 Change	A1B Change	A2 Change
Annual temperature	[1]	(+)	[1]		(+) 3.5-4 °C	
Seasonal temperature-Win	[1]	(+)	[2]	(+) 2.8±1°C		(+) 3.5±0.7 °C
	[4]	(+) 1.5°C				
Seasonal temperature-Spr			[2]	(+) 2.4±1.1°C		(+) 3.4±1.1°C
Seasonal temperature-Sum	[1]	(+) 2°C	[2]	(+) 4.1±1°C		(+) 5±1.5 °C
Seasonal temperature - Aut			[2]	(+) 3.2±1°C		(+) 4.1±1°C
Annual precipitation	[1]	(-)	[1]		(-)	
	[4]	(-) 5%				
Seasonal precipitation- Sum			[1]		(-) 40%	
Seasonal precipitation- win			[2]	(+) 10±11%		(+) 18±12%
Seasonal precipitation- Spr			[2]	(-) 4±24%		(-) 8±12%
Seasonal precipitation- Sum			[2]	(-) 18±18%		(-) 30±15%
Seasonal precipitation - Aut			[2]	(-) 7±15%		(-) 4±12%
Mean number of days with snow cover			[1]		(-) 10-50	
Mean number of summer days (>25 °C)			[1]		(+) 20-50	
Heat wave frequency*	[3]	(+) 3-9 times more frequent	[3]		(+) 15-20 times more frequent	
Heat wave amplitude**	[3]	(+) 2-2.5 °C	[3]		(+) 5-5.5 °C	

* Heat waves defined in [3] as the spell of at least six consecutive days with maximum temperatures exceeding the local 90th percentile of the control period (1961-1990). **The average peak temperature of the hottest heat wave per summer

- [1] ENSEMBLES Europe (ClimateAdapt), risoluzione 25 km2;
 [2] ENSEMBLES Europe (ClimateAdapt), risoluzione Nuts3 (Province);
 [3] PRUDENCE Northern Italia (Coppola and Giorgi 2010);
 [4] ENSEMBLES Europe (Fischer et al. 2010)
 [5] CIRCE Mediterranean basin (Gualdi et al. 2011)

The challenge of climate change requires two types of response. The first one contemplates the adoption of measures to reduce greenhouse gases emissions (i.e., mitigation strategies). The second one consists in measures and actions aimed to reduce vulnerability of natural and socio-economic systems, in order to increase their resilience towards the inevitable impacts of a changing climate (i.e. adaptation interventions).

With respect to the mitigation strategies, many efforts have been undertaken by industrialized countries to control the atmospheric pollutant and greenhouse gases emissions. Nevertheless, the goal of the United Nations Framework Convention on Climate Change (UNFCCC) to stabilize the atmospheric concentrations of greenhouse gases is still far from being reached. Moreover, even if at global level greenhouse gas emissions could be significantly reduced, the impacts of GCC would remain elevated for at least several decades due to the inertia of climate systems [5]. Consequently, there is an urgent need to evaluate the socioeconomic and natural systems' vulnerability to the likely consequences of climate change and to initiate subsequent adaptation strategies. It should be noted that, while mitigation actions require a joint response and coordination at the international level, adaptation initiatives could be instead defined and implemented at national and especially regional level, as suggested by the European Commission [6].

In the follow, we first present a brief review of the main impacts that such climatic stressors can exert on selected more vulnerable sectors, namely human health, soil defense, water supply, tourism, agriculture, mountain areas, biodiversity, energy, transportation and air quality. The likely impacts and the list of preliminary adaptation measures results from a participatory process with the main political actors of the Lombardy Region.

In the second section, we summarized the key strategic factors that should be taken into account for the definition of a comprehensive and effective adaptation strategy at regional level in Lombardy.

2. MAIN CLIMATIC CHALLENGE AND PRELIMINARY ADAPTATION DIRECTIONS PER SECTOR IN LOMBARDY

2.1 Human health: heat wave

Studies regarding future climatic variability projections agree with the fact that in the next decades heat waves could appear with major frequency, intensity and duration in the Mediterranean Basin [3]. Several local factors contribute to the increase of daytime heating and a lower night cooling especially in urban areas. As evidenced by a series of epidemiological studies [7] such changes can provoke an increase in public health emergencies. The regional healthcare sector will likely face an accentuation of these phenomena in terms of an increase in thermal shock mobility and so in hospital admissions, and hence to an increasing in health care costs. Aged people (over 65 years old) and chronically ill (specially cardio-respiratory ones) will likely constitute the social group most vulnerable to thermic stress [8].

Strategic directions for adaptation:

- Reinforce healthcare services in response to the major frequency and intensity of the summer heat waves;
- Increase efforts and resources in prevention and control considering explicitly climate change projections;
- Intensify efforts in reducing the 'heat urban island' effect in metropolitan areas (e.g. expand green spaces and urban parks, bulding bioclimatization, etc.);
- Promote campaigns of hygiene habits, food safety and healthy life style;
- Ensure adequate energetic supplies for air conditioning during periods of high demand.

2.2 Soil defense: increase in hydro-geological hazard

The change in rainfall patterns (increase of extreme events of heavy rainfall) and temperature (rise of freezing-level height), accompanied by the accelerated retreat of glaciers and melting of alpine permafrost, will likely increase the frequency and intensity of dangerous hydrological events (floods,

flash floods, landslides, avalanches) [9]. The derived impacts will concern mainly soil erosion, water management, transports and infrastructure protection.

Strategic directions for adaptation:

- Reevaluate the hydro-geological hazard mapping and integrated risk management protocols of the Lombardy territory by explicitly considering the expected changes in climate variables;
- Adequate current policies and protection systems in response to the expected increase in flood and flash flood hazards;
- Guarantee the necessary space for water streams, limit the extensions of sealed areas to ensure the natural soil capability of water retention and flood control;
- Adapt the present warning system and emergency management to the increase in frequency of flash flood events.

2.3 Water supply: increase in water stress

According to the main climatic projections, it is likely that the intensity and frequency of droughts events will increase in the coming decades [10]. Subsequent impacts on the hydrological cycle will affect both the offer and the demand of water resources in terms of quality and quantity. Water scarcity is likely to affect different socio-economic sectors of great importance, including agriculture (less availability for irrigation), electricity production (hydroelectric reservoirs and cooling of thermal power plants), tourism development and the management of wastewater and fresh water supplies.

Strategic directions for adaptation:

- Reduce water demand in hydro-demanding sectors;
- Optimize available water reservoirs;
- Optimize agriculture and farming systems and techniques (efficient irrigation, optimization of water resources distribution systems, adoption of conservative farming techniques to increase water storing capacity);

- Reinforce present monitoring systems of the state of the reservoirs and consumptions.

2.4 Tourism: rise of the limit of snow cover

The increase in temperatures projected for the coming decades will provoke a progressive decrease in the thickness and duration of snow cover and the elevation of the snow reliability line towards higher altitudes [11]. The ski areas are expected to face snow scarcity and will depend on artificial snow for their maintenance, increasing hence the need of water and energy supplies, with negative consequences at the environmental and economic level [12]. On the contrary, an increase in demand for summer tourism in mountain areas could be expected. However, increase in hydro-geological risk in mountain areas and proliferation of toxic algal blooms in lake could further reduce tourism attraction of Lombardy region [13].

Strategic directions for adaptation:

- Diversify touristic offer as an alternative to winter sports stimulating summer tourism;
- Promote the flexibility of existing ski areas activities by adapting the opening season to the real snow availability;
- Promote the application of cost-benefit analyses to existing ski areas to evaluate the environmental and economic suitability with regards to future scenarios;
- Include climatic consideration in the feasibility assessment of future ski areas, discouraging the use of massive artificial snow;
- Enforce the actual wear monitoring systems and natural risks protection (avalanches) for safeguard of alpine tourism.

2.5 Agriculture: water stress and diffusion of pests

The main climate threats on agro-ecosystems are represented by thermic and water stress on crops, loss of agricultural land due to the increase of hydrogeological instability, increase in pests and disease diffusion, modification of the suitable areas for cultures, increased in crop damage due to a higher

ozone exposure [14,15]. Jointly, these factors can lead to a decrease in crop productivity but can also offer opportunities depending on the crop variety [16].

Strategic directions for adaptation:

- Promote the introduction of new agricultural techniques to adapt the sector to the climate changes and to minimize extreme events damages to the cultivation (in harmony with the objectives of mitigation and management of water);
- Incentive good soil management practices to maintain its main functions: natural fertility, capacity to act as carbon sink, capacity to hold water and to protect biodiversity;
- Diversify regional cultivations adapting to the new climatic conditions, introducing more resistant varieties, adapting the present varieties to new suitable areas;
- Define intervention measures to support farmers during the CC adapting process, and the fight against plant diseases (e.g. providing ad hoc insurance mechanisms)

2.6 Mountain areas: melting of permafrost and glaciers

In the coming decades the melting of glaciers and of Alpine permafrost (permanently frozen soil at high altitudes) will undergo an intense acceleration [17]. The affected areas, stable so far, will become progressively more unstable and subjected to greater risk of collapse [18], avalanches and landslides in steeper slopes [19]. These events can endanger touristic localities, residential areas and others infrastructures (energetic, transport, skiing) especially in alpine valleys.

Strategic directions for adaptation:

- Update in a continuous way the cartography of risk in alpine areas explicitly accounting for the new climatic characteristics
- Analyze and update (if necessary) existing protection systems considering the evolution of natural risks and privileging the use of natural protection system in supplementary protection activities.

2.7 Biodiversity and protected areas: extinction of species, habitat modification and shifts in species distribution

Biodiversity and natural ecosystems provide valuable goods and services to the entire Lombardy society. Several researches agree that by the end of this century the main common driver of biodiversity loss and species extinctions on global level will be the change of climatic conditions [5]. GCC affects plants and animal's physiology and phenology, causing changes in the length of their development duration, changes in population's distribution and dimension and exotic species distribution.

Strategic directions for adaptation:

- Safeguard the most representative areas in terms of biology conservation, with special attention to the rare habitats or in delicate state of equilibrium;
- Reduce cognitive gaps and uncertainties in relation to the appearance, settlement, diffusion and fight against alien species and vector disease;
- Reduce fragmentation of habitats and ensure the progressive connectivity of regional protected areas;
- Expand existing protected areas to preserve those species which spatial distribution that is expected to be largely reduced due to GCC.

2.8 Energetic sector: decrease in hydroelectric production capacity

The present and future changes in the spatial and temporal distribution of rainfalls, the consequent river runoff reduction and the insufficient storage capacity of existing dams can significantly reduce the capacity of hydroelectric production in our region [10].

Furthermore, the increase in temperature of watercourses will provoke further limitations to the thermoelectric energy production, due to a lower efficiency of the power stations cooling systems especially during the summer season [20].

Strategic directions for adaptation:

- Promote information campaigns to raise awareness about energetic problems and encourage forms of energy saving and reduction of consumptions;
- Promote the use of passive conditioning of infrastructure, especially in summer, to reduce energy demand during for cooling purposes;
- Enhance the study of the sensitivity of the main sources of renewable energy to the new conditions (e.g. possible expansion of solar energy opportunities.)

2.9 Transports and mobility: impacts on transport infrastructure

The expected GCC will induce both impacts on transport infrastructures (road and rail artifacts stability, bridges resistance, asphalt endurance) [21] as well as effects on the dynamics of the sector in terms of transport modality [22].

Strategic directions for adaptation:

- Strengthen the existing monitoring and risk analysis plans to identify main vulnerabilities and priorities for transportation infrastructure;
- Promote the adoption of transport infrastructure that can resist meteorological extremes (thermally stable materials, draining asphalt);
- Combine the adaptation efforts with the promotion of the use of low emission transportation facilities;
- Review and update if necessary the authorization processes and normative bases of transport infrastructure's planning considering future climate changes.

2.10 Air quality: favorable condition for air Pollutants accumulation

Climatic variables can affect air quality at local and regional level by influencing the chemical reactions of pollutants production and transformation in the atmosphere, the altitude of pollutants mixing layer, and the rate of deposition of pollutants on soil. In particular, ongoing climate changes seem to favor

the formation and persistence of secondary pollutants such as ozone and fine particulate (PM₁₀ and PM_{2.5}) in the atmosphere [23].

Strategic directions for adaptation:

- Cover the cognitive gaps concerning climate change implications in atmospheric pollution (mechanism of influence of climatic variables on the dynamic of main atmospheric pollutants);
- Adequate the present surveillance and alarm systems to the future increase of acute atmospheric pollution situations;
- Strengthen technical measures to decrease emissions of fine particulate and precursors of tropospheric ozone;
- Ensure adequate warning systems during episodes of intense air pollution to reduce health risks for population.
- Promote soil management practices that can enhance the adsorption of pollutants and concomitantly ensure carbon sequestration.

3. KEY ASPECTS FOR IMPLEMENTING THE REGIONAL ADAPTATION STRATEGY IN LOMBARDY

3.1 Harmonization with the National Adaptation Strategy to climate changes

The RAS of Lombardy should carefully consider the information produced by institutional bodies and environmental agencies at the European level, analyze already implemented adaptation strategies formulated by EU Member States and by European regions, and work in closed coordination with the Italian National Strategy, which is currently in definition.

3.2 Cover knowledge gaps

A solid adaptation strategy must be based on solid scientific basis as well as on the best available scientific information. It is therefore necessary to cover the cognitive gaps about climate change and climate projections on a spatial-temporal scale coherent with the regional territory.

3.3 Definition of vulnerabilities of the territory

The process of vulnerability evaluation includes the quantification of the most significant impacts; the sensibility analysis of key systems and their resilience capacity and the integrated evaluation of the main risks linked directly or indirectly to climate changes.

3.4 Identification of priorities

Priority sectors and geographical areas for adaptation interventions must be evaluated in function of their intrinsic vulnerability, resilience, and the overall implications in population risk, infrastructures, and environmental goods and services, as well as on the potential costs and benefits of possible adaptation actions. Appropriate tools - including multi-criteria analysis, expert panels and Evaluation Impact Assessment studies- should be developed to support decision making process concerning adaptation priorities.

3.5 Sectoral and inter-sectoral action plans: multilevel governance

Effective and coherent adaptation policies require a high degree of consensus between the different levels of governance that operate in the same region. The planning and the implementation of the Lombardy's future regional adaptation strategy should face the challenges of vertical coordination (ensuring its complementarity with the inter-regional and national adaptation strategies) and of horizontal coordination (among distinct sectoral interests)

3.6 Integration into sectoral policies

The adaptation to climate change risks should be an essential component in all sectoral regional policies, mainstreaming them into existing programs at both national and regional levels. In this regard, we must consider the need for tools and methodologies in order to support the integration process of regional adaptation strategy.

3.7 Financing

The implementation of adaptation measures, within the framework of existing sectoral policies, must be based on a list of priorities within the budget available for individual sectors, in order to optimize the costs of adaptation. If additional financial resources are required, proposals should be formulated for EU funds (European Regional Development Fund, Cohesion Fund, Rural Development Funds, INTERREG funding and research funding from European Commission) as suggested by the recently published European Adaptation Strategy [24].

3.8 Operational and administrative management of the strategy

In the framework of the Regional Adaptation Strategy, a responsible unit for coordination, management and monitoring of the process should be identified. It should also be designed an institutional scheme in which a structure for coordination of the RAS is defined.

3.9 Monitoring and follow up of the RAS

The future Lombardy Regional Adaptation Strategy should include mechanisms to periodically revise the strategy and to propose next updates. In this regard, it would be appropriate to consider the drafting of specific protocols for the progress state and follow-up of the adaptation plan. They must include the periodic review of common strategies and sectoral adaptation initiatives.

3.10 Communication, awareness rising and participation

The communication, training and awareness rising processes, are social tools that, in addition to participation, are key elements to achieve the desired results from any adaptation strategy. Therefore, the progresses and results of the RAS should be disseminated and effectively communicated to all stakeholders and social actors involved, such as municipalities, organizations, associations and all citizens in general. Such process should also ensure an adequate perception of the identified risks and a satisfactory degree of acceptance of the adopted adaptation measures.

4. ACKNOWLEDGEMENTS

The Guidelines for the implementation of the Regional Adaptation Strategy in Lombardy (RAS) was performed by researchers of the Lombardy Foundation for the Environment (FLA) and assisted by experts of the University of Parma and Stanford University (USA). The activities were coordinated and supervised by the Department of Air Quality and Climate Change of Lombardy Foundation for the Environment, together with the Unit for Prevention and Air quality Protection from the DG Environment, Energy and Networks of the Lombardy Region, in particular, with the advice of Ing. Gian Luca Gurrieri and the official support of Ing. Debora Dazzi. We specially thank the very valuable contribution of the 44 technicians, engineers, officials and leaders of the Lombardy Region who participated enthusiastically to the formative workshops carried out for the implementation of these guidelines.

5. REFERENCES

<http://climwatadapt.eu/> (1)

Coppola E. & Giorgi F. (2010). *An assessment of temperature and precipitation change projections over Italy from recent global and regional climate model simulations*. International Journal of Climatology, 30: 11-32. (2)

Fischer E.M. & C. Schaer (2010). *Consistent geographical patterns of changes in high-impact European heat waves*. Nature Geoscience, 3:398-403 (3)

Gualdi S., Somot S., May W., Castellari S., Déqué M., Adani M., Artale V., Bellucci A., Breitgand J.S., Carillo A., Cornes R., Dell'Aquila A., Dubois C., Efthymiadis D., Elizalde A., Gimeno L., Goodess C.M., Harzallah A., Krichak S.O., Kuglitsch F.G., Leckebusch G.C., L'Heveder B.P., Li L., Lionello P., Luterbacher J., Mariotti A., Nieto R., Nissen K.M., Oddo P., Ruti P., Sanna A., Sannino G., Scoccimarro E., Struglia M.V., Toreti A., Ulbrich U., and Xoplaki E. (2011) *Future Climate Projections. In Regional Assessment of Climate Change in the Mediterranean*. A. Navarra, L. Tubiana (eds.), Springer, Dordrecht, The Netherlands (4)

IPCC (2007). *SRES: Special Report on Emission Scenarios*. (5)

White paper (2009). *Adapting climate change in Europe*. Options for EU actions. (6)

Report APAT-OMS (2007). *Cambiamenti climatici ed eventi estremi: rischi per la salute in Italia*. (7)

Michelozzi P., De Sario M., Accetta G., De Donato F., Kirchmayer U., et al. (2006). *Temperature and summer mortality: geographical and temporal variations in four Italian cities*. Journal of Epidemiology Community Health 60: 417-423. (8)

Beniston, M. (2007). *Linking extreme climate events and economic impacts: Examples from the Swiss Alps*. Energy Policy 35: 5384–5392. (9)

Lehner B., Czisch G. & Vassolo S. (2005). *The impact of global change on the hydropower potential of Europe: a model-based analysis*. Energy Policy, 33: 839- 855. (10)

Bigano A. & F. Bosello (2007). *Impacts of Climate Change on Tourism in the Italian Alps: An Economic Assessment*. Report for the ClimChalp Project. (11)

OECD Annual Report (2007). Organisation for Economic Co-operation and Development. (12)

Fondazione Lombardia per l'Ambiente (2008). *Progetto Kyoto Lombardia* (13)

Moriondo M., Giannakopoulos C., & Bindi M. (2011). *Climate change impact assessment: the role of climate*

- extremes in crop yield simulation*. *Climatic Change*, 104: 679-701. (14)
- Lobell D. B., Schlenker W., & Costa-Roberts J. (2011). *Climate trends and global crop production since 1980*. *Science*, 333, 616-620. (15)
- Mereu V., et al. (2008) *Land suitability and potential yield variations of wheat and olive crops determined by climate change in Italy*. Atti del X Congresso della Società Europea di Agronomia, Bologna. 2008. (16)
- Zemp M., Haeberli W., Hoelzle M. & Paul F. (2006) *Alpine glaciers to disappear within decades?* *Geophysical Research Letters* 33: 13. (17)
- Smiraglia C., Morandi G., Dialaiuti G. (2008). *Clima e ghiacciai. L'evoluzione delle risorse glaciali in Lombardia*. Consiglio Nazionale delle Ricerche. (18)
- Diolaiuti G., Bocchiola D., D'agata C., & Smiraglia C. (2012) *Evidence of climate change impact upon glaciers' recession within the Italian Alps*. *Theoretical and Applied Climatology*, 109: 429-445. (19)
- van Vliet M. T. H., Yearsley J. R., Franssen W. H. P., Ludwig F., Haddeland I., Lettenmaier D. P., & Kabat P. (2012). *Coupled daily streamflow and water temperature modelling in large river basins*. *Hydrology and Earth System Sciences*, 16: 4303-4321. (20)
- Giorgi F., & Lionello P. (2008). *Climate change projections for the Mediterranean region*. *Global and Planetary Change*, 63:90-104. (21)
- Caserini S., & Pignatelli R. (2009) *Cambiamenti climatici e trasporti: il contesto e gli impatti*. In Castellari S., Artale V. (a cura di) *I cambiamenti climatici in Italia: evidenze, vulnerabilità e impatti*. Bononia University Press, Bologna, 18: 535-556. (22)
- Jacob D. J. & Winner D. A. (2009) *Effect of climate change on air quality*. *Atmospheric Environment* 43:51- 63. (23)
- COM (2013). *An EU Strategy on adaptation to climate change*. (24)

Beyond stationarity in planning renewables: The CLIM-RUN experience for the Euro-Mediterranean region

Calmanti S. and Dell'Aquila A.*

UTMEA-CLIM, ENEA, Rome, Italy

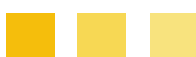
**Corresponding author: alessandro.dellaquila@enea.it*

Abstract

During the first phase of EU-FP7 CLIMRUN project, wind speed has been identified as a key climate variable of interest for the case studies on energy that cover the Greater Mediterranean region involving Morocco, Spain and Cyprus. Most of the interest concerning wind modelling focuses on the very short-range (nowcasting) and on seasonal forecasts, because the largest part of the manageable risk is concentrated on these time-scales. However, the interaction with stakeholders, especially in the energy sector, has highlighted the need for more in depth understanding of wind modelling capacities at a longer time scale, which may contribute to both site evaluation in the absence of very accurate wind atlases and on the assessments of risks that may affect the return on investments on longer time scale.

In this framework, climate experts involved in CLIM-RUN EU FP7 project are exploring the potential of seasonal to decadal climate forecast techniques (time-frame 2012-2040) and regional climate scenarios (time horizon 2040+) over the Mediterranean Region as a tool for assessing the impact of changes in climate patterns on the energy output of wind power plants. Subsequently, we will give here a brief overview of these techniques as well as first results related to wind projections for different sites across the Mediterranean Region. We will highlight that regional climate models have a large potential for enhancing the quality of climate projections in the presence of complex orography and in the proximity of coastal areas.

Keywords: *Climate services, Wind energy, Regional models*



During the first phase of CLIM-RUN EU-FP7, wind fields have been identified as a key climate variable of interest for the case studies on energy (Morocco, Spain) and natural hazards (wild fires, Greece).

According to the World Wind Energy Association the total wind generation capacity worldwide has come close to cover 3% of the world's electricity demand (<http://www.wwindea.org>), due to the relatively low costs of construction and maintenance, it's still attracting large investments.

Most of the interest concerning wind modelling focuses on the very short-range (nowcasting) and on seasonal forecasts, because the largest part of the manageable risk is concentrated on these time-scales [3]. More in detail, stakeholders surveys conducted during the initial phase of CLIM-RUN project have highlighted the interest in wind scenarios, as a potential component of the planning phase. By using climate model data the assumption of stationary wind regimes can be compared to other scenarios where large scale changes in atmospheric circulation patterns may affect local wind regimes. The interaction with CLIMRUN stakeholders, especially in the energy sector, has highlighted the need for more in depth understanding of wind modelling capacities at a longer time scale, which may contribute to both site evaluation in the absence of very accurate wind atlases and on the assessments of risks that may affect the return on investments on longer time scale.

Recent studies have demonstrated that regional climate models (RCMs) have a large potential for enhancing the quality of climate projections in the presence of complex orography [1] and in the proximity of coastal areas [1, 4]. Under CLIMRUN, we have moved one step forward and started the evaluation of wind modelling in the context of today's largest and most consolidated ensemble of RCMs produced during the EU-FP6 ENSEMBLES RCMs simulations over Euro-Mediterranean region [2].

Purpose of this activity is twofold. First, we wish to address the fundamental issue of uncertainty by highlighting the deficiencies of this particular ensemble of climate models in describing specific characteristics of the wind field over the Mediterranean. On the other hand we wish to build examples of the kind of climate information that can be extracted from such a huge - to a large extent still not exploited - resource of model data

The map below (Figure 1.) shows the projected changes in 10m wind speed over the Mediterranean. The map is obtained by averaging the mean annual wind speed of 16 regional climate models that have

produced climate scenarios for the ENSEMBLES project. According to those projections, most of the Mediterranean is expected to see a decrease in mean wind speed which would imply an overall loss of the expected productivity. In particular, a consistent negative trend of the monthly mean wind speed along the coast of North Africa (Figure 2), amounting to 5-10% of the corresponding long term average. Such climate scenarios may be an input for the more insightful and spatially accurate analysis that would be required to assess the potential changes in energy productivity at any specific site.

Climate modelers of the CLIM-RUN consortium are contributing to international coordinated efforts for the production of long-term climate scenarios, such as the Med-CORDEX initiative (www.med-cordex.eu) that will continue to provide more data for the assessment of the impact of climate variability and change on wind energy.

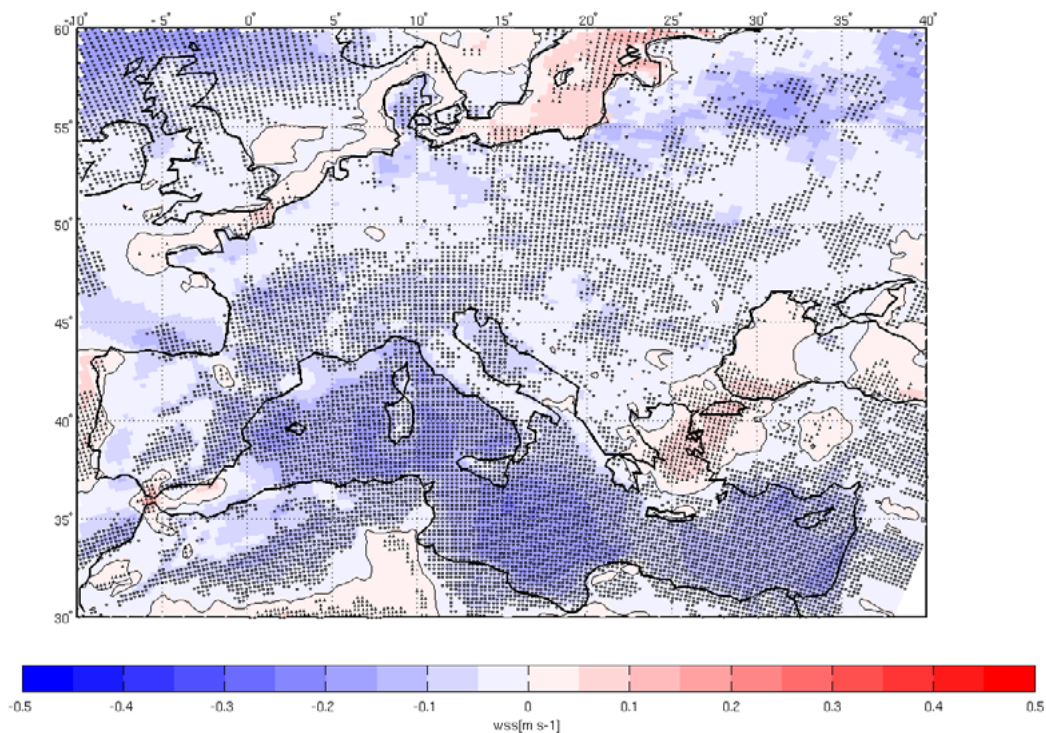


Fig. 1. Annual mean change in wind speed [m s⁻¹] at 10 m height projected by 16 regional climate models. Colours represent the average long term change in wind speed projected for the decade 2040-2050 with respect to 1990-2000. Model data are produced at an horizontal resolution of about 50Km. Hatched areas represent areas where more than 66% of the model agree in the sign of the long term change.

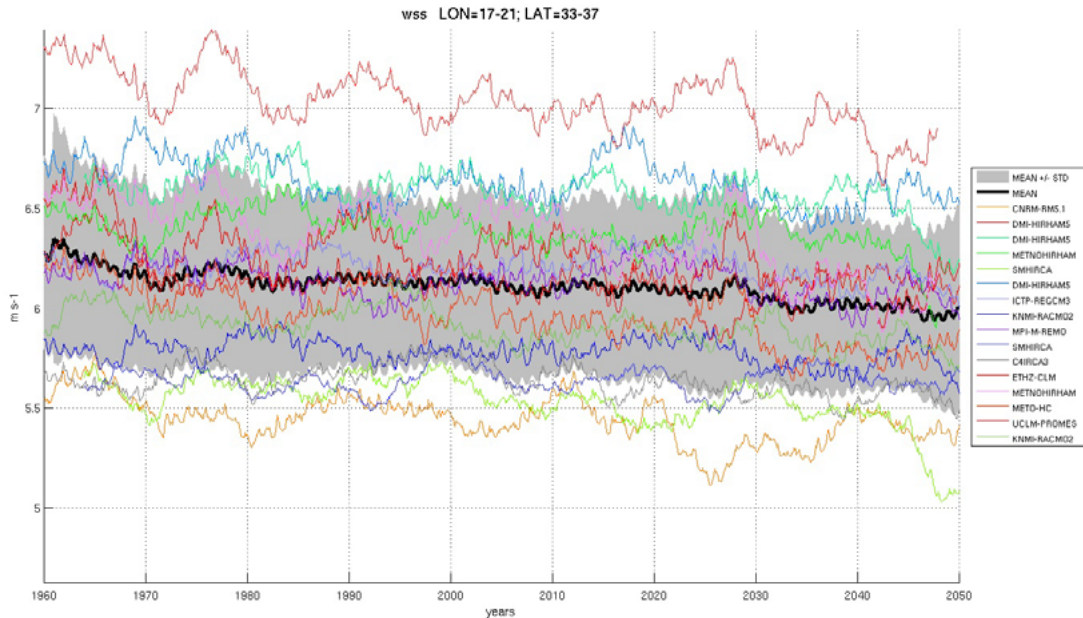


Fig. 2. Monthly wind speed simulated by 16 regional climate models in the area included between (17°E, 37°N) and (21°E, 33°N) over the coast of North Africa. Thin lines represent the monthly wind speed simulated by each model. The thick line indicates the ensemble average. The shaded area represents one standard deviation of the model spread around the mean.

ACKNOWLEDGMENTS

This work was supported by the FP7 European Commission project CLIMRUN under contract FP7-ENV-2010-265192

REFERENCES

- Artale V. et al. (2010). *An atmosphere-ocean regional climate model for the Mediterranean area: assessment of a present climate simulation*. *Clim. Dyn.* (1)
- Christensen J.H., Rummukainen M., Lenderink G., (2009). *Formulation of very-high-resolution regional climate model ensembles for Europe*. In: van der Linden P., and Mitchell J.F.B. (eds.). *ENSEMBLES: Climate Change and its Impacts: Summary of research and results from the ENSEMBLES project*. Met Office Hadley Centre, FitzRoy Road, Exeter EX1 3PB, UK. 160pp (2)

- Marquis et al. (2012). *Forecasting the Wind to Reach Significant Penetration Levels of Wind Energy*. Bull. of Am. Met. Soc. (3)
- Winterfeldt J. and Weisse R. (2009). *Assessment of value added for surface marine wind speed obtained from two regional climate models*. Mon. Wea. Rev. (4)

Eni's approach to mitigation and adaptation

Baldarelli T., Crisari A., De Filippo R., Fusco R. *, Ricci G.

ENI

*Corresponding author: rosanna.fusco@eni.com

Abstract

According to the IPCC¹, global temperature increase is causing several effects on the environment: in particular, extreme events are occurring more frequently and with a growing magnitude. On the other hand, in the next 20 years fossil fuels will continue to be fundamental to meet the increasing energy demand.

As a global energy company operating in about 80 countries and in areas subjected to extreme events, Eni is aware of its role related to reducing its carbon footprint as well as to facing higher risks generated by climate change effects.

Eni believes that the Oil & Gas sector must proactively collaborate with decision-makers and therefore, since a decade Eni has been contributing to the European and International debate on climate policy: post Kyoto, post 2020, EU-ETS², CCS³.

Moreover, in Eni's view the Oil&Gas sector should improve its GHG performances also beyond the pure compliance requirements; on its own, Eni has set up a Climate Strategy including compulsory and voluntary measures aimed at improving its carbon performances and developing mitigation and adaptation measures.

Among the GHG mitigation actions, flaring reduction, energy efficiency and voluntary validation⁴ of its GHG inventory and GHG targets can be highlighted. Thanks to its efforts in 2012 Eni was the only company of the energy sector in the CDP's⁵ *Carbon Performance Leadership Index*.

¹ Intergovernmental Panel on Climate Change

² EU – Emission Trading Scheme

³ Carbon Capture and Storage

⁴ Performed by a third party in accordance to the international standard ISO 14064.

⁵ The CDP (Carbon Disclosure Project) is an international, not-for-profit organization providing a global system for companies and cities to measure, disclose, manage and share GHG and other environmental informations. CDP works with the

Regarding adaptation, among other options (engineering, emergency management procedures and new insurance contracts), Eni strategically looks at the benefits generated by forestry conservation.

***Keywords:** Oil&Gas, Flaring, Energy Efficiency, Risk Management, Forestry*

largest corporations in the world to help them ensure that an effective carbon emissions / reductions strategy is made integral to their business. This effort taken seriously because of the size of the shareholders backing CDP - 655 institutional investors with \$78 trillion under management.



ENI'S APPROACH TO MITIGATION AND ADAPTATION

The IPCC predicts a significant increase in global mean temperature by the end of the century. Warming of the climate system is unequivocal, as it is evident also from observations of ocean temperatures, widespread melting of snow and ice, rising global average sea level, growing magnitude and frequency of extreme events.

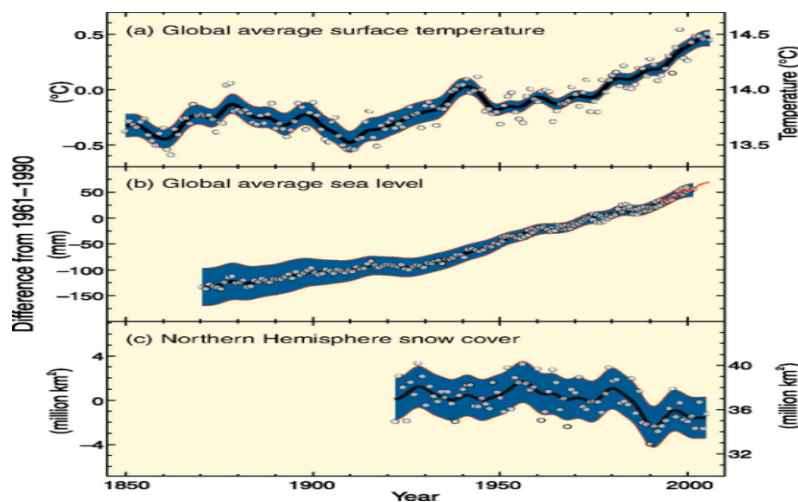


Fig.1: Changes in temperature, sea level and Northern Hemisphere snow cover (source IPCC)

In the future climate change will put global energy companies like Eni at a greater risk to experience various extreme events, since the company operates in about 80 countries and in a range of environments which are vulnerable and subjected to extremes (e.g. the arctic area, the Gulf of Mexico, Australia, etc...).

Moreover, according to the International Energy Agency, fossil fuels will dominate the energy supply up to 2030 and natural gas will become more and more important to foster the economic growth in a sustainable way.

Therefore since a decade Eni has assumed a leading role in the international arena in identifying and implementing innovative solutions for this challenge, not limiting its actions to pure compliance

activities. This commitment is pursued by reducing its carbon footprint and, on the other hand, mitigating the risks related to extreme events on its facilities and local communities. Eni’s approach to mitigation and adaptation foresees the interaction with decision-makers in shaping the Climate Policy and the implementation of a Climate Strategy that combines mitigation measures (in particular flaring down and energy efficiency projects) with the development of research into innovative technology (renewables and CCS) and the implementation of adaptation initiatives (special focus is given to water resources management and forestry conservation).

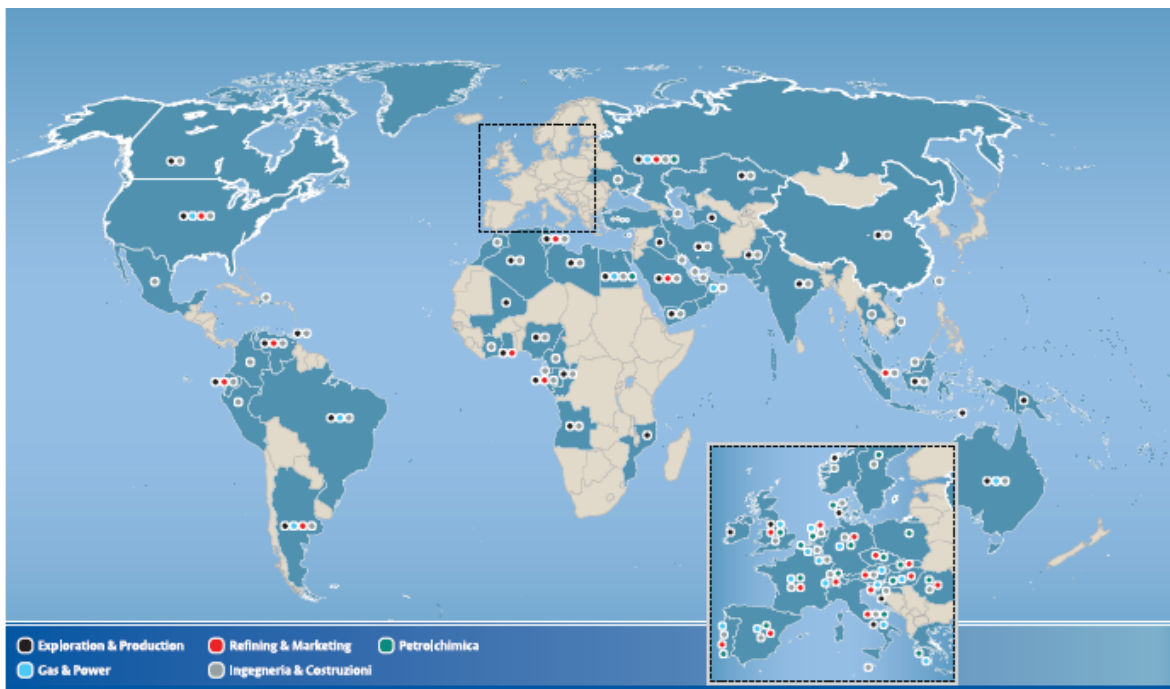


Fig. 2: Eni in the world

Regarding the *Climate Policy* Eni has been contributing to the European and International debate for 10 years and is currently committed to take part in the dialogue on the post 2020 climate regulatory framework. In Eni’s view the “post 2020 international climate agreement” should include emerging economies and expand the existing tools as well as identify new and more efficient options in order to

achieve concrete mitigation results and a more equitable development. The reform of Kyoto's CDM⁶ and its evolution to sectoral mechanisms⁷ is fundamental to involve major developing countries and the private sector in the post 2020 efforts. More generally, the launch of new emission trading systems (also in emerging economies) and sectoral mechanisms entails the necessity of designing a new framework that can govern under the UNFCCC aegis all these new programs.

Regarding the "EU Climate Policy post 2020," the EU-ETS shall be the central pillar of the European climate policy towards 2030, since it can drive industrial choices in favour of energy efficiency and low carbon fuels. EU-ETS should not be a self-standing scheme but positive interactions and synergies should be pursued with other major regulatory issues, such as renewables, energy efficiency and fuels taxation. Furthermore, it is important to sustain efforts to link the EU-ETS with new Emission Trading Schemes that are currently starting up like those in Australia, California, China, S. Korea.

ENI'S CLIMATE STRATEGY

Eni's Climate Strategy has been set up since early 2000s with the aim of reducing its GHG emissions and mitigating risks related to the global change. The measures are not only compulsory but mainly voluntary, thus witnessing Eni's pro-activity in facing the climate challenge:

- an ambitious flaring down program that will enable Eni to achieve zero flaring in 2017;
- challenging programs aimed at achieving continuous energy efficiency improvements in the industrial plants;
- adoption of certified energy management systems (ISO 50001) for industrial plants and buildings;
- promotion and replacement of high carbon content fuels with natural gas;
- research and development of new technological options, such as Carbon Capture and Storage and breakthrough renewables;

⁶ Clean Development Mechanisms

⁷ Offset programs regarding entire economic and industrial sectors like, for instance, steel and cement industry, households or transportation

- validation by a third party - in accordance to the international standard ISO 14064 - of its worldwide GHG inventory and GHG targets;
- promotion of energy-saving behaviours among employees, suppliers, consumers and customers;
- inclusion of climate change impacts (including the water stressed areas) in the risk management plans and procedures.

The most significant mitigation measures are represented by flaring down projects and energy efficiency programs. The *reduction of flaring* of associated gas produced with oil is a massive program (entailing some billion Euros) mainly located in Nigeria, Congo and Libya, and related to Eni's commitment to promote *Access to Energy* in Africa. Indeed, major investments in Nigeria and Congo have led Eni to reduce flaring emissions and provide the national grids with brand new power plants, currently providing 20% and 60% of the electricity of Nigeria and Congo.

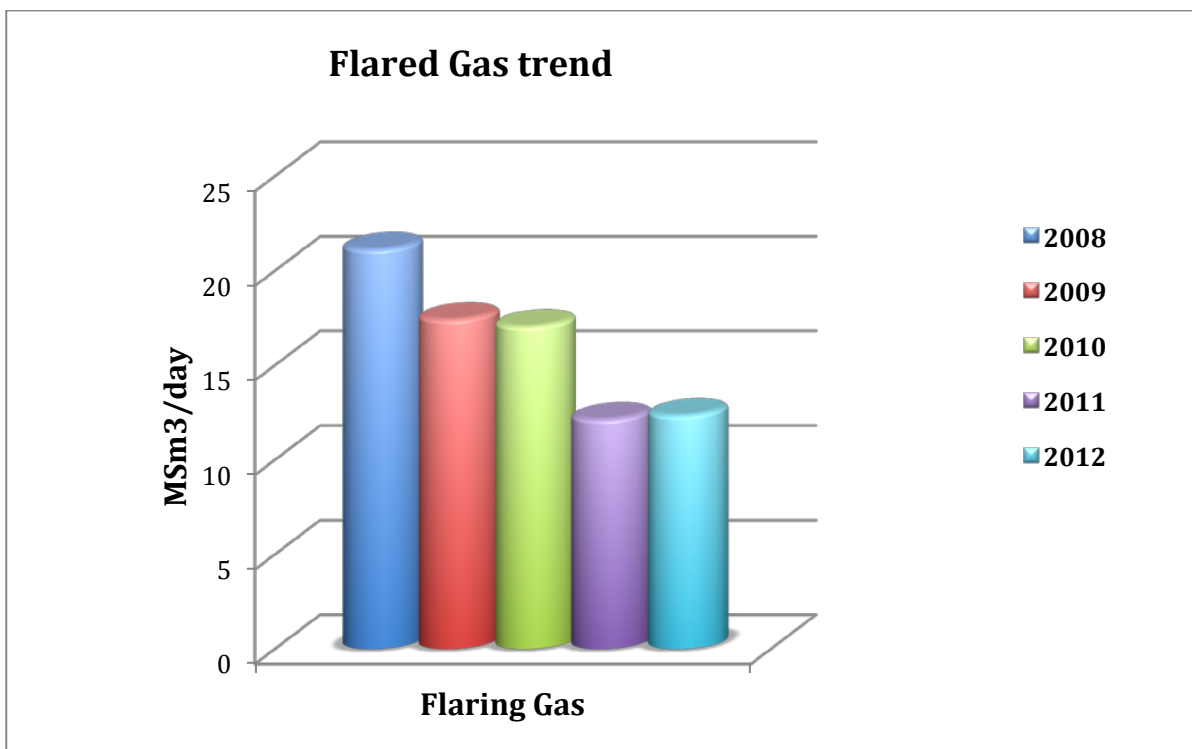


Fig.3 Flaring down in Eni

Regarding the *energy efficiency* Eni's programs are aimed at an efficient use of energy and find the best process solutions. Initiatives to improve energy efficiency include management initiatives such as the adoption of Energy Management Systems (EMS). The energy saving projects completed over the 2010-2012 period allow, under normal running conditions, a saving of 218 ktoe/year (almost 630 ktCO₂/year) with an estimated equivalent value of about €100 million. Moreover, the Project "Green Refinery" (investment of about € 100 million) will transform the Refinery of Venice in an innovative *bio-refinery* for the production of high quality bio-fuels, with a reduction of emissions of CO₂, SO₂ and NO_x from the refining process. Both projects allow a reduction in the consumption of fossil fuels and the use of biomass.

This commitment to improve its GHG performances has led *Eni in 2012 to be the only company belonging to the energy sector joining the Carbon Performance Leadership Index of the CDP.*

As per *adaptation* - either related to the protection of its operations and local communities - Eni has introduced the climate change issue in its risk management plans. The risk is firstly managed by identifying vulnerabilities and, afterwards, by properly assessing likelihood and magnitude associated to major risk factors in extreme environments like hurricanes, storms (South East Asia and Gulf of Mexico), water scarcity (Sahara), iceberg and snow storms (Alaska, W. Siberia or Barents sea). The subsequent step is the implementation of the appropriate risk management measures like new engineering choices for improving the robustness of installations, new procedures for facing emergencies caused by extreme events, specific insurance contracts for covering costs of damages.

In particular Eni has been addressing and managing *risks related to water for years*. Indeed areas that are susceptible to desertification and drought are growing and this issue has determined a different approach toward the protection of water resources for local communities. The risk assessment of water stressed areas foresees the identification and evaluation of water related risks near Eni's operational sites, taking into consideration social, ethical, environmental and industrial issues. Among the risk mitigation measures Eni is committed in particular to the recycling and re-injection of water produced with oil in order to reduce the use of fresh water for reservoir pressure maintenance. This action enables Eni to preserve fresh water resources for local communities in sensible areas like in particular the Sahara.

FORESTRY MANAGEMENT FOR MITIGATION AND ADAPTATION

Deforestation contributes as much as 18% to annual GHG emissions (IPCC 2007). Forests conservation is therefore one of the greatest environmental challenges and opportunities facing the world in the 21st century (World Resources Institute 2010). In particular REDD+ projects⁸ are important topics of the negotiations on post 2020 international climate policy regime. Many developed countries, organizations, private institutions and oil companies see REDD+ as a positive way to contribute to global mitigation efforts. REDD+ is also often described as an important factor in enabling adaptation to climate change, helping to protect biodiversity and reducing erosion and building resilience of local livelihoods and resources. With these perspectives the Oil&Gas sector is getting conscious of the opportunities related to forest management as an appropriate response to climate risks, and is thus developing in recent years some REDD projects in developing countries.

Eni considers that the implementation of specific projects can maintain or enhance the adaptive capacity of forests to global climate change. For this reason Eni with DIBAF (Department for Innovation in Biological, Agro-food and Forest systems of the University of Tuscia) is studying potential projects aimed at reducing deforestation (REDD+) of forestries and mangroves that can increase the carbon stocks (mitigation) and environmental safeguards (adaptation) in some developing countries where Eni operates. In addition, Eni agrees with IPCC that reducing both loss of natural habitat and deforestation can generate significant benefits also to biodiversity, soil and water conservation. Furthermore, in Eni's view REDD+ projects can have positive impacts on socio-economic development of local communities.

Regarding mangroves, their capacity to sequester carbon dioxide from the atmosphere is becoming increasingly recognized at international level. Indeed more than half (55%) of global biological carbon is captured by mangroves, sea grasses, salt marshes (UNEP 2009). Cutting down mangroves means releasing larger amounts of carbon into the atmosphere, a range of between 150 million to 1 billion tonnes of CO₂ that is emitted annually due to the destruction of mangrove forests globally. In some cases oil and gas deposits are found in site underlying mangroves and can cause their significant environmental damage. Therefore activities to re-establish or rehabilitate mangrove forests

⁸ Reducing emissions from deforestation and forest degradation in developing countries, and the roles of conservation, sustainable management of forests and enhancement of forest carbon stocks in developing countries

(reforestation) or to establish them in areas where they previously did not occur (afforestation) are interesting options for Eni.

Concluding, for Eni forests and mangroves management is a strategic option to reduce GHG emissions, mitigate climate risks and also preserve a variety of useful ecological, bio-physical and socio-economic functions of ecosystems in developing countries, thus delivering benefits to local communities.



Fig. 4: Mangroves

Climatic change impacts on energy sectors over Italian Region

Faggian P. *, Ronzio D., Decimi G.

RSE S.p.A. Milano - Italy

**Corresponding author: paola.faggian@rse-web.it*

Abstract

Future climate change impacts pose challenges to the security and efficiency of electricity supply. Future climate change scenarios over Italian Region have been elaborated on the basis of regional model outputs developed in the framework of European Project ENSEMBLES, together with gridded observation data from E-OBS. Some future projections at Italian Regions scale are available through the web-gis site CLIMED (<http://climed.rse-web.it>)

Keywords: *climate changes, ensemble means, heating/cooling degree days*



CLIMATIC CHANGE IMPACTS ON ENERGY SECTORS OVER ITALIAN REGION

Climate changes are becoming ever more evident: heat waves and droughts, flooding and desertification, melting glaciers and permafrost are extensively observed in the world and are causing serious impacts with enormous economic, environmental and social costs (EEA Report N° 12/2012).

In energy sector gradual changes in the climate and extreme weather events are likely to have adverse effects on the resilience of electricity networks and can potentially lead to interruptions of the power supply and cause extensive blackouts.

The infrastructures identified as vulnerable to long-term climate impacts are:

- Fossil power generation because of the loss of efficiency due to increased temperatures.
- Hydroelectric generation due to a reduce water supply if periods of drought increase.
- Renewable power generation due to increased storminess.
- Energy distribution system as the capacity of distribution network is reduced if temperatures and precipitation storminess increase.

Beside energy supply, power demand also is linked to several weather variables, particularly to daily temperature.

To investigate the influence of climate change over Southern Europe with focus Italian Region, future climate change scenarios have been elaborated on the basis of ten regional simulations with a horizontal resolution of 25 km and driven by the SRES A1B scenario forcing [1], provided by the ENSEMBLES Project (Tab.1) (<http://www.ensembles-eu.org>), together with gridded observation data from E-OBS (<http://eca.knmi.nl/dailydata>) [2].

Future scenarios have been elaborated using two *ensemble mean* methodologies: in the first one, only few models have been used, those with the best performances in the description of climate variability; in the second one all models have been considered, using a *bias correction* technique.

Climate change Projections for the thirty-year period 2021-2050 have been elaborated considering as reference period 1961-1990.

A significant warming is projected, above all in the summer season with a greater occurrence of extremely high temperature events (Fig.1). The precipitation change signal is of more difficult interpretation but it is found a likely precipitation decrease during the summer season above all in the Southern of Italy.

In addition, heating degree days (HDD) and cooling degree days (CDD) have been calculated [2] in order to examine the change in energy requirements.

HDD decrease substantially and CDD increase everywhere (Fig.2), especially in the Po Valley and in the Southern of Italy. This change can potentially shift the peak in energy demand to summer season with implications for the need for additional energy capacity and increased stress on water resources.

The web-gis site CLIMED (<http://climed.rse-web.it>) presents future projections at daily, monthly, seasonal, annual scales for each Italian Region.

Istituto	Driving GCM	Modello RCM	Simulazione	Acronimo
CNRM ⁽¹⁾	ARPEGE_RM5.1	Aladin	CNRM-RM5.1_ARPEGE	C&A
DMI ⁽²⁾	ARPEGE	HIRHAM5	DMI-HIRHAM5_ARPEGE	D&A
DMI	BCM	HIRHAM5	DMI-HIRHAM5_BCM	D&B
ETHZ ⁽³⁾	HadCM3Q0	CLM	ETHZ-CLM_HadCM3Q0	E&H
ICTP ⁽⁴⁾	ECHAM5-r3	ICTP-REGCM3	ICTP-REGCM3_ECHAM5	I&E
KNMI ⁽⁵⁾	ECHAM5-r3	RACMO	KNMI-RACMO2_ECHAM5	K&E
IIC ⁽⁶⁾	HadCM3Q0	HadRM3Q0	METO-IIC_HadCM3Q0	M&H
SMHI ⁽⁷⁾	HadCM3Q0	RCA	SMHIRCA_HadCM3Q3	S&H
SMHI	ECHAM5-r3	RCA	SMHIRCA_ECHAM5	S&E
SMHI	BCM	RCA	SMHIRCA_BCM	S&B

(1) Météo-France (CNRM)

(2) Danish Meteorological Institute (DMI)

(3) Swiss Institute of Technology (ETHZ)

(4) The Abdus- Salam International Centre for Theoretical Physics (ICTP)

(5) The Royal Netherlands Meteorological Institute (KNMI)

(6) UK Met Office, Hadley Centre for Climate Prediction and Research (HC)

(7) Swedish Meteorological and Hydrological Institute (SMHI)

Tab. 1 List of Regional Circulation Models considered in this study provided by ENSEMBLES Archive

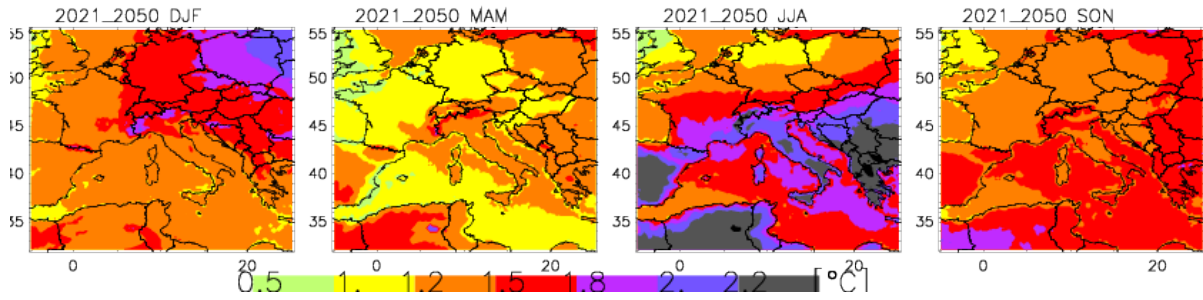


Fig. 1 Seasonal surface air temperature anomalies projected by 2021-2050, through an ensemble mean of ENSEMBLES models, compared to 1961-1990 scenario, ordered from left to right for winter (DJF), spring (MAM), summer (JJA) and autumn (SON)

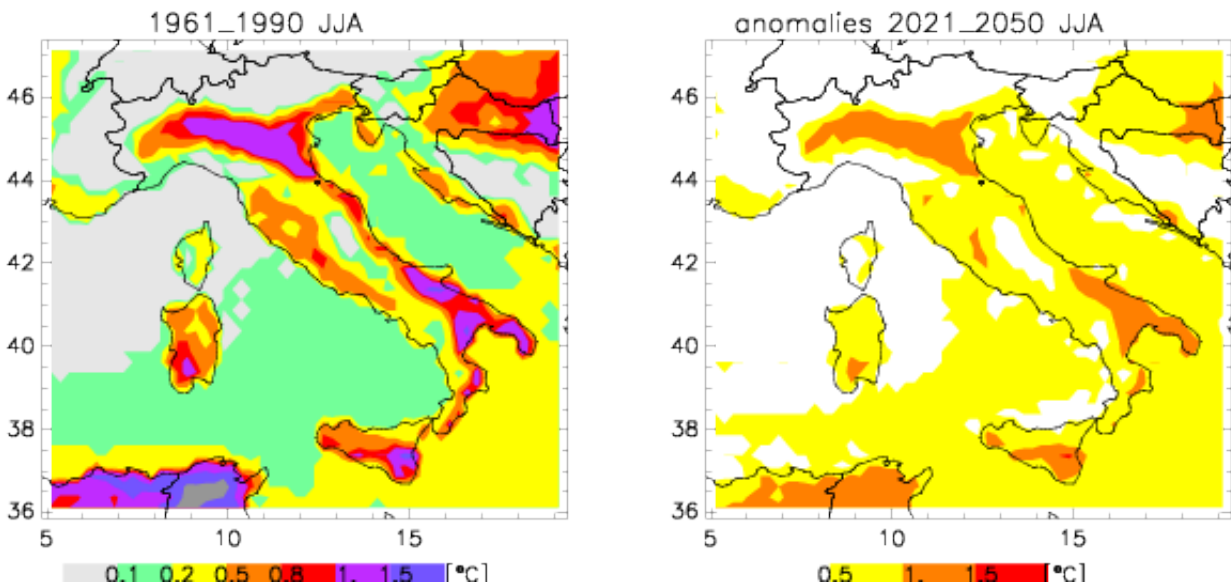


Fig.2 Summer CDD in reference scenario (left-hand panel) and CDD anomalies projected by 2021-2050 (right-hand panel)

ACKNOWLEDGMENTS

This work has been financed by the Research Fund for the Italian Electrical System under the Contract Agreement between RSE (formerly known as ERSE) and the Ministry of Economic Development - General Directorate for Nuclear Energy, Renewable Energy and Energy Efficiency stipulated on July 29, 2009 in compliance with the Decree of March 19, 2009.

The ENSEMBLES data used in this work was funded by the EU FP6 Integrated Project ENSEMBLES (Contract number 505539) whose support is gratefully acknowledged

We acknowledge the E-OBS dataset from the EU-FP6 project ENSEMBLES (<http://ensembles-eu.metoffice.com>) and the data providers in the ECA&D project (<http://www.ecad.eu>)"

REFERENCES

- Nakicenovic N., and Coauthors, 2000: *Special report on emissions scenarios: a special report of Working Group III in the Intergovernmental Panel on Climate Change*. Cambridge University Press, p 600. (1)
- Haylock M. R., Hofstra N., Klein Tank A. M. G., Klok E. J., Jones P. D., New M.: *A European daily high-resolution gridded dataset of surface temperature and precipitation*, J. Geophys. Res (Atmospheres), n.113, D20119, doi:10.1029/2008JD10201, 2008. (2)
- Giannakopoulos C., Hadjinicolaou P., Zerefos C., Demosthenous G. 2009, *Changing Energy Requirements in the Mediterranean Under Changing Climatic Conditions*. *Energies* **2**, 805-815; doi:10.3390/en20400805. (3)

CLIMATE POLICY AND ECONOMIC ASSESSMENT

Air quality and climate change mitigation policies

Including air pollutants' emissions in integrated assessment climate change modelling

Aleluia Reis L.^{1,2*}, Drouet L.^{1,2} and Tavoni M.^{1,2}

¹*Euro-Mediterranean Center on Climate Change - CIP Division, Italy*

²*Fondazione Eni Enrico Mattei, Italy*

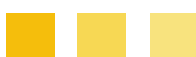
*Corresponding author: lara.aleluia@feem.it

Abstract

Climate change and air quality are two major topics in what concerns international policy. Climate change mitigation policies are based on restructuring the energy system in order to reduce the emissions of greenhouse. These actions have impacts beyond the climate change mitigation effects, namely in air quality policies. In this context, integrated assessment modelling is evolving towards the integration of air pollution emissions in order to account for potential synergies and trade-offs between global climate change measures and air pollution control strategies.

We discuss on the methodology to include air pollutants' emissions into the WITCH integrated assessment model. Additionally, we present the preliminary SO₂ emission results of the WITCH model.

Keywords: *integrated assessment, climate change, air pollution, synergies, trade-offs.*



1. THE CONNECTIONS BETWEEN AIR POLLUTION AND CLIMATE CHANGE

During a long period global climate change was seen as a phenomenon mainly driven by the emissions of carbon dioxide (CO₂) and other Greenhouse Gases (GHG), such as methane (CH₄) and nitrous oxide (N₂O)[1]. However connections between some air pollutants and climate exist and are more and more studied [2]. Aerosols are known to play an important role in the earth net radiative forcing, directly by changing the absorbing properties of the atmosphere and indirectly interfering with properties of the clouds. Organic Carbons (OC) and sulphur dioxide (SO₂) aerosols scatter the sunlight therefore cooling the earth's atmosphere. Moreover they increase cloud droplet concentration augmenting the cloud's albedo and lifetime by retarding precipitation. This effect is considered as a significant "mask" of the warming effects of the GHG emissions [2].

On the other hand, anthropogenic emissions of Black Carbon (BC) aerosols, also called soot, have absorbing properties and thus contribute to a warming effect. This type of particles has a characteristic black colour which absorbs light. A second effect of BC is the reduction of surface albedo when deposited, especially on ice and snow. The reduction of the ice albedo reduces the reflection of light and increases the melting of the ice due to a higher absorption [3].

Moreover, the temperature increase caused by the climatic change has consequences on the reaction rates of the pollutants in the atmosphere. Likewise the changes in global circulation and weather patterns influence the concentration and spatial distribution of the pollutants. Additionally, climate change might affect the biogenic emissions and photochemical smog [4] [5].

The relation between air pollution and climate change goes beyond the physical interplay of aerosols and the radiative forcing. The emission sources of GHG and of air pollutants are often identical, thus mitigation policies on climate change may also contribute to local air quality control policies [6] [7]. Contrarily air pollution control policies might lead to increasing efforts of climate change mitigation policies, due to the decrease in cooling aerosol emissions.

The negative effects, on human health and society, of both climate change and air pollution are well known and both topics have great importance in terms of policy.

Amongst the most known effects of climate change are the increase of extreme events like the frequency of cold and hot days, precipitation days, cyclones, floods, droughts and heat waves; sea level rising, the decrease of glacier and ice caps and changes in ecosystems [8]. Major concerns include the

impact on urban environments, where a great part of the population lives, such as sea level rise on coastal cities, degradation of built infrastructure, increase in energy use and the decrease of the quality and availability of water and other resources [9] [10]. Ultimately leading to the increase human mortality and morbidity due to extreme heat or cold, droughts, storms, water and air quality and the increase of infectious diseases incidence, such as Dengue and Malaria [11]. In what concerns air pollution, it is found to fasten the degradation of materials, to affect ecosystems reducing crop yield, and to increase mortality and morbidity by aggravation of respiratory and heart diseases and lung cancer [12] [13] [14]. The effects of air pollution are more damaging in cities, where the population exposure is higher and several air quality standards are still breached [15].

In terms of international policy, also both topics are dealt separately, examples of that are the UN Framework Convention on Climate Change and the Convention on Long-Range Transboundary Air Pollution [16].

Despite the links between these two environmental problems and their importance, integrated assessment models tend to treat them separately, using different methodologies and focuses [6]. Historically, air pollution management tends to be based on End Of Pipe (EOP) measures which normally are pollutant specific. Climate change mitigation, on the other hand, focuses on the management of fuels shares and energy technological options [1]. Additionally climate change mitigation policies are often in contrast with local and regional policy objectives, due to the global and long term objectives characteristic of climate change. In this context the success of climate change policies would benefit greatly from a deeper knowledge of the economic and environmental implications of climate change policies in air quality.

Accordingly integrated assessment models are evolving towards the integration of air pollutants' emissions. In this context, we present a methodology to incorporate this relationship within the World Induced Technical Change Hybrid (WITCH) model.

2. OBJECTIVES

The ultimate goal of this study is to quantify the contribution of climate change mitigation to the achievement of air pollution goals. The inclusion of the air pollution emissions which are relevant for climate change interactions allows for the quantification of the air pollution abatements caused by stringent climate mitigation. Additionally, this model configuration permits to explore which are the climate policies that lead to the greatest synergies with air quality policies which ultimately will lead to an increase in human health.

Moreover, as previously mentioned, the relationship between climate and aerosols can generate conflicts between air quality objectives and climate targets. This happens due to the possible trade-offs between the cooling effects of some air pollutants and the temperature targets of the climate global policies. These trade-offs are still uncertain and should be better evaluated and analysed. Finally the model will be prepared to estimate the amount of investment that is also contributing to reduce air pollution. This will provide a picture of the importance of integrated policies in achieving air pollution reductions.

3. THE WITCH ENERGY-ECONOMIC-CLIMATE MODEL

The WITCH model is an economic growth model designed to study optimal economic and climate change policies [17]. The energy-economic system covers the whole world, grouping the countries into sub-regions which share economic, energetic and/or geographical characteristics. The energy sector is well represented and it includes electric and non-electric use, six types of fuels and seven electricity generation technologies. The climate module is connected to the economic system using a damage function. This function uses the CO₂ emissions generated by the economy to derive a temperature differential (increase) that feeds back into the model as an economic gain or loss of a given region. Additionally, the model accounts for acquired technological knowledge due to experience and also for research and development investments to increase energy efficiency and reduce costs of biofuels.

The model has been used in several economic and climate change policy studies [18] [19] [20]. In this study we propose to incorporate the air quality pollutants (OC, BC, SO₂, Nitrogen oxides (NO_x), Particulate Matter (PM), Non-Methane Volatile Organic Compounds (NMVOC) and carbon monoxide

(CO) and ammonia (NH₃) into the WITCH model endogenously, i.e. based on the temporal evolution of the model variables.

4. ENDOGENOUS EMISSIONS OF AIR POLLUTANTS

Anthropogenic emissions of air pollutants can be associated with a given economic activity, for instance the NO_x from fuel combustion can be associated with the combustion of fossil fuels and a given burning efficiency [21] [22]. Likewise emissions of SO₂, OC and BC can be seen as a function of the sectorial or technological activity [23] [24]. An activity is the quantification of a process which leads to emissions (e.g. fuel combusted or product produced) [22]. In the WITCH model we use the activities related with the fuel use and the type of electricity generation technologies in order to compute the emissions E of pollutant p at time period t according to:

$$E_p = \sum_s A_s ef_{s,p}(t),$$

where $ef_{s,p}(t)$ is the controlled emission factor for activity category s and for pollutant p .

Another method to incorporate pollutants, about which little information on emission factors is known, is to use the emissions of pollutants which share the same emission sources as a proxy, as for example PM as a proxy for OC and BC [25]. Although in this case the fraction of OC or BC in PM must be known for each source category.

In order to account for EOP options, a removal efficiency rate should be added. These rates can be stipulated values found in literature [26], or they can be simulated as a function of Gross Domestic Product (GDP), where it is assumed that the air pollution controls are a function of income [27]. Accordingly, the controlled emission factor is then given by [22]:

$$ef_{s,p}(t) = ef'_{s,p} (1 - fc_{s,p}(t)),$$

where $ef'_{s,p}$ is the uncontrolled emission factor and $fc_{s,p}(t)$ is given by [27]:

$$f c_{s,p}(t) = \frac{f \max_{s,p}}{\left(1 + e^{-\frac{c}{\tau}(GDPcap - GDPcap_0)}\right)},$$

where $f \max_{s,p}$ is the maximal control fraction, c is a known constant, τ is the range of GDP per capita where 10 to 90% of the control happens, $GDPcap$ is the GDP per capita and $GDPcap_0$ is the point at which the $f \max_{s,p}$ is half. In this context the control might mean EOP measures or reduction of sulphur content for the case of SO_2 pollutant.

These methodologies are essential to macro-economic-climate-air modelling, where data is often scarce, although they underlie approximations, and more complex and complete methods may be considered in the future.

5. PRELIMINARY RESULTS

We show some preliminary results of the WITCH model for SO_2 . These results are based on the RCP 8.5 scenario [28]. The emitting regions on the WICTH model are organised as detailed in Tab. 1.

Region	Countries
cajaz	Canada, Japan, New Zeland
china	China, including Taiwan
esia	South East Asia, including Indonesia
india	India
kosau	South Korea, South Africa, Australia
laca	Latin America, Mexico and Caribbean
mena	Middle East and North Africa
neweuro	EU new countries + Switzerland + Norway
oldeuro	EU old countries
sasia	South Asia
ssa	Sub Saharan Africa
te	Non-EU Eastern European countries, including Russia
usa	United States of America

Tab. 1- WITCH world Regions.

Fig. 1 presents the sectorial results of SO₂ emissions for each of the WITCH regions. It shows that for the case of SO₂ the energy related sector, which includes emissions from power plants, energy conversion, extraction, and distribution, is the greatest contributor. The energy related sector is followed by the Industry sector, which comprises industrial combustion and processing. These are sectors witch are endogenously related to the WITCH economical model.

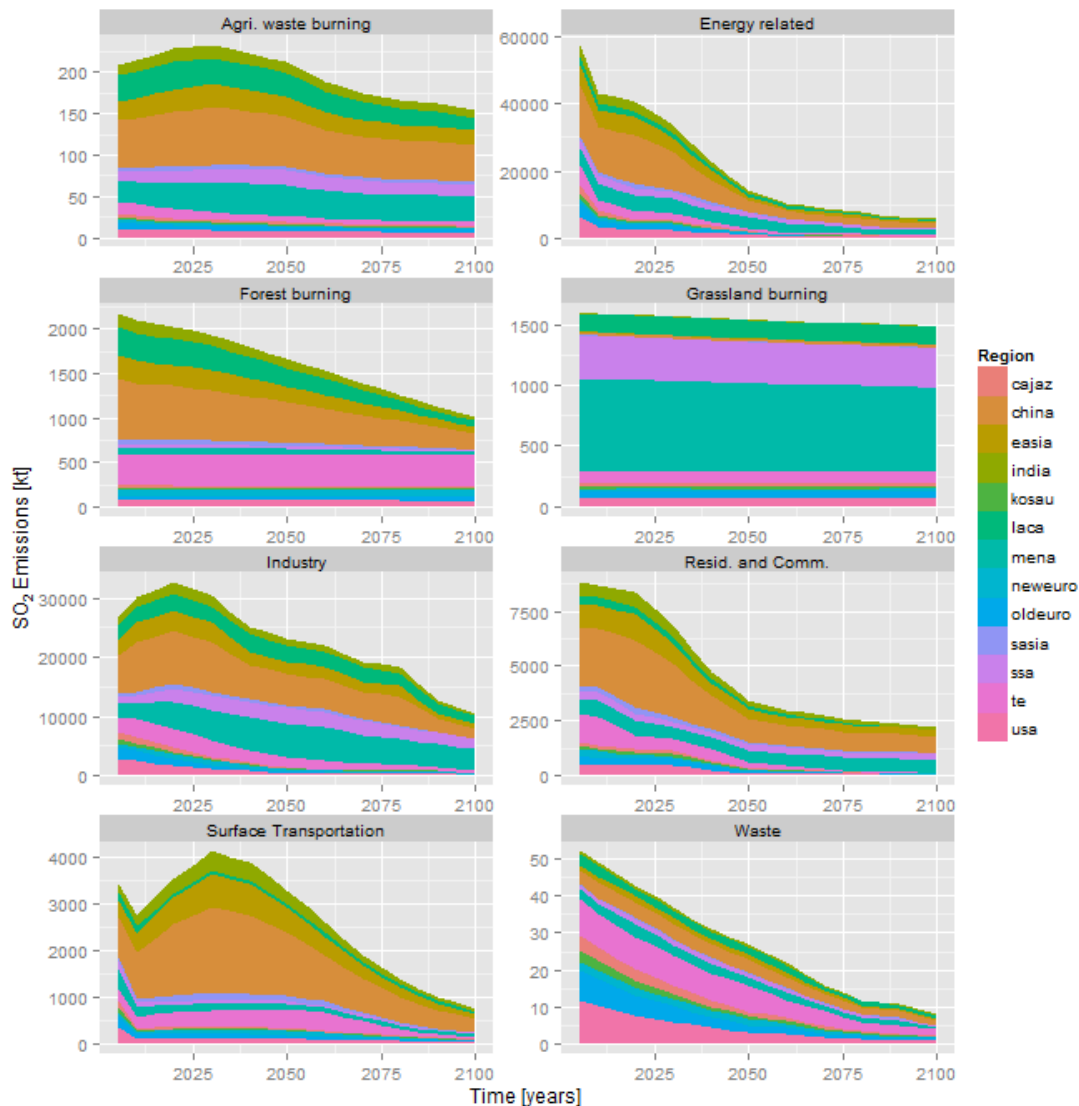


Fig. 1- SO₂ emissions from the WITCH model. Where “Agri.” stands for agriculture, “Resid.” for residential and “Comm.” for commercial.

6. CONCLUSIONS

Climate change and air pollution are two environmental issues which affect greatly society’s development and human population health. They both play a significant role in policy and political

agendas. Despite their inherent different time scales, they influence each other, thus also their policy management strategies have overlapping areas.

Furthermore, the analysis of integrated air pollution-climate policies is of extreme importance for the success of climate mitigation policies application. The inclusion of air pollution emissions in the WITCH model is therefore a step further towards a more complete climate-air pollution-economic integrated assessment modelling framework.

7. ACKNOWLEDGMENTS

The research leading to these results has received funding from the Italian Ministry of Education, University and Research and the Italian Ministry of Environment, Land and Sea under the GEMINA project.

Additionally, this research has received funding from the European Union Seventh Framework Programme (FP7/2007-2013) under grant agreement n° 282846(LIMITS).

8. REFERENCES

- Bollen J., Zwaan, B. Brink, C., & Eerens H. (2013). *Local Air Pollution and Global Climate Change: A Combined Cost-Benefit Analysis*. submitted to the Energy Journal. (1)
- Ramanathan V., & Feng Y. (2009). *Air pollution, greenhouse gases and climate change: Global and regional perspectives*. Atmospheric Environment, 43, 37-50. (2)
- UNEP. (2011). *Near-term Climate Protection and Clean Air Benefits: Actions for Controlling Short-Lived Climate Forcers*. United Nations Environment Programme. (3)
- Kelly J., Makar P., & Plummer D. A. (2012). *Projections of mid-century summer air-quality for North America: effects of changes in climate and precursor emissions*. Atmospheric Chemistry and Physics, 12, 5367-5390. (4)
- Jacob D., & Winner D. A. (2009). *Effect of climate change on air quality*. Atmospheric Environment, 43, 51-63. (5)
- Vuuren D. v., Cofala J., Eerens H., Oostenrijk R., Heyes C., Klimont Z., et al. (2004). *Exploring the ancillary benefits of the Kyoto Protocol for air pollution in Europe*. EEA. (6)

- Muller N. (2012). *The design of optimal climate policy with air pollution co-benefits*. Resource and Energy Economics, 34, 696-722. (7)
- Bernstein L. P. and, O. B., Chen Z., Christ R., Davidson O., & and G. H. (2007). *Climate Change 2007: Synthesis Report*. IPCC, Intergovernmental Panel on Climate Change. (8)
- Hunt A., & Watkiss P. (2011). *Climate change impacts and adaptation in cities: a review of the literature*. Climatic Change, 104, 13-49. (9)
- Patz J., D., C.-L., Holloway T., & Foley J. A. (2005). *Impact of regional climate change on human health*. Nature, 438, 310-317. (10)
- Wilby R. (2007). *A Review of Climate Change Impacts on the Built Environment*. Built Environment, 33(1), 31-45. (11)
- Cullis C. F., & Hirschler M. M., (1989). *Man's Emissions of Carbon Monoxide and Hydrocarbons into the Atmosphere*. Atmospheric Environment, 23(6), 1195-1203. (12)
- Navrud S. (2001). *Valuing Health Impacts from Air Pollution in Europe*. Environmental and Resource Economics, 20, 305-329. (13)
- O'Neill M., Jerrett M., Kawachi I., Levy J., Cohen A., Gouveia N., et al. (2003). *Health, Wealth, and Air Pollution: Advancing Theory and Methods*. Environmental Health Perspectives, 111(16), 1861-1870. (14)
- EEA. (2012). *Air quality in Europe --- 2012 report*. European Environment Agency. (15)
- Nemet G. F., Holloway T., & Meier P. (2010). *Implications of incorporating air-quality co-benefits into climate change policymaking*. Environ. Res. Lett., 5, 014007 (9pp). (16)
- Bosetti V., Massetti E., & Tavoni M. (2007). *The WITCH Model. Structure, Baseline, Solutions*. FEEM, Fondazione Eni Enrico Mattei. (17)
- Bosetti V., Carraro C., & Tavoni M. (2012). *Timing of Mitigation and Technology Availability in Achieving a Low-Carbon World*. Environment and Resource Economics, 51, 353-369. (18)
- Bosetti V., Carraro C., Cian E. D., Massetti E., & Tavoni M. (2013). *Incentives and Stability of International Climate Coalitions: An Integrated Assessment*. Energy Policy, 55, 44-56. (19)
- Höhne N., C. and, Elzen R. T., Riahi v, Chen K., C., Rogelj J., et al. (2012). *National greenhouse gas emissions reduction pledges and 2°C --- comparison of studies*. Climate Policy, 12, 356-377. (20)

- Delmas R., Serça D., & Jambert C. (1997). *Global inventory of NO_x sources*. *Nutrient Cycling in Agroecosystems*, 48, 51-60. (21)
- Bond T. C., Doherty S. J., Fahey D. W., Forster P. M., Berntsen T., DeAngelo B. J., et al. (2013). *Bounding the role of black carbon in the climate system: A scientific assessment*. American Geophysical Union. (22)
- Klimont Z., Streets D. G., Gupta S., Cofala J., Lixin F., & Ichikawa, Y. (2002). *Anthropogenic emissions of non-methane volatile organic compounds in China*. *Atmospheric Environment*, 36, 1309-1322. (23)
- Ohara T., Akimoto H., Kurokawa J., Horii N., Yamaji K., Yan X., et al. (2007). *An Asian emission inventory of anthropogenic emission sources for the period 1980--2020*. *Atmospheric Chemistry and Physics*, 7, 4419-4444. (24)
- Cao G., Zhang X., & Zheng F. (2006). *Inventory of black carbon and organic carbon emissions from China*. *Atmospheric Environment*, 40, 6516-6527. (25)
- Wang J., Yang J., Ma Z., & Benkovic S. (2000). *SO₂ Emission Trading Program-US Experience and China's Perspective*. China Environmental Science Publishing Company. (26)
- Smith S., Pitcher H., & Wigley T. (2005). *Future Sulfur Dioxide Emissions*. *Climatic Change*, 73, 267-318. (27)
- Riahi K., Gruebler A., & Nakicenovic N.: (2007). *Scenarios of long-term socio-economic and environmental development under climate stabilization*. *Technological Forecasting and Social Change* 74, 7, 887-935. (28)

Synergies and trade-offs between climate change mitigation strategies and air quality policies: the case of wood burning in domestic appliances

Caserini S.*, Galante S., Ozgen S.

Politecnico di Milano, D.I.C.A. Sez. Ambientale Milano, Italy

**Corresponding author: stefano.caserini@polimi.it*

Abstract

The availability of a comprehensive picture of atmospheric emissions from different sources allows to understand trade-offs and co-benefits between different policies in the sector of household heating. Wood combustion in small domestic appliances has relevant emissions of pollutants dangerous for human health, such as fine particulates and B(a)P, as well as carbonaceous particles with a radiative forcing for the atmosphere such as elemental carbon (EC, called also black carbon) and organic carbon (OC).

EC+OC contribution to the CO₂eq emissions in Lombardy in 2008, estimated on the basis of GWP100 values proposed in literature, results to be on average about 2.7 % of other greenhouse gas CO₂eq emissions in Lombardy in 2008. If the upper range of EC and OC emissions or GWP20 were assumed, EC+OC contribution to regional CO₂eq emissions would increase and the carbonaceous fractions of particulate matter would become an important radiative forcing source.

Residential wood combustion contribute to 20% of total EC+OC emissions and is due mainly to old appliances (open fireplace and stoves) that give also the greatest contribute to PM and B(a)P emissions.

The resulting evidences indicate that the natural renewal of appliances will allow a reduction of all the emissions from RWC in the 2010-2020 period. Specific policies (such as information campaigns to raise awareness on the impact of RWC on air quality, as well as accelerating the ratio of appliance renewal and improving the available technologies towards lower emission levels and higher thermal yield), will be needed to further reduce emissions and to better integrate air quality policies and the strategies for mitigation of climate change.

Keywords: Residential wood combustion, emissions, black carbon, organic carbon, particulate.



1. INTRODUCTION

Residential wood combustion (RWC) is extensively widespread in Italy and Europe and its usage is increasing because of the combination of high fossil prices and international efforts to decrease greenhouse gas emissions with associated incentives for bioenergy. Although recently some studies have opened a debate on the validity of the assumption of carbon neutrality for biomass from forestry where the cycles of carbon can be as long as centuries [1, 2, 3], GHGs (greenhouse gases) emission savings are expected when biomass substitutes fossil fuels in different types of combustion technologies [4].

Nevertheless it has to be considered that RWC emissions have an important impact on local air quality in several European countries, as has been confirmed with different methods such as using emission inventories, air quality data analysis, air quality modeling and source receptors modeling [5]. In fact, in addition to a high level of particulate matter (PM), RWC produces volatile organic compounds (VOC) with a high content of various toxic and carcinogenic compounds such as polycyclic aromatic hydrocarbons (PAH) and Dioxins. In particular, benzo(a)pyrene (B(a)P) is one of the four PAHs considered in UN-ECE Convention on Long-range Transboundary Air Pollution – CLRTAP and has been proposed by the EU Directive 2004/107/EC as a marker for the carcinogenic risk of PAH in ambient air. RWC is also an important source of black carbon (BC) and organic carbon emissions (OC) and thus has an impact on climate, given the potential of BC and OC to alter the Earth's energy balance through a complex net of processes [6]. Reducing BC emissions is thought to be a potential powerful tool to combat global warming [7].

The attention of this work is focused on RWC and aims to identify, through an analysis of detailed and reliable emission inventories of four pollutants (particles with aerodynamic diameters less than 10 μm -PM₁₀, B(a)P, EC and OC), synergies and trade-offs between climate change mitigation strategies and air quality policies on wood burning in domestic appliances.

The focus area considered is Lombardy, a 9 million-inhabitant-region in northern Italy, characterized by a high density of population, industrial activities and private transport; due to unfavourable meteorological conditions, PM₁₀ and NO₂ concentrations in air are particularly high, and exceed air quality standard in many monitoring points, particularly during the winter. Benzo(a)Pyrene ambient air objectives are also exceeded in many sites outside the main cities.

Residential wood combustion (RWC) has been identified as a key source for particulate emissions in Lombardy since the 2005 inventory [8].

It's worth mentioning that the terms black carbon and elemental carbon (EC) are frequently used to specify non-organic, non-carbonate part of the carbonaceous aerosol fraction. The term BC is usually employed when pure optical methods are used in the quantification, whereas EC is frequently employed to refer to refractory carbon determined with physical and chemical analyses (e.g. thermo-optical methods). Thus BC and EC are correlated but not coincident. BC inventories nearly always use EC from particulate matter (PM) source emission samples [9]; for this reason the following analyses use the term EC in reference to the emission values.

2. METHODOLOGIES

PM₁₀, B(a)P, CO₂, EC and OC emissions in Lombardy have been assessed by the 2008 regional emission inventory INEMAR [10] as well as in [11] and [12]. The emissions of the first three pollutants have been calculated by the product between activity data and emission factors, whereas EC and OC emissions have been derived from the PM inventory considering a specific fraction ratio of EC and OC in the particulate taken from a detailed literature survey [13]. The detailed EC and OC inventory has also considered contributions of minor relevance, such as tobacco smoking, which although lower in absolute terms, is relevant for the closeness with exposed people.

Emission factors have been taken from the AEIG-Atmospheric Emission Inventory Guidebook [14] and EC and OC abundances in PM from a detailed analysis of available scientific literature.

As far as RWC is concerned, results from a detailed telephone survey have been used to assess the biomass consumption (activity data) and the occurrence of the main categories of small combustion installations in the Region [15].

A specific and detailed literature review considering many experimental studies has been used to identify PM₁₀, B(a)P, EC and OC emission factors for RWC in different appliances such as open and closed fireplaces, old and modern stoves and pellet stoves. Emission factors have a great variability and uncertainty due to the diffuse character of this source, the differences in operating and combustion conditions (in particular temperature and excess air) and the lack of specific studies for some appliances typical of southern Europe, i.e., closed fireplaces [16]. Emission factors from RWC have been selected

from the data available in literature; the large variability of emission factors for RWC (depending mainly on wood use, appliance type and conditions) is furthermore an important source of uncertainty for PM, non-methane VOC, EC, OC and B(a)P emissions.

In order to have a first level assessment of the climate impact of the carbonaceous aerosols, CO₂eq emissions from EC and OC sources are calculated considering the average, minimum and maximum Global Warming Potential values for a time horizon of 100 years (GWP100) suggested in the UNEP-WMO report [7]: 680, 210, 1500 for BC (or EC), and as -69, -129, -25 for OC.

3. RESULTS

Tab.1 reports the summary of average PM₁₀, B(a)P, CO₂, EC and OC emissions in Lombardy in 2008 for SNAP (Selected Nomenclature for Air Pollutants) Level 1 categories. RWC in small appliances results to be a major source of PM₁₀ (47% of total emission), B(a)P (77%), EC (31%) and OC (74%).

SNAP group	PM ₁₀ t year ⁻¹	B(a)P kg year ⁻¹	CO ₂ kt year ⁻¹	EC t year ⁻¹	OC t year ⁻¹
1 Combustion in energy and transformation industries	482	1	19,007	40	178
2 Non-industrial combustion plants (of wich residential wood combustion)	11,931 11,345	2,992 2,880	17,150	1,286 1,151	6,332 5,807
3 Combustion in manufacturing industry	1,056	398	10,096	104	138
4 Production processes	955	17	4,569	2.1	7.1
6 Solvent and other product use	250			0.0	0.0
7 Road transport	6,540	103	19,356	2,340	1,185
8 Other mobile sources and machinery	760	12	1,732	288	199
9 Waste treatment and disposal	80	1	940	4.3	7.1
10 Agriculture	1,212	204		48	143
11 Other sources	735	31	-3,040	109	354
Total	24,001	3,758	69,810	4,222	8,543

Tab.1: Summary PM₁₀, B(a)P, CO₂, EC and OC emissions in Lombardy in 2008 (t year⁻¹)

Traditional wood stoves, closed fireplaces and open fireplaces are the major contributors of B(a)P emission, accounting respectively for 32%, 23% and 19%. The relevance of wood burning in small residential appliances to B(a)P concentration has also been highlighted by a detailed analysis of three years of particle phase B(a)P air concentration measurements in 13 sites in Lombardy [12]. The

dominance of the wood combustion originating, according to the emission inventory from the residential sector and from pizzerias in the city of Milan, is consistent with the findings of other studies based on a source apportionment approach or air quality modelling.

On-road diesel vehicles and RWC account for more than 80% of carbonaceous particles in PM, whereas for particulate emissions their contribution results to be less than 60%. On the whole, non-combustion sources are observed to have a very small contribution to the regional OC and EC emissions. In comparison with other European contexts, the importance of diesel and RWC in Lombardy is enhanced by the very limited use of coal and fuel oil, and by the rigorous standards in use for the industrial sector. On the contrary, traffic and in particular the use of diesel passenger cars is extremely important.

For a better understanding of the differences between the contributions of the different appliances burning woody biomasses to carbonaceous particle emissions, the implied emission factors for EC and OC are shown in Tab.2. It can be noticed that the most polluting device, in terms of EC, OC and TSP emission factors, is the open fireplace, followed by the traditional stove, the closed fireplace, the innovative wood stove and the pellet stove. While the open fireplaces have a greater fraction of OC, due to larger contributions of incomplete combustion products in the effluent, pellets stoves are characterized by drastically lower implied emission factors, particularly for OC.

Appliance type	PM10	B(a)P	EC	OC
Open fireplace	860	0.18	72	493
Traditional wood stove	810	0.25	101	422
Closed fireplace or insert	450	0.1	42	208
Innovative wood stove	240	0.1	50	113
Pellets stove	76	0.05	7.9	20

Tab. 2: PM10, B(a)P, EC and OC emission factor (g GJ⁻¹) for residential wood combustion

The results obtained in the case of Lombardy are consistent with other works available in literature. At the European level, residential combustion contribution (dominated by RWC) is a major source of BC and OC emissions [17]. A recent work assessed BC and OC emissions in Denmark [18], estimating the

share of the residential sector as 62% for BC and 84% for OC; it is interesting to notice that, regarding the RWC sector, the OC/BC ratio is reported to be 2 in Denmark whereas it is estimated as 4 in the present work. The cause for this difference is the larger presence in Lombardy of small and inefficient combustion appliances (in particular open fireplaces) which are responsible for higher OC emissions. EC pro-capita emission in Lombardy (0.51 kg y^{-1}) is lower than the average assessed in [17], 0.67 kg y^{-1} , whereas for OC the Lombardy pro-capita is 0.99 kg y^{-1} against 0.79 kg y^{-1} . This is mainly due to fact that the pro capita PM10 and OC from RWC is almost two times the western European average.

CO₂ equivalent emissions from BC and OC

Black carbon in soot is the dominant absorber of visible solar radiation in the atmosphere and is estimated to be at global level the second largest contributor to global warming after carbon dioxide [19]. There is a range of quantitative estimates in the literature for global average radiative forcing due to BC. According to a recent report by United Nations Environment Programme and World Meteorological Organization, global average net radiative forcing for BC is likely to be positive with a best estimate of 0.6 W m^{-2} [7]. The same assessment reports for OC particles, which generally tend to produce a cooling influence on climate, central values in the range of -0.08 to -0.30 W m^{-2} , with a best estimate of -0.19 W m^{-2} .

Up to now, there is no general consensus on the global warming potential (GWP) associated to the carbon content of particulate matter; furthermore, as EC and OC are short-living species, GWP is not an adequate metric of warming potential and its value depends on the geographical location in which emissions take place [20]. Nevertheless, due to its short-term effect BC reduction is envisaged as a tool to mitigate climate change in the first half of this century, and therefore its useful to quantify its effect in comparison with the CO₂, in order to identify the most effective measures [21, 7]. The CO₂equivalent emissions due to EC and OC, obtained as explained previously with GWP100, are shown in Tab.3; the warming potential in terms of CO₂eq is positive for every sector, even in the subsector with the lowest EC/OC ratio, RWC, that accounts to 20% of total CO₂eq associated to EC+OC.

	CO ₂ eq (EC)			CO ₂ eq (OC)			CO ₂ eq (EC+OC)		
	GWP100 average	GWP100 min	GWP100 max	GWP100 average	GWP100 min	GWP100 max	GWP100 average	GWP100 min	GWP100 max
Diesel	1518	469	3348	-50	-18	-93	1468	451	3255
Biomass combustion	892	275	1968	-437	-158	-817	455	117	1150
Other combustions	423	131	934	-79	-29	-148	344	102	786
Other sources	40	12	88	-23	-8	-43	17	4	45
Total	2873	887	6338	-589	-213	-1101	2284	674	5236

Tab. 3: CO₂eq emission from EC and OC in Lombardy (kt y⁻¹) for different GWP values

The overall CO₂eq associated to EC+OC emissions in Lombardy is 2.3 Mt year⁻¹, 2.7% of the regional CO₂eq emissions from the six greenhouse gases covered by the Kyoto Protocol (84.2 Mt year⁻¹) [10], whereas using the maximum value proposed for the GWP100 the EC and OC contribution in terms of CO₂eq accounts for up to the 6.3% of all other greenhouse gas emissions. It's worth noting that considering the warming potential on a shorter reference time would further increase this contribution: for example, assuming the GWP20 3.5 times the GWP100 [20], the CO₂eq associated to EC+OC increases to 8.0 Mt year⁻¹, 9.6% of Kyoto gases emissions with a range between 3 and 21% when minimum and maximum values of GWPs are considered.

Scenario to 2020

PM emissions from RWC in Lombardy in the period 2010-2020 have been calculated in [22] on the basis of biomass use trend and appliance renewal rate, considering two types of scenarios: a “business as usual” (BAU) scenario, which assumes a constant legislative framework, and other scenarios considering the implementation, after 2010, of several regulatory measures to limit RWC emissions. The BAU scenario implemented takes into account the natural trend of appliance renewal as well as technological improvements. The information on the trend of the different appliances are of great importance, as PM and toxic emission factors as shown are directly linked to combustion technologies, and higher for old stoves and fireplaces.

Starting from the BAU scenario, the impact of policies was studied. In the alternative scenario the following measures were selected:

- the introduction of new regulation for a periodic maintenance;
- information campaign to raise awareness of the impact of RWC;
- campaign to enforce the respect of the existing regional law, that banishes the use of open fireplaces in the plain area of the region;
- introduction of emission standards for new appliances sold after 2015.

Results show that it is possible to forecast for the next decade (in the absence of specific measures) an enhancement in the use of biomass, mainly related with a major use of pellets and better energy efficiency of new appliances. In the meantime, in the BAU scenario PM10 emissions decrease, because although a development of biomass use in the residential sector the increase in pellets use lead to a reduction in total emission. Anyway, in the absence of specific policies aimed to the renewal of appliances and to a sharp improvement in the efficiency, 2020 emissions will be still very high, unless regulatory acts aimed to a drastic improvement in the appliance quality are implemented.

In the “scenario with regulatory measures” PM10 emission decreases of 53% by the year 2020 (see Fig.1). The introduction of compulsory standards for appliances sold after 2015 is associated with the most rapid decrease in emissions; nevertheless to the slowness of technological renewal, the major part of benefits would be concentrated after 2020. Emission reductions are not simply additive.

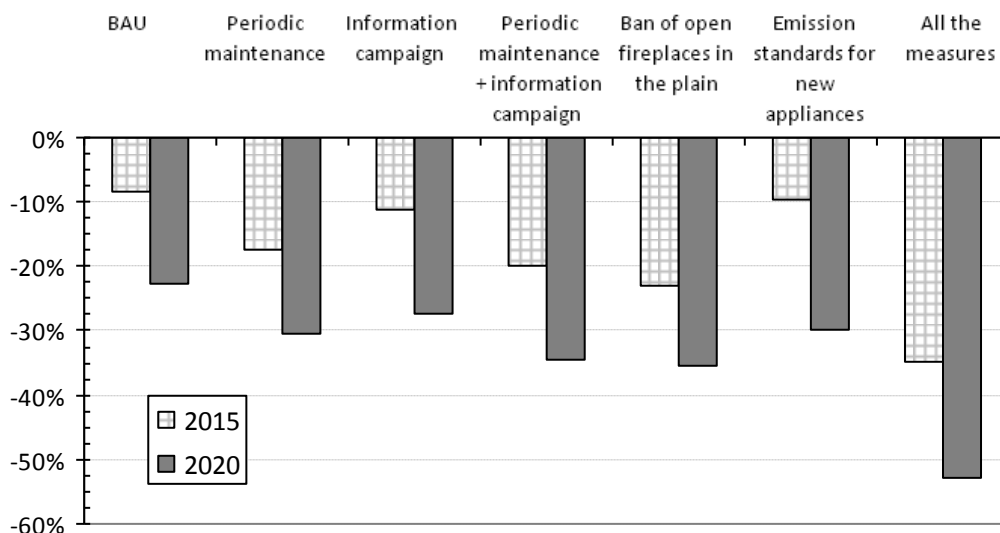


Fig.1 – Reduction in PM10 emission from RWC in 2015 and 2020 (compared to 2010 emissions) due to different measures

Emission scenarios for PM10 can be used to assess EC and OC, using the estimate of carbonaceous fractions proposed in [13]. Results are shown in Fig.2: as it can be noticed, the most important variation is related to OC emissions, since it's the fraction most influenced from the improvement of the combustion process. Therefore in the BAU scenario the CO₂eq calculated with an average GW100 has a 5% variation only in the decade 2010-2020, since the warming potential of EC is less mitigated from the cooling potential of OC. In the “With measure” scenario, the reduction of CO₂eq emission from RWC in the 2010-2020 period accounts for 32%, but is not relevant in absolute terms. Even using GWP20 the reduction in CO₂eq accounts for 400 kt y-1, less than 0.5% of total CO₂eq emissions in Lombardy.

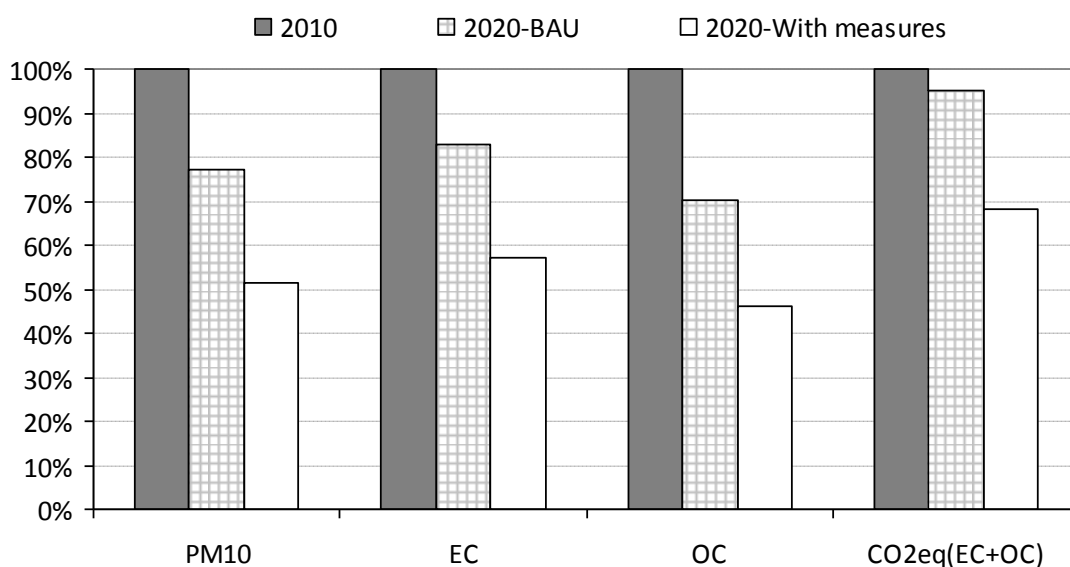


Fig.2 – PM10, EC, OC and CO₂eq emission reduction in 2020 (compared to 2010 emissions) for the two scenarios.

Integrated policies and measures

Tab. 1 has shown that a significant fraction of CO₂, NO_x and PM10 is due to energy production through fossil fuels (88%, 90% and 23% respectively). Thus, policies aimed to energy efficiency and energy savings have benefits to all these pollutants and deserve the priority given by EU directive on air quality and climate change. Tab.4 reports a summary of the total emissions of NO_x, PM10 and CO₂ in the SNAP 2 sector (commercial, institutional and residential combustions) in Lombardy, considering

different fuel types and average emission factors weighted on the distribution in the region of each type of small domestic appliances.

It can be highlighted that although RWC produces 6% of the total heat and has no net CO₂ emissions, it determines about 99% of the emissions of PM10, B(a)P, EC and OC of this sector. On the other side, the use of natural gas meets the 86% of the heat demand in the same sector and produces 80% and 90% of NO_x and CO₂ emissions respectively, but is responsible of less than 1% of PM10, B(a)P, EC and OC emissions.

Fuel use	CO ₂		NO _x		PM10		B(a)P		EC		OC		
	% energy	E.F. kg/GJ	% emis.	E.F. g/GJ	% emis.	E.F. g/GJ	% emis.	E.F. mg/GJ	% emis.	E.F. g/GJ	% emis.	E.F. g/GJ	% emis.
Natural gas	86%	56	90%	38	79.6%	0.2	0.47%	0.0006	0.01%	0.014	0.2%	0.15	0.6%
Gas oil	5.4%	73	7.4%	58	7.5%	5.0	0.72%	0.079	0.05%	1.6	1.7%	0.40	0.1%
LPG	2.3%	63	2.7%	58	3.2%	0.2	0.01%	-	-	0.02	0.01%	0.2	0.02%
RWC (average)	6.3%	-	-	63	9.6%	580	98.8%	147	99.9%	80	98.1%	335	99.3%

Tab. 4. Emissions factors and share of emissions in the residential sector in Lombardy, year 2008.

In the last decades many regulations have tried to limit emissions in the residential sector: for instance, coal is now of very limited use, the use of coal and fuel oil in the residential sector is banned, methane is largely the dominant fuel in the power sector.

The results of this work suggest that technological improvements in RWC appliances as well as new policies to accelerate the ratio of substitution of old and obsolete stoves and fireplaces with new burners with lower emissions and higher thermal yield (i.e. pellets stoves), are one of the most important strategies to reduce emissions and comply with PM10 and B(a)P standards. These reductions may coexist with the increase in the use of biomass (with the subsequent effect of CO₂ emission mitigation) and the reduction of EC and OC emissions. Although the reduction in OC emissions (that have a negative GWP, thus a cooling effect for the atmosphere) is slightly higher than the reduction in

EC emissions, the warming contribution of carbonaceous PM from RWC remains low compared to other radiative forcing agents such as the main GHGs.

Further work will be necessary to improve the reliability of PM₁₀, B(a)P, EC and OC emission assessment in the RWC sector, that is the most important source of uncertainty identified for Lombardy for these pollutants. Because these emissions are the weak point for the environmental compliance of biomass use in the residential sector, this refinements will allow to reduce the uncertainty on how the increase in the use of biomass in the residential sector which is boosted by the minor price of biomass in relation to fossil fuels and welcomed by renewable energy legislations in order to decrease the fossil fuel use and mitigate CO₂ emissions, could be integrated with existing restrictive air quality standards.

4. REFERENCES

- Cherubini F, Peters GP, Berntsen T, Strømman AH, Hertwich E (2011) *CO₂ emissions from biomass combustion for bioenergy: atmospheric decay and contribution to global warming*. GCB Bioenergy, 3, 413-426. (1)
- Zanchi G, Pena N, Bird N (2011) *Is woody bioenergy carbon neutral? A comparative assessment of emissions from consumption of woody bioenergy and fossil fuel*. GCB Bioenergy, 4, 761-772. (2)
- Holtmark B (2012) *Harvesting in boreal forests and the biofuel carbon debt*. Climatic Change, 112, 415-428. (3)
- Caserini S., Livio S., Giugliano M., Grosso M., Rigamonti L. (2010) *LCA of domestic and centralized biomass combustion: The case of Lombardy (Italy)*. Biomass & Bioenergy, 34, 4, 474-482. (4)
- Angelino S., Lanzani G., Caserini S., Marongiu M., Bellinzona S.A. (2012) *Domestic wood combustion impact on air quality in Lombardy region*. *Air Quality 2012*, 8th International Conference on Air Quality - Science and Application. Athens, 19-23 March. (5)
- US-EPA (2012) Report to Congress on Black Carbon. *Department of the Interior, Environment, and Related Agencies Appropriations Act, 2010*. March 2012. (6)
- UNEP-WMO (2012) *Integrated assessment of black carbon and tropospheric ozone*. By the United Nations Environment Programme and World Meteorological Organization. (7)

- Caserini S., Fraccaroli A., Monguzzi A.M., Moretti M., Angelino E., Leonardi A., De Lauretis R., Zanella V. (2007) *New insight into the role of wood combustion as key PM source in Italy and in Lombardy region*. 16th Annual International Emissions Inventory Conference “Emission Inventories: Integration, Analysis, and Communications” Raleigh, North Carolina, May 14 – 17. (8)
- Chow J.C., Watson J.G., Lowenthal D.H., Chen L.A., Motallebi N. (2010) *Black and organic carbon emission inventories: review and application to California*. *J Air Waste Manage*, 60:497-507. (9)
- ARPA Lombardia. *INEMAR - Inventario emissioni aria anno 2008– Lombardia, 2011*. www.inemar.eu (accessed 20/5/2012). (10)
- Caserini S., Angelino E., Antognazza F., Fossati G., Lanzani G., Marongiu M., Moretti M. (2012) *Atmospheric emissions in Lombardy: findings from the INEMAR emission inventory*. SIDISA 2012 Sustainable Technology for Environmental Protection. International Symposium of Sanitary and Environmental Engineering 9th Edition. Italian-Brazilian Symposium of Sanitary and Environmental Engineering 11th Edition. Milan, 26 – 29 June. (11)
- Gianelle V., Colombi C., Caserini S., Ozgen S., Galante S., Marongiu A., Lanzani G. (2013). *Benz(a)pyrene air concentrations and emission inventory in Lombardy region*. *Atmospheric Pollution Research*, 4, 257-266. (12)
- Caserini S., Galante S., Ozgen S., Cucco S., de Gregorio K., Moretti M. (2013) *A methodology for elemental and organic carbon emissions inventory and results for Lombardy region, Italy*. *Science of the Total Environment*, vol. 450–451, pp. 22–30. (13)
- EEA (2010) *EMEP/EEA Air pollutant Emission Inventory Guidebook 2009*. Chapter 1.A.4 Small Combustion. (14)
- Pastorello C., Caserini S., Galante S., Dilara P., Galletti F. (2011) *Importance of activity data for improving the residential wood combustion emission inventory at regional level*. *Atmospheric Environment*, 45, 2869-2876. (15)
- Galante S. (2013) *Biomass combustion in small residential plants: emissions, uncertainty, scenarios of reduction*. *PdD Thesis*, Politecnico di Milano. (16)
- Kupiainen K, Klimont Z. (2007) *Primary emissions of fine carbonaceous particles in Europe*. *Atmospheric Environment*, 41:2156-70. (17)

- Winther M, Nielsen OK. *Technology dependent BC and OC emissions for Denmark, Greenland and the Faroe Islands calculated for the time period 1990-2030* (2011) *Atmospheric Environment*, 45:5880-95. (18)
- Ramanathan V, Carmichael G. (2008) *Global and regional climate changes due to black carbon*. *Nature Geoscience*, 1:221-27. (19)
- Rypdal K., Rive N., Berntsen T.K., Klimont Z., Mideksa T., Myhre G., Skeie B. (2009) *Costs and global impacts of black carbon abatement strategies*. *Tellus*, 61:625-41. (20)
- Bond T, Sun H. (2005) *Can reducing black carbon counteract global warming?* *Env Sci Tech*, 39:5921-26. (21)
- Galante S., Caserini S., Ozgen S. (2012) *PM emission scenario from domestic biomass burning: data and uncertainties*. In: *20th European Biomass Conference. Setting the course of a biobased economy* (Eds.) 20th European Biomass Conference. Setting the course of a biobased economy - Proceedings of the 20th European Biomass Conference and Exhibition, Milan, Italy, 18-22 June. ISBN 978-88-89407-54-7, 2268-2273. (22)

Ancillary benefits of climate change policy in China: air pollution impacts on household health, adaptation and government-controlled information in Beijing

Ravetti C.^{1*}, Quan M.², and Popp Jin Y.²

¹Centre for International Environmental Studies, IHEID Geneva,

²Peking University, College of Environmental Sciences and Engineering

*Corresponding author: chiara.ravetti@graduateinstitute.ch

Abstract

This paper analyses one important element for evaluating the ancillary benefits that China could reap from greenhouse gas abatement policies, which is information about air pollution. Information is critical especially given the scarce adaptive capacity of Chinese urban population, which can hardly avert the health damages of pollution and heavily relies on government media. In this study we consider on the one hand how the government handles information relative to daily air pollution levels, and on the other how households use information and try to avoid health damages in a highly polluted city, Beijing. The analysis is based on air pollution data from different sources and on original survey data about averting behaviour, health and access to information. These two sets of data allow us to explore the incentives behind people's adaptation (or lack of it). We find that indeed official Chinese data provides a distorted signal with respect to alternative measurements. For households, which rarely use the internet to double-check pollution values, this may imply a distorted capacity to adapt, especially for those more financially constrained and for individuals with less time flexibility. Effectively, China's authoritarian government is impeding any adaptive response by urban dwellers, disregarding people's individual preferences about pollution, health or adaptation to environmental risks and damages.

Keywords: *Ancillary benefits, Averting Behaviour, Information, Air Pollution, Health*



The debate about ancillary benefits of climate change policies aimed at reducing greenhouse gas (GHG) emissions has paid increasing attention to developing countries in recent years. Numerous studies examine how developing countries evaluate the side-effects, externalities and spillovers that derive from climate change mitigation, typically looking at air pollution reduction and health¹. In theory, developing countries could benefit from short-term, less uncertain and localized spillovers if they commit to reduce GHG, even if they face higher opportunity costs of allocating resources to this task, and this can create an incentive for participation in international mitigation efforts (Pittel and Rübhelke 2008). Nonetheless, the political, demographic and socio-economic characteristics of a country can affect significantly the way these ancillary benefits are attained.

The objective of this study is to draw attention to one key element which can affect the adaptation of households to environmental damages, and hence the analyses of ancillary benefits: information. We study the significance of access to information by looking at different responses of the government and households to high levels of air pollution in urban Beijing, China. This gives a useful indication of what distortions the country should consider if it adopted measures that simultaneously addressed local and global emissions. The paper is organized as follows: first we examine the role of the government in providing information about air pollution, analysing the discrepancy between Chinese reported levels of pollution and those indicated by the US embassy in Beijing. Afterwards, we study the household dimension of the problem, focusing on the impact of information on the choice between costly defensive behaviours, such as the purchase of durable goods for self-protection (e.g. air purifiers), and cheaper behaviours that are more time-consuming, such as reducing leisure time outdoor or changing means of transportation.

GOVERNMENT

First, we explore how the government communicates to the public the monitored levels of pollutants' concentration at a given point in time. This can be indicative also of how information about other environmental issues diffuses, including global warming. Government agencies monitor and diffuse

¹ See for instance Alberini et al. (1997) for Taiwan, Alberini et al. (2007) in Delhi, Citifuentes et al. (2001) for Chile, El-Fadel and Massoud (2000) in Beirut, Lebanon, Hammit and Zhou (2006), Wang and Mullahy (2006) and Desheng et al. (2012) for China.

information about a city's pollution parameters, providing a public good which otherwise would be under-supplied by the private sector. Hence the government has a pivotal role in determining the population's awareness of pollution risks.

The standard tools used in the USA and many other countries to communicate to the general public the level of pollution are standardized indexes - Air Quality Indexes or AQI - that convey information about the level of pollution through a simple rating of air quality. The index score is then associated with the health damages that can derive from it. China has also an Air Pollution Index (API) that is in many aspects similar to the one developed by the US Environmental Protection Agency (EPA). A comparison is presented in Fig.1.

Index and Definition		Health Implications	PM10 (µg/m³)		SOx		NOx		Others
AQI US	API China		US	China	US (ppm)	China (µg/m³)	US	China (µg/m³)	US
0 – 50 Good	0-50 Excellent	Air quality is considered satisfactory, and air pollution poses little or no risk	0-50	0-50	0 - 0.03	0-50	Under revision	0-80	Ozone (8 hour and 1 hour), Carbon monoxide, PM2.5
51-100 Moderate	51-100 Good	Air quality is acceptable; however, for some pollutants there may be a moderate health concern for a very small number of people who are unusually sensitive to air pollution.	>50-150	50-150	>0.03 - 0.14	50-150		80-120	
101-150 Unhealthy for sensitive groups	100-200 Slightly polluted	Members of sensitive groups may experience health effects. The general public is not likely to be affected.	>150-250	150-350	>0.14 - 0.22	150-800		120-280	
151-200 Unhealthy	Light polluted	Everyone may begin to experience health effects; more serious effects for members of sensitive groups.	>250-350		>0.22 - 0.30				
201-300 Very Unhealthy	200-300 Moderately polluted Moderate-heavy polluted	Health warnings of emergency conditions. The entire population is more likely to be affected.	>350-420	350-420	>0.30 - 0.60	800-1600		280-565	
300+ Hazardous	300-400 Heavy polluted	Health alert: everyone may experience more serious health effects	>420-500	420-500	>0.60 - 1.0	1600-2100		565-750	
	400-500		500-600	2100-2620		750-940			
	500		> 600	> 2620		> 940			

Fig.1 - US versus China's pollution indexes (Source: own elaboration from US EPA and MEP)

The Chinese API or the US AQI on a given day correspond to the highest value of any of the pollutants which compose it.

$$API = \max(I_1, I_2, \dots, I_n) \quad (1)$$

The index for an observed concentration C of pollutant i is:

$$I_i = (C - C_{low}) \frac{I_{high} - I_{low}}{C_{high} - C_{low}} + I_{low} \quad (2)$$

where *high* and *low* indicate the boundaries of each category mentioned in the above table (Beijing Municipal Environment Monitoring Centre and US-EPA 2006). While the construction of the index is identical between the two countries, the boundaries of concentration for some of the pollutants are sometimes different (e.g. SO_x).

Incentives to distort information

Chinese politics presents a unique institutional structure in its hierarchical relationship between local and central government. This is based on a system of vertical bureaucratic control that allows some flexibility at the local level, but no true decentralization (Tsui and Wang 2004). Government officers are responsible for economic targets and, more recently, also for some environmental performance, which however represent a secondary concern (Xu 2011). The observation that organization and hierarchy can generate different incentives and outcomes is not new², but in the context of diffusing information about an environmental problem has not been studied extensively.

It is therefore interesting to consider in this authoritarian system whether there are incentives for distorting information about environmental problems, to make them appear less significant to the central government. Some evidence of this data distortion has been found by Andrews (2008) and Chen et al. (2013), who analysed API data officially reported. Both studies find that air pollution data has been manipulated in various ways: from shifting monitoring stations to less polluted areas, to down-playing some numbers around the threshold of “blue sky days” (API of less than 100). Indeed a

² Maskin et al. (2000), for instance, test this hypothesis with Chinese data on managers' incentives, using a broader model applicable to government structures.

clear incentive for distortions comes from the National Environmental Protection City award, started in 2003, which prizes cities that, among other things, can achieve more than 85% of blue sky days in a year.

Comparing the US AQI with Chinese API

Given that incentives may indeed exist to distort air pollution information, Beijing presents the unique feature of having a counter-check to official data: the United States embassy, with its own monitor for particulate matter. Therefore, it is possible to conduct a comparative analysis of the two indexes produced by the Chinese and US for the same time period. Fig. 2 below shows the comparison of the daily indexes during some months of 2008.

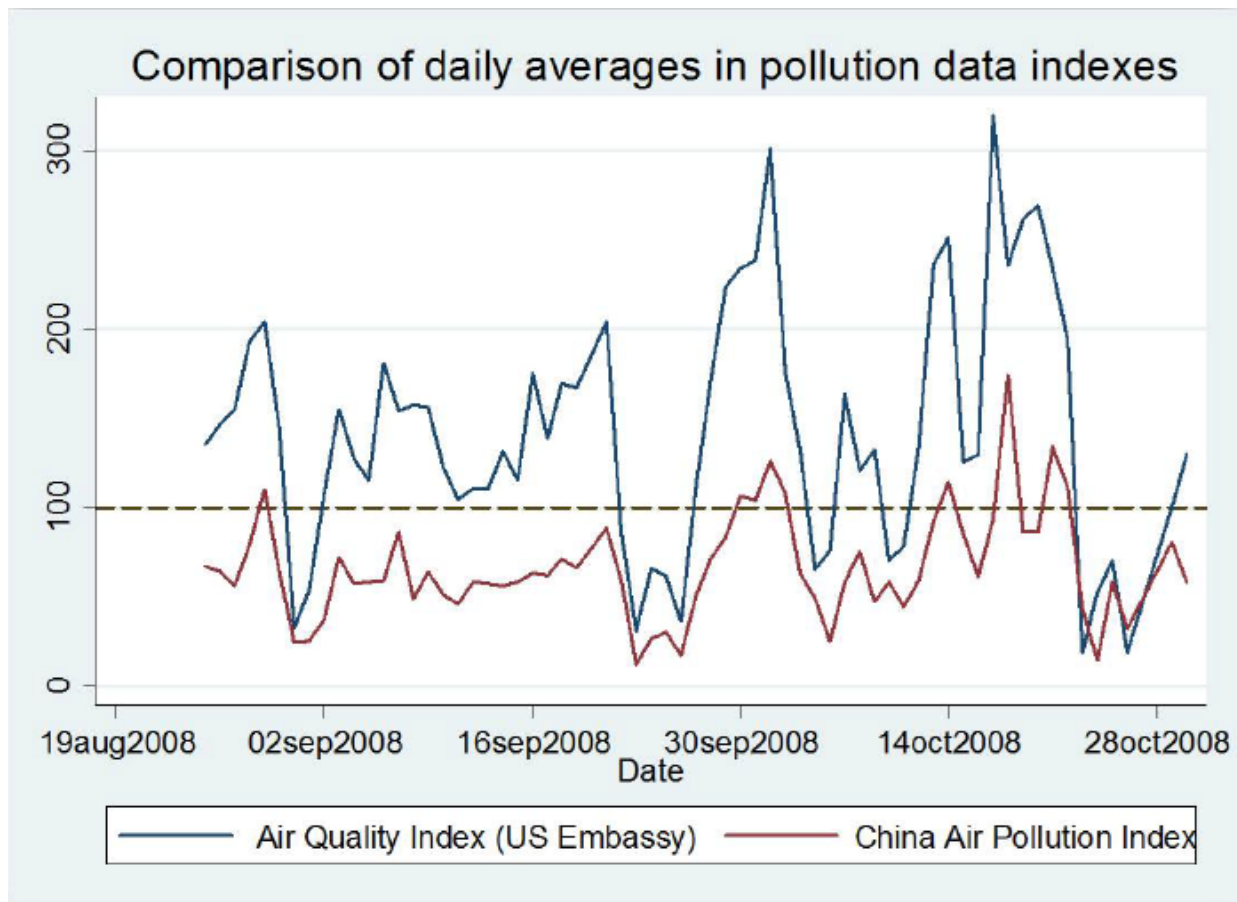


Fig.2 – Mismatch between the Chinese and US pollution indexes

From the graph, it is clear that the indexes take very different values in the same day. The Chinese index, in red, tends to be lower than the US one (blue) and rarely surpasses the blue sky day limit of 100. Moreover, the Chinese index tends to be downward biased especially in highly polluted days, when the difference from the US AQI becomes greater³. For a more formal analysis of the systematic ways in which Chinese officials might manipulate Beijing's API, we conduct the following time-series analysis using data from 2008 to 2013:

³ We assume that the US embassy does not have itself any incentive to distort pollution reporting. In particular, it is reasonable to assume that it would not scale the index upwards, since this would easily cause diplomatic tensions. Therefore in the following analysis we consider the US measurement to be fairly representative of actual pollution levels.

$$\frac{API_t}{AQI_t} = \alpha + \beta_1 AQI_t + \beta_2 Politics_t + \sum_{i=1}^p \gamma_i Thresholds_i + \sum_{i=1}^q \phi_i \frac{API_{t-i}}{AQI_{t-i}} + \sum_{i=1}^r \theta_i \epsilon_{t-i} + \eta_m + \sigma_y + \epsilon_t$$

We consider whether the AQI significantly affects the ratio API/AQI. If the two indexes are similar, the ratio will be close to one and the effect insignificant; the more discrepancy between the two, however, the more of a (negative) significant impact we should observe. Moreover, we include controls for political events that could make local officials more willing to distort pollution data: the Beijing Olympics (August 2008), the celebration of the Communist Party's 60 years (October 2009), Bo Xilai's scandal during China's parliamentary session in Beijing (March 2012), the diplomatic tension with the US embassy for the publication of air pollution tweets (June 2012), and the 17th National Congress of the CPC (November 2012). We also include dummies for thresholds that could matter for politicians, such as the API at 100 on blue sky days and (considering Fig. 1) 200 and 300. In addition, to capture persistence in shocks and in pollution stocks, we add an autoregressive and a moving average component. Finally, we include month and year fixed effects. We consider only days when PM10 is the main pollutant, since for SOx the comparison would not be possible. Results of various autoregressive-moving average specifications are presented in Table 1.

The average value of the dependent variable is 0.87, reasonably indicating that the Chinese API tends to be smaller, on average, than the US index. Whenever pollution (as registered by the US AQI) rises, the effect on the ratio AQI/API is unambiguously negative and significant: a 1% increase in the AQI causes a fall in the Chinese/US ratio of 0.3%. But more interestingly, thresholds and political events do seem to play a role in moving the asymmetric relation between the two indexes. Political events *per se* give a slightly higher intercept, but at high levels of pollution (i.e. when the political event is interacted with air quality) the dampening effect on Chinese API compounds the negative effect of the AQI. Of all thresholds, 100 is significant and large, as one could expect given the blue sky days policy, but also at 300 there is significant alert, since the air quality is reaching heavily polluted levels. In interaction with the score of the AQI, the 100 threshold almost cancels out (-0.3 and 0.2, leaving still a slight negative impact on the ratio), while the interaction of the 300 threshold does not dampen much the negative effect of AQI.

Table 1: Ratio of Chinese to US pollution indexes (logs)

	Chinese/US index	Chinese/US index	Chinese/US index	Chinese/US index
AQI (US)	-0.294*** (0.007)	-0.297*** (0.007)	-0.294*** (0.007)	-0.295*** (0.007)
Political Events	0.131*** (0.031)	0.130*** (0.031)	0.126*** (0.031)	0.132*** (0.031)
Politics* AQI	-0.029*** (0.006)	-0.029*** (0.006)	-0.028*** (0.006)	-0.029*** (0.006)
AQI threshold(100)	-0.943*** (0.065)	-0.948*** (0.065)	-0.943*** (0.066)	-0.951*** (0.067)
AQI threshold(200)	0.013 (0.185)	0.025 (0.191)	0.013 (0.185)	0.031 (0.191)
AQI threshold(300)	-0.480** (0.231)	-0.525** (0.235)	-0.477** (0.231)	-0.486** (0.234)
T100*avg. AQI	0.210*** (0.014)	0.211*** (0.014)	0.210*** (0.014)	0.211*** (0.014)
T200*avg. AQI	0.002 (0.034)	0.000 (0.035)	0.002 (0.034)	-0.001 (0.035)
T300*avg. AQI	0.084** (0.041)	0.092** (0.042)	0.083** (0.041)	0.085** (0.041)
Constant	2.190*** (0.037)	2.204*** (0.036)	2.189*** (0.037)	2.195*** (0.037)
ARMA				
L.ar	0.349*** (0.028)			-0.639*** (0.033)
L2.ar				0.351*** (0.029)
L.ma		0.316*** (0.031)	0.340*** (0.031)	0.987*** (0.024)
L2.ma			0.139*** (0.033)	
sigma				
Constant	0.043*** (0.001)	0.044*** (0.001)	0.043*** (0.001)	0.043*** (0.001)
Observations	876	876	876	876
AIC	-2934.260	-2921.662	-2932.724	-2931.349
BIC	-2800.550	-2787.951	-2794.238	-2788.088

Standard errors in parentheses

 * $p < 0.10$, ** $p < 0.05$, *** $p < 0.01$

The four models are compared using the Akaike and Bayesian Information Criterion (AIC and BIC)⁴. Choosing the two models with lowest information criteria, i.e. the AR(1) and the MA(2) models, we compute in-sample forecasts to see which of the specified models performs best in terms of predictive power. Comparing the mean squared errors of our forecasts, we select the moving average with two lags, MA(2). Its forecasts are plotted in Fig. 3, which shows that overall the model performs quite well in predicting 100 days inside of our sample.

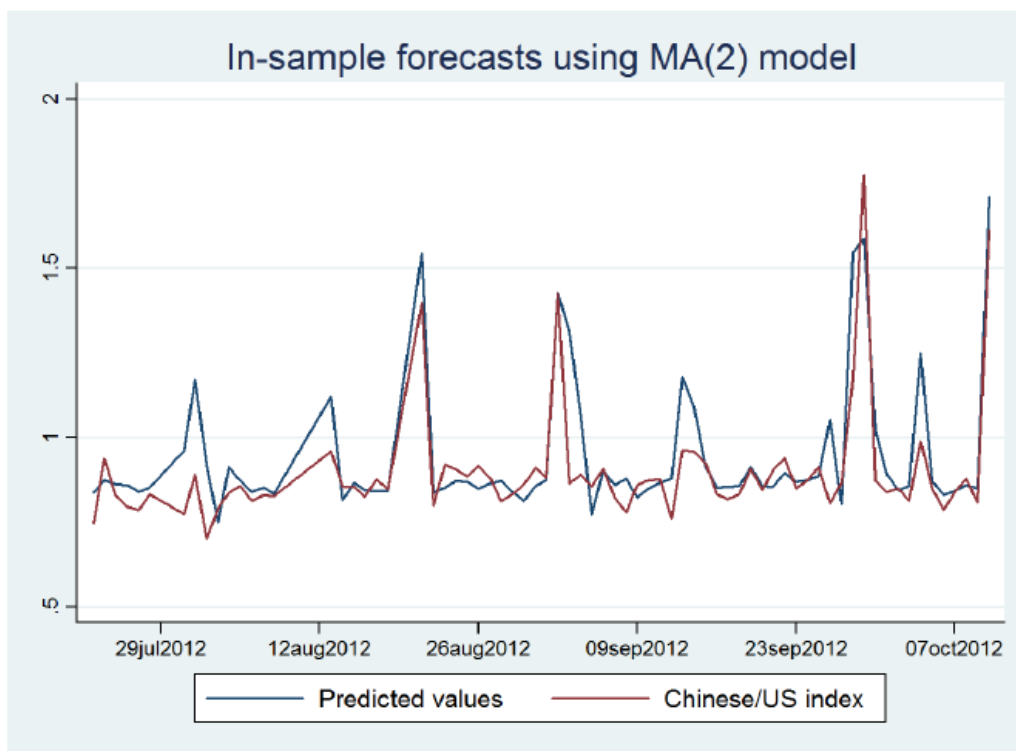


Fig 3 – How well the model performs in predicting the indexes' ratio

This analysis shows that the Chinese API is systematically manipulated, and this may be due to political pressure during sensitive events, or to the institutionalization of thresholds that government officers must care about. Next, we analyse whether this distorted signal from the government can affect household responses to air pollution.

⁴ Note that these criteria are only interpretable as relative measures to compare different models, they have no absolute meaning relative to goodness of fit, as the classical R squared would have.

HOUSEHOLDS

Individuals living in Beijing choose if and how to respond to the environmental and health hazard presented by air pollution, by virtue of incurring a cost, monetary or in terms of time, for protecting themselves and their families from the damages of pollution. This decision for individual and intra-household allocation of this public good, clean air, then translates into the health outcomes of the whole family. Each household member faces a trade-off between income and non-market activities (leisure, averting behaviour, taking care of children, etc.), so agents bargain for who dedicates more time to a tasks, depending on relative opportunity costs⁵. Furthermore, households decide how to obtain information about air pollution, either by relying on government-controlled sources (TV, newspapers, radio), on their own perception (for instance through visibility or smell of the air), or on independent sources, which are still relatively less popular in China, such as the internet. The US embassy measurements are available hourly through an online tweet, which can even be downloaded on a mobile device. The internet is restricted in China, but young people nowadays are able to access this sort of information through the web.

In order to examine the behaviour of households with respect to air pollution and health, we conducted a household survey in urban Beijing, to elicit expenditure and time allocation to averting activities. The interviews were conducted in three districts of Beijing, Haidian, Chaoyan and Dongcheng, for a total of 1672 individuals (578 households). Sample selection was designed to ensure representativeness, using probability proportional to size (PPS) at the district and street level and random selection at the community and household level.

The questionnaire inquired in detail about a) the socio-economic characteristics of the household, b) habits and averting behaviours (wearing masks, reducing time outdoor, changing means of transportation, buying air purifiers, doing preventive health checks - more detail below), c) how the family gathered information about air pollution and d) health of family members, particularly airborne diseases, cost of illness and insurance.

Health and pollution

⁵ For a formal analysis of the possible bargaining solutions inside the household, see a summary of intra-household allocation models by Browning et al. 2010.

Preliminary analysis of the data indicates that in our sample we observe the standard epidemiological correlation between air pollution and illness episodes outcomes (Fig.4). This however is not the major aim of this analysis, since the linkage between air pollution and airborne diseases has been extensively studied by medical experiments (Ren and Tong 2008). Rather we would like to examine how the adaptive behaviour of the household comes into play and what is the role of information access.

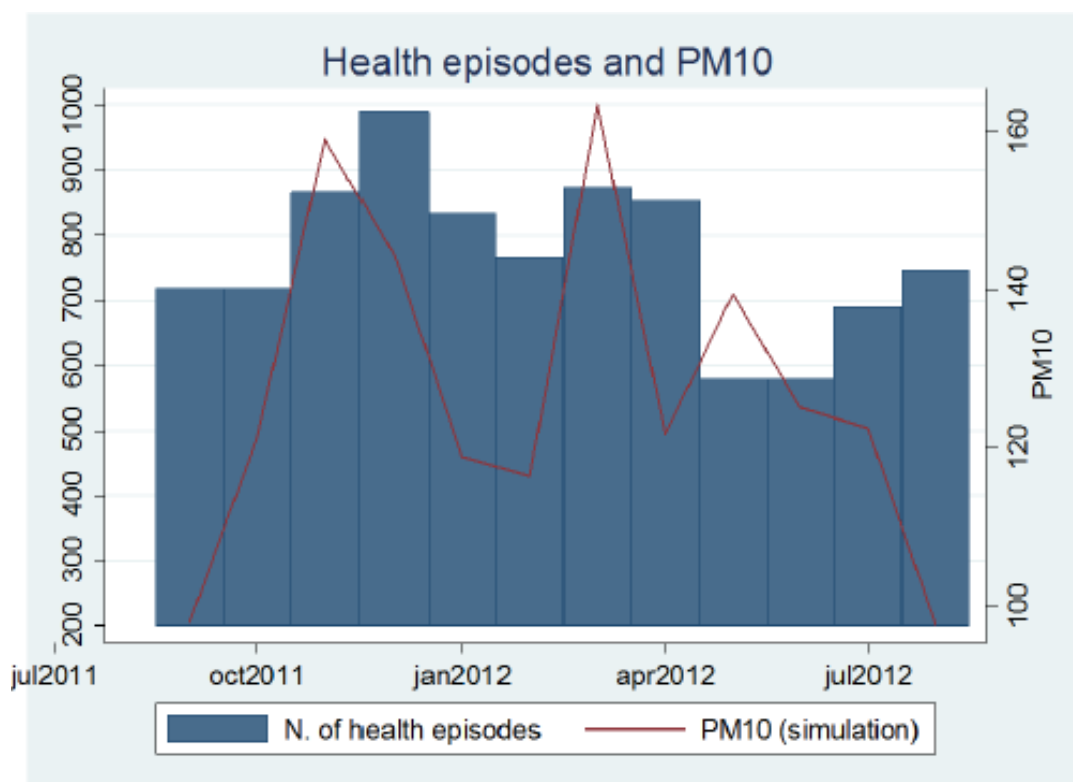


Fig. 4 – Number of illness episodes and pollution levels

Averting behaviours

The averting behaviours considered are quite heterogeneous: they range from time-consuming activities to more expensive ones; some are undertaken by almost everybody, while others are rarely adopted. Table 2 illustrates the characteristics of averting choices, their correlation with income and also,

following the original literature on self-protection versus market protection (Ehrlich and Becker 1972), with insurance.

Table 2: Characteristics of averting behaviours

AVERTING BEHAVIOUR	FREQUENCY	INCOME	INSURANCE
Reduce time outdoor	58 %	0.01	-0.02
Transport change	6 %	-0.01	0.03
Mask	11 %	0.1 **	0.01
Preventive health checks	62 %	0.1 ***	0.1 **
Air purifier	21 %	0.2 ***	0.3 ***

“Reduce time outdoor” combines two questions, one about leisure outdoor and one about exercise. “Transport change” implies switching from means of transportation with high exposure to pollution (i.e. walking) to relatively safer ones, such as car. For facial masks we asked the respondents to mention if they choose a simple paper mask or a more sophisticated one⁶, but only few people used higher quality masks (2% of the sample). Finally, two expensive strategies are presented: buying an air purifier, whose price reaches 30,000 yuan (with an average monthly income of around 4,000¥) or going for preventive medical checks whose price ranged from 10 to 15,000¥ annually. These latter behaviours correlate more strongly with income and private insurance expenditure.

Information about pollution

Internet use for the collection of information about air pollution is still limited. The majority of people interviewed relied on government-controlled sources of information, such as TV, radio or newspapers - see Table 3. Furthermore, 70% of our sample considers the information available on air pollution sufficient and only 8% of the remaining respondents indicated they would like more detailed information through the internet. Therefore, the government can exert a direct influence on the choices of most people when deciding what data to publish for the API.

⁶There exist more expensive masks on the market that filter much more efficiently particulate matter.

Table 3: Different sources of information about air pollution

SOURCE OF INFORMATION	FREQUENCY
Government sources (TV, radio, newspapers)	77 %
Internet (PC or mobile device)	6 %
Self-perception, other people	17 %
Doesn't care	0.1 %

An important point is whether we consider using the internet as a form of averting behaviour. Table 4 shows that this choice does not correlate significantly with the other averting decisions. All other behaviours are instead highly correlated, with the exception of preventive health checks, which are an ex-ante measure that cannot be considered as an immediate response to highly polluted days, but rather a long-term concern for the health hazard posed by pollution.

Table 4: Correlations of internet and averting behaviour

	Internet	Reduce time outdoor	Transport change	Mask	Preventive health checks	Air purifier
Internet	1.00					
Reduce time outdoor	-0.02 (0.60)	1.00				
Transport change	0.08* (0.07)	0.20*** (0.00)	1.00			
Mask	0.03 (0.45)	0.19*** (0.00)	0.28*** (0.00)	1.00		
Preventive health checks	0.04 (0.30)	0.02 (0.46)	0.04 (0.14)	0.06** (0.02)	1.00	
Air purifier	0.02 (0.69)	0.11*** (0.00)	0.07*** (0.01)	0.11*** (0.00)	0.07*** (0.00)	1.00

Awareness of the problem

Despite not being a primary goal of the survey (i.e. we did not use any experimental setting to elicit the exact value given to clean air), from some answers we can get a sense about the awareness about the environmental problem posed by air pollution. For instance, only 66 % of respondents had noticed and remembered the 2 most polluted haze days in Beijing, indicating that individual perception and interest in the issue might be still relatively limited. For those who did remember the extremely bad haze days, Table 5 shows how people reacted afterwards.

Table 5: What did you do after the peak pollution days last year?

Nothing	38 %
I started worrying more about air pollution	25 %
I look for more information	9 %
I worry more about air pollution and look for more information about it	27 %
Other	1 %

Empirical model

Starting from these stylized facts, we analyse more formally the determinants of averting behaviour and of the source of information. First of all, we distinguish the agents that use internet as opposed to relying on government sources or none. We set a general empirical model of information, as follows:

$$Info_i = \beta_0 + \mathbf{X}_i\beta_1 + \beta_2 Exposure_i + \beta_3 Income_i + \beta_4 TimeFlexibility_i + \delta_j Illnesses_{ji} + \epsilon_{ui}$$

and we test it using as a dependent variable different types of information sources. Such specification may pose problems in terms of reverse causality, especially once we introduce illnesses (j corresponds

to either acute or chronic airborne diseases, symptoms, total diseases or self-rated health), so we also try a model without any disease. Overall, we will be cautious in making causal statements, since there could be biases arising from potential omitted variables. The controls in \mathbf{X} are age, gender, education level and smoking status, to capture risk attitude towards pollution and lung diseases. “Exposure” is the total amount of hours that a person spends outdoor, mostly predetermined. Income is measured at the household level, while time flexibility at the individual level, and corresponds to the amount of hours spent working (assuming that someone who is retired or unemployed is more flexible to get interested into air pollution and avert its damages).

We consider as left-hand-side variable the binary choice between using or not the internet to check air pollution information. The dependent variable is a dummy equals to 1 if the respondent said (s)he uses internet as a source of information, zero otherwise. Since the occurrence of a 1 is rare, we use a complementary log-log specification to account for the asymmetric nature of the variable (Hilbe 1996). The results are displayed in Table 6.

With averting behaviours, we specify a similar model and test it with different behaviours.

$$Avert_i = \beta_0 + \mathbf{X}_i\beta_1 + \beta_2 Exposure_i + \beta_3 Income_h + \beta_4 Time_i + \beta_5 Other_i + \delta_j Illnesses_{ji} + \epsilon_{it}$$

Beyond the controls used in the previous specification, we add a measure of insurance payment, following the literature on market protection versus self-protection, and a control for car ownership. The use of internet is also included, although it was already seen from the correlation table in the stylized facts that it will probably not relate with any averting behaviours.

Results

Tables 6 and 7 present the results from a simple econometric examination of the household survey. Considering that the sample is small, only the strongest effects should emerge. Only individual characteristics, as being young and educated, have a significant explanatory power for the choice of using internet. This indicates that this choice is not constrained by income considerations or by lack of time, nor by concerns about one's health and exposure. As a robustness check, we repeated a similar exercise using other formulations of the dependent variable, and results remain the same. For averting behaviour, the cross-sectional logit displayed in Table 7 indicates that, as expected, income matters only for the most expensive behaviours, i.e. preventive health checks and ownership of air purifiers.

Insurance is only significant in determining medical check-ups, which clearly indicates that other averting behaviours are too short term to create a trade-off or complementarity between market insurance and self-protection. The number of hours that a person normally spends outdoor and the number of hours worked both correlate negatively with an averting behaviour of time change (spending less time in the open air for leisure or exercise), confirming that for some averting behaviours the problem is not given by income constraints, but by scarce flexibility to change schedule. Internet usage, as one could expect from the correlations displayed in the stylized facts, is not significantly related to any of these averting choices.

Overall, given that China is a developing nation and its environmental priorities should be quite different from those of richer nations, it is interesting to find that averting behaviours indeed depends on time availability (for relatively inexpensive behaviours) and on monetary constraints (for more expensive behaviours). This indicates that inside the household we have an allocation of tasks which reflects relative opportunity costs, which then translate in different capacities to avert. But since internet usage is not common to check pollution information, the government can fully shape the preferences of the population about environmental risks.

Table 7: Cross Section - Averting behaviours

	Time outdoor	Transport	Mask	Health checks	Air purifier
Age	0.008 (0.008)	-0.022*** (0.009)	-0.016** (0.008)	-0.002 (0.001)	0.006 (0.007)
Male	-0.327* (0.179)	0.069 (0.142)	-0.537*** (0.178)	0.020 (0.033)	0.015 (0.120)
Education	-0.032 (0.121)	0.069 (0.124)	0.056 (0.118)	0.102*** (0.019)	0.175* (0.105)
N. of cigarettes	-0.008 (0.014)	-0.008 (0.018)	-0.054** (0.024)	-0.003 (0.003)	-0.008 (0.015)
Hours outdoor	-0.020** (0.009)	0.033*** (0.010)	0.003 (0.009)	0.002 (0.002)	-0.001 (0.011)
Household Income	1.822 (1.906)	0.772 (2.615)	-1.423 (1.810)	0.378** (0.186)	3.559** (1.761)
Hours work	-0.010* (0.006)	-0.011* (0.006)	-0.004 (0.005)	-0.001 (0.001)	-0.008 (0.006)
Insurance coverage	0.005 (0.008)	0.007 (0.009)	0.011 (0.008)	0.004*** (0.001)	0.000 (0.006)
Car	0.078 (0.359)	0.685* (0.395)	0.493* (0.276)	0.057 (0.047)	1.433*** (0.319)
Self-rated health	0.195 (0.150)	0.202 (0.172)	-0.049 (0.135)	-0.006 (0.032)	-0.292** (0.143)
Internet	-0.010 (0.750)	0.410 (0.622)	0.264 (0.376)	0.007 (0.107)	-1.238 (0.874)
Constant	0.609 (0.891)	-2.673*** (0.740)	-1.282* (0.748)	0.158 (0.137)	-2.374*** (0.688)
Observations	712	709	716	896	898

Standard errors clustered at household level in parentheses

* $p < 0.10$, ** $p < 0.05$, *** $p < 0.01$

CONCLUSION

This analysis has shown that the Chinese government has incentives to manipulate information about pollution and generate a distorted signal; since most people use only government-controlled media as sources of information about pollution, this remains relevant for the majority of the population. In particular, this may penalize older people and less educated people who do not use alternative means of information and overall might be less aware of the problem. Households, however, are able to mildly adjust to air pollution depending on their income, time flexibility, and other contingent factors, but not in relation to the way they obtain information. In a way, the population delegates it to the central government to decide for them when they should worry about pollution, and the government paternalistically reassures the country that air pollution is generally not a problem. In the future this is bound to change, but for the moment the socio-economic mechanisms for individual adaptation in China are fully conditioned by the government, which is not willing to provide accurate information for people to freely decide how to respond to these risks. And this could be very problematic not only for adaptation to air pollution peaks, but for many other cases of environmental degradation, or for more drastic climatic changes.

ACKNOWLEDGMENTS

We would like to thank Professor Zhang Shiqiu and all the economics team of the College of environmental Science and Engineering for their support, especially in the preparation of the household survey; Professor Tim Swanson, for invaluable advice and guidance; the participants to the Ferrara IAERE conference and those to the CIES Seminars Series for many useful comments and suggestions. The research leading to these results and particularly the households survey in Beijing has received funding from the European Union's Seventh Framework Programme (FP7/2007-2013) under the grant agreement n° 266992 (GLOBAL IQ). All the usual disclaimers apply.

REFERENCES

- Alberini A., Bhattacharya S., & Cropper M. L. (2007). *The value of mortality risk reductions in Delhi, India*. Journal of Risk and Uncertainty, Springer US, 34, 21-47. (1)
- Alberini A., Cropper M., Fu T.-T., Krupnick A., Liu J.-T., Shaw D., et al. (1997). *Valuing Health Effects of Air Pollution in Developing Countries: The Case of Taiwan*. Journal of Environmental Economics and Management, 34(2), 107-126. (2)
- Andrews S. Q. (2008). *Inconsistencies in air quality metrics: 'Blue Sky' days and PM10 concentrations in Beijing*. Environmental Research Letters, 3, No. 3. (3)
- Apps P. F., & Rees R. (1997). *Collective Labor Supply and Household Production*. Journal of Political Economy, 105(1), pp. 178-190. (4)
- Aunan K., & Pan X.-C. (2004). *Exposure-response functions for health effects of ambient air pollution applicable for China a meta-analysis*. Science of The Total Environment, 329, 3-16. (5)
- Bartik T. J. (2008). *Evaluating the Benefits of Non-marginal Reductions in Pollution Using Information on Defensive Expenditures*. Dans J. Herriges, & C. L. Kling (Eds.), *Revealed Preference Approaches to Environmental Valuation* (pp. 459-475). W.E. Upjohn Institute for Employment Research. (6)
- Becker G. S. (1965). *A Theory of the Allocation of Time*. The Economic Journal, 75(299), pp. 493-517. (7)
- Bjørn Sætterstrøm M. K.-H., & Sørensen J. (2012). *A Method to Assess the Potential Effects of Air Pollution Mitigation on Healthcare Costs*. Journal of Environmental and Public Health, vol. 2012. (8)
- Bohara A. K., McKee M., Berrens R. P., Jenkins-Smith H., Silva C. L., & Brookshire D. S. (1998). *Effects of Total Cost and Group-Size Information on Willingness to Pay Responses: Open Ended vs. Dichotomous Choice*. Journal of Environmental Economics and Management, 35(2), 142-163. (9)
- Bousquet J., Khaltayev N., Cruz A., & Organization W. H. (2007). *Global Surveillance, Prevention And Control Of Chronic Respiratory Diseases: A Comprehensive Approach*. (WHO, Ed.) World Health Organization. (10)
- Braga A. L., Saldiva P. H., Pereira L. A., Menezes J. J., Conceicao G. M., Lin C. A., et al. (2001). *Health effects of air pollution exposure on children and adolescents in São Paulo, Brazil*. Pediatric Pulmonology, 31(2), 106-113. (11)
- Bresnahan B. W., Dickie M., & Gerking S. (1997). *Averting Behavior and Urban Air Pollution*. Land Economics, 73(3), pp. 340-357. (12)

- Bresnahan B., & Dickie M. (1995). *Averting Behavior and Policy Evaluation*. Journal of Environmental Economics and Management(397e). (13)
- Browning M., & Gortz M. (2012). *Spending Time and Money within the Household*. The Scandinavian Journal of Economics, 114(3), 681-704. (14)
- Browning M., Bourguignon F., Chiappori P.-A., & Lechene V. (1994). *Income and Outcomes: A Structural Model of Intrahousehold Allocation*. Journal of Political Economy, 102(6), 1067-96. (15)
- Browning M., Chiappori P.-A., & Lechene V. (2010). *Distributional Effects in Household Models: Separate Spheres and Income Pooling*. The Economic Journal, 120(545), 786-799. (16)
- Calthrop E., & Maddison D. (1996). *The dose-response function approach to modelling the health effects of air pollution*. Energy Policy , 24(7), 599-607. (17)
- Carter M., & Katz E. (1997). *Intrahousehold Resource Allocation in Developing Countries: Methods, Models and Policies*. Dans H. J. Haddad L (Ed.). (18)
- Chen Y., Jin G. Z., Kumar N., & Shi G. (2013). *Gaming in Air Pollution Data? Lessons from China*. NBER Working Paper No. 18729(18729). (19)
- Chiappori P.-A. (1992). *Collective Labor Supply and Welfare*. Journal of Political Economy, 100(3), 437-67. (20)
- Cook P. J., & Graham D. A. (1977). *The Demand for Insurance and Protection: The Case of Irreplaceable Commodities*. The Quarterly Journal of Economics, 91(1), pp. 143-156. (21)
- Courant P. N., & Porter R. C. (1981). *Averting expenditure and the cost of pollution*. Journal of Environmental Economics and Management, 8(4), 321-329. (22)
- Cropper M. L. (1981). *Measuring the Benefits from Reduced Morbidity*. The American Economic Review, 71(2), pp. 235-240. (23)
- Dixit A. K. (1990). *Optimization in Economic Theory*. Oxford University Press. (24)
- Ehrlich I., & Becker G. S. (1972). *Market Insurance, Self-Insurance, and Self-Protection*. Journal of Political Economy, 80(4), 623-48. (25)
- El-Fadel M., & Massoud M. (2000). *Particulate matter in urban areas: health-based economic assessment*. Science of The Total Environment, 257, 133-146. (26)
- (EPA) U. E. (2006). *Guideline for Reporting of Daily Air Quality – Air Quality Index (AQI)*. EPA-454/B-06-001, May 2006. (27)
- Foster A., & Kumar N. (2011). *Health effects of air quality regulations in Delhi, India*. Atmospheric Environment, 45, 1675-1683. (28)

- Grossman M. (1972). *On the Concept of Health Capital and the Demand for Health*. *Journal of Political Economy*, 80(2), pp. 223-255. (29)
- Hausman J. A., & Taylor W. E. (1981). *Panel Data and Unobservable Individual Effects*. *Econometrica*, 49(6), pp. 1377-1398. (30)
- Hilbe J. M. (1996). *Maximum-likelihood complementary log-log regression*. *Stata Technical Bulletin Reprints*, Stata Press, 6, 129–131. (31)
- Qiu H., Yu I.T., Tian L., Wang X., Tse L.A., Tam W., Wong T.W. (2012). *Effects of Coarse Particulate Matter on Emergency Hospital Admissions for Respiratory Diseases: A Time-Series Analysis in Hong Kong*. *Environmental Health Perspectives*, 120(4), 572–576. (32)
- Hubbell B., & Jordan J. L. (2000). *Joint Production and Averting Expenditure Measures of Willingness to Pay: Do Water Expenditures Really Measure Avoidance Costs?* *American Journal of Agricultural Economics*, 82(2), 427-437. (33)
- Jalan J., & Ravallion M. (2003). *Does piped water reduce diarrhea for children in rural India?* *Journal of Econometrics*, 112(1), 153-173. (34)
- Jalan J., & Somanathan E. (2008). *The importance of being informed: Experimental evidence on demand for environmental quality*. *Journal of Development Economics*, 87(1), 14-28. (35)
- Kerry Smith V., & Desvousges W. H. (1986). *Averting behavior: Does it exist?* *Economics Letters*, 20(3), 291-296. (36)
- Li J., Guttikunda S. K., Carmichael G. R., Streets D. G., Chang Y.-S., & Fung V. (2004). *Quantifying the human health benefits of curbing air pollution in Shanghai*. *Journal of Environmental Management*, 70(1), 49-62. (37)
- Maskin E., Qian Y., & Xu C. (2000). *Incentives, Information, and Organizational Form*. *The Review of Economic Studies*, 67(2), pp. 359-378. (38)
- Moretti E., & Neidell M. (2011). *Pollution, Health, and Avoidance Behavior: Evidence from the Ports of Los Angeles*. *Journal of Human Resources*, 46(1), 154-175. (39)
- Neidell M. J. (2008). *Information, Avoidance Behavior, and Health: The Effect of Ozone on Asthma Hospitalizations*. NBER Working Papers, National Bureau of Economic Research, Inc. (40)
- Pitt M. M., & Rosenzweig M. R. (1990). *Estimating the Intrahousehold Incidence of Illness: Child Health and Gender-Inequality in the Allocation of Time*. *International Economic Review*, 31(4), 969-80. (41)

- Pitt M. M., Rosenzweig M. R., & Hassan M. N. (1990). *Productivity, Health, and Inequality in the Intrahousehold Distribution of Food in Low-Income Countries*. *The American Economic Review*, 80(5), pp. 1139-1156. (42)
- Pittel K., & Rübbelke D. T. (2008). *Climate policy and ancillary benefits: A survey and integration into the modelling of international negotiations on climate change*. *Ecological Economics*, 68(1-2), 210-220. (43)
- Quiggin J. (1992). *Risk, self-protection and ex ante economic value--some positive results*. *Journal of Environmental Economics and Management*, 23(1), 40-53. (44)
- Quiggin J. (2002). *Risk and Self-Protection: A State-Contingent View*. *Journal of Risk and Uncertainty*, 25(2), 133-45. (45)
- Ren C., & Tong S. (2008). *Health effects of ambient air pollution - recent research development and contemporary methodological challenges*. *Environmental Health*, 7(1), 56. (46)
- Shogren J. F., & Crocker T. D. (1999). *Risk and Its Consequences*. *Journal of Environmental Economics and Management*, 37(1), 44-51. (47)
- Simmons K. M., & Kruse J. B. (2000). *Market Value of Mitigation and Perceived Risk: Empirical Results*. *The Journal of Economics*, 26(1), 41-51. (48)
- Somanathan E. (2010). *Effects of Information on Environmental Quality in Developing Countries*. *Review of Environmental Economics and Policy*. (49)
- Strand J. (2007). *Public-good valuation and intra-family allocation*. *Environmental and Resource Economics*, 38, 527-543. (50)
- Talberth J., Berrens, R. P., Mckee M., & Jones M. (2006). *Averting And Insurance Decisions In The Wildland-Urban Interface: Implications Of Survey And Experimental Data For Wildfire Risk Reduction Policy*. *Contemporary Economic Policy*, 24(2), 203-223. (51)
- Tsui K.-y., & Wang Y. (2004). *Between Separate Stoves and a Single Menu: Fiscal Decentralization in China*. *The China Quarterly*, 177, 71-90. (52)
- Um M.-J., Kwak S.-J., & Kim T.-Y. (2002). *Estimating Willingness to Pay for Improved Drinking Water Quality Using Averting Behavior Method with Perception Measure*. *Environmental and Resource Economics*, 21, 285-300. (53)
- Viscusi W. K., & Aldy J. E. (2003). *The Value of a Statistical Life: A Critical Review of Market Estimates throughout the World*. *Journal of Risk and Uncertainty*, 27(1), 5-76. (54)
- Wang W., Primbs T., Tao S., & Simonich S. L. (2009). *Atmospheric Particulate Matter Pollution during the 2008 Beijing Olympics*. *Environmental Science & Technology*, 43(14), 5314-5320. (55)

- Whitehead J. (2005). *Environmental Risk and Averting Behavior: Predictive Validity of Jointly Estimated Revealed and Stated Behavior Data*. *Environmental & Resource Economics*, 32(3), 301-316. (56)
- WHO. (2005). *Air quality guidelines for particulate matter, ozone, nitrogen dioxide and sulfur dioxide. Global update 2005. Summary of risk assessment*. World Health Organization. (57)
- Xu C. (2011). *The Fundamental Institutions of China's Reforms and Development*. *Journal of Economic Literature*, 49(4), 1076-1151. (58)
- Zhang P. a. (2012). *Long-Term Exposure to Ambient Air Pollution and Mortality Due to Cardiovascular Disease and Cerebrovascular Disease in Shenyang, China*. *Respiration*, 84 (5)(6), 360-368. (59)

CLIMATE POLICY AND ECONOMIC ASSESSMENT

Climate change and urbanization:
implications, feedback and evaluation of strategies

Integrating the human dimension in ecosystem based adaptation to global changes

L. Ilieva ^{1*}, C. Giupponi ^{1,2}

¹*Dipartimento di Economia, Università Ca' Foscari di Venezia Venezia, Italy*

²*Centro Euro-Mediterraneo sui Cambiamenti Climatici (CMCC), Venezia, Italy*

*Corresponding author: lili.ilieva@unive.it

Abstract

In the quest for adaptation to climate change, ecosystems in good structural and functional status are widely recognised as fundamental asset for the enhancement of resilience of the broader system called socio-ecosystem (SES), by delivering benefits to communities via their services. In parallel, society is able to strengthen SES's adaptive capacity, through for example ad hoc climate change adaptation plans (CCAP). Unfortunately, only limited efforts are in place to integrate ecosystems' and society's adaptive capacities, while instead the potential for synergies is evident. By taking the challenge of including the complex set of natural and human providers and beneficiaries in the dynamic analysis of the SES, a truly holistic approach can be implemented and adaptive effectiveness can substantially improve. Exploring the notion of ecosystem services (i.e. regulating, provisioning, supporting and cultural) and social services (e.g. maintenance and sustainable management of land and resources to limit vulnerability) being an integral part of a unique adaptation response strategy provides an avenue for an innovative approach based upon the notion of socio-ecosystem services (SES-S).

Ecosystem Based Adaptation (EbA) is an already established approach, which we propose to be further developed by integrating the human dimension, through capabilities for integrated system dynamic. The aim of the research reported in this work is to go beyond the usual approach in exploring factors contributing to vulnerability and pathways to strengthen resilience of communities, by means of a dynamic integration of nature and the human dimension. With the proposed approach both humans and ecosystems are recognised as being the entities of the same process to respond to threats and exploit opportunities that may derive from global change and, in particular from climate variability and extreme events. Capturing the essence of this approach in the context of adaptation and effectively communicating it to policy makers requires effective interfaces between the various actors involved. A consolidated framework for communicating societal and environmental issues can be used to introduce

a system dynamics approach can be applied in the DPSIR (Drivers–Pressures–State Change–Impact–Response) framework. The original framework has been further developed by the authors to include exogenous drivers for the formalisation of the adaptation problem according to the notion of SES-S based adaptation. An illustration of the proposed approach provided through the presentation of a case study on the coastal zone in Guyana.

Keywords: *Ecosystem services, ecosystem-based adaptation, coastal ecosystems, Guyana*



1. INTRODUCTION

It is widely asserted that environmental and climatic changes pose most tangible effects on communities highly dependent on natural ecosystems to support their livelihoods [1]. Environmental and human-induced disruption of ecosystem functions (e.g. operation of hydrological cycle contributing to flood control and drinking water supply) makes socio-ecological system more vulnerable to external threats [2]. Hence the maintenance of an integrated and functional natural capital to deliver environmental goods and services is a precondition for development of a resilient socio-economic system [3]. Adapting to climatic changes can be perceived as a systematic response formed via the interconnection between ecosystem services (e.g. provisioning, supporting, regulating and cultural) and social services (e.g. maintenance, conservation and sustainable management of natural resources) for the design of a holistic approach to address the complexity of climate impacts.

The role of ecosystems in protecting coastal shorelines, mitigating floods and contributing to food security is evident, yet the emergence of ecosystem-based approach to adaptation (EbA) is a rather recently introduced concept [4][5]. By combining practices for biodiversity conservation and maintenance of ecosystem services into a broader adaptation framework, the ecosystem approach is embedded into the concept of socio-ecological system resilience [6].

The ecosystem-based adaptation (EbA) calls not only for the consideration of natural (i.e. environment, resources, biodiversity) elements but provides a foundation for an integrated view in which human (i.e. socio-economic, cultural, religious) elements of the social-ecological system and their interactions are as well explored. The opportunity thus emerges to develop innovative assessment and management approaches which go beyond the rather consolidated approach based upon the analysis of ecosystem services. An avenue for innovative and more effective approaches can come from the development of consolidated ES analysis towards a novel notion of SES (here Socio-Ecosystem Services), in which not only the provision of services from ecosystems to humans is considered, but also the services provided by society (e.g. maintenance of land in rural areas to limit vulnerability) and the fluxes between any kind of provider and any beneficiary. An opportunity emerges to develop innovative assessment and management approaches which go beyond the rather consolidated approach based upon the analysis of ecosystem services and, in case, on the establishment of PES mechanisms (Payment for ecosystem services) as a policy solution for nature valorisation and poverty alleviation.

2. STUDY AREA

The coastal zone of Guyana is in many areas 0.5 – 1.0 m and more below sea level, making it prone to strong tidal influences and extremely vulnerable to storm surges and sea level rise. The coastline constitutes only 7% (216,000km²) of the country's total land, yet it is where human settlements are most concentrated and 76.6% (ca. 540 000 people) of the population live predominantly in rural settings [7]. In addition to human settlements most of the country's economic assets e.g. infrastructure and agriculture (e.g. sugar cane and rice fields) are located at the coastal plain as well. The coastal area is a mosaic of natural systems (e.g. mangroves, mud banks) and man-made sea defenses (e.g. seawalls, drainage system), which serve to protect the coast from inundation and flooding. It is divided into two zones with different level of impact and developmental status – *Coastal zone I and II*. *Coastal zone I* is densely populated region of eastern Essequibo and up to Berbice and Demerara. *Coastal zone II* is the western Essequibo area where the coast comprises largely of natural ecosystems and limited built coastal protection. The coast is characterised by partly degraded ecosystems and extensive engineered coastal protection [7].

Extreme events as floods have been observed to intensify in Guyana over the last decade causing large damage on livelihoods and major economic sectors located at the coastal zone. In the last decade rice production has been observed to decline by almost 30% in the period 1997 - 2009, which is attributed to crop diseases and inconsistent weather [8]. The damages from the flood in 2005 alone resulted in total loss of 60% from GDP from which agriculture e.g. rice crops, experiencing the greatest damage and highest cost of US\$ 8.8 million [8]. Adaptation measures in the form of coastal protection and agricultural intensification has been implemented in the past, yet threats from natural hazards continue to increase exposing communities dependent on subsistence agriculture to more severe impacts. Climate projections reveal economic losses to reach US\$150 million by 2030 [9]. Based on IPCC scenarios, projections show loss of agricultural land to be between 48,393 ha and 85,585 ha by 2031 resulting in estimated economic cost between USD\$ 794 - 1,577 million for rice and USD\$ 144 - 300 million. Subsistence agriculture is expected to be highly impacted and endangering livelihoods [8].

3. METHODS

By taking the challenge of including the complex set of natural and human providers of services and beneficiaries in the analysis a truly holistic approach can be implemented and operational effectiveness can substantially improve. The integration of this approach into the complex scene of adaptation efforts would be analysed through system dynamic modeling of the socio-ecological setting with the intention to explore the behavior of the system and inform decision-makers. The system analysis will take form of four consecutive steps build upon the theoretical foundation of system dynamic modeling[10]. An initial step is the development of Cognitive Map describing the system, with its endogenous and exogenous elements in the form of a DPSIR (Drivers–Pressures–State Change–Impact–Response) framework. The initial application of DPSIR would provide an opportunity to explore key elements and their functionality in a system boundary and enable a better understanding and communication in the policy-making arena [11]. Build upon this knowledge the causal loop diagram will provide an overview of interactions and functional dependencies of the key system variables, which will be further applied in the development of a stock and flow map. Such a conceptual map will characterize the system and generate information upon which policy decisions can be formulated and tested. The modeling steps will be performed using the visual modeling tool VENSIM.

The development of this concept can be illustrated with a case study of the coastal socio-ecological system in the context of highly vulnerable predominantly rural agricultural setting in Guyana. Outcomes would provide a scientific framework for policy making to integrate such approach in the development of a national adaptation strategy to provide a coherent and effective response to climate-related impacts..

4. PRELIMINARY ANALYSIS

Tropical coastal social–ecological systems differ from other social–ecological systems (SES) due to the higher degree of risk and uncertainty associated with coastal and marine resource extraction, land use change and natural hazards. Analysing the elements of the coastal system and their causal relationships applying the DPSIR approach as a framework will provide a systematic analysis of the environmental changes and potential responses in a holistic manner [12]. The preliminary analysis aims to integrate the ecosystem-based adaptation as a response addressing pressures and drivers to facilitate the

communication of the role of maintaining and restoring ecosystems and their services in adaptation measures in Guyana. Tables 1 and 2 illustrate the socio-ecological elements of the DPSIR framework for the coastal zone of Guyana taking into account exogenous drivers as sea level rise (SLR). The framework illustrates the role of ecosystem services as defined by Millennium Ecosystem Assessment (2006) (e.g. Supporting, Provisioning, Regulating and Cultural) in reducing the vulnerability of the system. Ecosystem-based adaptation practices analysed in the framework include:

- a) Ecosystem approach to fishing,
- b) Sustainable harvesting,
- c) Agro-environmental measures,
- d) Restoration of ecosystems,
- e) Monitoring & research and
- f) Extension of protected areas

These practices are only a fraction of the possible ecosystem-based adaptation measures, yet they represent the major principles of the concept and provide an image of their role in the system. The approach provides a systematic analysis of the two coastal zones - *i) Coastal Zone I and ii) Coastal Zone II* thus visualising the difference of the elements and links under different scenarios.

The cognitive map in Figure 1 shows the DPSIR elements and causal links of the socio-ecological system of *Coastal Zone I* in Guyana, characterized with high population density, developed economic activity, intensive agricultural fields and fishing industry with a mixed urban and rural landscape, where the capital of Georgetown is also located.

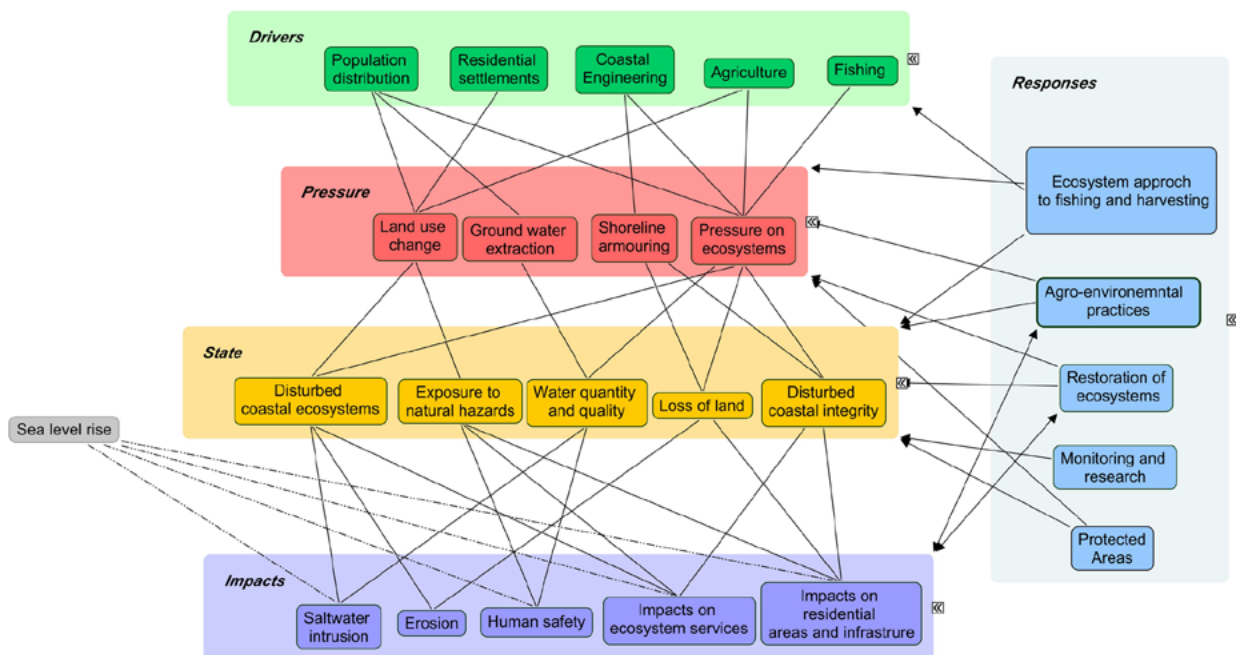


Fig 1: A conceptual map for DPSIR framework for Coastal Zone I in Guyana: From top to bottom i) Drivers, ii) Pressures, iii) State, iv) Exogenous driver – Sea level rise, v) Impacts and EbA Responses

Major endogenous socio-economic drivers of the system are population distribution due to migration from hinterland to the coast thus resulting in demand for additional residential settlements in areas with high exposure to floods. Coastal engineering is present at large in the area and often being a reason for disturbance in coastal ecosystems which are under pressure from intensive agriculture (e.g. monoculture) and fishing practices lead to pressures on the coastal ecosystems as well. Harvesting of mangroves is not a major driver in this area due to better awareness and monitoring of the forests.

The conceptual map in Figure 2 illustrates the elements of the DPSIR framework of the *Coastal Zone II* of Guyana characterized by relatively low population density, rural landscape and sustainable small-scale agriculture and subsistence fishing.

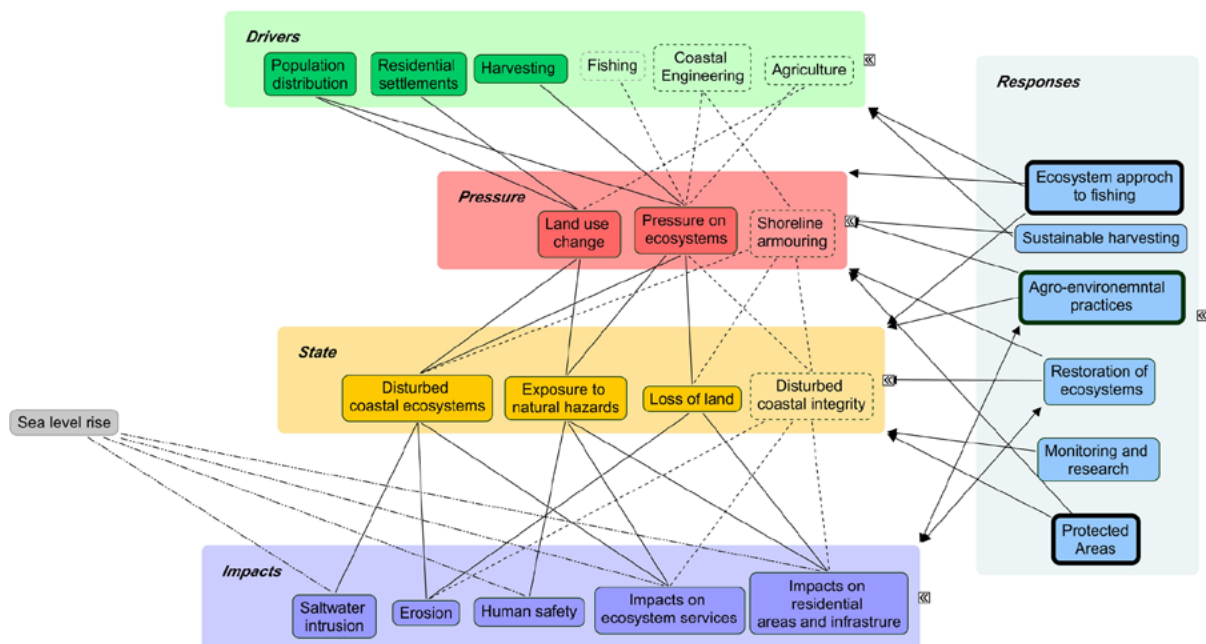


Fig 2: A conceptual map of DPSIR framework for Coastal Zone II in Guyana: From top to bottom *i) Drivers, ii) Pressures, iii) State, iv) Exogenous driver – Sea level rise, v) Impacts and vi) EbA Responses*

Coastal ecosystems are disturbed through unsustainable harvesting of predominantly mangrove trees. Fishing and extensive agriculture in this region is at present not at large scale yet it is a potential threat in the path to economic development these elements to turn to driving forces. Hence, these components and related outcomes are presented in dotted lines. It can be observed in the previous conceptual map for Coastal Zone I that the existence of the additional drivers would lead to more pressure in the socio-ecological system and negatively alter its state making it unstable and vulnerable. The highlighted practices are the ones already applied to a certain scale by the coastal communities providing an example of an autonomous adaptation process integrating both the notion of social and ecosystem services.

5. FURTHER RESEARCH STEPS

For the purpose of developing the next steps in the system dynamic analysis and develop causal loop with focus on climate change impacts in the agricultural system and factors affecting its stability and enhancing resilience. The system dynamic model will analyse proposed ecosystem-based adaptation efforts emphasising on the human dimension of managed agri-environmental measures as agro-

ecology.. In the process of developing the model quantification could either be based on hard-source data or qualitative data could be converted.

6. REFERENCES

- Adger W.N., Hughes T.P., Folke C., et al. (2005). *Social-ecological resilience to coastal disasters*. Science 309: 1036-1039. (1)
- MEA, 2005. *Millennium Ecosystem Assessment – Ecosystems and Human Wellbeing Biodiversity Synthesis*. Island Press, Washington, DC. (2)
- Daily G.C., 1997. *Nature's Services: Societal Dependence on Natural Ecosystems*. Island Press, Washington, DC, USA. Adger, W.N., Hughes T.P., Folke, C., et al. (2005). Social-ecological resilience to coastal disasters. Science 309: 1036-1039 (3)
- Barbier EB: Natural barriers to natural disasters: replanting mangroves after the tsunami. *Front Ecol Environ* 2006, 4:124- 131. (4)
- Munang, R., Thiaw, I., Alverson, K., Liu, J. and Han, Z. (2013). The role of ecosystem services in climate change adaptation and disaster risk reduction. *Current Opinion in Environmental Sustainability* 2013, 5:47–52 (5)
- Berkes, F., Colding, J. and Folke,C.(eds). (2003) *Navigating Social-Ecological Systems: Building Resilience for Complexity and Change*. Cambridge University Press, Cambridge. (6)
- Government of Guyana 2010. *A Low Carbon Development Strategy. Transforming Guyana's Economy While Combating Climate Change*, May 2010. Office of the President, Republic of Guyana. (7)
- GoG (Government of Guyana) 2012. *Second National Communication to UNFCCC*. (8)
- ECLAC, 2011. *An assessment of the economic impact of climate change in agricultural sector*. (9)

Sterman, John. 2000. *Business dynamics : systems thinking and modeling for a complex world* / John D. Sterman.

Elliott, M., 2002. The role of the DPSIR approach and conceptual models in marine environmental management: an example for offshore wind power. *Marine Pollution Bulletin*, 44, iii–vii. (10)

Kristensen, P. 2004. *The DPSIR Framework*. National Environmental Research Institute. Department of Policy Analysis. Denmark. (11)

Vulnerability and adaptation of Paris metropolitan area to future heat waves

Lemonsu A.^{1*}, Vigié V.², Beulant A.L.¹, Hallegatte S.³, Marchadier C.¹,
Masson V.¹, Pigeon G.¹, Salagnac J.-L.⁴, Somot S.¹

¹CNRM/GAME (Météo-France, CNRS), Toulouse, France;

²Centre International de Recherche sur l'Environnement et le Développement, Nogent-sur-Marne, France ;

³France World Bank, Washington DC, USA; ⁴Centre Scientifique et Technique du Bâtiment, Vincennes, France

*Corresponding author: aude.lemonsu@meteo.fr

Abstract

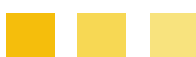
The VURCA project studies the vulnerability of Paris to future heat waves. Through an interdisciplinary team of climatologists, atmospheric physicists, economists and specialists in construction, it was able to develop a framework to analyze prospective effects of different policies aiming at reducing heat waves impacts.

A numerical set-up is implemented to simulate the urban climate of Paris in the future (under different scenarios of urban expansion, adaptation measures for buildings, and use air-conditioning) for various heat-wave conditions representative of a large span of possible future events. For each simulation, indicators of heat stress for population and energy consumption for air-conditioning (AC) are produced.

The results show that Paris could be strongly affected by heat waves at the end of the century (almost 11 heat-wave days per year in average, according to the analysis of climate projections). In a reference scenario without AC, 7.5 hours per heat-wave day would be spent in average in high heat-stress conditions inside buildings, and 15 hours in the streets. It is also shown that alternative scenario favoring a "compact city" could worsen heat-wave impacts through an increased heat island effect.

It is simulated that massive use of AC to insure indoor thermal comfort would lead to more than 1 TWh per year of extra final energy consumption, while degrading the outdoor microclimate because of heat releases. It is also simulated that adaptation policies could be implemented to significantly reduce AC energy demand thanks to massive creation of green spaces in Paris, stricter building insulation rules, and effective recommendations leading to a careful use of AC (with temperature set points higher than 23°C). Finally, it is noted that greening and insulation strategies only do not allow to ensure a quite satisfying comfort, so that it seems difficult not to equip cities with AC in the future.

Keywords: Heat waves; Urban heat island ; Urban vulnerability ; Heat stress ; Air-conditioning ; Energy consumption; Adaptation to climate change



1. INTRODUCTION

Because more than half of the world population lives there, and because most of the economic activity takes place within them, cities vulnerability appears of particular importance when looking at the potential impacts of climate change. Climate change can affect cities in many different ways. One of them is the increased risk of summer heat waves, which can be dangerous for human health and can significantly impact energy consumption. Such a risk is reflected in climate-model projections, for all emission scenarios, by both an increase in average summer temperatures and in temperature variability from one year to another.

Cities are particularly vulnerable to heat waves because of the urban heat island (UHI) effect, which magnifies the air temperatures in urbanized areas. In terms of thermal comfort, the impacts are especially significant at night, when the UHI reaches its maximum. This prevents a correct recovery of the human bodies and can lead to severe sanitary consequences as it was the case during the 2003 heat wave in France (with an excess of mortality more important in Paris region). This impact can be mitigated thanks to the use of air conditioning. However, a massive usage of air-conditioning to face to heat wave conditions can induce a sharp increase in energy demand which could be an important burden in a context of greenhouse gases reduction efforts. At city scale, some mitigation and adaptation strategies can however be implemented to reduce this demand.

The VURCA project – funded by the French Agency for Research (2009-2012) – studies cities vulnerability to future heat wave events. Through an interdisciplinary team consisting of climatologists, atmospheric physicists, economists and specialists in construction, it was able to develop a framework to analyze prospective effects of different policies aiming at reducing heat waves impacts. This project takes Paris urban area in 2100 as a case study.

2. INTEGRATED CITY SCENARIOS

Several scenarios were simulated to assess the consequences of different adaptation strategies. These scenarios are the combination of several alternatives:

1. Three city expansion scenario alternatives (**Fig. 1**) were used. These scenarios were simulated by NEDUM2D model (a socio-economic land-use/transport interaction model [1]) and based on demographic and macro-economic trends:

- *Spread-out city*: No effective containment policy is carried out. Urbanization is supposed to be driven only by market forces.
- *Compact city*: A “green-belt policy” forbids from 2020 on any new construction in locations which are not already densely inhabited. Additional development is therefore carried out through densification of the city center.
- *Green city*: No effective containment policy is carried out, but numerous parks are introduced in the city. We suppose that, in 2020, 10% of all built surfaces has to be relocated elsewhere in the urban area to leave space for urban parks. Urban extension is therefore bigger in this scenario than in the « Spread-out city » scenario.



Fig. 1: Urban expansion of the Paris metropolitan area simulated by NEDUM2d socio-economic land-use/transport interaction model from 2010 to 2100 for three scenarios of urban policies.

2. Two alternatives for building adaptation measures:

The Paris built environment can be presented according to main building characteristics associated to periods of construction. They reflect the evolution of the know-how, the introduction of innovation and the architectural choices. For the future, the VURCA project proposes two scenarios for building adaptation measures that translate more - *Virtuous buildings* - or less - *Business-as-usual buildings* - interventionist strategies in terms of new regulations and technical improvements.

3. Three alternatives for air-conditioning (AC) use: *No AC*, *Moderate use of AC* with temperature set points of 26°C for offices and 28°C for housings, or *Intensive use of AC* with a temperature set point of 23°C

3. MODELING METHODOLOGY

The objective is to perform simulations of urban climate in Paris (under the different scenarios of urban expansion, adaptation measures for buildings, and use air conditioning) for a large set of heat wave conditions that is representative of a large span of future events, in order to assess the vulnerability of the city to 2100 summer climate.

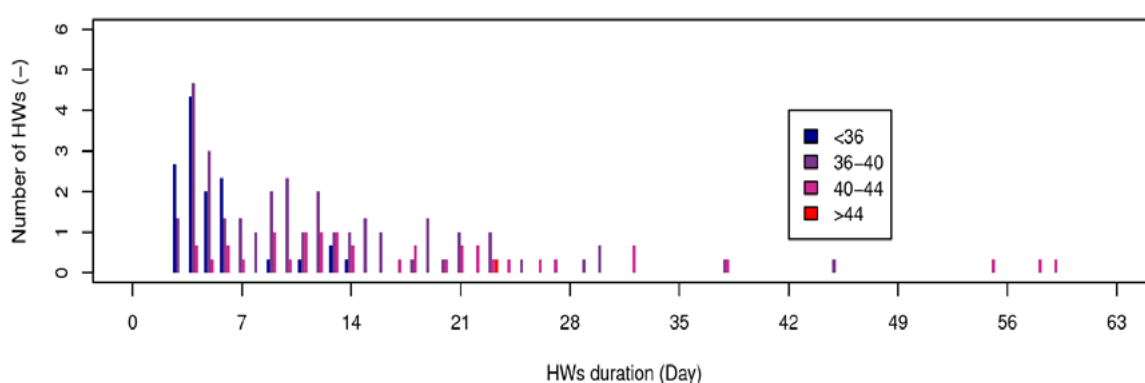


Fig.2- Distribution of future heat waves over 2070-2099 by class of intensity, extracted from climate model projections over the Paris region

Future heat waves over the Paris region are extracted from an ensemble of climate-model projections following the SRES A1B emission scenario (provided by the European ENSEMBLES database) over the 2070-2099 time period [2]. These future heat waves are classified into 4 classes according to their intensity (distribution presented in Fig.2). The heat wave durations vary between 3 days (by definition) and 60 days. But the majority of heat waves have a duration which is smaller than two weeks.

The urban microclimate of Paris is simulated with the SURFEX land surface modeling system that includes an advanced version of the TEB urban canopy model [3] with a better representation of urban green areas [4], a new parameterization for building energy and air-conditioning [5], and a calculation of the Universal Thermal Climate Index that translates into indoor and outdoor thermal heat stress. The SURFEX system is run in offline mode (in order to achieve a large number of simulations) over a spatial domain of 100 x 100 points, centered on Paris, with a horizontal resolution of 1 km. A set of synthetic (or idealized) heat waves is modeled, based on the 2003 heat wave but corrected in duration and intensity in order to replicate the different classes of heat waves that are statistically representative

of future climate. A 3 steps comprehensive methodology (Fig.3) is developed in order to build the atmospheric forcing and to implement the simulations.

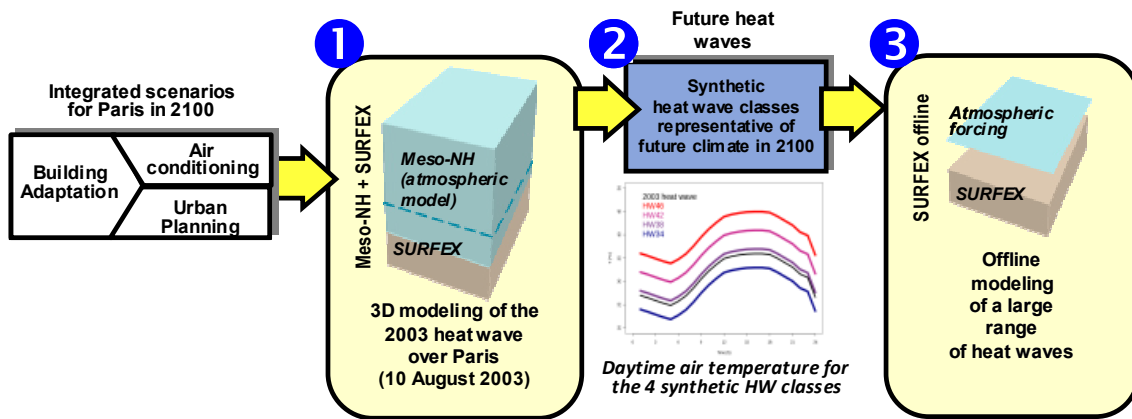


Fig.3 - Description of the modelling methodology.

4. SERIOUSNESS AND GRAVITY INDICATORS

For each heat wave, two sets of indicators are calculated to quantify the seriousness of the event. The first one is the cumulative energy consumed by AC systems (kWh) of the whole Paris metropolitan area. The second one is the number of hours per day during which inhabitants are at least in condition of high heat stress, i.e. with a perceived temperature higher than 32°C, for indoor and outdoor conditions.

For each integrated scenario, the seriousness indicators are weighted according to the occurrence probabilities of futures heat waves in order to build vulnerability indicators. They make possible the assessment of the efficiency of the adaptation strategies implemented to face future summer climate and their comparison.

5. ANALYSIS AND KEY INSIGHTS

A number of results are available from this work, answering three main questions:

1. To what extent will Paris be vulnerable to heat waves?

Paris can be strongly affected by heat waves. We computed that, without air conditioning, at the end of the century, almost 11 heat wave days per year in average should be expected to be spent in Paris urban area. During these days, in residential buildings, if no AC is used, almost 7 hours and a half would be in average spent in high heat stress conditions, i.e. with an apparent air temperature (UTCI) greater than 32°C. This could lead to serious health consequences. In the streets, even in shadow, this duration is higher, and almost 15 hours have to be spent in these conditions.

Urban expansion, through an increased heat island effect, could worsen heat waves impacts. We computed that, in the scenario of high city densification (the “compact city scenario”), in the streets, 20 minutes in high heat stress conditions should be added.

2. What would be the effect of a massive development of air-conditioning?

If a massive development of air conditioning happens to prevent health issues, about 1.1 TWh per year of extra final energy consumption should be expected, if a 23° temperature is to be maintained in all residential and office buildings.

Heat released by AC engines causes a degradation of external thermal comfort, and the duration spent under high heat stress conditions in the streets is increased by about 20 minutes.

These results were computed with the hypothesis that existing urban green spaces are adequately watered, and this plays an important role in reducing Paris sensitivity to heat waves. In case of water shortage, (which is almost equivalent to an urban green spaces removal), we simulated that energy consumption would be increased by about 8%, and that almost one hour of outdoor thermal discomfort would be added.

3. Could alternative adaptation policies enable to reduce energy demand for air conditioning and thermal discomfort?

Energy demand for air conditioning could be an important burden in a context of greenhouse gases reduction efforts, but adaptation policies could be implemented to reduce this demand. We computed that

- a massive creation of parks and green spaces in Paris urban area (devoting 10% of land surface to new parks),
- stricter building insulation rules and the use of reflective materials for walls and roofs,
- and effective recommendations or policies leading to air conditioning used to maintain 28°C in residential buildings and 26°C in offices instead of 23°C,

could together enable to reduce energy consumption by 0.7 TWh, i.e. reduce energy consumption for AC by more than 50%. This would also reduce outdoor thermal discomfort time by about 1 hour.

However, these policies could not a priori totally replace AC use, as 6 hours per day would still have to be spent in high heat stress conditions in residential buildings if no AC is to be used at all.

In conclusion, several alternative options to air-conditioning are able significantly reducing the vulnerability of the city in terms of both indoor and outdoor comfort. Nevertheless, at best, a third of the day is spent under conditions of strong heat stress inside buildings without air-conditioning.

6. ADAPTATION POLICIES EFFICIENCY DEPENDS ON THE HEAT WAVE CHARACTERISTICS

Various adaptation policies have efficiencies which vary according to the type of heat wave. For instance, cities sensitivity to heat waves varies greatly with the duration of the event. Continuously high temperatures are required during a few days before indoor temperatures reach their maximum equilibrium value. This duration was found to be about 5 days in Paris. Building insulation enables to increase this duration and therefore to be less sensitive to short heat waves.

7. ISSUES OF IMPLEMENTATION OF ADAPTATION POLICIES

Implementing these policies is however no easy task. Beside the operational difficulty to change air conditioning use habits, stricter building insulation would be expensive, and green spaces creation would have a high cost in terms of land use (by decreasing residential land supply, it could increase all rents and real estate prices by 2 %, when compared to reference scenario). Green spaces creation would also reduce the city density and could lead to increased urbanized surface, and to increased transport-

related greenhouse gases emissions (+10%). They would finally require a huge amount of water to be efficient. If water availability stops, green spaces are found to have almost no effect.

Among the three policies we have studied, changing AC use habits (increasing temperature set points) is the policy which has, individually, the greatest impact. This policy, moreover, has none of the costs or collateral effects that the two other adaptation policies have. However, it is rather unclear how such a policy could be implemented in practice.

8. ACKNOWLEDGMENTS

The VURCA project (French acronym for Urban vulnerability to heat waves and adaptation strategies) is funded by the French Agency for Research (ANR-08-VULN-013).

9. REFERENCES

- Viguié V., & Hallegatte S. (2012), *Trade-Offs and Synergies in Urban Climate Policies*, Nature Climate Change, 2, 334-337. (1)
- Beuland A.L., Lemonsu A., Somot S. & Masson V. (2012), *Future Heat Waves over Paris Metropolitan Area, National Security and Human Health Implications of Climate Change*. NATO Science for Peace and Security Series C: Environmental Security, 135-145, DOI : 10.1007/978-94-007-2430-3_12. (2)
- Masson V. (2000), *A Physically-based scheme for the Urban Energy Budget in atmospheric models*, Boundary-Layer Meteorol., 94, 357-397. (3)
- Lemonsu A., Masson V., Shashua-Bar L., Erell E., & Pearlmutter D. (2012), *Inclusion of vegetation in the Town Energy Balance model for modeling urban green areas*, Geoscientific Model Development, 5, 1377-1393. (4)
- Bueno B., Pigeon G., Norford L. K., Zibouche K. & Marchadier C. (2012), *Development and evaluation of a building energy model integrated in the TEB scheme*, Geoscientific Model Development, 5, 433-448. (5)

The role of climatic variability on cholera spreading in Bangladesh

Ciddio M.^{1*}, Righetto L.², and Mari L.^{1,2}

¹*Dipartimento di Elettronica, Informazione e Bioingegneria, Politecnico di Milano, Milano, Italy,*

²*Laboratory of Ecohydrology, École Polytechnique Fédérale de Lausanne, Lausanne, Switzerland*

*Corresponding author: manuela.ciddio@mail.polimi.it

Abstract

Cholera is a disease transmitted through exposure to water contaminated by the bacterium *Vibrio cholerae*. The disease is clearly linked to the variability of climatic factors, as infections are enhanced by intense seasonal precipitation (e.g. monsoon season). Here we propose a spatially explicit model for cholera and apply it to Bangladesh, where the disease is endemic, integrating the role of precipitation and temperature annual cycles. River networks represent one of the major pathways of disease spreading. The data structure designed for the application of the model is thus based on the hydrological connectivity network, as well as on the spatial distribution of the population and on the connections that regulate human mobility among communities. In this region, cholera incidence exhibits two annual peaks, although the main environmental drivers peak once per year during the monsoon season (from June to September). The proposed model attempts to explain these particular dynamics taking into account the annual fluctuations of water availability and considering hydro-climatological forcings as inputs for the model. For this purpose, a compartmental SIRB (Susceptible-Infected-Recovered-Bacteria) epidemiological model is integrated with a hydrological model. Results show that the introduction of two terms of transport (hydrological transport and human mobility) allows to generate spatial patterns of cholera prevalence that reproduce the bimodal pattern typically observed in this region.

Keywords: *Epidemiology; Spatially explicit models; Climatic factors; Hydro-climatological forcings.*



Cholera is an acute water-borne disease caused by the bacterium *Vibrio cholerae*, which colonizes the human intestine and produces an enterotoxin responsible for a watery diarrhea. Since cholera outbreaks are generally associated with the ingestion of contaminated food or water, it represents one of the most serious public health problems especially among populations in developing countries, which lack access to safe water and appropriate sanitation. According to the World Health Organization (WHO), almost 590,000 cases were recorded worldwide in 2011 and the number of cases is increasing [22].

The Bay of Bengal, with its extensive estuary formed by the delta of the Ganges-Brahmaputra-Meghna (GBM) system, is considered the native habitat of *Vibrio cholerae* [19]. This region is characterized by seasonal outbreaks that occur throughout the year with a bimodal annual distribution [1], while single annual peaks can be seen elsewhere (e.g. parts of Africa, South-east Asia and Latin America [10]). This seasonality suggests a clear key role of climatic factors in the dynamic of the disease. The annual cycle of epidemics in this particular endemic context has been historically linked to a range of environmental and climatic variables including precipitation [10], river discharge [1], sea surface temperature [6], and El Niño-Southern Oscillation [18].

Our aim is to develop a spatially explicit model of cholera transmission that integrates the role of the precipitation and temperature annual cycles on the dynamics of the disease. The model has been applied to the case of Bangladesh and includes two terms of pathogen transport: hydrological transport and human mobility.

The territory of Bangladesh is divided into more than 800 hydrological entities (Figure 1), identified on the basis of a Digital Elevation Model (DEM). Specifically, we traced the river network combining flow directions and flow accumulations maps, results of DEM manipulation, in order to identify the watersheds.

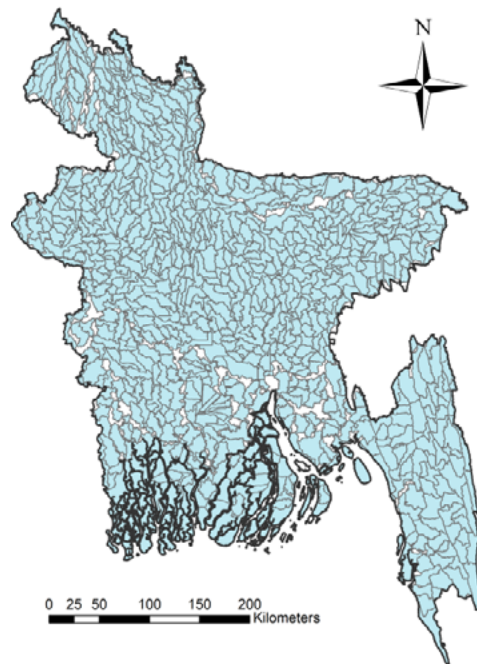


Fig. 1: Subdivision of Bangladesh in hydrological entities: the territory is divided into 880 watersheds, that are defined through elaboration of the DEM of the area.

The dispersion of bacteria depends on a complex set of processes. The network used to implement these mechanisms is described by a series of nodes, representing hydrological entities (where human communities live), and edges, representing pathways for the spread of the disease. We placed nodes at the centroid of each hydrological entity weighed on population and we considered two terms of transport that identify different edges:

- a first mechanism of propagation related to the dispersion through the river network;
- a second mechanism of propagation related to human mobility, described by fluxes of individuals on a completely connected graph.

For each node we model the dynamics of the number of susceptibles to the disease (initially coinciding with the total population), infected individuals, recovered and immune individuals, *V. cholerae* abundance in the aquatic environment, and water availability.

Epidemiological dynamics and pathogen transport in a generic node *i* of the network are therefore described via a compartmental SIRB-like model similar to [5] represented by the following system of nonlinear differential equations:

$$\frac{dS_i}{dt} = \mu(H_i - S_i) - \beta_i(J)(1-m)\frac{B_i}{K+B_i}S_i - m\left(\sum_{j=1}^n Q_{ij}\beta_j(J)\frac{B_j}{K+B_j}\right)S_i + \rho R_i$$

$$\frac{dI_i}{dt} = \beta_i(J)(1-m)\frac{B_i}{K+B_i}S_i + m\left(\sum_{j=1}^n Q_{ij}\beta_j(J)\frac{B_j}{K+B_j}\right)S_i - (\gamma + \alpha + \mu)I_i$$

$$\frac{dR_i}{dt} = \gamma I_i - (\rho + \mu)R_i$$

$$\frac{dB_i}{dt} = -\mu_B(T)B_i + (1-m)p_i(J)I_i + mp_i(J)\sum_{j=1}^n Q_{ji}I_j - \lambda f_i B_i + \lambda \sum_{j=1}^{d_{in}} P_{ji} \frac{W_j}{W_i} B_j$$

$$\frac{dW_i}{dt} = J_i(t)A_i - ET_i(t)A_i - \lambda W_i + \lambda \sum_{j=1}^{d_{in}} W_j$$

where S_i , I_i , R_i , B_i and W_i are respectively susceptibles, infected, and recovered individuals, pathogen concentration and water availability in each node of the spatial network at time t . Figure 2 shows a schematic diagram of the model.

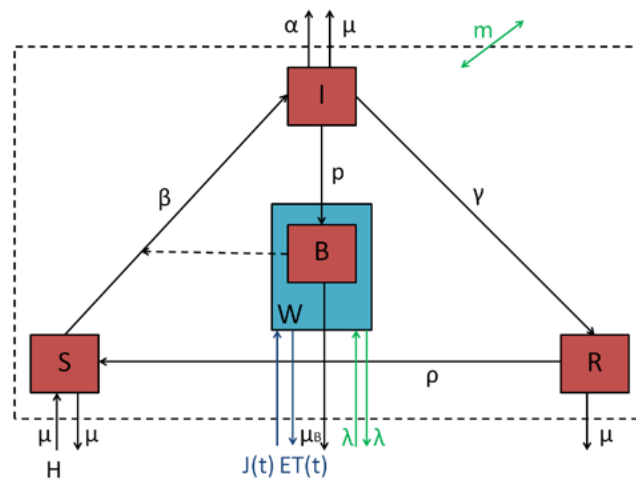


Fig. 2: Schematic diagram of the model: red blocks represent the state variables of the epidemiological model, the blue block represents the state variable of the hydrological model, the arrows describe the fluxes. The dashed arrow that starts from the bacteria in the local water reservoir indicates that their abundance indirectly acts on the fluxes of individuals from susceptible to infected compartment.

The dynamics of the susceptible compartment is described by the balance among population demography, infections due to contact with *V. cholerae* and immunity loss. The host population is assumed to be at a demographic equilibrium, where μ is the human mortality rate and H_i is the size of the local community. The fraction $B_i/(K+B_i)$ is the logistic dose-response curve [8] representing the probability of becoming infected due to the exposure to a concentration B_i of vibrios, K being the half-saturation constant. The parameter $\beta_i(J)$ represents the rate of exposure to contaminated water, depending on precipitation J . Individuals can get infected in their original node i or during a daily trip in a different node j , with m and Q_{ij} being the fraction of moving people and the probability of moving between any two nodes i and j , respectively.

Infected individuals recover at a rate γ , or die for natural or cholera-induced mortality at a rate μ or α , respectively. Recovered from the disease lose their immunity and become susceptibles again at a rate ρ . Infected individuals contribute to the concentration of free-living vibrios at a rate $p_i(J)$, which represents the concentration of bacteria excreted by one infected individual that reach and contaminate the local water reservoir, depending on precipitation J . Bacteria are assumed to die at a rate $\mu_B(T)$, function of temperature T , and undergo dispersal through the river network at rate λ , with f_i being the fraction of bacteria that leave the node. Local water availability is expression of the water balance between precipitation $J_i(t)$ and losses due to evapotranspiration $ET_i(T)$, computed with Blaney-Criddle formula [17], and river flow, A_i being the area of the hydrological entity in node i .

To simulate the spread of the disease, we describe the propagation due to hydrological transport as a random walk process on an oriented graph [2], where edges are represented by segments of the river network in each hydrological entity. We assume that vibrios move between any two nodes of the network with a probability given by:

$$P_{ij} = \begin{cases} \frac{P_{out}}{d_{out}(i)P_{out} + d_{in}(i)P_{in}} & \text{if } i \rightarrow j \\ \frac{P_{in}}{d_{out}(i)P_{out} + d_{in}(i)P_{in}} & \text{if } i \leftarrow j \\ 0 & \text{elsewhere} \end{cases}$$

where P_{out} and P_{in} are the probabilities of moving along an outward or inward edge respectively, and d_{out} and d_{in} are the out-degree or in-degree of each node, defined through the elaboration of the DEM.

Bangladesh extends over most of the delta of the GBM basin, which covers a total area of over one million square kilometers. For a more realistic analysis, we also consider the volume of water that enters the system through the river flow from portions of the GBM network located outside the administrative boundaries of Bangladesh. The water volume is proportional to drainage area [14] and it has been estimated for the three nodes shown in the left panel of Figure 3.

Cholera spread is affected also by human mobility. Fluxes of individuals that move among the nodes of the river network are described as a function of local population size and distance between any two nodes, with a gravitational model:

$$Q_{ij} = \frac{H_j e^{-d_{ij}/D}}{\sum_{k \neq i}^n H_k e^{-d_{ik}/D}}$$

where H_i is the population living in node i , d_{ij} is the distance between two nodes i and j , D is the mean dispersal distance characterizing human movement and n is the total number of nodes in the network.

The right panel of Figure 3 shows the most important connections in a small portion of the territory. For each node the three connections with the highest values of mobility fluxes are shown.

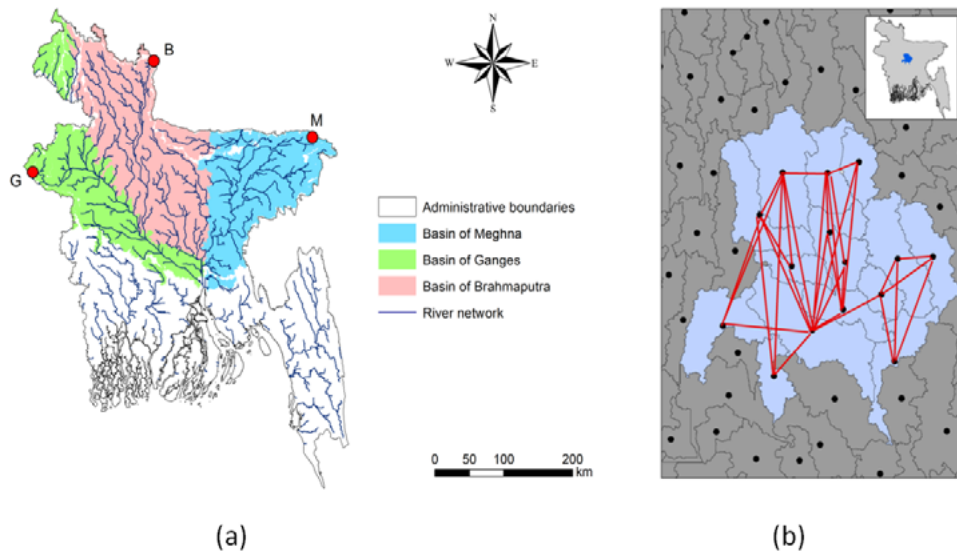


Fig. 3: Network connectivity. (a) River network and basins of the Ganges, Brahmaputra and Meghna in the territory of Bangladesh. Red circles represent the points where the three rivers cross the administrative boundaries of Bangladesh. (b) Most important connections of the mobility graph for a small part of the territory.

In order to study the role of hydro-climatological forcings on cholera dynamics, we calculated for each node of the network the annual pattern of precipitation and temperature, as moving averages of the available time series [11, 12] (Figure 4). Both environmental variables are used as direct inputs in the model, forcing specific processes as detailed below.

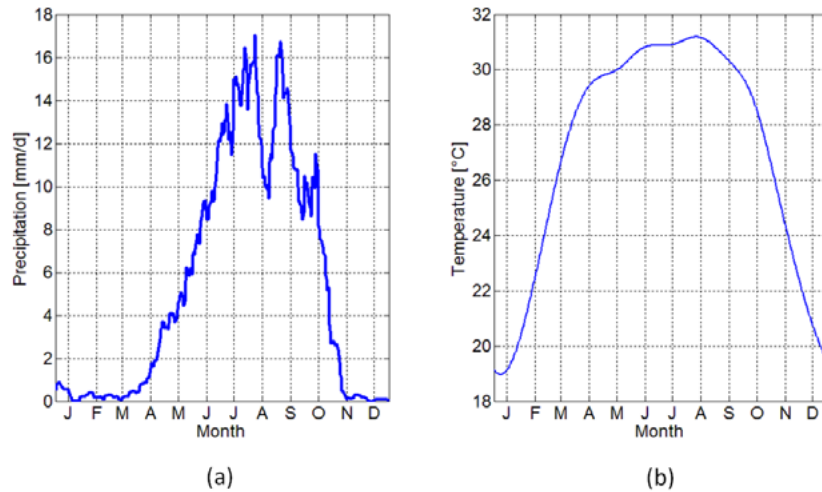


Fig. 4: Average annual pattern of precipitation and temperature in the node representing Dhaka, the capital of Bangladesh. (a) Annual pattern elaborated from 13 years of daily data of precipitation. (b) Annual pattern elaborated from 64 years of monthly data of temperature.

We consider that during and after the monsoon season, when rainfall is more abundant, a large part of the region is flooded and people crowd not affected areas; this is typically accompanied by a deterioration of sanitation systems, which results in an increase of environmental contamination and in a reduced access to treated water [5]. From a modeling point of view, this is reflected in the following formulation for the exposure and contamination rates $\beta(J)$ and $p(J)$:

$$\beta_i(J_i(t)) = \beta_0(1 + \phi J_i(t))$$

$$p_i(J_i(t)) = p_0(1 + \phi J_i(t))$$

where β_0 and p_0 are the baseline values for the exposure and contamination rates, and ϕ quantifies the effect of precipitation J on these parameters at each time t .

We also include the effect of temperature on the ability of cholera bacteria to survive and multiply in the environment. Since warmer temperatures are known to favor the growth of *V. cholerae* in the surface water [5], we assume that mortality of the bacteria depends on temperature as follows:

$$\mu_B(T) = \bar{\mu}_B \left(1 - \varepsilon \frac{T - \bar{T}}{T_{max} - \bar{T}} \right)$$

where $\bar{\mu}_B$ is the average vibrio mortality, T_{max} and \bar{T} are the maximum and the mean temperature during the year, and ε quantifies the effect of temperature on *V. cholerae* mortality. Temperature also influences evapotranspiration as detailed above.

We are interested in the long-term behavior of the system, thus we simulate the process for 10 years (each year with the same hydro-climatological pattern) and we analyze the patterns of cholera prevalence in the final year of the simulation. Epidemiological parameters used to run the model can be found in the literature (Table 1), while the parameters related to pathogen transport have been set as follows:

- for hydrological transport, we assume that the probability of moving along an outward edge is $P_{out} = 0.5$ and that the dispersal rate through the river network is $\lambda = 0.01 \text{ d}^{-1}$; we consider the sea as a bacterial reservoir, so that $f_i = 0.25$ in the outlet nodes, 1 elsewhere;
- for human mobility, we assume a mean dispersal distance $D = 10 \text{ km}$ for daily trips and a value for the fraction m of moving population of 0.2.

Parameter	Value	Units	References
μ	$1/(70.6 \cdot 365)$	d^{-1}	[7]
β_0	1	d^{-1}	[3, 8, 15, 20]
ρ	$1/(3 \cdot 365)$	d^{-1}	[13]
γ	0.2	d^{-1}	[3, 4, 8, 15]
α	0	d^{-1}	[20]
$\bar{\mu}_B$	0.2	d^{-1}	[3, 4, 8, 15, 16, 20]
p_0/K	10^{-6}	individual ⁻¹ $\text{d}^{-1} \text{ m}^{-3}$	[9, 21]

Tab. 1: Epidemiological parameter values used for simulation, with units and references.

Figure 5 shows two temporal patterns of global prevalence generated by our model. The annual prevalence is characterized by one or two peaks per year, depending on whether we want to consider the effect of precipitation or not.

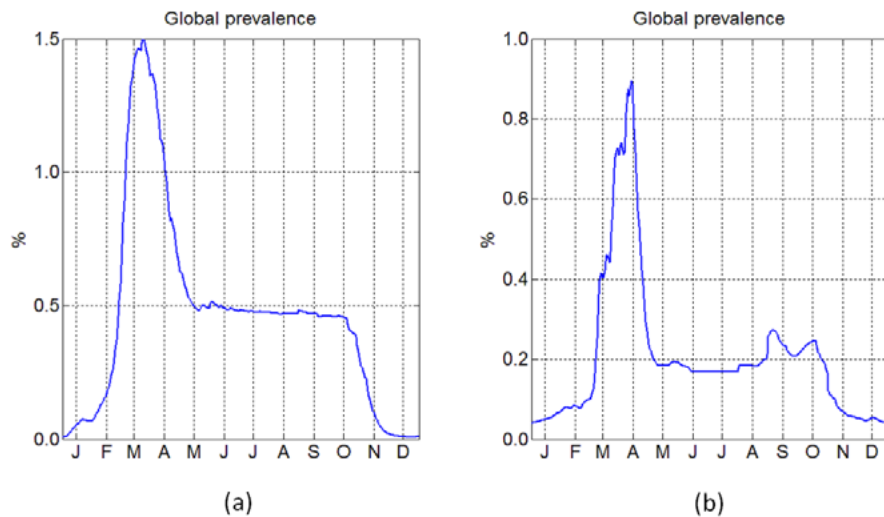


Fig. 5: Global prevalence simulated with our model. (a) Global prevalence in absence of rainfall dependence ($\phi = 0$): the pattern exhibits a single peak in spring, due to low bacterial dilution. (b) Global prevalence considering the effect of precipitation on cholera spreading ($\phi = 0.8$): the pattern exhibits also a second outbreak in autumn, caused by increase in the rates of exposure and contamination.

The global patterns generated by the model suggest some considerations:

- low dilution of cholera bacteria in water is responsible for the spring peak;
- the effect of intense precipitation characterizing the monsoon season determines the increase in the rates of exposure and contamination, so that the fall peak occurs only including in the model the dependence on rainfall. However, the summer flood washes out the system and thus the second peak is less important than the first one.

At a local level, it can be noticed that prevalence patterns are qualitatively different according to the position of the nodes in the network (Figure 6). The spring outbreak occurs earlier in the communities near the coast, but its intensity is greater in upstream nodes. During the spring peak, people can get infected earlier in the coastal areas because of bacteria that colonize permanently the coastal region (i.e. the outlet nodes). Then, bacteria reach inland areas through the river network and movement of infected individuals. Prevalence is higher where bacterial concentration is higher (i.e. water volume is

lower), so that the most intense peaks occur far from the coast, in the upstream nodes of the river network. Coastal communities do not exhibit the fall outbreak because of bacterial dilution in the downstream nodes, where water volume is higher.

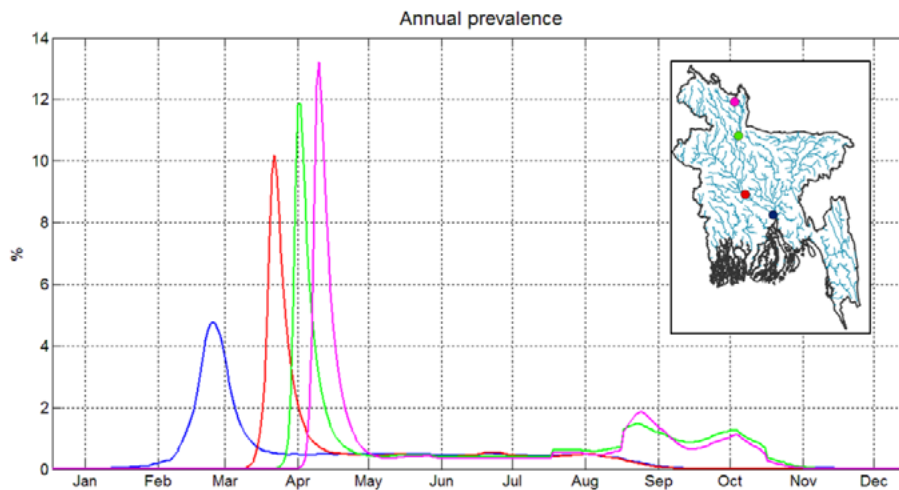


Fig. 6: Annual prevalence in different communities. The disease starts spreading near the coast and then reaches the inland areas, where there is also a second outbreak in autumn.

Overall the results presented in this work support the crucial role of hydro-climatological factors in controlling the spatiotemporal progression of the disease in Bangladesh, identifying both seasonal and spatial dynamics (from spring to fall and from coast to inland). The importance of climatic variability suggests the need of a more detailed study of the environmental forcings. Predictive models for the relevant hydro-climatological variables, coupled with spatially explicit eco-epidemiological models, will be key tools to better understand, forecast and possibly control cholera dynamics.

ACKNOWLEDGMENTS

The authors wish to thank Dr. Enrico Bertuzzo (École Polytechnique Fédérale de Lausanne) and Prof. Marino Gatto (Politecnico di Milano) for helpful discussions on cholera dynamics. MC acknowledges the support provided by project Contr. Ric. "CNR-ISAC" 10/11/10 (GCB0RICC01). LR and LM acknowledge the support provided by the ERC project RINEC-227612 and by the SFN/FNS projects 200021_124930/1 and CR2312_138104/1.

REFERENCES

- Akanda A.S., Jutla S., Islam S. (2009), *Dual peak cholera transmission in Bengal Delta: a hydroclimatological explanation*, Geophysical Research Letters 36, L19401. (1)
- Bertuzzo E., Maritan A., Gatto M., Rodriguez-Iturbe I., Rinaldo A. (2007), *River networks and ecological corridors: reactive transport on fractals, migration fronts, hydrochory*, Water Resources Research 43, W04419. (2)
- Bertuzzo E., Azaele S., Maritan A., Gatto M., Rodriguez-Iturbe I., Rinaldo A. (2008), *On the space-time evolution of a cholera epidemic*, Water Resources Research 44, W01424. (3)
- Bertuzzo E., Mari L., Righetto L., Gatto M., Casagrandi R., Blokesch M., Rodriguez-Iturbe I., Rinaldo A. (2011), *Prediction of the spatial evolution and effects of control measures for the unfolding Haiti cholera outbreak*, Geophysical Research Letters 38, L06403. (4)
- Bertuzzo E., Mari L., Righetto L., Gatto M., Casagrandi R., Rodriguez-Iturbe I., Rinaldo A. (2012), *Hydroclimatology of Dual-Peak Annual Cholera Incidence: Insights from a Spatially Explicit Model*, Geophysical Research Letters 39, L05403. (5)
- Bouma M.J., Pascual M. (2001), *Seasonal and interannual cycles of endemic cholera in Bengal 1891-1940 in relation to climate and geography*, Hydrobiologia 460, 147-156. (6)
- Central Intelligence Agency (CIA). The World Factbook. Link: <https://www.cia.gov/library/publications/the-worldfactbook/index.html>. (7)
- Codeco C. (2001), *Endemic and epidemic dynamics of cholera: the role of the aquatic reservoir*, BMC Infectious Diseases 1. (8)
- Feachem, R., Bradley D.J., Garelick H., Mara D.D. (1983), *Vibrio cholera and cholera*, In Sanitation and disease. Health aspects of excreta and wastewater management, John Wiley & Sons 297-325. (9)
- Hashizume M., Armstrong B., Hajat S., Wagatsuma Y., Faruque A.S.G., Hayashi T., Sack D.A. (2008), *The effect of rainfall on the incidence of cholera in Bangladesh*, Epidemiology 19(1) 103-110. (10)
- International Research Institute for Climate and Society (IRI). *Air Temperature data*. Link: <http://portal.iri.columbia.edu/portal/server.pt>. (11)

- International Research Institute for Climate and Society (IRI). *Surface Rain from all Satellite and Surface data*. Link: <http://portal.iri.columbia.edu/portal/server.pt>. (12)
- Koelle K., Rodò X., Pascual M., Yunus Md., Mostafa G. (2005), *Refractory periods and climate forcing in cholera dynamics*, Nature 436, 696-700. (13)
- Leopold L.B., Wolman M.G., Miller J. (1964), *Fluvial Processes in Geomorphology*, Freeman, San Francisco. (14)
- Mari L., Bertuzzo E., Righetto L., Casagrandi R., Gatto M., Rodriguez-Iturbe I., Rinaldo A. (2011), *Modelling cholera epidemics: the role of waterways, human mobility and sanitation*, Journal of the Royal Society Interface 9, 376-388. (15)
- Mari L., Bertuzzo E., Righetto L., Casagrandi R., Gatto M., Rodriguez-Iturbe I., Rinaldo A. (2012), *On the role of human mobility in the spread of cholera epidemics: towards an epidemiological movement ecology*. Ecohydrology 5, 531-540. (16)
- Moisello U. (1998), *Idrologia tecnica*, La Goliardica Pavese. (17)
- Pascual M., Rodo X., Ellner S., Colwell R., Bouma M.J. (2000), *Cholera Dynamics and El-Niño-Southern Oscillation*, Science 289, 1766-1769. (18)
- Pascual, M., Bouma M., Dobson A.P. (2002), *Cholera and climate: revisiting the quantitative evidence*, Microbes and Infection 4, 237-245. (19)
- Righetto L., Casagrandi R., Bertuzzo E., Mari L., Gatto M., Rodriguez-Iturbe I., Rinaldo A. (2012), *The role of aquatic reservoir fluctuations in long-term cholera patterns*, Epidemics 4, 33-42. (20)
- Sack R.B., Siddique A.K., Longini I.M., Nizam A., Yunus M.D., Islam M.S., Morris J.G., Ali A., Huq A., Nair G.B., Qadri F., Faruque S.M., Sack D.A., Colwell R.R. (2003), *A 4-Year Study of the Epidemiology of Vibrio cholerae in Four Rural Areas of Bangladesh*, The Journal of Infectious Diseases 187, 96-101. (21)
- World Health Organization (WHO) (2012), *Weekly epidemiological record*, Technical Report 31, Geneva. (22)

Albedo modifications as global mitigation and local adaptation strategy in European cities: a geographically explicit investigation

Susca T.^{1,2*}, and Creutzig F.^{2,3}

¹Hertie School of Governance, Berlin, Germany;

²MCC - Mercator Research Institute on Global Commons and Climate Change, Berlin, Germany;

³Technical University Berlin, Berlin, Germany

*Corresponding author: susca@hertie-school.org

Abstract

Climate change becomes an important focus of urban policy agendas in cities world-wide. The consequences of the greenhouse gas effects, such as heat waves, are already observed in numerous locations. While climate change mitigation appears as a policy option, local adaptation develops into a necessity. Albedo addresses both objectives. The current literature sees albedo as a mitigation policy option, while other literature points to the potential of albedo changes to also reduce the local urban heat island effect. The two literature strands investigate different spatial scales. Here, we take a regional perspective and assess the combined mitigation and adaptation potential of albedo changes in European cities. As an example, we estimate the adaptation and mitigation of three European cities, based on latitude and resulting radiation, surface, population and cloudiness. The cities are chosen from northern, central and southern Europe which have significantly different mitigation potential albeit in an unexpected manner. While total mitigation effects are miniscule, the adaptation effects on population can be considerable.

Keywords: *Urban Climate; Albedo; Adaptation Strategy; Climate Mitigation*



Climate change already impacts living systems [1] and livelihoods worldwide [2]. The Earth is experiencing an increase in the average temperature of about 0.8°C since preindustrial times [3]. Arguably, the consequences of climate change are most relevant where most people are affected: in cities. In the last years densely urbanized areas are experiencing catastrophic consequences of climate change with very heavy social and economic consequences. For instance, in 2005 the hurricane Katrina provoked about 1500 deaths in Louisiana and caused damages of around \$ 40-50 billion [4]. On October 29th 2012 hurricane Sandy hit New York City flooding streets and interrupting the normal use of the subway causing damages for about \$50 billion [5]. In Europe, between 1980 and 2011, extreme climate conditions caused more than € 90 billion for damages due to flooding and more than 2500 fatalities with high social costs [6]. In 2003 Paris experienced a heat wave that provoked a severe increase in the urban population deaths [7]. In 2010 Moscow more than 15000 excess deaths were recorded as a consequence of a summer heat wave [8].

At the same time, cities are the major contributors to climate change being responsible of about 78% of carbon dioxide (CO₂) emissions and for this reason they have also the potential to positively affect the global climate [9]. Mitigation and adaptation strategies applied to the urban environment can be useful to decrease the effect of urbanization on climate.

The European Commission (EC) is putting efforts in designing guidelines or documents able to support project managers to make their physical assets more climate-resilient. For instance the Commission published, as part of the European Union (EU) Adaptation Strategy package, "Guidelines for project managers: Making vulnerable investment climate resilient" [10]. Furthermore, in March 2012 the EC launched the European Climate Adaptation Platform [11-12] with the aim to support European countries to adapt to climate change considering both national and transnational adaptation strategies and proposing tools for supporting adaptation plans [12]. In April 2013 the EC adopted the EU strategy [13] on adaptation to climate change that has the aims to:

- encourage Member States to adopt adaptation strategies providing funds – for instance through the LIFE Programme and some international financing institution as the Investment Bank and the European Bank for Reconstruction and Development – to take action and launching a voluntary commitment based on the Covenant of Mayor Initiative;

- promote adaptation strategies and the use of insurance in key sectors such as, for instance, agriculture and fisheries;
- promote to address knowledge – especially among decision-makers – about adaptation strategies.

Moreover, the EC is promoting the “Adaptation Strategies for European Cities” project [6]. This project aims to provide assistance for cities in developing and implementing adaptation strategies. The project has the objective to expand the knowledge and raise awareness about the impacts related to climate change that cities are facing. The project wants also to facilitate the exchange of knowledge and good practices for coping with climate change in order to provide guidance and develop projects for the urban adaptation.

Recent studies demonstrated that the variation in surface albedo can affect the Earth’s energy balance and, as a consequence, global climate (e.g., 14-18). Albedo effects are relevant: a 1% change in average global albedo equals $3.4\text{W}/\text{m}^2$ – a rate similar to that caused by a doubling of CO_2 emissions from current levels [19]. Cities are particularly relevant from a heat flux perspective: In large cities the sensible heat flux can exceed $300\text{W}/\text{m}^2$, topping that of deserts [19]. Hence, the increase in surface albedo simultaneously addresses a common urban exuberance worsened both by global warming and sometimes unfortunate urban planning: the urban heat island (UHI) effect [20-21]. The urban-wide increase in albedo can be obtained by substituting dark surfaces, for instance asphalt surfaces, with vegetated or high reflective ones and/or enhancing urban vegetation. In densely urbanized areas where there are just few residual spaces that can be converted in green areas, a possible solution can be the conversion of black traditional roofs into green or white ones as well as the enhancement of pavement’s albedo. Rooftops and pavements are available urban surfaces that can be easily enhanced.

Previous studies show that the increase in urban albedo is more effective at local scale than at global one since it is able to mitigate UHI. Specifically, the mitigation of the UHI is an important issue since high urban temperature, especially in summer, correlates with heat-related mortality especially among old people or people with physical or social vulnerability [22-24]. In the US extreme temperatures are the main cause of weather-related mortality [25]. The increase in urban albedo can also accrue several other benefits such as the enhancement in air quality and the decrease in energy use for summer cooling [20]. Rosenfeld and colleagues [20] state that the increase in albedo from 0.13 to 0.26 in Los

Angeles can reduce the air temperature recorded at 12pm of about 2°C and at 3pm about 3°C. The reduction of urban temperature also mitigates the formation of smog and ozone [26-28] with positive effects on human health.

In some countries, local authorities are pushing towards an overall increase in urban albedo in order to mitigate local climate. For instance, in the United States, Mayor Michael Bloomberg is carrying forward an urban plan for New York City [29] with the aim to convert black flat roofs into white ones for reducing summer temperatures [30]. The European project ‘Cool roof Europe’, co-financed by the EU in the framework of the Intelligent Energy Europe Program, has the aim to work on action plan for cool roofs in Europe [31].

The urban-wide increase in albedo can be coupled with other mitigation or adaptation strategies – for instance the increase in urban vegetation, the substitution of impervious man-made surfaces with pervious ones, the enhancement in urban water-bodies – in order to strengthen its efficiency and sustain the global and regional precipitation patterns [32]. The increase in urban albedo can be integrated in urban policies. For instance, it can be considered in ordinary building maintenance plans without requesting economic investments. Furthermore, the urban increase in albedo can be coordinated at European level contributing to positively affect climate change.

In this study we present a framework to investigate the capacity of cities to utilize albedo for addressing both mitigation and adaptation. We focus on the urban-wide increase in rooftops and pavements albedo. The developed theoretical framework is then applied to the 3 European cities. European countries were divided in three geographical areas featured by similar climatological and geographical characteristics such as latitude: Scandinavian countries; northern and central European countries; southern European countries. Each geographical area is represented by one city. The effectiveness of the increase in albedo is mainly dependent on two characteristics: the incoming solar radiation and the clearness index. The incoming solar radiation is mainly dependent on latitude. The clearness index depends on the cloud cover that is impacted, among others, by the closeness to the sea or ocean. For each of the three cities both the average annual clearness index and the incoming solar radiation at the top-of-the-atmosphere (TOA) were retrieved from NASA [33]. The climatological data from NASA are referred to average values calculated on a dataset of 22 years for a grid with cells’ resolution of 1x1°. For each city the coordinates are placed in a cell of the grid.

At the global scale the variation in surface albedo influences radiative forcing (RF) and, as a consequence, global climate. First, in this study the effect of the variation of surface albedo on RF was calculated for a surface of one square meter as follows (Eq. 1):

$$\Delta RF_{TOA} = SR_{TOA} \Delta \alpha_{TOA}$$

Equation 1

The variation in RF deriving by the change in surface albedo is expressed in Wm^{-2} as well as the incoming solar radiation at TOA (i.e., SR_{TOA}). The effect of the variation in surface albedo at TOA is dependent on the two-way transmittance parameter (i.e., f_a):

$$\Delta \alpha_{TOA} = f_a \Delta \alpha_s$$

Equation 2

f_a considers both the clearness index, K_T (i.e., the fraction of radiation at TOA that reaches the Earth's surface) and the transmittance factor T_a (i.e., the fraction of the radiation reflected from the surface that arrives back at the TOA) [34]. Since the physical mechanism that affects T_a is the same that affects K_T [34], equation 2 was approximated to the following relation:

$$f_a = K_T^2$$

Equation 3

Each city is characterized by a potential unitary effect on climate close to the average potential effect on global climate of all the cities examined for each area. For the Scandinavian countries Helsinki was selected, for the central European cities Krakow and for the south European cities Porto. The climatological data about the three cities are reported in table 1.

Location	Geographical coordinates	$SR_{TOA} [W/m^2]^{a,b}$	$K_T^{a,c}$
Helsinki	60°10' 15" N 24°56' 15" E	235	0.45
Krakow	50° 3' 42" N 19° 56' 14" E	269	0.39
Porto	41° 10' 0" N -8° 35' 0" E	323	0.53

^a Data retrieved from NASA [33]
^b Annual Averaged Top-of-atmosphere Insolation
^c Annual Averaged Insolation Clearness Index

Table 1 Geographical and climatological data of the three representative cities

In addition the snow cover was considered in order to take into account the effectiveness of the variation in urban albedo. For instance, since during winter the urban albedos in Helsinki and Krakow are influenced by the presence of snow, the increase in albedo does not provide any beneficial to the global and local climate. The monthly effect of the change in urban albedo on RF was averaged considering the months during which its change does not affect climate in order to obtain the average annual effect on RF.

The effect of the variation in urban albedo on climate is also dependent on the urban morphology. The wider is the urban surface can be enhanced the more effective is the strategy on climate.

The amount of urban surface for pavements and rooftop (Tab. 2) was considered in order to calculate how the increase in their albedo can potentially affect climate in addition to geographical and climatological data:

$$\Delta RF_{TOA Potential} = f(\text{clearness, solar radiation, urban surface})$$

Equation 4

City	Area for residential use [km ²] ^a	Area used for commercial activities (industry, trade, offices) [km ²] ^a	Area used for transport (road, rail air, ports) [km ²] ^a	Total land area [km ²] ^a
Helsinki	246.5	83.16	204.92	2969.9
Krakow	53.85	65.81	122.65	2991.5
Porto	163.54	62.38	9.55	562

^a Data retrieved from Eurostat [35]

Table 2 Urban characteristics of the three representative cities

The data related to the urban morphology of the cities were retrieved from Eurostat Urban Audit [35].

The data about the urban surface for residential use, for commercial activities and that one used for transport were used in order to calculate the average increase in urban albedo for each city (Eq. 5)

$$\Delta\alpha_{Avg Un} = \sum_i \frac{\Delta\alpha_i S_i}{S_{Urb}}$$

Equation 5

$\Delta\alpha_{AvgUn}$ is the average change in urban albedo due to the variation in albedo of pavements and rooftops; $\Delta\alpha_i$ is the potential change in albedo for the different typologies of urban surfaces (i.e., pavements and rooftops) and S_i is the potential amount of surfaces that can be enhanced. S_{Urb} is the total urban surface for each city (Tab. 2).

$$\Delta RF_{TOA Potential} = -SR_{TOA} K_T^2 \Delta\alpha_{Avg Un} S_{Urb}$$

Equation 6

For the evaluation of the effect of the surface change in albedo on climate, previous studies (e.g., 36) considered as reasonable an increase in rooftop and pavement albedo of respectively 0.25 and 0.15. In this study the same increase in albedo (i.e., $\Delta\alpha_i$) was considered. Furthermore, in order to provide a measure that can be easily understood, the potential change in RF was translated into kilograms of carbon dioxide equivalents (i.e., CO₂eq) as follows:

$$\Delta CO_2 eq = \Delta RF_{Pl} \frac{\ln(2)}{\Delta F_{2X}} \left(\frac{p_{CO_2} M_{CO_2} m_{air}}{1.0 \times 10^6 M_{air}} \right) \frac{t}{\int_0^t Decay CO_2(t) dt}$$

Equation 7

$\Delta CO_2 eq$ is the amount of CO₂ that should be released in the atmosphere in order to produce the same effect on global climate that the change of albedo is able to produce. $\Delta CO_2 eq$, in equation 7, is expressed into grams. ΔRF_{Pl} is the variation in RF at TOA due to the change in planetary albedo. ΔRF_{Pl} is calculated as follows:

$$\Delta RF_{Pl} = -SR_{TOA} \frac{\Delta\alpha_{Avg Un} S_{Urb}}{A_{Earth}}$$

Equation 8

A_{Earth} is the Earth's surface ($5.1 \cdot 10^{14} \text{ m}^2$). p_{CO_2} is the partial pressure considered as reference (383 ppmv). M_{CO_2} is the molecular mass of CO₂ ($44.0095 \text{ g mol}^{-1}$); m_{air} is the mass of the atmosphere ($5.148 \cdot 10^{21} \text{ g}$). ΔF_{2X} is the variation in RF due to the doubling of the amount of CO₂ in the atmosphere (3.7 Wm^{-2}). M_{air} is the dry air molecular mass (28.95 g mol^{-1}) [3]. The decay of CO₂ over time is expressed in the following equation by Joos and colleagues [37]:

$$Decay CO_2(t) = 0.217 + 0.259e^{\frac{-t}{172.9}} + 0.338e^{\frac{-t}{18.51}} + 0.186e^{\frac{-t}{1.186}}$$

Equation 9

Since the change in surface albedo is particularly important at local scale, the effects on urban scale were evaluated. Previous studies demonstrated that the effect of change in albedo on urban climate is highly correlated with the incoming solar radiation and the urban characteristics [38]. In this study the mitigation in the peak of temperature has been calculated through the use of a regression analysis developed by Santamouris [39].

We find that low latitude cities (e.g., Porto) are characterized by a higher amount of incoming solar radiation as well as clearness index (Tab. 1). In contrast, northern and central European cities are featured by a higher incoming solar radiation than Scandinavian cities but by a less clearness index (Tab. 1). This means that the unitary variation in surface albedo (e.g., one square meter) in Scandinavian cities, in some cases, could be more effective than the same change in albedo in northern and central European cities. We observe this effect when comparing Krakow with Helsinki.

Since this study was developed to evaluate the potential in urban context to influence global climate, the amount of urban surface that can potentially be enhanced plays an important role. Table 2 shows that the amount of urban surface that can be enhanced is considerably larger in Helsinki than in Porto. Since the total urban area in Porto is less extensive than in the other two cities, the potential average increase in Porto is higher than in Helsinki and Krakow (Tab. 3). The effects of the change in urban-wide albedo in Helsinki and Krakow are reduced by the winter snow cover. However, despite this, it surprisingly results that the potential urban-wide increase in rooftops and pavements' albedo in Helsinki can be more effective on climate than the increase in albedo in the other two cities. From figure 1 – that shows the correspondent amount of CO₂ that provoke the same effect on climate of the change of albedo – it clearly results that, the potential effect in Helsinki is slightly higher than the effect in Porto because of Helsinki's large urban surface. Besides, the potential in Krakow is quite low, compared to the other two cities, because of the low solar incoming radiation, low clearness index, the contribution of the snow cover during winter and the relatively low amount of urban surface that can be enhanced.

The effect of the increase in albedo in Helsinki evaluated in a time-frame of 100 years is equal to a decrease of the emission in the same time frame of 13 Mt of CO₂. The increase in albedo in Porto and in Krakow corresponds – in the same time-frame – to a decrease in the emissions of CO₂ of respectively 11.7 and 5.6 Mt (Fig. 1)

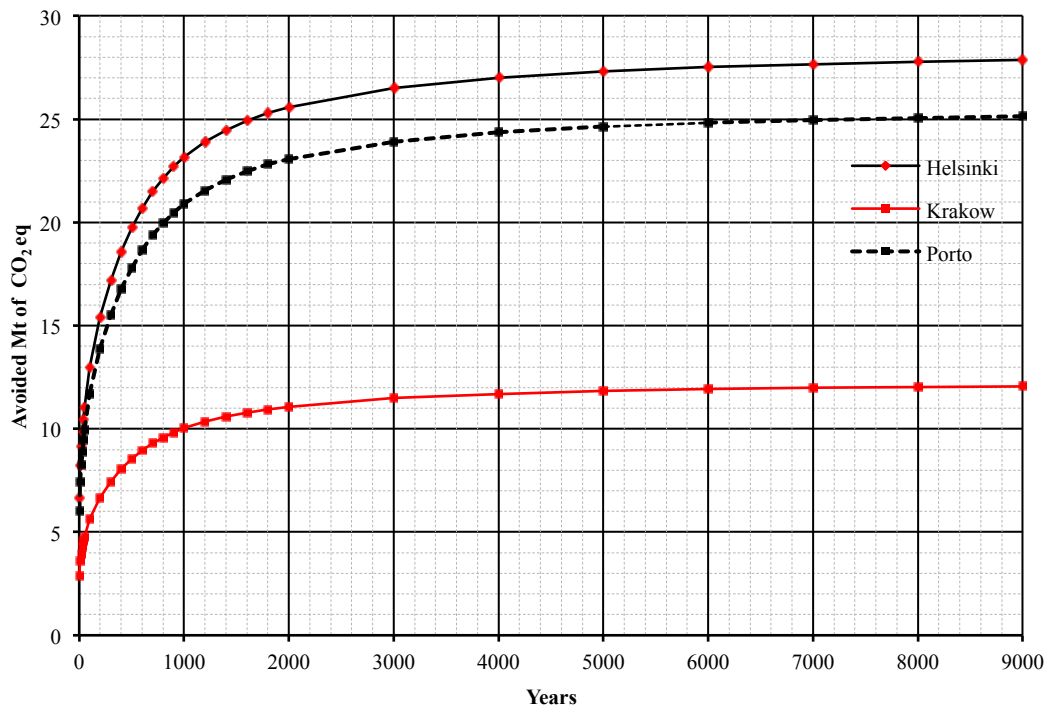


Fig. 1: Time-dependent avoided emission of CO₂ eq for the increase in urban albedo

On the contrary, in Porto the increase in urban albedo can be more effective on urban scale than in the two other cities. The urban-wide increase in albedo mitigates the peak in summer temperature (Tab. 3, third column) of about 1°C (Tab. 3 fourth column). The beneficial effect is due to the high potential increase in the average urban albedo. The high population density in Porto (Tab. 3 fifth column), compared to the other two cities, amplifies the beneficial effects of the increase in albedo. Indeed, a large number of people would benefit of the decrease in summer peak of temperature.

City	Potential increase in average urban albedo	Monthly average air temperature at 2 m above the surface of the Earth [°C] ^a	Potential mitigation in peak in temperature [°C]	Population density [Inb/km ²] ^b
Helsinki	0.04	21.8 (July)	0.34	430.88
Krakow	0.02	24 (July)	0.15	426.69
Porto	0.10	28.6 (July)	0.93	1980.42

^a Data retrieved from NASA [33]
^b Data retrieved from Eurostat [35]

Table 3 Potential change in urban albedo and potential mitigation in peak in temperature in the three representative cities

The decrease in extreme temperatures is also associated to a decrease in the anthropogenic ozone formation. Thus, the decrease of summer peak in temperature not only has positive effects on heat-stress and heat related mortality, but also reduces morbidity associated with respiratory diseases.

Altogether, this study shows that the increase in urban albedo can be an efficient adaptation strategy to mitigate the UHI and to cope with climate change. In addition, this study demonstrates the importance of a site-dependent evaluation of the potential adaptation related to this urban strategy. Indeed, not just geographical and climatological characteristics play a role, but also the urban morphology can be decisive to make the strategy successful. This underlines the necessity to tailor urban policy on the effective potentialities of each city.

REFERENCES

- Parmesan C. & Yohe G. (2003), *A globally coherent fingerprint of climate change impacts across natural systems*, Nature, Vol. 421, No. 2, pp. 37-42. (1)
- Morton J.F. (2007), *The impact of climate change on smallholder and subsistence agriculture*, PNAS, Vol. 104, No. 50, pp. 19680-19685. (2)
- IPCC (2007), *Climate Change 2007*. Cambridge University Press, Cambridge, United Kingdom and New York, NY, USA. (3)
- Kates R.W., Colten C.E., Laska S. & Leatherman S.P. (2006), *Reconstruction of New Orleans after Hurricane Katrina: A research perspective*, PNAS, Vol. 103, No. 40, pp. 14653-14660. (4)
- National Oceanic and Atmosphere Administration (2013), *Sandy retired from list of Atlantic Basin tropical cyclone names*, Retrieved on April 2013 from:
http://www.noaa.gov/stories2013/20130411_sandynameretiredt.html (5)
- European Commission (2013), *Adaptation strategies for European cities*. Retrieved on April 2013 from:
<http://eucities-adapt.eu/cms/> (6)
- Canouï-Poitrine F., Cadot E. & Spira A. (2006), *Excess deaths during the August 2003 heat wave in Paris, France*. Rev Epidemiol Sante Publique, Volume 54, No 2, pp. 127-35. (7)

- Henson B. (2010), *How unusual is Moskow's heat?* Retrieved on May 2013 from:
<https://www2.ucar.edu/atmosnews/opinion/2346/how-unusual-moscows-heat> (8)
- Grimm N.B., Faeth S.H., Golubiewski N.E., Redman C.L., Wu, J., Bai X. & Briggs J.M. (2008), *Global change and the ecology of cities*, Science, Vol. 319, pp. 756-760. (9)
- European Commission (2012), *Guidelines for Project Managers: Making vulnerable investments climate resilient*, conducted by Acclimatise and COWI A/S, contract no. 071303/2011/610951/SER/CLIMA.C3. (10)
- European Commission (2013), *An EU strategy on adaptation to climate change*. Retrieved on April 2013 from: http://ec.europa.eu/clima/policies/adaptation/index_en.htm (11)
- European Commission (2013), *Climate Change Adaptation in Europe*. Retrieved on April 2013 from: <http://climate-adapt.eea.europa.eu/> (12)
- European Commission (2013), *Climate Action*. Retrieved on April 2013 from http://ec.europa.eu/clima/policies/adaptation/what/index_en.htm (13)
- Hamley R.M. (2007), *Active amplification of the terrestrial albedo to mitigate climate change: an exploratory study*. Mitigation and Adaptation Strategies for Global Change, Volume 12, No 4, pp. 419-439. (14)
- Akbari H., Menon S. & Rosenfeld A. (2009), *Global cooling: increasing world-wide urban albedos to offset CO₂*. Climatic change, Vol. 94, pp. 275-286. (15)
- Akbari H., Matthews H.D. & Seto D. (2012). *The long-term effect of increasing the albedo of urban areas*. Environmental Research Letter, Vol. 7. (16)
- Susca, T. (2012), *Enhancement of life cycle assessment (LCA) methodology to include the effect of surface albedo on climate change: Comparing black and white roofs*. Environmental Pollution, No 163, pp. 48-54. (17)
- Lenton M.T. & Vaughan N.E. (2009), *The radiative forcing potential of different climate geoengineering options*. Atmospheric Chemistry and Physics, No 9, pp. 5539-5561. (18)
- Smil (2008), *Energy in nature and society: general energetics of complex systems*, MIT Press. (19)
- Rosenfeld A.H., Akbari H., Bretz S., Fishman B.L., Kurn D.M., Sailor D. & Taha H. (1995), *Mitigation of urban heat islands: materials, utility programs, updates*. Energy and Buildings, No 22, pp. 255-265. (20)

- Akbari H. & Levinsson R. (2008), *Evolution of Cool-Roof Standards in the US*. in M. Santamouris, “Advances in Building Energy Research” (pp. 1-32). Athens: Earth Scan. (21)
- Basu R. & Samet J.M. (2002), *Relation between elevated ambient temperature and mortality: A review of the epidemiologic evidence*. *Epidemiologic Reviews*, No. 24, pp. 190-202. (22)
- Kovats R.S. & Hajat S. (2008), *Heat stress and public health: A critical review*. *Annual Review of Public Health*, No. 29 (1), pp. 41-55. (23)
- WHO (World Health Organization)(2009), *Protecting health from climate change. Connecting science, policy and people*. Retrieved on May 2011 from:
http://whqlibdoc.who.int/publications/2009/9789241598880_eng.pdf. (24)
- Luber G. & McGeehin M. (2008), *Climate change and extreme heat events*. *American Journal of Preventive Medicine*, No. 35 (5), pp. 429-435. (25)
- Taha H. (2008), *Urban surface modification as a potential ozone air-quality improvement strategy in California: a mesoscale modelling study*. *Boundary-Layer Meteorology*, No 127, pp. 219-239. (26)
- Taha H. (2001), *Potential impacts of climate change on tropospheric ozone in California: a preliminary episodic modeling assessment of the Los Angeles basin and the Sacramento valley*. Berkeley: Lawrence Berkeley National Laboratory. (27)
- Akbari H., Levinson R., Miller W. & Berdahl P. (2005), *Cool colored roofs to save energy and improve air quality. Passive and Low Energy Cooling*, pp. 89-100. Santorini: Palenc. (28)
- NYC °CoolRoofs (2010). Retrieved on March 2013 from:
<http://www.nyc.gov/html/coolroofs/html/home/home.shtml> (29)
- Bloomberg Hypes Energy-Efficient Rooftop Painting* (2009). Retrieved on December 2009, from:
http://www.nypost.com/p/news/local/bloomberg_hypes_energy_efficient_w4c1QCjsR3n0qctCJQaFHL (30)
- Cool Roofs* (2010). Retrieved on October 2010 from: <http://www.coolroofseu.eu/> (31)
- Jacobson M.Z. & Ten Hoeve J.E. (2012), *Effects of urban surfaces and white roofs on global and regional climate*. *Journal of climate*, Vol. 25, pp. 1028-1044. (32)

- NASA (2013). *NASA Surface meteorology and Solar Energy - Available Tables* Retrieved on February 2013 from: http://power.larc.nasa.gov/cgi-bin/cgiwrap/solar/grid.cgi?&p=grid_id&p=swvdowncook&p=avg_kt&p=daylight&p=day_cld&p=toa_dwn&p=srf_alb&num=197132&lat=41&veg=17&hgt=100&submit=Submit&email=grid@larc.nasa.gov&lon=16&step=2&sitelev= (33)
- Bright R.M., Strømman A.H. & Peters G.P. (2011), *Radiative forcing impacts of boreal forest biofuels: a scenario study for Norway in light of albedo*. Environmental Science and Technology, No. 45, pp. 7570-7580. (34)
- Eurostat, 2013. *Statistics*. Retrieved on February 2013 from: http://epp.eurostat.ec.europa.eu/portal/page/portal/statistics/search_database (35)
- Akbari H., Menon S. & Rosenfeld A. (2009), *Global cooling: increasing world-wide urban albedos to offset CO₂*. Climatic Change, No. 94, pp. 275-286. (36)
- Joos F., Prentice I.C., Sitch S., Meyer R.H., Platter G., Gerber S. & Hasselmann K. (2001), *Global warming feedbacks on terrestrial carbon uptake under the Intergovernmental Panel on Climate Change (IPCC) emission scenarios*. Global biogeochemical cycles, No. 15 (4), pp. 891-907. (37)
- Oleson, K.W., Bonan, G.B. & Feddema, J. (2010), *Effects of white roofs on urban temperature in a global climate model*. Geophysical research letters, No. 37 L03701. (38)
- Santamouris M. (2012), *Cooling the cities – A review of reflective and green roof mitigation technologies to fight heat island and improve comfort in urban environments*. Solar Energy, <http://dx.doi.org/10.1016/j.solener.2012.07.003>. (39)

CLIMATE POLICY AND ECONOMIC ASSESSMENT

Economic assessment of climate change impacts

An indicator-based assessment of vulnerability to climate change in Italian coastal cities

Breil M.^{1,2,*}, Johnson K.^{1,3}, Bucchignani E.^{1,4}

¹ *Centro Euro-Mediterraneo sui Cambiamenti Climatici, Fondazione Eni Enrico Mattei;*

³ *Università Ca'Foscari Venezia,* ⁴ *Centro Italiano Ricerche Aerospaziali*

**Corresponding author: margaretha.breil@cmcc.it*

Abstract

The article describes a top-down methodology to assess vulnerabilities to climate change impacts in Italian coastal cities. Spatially explicit socio-economic indicators are used to represent sensitivity and adaptive capacity, while land use and climate data provide projections for exposure to inland and coastal flooding and heat waves. Using the eight major Italian coastal cities as objects for a scoping study, the extent of current vulnerable populations and infrastructure networks is analyzed relative to future impacts of climate change. Vulnerability indicators are derived from the literature and applied to statistical and GIS data to assess urban areas, specifically infrastructures and the number of inhabitants potentially at risk, based on land use information and census data. Anticipated changes in future urban climate conditions are described using regional climate projections for the first half of the 21st century and are compared with historically observed climate data. Results indicate different patterns of vulnerability across the eight cities due to topographic, climatic, and socio-economic characteristics.

Keywords: *Climate change, adaptation, indicators, urban areas, coastal cities, Italy*



1. INTRODUCTION

Cities are vulnerable to the impacts of climate change due in part to the geographic concentration of population, values and assets. Hence cities and infrastructures represent key areas for adaptation efforts [1]. Coastal cities are particularly vulnerable to climate change due to rising sea levels and storm surges, which increase the risks of erosion and coastal flooding. Coastal vulnerabilities are additional to those vulnerabilities common to all cities, which are largely caused by surface sealing, making cities more susceptible to flash floods and river flooding, and by pollution and Urban Heat Island effects that are exacerbated by heat waves [2,3]. Addressing urban climate change vulnerabilities is becoming an increasingly relevant issue for local authorities, although neither the problems posed, nor the types of tasks connected to urban adaptation are entirely novel issues for urban governance. Nevertheless, new kinds of approaches, resources, and information regarding future variability of impacts and vulnerabilities are required to create suitable and efficient adaptation measures, especially with respect to the uncertainty surrounding climate impacts [1].

1.1 Characterizing urban vulnerability

An analysis of urban vulnerability should accomplish two things: identify direct and indirect climate change impacts, and identify the urban functions and stakeholders potentially affected. This paper defines a set of indicators for a preliminary assessment of urban vulnerabilities to climate change, which are analysed together with projections on future climate conditions for eight major Italian coastal cities. This is a screening study to identify the climate change vulnerabilities and adaptation needs of these cities, from now until 2050. Top-down analyses such as this one are useful for identifying urban vulnerabilities and adaptation needs and comparing them across different local contexts, detecting particular policy needs, thereby potentially assisting regional or national authorities in the design of adaptation policies.

Here vulnerability is defined as “the degree to which a system is susceptible to, or unable to cope with, adverse effects of climate change, including climate variability and extremes; it is a function of the character, magnitude, and rate of climate change and variation to which a system is exposed, its sensitivity, and its adaptive capacity” [4].

Understanding urban vulnerability is crucial for the design of efficient urban adaptation measures. Decision-makers therefore must take into account the exposure of single parts of the urban area to climatic variations, the extent to which they are sensitive to these impacts, and the capacity of urban inhabitants and functions to adapt to or cope with these changes.

Following this definition, a conceptual model for the definition of indicators is proposed which characterizes the elements of vulnerability to climate change impacts. It is assumed that an appropriate definition of urban vulnerabilities and associated indicators for each specific urban area can assist the integration of adaptation into urban policies addressing core considerations on the nexus of climate impacts, vulnerability and adaptive capacity.

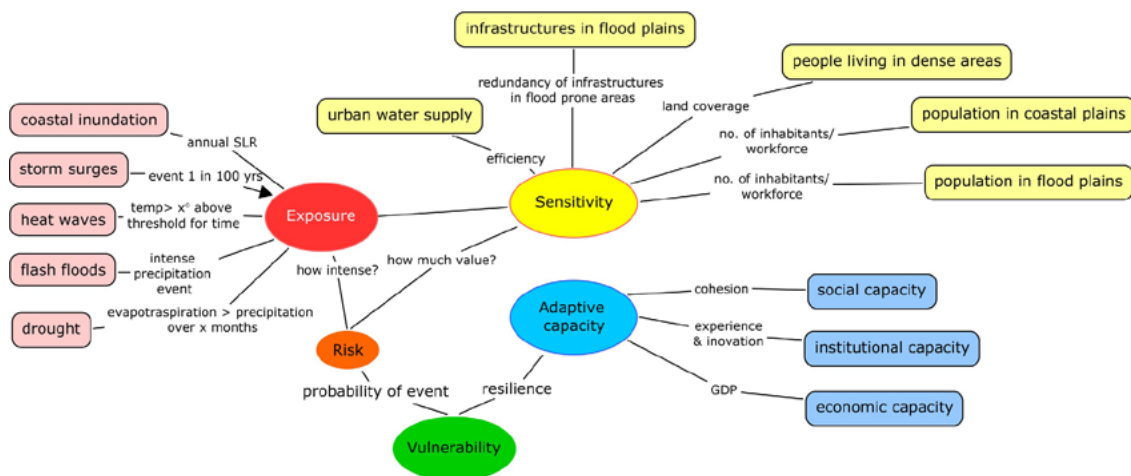


Fig. 1: Conceptual representation of urban vulnerability

1.2 Vulnerability indicators

The limitations of a top-down analysis have confined the selection of indicators to data that is coarser than what would be used in a local level assessment. In local level assessments more specific local knowledge and a greater amount of resources can be involved, however the possibility of producing comparable results across different urban contexts is limited. Top-down assessments are suitable for identifying vulnerabilities that warrant – in a second step – a more in depth analysis.

Indicators are commonly used for assessing vulnerabilities to climate change, especially in contexts where either comparable measures across different contexts or across longer timescales are needed. For instance, an EU white paper calls for the development of indicators for monitoring impacts and adaptation measures [5]. Specific indicators for cities are requested in an EU document focussing urban policies [3], and explored in a scoping study relying mostly on the impact-receptor connection and the type of damages experienced [2]. Following the proposal made by Schauer et. al [2], this study intends to operationalize the concept of climate change vulnerability in urban contexts using spatially explicit indicators to detect spatial distribution of vulnerabilities, and as a final consequence, specific adaptation needs. The choice of indicators has been driven furthermore by the possibility of feeding the indicators with data that is easy to access and available for a large range of urban contexts. Following the conceptual model for urban vulnerability presented above, urban characteristics of sensitivity and adaptive capacity are identified and associated with land-use or statistical data, while climate data is used to define exposure. Indicators used in this study are consistent with those represented in the literature.

1.3 The Italian case study

To characterize the vulnerability of Italian coastal cities, this paper details a screening study that uses indicators to estimate the vulnerability of urban sensitivities to the changing climate impacts of coastal and urban flooding, and heat waves, from today to the 2050s. Vulnerabilities to future climate change are considered relative to the sensitivities of current populations, land use patterns and adaptive capacities. This approach is powerful with regards to the possibility of screening and summarizing a greater number of local situations in a shorter period of time, but some limitations exist, as local specificities regarding the physical impacts, as well as sensitivity and adaptive capacity cannot be considered, and require further detailed analysis.

2. METHODS AND DATA

The eight coastal Italian cities analysed in this study were selected based on their size and the availability of GIS and climate data. Land use data is available in the Urban Atlas [6] for eight out of the nine Italian coastal cities with a population greater than 200,000. The area of Messina, the ninth among the major Italian coastal cities, had to be excluded in order to maintain consistency and comparability

of data across the case study cities. Therefore this assessment focuses on the eight coastal Italian cities of Rome, Naples, Palermo, Genoa, Bari, Catania, Venice, and Trieste.

Following the definition of vulnerability, indicators were selected for assessing spatial distribution of exposure, sensitivity, and adaptive capacity in the cities to the three climate impacts considered here: coastal flooding, urban inland flooding, and heat waves.

2.1 Exposure to climate impacts

The **exposure** to impacts from meteorological events was assessed using climate projections of extreme heat and precipitation events for the period from 2025 to 2055, which have been modelled for all case study cities and compared to baseline data from 1971 to 2001. The study focuses on near-term climate changes because there are fewer uncertainties, changes are evident even over this time frame, and the data is more relevant for local policymakers. Numerical simulations have been performed at a very high spatial resolution (about 8 km) using the regional model COSMO-CLM [7], which has good capabilities in simulating the main features of the Italian climate [8].

2.1.1 Precipitation contributing to urban inland flooding

Daily precipitation projections for the period from 2025 to 2055 are compared with data from past climate (1971-2000) for three cities; furthermore, the remaining cities, trends for the decades of the 2030s and the 2050s are compared with historic data. The number of days of projected precipitation quantities greater or equal to the 95th percentile precipitation for a given year is calculated, based on comparison with the average of projections for the 2030s and 2050s. The number of days per month with precipitation greater than or equal to the 95th percentile precipitation amounts is representative of potential extreme precipitation days, potentially contributing to flood events.

2.1.2 High temperatures and heat waves

In a similar manner, climate model projections of daily mean temperatures for 2025 to 2055 are used to estimate the number of extremely hot days in the 2030s and 2050s. The definition of “extremely hot” used in this context actually should refer to a relative measure rather than an absolute threshold value,

as negative health impacts and mortality vary regionally according to the population and its preparedness for coping with excess heat [9]. Nevertheless, for the sake of comparability, rather than a dynamic reference to annual or decadal mean or peak temperatures, this study refers to a fixed threshold (mean 24hours temperatures above 28°C) for detecting trends in extremely high temperatures across the two decades modelled.

2.1.3 Sea level rise

Sea level rise (SLR) data is from the most recent projections for the Mediterranean [10–12], summing up steric and mass addition contributions to a SLR projection of 7 to 12 cm for 2050. This increase is applied to the storm surge level indicated by the DINAS Coast database [13] for events with a 1-in-100-year probability. Further to rising sea levels, the compounded effects of tectonic tendencies are calculated for each urban area in order to obtain the relative changes for each local context. SLR projections used refer to the A1B climate scenario. The calculations are made in 5-year increments from 2000 until 2050. Potential losses from erosion have not been included in this equation because all coastlines along the urban areas considered are considered “artificial” [14].

The data on relative SLR could not be directly related to GIS data for a determination of sensitivity, as the vertical accuracy of GIS data is lower than the expected change in sea level over the timeframe considered. A buffer along the coastline has thus been applied in order to quantify and characterize population and infrastructure potentially threatened by increasing sea levels.

2.2 Sensitivity

Land use data and urban densities, and the proximity to green and blue areas, are used as indicators defining spatially differentiated sensitivities. This information is derived from satellite data, using the data provided by the EEA with the Urban Atlas, which provides a set of comparable land use and land cover data at the scale of 1:10.000 [6].

To provide some insight on potential flood risk without access to hydraulic modelling, a simple buffer of 150 meters is applied on both sides of all elements of the hydraulic network present in the urban

areas. Persons living in these areas and infrastructures crossing them are considered at risk of inundation.

Due to the lack of other means of comparison and valuation of the relative importance of these areas within the urban context, the territorial extension of the area of infrastructures and the number of inhabitants have been compared with city averages, providing thus both absolute and relative information on the population at risk. Due to the lack of comparable data on the levels of coastlines for the urban zones considered, an analogous, distance based approach has been applied to the areas along the shorelines, identifying infrastructures, urban areas and populations lying in a distance of 100 meters from the coastas defined by the land use data.

Physical factors that create UHI effects, like sealed surfaces and high-density urban areas, were identified using from land use data. Within these areas, buffer zones of 500 meters and 150 meters are placed around the shoreline and urban green and blue areas, respectively, assuming that these areas will benefit from mitigating effects generated by urban vegetation. For the remaining sensitive areas, the average density of residential population, old and very old persons was determined using the ISTAT 2001 census.

2.3 Adaptive capacity of vulnerable populations

Adaptive capacity is defined mainly by socio economic data obtained from census results, available by census section. Because the most recent census data has not yet been published at a sufficiently detailed spatial scale, 2001 census data is used [15] for all municipalities included in the large urban zones as defined by the Urban Audit. Statistical data provides only scarce information on socio-economic characteristics connected to a potential lack of adaptive capacity of the residential population. Census data, allows for the quantification of populations with a low education level¹, of unemployed, retired, or migrants². Further to these socio-economic characteristics, the presence of dwellings without a telephone line has been considered a factor indicating potential difficulties in coping with the consequences of urban flooding. With respect to heat waves, elderly and persons affected by specific

¹ This indicator refers to adults with only primary education.

² In this case, foreigners from Africa, Asia and Oceania have been considered as migrants with a potentially reduced capacity to adapt to flooding.

health problem are known to have the lowest adaptive capacity to extreme high temperatures and heat waves. From census data, the presence of the first of these groups can be derived.

In a similar manner, further to the overall population living in areas potentially affected by flooding, census data has been used to assess the number of persons considered particularly vulnerable because of particular socio-economic characteristics. In this case, statistical categories describing children and elderly persons are referenced.

3. RESULTS

3.1 Exposure: Trends in extreme temperatures

In all 8 cities, summer mean temperatures for the period 2025 to 2055 are expected to be between 1 and 2°C higher than those experienced between 1971 and 2000, considering the highest 5% of daily mean temperatures (95th%). From these projections, extreme temperatures potentially connoting events of heat waves are expected to rise in approximately the same range. Most importantly, the number of days with very high mean temperatures is increasing significantly in all cities. These values represent daily means, so daily absolute maximum values will be superior to the average of day and night-time temperatures.

	Venice	Genoa	Naples	Trieste	Rome	Bari	Catania	Palermo
	Summer average temperatures (95 th %)							
1971-2000	26,66	24,20	27,26	26,33	27,00	28,77	25,66	27,59
2025 - 2055	28,30	25,79	28,78	29,04	29,94	30,63	26,74	29,46
variation	1,64	1,59	1,52	2,70	2,95	1,86	1,07	1,87
	Summer maximum temperatures							
1971-2000	31,52	31,78	33,70	31,25	35,07	34,39	28,49	36,21
2025 - 2055	32,99	33,24	33,99	33,64	33,90	36,33	30,31	39,15
variation	1,47	1,46	0,29	2,39	-1,17	1,93	1,82	2,94
	Number of days >28°C							
1971-2000	3,67	5,33	5,33	3,10	8,73	11,77	0,13	5,87
2025 - 2055	10,74	14,55	14,55	10,50	27,23	28,95	1,64	15,55
variation	7,08	9,22	9,22	7,40	18,49	17,19	1,50	9,68

Table 1: Exposure to heat waves: changes in daily mean summer temperatures

The urban heat island effect results in part from reduced evapotranspiration; urban green areas and aquatic surfaces provide mitigating effects. Here the projected number of days without rain gives some insight on potentially increasing water stress in cities, as the maintenance of urban green space may depend more frequently on irrigation, placing more stress on shrinking water reserves.

	Venice	Genoa	Naples	Trieste	Rome	Bari	Catania	Palermo
1971-2000	1,2725	2,9036	1,0759	1,9875	1,2014	0,6331	0,3840	0,6919
2025 - 2055	1,2825	2,6035	0,8279	1,8605	0,9809	0,5726	0,2258	0,6514
variation	0,0100	-0,3001	-0,2480	-0,1270	-0,2205	-0,0604	-0,1582	-0,0405

Table 2: Precipitation trends, daily mean values

Additionally, problems may arise for urban aquatic surfaces, where reduced water levels will increase the concentration of pollutants and sanitation problems related to the water quality. Projections show that the precipitation is expected to decrease slightly in all cities but Venice.

3.2 Exposure: Trends in Sea level rise

Projections for sea level rise in the Mediterranean are combined with information on local subsidence/uplift trends, in order to derive the potential level that can be reached by an extreme event (1-in-100-year). For the cities considered, according to the different trends in subsidence/uplift, local sea levels of 0,011 to 0,016 m above the actual mean sea level are projected.

	Venice	Genoa	Naples	Trieste	Rome	Bari	Catania	Palermo
Sea level rise 2050	0,16	0,11	0,12	0,11	0,12	0,12	0,13	0,12
Storm surge level 2050	2,06	0,56	0,69	1,33	0,76	0,77	0,48	0,65

Table 3: Trends in local sea level rise (m)

4. LOCAL TRENDS FOR SENSITIVITY AND ADAPTIVE CAPACITY

To relate these projections of climate impacts to the sensitivity of urban areas and to derive information on their specific vulnerabilities, indicators for sensitivity and adaptive capacity are applied to GIS and statistical data to assess the vulnerability of each urban area with respect to heat waves, flash floods and coastal flooding.

Not surprisingly, in all cities the urban heat island effect is concentrated in the central areas, and is particularly significant in terms of population affected. Naples appears to be the most affected, with more than half of the urban population and more than 17% of the urban areas interested. For all cities except Trieste, the group of elderly inhabitants (over 65 and especially over 75 years of age) is particularly exposed, due to the higher concentration of elderly in most of the densely built central urban areas.

Comparing climate data from the period 1971 to 2000 with projections (see table 1), the number of extremely hot days is increasing in all cities. Hot days are defined, in this case, as days with medium temperatures (that is 24 hour means) above 28°C. As the occurrence of hot days are expected to increase, major problems related to urban heat island effects are to be expected in all cities considered, especially in Rome and Bari, where the highest increases in hot days are expected..

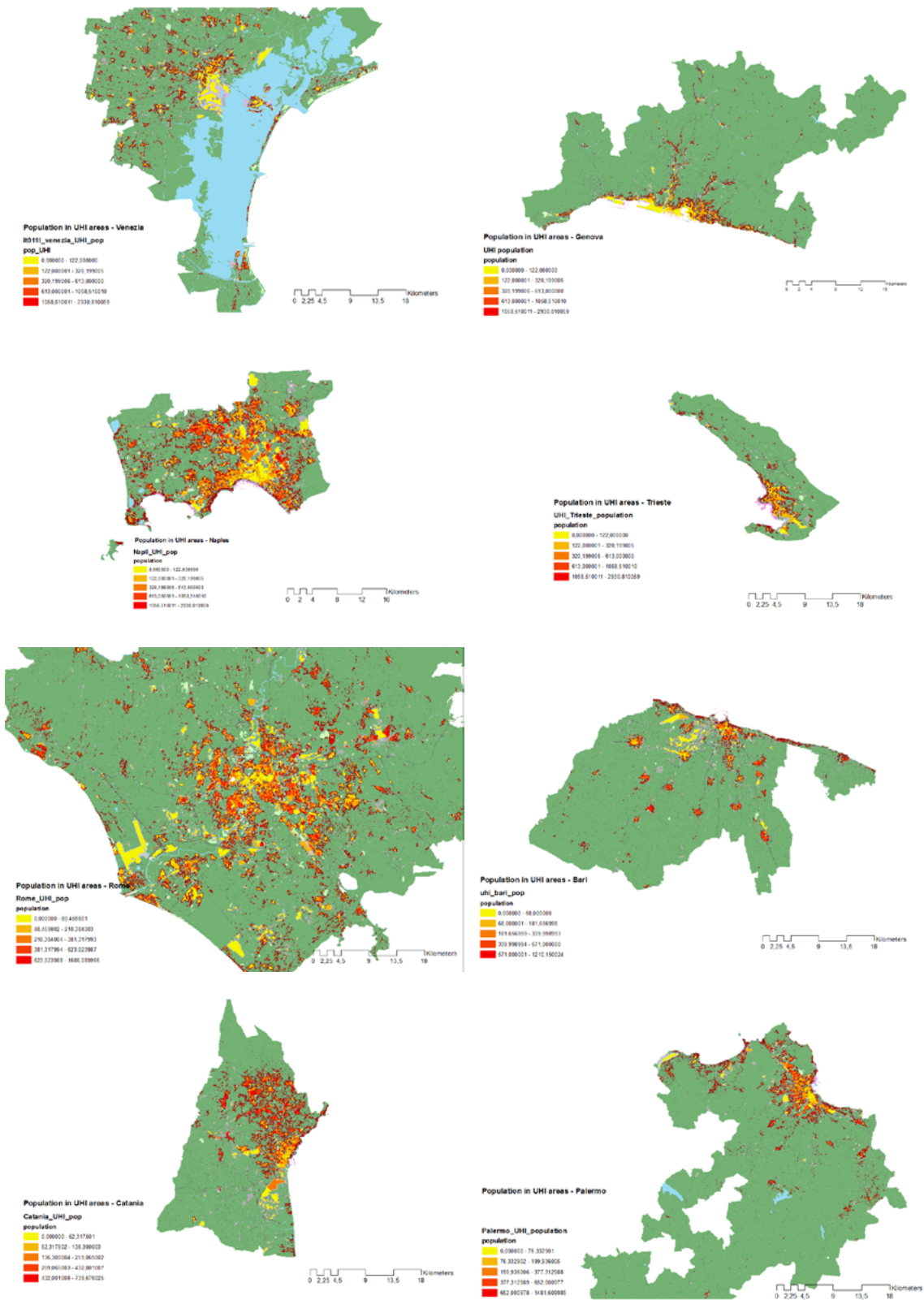


Table 4: Population densities in UHI - prone areas

The results obtained evidence a high level of risk of urban flooding in all coastal cities considered, regarding both infrastructures and populations living in buildings close to the shoreline. Although absolute quantities of precipitation projected do not reach levels experienced in recent events³, a trend of increasing precipitations during extreme events can be derived from the projections. The portions of urban territory, population and infrastructure vary from nearly 30% of the urban population identified as vulnerable to river flooding in Genoa, 25% of the surfaces of transport infrastructures and 6,5% of the population in Rome.

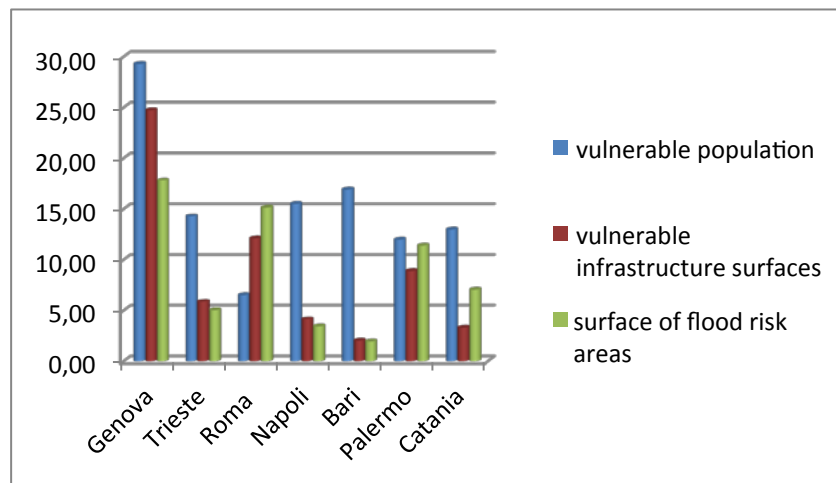


Fig. 2: River flooding, vulnerable assets in relation to urban total (%)

Nevertheless, the fact that exposure rates calculated for Catania and Naples are well beyond the average of the sample is contradicted by some extreme recent events with dramatic consequences. This points to the necessity of considering, further to flooding, also the incidence of land slides in relation to heavy precipitation events.

With regards to coastal flooding, rates of exposure and vulnerabilities are limited to relatively small portions of the urban territories, but can potentially reach, in some cases, almost 5% of the overall population (Bari) or almost 4 % of infrastructure, (excluding port areas), and population in Genoa. Bari is, along with Trieste (and Rome where the vulnerability results are quite low), one of the cities expected to face the most significant rise in storm surge levels among the cities considered.

³ This is due to the short timeframe used, which may not capture events with return periods of 100-years.

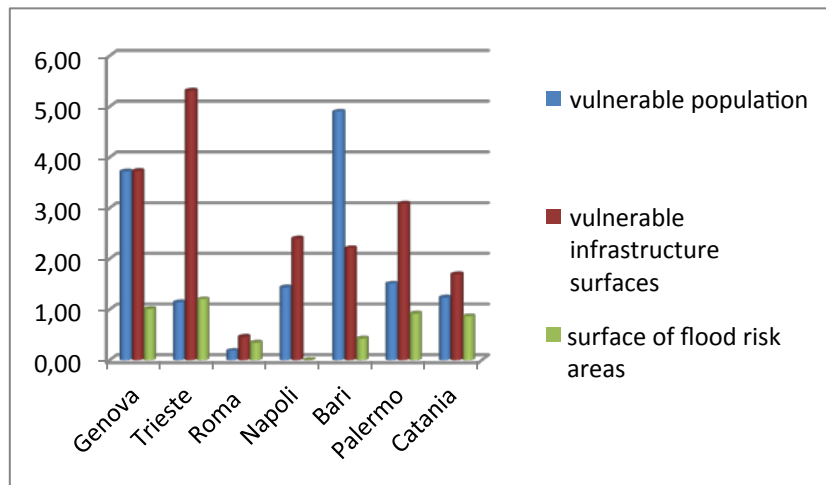


Fig. 3: Coastal flooding, vulnerable assets in relation to urban total (%)

5. CONCLUSIONS

Vulnerabilities to climate change impacts are quite pronounced among the eight coastal Italian cities considered, but not evenly distributed, due to different socio-economic, morphologic and climate conditions. For instance, the particular vulnerability of Genoa’s urban area to inland flooding is confirmed by our GIS model, with circa 30% of surface of infrastructures and 18% of the residential population potentially interested by flood events and a relatively high exposure to coastal inundation due to a strong concentration of infrastructures and residential areas near shorelines. Similar or higher vulnerabilities to coastal flooding are detected for Trieste, Bari and Palermo. These results will need to be confirmed using accurate elevation data.

Naples on the other side shows a particularly low rate of exposure to flood risk, which does not correspond to the actual risk made evident in recent years; similar conclusions are drawn for Catania. In both cases the results indicate that a further investigation is needed with regards to the interaction between intense rainfall events and landslides, as a further issue not considered in this context. Projections and exposure to UHI effects differ between the cities, with Naples showing the highest rate of exposure of vulnerable populations, alongside with a medium-high increases in the number of heat days.

The issue of SLR represents a concern for all cities considered. An assessment of vulnerabilities in this context has been hampered by a lack of accurate, high-resolution digital elevation data, which has not allowed for the modelling of spatial impacts in this research. Indications with regards to these vulnerabilities are limited to the spatial concentrations of assets and population in areas close to the shoreline.

Albeit, this analysis has used very rough but comparable criteria for the analysis of urban risks and vulnerabilities, the results are confirmed by recent experiences, for instance in occasion of heavy precipitation events, which have caused important damages in Genoa.

6. ACKNOWLEDGMENTS

The research leading to these results has received funding from the Italian Ministry of Education, University and Research and the Italian Ministry of Environment, Land and Sea under the GEMINA project.

7. REFERENCES

- EC. *An EU Strategy on adaptation to climate change. Communication from the Commission to the European Parliament, the Council, the European Economic and Social committee and the Committee of the Regions.* 2013. (1)
- Schauser I., Otto S., Schneiderbauer S., Harvey A., Hodgson N., Robrecht H., et al. *Urban regions: Vulnerabilities, Vulnerability assessments by indicators and adaptation options for climate change impacts - Scoping Study.* 2010; 208. (2)
- EU. *Adaptation to Climate Change. Policy instruments for adaptation to climate change in big European cities and metropolitan areas.* 2011. (3)
- Parry M., Canziani O., Palutikof J., Linden P. van der, Hanson C. (Eds.). *Climate change 2007: Impacts, Adaptation and Vulnerability.* Contribution of Working Group II to the Fourth Assessment Report of the Intergovernmental Panel on Climate Change. Cambridge, United Kingdom and New York, NY, USA: Cambridge University Press; 2007. (4)
- EC. *WHITE PAPER Adapting to climate change: Towards a European framework for action.* 2009. (5)

- EEA. *Urban Atlas*. 2010. (6)
- Rockel B., Will A., Hense A. *The Regional Climate Model COSMO-CLM(CCLM)*. *Meteorologische Zeitschrift* 2008; 17: 347–8. (7)
- Bellafiore D., Bucchignani E., Gualdi S., Carniel S., Djurdjevic V., Umgiesser G. *Assessment of meteorological climate models as inputs for coastal studies*. *Ocean Dynamics* 2012; 62: 555–68. (8)
- Wilhelmi O.V., Purvis K.L., Harriss R.C. *Designing a geospatial information infrastructure for mitigation of heat wave hazards in urban areas*. *Natural Hazards Review* 2004; 5: 147–58. (9)
- Marcos M, Tsimplis MN. *Comparison of results of AOGCMs in the Mediterranean Sea during the 21st century*. *Journal of Geophys. Research* 2008; 113. (10)
- IPCC, Solomon S., Qin D., Manning M., Chen Z., Marquis M., et al. *Climate Change 2007: The Physical Science Basis, Contribution of Working Group I to the Fourth Assessment Report of the IPCC*. 2007. (11)
- Gualdi S., Somot S., Li L., Artale V., Adani M., Bellucci A., et al. *The CIRCE simulations: a new set of regional climate change projections performed with a realistic representation of the Mediterranean Sea*. *Bulletin of the American Meteorological Society* 2012; 120702121511006. (12)
- DINAS-COAST Consortium. *Dynamic Interactive Vulnerability Assessment (DIVA)*. 2006. (13)
- APAT. *Atlante delle Coste*. s.d.; (14)
- ISTAT. *Descrizione dei dati geografici e delle variabili censuarie per sezione di censimento Anni 1991, 2001, 2011*. 2012. (15)

Climate Change, Smoothing with Water Stock and Impact on the Agricultural Sector in the Po Valley (Italy)

Martina Bozzola

Graduate Institute of International and Development Studies, Geneva (CH).

martina.bozzola@graduateinstitute.ch

Abstract

This paper uses a simple dynamic optimization model to illustrate the potential for suboptimal management of water resources. We analyze the manner in which decentralized decision making and heterogeneous costs in accessing the water resource imply a water storage problem and causes suboptimal allocation of the water resources. This is increasingly relevant with greater uncertainty inherent in climate change. Heterogeneity in access causes suboptimal allocation of the water resources and makes a case for government intervention, especially as water stocks are attributed a buffer value against climate fluctuations.

We illustrate the particularities of our model in the context of the Po river basin in the north of the Italian peninsula. This area is overall characterized by heterogeneous topographical feature and intensive water use in agriculture. We show that a more efficient water management system, integrated along the watershed, is needed to cope with an increasingly unpredictable weather.

Keywords: *externalities, water management, heterogeneous water extraction costs, mountain watershed, agricultural yields.*

JEL Classification : Q19, Q25, Q54

1. INTRODUCTION

With regard to water resources, climate change is expected to result in increased variability, enhanced uncertainty, and generally increased scarcity (Strzepek et al. 2011). It is expected that climate change will significantly impact water supply and demand throughout the world. This will have implications for localized planning and water resources management, even in those areas that have not traditionally faced fresh water shortage, such as the Alpine Region. This paper highlights the potential for suboptimal management of the quantity and spatial allocation of water resources.

We use a dynamic optimization model to illustrate that heterogeneous water extraction costs imply a water storage problem, increasingly relevant under climate variability. In such an environment, spatial externalities arise in the form of suboptimal water resources allocation to early users, as water users have different incentive to overexploit the aquifer or other water resources stocks. Aquifers or other water stocks can be used to smooth the volatility in water supply, but heterogeneity in access to the groundwater resource makes a case for government intervention.

We discuss these issues in the context of the Po river basin, a mountain based watershed in the north of the Italian peninsula. This area is characterized by high water availability and intensive water use in agriculture. Several studies have concluded that climate change induced effects are already affecting the Alpine area and will do so increasingly in the future.¹ Increasing climate variability in the Po basin implies a water storage problem. Aquifers and other forms of water stock can be used to mitigate this problem, if managed as a tool to smooth fluctuations in water supply. In this paper, we focus on policies that can help to smooth water input fluctuations.

We show that agricultural production has suffered when unanticipated climate variability occurs. In terms of the area irrigated and the amount of water used, water demand for irrigation in Italy is very significant. A study of the European Commission includes Northern Italy among those European regions in which irrigation is carried out mainly as a complement to natural rainfall. In these countries or regions the areas of irrigated agriculture tend to be increasing, as farmers invest in irrigation equipment, primarily in order to reduce risk and increase yields of certain drought-prone crops.² We address the different roles of farmers and the public sector in adapting to these changes.

¹Toreti et al., 2009 and 2010; Beniston et al., 2003 and 2011; Beniston, 2003 and 2010; Lòpez-Moreno et al., 2011, The European Environment Agency, 2009

²Source: "The Environmental Impacts of Irrigation in the European Union" (2000).

In the following section of the paper (Section 2) we extend the basic dynamic optimization model by including heterogeneous water extraction costs. We show that a water storage problem may arise as a consequence of heterogeneity in access to the water stock and this may require government intervention. Section 3 presents an application to the Po river basin. Section 4 concludes.

2. THEORY: HETEROGENEOUS COSTS AND WATER ALLOCATION PROBLEMS

We present in this section a simple model showing that the lack of government intervention, along with heterogeneity in access to the water stock, causes externalities and reduce the agents' capability to use the water stock to smooth fluctuations in water supply.

The “common pool problem” refers to the idea that the efficient intertemporal allocation of resources requires that any decision on the current rate of use takes into account the entailments for future supply.³

Available water storage and flow are factors driving important water management decisions such as when to release water from reservoirs, or the rate of extraction of water from an aquifer at a given point in time (Kelso, 1961; Renshaw, 1963; Knapp and Olson, 1995). The distinction between flow and stock resources in the water sector and the importance of including stock values in determining optimal water allocation has long been recognized in the literature (Kelso, 1961; Renshaw, 1963; Noel et al., 1980; Knapp and Olson, 1995; Trenberth et al. 2000; Rubio and Casino, 2003).

Since the nineties, a stream of literature has given more importance to the study of risk externalities.⁴ This literature considers the *buffer value* of groundwater against uncertain surface water supply, modeling groundwater as insurance for stochastic fluctuations in surface water flows.⁵ Tsur (1990), Tsur and Graham-Tomasi (1991) and Masahiko and Tsur (2007) highlight the stabilization role of pumped groundwater when used in conjunction with surface water for irrigation, characterized by supply variability. In general, the capacity of groundwater projects should lead to an increase in the variability of the supply of surface water (Tsur, 1990). Furthermore, under high

³Neher (1990), p. 256.

⁴Provencher and Burt (1993) define risk externality as a type of common property externalities in groundwater. These arise because the income risk of all firms is affected by the total amount of groundwater stock available for pumping.

⁵Tsur, 1990; Tsur and Graham-Tomasi, 1991; Provencher and Burt, 1994; Knapp and Olson, 1995; Groom and Swanson, 2003; Masahiko and Tsur, 2007.

precipitation variability, the stabilization value of groundwater to wheat growers well exceeds the benefits associated with the increase water supply (Tsur, 1990). Knapp and Olson (1995) define aquifers as a natural inventory system for smoothing annual fluctuations in surface flows. Domestic, industrial and agricultural water demanders all place a higher value on reliable water supplies than on supplies with high risk of availability (Taylor and Young, 1995). Water supply unreliability comes from normal hydrological risks, reflecting the variance in precipitation and runoff.

We contribute to the literature on groundwater management, as it is usually assumed that agents exploit an aquifer characterized by a flat bottom, by pumping water perpendicularly from equal distances (i.e. pumping costs are homogeneous across agents).⁶ The key feature of this model is that each unit of groundwater can be pumped at the per unit m^3 extraction cost, z_i , which is *heterogeneous across agents*, as indicated by the subscript i .

We assume that farmers operates in a territory characterized by significant topographic heterogeneity. Therefore the differences in pumping costs across farmers depends on the geographical location of their farm along the watershed. That is, agents' location with respect to the aquifer indicates the relative accessibility to the water storage. Figure (1) illustrates graphically this situation, where the dashed line represents the water table.

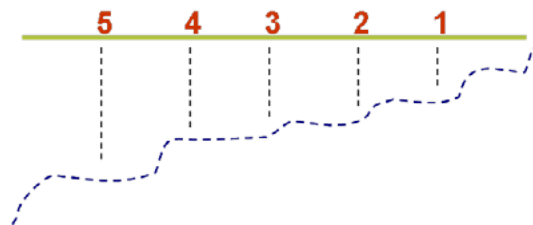


Figure 1: Heterogeneity in access to the aquifer.

The absence of a governance framework leads to a situation where each agent does not perceive any individual benefit from conservation today to permit lower extraction costs in the future. Each farmer determines the optimal groundwater extraction path q_{it}^* according to the following program:

$$\max_{q_{it}} R_i = \int_0^{\infty} \left[p * f(q_{it}) - z_i(x_t) * q_{it} \right] e^{-rt} dt \quad (1)$$

⁶See, for example, Provencher, 1993 and 1995; Provencher and Burt, 1994; Rubio and Casino, 2003.

Each individual is operating under given costs of resources (crop's price p , interest rate r) and the following stock constraint:

$$\frac{\partial x}{\partial t} = \dot{x} = G_t - Q_t \quad (2)$$

R_i is the present value of the resource to farmer i . The net benefit increases in water input, but at a decreasing rate: $R'(q) > 0$, $R''(q) < 0$.

$f(\cdot)$ is the crop yield response function to water input. Hence, $p^* f(q_{it})$ is the gross revenue of the agent i at time t . In order to focus on the externalities related to heterogeneity in access to the water stock, we assume that farmers rely only on the water pumped from the aquifer as input in the production function, which determines their income.

q_{it} is the groundwater converted into available water flow at time t by farmer i at a given per unit m^3 extraction cost, z . x_t is the basin-wide stock of groundwater available to the agents at time t . Each individual considers the resource stock exogenous with respect to its own actions. However, the stock at any point in time depends on the *collective* extraction (present and past). Water extraction costs are a function of the water stock available, i.e. $z_i(x_t)$. These cost functions are assumed continuous, concave and twice differentiable. Extraction costs are higher the lower is the water table i.e. $z'_i(x) < 0$. This is the so call *depth externality*.

Q_t is the total amount of water extracted from the aquifer at time t . We abandon the symmetry assumption that the optimal volume of water extracted at time t is the same for each farmer. This is due to the farmers' heterogeneous access to the water stock.

As a consequence, Q_t is defined as follows:

$$Q_t = \sum_{i=1}^N q_{it} \neq N * q_{it} \quad (3)$$

G_t is the *exogenous* recharge rate (megaliters per unit of time). The exogeneity assumption is accepted in the literature for the case of mountain watersheds, often characterized by the presence of underground water flows coming from distant regions and dependent on factors such as snowmelt rate or precipitations in the upper part of the watershed. The recharge rate of water is not biological thus it is modeled as if it is not at all stock dependent, as in Neher (1990). The water table falls

if $Q_t > G_t$, reducing x : $\dot{x} < 0$.

The Farmers' Program:

$$H^{pv} = \left[p * f(q_{it}) - z_i(x_t) * q_{it} \right] e^{-rt} dt + \phi_{it} \left[G_t - Q_t \right] \quad (4)$$

$$= \left\{ \left[p * f(q_{it}) - z_i(x_t) * q_{it} \right] dt + \lambda_{it} \left[G_t - Q_t \right] \right\} * e^{-rt} \quad (5)$$

$$= H^{cv} * e^{-rt} \quad (6)$$

H^{pv} is the hamiltonian present value, H^{cv} is the hamiltonian current value and $\lambda_{it} = \phi_{it} * e^{rt}$.

λ_i is the value of a unit of stock water invested in the aquifer from the perspective of farmer i . The value of a unit of stock of water invested in the aquifer, from the perspective of *all users*, is then given by:

$$\lambda = \sum_{i=1}^N \lambda_i \quad (7)$$

Proposition 1: if the state failure to govern and provide coordination among agents results in unrestricted access to the groundwater stock, each farmer perceives the *rental value* (λ_i) of leaving a unit of water in the aquifer as zero. This causes inefficient water pumping by each individual.

The optimal quantity of water extracted by each farmer at a given point in time is derived by solving the *first-order condition*:

$$\frac{\partial H^{cv}}{\partial q_{it}} = 0 \quad (8)$$

$$p * \frac{\partial f(q_{it})}{\partial q_{it}} - z_i(x_t) = \lambda_{it} \quad (9)$$

For each farmer, the optimal quantity of groundwater extracted at time t (q_{it}^*) is:

$$q_{it}^* = 0 \quad \text{if} \quad p < z_i(x_t) + \lambda_{it} \quad (10)$$

$$> 0 \quad \text{if} \quad p \geq z_i(x_t) + \lambda_{it} \quad (11)$$

With unrestricted access ($N \rightarrow \infty$) to the resource, there is no perceived value in not consuming immediately the water stock. Industry's profit goes to zero and $\lambda_i \rightarrow 0$. If many competitive users are granted unregulated, open access to the water stock resource, no actor will perceive the benefit from the stock's conservation. Each farmer will pump groundwater until the unit cost of extracting one unit (e.g. one m^3) of water from the ground is equal to the marginal revenue generated by that unit through the production function, that will equate the price of the produced crop.

We have shown the possible existence of *common pools* externalities, as per our *proposition 1*. The fact that each farmer perceives the rental value λ_i of leaving a unit of water in the aquifer as zero results in inefficient (too high) water pumping by each individual. Indeed, efficient water resources allocation is sometimes beyond the reach of the private sector if this is left unregulated. A Planning Authority may be able to play a constructive role by regulating the extraction efforts (Neher, 1990).

We have presented the basic concepts of the *common pool problem* in water resource. We now turn to the main contribution of this paper, showing that heterogeneity in access to the water resource may be a stronger reason for government intervention.

Proposition 2: Assume $z_1 < z_2 < z_3$, where $i=1, 2, 3$ indicates the geographical position of the agent with respect to the aquifer. Unmanaged pumping with heterogenous costs will cause an allocation to *early users* (those users that access the water stock at lower costs). With no coordination these users will deplete more water than other users. This causes the externalities discussed above plus *spatial externalities*. Given heterogeneous water extraction costs, there is an inefficient allocation of water to *early users*.

As discussed, with unrestricted access the value of a unit of stock of water invested in the aquifer from the perspective of each farmers goes to zero ($\lambda_i \rightarrow 0$). The solution for the optimal groundwater quantity extracted by each agent at time t is:

$$q_{it}^* = 0 \quad \text{if} \quad p < z_i(x_t) \tag{I2}$$

$$> 0 \quad \text{if} \quad p \geq z_i(x_t) \tag{I3}$$

$$q_{it}^* : p = z_i(x_t) \tag{I4}$$

Given the assumption on pumping costs stated in *Proposition 2* the above conditions for optimality imply: $q_{1t} > q_{2t} > q_{3t}$ where $i = 1, 2, 3$ indicate the geographical position of the agents along the watershed, with agent 1 being located in the most favorable position with respect to accessing the aquifer and agent 3 located in the most disadvantageous area (Figure 2).

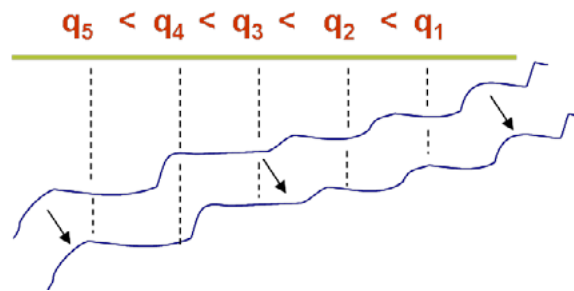


Figure 2: Heterogeneity in optimal quantity extracted from the aquifer.

Ceteris paribus some farmers will reach the maximum sustainable pumping cost earlier than others, due to heterogeneous groundwater extraction costs (Figure 3).

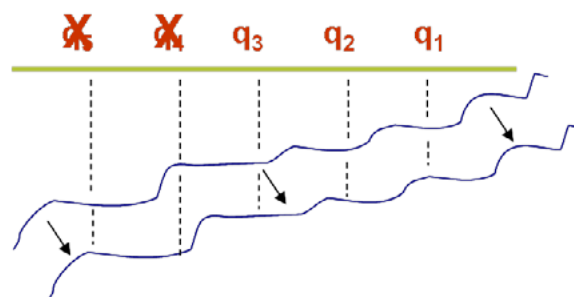


Figure 3: The effect of heterogeneous groundwater extraction costs and aquifer's depletion.

This scenario, characterized by heterogeneous water extraction costs works against the establishment of a cooperative environment in water extraction policies. Some farmers have stronger incentives to lobby for a collaborative scenario, for example based on water extraction permits distributed by a local authority. Another desirable solution for these actors is to centralize the water extraction and storage.

In some areas of the Po river basin, some farm ponds which existence is documented since the sixties, have recently felt into disuse due to the lowering of the water table, mainly because of a heavy water pumping for agricultural and industrial use.⁷ We describe in more details an application to the Po river basin in the next section.

⁷The Italian National Institute of Statistics (ISTAT). 2006. "Water Resources Assessment and Water Use in Agriculture".

3. AN APPLICATION TO THE PO VALLEY (ITALY)

3.1 Territorial Heterogeneity

The Po river basin is a mountain based watershed in the north of the Italian peninsula. This area is characterized by heterogeneous topographical features and intensive water use in agriculture. This basin has not traditionally faced hydrological constraints. However, recent drought periods, along with increasing pressure by growing population and economic activities, have highlighted the need for a better and more integrated water resources planning.

This is the longest river in Italy, with a total length of over 650 km (Figure 4). The whole watershed covers 74,000 km². About 35% of the Italian agricultural production comes from this area.

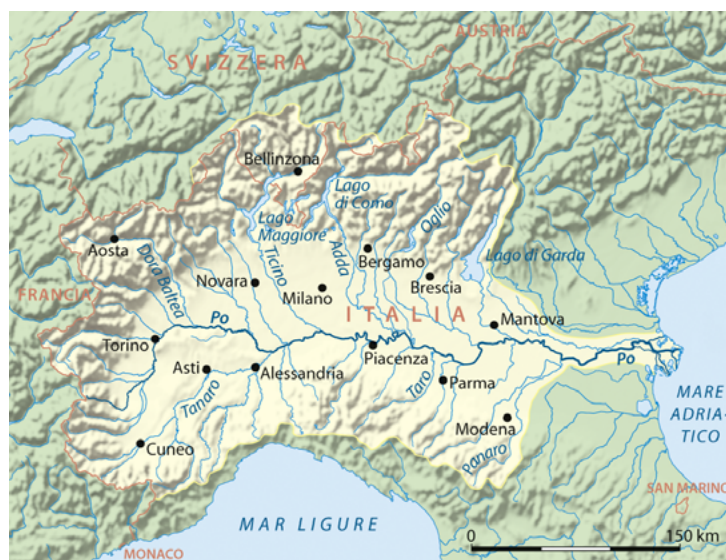


Figure 4: The Po River Basin.

Most of the Usable Agricultural Land (AUL) is concentrated in three regions: 37% in Lombardy, 31.5% in Piedmont and 30% in Emilia Romagna.⁸ Agriculture accounts for about 1.5% of the GDP produced.⁹ Figure (5) shows the topographic features of the land dedicated to agriculture in each region. Data at the provincial administrative level show a significant topographic heterogeneity within and between provinces.

The Po basin is also heterogeneous in terms of soil texture (e.g., sand and clay), which impacts crops' productivity and water infiltration rate. These considerations have direct implications for

⁸Po River Watershed Authority, 2006; Giupponi, 2000.

⁹Source: own calculations on data ISTAT, based on the 10-years average 2000 - 2010.

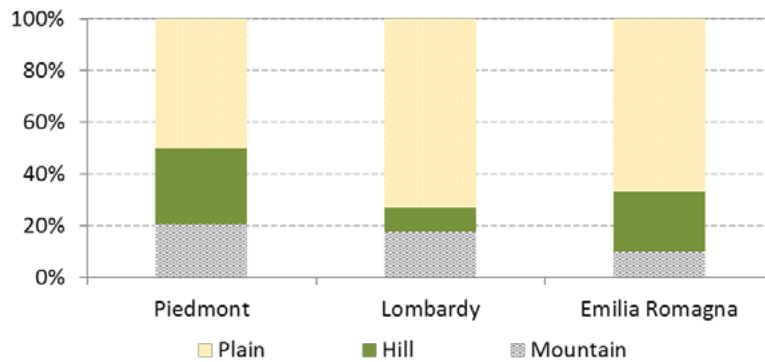


Figure 5: Topographic features of the usable agricultural land, by region. *Source: own elaboration on data ISTAT (Agricultural Census, 2010).*

accessibility to the water resource, crop selection, and irrigation methods adopted.

3.2 Climate Change in the Po Basin

Climate change has been observed to occur over the past four decades in the Po valley (Figure 6).¹⁰

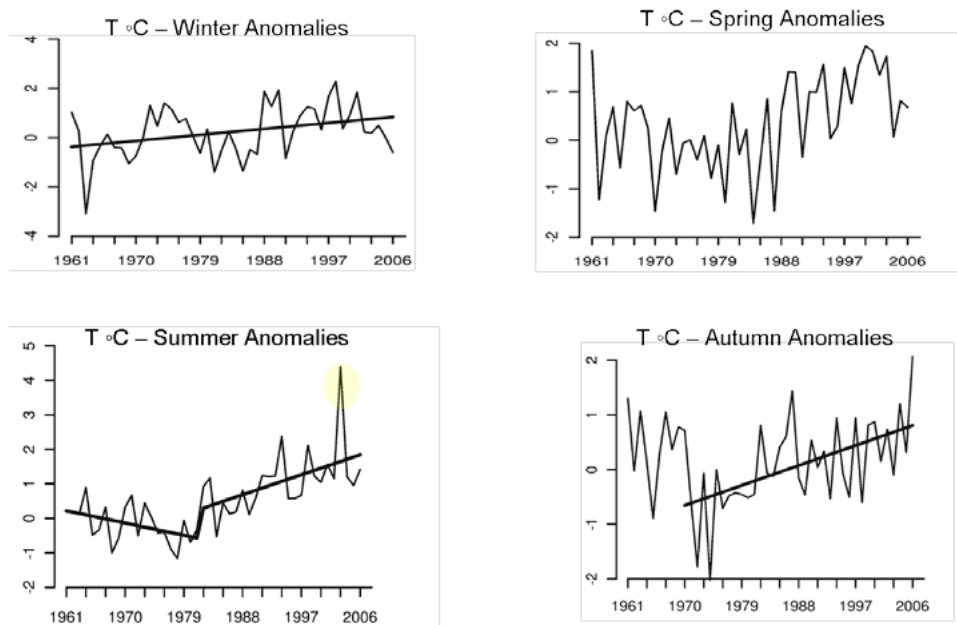


Figure 6: Seasonal temperature anomalies, North of Italy. *Source: Toreti et al. (2010).*

¹⁰Ciccarelli et al. (2008), Cacciamani et al. (2008) Toreti et al. (2010)

The literature analyzing precipitation trends has generated less straightforward results, leading to greater uncertainty regarding the impacts of climate-change on regional rainfall.

Climate change affects not only the mean values of climatic variables, but also their variability. Figure 7 shows the standard deviations during each twenty-year period between 1880 and 2010, for meteorological stations across the Po basin.¹¹ With the exception of the city of Reggio Emilia, we see a trend towards increasing variability in precipitation over time. This increased variability is something that is more difficult to “plan for” on the part of local farmers, and so implies a more important role for policy makers. In this scenario, groundwater plays an increasing stabilization role as a buffer against erratic precipitation patterns and increasing variability in surface water flows, despite the latter remain the main water source irrigation in the Po basin.

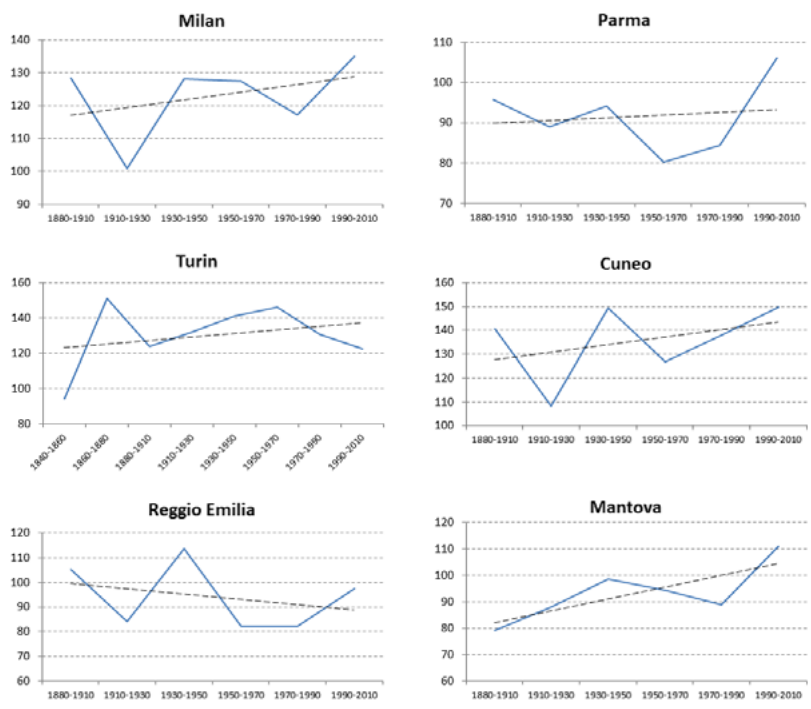


Figure 7: Standard deviation of precipitation and its long term trend. *Source: Own elaboration on data HISTALP and SCIA SINANET.*

The results discussed in this section suggest the need for deeper integration between different institutions involved at different levels in the management and use of water resources.

¹¹These data refer to specific meteorological stations. Missing data for most recent years, not included in the HISTALP dataset, have been integrated with the nearest meteorological station for which data are available on the SCIA SINANET website.

3.3 Climate Forecasting: Expected Impacts

Existing climate models confirm that the distribution of precipitation over the growing season, for a given location, is projected to vary substantially across the alpine region.¹² These models confirm positive trends in temperature and negative in precipitation, as shown in Figure 8.

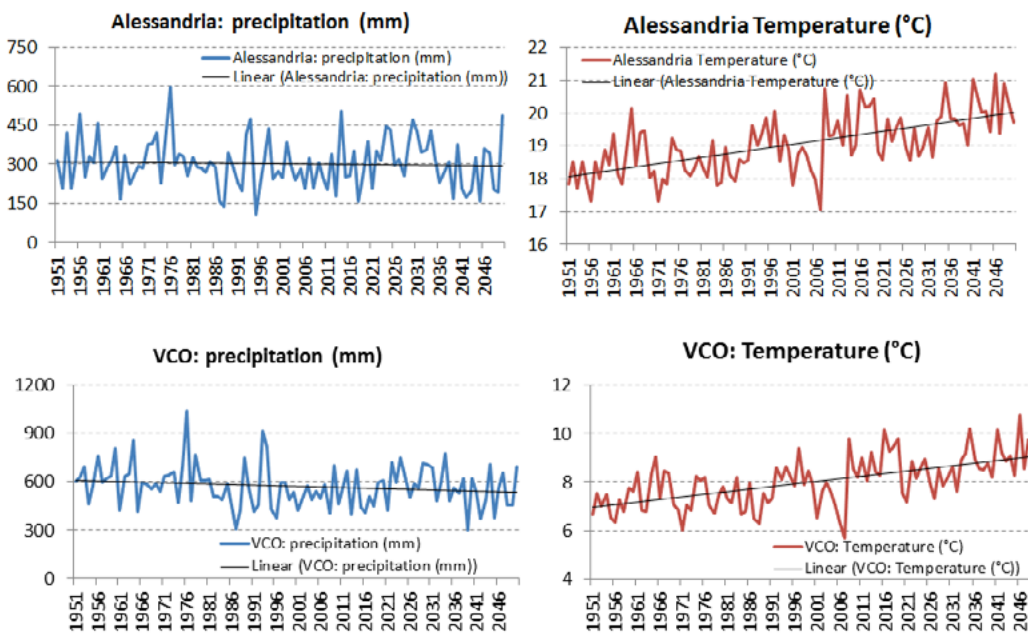


Figure 8: Climate simulations of precipitations and temperature during the growing season (1st March - 31st August) from 1951 to 2050. *Source: Own elaboration on RegCM3 Model data, averaged at provincial administrative level, provided by the Department of Civil and Environmental Engineering of the Milan Polytechnic.*

The graphs show the total precipitation and average temperature within the provincial administrative border of the north most and south-west most provinces in the Piedmont region (VCO and Alessandria, respectively), from 1951 to 2050.¹³ This scenario is characterized by higher variability of precipitation, a slightly decreasing precipitations trend, and clear evidence of warming. These forecasted impacts would be expected to place increasing pressure for adaptation on all economic activities within the Po basin.

¹²We refer, in particular, to climate models developed within the EU-funded project ACQWA. The numerical models analyzed include simulations of temperatures and precipitations from 1951 to 2050.

¹³Our conclusions are consistent for all provinces in Piedmont region.

Our short review of the scientific evidence indicates that the direct and indirect impacts of higher precipitation variability over the next fifty years are likely to increase costs of any poor water management, as groundwater can increasingly serve as a buffer against higher variability in surface water flows and erratic precipitations patterns. The complex topographical characteristics of the Po basin (and in general of a mountain based watershed) makes the effects of climate change across space and time even more uncertain.

The following section presents evidences on the impact of climate variability on agriculture. We will discuss how water management can be expected to aid in the adaptation to these changes (first at farmer level), and then to the nature of policy interventions that might be recommended to aid adaptation and to deal with residual effects.

3.4 Impacts on Agriculture

We assume farmers are interested in water management in aid of climate adaptation, because this is consistent with the pursuit of profit maximisation in agriculture (as well as with aversion to variability). Farmers' adaptation to expected climate change will often take the form of investment in assets to shift water temporally, using locally appropriate water storage techniques. For instance, farm ponds and artificial lakes can be used to smooth the volatility in rainfall. A study in the neighboring region of Tuscany demonstrates this strategy. The study shows that the number of farm ponds has increased 69% from 1980 to 2006 (from 1707 ponds to 2462). Overall the water stored at farm level increased from 40 to about 59 million m^3 (Orlandini et al. 2009).

Table 2 shows the results of a simple correlation analysis of the relationship between variability in temperature, precipitation (during the months March to August) and agricultural yields.¹⁴

All the statistically significant correlation coefficients are of negative sign, suggesting that relevant uncertainty remains, even after farmers invest in assets to deal with expected variability. The negative correlation between agricultural yields and observed anomalies may indicate that agricultural production has suffered when unanticipated climatic variability occurs.

¹⁴We combine data sets on crops production with monthly average temperature and precipitations. To determine climate anomalies we use the standard deviation for 28 provinces. We calculate this correlation for the 20-years period 1990-2010, considering the months March to August. Data sources: ISTAT, the Italian Environmental Agency, HISTALP and ILMETEO SRL.

Table 1: Correlation between crops yields and standard deviation of precipitation and temperature

Yields	precipitation anomalies	temperature anomalies
Maize	-0.161***	0.023
Barley	-0.280***	-0.147***
Soft Wheat	-0.425***	-0.1*
Sugarbeet	-0.206***	-0.199***
Soya	-0.226***	0.077

Table 2: Significance level of the correlation coefficients at: * 1%; ** 5%; * 10%.**

4. CONCLUSIONS AND POLICY IMPLICATIONS

The Po basin is characterized by high territorial heterogeneity and a complicated governance structure in the water management sector. Roles and responsibilities often overlap and are not clearly defined between different levels of governance and a multiplicity of institutional actors. Higher uncertainty in climate stresses the need for deeper integration between different institutions involved in the management and use of water resources. Due to the traditionally high availability of water resources, the coordination challenges of a topographically heterogeneous territory and the complex governance and institutional framework, rules regarding water access and abstraction have traditionally been weakly implemented.

As discussed in section 2, the existence of heterogeneous access to water resources is an obstacle to the implementation of collaborative water management solutions. The heterogeneity in access to water resources is one of the main causes of the existence of a high number of drainage and irrigation consortia, sometimes of very small dimensions.¹⁵ Efficient water management is particularly important in a scenario characterized by increasing variability in precipitations, as groundwater becomes an important *buffer* against uncertain surface water supply and increasingly erratic precipitation patterns. In this perspective, groundwater can be valued as an insurance for stochastic fluctuations in surface water flows. In line with the existing literature, we highlighted the stabilization role of groundwater when used in conjunction with surface water for irrigation, characterized

¹⁵Source: Po River Basin Authority.

by supply variability.

Despite these institutional problems, there are clear policy directions to consider for addressing the remaining variability. One approach would be to consider the integration of all water resources across the entire watershed (at a particular point in time) - this is the point of “water trading”. Another approach would be to try to smooth variability by means of integration of water across time - this is the point of “water storage”. Optimal policies should respond to both the existing institutional characteristics, as well as future climatic trends. These are characterized by higher variability of precipitation, a slightly decreasing or null precipitation trend, and clear evidences on warming trends. This has triggered a debate on the role of groundwater management policies and investment in water infrastructure in those areas that are rich in water resource but possibly (increasingly) exposed to surface water variability, related to climate change effects.

This paper provides a theoretical background to understand, in the context of increasing variability in climatic variables and of heterogeneous pumping costs, the role of risk, stock and depth externalities. We discussed why given the current climate scenarios, groundwater plays an increasing stabilization role against increasing variability in surface water flows, despite the latter remain the main water source irrigation in the Po basin. If policymakers do not consider the stabilization role of groundwater, but only the existence of stock and depth externalizes, this can result in underestimating the risks of poor water management policies, even in those agricultural regions, such as the Po basin, where variable surface water supplies are a primary source of irrigation water, while groundwater or other resources’ stock are used as a contingent source of water.

5. ACKNOWLEDGMENTS

Financial support by the EU project ACQWA (Framework Program 7 of the European Commission under Grant Nr.212250; www.acqwa.ch) is gratefully acknowledged. The usual disclaimer applies.

6. REFERENCES

Beniston, Martin, M. Stoffel, M. Hill, 2011. "Impacts of climatic change on water and natural hazards in the Alps: Can current water governance cope with future challenges? Examples from the European "ACQWA" project". *Environmental Science and Policy*. 14: 734-743.

Beniston, Martin., F. Keller, and S. Goyette. 2003. "Snow pack in the Swiss Alps under changing climatic conditions: an empirical approach for climate impacts studies". *Theoretical and Applied Climatology* 74 (1-2) (January 1): 19-31.

Beniston, Martin. 2003. "Climatic Change in Mountain Regions: a Review of Possible Impacts". *Climatic Change* 59: 5-31.

Beniston, Martin. 2010. "Impacts of climatic change on water and associated economic activities in the Swiss Alps". *Journal of Hydrology* 412-413 (January): 291-296.

Cacciamani, Carlo, S. Tibaldi, and S. Pecora. 2008. "Quanto il clima pesa sul bacino del Po?". *Rivista ARPA* 3 (May-June): 12-13.

Ciccarelli, Nadia, J. von Hardenberg, A. Provenzale, C. Ronchi, A. Vargiu, R. Pelosini. 2008. "Climate variability in north-western Italy during the second half of the 20th century." *Global and Planetary Change* 63: 185-195.

Commission of the European Communities. 2009. 147 WHITE PAPER. "Adapting to climate change: Towards a European framework for action". COM/2009/0147 Brussels, 1.4.2009.

COPA, COGECA. 2009. "Water and Agriculture Under Climate Change". Info Sheet EN(09)5660.

Deschênes, Olivier and M. Greenstone. 2007. "The Economic Impacts of Climate Change: Evidence from Agricultural Profits and Random Fluctuations in Weather". *American Economic Review* 97, 1: 354-385.

Directive 2000/60/EC of the European Parliament and of the Council of 23 October 2000 establishing a framework for Community action in the field of water policy (European Water Framework Directive - WFD).

EEA - European Environment Agency. 2009. "Regional Climate Change and Adaptation. The Alps Facing the Challenge of Changing Water Resources". EEA Report 8/2009. 143 pp.

Giupponi, Carlo. 2000. "The Environmental Impact of Maize Cultivation in the European Union: Practical Options for the Improvement of the Environmental Impact: Italian Case Study". The European Commission DG XI. D.1. 46 pp.

Gleick, Peter H., G. Wolff, E. L. Chalecki, R. Reyes. 2002. "The new economy of water: the risks and benefits of globalization and privatization of fresh water". Pacific Institute for Studies in Development, Environment, and Security.

Groom, Ben and Tim Swanson, 2003. "Missing Markets and Redundant Reservoirs" *Environmental and Resource Economics*, European Association of Environmental and Resource Economists, 26 (1): 125-144.

INEA (The Italian National Institute of Agricultural Economics). 2011. "Atlante Nazionale dell'irrigazione". Edited by Raffaella Zucaro.

ISTAT (The Italian National Institute of Statistics). 2006. "Water resources assessment and water use in agriculture" [M. Cammarrota, G. Bellini, A. Femia, I. Pierantoni, S. Tersigni]. Essays n. 18 - 2006. Italian National Institute of Statistics (Istat).

Kelso, Maurice M. 1961. "The Stock Resource Value of Water". *Journal of Farm Economics* 43 (5): 1112-1129.

Knapp, Keith and Lars Olson. 1995. "The economics of conjunctive groundwater management with stochastic surface supplies". *Journal of Environmental Economics and Management* 28: 340-356.

Koundoury, Phoebe. 2004. "Current issues in the economics of groundwater resource management". *Journal of Economic Surveys*. 18 (5): 703-740.

López-Moreno, J.I., Vicente-Serrano S.M., Mórán-Tejeda E., Lorenzo J., Kenawy, A. and Beniston, M. 2011. "NAO Effects on Combined Temperature Precipitation Winter Modes in the Mediterranean Mountains: Observed Relationships and Projections for the 21st Century". *Global and Planetary Change*, 77: 62-76.

Masahiko, Gemma and Tsur, Y. 2007. "The Stabilization value of Groundwater and Conjunctive Water Management under Uncertainty". *Review of Agricultural Economics*. 29 (3): 540-548.

Neher, Philip A. 1990. "Natural Resource Economics: Conservation and Exploitation". Cambridge University Press. 360 pp.

Noel, Jay E., B. Delworth Gardner, and C. V. Moore. 1980. "Optimal Regional Conjunctive Water Management". *American Journal of Agricultural Economics* 62 (3): 489-498.

Orlandini, Simone, Natali, F. and Dalla Marta, A. 2009. "Water Use In Italian Agriculture: Analysis of Rainfall Patters, Irrigation Systems and Water Storage Capacity of Farm Ponds". *Rivista Italiana di Agrometeorologia*, vol. anno 14(3): 55-59.

Po River Watershed Authority. 2006. "Caratteristiche del bacino del fiume Po e primo esame dell' impatto ambientale delle attività umane sulle risorse idriche". www.adbpo.it

Provencher, Bill and Oscar Burt. 1993. "The Externalities Associated with the Common Property Exploitation of Groundwater". *Journal of Environmental Economics and Management*. 24 (2): 139-158.

Provencher, Bill. 1993. "A Private Property Rights Regime to Replenish a Groundwater Aquifer". *Land Economics* 69 (4): 325-340.

Provencher, Bill, and Oscar Burt. 1994. "A Private Property Rights Regime for the Commons: The Case for Groundwater". *American Journal of Agricultural Economics* 76 (4): 875-888

Provencher, Bill. 1995. "Issues in the conjunctive use of surface water and groundwater". *The Handbook of Environmental Economics*, D. Bromley, Editor, Blackwell, Oxford: 503-528.

Renshaw, Edward F. 1963. "The Management of Ground Water Reservoirs". *Journal of Farm Economics* 45 (2): 285-295.

Rubio, Santiago and B. Casino. 2003. "Strategic Behaviour and Efficiency in the Common Property Extraction of Groundwater". *Environmental and Resource Economics*. 26 (1): 73-87.

Strzepek, Kenneth, McCluskey, A. Boehlert, B., Jacobsen, M., and Fant IV, C. 2011. "Climate Variability and Change: A Basin Scale Indicator Approach to Understanding the Risk to Water Resources Development and Management". The World Bank. Washington, DC. September 2011. 139 pp.

Taylor, R. G. and Young, R. A. 1995. "Rural-to-urban water transfers: measuring direct foregone benefits of irrigation water under uncertain water supplies". *Journal of Agricultural and Resource Economics* 20: 247-262.

Trenberth, Kevin E., Miller Kathleen, Mearns, Linda and Rhodes, Steven. 2000. "Effects of Changing Climate on Weather and Human Activities". *Understanding Global Change: Earth Science and Human Impacts Series, Global Change Instruction Program, UCAR*. University Science Books Publisher: Sausalito, CA. University Science Books. 46 pp.

Toreti, Andrea, G. Fioravanti, W. Perconti and F. Desiato. 2009. "Annual and Seasonal Precipitation Over Italy from 1961 to 2006". *International Journal of Climatology*. 29: 1976-1987.

Toreti, Andrea, F. Desiato, G. Fioravanti and W. Perconti. 2010. "Seasonal Temperatures Over Italy and Their Relationship with Low-Frequency Atmospheric Circulation Patterns". *Climatic Change*. 99 (1-2): 211-227.

Tsur, Y. 1990. "Stabilization role of groundwater when surface water supplies are uncertain: the implications for groundwater development". *Water Resource Research* 26, 811-818.

Tsur, Y. and Graham-Tomasi, T. 1991. "The buffer value of groundwater with stochastic surface water supplies". *Journal of Environmental Economics and Management* 21, 201-224.

The economics of tropical cyclones under climate change: incorporating the impact of global hurricane characteristics and level of development

Bakkensen L.

Centro Euro-Mediterraneo sui Cambiamenti Climatici, Venice, Italy

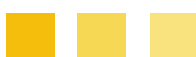
Yale University, New Haven, U.S.A.

**Corresponding author: laura.bakkensen@yale.edu*

Abstract

Building on the analysis of Mendelsohn, Emanuel, Chonabayashi, and Bakkensen (2012), the present study advances the understanding of the impact of climate change on tropical cyclones by refining the global tropical cyclone damages function. It differentiates marginal impacts on developed and developing countries and estimates, for the first time, the marginal impact of global tropical cyclone characteristics on damages. With this refined understanding of damages, the estimated relationships are applied to calculate expected damages of simulated hurricane tracks in the years 2008 and 2100 under four different climate scenarios. Finally, the impact of climate change on aggregate damages, as well as the global distribution of damages, is calculated. The results show that, while tropical cyclones currently cause approximately \$25 billion per year in real damages, socioeconomic change will add approximately \$112 billion in real damages to the global total. Climate change will result in additional damages of \$110 billion. Future damages will be heterogeneous across the globe, with the United States and small island nations being harmed disproportionately more than other regions.

Keywords: *Natural Disasters, Economics, Climate Change, Integrated Assessment Modeling*



1. INTRODUCTION

Tropical cyclones currently cause approximately \$26 billion of damages per year globally (Mendelsohn, Emanuel, Chonabayashi, and Bakkensen, 2012) with approximately \$9 billion per year of damages in the United States (Nordhaus, 2010). Global damages are expected to double over the next hundred years due to socioeconomic change and double again due to climate change (Mendelsohn et al., 2012). Further study of damages is fundamental to understanding how to properly reduce coastal and inland vulnerability to future hurricane damages through appropriate public policy, insurance, education, and adaptation efforts.

The current research effort builds on the 2011 analysis of Mendelsohn, Emanuel, and Chonabayashi and the 2012 analysis of Mendelsohn, Emanuel, Chonabayashi, and Bakkensen. In their initial work, Mendelsohn et al. (2011) used the Hurricane Integrated Assessment Model (HIAM) to link climate conditions with hurricane damages in order to predict both the distribution and magnitude of hurricane damages in the United States by 2100, under four climate scenarios. As part of the model, 5,000 simulated hurricane tracks were generated for present and future climate in the year 2100 using four climate models. Then, a historical damage function was estimated by regressing local socioeconomic and hurricane characteristics on aggregate hurricane damage data. The resulting estimated relationship was used to calculate the aggregate damages for each of the four climate models in the year 2100. It was also found that the minimum barometric pressure of a hurricane is a better predictor of resulting damages than maximum sustained wind speed, which had been used in previous literature.

The results showed that at the present time, the United States has an annual expected hurricane damage of \$9 billion per year. In the year 2100, due only to population and economic growth, the U.S. is expected to incur \$27 to \$55 billion per year in real damages, with an additional \$25 billion per year of predicted damages due to climate change. Although these are expected values, predicting damages in a single year remains elusive, and the distribution of damages is such that the largest storms produce a very large percentage of expected damages.

In addition to the U.S. analysis, Mendelsohn et al. (2012) conducted a parallel analysis using the Tropical Cyclone Integrated Assessment Model of the impact of climate change on tropical cyclone (including tropical cyclone, typhoon, and hurricane) damages around the globe. They estimate current global tropical cyclone damages to be \$26 billion per year. They predict that in 2100, without climate change, tropical cyclones will cause an estimated \$56 billion in real damages per year, with climate

change adding an additional \$53 billion per year in expected damages. The distribution of damages is likely to change, with North America facing \$26 billion in damages per year and \$15 billion per year in East Asia. Caribbean islands will likely face the highest damages as a percentage of their total gross domestic product.

Both of these studies laid a solid theoretical and analytical foundation for many directions of future research. The current study adds to the research by differentiating marginal impacts on damages for developed and developing countries. New variables of global historical tropical cyclone characteristics were added to the model. This additional data allows calculation of the estimated parameters for global tropical cyclone characteristics, while past literature applied U.S. coefficients to the global analysis. These results were used to predict the impact of climate change on aggregated global tropical cyclone damages under four climate scenarios in the year 2000 and 2100.

1.1 Review of the Relevant Literature

Modeling tropical cyclones, tropical cyclone damages, and the impacts of climate change have received complementary effort from both the natural and social sciences. Both areas have made advancements but much debate and future work remains, especially with regard to the social science side, as it necessarily follows new developments in the understanding of cyclones by the natural sciences.

Several points of academic debate in the natural sciences center on the relationship between hurricanes and climate change. While there is convincing evidence that rising sea surface temperature will increase the potential intensity and maximum wind speed of hurricanes, especially the most powerful hurricanes, it is still unclear by how much these factors will rise over time due to climate change (Emanuel, 2005; Montaigne 2010). With regard to the impact of climate change on hurricane frequency, some see evidence that climate change will increase hurricane frequency, while others contend that it is still too early to tell (Hallegate, 2007). Lastly, debate remains surrounding the evidence in the historical hurricane data, as some calculate climate impacts already on hurricane activity, while others claim the observed hurricane characteristics over past years to be within the range of historical trends and see no clear impact of climate change on hurricanes in recent decades (Pielke, 2005).

Among social scientists, various modeling efforts have been conducted to understand the relationship between hurricanes, hurricane damages, and climate change. In addition to the results by Mendelsohn,

Emanuel, and Chonabayashi (2011) and Mendelsohn, Emanuel, Chonabayashi, and Bakkensen (2012), the following results are noteworthy. Nordhaus (2009) estimated that climate change will result in \$10 billion per year in additional hurricane damages to the United States, but notes this could be an underestimate, given current hurricane models. Further, warming temperatures will increase vulnerability of many coastal communities in the U.S., especially high valued areas near the Gulf of Mexico and in Florida. Narita et al. (2009) find that, by the year 2100, climate change will result in an expected \$19 billion in additional damages per year globally, with the U.S. and China bearing the largest absolute damages and, similar to Mendelsohn et al. (2010), small island nations will suffer the largest percentage damages compared with their gross domestic product. Pielke (2007) observes that future hurricane damages will increase not only because of climate change, but also because additional population and assets will be located in the hurricane path, given population growth and economic development. Thus, he finds that increasing human adaptation to climate change will have a much greater impact than climate mitigation in reducing future damages. Pielke contends that human adaptation will lead to a reduction in vulnerability not only from the impacts of climate change, but it will also better protect expanding population and capital in harm's way. All papers call for more research, especially with regard to decreasing vulnerability and increasing adaptation efforts, as well as gathering greater detail in hurricane, geographic, and socioeconomic data.

2. THEORETICAL FOUNDATION

The theoretical foundation of this analysis is based on the previous work of Mendelsohn et al. (2011). They note that the economic damage from tropical cyclone (D) is equal to the total of all destruction caused by the tropical cyclone. In their analysis, damages were limited to losses of buildings and infrastructure. The expected value of damages from tropical cyclones can be calculated by:

$$E[D] = \sum_j \sum_i \pi(X_{ij}, C) D(X_{ij}, Z_j)$$

where $\pi(X_{ij}, C)$ is the probability that tropical cyclone i will make landfall at location j , given tropical cyclone characteristics X and climate conditions C . $D(X_{ij}, Z_j)$ represents the damages from tropical cyclone i at location j , given characteristics X of tropical cyclone i at location j and local socioeconomic conditions Z at location j . Expected damages equal the probability of a landfall at a given location

multiplied by the damage from the tropical cyclone, summed across all locations and tropical cyclones. Atmospheric experts are key to estimating the probability function, while economists specialize in the damages portion (Mendelsohn et al., 2011).

The impact W of climate change, or a change in atmospheric conditions from current climate $C0$ to a new climate $C1$, on tropical cyclone damages can be calculated by:

$$W = E[D(C1)] - E[D(C0)]$$

which is the difference between the expected damages of each climate, holding all other factors constant. The frequency distribution of damages, or the probability of a range of damage magnitudes given a storm, can be calculated by:

$$Prob(D) = f(D(X))$$

which describes the hurricane risk distribution of a certain location. Finally, the return rate for storm damage (RR) can be found by:

$$RR = \frac{1}{Prob(D)} = \frac{1}{f(D(X))}$$

which is the expected length of time between events of a certain damage level (Mendelsohn, et al., 2011).

3. METHODOLOGY AND DATA

The current project answers the following questions: (1) what are the marginal effects of development on tropical cyclone damages across the globe; (2) what are the marginal impacts of tropical cyclone storm characteristics, such as minimum sea level barometric pressure and maximum wind speed, in global damages from tropical cyclones; (3) given the results from (1) and (2), what are the estimated damages per country from tropical cyclones in 2100 using four climate change models; and (4) what is the distribution of damages across the globe and which countries are most vulnerable to tropical cyclone impacts?

3.1 Methodology

Following the methodology of Mendelsohn et al. (2012), the analysis takes place in three steps. First, a damage function is estimated using an ordinary least squares estimator on historical hurricane and socioeconomic data. Second, the estimated damage function is used to calculate the damages from tropical cyclone tracks simulated both for the current climate and for climate in the year 2100 using four climate models. Lastly, the impacts of climate and socioeconomic change on tropical cyclone damages are computed.

To estimate the historical tropical cyclone damages function, the regression equation is structured in the following form:

$$D_{ij} = \beta_0 MSLP_{ij} * NonOECD_j + \beta_1 MSLP_{ij} * OECD_j + \beta_2 NonOECD_j + \beta_3 OECD_j + \beta_4 P_j * NonOECD_j + \beta_5 P_j * OECD_j + \beta_6 Y_j * NonOECD_j + \beta_7 Y_j * OECD_j + \varepsilon_{ij}$$

where D_{ij} is a record of tropical cyclone damages from storm i in country j and $MSLP_{ij}$ is the minimum sea level barometric pressure at landfall¹ for tropical cyclone i in country j . P_j and Y_j are average country-level population density and per capita income terms, respectively. $OECD_j$ is an indicator variable for countries that are members of the Organization for Economic Cooperation and Development, a proxy for development. $NonOECD_j$ represent countries not in OECD and is an indicator variable equal to $(1-OECD)$. Lastly, the NonOECD and OECD variables are interacted with the hurricane characteristic and socioeconomic variables to discover any variation in the impacts of these explanatory variables over levels of development. Note that, since OECD and NonOECD would together be perfectly collinear with a constant term, no constant is included in the regression. Goodness of fit statistics, such as the F and R^2 statistics, are adjusted accordingly. With this, the first stage of the analysis is complete.

For the second stage, the estimated damage function was used to approximate the damages from the simulated tropical cyclone data. First, damages from tropical cyclones simulated under current climate conditions by four climate models are calculated, using current socioeconomic condition in the year 2008. These same current climate tropical cyclone damages are then re-calculated with socioeconomic projections for the year 2100. The difference between the future damages and present damages, given

¹ If a tropical cyclone does not make landfall in a country and damages were observed in the historical evidence, characteristics were used from the storm when it was at its closest point to the given country.

current climate, show the increase in damages from tropical cyclones due only to changes in population and economic growth. To calculate the impact of climate change on tropical cyclone damages, another set of tropical cyclones was simulated under year 2100 climate conditions based on the projections of the same four climate models. Damages were calculated using future climate and future socioeconomic projections. The impact of climate change is the difference between the expected damages from the future climate, future socioeconomic damages and the current climate, future socioeconomic damage projections.

3.2 Data

The analysis utilizes data from multiple sources. The first part of the analysis relies on country-level historical tropical cyclone damages data, as well as affiliated historical country population and income data. Data on tropical cyclone damages are obtained from EM-DAT, the International Disaster Database managed by the Center for Research on the Epidemiology of Disasters. The EM-DAT database includes information on more than 17,000 natural and technological disasters and is sponsored in part by the United Nations and United States Agency for International Development. Data on historical country population and income data are gathered from the U.S. Department of Agriculture's Economic Research Service International Macroeconomic Data Sets. The historical data includes various country-level macroeconomic variables including real gross domestic product and population from 1969 to 2010.

Historical tropical cyclone data are collected from several sources including the U.S. National Oceanic and Atmospheric Administration's International Best Track Archive for Climate Stewardship (IBTrACS) and the U.S. Navy's Joint Typhoon Warning Center's Tropical Cyclone Reports. These sources include variables such as location, wind speed, and minimum barometric pressure at 6-hour intervals for each hurricane since the mid-1800s (NOAA, 2010). Affiliated tropical cyclone characteristics from these sources were matched by hand with the country level damages data to complete the historical data set. Currently, 611 hurricane characteristics at landfall have been matched with economic damages data. The dataset includes tropical cyclones from the Atlantic, Eastern, Central, and Western Pacific, and Indian Oceans, as well as the Southern Hemisphere. The second half of the study utilizes simulation data for the years 1980-2000 and 2080-2100. Tropical cyclone tracks and characteristics are simulated by Professor Kerry Emanuel of the Massachusetts Institute of Technology.

These data include 5,000 simulated hurricane tracks for the Atlantic basin and 3,000 simulated tropical cyclone tracks for each of the Western and Eastern Pacific, Indian Ocean, and Southern Hemisphere basins, for each of four climate models and for both current and future climate, resulting in a total of 136,000 storms. Each track contains tropical cyclone location and characteristics at six-hour intervals for the life of the storm. The climate models are: CNRM (Gueremy et al. 2005), ECHAM (Cubasch et al 1997), GFDL (Manabe et al. 1991), and MIROC (Hasumi and Emori 2004). The models are based on an A1B SRES climate scenario which assumes carbon dioxide concentrations stabilize at 720 ppm (IPCC, 2000). See Mendelsohn et al. (2011) for a more detailed description. Future economic data by country are projected by the World Bank and projections of population are compiled by the United Nations.

4. RESULTS

4.1 Historical Global Damages Function

Table 1 below contains the results from the estimation of the historical tropical cyclone damages function. Socioeconomic variables (P, population density; and Y, per capita income) and tropical cyclone intensity (MSLP, minimum barometric sea level pressure) are included. Level of development is interacted with each variable.

	NonOECD	OECD	P*	P*	Y*	Y*	MSLP*	MSLP*
			NonOECD	OECD	NonOECD	OECD	NonOECD	OECD
Estimated								
Coefficient	210.30	339.83	-0.29	-0.23	0.24	1.09	-28.16	-48.07
(Standard	(45.08)	(81.91)	(0.18)	(0.22)	(0.15)	(0.40)	(6.53)	(11.85)
Error)								

Table 1: Estimated Coefficients of the Historical Tropical Cyclone Damages Function

The estimated coefficients for variables in the historical global tropical cyclone damage function are shown in the table above. Standard errors are in the parentheses. The F statistic is 14.91 and the adjusted R^2 value is 0.23 with 355 observations. The F and R^2 statistics were adjusted for the fact that no constant was included in the regression (see a full explanation in Section 3.1 *Methodology*).

Recall from Section 3.1 (Methodology) that D_{ij} is a record of tropical cyclone damages from storm i in country j . P_j and Y_j are average country-level population density and per capita income terms, respectively. $OECD_j$ is an indicator variable for countries that are members of the Organization for Economic Cooperation and Development, a proxy for development. $NonOECD$ represent countries not in the OECD and is an indicator variable equal to $(1-OECD)$.

The above regression was estimated using Ordinary Least Squares with logged variables. Thus, the resulting estimated coefficients are interpreted as elasticities. The results shed new light on the structure of tropical cyclone damages, as well as the distribution of vulnerability. The estimated coefficient of 339.83 for OECD countries versus 210.30 for non-OECD countries implies that, holding everything else constant, developed countries are more vulnerable to damages from tropical cyclones than developing countries, although the difference is not statistically significant.

Turning to the interaction coefficients, a one percent increase in population density will decrease damages slightly by 0.29 percent for NonOECD countries and 0.23 percent for OECD countries. This elasticity implies that as countries transitioning from more rural to more urban living will have a modest reduction in vulnerability from tropical cyclone damages. Although both estimated coefficients are similar in magnitude and not statistically different than an estimated zero, it is also important to note that these results show evidence that there is not a strong positive relationship between population density and tropical cyclone damages. This is an important distinction because it is often assumed in the literature that increasing population density will lead to increased damages from tropical cyclones with an elasticity of one (Nordhaus, 2010; Pielke et al, 2008).

Turning to income, a one percent increase in income in a non-OECD country will increase damages by an estimated 0.24 percent. This implies developing countries, although still vulnerable to damages, are taking steps to protect their assets through growth. More analysis should be directed into this area to find out what strategies are undertaken by these countries to reduce vulnerability. However, one should not assume that development will necessarily result in low damages in non-OECD countries, because

OECD countries have a strikingly different result. The estimated interaction coefficient for income and OECD country status robustly implies that a one percent increase in income in a developed country will increase damages by 1.09 percent. Three theories could be at play, and further investigation is needed to determine what hypothesis is supported empirically. First, there could be limits on available strategies to reduce vulnerability from tropical cyclone damages. Low hanging fruits, based on inexpensive technological and structural protection, could be implemented during earlier stages of development at relatively low cost. But once a country reaches a certain level of development, these methods may no longer be sufficient. Second, it is possible that developed countries may have maladaptive policies in place. For example, government policies and insurance contracts could be encouraging development of expensive assets situated in harm's way. Careful study is needed to determine precisely what is the causal factor and what measures can be taken to decrease vulnerability of developed countries and ensure that developing countries can continue to reap the benefits of reduced vulnerability through development. Third, work by Bakkensen (2013) points to the United States as an outlier with high income elasticity of damages compared with other OECD countries. Thus, further work is needed to see the extent to which the United States drives the OECD results.

Turning lastly to the hurricane intensity coefficient, we find damages are highly and significantly influenced by hurricane intensity. Note that minimum sea level barometric pressure is inversely related to maximum wind speed and also damages. A lower pressure is indicative of a more powerful storm. Thus, a one percent decrease in minimum sea level barometric pressure will increase damages by 28.16 percent in non-OECD countries and 48.07 percent in OECD countries. Although these are lower numbers than that of Mendelsohn et al. (2011) who estimated the minimum sea level barometric pressure elasticity of damages to be 86 for the United States, the results reinforce the importance of storm intensity in damages. Also, they show that OECD countries are more vulnerable to damages than are non-OECD countries, although the difference is not statistically significant. Further work is needed to explain the underlying relationship between hurricane pressure and damages, and their interaction with level of development. Heterogeneity in the potential range of adaptation strategies to reduce vulnerability may occur. It may be easier to more fully protect against damages from lower category storms yet difficult, based on available technology and cost constraints, to protect against damages from very intense (low minimum pressure) and low probability storms.

4.2 Socioeconomic Change Impact on Tropical Cyclone Damages

The second part of the analysis calculates the impact of socioeconomic change on tropical cyclone damages, from the present global levels of development to the world in 2100, holding climate constant. Currently, average annual global tropical cyclone damages are approximately \$26 billion per year and socioeconomic change is expected to increase this number by about \$112 billion by the year 2100. In Table 2 and Figure 1 below, regional total expected damages are compared, given current and future socioeconomic conditions, holding climate conditions constant at the present day.

Region	Current Economy Damages (\$ millions)	Future Economy Damages (\$ millions)
Oceania	255	998
East Asia	6,343	44,591
South Asia	814	1,303
North Africa & Middle East	174	176
Sub-Sahara Africa	94	115
Western Europe	32	383
North America	16,103	87,072
Central America & Caribbean	1,918	3,117
South America	1	2
World	25,734	137,757

Table 2: Annual Expected Regional Damages for Current and Future Socioeconomic Conditions, Given Current Climate Conditions

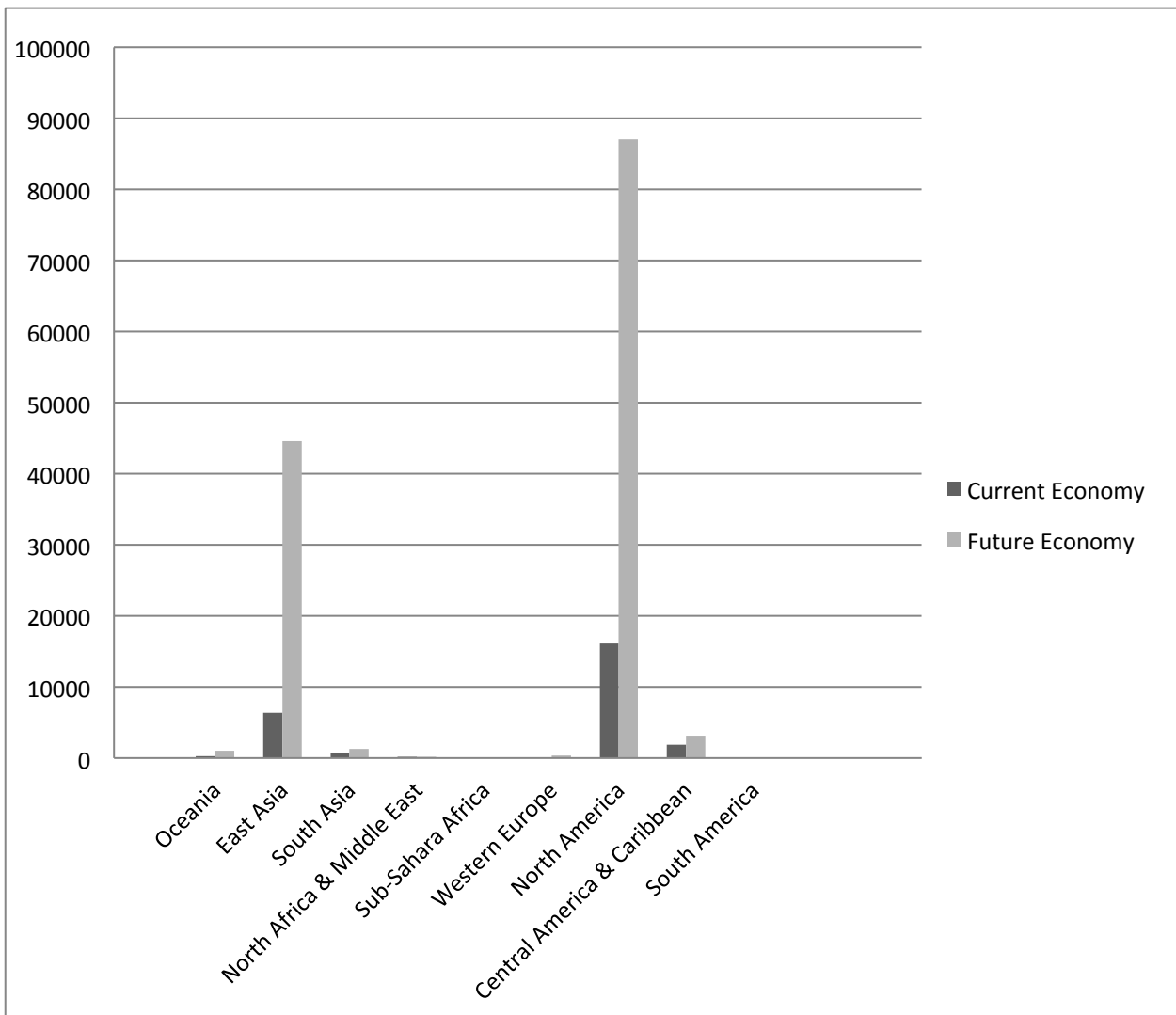


Figure 1: Annual Expected Regional Damages for Current and Future Socioeconomic Conditions, Given Current Climate Conditions, in millions of U.S. dollars

As seen in the results, damages and vulnerability due to tropical cyclones are regional in nature. East Asia and North America bear the vast majority of global damages, both currently and in the future. Of the approximately \$112 billion expected increase in tropical cyclone damages due to socioeconomic change, North America will bear about 63 percent of the increase, followed by East Asia sustaining approximately 34 percent of the damages. Although continued development will no doubt put more infrastructure and assets in harm's way, these results should not be interpreted as an argument against future development. Rather they serve as a reminder that smart strategies in adaptation and

development are essential in order to reduce or mitigate future tropical cyclone damages and vulnerability.

Recall from Section 4.1 that the estimated population density coefficients for OECD and non-OECD countries are of similar magnitude, so changes in population density from present to future socioeconomic conditions will impact countries similarly. Growth in per capita income, however, was found to increase damages more quickly in OECD countries than in non-OECD countries. This greatly impacts expected damages due to socioeconomic change, as OECD country damages are predicted to increase sharply over the next century due to development alone. Caution should be exercised with these numbers, as the analysis assumes no countries will change OECD status over the next one hundred years, an unlikely outcome. It is possible that, with continued development, income elasticities for developing countries may increase, leading to greater damages than predicted above. It is also possible that the United States is driving the OECD results, and therefore results may not be representative. Further research is needed to understand and better model the transition in damage elasticity across levels of development.

4.3 Climate Change Impact on Global Tropical Cyclone Damages

The results from the impact of climate change on tropical cyclone damages are presented below. Holding future socioeconomic conditions fixed, climate change is expected to increase tropical cyclone damages by approximately \$110 billion per year. Impacts will be highly regionalized, as North America will be hit hardest by climate change impacts, followed by the Caribbean region and Central America. Results below are summarized on a regional basis. Below in Table 3 are annual expected regional damages associated with climate change.

Region	Current Climate, Future Economy Baseline	CNRM Climate Change Impact	ECHAM Climate Change Impact	GFDL Climate Change Impact	MIROC Climate Change Impact	Average Climate Change Impact
Central America & Caribbean	3,117	643	-337	3,855	744	1,226
East Asia	44,591	1,316	-11,821	-17,551	21,501	-1,639
North Africa & Middle East	176	105	63	55	43	67
North America	87,072	78,119	26,492	329,264	5,824	109,925
Oceania	998	736	484	-781	-74	91
South America	2	1	0	-1	0	0
South Asia	1,303	-33	-7	-782	317	-126
Sub-Saharan Africa	115	-13	168	124	103	96
Western Europe	383	-100	377	-54	165	97
World	137,757	80,773	15,420	314,130	28,623	109,736

Table 3: Annual Expected Regional Damages for Climate Change, Given Future Socioeconomic Conditions, in millions of U.S. dollars

As seen above, climate change impacts on tropical cyclone damages are highly regional in nature. On average, damages in North America are expected to double and are predicted to rise in all four climate models. Damages from the Caribbean region and Central America will increase, on average, by almost fifty percent. It is important to note the large variability in climate model predictions within regions. For Central America and the Caribbean region, all models except for the ECHAM model predict increases from the future baseline. East Asia, another region facing large increases in expected future damages due to socioeconomic change, has higher variability in expected future climate damages, with MIROC predicting an approximately 50 percent increase in damages due to the changed climate, while ECHAM and GFDL predict decreased damages by 25 to 40 percent. Somewhat masked by the average value over the four climate models, Oceania also shows high variability in the estimated climate change impacts. ECHAM and CNRM predict an average increase in future baseline damages of approximately 48 to 74 percent, respectively. Sub-Saharan Africa shows more consistency, as three of the four models predict at least an approximately 90 percent increase in damages.

Although future tropical cyclone damages from socioeconomic and climate changes seem large compared with current damages, the future global economy will also be much larger in the year 2100. Thus, contextualizing damages as a percentage of future Gross Domestic Product (GDP) is vital for balanced analysis. In Figure 2 below, regional annual damages from climate change are given as a percentage of total regional Gross Domestic Product². Table 4 below shows the top ten countries expected to lose the greatest amount of their annual gross domestic product due to total expected tropical cyclone damages, given future socioeconomic and climate conditions.

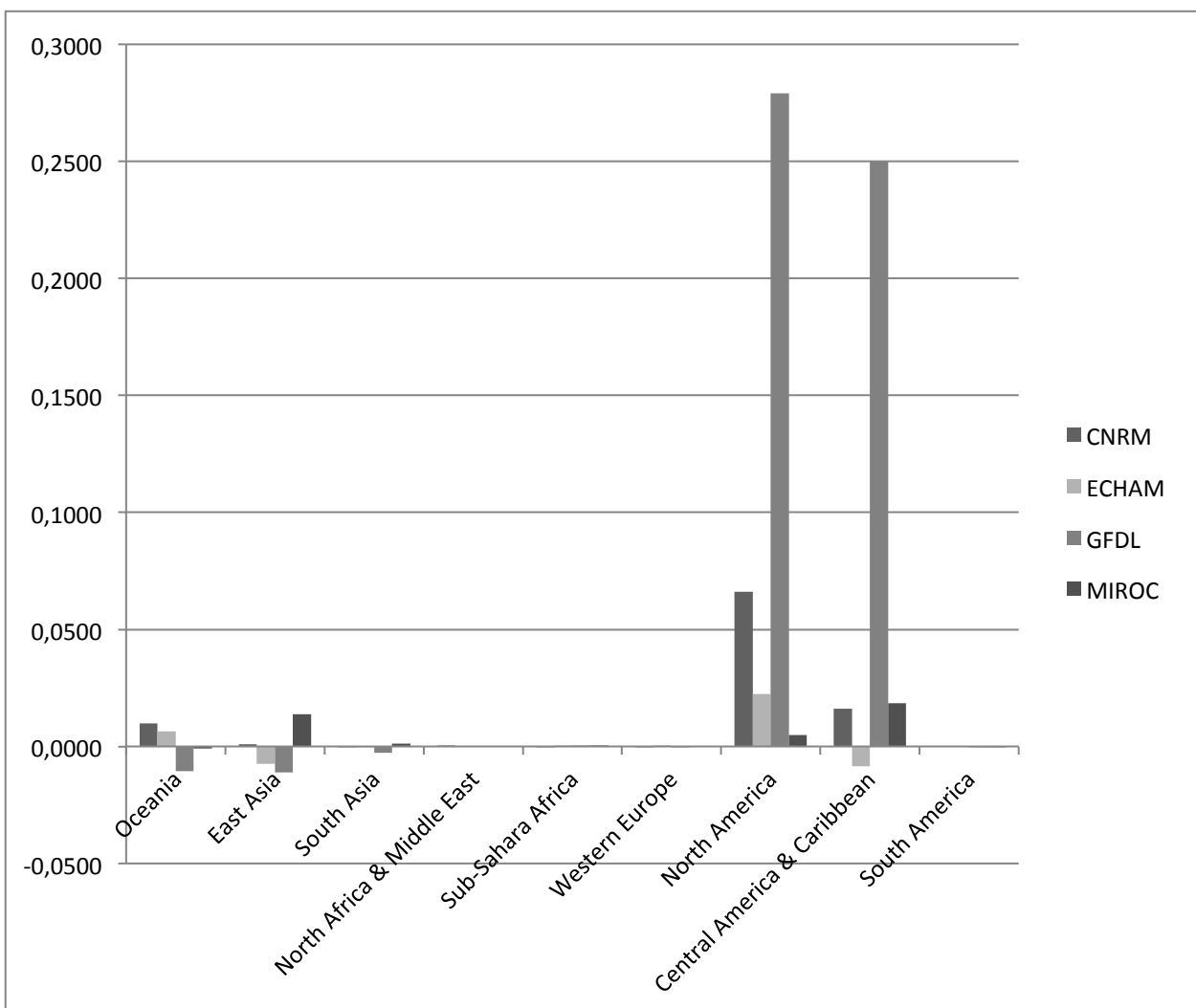


Figure 2: Expected Regional Annual Damages from Climate Change, as a percentage of Regional Gross Domestic Product

² Regional gross domestic product is defined in this paper as the sum gross domestic product across all countries in the region, regardless if the country is at risk for tropical cyclones or not.

Rescaling damages by projections for the future economy, Atlantic basin storms will lead to the largest percentage of loss in regional Gross Domestic Product, with North America, the Caribbean region, and Central America losing up to approximately 0.25 percent of their GDP per year due to climate change. Note that the above graph only represents the impact of climate change and not total expected tropical cyclone damages in the year 2100. Also note that regional GDP was calculated by including the GDP of all countries within the region, regardless of whether they are at risk for tropical cyclones.

Cayman Is.	1.93
British Virgin Is.	1.47
St. Kitts & Nevis	1.47
Virgin Is.	1.20
Turks & Caicos Is.	1.18
Samoa	0.75
Grenada	0.68
Antigua & Barbuda	0.64
The Bahamas	0.61
Dominica	0.50

Table 4: Annual Expected Damages, as a percent of Country GDP

Table 4 above shows the ten countries with greatest annual expected losses, as a percentage of future GDP, due to tropical cyclone damages in the year 2100. Small island nations are at greatest risk, including islands in the Caribbean region, as well as some in Oceania and Sub-Saharan Africa around Madagascar. Small island nations are at particular risk, not only due to the large expected damages as a percentage of their GDP, but also because they may have more limited adaptive ability compared with larger countries, given smaller land area for evacuation and development retreat for coastal communities.

5. CONCLUSION

The current project answers the following questions: (1) what are the marginal and interaction effects of development on tropical cyclone damages across the globe; (2) what are the marginal impacts of tropical cyclone storm characteristics, such as minimum sea level barometric pressure, in global damages from tropical cyclones; (3) given the results from (1) and (2), what are the estimated damages per country from tropical cyclones in 2100 using four general circulation models; and (4) what is the distribution of damages across the globe and which countries are most vulnerable to tropical cyclone impacts? The study analyzes these questions through estimation of a refined global damages function and then applies the estimated relationships to simulation data of hurricane tracks in the years 2000 and 2100 under four different climate models. The results show that, from a base of approximately \$25 billion per year in damages from tropical cyclones, socioeconomic change will increase the global total by approximately \$112 billion, and climate change will result in additional losses of \$110 billion. Damages will be heterogeneous across the globe, with the United States and small island nations being hit disproportionately more. Although tropical cyclone damages will never be entirely eliminated, further research efforts in this area including efficient adaptation, insurance, and public policy choices can help to reduce vulnerability and hopefully decrease future damages and deaths from tropical cyclones.

6. ACKNOWLEDGMENTS

The author would like to thank Robert Mendelsohn, Kerry Emanuel, Kenneth Gillingham, Alexey Fedorov, William Nordhaus, Gokay Saher, Shun Chonabayashi, and the participants of the Yale Environmental Economics Seminar and the 2011 Belpasso International Summer School for their helpful suggestions. The author also acknowledges the Yale Institute for Biospheric Studies, the Centro Euro-Mediterraneo sui Cambiamenti Climatici, the Italian Ministry of Education, University and Research, and the Italian Ministry of Environment, Land and Sea under the GEMINA project for funding. All errors are attributed to the author.

7. REFERENCES

- Bakkensen, Laura A. 2013. *Adaptation and Natural Disasters: Evidence from Global Tropical Cyclone Damages and Fatalities*. Working paper.
- Cubasch U, Voss R., Hegerl G., Waskiewicz J., and Crowley T. 1997. *Simulation of the Influence of Solar Radiation Variations on the Global Climate with an Ocean-Atmosphere General Circulation Model* *Climate Dynamics* **13**: 757-767.
- Emanuel K. 2005. *Divine Wind*. New York: Oxford University Press.
- Gueremy J.F., Deque M., Braun A., Evre J.P.. 2005. *Actual and potential skill of seasonal predictions using the CNRM contribution to DEMETER: coupled versus uncoupled model*, *Tellus* 57: 308–319.
- Hallegate S. 2007, *The use of synthetic hurricane tracks in risk analysis and climate change damage assessment*, *Journal of Applied Meteorology and Climatology* 46: 1956–1966.
- Hasumi H. and Emori S. 2004. *K-1 Coupled GCM (MIROC) Description*, Center for Climate System Research, University of Tokyo, Tokyo.
- Holland G.J. 1993. *Global Guide to Tropical Cyclone Forecasting*, WMO/TC-No. 560, Report No. TCP-31. Geneva, Switzerland: World Meteorological Organization.
- IPCC (Intergovernmental Panel on Climate Change). 2000. *Special Report on Emissions Scenarios*, Cambridge University Press, Cambridge, UK.
- Manabe S., Stouffer J., Spelman M.J., and Bryan K.. 1991. *Transient Responses of a Coupled Ocean-Atmosphere Model to Gradual changes of Atmospheric CO₂. Part I: mean annual response*, *Journal of Climate* **4**: 785-818.
- Mendelsohn R., Emanuel K., and Chonabayashi S. 2011. *The Impact of Climate Change on Hurricane Damages in the United States*. *World Bank working paper*.
- Mendelsohn, R., Emanuel, K., Chonabayashi, S., & Bakkensen, L. 2012. *The impact of climate change on global tropical cyclone damage*. *Nature Climate Change*, 2(3), 205-209.
- Montaigne F. 2010. *Exploring the Links Between Hurricanes and Ocean Warming*. *Yale Environment* 360. Retrieved December 2010 from:
http://e360.yale.edu/feature/exploring_the_links_between_hurricanes_and_ocean_warming/2318/.

- Narita D., Tol R.S.J., and Anthoff D. 2009. *Damage costs of climate change through intensification of tropical cyclone activities: An application of FUND*, ESRI Working Paper 259.
- National Hurricane Center (NHC). 2010. *Hurricane Research Division: Frequently Asked Questions*. Retrieved December 2010 from: <http://www.aoml.noaa.gov/hrd/tcfaq/A1.html>.
- National Oceanic and Atmospheric Administration (NOAA). 2010. *Hurricane Research Division: Re-analysis project*. Retrieved December 2010 from: <http://www.aoml.noaa.gov/hrd/hurdat/>.
- Nordhaus W. 2010. *The Economics of Hurricanes and Implications of Climate Change*. Climate Change Economics (forthcoming).
- Pielke R. A. Jr. 2005. *Are There Trends in Hurricane Destruction?* Nature 438: E11
- Pielke R. A. Jr., Gratz J., Landsea C. W., Collins D., Saunders M. A. and Musulin R.. 2008. *Normalized Tropical cyclone Damage in the United States: 1900–2005*. Natural Hazards Review, 9: 1-29.

CLIMATE POLICY AND ECONOMIC ASSESSMENT

Poster Session

The Cost of Climate Change Inaction in the EU. A CGE Approach

Pierfederici R.^{1*}, Bosello F.² and Eboli F.³

¹Fondazione Eni Enrico Mattei and Euro-Mediterranean Center on Climate Change

²Fondazione Eni Enrico Mattei, University of Milan and Euro-Mediterranean Center on Climate Change

³Fondazione Eni Enrico Mattei and Euro-Mediterranean Center on Climate Change

*Corresponding author: roberta.pierfederici@feem.it

Abstract

The present research describes a climate change integrated impact assessment exercise, whose economic evaluation is based on a CGE approach and modeling effort. Impacts are economically assessed for a 2 °C and 4 °C warming scenarios with respect to pre-industrial temperature, as a range of climate responses driven by economic growth up to 2050. Impact types considered are those originated by: ecosystem losses, sea-level rise, changes of energy demand, of crops productivity, of fish stock productivity, of tourism flows, flooding and health.

Estimates indicate that a temperature increase of 2°C in 2050 could lead to global GDP losses of about 0.7% compared to a hypothetical scenario where no climate change is assumed to occur. Doubling the temperature increase world losses are -1.8% of GDP.

The EU 27 as a whole experiences a GDP loss of 0.16% and 0.74% in the 2°C and 4°C cases respectively. The southern EU region is more severely hit with Greece top-loser (-1.76% and -6.24% of GDP in 2050 in the 2°C and 4°C temperature increase scenarios respectively), the Northern one gaining or remaining basically unaffected. Regarding the impacts type, the two major drivers of climate change impacts are agriculture and tourism, followed by the impacts related to ecosystem losses.

The analysis also reveals a redistribution of the labour force due to climate change, leading to labour demand contractions in different sectors. In 2050, when the temperature increases 2°C, higher labour demand contractions are concentrated in the agricultural sector especially in Greece (-5.7%), Spain (-5.9%) and Portugal (-2.7%); in the fishing sector in Italy (-7.9%) and Spain (-4.5%); in the service sector in Hungary (-1.3%), Italy (-0.7%) and Portugal (-0.5%). Industrial labour demand declines particularly in Finland (-4%), Sweden (-1.6%) and Hungary (-1.4%); energy sectors tend also to expel labour force.

Keywords: Computable General Equilibrium Modeling, Impact Assessment, Climate Change, Ecosystems



1. INTRODUCTION

In recent years a number of studies have investigated the economic cost of climate change in Europe. Nevertheless, most of these studies have either adopted a sectoral focus assessing the cost for a particular sector (ClimWatAdapt Project¹, SESAME Project²), or have assessed the cost in a specific EU country or region (CIRCE Project³). In order to close these gaps we have applied a CGE model to assess the economic consequences of climate change in a wider set of climate change impacts, including even those sectors in which only very limited information is available, such as ecosystems and fishery sectors. Furthermore we used a more detailed regional coverage, focusing on EU-27 at a country level.

Computable General Equilibrium (CGE) models are increasingly used to assess costs and benefits associated with climate change impacts (for a partial list, see e.g. Deke *et al.* [17]; Darwin and Tol [15]; Bosello *et al.* [4] on sea-level rise; Bosello *et al.* [5] on health; Darwin [15]; Ronneberger *et al.* [24] on agriculture; Berritella *et al.* [2]; Calzadilla *et al.* [7] on water scarcity; Aaheim and Wey [1] on sea-level rise, agriculture, health, energy demand, tourism, forestry, fisheries, extreme events, energy supply; Ciscar [11] on sea-level rise, agriculture, tourism, river floods).

The appeal of such tools is the explicit modelling of market interactions between sectors and regions (inter industry and international trade flows are accounted for by databases relying upon input output Social Accounting Matrices). This allows tracing adjustment mechanisms in the whole economic system triggered by a “shock” concerning initially just one part of it (region or sector). Putting it differently, not only direct costs, but higher-order effects as well can be determined.

Following this approach, the Intertemporal Computable Equilibrium System (ICES) CGE model (Eboli *et al.* [18]), is hereby used as a unifying platform to assess the economic consequences of a wide set of climate change impacts, assessed for a 2 °C and 4 °C

warming scenarios, both assumed to occur in 2050 and representing two extreme potential climate outcomes connected to a specific economic scenario.

¹ <http://climwatadapt.eu/>

² http://www.clamer.eu/index.php?option=com_clamerprojects&ProjectId=73

³ <http://www.circeproject.eu/>

In what follows, section 2 briefly introduces the model used and the baseline scenario, section 3 describes the impacts assessed, section 4 focuses on the implementation of climate change impacts into the ICES model, section 5 presents simulation results and section 6 concludes.

2. THE ICES MODEL AND THE BASELINE SCENARIO

ICES is a recursive-dynamic CGE model improving upon the static structure of the GTAP-E model (Burniaux and Troung [6]). The calibration year is 2004, data collecting input-output data for the world economy come from the GTAP7 database (Narayanan and Walmsley [22]) and the simulation time is 2004-2050.

Tab. 1 reports region and sector aggregations for this study. Regions have been chosen in order to detail as much as possible the EU countries, whereas industries' detail is the closest possible to the sectoral impacts estimated by source studies.

Countries/Regions	Sectors
Austria	
Belgium	
Czech Republic	Agriculture
Denmark	Timber
Finland	Fishing
France	Coal
Germany	Oil
Greece	Gas
Hungary	Oil Products
Ireland	Electricity
Italy	Other Industry
Netherlands	Transportation
Poland	Residential
Portugal	Market Services
Spain	Public Services
Sweden	
UK	
Rest of EU	

Tab. 1: Regional and sectoral coverage of the ICES model (this study)

EU GDP national and regional growth rates reported in figure 1 derive from the 2012 Ageing Report issued by EU Commission⁴

Population trends also replicate the 2012 Ageing Report for EU27. For non-EU27 regions, population evolves according to United Nations [25].

⁴ <http://ec.europa.eu/social/main.jsp?langId=en&catId=89&newsId=1326&furtherNews=yes>

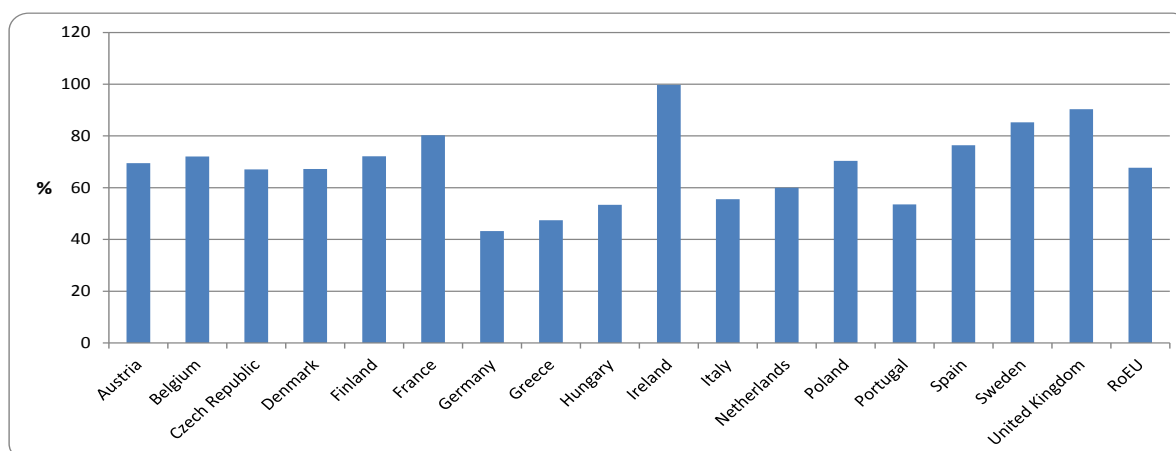


Fig. 1: Baseline GDP growth rates by country (% change 2004-2050)

3. ASSESSING CLIMATE CHANGE IMPACTS BY CATEGORY

The inputs to the CGE exercise derive from the results of a set of bottom-up partial-equilibrium exercises performed within different EU FP projects and other research initiatives referenced in Tab. 2.

Climate Change Impact	Source Model	Reference Project	Reference Publication
Ecosystem	Na	Na	Manne et al. [21]; Warren [26]
Tourism Flows	HTM	ClimateCost ⁵	Bigano et al. [3]
Crops' Productivity	ClimateCrop	ClimateCost	Iglesias et al. [20]
Residential Energy Demand	POLES	ClimateCost	Criqui [13]; Criqui et al. [14]
River Floods	LISFLOOD	ClimateCost	Feyen [19]
Health	Na	PESETA ⁶	Ciscar et al. [11]
Fishery		SESAME ⁷	Cheung et al. [9]
Sea-Level Rise	DIVA	ClimateCost	Vafeidis et al. [27]

Tab. 2: Impact types and source studies for the ICES CGE modelling exercise

⁵ <http://www.climatecost.cc/>

⁶ <http://peseta.jrc.ec.europa.eu/>

⁷ <http://www.sesame-ip.eu/>

These allow physically quantifying climate change consequences on ecosystem, energy demand, agricultural productivity, tourism flows, river floods, health, fishery and sea-level rise. All the studies, except those on floods and health, have a global coverage. The majority of them is based on a geographic information system. When this is the case, results have been aggregated to match the geographical resolution of the CGE exercise. An important novelty of this work is the estimate of climate change impacts on ecosystems.

4. ICES: MODELING AND ESTIMATION OF IMPACTS

To determine with a CGE model the economic consequences of the different impacts assessed, these need to be firstly translated into changes in economic variables existing in the model.

Two broad categories of impacts can be distinguished in this analysis. The first relates to the supply-side of the economic system, affects exogenous variables in the model - stock or productivity of primary factors - and thus can be easily accommodated. Impacts on ecosystems, sea-level rise, agriculture, floods, fishery and human health belong to this category. They do not require any substantial change in the basic structure of the model to be implemented. Within this group, impacts ecosystems are modeled as a loss in the physical capital stock. The assumption made thus is that ecosystems offer a set of support services to the production activity which are all embedded in capital services. When ecosystem deteriorates, its production support services deteriorates and thus (through deterioration of the capital stock) capital services.

The second affects changes in the demand side. Impacts on tourism and on energy consumption are of this kind. This implies to intervene on variables which are endogenous to (i.e. output of) the model through shifting factors in demand functions.

Tables 3a to 4c summarize the results of all this procedure presenting the computed inputs for the ICES CGE model necessary to run the climate-change simulations.

	Demand-side Impacts				
	Energy			Tourism	
	Gas	Oil Products	Electricity	Mserv Demand	Expenditure*
Austria	-0.13	0.58	-0.12	1.61	1.29
Belgium	-0.16	0.46	0.15	-0.17	-0.40
Czech Republic	0.16	1.47	-2.62	0.47	0.09
Denmark	-0.48	0.07	2.95	1.12	0.75
Finland	-1.32	-0.17	-0.44	5.15	2.61
France	0.34	1.12	0.14	-0.43	-6.75
Germany	-0.69	-0.07	-0.25	1.26	9.90
Greece	3.48	-0.14	11.42	-2.13	-2.26
Hungary	2.50	3.83	6.92	-0.43	-0.41
Ireland	-0.88	-0.02	1.17	-0.12	-0.08
Italy	-0.19	0.70	15.22	-0.96	-17.05
Netherlands	-0.47	0.36	2.20	0.28	0.41
Poland	-0.30	0.60	-1.67	0.71	0.53
Portugal	-0.17	0.31	10.91	-2.72	-2.63
Spain	-0.40	0.31	17.52	-2.26	-17.61
Sweden	-1.42	-0.27	0.59	4.00	4.39
United Kingdom	-0.49	0.42	0.44	1.28	12.67
RoEU	0.28	1.27	2.17	0.28	0.26
RoOECD	0.88	1.60	6.94	3.04	297.28
CHIND	2.24	2.83	6.52	-2.81	-102.28
TE	0.17	2.18	-2.94	4.66	31.90
RoW	-0.36	0.89	9.32	-2.40	-212.60

Table 3a. Demand-side impacts: 2° C temperature increase, ref. year 2050

Note: *US\$ billion

	Supply-side Impacts (1)				
	SLR	Fishery	Agriculture	Ecosystems	Health
	Land and K Stock	Fish Stock	Land productivity	K Stock	L Productivity
Austria	0	<i>n.a. -> 0</i>	7.63	-0.13	0.0024
Belgium	-0.00390	0.21	-3.79	-0.12	0.0016
Czech Republic	0	<i>n.a. -> 0</i>	-3.95	-0.10	0.0024
Denmark	-0.00369	7.87	20.35	-0.15	0
Finland	-0.00008	14.86	31.33	-0.11	0
France	-0.01929	0.27	-5.36	-0.11	0.0024
Germany	-0.01706	<i>n.a. -> 0</i>	-0.77	-0.12	0.0016
Greece	-0.00145	0.14	-20.88	-0.13	0.0136
Hungary	0	<i>n.a. -> 0</i>	3.33	-0.13	0.0024
Ireland	-0.00540	-1.43	-2.11	-0.22	0.0184
Italy	-0.00552	-12.37	-9.27	-0.19	0.0136
Netherlands	-0.13763	7.79	0.08	-0.29	0.0016
Poland	-0.00040	7.65	-1.76	-0.07	0.0016
Portugal	-0.01128	3.80	-15.70	-0.11	0.0136
Spain	-0.00147	-6.49	-17.71	-0.06	0.0136
Sweden	-0.00007	10.96	28.59	-0.08	0
United Kingdom	-0.00344	1.84	5.12	-0.12	0.0184
RoEU	-0.00515	2.28	-0.90	-0.04	0.0072
RoOECD	-0.15174	6.34	-2.87	-0.08	<i>n.a. -> 0</i>
CHIND	-0.13254	-2.02	0.30	-0.02	<i>n.a. -> 0</i>
TE	-0.09475	2.95	-4.14	-0.07	<i>n.a. -> 0</i>
RoW	-0.11420	-4.21	-7.30	0.00	<i>n.a. -> 0</i>

Table 3b. Supply-side impacts (1): 2° C temperature increase, *ref. year 2050*

	Supply-side Impacts (2)					
	Floodings					
	Agriculture (land stock)	Residential (K prod.)	Transport (K prod.)	Commerce (K prod.)	Industry (K prod.)	Population (L prod.)
Austria	-0.009131	-0.635930	-0.005735	-0.000753	-0.002799	0.001251
Belgium	-0.015736	-0.048307	-0.003496	-0.005481	-0.019250	0.001245
Czech Republic	-0.000834	-0.112179	-0.002207	-0.003253	-0.009282	0.000482
Denmark	-0.000044	0.000435	0.000018	0.000015	0.000132	0.000000
Finland	-0.009900	-0.212826	-0.007250	-0.004996	-0.007816	0.001105
France	-0.001524	0.018805	0.000825	0.000173	0.000944	0.000452
Germany	0.001652	0.004830	0.000533	0.000093	0.000691	0.000167
Greece	-0.002600	-0.030850	-0.000498	-0.000283	-0.002170	0.000305
Hungary	-0.008180	-0.297233	-0.007311	-0.001823	-0.005408	0.000319
Ireland	-0.011957	-0.205516	-0.006128	-0.000513	-0.000307	0.000227
Italy	-0.014730	-1.340414	-0.003075	-0.000960	-0.004711	0.000839
Netherlands	-0.008952	-0.021213	-0.000869	-0.000062	-0.000342	0.001168
Poland	0.005314	0.032759	0.000609	-0.000186	-0.000677	-0.000008
Portugal	-0.011786	-0.010840	-0.001154	-0.000127	-0.000446	0.000082
Spain	-0.014978	-0.105708	-0.001926	-0.001412	-0.004107	0.000424
Sweden	-0.001952	-0.063190	-0.001366	-0.000526	-0.001764	0.000081
United Kingdom	-0.037875	-0.377944	-0.011255	-0.003419	-0.024845	0.000918
RoEU	-0.006674	-0.352415	-0.005959	-0.003333	-0.008521	0.000968
RoOECD	n.a. -> 0	n.a. -> 0	n.a. -> 0	n.a. -> 0	n.a. -> 0	n.a. -> 0
CHIND	n.a. -> 0	n.a. -> 0	n.a. -> 0	n.a. -> 0	n.a. -> 0	n.a. -> 0
TE	n.a. -> 0	n.a. -> 0	n.a. -> 0	n.a. -> 0	n.a. -> 0	n.a. -> 0
RoW	n.a. -> 0	n.a. -> 0	n.a. -> 0	n.a. -> 0	n.a. -> 0	n.a. -> 0

Table 3c. Supply-side impacts (2): 2° C temperature increase, ref. year 2050

	Demand-side Impacts				
	Energy			Tourism	
	Gas	Oil Products	Electricity	Mserv Demand	Expenditure*
Austria	-0.27	1.21	-0.26	4.24	4.90
Belgium	-0.34	0.95	0.31	0.37	0.59
Czech Republic	0.33	3.07	-5.48	2.06	0.55
Denmark	-0.99	0.15	6.17	2.87	2.77
Finland	-2.76	-0.36	-0.91	12.74	9.33
France	0.71	2.34	0.29	-0.01	-0.30
Germany	-1.45	-0.14	-0.52	3.30	37.33
Greece	7.26	-0.29	23.83	-3.39	-8.16
Hungary	5.21	7.99	14.44	-0.30	-0.66
Ireland	-1.84	-0.04	2.44	0.27	0.11
Italy	-0.39	1.46	31.76	-1.30	-52.11
Netherlands	-0.98	0.76	4.60	1.17	2.46
Poland	-0.63	1.25	-3.49	1.49	1.60
Portugal	-0.35	0.65	22.78	-3.98	-8.70
Spain	-0.84	0.65	36.57	-3.08	-54.21
Sweden	-2.96	-0.57	1.23	9.65	15.28
United Kingdom	-1.01	0.87	0.93	2.65	37.69
RoEU	0.58	2.66	4.53	1.82	2.46
RoOECD	1.83	3.34	14.49	7.22	1018.28
CHIND	4.68	5.91	13.61	-4.37	-358.91
TE	0.35	4.55	-6.13	14.61	144.42
RoW	-0.75	1.87	19.45	-3.98	-794.71

Table 4a. Demand-side impacts: 4° C temperature increase, ref. year 2050

Note: * US\$ billion

	Supply-side Impacts (1)				
	SLR	Fishery	Agriculture	Ecosystems	Health
	Land and K Stock	Fish Stock	Land productivity	K Stock	L Productivity
Austria	0	<i>n.a. -> 0</i>	6.51	-0.52	0.0070
Belgium	-0.01351	0.44	-9.29	-0.47	0.0040
Czech Republic	0	<i>n.a. -> 0</i>	-9.70	-0.38	0.0070
Denmark	-0.01164	16.42	17.35	-0.59	0
Finland	-0.00026	31.01	26.72	-0.44	0
France	-0.09245	0.57	-13.14	-0.46	0.0070
Germany	-0.05916	<i>n.a. -> 0</i>	-1.89	-0.49	0.0040
Greece	-0.14124	0.29	-51.19	-0.52	0.0325
Hungary	0	<i>n.a. -> 0</i>	2.84	-0.54	0.0070
Ireland	-0.45826	-2.99	-5.18	-0.90	0.0450
Italy	-0.02250	-25.81	-22.72	-0.75	0.0325
Netherlands	-0.50368	16.26	0.07	-1.17	0.0040
Poland	-0.06546	15.96	-4.33	-0.26	0.0040
Portugal	-0.06294	7.93	-38.49	-0.44	0.0325
Spain	-0.02724	-13.54	-43.43	-0.24	0.0325
Sweden	-0.00019	22.86	24.38	-0.31	0
United Kingdom	-0.35276	3.83	4.36	-0.46	0.0450
RoEU	-0.08152	4.75	-2.20	-0.15	0.0175
RoOECD	-0.38697	13.24	-7.03	-0.34	<i>n.a. -> 0</i>
CHIND	-0.63032	-4.21	0.25	-0.06	<i>n.a. -> 0</i>
TE	-0.27001	6.15	-10.14	-0.28	<i>n.a. -> 0</i>
RoW	-0.24184	-8.78	-17.89	-0.02	<i>n.a. -> 0</i>

Table 4b. Supply-side impacts (1): 4° C temperature increase, ref. year 2050

	Supply-side Impacts (2)					
	Floodings					
	Agriculture (land stock)	Residential (K prod.)	Transport (K prod.)	Commerce (K prod.)	Industry (K prod.)	Population (L prod.)
Austria	-0.019844	-1.351235	-0.012211	-0.001854	-0.006816	0.002273
Belgium	-0.043552	-0.101259	-0.006539	-0.009657	-0.034333	0.001879
Czech Republic	-0.003306	-0.297799	-0.005237	-0.007026	-0.019762	0.000842
Denmark	-0.004319	-0.031111	-0.000603	-0.000121	-0.000440	0.000072
Finland	-0.018154	-0.411370	-0.014361	-0.008443	-0.013213	0.001746
France	-0.014930	-0.136315	-0.008830	-0.001716	-0.008446	0.001177
Germany	-0.005323	-0.006574	-0.000632	-0.000087	-0.000772	0.000424
Greece	-0.005643	-0.094077	-0.001396	-0.000721	-0.005516	0.000442
Hungary	-0.017378	-0.582444	-0.011749	-0.003160	-0.009341	0.000772
Ireland	-0.035354	-0.614801	-0.018013	-0.001521	-0.001024	0.000623
Italy	-0.030584	-2.954311	-0.006971	-0.002166	-0.010472	0.001318
Netherlands	-0.062254	-0.109728	-0.004355	-0.001034	-0.005382	0.002099
Poland	0.010549	0.077988	0.001652	-0.000182	-0.000619	-0.000069
Portugal	-0.010016	-0.018937	-0.001490	-0.000196	-0.000763	0.000096
Spain	-0.015747	-0.125104	-0.002292	-0.001702	-0.004995	0.000467
Sweden	-0.002559	-0.095156	-0.002931	-0.001439	-0.004791	0.000095
United Kingdom	-0.100310	-1.021074	-0.028817	-0.008138	-0.057809	0.002078
RoEU	-0.008616	-0.461287	-0.008151	-0.004495	-0.011618	0.001208
RoOECD	n.a. > 0	n.a. > 0	n.a. > 0	n.a. > 0	n.a. > 0	n.a. > 0
CHIND	n.a. > 0	n.a. > 0	n.a. > 0	n.a. > 0	n.a. > 0	n.a. > 0
TE	n.a. > 0	n.a. > 0	n.a. > 0	n.a. > 0	n.a. > 0	n.a. > 0
RoW	n.a. > 0	n.a. > 0	n.a. > 0	n.a. > 0	n.a. > 0	n.a. > 0

Table 4c. Supply-side impacts (2): 4° C temperature increase, ref. year 2050

From a quick inspection of the inputs, sea-level rise and ecosystem effects entail unambiguous negative impacts in all the countries/regions considered; the same for flooding; whereas net health impacts of climate change are everywhere positive. Tourism is positively affected by climate change in Northern European countries, where warming increases climatic attractiveness, and negatively affected in Southern European countries, becoming “too hot”. Both climate change consequences on crops and the fish stock productivity are mixed depending on the country. In general crops productivity tend to benefit from climatic change, through positive temperature and CO₂ concentration-fertilization effect, in

Centre-North EU and to decrease in the South. Reduced catches affect mainly Mediterranean countries, primarily Italy and Spain, whereas Greece is almost unaffected. On the contrary Northern EU fishery is apparently advantaged by climatic change. Electricity consumption with the only exceptions of Austria, Finland, Czech Republic, Germany and Poland is expected to increase in the EU for the prevalence of a cooling effect, i.e. more air conditioning in the summer. In gas and partly oil product demand there is a prevalence of “minus signs” as a consequence of the warming effect: less energy used to warm in the winter. Note that when demand side impacts are concerned (tourism and energy), these imply by construction a re-composition rather than a shrinking/expansion of agents demand as their total budget is unaltered. Accordingly, it is very difficult to assess since the beginning if the final consequences are positive or negative for the economic system. In fact, a negative physical impact does not necessarily imply an economic loss but may even turn in economic benefit. This may happen for instance when in a region physical impact itself turns to be relatively smaller in absolute terms to other regions, or because the importance of the impacted sector is relatively low important in the regional economic system, or again because international trade can drive unexpected outcomes as relative prices in the different regions vary. To do so a CGE analysis is needed which is the focus of the next session.

5. RESULTS

Fig. 2 reports climate change dynamic impact on the EU GDP. Fig. 3 and 4 report GDP impacts in 2050 for the 2°C and 4°C temperature increase scenarios and the decomposition of impacts by category.

The EU 27 as a whole experiences a GDP loss of the -0.16% and the -0.74% in the 2°C and 4°C cases respectively. (The loss for the world as a whole is larger: -0.7% and -1.8% of GDP in 2050 for 2°C and 4°C respectively). Impacts therefore are not linear in temperature. They are also rather moderate in aggregate⁸. However, they are highly differentiated by country, ranging from the +0.56% of GDP in Denmark to the -1.76% in Greece in the 2°C temperature increase scenario; from the +0.59% of GDP

⁸ Note that only river flooding are included in the assessment and just for the EU countries and that catastrophic events are not considered.

in Finland to the -6.24% in Greece in the 4°C temperature increase scenario. In general they are slightly positive or basically null in the Northern European countries (Denmark, Finland, Germany, Sweden the UK), negative in the Southern EU, highlighting its higher vulnerability. Among impacts type, agriculture clearly dominates, followed by tourism and ecosystem. These three impacts together build more than 70% of the final GDP result in the majority of the EU countries. Interesting is also country specific vulnerability. For instance, in Greece, Spain and Portugal, agriculture and tourism impacts are by large the more concerning; agriculture is less of an issue in Italy, Ireland and the Netherlands, where on the contrary ecosystem losses there appear to be more important.

Tables 5 and 6 report climate change impacts on sectoral production. These tend to follow generally the direction of the climatic shocks, but not always. In fact they are the final resultant of all the climatic shocks jointly implemented. Therefore, impacts interactions and aggregate effects also play a role in determining the final outcome. A straightforward example is what happens in the energy sectors. Take for instance Greece: household electricity demand is expected to increase because of a strong cooling effect, however the final production of the sector is negative. Indeed Greece experiences a severe aggregate GDP loss because of climate change which prevails on any single shock. Accordingly also its total energy demand, including that of electricity net of the cooling effect, declines. Aggregate GDP effects are also the major drivers of production performances in the “industry” macro-sector which is directly affected just by a very tiny productivity decline induced by increased expected losses from floods.

Picking some highlights: it is evident the negative performance of agricultural sectors especially in Spain, Greece, Portugal (-8.7%, -8.5%, -5.2% respectively in the 2°C temperature increase scenario in 2050) and partly in Italy and France (-2.7%, -2.3% respectively in the 2°C temperature increase scenario in 2050); the negative impacts on the service sector in the same countries (-2.08% in Greece, -1.01% in Spain, -0.97 in Portugal, -1.34% in Italy in the 2°C 2050) encompassing recreational tourism services which are negatively hit; the decline in fishery production in Italy and Spain (-8.27%, -3.91% respectively in the 2°C scenario in 2050); the generalized prevalence of production contraction in the energy sectors driven as said by the slump of world energy demand. Note also that industrial production is negatively affected in Finland and Sweden (-3.08%, -1.41% respectively in 2050 in the 2°C temperature increase scenario) notwithstanding the positive GDP impact of climate change in

those countries. This is another case where rebound effects play a role. The contraction in world demand can in fact impact negatively industrial production also in those countries where climate change is in fact positive.

Tables 7 and 8 report effects on labour demand. It is important to stress that the ICES CGE model depicts a Walrasian, perfectly clearing/full employment labour market. The first and most obvious consequence is that unemployment is not modelled. The second is that any shock on the labour market implies just a re-distribution of the labour forces from those sectors whose production, and factor prices, are declining more in relative terms, toward those sectors where the opposite happens. Accordingly, one or more sectors will be always gaining in terms of labour demand. This said, the redistribution of the labour force could indirectly provide some insights of possible tensions on the labour market that climate change may originate. Higher labour demand contractions (Table 7)⁹ are concentrated in the agricultural sector especially in Greece (-5.7%), Spain (-5.9%) and Portugal (2.7%); in the fishing sector in Italy (-7.9%) and Spain (-4.5%); in the service sector in Hungary (-1.3%), Italy and Portugal (-0.5% both). Industrial labour demand declines particularly in Finland (-4%), Sweden (-1.6%) and Hungary (-1.4%); energy sectors tend also to expel labour force.

To conclude, Fig. 5 and 6 and Tab. 9 report climate change impacts on world prices and Fig. 7 and 8 on terms of trade. Prices highlight a generalized decline consistently with the demand decrease at the world level induced by GDP contraction. The reduction is particularly evident for the forestry and fishing products and for energy commodities. Agricultural prices show an opposite trend however, as the land scarcity induced by flooding and sea-level rise and the decreased land productivity especially at the mid-low latitudes induces a negative supply-side effect more than offsetting the reduced demand.

This has direct implication for terms of trade. In general, EU countries which are, broadly speaking, energy importers and food exporters, benefit from the price shifts and gain. Exceptions are those southern countries like Greece, Spain, Portugal and also Italy where the GDP contraction is particularly high and domestic prices decreases more compared to imported prices.

⁹ The comments on Table 8 are similar qualitatively

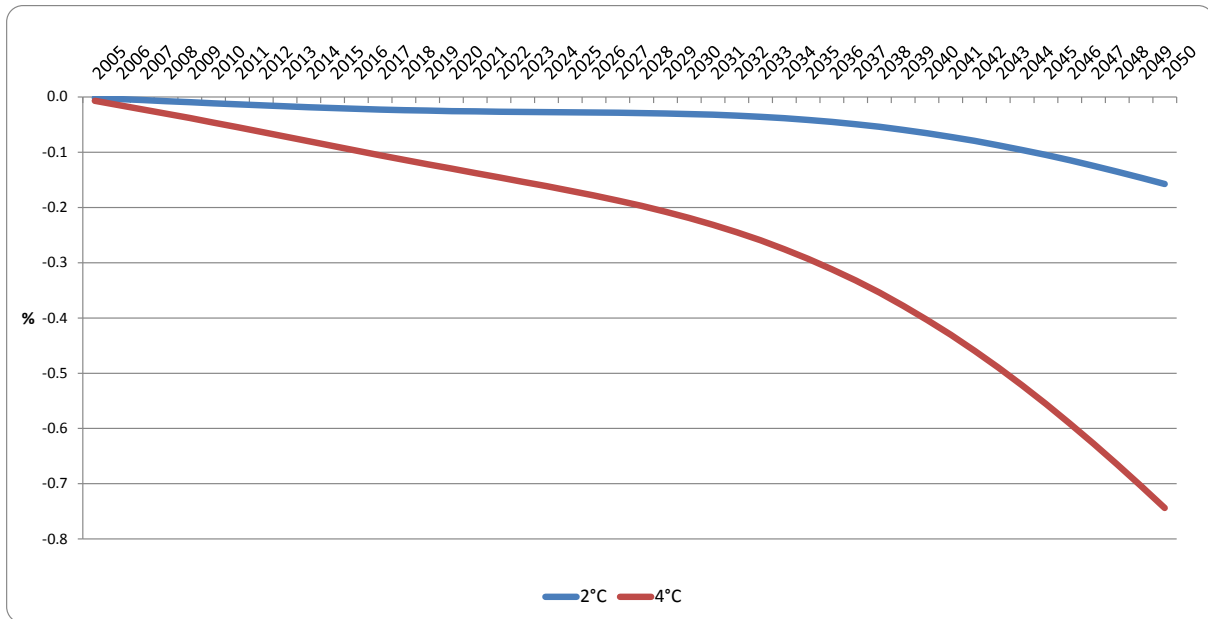


Fig. 2. Climate change impacts on EU real GDP (% change wrt baseline) - 2 °C and 4 °C temperature increase

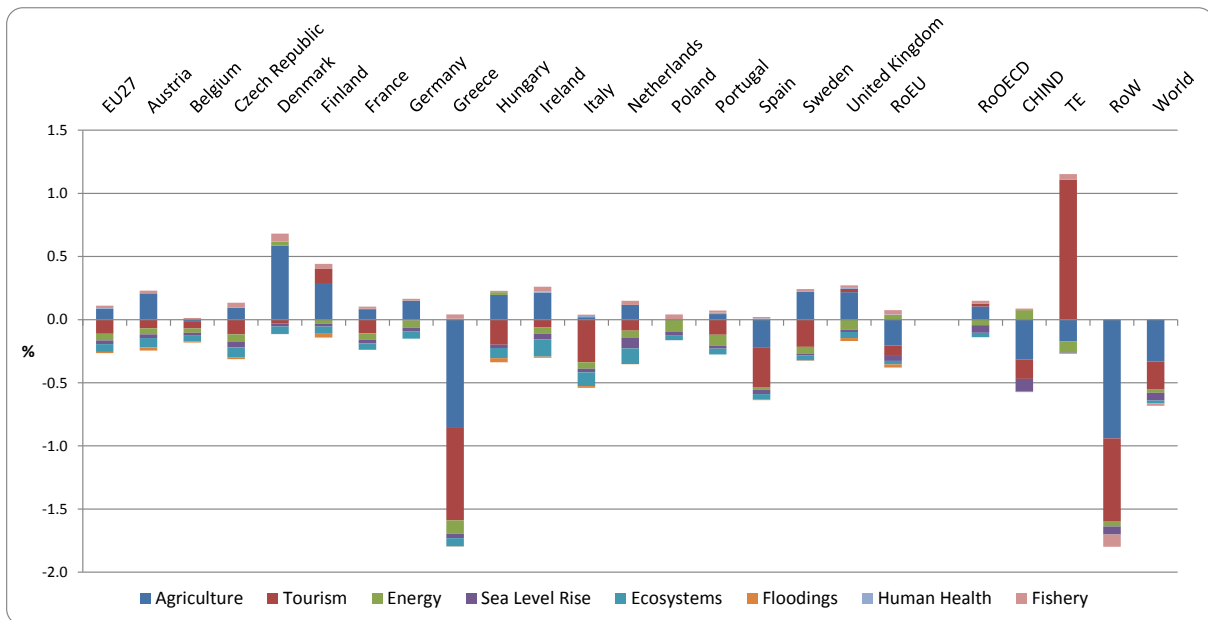


Fig. 3. Climate Change impacts on real GDP (% change wrt Baseline) and impact decomposition. 2°C temperature increase ref. year 2050

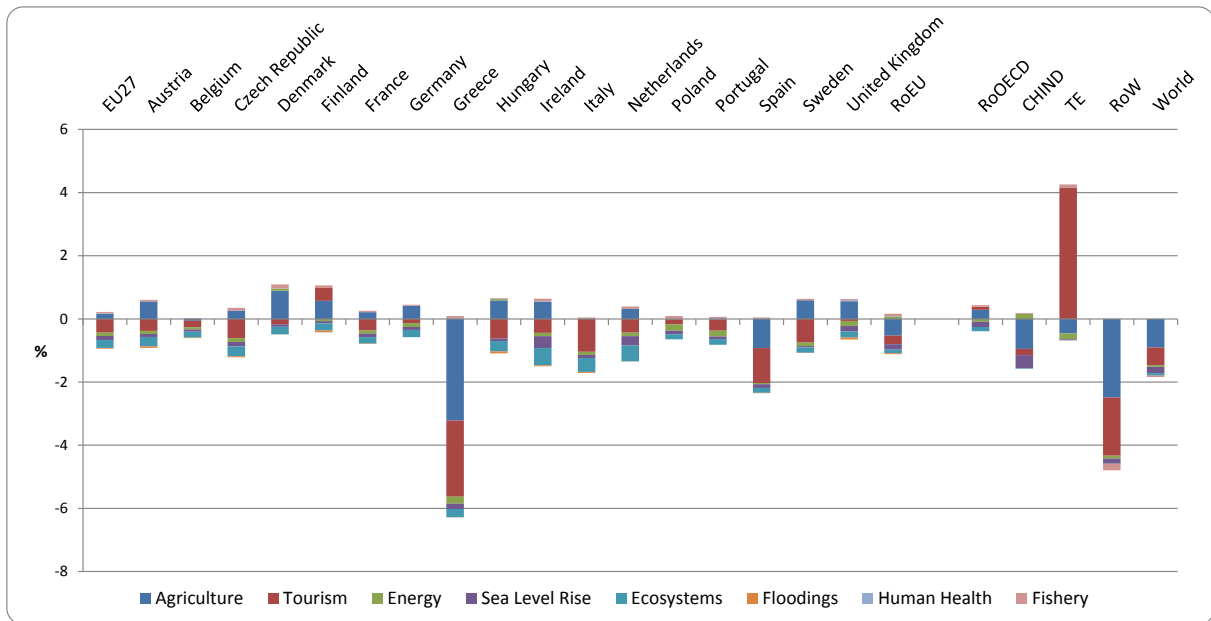


Fig. 4. Climate Change impacts on real GDP (% change wrt Baseline) and impact decomposition. 4°C temperature increase ref. year 2050

Tab. 5 Sectoral Production in 2050 (% change wrt Baseline) - 2 °C temperature increase

	Agriculture	Forestry	Fishing	Coal	Oil	Gas	Oil Pcts	Electricity	Industries	Transport	Residential	Mkt Services	Public Services
Austria	5.47	-1.10	-0.62	-0.01	-0.02	-1.23	0.37	-0.34	-0.10	-1.25	-0.69	-0.07	0.09
Belgium	-1.58	-1.06	-1.44	0.01	-0.02	-0.09	0.09	-0.08	0.46	-0.28	-0.24	-0.45	-0.13
Czech Republic	-0.03	-1.38	-1.39	-0.02	-0.02	-0.15	0.32	-1.12	0.01	-0.60	-0.06	-0.24	0.12
Denmark	13.46	-2.71	3.71	-0.01	-0.06	-0.45	0.82	0.67	-0.84	-1.87	0.46	-0.01	0.50
Finland	19.09	-2.19	8.85	-0.04	-0.06	-3.63	0.91	-1.00	-3.08	-1.85	-0.72	0.86	1.04
France	-2.33	-2.04	-1.21	0.05	-0.01	-0.28	0.30	0.39	0.70	-0.16	-0.17	-0.28	-0.15
Germany	0.38	-2.68	-0.81	-0.03	-0.02	-0.69	0.27	-0.65	-0.38	-0.73	-0.44	0.20	0.12
Greece	-8.47	-1.95	-0.80	0.21	0.09	0.13	-0.25	0.72	-0.49	4.74	-3.66	-2.08	-1.40
Hungary	2.11	-3.57	-2.77	0.03	-0.06	1.09	0.49	1.79	-0.86	-0.66	0.12	-0.72	0.07
Ireland	-0.11	-2.65	-1.56	0.00	-0.02	-0.64	0.30	0.12	0.35	-0.73	-0.01	-0.60	-0.07
Italy	-2.66	-0.98	-8.27	0.11	0.01	0.35	0.20	1.87	1.78	0.30	-0.79	-1.34	-0.97
Netherlands	0.81	-2.17	3.65	0.00	-0.03	-0.14	-0.50	-0.06	-0.20	-0.45	-0.29	-0.41	-0.03
Poland	-0.40	-1.45	1.14	-0.01	-0.01	-0.58	0.35	-0.82	-0.35	-0.52	-0.04	0.00	0.29
Portugal	-5.26	-2.51	-3.34	0.10	0.01	0.59	0.33	2.10	2.80	0.45	-0.99	-0.97	-1.34
Spain	-8.74	-0.78	-3.91	0.09	0.04	-0.60	-0.04	2.79	2.98	1.36	-3.05	-1.01	-1.16
Sweden	17.12	-1.86	4.61	-0.01	-0.01	-0.22	-0.01	-1.23	-1.41	-1.38	-2.06	0.69	0.36
United Kingdom	3.60	-1.71	0.35	-0.01	-0.04	-0.60	0.11	-0.37	-0.55	-0.74	-0.53	0.28	0.15
RoEU	1.85	-4.61	-2.61	-0.09	-0.12	-0.65	-0.21	-0.72	-1.04	-1.22	0.25	-0.59	0.19
RoOECD	-1.21	-2.73	2.42	-0.02	-0.07	-0.42	0.92	0.85	-2.30	-1.06	-1.23	1.08	0.09
CHIND	0.03	-0.57	-0.60	0.04	0.00	0.24	0.52	0.30	0.13	-0.59	-0.93	-1.45	-0.57
TE	-1.14	-0.31	0.54	-0.02	-0.03	-0.52	0.28	-1.55	-0.60	0.01	-1.13	3.11	0.50
RoW	-1.85	-0.26	-0.97	0.03	0.02	0.13	-0.88	1.27	-1.31	0.10	-2.03	-2.24	-1.11

Tab. 6 Sectoral Production in 2050 (% change wrt Baseline Scenario) - 4 °C temperature increase

	Agriculture	Forestry	Fishing	Coal	Oil	Gas	Oil Pcts	Electricity	Industries	Transport	Residential	Mkt Services	Public Services
Austria	6.42	-2.98	-2.11	-0.05	-0.09	-3.97	1.73	-1.35	-0.46	-3.01	-1.63	-0.49	0.63
Belgium	-3.89	-3.13	-4.93	-0.01	-0.08	0.01	0.67	-1.20	0.47	-0.56	-0.98	-1.21	0.04
Czech Republic	-0.08	-3.78	-4.57	-0.10	-0.08	0.06	1.20	-3.86	-0.57	-1.61	-0.44	-1.05	0.27
Denmark	12.07	-7.74	5.97	-0.03	-0.14	-1.14	1.82	1.13	-1.00	-2.78	-0.42	-0.30	0.81
Finland	16.83	-5.16	16.85	-0.10	-0.15	-8.31	2.22	-2.46	-6.75	-3.47	-1.28	2.64	3.69
France	-5.94	-6.06	-4.09	-0.04	-0.08	-1.76	1.24	-0.48	0.61	-0.77	-0.60	-0.77	-0.06
Germany	1.05	-7.57	-2.65	-0.11	-0.08	-2.14	1.59	-2.15	-1.53	-1.81	-0.75	0.24	0.62
Greece	-24.13	-4.70	-2.81	0.27	-0.11	-5.14	-0.94	-1.79	-3.61	16.61	-15.32	-6.54	-6.97
Hungary	3.99	-8.85	-8.39	-0.02	-0.24	1.66	0.81	2.86	-2.81	-1.64	0.21	-1.67	0.18
Ireland	-0.45	-7.07	-4.26	-0.04	-0.08	-2.50	0.88	-0.67	-0.02	-2.39	-0.71	-2.40	-0.43
Italy	-7.28	-2.28	-17.91	0.18	-0.03	-0.81	0.02	3.44	4.35	0.23	-4.86	-3.71	-3.17
Netherlands	1.89	-6.53	6.49	-0.03	-0.14	-0.72	-1.59	-1.24	-1.28	-0.76	-1.19	-1.64	-0.29
Poland	-0.93	-3.74	-0.22	-0.08	-0.07	-1.68	1.46	-2.11	-1.24	-1.22	-0.01	-0.43	0.72
Portugal	-15.75	-6.16	-10.48	0.22	0.01	0.89	0.50	3.91	7.98	1.59	-6.67	-2.30	-4.96
Spain	-22.96	-1.71	-9.23	0.19	0.08	-4.27	-0.98	4.55	7.59	3.62	-12.90	-2.66	-5.02
Sweden	16.00	-4.77	7.67	-0.02	-0.02	0.16	0.25	-3.67	-3.78	-3.17	-4.30	1.39	1.75
United Kingdom	3.62	-4.49	-0.07	-0.06	-0.16	-1.93	0.67	-1.41	-1.41	-1.84	-1.03	0.18	0.36
RoEU	4.71	-11.52	-10.45	-0.37	-0.42	-2.08	-0.68	-3.01	-3.56	-3.45	0.68	-1.44	1.09
RoOECD	-3.05	-8.09	3.37	-0.13	-0.27	-1.66	3.79	1.41	-7.31	-2.90	-2.03	2.69	1.16
CHIND	-0.31	-1.50	-1.53	0.06	-0.02	0.28	0.66	0.03	0.59	-1.56	-4.04	-3.51	-2.52
TE	-2.95	-0.95	1.15	-0.15	-0.15	-1.52	1.65	-3.61	-2.89	0.24	-2.54	10.93	2.51
RoW	-4.47	-0.75	-2.18	0.07	0.03	0.03	-3.17	1.11	-2.63	0.68	-7.82	-5.30	-4.39

Tab. 7 Labour demand in 2050 (% change wrt Baseline Scenario) - 2 °C temperature increase

	Agriculture	Forestry	Fishing	Coal	Oil	Gas	Oil_Pcts	Electricity	Industries	Transport	Residential	Mkt Services	Public Services
Austria	5.68	-1.83	-3.26	-0.19	-0.35	-1.53	-1.50	-0.69	-0.18	-2.03	-0.27	-0.08	0.18
Belgium	-0.24	-2.24	-3.28	0.10	-0.14	-0.27	-0.48	0.18	0.55	-0.38	0.18	-0.24	-0.11
Czech Republic	1.14	-1.66	-3.57	-0.13	-0.22	-0.38	-0.89	-1.37	-0.11	-1.14	0.09	-0.19	0.19
Denmark	12.40	-3.63	0.19	-0.33	-0.61	-1.70	-2.51	-0.39	-1.13	-3.63	0.26	-0.30	0.39
Finland	16.88	-3.40	3.89	-0.69	-0.89	-4.50	-4.08	-2.94	-4.03	-4.51	-1.68	0.07	0.84
France	-0.96	-2.87	-3.04	0.20	-0.14	-0.29	-0.34	0.50	0.76	-0.42	-0.04	-0.09	-0.07
Germany	1.23	-3.42	-3.27	-0.17	-0.36	-0.95	-1.30	-0.75	-0.39	-1.49	-0.29	0.40	0.19
Greece	-5.70	-1.93	-2.02	0.83	0.87	2.46	4.75	4.14	1.51	8.70	-1.31	1.26	-0.52
Hungary	2.66	-3.85	-4.50	0.12	-0.41	0.89	-1.67	0.98	-1.37	-2.15	-0.04	-1.26	-0.07
Ireland	0.71	-2.76	-3.24	-0.02	-0.27	-0.59	-0.90	-0.04	0.52	-1.54	0.33	-0.41	0.01
Italy	-0.93	-1.04	-7.93	0.50	0.12	0.65	0.87	2.46	2.18	0.96	0.72	-0.73	-0.90
Netherlands	1.70	-3.45	0.97	-0.04	-0.27	-0.27	-1.67	-0.21	-0.31	-1.15	-0.04	-0.14	0.10
Poland	0.67	-1.82	-2.89	-0.08	-0.25	-0.88	-0.85	-0.98	-0.35	-1.11	0.09	0.19	0.35
Portugal	-2.68	-3.16	-3.90	0.59	0.22	1.56	1.56	2.87	3.20	1.54	-0.24	-0.50	-1.27
Spain	-5.85	-0.91	-4.47	0.97	0.51	0.79	3.08	4.94	3.89	3.89	-2.08	-0.12	-0.80
Sweden	14.49	-2.49	0.01	-0.30	-0.60	-1.56	-2.80	-1.41	-1.62	-2.48	-2.06	0.63	0.34
United Kingdom	3.83	-2.64	-2.34	-0.19	-0.38	-1.04	-1.73	-0.59	-0.66	-1.72	-0.23	0.38	0.25
RoEU	2.36	-4.76	-7.03	-0.39	-0.55	-1.20	-2.64	-2.05	-1.69	-3.07	-0.22	-1.35	0.01
RoOECD	-0.86	-3.94	-0.98	-0.26	-0.61	-1.10	-2.42	-0.07	-2.54	-2.70	-1.14	1.06	0.06
CHIND	0.74	-1.20	-1.54	0.33	0.09	0.93	0.96	1.39	0.60	-0.16	-0.41	-1.02	-0.40
TE	-0.42	-0.95	-1.19	-0.18	-0.31	-1.70	-1.35	-2.78	-1.00	-0.78	-0.38	3.96	0.48
RoW	-0.07	-1.23	-1.96	0.79	0.55	1.31	2.42	3.67	0.11	2.31	-0.30	-0.92	-0.59

Tab. 8 Labour demand in 2050 (% change wrt Baseline Scenario) - 4 °C temperature increase

	Agriculture	Forestry	Fishing	Coal	Oil	Gas	Oil_Pcts	Electricity	Industries	Transport	Residential	Mkt Services	Public Services
Austria	8.16	-4.76	-9.65	-0.67	-1.17	-4.71	-4.49	-2.08	-0.35	-5.21	-0.25	0.10	0.93
Belgium	-0.37	-6.25	-10.21	-0.11	-0.73	-0.88	-2.79	-0.50	0.71	-1.48	0.73	-0.29	0.08
Czech Republic	3.09	-4.47	-10.50	-0.65	-0.89	-0.86	-3.51	-4.40	-0.64	-3.28	0.50	-0.27	0.77
Denmark	12.62	-9.92	-2.58	-0.71	-1.35	-3.73	-5.37	-0.44	-1.20	-6.18	-0.29	-0.21	0.81
Finland	15.26	-7.64	6.06	-1.62	-2.22	-9.94	-9.51	-6.16	-8.43	-9.06	-2.66	1.29	3.35
France	-2.47	-8.16	-9.23	-0.03	-0.84	-1.76	-2.72	-0.13	0.88	-2.47	0.19	0.10	0.39
Germany	3.38	-9.34	-9.40	-0.73	-1.35	-2.86	-4.36	-2.53	-1.51	-4.55	-0.03	1.22	0.95
Greece	-16.79	-4.57	-6.32	1.21	2.29	3.32	14.96	8.10	3.07	31.83	-7.80	5.21	-4.08
Hungary	5.80	-9.44	-12.60	-0.16	-1.43	1.34	-5.99	1.19	-3.67	-5.56	0.36	-2.16	0.15
Ireland	1.93	-7.31	-8.93	-0.44	-1.01	-2.12	-3.47	-1.12	1.33	-5.05	1.13	-0.95	0.05
Italy	-2.58	-2.40	-17.91	0.97	0.05	0.12	0.76	5.13	6.06	2.08	-0.49	-0.85	-2.96
Netherlands	4.46	-9.74	-1.43	-0.52	-1.07	-1.22	-6.11	-1.60	-1.49	-3.32	0.12	-0.17	0.44
Poland	1.98	-4.62	-9.03	-0.49	-0.97	-2.19	-3.19	-2.83	-1.08	-3.35	0.77	0.60	1.05
Portugal	-8.63	-7.40	-11.66	1.33	0.49	2.92	3.64	6.26	9.59	4.78	-3.31	-0.16	-4.64
Spain	-15.61	-1.84	-11.78	2.22	1.22	-0.63	7.30	10.91	10.68	11.15	-9.81	0.65	-3.83
Sweden	15.07	-6.19	-4.26	-1.02	-1.81	-3.85	-7.98	-3.76	-4.14	-6.17	-4.08	1.55	1.77
United Kingdom	5.37	-6.65	-7.46	-0.74	-1.25	-3.07	-5.28	-1.78	-1.55	-4.86	0.24	1.08	0.80
RoEU	6.14	-11.85	-20.68	-1.56	-1.91	-3.70	-8.82	-6.73	-5.12	-8.91	-0.48	-2.97	0.63
RoOECD	-2.33	-11.06	-5.51	-1.32	-2.20	-4.07	-8.10	-2.02	-8.01	-8.49	-1.18	2.84	1.18
CHIND	1.93	-3.07	-4.72	0.59	-0.06	1.11	0.48	2.28	1.91	-0.78	-1.68	-1.75	-1.92
TE	-1.49	-2.93	-2.10	-1.07	-1.49	-4.95	-6.11	-7.89	-4.60	-3.62	-0.45	13.24	2.27
RoW	0.38	-3.28	-6.04	1.86	1.28	2.31	4.56	6.94	1.21	6.25	-2.61	-1.38	-2.92

Tab.9 World prices in 2050 (% change wrt Baseline Scenario) – 2 °C and 4 °C temperature increase

	2 °C	4 °C
Agriculture	2.00	5.42
Forestry	-5.60	-14.51
Fishing	-8.76	-25.43
Coal	-0.75	-4.03
Oil	-1.97	-7.12
Gas	-1.82	-5.50
Oil_Pcts	-1.93	-6.90
Electricity	-1.11	-3.44
Industries	-0.26	-0.89
Transport	-1.06	-3.34
Residential	0.46	2.89
Mkt Services	0.12	0.49
Public Services	-0.01	0.55

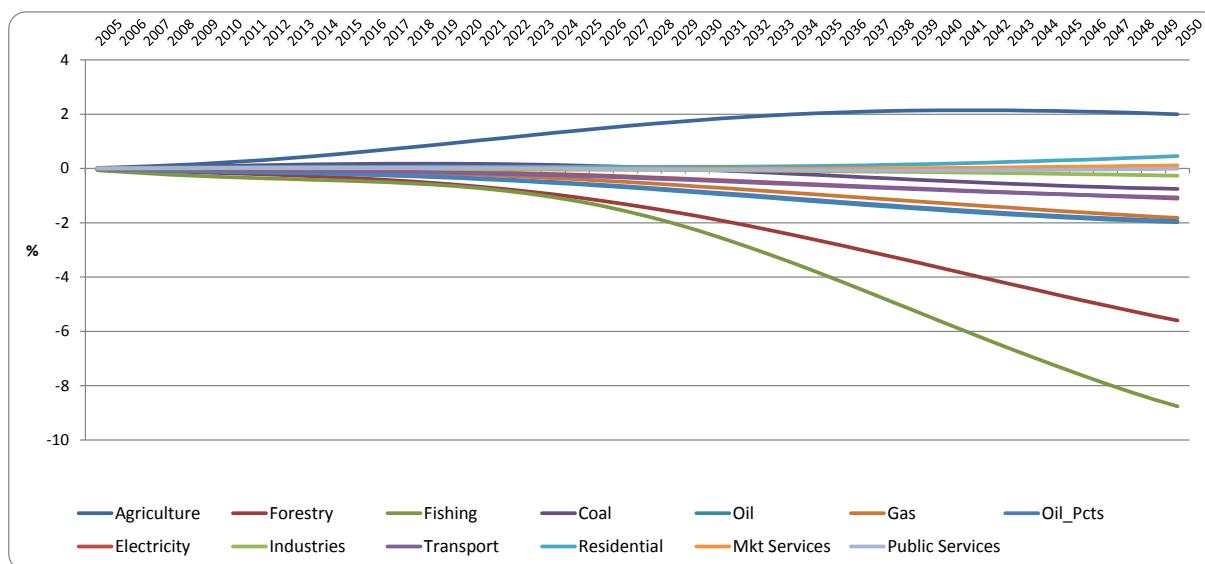


Fig. 5 World prices: % change wrt baseline - 2 °C temperature increase

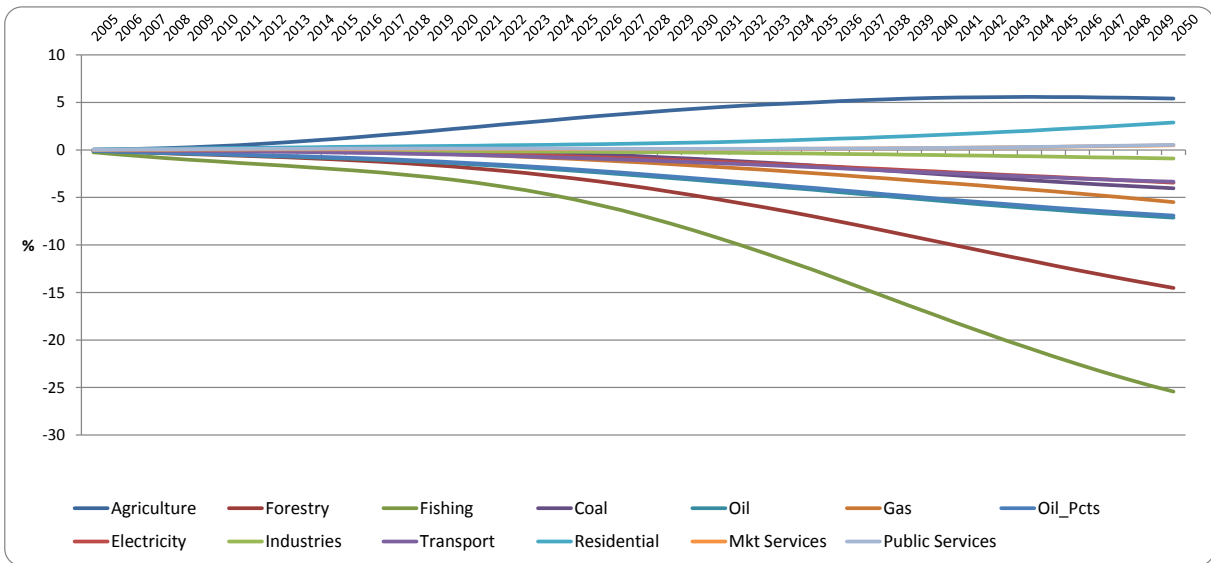


Fig. 6 World prices: % change wrt baseline - 4 °C temperature increase

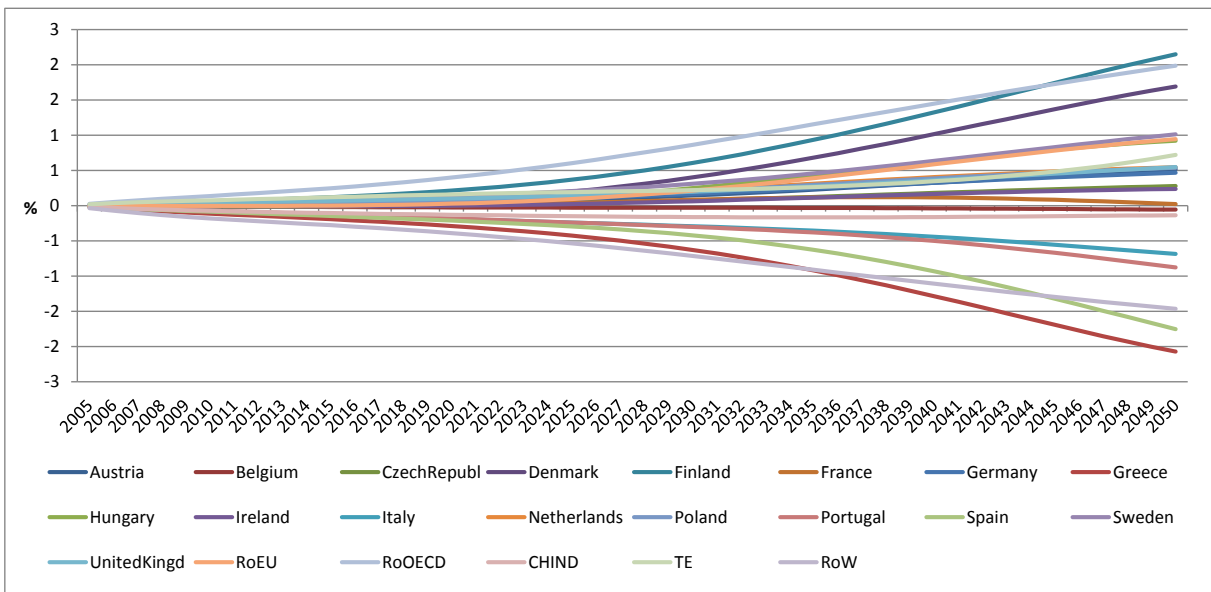


Fig. 7 Terms of trade: % change wrt baseline - 2 °C temperature increase

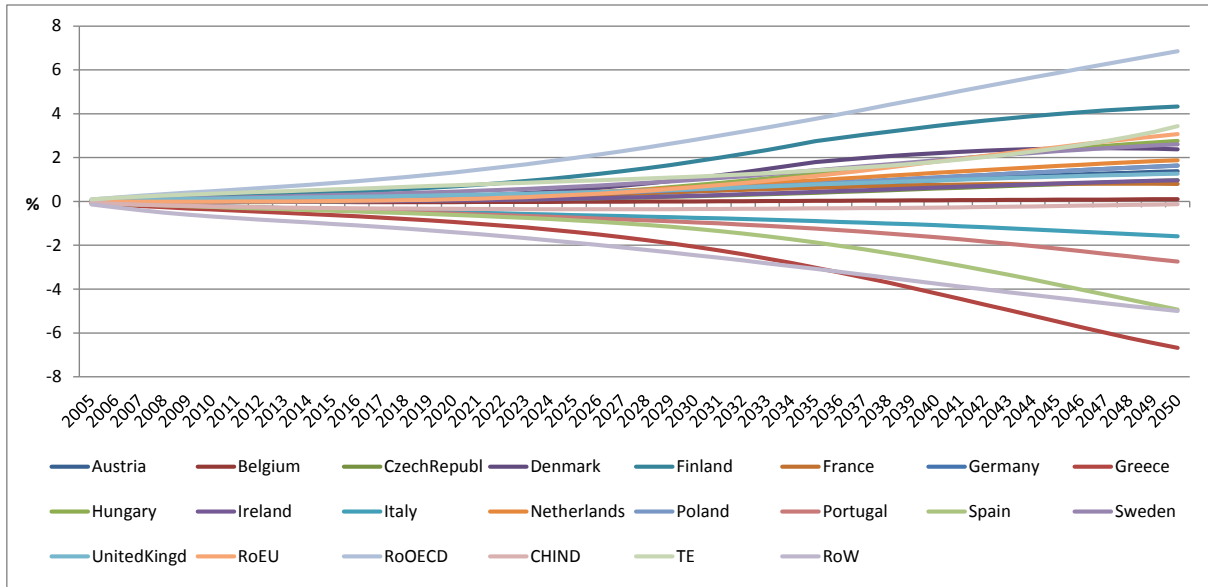


Fig. 8 Terms of trade: % change wrt baseline - 4 °C temperature increase

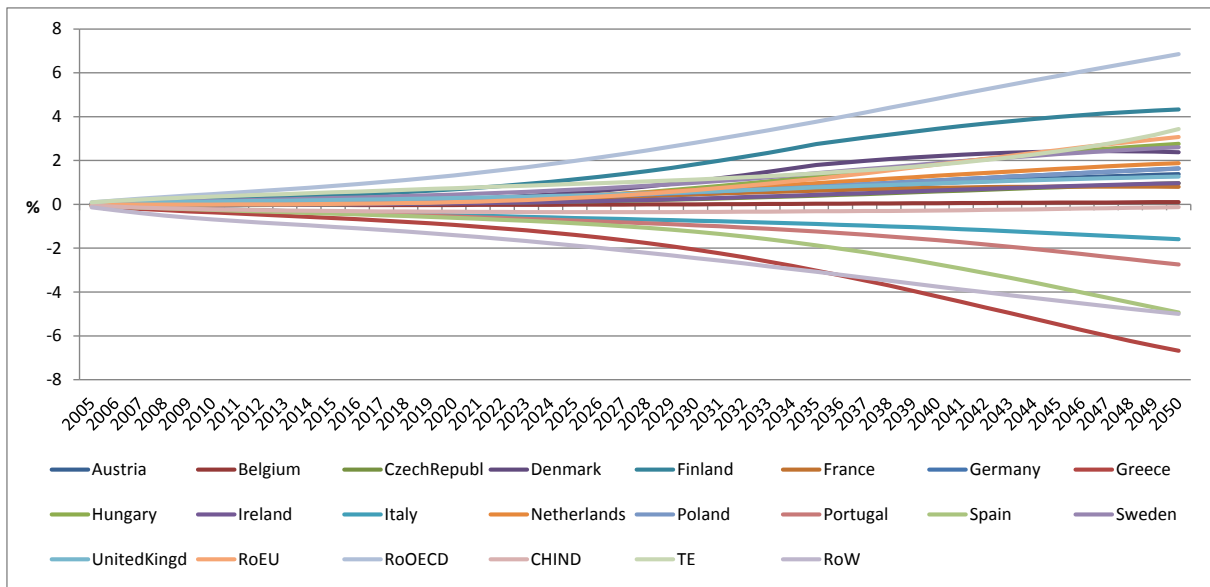


Fig. 8 Terms of trade: % change wrt baseline - 4 °C temperature increase

6. CONCLUSIONS

The present research describes a climate change integrated impact assessment exercise, whose economic evaluation is based on a CGE approach and modelling effort.

Impact types considered are those originated by: ecosystem losses, sea-level rise, changes of energy demand, of crops productivity, of fish stock productivity, of tourism flows, flooding and health. Impacts are also economically assessed for a 2 °C and 4 °C warming scenarios, both assumed to occur in 2050.

ICES estimates indicate that a temperature increase of 2°C compared to pre-industrial levels in 2050 could lead to global GDP losses of about 0.7% compared to a hypothetical scenario where no climate change is assumed to occur. Doubling the temperature increase, world losses are the -1.8% of GDP.

The EU 27 as a whole experiences a GDP loss of the -0.16% and the -0.74% in the 2°C and 4°C cases respectively. The apparent low vulnerability of the EU hide important country specificities: the southern EU region is more severely hit with Greece top-loser (-1.76% and -6.24% of GDP in 2050 in the 2°C and 4°C temperature increase scenarios respectively), the Northern one gaining or remaining basically unaffected. Among impacts type, agriculture clearly dominates, followed by tourism and ecosystem. These three impacts together build more than 70% of the final GDP result in the majority of the EU countries. Interesting is also country specific vulnerability. For instance, in Greece, Spain and Portugal, agriculture and tourism impacts are by large the more concerning; agriculture is less of an issue in Italy, Ireland and the Netherlands, where on the contrary ecosystem losses there appear to be more important.

Sectoral production tends to follow generally the direction of the climatic shocks, but not always as impacts interactions and aggregate effects also play a role in determining the final outcome. In 2050, when the temperature increases 2°C, higher labour demand contractions are concentrated in the agricultural sector especially in Spain (8.7%), Greece (-8.5%), Portugal (-5.2%); in the fishing sector in Italy (-8.27%) and Spain (-3.9%); in the service sector in Greece (-2.08%), Italy (-1.34%) and Spain (-1.01%). Industrial labour demand declines particularly in Finland (-3.8%), Sweden (-1.41%); energy sectors tend also to expel labour force.

Finally, the dynamics induced on world prices - generalized decline except of those of agricultural commodities - tends to benefit EU countries terms of trade with the exception of Greece, Spain, Portugal and also Italy where the GDP contraction is particularly high and domestic prices decreases more compared to imported prices.

7. REFERENCES

- Aaheim A., Dokken T., Hochrainer S., Hof A., Jochem E., Mechler R., and van Vuuren D.P., (2010), *National responsibilities for adaptation strategies: Lessons from four modelling framework* In: Making climate change work for us: European perspectives on adaptation and mitigation strategies. [Hulme, M. and H. Neufeldt(eds.)]. Cambridge University Press, Cambridge, pp. 87-112. (1)
- Berrittella M., Hoekstra A.Y., Rehdanz K., Roson R. and Tol R.S.J. (2007), *The Economic Impact of Restricted Water Supply: A Computable General Equilibrium Analysis*. Water Research 42, 1799-1813. (2)
- Bigano A., Hamilton J.M. and Tol R.S.J. (2005), *The Impact of Climate Change on Domestic and International Tourism: A Simulation Study*, Research unit Sustainability and Global Change FNU-58, Hamburg University and Centre for Marine and Atmospheric Science, Hamburg. (3)
- Bosello F., Lazzarin M., Roson R. and Tol R.S.J. (2007), *Economy-wide estimates of climate change implications: sea-level rise*, Environment and Development Economics, 37:549–571. (4)
- Bosello F., Roson R. and Tol R.S.J. (2006), *Economy wide estimates of the implications of climate change: human health*, Ecological Economics, 58, 579-591. (5)
- Burniaux J.-M. and Truong T.P. (2002), *GTAP-E: An energy environmental version of the GTAP model*, GTAP Technical Paper n. 16. (6)
- Calzadilla A., Rehdanz K., & Tol R. (2008), *The Economic Impact of More Sustainable Water Use in Agriculture: A CGE Analysis*, Research Unit Sustainability and Global Change, FNU-169. Hamburg University. (7)
- Cheung W.W.L., Close C., Lam V. *et al.* (2008a), *Application of macroecological theory to predict effects of climate change on global fisheries potential*, Marine Ecology Progress Series, 365, 187–197. (8)
- Cheung W. W. L., Lam V. W. Y., Sarmiento J.L., Kearney K., Watson R., Zeller D.I. R. K. and Pauly D. (2010), *Large-scale redistribution of maximum fisheries catch potential in the global ocean under climate change*, Global Change Biology 16, 24–35, doi: 10.1111/j.1365-2486.2009.01995.x (9)
- Cheung W.W.L., Lam V.W.Y. and Pauly D. (2008b), *Dynamic bioclimate envelope model to predict climate-induced changes in distribution of marine fishes and invertebrates*, in: Modelling Present and Climate-Shifted

- Distributions of Marine Fishes and Invertebrates. Fisheries Centre Research Reports 16(3) (eds Cheung WWL, Lam VWY, Pauly D), pp. 5–50. University of British Columbia, Vancouver. (10)
- Ciscar J.C. (2009), *Climate change impacts in Europe: Final report of the PESETA project*, JRC Technical Report, EUR 24093 EN, Spain. (11)
- Close C., Cheung W.W.L., Hodgson S. *et al.* (2006), *Distribution ranges of commercial fishes and invertebrates*, in: *Fishes in Databases and Ecosystems*. Fisheries Centre Research Report 14(4) (eds Palomares D, Stergiou KI, Pauly D), pp. 27–37. University of British Columbia, Vancouver. (12)
- Criqui P., (2001), *POLES: Prospective Outlook on Long-term Energy Systems*, Institut d'Economie et de Politique de l'Energie, available on line at: http://webu2.upmf-grenoble.fr/iepe/textes/POLES8p_01.pdf (13)
- Criqui P., Mima S., Menanteau P. (2009). *Trajectories of new energy technologies in carbon constraint cases with the POLES Model*, IARU International Scientific Congress on Climate Change, p. 16. (14)
- Darwin R. F. (1999), *A FARMer's View of the Ricardian Approach to Measuring Agricultural Effects of Climatic Change*, *Climatic Change*, 41 (3-4), 371-411. (15)
- Darwin R. F. and Tol R. S. J. (2001), *Estimates of the Economic Effects of Sea Level Rise*, *Environmental and Resource Economics*, 19, 113-129. (16)
- Deke O., Hooss K. G., Kasten C., Klepper G. and Springer K. (2002), *Economic Impact of Climate Change: Simulations with a Regionalized Climate-Economy Model*, Kiel Institute of World Economics, Kiel, 1065. (17)
- Eboli F., Parrado R. and Roson R. (2010), *Climate Change Feedback on Economic Growth: Explorations with a Dynamic General Equilibrium Model?*, *Environment and Development Economics*, Volume 15 (5), pp 515 -533. (18)
- Feyen L., Dankers R., 2009. *The impact of global warming on streamflow drought in Europe*, *J. Geophys. Res.*, 114, D17116, doi:10.1029/2008JD011438. (19)

- Iglesias A., Garrote L., Quiroga S. and Moneo M., (2009), *Impacts of climate change in agriculture in Europe*, PESETA FP6 project, available on line at: <http://ipts.jrc.ec.europa.eu/publications/pub.cfm?id=2900> (20)
- Manne A. and Richels R. (2005), *Merge: An Integrated Assessment Model for Global Climate Change, Energy and Environment*”, 175-189. (21)
- Narayanan B.G. and Walmsley T.L., (2008), *Global Trade, Assistance, and Production: The GTAP 7 Data Base*, Center for Global Trade Analysis, Purdue University. (22)
- Nakicenovic N. and Swart R. (2000), *Special Report on Emissions Scenarios: A Special Report of Working Group III of the Intergovernmental Panel on Climate Change*, Cambridge University Press, Cambridge, U.K. (23)
- Ronneberger K., Berrittella M., Bosello F. and Tol R.S.J. (2009), *KLUM@GTAP: introducing biophysical aspects of land use decisions into a general equilibrium model. A coupling experiment*, Environmental Modelling and Assessment, Vol. 14, n. 2. (24)
- UN - United Nations, Department of Economic and Social Affairs, Population Division (2011). *World Population Prospects: The 2010 Revision*, available at: <http://esa.un.org/unpd/wpp/index.htm> (25)
- Warren et al. (2006), *Spotlighting impacts functions in integrated assessment*, WP 91, Tyndall Centre for Climate Change Research. (26)
- Vafeidis A. T., Nicholls R. J., Boot G., Cox J., Grashoff P. S., Hinkel J., Maatens R., McFadden L., Spence T. & Tol R. S. J. (2008), *A new global coastal database for impact and vulnerability analysis to sea-level rise*, Journal of Coastal Research, 24(4):917-924. (27)

The informative role of farmers' perceptions of change for the development of robust climate change adaptation policies – a case study from Italy

Bonzanigo L.^{1,2,3*}, Bojovic D.^{1,2}, Maziotis A.³, Giupponi C.^{1,2,3}

¹Ca' Foscari University of Venice, Department of Economics, Venezia, Italy;

²Euro-Mediterranean Center on Climate Change, Climate Change Impacts and Policy Division, Venezia, Italy

³Fondazione Eni Enrico Mattei, Sustainable Development Group, Venezia, Italy

*Corresponding author: laura.bonzanigo@cmcc.it

Abstract

Most likely unavoidable, the changing climate calls for fast adaptive actions. The recent EU Strategy on Adaptation to Climate Change promotes National Adaptation Strategies as a key instrument to inform and prioritise adaptation measures. The agricultural sector in particular has always been adapting at the farm level. Today, it needs that on-going autonomous farm adaptations are complemented with medium-term structural and planned adaptive actions, in order to reduce the overall vulnerability of the agricultural sector. To investigate the individual adaptations and understand which are motivated by a changing climate and why - is a fundamental step when designing policies, to increase their chance of adoption and maximise the resources available. This research combines (i) an online participatory approach –eParticipation – to collect Veneto Region (VR, Italy) farmers' responses and identify their adaptation measures and (ii) a Heckman selection model to analyse the factors determining farmers' perceptions of change and the choice (if any) of adaptation options. The results both confirmed that this is an efficient approach for ensuring broad participation, and demonstrated that planned adaptation measures designed with informed consideration of farmers' concerns and responses to change have a higher chance of being accepted by farmers. These preliminary results could importantly contribute to the quality of the Italian NAS. Particularly, this paper offers an approach for a bottom-up, robust development of further adaptation policies. For the methodology's transfer to "real" policy-making, we recommend extending this proposed method for the design and assessment of adaptation policies to farmers' organisations and local decision-makers, in order to increase the representativeness of the interested parties. This would both ensure the policies' aptness and their broader acceptability.

Keywords: *Climate Change, Autonomous and Planned Adaptation, Agriculture, Decision-Support, eParticipation, Heckman model*



Evaluation of flood disaster risk in the Polesine sub-region

Amadio M.^{1*}, Mysiak J.¹, Pecora S.², Agnetti A.²

¹Fondazione ENI Enrico Mattei, Venezia, Italy

²ARPA Emilia-Romagna, HydroMeteoClimate Service, Hydrology Area, Parma, Italy

*Corresponding author: mattia.amadio@feem.it

Abstract

River flooding is the most common natural disaster in Europe, causing deaths and huge amount of economic losses. Disastrous flood events are often related to extreme meteorological conditions; therefore, climate change is expected to have an important influence over the intensity and frequency of major floods. While approximated large-scale assessments of flood risk scenarios have been carried out by EU Joint Research Center, the knowledge of the effects at smaller scales is poor or incomplete, with few localized studies. Also, the methods are still coarse and uneven. The approach of this study starts from the definition of the risk paradigm and the elaboration of local climatic scenarios to track a methodology aimed at elaborating and combining the three elements concurring to the determination of risk: hydrological hazard, value exposure and vulnerability. First, hydrological hazard scenarios are provided by hydrological and hydrodynamic models, used in to a flood forecasting system capable to define “what-if” scenario in a flexible way. These results are then integrated with land-use data (exposure) and depth-damage functions (vulnerability) in a GIS environment, to assess the final risk value (potential flood damage) and visualize it in form of risk maps. In this paper results from a pilot study in the Polesine area are presented, where four simulated levee breach scenarios are compared. The outcomes of the analysis may be instrumental to authorities to increase the knowledge of possible direct losses and guide decision making and planning processes also. As future perspective, the employed methodology can also be extended at the basin scale through integration with the existent flood warning system to gain a real-time estimate of floods direct costs.

Keywords: *Flood risk hazard Po river*



1. RESEARCH OBJECTIVE

The aim of this paper is to estimate the effects of climate change on the magnitude and frequency of extreme flood events in the Po River basin, and to understand how these effects will qualitatively and quantitatively reflect in terms of direct socio-economic risk. The study will focus on a pilot case study located in Polesine (Rovigo province). The estimated projections of hydro-climatic change in the river basin will be used as starting conditions for a hydro-meteorological model run to simulate the effects of an extraordinary discharge event on a flood scenario, producing a potential value of Hazard for each climatic scenario. This Hazard value will be compared with Exposure and Vulnerability values through GIS elaboration to estimate the direct socio-economic Risk (economic losses) potentially occurring in the pilot case study area during each scenario. The Risk outputs of different scenarios are conclusively compared.

2. DESCRIPTION OF CASE STUDY AREA

The term “Polesine” identifies the area located between the final section of the two major Italian rivers Po and Adige, before the Adriatic Sea. It is an hybrid river basin called “Fissero-Tartaro-Canalbianco”. This basin is a strip of land with an area of 1930 km² including 50 municipalities, which are a significant part of the Rovigo province. It is delimited for almost all its perimeter by embankments and barriers, similarly to a polder, and it is characterized by a strong agricultural connotation, lack of forestry, consistent water projects to defend the province and provide irrigation, and sparse, scattered urbanization through the monotonous landscape. The inner hydrographic network includes more than 2,000 km of canals and 80 dewatering pumps, constantly working to drain the excess of meteoric water. This system is strongly stressed during intense precipitation event, causing the risk of flooding from the inner network. Moreover, the sea level rising adds supplemental pressure to the dewatering system. In fact, the drainage of the basin is completely artificial. In some periods of the year (mostly spring and autumn) the rivers reach a higher altimetric level, meaning they flow pensile compared with the surrounding territory. This is the result of both subsidence of the floodplain (5 mm/year) and the constant deposit of sediments in the riverbed. Despite the massive amount of water defenses, numerous flood events involved this territory, with the 1951 being the more disastrous of last centuries. From 1952 to 1966, some 20 flood events from the rivers and from the sea engaged this province; after

that, methane extraction wells were closed to avoid further subsidence, and massive defense measures were built to avoid any disastrous events in the future.

Around 250,000 people live in Polesine, 50,000 of which are located in the chief town of Rovigo. The Population density (138 people/km²) is low compared with both the regional mean (268 people/km²) and the national mean (201 people/km²). The growth trend is almost flat since the disaster of 1951 (fig.1) and projections suggest it will remain stable for the next 40 years, while the average age will increase [12]. After the 1951 flooding, 150,000 people left the province and entrepreneurs start preferring other territories to invest and create business. This territory maintained a marked agricultural vocation and it was just marginally affected by the fast industrializing process happening in the Italian north-east area from the '70-'80s.

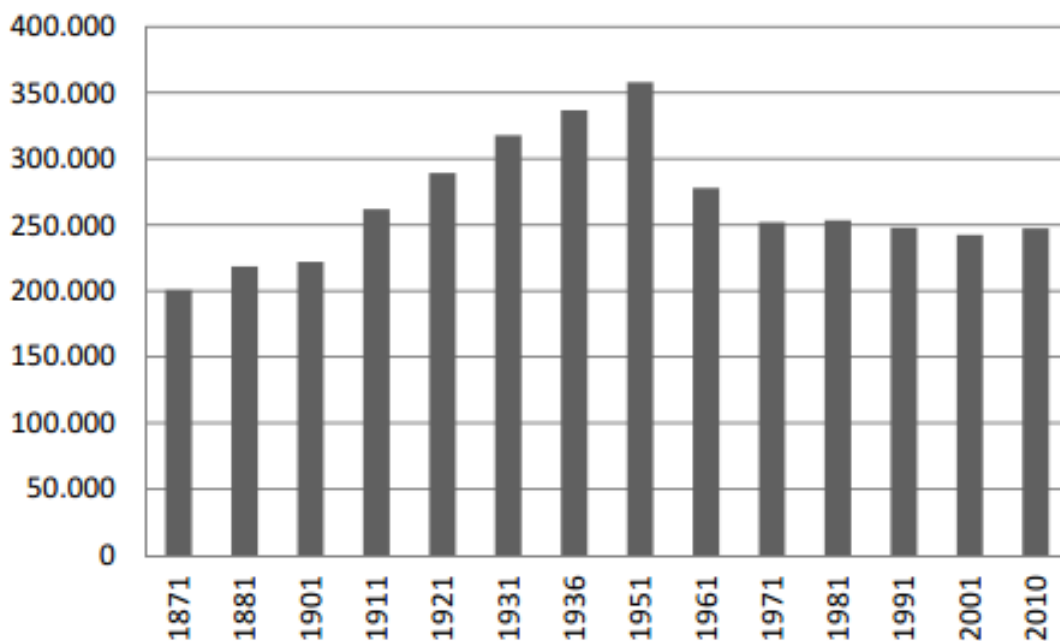


Fig. 1: People living in Polesine since 1871. The trend shows no significant changes in the last 40 years. The massive emigration happened after 1951 is clearly visible (Santato, 2010).

3. REFERENCE FLOOD EVENT: 1951, POLESINE

The November 1951 disastrous event affected the lower fraction of the Po River, exceeding all previous registered events in that area. The discharge levels reached a peak of 12,000 m³/s (4.28 m hydrometric height). The most affected regions were Veneto, Emilia Romagna and Piedmont [1;10]. The causes of this catastrophic event have been investigated. The structure and morphology of the Po riverbed and embankments was unaltered since the beginning of the century, so the explanation for such extraordinary flood must be found in the distribution, intensity and duration of the precipitation preceding the event, and in the unfortunate coincidence of flood waves from the river tributaries [1,9,10,15].

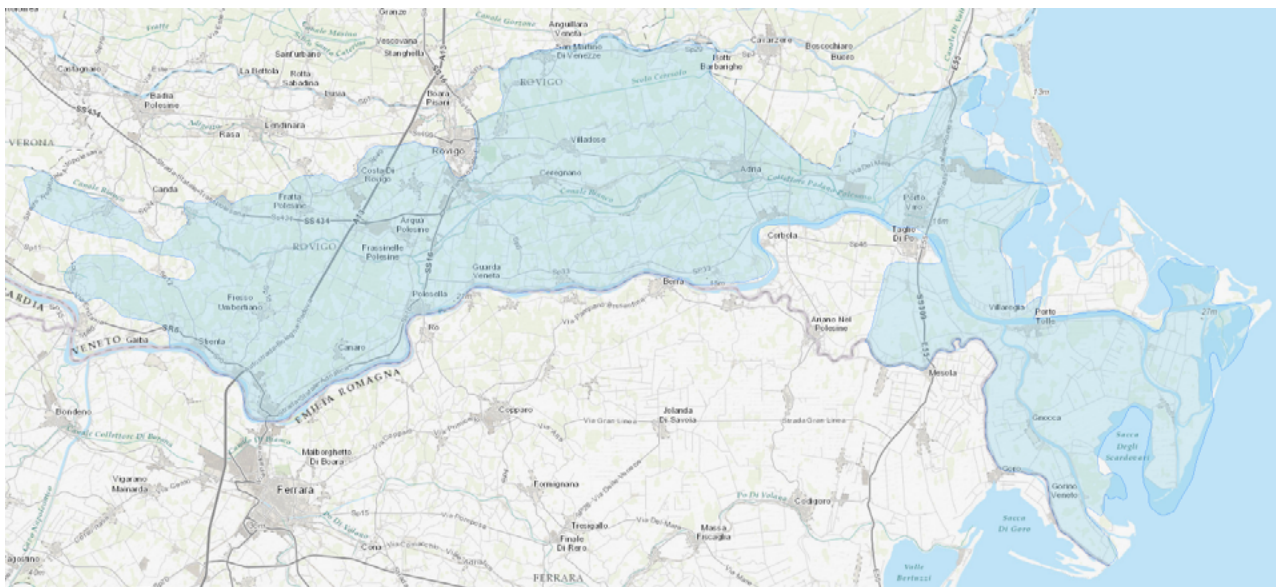


Fig. 2: Flood expansion during the 1951 event in Polesine (Rovigo Province). The numbers show the three breaks in the embankments system.

This catastrophic event caused 100 casualties and an estimated total damage of € 206.59 million (uninflated), equal to 3.7216% of 1951 GDP [9]. Compared to an inflation rate of 2,434% (up to year 2000), it is equal to € 5,235 million in 2000 value. 38 Municipalities were involved, with 900 houses destroyed, 160,000 people evacuated, and important damages to the country economy, with dead cattle and fields covered by sediments. Some 60 km of embankments were damaged, and 52 bridges were destroyed [15].

4. CLIMATIC FRAMEWORK

Both dynamical and statistical downscaling models (SDMs) of European macro-scale models were employed to provide high-resolution climate change scenarios for Emilia Romagna[3]. Coherently with the RCM HIRHAM models [5], the temperature signal obtained from project STARDEX [13;16] is homogenous for most of Europe, with a maximal increase of 1.5-2 °C, and the precipitation trend shows dissimilarity between northern and southern Europe: increasing in north-east and decreasing in south-west (fig.3). Results from different models used in the ensemble are comparable with modest variability throughout Europe, which imply a strong credibility [4].

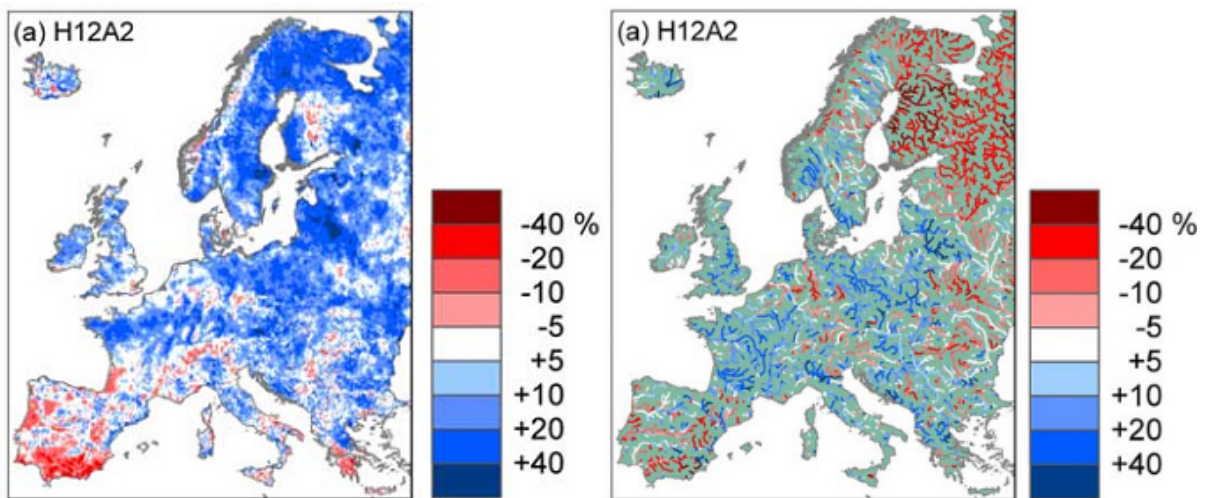


Fig. 3: RCM HIRHAM simulation of variation in the annual 5-day accumulated rainfall(a) and 100-years discharge levels (b) for scenario A2 and B2 (2071-20100). Values are compared to a 30-year average control run (1961-1990) (adapted from Dankers et al., 2008).

For Emilia Romagna, results about temperature are expressed as Probability Density Function (PDF) for 2021-2050. An increase in T_{min} and T_{max} is expected for all seasons, with an average shift of +2/+2.5°C. The T_{min} increases more than T_{max} during autumn and winter (+2°C), while T_{max} increases more in spring (+3°C) and summer (+5°C). There is no quantitative data reported about precipitation change, but scenarios indicate a marked decrease in winter (-10%) and summer (-20%) rainfall, while a slight increase in autumn precipitation is expected. Furthermore, rainfall magnitude during short-time extreme events are “very likely to increase” during spring-summer, alternated with longer and more frequent droughts [4,13,14].

5. ASSESSMENT METHODOLOGY: HAZARD CHARACTERISTICS VS VALUE AT RISK

Four main parameters are defined for this step:

1) Flood characteristics (*Hazard* value): water depth has the strongest influence on damage magnitude, while speed and duration are rarely taken on account. The dominant approach, as suggested by Merz et al. [11], employs depth-damage functions. Flood discharges, extent and depth can be calculated by means of 1D-2D models and simple GIS functionality. A combination of hydrological and hydraulic models has been employed by ARPA-SIM Emilia-Romagna for the definition of our scenarios.

- Hydrological model: DHI-Mike11 NAM Rainfall-Runoff
- 1D hydrodynamic model: DHI-Mike11 HD
- 2D hydrodynamic model DHI-Mike21 HD

The propagation of the flood is mainly regulated by the topography of the area, which is described by a 10-meters grid DEM (Digital Elevation Model). The inner canals of the floodplain (such as Canalbianco, Adigetto and Ceresolo) are not considered as streams contributing the flood, but their embankments are accounted as surmountable obstacles. Climate Change conditions forcing have been discussed with the experts from ARPA-SIM and applied on the base scenario (Autumn 2000 event) to produce two future discharge scenarios: +10% rainfall on the base event (2021-2050 scenario) and +30% rainfall on the base event (2071-2100 scenario). Four different rupture scenarios (tab.1) have been derived from these discharge scenarios, supposing a failure of the left embankments caused by erosion at Occhiobello, near Pontelagoscuro station. This rupture scenario resembles the reference event of 1951. The rupture length extension is 200 meters for three scenarios, while the last scenario figures a 400 meters break.

<i>Scenarios</i>	<i>Definition</i>	<i>Rainfall rates (compared to 2000 event)</i>	<i>Rupture</i>
Discharge scenarios	Base scenario	+0%	
	2021-2050	+10%	
	2071-2100	+30%	
Rupture scenarios	Base scenario	+0%	200 m
	2021-2050	+10%	200 m
	2071-2100	+30%	200 m
	2071-2100	+30%	400 m

Tab.1: Summary of different flood scenarios elaborated by ARPA ER

2) Assets at risk (*Exposure* value): land-use data about the number and typology of affected properties can be obtained from regional web-database [12], which provides with a detailed datasets about regional land-use in GIS vector format (2006, resolution: 1:10,000). There are 62 land-use categories, divided in 5 hierarchic levels. Several classes are aggregated together to identify few main categories. Classes are listed in tab2. Forest and semi-natural areas, wetlands and water bodies are other main categories not taken in account in the impact assessment.

<i>Urban surface</i>	<i>Agricultural surface</i>
<ul style="list-style-type: none"> • Continuous urban fabric (density >50%) • Discontinuous urban fabric (density <50%) • Industrial and commercial • Mine, dump and construction sites • Other artificial areas 	<ul style="list-style-type: none"> • Arable land (maize, cereals, soya, beet, sunflower) • Permanent crops (fruit trees, vineyards) • Pastures

Tab.2: Aggregated land-use categories which are significant for the analysis.

Population and vehicle density for km² of residential buildings have been also included from ISTAT to attain a coarse estimation of the exposed value, ignoring the sparse houses which are not mapped. Private vehicles density over population for each municipality is obtained from official statistics [2], assuming vehicles are parked in the urban areas. The resulting data is compared with the hazard extension, to assess the number of involved vehicles per depth categories over urban fabric areas.

3) Value of assets at risk: the value of elements at risk must be assessed on the basis of available statistical data or approximating land-use values from similar studies. These values are then integrated in the absolute depth-damage functions for each category to estimate the absolute damage. Maximal damage values for each land-use category in Italy are obtained from HKV Consultants [6]. Other discretionary categories taken in account are vehicles, furniture and agricultural products. The average value of vehicles in Italy (2011) is obtained from official statistics [2], while the value of furniture and agricultural products is accounted as a part of the damage share for their respective land-use categories.

4) Susceptibility of assets at risk (*Vulnerability* value): using a set of previously developed absolute damage functions, only land-use data are required. Each land-use category needs its own damage function. Generally, damage curves can be roughly described as:

$$Damage = a \times \sqrt[3]{depth}$$

with “a” being the parameter dependent on the category.

Absolute depth-damage functions have been developed by HKV consultants [6] for each European country on the basis of empirical data previously collected in other studies. The water depth range from 0 to 6 meters, where 6 is the maximum damage level (damage ratio = 1). They take in account five land-use categories (including inventories), chosen to cover at least 80% of the total damage. The total damage values are calculated on the basis of economical country-specific characteristic, deduced from Eurostat and World Bank data. These values are then actualized to 2007 and harmonized using the average national annual inflation rate (equal to 0.3 for 2000-2010 in Italy). Tab.3 summarizes the average functions for each land-use category.

Water depth (m)	Damage factor				
	Residential buildings including inventory	Commercial and Industrial including inventory	Agriculture including products	Transport infrastructures (roads and railroads)	Cars
0	0	0	0	0	0
1	0.4	0.3	0.55	0.42	0.5
2	0.6	0.55	0.75	0.65	1
3	0.75	0.75	0.85	0.8	1
4	0.85	0.90	0.95	0.9	1
5	0.95	1	1	1	1
6	1	1	1	1	1
	Maximum damage value (€/m²)				(€/n)
	618	475	0.63	20	14,450

Tab. 3: Depth-damage factors and maximal damage for each category (adapted from HKV Consultants, 2007).

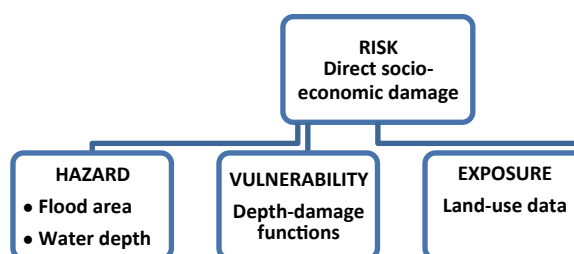


Fig. 4: Schematic representation of the flood damage evaluation process.

Fig.4 summarizes the evaluation process discussed until now. The final risk map represents the value of the potential socio-economic damage in monetary terms for each flood scenario, with a spatial resolution of 50x50 meters. It must be specified that risk maps shows the damage as occurring simultaneously in the whole area. The methodological approach described in this chapter is summarized in tab4.

Step 1	Approach and data requirements	<ul style="list-style-type: none"> • Meso-scale (province, municipalities) • Flood scenarios and characteristics • Aggregated land-use data • Approximate values for land-use categories • Damage functions
Step 2	Damage categories considered	<ul style="list-style-type: none"> • Land-use categories • Furniture • Cars • Agricultural products
Step 3	Flood characteristics	<ul style="list-style-type: none"> • 4 different flood scenarios • Area • Depth
	Land-use data	<ul style="list-style-type: none"> • Regional GIS dataset: 4 aggregated categories • ISTAT: population and vehicles numbers
	Determination of values of assets	<ul style="list-style-type: none"> • Transfer from previous studies
	Damage functions	<ul style="list-style-type: none"> • 5 depth-damage functions (matched with damage categories) transferred from previous studies
Step 4	Damage calculation and presentation	<ul style="list-style-type: none"> • ArcGIS overlay and spatial analyst • Shapefile data and maps

Tab. 4: Summary for damage evaluation approach.

6. RESULTS AND DISCUSSION

Discharge and rupture scenarios

Our simulated breach is located in Occhiobello, like in the 1951 event. This choice is motivated by the fact that, in this sector of the basin, the mitigation system already reached its structural limit, and therefore it won't be increased with further intervention in the next decades. Other mitigation measures or the influence of the mechanical drainage system (waterpumps) are not taken in account in the discussion. The discharge time series 1924-2010 for the Po station of Borgoforte have been analyzed through the Generalized Extreme Values (GEV) distribution [8]. The shape of the probability distribution has been then summarized by ARPA-SIM through the L-moments method [7]. Fig.5

presents the adapted probabilistic Gumbel distribution of the time series, which is employed to calculate the frequency of the events in our scenarios.

The Canalbianco embankments represents an obstacle for the further extension of the flood in the base scenario and in the 2021-2051 scenario, while in the 2071-2100 scenario this barrier is not sufficient to stop the flooding towards northern municipalities, involving the urban areas of Adria, Cavarzere and part of the Rovigo discontinuous urban fabric. The eastern section of the depressed basin (-1/-2 a.s.l.) is separated from the coastal area by the canal Brondolo, whereof embankments are some meters high over the floodplain. In none of our simulations this canal have been surmounted, thus avoiding the flood to reach the urban areas of Rosolina, Porto Viro and Chioggia, which are situated at circa 0/1 meters a.s.l. and would present an important exposed value either as urban, touristic and fish-farming area.

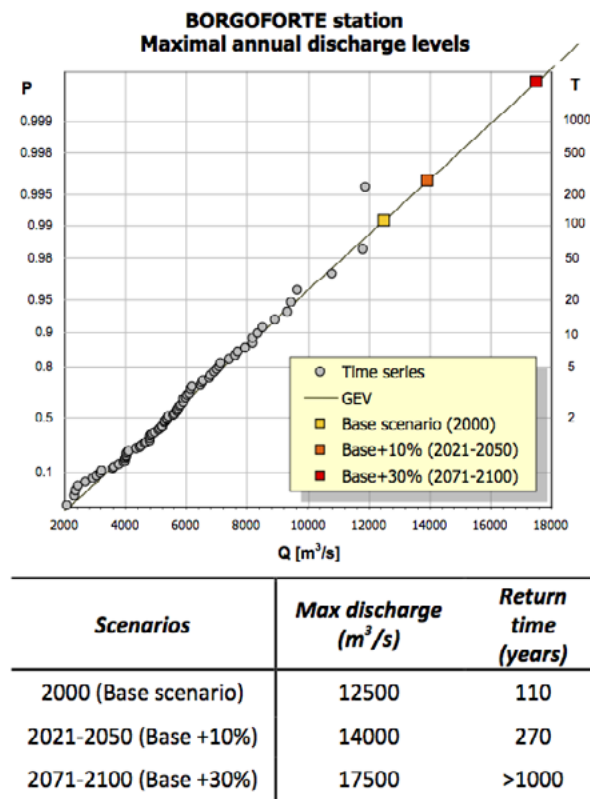


Fig.5: Probabilistic Gumbel distribution of discharge flow for the three discharge scenarios at Borgoforte station.

Exposure: Area affected

The total area of involved municipalities measures 868.5 km². Polesine region is mainly agricultural: in the impact area, 63.7% of the territory is employed for agriculture, corresponding to 86% of artificial areas. Forest, wetlands and water bodies are excluded from the discussion, since they do not carry any significant flood-prone value. Agricultural products are mainly from arable land (maize, other cereals and soy) with few scattered permanent cultures (fruit trees, vineyards and others). Residential buildings, which have the higher value density, account for just 6% of the total. Industrial and commercial activities are not widespread, accounting for just 2% of the artificial coverage. The transport network in the exposed area is mainly constituted of second and third order roads, but two important first-order transport ways are heavily exposed to the flood: the Padova-Bologna A13 highway and the Padova-Bologna railroad, which is served by hi-speed trains (Intercity and Eurostar). The A13 highway is exposed in the section between Rovigo and Occhiobello (20 km north-south) to an average flood depth of 2.5 meters, while the railroad follows a longer path (around 45 km) through Polesella and Canaro, so being exposed for a higher percent (from 70% to 90% depending on the scenario) of the total section to an average of 3 meters depth water. Both transport ways are not significantly elevated over the floodplain level. Discretionary values such as agricultural products and private vehicles need to be discussed separately. Our flood scenario is ideally placed during the first or second week of October, similarly to the October 2000 event. At this time, arable crops have been usually harvested already in Polesine, except in case of extraordinary rainy weather in September. However, this period is sensible for sowing cereal crops such wheat, oat and barley. We can therefore argue that an October flood would be more impacting on cereal crops that have been just sowed, compromising the next year's yield. For what concerns cars, their distribution strictly reflects that of population among the 25 municipalities, with Rovigo being the larger urban area, and thus the most populated (51,872). Adria and Cavarzere municipalities follows, with 20,549 and 15,005 respectively, while Occhiobello is forth with 11,315 (ISTAT, 2008). However, the urban area of Rovigo is for the most not interested by the flooding in any scenario, so the higher exposure of population and vehicles is located in Adria and Cavarzere municipalities.

Estimated impacts: population affected and economic damage

Full maps representing the damage classes for each flood scenario can be found in the Annex. The resolution of the risk layer pixel is 50x50m. Damage is expressed in million € at the 2000 value for each scenario. The percentage of damage among the land-use categories is compared to their corresponding coverage area in fig.6. The total population of 161,864 is distributed for the most over a total urban area of 47.61 km², corresponding to a density of 3,400 people over urban km². For each municipality the amount of flooded urban area is multiplied by the local density. The damage function for private vehicles is employed over their distribution using a maximal value of 14,450 € to assess the total damage induced by flooding.

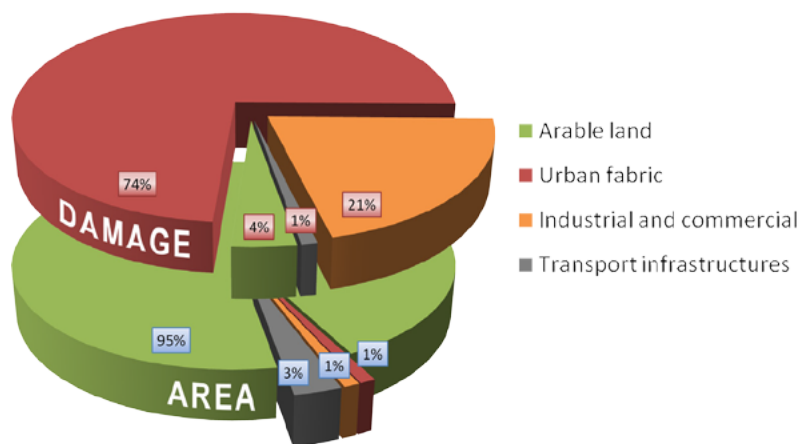


Fig. 6: Comparison between covered area and related damage for land-use categories in the Base Scenario.

Estimation of total damage

Finally, tab.5 is drawn summing up the results from both land-use categories and vehicles, approximating to the integer. The third column show the same values converted in \$ PPPs (conversion factor = 0.87).

<i>Scenarios</i>	<i>Involved area (km²)</i>	<i>Involved urban area (km²)</i>	<i>Total exposed population</i>	<i>Flooded vehicles</i>	<i>Vehicles damage (mil €)</i>	<i>Total damage (mil €)</i>	<i>Total damage (mil PPPs \$)</i>
2000 (Base scenario)	277.36	7.77	23,255	13,804	128.106	3,133	3,601
2021-2050 (Base +10%)	355.36	11.52	35,733	21,120	216.128	4,956	5,696
2071-2100 (Base +30%)	507.56	17.29	54,067	32,209	362.861	8,083	9,291
2071-2100 (Base +30%) 400 m	590.08	22.21	70,132	41,744	507.896	11,079	12,734

Tab. 5: Total flooded area, urban flooded area, amount of population exposed to the hazard, flooded vehicles and their corresponding damage cost, and comprehensive damage for each flood scenario.

The percentage of damage spread among the damage categories is represented in fig.7 for all scenarios. The relative shares of damage do not differ much comparing the four scenarios, showing how the increase in flood hazard level is constantly distributed among all the categories. The arable land area covers the most of the exposed area in terms of surface, but because of its low maximal value it accounts for just 2-4% of the total damage.

This share is even lower considering just the cereal production (20% of the total crops), which would be probably the only impacted crop according to the seasonality. Roads and railroads are also not significant in the total share, with just 1%. However, the A13 highway and the Padova-Bologna railway are two main arteries connecting highly developed areas, which likely means that a huge indirect impact would be caused by this negligible direct damage. Industrial-commercial (20-21%) and urban fabric (71-72%) hold the biggest shares of damage from hazard, despite the low shares of covered surface (roughly 1% and 3%). The damage assessment of the four potential scenarios can be compared with the reference events of 1951 to gain a denotative appreciation of both the physical and the economical scale of the event, using the same monetary measure (\$ PPPs updated to 2000 value). Tab.6 summarizes the characteristics of each event.

Total damage shares (mean for all scenarios)

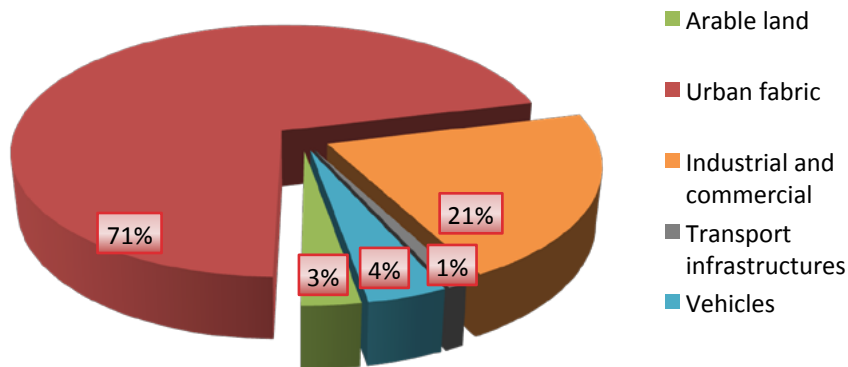


Fig. 7: Percentage of damage related to each land-use category and vehicles for the mean rupture scenario.

Regarding peak discharge, it must be highlighted that simulated events do not take in account any former outpouring of water before the rupture area. This practical approximation may be unrealistic and exaggerate the actual amount of water reaching the rupture. In fact, ARPA experts confirm that discharge values higher than 13,000 m³/s would probably cause some flood scenario in previous sections of the basin, allowing to reduce the water load downstream. The estimation of population exposure is based on the actual census (2008). Trends about population growth in Polesine are flat or slightly negative since 1951, suggesting that the real future scenarios may not change much compared to the simulations. This observation can be extended to the urban and economic development scenarios, which are strongly dependent on the population rates: as already pointed, also the primary sector has a flat or slightly negative trend in the whole eastern part of the basin. However, the comparison of estimated risk with registered damage of previous events is hindered by

the fact that only a portion of the total damage categories is considered in the analysis of simulated events. In fact, the total cost of damage estimated on reference events includes much more sources of loss, but their share on the total is not indicated and it is therefore impossible to produce an item-by-item comparison with the potential scenarios. Accordingly to this, the estimation of potential damage has to be considered as a conservative approximation of the full cost of the flood. Another important distinction must be made taking in account the existent Early Flood Warning System by ARPA, which gives a reliable forecasting and a timely warning should therefore be expected for any kind of important event. This would lead to an important saving of costs by reducing the exposed value (for example the private

vehicles) and by the execution of hazard mitigation measures (for example preventive controlled flooding) by the Civil Protection and other authorities.

<i>Flood event</i>	<i>Peak river discharge at Borgoforte (m³/s)</i>	<i>Estimated damage (mil \$ PPPs)</i>	<i>Affected population</i>
REFERENCE EVENTS			
1951	11,800	6,000	170,000
2000	11,800	8,000	43,000
SIMULATED EVENTS			
2000 (Base scenario)	12,500	3,601	23,255
2021-2050 (Base +10%)	14,000	5,696	35,733
2071-2100 (Base +30%)	17,500	9,291	54,067
2071-2100 (Base +30%) 400 m	17,500	12,734	70,132

Tab. 6: Comparison between reference events and simulated flood scenarios considering flood discharge rates, total economic damage and affected population.

The uncertainty related to the results of the assessment is likely to be high due to the simplified assumptions on the development of the hazard scenarios and the choice of the damage categories. That is, the final uncertainty sums up the numerous sources of approximation on the three components of the risk paradigm and it is hardly evaluable without a tangible comparison with factual data about the forecasted event.

7. CONCLUSIONS

Future climate change is likely going to positively influence the intensity and frequency of extreme flood events. However, the risk related to this increased hazard will be strongly dependent on both socio-economic conditions and anticipatory capacities. The integrated analysis of hazard, exposure and vulnerability values in GIS environment can provide a valuable approach to achieve a fast evaluation of potential damage regarding the most important categories of direct damage to help high-level decision making, without being much data-intensive and time-consuming. Moreover, after the pilot study, this methodology can be easily extended to larger parts of the basin using the same tools. They can be easily integrated in an automated chain model connected to the Early Flood Warning System to gain an

appraisal of potential risk right after the meteorological forecasting. However, a calibration and validation of the model would be needed to assess and reduce uncertainty, which is still not measurable at this time. In addition to this, more complex and comprehensive statistical indicators about socio-economic trends in the impact area would be needed to correctly evaluate the changes in the exposure value for future scenarios.

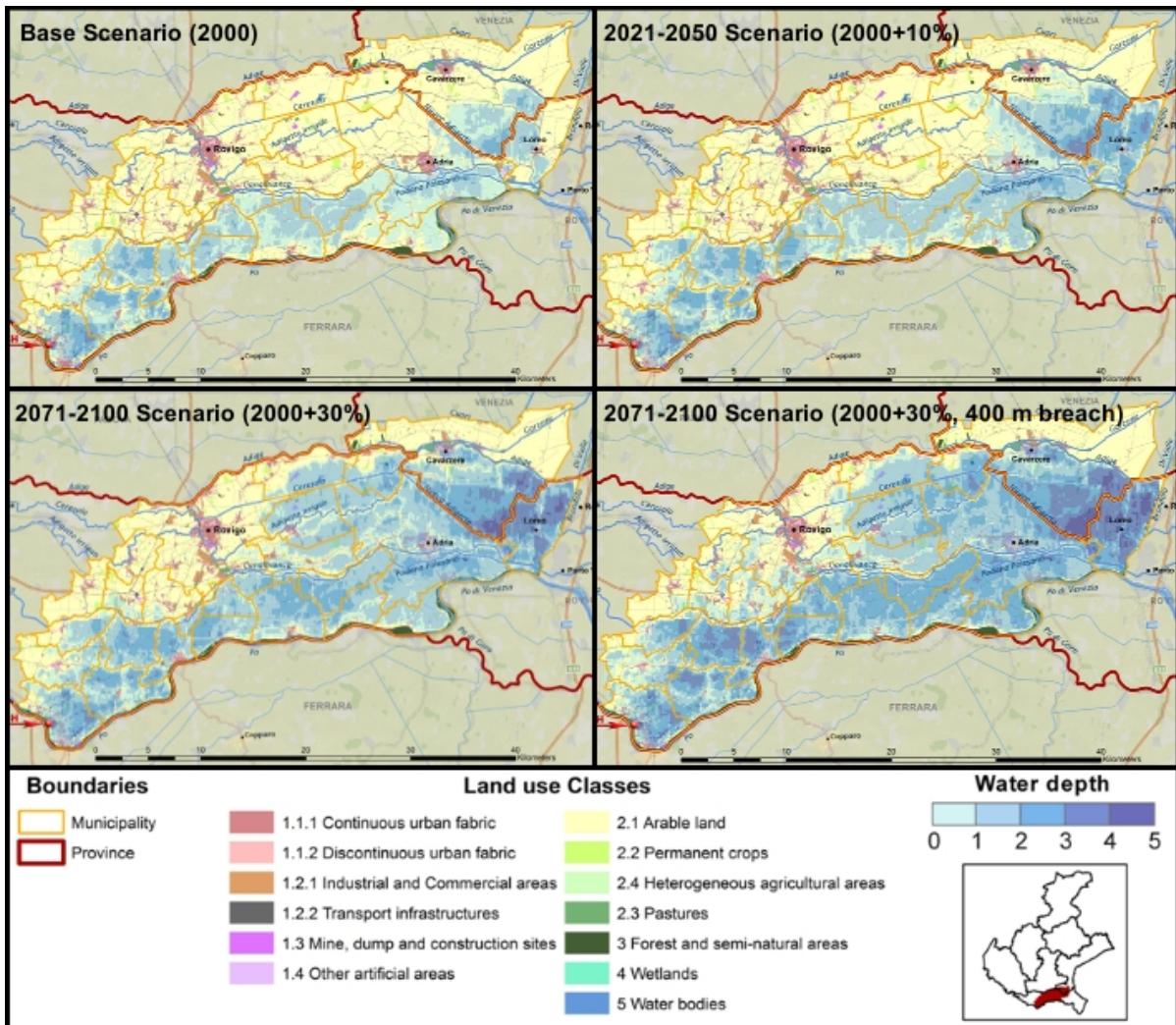


Fig. 8: Geographical representation of the four flood hazard scenarios simulated by ARPA-SIM.

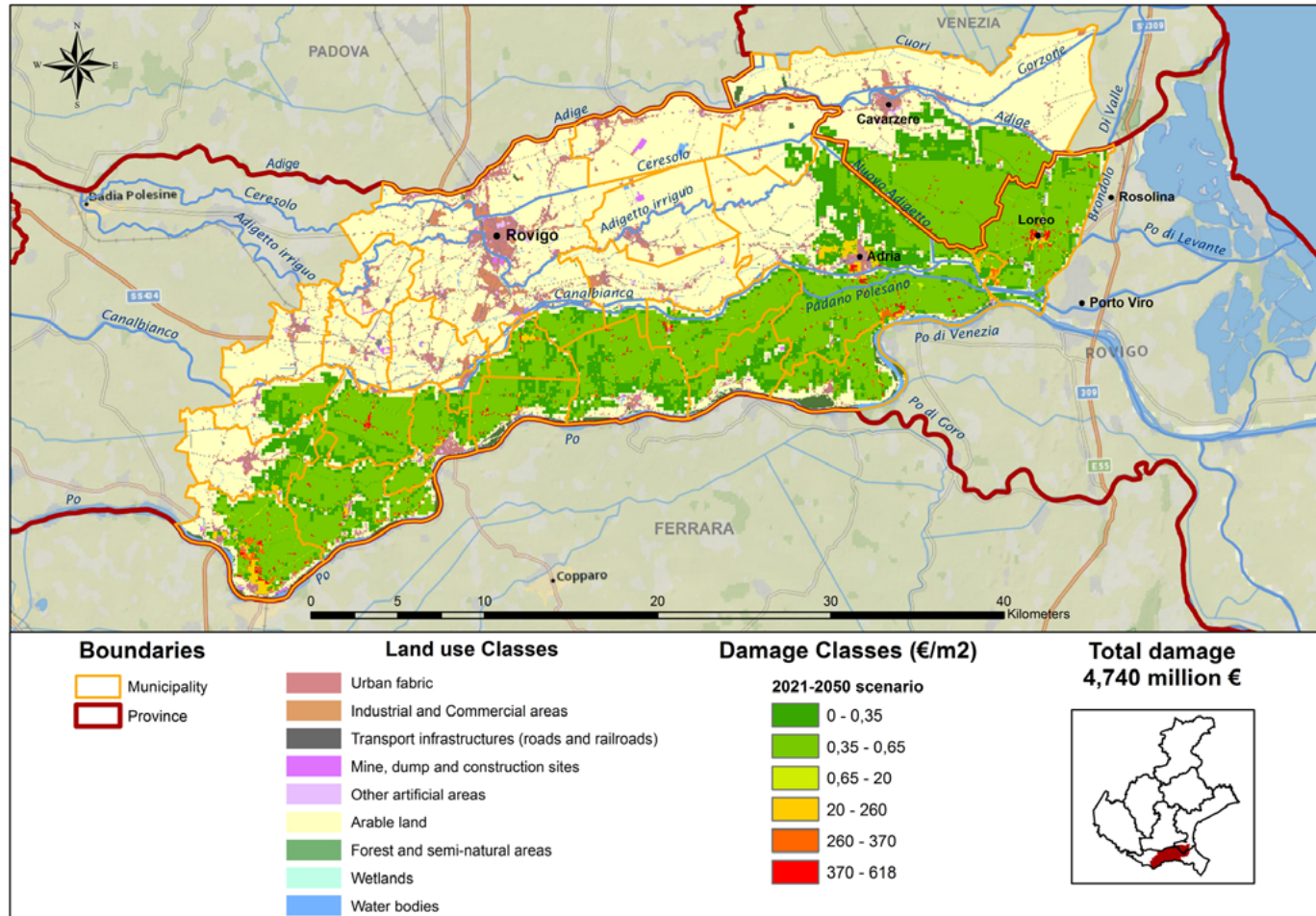


Fig. 9: Flood risk map for the 2021-2050 scenario (2000+10%) – 200m breach

8. ACKNOWLEDGMENTS

The author wish to thank ARPA-SIM team for the elaboration of the hydrological simulations.

9. REFERENCES

- AdBPo (2009), *Il rischio alluvionale sui fiumi di pianura - Stato dell'arte in materia di valutazione e gestione del rischio alluvioni*. Parma : Diabasis - Autorità di Bacino Fiume Po, 2009. (1)
- Automobile Club Italia (2009), *Parco veicolare Provincia di Rovigo*. Comuni-Italiani.it. [Online] 2009. [Riportato: 16 02 20120.] <http://www.comuni-italiani.it/029/statistiche/veicoli.html>. (2)
- Cacciamani C., et al. (2007), *Dal globale al locale, gli scenari futuri in Emilia-Romagna*. ARPA Rivista. 2007, 1, p. 19-21. (3)
- Cacciamani C., Pavan V., and Tomozeiu R. (2010), *Cambiamenti climatici, impatti e adattamento*. Ecoscienza. 2010, 2. (4)
- Dankers R., and Feyen L.(2008), *Climate change impact on flood hazard in Europe: An assessment based on high-resolution climate simulations*. Journal of Geophysical Research. 2008, Vol. 113. (5)
- HKV Consultants. 2007. *Flood damage functions for EU member states*. s.l.: Joint Research Centre, 2007. (6)
- Hosking J.R.M. (1990), *L-moments: analysis and estimation of distributions using linear combinations of order statistics*. Journal of the Royal Statistical Society. 1990, Vol. B, 52, p. 105–124. (7)
- Jenkinson A. F. (1955). *The frequency distribution of the annual maximum (or minimum) values of meteorological elements*. Quarterly Journal of the Royal Meteorology Society. 1955, 87, p. 145–158. (8)
- Lastoria B., et al. 2006. Socio-economic impacts of major floods in Italy from 1951 to 2003. *Advances in Geosciences*. 2006, 7, p. 223.229. (9)
- Marchi E., Roth G., and Siccardi F. 1995. *The november 1994 flood event on the Po River: structural and non-structural measures against inundations*. Hydrometeorology, Impacts, and Management of Extreme Floods. 1995. (10)
- Merz B. et al. 2010. *Assessment of economic flood damage*. Natural Hazards and Earth System Sciences. 2010, 10. (11)

- Regione Veneto, 2009. *Banca Dati della Copertura del Suolo della Regione Veneto. Regione del Veneto*. [Online] Unità di Progetto per il SIT e la cartografia, 30 06 2009. [Riportato: 2012 01 01.] <http://idt.regione.veneto.it/app/metacatalog/>. (12)
- STARDEX. 2005. *STARDEX final report. s.l.*: European Commission, 2005. (13)
- Tomei F. et al. 2010. *Analysis of precipitation in Emilia Romagna (Italy) and impacts of climate change scenarios*. Taormina, Italy: s.n., 2010. *Advances in Statistical Hydrology*. (14)
- Turitto O. 2004. *Extreme Po River flood in November 1951 and inundation of Polesine territory (Norther Italy)*. *Houille blanche - Revue internationale de l'eau*. 2004, 4, p. 64-70. (15)
- Van der Linden P., and Mitchell J.F.B. 2009. *ENSEMBLES: Climate Change and its Impacts. Summary of research and results from the ENSEMBLES project. s.l.*: Met Office Hadley Centre, 2009. (16)

AUTHORS INDEX

A

Ager A.A., 685
Agnetti A., 1126
Alcasena F., 685
Aleluia Reis L., 950
Amadio M., 1126
Amendola S., 41
Antonoli F., 256
Arca B., 670, 685
Arduini J., 250
Argenti G., 578
Attanasio A., 91

B

Bacciu V., 685, 720, 808
Bajocco S., 461
Bakkensen L., 1076
Baldarelli T., 935
Ballarin Denti A., 915
Barbarino S., 57
Barbarino S., 707
Bassini S., 428
Beaulant A.L., 1008
Bellucci A., 119
Bianco G., 271
Bindi M., 578
Blecic I., 819
Boero F., 382
Bojovic D., 1125
Bonamano S., 361
Bonanno R., 555
Bonasoni P., 250
Bonaventura L., 566
Bonzanigo L., 1125
Bortolu S., 670
Bosello F., 863, 1096
Bosetti V., 835
Botarelli L., 496
Bozzola M., 1057
Breil M., 1042
Brunetti M., 198
Bucchignani E., 78, 1042
Budillon G., 167, 303, 410

C

Cacciamani C., 496
Cagnazzi B., 555
Cagnazzo C., 138
Calmanti S., 71, 930
Caloiero T., 349
Candini A., 742
Cane D., 57, 707
Capozzi V., 303
Carboni G., 637
Carli B., 291
Casagrandi R., 566, 587
Caserini S., 961
Castaldi S., 611
Casula F., 685
Cavazzoni C., 428
Ceccarelli T., 461
Cecchini A., 819
Cerrone D., 167
Cervigni R., 637
Cherchi A., 3
Cherubini A. M., 738
Ciciulla F., 41
Ciddio M., 1016
Collalti A., 742
Comegna L., 507
Conte D., 184
Coomes D. A., 611
Corrado R., 738
Cortesi U., 291
Corti S., 102
Coscarelli R., 349
Cotroneo Y., 167
Creutzig F., 1028
Crisari A., 935
Critto A., 468, 478, 486
Czaja A., 152

D

D'Agostino R., 410
D'Alessandro F., 419
D'Onofrio D., 71
Daccache A., 773
Davini P., 138

De Cian E., 756
De Filippo R., 935
De Franceschi M., 235
De Leo G. A., 915
De Pace C., 650
Decimi G., 944
Del Bianco S., 291
Dell'Aquila A., 930
Di Paola A., 611, 624
Dibari C., 578
Dijkstra H.A., 263
Drouet L., 835, 950
Dubrovsky M., 670
Duce P., 670

E

Eboli F., 1096
Elefante C., 340
Emmerling J., 891
Enrica De Cian, 863
Erbacci G., 428

F

Faggian P., 944
Falk M., 819
Farneti R., 30
Ferranna, 863
Ferrari E., 349
Filippi L., 131
Fraschetti S., 382
Furlan E., 468, 486
Furlani F., 250
Fusco G., 167, 410
Fusco R., 935

G

Gai M., 291
Galante S., 961
Gallina V., 468, 478
Gallo A., 637
Garcia-Herrera R., 210
Gatti Cazzolla R., 611
Gatto M., 542, 566, 587
Giannini V., 440
Giostra U., 250
Giovannini L., 235
Giupponi C., 852, 998, 1125
Grasso F., 340

Graziosi F., 250
Gualdi S., 119, 138, 339

H

Hallegatte S., 1008
Herrera-Pantoja M., 599

I

Ilieva L., 998

J

Johnson K., 1042

L

Laiti L., 235
Lapi M., 915
Laurenza L., 291
Laviola S., 193
Lazzari M., 328
Lemonsu A., 1008
Levizzani V., 193
Lindsell J. A., 611
Lionello P., 184, 210, 382, 410
Lo Vullo E., 250
Lotti C., 650

M

Madonna F., 279
Maesano M., 611
Maimone F., 41
Maione M., 250
Manara V., 198
Mancosu N., 793
Manzi M., 78
Marcelli M., 361, 388
Marchadier C., 1008
Marchetti M., 611
Marcomini A., 468, 478, 486
Marconi S., 742
Mari L., 587, 1016
Marras S., 819
Martano P., 340
Martellucci R., 388
Masala F., 808
Masina S., 3, 19, 566, 587
Masseti E., 845, 848
Masson V., 1008
Mattiuzzi M., 742

Maugeri M., 198
Maziotis A., 1125
Melià P., 566, 587
Mendelsohn R., 845
Mercogliano P., 78, 222, 507
Mereu V., 637, 773
Messori G., 152
Metzger M.J., 524
Miglietta M.M., 193
Mignatti A., 542
Miyakoda K., 3
Montesarchio M., 78
Moriondo M., 578
Mysiak J., 1126

N

Natali S., 742
Navarra A., 3, 119, 138, 339
Nolè A., 742

O

Ozgen S., 961

P

Pace B., 271
Pacione R., 271
Paladini de Mendoza F., 388
Palazzi E., 71, 110, 131
Paparella F., 19, 611, 624
Pappalardo G., 279, 284
Pasini A., 91, 328, 486
Pasotti L., 198
Pasqui M., 496
Pavan S., 650
Pecora S., 1126
Pelino V., 41
Pellizzaro G., 670
Pelosini R., 707
Pennetta C., 738
Perini L., 461
Piazzolla D., 388
Piccarreta M., 328
Pierattini A., 388
Pierfederici R., 1096
Pierini S., 11, 263
Pigeon G., 1008
Ploshay J., 3
Popp Jin Y., 974

Provenzale A., 71, 110, 131, 542, 555, 707
Pyles R.D., 819

Q

Quan M., 974
Quaresima S., 496

R

Ravetti C., 974
Renato Casagrandi, 542
Renier L. A., 57
Rianna G., 507
Ricci G., 935
Ricciardi L., 650
Righetto L., 1016
Rivetti I., 382
Rizzi J., 468, 486
Ronchi C., 57, 222, 555
Ronco P., 478
Ronzio D., 944
Rosoldi M., 279
Rossetto M., 915
Ruggio R., 19

S

Salagnac J.-L., 1008
Salcedo-Sanz S., 210
Salis M., 685, 720
Salvadori G., 419
Salvati L., 461
Sannino G.M., 256
Santini M., 742
Scarascia L., 210
Schiavina M., 566
Scoccimarro E., 119, 339
Semenzin E., 478
Sgubin G., 263
Sharma A., 898
Simolo C., 198
Sirangelo B., 349
Sirca C., 808
Siva Chaudhry B., 898
Smiraglia D., 461
Snyder R.L., 793
Somot S., 1008
Spano D., 524, 637, 685, 720, 773, 793, 808, 819
Spinoni J., 198

Staglianò N., 578
Stefanì C., 361
Storto A., 587
Sue Wing I., 756
Susca T., 1028

T

Targetti S., 578
Tavoni M., 835, 891, 950
Terradez Mas J., 915
Terzago S., 110
Tomasicchio G.R., 419
Tommasi P., 507
Tomozeiu R., 496
Torresan S., 468, 478, 486
Trabucco A., 524, 773
Triacca U., 91
Trunfio G.A., 819
Turco M., 222

V

Valentini R., 611, 624, 742
Van Passel S., 845
Ventura A., 670
Vezzoli R., 222
Vichi M., 19, 587
Viguié V., 1008
von Hardenberg J., 71, 110, 131, 707

Z

Zabeo A., 468, 478, 486
Zambianchi E., 382
Zampieri M., 119, 339
Zardi D., 235
Zollo A.L., 78, 222
Zomer R., 524



Società Italiana per le Scienze del Clima

Isola di San Giorgio Maggiore, n. 8
I-30124, Venezia – Italia
Tel. 041.2700431 - Fax. 041.2700412
E-mail: info@sisclima.it

www.sisclima.it